Hans J. Welkoborsky
Peter Jecker
Editors

Ultrasonography of the Head and Neck

An Imaging Atlas

Springer

EXTRAS ONLINE

Ultrasonography of the Head and Neck

Hans J. Welkoborsky • Peter Jecker
Editors

Ultrasonography of the Head and Neck

An Imaging Atlas

Springer

Editors
Hans J. Welkoborsky, MD, DDS, PhD
Department of Otorhinolaryngology
Head and Neck Surgery
KRH Nordstadt Clinic-Academic Hospital
Hannover
Germany

Peter Jecker, MD, PhD
Department of Otorhinolaryngology and Plastic
Head and Neck Surgery
Klinikum Bad Salzungen GmbH
Bad Salzungen
Germany

ISBN 978-3-030-12640-7 ISBN 978-3-030-12641-4 (eBook)
https://doi.org/10.1007/978-3-030-12641-4

© Springer Nature Switzerland AG 2019
This work is subject to copyright. All rights are reserved by the Publisher, whether the whole or part of the material is concerned, specifically the rights of translation, reprinting, reuse of illustrations, recitation, broadcasting, reproduction on microfilms or in any other physical way, and transmission or information storage and retrieval, electronic adaptation, computer software, or by similar or dissimilar methodology now known or hereafter developed.
The use of general descriptive names, registered names, trademarks, service marks, etc. in this publication does not imply, even in the absence of a specific statement, that such names are exempt from the relevant protective laws and regulations and therefore free for general use.
The publisher, the authors, and the editors are safe to assume that the advice and information in this book are believed to be true and accurate at the date of publication. Neither the publisher nor the authors or the editors give a warranty, express or implied, with respect to the material contained herein or for any errors or omissions that may have been made. The publisher remains neutral with regard to jurisdictional claims in published maps and institutional affiliations.

This Springer imprint is published by the registered company Springer Nature Switzerland AG
The registered company address is: Gewerbestrasse 11, 6330 Cham, Switzerland

Preface

Ultrasound is a dynamic and interactive process between physician and patient. In the last decades, ultrasound has experienced an enormous expansion in clinical application and indication in the head and neck.

Although established in clinical medicine for many decades, ultrasound is an emerging technique. In recent years, it has been developed into the basic diagnostic imaging technique for examination of the entire neck, salivary glands, thyroid and parathyroid glands, and neck vessels. Other applications comprise the examination of the paranasal sinuses and orbit. Its advantages include the lack of radiation exposure, which makes it suitable, for example, for children or pregnant women, the high resolution of modern ultrasound transducers, and the possibility for a surgeon to correlate ultrasound findings to the intraoperative situation.

Ultrasound is now regarded as the technique that provides the highest sensitivity and diagnostic accuracy for detection of lymph node metastases and salivary gland tumors. New techniques, such as contrast-enhanced ultrasonography, elastography, and 3-D ultrasound, have enhanced the diagnostic accuracy and also the indications for sonographic examinations in the head and neck.

This *Atlas* is dedicated to the office-based use of head and neck ultrasound to provide the best care for patients with head and neck diseases. It covers the physical principles and fundamentals of ultrasonography. The ultrasound characteristics of particular diseases are described in detail in many chapters. Other chapters focus on endosonography, contrast-enhanced ultrasonography, ultrasound in pediatric patients, sonography of large neck vessels, transcranial Doppler sonography, and interventional techniques. Beside many figures with ultrasound characteristics, additional video clips showing typical findings are presented online to demonstrate the dynamic procedure of ultrasound examinations.

Many specialists in head and neck ultrasound have contributed chapters to this book, resulting in a textbook and atlas covering all aspects of head and neck ultrasound. We would like to give special thanks to all the contributing authors for their hard work to make this book successful. We would like to appreciate the fruitful discussions and scientific exchanges that we have experienced with the authors over the years. With some of them, we continue to teach ultrasound courses in Europe and in the United States.

Last but not least, we would like to thank our wives and families for their patience as we worked on this book, as well as Lee Klein, Samantha Lonuzzi and Keerthana Gnanasekeran from Springer for their valuable support and advice. Without the help of all of these amazing people, this book would not have been possible. Thank you all.

Hannover, Germany — Hans J. Welkoborsky
Bad Salzungen, Germany — Peter Jecker

Contents

1 **History of Head and Neck Ultrasonography** 1
Wolf J. Mann

2 **Physics and Principles of Ultrasound** 7
Ryan K. Orosco and Lisa A. Orloff

3 **Ultrasound Anatomy of the Head and the Neck** 15
Peter Jecker

4 **Interventional Ultrasonography** 41
Urban W. Geisthoff and Lisa A. Orloff

5 **Sonography of Lymph Nodes in the Neck** 53
Jens E. Meyer

6 **Sonography of Other Neck Masses** 95
Peter Jecker

7 **Sonography of the Oropharynx, Hypopharynx, Larynx, and Cervical Esophagus** 139
Peter Jecker

8 **Sonography of Parapharyngeal Masses** 167
Courtney M. Tomblinson and Michael L. Hinni

9 **Pediatric Sonography of the Neck: Characteristic Findings** 187
Jürgen Weidemann and Gabriele H. A. Engelcke

10 **Sonography of the Large Neck Vessels and of Tumors with Suspected Infiltration of the Large Neck Vessels** 205
Hans J. Welkoborsky

11 **Sonography of Major Salivary Glands** 235
Andreas Knopf

12 **Ultrasound of the Thyroid Gland** 259
Tomislav Novosel and Peter Jecker

13 **Ultrasound of the Parathyroid Glands** 279
Julia E. Noel and Lisa A. Orloff

14 **Sonography of the Paranasal Sinuses, Soft Tissues of the Face, Orbit, and Bony Structures of the Face** 291
Hans J. Welkoborsky

15 Endoscopic Ultrasound 321
Christoph Arens and Nikolaos Davaris

16 Contrast-Enhanced Ultrasonography: Clinical Applications 331
Julian Küstermeyer

17 Future Developments of Sonography 349
Hans J. Welkoborsky

Index 357

Contributors

Christoph Arens, MD, PhD Department of Otorhinolaryngology, Head and Neck Surgery, University Hospital Magdeburg, Otto-von-Guericke University, Magdeburg, Germany

Nikolaos Davaris, MD Department of Otorhinolaryngology, Head and Neck Surgery, University Hospital Magdeburg, Otto-von-Guericke University, Magdeburg, Germany

Gabriele H. A. Engelcke, MD Department of Pediatric Radiology, Kinder- und Jugendkrankenhaus Auf der Bult, Hannover, Germany

Urban W. Geisthoff, MD, PhD Department of Otorhinolaryngology, Marburg University Hospital, Marburg, Germany

Michael L. Hinni, MD Department of Otolaryngology–Head and Neck Surgery, Mayo Clinic, Phoenix, AZ, USA

Peter Jecker, MD, PhD Department of Otorhinolaryngology and Plastic Head and Neck Surgery, Klinikum Bad Salzungen GmbH, Bad Salzungen, Germany

Andreas Knopf, MD, PhD Department of Otorhinolaryngology–Head and Neck Surgery, University of Freiburg, Freiburg, Germany

Julian Küstermeyer, MD Department of Otorhinolaryngology, Head and Neck Surgery, KRH Nordstadt Clinic–Academic Hospital, Hannover, Germany

Wolf J. Mann, MD, PhD Department of Otolaryngology, Roemerwall Hospital, Mainz, Germany

Jens E. Meyer, MD, PhD Department of ENT, Head, Neck, and Plastic Surgery, Semmelweis University, Hamburg, Germany

Julia E. Noel, MD Department of Otolaryngology–Head and Neck Surgery, Stanford University School of Medicine, Stanford, CA, USA

Tomislav Novosel, MD Department of Otorhinolaryngology and Plastic Head and Neck Surgery, Klinikum Bad Salzungen GmbH, Bad Salzungen, Germany

Lisa A. Orloff, MD, FACS Department of Otolaryngology–Head and Neck Surgery, Stanford University School of Medicine, Stanford, CA, USA

Ryan K. Orosco, MD Department of Surgery, Division of Otolaryngology–Head and Neck Surgery, University of California San Diego, Moores Cancer Center, La Jolla, CA, USA

Courtney M. Tomblinson, MD Department of Radiology and Radiological Sciences, Vanderbilt University Medical Center, Nashville, TN, USA

Jürgen Weidemann, MD Department of Pediatric Radiology, Kinder- und Jugendkrankenhaus Auf der Bult, Hannover, Germany

Hans J. Welkoborsky, MD, DDS, PhD Department of Otorhinolaryngology, Head and Neck Surgery, KRH Nordstadt Clinic–Academic Hospital, Hannover, Germany

History of Head and Neck Ultrasonography

1

Wolf J. Mann

From neurology to obstetrics/gynecology to internal medicine and finally to all medical and surgical subspecialties, diagnostic ultrasound has its roots in the United States and Europe. Now, each medical discipline worldwide is taking advantage of the wealth of information provided by this technology. Ultrasound has found its place in the scope of modern imaging technology. Since the 60 th of last century, this is true also for the ENT specialty.

1.1 Earliest History

The history of ultrasound started with the discovery of the piezoelectric effect in certain crystals by Pierre Curie and his brother Jacques Curie in Paris in 1880 [1]. A milestone in the development of ultrasound was the tragedy of the *Titanic* in 1912, the same year when Alexander Behm, a physicist from Vienna, invented maritime sonar [2]. In the succeeding decades, the first medical application of ultrasound for therapy was designed, using high-intensity ultrasound to perform craniotomies or destruction of parts of the brain (mainly in the United States) and also to treat patients with rheumatic arthritis or Meniere's disease [3]. At about the same time, Gohr and Wedekind at the University of Köln in 1940 presented the possibility of ultrasonic diagnosis based on echo-reflection methods similar to the one used to detect flaws in metal. However, it was Karl T. Dussik [4], a neurologist and psychiatrist at the University of Vienna, Austria, who applied ultrasound to locate brain tumors and ventricular shift by transmission of ultrasound to the scalp. He presented his initial paper in 1942 and reported further results of the procedure, called "hyperphonography," in 1947. The registrations, called "ventriculograms," were the earliest attempt at the concept of scanning human organs.

W. J. Mann (✉)
Department of Otolaryngology, Roemerwall Hospital, Mainz, Germany
e-mail: Wolf.mann@roemerwallklinik.de

In the mid-1940s, Wolf-Dieter Keidel [5], a German physicist at the Physikalisch-Medizinischen Laboratorium at the University of Erlangen, studied the possibility of using ultrasound as a medical diagnostic tool, mainly for cardiac and thoracic measurements. He discussed his ideas with the engineers of Siemens and at that time also reported the use of ultrasound for diagnosis of paranasal sinus disease.

1.2 The 1950s and 1960s

Between 1950 and 1968, it was mostly echoencephalography that established the role of ultrasound in neurologic diagnosis for endocranial space-occupying lesions [6–8]. However, simultaneous developments took place in gynecology, perinatology [9–11], ophthalmology, cardiology, and other medical disciplines, at that time allowing for the differentiation between cysts and solid tumors [12]. In 1963, Holmes and Howry [13] used ultrasonic scanners through water to examine the head and neck area, in addition to examining the abdomen and the kidney. This diagnostic tool was extended also for examination of neck tumors, for assessment of motion of the lateral pharyngeal wall, and for examination of the thyroid [14–17].

Kitamura et al. [18] used ultrasound for recording of vocal fold motions, and Abramson et al. [19] used ultrasound for the diagnosis of middle-ear effusions. In the 1960s, Kitamura and Kanecko [20] and Gilbricht and Heidelbach [21] reported the use of amplitude-scan (A-scan) ultrasonography for diagnosis of paranasal sinus diseases.

1.3 The 1970s

Between 1970 and 1973, while acting as a surgical intern / resident at the Medical College of Ohio, Toledo (MCO), I met and was inspired by George Döring-Ludwig, an American professor and the founding chairman of the MCO Department of Medicine, who had developed the first appli-

© Springer Nature Switzerland AG 2019

H. J. Welkoborsky, P. Jecker (eds.), *Ultrasonography of the Head and Neck*, https://doi.org/10.1007/978-3-030-12641-4_1

cation of ultrasound to the human body for diagnostic medical purposes at the Naval Medical Research Institute in Maryland in the late 1940s [3]. His research at the Naval Institute focused on detecting gallstones and was classified by the Department of Defense until October 1949. At MCO, I also had the privilege of rotating through the Department of Radiology, which at that time was chaired by Atis K. Freimanis, who had graduated from the medical school of the University of Hamburg, Germany, in 1951. Freimanis was one of the pioneers of B-mode (brightness-mode) ultrasonography at the time of the ultrasonic boom in the 1960s, and he was a gifted teacher. He was well known for his work on the abdomen, the retroperitoneum, the pancreas, aortic aneurysms, and lymph node enlargements. He published seminal papers on sonographic detection of abdominal lymph node enlargement in 1969 and sonography in pancreatic diseases in 1970 [3]. During our discussions, he supported my interest in ultrasound examination of the head and neck, but he was skeptical about whether ultrasound could be used to diagnose sinus diseases.

When I returned to the medical school in Freiburg, Germany, in 1973, I met an engineer, Hermann Kapp, who was working in the Department of Neurology. He generously provided me with a Krautkrämer echoencephalograph, allowing my first attempts to diagnose paranasal sinus disease in Freiburg.

In 1971 the ultrasonic research section at the National Acoustic Laboratory in Sydney, Australia, headed by George Kossoff and William Garrett, reported the use of gray-scale obstetric scans [2]. As early as 1974, initiated by the Department of Neurology at Freiburg Medical School, which at that time had already focused interest on cerebral blood flow using ultrasound, contact was made with Carl Kretz, Chief of Ultrasound Technology in Zipf, Austria, who provided an echograph Type 4100 and, later, a compound B-mode scanner, so that in 1974, using the Combisone (KretzTechnik Zipf, Austria), the first gray-scale imaging of the maxillary and frontal sinus took place.

1975 was the year of my first publication regarding examination of the paranasal sinuses with ultrasound A-scan (Fig. 1.1) [22], and the next year I wrote about examining the

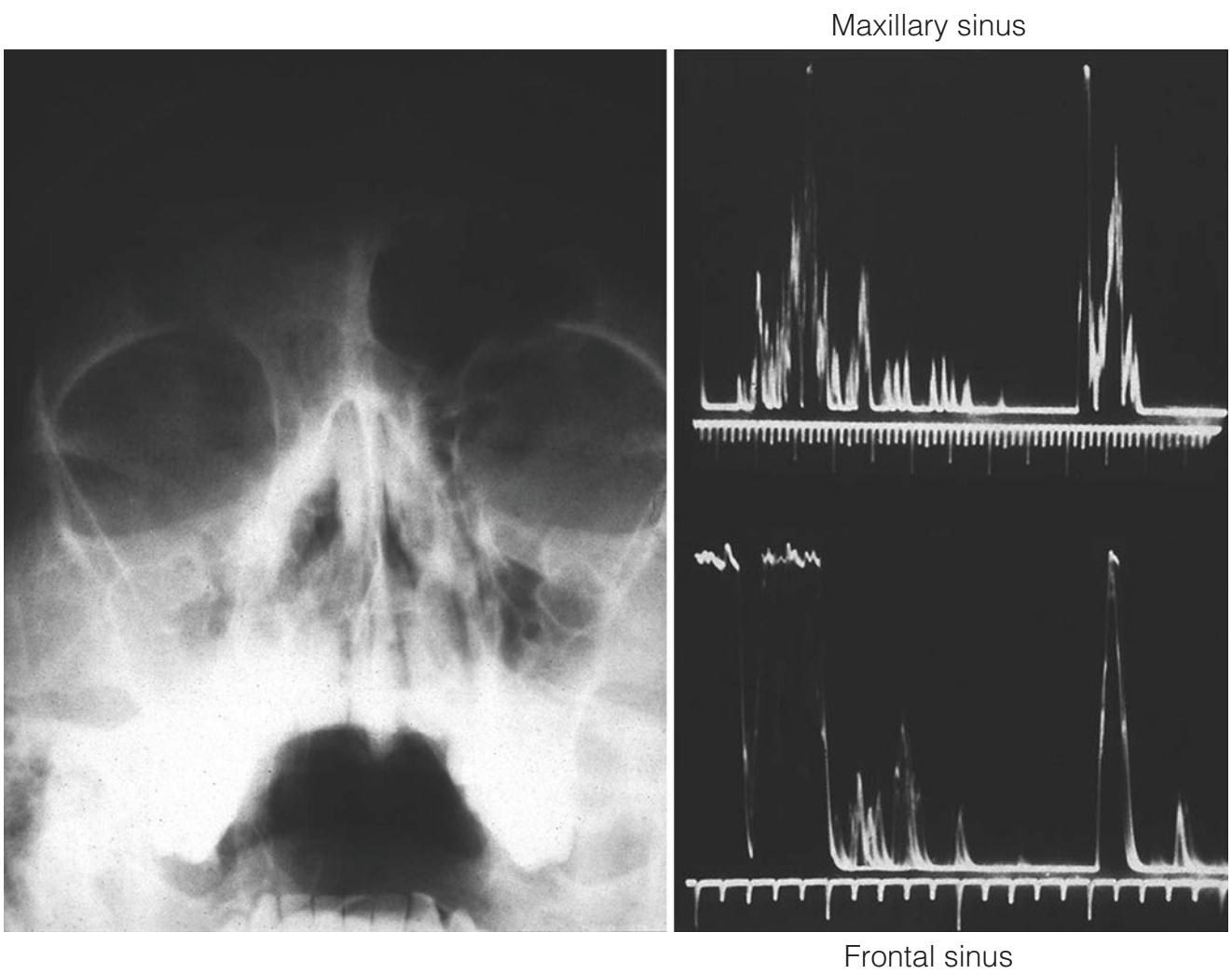

Fig. 1.1 The first gray-scale A scan imaging of the maxillary and frontal sinus

paranasal sinus with compound scanning in a two-dimensional plane [23]. That time, the first real-time ultrasonic scanner (Vidoson, Siemens, Germany) allowed for the generation of 16 black-and-white images per second, although it was too bulky for application in sinus examinations. In the mid-1970s, Wiley et al. [24], Gooding et al. [25], and Scheible and Leopold [26] used B-mode ultrasound technology for clinical evaluation of neck masses. And in the late 1970s and early 1980s, ultrasound was increasingly described in the English, German, and French literature for examination of head and neck lesions, including lesions of the salivary glands [27–29]. Revonta [30] in 1980 introduced A-scan ultrasonography for sinus examination in Finland, and a little later, this technology was also used at Lund University in Sweden by Jannert et al. [31].

1.4 The 1980s and 1990s

In the following years, tissue differentiation technology using gray-scale imaging was combined with A-scan sonography to display tissue differentiation and anatomic orientation in one image. Many new machines designed in the 1980s were based on linear, compound, or sector scanning, using increasing numbers of detectors, higher resolution, and increased storage capacity. Only after the introduction of so-called small parts transducers was the cumbersome examination of the head using abdominal transducers replaced step-by-step. These modern small parts transducers, with variable frequencies, had a dimension of 4 cm or less, improving contact with the surface of the head and neck region (Fig. 1.2). It is understandable that head and neck examination was first validated for parenchymatous organs like the parotid gland or thyroid gland, because their homogenous echostructure allowed for detection of tumors within these organs.

1.5 Expanded Applications

In the mid-1990s, color-coded Doppler sonography was applied to the examination of head and neck lymph nodes, with the aim of differentiating benign from malignant lymphadenopathy by analysis of the vascular perfusion pattern [32]. Transcranial sonography was introduced by otolaryngologists, neurosurgeons, and neurologists to evaluate blood

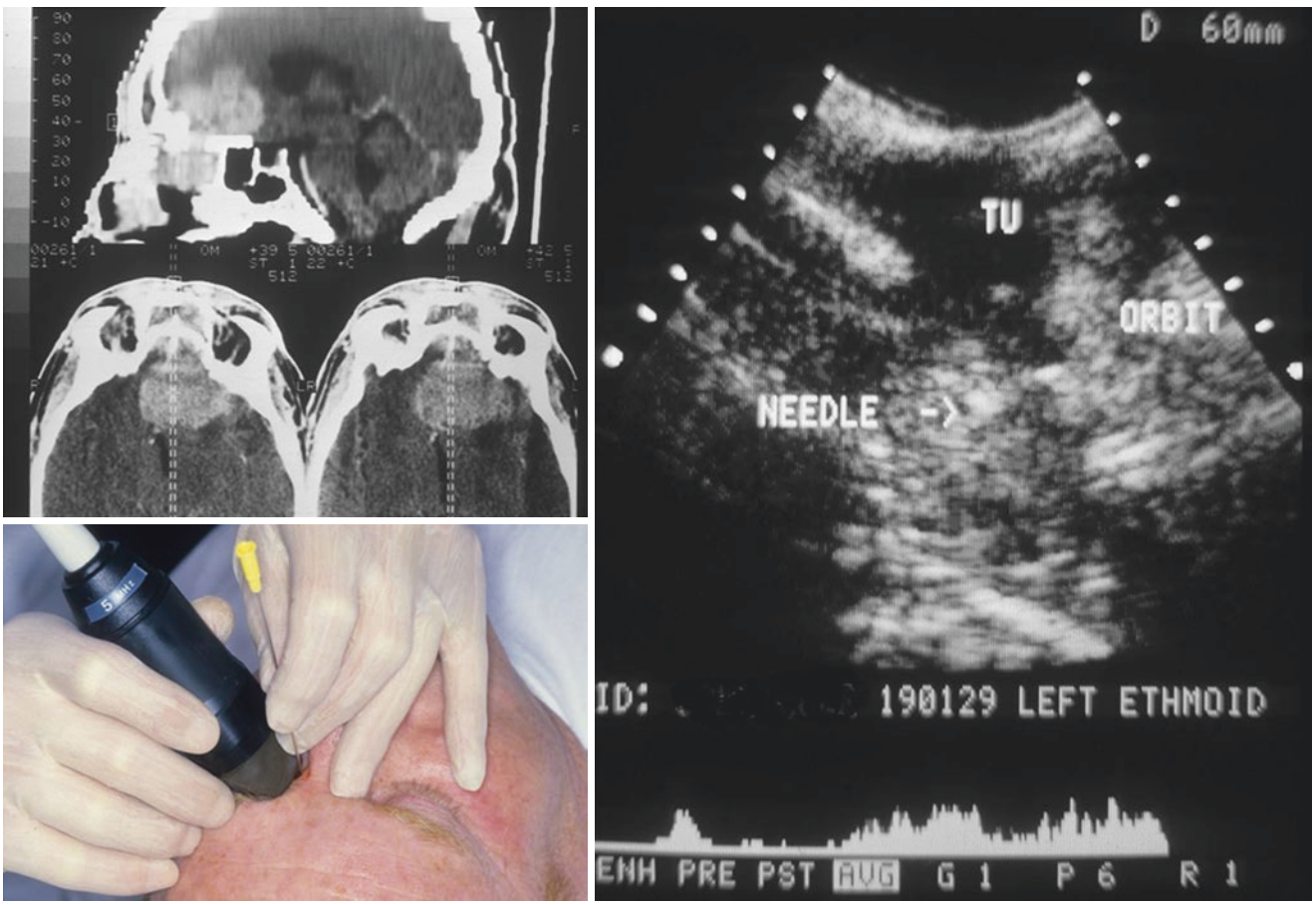

Fig. 1.2 Use of a small parts transducer for guided puncture of a frontal tumor in sonography of the head

flow within the common carotid artery during neck surgery [33, 34], and ultrasound-guided needle aspiration for cytologic examination of diseases of the thyroid, the parotid gland, and the neck became standard [35]. With the introduction of color-coded duplex sonography, it became possible not only to demonstrate vascularity of head and neck tumors and lymph nodes but also to quantify the vascularity and pattern of vascularization. "High-end" ultrasound systems with improved small parts transducers and various frequencies were used for head and neck examinations and were even applied intraoperatively [36, 37]. The introduction of so-called panoramic imaging (which allows for serial images of an entire anatomic area to be composed into ultrasonic tomographic pictures), harmonic imaging [38], 3D imaging, and elastography and the introduction of so-called signal enhancers combined with color-coded-duplex sonography [39] provided additional information on the vascularity of certain neck masses. For example, paragangliomas could be diagnosed in the head and neck without angiography. Parallel to this technical development and the shift from analog to digital technology, this imaging modality became commonplace for almost all medical subspecialties.

National ultrasound societies had been founded in the United States, Germany, Japan, the United Kingdom, Switzerland, and Austria in the 1970s, but specialists focusing on head and neck diseases were nonexistent, except for those performing an initial examination of the neck and thyroid by means of water-bath examination. Umbrella organizations like the American Institute of Ultrasound in Medicine (AIUM), the European Federation for Ultrasound in Medicine (EFSUM), and the World Federation of Ultrasound in Medicine and Biology (WFUMB) evolved. In 1964, the AIUM had broadened its interests away from therapeutic ultrasound applications, focusing on only diagnostic applications.

This focus has grown and diversified ever since. Among regular trinational meetings of the national ultrasound societies of Austria (ÖGUM), Germany (DEGUM), and Switzerland (SGUM), only one presentation in 1979 focused on examination of the head and neck, but a meeting in 2001 included 30 oral presentations on various topics related to head and neck ultrasound examinations. The first textbook summarizing the possible clinical applications of ultrasound to a spectrum of diseases of the head and neck was published in 1984 [40]. Additional textbooks on the topic were published in German in the 1990s [41, 42]. The English literature featured books by Lisa A. Orloff in 2007 [43] and Robert Sofferman and Anil Akuja in 2012 [44]. It was because of individuals like Bruneton in Nice, France, Gritzmann in Austria, van den Brekel in the Netherlands, and Akuja at the Prince of Wales Hospital in Hong Kong that ultrasound has become an integral part of head and neck examination, with a broad spectrum of indications. In the mid-1990s, ultrasound examination of the head and neck became part of the training requirement for a board certification in otolaryngology in Germany, so it became mandatory for each training program to acquire appropriate expertise. At that time, ultrasound schools had developed internationally in Aachen (Westhofen, Jecker), Freiburg (Mann), Erlangen (Iro), Hamburg (Hell), Mainz (Mann, Maurer, Jecker, Welkoborsky, Orloff), Hong Kong (Akuja, Soffermann, Orloff), Amsterdam (van den Brekel), and elsewhere. These programs at first were not found in the United States, but the regular presentation of courses at academy meetings led to the elimination of long-standing obstacles to the incorporation of ultrasound into clinical otolaryngologic practice. In 1998, the American College of Surgeons supported the use of ultrasound by appropriately trained surgeons, and the American Medical Association confirmed ultrasound imaging as being within the scope of practice for appropriately trained physicians.

References

1. Jecker P, Frentzel-Beyme B. The history of head and neck sonography. Laryngorhinootologie. 2002;81:900–5. German.
2. Frentzel-Beyme B. Sonography of head and neck. Praxis (Bern 1994). 2004;93:701–6. German.
3. Woo J. A short history of the development of ultrasound in obstetrics and gynecology. 2002. http://www.ob-ultrasound.net/history1.html. Accessed 15 Feb 2018.
4. Dussik K. Über die Möglichkeit hochfrequente mechanische Schwingungen als diagnostisches Hilfsmittel zu verwerten. Z ges Neurol Psychiat. 1942;174:153–6.
5. Keidel W. Über die Verwendung des Ultraschalls in der klinischen Diagnostik. Ärztl Forsch Z Forschungsergebn Med. 1947;1:349–55.
6. French LA, Wild J, Neal D. Detection of cerebral tumors by ultrasonic pulses: pilot studies on post mortem material. Cancer. 1950;3:705–9.
7. Leksell L. Echoencephalography, I. Detection of intracranial complications following head injury. Acta Chir Scand. 1955;110:301–4.
8. Kazner E, Kunze S, Schiefer E. Die Bedeutung der Echoenzephalographie für die Erkennung epiduraler Hämatome. Langenbecks Arch klin Chir. 1965;310:267–70.
9. Willocks J, Donald I, Duggan TC, Day N. Foetal cephalometry by ultrasound. J Obstet Gynaecol Br Commonw. 1964;71:11–20.
10. Kratochwil A. Ultraschalldiagnostik in Geburtshilfe und Gynäkologie. Stuuttgart: Thieme; 1968.
11. Hoffbauer H. Die Bedeutung der Ultraschalldiagnostik in der Frühschwangerschaft. Elektromedica. 1970;3:227–31.
12. Donald J, Brown TG. Demonstration of tissue interfaces within the body by ultrasonic echo sounding. Br J Radiol. 1961;34:539–42.
13. Holmes JH, Howry DH. Ultrasonic diagnosis of abdominal disease. Am J Dig Dis. 1963;8:12–6.
14. Baum G, Greenwood I. The application of ultrasonic locating techniques to ophthalmology. II. Ultrasonic slit lamp in the ultrasonic visualization of soft tissues. AMA Arch Ophthalmol. 1958;60:263–79.
15. Ossoinig K. Zur Ultraschalldiagnostik der Tumoren des Auges. Mbl Augenheilkunde. 1965;146:321–6.
16. Edler J. The diagnostic use of ultrasound in heart diseases. Acta Med Scand Suppl. 1955;308:32–7.

17. Effert S. Diagnostic value of ultrasonic cardiography. Br J Radiol. 1963;36:302–5.
18. Kitamura T, Kaneko T, Asano H, Muira T. Ultrasonic diagnosis in otorhinolaryngology. Eye Ear Nose Throat Mon. 1969;48:329–37.
19. Abramson DH, Abramson AL, Coleman DJ. Ultrasonics in otolaryngology. An aid in the diagnosis of middle ear fluid. Arch Otolaryngol. 1972;96:146–50.
20. Kitamura TA, Kanecko T. Le diagnostic des affections du sinus maxillaire par ultrasons impulsifs. Ann Oto-Laryngol (Paris). 1965;82:711–4.
21. Gilbricht E, Heidelbach JG. Ultraschall in der Medizin und ihre Anwendungsmöglichkeiten im HNO-Bereich. Z Laryngol Rhino Otol. 1968;47:737–46.
22. Mann W. Die Ultraschalldiagnostik der Nasennebenhöhlen und ihre Anwendung in der Freiburger HNO-Klinik. Arch Otorhinolaryngol. 1975;211:154–5.
23. Mann W. Die Ultraschalldiagnostik der NNH-Erkrankungen mit A- und B-Scan. Laryng Rhinol. 1976;55:48–53.
24. Wiley AL, Zagzebski JA, Tolbert DD, Baujavic RA. Ultrasound B-scans for clinical evaluation of neoplastic neck nodes. Arch Otolaryngol. 1975;101:509–13.
25. Gooding GA, Herzog KA, Lang FC. Ultrasonographic assessment of neck masses. J Clin Ultrasound. 1976;5:248–52.
26. Scheible FW, Leopold GR. Diagnostic imaging in head and neck disease: current applications of ultrasound. Head Neck Surg. 1978;1:1–7.
27. Macridis CA, Kouloulas LA, Kotsimbelas B, Yanoulis G. Zur Diagnose von Speicheldrüsentumoren mit Ultraschall. Elektromedica. 1975;4:130–6.
28. Bruneton JN, Fenart D, Vallicioni J, Demard F. Ultrasonic findings of parotid tumours in 40 patients. J Radiol. 1980;61:151–4. French.
29. Chodosh PL, Silbey R, Oen KT. Diagnostic use of ultrasound in diseases of the head and neck. Laryngoscope. 1980;90:814–7.
30. Revonta M. Ultrasound in the diagnosis of maxillary and frontal sinusitis. Acta Otolaryngol Suppl. 1980;370:1–55.
31. Jannert M, Andreasson L, Holmer N-G, Lörinc P. Ultrasonic examination of the paranasal sinuses. Acta Otolaryngol Suppl. 1982;389:1–52.
32. Schreiber J, Mann W, Lieb W. Farbduplexsonographische Messung der Lymphknotenperfusion. Ein Beitrag zur Diagnostik der zervikalen Metastasierung. Laryngo Rhino Otol. 1993;72:187–92.
33. Mann WJ, Beck A, Schreiber J, Maurer J, Amedee RG, Gluckmann JL. Ultrasonography for evaluation of the carotid artery in head and neck cancer. Laryngoscope. 1994;104:885–8.
34. Maurer J, Ungersböck K, Amedee RG, Mann WJ, Perneczky A. Transcranial Doppler ultrasound recording with compression tests in patients with tumors involving the carotid artery. Skull Base Surg. 1993;3:11–5.
35. Knapp I, Mann W, Wachter W. The value of ultrasound-controlled fine-needle biopsy in the diagnosis of possible neck tumors. Laryngorhinootologie. 1989;68:683–9. German.
36. Ecke U, Gosepath J, Mann WJ. Initial experience with intraoperative ultrasound in navigated soft tissue operations of the neck and below the base of the skull. Ultraschall Med. 2006;27:49–54.
37. Stetter S, Jecker P, Mann WJ. Einsatz des intraoperativen Ultraschalls in der Speicheldrüsenchirurgie. Ultraschall Med. 2006;27:159–63.
38. Jecker P, Maurer J, Mann WJ. Improved tumor site and contrast resolution in ultrasound diagnosis by using harmonic frequencies. Laryngorhinootologie. 2001;80:203–8. German.
39. Jecker P, Engelke JC, Westhofen M. Possible application of a signal enhancer for duplex ultrasound in otorhinolaryngology. Laryngorhinootologie. 1998;77:289–93. German.
40. Mann W. Ultraschall im Kopf/Hals-Bereich. Berlin/Heidelberg: Springer; 1984.
41. Hell B. Atlas der Ultraschalldiagnostik im Kopf-Hals-Bereich. New York: Georg-Thieme-Verlag; 1990.
42. Mann W, Welkoborsky HJ, Maurer J. Kompendium Ultraschall im Kopf-Hals-Bereich. New York: Thieme-Stuttgart; 1997.
43. Orloff LA. Head and neck ultrasonography. San Diego: Plural Publishing; 2007.
44. Soffermann RA, Akuja AT. Ultrasound of the thyroid and parathyroid glands. Heidelberg/New York: Springer; 2012.

Physics and Principles of Ultrasound

2

Ryan K. Orosco and Lisa A. Orloff

2.1 Introduction

This book contains a wealth of information about head and neck ultrasound. In order to take full advantage of this content, one must possess a strong understanding of the physics of ultrasound and the fundamentals of ultrasound imaging. Knowledge of the principles of ultrasound physics is not an absolute requisite for utilizing ultrasound, but it will make possible a higher level of technical mastery and will allow for high-quality implementation of ultrasound into clinical practice.

A clinical ultrasound image is the end result of complex interaction between hardware design elements and software processing. The goal of this chapter is to ensure that clinicians using this technology are aware of the key concepts and principles of ultrasound physics, without having to possess advanced understanding of the underlying engineering. This chapter addresses the basics of wave properties, ultrasound wave generation and reception, and the behavior of sound in tissue. Common ultrasound artifacts are explained from the physics perspective, and the special case of Doppler is discussed.

R. K. Orosco
Department of Surgery, Division of Otolaryngology–Head and Neck Surgery, University of California San Diego, Moores Cancer Center, La Jolla, CA, USA

L. A. Orloff (✉)
Department of Otolaryngology–Head and Neck Surgery, Stanford University School of Medicine, Stanford, CA, USA
e-mail: lorloff@stanford.edu

2.2 Sound and Ultrasound Waves

Sound waves are longitudinal waves, which cause particles and energy to move (propagate) through a medium (gas, liquid, solid). This is in contrast to transverse waves, which are like the ripples caused by dropping a stone in a bucket of water. In the water ripple example, the wave energy moves across the surface of the water, but the water particles themselves do not propagate—they just move vertically up and down.

Sound wave propagation is a familiar concept that we encounter frequently in daily life. Sound travels through the air, water, and ground. Sound energy causes compression and rarefaction of the molecules in the material through which it travels. These compressions and rarefactions are displayed graphically and mathematically as a sinusoidal wave. Ultrasound waves and audible sound waves behave in a similar fashion. They travel (propagate), reflect (echo), and are absorbed to varying degrees depending on the material with which they interact. For clinical ultrasound, the sound within the echo wave that is received by the ultrasound transducer is translated into an image, with brightness (B-mode) proportional to the amplitude of reflection.

The mathematical characteristics of a sine wave are amplitude, frequency, and wavelength. Amplitude is the height of a wave, which can be thought of as a corollary of sound intensity. Wave velocity can be calculated as the product of the frequency (f) and wavelength (λ): wave velocity = $f\lambda$. The higher the sound frequency, the shorter the wavelength. The frequency is reported in hertz (Hz), which represents the number of wave cycles per second: f = cycles/second. A 1 Hz wave has one cycle per second. A 1 MHz (1,000,000 Hz) wave has one million cycles per second. The normal hearing spectrum (20 Hz–20 kHz) includes frequencies well below those used in ultrasonic applications (Fig. 2.1). In general, 7.5–15 MHz is the ideal ultrasound frequency range for neck imaging.

© Springer Nature Switzerland AG 2019

H. J. Welkoborsky, P. Jecker (eds.), *Ultrasonography of the Head and Neck*, https://doi.org/10.1007/978-3-030-12641-4_2

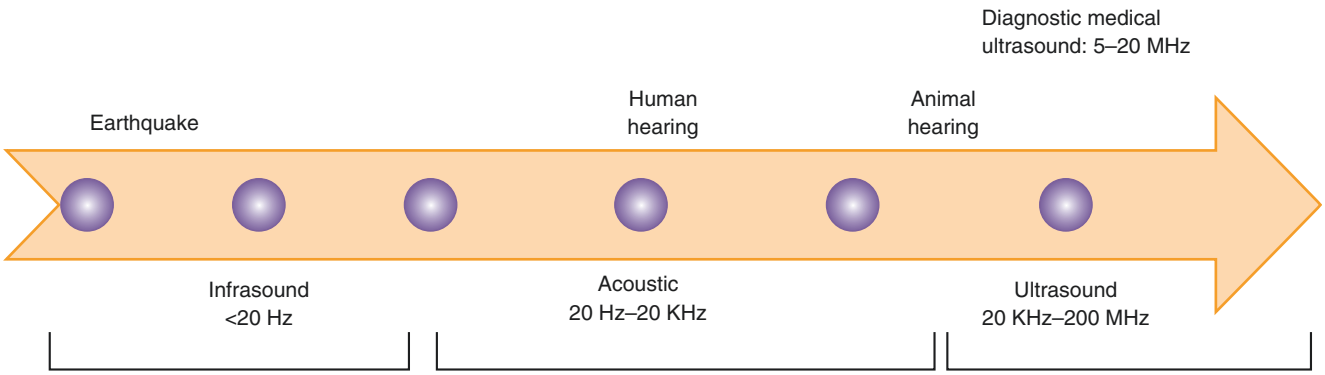

Fig. 2.1 Sound frequency spectrum

2.3 Ultrasound Wave Generation and Reception

Ultrasound waves are generated by an array of microscopic piezoelectric crystals. When subjected to electrical energy, the crystals change shape and generate ultrasound waves that are passed into tissues for clinical ultrasound imaging. Reflecting back, the ultrasound echo vibrates and distorts the crystal shape, translating an electrical signal back to a computer. The same crystal can be used to generate and receive ultrasound signals. Any given crystal—or the group of crystals called a "sector"—spends most of its time receiving sound information. The ultrasound machine has complex algorithms that alternate between generating and receiving modes in order to optimize image quality. It should be noted that piezoelectric crystals can be damaged by heat and mechanical forces, so care should be taken when handling the ultrasound transducer, and it should not be heat sterilized.

The piezoelectric crystals in clinical ultrasound devices are made of inorganic synthetic materials, commonly lead zirconate titanate (PZT). The ultrasound transducer consists of the electrical interface, material used for insulation and acoustic matching, and an array of crystals. For head and neck applications, the crystal array is linear, but other geometries exist. Depending on the ultrasound transducer, there may be multiple rows of crystals. The linear configuration affords planar ultrasound imaging, which is analogous to the familiar planar imaging of CT and MRI.

2.4 Ultrasound in Tissues

Sound speed, or velocity, depends on the material through which the wave is traveling. This velocity is positively correlated with the material's density—the denser the material, the faster the sound waves travel. In air, the velocity of sound is about 330 m/s. Knowing the wave velocity in a given medium and the time from sound generation to reception allows calculation of the distance that a wave has traveled from the source to the receiver. This is why one can estimate how far away one is from a lightning strike by counting the seconds between seeing the flash (source) and hearing the thunder crack (receiver). To bring this into medical context, consider the sound velocity in various body tissues: 1459 m/s in adipose tissue, 1480 m/s in water, and 1580 m/s in muscle. The velocity of sound in dense bone tissue is even faster: >4000 m/s. Ultrasound machines take into account the wave parameters of frequency, amplitude, and velocity as they generate the clinical images. Several more key concepts related to wave propagation in tissues will be addressed in the next sections: impedance, reflection, transmission, attenuation, and spatial resolution.

2.4.1 Acoustic Impedance, Reflection, and Transmission

Acoustic impedance is the product of material density and the acoustic velocity: Impedance = density × acoustic velocity. Because different materials have different densities, they also have different impedances. When a sound wave reaches the interface between two dissimilar materials, some of the energy is *transmitted* into that new medium, and some is *reflected* back. The magnitude and direction of the reflected and transmitted energy depend on the angle of the initial wave signal (the incident angle) and the difference in impedance properties of the two materials. Similar to the scenario of a laser beam fired at a mirror, the reflected energy returns at the same angle (compared with a normal, or perpendicular, reference), but in the negative direction of the incident beam. The portion of the wave that is not reflected will pass into the second material, but it does so at a slightly different angle. This new angle occurs because of the property of *refraction*,

explained by Snell's law. For now, just focus on wave transmission and reflection in the purest situation—when the sound wave hits the boundary interface at a 90-degree angle (perpendicular to the interface). In this situation, the speed and wavelength of this reflected wave are the same as that of the incident wave.

The greater the difference, or mismatch, in material *impedance*, the more wave energy is reflected. Imagine a ball passing through a material with low impedance (air) that strikes an interface with high impedance (a brick wall)—most of the energy is reflected back. This imperfect example should suffice to convey the concept of reflection: If there is a small mismatch in impedance between the two mediums at the interface, most of the sound energy is transmitted through, with little reflected.

Understanding the concepts of impedance, reflection, and transmission provides a physics-based explanation of what we intuitively understand when we are unable to see beyond the interface of two very dissimilar tissues, such as the soft tissues of the neck and the air-filled lumen of the trachea or the soft tissues of the parotid and the bony mandible. This also explains why ultrasound gel is needed for "contact coupling." The gel removes two boundary conditions (ultrasound transducer/air and air/skin) that would otherwise cause considerable signal loss and prevent imaging altogether.

2.4.2 Attenuation

Attenuation is another important concept that is likely to be familiar in our daily lives. The concept is that the amplitude of a sound pressure wave degrades, or decreases, as it travels through a medium. This degradation is a result of energy being absorbed by the medium, and some energy loss through scattering effects. When performing ultrasound, it is important to recognize that energy is deposited into the patient's tissues and converted into heat. Practically, routine clinical ultrasonography of the head and neck does not raise the tissue temperatures enough to cause harm. Still, the concept of "ALARA"—as low as reasonably achievable—is advocated in the practice of clinical ultrasonography. Making every reasonable effort to maintain exposures to ultrasound heat as low as practical serves to minimize the risk of potential thermal injury to the patient.

Intuitively, the greater the distance a wave travels through a medium, the greater the attenuation along that path. It is important to note that attenuation is not a linear phenomenon; it follows the inverse square law. The signal intensity (wave amplitude) decreases by the square of the distance: Intensity = $1/\text{distance}^2$. Attenuation is also proportional to the frequency: Attenuation (measured in decibels [dB]) = ½ × frequency × distance. There is less attenuation with waves that have a longer wavelength (lower frequency). Based on these characteristics, extremely low-frequency waves can pass through the ocean and even the earth's surface to communicate across distances. The clinical correlate of this concept is that the imaging of superficial structures is best accomplished with high-frequency ultrasound transducers, whereas deeper structures require lower-frequency transducers (or alterations in sound frequency generation).

Clinical ultrasound devices automatically compensate for attenuation using "time-gain compensation." The signal from more distant objects is increased (scaled) in order to counteract the signal attenuation. Because higher-frequency signals attenuate faster (in shorter distances from the source), more time-gain compensation is required. *Gain* (or in B-mode, brightness) can also be manually adjusted on most modern clinical ultrasound devices, either as a global (overall) gain or at various image depths. Note that there are limits to the usefulness of gain because it amplifies noise, or undesirable signal information, in addition to the true echo signal of interest.

2.4.3 Spatial Resolution

Spatial resolution is the final key concept to consider when performing clinical ultrasound. In today's digital world, resolution is an intuitive concept, as it is analogous to pixel resolution. When we ask ourselves how clear the ultrasound image is, we are really talking about the ability of the imaging system to differentiate between two objects, or two points. If two points are closer to each other than the spatial resolution of the system, the resultant image will display a single point that is a conglomeration of the two separate points. In clinical ultrasound systems, spatial resolution differs depending on whether the objects are perpendicular to the transducer or parallel with it (lateral or axial resolution).

The lateral resolution depends on the width of the ultrasound beam. Depending on the ultrasound system, the beam can be focused at one or multiple distances to alter the lateral resolution. Resolving two side-by-side points that are in line with or parallel to the transducer (axial resolution) is a function of ultrasound wavelength. The higher the frequency, the finer the axial resolution. But because these higher frequencies also come with more attenuation, there is always a trade-off. Just as with other imaging parameters, most clinical ultrasound systems allow for the depth of focus and frequency to be adjusted. These adjustments allow one to optimize the resolution in various clinical situations.

2.5 Artifacts in Ultrasound Imaging

Ultrasound imaging artifacts are erroneous representations of the anatomy that result from the physical interaction between sound waves and tissues and the manner in which the resul-

tant sound echo is processed and displayed by the computer. Several assumptions are made by the ultrasound computer: that the echoes received by the transducer originated from the main ultrasound beam from the same transducer; that an echo returns to the transducer after a single reflection; that the depth of an object is directly related to the amount of time for an ultrasound pulse to return to the transducer as an echo; that the speed of sound in human tissue is constant (generally about 1540 m/s); that ultrasound waves (incident beam and reflection) travel in a straight path (without refraction); and that the signal is uniformly attenuated in human tissue [1]. When these generalized assumptions are applied to real-world systems, ultrasound artifacts invariably result.

Without a thorough understanding of ultrasound physics, imaging artifacts can be misinterpreted, misclassified, and misunderstood. Although incorrect interpretation of artifacts can interfere with accurate diagnosis, proper interpretation can actually provide clues and be diagnostic for certain entities.

Two-dimensional ultrasound mode (2D mode), sometimes referred to as brightness (B-mode), is the standard mode used for head and neck ultrasound. In this mode, one will encounter reverberation, comet tail, mirror image, shadowing, and posterior enhancement artifacts. The key concepts presented earlier can be applied to understand these common artifacts. In 2D mode, refraction, beam width, range ambiguity, and speed error artifacts can also occur [2], but these are infrequently applicable in head and neck ultrasonography. Doppler imaging artifacts also exist [2] but are seldom encountered in head and neck ultrasound practice, which focuses more on anatomic architecture and qualitative vascular flow than quantitative Doppler.

2.5.1 Reverberation Artifact

Because the computer assumes that an echo returns to the transducer after a single reflection, reverberation artifact occurs in the presence of parallel highly reflective interfaces that cause repeated reflections (Fig. 2.2). This artifact is encountered when imaging the trachea, because of a marked impedance mismatch. The ultrasound waves encounter the interface between the soft tissue and tracheal cartilage, and a reflected signal echoes back to the transducer. This surface of the cartilage is displayed on the image at its true anatomical depth, but some ultrasound waves pass into the air of the tracheal lumen and encounter another interface (air/soft tissue) at the posterior trachea, again with a high-impedance mismatch. This causes another reflected wave, resulting in another echo back to the transducer. The second echo takes longer to return to the transducer and therefore has a longer apparent distance traveled. The result is an artifact signal that is deeper than the true anterior tracheal location. This same process repeats when the echo, traveling toward the transducer, hits the anterior tracheal wall: Some of the wave is reflected back through the air, and some makes its way back to the transducer. The reverberation artifact is displayed as multiple evenly spaced linear reflections deep to the true object boundary. Because the signal intensity attenuates each time, the size of the artifact reflections diminishes with each reflection. Moving the transducer to view the trachea from different incident angles can help identify and reduce confusion from reverberation artifact.

2.5.2 Comet-Tail Artifact

Comet-tail artifact (Fig. 2.3) is a special type of reverberation artifact that is commonly encountered in the thyroid. Echogenic foci within the thyroid can be microcalcifications, which are highly suggestive of malignancy, but they can also be caused by inspissated or clustered colloid crystals that produce a comet-tail artifact [3]. Although indicative of a

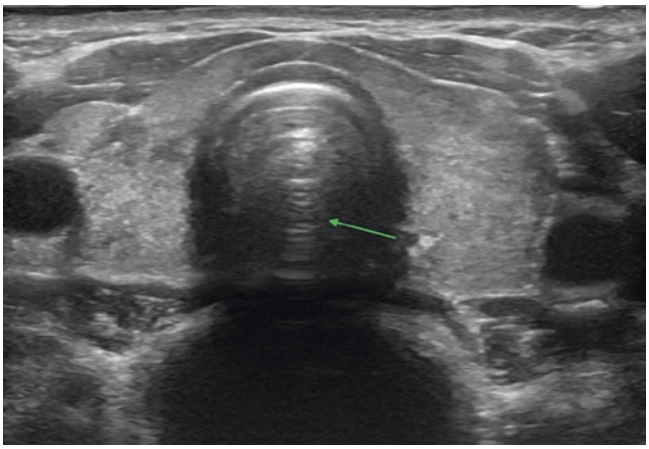

Fig. 2.2 Midline transverse view of the trachea with reverberation artifact (*green arrow*)

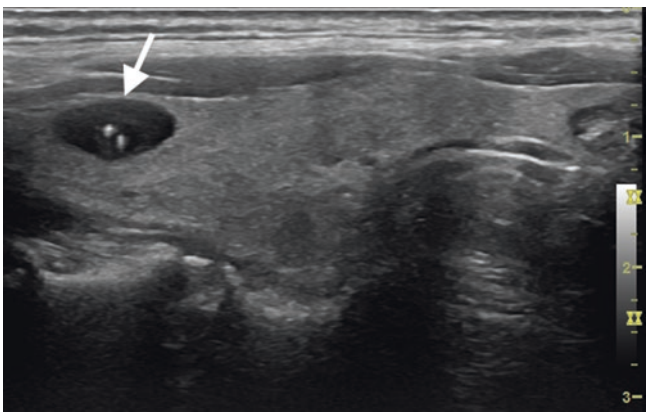

Fig. 2.3 Colloid cyst within the thyroid (*arrow*) with internal comet-tail artifact

benign nodule, it is not absolutely pathognomonic for such [4]. The distance between the two high-impedance mismatch interfaces is so small in these collections that individual reverberations are not visible. Instead of seeing multiple parallel reverberation artifact reflections of decreasing size, as with the trachea example in Fig. 2.2, a smeared "comet-tail" artifact is seen on the image.

2.5.3 Mirror-Image Artifact

The mirror-image artifact occurs when an object of interest is located near and superficial to a surface with high impedance. It is manifested as a "mirror image" or false object that is displayed equidistant from the reflective surface but on the opposite, deep side (Fig. 2.4). It occurs because reverberations between the reflective surface and the object effectively prolong the path time for the beam. Changing the incident angle of the transducer can help distinguish this artifact.

2.5.4 Shadowing Artifact

When ultrasound waves encounter a high-impedance tissue, most of the energy is reflected. As a result, the tissue immediately beyond the high-impedance interface appears obscured or void. This shadowing artifact (Fig. 2.5) is seen with dense structures such as bone, salivary calculi, and coarse calcifications within the thyroid. Knowledge of this artifact can help distinguish calcifications from colloid-related echogenic foci within the thyroid. Microcalcifications may be more difficult to distinguish, however, because they are echogenic or bright, but too small to produce a significant shadow.

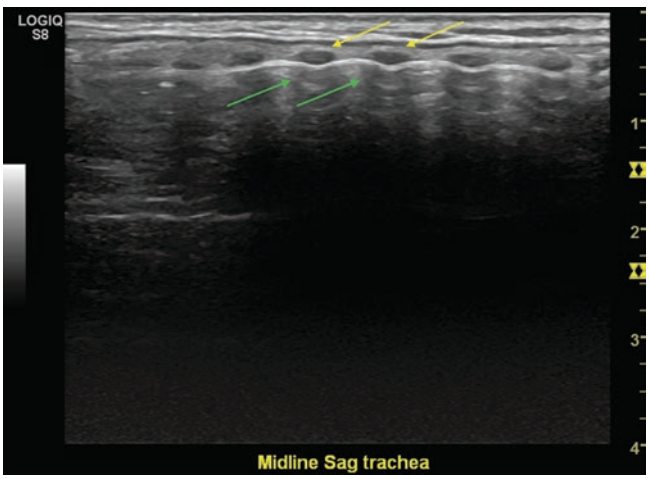

Fig. 2.4 Midline sagittal view of the trachea shows mirror-image artifact (*green arrows*) deep to the cartilaginous rings (*yellow arrows*)

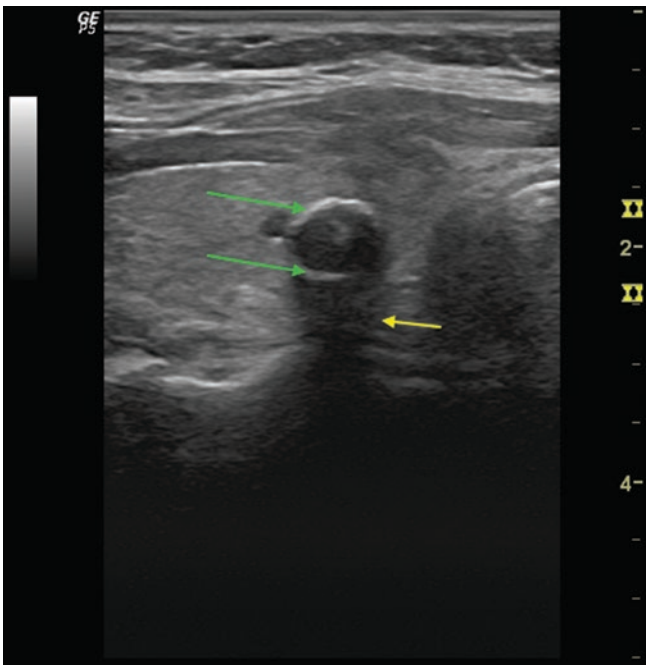

Fig. 2.5 Coarse rim calcification (*green arrows*) of a small thyroid nodule causes shadowing artifact both within the nodule and posterior (deep) to the nodule (*yellow arrow*)

2.5.5 Posterior Enhancement Artifact

Enhancement (Fig. 2.6) appears as a bright area deep to a hypoechoic or anechoic area or a low-impedance object. Compared with the tissue immediately lateral (beside) it, more sound energy passes through the object. Subsequently, there is more sound energy striking the area behind the object. These waves with relatively higher energy are reflected back to the transducer and displayed as a brighter signal behind (posterior) to the object. Posterior enhancement occurs when imaging cysts and some tumors such as pleomorphic adenomas within salivary tissue.

2.6 Doppler

Up to this point, we have been thinking about ultrasound imaging situations where the signal generator/receiver (ultrasound transducer) and the target object (anatomic tissue) are both stationary. The Doppler effect comes into play in situations where either the sound source, sound receiver, or target object are moving. The Doppler effect occurs when reflected sound waves get compressed or rarefied due to relative motion among these elements. This artificial compression or rarefication results in a sound frequency change.

This phenomenon is commonly explained using the real-world example of a siren on an ambulance as it drives down the road and passes an observer. The observer hears the high-pitched siren sound as the ambulance approaches. Because the

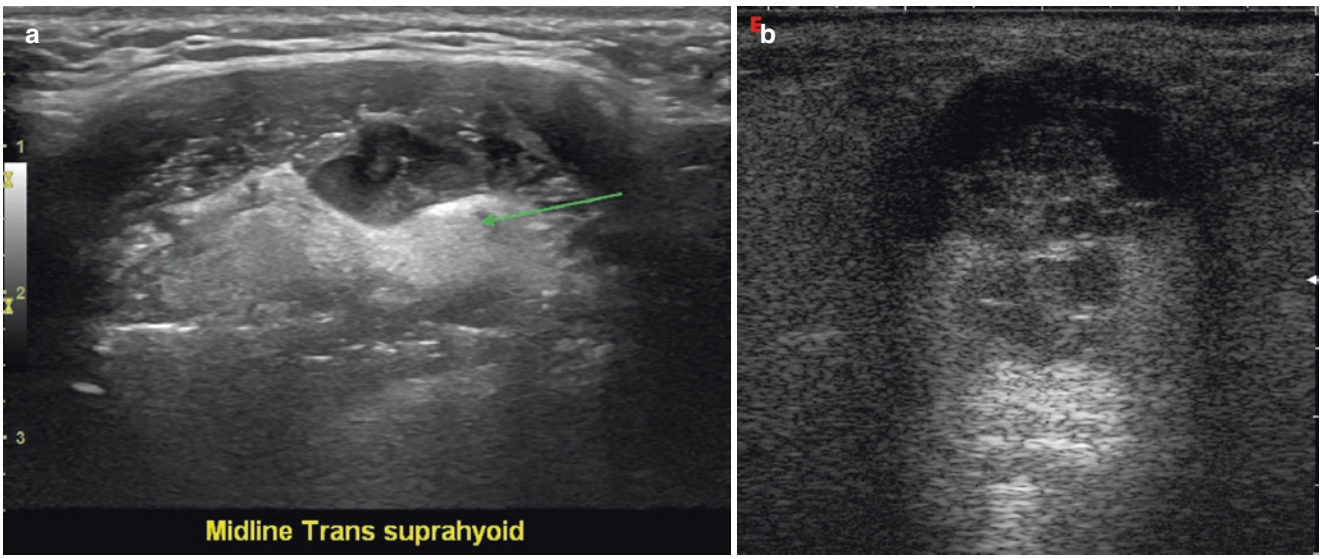

Fig. 2.6 Posterior enhancement artifact. (**a**) Midline transverse view of an incidentally noted thyroglossal duct cyst with posterior enhancement artifact (*green arrow*). (**b**) Pleomorphic adenoma of the parotid gland with posterior enhancement artifact

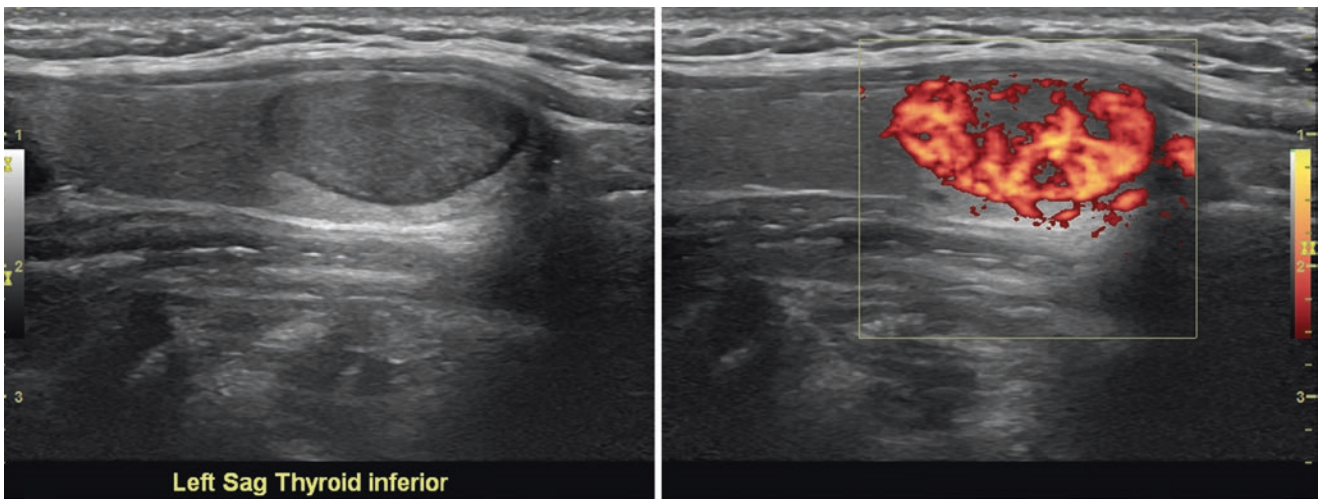

Fig. 2.7 *Left*, B-mode view of a hypoechoic thyroid nodule (follicular neoplasm by cytology). *Right*, Power Doppler view showing intense vascularity

sound waves and the sound source (siren) are moving toward the observer, this pitch (frequency) is artificially higher. For the split second when the vehicle has moved right next to the observer (perpendicular to the observer), the pitch of the siren is just as it would be if the vehicle were stopped. As the ambulance speeds on past the observer, the siren sounds lower-pitched (lower-frequency). In this scenario, the observer is stationary, and the sound source is moving. For clinical ultrasound scenarios, it is the target tissue (or fluid, such as blood) that is moving, with the sound generator/receiver in a fixed position. Phase changes can also be used for motion detection, but we will focus on the concept of frequency change for the purposes of understanding the concept.

The Doppler effect principle is applied to evaluate vascular flow with clinical ultrasound. The two main Doppler modes are *color-flow Doppler* and *power Doppler*. Color-flow Doppler distinguishes the directionality of flow (away or toward the transducer) and displays the different directions with a color scale. The algorithm used to produce color-flow Doppler images is affected by noisy signals (high signal/noise ratio), so it automatically filters out low-flow information in an effort to minimize this shortcoming. Accordingly, small veins and low-flow structures are not visible in color-flow mode. The power Doppler mode overcomes the shortcoming with regard to low-flow signals by mapping an integrated power map of the Doppler signal, effectively increasing the signal/noise ratio. This setting shows flow regardless of directionality and is better for detecting low-flow structures, but the information about

flow direction is lost (Fig. 2.7). For most head and neck ultrasound purposes, information about flow direction is less important than the detection of flow itself, so power Doppler is commonly used.

2.7 Summary

The principles discussed in this chapter represent the minimum knowledge of sound wave physics needed to optimize the performance and interpretation of ultrasound studies. Fortunately for the modern-day ultrasonographer, the powerful computer engineering available in even entry-level ultrasound systems enables acquisition of high-resolution anatomic images with little effort. The examiner can focus on image interpretation, with only minor adjustments in equipment settings and accommodations for artifacts. For more in-depth discussion, the reader is referred to the suggested resources below.

References

1. Feldman MK, Katyal S, Blackwood MS. US artifacts. Radiographics. 2009;29:1179–89.
2. Prabhu SJ, Kanal K, Bhargava P, Vaidya S, Dighe MK. Ultrasound artifacts: classification, applied physics with illustrations, and imaging appearances. Ultrasound Q. 2014;30:145–57.
3. Hoang JK, Lee WK, Lee M, Johnson D, Farrell S. US Features of thyroid malignancy: pearls and pitfalls. Radiographics. 2007;27:847–60; discussion 861–5.
4. Wu H, Zhang B, Li J, Liu Q, Zhao T. Echogenic foci with comet-tail artifact in resected thyroid nodules: not an absolute predictor of benign disease. PLoS One. 2018;13:e0191505.

Suggested Reading

Gibbs V, Cole D, Sassano A. Ultrasound physics and technology E-book: how, why and when. Philadelphia: Elsevier Health Sciences; 2011.

Hoskins PR, Martin K, Thrush A. Diagnostic ultrasound: physics and equipment. Cambridge: Cambridge University Press; 2010.

Zagzebski JA. Essentials of ultrasound physics. St. Louis: Mosby; 1996.

Ultrasound Anatomy of the Head and the Neck

3

Peter Jecker

3.1 General Notes

The correct interpretation of ultrasound findings requires an excellent knowledge of the neck anatomy. Thus, an anatomic atlas should always be available in case of unknown findings. Furthermore, the examiner should be familiar with the sonographic appearance of the normal neck structures, which are often used as landmarks to facilitate the reproducibility of ultrasound findings by different examiners. These structures or landmarks include organs (such as the thyroid or salivary glands), bony structures or cartilages, muscles, blood vessels, and nerves. The purpose of this chapter is to present these structures in the healthy neck.

3.2 Settings of the Ultrasound Device and Starting the Examination

Normally we prefer a linear scanner with a frequency between 7.5 and 10 MHz. If postoperative scar formation of the neck tissue is present, the use of a lower frequency is necessary. Additionally, sector imaging is sometimes advantageous, especially if large structures should be described.

The neck examination should always start with an area where the device adjustment can be checked [1]. We prefer starting the examination with a view of the thyroid gland and the surrounding vessels, i.e., the common carotid artery and internal jugular vein (Fig. 3.1). In this section, the carotid artery wall shows a high echogenicity, whereas the lumen of the vessels should be hypoechoic (Video 3.1). The quality of the thyroid's echo is between the echogenicity of both structures. This section through the thyroid gland allows fast and easy adjustment of the device. Then we examine the medial neck compartment, followed by both lateral compartments. After this, the region of the salivary glands is examined, followed by the tongue and the tongue base.

3.3 Systematic Head and Neck Ultrasound Examination: Normal Findings

3.3.1 The Medial Neck Compartment, Thyroid, and Larynx

The thyroid is the main organ in the medial neck compartment (Video 3.2). The thyroid lobes are connected by the isthmus, which can be seen in both transverse and sagittal section (Figs. 3.2 and 3.3). The thyroid of the healthy patient is more or less homogenous, and its echogenicity is similar to the echogenicity of the large salivary glands [1, 2]. The tracheal cartilages can also be seen, producing artificial reverberation echoes (Fig. 3.2). Lateral to the thyroid, the large blood vessels (the common carotid artery and more laterally, the internal jugular vein) can be found (Fig. 3.4). Sometimes, the vagal nerve becomes visible next to the blood vessels (Fig. 3.1). In the depth, the thyroid adjoins the scalene muscles and the vertebral column. Infrahyoid muscles can be seen in front of the thyroid gland. Differentiation of the infrahyoid muscles would be possible without any problem when using a modern ultrasound device.

The upper esophagus (Fig. 3.5) can commonly be seen under the left thyroid lobe, next to the vertebral column [3]. Parts of the esophagus are covered by the acoustic shadow of the trachea. The esophagus is characterized by an onion-like pattern. Especially in the sagittal plane, swallowing of saliva can be observed (Video 3.3). Sometimes, the esophagus also can be seen under the right thyroid lobe (Fig. 3.6); in rare

Electronic Supplementary Material The online version of this chapter (https://doi.org/10.1007/978-3-030-12641-4_3) contains supplementary material, which is available to authorized users.

P. Jecker (✉)
Department of Otorhinolaryngology and Plastic Head and Neck Surgery, Klinikum Bad Salzungen GmbH, Bad Salzungen, Germany
e-mail: peter.jecker@klinikum-badsalzungen.de

© Springer Nature Switzerland AG 2019

H. J. Welkoborsky, P. Jecker (eds.), *Ultrasonography of the Head and Neck*, https://doi.org/10.1007/978-3-030-12641-4_3

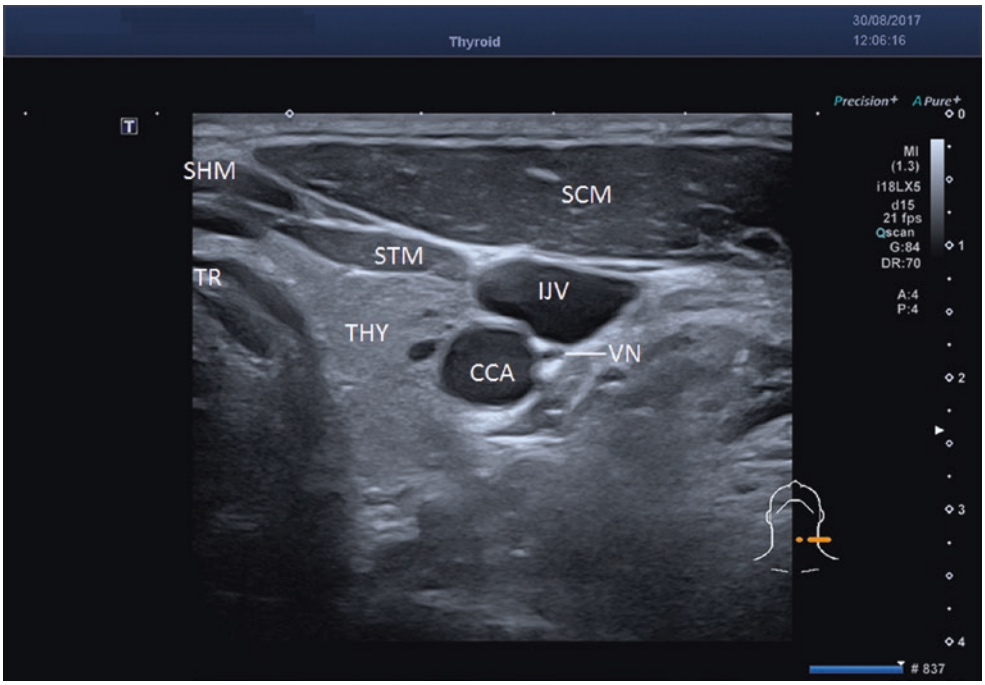

Fig. 3.1 Basic adjustment of the ultrasound device using a standardized plane through the thyroid gland (THY), the common carotid artery (CCA), and the internal jugular vein (IJV). SCM sternocleidomastoid muscle, SHM sternohyoid muscle, STM sternothyroid muscle, TR trachea, VN vagal nerve

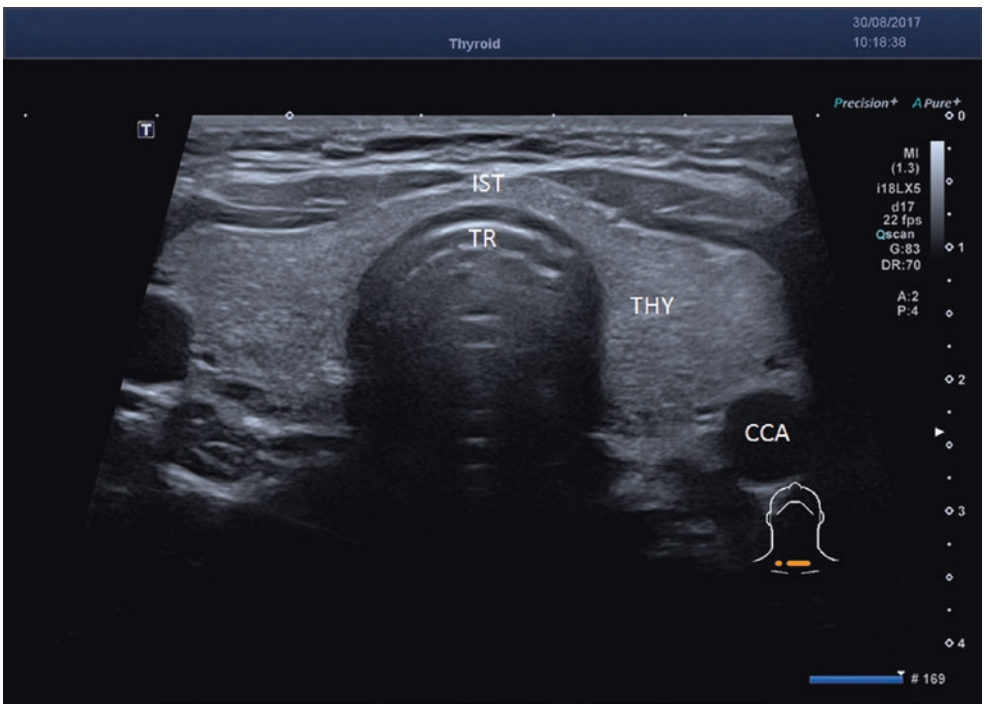

Fig. 3.2 Lower medial cervical compartment with the homogenous thyroid gland (THY), transverse plane. CCA common carotid artery, IST isthmus, TR trachea

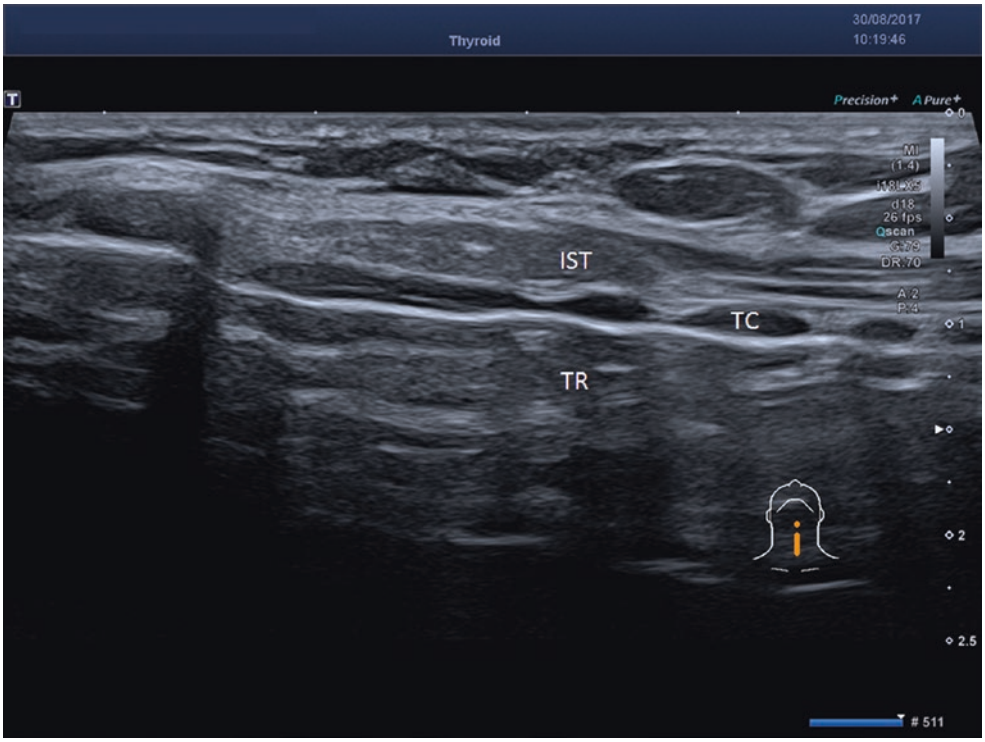

Fig. 3.3 Isthmus of the thyroid (IST), sagittal plane. TC tracheal cartilage, TR tracheal lumen

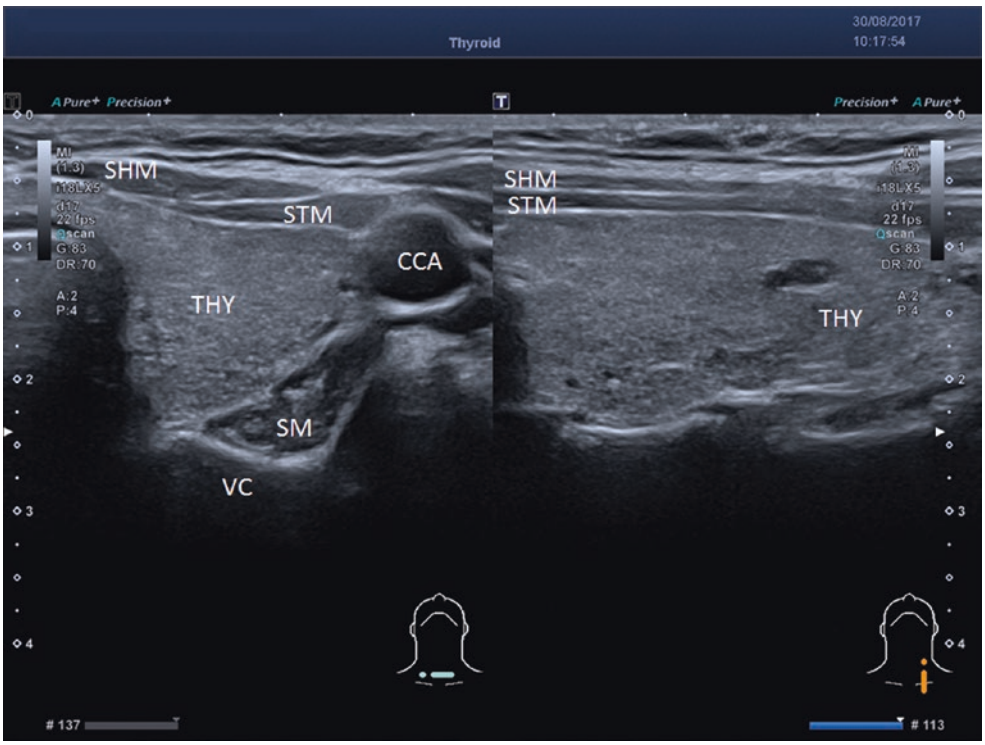

Fig. 3.4 Left thyroid lobe area, transverse plane (*left*) and sagittal plane (*right*). CCA common carotid artery, SHM sternohyoid muscle, SM scalene muscles, STM sternothyroid muscle, THY thyroid gland, VC vertebral column

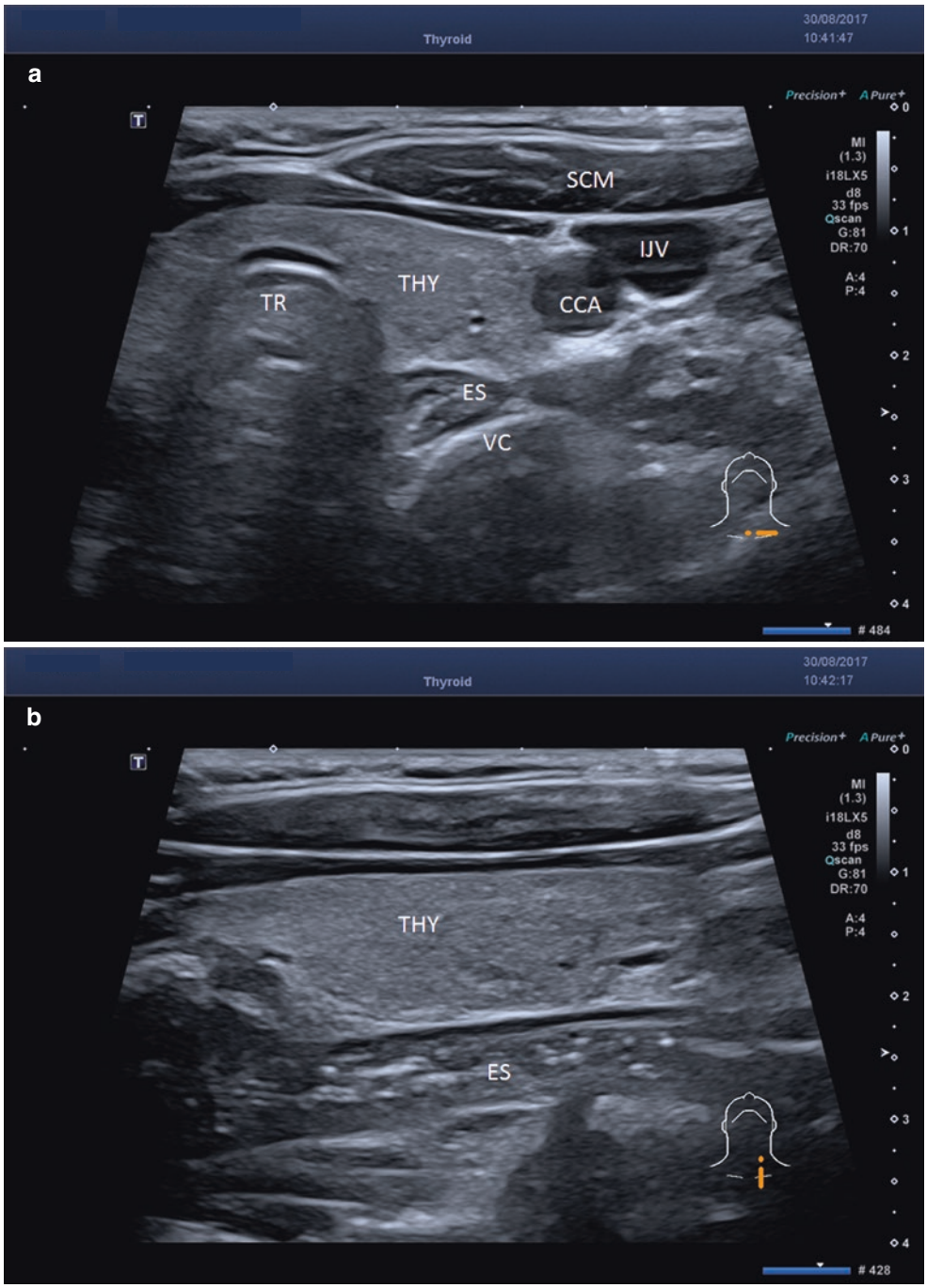

Fig. 3.5 Esophagus (ES) dorsal to the left thyroid lobe (THY), in transverse plane (**a**) and sagittal plane (**b**). CCA common carotid artery, IJV internal jugular vein, SCM sternocleidomastoid muscle, TR trachea, VC vertebral column

cases, the esophagus cannot be seen at all, because it can be completely covered by the acoustic shadow of the trachea.

The cricoid and thyroid cartilages can be seen cranial to the thyroid (Figs. 3.7 and 3.8). In younger patients, the cartilages are not ossified, which allows a sonographic view into the larynx. Then structures such as the vestibular folds can be examined (Video 3.4). With increasing ossification, the examination of intralaryngeal structures becomes more and more difficult, but not impossible [4].

3.3.2 The Jugular Fossa and the Supraclavicular Region

In clinical practice, it is often forgotten to examine the jugular fossa and the supraclavicular region, because most diseases of the head and neck become clinically apparent more cranially. Nevertheless, we have often found metastatic lymph nodes in this area, especially in patients suffering from thyroid cancer, breast cancer, or even colon or

Fig. 3.6 Esophagus (ES) next to the right thyroid lobe (THY). CCA common carotid artery, TR trachea

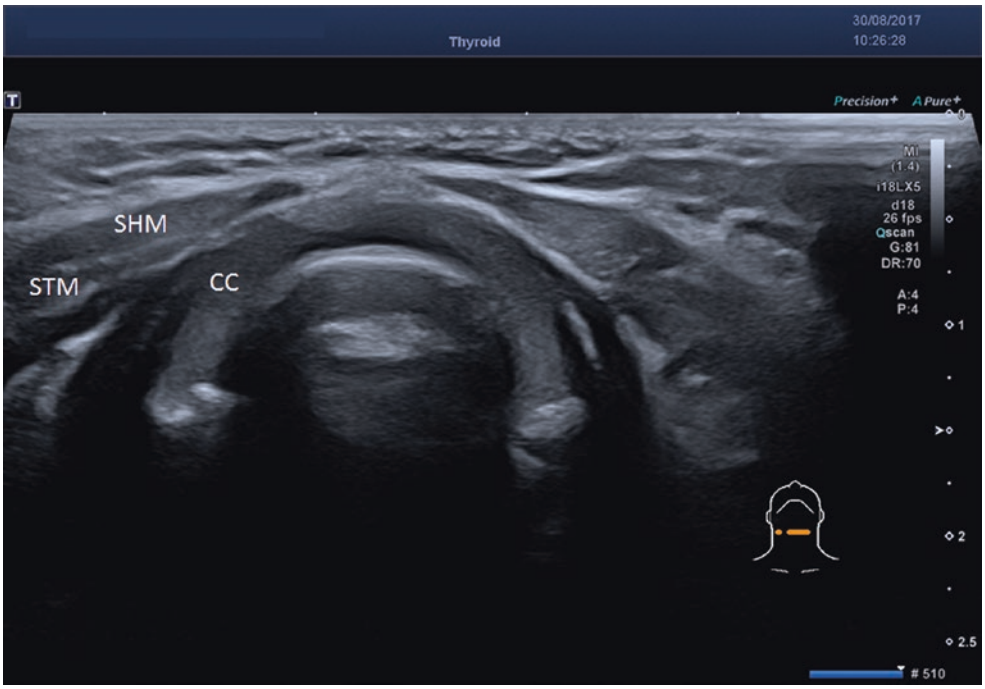

Fig. 3.7 Cricoid cartilage (CC). SHM sternohyoid muscle, STM sternothyroid muscle

prostate cancer. Furthermore, the sonographic examination of the jugular fossa allows a view into the upper mediastinum, where, for example, parathyroid adenomas can be found.

In young patients, parts of the thymus can be seen in the jugular fossa (Fig. 3.9). Likewise, in this area, blood vessels often can be seen in healthy patients. Thus, sometimes, the aortic arch becomes visible (Fig. 3.10). Furthermore, the brachiocephalic artery, the supraclavicular artery, and the common carotid artery can be detected next to the pleura (Figs. 3.11 and 3.12). At last, in this area, the nerves of the cervical plexus can be seen well between both scalene muscles (Figs. 3.13 and 3.14), allowing ultrasound-guided plexus anesthesia.

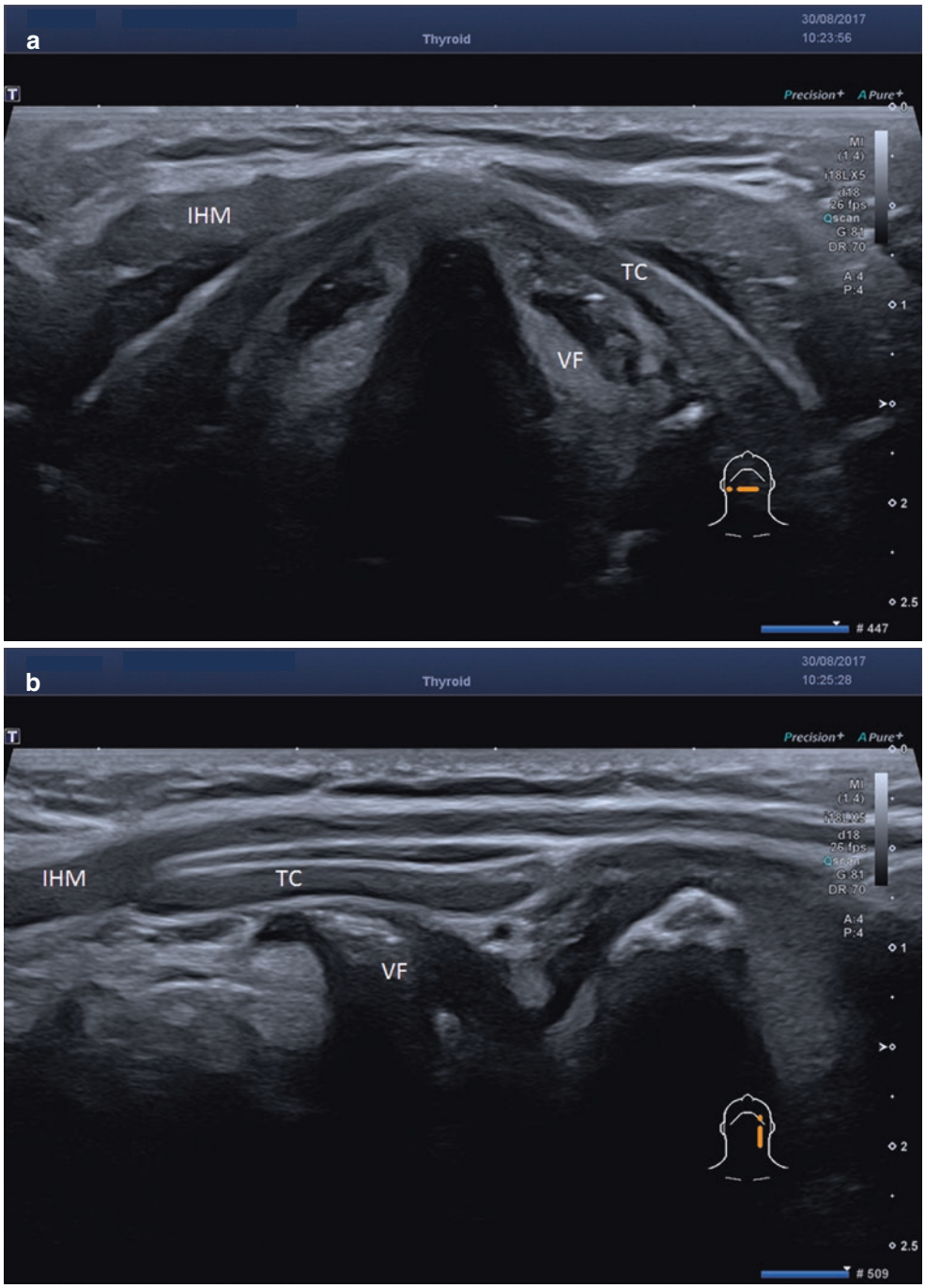

Fig. 3.8 Transverse (**a**) and sagittal (**b** and **c**) sections through the larynx at the level of the thyroid cartilage (TC). IHM infrahyoid muscle, SHM sternohyoid muscle, STM sternothyroid muscle, THM thyrohyoid muscle, VF vestibular fold

Fig. 3.8 (continued)

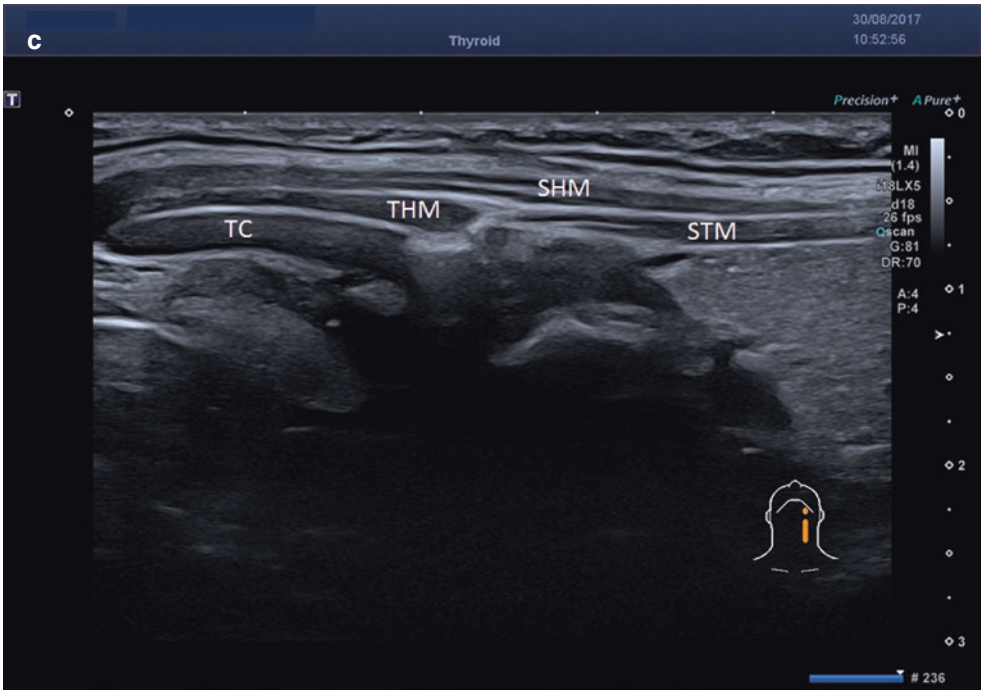

Fig. 3.9 In children, the thymus can be detected in the upper mediastinum through the sternum (**a**) and sometimes also through the jugular fossa (**b**). AO aorta, CL clavicle

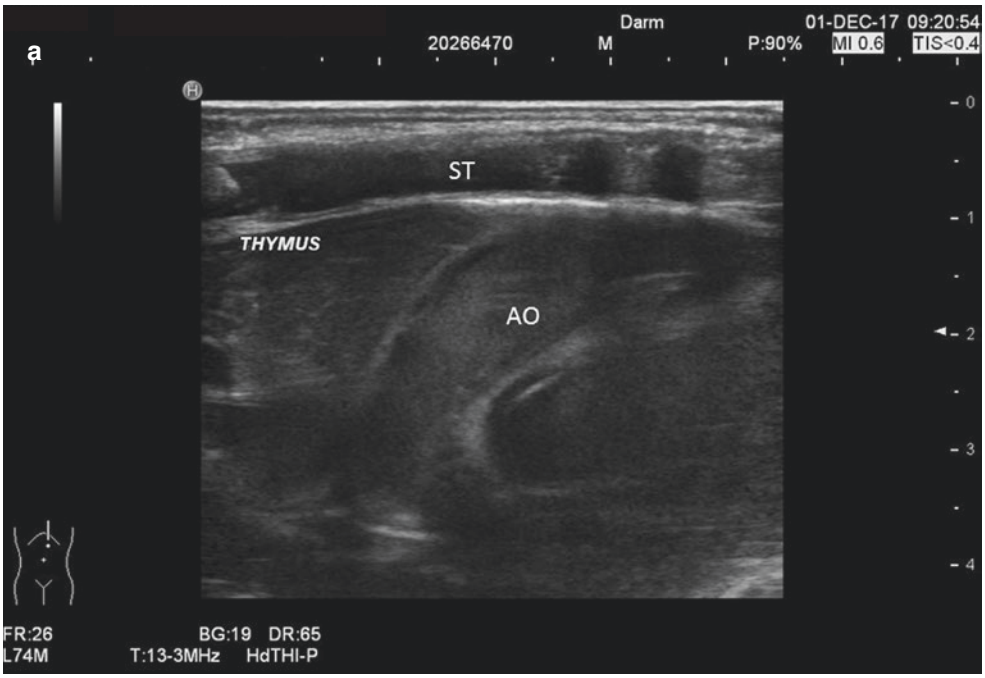

Fig. 3.9 (continued)

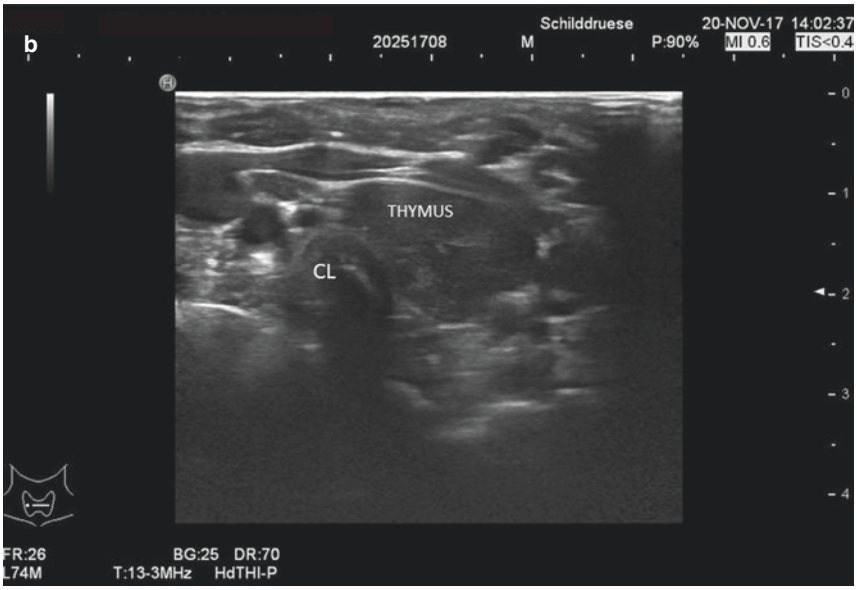

Fig. 3.10 The jugular fossa with the arch of the aorta (AO). (**a**) B-Scan and color-coded sonography. (**b**) Doppler sonography

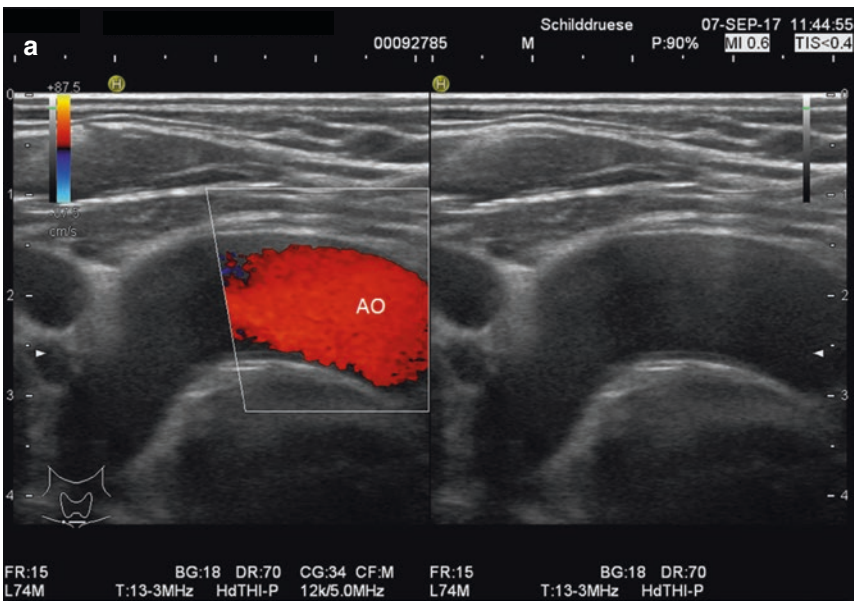

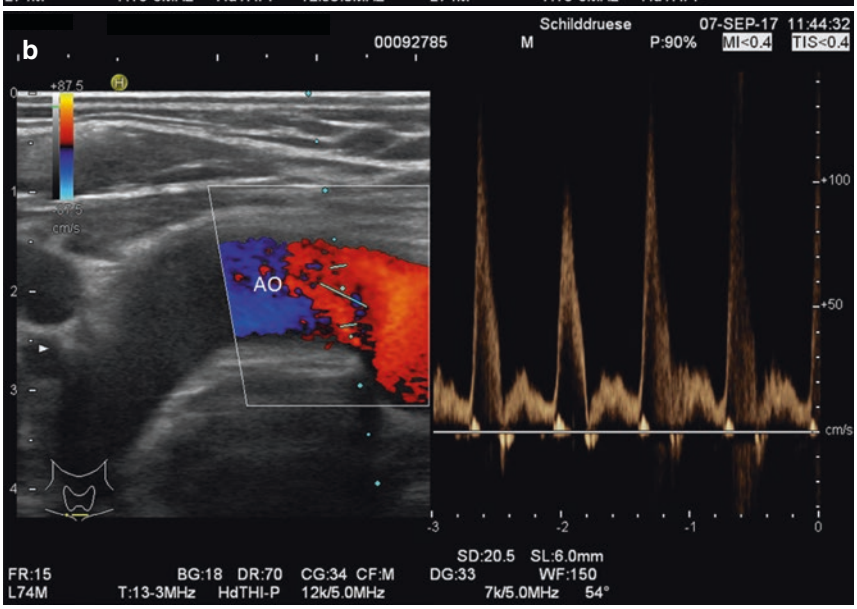

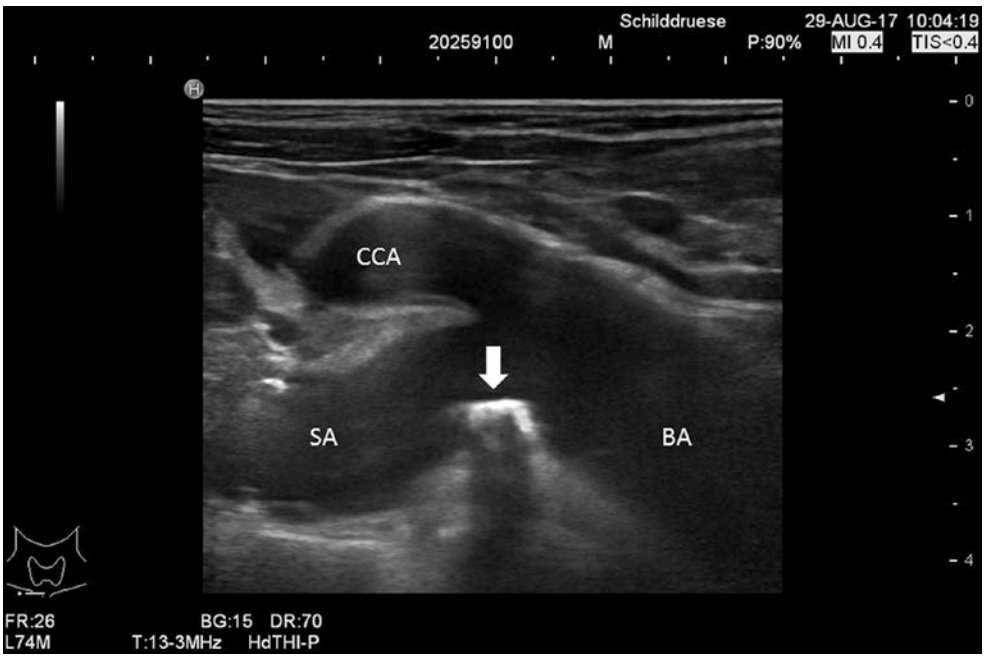

Fig. 3.11 Right supraclavicular region with the brachiocephalic artery (BA) and its bifurcation; the *arrow* indicates a calcified plaque. CCA common carotid artery, SA supraclavicular artery

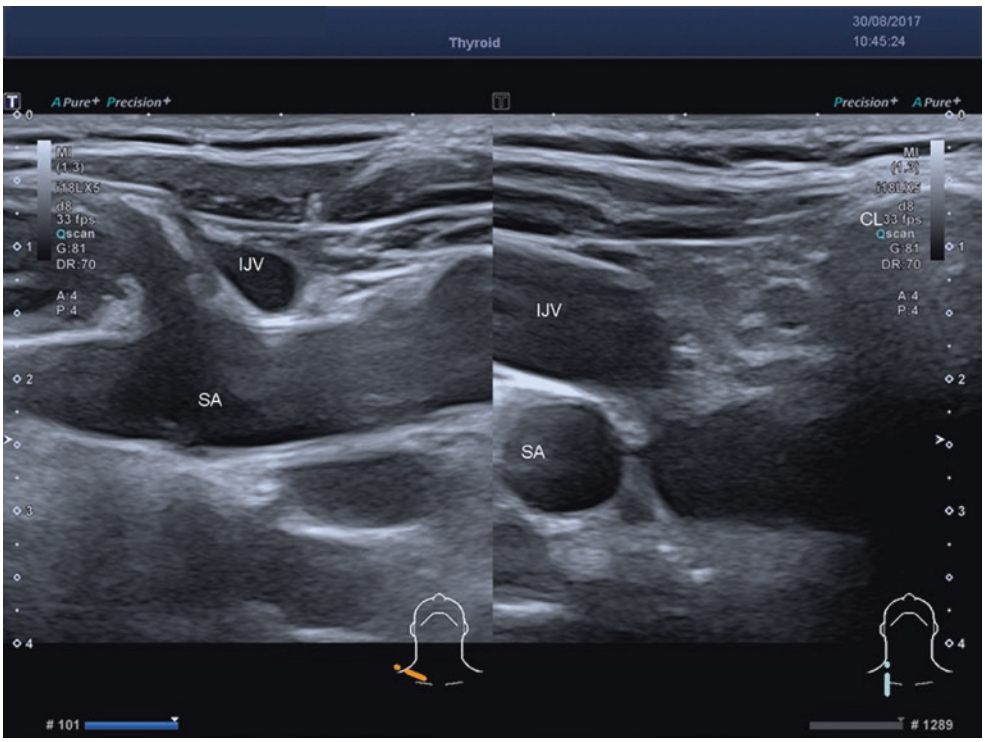

Fig. 3.12 Right supraclavicular region, transverse plane (*left*) and sagittal plane (*right*). CL clavicle, IJV internal jugular vein, SA supraclavicular artery

3.3.3 The Lateral Neck Compartment

The examination of the lateral neck compartments starts with the general view through the appropriate thyroid lobe, the large blood vessels, and the sternocleidomastoid muscle (Fig. 3.15). Too much pressure with the array on the patient's neck results in a collapse of the internal jugular vein. In contrast to the common carotid artery, the wall of the vein is very thin, and sometimes venous valves can be detected (Fig. 3.16; (Video 3.5). The external jugular vein can be seen in the superficial area of the lateral neck (Fig. 3.17). The omohyoid muscle (Fig. 3.18) is characterized by an oblique course in this area. This muscle is located between the sternocleidomastoid muscle and the large vessels and can easily be misdiagnosed as a lymph node in this area.

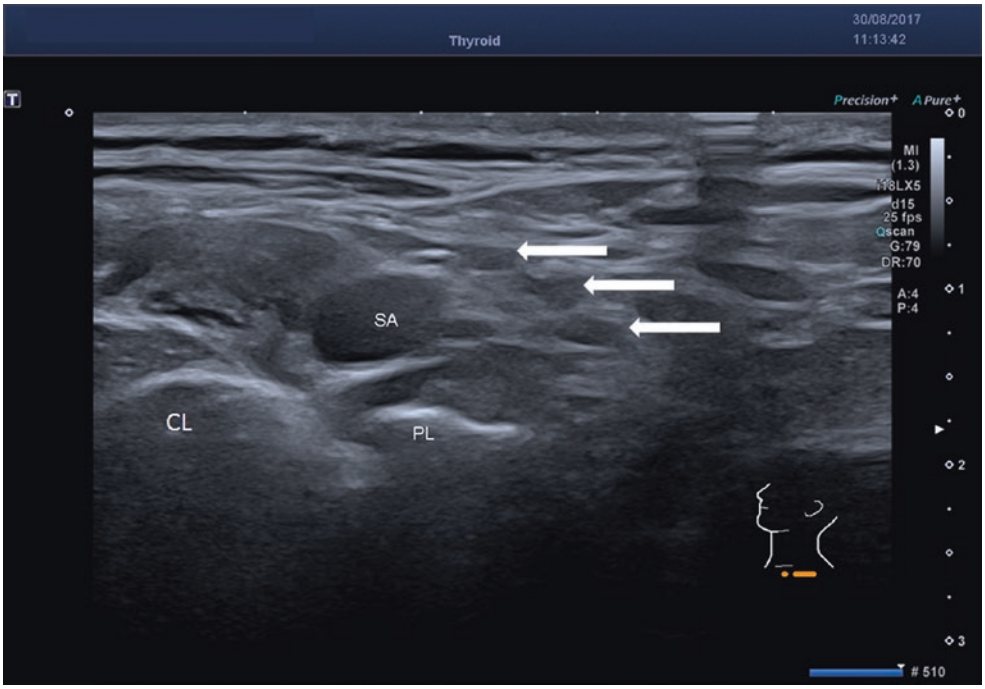

Fig. 3.13 Left supraclavicular region with parts of the supraclavicular plexus (*arrows*). CL clavicle, PL pleura, SA supraclavicular artery

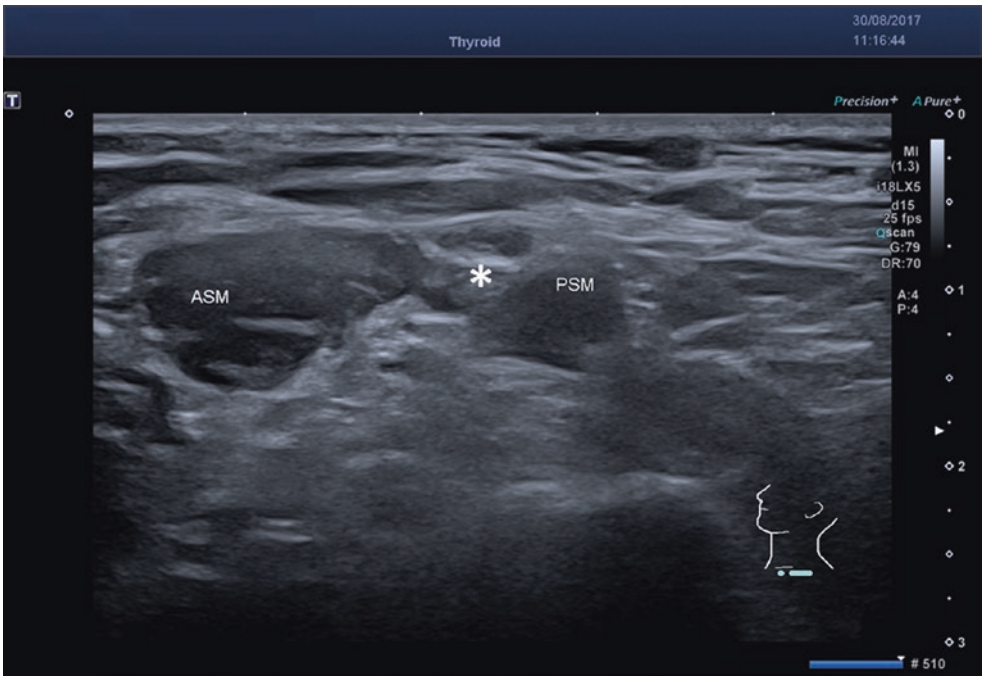

Fig. 3.14 Parts of the cervical plexus (*asterisk*) can be seen between the anterior scalene muscle (ASM) and the posterior scalene muscle (PSM)

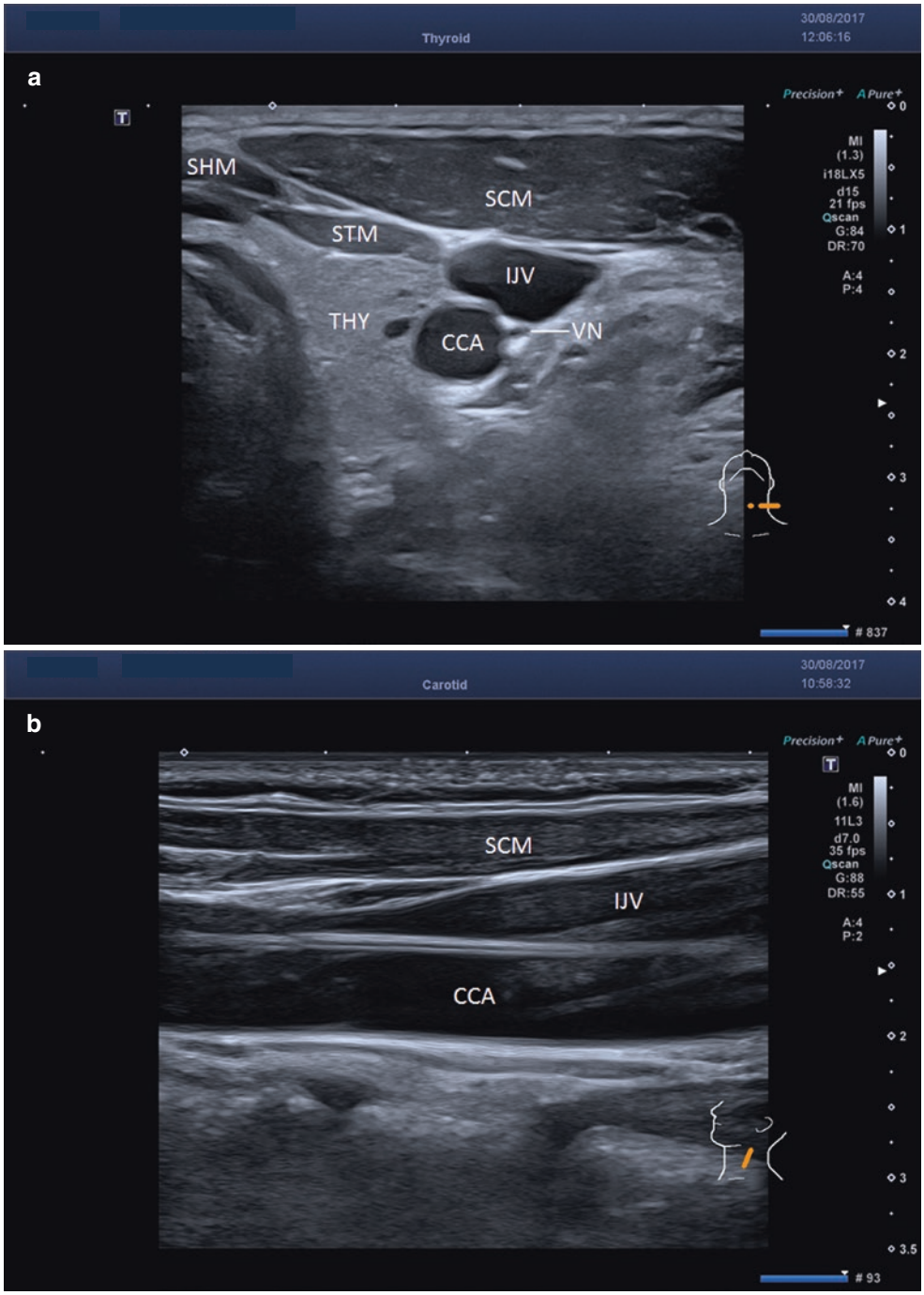

Fig. 3.15 Lateral cervical compartment. (**a**) Transverse plane. (**b**) Sagittal plane. CCA common carotid artery, IJV internal jugular vein, SCM sternocleidomastoid muscle, SHM sternohyoid muscle, STM sternothyroid muscle, THY thyroid, VN vagal nerve

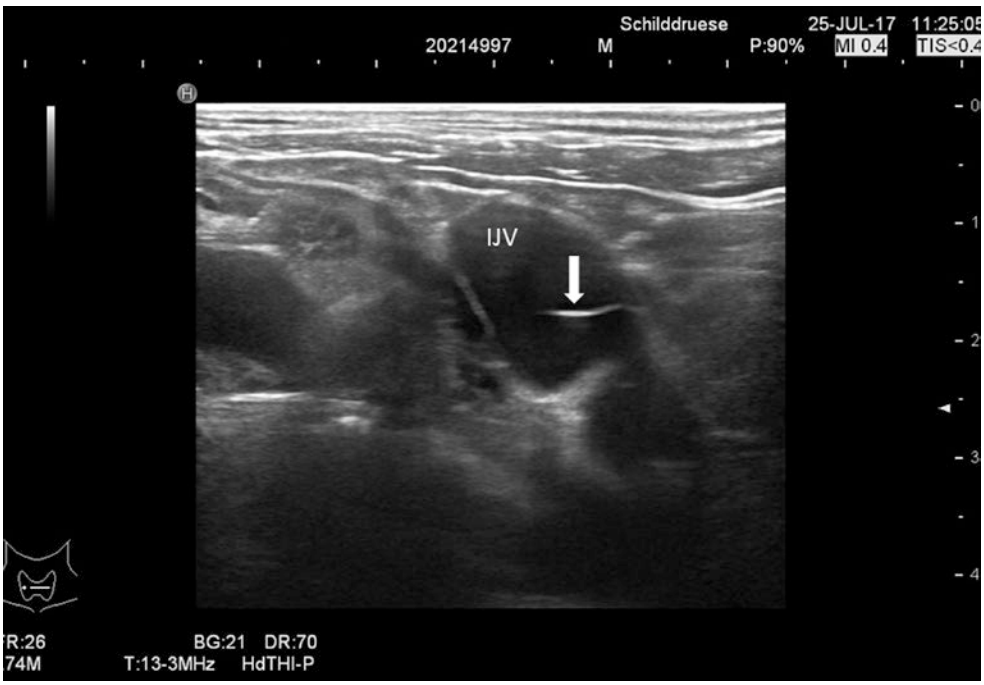

Fig. 3.16 Venous valve (*arrow*) in the left internal jugular vein (IJV)

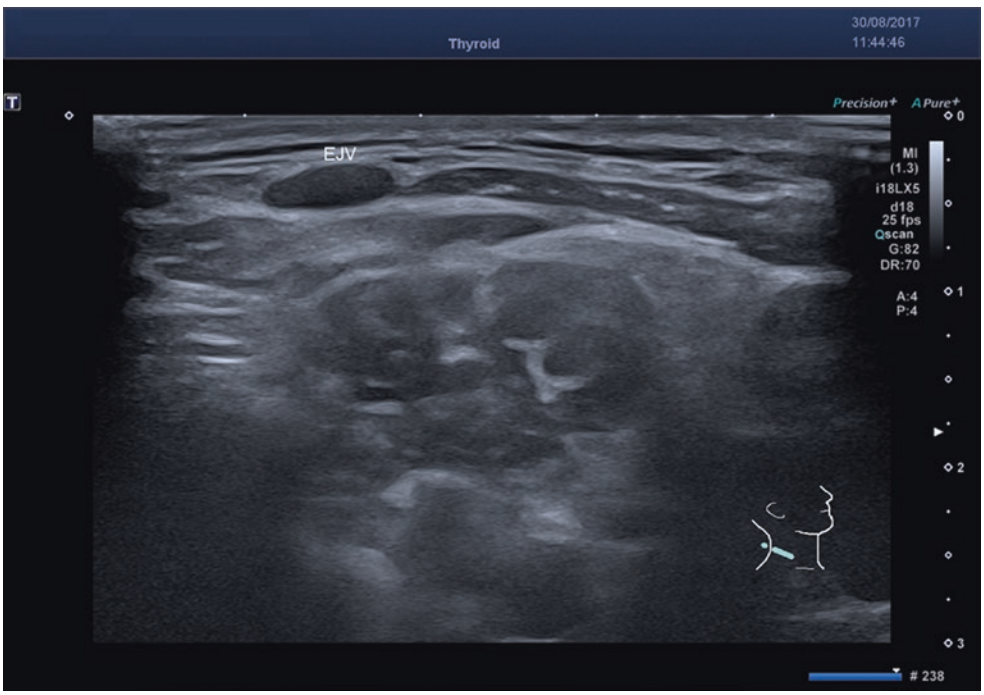

Fig. 3.17 External jugular vein (EJV)

More cranially, the bifurcation and the jugulofacial vein angle become obvious (Fig. 3.19). The relation of both structures to each other differs. Often it is necessary to differentiate between the large arteries of the neck. A differentiation is possible using Doppler ultrasound. The color-coded examination and the Doppler examination of the common carotid artery are easy (Fig. 3.20, Video 3.6). In contrast, the detection of the internal and the external carotid artery is more difficult, especially if the bifurcation is more cranial. Depending on the anatomy of the bifurcation, the internal and external carotid arteries can be seen in a more sagittal plane or a frontal plane (Fig. 3.21). The pulsed-wave (pw) Doppler allows a distinction between both blood vessels (Video 3.7). Whereas the end-diastolic pressure is nearly

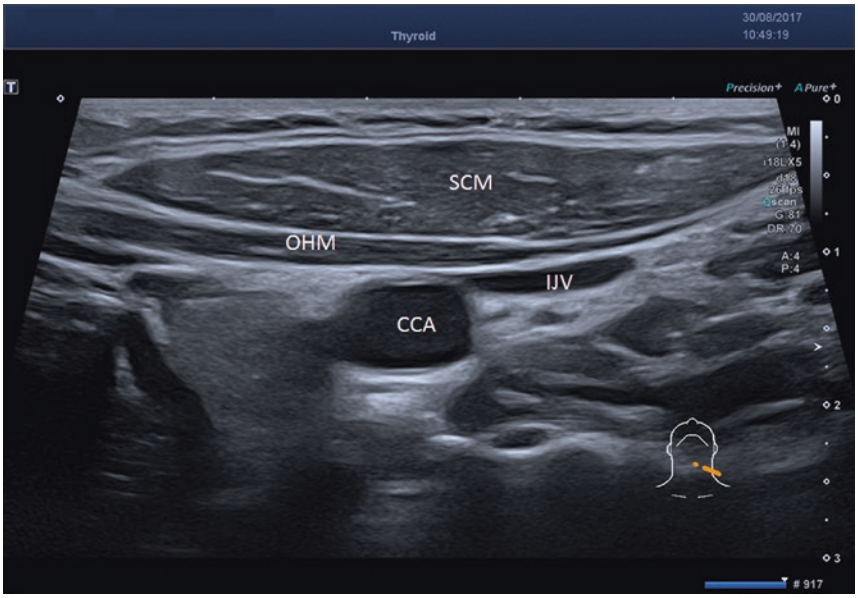

Fig. 3.18 The omohyoid muscle (OHM) can be seen in an oblique plane under the sternocleidomastoid muscle (SCM). CCA common carotid artery, IJV internal jugular vein

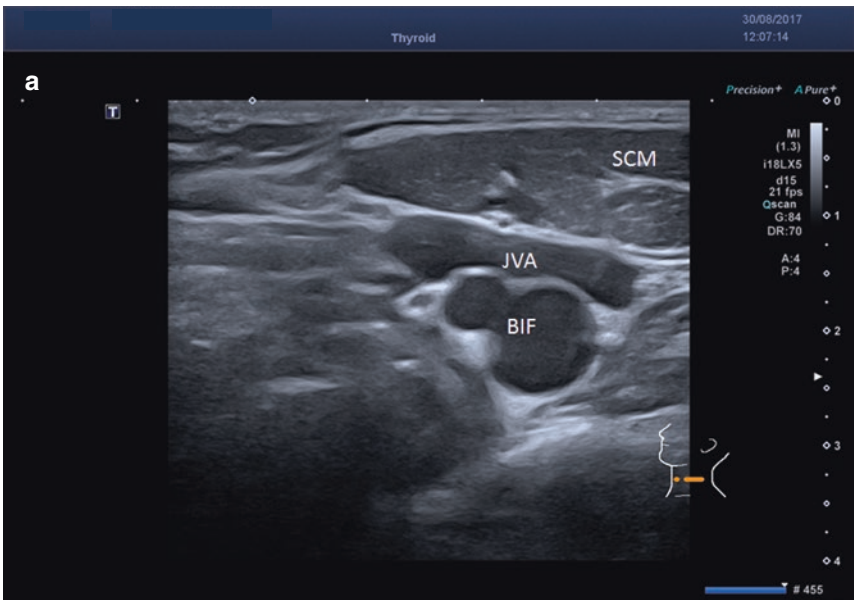

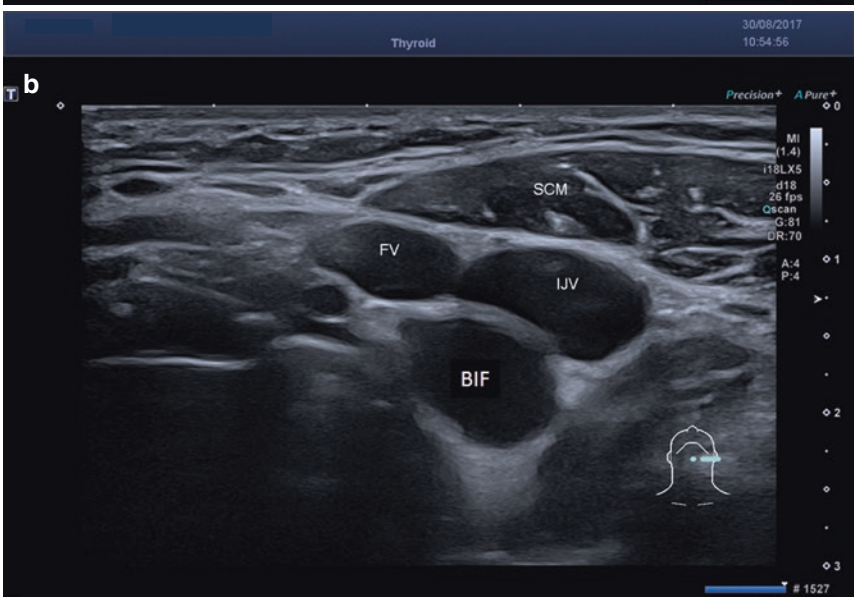

Fig. 3.19 Carotid bulb, bifurcation (BIF) and jugulofacial vein angle (JVA) in a transverse view (**a**, **b**, different patients) and a sagittal (**c**) view. FV facial vein, IJV internal jugular vein, SCM sternocleidomastoid muscle

Fig. 3.19 (continued)

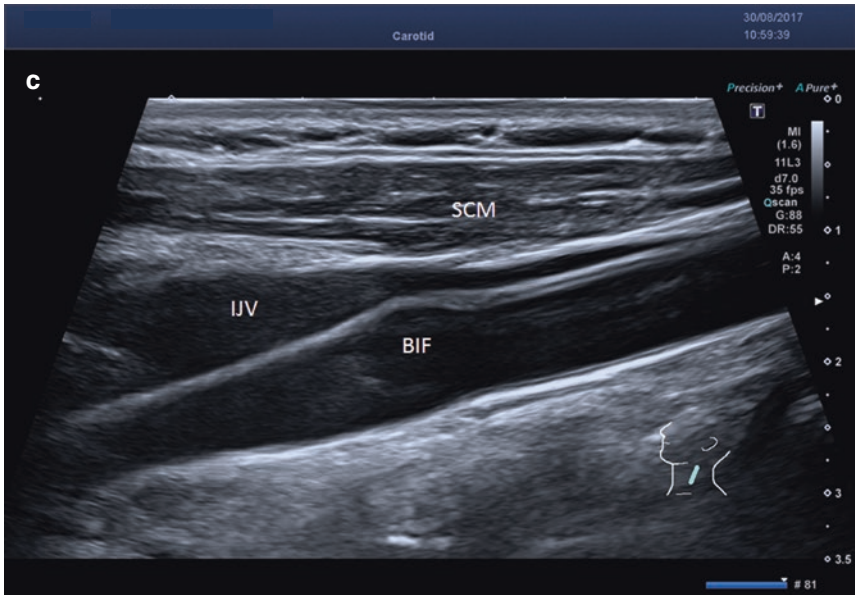

Fig. 3.20 Common carotid artery (CCA). (**a**) B-scan. (**b**) Color-coded sonography. (**c**) Doppler sonography

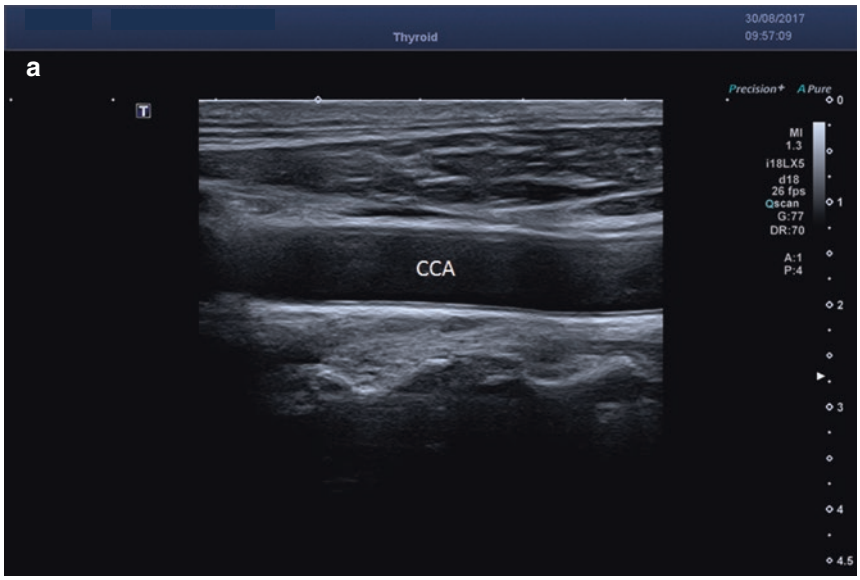

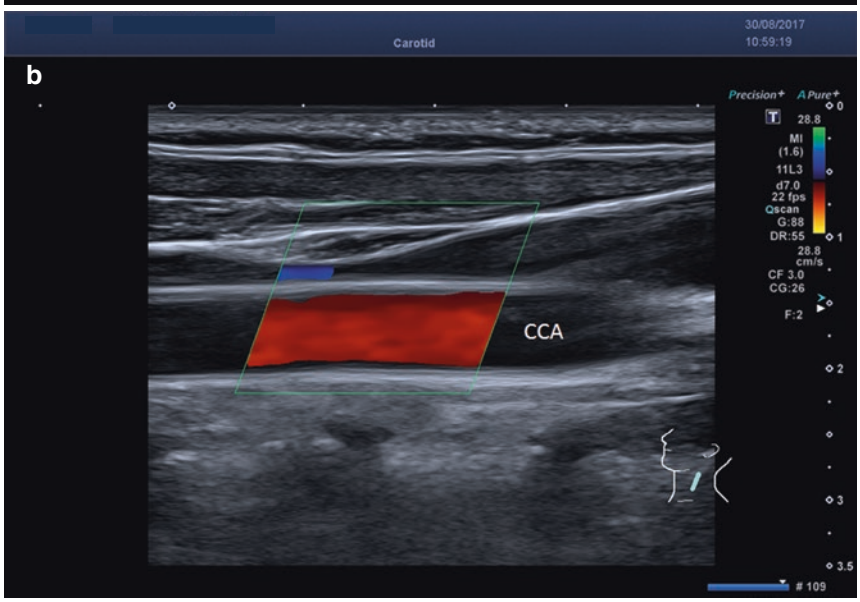

Fig. 3.20 (continued)

Fig. 3.21 Carotid bifurcation with a calcified plaque (*arrow*). (**a**) B-scan. (**b**) Color-coded sonography. CCA common carotid artery, ECA external carotid artery, ICA internal carotid artery

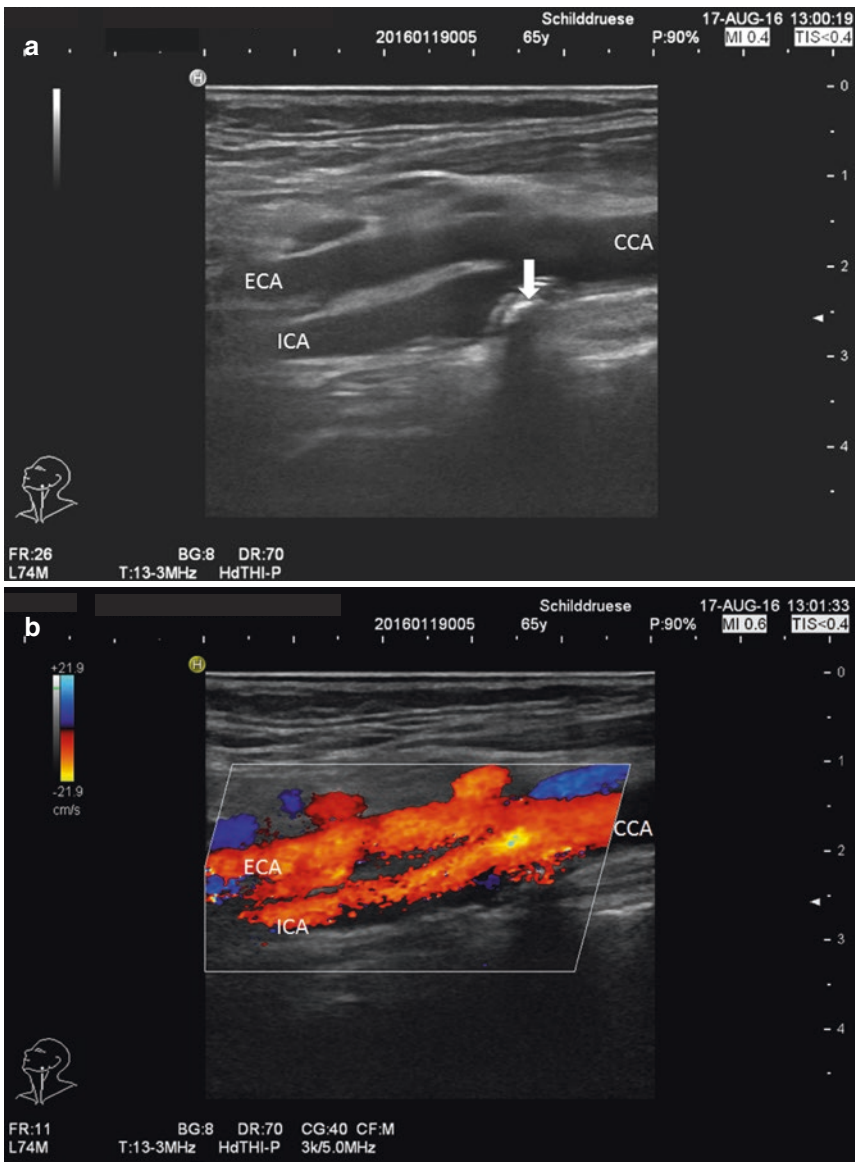

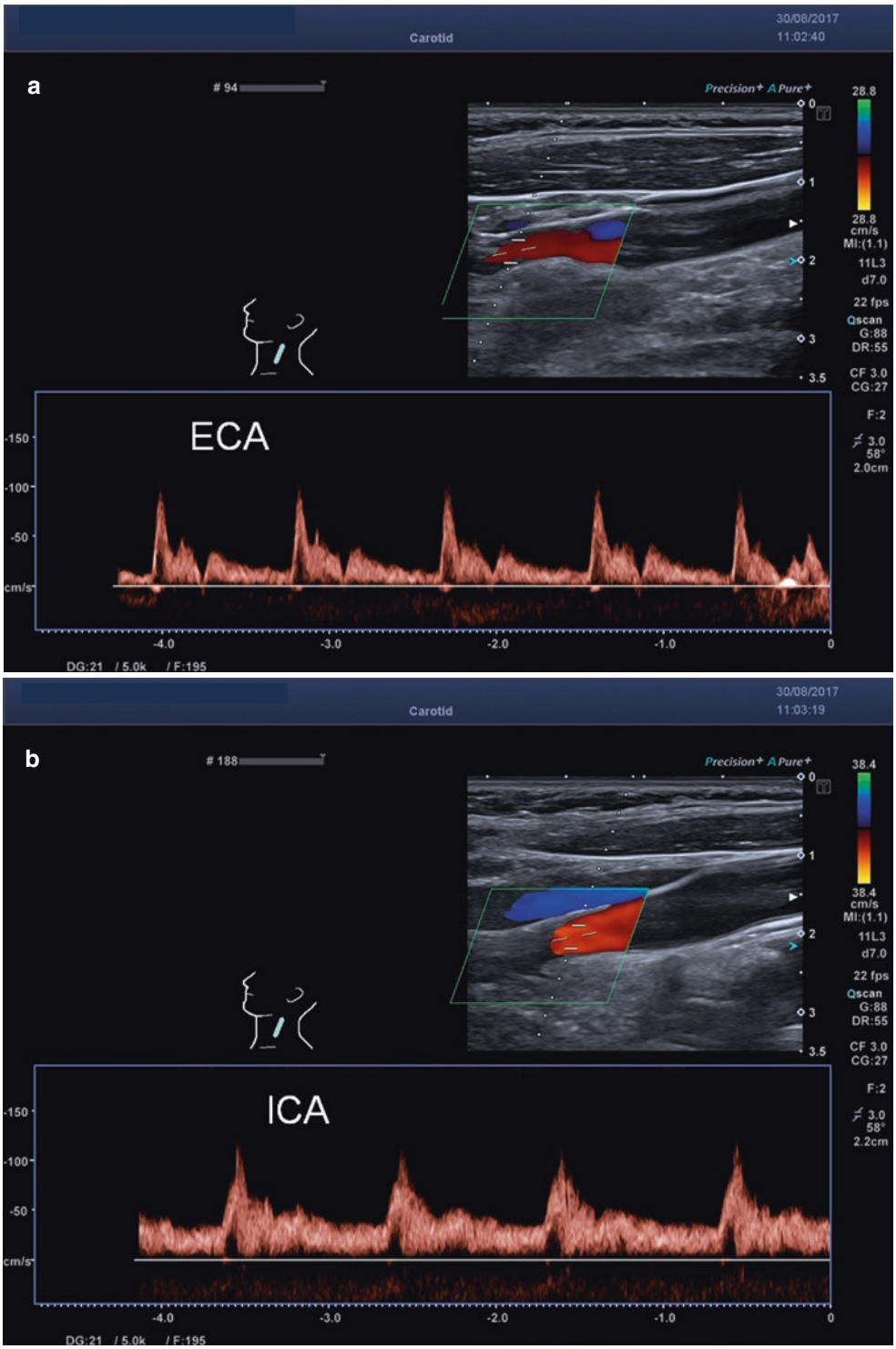

Fig. 3.22 Doppler sonography of the external carotid artery (ECA) (**a**) and internal carotid artery (ICA) (**b**)

zero in the external carotid artery, it is much higher in the internal carotid artery (Fig. 3.22).

If the probe is moved laterally in a sagittal view, the vertebral artery can be detected (Fig. 3.23). Its lumen is frequently covered by the acoustic shadows of the transverse processes of the vertebra (Videos 3.8 and 3.9).

3.3.4 The Floor of the Mouth, Including Submandibular and Sublingual Glands

Cranial to the bifurcation and the jugulofacial vein angle, the submandibular gland can be detected (Fig. 3.24). In healthy persons, the gland is homogeneous, and the echogenicity is

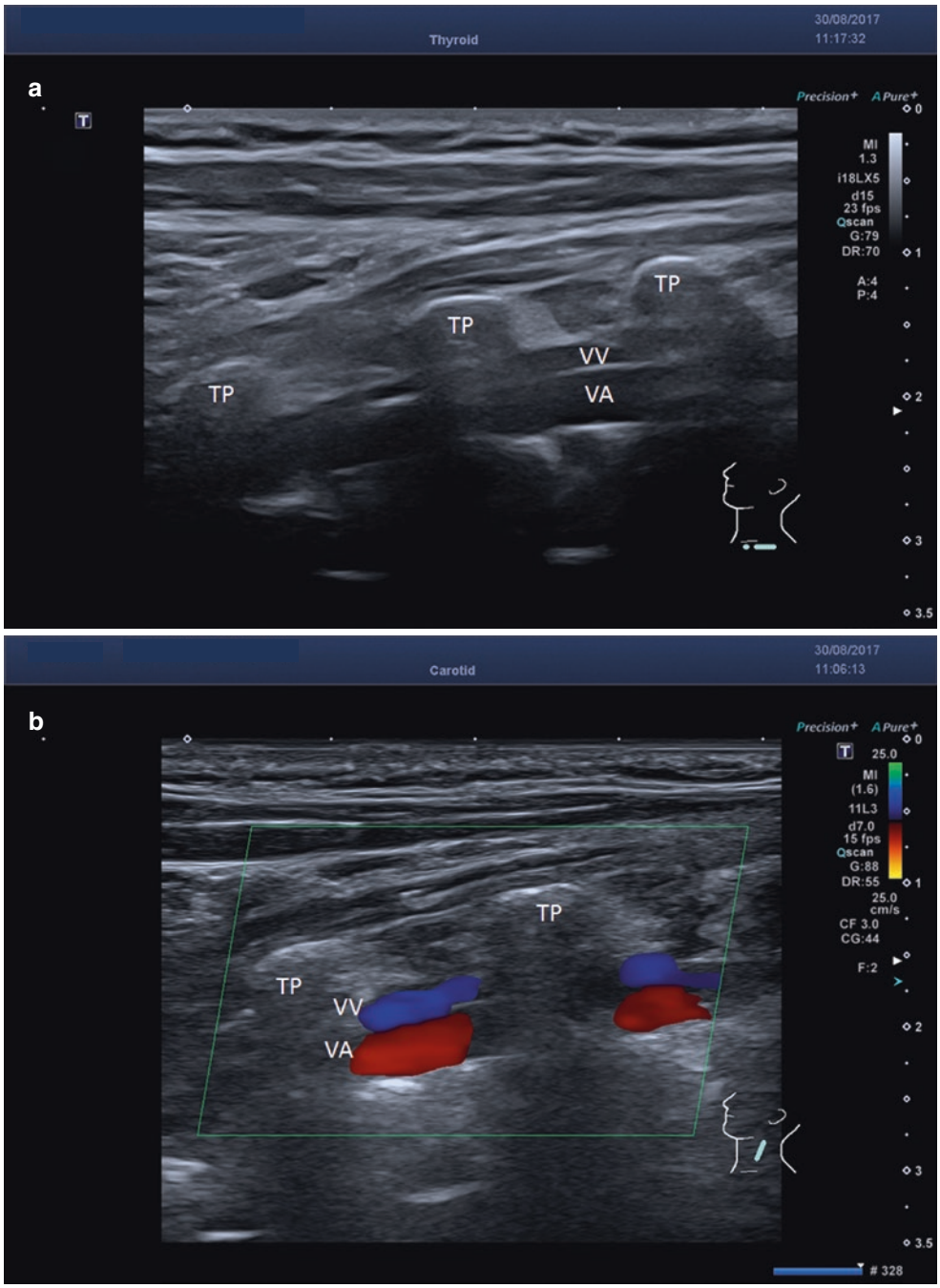

Fig. 3.23 Vertebral artery (VA) and vertebral vein (VV) in a sagittal section. (**a**) B-Scan. (**b**) Color-coded sonography. (**c**) Doppler sonography. TP transverse process of the vertebra

Fig. 3.23 (continued)

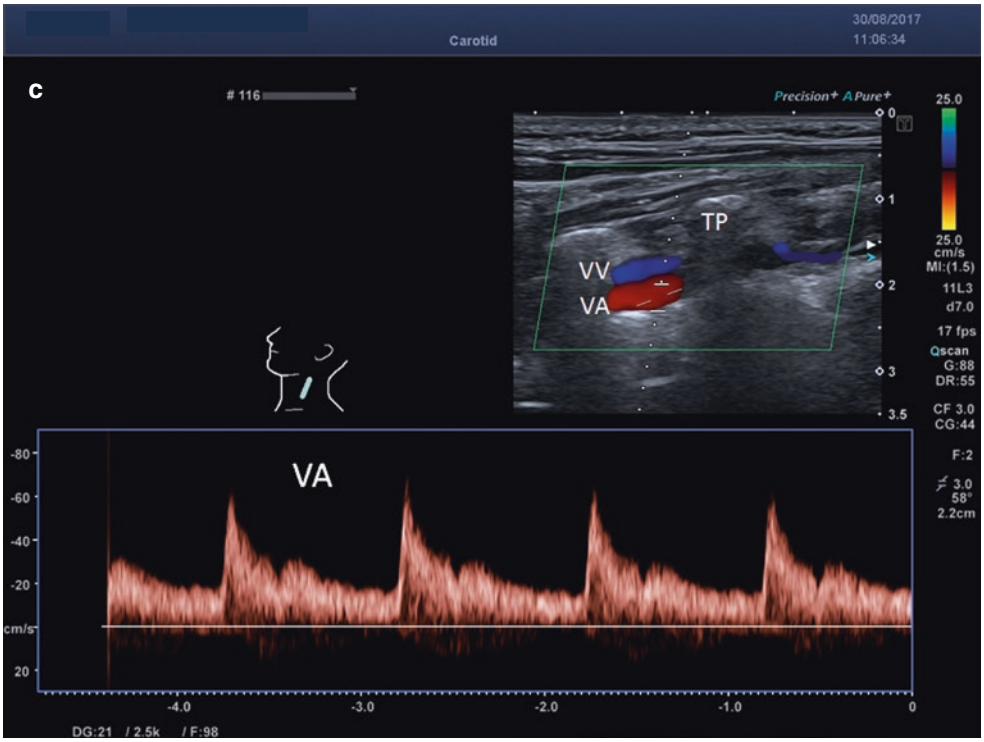

Fig. 3.24 Oblique section through the jaw angle. SM submandibular gland, TO tongue

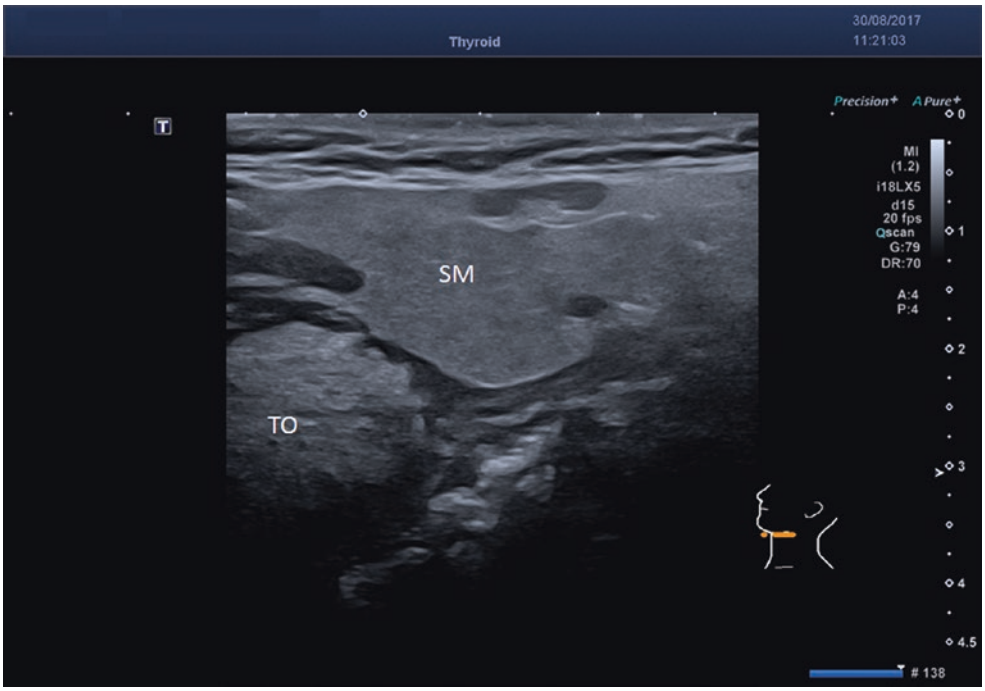

similar to that of the thyroid gland (Video 3.10). The submandibular gland has direct contact with the inferior part of the parotid gland, and the echo of the two glands is somewhat different (Fig. 3.25). Within the submandibular gland, the hilus can sometimes be seen; it should not be confused with intraglandular vessels (Fig. 3.26). The facial artery also can be detected in this region (Fig. 3.27).

From the submandibular gland, the array should be moved in the direction of the mouth floor (Video 3.11). In the ventral portion of the mouth floor, a figure like the "head of

Fig. 3.25 Contact between submandibular gland (SM) and parotid gland (PAR). LN lymph node, TO tongue

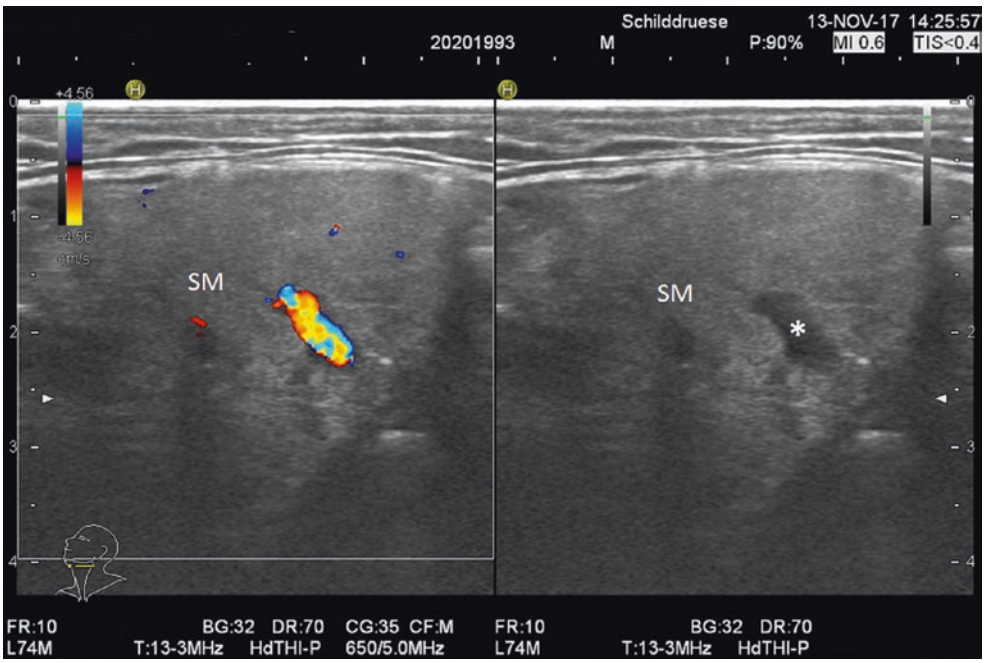

Fig. 3.26 A hilus-like structure (*asterisk*) in the submandibular gland (SM), diagnosed as an intraglandular blood vessel by using color-coded ultrasound

Mickey Mouse" can be seen (Fig. 3.28). The single muscles of the mouth floor can be identified as structures of poor echo (Figs. 3.28 and 3.29). Furthermore, the sublingual glands can be seen beside the mandible. They are characterized by the typical echo similar to that of other major salivary glands. Finally, the sublingual artery can be seen with B-scan and with color-coded sonography (Fig. 3.30).

3.3.5 Tongue, Tongue Base, and Tonsils

Although the tongue (Video 3.12) can also be seen in a frontal section, the optimal visualization of its whole body requires a sagittal view (Fig. 3.31). In this view, the caudal parts of the tongue base can also be identified (Video 3.13). Within the tongue base, a small area is always covered by the

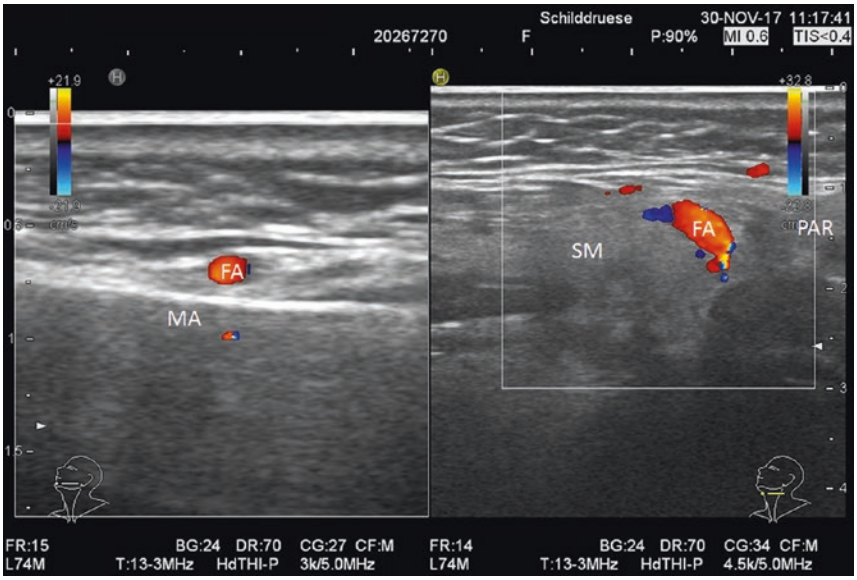

Fig. 3.27 The facial artery (FA) can be detected upon the mandible (MA) and next to the posterior end of the submandibular gland (SM). PAR parotid gland

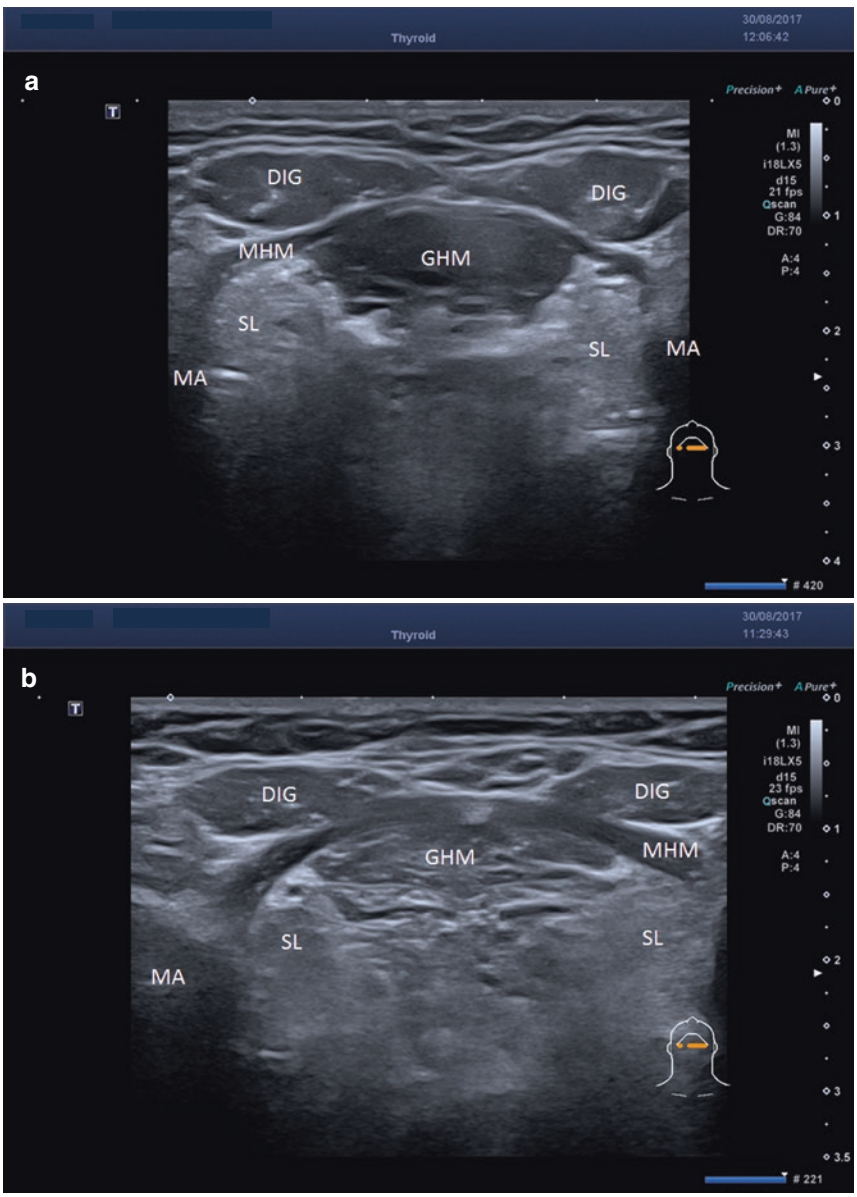

Fig. 3.28 Frontal section through the anterior mouth floor (**a**) and posterior mouth floor (**b**). DIG digastric muscle, GHM geniohyoid muscle, MA mandible, MHM mylohyoid muscle, SL sublingual gland

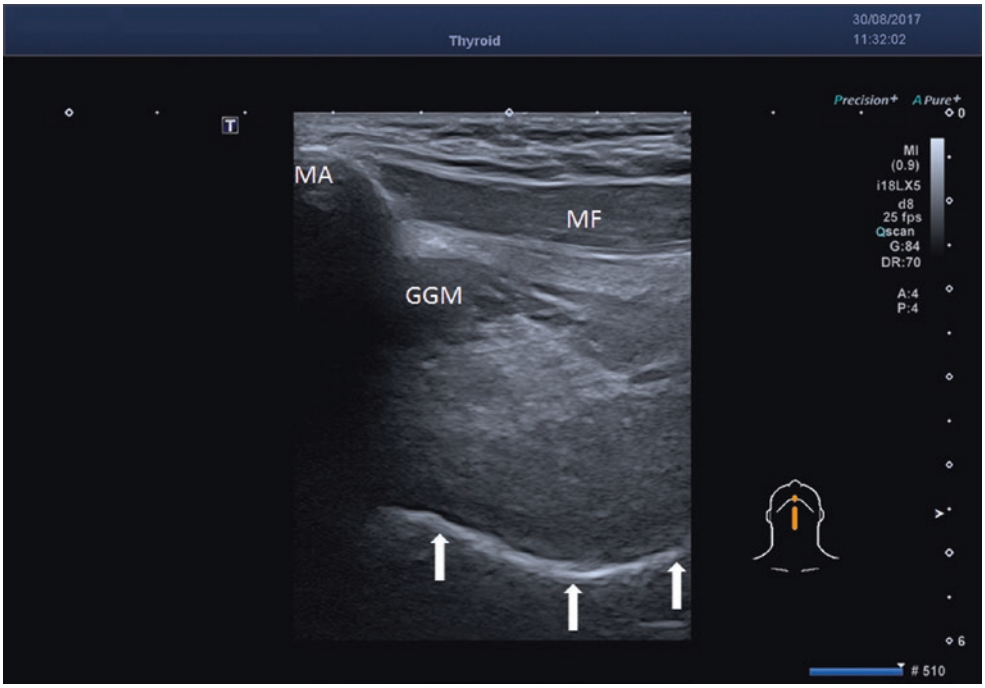

Fig. 3.29 Sagittal section through the mouth floor. The *arrows* mark the tongue surface. GGM genioglossus muscle, MA mandible, MF mouth floor

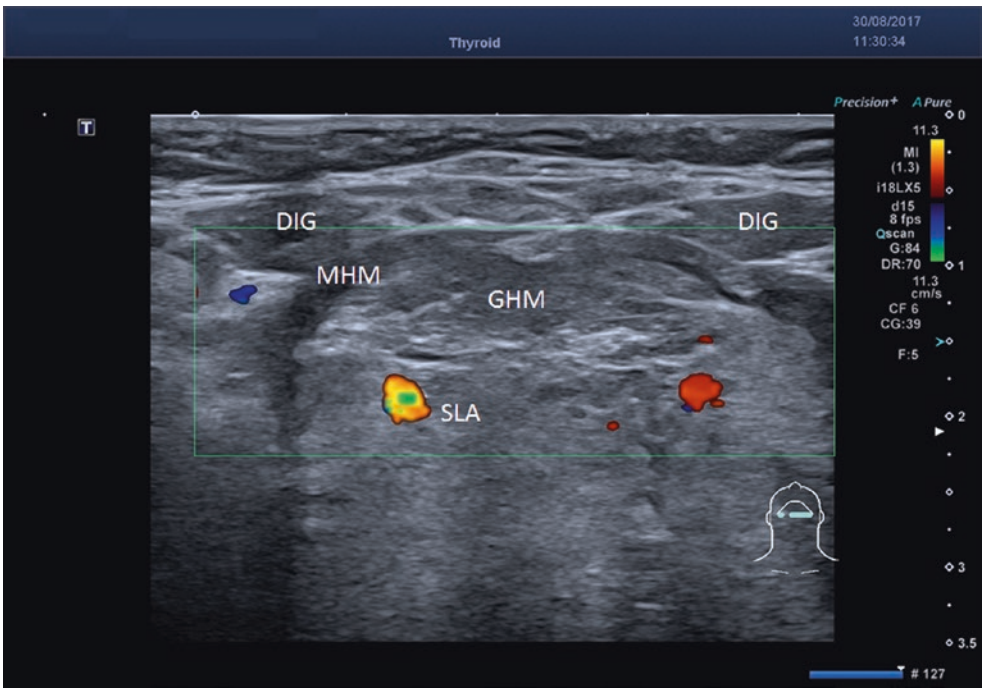

Fig. 3.30 Frontal section through the mouth floor; color-coded sonography detects both sublingual arteries. DIG digastric muscle, GHM geniohyoid muscle, MHM mylohyoid muscle

acoustic shadow of the hyoid (Fig. 3.32), and the examiner should be aware that pathological changes of this region can be overlooked.

The tonsillar region can be seen with an oblique section through the submandibular gland (Fig. 3.33). The tonsils are located next to the tongue and the dorsal part of the submandibular gland [5]. A sonographic differentiation between small tonsils in adults and status after tonsillectomy is often impossible. Compared with adults, in children the tonsils can appear very imposing.

3.3.6 The Parotid Gland and the Cheek

As mentioned before, the parotid gland can be detected next to the submandibular gland. Thus, the array has only to be

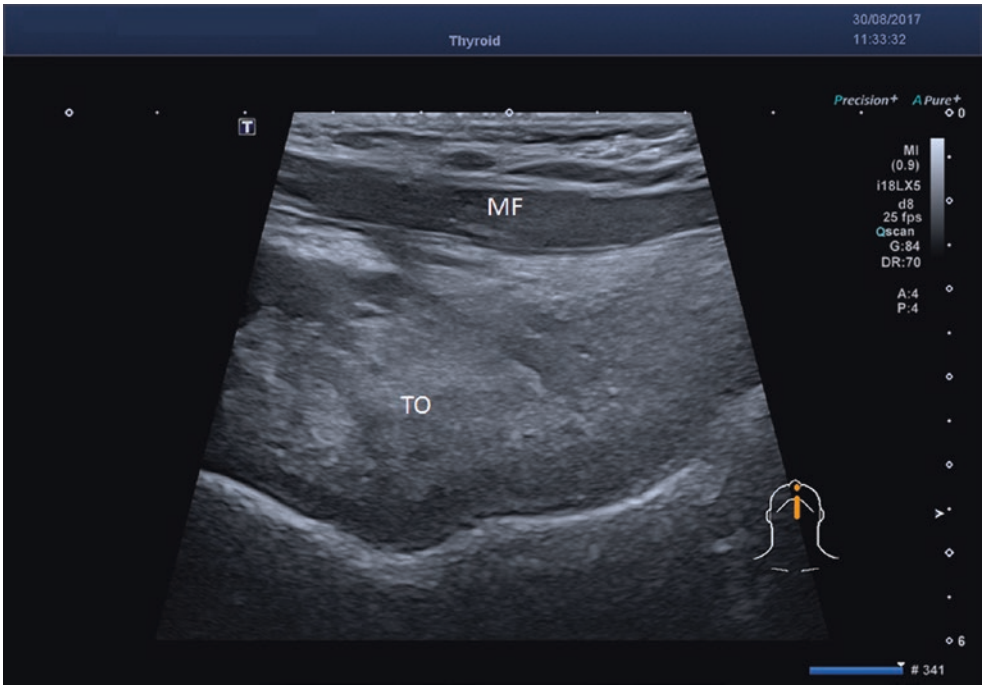

Fig. 3.31 Sagittal view of the tongue body (TO), MF mouth floor

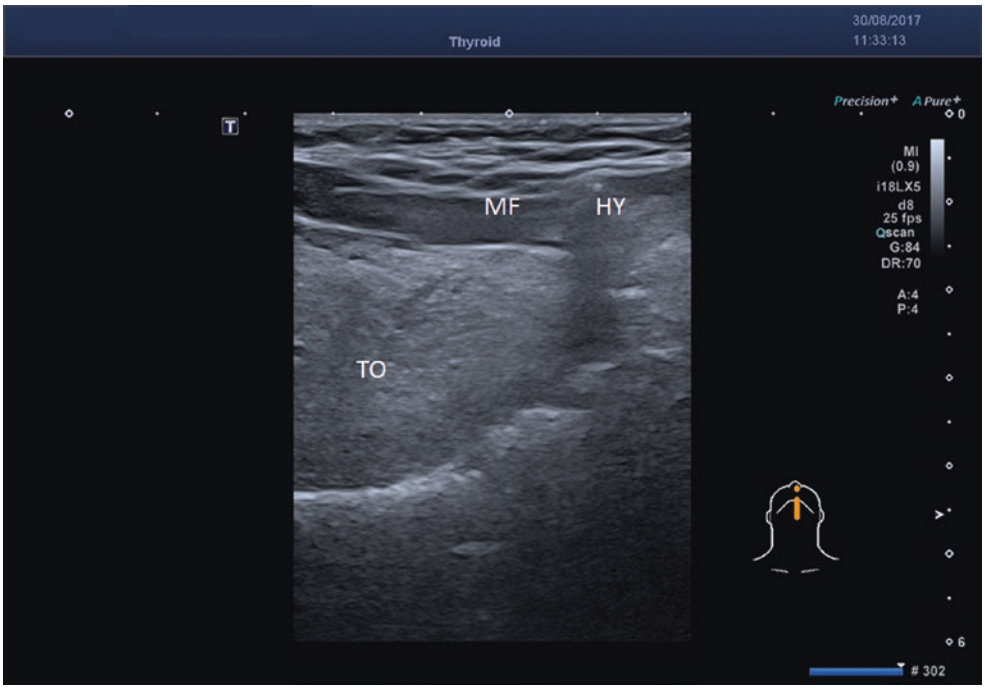

Fig. 3.32 Sagittal view of the tongue base (TO). MF mouth floor, HY hyoid

moved dorsally until the mastoid can be seen. Then, the anterior part of the array must be raised over the mandible to get the standard view of the parotid gland (Fig. 3.34). In the depth, the retromandibular vein can be seen; it divides the gland into a superior and a deep portion (Fig. 3.35). The anterior parts of the gland can be detected if the examiner follows the glandular tissue above the masseter (Fig. 3.36). While the patient bites firmly, a thickening of the masseter can be detected impressively (Fig. 3.37). Similar to the other major glands, the Stensen duct can only be seen in pathological situations. Anterior to the masseter, the cheek and the teeth become visible (Fig. 3.38).

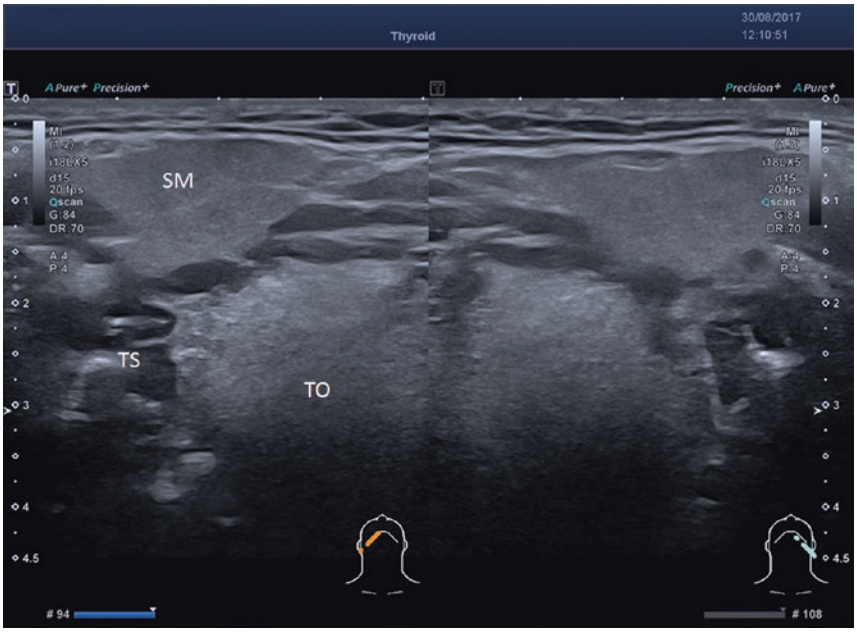

Fig. 3.33 Right and left tonsillar region (TS); SM submandibular gland, TO tongue

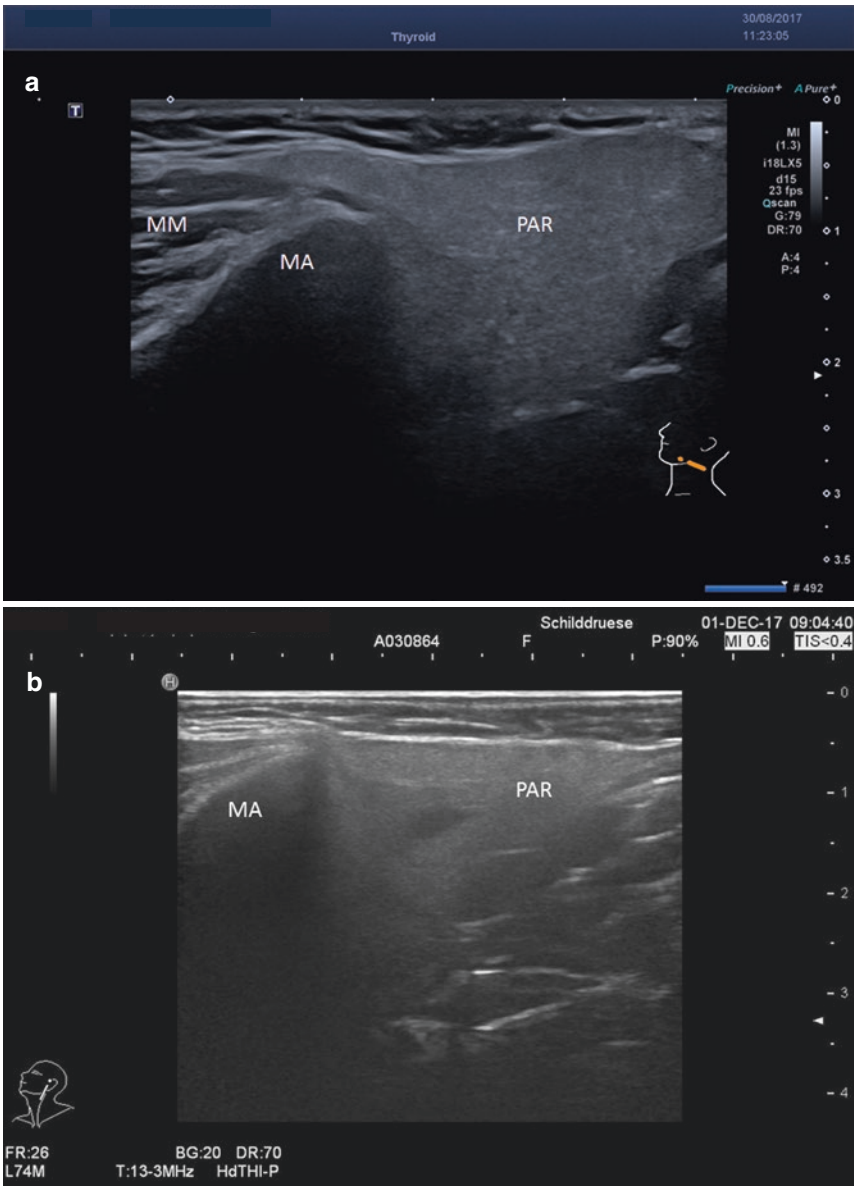

Fig. 3.34 Transverse (**a**) and frontal section (**b**) through the parotid gland (PAR). MA mandible, MM masseter muscle

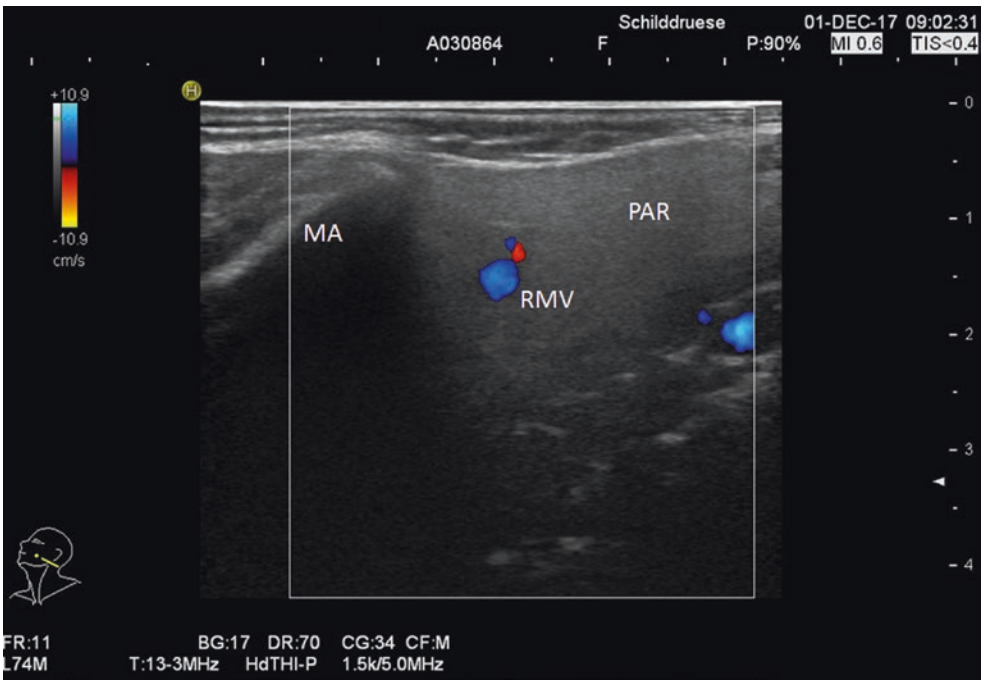

Fig. 3.35 The retromandibular vein (RMV) divides the parotid gland (PAR) into a superficial portion and a deep portion. MA mandible

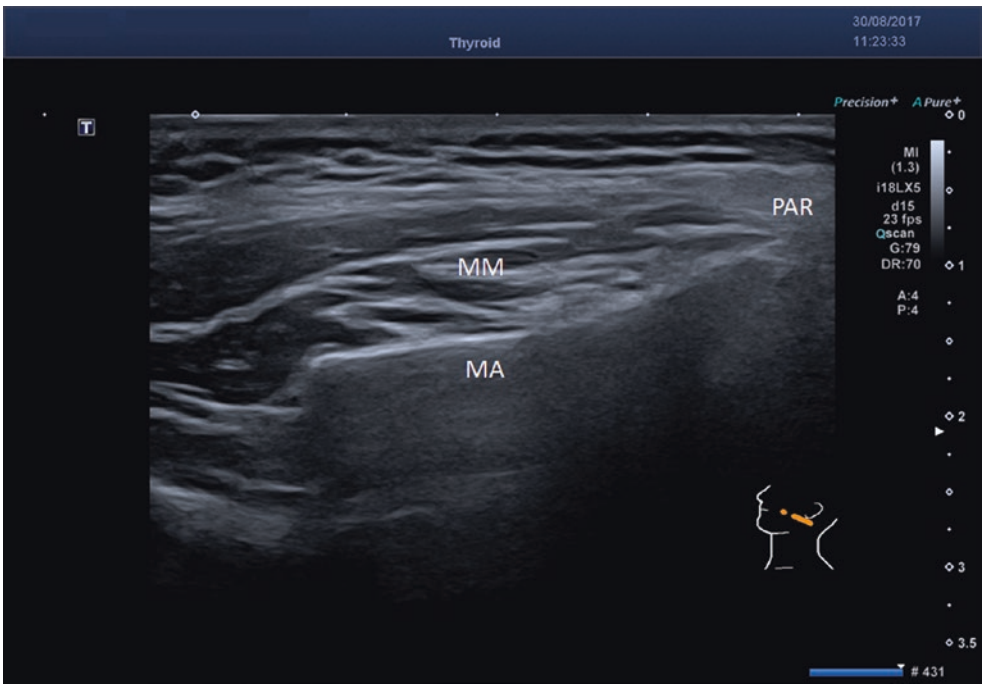

Fig. 3.36 Transverse section through the masseter muscle (MM). MA maxilla, PAR parotid gland

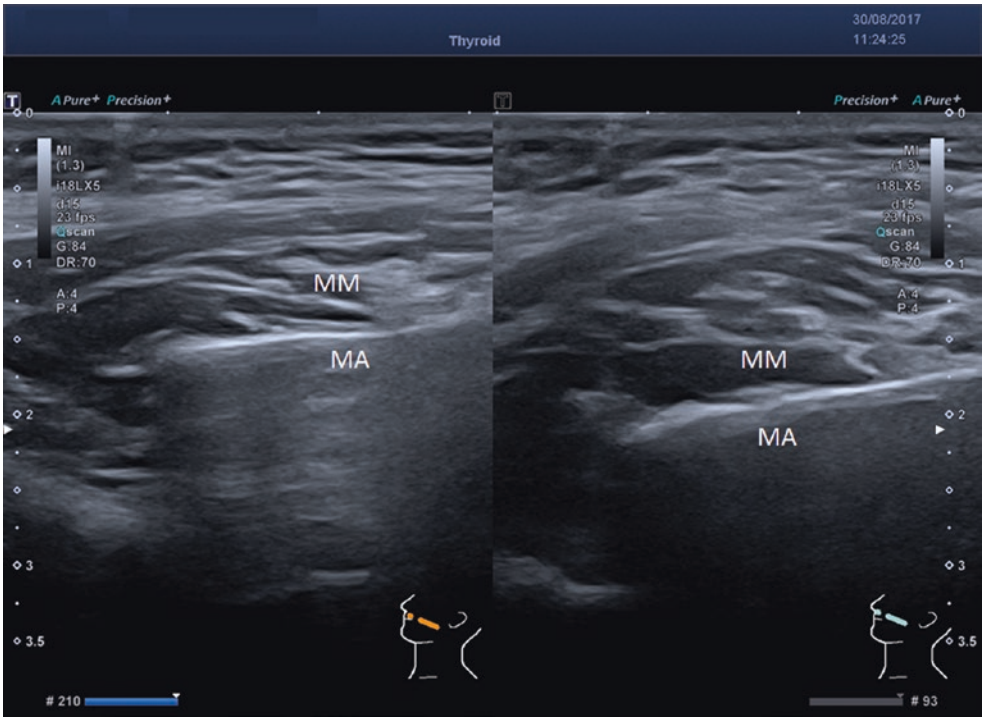

Fig. 3.37 Masseter muscle (MM) during relaxation (*left*) and during biting (*right*). MA maxilla

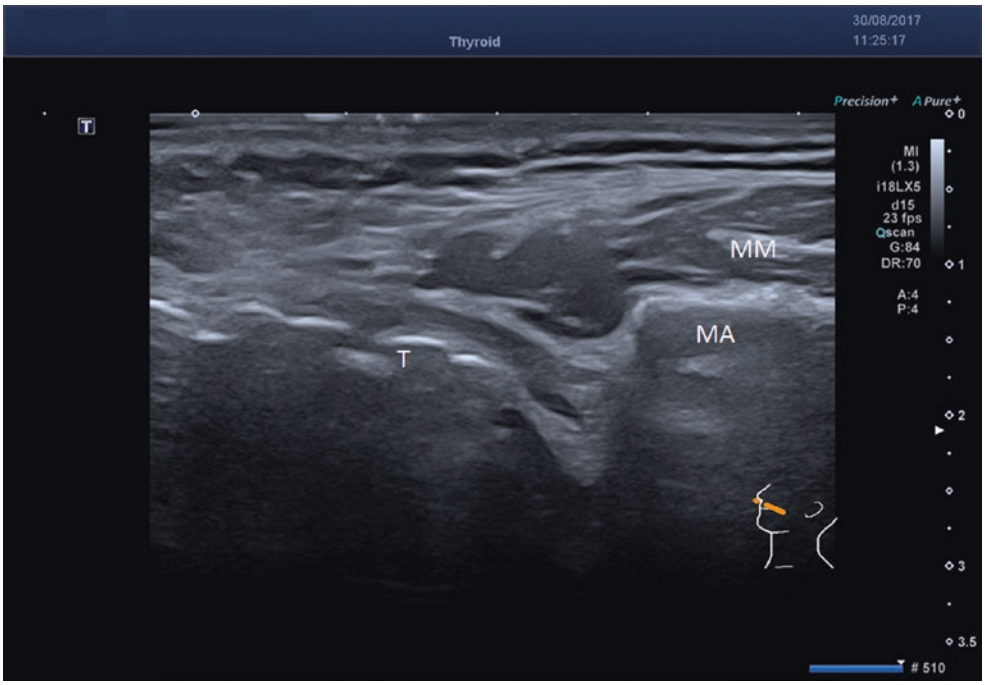

Fig. 3.38 Anterior cheek, transverse plane. MA maxilla, MM masseter muscle, T teeth

References

1. Welkoborsky HJ, Jecker P, Maurer J, Mann WJ. Ultraschalldiagnostik Kopf-Hals. Stuttgart: Thieme; 2013.
2. Orloff LA. Head and neck ultrasonography. 2nd ed. San Diego: Plural Publishing; 2017.
3. Jecker P, Schuon R, Hlawatsch A. Ultrasound of hypopharyngeal and oesophageal cancer: possibilities and limitations to staging and planning of therapy. Ultraschall Med. 2005;26:312–7. German.
4. Bozzato A, Zenk J, Gottwald F, Koch M, Iro H. Influence of thyroid cartilage ossification in laryngeal ultrasound. Laryngorhinootologie. 2007;86:276–81. German.
5. Bandarkar AN, Adeyiga AO, Fordham MT, Preciado D, Reilly BK. Tonsil ultrasound: technical approach and spectrum of pediatric peritonsillar infections. Pediatr Radiol. 2016;46:1059–67.

Interventional Ultrasonography

4

Urban W. Geisthoff and Lisa A. Orloff

4.1 Introduction

Ultrasound guidance can be used to control percutaneous interventions [1]. With fine needles, tissue consistency can be explored, fluids from cysts or other cavities can be aspirated, and chemical agents can be injected for pharmacological therapy or to tattoo regions. Thin needles are used to aspirate cells for cytology, and larger-core biopsy needles can harvest tissue for histological examinations. Laser fibers and radiofrequency probes advanced through needles can coagulate vascular lesions, which can be monitored by ultrasonography. Catheterization of vessels for vascular access or of salivary ducts for drainage is possible. Salivary gland stones can be fragmented and extracted in a minimally invasive way using ultrasound control.

4.2 General Techniques

For the setup, it is advantageous if the patient is positioned between the ultrasound screen and the examiner (Fig. 4.1), so that the examiner can observe both the patient and screen without having to turn around. Depending on the intervention planned, it may be advisable to move the ultrasound machine or the position of the examiner. For example, for a sonographically controlled intervention involving the left parotid gland, the examiner would sit on the opposite (right) side, and the ultrasound screen would be placed on the left side of the patient.

Fig. 4.1 Setting for interventions under sonographic control in the office (**a**) and in the surgery room (**b**). The patient is located between the ultrasound screen and the examiner, allowing the examiner to control the procedure both on the screen and under direct vision without having to turn around

Two major approaches are commonly used to guide interventions with ultrasound: long axis (parallel) and short axis (perpendicular). In the long-axis technique, the long axis of

Electronic Supplementary Material The online version of this chapter (https://doi.org/10.1007/978-3-030-12641-4_4) contains supplementary material, which is available to authorized users.

U. W. Geisthoff
Department of Otorhinolaryngology, Marburg University Hospital, Marburg, Germany

L. A. Orloff (✉)
Department of Otolaryngology–Head and Neck Surgery, Stanford University School of Medicine, Stanford, CA, USA
e-mail: lorloff@stanford.edu

© Springer Nature Switzerland AG 2019

H. J. Welkoborsky, P. Jecker (eds.), *Ultrasonography of the Head and Neck*, https://doi.org/10.1007/978-3-030-12641-4_4

the ultrasound transducer is placed parallel to the planned trajectory of the instrument (Fig. 4.2). The major advantage of this technique is that the needle or instrument can be monitored throughout its entire course toward the target. In the short-axis technique, the instrument is inserted to cross underneath the short axis of the transducer within the patient; the trajectory is perpendicular rather than parallel (Fig. 4.3). In this approach, the instrument is visualized only over a short distance as it passes immediately deep to the ultrasound beam, most often when it is within the target structure. It can be helpful to tilt the transducer very slightly to increase the monitored part of the trajectory. Benefits of this technique are that it also allows the simultaneous visualization of structures that are outside the plane of the target structure and the instrument trajectory. Additionally, sometimes the space on the surface is not sufficient to place the transducer parallel to the axis of the instrument (e.g., in the retromandibular space). Also, the distance the instrument must travel within the tissues is usually shorter than by the parallel approach.

Fig. 4.2 Long-axis technique: The planned trajectory of the instrument is within the plane of the ultrasound transducer; that is, they are parallel

Fig. 4.3 Short-axis technique: The planned trajectory of the instrument is not parallel to the plane of the ultrasound transducer; that is, it will cross this plane at only one point. This technique is often called "perpendicular," but in fact the trajectory is seldom perpendicular to the plane of the ultrasound transducer

The following order is suggested to perform the procedure:

- Visualize the target structure.
- Plan a trajectory avoiding sensitive structures.
- Align the ultrasound transducer and the instrument.
- Start with some distance to the transducer (otherwise, the instrument may not be deep enough or the angle of insertion may be difficult).
- Correct the ultrasound transducer position by very slight adjustments to visualize the target and instrument at the same time. (Avoid gross movements.)
- Visualization of the tip of the instrument is most important to avoid collateral damage and to confirm biopsy or therapy in the correct location.
- If it is not possible to reach the target with the instrument, pull it back. Do not bend the instrument.

The following paragraphs present different applications. This list is not complete, as overlaps, modifications, and additional nonlisted options exist.

4.3 Indications

4.3.1 Punctures

Punctures (or percutaneous insertions) are usually performed using sharp needles penetrating the tissue. Punctures with fine needles or small diameters often do not require local anesthesia. For larger diameters, at least anesthesia of the skin is recommended. Sometimes it even may be advisable to incise the skin with a scalpel before introduction of the puncture device. Local anesthesia too close to the target increases the risk of bloody biopsy specimens. In certain cases with acute infections (such as a deep neck abscess in a child), local anesthesia may not be effective because of the altered pH of the tissues, so that general anesthesia becomes necessary.

Testing of Tissue Consistency

High contrast of acoustical impedance between tissues can result in total reflections. Typically, this can be seen on the surface of calcifications or air-filled structures. Calcifications can be solid stones or accumulations of small calcified structures in the tissue, such as lymph nodes with tuberculosis. The differentiation of these structures using ultrasound can be difficult. Sometimes stones or air can be moved by applying

pressure from the outside, either with the transducer or by palpation (e.g., a finger inside the mouth). The additional use of a needle can add essential information, as air can be aspirated, and solid stones offer resistance to the needle and will be moved visibly (Video 4.1). Small calcifications or soft stones will easily be penetrated by the needle, so that no relevant movement of the structure in relation to the surrounding tissue will result. After identification of a parotid stone by this technique, the needle can also be used to guide a surgeon toward the stone for extraction during open surgery [2].

Aspiration of Liquids and/or Instillation of Therapeutic Liquids or Liquids for Marking Structures

The lumen of the needle can be used both to aspirate and to inject liquids. Aspiration can be used to drain liquid-filled cavities like infected cysts, sialoceles, abscesses, and hematomas (Video 4.2). Fluid for microbial culture can be obtained at the same time. Therapeutic liquids like 96–98% alcohol, picibanil (OKT432), or doxycycline can be injected to sclerose thyroid cysts, lymphoepithelial cysts of the parotid gland, or vascular lesions like lymphatic malformations [3]. The procedure typically involves first aspiration to empty the lesion, followed by injection of the sclerosing agent.

It is important to note that nerve damage (e.g., vocal fold paralysis or facial paralysis, depending on the site of the lesion) can occur [4]. It has been recognized that seepage of the sclerosing agent or nerve compression by a sudden increase in the tissue pressure around the lesion might cause adjacent nerve injury.

In addition to ultrasound guidance for injecting liquid-filled lesions, additional indications include injections into parenchyma, such as the salivary glands, typically in a diffuse (fanlike) manner. An important drug for these injections is botulinum toxin. Botulinum toxin is a bacterial neurotoxic protein that inhibits the release of acetylcholine from axon endings. Type A of this toxin is used for a variety of indications, including muscular hyperactivity (e.g., blepharospasm or cervical dystonia) or to decrease secretion from glands (e.g., hyperhidrosis or hypersalivation) [5–8]. The use of ultrasound can be helpful to ensure that the toxin is delivered near to the relevant axon endings. If the patient has become refractory to botulinum toxin type A, a possible alternative is botulinum toxin type B.

The spectrum of therapeutic options in the head and neck region includes several uses:

- Injection of botulinum toxin into the salivary glands for sialorrhea (Video 4.3) (25 G–27 G needle, total of 100–400 IU per session, distributed onto the large salivary glands. For children, e.g., 30 IE into each parotid and 20 IE into each submandibular gland). Repetition might be necessary after 2–4 months. Recent publications have shown that the use of botulinum toxin for this indication is safe even in the pediatric population [9–11]. Side effects include swallowing disorders, which are usually temporary [12, 13].
- Injection of botulinum toxin into sialoceles or into the gland parenchyma for salivary fistulas after open gland surgery (30–100 IU per gland or lesion, diluted in about 10 mL of saline) [14–16].
- Injection of botulinum toxin into the area of maximum pain for first bite syndrome, occasionally occurring after parapharyngeal space surgery [12, 13]. This procedure often causes very brief but intense pain for the first 5–10 seconds after injection. Therefore, it can be helpful to use an ice pack or ice spray before and after the procedure.
- In contrast to these techniques, the injection of botulinum toxin into the skin for Frey's syndrome after parotidectomy (0.1 IU/cm^2) is usually done without ultrasound control [17–19].

Lesions such as lymph nodes can be marked by dyes before extirpation to facilitate intraoperative identification and ensure retrieval of the intended target [20, 21]. The volumes of dye used are small (up to 0.2 mL), as too much can result in a diffuse staining of a large tissue area. Activated charcoal can be injected even 3 weeks before the procedure, whereas methylene blue is usually injected immediately preoperatively. Intraoperative identification can also be achieved by ultrasound-guided needle localization. The principle is described in detail above, as it can also be used to test for tissue consistency. Foreign bodies in soft tissue (such as wood, plastic, or metal) can be visualized sonographically and marked with a needle before instruments like hemostats are introduced through wound channels to remove the objects or before open surgery is performed for removal [22, 23].

Cytologic Examinations (Fine Needle Aspiration)

Ultrasound-guided fine needle biopsies provide aspirate samples for cytologic, immunocytochemical, and chemical diagnosis (Fig. 4.4) [24–26]. It is important to ensure for fine needle aspiration (FNA) cytology that the needle tip is within the target lesion, to ensure that the cells examined are from the area of interest. Larger needle sizes may gain larger tissue samples but also increase the risk of cell seeding, bleeding, and discomfort for patients. Preferred needle diameters range between 23 G and 27 G, with larger diameters (up to 14 G) used for core biopsies. There is debate about the optimal number of needle passes, which is influenced by many factors, including operator experience, tissue source, technique, and ability to perform on-site microscopic assessment of adequacy. Negative pressure or suction can increase the sample size but also increases the risk of collecting blood, which may hinder the cytologic

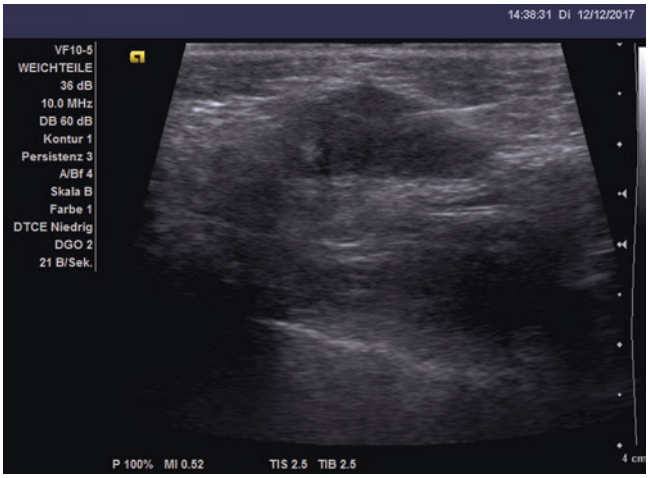

Fig. 4.4 Fine needle aspiration (FNA) cytology under sonographic control in the patient from the figures above. The needle tip can be seen inside the lesion of the anterior parotid gland. In this case, an adenoid cystic carcinoma was diagnosed by cytology

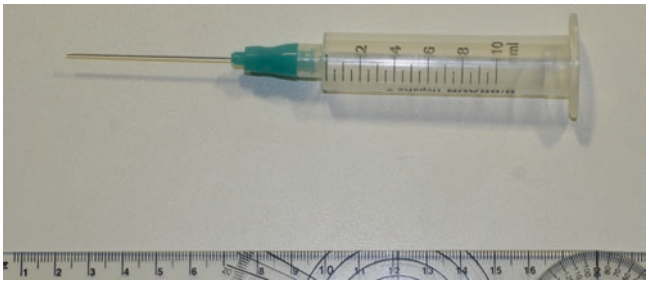

Fig. 4.5 Set for performing FNA with the capillary technique: the plunger of the syringe has been removed. The tissue sample is obtained without any suction, but the plunger can be reinserted to harvest the cells from inside the injection needle

Fig. 4.6 A handle can facilitate FNA using the suction technique (device from Cameco AB, Täby, Sweden)

interpretation. Without suction, only capillary forces and the pressure of the needle perforating the tissue will collect the sample (Fig. 4.5). Suction is usually achieved via a syringe. Specially designed handles facilitate one-handed use (Fig. 4.6). If an assistant is available, the needle might be connected to the syringe by extension tubing. Alternatively, a stopcock between the needle and tube allows the syringe to be "pre-loaded" for one-person use.

Before obtaining the specimen, the preferred method of preparing the sample should be discussed with the pathologist. Some pathologists prefer that a smear be performed on glass slides, while others prefer rinsing the cells for liquid-based processing. The preferred liquid and fixative should also be discussed. The needle also can be rinsed with saline after expelling the specimen, with the needle washout submitted for chemical testing (such as for thyroglobulin or parathyroid hormone).

Histologic Examinations (Core Biopsy)

The diameters of devices for core biopsy (CB) are typically larger than for FNA cytology [25, 26]. Additionally, they usually include a mechanism to cut out a cylindrical specimen from the tissue. Figure 4.7 shows different devices. It is important to note that in some devices the total advancement of the needle is controlled manually (Video 4.4). In other devices, however, the operator must aim and then release the needle, which then advances rapidly by a spring mechanism (Video 4.5). These devices require special caution, as miscalculation of the advancing distance, wrong settings of the device, or movements of the patient can lead to painful or even dangerous complications. One of the authors once hit the vertebral column of a patient, fortunately without adverse results, but we are aware of one tragic, unpublished case from a regional colleague in which the core biopsy included parts of the carotid artery, resulting in a lethal outcome.

The specimen obtained is usually processed like any other histologic sample by being placed in formalin. However, pathologists might ask that tissue for lymphoma studies should be submitted fresh, in saline or tissue support medium.

4.3.2 Destruction of Tissues

Laser therapy of vascular lesions such as venous malformations can be performed percutaneously with ultrasound guidance [27]. However, when using a Nd:YAG laser, the maximum depth of the coagulative effect is about 1 cm. To reach deeper parts of a lesion or to spare the superficial tissue, interstitial therapy is delivered via a cannula that is introduced into the lesion and advanced as far as the coagulation is planned. Larger vessels or high-flow areas should be avoided, as laser coagulation might not achieve sufficient coagulation of these areas. The bare fiber is introduced through the lumen of the steel needle. The tip of the bare fiber can be seen on ultrasound (Fig. 4.8, Video 4.6). However, it is advantageous to mark the bare fiber (e.g., with a Band-Aid or other stop) at the distance to which it

Fig. 4.7 A multitude of devices can be used to obtain core bore biopsies. (**a**) A selection of devices (from left to right, without preference): Chiba Biopsy Needle, 23 G × 5 cm, with "echotip" (a roughened surface near the tip for better echogenicity), Cook Inc., Bloomington, IN, USA; Quick-Core Biopsy Needle, 20 G × 15 cm, Cook Inc., Bloomington, IN, USA; Temno Biopsy System, 20 G × 6 cm, Carefusion/Becton Dickinson, Franklin Lakes, NJ, USA; Magnum Biopsy System, C.R. Bard Inc., Murray Hill, NJ, USA; BioPince, Full Core Biopsy Instrument, 18 G × 10 cm, Argon Medical Devices Inc., Athens, TX, USA; Tru-Cut biopsy device, 18 G × 24 cm, Angiomed, Becton Dickinson, Franklin Lakes, NJ, USA; Spirotome, Soft Tissue Biopsy Needle Set, outer needle (right side around the trocar): 8 G × 15 cm; inner needle with spiral cutting tip (left side): 10 G × 22 cm, Cook Inc., Bloomington, IN, USA; Biopsie Handy, 18 G × 10 cm, Somatex Medical Technologies GmbH, Teltow, Germany. (**b**) Tips of the devices shown. (**c**) Using the Spirotome: outside view. (**d**) Using the Spirotome: sonographic view. Optional port systems (e.g., coaxial introducer systems) are available that allow multiple tissue samples to be obtained through a single insertion site

should be introduced into the cannula, so that either retraction into the plastic cannula or too much protrusion can be avoided. Retraction can result in the coagulation of plastic, and protrusion can result in a broken fiber. After making sure that the fiber is introduced well and aims at the target tissue, coagulation is started. (The Nd:YAG laser can be set to 5–20 W, but the tissue response should be observed.) The tissue usually responds with increasing echogenicity. Both the fiber and the outer plastic cannula are retracted simultaneously, observing the effect on the tissue. In this way, a cylindrical coagulation zone is created. It can be helpful to stop the laser only after total removal of the fiber and cannula, as otherwise bleeding from the puncture site may result.

4.4 Catheterization

4.4.1 Treatment of Stenotic Salivary Ducts

Obstructive sialadenitis is caused either by sialolithiasis (discussed below) or by ductal stenosis. Ultrasound can allow assessment of the length of the stenosis without having to pass through it. Often the duct is dilated proximal to the stenosis because of the blockage of the saliva flow. This dilatation of the proximal part can be increased using a sialagogue, while the distal part can be dilated by flushing the duct from its distal opening with saline, using a plastic IV cannula. Under sonographic control, metal or plastic dilators or balloons can be used to increase the

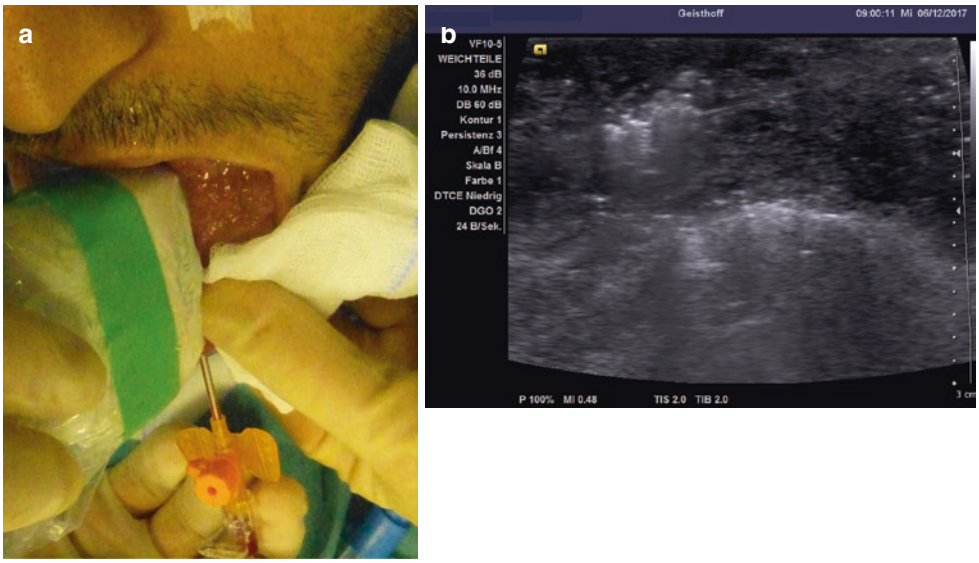

Fig. 4.8 (**a**) A cannula is introduced into a venous malformation of the tongue under sonographic control. In the middle of the steel needle lies a bare fiber, which is advanced to coagulate the tissue. (**b**) The coagulation effect can be monitored by ultrasound

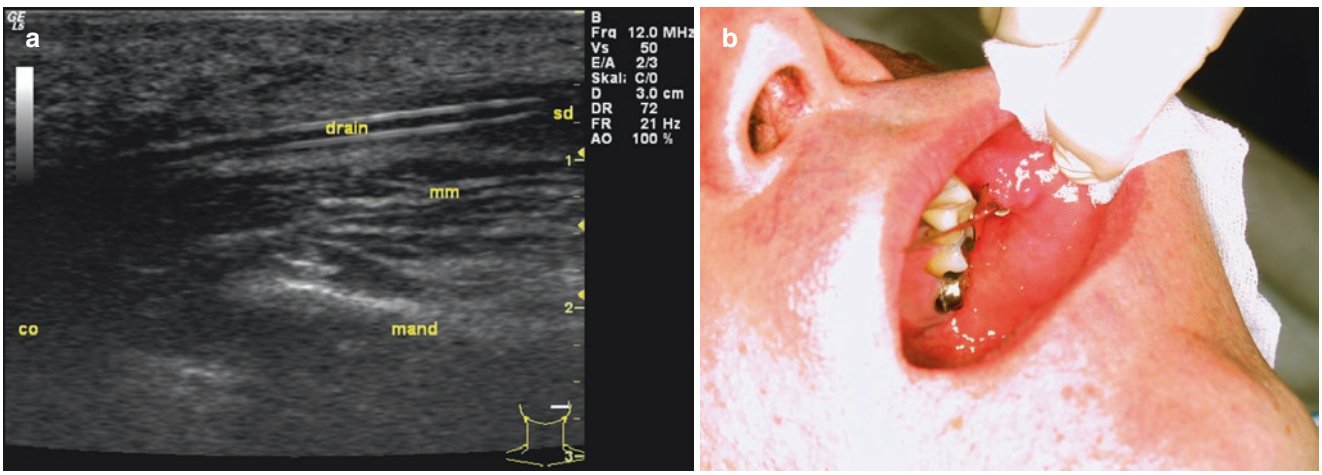

Fig. 4.9 (**a**) A drain has been placed into a stenotic left Stensen's duct under sonographic control. (From Jecker et al. [29], with permission.) (**b**) The probe that has been used for positioning the drain is still inside the drain. co oral cavity (cavitas oris), mand mandible, mm masseter muscle, sd Stensen's duct

diameter of the duct [28, 29]. The effect of the dilation process can be well seen by ultrasound. Plastic or metal dilators can be placed from distal to the stenosis by sonographic control. However, the process of dilation is usually difficult to visualize, as the dilators not only widen the duct but also move it parallel or sideward to the ultrasound transducer (Video 4.7).

Stents or drains can be used to keep the lumen of the dilated duct open (Fig. 4.9). However, this is not universally recommended. Some authors favor only irrigation of the fresh wound with corticosteroids. Stents can be placed under sonographic control (*see* Video 4.7).

4.4.2 Vascular Access/Cannulas

Ultrasound-guided vascular access, which is increasingly used by anesthesiologists and hospitalists, can also be used by head and neck surgeons [30]. After identification of the target vessel, the catheter is usually introduced by either the short-axis or long-axis technique (Video 4.8). It is important to remember that the venous pressure in the area of interest must be sufficient, which can be achieved by placing the region of interest in a dependent position, by the Valsalva maneuver, or by asking the anesthesiologist to increase the PEEP (positive end-expiratory pressure).

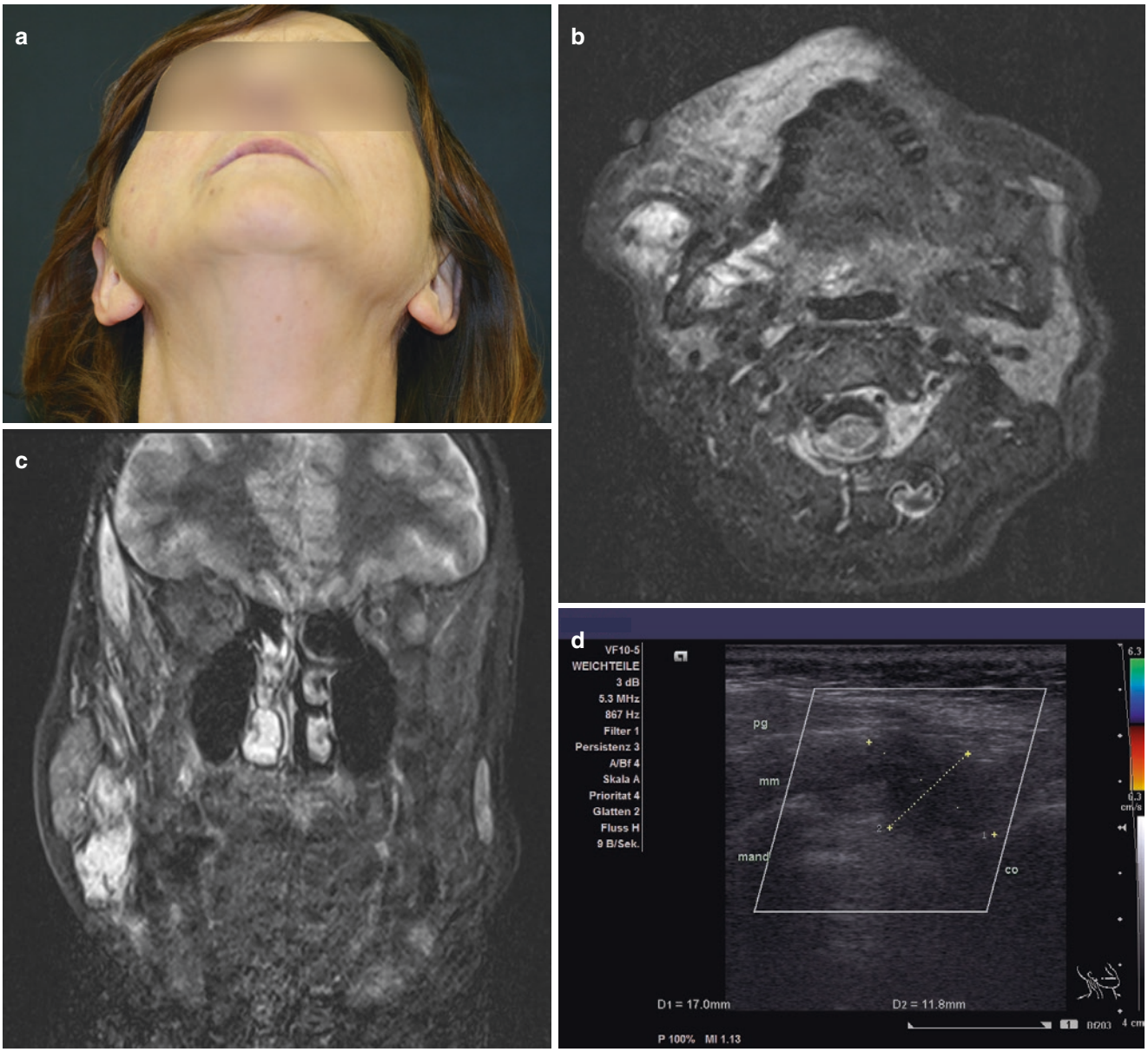

Fig. 4.10 (**a**) Outer aspect of a venous malformation of the right cheek. The intermittent swelling led to recurrent asymmetry and discomfort. (**b, c**) Axial and coronal MRI views of this venous malformation (Courtesy of Prof. Dr. Bien and Dr. Gurschi, Neuroradiology, Univ. of Marburg). (**d**) Sonographic view of the same venous malformation. Sometimes the flow is very low and can barely be detected by duplex sonography. In this case, slight compression of the lesion can induce a visible flow, as in Video 4.9a

A special form of vascular access is the catheterization of a vascular anomaly for radiologically controlled sclerosis, a technique that overlaps with the instillation of therapeutic liquids as discussed above. In this case, the lesion is only identified and punctured under sonographic control. After establishing the access, the sclerosing procedure is performed under sonographic control. Figure 4.10 shows the outer and imaging aspects of a venous malformation before therapy. Video 4.9 demonstrates the flow inside the lesion and the needle inside it. Figure 4.11 shows the angiographic aspect of the lesion after injection of contrast material and Histoacryl glue.

Ultrasound also can be used to select the more suitable side for implantation of a port into the cephalic vein.

4.5 Treatment of Sialolithiasis

4.5.1 Mobilization of the Stone for Drainage

Stones can be mobilized either using the finger (Video 4.10) or by inserting a probe into the duct (Video 4.11), allowing blocked saliva or pus to be excreted. The effect is often only of short

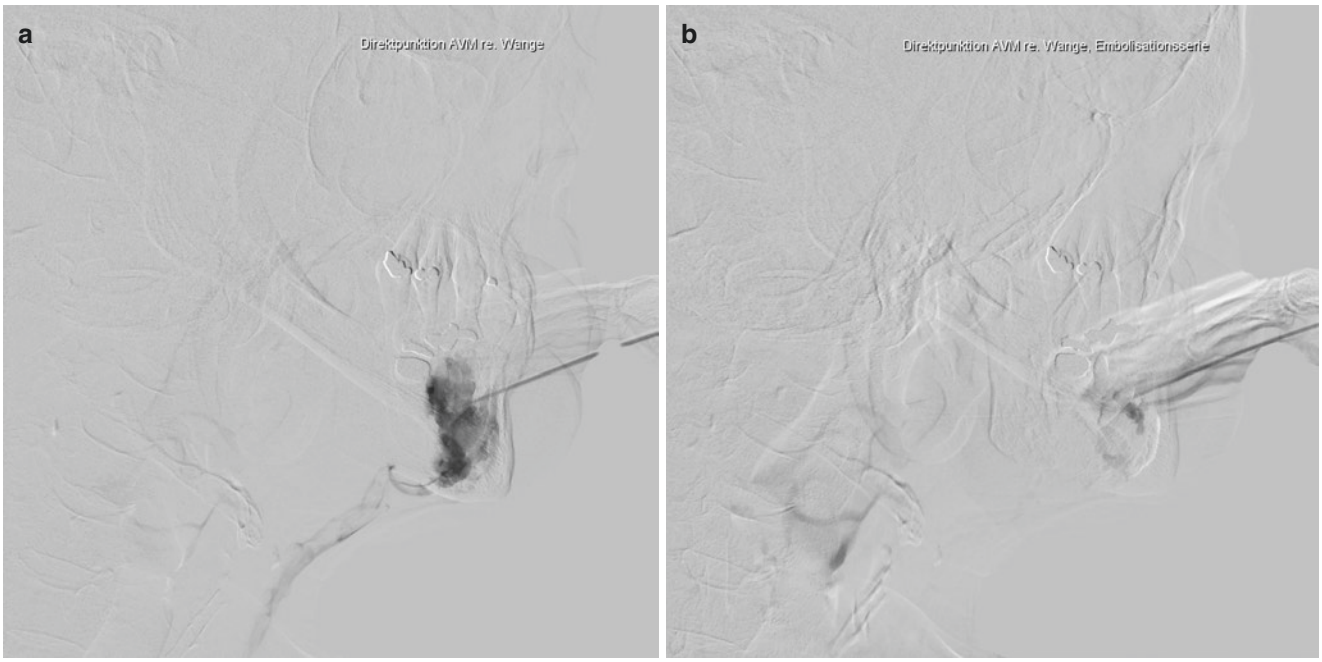

Fig. 4.11 Angiography performed after direct puncture of the venous malformation shown in Fig. 4.10 and Video 4.9, with injection of contrast material (**a**) and Histoacryl glue mixed with contrast material for sclerosis (**b**). (Courtesy of Prof. Dr. Bien and Dr. Gurschi, Neuroradiology, Univ. of Marburg)

duration, as the flow of the secretion will return most stones to the same position, but sometimes a different position is achieved, which leaves enough space next to the stone for secretion.

4.5.2 Extraction of the Stones (Basket or Forceps)

Not only probes but also other instruments can be introduced into the duct through the natural papilla. In addition to ultrasound control, other methods of guidance can be used, including sialendoscopy, haptics, or x-ray (with the disadvantage of radiation exposure) [29]. Haptics are often only sufficient if the pathology is very near to the papilla. Sialendoscopy is often an excellent measure, but it requires special instrumentation and experience. Additionally, part of the duct lumen is occupied by the endoscope, which can prevent the use of larger instruments. It can be helpful to combine different methods (multimodal therapy) to increase the success rate [31].

Both baskets (Fig. 4.12) and miniforceps (such as those used for ear surgery) (Figs. 4.13, 4.14, and 4.15) can be introduced into the lumen of Stensen's or Wharton's duct. This frequently first requires the dilation of the papilla. Afterward, the instrument is directed toward the stone. Reaching the stone can be difficult or even impossible if the duct is tortuous, stenotic, or bifurcated distal to the stone. When the stone is reached, the instrument jaws or wires are opened, and the stone is grasped and extracted (Video 4.12). Extraction is possible only if the duct diameter allows it, however. If in doubt, instruments such as forceps or half-open baskets should be used, which can release the stone in case of blockage. Sometimes, a mini-papillotomy is necessary to overcome the papilla.

4.5.3 Fragmentation of Stones

If the diameter of the stone is too large in relationship to the duct, either the duct has to be dilated, or the stone must be broken into smaller pieces by methods such as extracorporeal shock wave lithotripsy (ESWL) or intraductal pneumatic or laser lithotripsy under sialendoscopic control. Fragmentation by forceps under sialendoscopic control is also possible, but because these forceps are often very small, they can crush only soft stones. Forceps for middle ear surgery, of different diameters and shapes, usually allow application of sufficient force and can be controlled by ultrasound [32, 33]. The fragmentation of the stone can often be felt, heard, and seen on the ultrasound screen (Fig. 4.14, Video 4.13). Often multiple crushing closures of the jaws are necessary. Afterward, the fragments are removed as described above (Fig. 4.15).

ESWL for salivary gland stones is also performed under sonographic control. Figures 4.16 and 4.17 show the setting of ESWL, and Video 4.14 shows the picture on the ultrasound screen during the procedure.

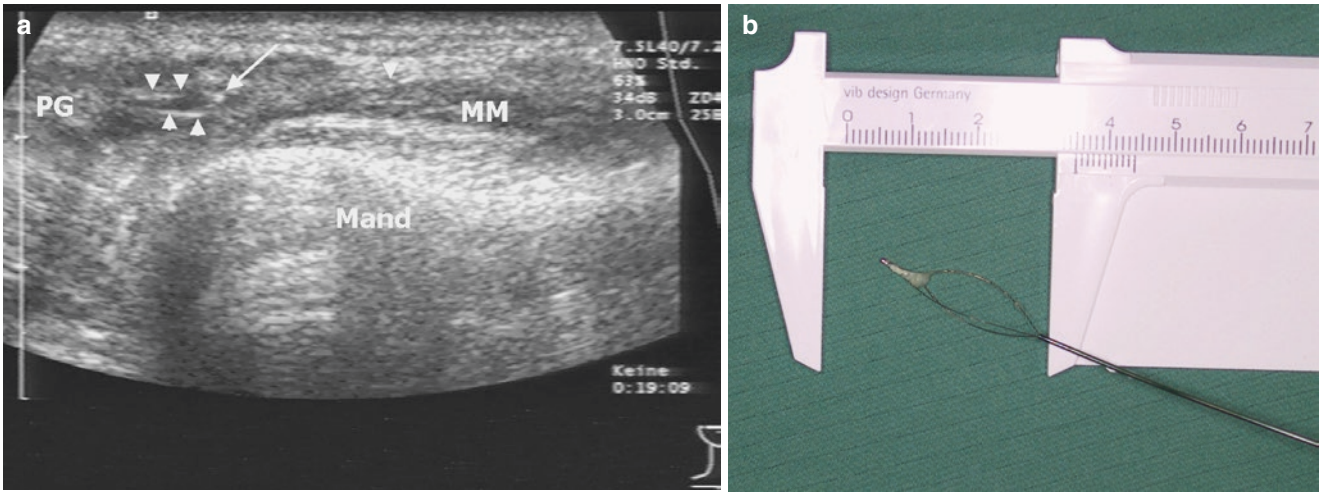

Fig. 4.12 (**a**) A small stone (*arrow*) inside the right Stensen's duct (*single arrowhead*) is grasped by a Dormia basket (*four arrowheads*). Mand mandible, MM masseter muscle, PG parotid gland. (**b**) A small stone has been extracted by a Dormia basket

Fig. 4.13 A small forceps has been introduced into the right Stensen's duct and is now monitored by ultrasonography

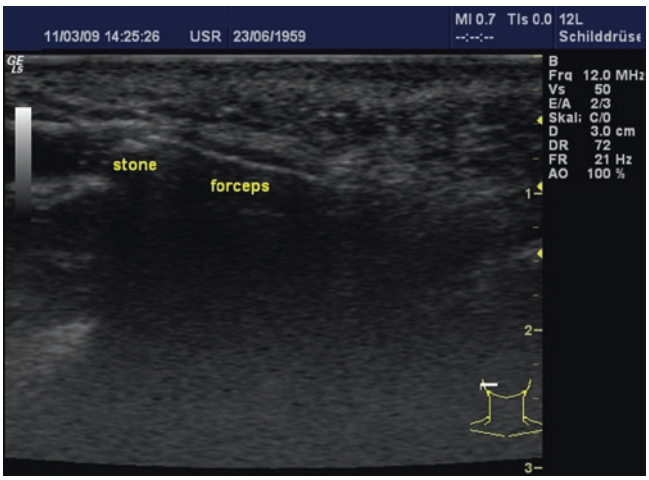

Fig. 4.14 Forceps introduced in right Stensen's duct and grasping a stone. (From Jecker et al. [29], with permission)

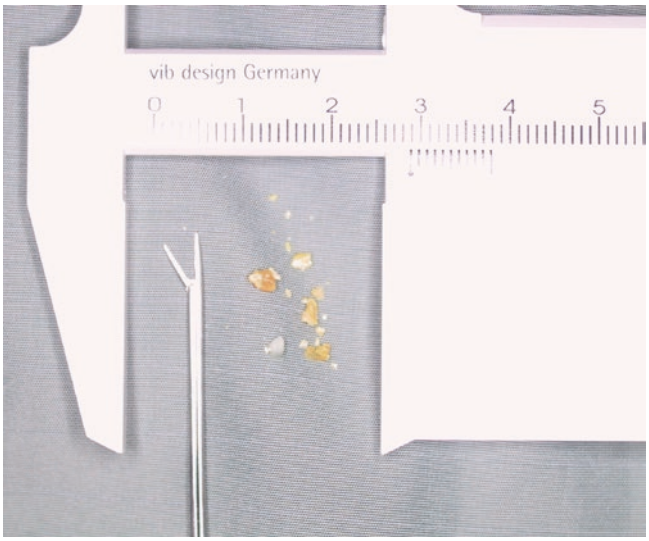

Fig. 4.15 A miniforceps and a salivary gland stone that was fragmented under sonographic control

4.6 Technical Remarks

Industry offers quite a variety of devices that can be used for ultrasound-guided procedures. Echogenicity of the tip of instruments can sometimes be improved by turning the tapered section of the needle tip toward the ultrasound transducer, as this leads to an additional reflection plane. A further increase of echogenicity is produced by the roughening of the polished metal surfaces near the needle tip (*see* Fig. 4.7). As the price is higher than that of normal needles, such needles are used only for more complex circumstances, such as for treatment of handicapped children under local anesthesia.

Fig. 4.16 Extracorporeal shock wave lithotripsy (ESWL) using the Minilith system (Storz Medical, Switzerland). The treatment cushion containing the ultrasound head and the electromagnetic shock wave generator are positioned over the stone

Fig. 4.17 The ultrasound screen of the ESWL machine shows crosshairs in which the stone must be positioned

Attachable needle guides available for some transducers correspond to diagonal lines projected onto the image on the screen. However, they limit flexibility in biopsy direction. Additionally, they can never compensate for a bend of the needle. Such guides are rarely necessary once experience with ultrasound guidance has been obtained.

References

1. Yuen HY, Lee YY, Bhatia K, Ahuja AT. A short review of basic head and neck interventional procedures in a general radiology department. Cancer Imaging. 2013;13:502–11.
2. Joshi AS, Sood AJ. Ultrasound-guided needle localization during open parotid sialolithotomy. Otolaryngol Head Neck Surg. 2014;151:59–64.
3. Kim JH. Ultrasound-guided sclerotherapy for benign non-thyroid cystic mass in the neck. Ultrasonography. 2014;33:83–90.
4. Berenguer B, Burrows PE, Zurakowski D, Mulliken JB. Sclerotherapy of craniofacial venous malformations: complications and results. Plast Reconstr Surg. 1999;104:1–11; discussion 2–5.
5. Karp BI, Alter K. Botulinum toxin treatment of blepharospasm, orofacial/oromandibular dystonia, and hemifacial spasm. Semin Neurol. 2016;36:84–91.
6. Schramm A, Baumer T, Fietzek U, Heitmann S, Walter U, Jost WH. Relevance of sonography for botulinum toxin treatment of cervical dystonia: an expert statement. J Neural Transm (Vienna). 2015;122:1457–63.
7. Farrugia MK, Nicholls EA. Intradermal botulinum A toxin injection for axillary hyperhydrosis. J Pediatr Surg. 2005;40:1668–9.
8. Barbero P, Busso M, Artusi CA, De Mercanti S, Tinivella M, Veltri A, et al. Ultrasound-guided botulinum toxin-A injections: a method of treating sialorrhea. J Vis Exp. 2016;(117) https://doi.org/10.3791/54606.
9. Petracca M, Guidubaldi A, Ricciardi L, Ialongo T, Del Grande A, Mulas D, et al. Botulinum toxin A and B in sialorrhea: Long-term data and literature overview. Toxicon. 2015;107(Pt A):129–40.
10. Porte M, Chaleat-Valayer E, Patte K, D'Anjou MC, Boulay C, Laffont I. Relevance of intraglandular injections of botulinum toxin for the treatment of sialorrhea in children with cerebral palsy: a review. Eur J Paediatr Neurol. 2014;18:649–57.
11. Shariat-Madar B, Chun RH, Sulman CG, Conley SF. Safety of ultrasound-guided botulinum toxin injections for sialorrhea as performed by pediatric otolaryngologists. Otolaryngol Head Neck Surg. 2016;154:924–7.
12. Ali MJ, Orloff LA, Lustig LR, Eisele DW. Botulinum toxin in the treatment of first bite syndrome. Otolaryngol Head Neck Surg. 2008;139:742–3.
13. Ghosh A, Mirza N. First bite syndrome: Our experience with intraparotid injections with botulinum toxin type A. Laryngoscope. 2016;126:104–7.
14. Capaccio P, Cuccarini V, Benicchio V, Minorati D, Spadari F, Ottaviani F. Treatment of iatrogenic submandibular sialocele with botulinum toxin. Case report. Br J Oral Maxillofac Surg. 2007;45:415–7.
15. Chow TL, Kwok SP. Use of botulinum toxin type A in a case of persistent parotid sialocele. Hong Kong Med J. 2003;9:293–4.
16. Pantel M, Volk GF, Guntinas-Lichius O, Wittekindt C. Botulinum toxin type B for the treatment of a sialocele after parotidectomy. Head Neck. 2013;35:E11–2.
17. Austin T, Davis J, Chan T. Sialolithiasis of submandibular gland. J Emerg Med. 2004;26:221–3.
18. de Bree R, Duyndam JE, Kuik DJ, Leemans CR. Repeated botulinum toxin type A injections to treat patients with Frey syndrome. Arch Otolaryngol Head Neck Surg. 2009;135:287–90.
19. Drobik C, Laskawi R, Schwab S. Therapy of Frey syndrome with botulinum toxin A. Experiences with a new method of treatment. [Article in German]. HNO. 1995;43:644–8.
20. Yamamoto S, Maeda N, Yoshimura K, Oka M. Intraoperative detection of sentinel lymph nodes in breast cancer patients using ultrasonography-guided direct indocyanine green dye-marking by real-time virtual sonography constructed with three-dimensional computed tomography-lymphography. Breast. 2013;22:933–7.

21. Eppstein AC, Munshi IA, Sakamoto B, Gwirtz K. Ultrasonography-guided identification with methylene blue tattooing of the ilioinguinal nerve for neurectomy for chronic pain: a case series. JAMA Surg. 2015;150:180–2.
22. Hiremath R, Reddy H, Ibrahim J, Haritha CH, Shah RS. Soft tissue foreign body: utility of high resolution ultrasonography. J Clin Diagn Res. 2017;11:TC14–6.
23. Paziana K, Fields JM, Rotte M, Au A, Ku B. Soft tissue foreign body removal technique using portable ultrasonography. Wilderness Environ Med. 2012;23:343–8.
24. Ahn D, Kim H, Sohn JH, Choi JH, Na KJ. Surgeon-performed ultrasound-guided fine-needle aspiration cytology of head and neck mass lesions: sampling adequacy and diagnostic accuracy. Ann Surg Oncol. 2015;22:1360–5.
25. Kraft M, Laeng H, Schmuziger N, Arnoux A, Gurtler N. Comparison of ultrasound-guided core-needle biopsy and fine-needle aspiration in the assessment of head and neck lesions. Head Neck. 2008;30:1457–63.
26. Saha S, Woodhouse NR, Gok G, Ramesar K, Moody A, Howlett DC. Ultrasound guided core biopsy, fine needle aspiration cytology and surgical excision biopsy in the diagnosis of metastatic squamous cell carcinoma in the head and neck: an eleven year experience. Eur J Radiol. 2011;80:792–5.
27. Werner JA, Lippert BM, Gottschlich S, Folz BJ, Fleiner B, Hoeft S, et al. Ultrasound-guided interstitial Nd: YAG laser treatment of voluminous hemangiomas and vascular malformations in 92 patients. Laryngoscope. 1998;108:463–70.
28. Geisthoff U, Hoffmanns L, Al-Habib A, Maune S. Sonographisch kontrollierte, minimal-invasive Verfahren zur Behandlung der obstruktiven Sialadenitis aktuelle Ergebnisse und neue Techniken. Abstractband zur 84 Jahresversammlung der Deutschen Gesellschaft für Hals-Nasen-Ohren-Heilkunde, Kopf- und Hals-Chirurgie eV, 8-1252013 Nürnberg. Mönchengladbach: Rheinware Verlag; 2013.
29. Jecker P, Geisthoff U, Meyer JE, Orloff LA. Salivary gland ultrasonography. In: Orloff LA, editor. Head and neck ultrasonography. 2nd ed. San Diego: Plural Publishing Inc.; 2017.
30. Wacker F, Wolf KJ, Fobbe F. Percutaneous vascular access guided by color duplex sonography. Eur Radiol. 1997;7:1501–4.
31. Geisthoff U. Techniques for multimodal salivary gland stone therapy. Oper Tech Otolaryngol. 2007;18:332–40.
32. Geisthoff UW, Lehnert BK, Verse T. Ultrasound-guided mechanical intraductal stone fragmentation and removal for sialolithiasis: a new technique. Surg Endosc. 2006;20:690–4.
33. Geisthoff UW, Maune S. Ultrasound-guided mechanical fragmentation of sialoliths (sonoguide forceps). Head Neck. 2010;32:1641–7.

Sonography of Lymph Nodes in the Neck

5

Jens E. Meyer

Lymph nodes occur frequently in the neck area. In most cases, they are benign, but it is always necessary to consider lymph node enlargement in combination with the patient's history, clinical signs, laboratory findings, and imaging results. In some cases, the application of interventional techniques such as ultrasound-guided fine-needle aspiration (USFNA) or ultrasound-guided core biopsy (USCB), contrast-enhanced ultrasound (CEUS), or lymphadenectomy with histology is required.

For a systematic evaluation of neck lymph nodes, it is recommended to begin the examination with plain B-mode ultrasonography at least in two different planes, mostly in a cross-sectional (axial, horizontal) and longitudinal (sagittal, vertical) plane. With this information, qualitative parameters such as homogeneity, presence or absence of a hilum, and the echostructure of the lymph node can be estimated (Table 5.1). As the next step, it is reasonable to switch to qualitative parameters and then measure the two cross-sectional/axial diameters and the longitudinal diameter. In a large study of head and neck squamous cell cancer (HNSCC), it could be shown in a multivariate analysis that diameters and derived values, e.g., volume and Steinkamp/Solbiati index, are the most significant parameters for detection of malignant transformation (Table 5.1) [1].

In addition, color-coded duplex and power Doppler sonography or the administration of contrast media can assist in further differential diagnosis (Tables 5.2 and 5.3) [2]. The ultrasound (US) report should convey nodule size (in three dimensions) and location (e.g., level IIA right) and a description of the nodule's sonographic features, including composition (solid, cystic proportion, or spongiform), echogenicity, margins, presence and type of calcifications, shape (if taller than wide), and vascularity. The pattern of sonographic features associated with a nodule confers the risk of malignancy and, combined with nodule size, guides FNA decision-making (Table 5.3).

5.1 Differential Diagnosis

5.1.1 Reactive Lymphadenopathy

Characteristics Oval, presence of hilum, normal cortex, longitudinal diameter <15–18 mm, short cross-sectional diameter <5–8 mm, Solbiati/Steinkamp's L/S ratio <2, absence of or hilar vascularization on color/Doppler mode, rarely peripheral vascularization type, no other suspicious signs.

Plain grayscale ultrasonography Reactive hyperplasia is a common cause of cervical lymph node (CLN) enlargement and by far the most frequent type of lymph node enlargement that ultrasonography can visualize. The number of normal CLNs varies considerably among individuals and decreases with age. Although reactive CLNs tend to be smaller than nodes of infectious or bacterial lymphadenitis and lymphoma nodes, the size alone cannot be used as the single criterion in the differential diagnosis of cervical lymphadenopathy [3, 4]. Especially in children, CLNs can reach diameters of 20 mm or more (Fig. 5.1), although less than 10 mm in diameter is considered to be normal in children younger than 12 years, and small CLNs in the anterior neck levels are usually regarded as benign in children [5, 6]. In adults, generally smaller diameters are thought to be reactive, whereas larger diameters, especially if the CLN is round in shape, are interpreted as a malignant condition, although exact sizes vary tremendously.

Electronic Supplementary Material The online version of this chapter (https://doi.org/10.1007/978-3-030-12641-4_5) contains supplementary material, which is available to authorized users.

J. E. Meyer (✉)
Department of ENT, Head, Neck, and Plastic Surgery,
Semmelweis University, Hamburg, Germany
e-mail: jens.meyer@asklepios.com

© Springer Nature Switzerland AG 2019

H. J. Welkoborsky, P. Jecker (eds.), *Ultrasonography of the Head and Neck*, https://doi.org/10.1007/978-3-030-12641-4_5

Table 5.1 Characteristics of different CLN diseases: plain grayscale US

Disease	Inflammatory lymphadenopathy					Malignant lymphadenopathy		
Sonographic signs	Reactive lymphadenopathy	Infectious mononucleosis	Tuberculous lymphadenopathy	Non-tuberculous lymphadenopathy	Suppurative/necrotizing lymphadenopathy/ abscesses	HNSCC lymph node metastases	Thyroid carcinoma lymph node metastases	Lymphoma nodes
Size	LD <15–18 mm SD <5–8 mm	Large longitudinal diameters	No specific sizes	19 mm > LD < 44 mm	No specific sizes	LD >18 mm SD >8–10 mm	No specific sizes Increased short axis	LD <18 mm SD >8–10 mm
Shape	Elliptical (L/S < 2)	Round (L/S > 2)	Round (L/S > 2)	Round, but not specific (satellite-like CLNs)	Not specific	Round (L/S > 2)	Round (L/S > 2)	Elliptical (L/S < 2)
Nodal borders	Unsharp	Sharp	Irregular>sharp (Nodal matting, soft tissue edema)	Irregular>sharp (Nodal matting, soft tissue edema)	Unsharp (Nodal matting, clumping, perinodal edema)	Sharp/unsharp (extracapsular spread)	Sharp	Sharp
Echogenic hilum	Present >5 mm	Hyperechoic hilum	Absent (displaced hilar vessels)	Absent (displaced hilar vessels)	Absent	Absent	Absent	Present
Echogenicity	Hypoechoic	Hyper-/ hypoechoic	Stage I/II hypoechoic >Stage III hypoechoic mass with heterogeneous echogenicity	Stage I marked decreases of echogenicity Stage II heterogeneous echogenicity	Hyper-/hypoechogenic areas following a salt-and-pepper pattern (lost echostructure, inhomogeneous)	Hyper-/ hypoechoic In-/ homogenous	Hyperechoic tissue looking like thyroid	Homogenous with intranodal reticulation (micronodular echopattern)
Calcifications	Absent	Absent	Single or multiple coarse, hyperechoic spots created by scattered calcifications or hyalinosis	Multiple intranodal calcifications characteristic of end-stage infection	Seldom	Absent	Punctate and peripheral microcalcifications	Seldom, mostly after treatment
Intranodal liquefaction	Absent	Seldom (abscess formation)	>Stage III (cold abscesses), IV (collar stud abscess), V (sinus tract formation)	>Stage II intranodal cystic necrosis (fluctuant appearance)	Obligate liquid areas	Common (intranodal necrosis)	Common (cystic areas)	Seldom unless pretreated or advanced disease

Table 5.2 Characteristics of different CLN diseases: Doppler US and CEUS

Disease	Inflammatory lymphadenopathy					Malignant lymphadenopathy		
Sonographic signs	Reactive lymphadenopathy	Infectious mononucleosis	Tuberculous lymphadenopathy	Non-tuberculous lymphadenopathy	Suppurative/ necrotizing lymphadenopathy/ abscesses	HNSCC lymph node metastases	Thyroid carcinoma lymph node metastases	Lymphoma nodes
Doppler sonographic vascular pattern	Hilar vasculature or avascular	Hilar vasculature with symmetric radial tree-like vascular pattern Low resistance index (RI < 0.6)	High vasculature	Variable vascularity depending on the rate of growth and the development of necrotic areas	High vasculature	Peripheral or mixed vasculature	Indeterminate: increased central vasculature Suspicious: peripheral or diffusely increased vasculature	High vasculature with mixed (hilar and peripheral) pattern
Contrast-enhancement US	Most accurate illustration of nodal vasculature and additional information on LN parenchymal perfusion	Unknown	Not specific	Not specific	Contrast media accumulation	Most accurate illustration of nodal vasculature and additional information on LN parenchymal perfusion	Not specific	Most accurate illustration of nodal vasculature and additional information on LN parenchymal perfusion

Table 5.3 Characteristics of different CLN diseases: supplemental characteristics

Disease	Inflammatory lymphadenopathy					Malignant lymphadenopathy		
Sonographic signs	Reactive lymphadenopathy	Infectious mononucleosis	Tuberculous lymph adenopathy	Non-tuberculous lymphadenopathy	Suppurative/ necrotizing lymphadenopathy/ abscesses	HNSCC lymph node metastases	Thyroid carcinoma lymph node metastases	Lymphoma nodes
Supplemental characteristics	Absent	Commonly matting or clumping	Nodal matting and adjacent soft tissue edema Echogenic thin layer Lymph node packages "Malignant appearance" Can mimic all other lymphadenopathies	Involved CLN levels submandibular, preauricular and rarely parotid Mainly unilateral Development of satellite-like nodules Nodal matting and adjacent soft tissue edema Livid discoloration and thinned out, shiny appearance ("parchment-like") of overlying skin Lymphocutaneous fistulas/ draining wound (sinus-like, echogenic intrinsic reflexes with and without acoustic shadows)	Fusion Huge conglomerates Nodal matting or clumping Perinodal edema	Perinodal edema through extracapsular spread and after previous radiation therapy	Uncommon	Uncommon
US elastography	Soft	Unknown	Stiff (induration)	Unknown	Variable stiffness	Stiff	Stiff	Soft
US-guided FNAC/CBC	High sensitivity, specificity, and accuracy	Laboratory diagnostics	Unknown	Unknown	Aspiration of pus helpful for antibiotic resistance testing	High sensitivity, specificity, and accuracy Stages correctly neck nodes in 93% of patients with HNSCC	High sensitivity, specificity, and accuracy Measurement of thyroglobulin in needle washouts	High sensitivity, specificity, and accuracy

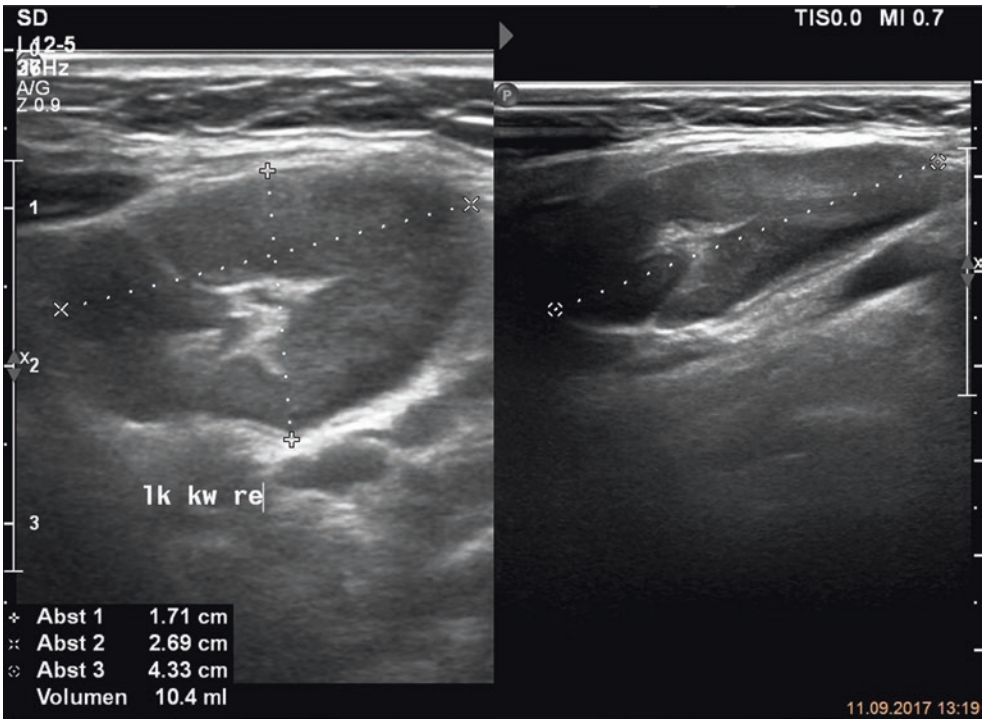

Fig. 5.1 Reactive, juvenile CLN with huge diameters

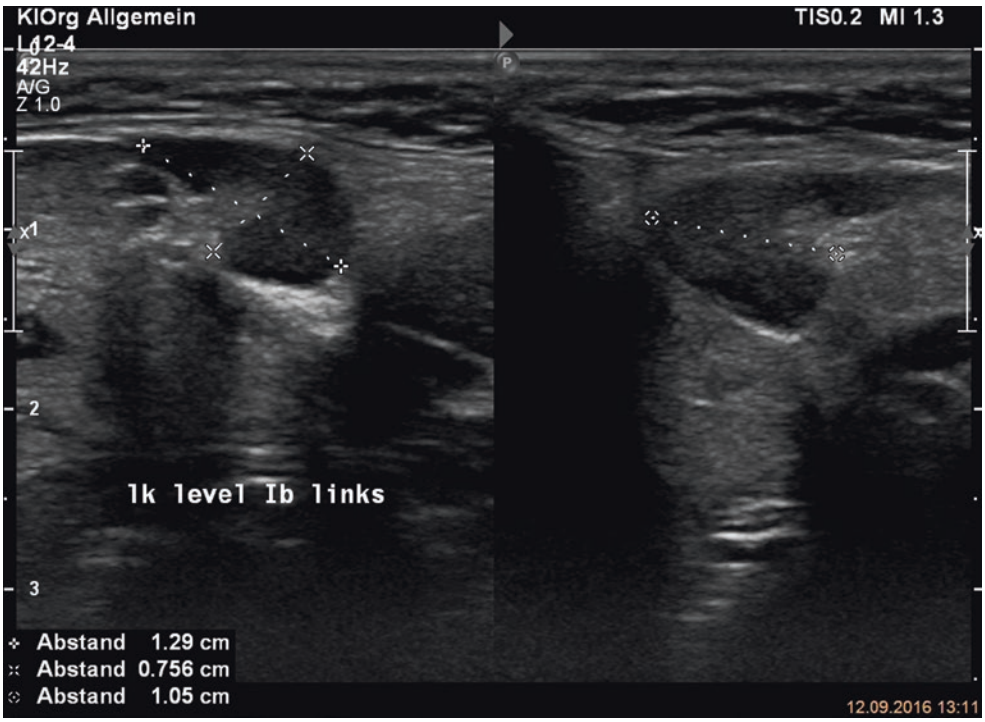

Fig. 5.2 Characteristic examples of a reactive CLN with a hilum and a longitudinal diameter less than 18 mm and a minimal diameter less than 8 mm

In various studies, the longitudinal, cross-sectional, and minimal transverse diameters have been recommended for the assessment of CLNs [7–11]. In a larger cohort study of 290 patients, interpretation of the ROC curve suggested that a long-axis measurement of 18 mm is a good cutoff value to distinguish reactive from malignant CLNs (Fig. 5.2) [1]. Because the data in the literature vary significantly, the longitudinal axis is of rather poor diagnostic value, however, and the shortest axis or the ratio of long to short axis diameters (Steinkamp/Solbiati index) should be considered [12]. Hajek and colleagues have suggested that reactive CLNs have a maximal shortest axis of no more than 5 mm, with a cutoff value for the minimal diameter of 8 mm, which was confirmed by several other groups (Fig. 5.2) [1, 13–15].

Another interesting issue is the calculation of ratios of diameters. On one hand, this reduces false-positive and false-negative results, and on the other hand, it is possible to estimate two-dimensional and three-dimensional forms of a lymph node. A ratio of long to short axis diameter above 2 is thought to be oval and reactive. The study group led by Vassallo presented a sensitivity of 85% and a specificity of 86% for this criterion [16]. Other published data in this field has concluded that the Steinkamp/Solbiati ratio (L/S, longer to shorter diameters) is the most conclusive parameter (Fig. 5.3) [12].

There is common agreement that round lymph nodes tend to be malignant and oval nodes tend to be benign [15, 17–20]. However, a round-shaped CLN (L/S ratio <2) can be found in up to 36% of healthy patients [21–25]. Furthermore, every malignant lymph node at an early stage of conversion can still be oval-shaped [18].

A lymph node hilum corresponds to the site where the afferent and efferent vessels pass the capsule of the lymph node. It can easily be visualized sonographically by both B-mode and color duplex sonography (Fig. 5.4). A hilum occurs in 28.6–87% of normal CLNs [21–24]. Nevertheless, the hilar vascularization is seen in only about two thirds of normal CLNs by B-mode grayscale sonography, so color duplex sonography is the method of choice to clarify whether a lymph node has hilar vascularization. The absence of a hilum or hilar vascularization may be without significance, but the presence of a normal hilum virtually eliminates suspicion of malignancy in the majority of cases. Although peripheral vascularization stands for malignant transformation of a CLN, it can also be seen in up to 18% of benign CLNs [21–24].

Doppler ultrasonographic assessment of intranodal vascular resistance Furthermore, Doppler sonography elicits an intranodal vascular pattern of CLNs, which has been reported to have a reproducibility of 85% [26]. Normal and reactive lymph nodes with maximal transverse diameter greater than 5 mm show a hilar vascular pattern in about 90% of all CLNs in a normal neck, whereas small CLNs with a maximal transverse diameter less than 5 mm usually appear avascular (Figs. 5.5 and 5.6; Video 5.1) [18, 27–31]. Evaluation of the vascular pattern of CLNs may not distinguish between different benign nodal diseases, however, as their vascular patterns vary with the duration of illness [32, 33].

Additionally, spectral Doppler US allows calculation of the vascular resistance of the intranodal vessels. Because of inconsistent results in previous studies and poor reproducibility, to date the value of spectral Doppler US evaluation of intranodal vascular resistance is limited in routine clinical practice, however [31, 32, 34–39].

Qualitative elastographic assessment It is well known that benign lymph nodes tend to be soft, whereas malignant lymph nodes are usually firm. The firmness is classified in qualitative real-time elastograms into four or five grades [40–43]. For qualitative US elastography as a single parameter to distinguish between benign and malignant conditions, the sensitivity, specificity, and overall accuracy have been reported to be 62.2–88.4%, 35.3–100%, and 66.3–89%,

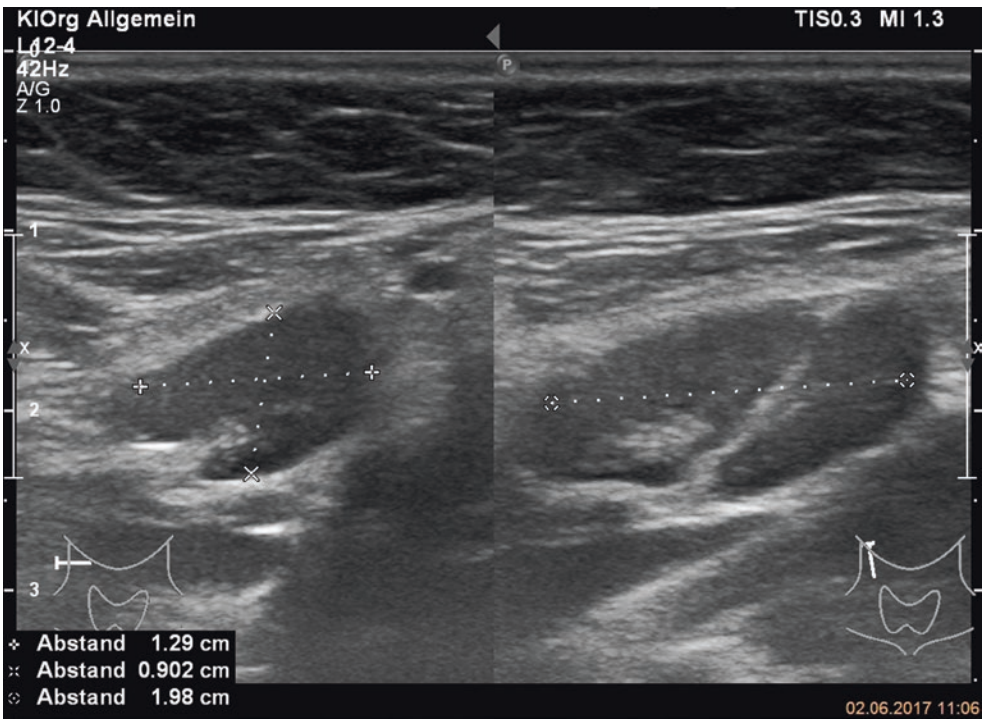

Fig. 5.3 Large, reactive CLN with a hilum and a ratio of long to short axis diameter above 2 (Solbiati/Steinkamp's ratio)

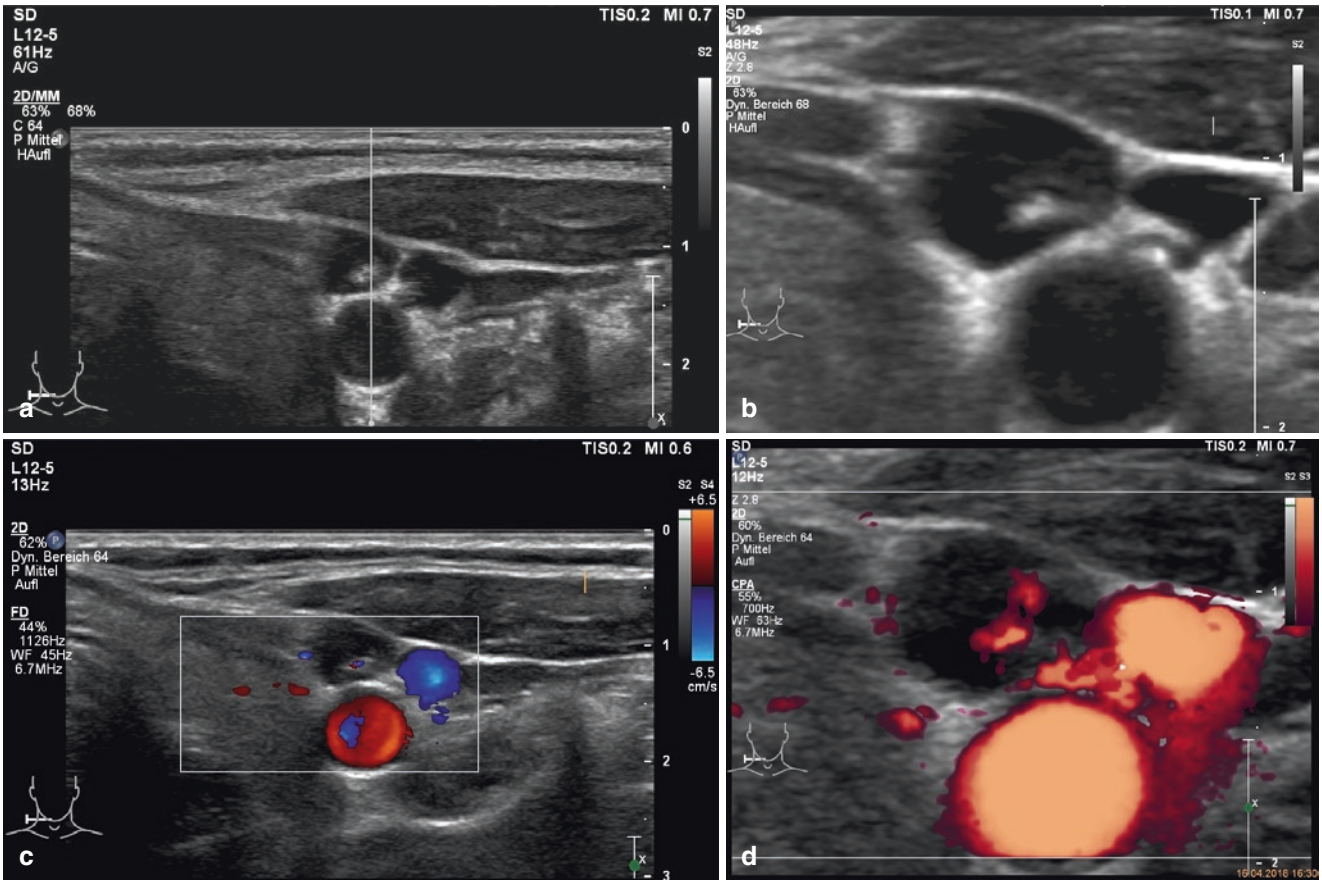

Fig. 5.4 (**a**–**d**) Presentation of a classical CLN's hilum corresponding to the site where the afferent and efferent vessels pass the capsule. (**a**) Normal B-mode scan. (**b**) Enlarged B-mode scan. (**c**) Color duplex sonography. (**d**) Power Doppler sonography

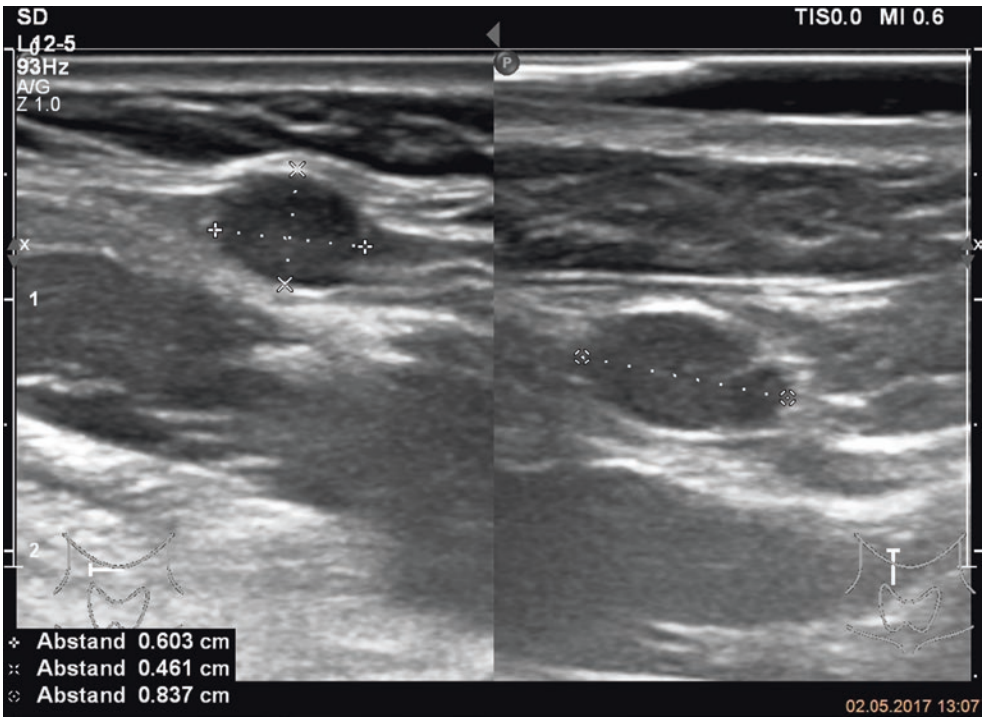

Fig. 5.5 A small CLN with a maximal transverse diameter less than 5 mm which usually appears apparently avascular without a hilum

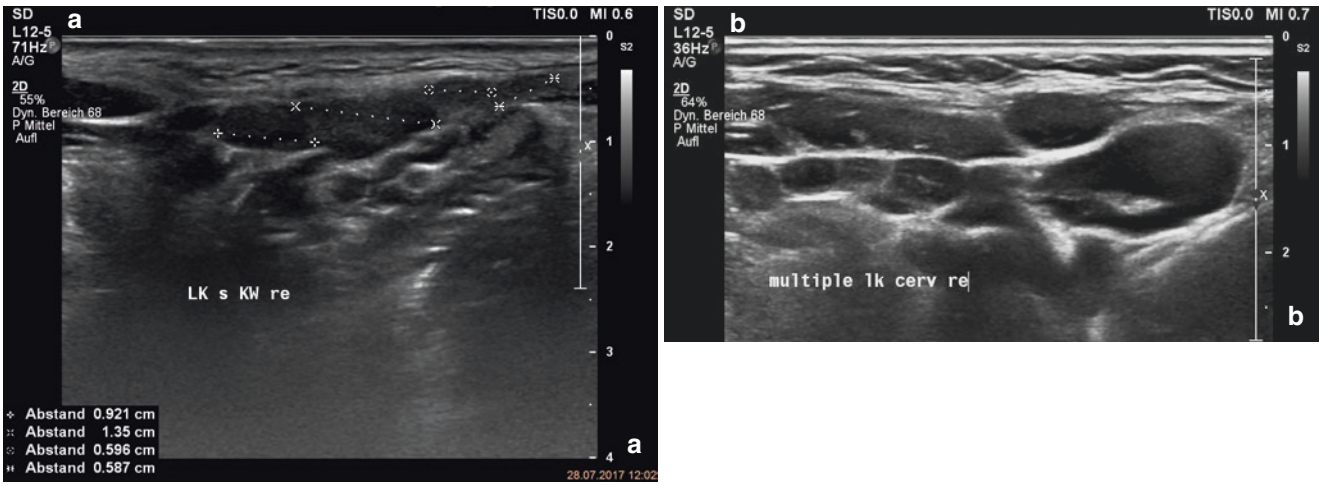

Fig. 5.6 A chain of small CLNs which is characteristically of reactive lymphadenopathy. (**a**) in a longitudinal view. (**b**) in a transverse view

respectively, whereas the combination of qualitative elastography and grayscale ultrasonography achieved an improved sensitivity (92%), specificity (94%), and overall accuracy (93%) [40–43].

Currently the major problems with qualitative US elastography are inconsistent scoring systems and approaches in the assessment of CLNs, which lead to contradictory results in the literature. Therefore, the value of real-time elastography in routine clinical practice remains unclear and limited.

Quantitative elastographic assessment On conventional strain elastography, benign lymph nodes tend to have a lower strain index, whereas malignant nodes usually have a higher strain index. Shear wave elastography (SWE) has been reported to have variable reliability in assessing the stiffness of neck lesions [44]. A recent study using SWE found that malignant nodes were stiffer than benign nodes [45]. Strain index and SWE allow quantification of lymph node stiffness, which provides additional information for the assessment of cervical lymphadenopathy. However, the results remain inconsistent and highly dependent on the cutoff values chosen, so its use in routine clinical practice is limited.

In conclusion, there is currently not one single sonographic parameter that gives a precise hint as to the status of a CLN, so the decision relies on the combination of multiple parameters; the most significant information currently are the absence of peripheral vascularization, short axis diameter, and Steinkamp's ratio [1].

5.1.2 Tuberculous Lymphadenopathy

Characteristics Can mimic all other lymphadenopathies. Inhomogeneous, lost echostructure, induration, lymph node packages, high vascularization, malignant appearance, hypoechoic, round, without echogenic hilum, displaced hilar vessels, liquid areas, intranodal cystic necrosis, "collar stud" abscess, hyperechoic spots with evident posterior acoustic shadowing, single or multiple coarse high-echo spots created by scattered calcifications or hyalinosis, nodal matting, adjacent soft tissue edema, echogenic thin layer.

Table 5.4 Stages and sonographic appearance of tuberculous cervical lymph nodes

Stage	Clinical changes of CLNs	US findings
I	Nonspecific, reactive changes as in other lymphadenitis	Simple nodal enlargement or rounding
II	Fixation to surrounding tissues because of periadenitis changes	Irregular borders
III	Cold abscesses	Hypoechoic mass with inhomogeneous texture
IV	Formation of collar stud abscesses	Nodal matting
V	Sinus tract formation	Extranodal spread into adjacent structures

Plain grayscale ultrasonography Suppurative, tuberculous lymphadenitis can mimic any other type of CLN diseases, because different US patterns can be apparent simultaneously in one patient who has multiple tuberculous cervical lymph nodes (TCLN) of different stages [46, 47]. The different stages of tuberculous lymphadenitis are depicted in Table 5.4 [48].

Therefore, evaluation of clinical symptoms (such as unilateral, enlarged CLN without pain or tenderness) and of other underlying diseases (most frequently, HIV) is very important [48]. In most cases in developed countries, TCLNs is a differential diagnosis of malignant CLN or neck abscess formation that usually involves the lymph nodes of the jugular chain, posterior triangle, and supraclavicular fossa [46, 49].

According to Ying et al. [50], stage I TCLNs commonly appear as round lesions (Fig. 5.7). In their study, 79% of 315

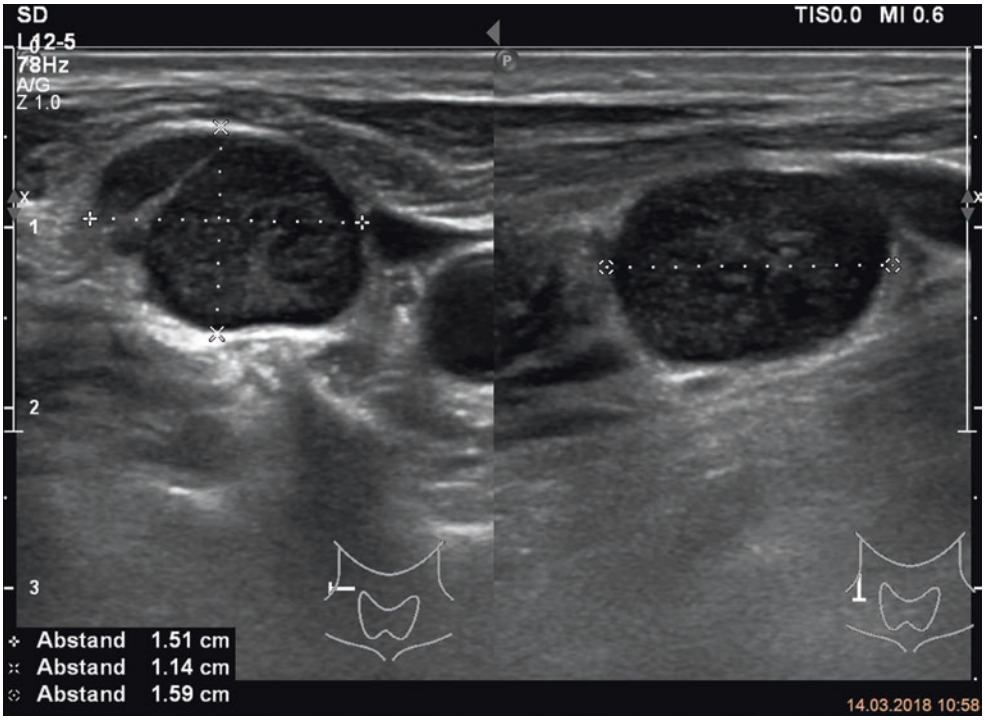

Fig. 5.7 Stage I of a tuberculous-infected CLN commonly appearing as a hypoechoic, round lesion with displaced hilar vessels

TCLNs showed a more round shape (S/L ratio more than 1/2), but the percentage was less than that of metastatic nodes (95%) [50].

Because the shape or size of TCLNs is rather unspecific, changes in the echogenic texture and echogenicity provide more clues to the diagnosis of TCLNs. The presence of a hilum within CLNs is usually a sign of benignity, whereas its absence points toward malignancy, but an absent hilum is also reported in 76–86% of TCLNs [50]. TCLNs are predominantly hypoechoic because of the high incidence of intranodal cystic necrosis with posterior acoustic enhancement (Fig. 5.8) [51].

By contrast, in a study reviewing CLNs in 192 patients, 84% of tuberculous nodes and 11% of metastatic nodes showed considerable internal echoes in B-mode sonography, whereas none of the reactive nodes had internal echoes [52]. The hyperechoic appearance is created by scattered calcifications or hyalinosis in caseous necrosis, which is thought to be highly specific for TCLNs (Fig. 5.8). Under US, they appear as single or multiple coarse, high-echo spots located focally in either the central or peripheral area within the nodes [48]. In cases of stage IV (Fig. 5.9) or V (Fig. 5.10) tuberculous infection, the evolving pathological process leads to clustered calcifications in several foci, which appear as hyperechoic spots with evident posterior acoustic shadowing under US. This finding was reported in about 25% of TCLNs [47, 53]. It is difficult, however, to differentiate between sprinkled calcifications of papillary thyroid carcinoma metastases and caseous necrosis of tuberculous nodes, so it is important to keep this possibility in mind during the investigation and take a routine look at the thyroid gland!

The so-called echogenic thin layer is another key US feature of TCLNs; it is usually located deep to the peripheral margin and measures 2–3 mm in thickness (Fig. 5.11). It is seen in 86.7% of pathologically confirmed cases and corresponds to the specific granulomatous tissue layer surrounding the caseous necrosis, reflecting the wall of body defense [46, 51]. Interestingly, Asai et al. showed that the concomitant presence of hyperechoic echoes and an echogenic thin layer has a sensitivity of 100% and a specificity of 100% for tuberculosis [51].

Further progression of the tuberculous infection leads to periadenitis (stage II disease) and subsequently to a loss of acoustic impedance difference between the TCLN and its surrounding soft tissues (Fig. 5.12). This usually results sonographically in unsharp borders of the TCLN [17]. More advanced inflammation (stage III) can leave the lymph nodes and spread into the adjacent subcutaneous tissue, eliciting soft tissue edema (Fig. 5.13). Nodal matting or clumping is considered to be a result of this periadenitis and adjacent soft tissue edema [17]. This phenomenon may also be seen in patients whose neck has been irradiated [54], but in patients without previous radiotherapy, the presence of soft tissue edema and nodal matting is highly suggestive of tuberculosis.

The "collar stud" abscess or a fistula tract can be seen in stage IV/V of CLN tuberculosis (Figs. 5.9 and 5.10) [47].

Doppler ultrasonographic assessment of intranodal vascular resistance On Doppler US, the vascular pattern of TCLNs varies depending on the degree of intranodal necrosis and the stage of the disease. In 81% of TCLNs, an

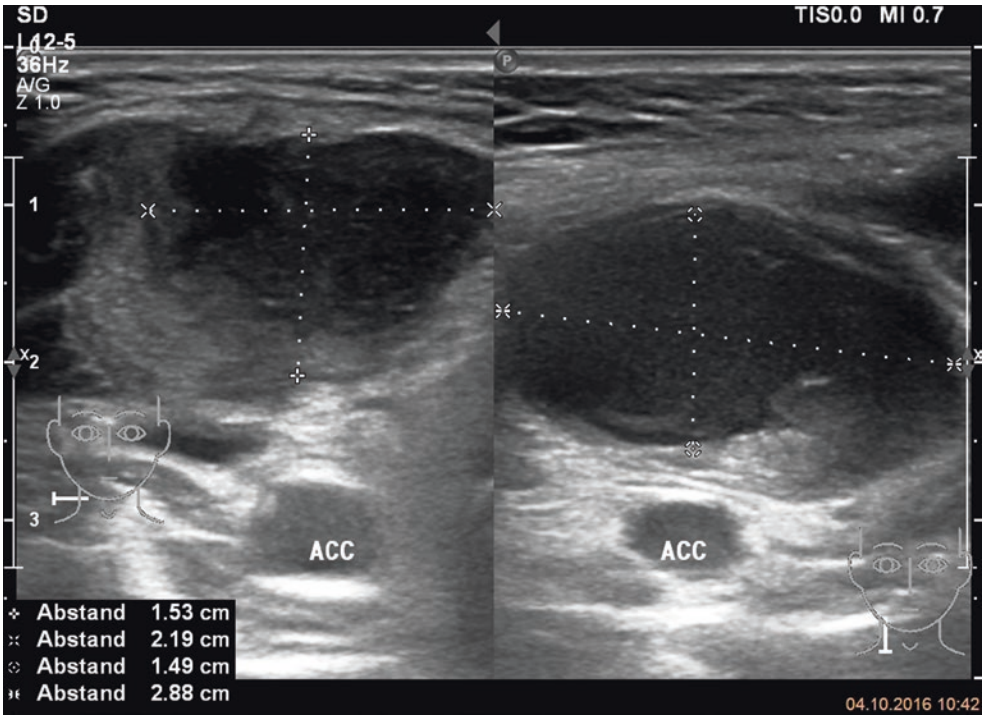

Fig. 5.8 Classical TCLN with an absent hilum, predominantly hypoechoic because of the high incidence of intranodal cystic necrosis with posterior acoustic enhancement and hyperechoic appearance created by scattered calcifications or hyalinosis

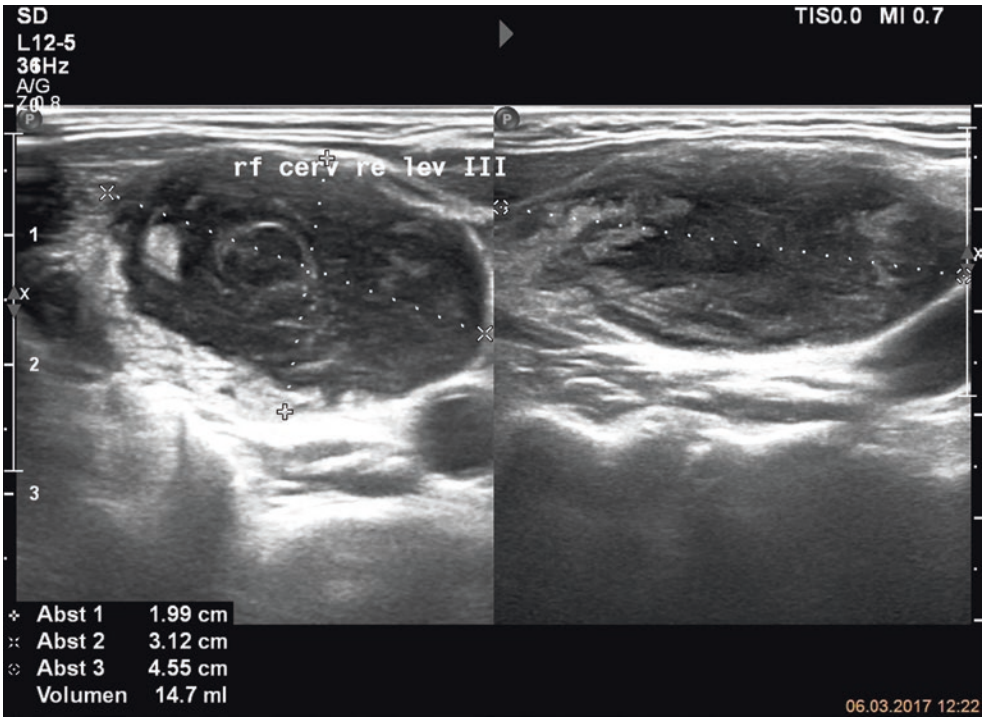

Fig. 5.9 CLN with a stage IV tuberculous infection with clustered calcifications in several foci appearing as hyperechoic spots with evident posterior acoustic shadowing under US

intranodal cystic necrosis pushes the hilum away and causes displaced vasculature (Fig. 5.7) [17]. As cystic necrosis aggravates, it eventually destroys the blood vessels in 6–41% of TCLNs and results in apparent avasculature (Fig. 5.14) [29, 31]. Avasculature may also reflect the healing process at later stages of the disease, when fibrosis and hyalinization cause compression and obliteration of intranodal vessels [55].

Qualitative/quantitative elastographic assessment The role of elastography is not yet fully understood, although differences between malignant, benign, and tuberculous CLNs have been identified in case reports [56].

Ultrasound-guided fine-needle aspiration (USFNA) and utrasound-guided core biopsy (USCB) cytology Although typical US features exist, none are pathognomonic, and

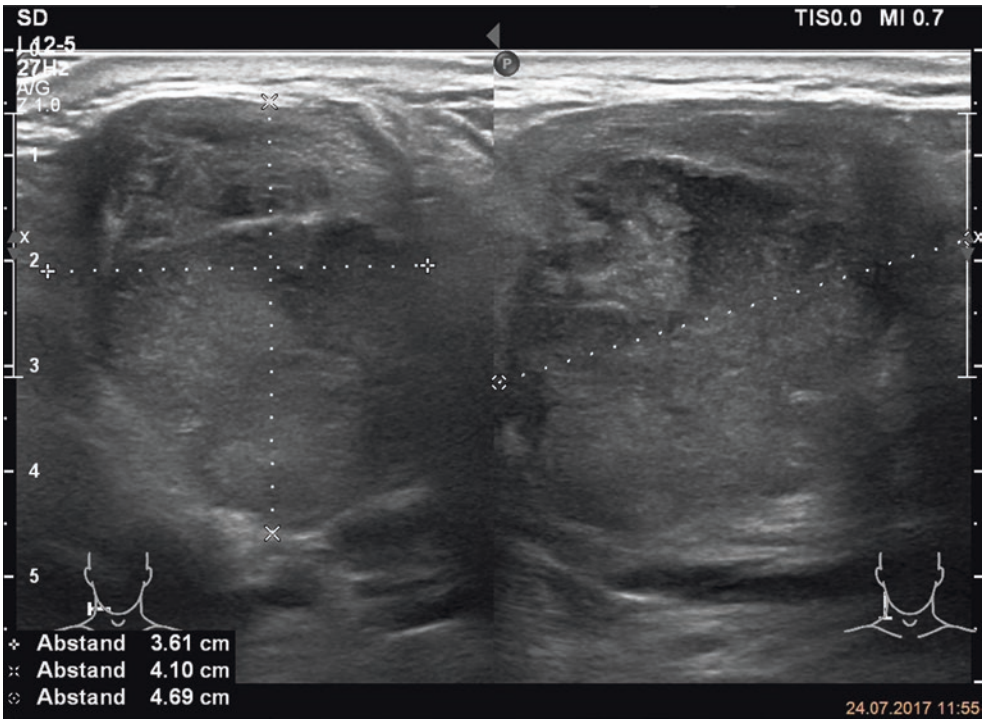

Fig. 5.10 TCLN in stage V with sinus tract formation and extranodal spread into adjacent structures

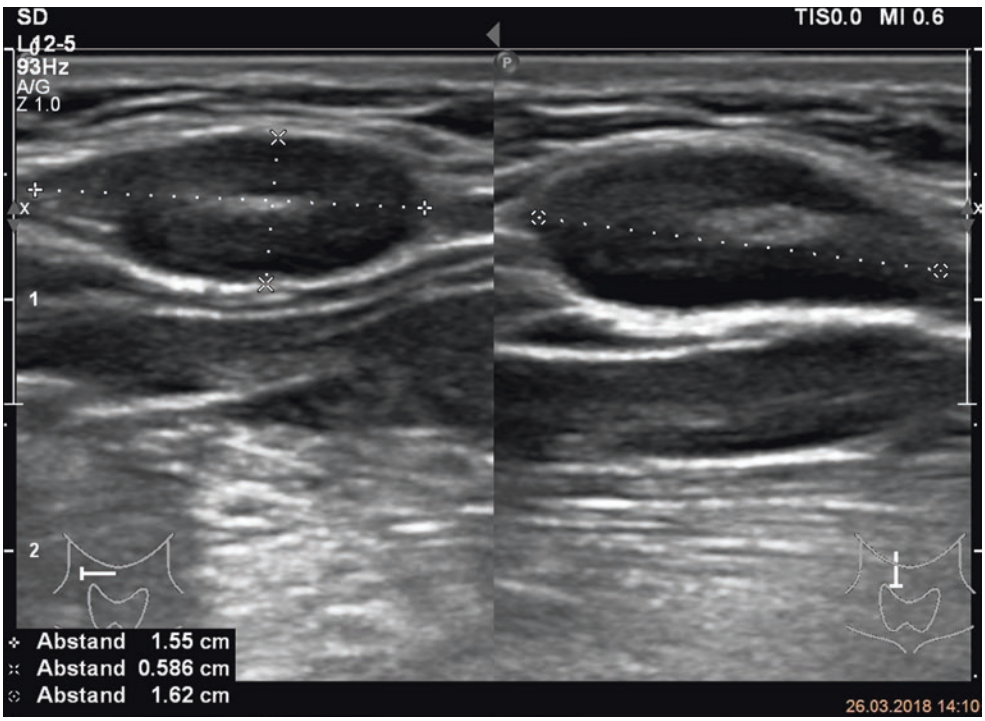

Fig. 5.11 TCLN depicting another key US feature the "echogenic thin layer" that shows in combination with hyperechoic echoes a sensitivity of 100% and a specificity of 100% for tuberculosis

TCLN cannot be diagnosed merely with US alone [48]. A confirmative diagnosis depends on ancillary tests such as USFNA, USCB, mycobacterial culture, or polymerase chain reaction (PCR) test for the *M. tuberculosis* gene [57]. The sensitivity of cultures performed on FNA specimens was reported to reach 86%, whereas the sensitivity of microscopy was 18% and of cytology from FNA specimens was 38% [58]. Surgical biopsy has long been considered the gold standard to obtain specimens for histology of TCLNs, but this is often followed by fistula formation and poor wound healing [59]. Instead, USCB provides a favorable alternative, which leaves a smaller scar and has lower chances of complications while offering similar diagnostic accuracy (Video 5.2) [60].

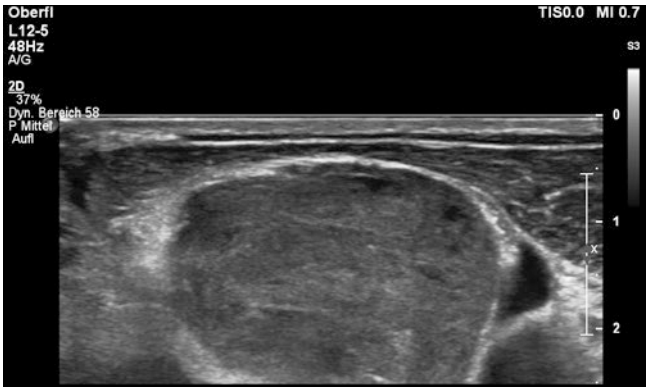

Fig. 5.12 TCLN with a stage II disease typically presented with periadenitis and subsequently a loss of acoustic impedance difference in comparison to its surrounding soft tissues, which is sonographically shown by unsharp borders

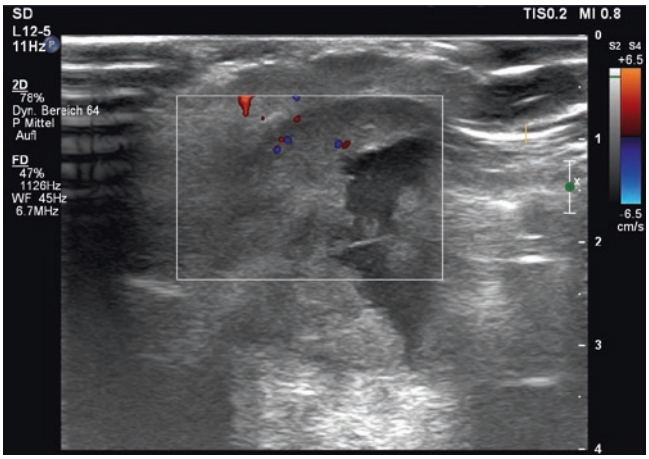

Fig. 5.14 TCLN with stage V disease. As cystic necrosis aggravates, it destroys the blood vessels and results in apparent avasculature

Fig. 5.13 More advanced tuberculous inflammation (stage III) spreads into the adjacent subcutaneous tissue eliciting soft tissue edema, nodal matting, or clumping

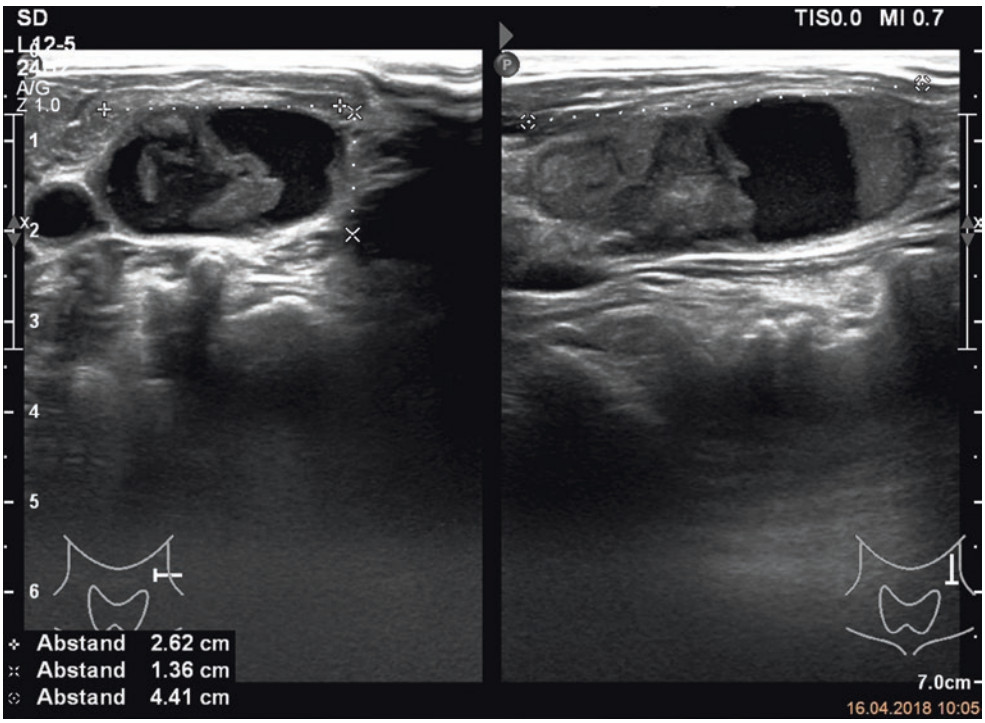

5.1.3 Non-tuberculous Mycobacteria (NTM) Lymphadenopathy

Characteristics Can mimic all other lymphadenopathies, primarily in children under the age of 6 years. Unilateral, most commonly (in order of incidence) in submandibular, preauricular, and parotid CLN levels; satellite-like nodules; "malignant" appearance; heterogeneous; lost echostructure; intranodal liquefaction with cystic necrosis (echolucent areas); overlying skin with livid discoloration and with a "parchment-like" shiny appearance; echogenic thin layer; sinus-like lymphocutaneous fistulas; echogenic intrinsic reflexes with and without acoustic shadowing; multiple intranodal calcifications; nodal matting; adjacent soft tissue edema.

The term non-tuberculous mycobacteria (NTM) refers to mycobacterial species other than the *Mycobacterium tuberculosis* complex (i.e., *M. bovis*, *M. africanum, M. microti*, *M. canetti*, *M. caprae*, *M. pinnipedii*, *M suricattae*, and *M. mungi*) and those organisms causing leprosy (*M. leprae* and *M. lepromatosis*). NTM are ubiquitous environmental organisms mostly found in soil and water; they cause lung-, sinus-, lymph

node-, joint-, CNS-, and catheter-related and disseminated infections in susceptible individuals [61, 62].

For any given level of host susceptibility, there seem to be a real increase in NTM infection rates, which has been associated with activities potentially increasing exposure to NTM in water (swimming), soils (gardening), and aerosols (showering, hot tubs) [63]. Furthermore, a number of immunodeficiencies have been associated with NTM infection [64, 65], including inherited disorders of cytokine signaling [66, 67] and immune cell function [68, 69], as well as acquired immunodeficiencies, including HIV/AIDS [70]. A number of immunosuppressive drugs, such as oral or inhaled corticosteroids [71–73] and the combined immunosuppressive therapy used in solid organ transplantation and in anticancer chemotherapy [70], have been associated with the acquisition of NTM infections, whereas direct person-to-person spread is unlikely [74].

Besides the most frequent pulmonary infections, NTM cause locally limited infections of the skin, connective tissue, eye, and bones [61, 75], as well as lymph nodes of the neck, most often in children less than 5 years of age, with a female predilection; immunocompetent teenagers and adults are usually not affected [76]. Predominantly isolated mycobacteria belong in 65–80% of cases to the *Mycobacterium avium/intracellulare* species; only about 10% are *Mycobacteria tuberculosis*, but the opposite applies to teenagers and adults [77]. Furthermore, the authors showed that the increasing incidence of NTM lymphadenopathies was linked to a change and diversification in NTM species from *M. avium/intracellulare* and *M. scrofulaceum* to *M. celatum*, *M. genavense*, *M. haemophilum*, *M. interjectum*, *M. kansasii*, *M. lentiflavum*, *M. malmoense*, and the fast-growing *M. abscessus/fortuitum*. The primary therapy includes the complete resection of the affected lymph nodes and surrounding tissue. Preoperative ultrasound is often the only imaging technique that is required.

Plain grayscale ultrasonography NTM lymphadenopathy of the head and neck can be divided into four distinctly segmented clinical phases by ultrasound imaging (Table 5.5). These are universal features but not entirely specific, and all the stages are similar to TCLNs [78]. Characteristically the submandibular nodes are most frequently involved, followed by the preauricular and rarely by the parotid gland lymph node levels. Most levels are unilaterally affected [79].

Stage I is characterized by a painless, hypervascular mass (Fig. 5.15). The diameter of the involved lymph nodes ranges from 1.9 cm to 4.4 cm (rather large in comparison) [79]. On sonography, marked decreases of echogenicity were characteristic in the early stages, with development of satellite-like nodules at the edge of the affected lymph node [79, 80].

Table 5.5 Stages and sonographic appearance of non-tuberculous cervical lymph nodes

Stages	Clinical changes of CLNs	US findings
I	Mostly over weeks persistent, painless, enlarged lymph nodes without symptoms as in other lymphadenitis	Unilateral, nonspecific, reactive nodal hypervascular enlargement or rounding Rather large diameters (1.9–4.4 cm) Marked decreases of echogenicity Development of satellite-like nodules at the edge of the lymph node Characteristically submandibular and preauricular; parotid lymph node levels rarely involved
II	Fluctuation as a result of intranodal liquefaction with cystic necrosis Fixation to surrounding tissues as a result of periadenitis changes	Hypoechoic mass with inhomogeneous texture with irregular borders and posterior shadowing Nodal matting and adjacent soft tissue edema
III	Livid discoloration and thinning with a shiny appearance (“parchment-like”) of overlying skin	Decreased distance of skin to lesion
IV	Lymphocutaneous fistulas/draining wound	Echogenic intrinsic reflexes, with and without acoustic shadows Multiple intranodal calcifications

In stage II, lymph nodes with heterogeneous echogenicity, incorporating intranodal echolucent areas, may indicate liquefaction with cystic necrosis, causing the mass to appear fluctuant. Additionally, nodal matting and adjacent soft tissue edema may be present in the neck (Fig. 5.16) [79, 81].

In stage III, the overlying skin of the affected CLN may develop livid discoloration and become notably thinner with a shiny appearance (“parchment-like”) (Fig. 5.17). During stage IV, the lesion fistulizes to the skin surface, causing a sinus-like, draining wound; echogenic intrinsic reflexes with and without acoustic shadows can be seen (Fig. 5.18; Video 5.3) [80, 81]. Multiple intranodal calcifications are rather characteristic of end-stage NTM infection [79, 82]. Calcification in juvenile CLNs is rather uncommon (Fig. 5.19), but calcification may also be found in metastatic nodes from papillary carcinoma of the thyroid in children [83, 84].

Most NTM patients present in stage III with lymph node fluctuation and violaceous skin discoloration following a history (over weeks) of unilateral, painless, enlarged lymph nodes without symptoms [80]. Then overnight the lymph nodes rapidly enlarge, fuse, and develop a lymphocutaneous fistula with secretions. Sometimes both sides are affected. Clinically the focally livid color of the skin covering the enlarged lymph node is characteristic.

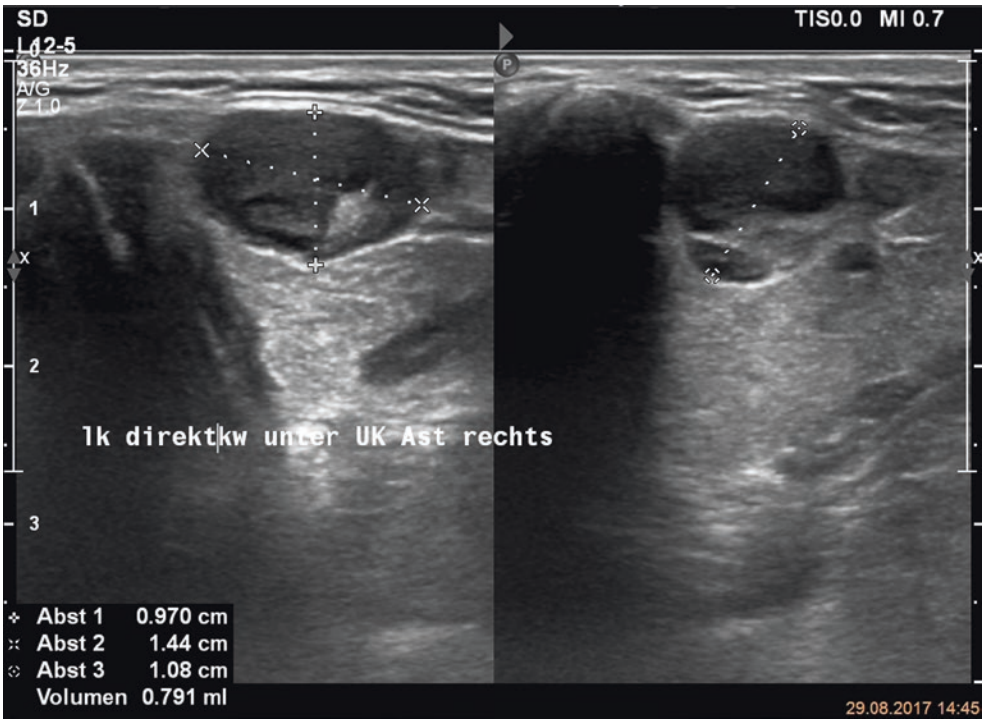

Fig. 5.15 Unilateral stage I NTM lymphadenopathy of the head and neck characterized by a painless, hypervascular mass

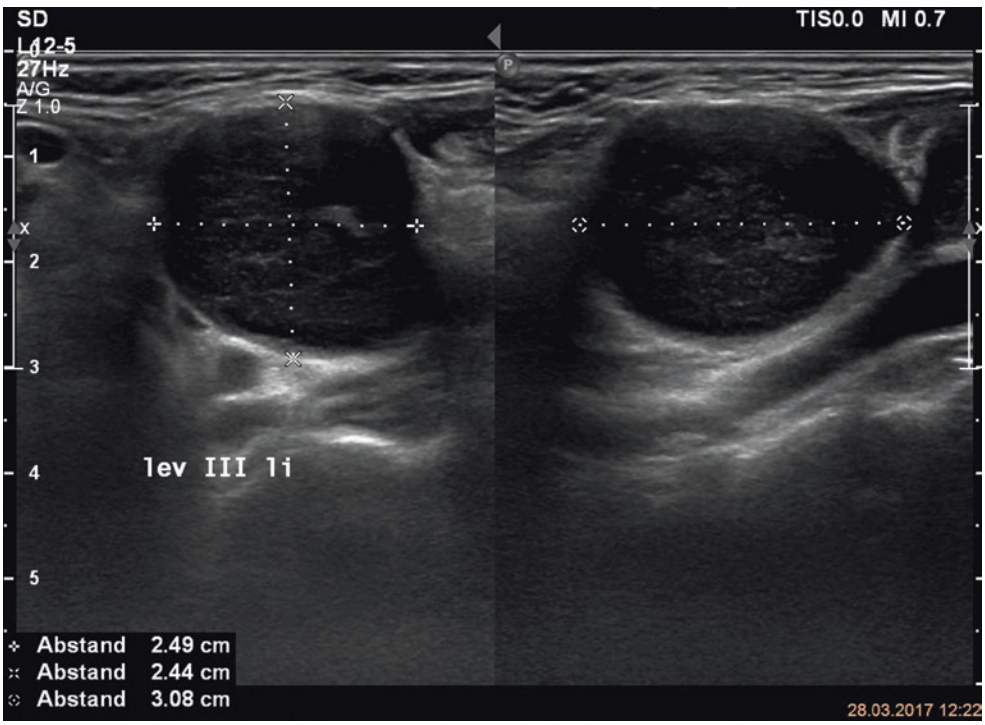

Fig. 5.16 Stage II non-tuberculous CLN with heterogeneous echogenicity, incorporating intranodal echolucent areas indicating liquefaction with cystic necrosis, nodal matting, and adjacent soft tissue edema

The differential diagnosis is challenging, including tuberculosis, cat scratch disease, EBV-driven mononucleosis, toxoplasmosis, or suppurative lymphadenitis. A clear differentiation from tuberculosis is not possible by imaging alone. Actinomycosis also leads to livid skin discoloration and fistula development, but it typically does not spread via the lymphatic system [85].

Doppler ultrasonographic assessment of intranodal vascular resistance The use of newer power Doppler equipment has increased the sensitivity of the detection of intranodal vascularity [86]. Still, to date no specific data have been published on the use of Doppler US in NTM infection. Benign processes may manifest with variable

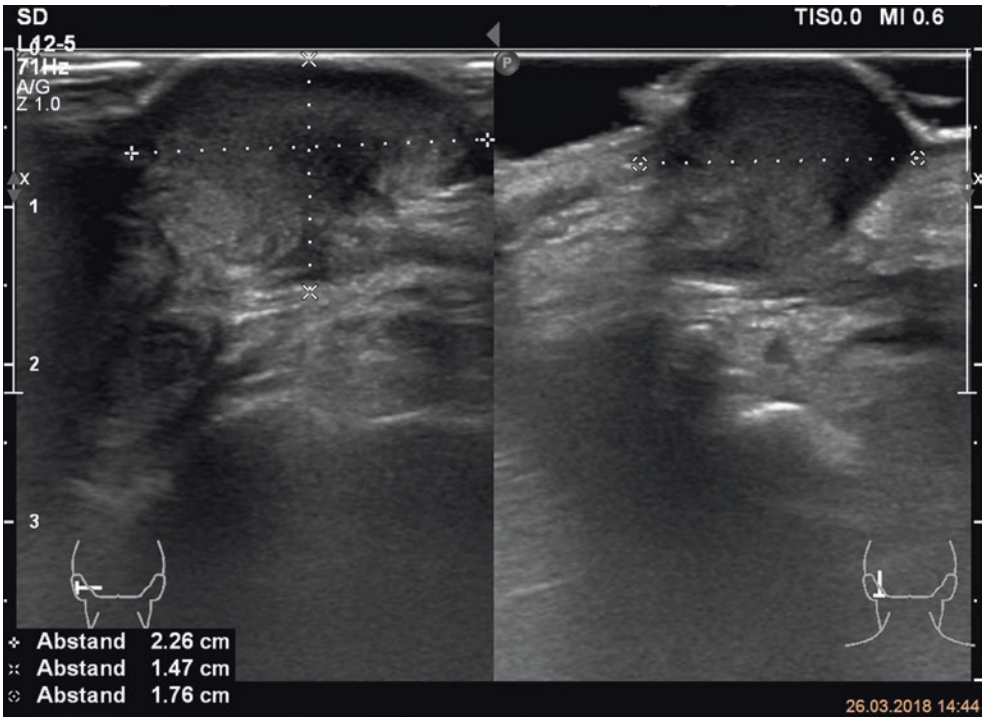

Fig. 5.17 Stage III non-tuberculous CLN with "parchment-like" appearance of the overlying skin and a livid discoloration

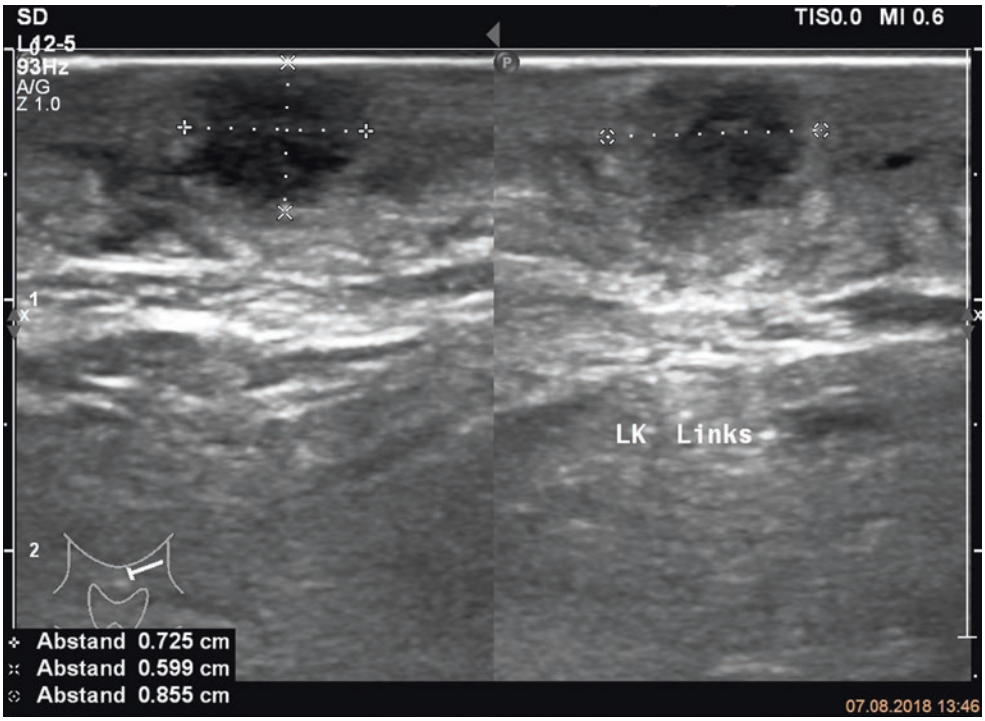

Fig. 5.18 In stage IV of non-tuberculous disease, the lesion fistulizes to the skin surface causing a sinus-like, draining wound and echogenic intrinsic reflexes with and without acoustic shadows

vascularity depending on the rate of growth and the development of necrotic areas, which cause perfusion defects that may mimic the Doppler US appearance of TCLNs. However, evaluation of the vascular pattern of CLNs may not distinguish between different benign nodal diseases, as their vascular patterns vary with the stage of disease [3, 87].

Qualitative/quantitative elastographic assessment No investigation has yet been done on this research field.

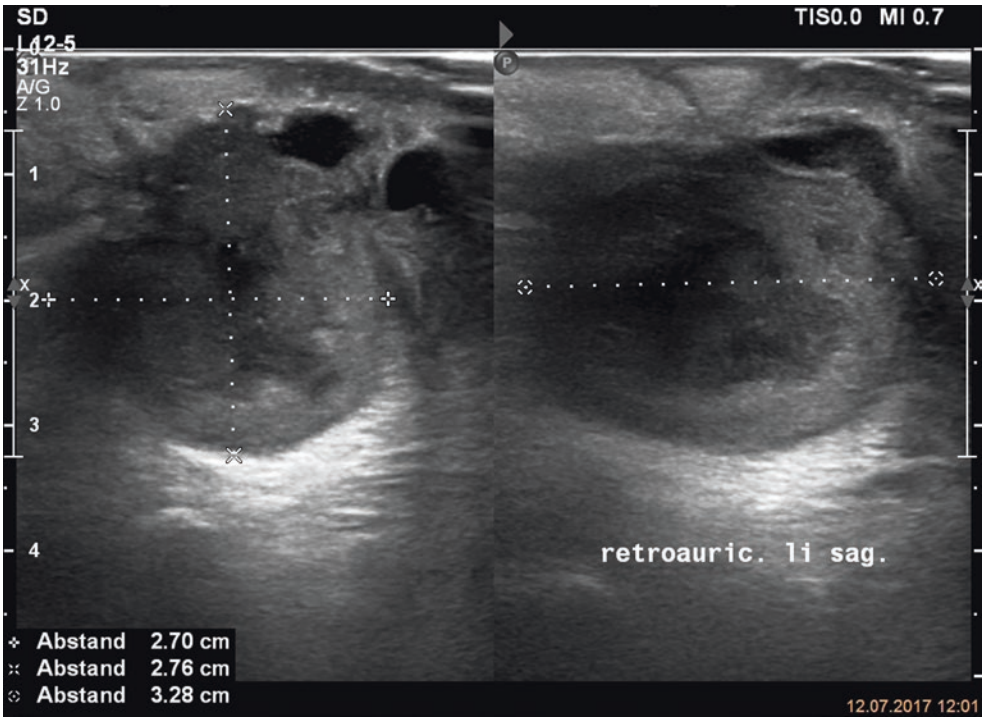

Fig. 5.19 End-stage non-tuberculous mycobacterial infection with multiple intranodal calcifications, which is rather uncommon in juvenile CLNs and can only be found in metastatic nodes from papillary carcinoma of the thyroid in children

5.1.4 Epstein-Barr Virus (EBV)-Triggered Lymphadenopathy (Infectious Mononucleosis)

Characteristics Round, Steinkamp's L/S ratio <2, large longitudinal diameters, hyperechoic hilum, sharp borders, commonly matting or clumping of CLNs, hypervascular, color/Doppler mode symmetric radial tree-like vascular pattern, low resistance index (RI <0.6).

About 90% or more of adults worldwide are seropositive for EBV [88]. Infections are more frequent before adolescence, but EBV can affect patients of all ages. Infection usually proceeds silently, and only 25–30% of cases become clinically apparent [88–90]. In those patients, a triad of moderate to high fever, pharyngitis, and moderately tender CLNs with splenomegaly (>50%) characterizes the course of the disease. Cytomegalovirus, toxoplasmosis, HIV, and human herpes virus type 1 infections elicit the same symptoms, so these diseases must be distinguished from infectious mononucleosis.

Plain grayscale ultrasonography In pediatric patients with acute infectious mononucleosis, 100% of CLNs show a wide, hyperechoic hilum and have sharp borders (Fig. 5.20) [3]. Hypoechoic foci can occasionally be observed within the hyperechoic hilum; this might be attributed to the development of germinal follicles in the pulp [91]. Additionally, matting or clumping of CLNs is common in these patients and is considered to be the result of periadenitis and adjacent soft tissue edema (Fig. 5.21) [3, 79, 87, 92].

In comparison to reactive lymphadenitis, the EBV-infected CLNs are considerably larger, round, and hypervascular (Fig. 5.21) [91]. Vassalo et al. mentioned that L/S ≥2 is a stronger criterion for benign conditions than L/S <2 for malignancy [93]. Papakonstantinou et al. [3] found that the majority of the acutely enlarged lymph nodes of infectious mononucleosis and bacterial lymphadenitis had L/S <2, as did the lymph nodes affected by malignant lymphoma. In contrast, the vast majority of hyperplastic lymph nodes exhibited L/S ≥2, but their size was considerably smaller. Therefore, round shape seems to be a function of size and rapid growth rather than of internal destruction of the node [3, 87, 92].

Doppler ultrasonographic assessment of intranodal vascular resistance Doppler US shows a central radial tree-like pattern of vessels in 75% of EBV-infected CLNs; the other 25% elicit a central hilar vessel (Fig. 5.22). This difference is statistically significant [3]. Spotted, peripheral, or avascular patterns of perfusion were not observed in any case of infectious mononucleosis or even reactive hyperplasia. In infective lymphadenopathy, extensive inflammatory changes in the central part of the CLN may displace normal lymphatic tissue to the periphery, resulting in huge enlargement and dilatation of subcapsular vessels,

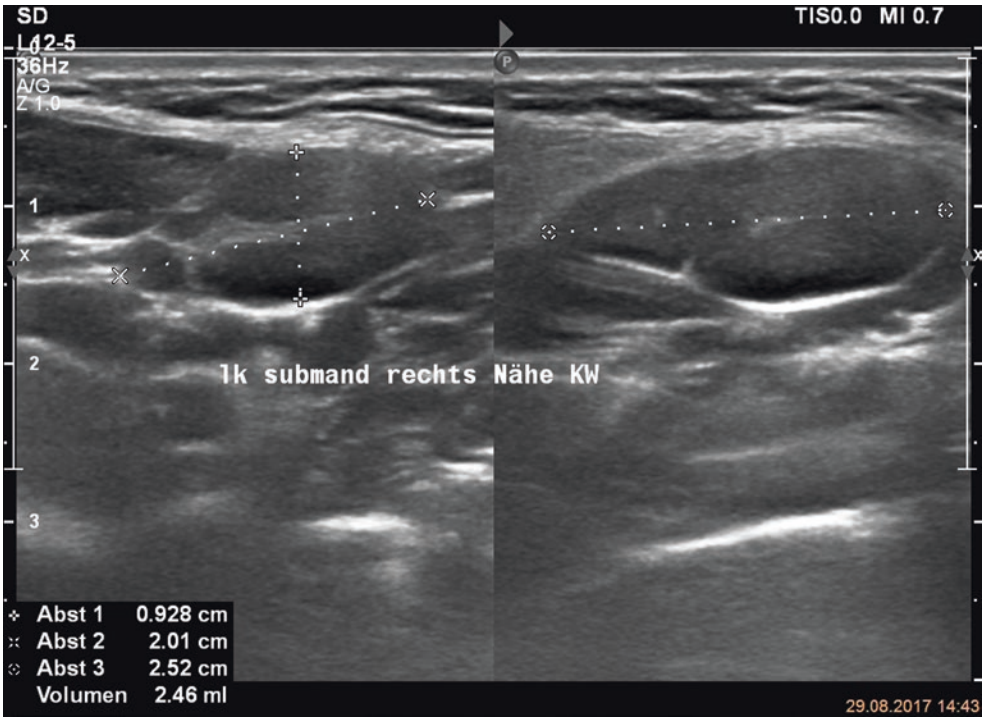

Fig. 5.20 CLNs with an acute infectious mononucleosis show a wide hyperechoic hilum and have sharp borders

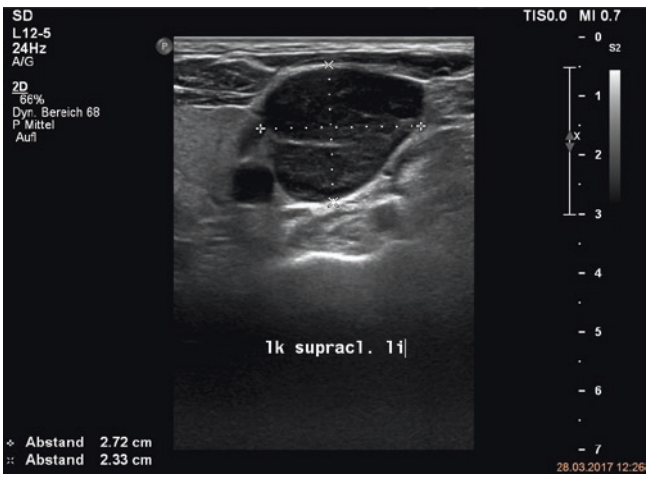

Fig. 5.21 EBV-infected CLNs are considerably larger, round, and hypervascular. Occasionally hypoechoic foci within the hyperechoic hilum and matting or clumping as the result of periadenitis and adjacent soft tissue edema may be seen

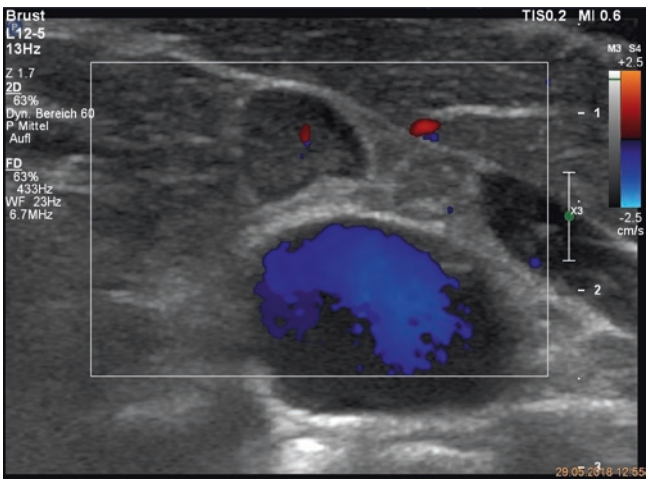

Fig. 5.22 Doppler ultrasonography shows a central radial tree-like pattern of vessels in 75% of EBV-infected CLNs, whereas the residual 25% elicit a central hilar vessel

whereas extension of the inflammation into adjacent fat planes incites enlargement of pericapsular vessels, similar to metastatic lymphadenopathy [3, 29, 31, 94]. Vascular densities are controversial. According to the results of Papakonstantinou et al. [3], benign processes may manifest with variable vascular density depending on the rate of growth and the development of necrotic areas, which cause perfusion defects. Power Doppler may provide more information about vascular density (Figs. 5.23 and 5.24) [95], but it does not seem to contribute to the final categorization of vascular patterns [94].

Color Doppler sonography is an established method for the noninvasive documentation and quantification of intravascular blood flow. In the study of Baltas et al., the resistance index (RI <0.6) of intranodal hilum vessels in infectious

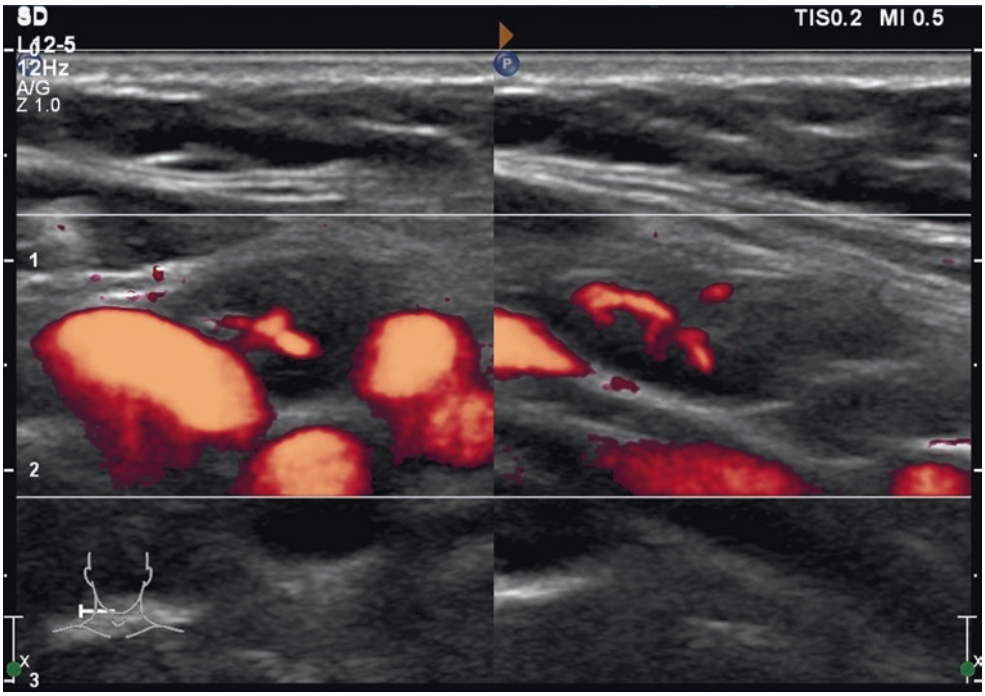

Fig. 5.23 Benign processes may manifest with variable vascular density, which can be investigated by power Doppler

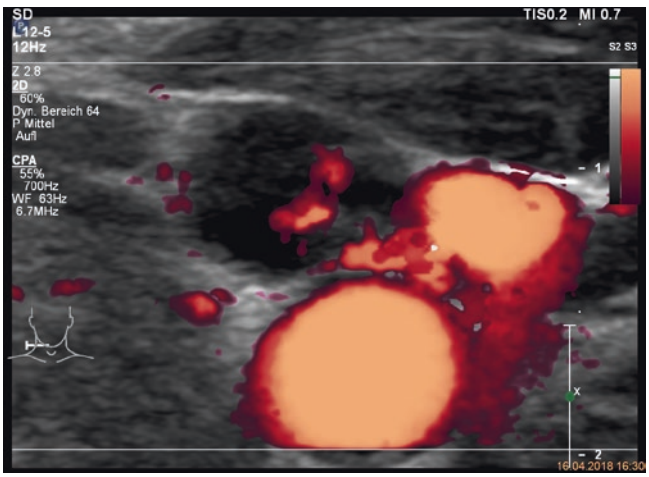

Fig. 5.24 A magnified view of Fig. 5.23

mononucleosis was low, which indicates a benign lesion; this finding was in accordance with previous investigations [96].

Qualitative/quantitative elastographic assessment No investigation has yet been done in this research field.

5.1.5 Suppurative Lymphadenopathy (Abscesses)

Characteristics Fusion, huge conglomerates, inhomogeneous, lost echotexture, liquid areas, induration, hyper/hypoechogenic areas in a salt-and-pepper pattern, color/Doppler mode high vascularization, contrast media accumulation, unsharp borders, nodal matting or clumping, adjacent soft tissue edema.

Plain grayscale ultrasonography The two kinds of abscesses—"cold" and "hot"—can be distinguished. Cold abscesses are more like a suppurative lymphadenopathy; the fulminant inflammation associated with a hot abscess is lacking. Therefore the sonographic characteristics of cold abscesses are quite similar to those of a necrotic CLN. In contrast, hot abscesses are the result of a severe infection, which usually also involves the surrounding connective tissue. Patients with hot abscesses are very often in bad general condition (high fever; swollen, reddish neck; pain). Thus, there are two main differential diagnoses: the tuberculosis stage IV/V and malignant, necrotic CLN disease with accompanying infection [97].

In both cases the abscess is predominantly hypoechoic or anechoic with a posterior acoustic enhancement. Moreover, destruction of the internal anatomy of the lymph node or nodes leads to loss of the hilar structure and vasculature. Occasionally, an area of suppuration with residual tissue is either hyperechoic or isoechoic relative to the surrounding tissue [98]. Cold abscesses usually have more sharp borders (Fig. 5.25) than hot abscesses (Fig. 5.26) [99–101]. Moreover, the periadenitis subsequently results in unsharp borders on US imaging, spreads into subcutaneous tissues with adjacent soft tissue edema, and shows nodal matting or clumping in the neck [17]. Intranodal necrosis or huge necrotic areas in CLN conglomerates also can be visible. Regardless of the nodal size, all lymph nodes with intranodal necrosis are considered pathologic [102].

On US, the abscess may appear in the beginning as a cystic area within a lymph node. Cystic necrosis appears as an

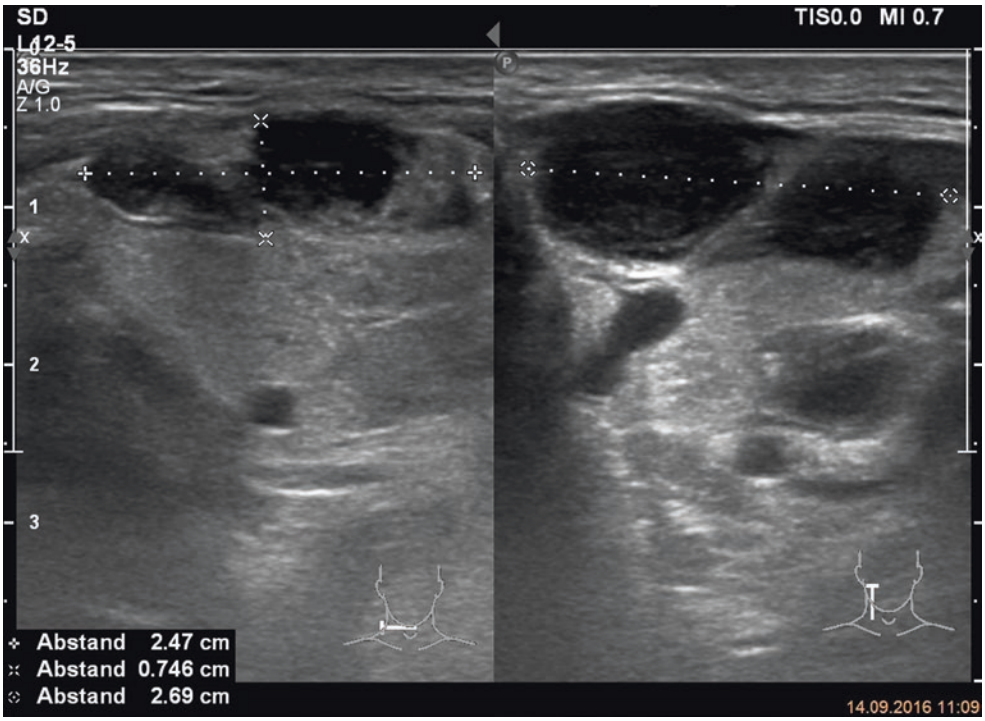

Fig. 5.25 Cold abscesses usually are more sharp-shaped with a predominantly hypoechoic or anechoic center

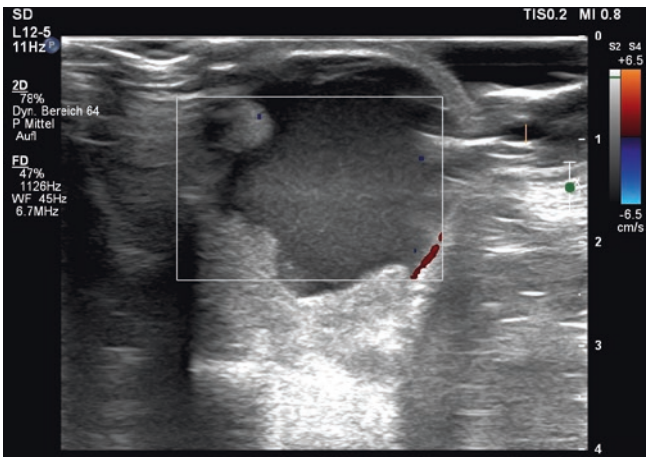

Fig. 5.26 Hot abscesses tend to be less sharp- or duller-shaped, with a predominantly hypoechoic or anechoic center and a posterior acoustic enhancement. Occasionally, an area of suppression with residual tissue is either hyperechoic or isoechoic relative to the surrounding tissue. No Doppler sonographic signs elicit loss of solid CLN tissue

echolucent area within the lymph node, with dorsal acoustic shadowing, whereas in huge conglomerates, echolucent areas change, with echogenic areas following a salt-and-pepper pattern [13, 103].

As a function of the grade of cellulitis and the size of the abscess, a mass effect with suppression of surrounding tissues occurs [104, 105]. Furthermore, to determine liquefaction within the lymph node, dynamic sonopalpation can be used. Briefly, a fluctuation and a compression of the liquid are induced by gentle, repetitive pressure with the transducer or the finger over the area of cellulitis. Thus, these simple maneuvers can demonstrate the presence and extent of liquefaction in an abscess.

Qualitative/quantitative elastographic assessment Elastography cannot yield any advantages for the diagnosis of a neck abscess, because abscesses display variable stiffness according to fluid content [106]. On the other hand, elastography visualizes induration of surrounding superficial skin abscesses. Thereby, asymmetry of abscess induration is associated with failure of standard therapy [107].

Ultrasound-guided fine-needle aspiration (USFNA) and ultrasound-guided core biopsy (USCB) Aspiration of pus is helpful for confirmation of suspected diagnosis and for antibiotic resistance testing at a microbiologic lab. Occassionally this might also be a therapeutic option.

5.1.6 Lymph Node Metastases of Head and Neck Squamous Cell Carcinoma (HNSCC)

Characteristics Round, inhomogenous or homogenous, absence of hilum structure, enlarged cortex, longitudinal diameter >18 mm, minimal cross-sectional diameter >8–10 mm, color/Doppler mode peripheral vascularization; Steinkamp/Solbiati index <2.

Plane grayscale ultrasonography The published studies have not achieved accord in regard to the best ultrasound criteria to indicate a lymph node metastasis of HNSCC. Nevertheless

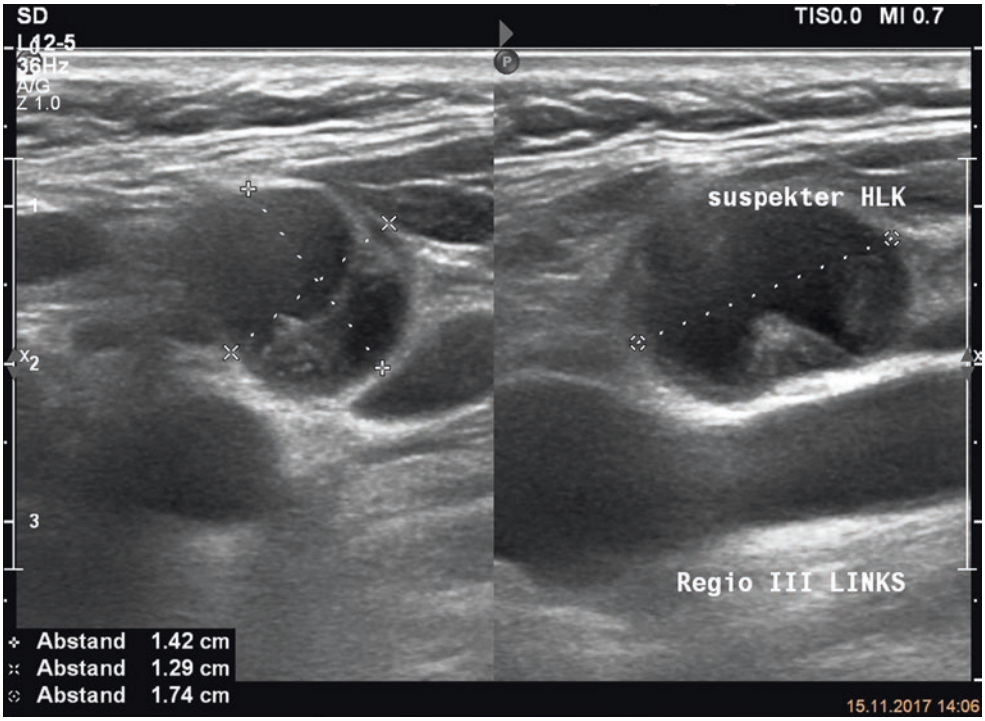

Fig. 5.27 A heterogeneous texture of a lymph node is considered as a sign of malignant transformation and can be found in more than 90.9% of all metastatic and only 11.8% of all reactive cervical lymph nodes

most authors agree that sonomorphologic criteria have a low sensitivity but a high specificity for differentiating metastatic from nonmetastatic lymph nodes [14, 15].

In the past, quantitative and sonomorphologic criteria were separately investigated [13, 16, 108, 109]. Heterogeneous texture of a lymph node was considered as a sign of malignant transformation [15, 110]. Hessling and coworkers found a heterogeneous echogenic structure in 90.9% of all metastatic cervical lymph nodes and only 11.8% of reactive CLNs (Fig. 5.27) [110]. In this study, the sensitivity of echogenic structure was just 23.5%, with a specificity of 76.5%, which is in accordance with the literature. In contrast, the groups led by Ahuja and Som concluded that metastases have a hypoechogenic structure and look more homogenous (Fig. 5.28) [17, 19, 102]. Therefore, echogenicity is not a significant criterion for diagnosing and confirming a lymph node metastasis; it is just one part of the puzzle. Nevertheless, the appearance of irregular borders points toward extracapsular spread (ECS) and therefore is a safe sign of malignancy (Video 5.4).

The appearance of an echogenic hilum in a cervical lymph node is a sign of a benign condition. Solbiati reported that only 4% of the investigated cervical lymph node metastases had a hilum [19], and studies by Rubaltelli and Vassallo showed that 84–92% of all benign lymph nodes were an echogenic lymph node with a hilum [13, 16]. In the study by Meyer et al., 96.5% of all benign cervical lymph nodes had a hilum, but also 91.5% of all metastases had a hilum [1]. This gives evidence that the

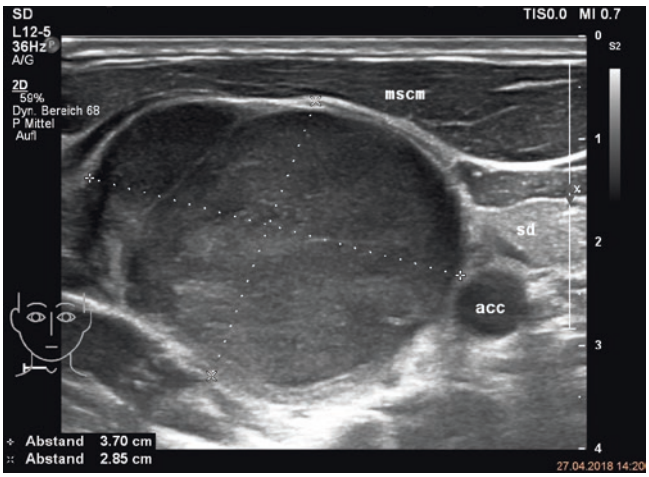

Fig. 5.28 Until now, echogenicity in HNSCC metastases can be hyperechogenic and heterogeneous as well as also hypoechogenic and more homogenous as in this figure. As a result, echogenicity is not a significant criterion for diagnosing and confirming a lymph node metastasis

qualitative criterion "hilum" might only give additional hints for the exact diagnosis of malignant transformation.

Quantitative parameters moved significantly into the foreground. In various studies, the longitudinal, cross-sectional, and minimal transverse diameters have been recommended for the assessment of the diagnosis [16–18, 108, 109]. In publications so far, the suggested longitudinal diameter of neck metastasis ranges from 5 to 15 mm [1, 14, 18, 102, 108, 109]; most of these reports have involved

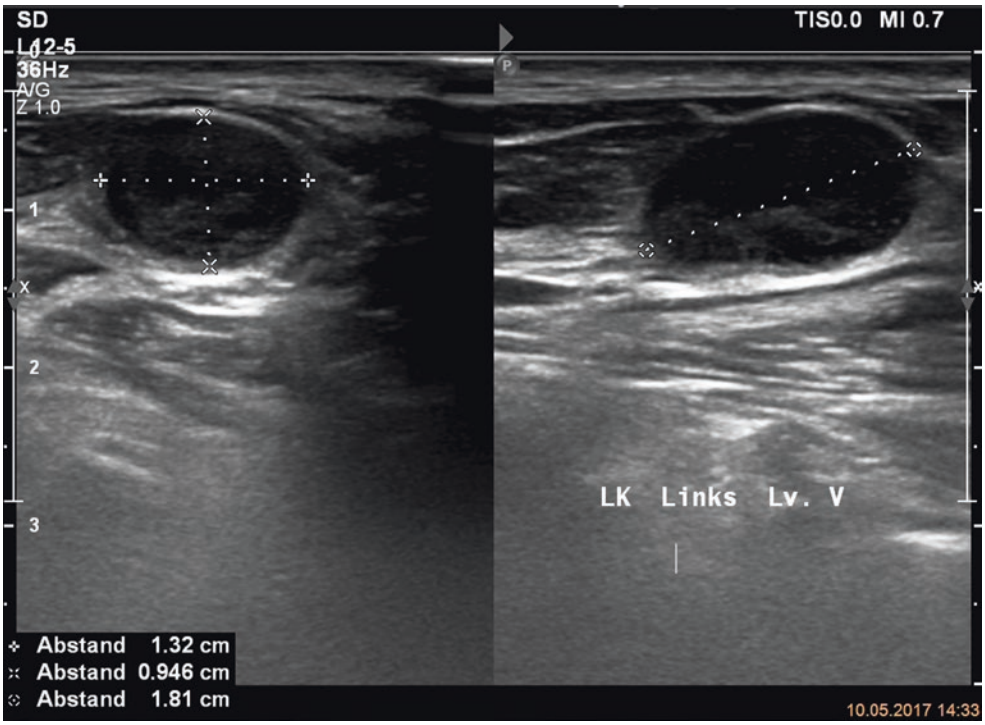

Fig. 5.29 In a larger cohort study, interpretation of the ROC curve suggested 18 mm to be a good cutoff value for the longitudinal diameter to distinguish metastatic from nonmetastatic cervical lymph nodes. To raise a higher sensitivity and specificity in an obviously metastatic neck, longitudinal diameters of suspected nodes should exceed 15–18 mm in length, whereas in clinically unsuspicious necks, the cutoff line should be lower, above 10 mm in length, to assume metastatic disease

small study cohorts. In a larger cohort study, interpretation of the ROC curve suggested 18 mm to be a good cutoff value to distinguish metastatic from nonmetastatic CLNs (Fig. 5.29). Sensitivity was 60.5%, whereas specificity was 74.3% [1]. In contrast, the group around Steinkamp proved the hypothesis that CLNs with a maximal longitudinal diameter above 10 mm could be considered as metastasis; they reported a sensitivity of 88% but a rather low specificity of 60% [111]. In an obviously metastatic neck, longitudinal diameters of suspected nodes should exceed 15–18 mm, whereas in clinically unsuspicious necks, the cutoff line to assume metastatic disease should be lower, >10 mm in length. In this way, the sensitivity is higher in a diagnostic situation with no clinically relevant neck disease, and specificity increases in a metastatic-neck.

Moreover, this shows that the use of multiple parameters will be most successful. More recent studies have investigated the minimal diameter of lymph nodes and found that minimal diameters exceeding 5–10 mm are suspect for the detection of lymph node metastases [13, 108, 112]. Most authors recommended 8 mm as the best cutoff value for the minimal diameter (Fig. 5.30) [1, 14].

Another interesting issue is the calculation of ratios of diameters to image two-dimensional forms of the lymph node. The workgroup of Vassallo presented a sensitivity of 85% and a specificity of 86% for the criterion "ratio of longitudinal to transverse diameter" [16]. When Steinkamp and coworkers applied this ratio, they improved their diagnostic accuracy from 52% to 93%, compared with the exclusive observation of the diameters of the lymph nodes [111]. It is commonly agreed that round-shaped lymph nodes are highly suspicious for malignancy, and oval-shaped nodes represent benign findings [15, 17–20]. On the other hand, a malignant lymph node at an early stage of conversion can still be oval [18], and round-shaped lymph nodes are the typical sonographic finding in Hodgkin's and non-Hodgkin's lymphoma [17, 19]. Considering a Steinkamp/Solbiati index of 0.67 to be the cutoff for round or oval-shaped lymph nodes, data showed a sensitivity of 64.5%, a specificity of 57.6%, and a predictor quality of 61.3% for lymph node metastasis (Fig. 5.31).

Along with the discussion of derived quantitative sonomorphologic criteria, the criterion "volume of lymph nodes" came into force and raised increased attention, because an enlargement of a lymph node in general is considered suspicious for malignancy [16, 17, 113], especially in cases of HNSCC [18]. On the other hand, reactive or resorptive inflammation may also lead to lymph node enlargement [19, 111], and more importantly, micrometastases smaller than 3 mm could not be detected by ultrasound technique [16, 17, 114]. By using the volume formula for ellipsoid objects, the possibility that a lymph node is malignant is doubled if its volume is >9 mm^3 in a patient with confirmed cancer in the head and neck area. This correlation is statistically highly significant ($p < 0.001$) (Fig. 5.32).

The use of single sonomorphologic aspects is definitively less valuable than the combination of multiple criteria. To simplify judgment of the different parameters and bring them

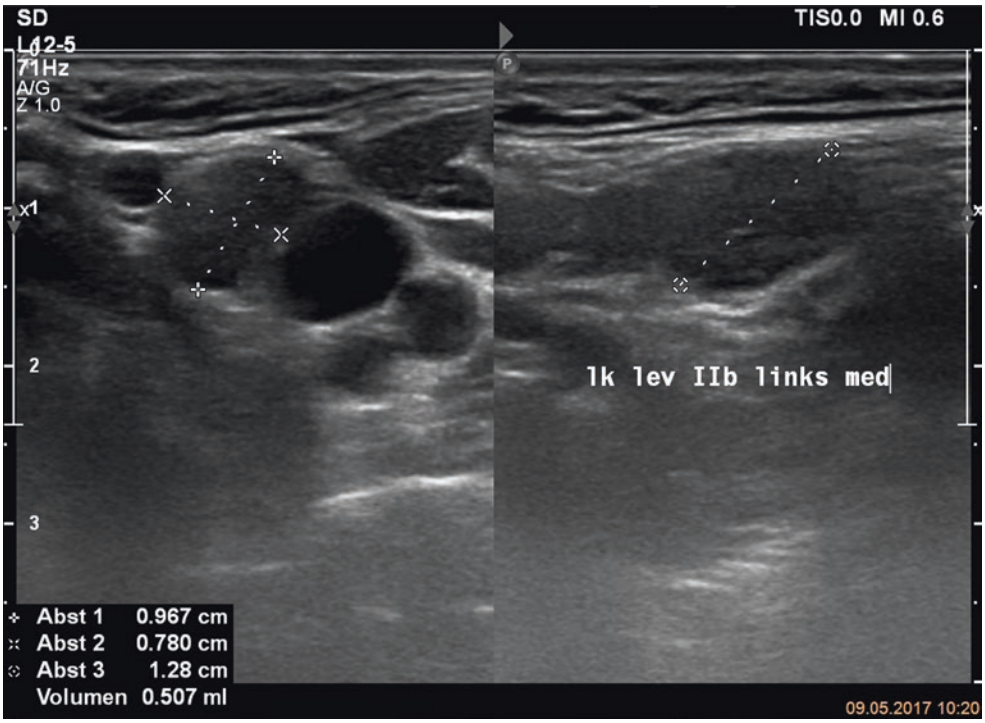

Fig. 5.30 Only determination of multiple diameters will be most successful. In more recent studies a minimal diameter exceeding 5–10 mm are suspect for the detection of lymph node metastases, recommending 8 mm as the best cutoff value

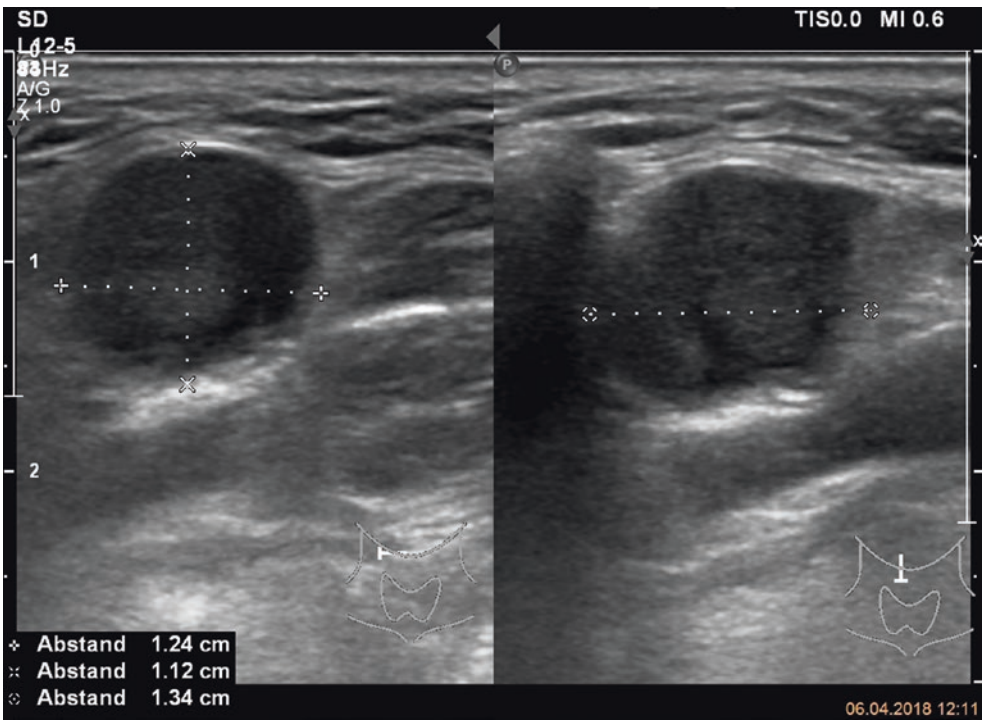

Fig. 5.31 Another interesting issue is the calculation of a Steinkamp/Solibiaty index "ratio of longitudinal to transverse diameter." A ratio of 0.67 is a good value for the cutoff between round- or oval-shaped lymph nodes and a predictor for lymph node metastasis

together, a statistically proven point scale system was recently published [1]. After multivariate analysis, it turned out that the three diameters (longitudinal, transverse, and minimal diameter) and dependent values were the most significant parameters to distinguish between reactive and malignant lymph nodes. The five values were adjusted to 100 points, each under 30 points (Table 5.6). As soon as two values turn positive, a critical sum of 30 points is exceeded, and malignant transformation is very probable, with a sensitivity of 82% and a specificity of 58%; these are comparable to the various published data for ultrasound in the literature, which have shown 78–98% sensitivity and 32–100% specificity [14, 108, 111].

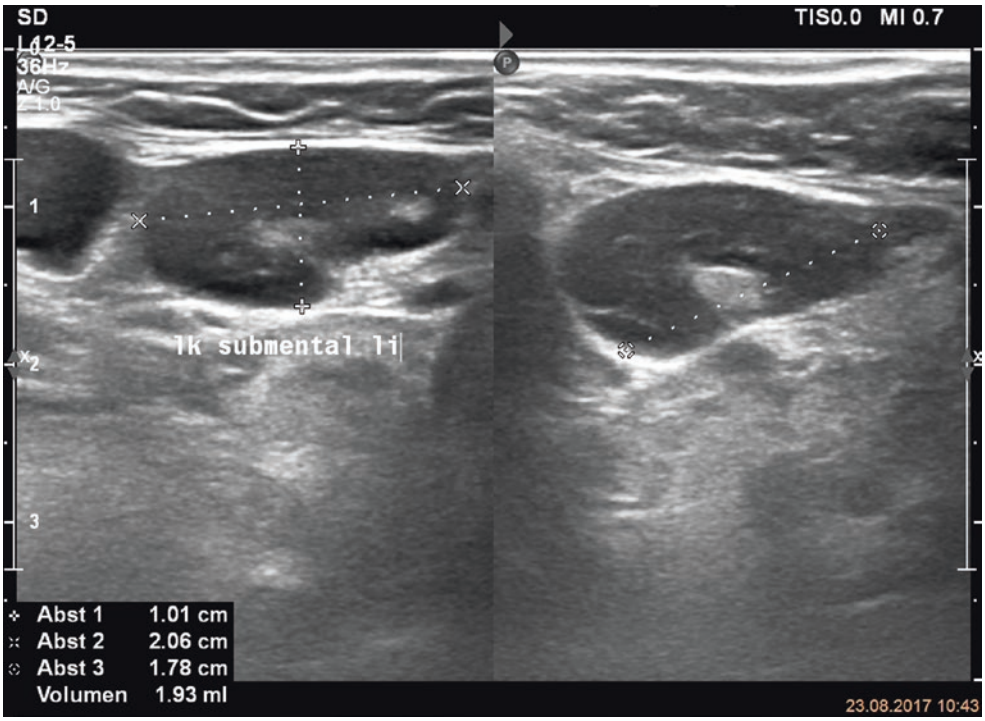

Fig. 5.32 Along with the discussion of derived quantitative sonomorphologic criteria, the criterion "volume of lymph nodes" came into force and raised increased attention. By applying the volume formula for ellipsoid objects, the possibility of a potential malignant lymph node is doubled in a volume above 9 mm^3 in case of a confirmed cancer disease in the head and neck area

Table 5.6 Point scale of quantitative ultrasound values[a]

Points	If	
25	Volume > 6 cm^3	
23	Longitudinal to transverse diameter > 0.7	
22	Longitudinal diameter > 19 mm	
17	Minimal diameter > 11 mm	
13	Minimal to maximal transverse diameter > 0.7	
100	If the total score is 30 points or more, a malignant transformation is very proable.	

[a]Each value was adjusted in the order of its statistical significance, so that sum accounts for 100 points. A malignant transformation is very probable if a critical sum of 30 points is exceeded

Doppler ultrasonographic assessment of intranodal vascular resistance Metastatic lymph nodes usually have a peripheral or mixed (hilar and peripheral) vascularization (Video 5.6) [18, 29, 31, 32, 34, 35, 115]. The presence of peripheral vascularization and perfusion in malignant nodes

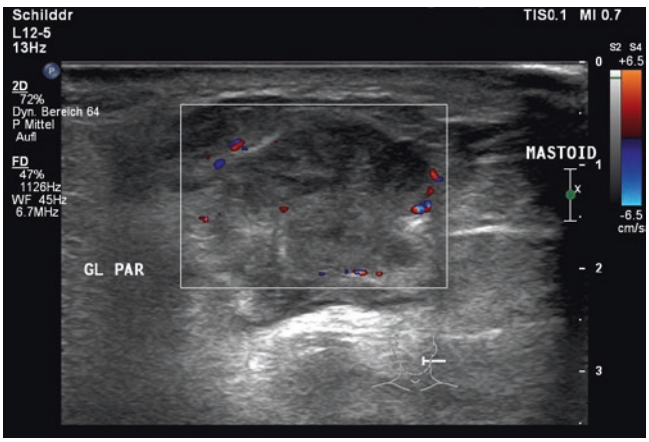

Fig. 5.33 Because peripheral vascularization is common in malignant nodes, its presence, regardless of the presence or absence of hilar vessels, is highly suggestive of malignancy

is thought to be related to tumor neoangiogenesis and recruitment of capsular vessels, whereas keratinization and intranodal necrosis often cause diminishing of hilar vessels [18, 29, 31, 35]. Because peripheral vascularization is common in malignant nodes, its presence, regardless of the presence or absence of hilar vessels, is highly suggestive of malignancy (Fig. 5.33). Power Doppler ultrasonographic evaluation of nodal vascular pattern has been reported to have high sensitivity (83–89%) and specificity (87–100%) for differentiating metastatic and reactive nodes (Video 5.7) [18, 29, 31, 35].

Power Doppler ultrasonography assessment of cervical nodes improves diagnostic accuracy, but its use may not be

necessary in all cases, because grayscale ultrasonography in combination with the features discussed above already has a high sensitivity (95%) and specificity (83%) in differentiating metastatic and nonmetastatic nodes [19]. Power Doppler ultrasonography is useful in patients in whom grayscale ultrasonography is equivocal, however.

Contrast-enhanced ultrasound Contrast-enhanced ultrasound (CEUS) facilitates more accurate illustration of nodal vascularization and provides additional information on lymph node parenchymal perfusion [116]. Its value in differentiating benign and malignant lymph nodes is controversial, however [116–119]. The value of CEUS in routine clinical practice is limited because it is expensive, time-consuming, and does not eliminate the need for fine-needle aspiration cytology (FNAC).

Ultrasound-guided fine-needle aspiration (USFNA) and ultrasound-guided core biopsy (USCB) cytology USFNA and USCB are both of tremendous importance in the differential diagnosis of malignant cervical lymphadenopathies. Fine-needle aspiration cytology (FNAC) is well established in adults and is becoming popular in children [120, 121]. Ultrasound-guided FNAC has been shown to be an accurate method for evaluating cervical lymphadenopathy, with a high sensitivity (89–98%), specificity (95–99%), and overall diagnostic accuracy (95–98%) [122–125]. It has been reported that ultrasound-guided FNAC correctly stages the neck nodes in 93% of patients with head and neck malignancy [123] and influences the indications for therapeutic and elective treatment [125]. In our experience, ultrasound-guided FNAC is performed to confirm the diagnosis whenever the ultrasonographic findings are equivocal. The technique aids in tumor staging and treatment planning [123–126] and also is useful in postoperative surveillance of neck nodes [127].

Although ultrasound-guided FNAC is useful in most cases, surgical excision of the lymph nodes and histology are usually considered mandatory for bulky and symptomatic lesions or when cytologic findings are inconclusive for the diagnosis [128]. It has been reported that ultrasound-guided core biopsy (USCB) of neck masses can be performed in pediatric patients under local anesthesia and that the procedure is well tolerated [129]. USCB therefore avoids unnecessary surgical procedures in this group of patients.

5.1.7 Thyroid Carcinoma Lymph Node Metastases

Characteristics *Indeterminate*: absence of a hilum and at least one of the following signs—round shape, increased short axis, increased central vascularization. *Suspicious*: cystic areas, microcalcifications, peripheral or diffusely increased vascularization, hyperechoic tissue looking like thyroid.

The European Thyroid Association (ETA) and the American Thyroid Association (ATA) recently published two essential review papers with guidelines on this issue [130, 131]. In addition to the workup of the thyroid gland itself, ultrasound should evaluate the presence or absence of any suspicious CLN in the central or lateral lymph node levels, though it can be difficult in the deep parapharyngeal and retropharyngeal lymph node levels. When attempting to identify malignant thyroid metastases, the level of the CLNs is of particular importance. Leboulleux et al. reported that almost half of metastatic CLNs are located in levels III and IV, and the other half are in level VI [22]. Up to 16% of CLN metastasis occurs bilaterally, whereas unilateral CLN metastases are most frequently located on the same side as the initial thyroid tumor [132].

Abnormal CLNs in thyroid cancer are classified in two categories: indeterminate and suspicious [130] (Fig. 5.33). *Indeterminate* CLNs lack a hilum and show at least one of the following characteristics:

- Rather round shape
- Increased short axis (≥8 mm in level II and ≥5 mm in levels III and IV)
- Increased central vascularization (Fig. 5.34).

In this context, the presence of a hilum and the absence of vascularization are the weakest ultrasonographical signs for CLNs in thyroid cancer because a hilum is also present in normal CLNs in 29–48% and 33–36% of the cases, respectively [133–137].

In contrast, *suspicious* CLNs demonstrate at least one of the following characteristics (Fig. 5.35) [130, 133–137]:

- Microcalcifications
- Partially cystic appearance
- Peripheral or diffusely increased vascularization
- Hyperechoic, thyroid-like tissue

Microcalcifications and cystic transformation are especially strong indicators for malignancy, because they do not occur in normal CLNs. Although their sensitivity is only moderate (5–69% for microcalcifications and 10–34% for cystic transformation), their specificity (93–100% and 91–100%, respectively) was very good, resulting in a high positive predictive value (PPV) of 88–100% and 77–100%, respectively, with fair accuracies of 56–72% and 48–65% (Fig. 5.36). Peripheral vascularization, hyperechogenicity, and round shape do have moderate sensitivity and specificity (of 40–86%,

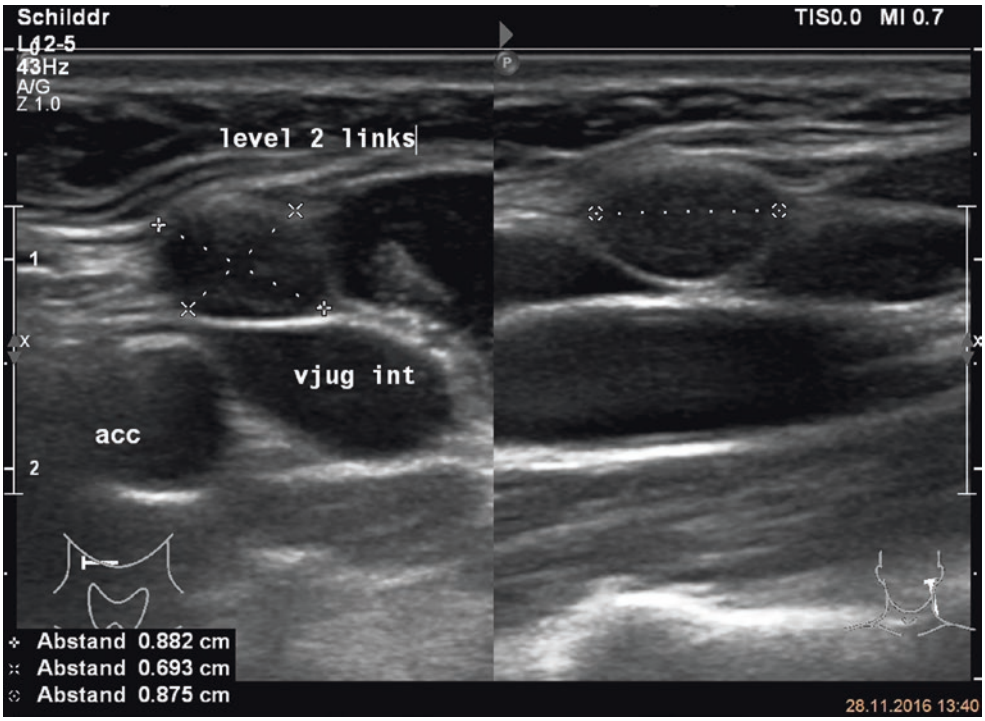

Fig. 5.34 Indeterminate CLNs are lacking a hilum and show at least one of the following characteristics: (1) rather a round shape; (2) an increased short axis (≥8 mm in level II and ≥5 mm in levels III and IV); and/or (3) an increased central vascularization

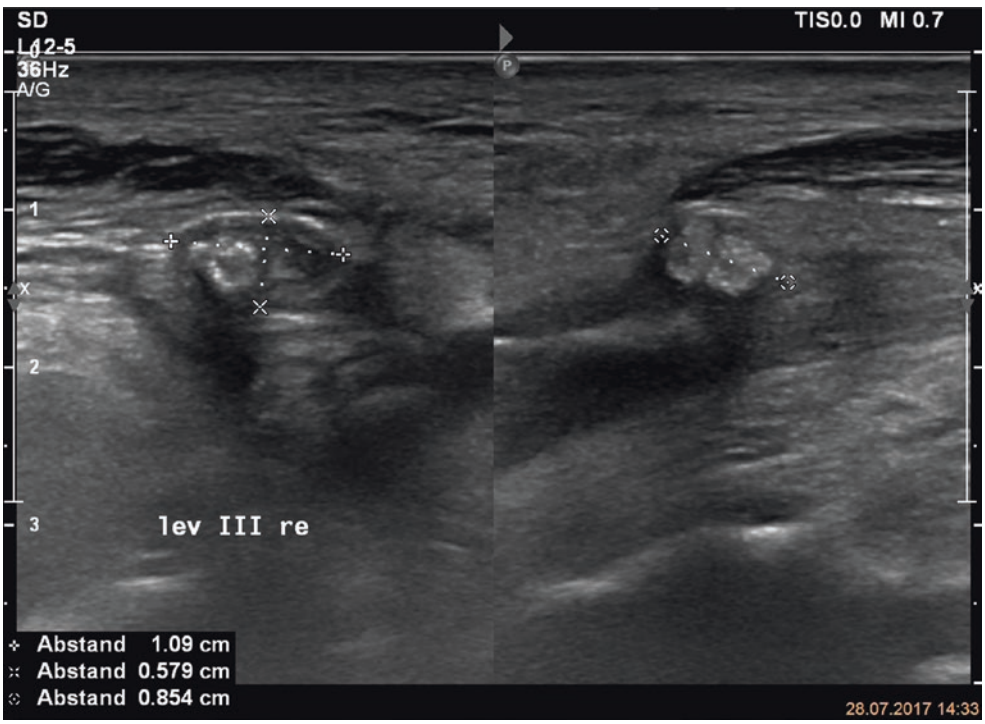

Fig. 5.35 Suspicious CLNs elicit at least one of the following characteristics: (1) microcalcifications, (2) partially cystic appearance, (3) peripheral or diffusely increased vascularization, and/or (4) hyperechoic, thyroid-like looking tissue

57–93%; 30–87%, 43–95%; 37%, 70%, respectively (Fig. 5.37)) but therefore have higher negative predictive values (NPVs) and also higher PPVs (31–70%, 77–80%; 38–84%, 66–96%; 45%, 63%, respectively) while rarely occur in normal CLNs (1–18%; 4–17%; 4–36%, respectively).

Qualitative/quantitative elastographic assessment Experience with US elastography (USE) is limited, with sensitivities of 83–85% and specificities of 98–100% [138, 139]. Nevertheless, USE could be applied selectively in nodules with indeterminate or equivocal US appearances and

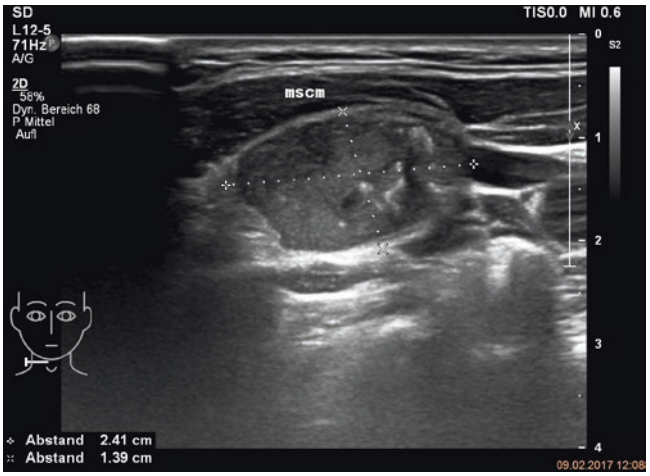

Fig. 5.36 Especially microcalcifications and cystic transformation are strong indicators for malignancy since these do not occur in normal CLNs

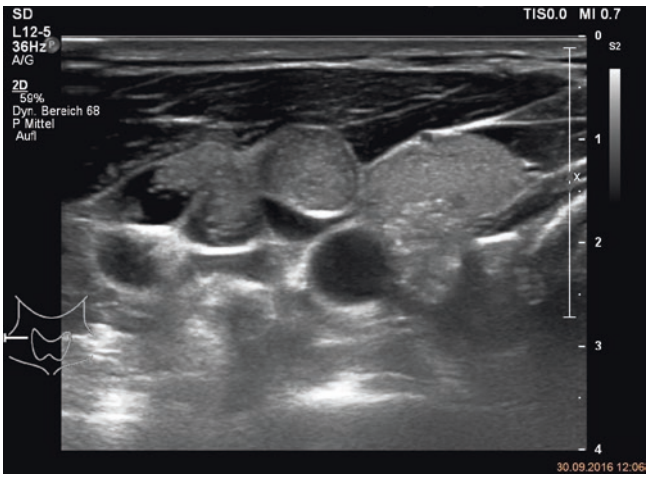

Fig. 5.37 Peripheral vascularization, hyperechogenicity, and round shape do have moderate sensitivity and specificity, respectively, but therefore have higher negative and positive predictive values, which rarely occur in normal CLNs

may improve decision-making for US-guided FNAC by upgrading or downgrading the risk of malignancy.

Ultrasound-guided fine-needle aspiration (USFNA) and ultrasound-guided core biopsy (USCB) cytology The confirmation of malignancy in CLNs is achieved by US-guided FNA for cytology and/or measurement of thyroglobulin (Tg) in the needle washout (Table 5.7). A Tg concentration <1 ng/mL is reassuring; the probability of N1 disease increases with higher Tg levels [140]. This FNA measurement of Tg is likely to be valid even in patients with circulating anti-Tg autoantibodies [141, 142], although one study scrutinizes the validity of this measurement in patients

Table 5.7 Recommendation for the use of ultrasound-guided fine-needle aspiration (FNA) cytology in CLNs of patients with thyroid cancer

	Recommendation for	Strength of recommendation/ quality of evidence
(A)	Preoperative neck US for cervical (central and especially lateral neck compartments) lymph nodes is recommended for all patients undergoing thyroidectomy for malignant or suspicious-for-malignancy cytologic or molecular findings	Strong recommendation Moderate-quality evidence
(B)	US-guided FNA of sonographically suspicious lymph nodes ≥8–10 mm in the smallest diameter should be performed to confirm malignancy, if this would change management	Strong recommendation Moderate-quality evidence
(C)	The addition of FNA thyroglobulin (Tg) washout in the evaluation of suspicious cervical lymph nodes is appropriate in selected patients, but interpretation may be difficult in patients with an intact thyroid gland	Weak recommendation Low-quality evidence

with anti-Tg autoantibodies [143]. Tg washout may be helpful, particularly in cases in which the lymph nodes are cystic, cytologic evaluation of the lymph node is inadequate, or the cytologic and sonographic evaluations are divergent (such as normal cytologic biopsy of a large lymph node with microcalcifications) [144]. In a retrospective study, additional FNA with Tg washout measurements (FNA-Tg) helped to diagnose a metastatic lymph node with one or two suspicious US features, but it did not offer incremental benefit for those lymph nodes with highly suspicious US features in which FNA alone was sufficient for diagnosis. Two recent systematic reviews showed that false-positive Tg washout may particularly occur in lymph nodes in the central compartment when the thyroid gland is still present [145, 146]; therefore an FNA-Tg cutoff of 32 ng/mL is suggested [146]. Others have interpreted FNA-Tg in the context of serum Tg and TSH in these patients [147, 148], so standardization of the interpretation of Tg washout is urgently required for determining the prognosis and tailoring treatment for patients with differentiated thyroid cancer. However, removal of the primary thyroid tumor and accessible locoregional disease remains an important component of initial treatment even in most patients with metastatic disease [149].

5.1.8 Malignant Lymphoma Nodes

Characteristics Elliptical, homogenous with intranodal reticulation, hilum present, sharp borders, longitudinal diam-

eter <18 mm, minimal cross-sectional diameter >8–10 mm, color/Doppler mode mixed vascularization.

Plane grayscale ultrasonography Lymph nodes can be affected by either Hodgkin's or non-Hodgkin's lymphoma. Affected nodes can appear in any level of the neck, unilaterally or bilaterally. It is not possible to distinguish between both lymphoma forms by sonography alone. The diameter of lymphomatous cervical nodes is not an accurate criterion for differentiating lymphomatous from normal or other pathologic CLNs, because they can vary significantly [150]. Typically, lymphomatous nodes are enlarged, with a minimal diameter of 10 mm or larger in the beginning [151, 152]; gradual and substantial reduction in size during treatment indicates a good treatment response [153].

A lymphomatous node is usually round and well-defined; it appears hypoechoic and lacks an echogenic hilum (Figs. 5.38 and 5.39) [152, 154, 155]. These features are unspecific and therefore may not be useful US criteria to differentiate lymphoma from metastatic CLNs.

Although previous studies suggested that a pseudocystic appearance with posterior acoustic enhancement is characteristic of lymphomatous nodes (Fig. 5.40) [152, 154, 155], with the use of newer high-resolution transducers, pseudocystic appearance is not often seen, but intranodal reticulation, a micronodular echo pattern, is commonly found (Figs. 5.41 and 5.42) [156].

Lymphomatous CLNs seldom show a real cystic necrosis unless the disease is advanced or the patient has received previous radiation or chemotherapy [151]. Similarly, intranodal dense calcification with posterior acoustic shadowing is uncommon and may be found only after treatment [157].

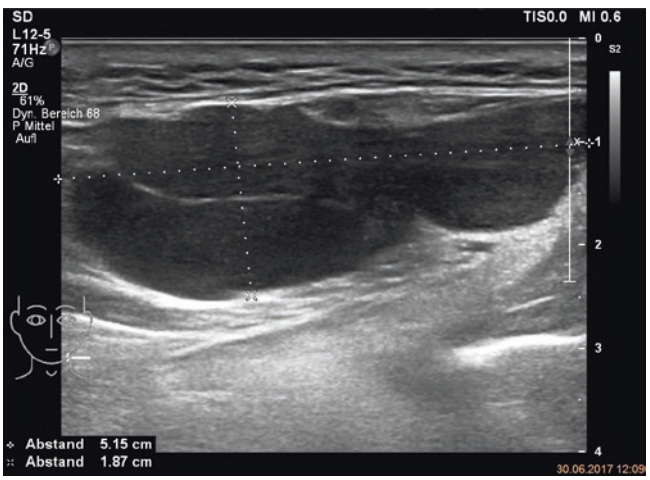

Fig. 5.38 A lymphomatous node is usually round-shaped, well-defined, appears hypoechoic, and without an echogenic hilum. These features are unspecific and therefore may not be useful ultrasonographic criteria to differentiate lymphoma from metastatic CLNs

Fig. 5.39 A characteristic longitudinal plane of a chain of hypoechoic lymphomatous CLNs packed back to back of each others

Doppler ultrasonographic assessment of intranodal vascular resistance Lymphomatous nodes tend to have a mixed vasculature (hilar and peripheral), whereas an isolated peripheral vasculature is uncommon (Fig. 5.43) [157]. The relatively high incidence of hilar vascularization in lymphomatous nodes is believed to be associated with the combination of malignant lymphatic and vascular hyperplasia of preexisting immune cells and vessels (Fig. 5.44). Since a peripheral vascularization is characteristic for malignant nodes, its presence is highly suggestive of malignancy, with a sensitivity of 67% and a specificity of 100% for distinguishing lymphomatous from reactive lymph nodes [158].

Furthermore, this sign is also used for monitoring of therapeutic success. Reduced intranodal vascularization is a sign of good treatment response in patients with non-Hodgkin lymphoma during chemotherapy, whereas lymph nodes with persistent vasculature tend to have poor clinical outcome [153].

The application of power Doppler US in the assessment of cervical nodes might not be necessary for all cases in routine clinical practice, because grayscale ultrasonography with the features described above already achieves a high sensitivity (95%) and high specificity (83%) in differentiating metastatic and nonmetastatic nodes [159]. Power Doppler US is useful in patients for whom grayscale ultrasonography is equivocal, however, and it improves diagnostic accuracy (Video 5.8) [159].

As with metastatic lymph nodes, the role of vascular resistance in the assessment of lymphomatous nodes is unclear, and further research is needed [31, 35, 160].

Qualitative elastographic assessment Tan et al. recently investigated elastography in lymphomatous nodes and reported that lymphomatous malignant and benign nodes could not be distinguished by the elastographic score alone; both show similar elastographic characteristics, whereas solid malignant lymphadenopathies are more stiff [43].

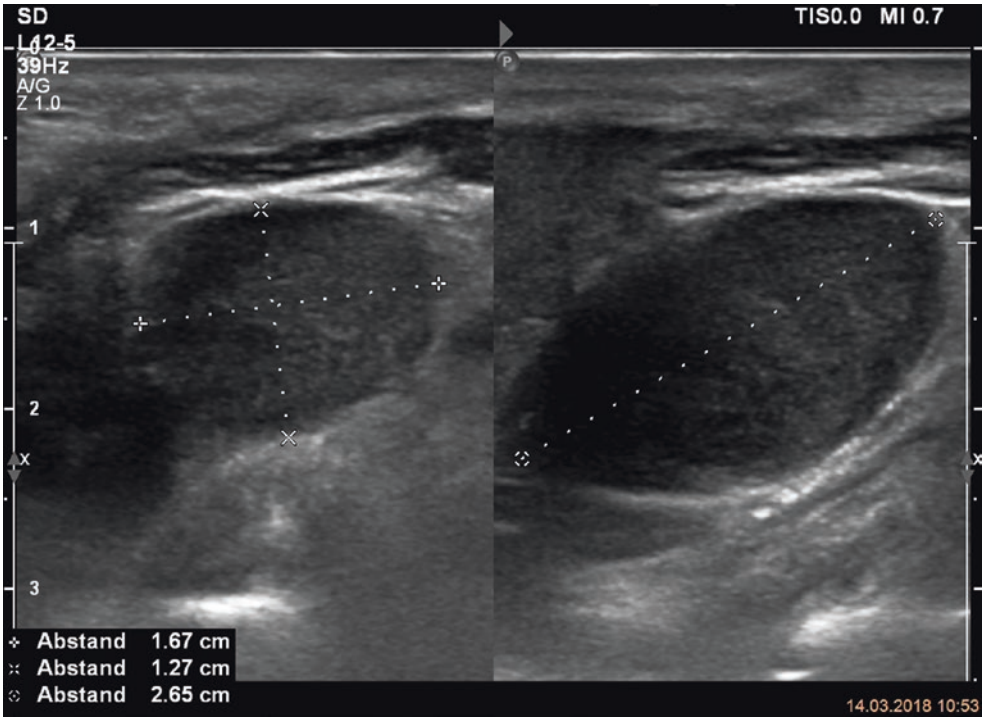

Fig. 5.40 Previous studies had suggested that pseudocystic appearance with posterior acoustic enhancement is characteristic features of lymphomatous nodes

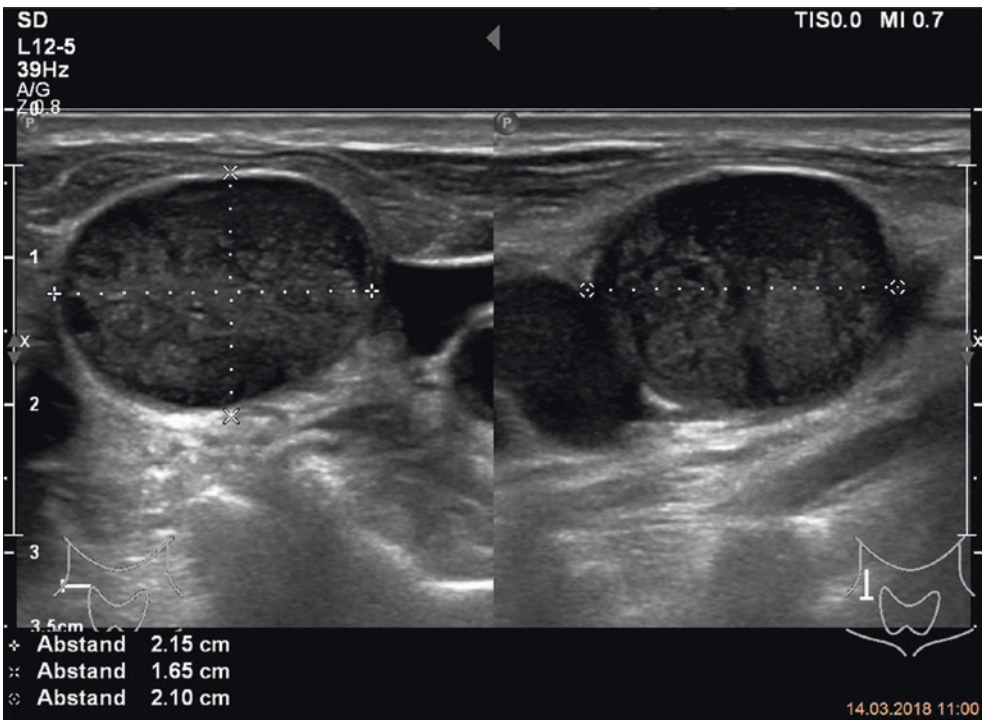

Fig. 5.41 With the use of newer high-resolution transducers, pseudocystic appearance is not often seen, while intranodal reticulation, a micronodular echopattern, is commonly found in lymphomatous nodes

Ultrasound-guided fine-needle aspiration (USFNA) and ultrasound-guided core biopsy (USCB) cytology Although USFNA or USCB cytology is very useful in the diagnosis of malignancies, in cases of lymphomatous nodes, surgical excision of the lymph node and a specified immunochemistry are mandatory to determine the subtype of lymphomas and plan the treatment regimen [128].

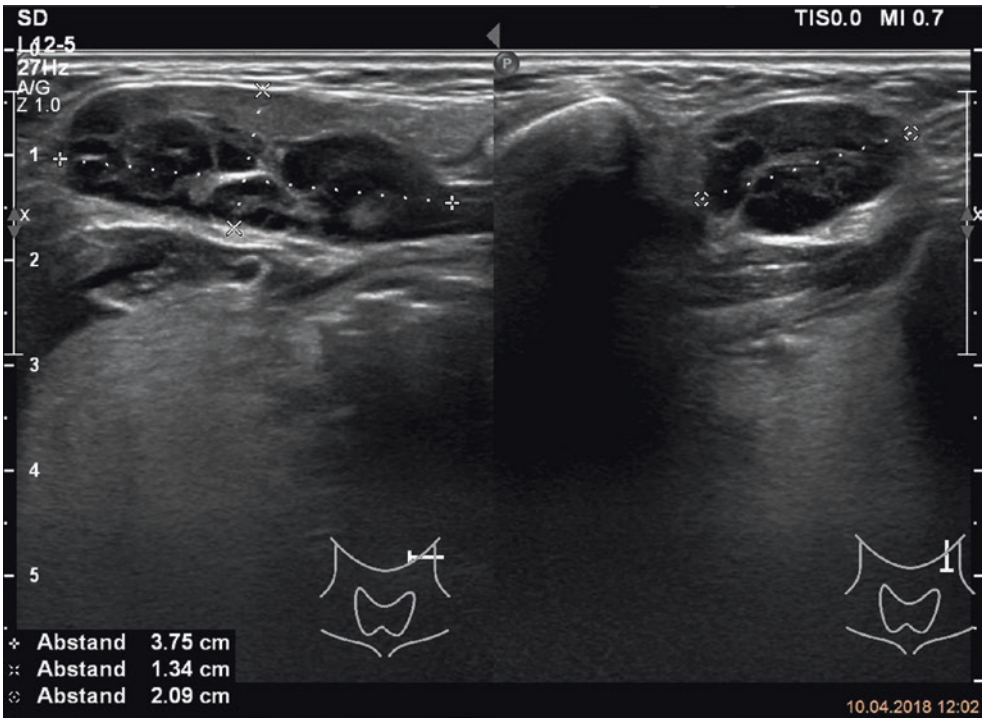

Fig. 5.42 Pseudocystic appearance of lymphpmatous CLN

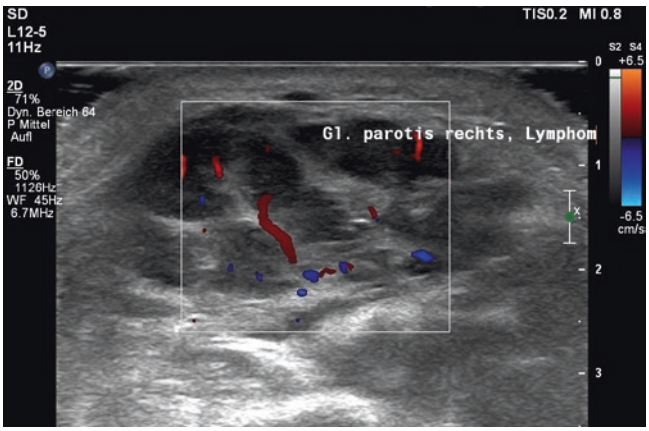

Fig. 5.43 Lymphomatous nodes tend to have a mixed vasculature (hilar and peripheral), whereas an isolated peripheral vasculature is uncommon

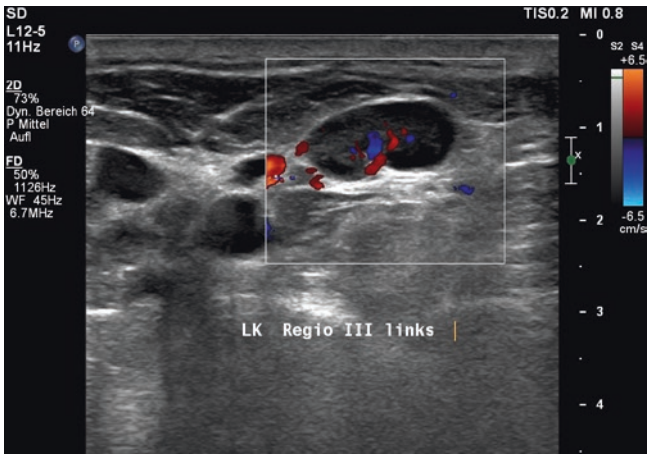

Fig. 5.44 The relatively high incidence of hilar vascularization in lymphomatous nodes is believed to be associated with the combination of malignant lymphatic and vascular hyperplasia of preexisting immune cells and vessels. Since a peripheral vascularization is characteristic for malignant nodes, its presence is highly suggestive for distinguishing lymphomatous from reactive lymph nodes

5.2 Regional Differential Diagnoses

Lymph node compartments are separated into levels and sublevels according to the last CLN classification of the American Head and Neck Society (Fig. 5.45) [161, 162]. Level VI contains the thyroid gland and the adjacent nodes bordered superiorly by the hyoid bone, inferiorly by the brachiocephalic artery defined by the suprasternal notch, and laterally on each side by the carotid sheaths. The level II, III, and IV nodes are arrayed along the jugular veins on each side, bordered anteromedially by level VI and laterally by the posterior border of the sternocleidomastoid muscle. The level III nodes are bounded superiorly by the level of the hyoid bone and inferiorly by the cricoid cartilage; level II is above level III, and level IV is below it. The level I node compartment includes the submental and submandibular

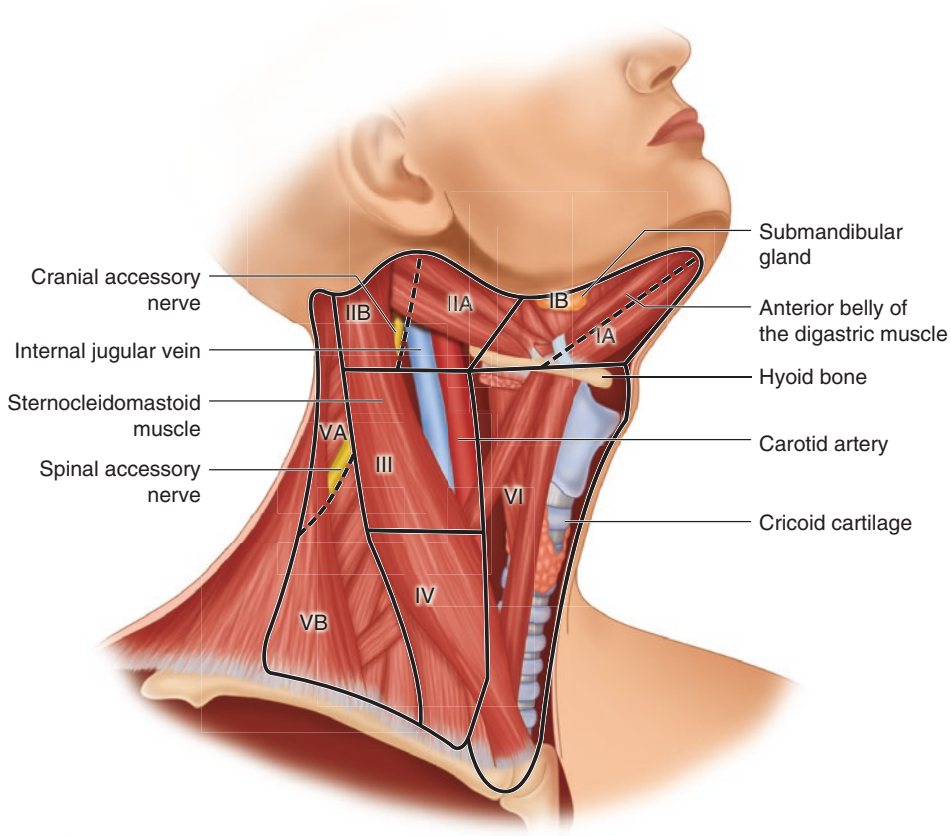

Fig. 5.45 Lymph node compartments are separated into levels and sublevels according to the last CLN classification of the American Head and Neck Society by Robbins et al. [162]

nodes, above the hyoid bone and anterior to the posterior edge of the submandibular gland. Finally, the level V nodes are in the posterior triangle, lateral to the lateral edge of the sternocleidomastoid muscle and medial to the trapezius muscle. Level VII includes the paratracheal and pretracheal superior mediastinal CLNs above the level of the brachiocephalic artery; it lies just caudal to level VI. Levels I, II, and V can be further subdivided into parts A and B, as noted in Fig. 5.45. Table 5.8 lists the primary tumor sites most likely to metastasize to each level.

5.2.1 Central/Anterior Lymphadenopathy

Head and Neck Squamous Cell Carcinoma (HNSCC)

The Delphian lymph node is frequently involved in metastatic laryngeal squamous cell carcinoma of the glottic and subglottic area and is found anterior to the thyroid cartilage. Furthermore, cancers arising from the apex of the piriform sinus and cervical esophagus metastasize to the anterior compartment group (level VI). Therefore, US investigation of the neck should always involve level VI in laryngeal, hypopharyngeal, and cervical esophageal cancer. Infrequently, level VII can also be involved, especially in advanced cancer of these locations.

Thyroid Cancer

A systematic sonographic evaluation of the anterior (and lateral) CLN levels VI and VII should be performed whenever thyroid nodules are detected. If US identifies suspicious CLNs, an US-guided FNAC of the suspicious lymph node (and the thyroid nodule) should be performed, and a washout for Tg measurement is indicated [131]. This approach also warrants US-guided FNA of nodules measuring less than a centimeter.

5.2.2 Lateral Lymphadenopathy

Head and Neck Squamous Cell Carcinoma

Submental CLNs (sublevel IA) are at greatest risk for harboring metastases from cancers arising from the floor of the mouth, anterior oral tongue, anterior mandibular alveolar

Table 5.8 Local distribution of underlying diseases to CLN levels

CLN level	Anatomic regions	Primary drainage sites/origins
IA	Submental lymph nodes	Floor of mouth, anterior oral tongue, anterior mandibular alveolar ridge, and lower lip
IB	Submandibular lymph nodes	Oral cavity, anterior nasal cavity, soft tissue structures of the midface, and submandibular gland Non-tuberculous lymphadenopathies
IIA	Anterior cervical	Oral cavity, nasal cavity, nasopharynx, oropharynx, hypopharynx, larynx, and parotid gland Thyroid gland (papillary cancer), tuberculous lymphadenopathies
IIB	Upper jugular	Oral cavity, nasal cavity, nasopharynx, oropharynx, hypopharynx, larynx, and parotid gland Thyroid gland (papillary cancer), tuberculous lymphadenopathies
III	Middle jugular	Oral cavity, nasopharynx, oropharynx, hypopharynx, and larynx Thyroid gland, tuberculous lymphadenopathies
IV	Lower jugular	Hypopharynx, cervical esophagus, and larynx Thyroid gland, tuberculous lymphadenopathies
VA	Upper accessory	Nasopharynx, oropharynx, and cutaneous structures of the posterior scalp and neck, tuberculous lymphadenopathies
VB	Lower accessory	Nasopharynx, oropharynx, and cutaneous structures of the posterior scalp and neck, tuberculous lymphadenopathies
VI	Prelaryngeal and pretracheal/ paratracheal	Glottic and subglottic area, apex of the piriform sinus, and cervical esophagus Thyroid gland
VII	Superior mediastinal	Glottic and subglottic area, apex of the piriform sinus, and cervical esophagus Thyroid gland

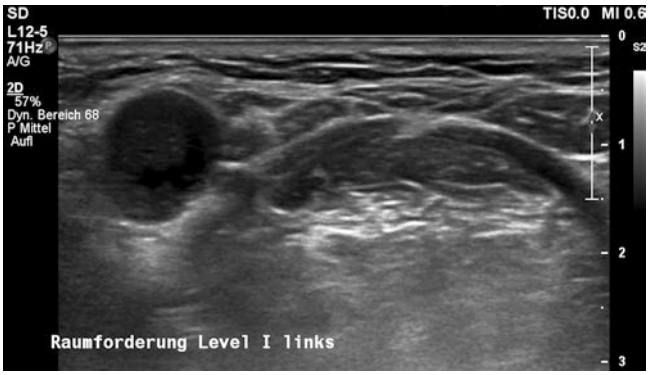

Fig. 5.46 Submandibular metastasis (level IB) from a cancer arising from the oral cavity

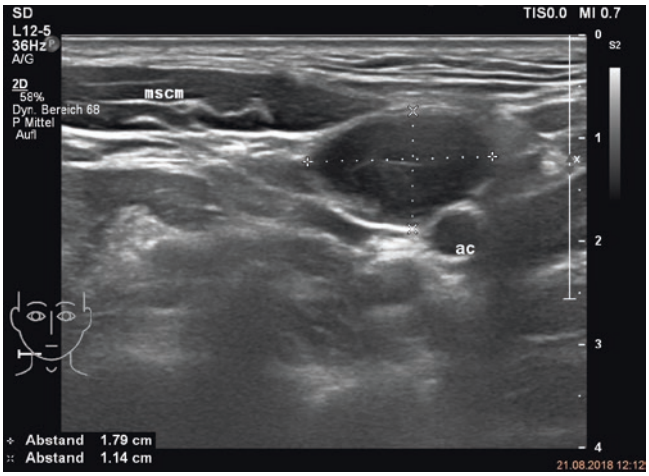

Fig. 5.47 Upper jugular metastasis (level IIA) from a cancer arising from the oropharynx

ridge, and lower lip, whereas submandibular CLNs (sublevel IB) harbor metastases from cancers arising from the oral cavity, anterior nasal cavity, soft tissue structures of the midface, and submandibular gland (Fig. 5.46) [161].

The upper jugular CLN chain (including sublevels IIA and IIB) bears metastases from cancers arising from the oral cavity, nasal cavity, nasopharynx, oropharynx, hypopharynx, larynx, and parotid gland (Fig. 5.47), whereas the middle jugular lymph nodes (level III) may be involved by cancers arising from the oral cavity, nasopharynx, oropharynx, hypopharynx, and larynx (Fig. 5.48). More caudally, the lower jugular CLNs (level IV) are at greatest risk for harboring metastases from cancers arising from the hypopharynx, cervical esophagus, and larynx (Fig. 5.49) [162].

Thyroid Gland Cancer

The location of the lymph nodes may also be useful for decision-making in thyroid gland carcinomas. Malignant lymph nodes are much more likely to occur in levels III, IV, and VI than in level II [21, 22], although this may not be true for papillary thyroid cancer (PTC) tumors arising in the upper pole of the thyroid, which have a higher propensity to demonstrate skip metastases to levels III and II (Fig. 5.50) [163].

Non-tuberculous Lymphadenopathy

Non-tuberculous lymphadenopathy involves primarily children under 5 years of age and submandibular (level IB), preauricular, and, rarely, parotid CLN levels.

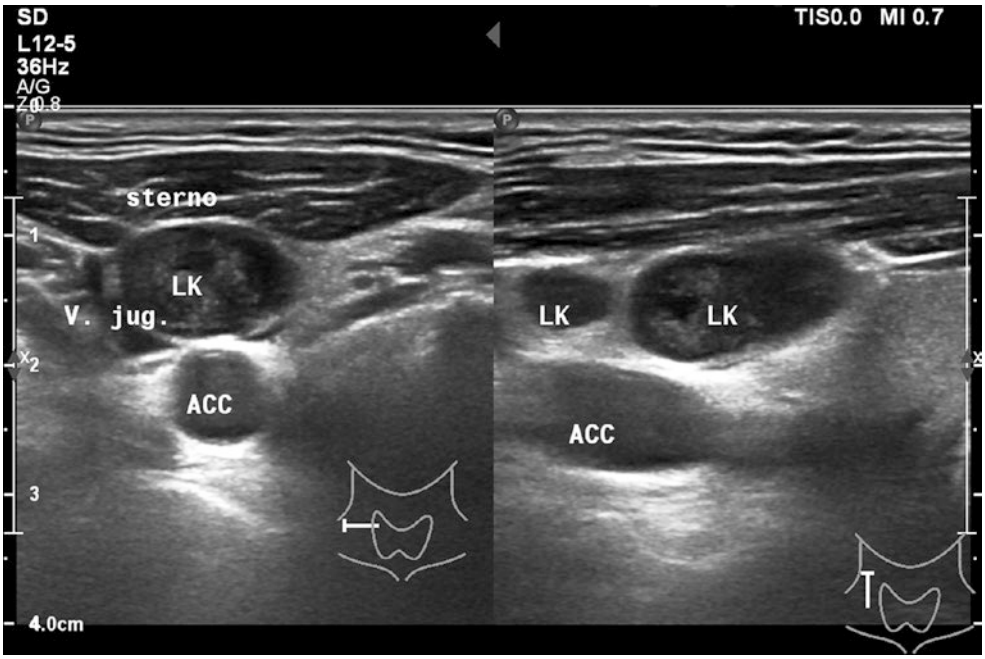

Fig. 5.48 Middle jugular metastasis (level III) arising from a cancer of the larynx

Fig. 5.49 Lower jugular metastasis (level IV) arising from a cancer of the hypopharynx

Tuberculous Lymphadenopathy

Tuberculous lymphadenopathy shows up in adults with a unilateral enlarged CLN without pain or tenderness; it usually involves the lymph nodes of levels II–IV, level V, and the supraclavicular fossa [47, 50].

5.2.3 Posterior Lymphadenopathy

HNSCC Lymph Node Metastases

The posterior triangle group, which includes sublevels VA and VB, is at greatest risk for harboring metastases from cancers arising from the nasopharynx, oropharynx, and cutaneous structures of the posterior scalp and neck (Figs. 5.51 and 5.52) [161]. In cases of cutaneous cancers, often the parotid gland is the first place of metastasis.

Tuberculous Lymphadenopathy

Tuberculous lymphadenopathy usually is an unilateral lymphadenopathy without pain or tenderness; it usually involves the lymph nodes of levels II–IV, level V, and the supraclavicular fossa [47, 50].

5.3 Cystic/Necrotic Lymphadenopathy

5.3.1 Inflammatory Lymphadenopathies

Cystic/necrotic transformation is absent in reactive lymphadenopathy and is infrequent in infectious mononucleosis, whereas liquid areas in suppurative/necrotizing lymphadenopathy or abscesses are obligatory. Moreover, liquefaction is characteristic of tuberculous lymphadenopathy ("collar stud" abscess) and non-tuberculous lymphadenopathy (stage II, intranodal cystic necrosis).

5.3.2 Malignant Lymphadenopathies

Cervical metastases are often the first sign in patients with carcinoma of the head and neck (HNSCC) or other origins. These metastatic nodes frequently undergo cystic degeneration and may be difficult to distinguish from other cystic lesions of the head and neck (Fig. 5.53). In the presence of a primary head and neck cancer, a nodal necrosis is the most

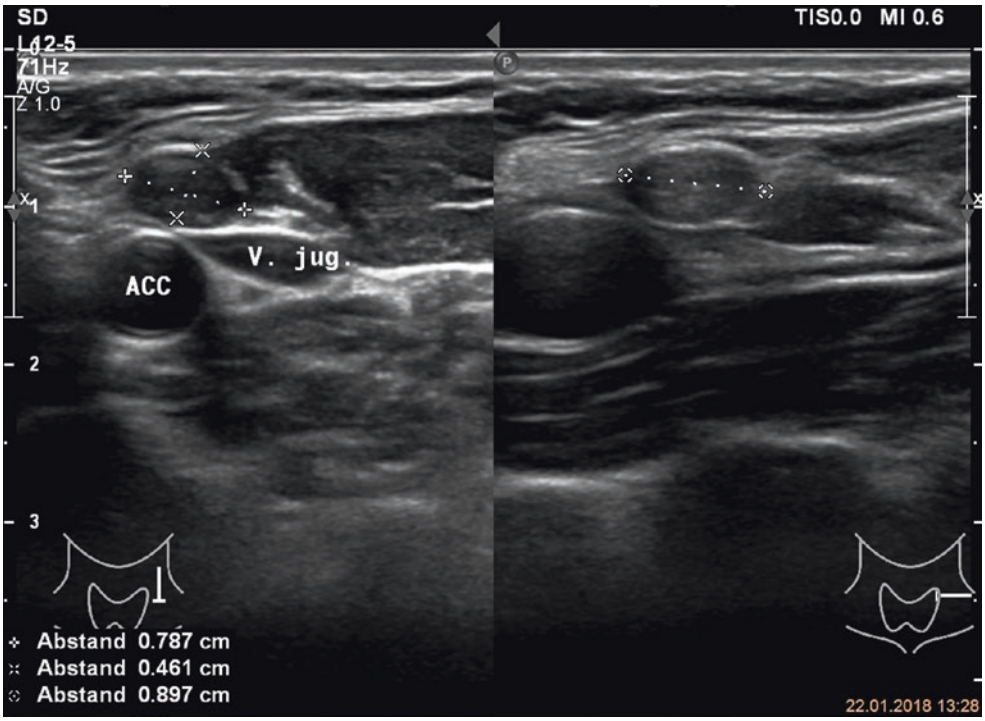

Fig. 5.50 PTC skip metastasis arising from the upper pole of the ipsilateral thyroid to level II/III

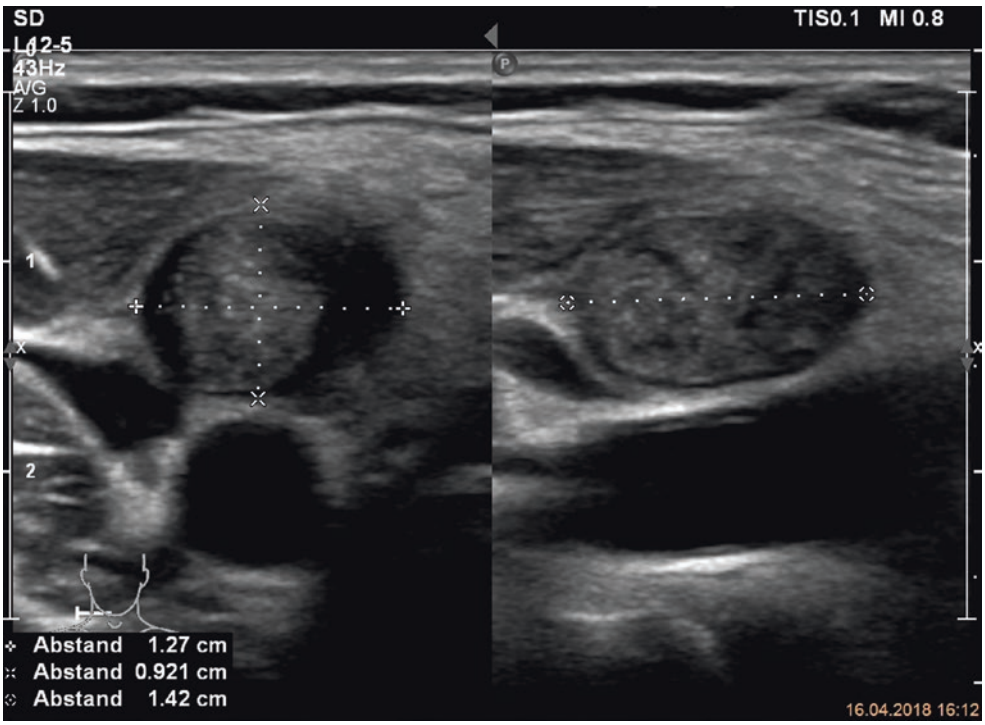

Fig. 5.51 A non-tuberculous lymphadenopathy in the submandibular level (level IB)

valuable sign of metastatic involvement, with specificity between 95% and 100% [164]. The following paragraphs describe some special entities.

HPV-Positive Metastases

Cervical metastases from primaries in the oropharynx have been shown to be more likely to undergo cystic changes than squamous cell carcinoma from other head and neck sites [166, 167]. This finding was one of the first hints of a new entity of HNSCCs, the HPV-positive HNSCC (Fig. 5.54). HPV-positive HNSCC show regularly small primaries, most of which are hidden in the palatine tonsil or the base of the tongue, with many CLN metastases, which may be cystic. In these cases, especially if no primary is seen,

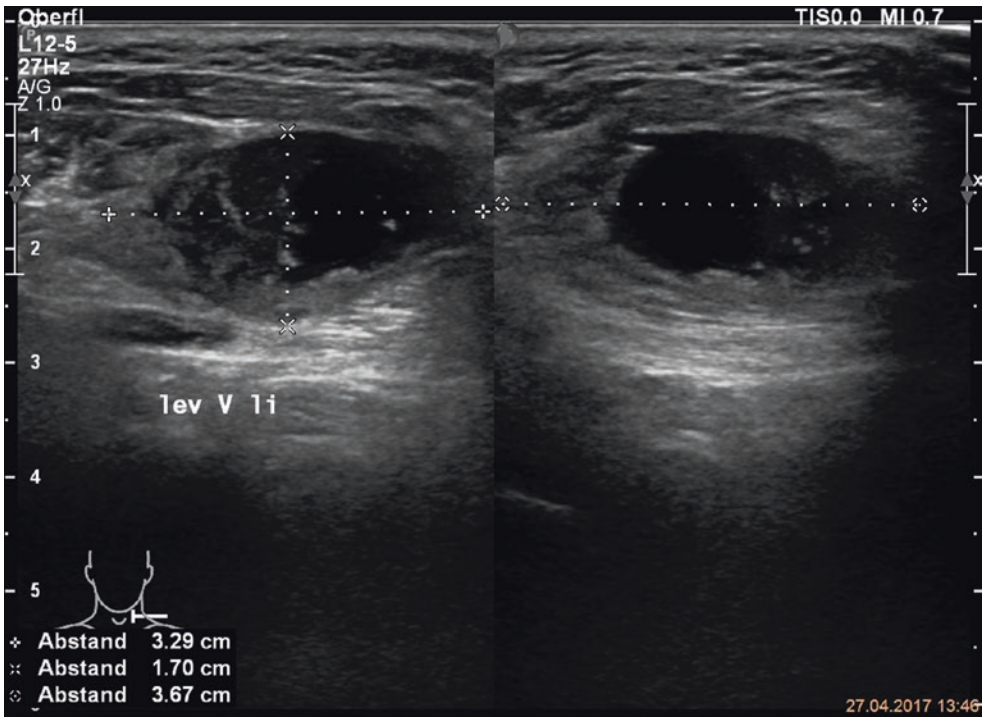

Fig. 5.52 Metastasis in the posterior triangle group arising from a cancer of the nasopharynx

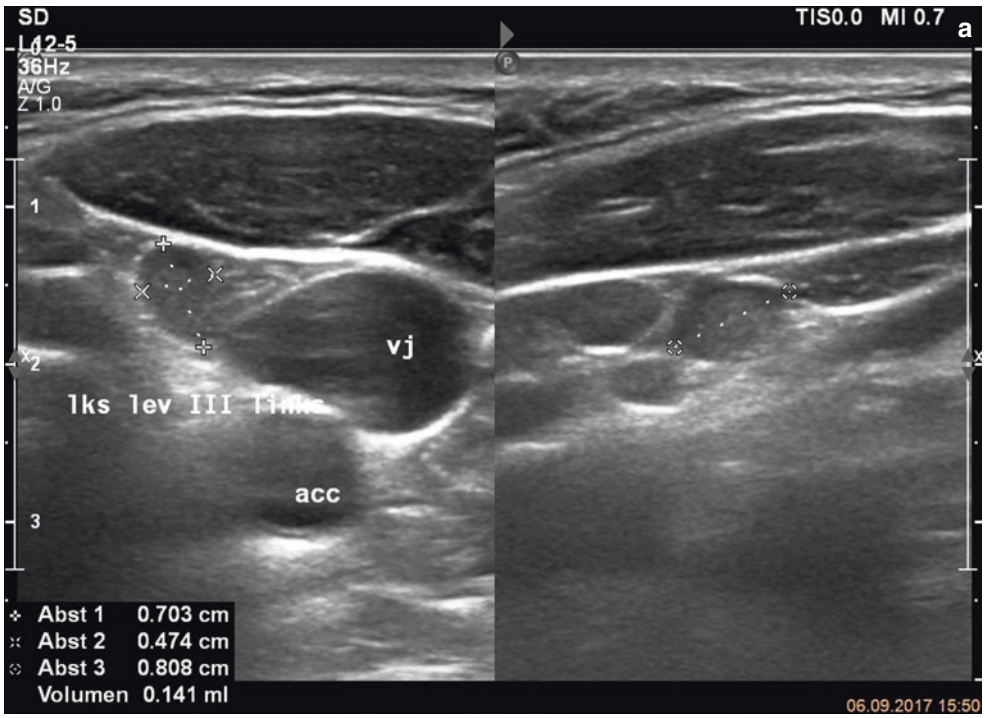

Fig. 5.53 (**a**–**c**) Cervical metastases are often the first sign in patients with carcinoma of the head and neck and frequently undergo cystic degeneration. This nodal necrosis is the most valuable sign of metastatic involvement. (**a**) A small and in the beginning indeterminate CLN. (**b**) Within 2 months this CLN elicited progressive growth and cystic degeneration. (**c**) Only 1 week later, further growth could be detected and nodal necrosis is apparent

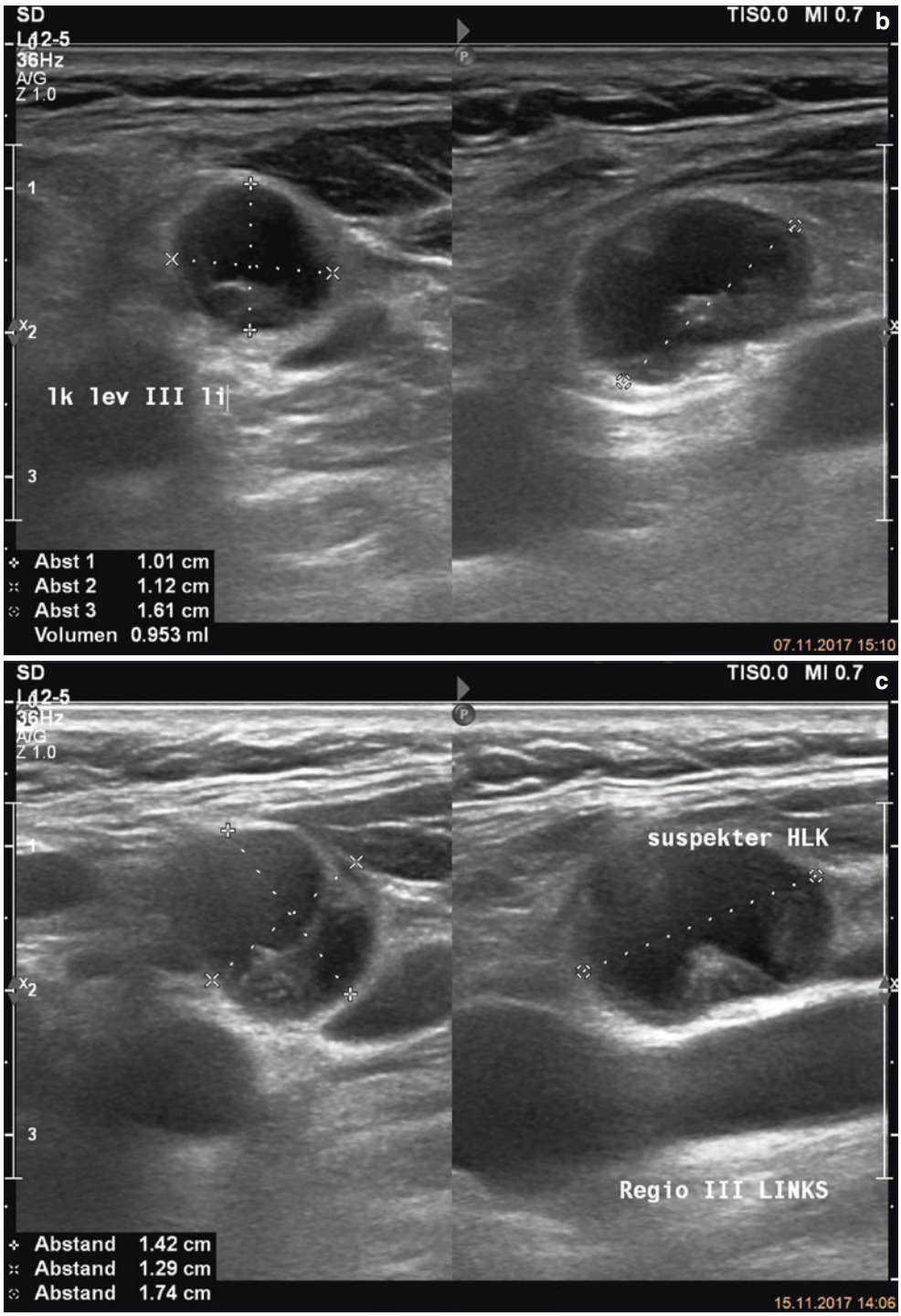

Fig. 5.53 (continued)

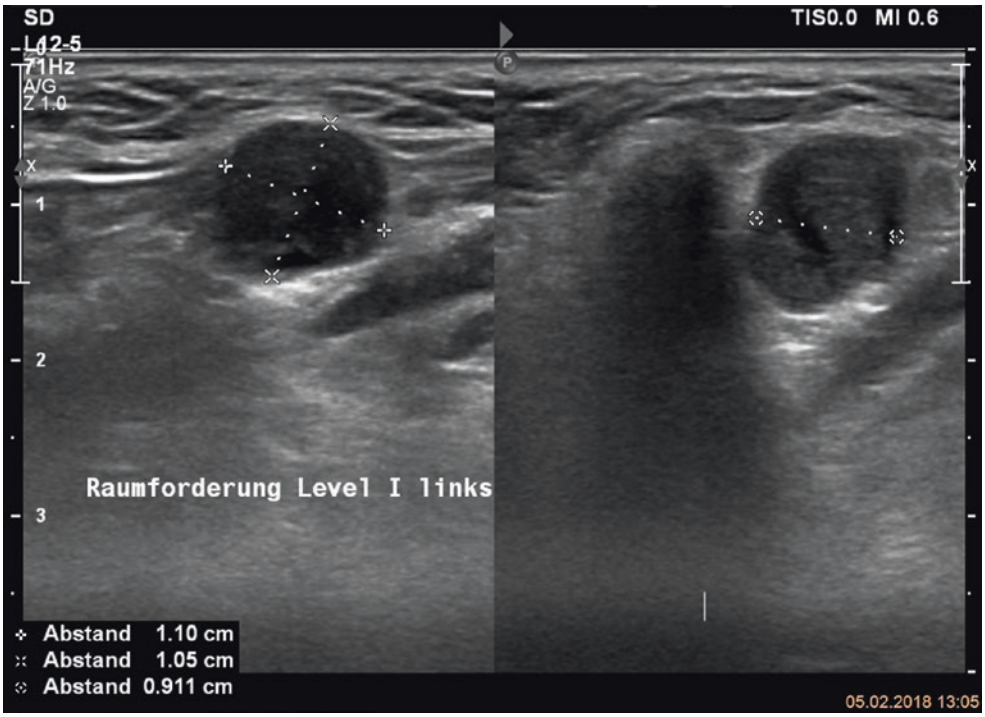

Fig. 5.54 HPV-driven cervical metastases from primaries of the oropharynx have been shown to be more likely to undergo cystic changes in comparison to squamous cell carcinoma from other head and neck sites

FNA cytology of the necrotic CLN may be performed in combination with a p16 immunohistochemistry and HPV-PCR [168, 169].

EBV-Positive Metastases

The strong association of nasopharyngeal carcinoma (NPC) with the Epstein-Barr virus (EBV) is well documented [170, 171]. NPC is frequently accompanied by CLN metastases, which are in many instances the only manifestation of this disease, as endoscopic examination or biopsy of the nasopharynx often fails to detect the primary site [172]. In many cases of NPC, the regional metastases are mostly bilateral and are larger than other HNSCC metastases, which have led to an individual TNM classification of those CLN metastases in NPCs. Necrosis is one of the most important features of the disease progression in CLNs and is a typical sign of NPCs (Fig. 5.55).

N2a and N3 Metastases

Another characteristic hallmark of CLN regional metastasis progression is the fact that with ongoing growth, it is difficult for the cervical metastasis to maintain alimentation at its center, leading to central necrosis. Therefore necrosis is a common feature of larger, singular metastases such as N2a or N3 metastases (Fig. 5.56).

Thyroid Carcinoma Lymph Node Metastases

Necrosis is an unfavorable prognostic indicator that can be found in metastases from both papillary thyroid carcinoma and undifferentiated thyroid cancer.

Lymphoma Nodes

Necrotic nodes most commonly arise from HNSCC, but they may occur uncommonly with lymphoma that has been pretreated or is advanced.

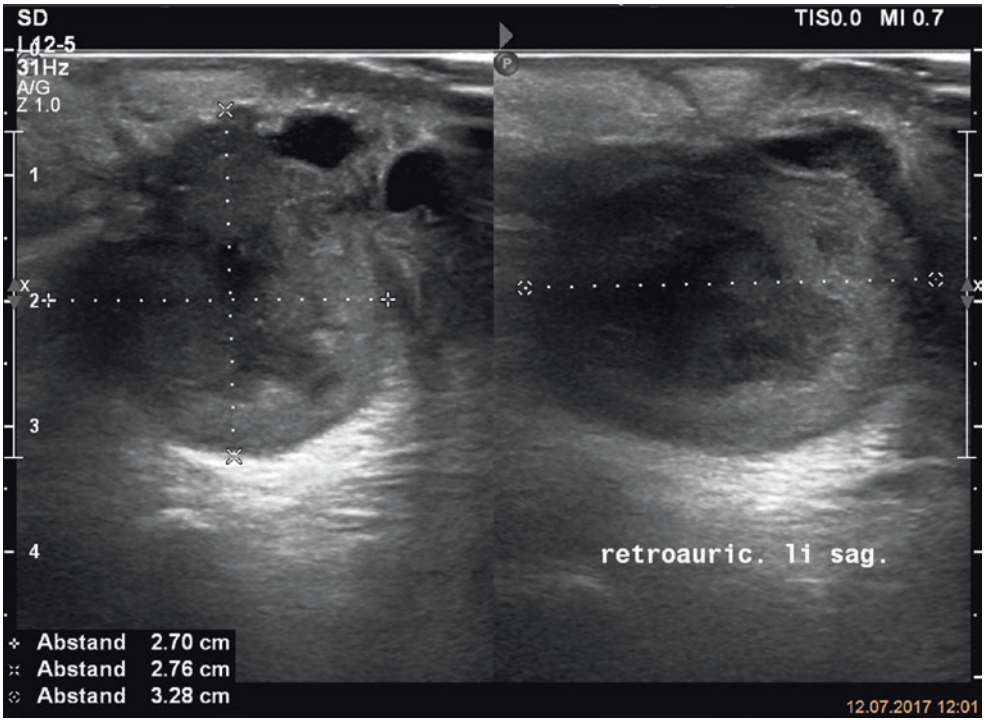

Fig. 5.55 Necrosis is one of the most important features of the disease progression and in association with level V involvement a typical sign of nasopharyngeal carcinoma associated with the Epstein-Barr virus

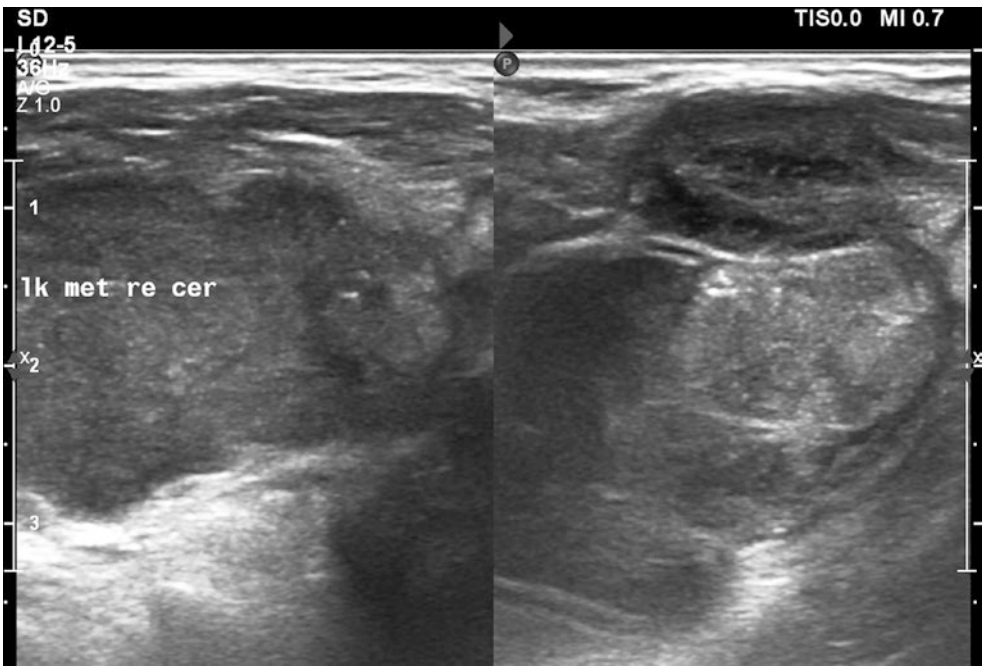

Fig. 5.56 In greater, singular metastases, e.g., N2a or N3 metastases, a common feature is necrosis often combined with extracapsular spread

References

1. Meyer JE, Steffen A, Bienemann M, Hedderich J, Schulz U, Laudien M, et al. Evaluation and development of a predictive model for ultrasound-guided investigation of neck metastases. Eur Arch Otorhinolaryngol. 2012;269:315–20.
2. Zenk J, Bozzato A, Steinhart H, Greess H, Iro H. Metastatic and inflammatory cervical lymph nodes as analyzed by contrast-enhanced color-coded Doppler ultrasonography: quantitative dynamic perfusion patterns and histopathologic correlation. Ann Otol Rhinol Laryngol. 2005;114:43–9.
3. Papakonstantinou O, Bakantaki A, Paspalaki P, Charoulakis N, Gourtsoyiannis N. High-resolution and color Doppler ultrasonography of cervical lymphadenopathy in children. Acta Radiol. 2001;42:470–6.
4. Ying M, Lee YY, Wong KT, Leung VY, Ahuja AT. Ultrasonography of neck lymph nodes in children. Hong Kong J Paediatr. 2009;14:29–36.
5. Park YW. Evaluation of neck masses in children. Am Fam Physician. 1995;51:1904–12.
6. Mohseni S, Shojaiefard A, Khorgami Z, Alinejad S, Ghorbani A, Ghafouri A. Peripheral lymphadenopathy: approach and diagnostic tools. Iran J Med Sci. 2014;39:158–70.
7. Mende U, Zöller J, Dietz A, Wannenmacher M, Born IA, Maier H. Ultrasound diagnosis in primary staging of head-neck tumors. Radiologe. 1996;36:207–16. German.
8. Dietz A, Knödler M, Lordick F. Primärtherapie der Kopf-Hals-Tumoren. Onkologe. 2014;2:144–51.
9. Ruffing S, Struffert T, Grgic A, Reith W. Imaging diagnostics of the pharynx and larynx. Radiologe. 2005;45:828–36. German.
10. Iro H, Waldfahrer F. Leitsymptome und Untersuchungsmethoden des äußeren Halses aus. In: Probst R, Grevers G, Iro H, editors. Hals-Nasen-Ohren-Heilkunde. Stuttgart: Georg Thieme Verlag; 2008. p. 287–9.
11. Rettenbacher T. Sonography of peripheral lymph nodes part 1: normal findings and B-image criteria. Ultraschall Med. 2010;31:344–62. English, German.
12. Steinkamp HJ, Cornehl M, Hosten N, Pegios W, Vogl T, Felix R. Cervical lymphadenopathy: ratio of long- to short-axis diameter as a predictor of malignancy. Br J Radiol. 1995;68:266–70.
13. Rubaltelli L, Proto E, Salmaso R, Bortoletto P, Candiani F, Cagol P. Sonography of abnormal lymph nodes in vitro: correlation of sonographic and histologic findings. AJR Am J Roentgenol. 1990;155:1241–4.
14. Gritzmann N. Sonography of the neck: current potentials and limitations. Ultraschall Med. 2005;26:185–96.
15. van den Brekel MW, Stel HV, Castelijns JA, Nauta JJ, van der Waal I, Valk J, et al. Cervical lymph node metastasis: assessment of radiologic criteria. Radiology. 1990;177:379–84.
16. Vassallo P, Wernecke K, Roos N, Peters PE. Differentiation of benign from malignant superficial lymphadenopathy: the role of high-resolution ultrasound. Radiology. 1992;183:215–20.
17. Ahuja A, Ying M. Sonography of neck lymph nodes. I-II. Abnormal lymph nodes. Clin Radiol. 2003;58:351–66.
18. Ariji Y, Kimura Y, Hayashi N, Onitsuka T, Yonetsu K, Hayashi K, et al. Power Doppler sonography of cervical lymph nodes in patients with head and neck cancer. AJNR Am J Neuroradiol. 1998;19:303–7.
19. Ahuja AT, Ying M. Sonographic evaluation of cervical lymph nodes. AJR Am J Roentgenol. 2005;184:1691–9.
20. Koischwitz D, Gritzmann N. Ultrasound of the neck. Radiol Clin N Am. 2000;38:1029–45.
21. Kuna SK, Bracic I, Tesic V, Kuna K, Herceg GH, Dodig D. Ultrasonographic differentiation of benign from malignant neck lymphadenopathy in thyroid cancer. J Ultrasound Med. 2006;25:1531–40.
22. Leboulleux S, Girard E, Rose M, Travagli JP, Sabbah N, Caillou B, et al. Ultrasound criteria of malignancy for cervical lymph nodes in patients followed up for differentiated thyroid cancer. J Clin Endocrinol Metab. 2007;92:3590–4.
23. Park JS, Son KR, Na DG, Kim E, Kim S. Performance of preoperative sonographic staging of papillary thyroid carcinoma based on the sixth edition of the AJCC/UICC TNM classification system. AJR Am J Roentgenol. 2009;192:66–72.
24. Sohn YM, Kwak JY, Kim EK, Moon HJ, Kim SJ, Kim MJ. Diagnostic approach for evaluation of lymph node metastasis from thyroid cancer using ultrasound and fine-needle aspiration biopsy. AJR Am J Roentgenol. 2010;194:38–43.
25. Do Rosario PW, Fagundes TA, Maia FF, Franco AC, Figueiredo MB, Purisch S. Sonography in the diagnosis of cervical recurrence in patients with differentiated thyroid carcinoma. J Ultrasound Med. 2004;23:915–20.
26. Ying M, Ahuja A, Brook F. Repeatability of power Doppler sonography of cervical lymph nodes. Ultrasound Med Biol. 2002;28:737–44.
27. Ying M, Ahuja A, Brook F, Metreweli C. Vascularity and gray-scale sonographic features of normal cervical lymph nodes: variations with nodal size. Clin Radiol. 2001;56:416–9.
28. Ying M, Ahuja A, Brook F, Metreweli C. Power Doppler sonography of normal cervical lymph nodes. J Ultrasound Med. 2000;19:511–7.
29. Wu CH, Chang YL, Hsu WC, Ko JY, Sheen TS, Hsieh FJ. Usefulness of Doppler spectral analysis and power Doppler sonography in the differentiation of cervical lymphadenopathies. AJR Am J Roentgenol. 1998;171:503–9.
30. Lyshchik A, Higashi T, Asato R, Tanaka S, Ito J, Hiraoka M, et al. Cervical lymph node metastases: diagnosis at sonoelastography–initial experience. Radiology. 2007;243:258–67.
31. Na DG, Lim HK, Byun HS, Kim HD, Ko YH, Baek JH. Differential diagnosis of cervical lymphadenopathy: usefulness of color Doppler sonography. AJR Am J Roentgenol. 1997;168:1311–6.
32. Ahuja AT, Ying M, Ho SS, Metreweli C. Distribution of intranodal vessels in differentiating benign from metastatic neck nodes. Clin Radiol. 2001;56:197–201.
33. Swartz JD, Yussen PS, Popky GL. Imaging of the neck: nodal disease. Crit Rev Diagn Imaging. 1991;31:413–69.
34. Gupta A, Rahman K, Shahid M, Kumar A, Qaseem SM, Hassan SA, Siddiqui FA. Sonographic assessment of cervical lymphadenopathy: role of high-resolution and color Doppler imaging. Head Neck. 2011;33:297–302.
35. Steinkamp HJ, Maurer J, Cornehl M, Knobber D, Hettwer H, Felix R. Recurrent cervical lymphadenopathy: differential diagnosis with color-duplex sonography. Eur Arch Otorhinolaryngol. 1994;251:404–9.
36. Mäurer J, Willam C, Schroeder R, Hidajad N, Hell B, Bier J, et al. Evaluation of metastases and reactive lymph nodes in Doppler sonography using an ultrasound contrast enhancer. Investig Radiol. 1997;32:441–6.
37. Dragoni F, Cartoni C, Pescarmona E, Chiarotti F, Puopolo M, Orsi E, et al. The role of high resolution pulsed and color Doppler ultrasound in the differential diagnosis of benign and malignant lymphadenopathy: results of multivariate analysis. Cancer. 1999;85:2485–90.
38. Chang DB, Yuan A, Yu CJ, Luh KT, Kuo SH, Yang PC. Differentiation of benign and malignant cervical lymph nodes with color Doppler sonography. AJR Am J Roentgenol. 1994;162:965–8.
39. Adibelli ZH, Unal G, Gül E, Uslu F, Koçak U, Abali Y. Differentiation of benign and malignant cervical lymph nodes:

value of B-mode and color Doppler sonography. Eur J Radiol. 1998;28:230–4.
40. Bhatia KS, Cho CC, Yuen YH, Rasalkar DD, King AD, Ahuja AT. Real-time qualitative ultrasound elastography of cervical lymph nodes in routine clinical practice: interobserver agreement and correlation with malignancy. Ultrasound Med Biol. 2010;36:1990–7.
41. Teng DK, Wang H, Lin YQ, Sui GQ, Guo F, Sun LN. Value of ultrasound elastography in assessment of enlarged cervical lymph nodes. Asian Pac J Cancer Prev. 2012;13:2081–5.
42. Alam F, Naito K, Horiguchi J, Fukuda H, Tachikake T, Ito K. Accuracy of sonographic elastography in the differential diagnosis of enlarged cervical lymph nodes: comparison with conventional B-mode sonography. AJR Am J Roentgenol. 2008;191:604–10.
43. Tan R, Xiao Y, He Q. Ultrasound elastography: its potential role in assessment of cervical lymphadenopathy. Acad Radiol. 2010;17:849–55.
44. Bhatia K, Tong CS, Cho CC, Yuen EH, Lee J, Ahuja AT. Reliability of shear wave ultrasound elastography for neck lesions identified in routine clinical practice. Ultraschall Med. 2012;33:463–8.
45. Bhatia KS, Cho CC, Tong CS, Yuen EH, Ahuja AT. Shear wave elasticity imaging of cervical lymph nodes. Ultrasound Med Biol. 2012;38:195–201.
46. Suh KW, Park CS, Lee JT, Lee KG. Diagnosis of cervical tuberculous lymphadenitis with fine needle aspiration biopsy and cytologic examination under ultrasonographic guides. Yonsei Med J. 1993;34:328–33.
47. Baatenburg de Jong RJ, Rongen RJ, Laméris JS, Knegt P, Verwoerd CD. Ultrasound in the diagnosis of cervical tuberculous adenitis. Auris Nasus Larynx. 1998;25:67–72.
48. Chou CH, Yang TL, Wang CP. Ultrasonographic features of tuberculous cervical lymphadenitis. J Med Ultrasound. 2014;22:158–63.
49. Yew WW, Lee J. Pathogenesis of cervical tuberculous lymphadenitis: pathways to anatomic localization. Tuber Lung Dis. 1995;76:275–6.
50. Ying M, Ahuja AT, Evans R, King W, Metreweli C. Cervical lymphadenopathy: sonographic differentiation between tuberculous nodes and nodal metastases from non-head and neck carcinomas. J Clin Ultrasound. 1998;26:383–9.
51. Asai S, Miyachi H, Suzuki K, Shimamura K, Ando Y. Ultrasonographic differentiation between tuberculous lymphadenitis and malignant lymph nodes. J Ultrasound Med. 2001;20:533–8.
52. Khanna R, Sharma AD, Khanna S, Kumar M, Shukla RC. Usefulness of ultrasonography for the evaluation of cervical lymphadenopathy. World J Surg Oncol. 2011;9:29.
53. Gupta KB, Kumar A, Sen R, Sen J, Vermas M. Role of ultrasonography and computed tomography in complicated cases of tuberculous cervical lymphadenitis. Indian J Tuberc. 2007;54:71–8.
54. Ahuja A, Ying M, Leung SF, Metreweli C. The sonographic appearance and significance of cervical metastatic nodes following radiotherapy for nasopharyngaeal carcinoma. Clin Radiol. 1996;51:698–701.
55. Ahuja A, Ying M, Yuen YH, Metreweli C. Power Doppler sonography to differentiate tuberculous cervical lymphadenopathy from nasopharyngeal carcinoma. AJNR Am J Neuroradiol. 2001;22:735–40.
56. Phatak SV, Gupta N, Phatak P. Tuberculous cervical lymphadenitis (scrofula): USG, Doppler and elastographic evaluation: report of two cases. Int J Res Med Sci. 2017;5:3257–60.
57. Choi EC, Moon WJ, Lim YC. Case report. Tuberculous cervical lymphadenitis mimicking metastatic lymph nodes from papillary thyroid carcinoma. Br J Radiol. 2009;82:e208–11.
58. Knox J, Lane G, Wong JS, Trevan PG, Karunajeewa H. Diagnosis of tuberculous lymphadenitis using fine needle aspiration biopsy. Intern Med J. 2012;42:1029–36.
59. Reede DL, Som SP. Lymph nodes. In: Som SP, Bergeron RT, editors. Head and neck imaging. 2nd ed. St Louis: Mosby Year Book; 1991. p. 573.
60. McAllister KA, MacGregor FB. Diagnosis of tuberculosis in the head and neck. J Laryngol Otol. 2011;125:603–7.
61. Griffith DE, Aksamit T, Brown-Elliott BA, Catanzaro A, Daley C, Gordin F, et al., American Thoracic Society, Infectious Disease Society of America. An official ATS/IDSA statement: diagnosis, treatment, and prevention of nontuberculous mycobacterial diseases. Am J Respir Crit Care Med. 2007;175:367–416.
62. Haworth CS, Banks J, Capstick T, Fisher AJ, Gorsuch T, Laurenson IF, et al. British Thoracic Society guidelines for the management of non-tuberculous mycobacterial pulmonary disease (NTM-PD). Thorax. 2017;72(Suppl 2):ii1–64.
63. Falkinham JO. Current epidemiologic trends of the nontuberculous mycobacteria (NTM). Curr Environ Health Rep. 2016;3:161–7.
64. Wu UI, Holland SM. Host susceptibility to non-tuberculous mycobacterial infections. Lancet Infect Dis. 2015;15:968–80.
65. Lake MA, Ambrose LR, Lipman MC, Lowe DM. "Why me, why now?" using clinical immunology and epidemiology to explain who gets nontuberculous mycobacterial infection. BMC Med. 2016;14:54.
66. Sologuren I, Boisson-Dupuis S, Pestano J, Vincent QB, Fernández-Pérez L, Chapgier A, et al. Partial recessive IFN-γR1 deficiency: genetic, immunological and clinical features of 14 patients from 11 kindreds. Hum Mol Genet. 2011;20:1509–23.
67. Kristensen IA, Veirum JE, Møller BK, Christiansen M. Novel STAT1 alleles in a patient with impaired resistance to mycobacteria. J Clin Immunol. 2011;31:265–71.
68. Hsu AP, Sampaio EP, Khan J, Calvo KR, Lemieux JE, Patel SY, et al. Mutations in *GATA2* are associated with the autosomal dominant and sporadic monocytopenia and mycobacterial infection (MonoMAC) syndrome. Blood. 2011;118:2653–5.
69. Sapkota BR, Hijikata M, Matsushita I, Tanaka G, Ieki R, Kobayashi N, et al. Association of *SLC11A1* (*NRAMP1*) polymorphisms with pulmonary *Mycobacterium avium* complex infection. Hum Immunol. 2012;73:529–36.
70. Henkle E, Winthrop KL. Nontuberculous mycobacteria infections in immunosuppressed hosts. Clin Chest Med. 2015;36:91–9.
71. Hojo M, Iikura M, Hirano S, Sugiyama H, Kobayashi N, Kudo K. Increased risk of nontuberculous mycobacterial infection in asthmatic patients using long-term inhaled corticosteroid therapy. Respirology. 2012;17:185–90.
72. Andréjak C, Nielsen R, Thomsen VØ, Duhaut P, Sørensen HT, Thomsen RW. Chronic respiratory disease, inhaled corticosteroids and risk of non-tuberculous mycobacteriosis. Thorax. 2013;68:256–62.
73. Dirac MA, Horan KL, Doody DR, Meschke JS, Park DR, Jackson LA, et al. Environment or host?: a case-control study of risk factors for *Mycobacterium avium* complex lung disease. Am J Respir Crit Care Med. 2012;186:684–91.
74. Bryant JM, Grogono DM, Greaves D, Foweraker J, Roddick I, Ianns T, et al. Whole-genome sequencing to identify transmission of *Mycobacterium abscessus* between patients with cystic fibrosis: a retrospective cohort study. Lancet. 2013;381:1551–60.
75. Brown-Elliott BA, Mann LB, Hail D, Whitney C, Wallace RJ Jr. Antimicrobial susceptibility of nontuberculous mycobacteria from eye infections. Cornea. 2012;31:900–6.
76. Kentrup H, Biesterfeld S, Haase G. Nichttuberkulöse Mykobakterien als Ursache zervikaler Lymphadenitiden im Kindesalter. Dtsch Ärztebl. 1997;94:A-2416–9.
77. Grange JM, Yates MD, Pozniak A. Bacteriologically confirmed non-tuberculous mycobacterial lymphadenitis in south east

England: a recent increase in the number of cases. Arch Dis Child. 1995;72:516–7.
78. Penn R, Steehler MK, Sokohl A, Harley EH. Nontuberculous mycobacterial cervicofacial lymphadenitis–a review and proposed classification system. Int J Pediatr Otorhinolaryngol. 2011;75:1599–603.
79. Lindeboom JA, Smets AM, Kuijper EJ, van Rijn RR, Prins JM. The sonographic characteristics of nontuberculous mycobacterial cervicofacial lymphadenitis in children. Pediatr Radiol. 2006;36:1063–7.
80. von Kalle T, Koitschev A. Pediatric radiology in oto-rhinolaryngology. GMS Curr Top Otorhinolaryngol Head Neck Surg. 2014;13:Doc03. https://doi.org/10.3205/cto000106.
81. Haber HP, Warmann SW, Fuchs J. Cervical atypical mycobacterial lymphadenitis in childhood: findings on sonography. Ultraschall Med. 2006;27:462–6.
82. Wolinsky E. Mycobacterial lymphadenitis in children: a prospective study of 105 nontuberculous cases with long-term follow-up. Clin Infect Dis. 1995;20:954–63.
83. Antonelli A, Miccoli P, Fallahi P, Grosso M, Nesti C, Spinelli C, Ferrannini E. Role of neck ultrasonography in the follow-up of children operated on for thyroid papillary cancer. Thyroid. 2003;13:479–84.
84. Ahuja AT, Chow L, Chick W, King W, Metreweli C. Metastatic cervical nodes in papillary carcinoma of the thyroid: ultrasound and histological correlation. Clin Radiol. 1995;50:229–31.
85. Park JK, Lee HK, Ha HK, Choi HY, Choi CG. Cervicofacial actinomycosis: CT and MR imaging findings in seven patients. AJNR Am J Neuroradiol. 2003;24:331–5.
86. Stramare R, Tregnaghi A, Fittà C, Torraco A, Khadivi Y, Rossi CR, Rubaltelli L. High-sensitivity power Doppler imaging of normal superficial lymph nodes. J Clin Ultrasound. 2004;32:273–6.
87. Niedzielska G, Kotowski M, Niedzielski A, Dybiec E, Wieczorek P. Cervical lymphadenopathy in children–incidence and diagnostic management. Int J Pediatr Otorhinolaryngol. 2007;71:51–6.
88. Luzuriaga K, Sullivan JL. Infectious mononucleosis. N Engl J Med. 2010;362:1993–2000.
89. Richner S, Laifer G. Peripheral lymphadenopathy in immunocompetent adults. Swiss Med Wkly. 2010;140:98–104.
90. Hurt C, Tammaro D. Diagnostic evaluation of mononucleosis-like illnesses. Am J Med. 2007;120:911.
91. Krishnan J, Danon A, Frizzera G. Reactive lymphadenopathies and atypical lymphoproliferative disorders. Am J Clin Pathol. 1993;99:385.
92. Tashiro N, Matsubara T, Uchida M, Katayama K, Ichiyama T, Furukawa S. Ultrasonographic evaluation of cervical lymph nodes in Kawasaki disease. Pediatrics. 2002;109:E77.
93. Vassallo P, Edel G, Roos N, Naguib A, Peters PE. In-vitro high-resolution ultrasonography of benign and malignant lymph nodes. A sonographic-pathologic correlation. Investig Radiol. 1993;28:698–705.
94. Tschammler A, Ott G, Schang T, Seelbach-Goebel B, Schwager K, Hahn D. Lymphadenopathy. Differentiation of benign from malignant disease – color Doppler US assessment of intranodal angioarchitecture. Radiology. 1998;208:117–23.
95. Giovagnorio F, Caiazzo R, Avitto A. Evaluation of vascular patterns of cervical lymph nodes with power Doppler sonography. J Clin Ultrasound. 1997;25:71–6.
96. Baltas C, Balanika A, Papakonstantinou O, Kominis C, Bizimi V, Alexopoulou E, et al. Gray-scale and color Doppler sonographic (CDUS) features of cervical lymph nodes in infectious mononucleosis. [Poster]. European Congress of Radiology (ECR). 2010; https://doi.org/10.1594/ecr2010/C-1828.
97. Ying M, Bhatia KS, Lee YP, Yuen HY, Ahuja AT. Review of ultrasonography of malignant neck nodes: greyscale, Doppler, contrast enhancement and elastography. Cancer Imaging. 2014;13:658–69.
98. Jasinski RW, Glazer GM, Francis IR, Harkness RL. CT and ultrasound in abscess detection at specific anatomic sites: a study of 198 patients. Comput Radiol. 1987;11:41–7.
99. Sandler MA, Alpern MB, Madrazo BL, Gitschlag KF. Inflammatory lesions of the groin: ultrasonic evaluation. Radiology. 1984;151:747–50.
100. vanSonnenberg E, Wittich GR, Casola G, Cabrera OA, Gosink BB, Resnick DL. Sonography of thigh abscess: detection, diagnosis, and drainage. AJR Am J Roentgenol. 1987;149:769–72.
101. Yeh HC, Rabinowitz JG. Ultrasonography and computed tomography of inflammatory abdominal wall lesions. Radiology. 1982;144:859–63.
102. Som PM. Lymph nodes of the neck. Radiology. 1987;165:593–600.
103. Sakai F, Kiyono K, Sone S, Kondo Y, Oguchi M, Watanabe T, et al. Ultrasonic evaluation of cervical metastatic lymphadenopathy. J Ultrasound Med. 1988;7:305–10.
104. Lawson JP, Keller MS, Rattner Z. Recent advances in pediatric musculoskeletal imaging. Radiol Clin N Am. 1994;32:353–75.
105. Loyer EM, Kaur H, David CL, DuBrow R, Eftekhari FM. Importance of dynamic assessment of the soft tissues in the sonographic diagnosis of echogenic superficial abscesses. J Ultrasound Med. 1995;14:669–71.
106. Bhatia KS, Rasalkar DD, Lee YP, Wong KT, King AD, Yuen YH, Ahuja AT. Real-time qualitative ultrasound elastography of miscellaneous non-nodal neck masses: applications and limitations. Ultrasound Med Biol. 2010;36:1644–52.
107. Gaspari R, Blehar D, Briones J, Dayno M. Sonoelastographic characteristics of abscess induration associated with therapy failure. J Ultrasound Med. 2012;31:1405–11.
108. Rainer T, Öfner G, Marckhgott E. Ultrasound diagnosis of regional lymph node metastasis of the neck in patients with head-neck neoplasms: sono-morphologic criteria and diagnostic accuracy. Laryngo Rhino Otologie. 1993;72:73–7.
109. Bruneton JN, Roux P, Caramella E, Demard F, Vallicioni J, Chauvel P. Ear, nose, and throat cancer: ultrasound diagnosis of metastasis to cervical lymph nodes. Radiology. 1984;152:771–3.
110. Hessling KH, Schmelzeisen R, Reimer P, Milbrandt H, Wittekind C. Die Bedeutung sonomorphologischer Kriterien in der Diagnostik von Halslymphknotenmetastasen. Dtsch Z Mund Kiefer Gesichtschir. 1994;18:42–6.
111. Steinkamp HJ. Halslymphknotenmetastasen. Sonographischer Malignitätsnachweis. Fortschr Geb Rontgenstr. 1992;56:135–41.
112. Van den Brekel MW, Castelijns JA, Snow GB. The size of lymph nodes in the neck on sonograms as a radiologic criterion for metastasis: how reliable is it? Am J Neuroradiol. 1998;19:695–700.
113. Steinkamp HJ, Zwicker C, Langer M, Mathe M, Ehritt C, Neumann K, Felix R. Reactive enlargement of cervical lymph nodes and cervical lymph node metastases: sonography (M/Q quotient) and computed tomography. Aktuelle Radiol. 1992;2:188–95. German.
114. Castelijns JA, van den Brekel MW. Detection of lymph node metastases in the neck: radiologic criteria. AJNR Am J Neuroradiol. 2001;22:3–4.
115. Imani Moghaddam M, Davachi B, Mostaan LV, Langaroodi AJ, Memar B, Azimi SA, Marouzi P. Evaluation of the sonographic features of metastatic cervical lymph nodes in patients with head and neck malignancy. J Craniofac Surg. 2011;22:2179–84.
116. Rubaltelli L, Khadivi Y, Tregnaghi A, Stramare R, Ferro F, Borsato S, et al. Evaluation of lymph node perfusion using continuous mode harmonic ultrasonography with a second-generation contrast agent. J Ultrasound Med. 2004;23:829–36.
117. Moritz JD, Ludwig A, Oestmann JW. Contrast-enhanced color Doppler sonography for evaluation of enlarged cervical lymph nodes in head and neck tumors. AJR Am J Roentgenol. 2000;174:1279–84.
118. Rickert D, Jecker P, Metzler V, Lehmann T, Ernst E, Westhofen M. Color-coded duplex sonography of the cervical lymph nodes:

improved differential diagnostic assessment after administration of the signal enhancer SH U 508A (Levovist). Eur Arch Otorhinolaryngol. 2000;257:453–8.
119. Zenk J, Bozzato A, Hornung J, Gottwald F, Rabe C, Gill S, Iro H. Neck lymph nodes: prediction by computer-assisted contrast medium analysis? Ultrasound Med Biol. 2007;33:246–53.
120. Umapathy N, De R, Donaldson I. Cervical lymphadenopathy in children. Hosp Med. 2003;64:104–7.
121. Ramadan HH, Wax MK, Boyd CB. Fine-needle aspiration of head and neck masses in children. Am J Otolaryngol. 1997;18:400–4.
122. Baatenburg de Jong RJ, Rongen RJ, Verwoerd CD, van Overhagen H, Lameris JS, Knegt P. Ultrasound-guided fineneedle aspiration biopsy of neck nodes. Arch Otolaryngol Head Neck Surg. 1991;117:402–4.
123. Knappe M, Louw M, Gregor RT. Ultrasonography-guided fine-needle aspiration for the assessment of cervical metastases. Arch Otolaryngol Head Neck Surg. 2000;126:1091–6.
124. Lo CP, Chen CY, Chin SC, Lee KW, Hsueh CJ, Juan CJ, et al. Detection of suspicious malignant cervical lymph nodes of unknown origin: diagnostic accuracy of ultrasound-guided fine-needle aspiration biopsy with nodal size and central necrosis correlate. Can Assoc Radiol J. 2007;58:286–91.
125. Robinson IA, Cozens NJ. Does a joint ultrasound guided cytology clinic optimize the cytological evaluation of head and neck masses? Clin Radiol. 1999;54:312–6.
126. Hodder SC, Evans RM, Patton DW, Silvester KC. Ultrasound and fine needle aspiration cytology in the staging of neck lymph nodes in oral squamous cell carcinoma. Br J Oral Maxillofac Surg. 2000;38:430–6.
127. van den Brekel MW, Reitsma LC, Quak JJ, Smeele LE, van der Linden JC, Snow GB, Castelijns JA. Sonographically guided aspiration cytology of neck nodes for selection of treatment and follow-up in patients with N0 head and neck cancer. AJNR Am J Neuroradiol. 1999;20:1727–31.
128. Ruggiero A, Attinà G, Maurizi P, Mulè A, Tarquini E, Barone G, et al. Rosai-Dorfman disease: two case reports and diagnostic role of fine-needle aspiration cytology. J Pediatr Hematol Oncol. 2006;28:103–6.
129. Bain G, Bearcroft PW, Berman LH, Grant JW. The use of ultrasound-guided cutting-needle biopsy in paediatric neck masses. Eur Radiol. 2000;10:512–5.
130. Leenhardt L, Erdogan MF, Hegedus L, Mandel SJ, Paschke R, Rago T, Russ G. 2013 European Thyroid Association guidelines for cervical ultrasound scan and ultrasound-guided techniques in the postoperative management of patients with thyroid cancer. Eur Thyroid J. 2013;2:147–59.
131. Haugen BR, Alexander EK, Bible KC, Doherty GM, Mandel SJ, Nikiforov YE, et al. 2015 American Thyroid Association management guidelines for adult patients with thyroid nodules and differentiated thyroid cancer. Thyroid. 2016;26:1–133.
132. Machens A, Holzhausen HJ, Dralle H. Skip metastases in thyroid cancer leaping the central lymph node compartment. Arch Surg. 2004;139:43–5.
133. American Thyroid Association (ATA) Guidelines Taskforce on Thyroid Nodules and Differentiated Thyroid Cancer, Cooper DS, Doherty GM, Haugen BR, Kloos RT, Lee SL, et al. Revised American Thyroid Association management guidelines for patients with thyroid nodules and differentiated thyroid cancer. Thyroid. 2009;19:1167–214.
134. Qaseem A, Snow V, Owens DK, Shekelle P. The development of clinical practice guidelines and guidance statements of the American College of Physicians: summary of methods. Ann Intern Med. 2010;153:194–9.
135. Schunemann HJ, Oxman AD, Brozek J, Glasziou P, Jaeschke R, Vist GE, et al. Grading quality of evidence and strength of recommendations for diagnostic tests and strategies. BMJ. 2008;336:1106–10.
136. Bossuyt PM, Reitsma JB, Bruns DE, Gatsonis CA, Glasziou PP, Irwig LM, et al. Towards complete and accurate reporting of studies of diagnostic accuracy: the STARD Initiative. Ann Intern Med. 2003;138:40–4.
137. Leung AN, Bull TM, Jaeschke R, Lockwood CJ, Boiselle PM, Hurwitz LM, et al. An official American Thoracic Society/Society of Thoracic Radiology clinical practice guideline: evaluation of suspected pulmonary embolism in pregnancy. Am J Respir Crit Care Med. 2011;184:1200–8.
138. Marqusee E, Benson CB, Frates MC, Doubilet PM, Larsen PR, Cibas ES, Mandel SJ. Usefulness of ultrasonography in the management of nodular thyroid disease. Ann Intern Med. 2000;133:696–700.
139. Hagag P, Strauss S, Weiss M. Role of ultrasound-guided fine-needle aspiration biopsy in evaluation of nonpalpable thyroid nodules. Thyroid. 1998;8:989–95.
140. Snozek CL, Chambers EP, Reading CC, Sebo TJ, Sistrunk JW, Singh RJ, Grebe SK. Serum thyroglobulin, high-resolution ultrasound, and lymph node thyroglobulin in diagnosis of differentiated thyroid carcinoma nodal metastases. J Clin Endocrinol Metab. 2007;92:4278–81.
141. Frasoldati A, Pesenti M, Gallo M, Caroggio A, Salvo D, Valcavi R. Diagnosis of neck recurrences in patients with differentiated thyroid carcinoma. Cancer. 2003;97:90–6.
142. Boi F, Baghino G, Atzeni F, Lai ML, Faa G, Mariotti S. The diagnostic value for differentiated thyroid carcinoma metastases of thyroglobulin (Tg) measurement in washout fluid from fine-needle aspiration biopsy of neck lymph nodes is maintained in the presence of circulating anti-Tg antibodies. J Clin Endocrinol Metab. 2006;91:1364–9.
143. Jeon MJ, Park JW, Han JM, Yim JH, Song DE, Gong G, et al. Serum antithyroglobulin antibodies interfere with thyroglobulin detection in fine-needle aspirates of metastatic neck nodes in papillary thyroid carcinoma. J Clin Endocrinol Metab. 2013;98:153–60.
144. Chung J, Kim EK, Lim H, Son EJ, Yoon JH, Youk JH, et al. Optimal indication of thyroglobulin measurement in fine-needle aspiration for detecting lateral metastatic lymph nodes in patients with papillary thyroid carcinoma. Head Neck. 2014;36:795–801.
145. Grani G, Fumarola A. Thyroglobulin in lymph node fine-needle aspiration wash-out: a systematic review and meta-analysis of diagnostic accuracy. J Clin Endocrinol Metab. 2014;99:1970–82.
146. Pak K, Suh S, Hong H, Cheon GJ, Hahn SK, Kang KW, et al. Diagnostic values of thyroglobulin measurement in fine-needle aspiration of lymph nodes in patients with thyroid cancer. Endocrine. 2015;49:70–7.
147. Pacini F, Fugazzola L, Lippi F, Ceccarelli C, Centoni R, Miccoli P, et al. Detection of thyroglobulin in fine needle aspirates of nonthyroidal neck masses: a clue to the diagnosis of metastatic differentiated thyroid cancer. J Clin Endocrinol Metab. 1992;74:1401–4.
148. Moon JH, Kim YI, Lim JA, Choi HS, Cho SW, Kim KW, et al. Thyroglobulin in washout fluid from lymph node fine-needle aspiration biopsy in papillary thyroid cancer: large-scale validation of the cutoff value to determine malignancy and evaluation of discrepant results. J Clin Endocrinol Metab. 2013;98:1061–8.
149. Giovanella L, Bongiovanni M, Trimboli P. Diagnostic value of thyroglobulin assay in cervical lymph node fine-needle aspirations for metastatic differentiated thyroid cancer. Curr Opin Oncol. 2013;25:6–13.
150. Lee YY, Van Tassel P, Nauert C, North LB, Jing BS. Lymphomas of the head and neck: CT findings at initial presentation. AJR Am J Roentgenol. 1987;149:575–81.
151. DePeña CA, Van Tassel P, Lee YY. Lymphoma of the head and neck. Radiol Clin N Am. 1990;28:723–43.

152. Bruneton JN, Normand F, Balu-Maestro C, Kerboul P, Santini N, Thyss A, Schneider M. Lymphomatous superficial lymph nodes: US detection. Radiology. 1987;165:233–5.
153. Ho SS, Ahuja AT, Yeo W, Chan TC, Kew J, Metreweli C. Longitudinal colour Doppler study of superficial lymph nodes in non-Hodgkin's lymphoma patients on chemotherapy. Clin Radiol. 2000;55:110.
154. Ahuja A, Ying M, Yang WT, Evans R, King W, Metreweli C. The use of sonography in differentiating cervical lymphomatous lymph nodes from cervical metastatic lymph nodes. Clin Radiol. 1996;51:186–90.
155. Ishii J, Fujii E, Suzuki H, Shinozuka K, Kawase N, Amagasa T. Ultrasonic diagnosis of oral and neck malignant lymphoma. Bull Tokyo Med Dent Univ. 1992;39:63–9.
156. Ahuja AT, Ying M, Yuen HY, Metreweli C. 'Pseudocystic' appearance of non-Hodgkin's lymphomatous nodes: an infrequent finding with high-resolution transducers. Clin Radiol. 2001;56:111–5.
157. Ahuja AT, Ying M, Ho SY, Antonio G, Lee YP, King AD, Wong KT. Ultrasound of malignant cervical lymph nodes. Cancer Imaging. 2008;8:48–56.
158. Ying M, Ahuja A, Brook F. Accuracy of sonographic vascular features in differentiating different causes of cervical lymphadenopathy. Ultrasound Med Biol. 2004;30:441–7.
159. Ahuja A, Ying M. Sonographic evaluation of cervical lymphadenopathy: is power Doppler sonography routinely indicated? Ultrasound Med Biol. 2003;29:353–9.
160. Ahuja A, Ying M. An overview of neck node sonography. Investig Radiol. 2002;37:333–42.
161. Robbins KT, Clayman G, Levine PA, Medina J, Sessions R, Shaha A, et al., American Head and Neck Society, American Academy of Otolaryngology–Head and Neck Surgery. Neck dissection classification update: revisions proposed by the American Head and Neck Society and the American Academy of Otolaryngology-Head and Neck Surgery. Arch Otolaryngol Head Neck Surg. 2002;128:751–8.
162. Robbins KT, Shaha AR, Medina JE, Califano JA, Wolf GT, et al., Committee for Neck Dissection Classification, American Head and Neck Society. Consensus statement on the classification and terminology of neck dissection. Arch Otolaryngol Head Neck Surg. 2008;134:536–8.
163. Park JH, Lee YS, Kim BW, Chang HS, Park CS. Skip lateral neck node metastases in papillary thyroid carcinoma. World J Surg. 2012;36:743–7.
164. Kaji AV, Mohuchy T, Swartz JD. Imaging of cervical lymphadenopathy. Semin Ultrasound CT MR. 1997;18:220–49.
165. Thompson LD, Heffner DK. The clinical importance of cystic squamous cell carcinomas in the neck: a study of 136 cases. Cancer. 1998;82:944–56.
166. Goldenberg D, Sciubba J, Koch WM. Cystic metastasis from head and neck squamous cell cancer: a distinct disease variant? Head Neck. 2006;28:633–8.
167. Goldenberg D, Begum S, Westra WH, Khan Z, Sciubba J, Pai SI, et al. Cystic lymph node metastasis in patients with head and neck cancer: an HPV-associated phenomenon. Head Neck. 2008;30:898–903.
168. Begum S, Gillison ML, Nicol TL, Westra WH. Detection of human papillomavirus-16 in fine-needle aspirates to determine tumor origin in patients with metastatic squamous cell carcinoma of the head and neck. Clin Cancer Res. 2007;13:1186–91.
169. Begum S, Gillison ML, Ansari-Lari MA, Shah K, Westra WH. Detection of human papillomavirus in cervical lymph nodes: a highly effective strategy for localising site of tumor origin. Clin Cancer Res. 2003;9:6469–75.
170. Henle G, Henle W. Epstein-Barr virus–specific IgA serum antibodies as an outstanding feature of nasopharyngeal carcinoma. Int J Cancer. 1976;17:1–7.
171. Fåhraeus R, Fu HL, Ernberg I, Finke J, Rowe M, Klein G, et al. Expression of Epstein-Barr virus-encoded proteins in nasopharyngeal carcinoma. Int J Cancer. 1988;42:329–38.
172. Nakao K, Yuge T, Mochiki M, Nibu K, Sugasawa M. Detection of Epstein-Barr virus in metastatic lymph nodes of patients with nasopharyngeal carcinoma and a primary unknown carcinoma. Arch Otolaryngol Head Neck Surg. 2003;129:338–40.

Sonography of Other Neck Masses

6

Peter Jecker

6.1 General Notes

Head and neck surgeons should use ultrasound frequently to diagnose neck diseases. Because ultrasound is very easy to perform, it gives us a fast overview and first impression about the nature of different diseases, their extension, and possible complications. It must be considered that some diseases present themselves with typical sonographic characteristics [1], whereas there are other diseases with relatively untypical findings. Therefore, the differential diagnosis should always be substantiated with the patient's history and clinical findings, as well as sonographic imaging.

6.2 Inflammatory Changes of the Neck

Inflammatory changes of the neck can be caused by various agents. The most common ones are bacterial or viral infections of lymph nodes in the neck, infections of teeth, tonsillitis, and salivary gland infection.

Soft tissue inflammation of the neck usually shows an associated surrounding tissue edema [2]. With ultrasound, we can detect an enlargement of the neck muscles with commonly hyperechoic changes within the tissue due to an increased retention of fluid in the infected area (Figs. 6.1, 6.2, and 6.3).

Lymph nodes frequently can be found around the inflamed tissue. The appearance of the lymph nodes depends not only on the nature of the infection but also on its strength. In addition to lymph nodes, blood vessels can always be detected, even in nodes with a diameter smaller than 1 cm (Fig. 6.1). Furthermore, an abscess of the neck caused by infective agents can be seen as a neck swelling. Abscesses must be detected as early as possible, to begin specific therapy and reduce the possibility of complications. It is important to differentiate between an abscess and a phlegmon of the neck tissue. Thus, it is a further purpose of the ultrasound examination to detect even small abscesses within the neck tissue or even in lymph nodes. Sometimes abscesses are difficult to detect, especially when they are small. They are characterized by different sonographic features. Usually they are hypoechoic, whereas the hypoechogeneity depends on the consistency of the fluid (Video 6.1). Furthermore, a hyperechoic acoustic shadow often can be seen behind the fluid area of the abscess. Duplex sonography often shows hypervascularization of the surrounding tissue, whereas the liquid area does not have blood vessels (Video 6.2).

In practice, we often detect lymph nodes within the edematous tissue of the neck. If the node contains hypoechoic areas with a hyperechoic acoustic shadow, it is highly suspicious for abscess formation (Fig. 6.3a). The next step is the use of duplex sonography, with which we can frequently see areas that lack blood vessels (Figs. 6.3b, 6.4 and 6.5). Abscesses can be large (Fig. 6.6) or even very small (Fig. 6.7) and can be positioned in every neck region. Whereas lymph node abscesses frequently show smooth borders surrounded by the capsule of the lymph node, the borders of diffuse abscess formation in the neck tissue are sometimes irregular.

Electronic Supplementary Material The online version of this chapter (https://doi.org/10.1007/978-3-030-12641-4_6) contains supplementary material, which is available to authorized users.

P. Jecker (✉)
Department of Otorhinolaryngology and Plastic Head and Neck Surgery, Klinikum Bad Salzungen GmbH,
Bad Salzungen, Germany
e-mail: peter.jecker@klinikum-badsalzungen.de

© Springer Nature Switzerland AG 2019

H. J. Welkoborsky, P. Jecker (eds.), *Ultrasonography of the Head and Neck*, https://doi.org/10.1007/978-3-030-12641-4_6

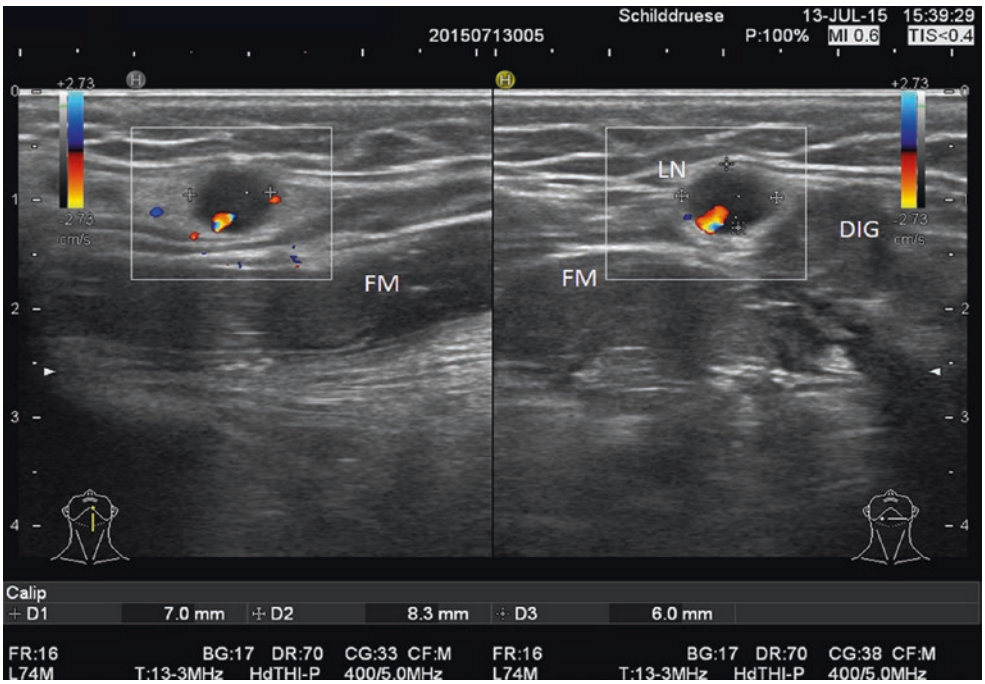

Fig. 6.1 Lymph nodes (LN) of the floor of the mouth (FM) with soft tissue inflammation. In this patient, the tissue in the area of the mouth floor is hyperechoic because of an inflammatory edema. DIG digastric muscle

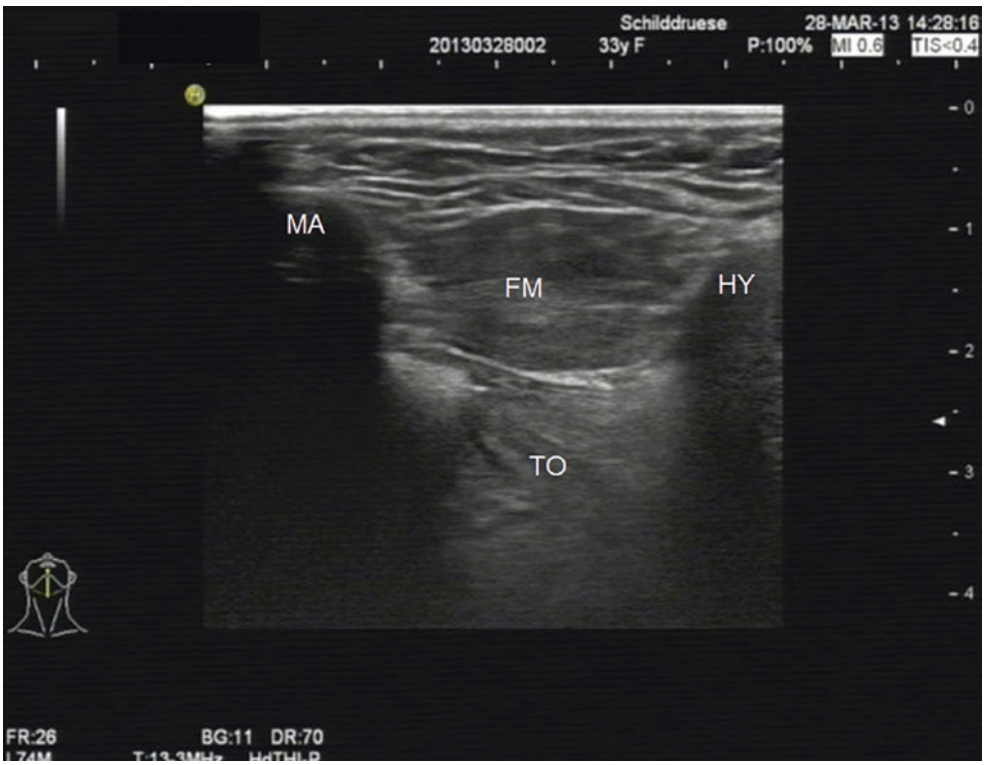

Fig. 6.2 Inflammation of the floor of the mouth (FM). The muscles between the mandible (MA) and the hyoid (HY) are typically thickened. TO tongue

6.3 Tumors of the Skin and Subcutaneous Tissue

6.3.1 Atheroma

An atheroma is an intradermal cyst originating from a hair follicle. Thus, it can be detected with ultrasound within the skin (Fig. 6.8). Generally, atheroma is a clinical diagnosis, but in rare cases (e.g., if the atheroma is located in the parotid region), ultrasound makes sense to differentiate it from other kinds of tumors, such as parotid tumors. Atheroma is characterized by a smooth capsule. Depending on the consistency of the fluid, its echogenicity may vary. Normally we detect atheroma as a hypoechoic structure, but in some cases the

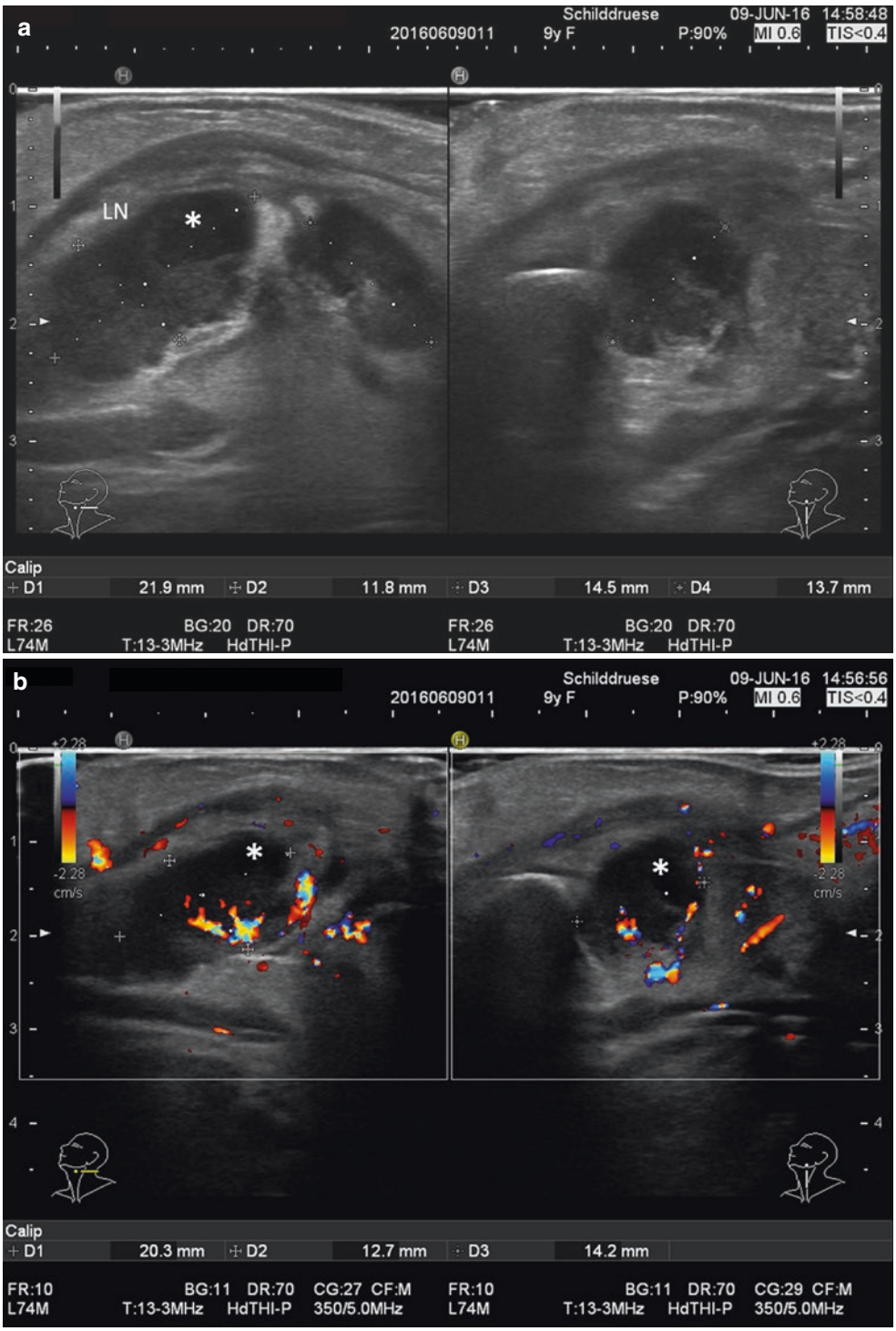

Fig. 6.3 Lymph nodes (LN) of the neck. (**a**) B-scan sonograph. (**b**) Color-coded sonography. The node includes a hypoechoic area without blood flow (*asterisk*), which is quite suspect for an abscess. Furthermore, the surrounding tissue is thickened as a result of the strong inflammation

echo is brighter (Fig. 6.9). Furthermore, an atheroma is characterized by a hyperechoic acoustic shadow. Blood vessels can only be detected in the capsule area. In case of an acute infection, the surrounding tissue shows edematous thickening (Fig. 6.10).

6.3.2 Lipoma

A lipoma can be found anywhere in the head and the neck [3]. In most cases, lipomas have a very thin capsule and a typically feathered echo inside (Fig. 6.11) (Video 6.3). The

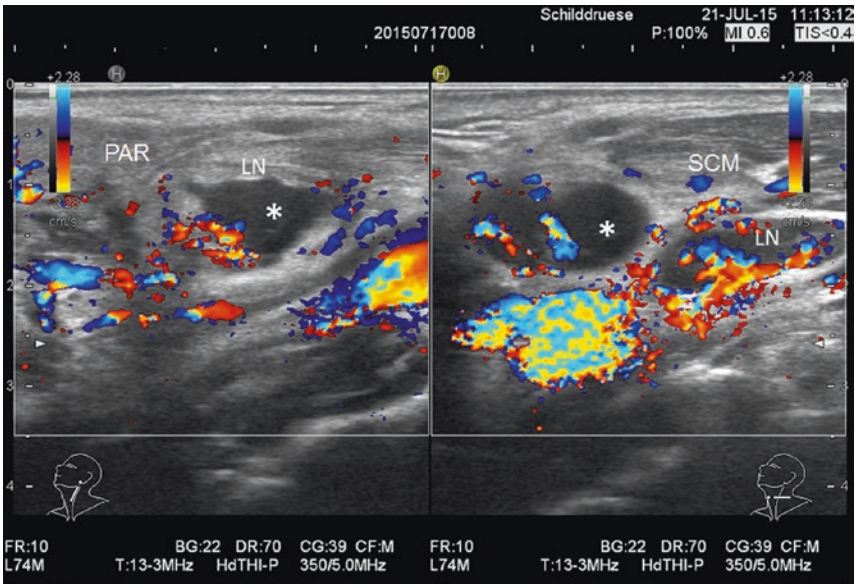

Fig. 6.4 Lymph node (LN) abscess next to the parotid gland (PAR). Note the hypoechoic abscess (*asterisk*) with a relative acoustic enhancement. Furthermore, the abscess lacks vascularity

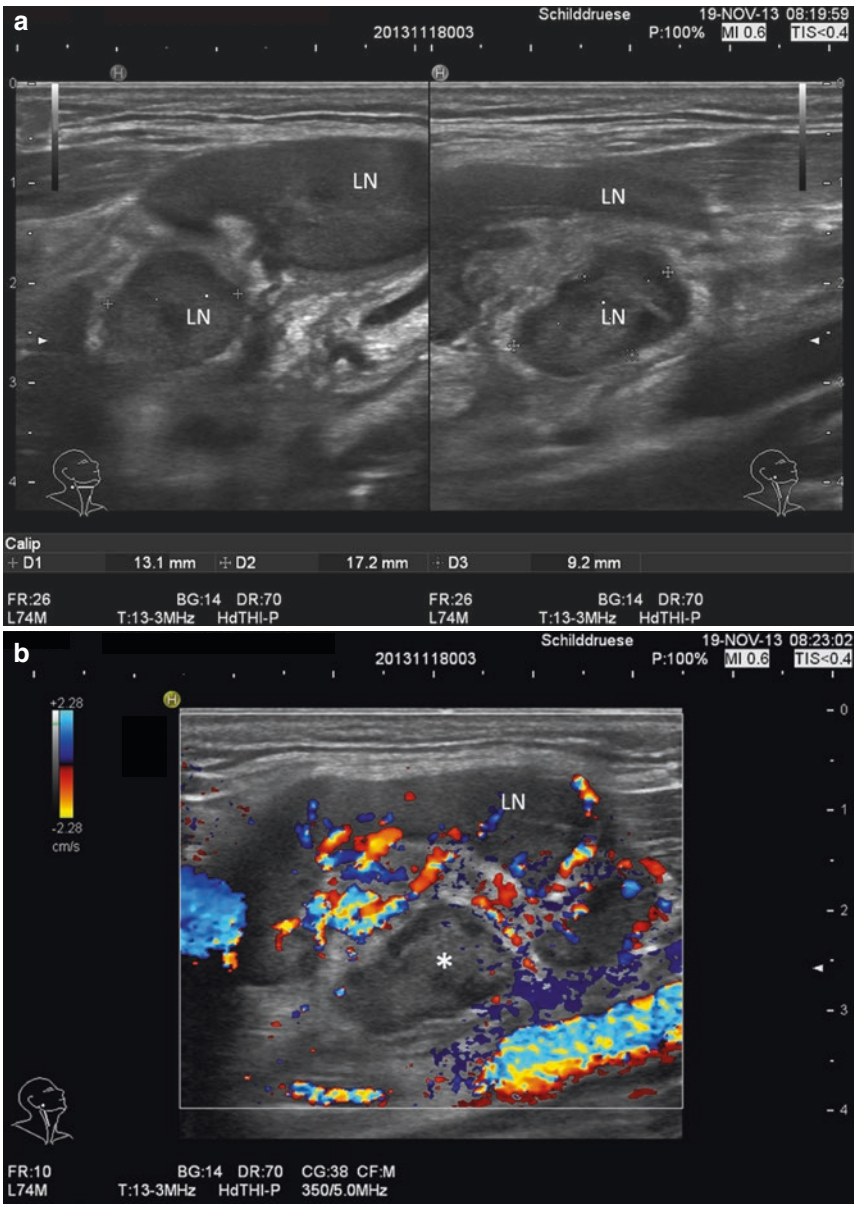

Fig. 6.5 Lymph node abscess in the left neck. (**a**) Using B-scan, the two nodes (LN) impress as inflamed lymph nodes. The surrounding tissue is hyperechoic owing to edema. (**b**) Using color-coded sonography, it becomes obvious that one or both nodes is not vascularized (*asterisk*), indicating necrosis or abscess

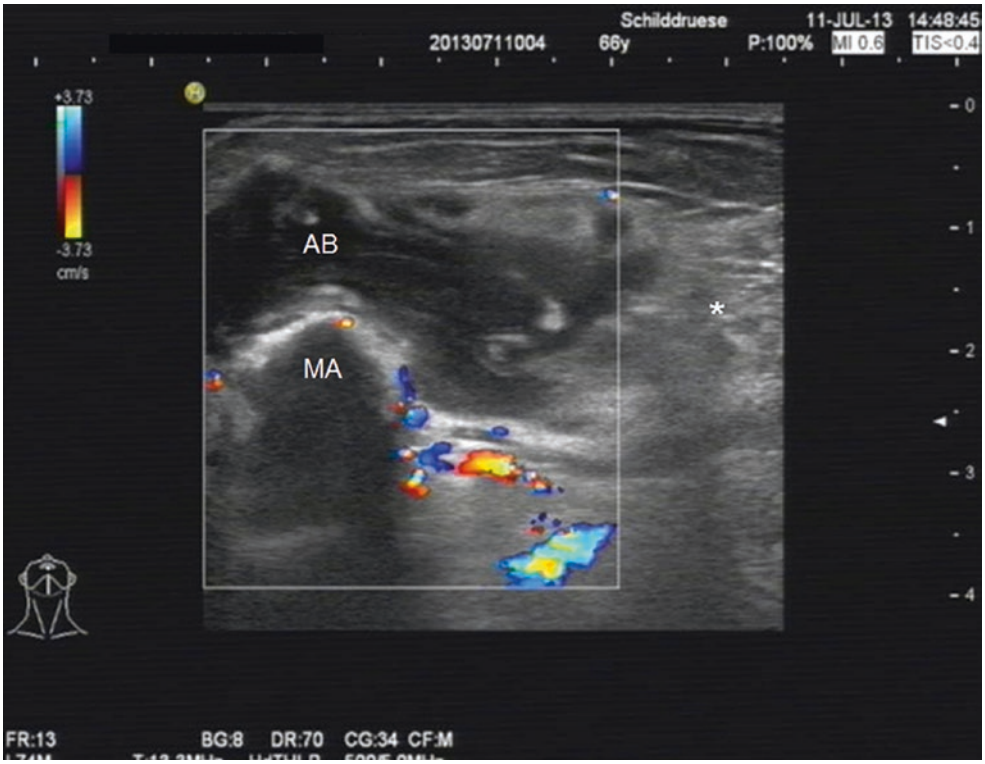

Fig. 6.6 Odontogenous abscess (AB) next to the mandible (MA). The abscess area is hypoechoic, without blood vessels. The surrounding tissue (*asterisk*) is hyperechoic and thickened because of the strong inflammation

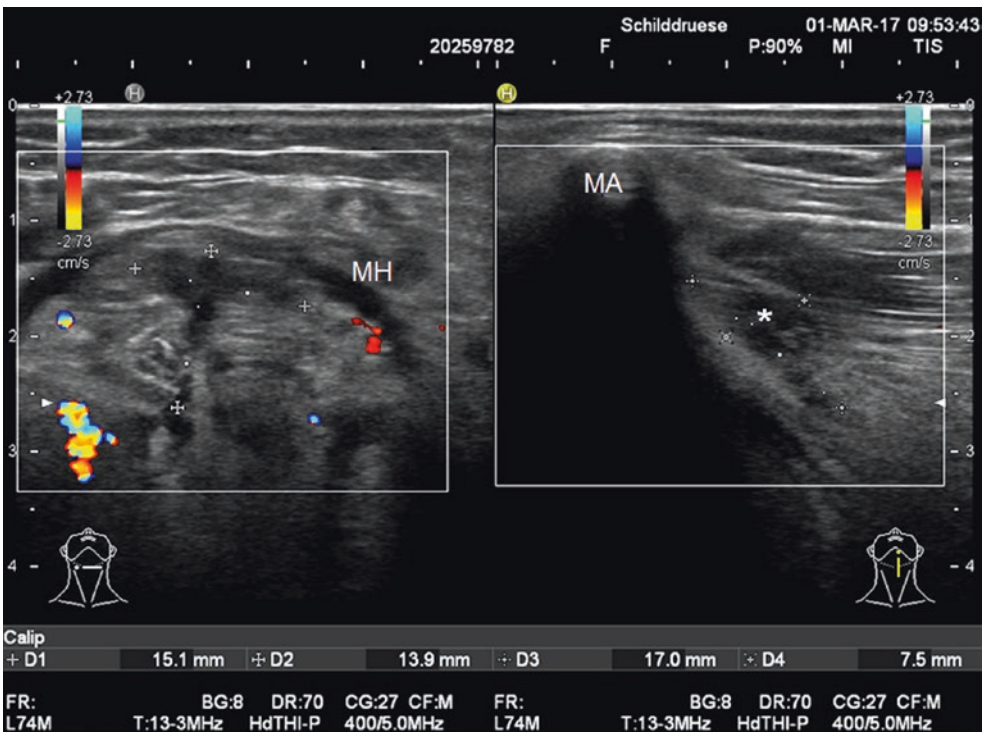

Fig. 6.7 Phlegmon and a small abscess (*asterisk*) of the left floor of the mouth. MA mandible, MH mylohyoid muscle

feathered echo is similar to the echo of the neck muscles (Fig. 6.12). Therefore it is sometimes difficult to differentiate normal neck muscles from a lipoma, especially if the lipoma is small and not palpable, which may occur if it is in a deep location (Fig. 6.13). Generally, its blood supply is weak, with only a few blood vessels that can be detected near the capsule (Fig. 6.13).

A diffuse lipomatosis of the neck, such as in Madelung disease, is characterized by the same pattern as the lipoma: thickened, fatty tissue showing a feathered structure

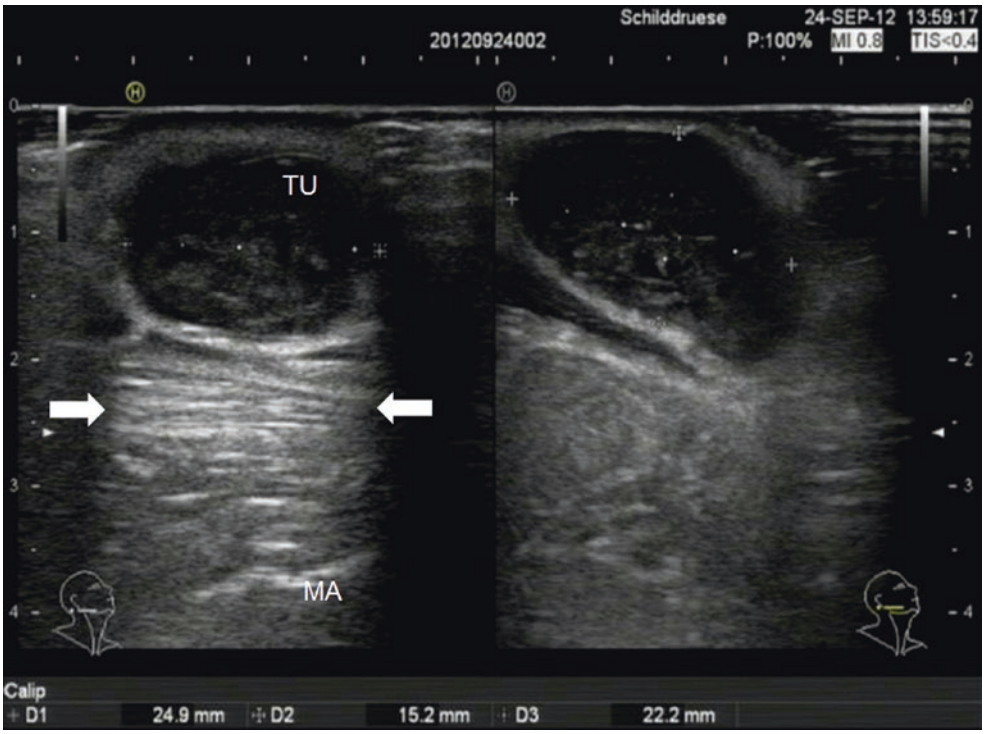

Fig. 6.8 Atheroma (TU) next to the right mandible (MA); the intracutaneous tumor often has a hypoechoic structure. Generally the structure depends on its consistency. Here, a strong enhancement of the acoustic signal is seen between the arrows

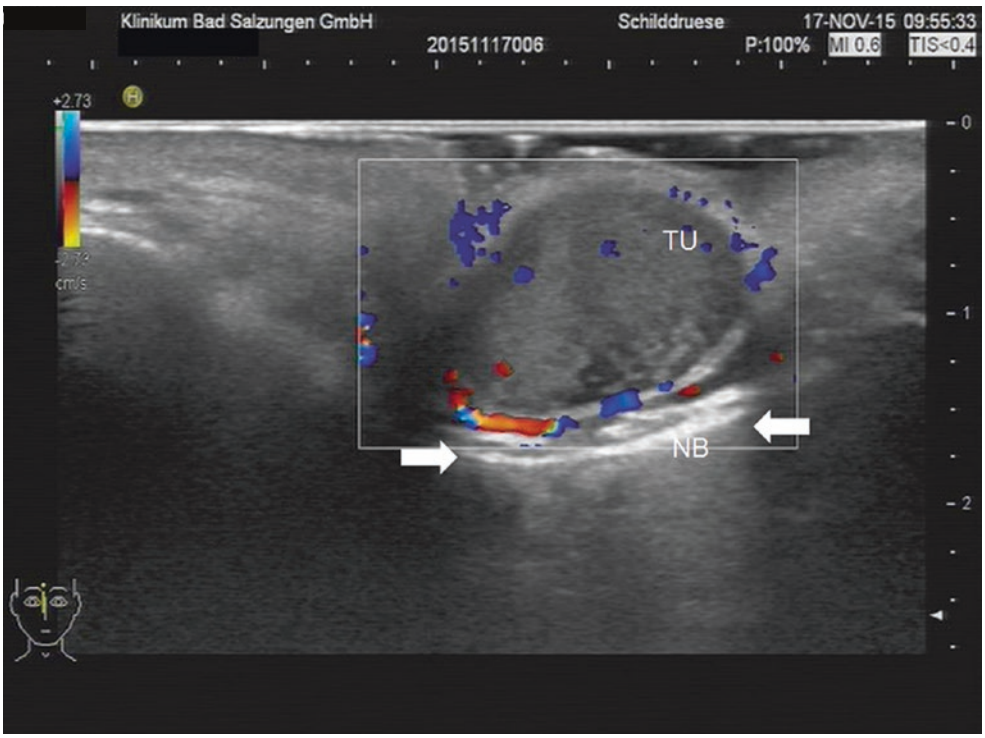

Fig. 6.9 Another atheroma (TU) next to the nasal bone (NB), with intracutaneous localization and strong enhancement of the acoustic signal behind the tumor (*between arrows*). Note that the tumor itself is more hyperechoic than the atheroma in Fig. 6.8

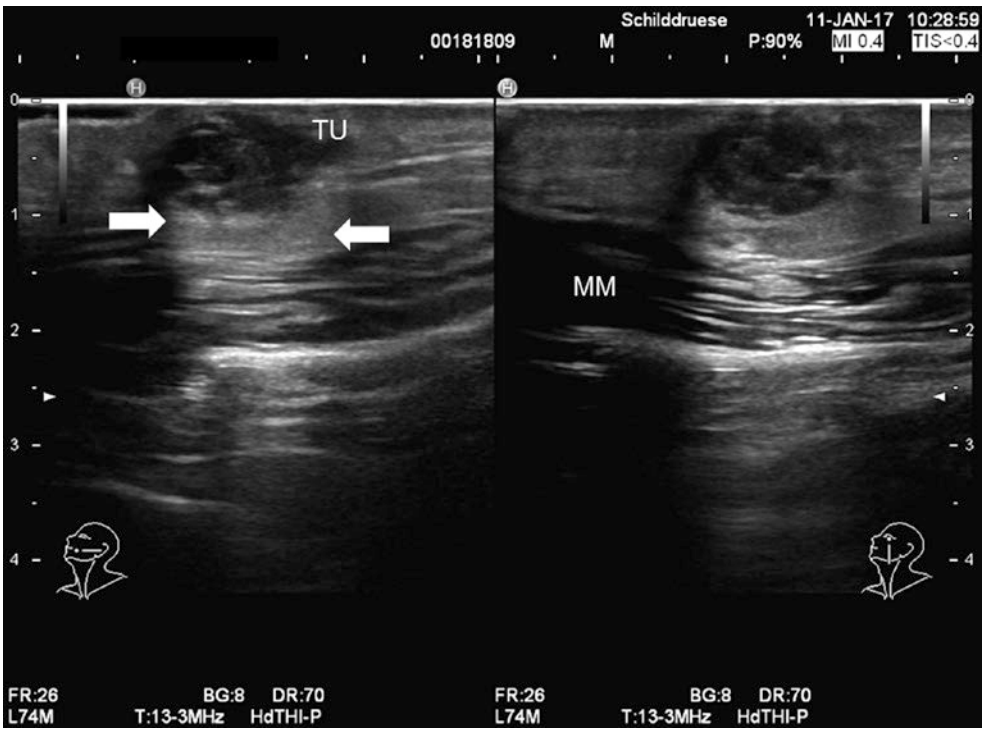

Fig. 6.10 Acute, infected atheroma (TU) of the cheek, with typical echo and typical intracutaneous location and enhancement of the echo (*between the arrows*). The surrounding tissue, especially the masseter muscle (MM), shows an edematous thickening due to inflammation

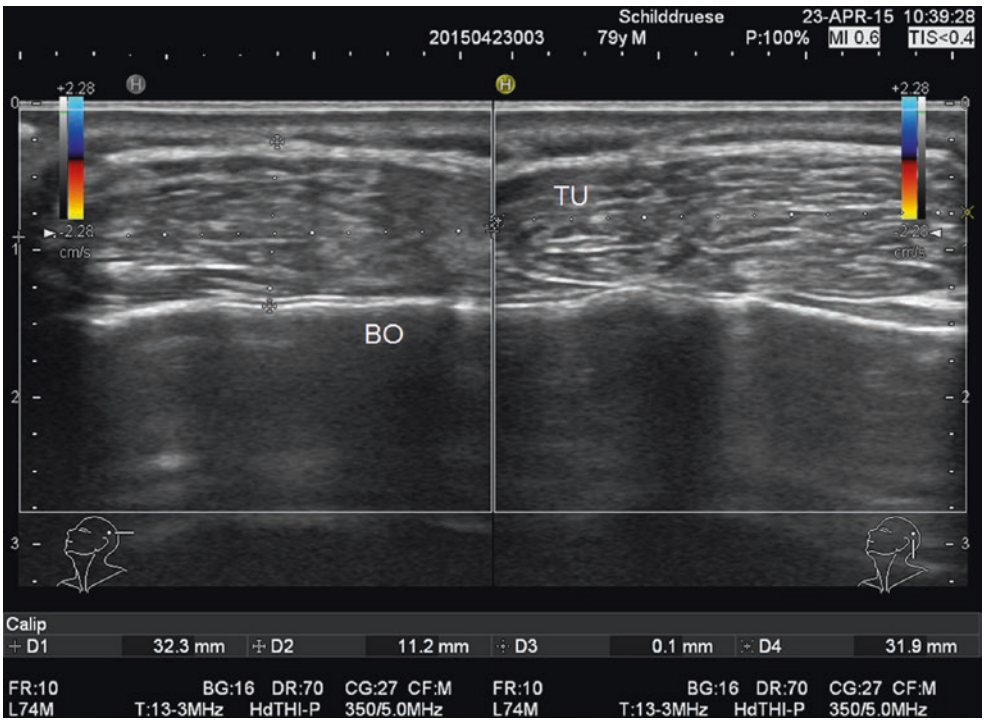

Fig. 6.11 A typical lipoma (TU) with a feathered echo and a thin capsule. BO bone

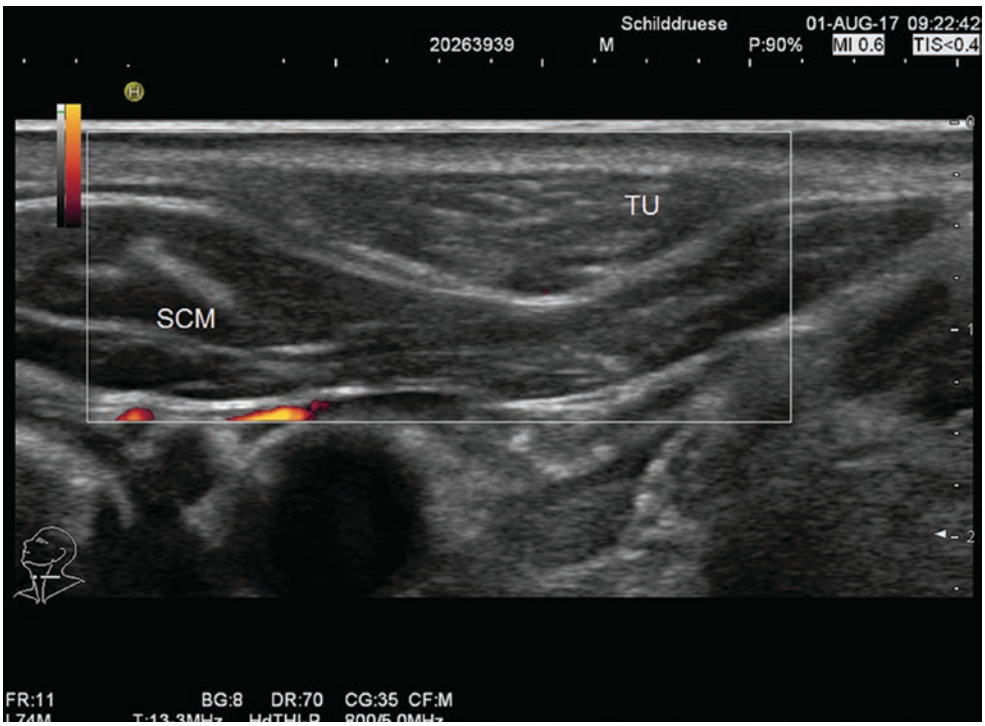

Fig. 6.12 Another lipoma (TU) of the lateral neck. Note that the echo often is nearly the same as the echo of the muscles (sternocleidomastoid, SCM)

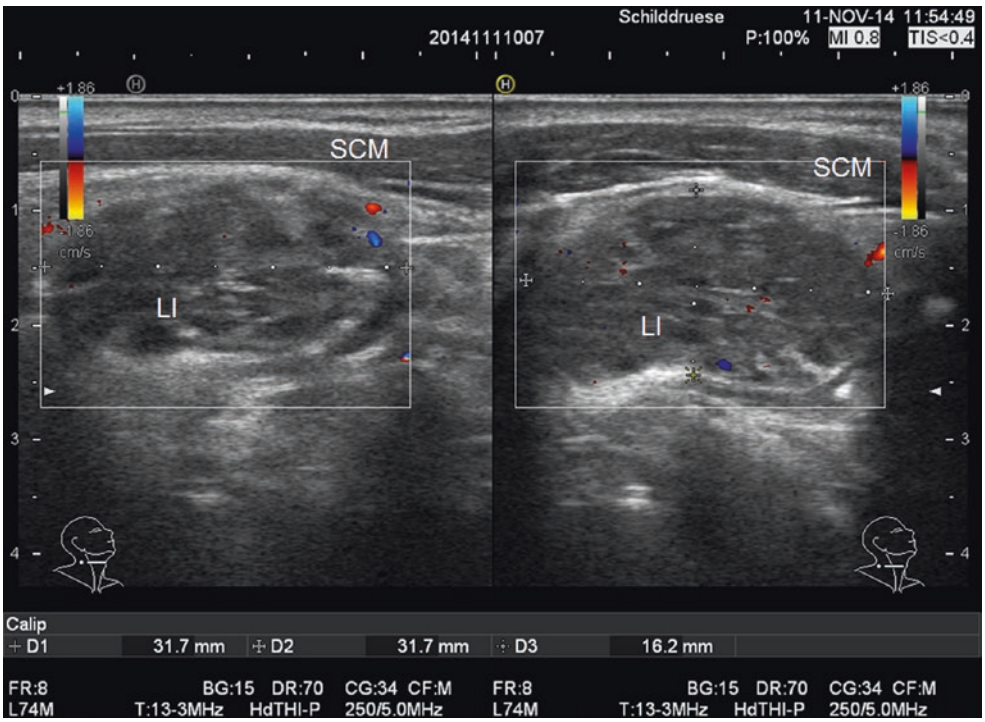

Fig. 6.13 Lipoma (LI) in a deep location under the sternocleidomastoid muscle (SCM). Typically, only a few blood vessels can be seen

(Fig. 6.14a). In these patients, the lipomatous tissue frequently can also be detected in deeper regions of the neck (Fig. 6.14b).

In rare cases, the lipoma does not show the typical feathered structure inside, but instead has a more homogenous and hypoechoic structure (Fig. 6.15). Especially in the submandibular region, such a lipoma can mimic a salivary gland tumor. We have found several lipomas with this pattern even within the head and neck muscles (Fig. 6.16).

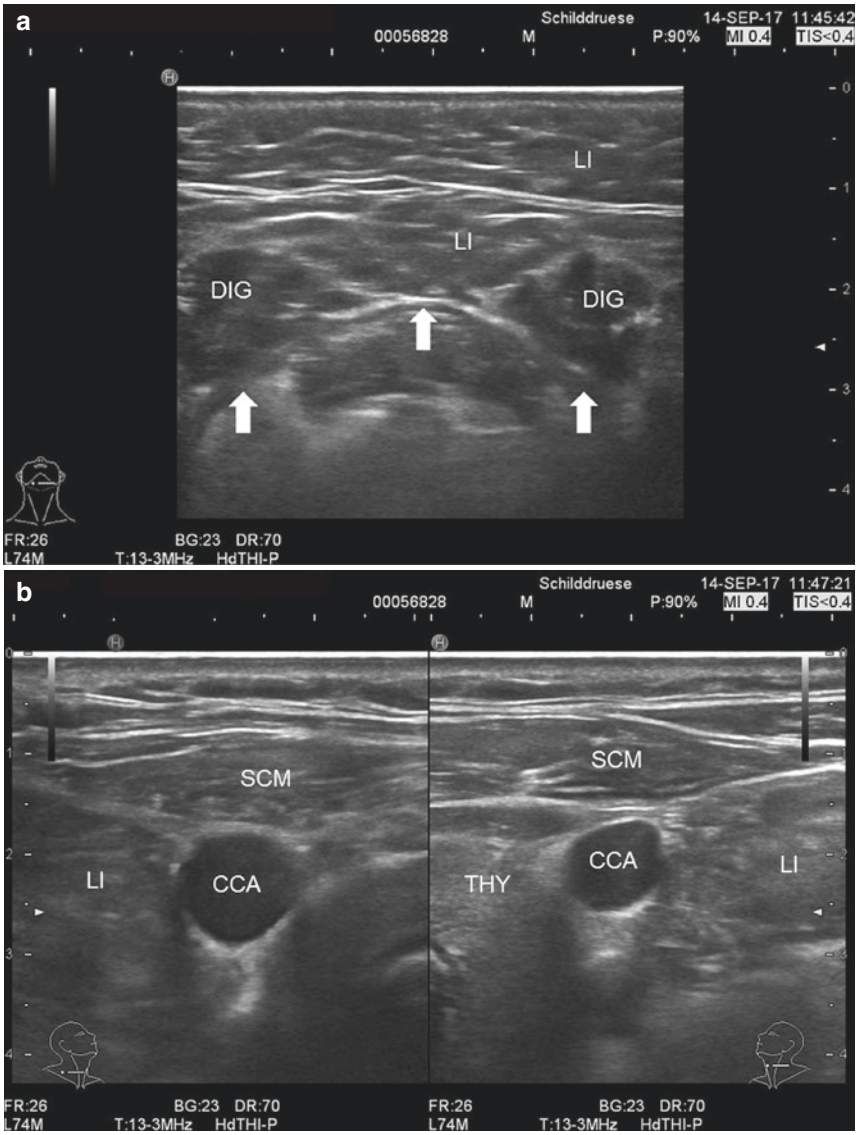

Fig. 6.14 (**a**, **b**) Diffuse lipomatosis (LI) of the neck, with a typical sonographic pattern of the subcutaneous tissue in the whole neck. The tissue shows a feathered echo, and no capsule can be detected. The *arrows* indicate the mylohyoid muscle. CCA common carotid artery, DIG digastric muscles, SCM sternocleidomastoid muscle, THY thyroid

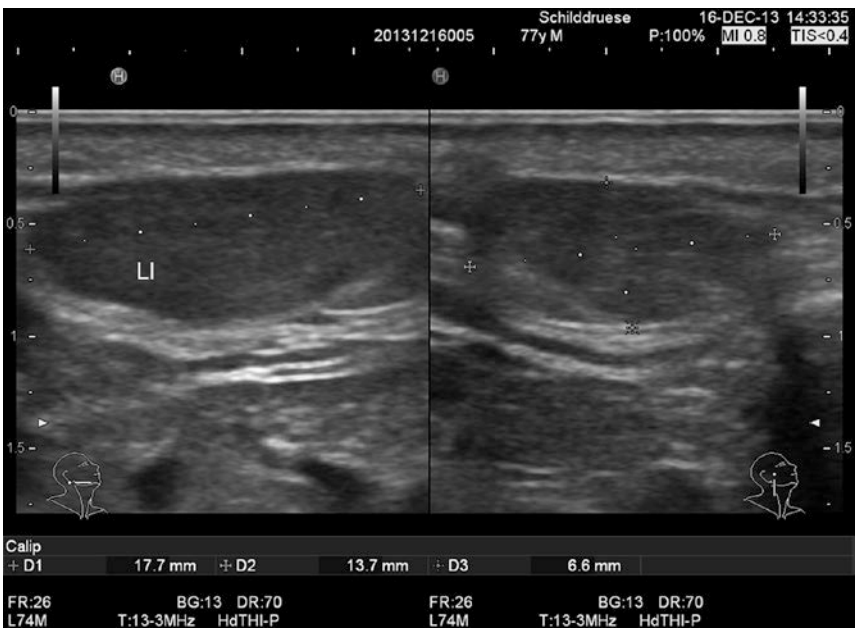

Fig. 6.15 An atypical lipoma (LI), in which the typical feathered structure cannot be seen

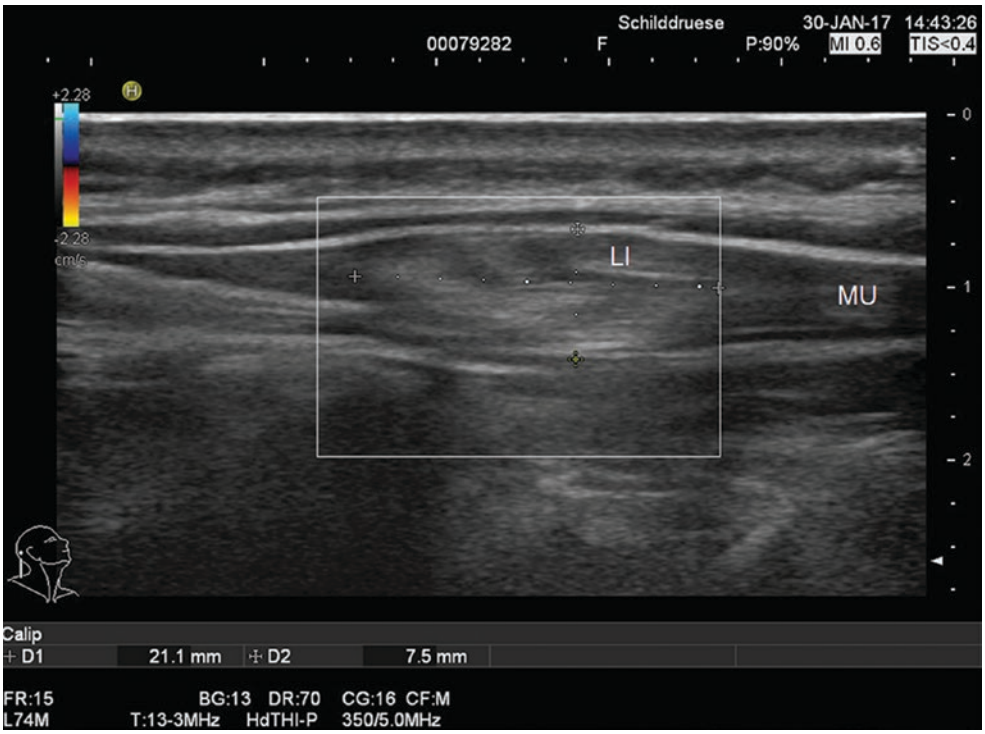

Fig. 6.16 Intramuscular (MU) lipoma (LI) with an atypical appearance

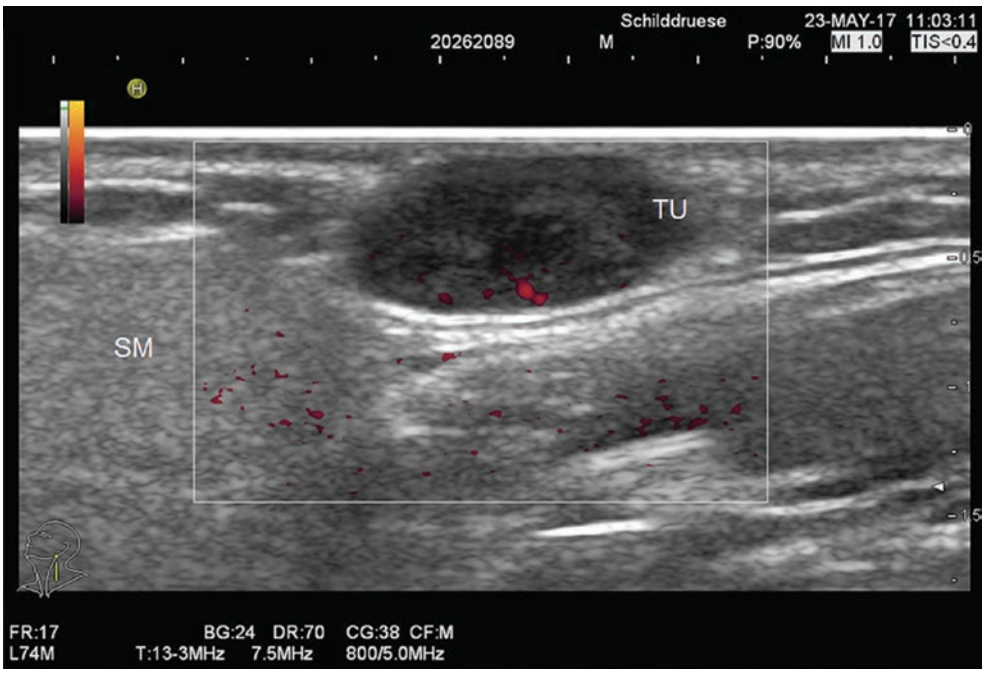

Fig. 6.17 Neurofibroma (TU) of the skin in a patient suffering from von Recklinghausen disease. SM submandibular gland

6.3.3 Skin Tumors and Infiltration of the Skin by Metastatic Disease

Skin tumors are very easily detectable by ultrasound. Of course, ultrasound of the skin is a domain of the dermatologist, who can use high-frequency ultrasound to determine the thickness of skin tumors and the infiltration of the various skin layers. Nevertheless, the head and neck surgeon will be confronted with skin tumors that require estimation of the extent of the tumor, rather than differentiation of malignant versus benign tumors. Different tumors can occur in different skin layers. Benign tumors (such as the atheroma described above) are characterized by a clear border, but other tumors, such as a neurofibroma (Fig. 6.17), show a similar B-scan pattern. Sometimes intratumoral blood ves-

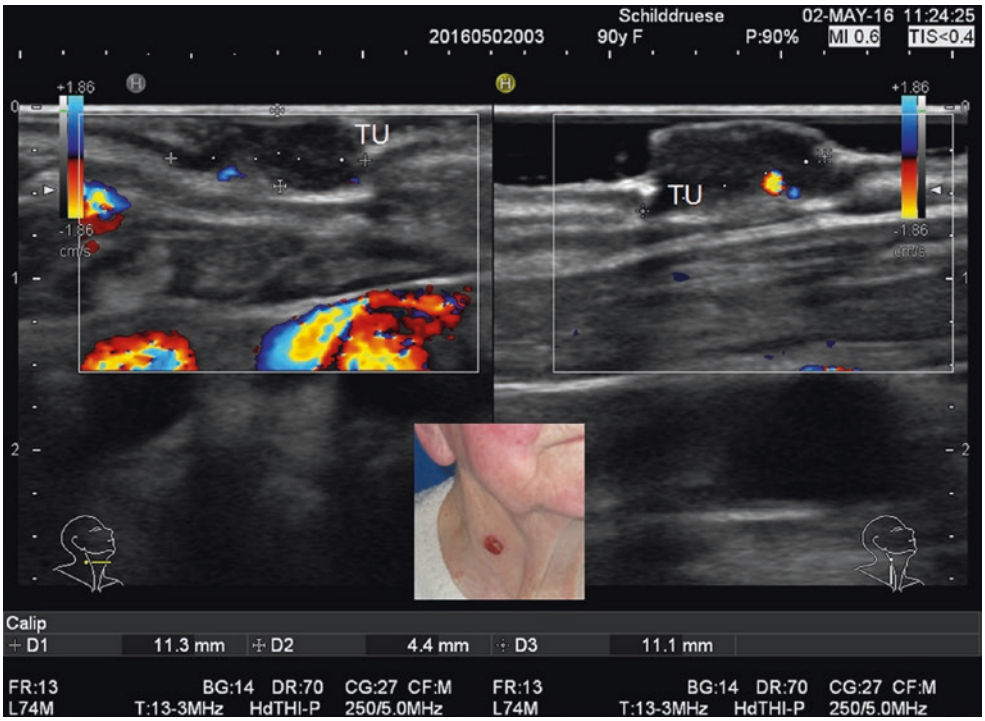

Fig. 6.18 Superficial tumor (TU) of the skin; sonographic picture and clinical aspect

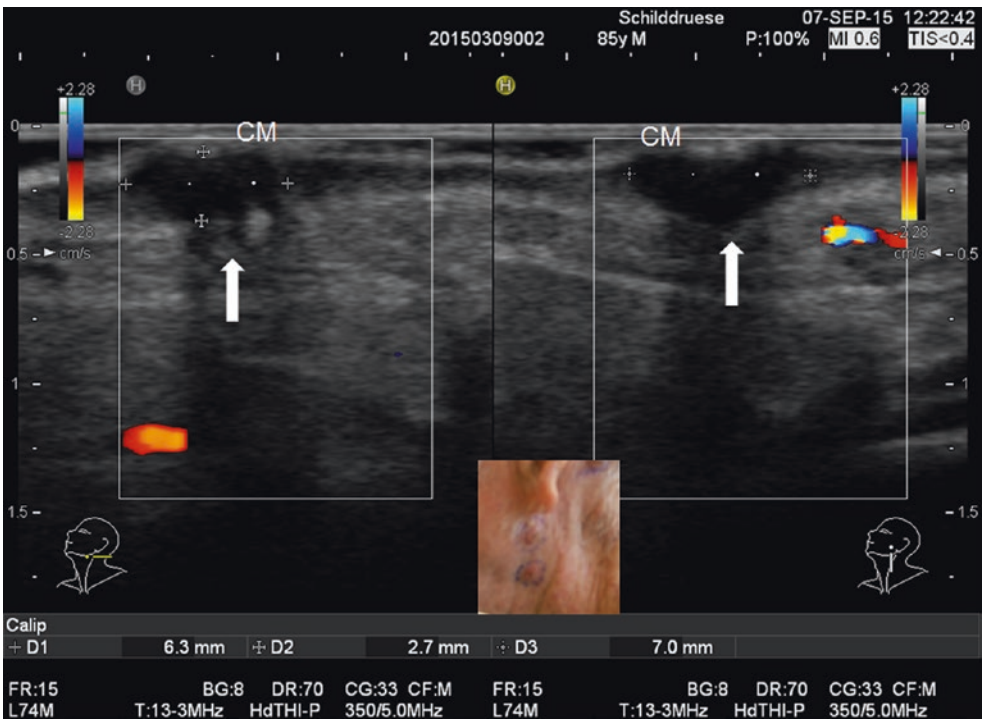

Fig. 6.19 Cutaneous metastases (CM). The metastasis is located superficially and has typical irregular borders (*arrows*)

sels can be detected, in contrast to the atheroma, which is filled with fluid. Most skin tumors are hypoechoic. They are located within the skin level or can be more prominent. With the ultrasound equipment of the head and neck surgeon, differentiating between kinds of skin tumors—such as between a basalioma (Fig. 6.18), squamous cell carcinomas, or skin metastasis (Fig. 6.19)—is only possible by knowing the clinical picture and the patient's history. In case of malignancy, the tumor may show an infiltration of deeper structures (Fig. 6.20). Therefore, preoperative ultrasound of skin tumors may influence the radicality of the surgery and should be part of the diagnostic routine.

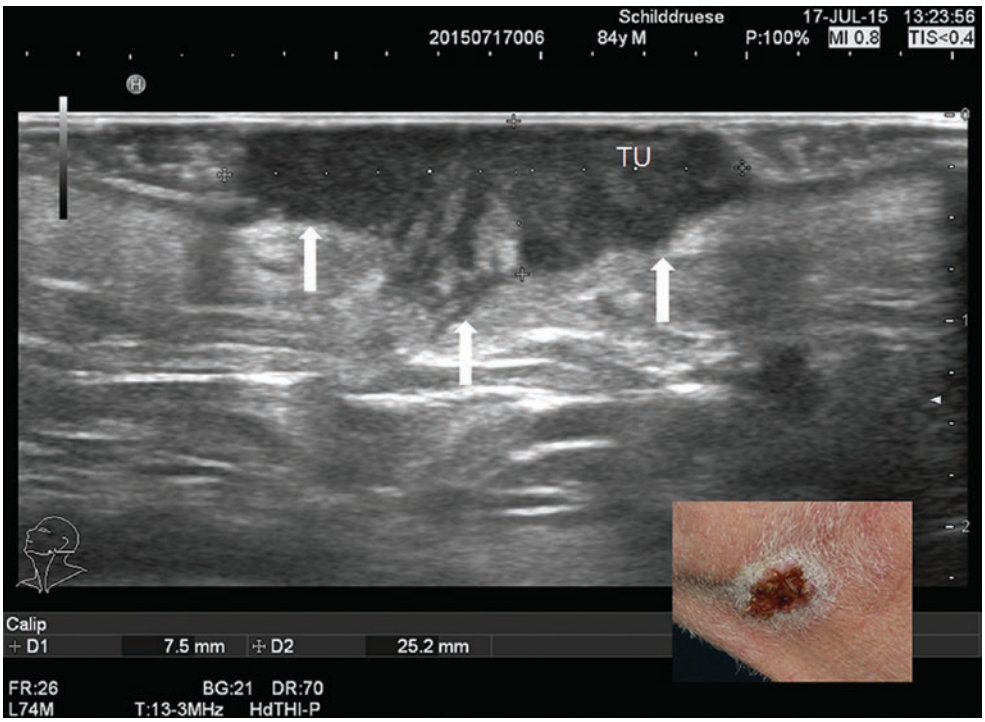

Fig. 6.20 Clinical aspect and ultrasound of a squamous cell carcinoma (TU). Note the superficial location and the irregular borders in the depth of the tumor (*arrows*)

Fig. 6.21 Subcutaneous process (*asterisk*) with a fistula (*between the arrows*)

6.3.4 Fistula

Fistulas can occur anywhere in the skin. Clinically, a fistula is often located in the area of the parotid gland, such as a postoperative fistula, congenital preauricular fistula, or lateral cervical fistula. Small fistulas cannot be seen with ultrasound. Of course, the fistula's duct can be filled with saline for better detection with sonography and to get an overview of its extension, but in practice, the clinical impact of this approach is low. Nevertheless, some fistulas can be seen very well by using ultrasound (Video 6.4). The examiner can frequently detect the connection to the skin (Fig. 6.21). Because of its fluid contents, the fistula itself is hypoechoic, with an increased echo behind it.

6.3.5 Hemangiomas and Vascular Malformations

In contrast to hemangiomas, *vascular malformation* does not describe proliferative vascular disease. Vascular malformations are congenital and can be arterial, venous, or lymphatic. Many of these tumors occur in the head and neck region, and ultrasound imaging should be the first step in diagnosis, especially because these tumors are often seen in children. Therefore, head and neck surgeons should be familiar with their typical sonographic features.

Hemangioma [4] is commonly characterized by a regular border and a heterogenous echo inside (Figs. 6.22 and 6.23). The detection of blood vessels may be difficult; color-coded

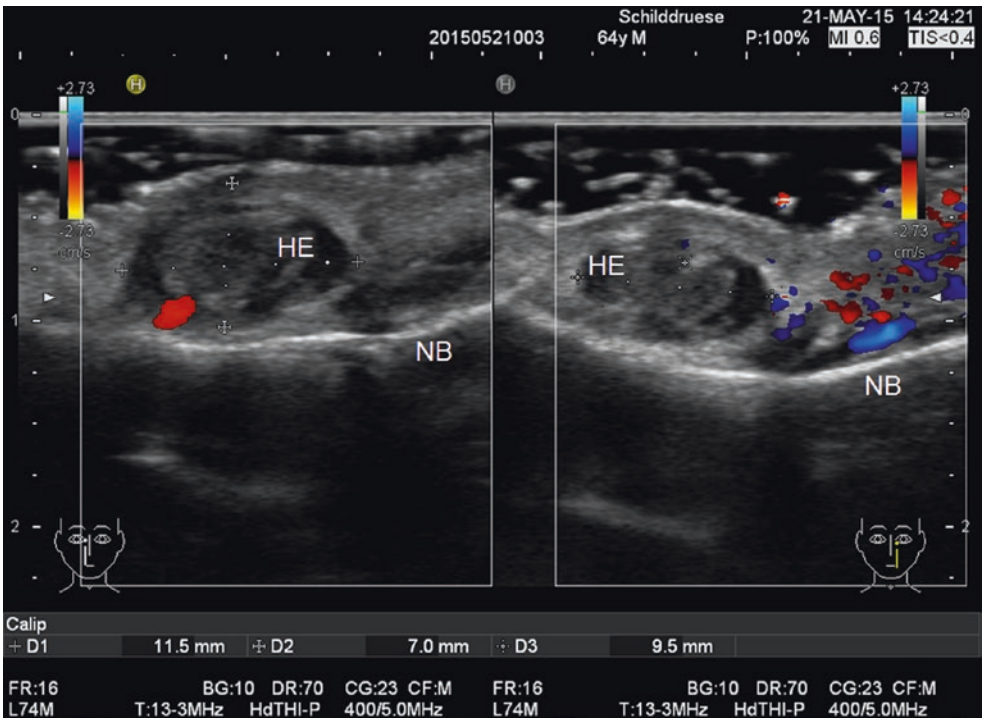

Fig. 6.22 Hemangioma (HE) of the face. Using color-coded sonography, only a few blood vessels can be detected even with a low pulse repetition frequency. NB nasal bone

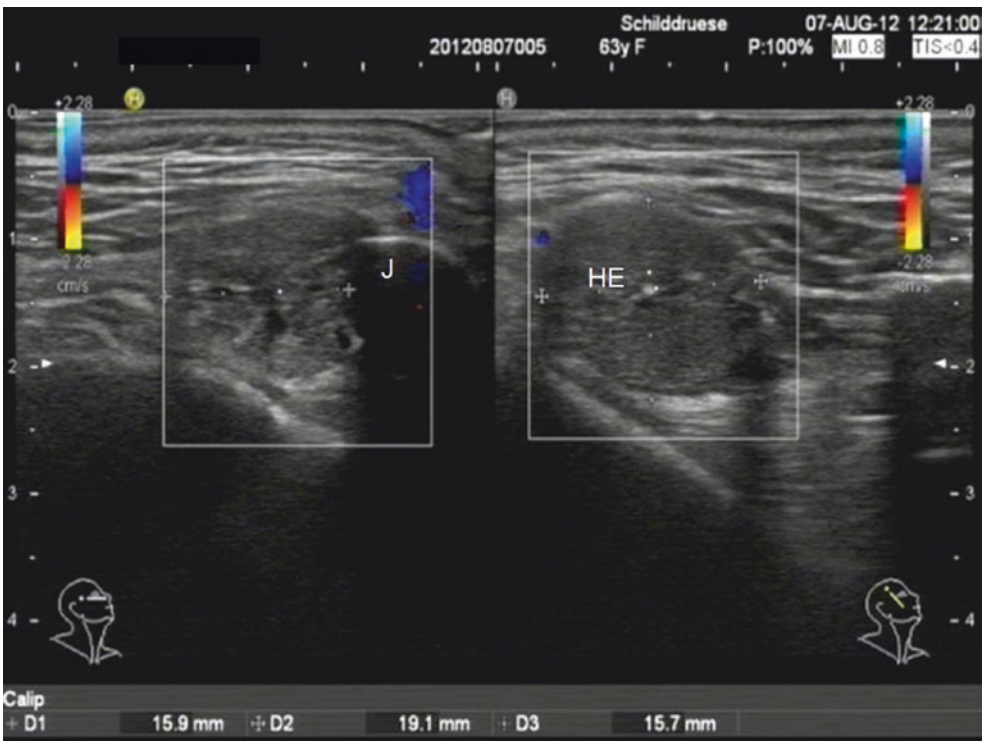

Fig. 6.23 Hemangioma (HE) next to the jaw (J)

sonography detects only the blood flow, not the extent of vascularity. Nevertheless, duplex sonography is an essential part of the examination, and the examiner should try to detect as many intratumoral vessels as possible. Therefore, the pulse repetition frequency (PRF) should be reduced to a minimum.

Vascular malformations are located subcutaneously. Often it is difficult to detect surrounding structures (Figs. 6.24 and 6.25). The echo resembles multicystic disease, so the depiction of blood vessels entering the tumor is mandatory. Using pulsed-wave (pw) Doppler, high systolic velocities can be detected as a result of intratumoral shunts. In venous malformations, an increasing tumor volume can be detected when the Valsalva maneuver is performed (Fig. 6.25).

Lymphatic malformations also look like a multicystic tumor (Fig. 6.26). They are localized in the head and neck region in 70–80% of cases [5].

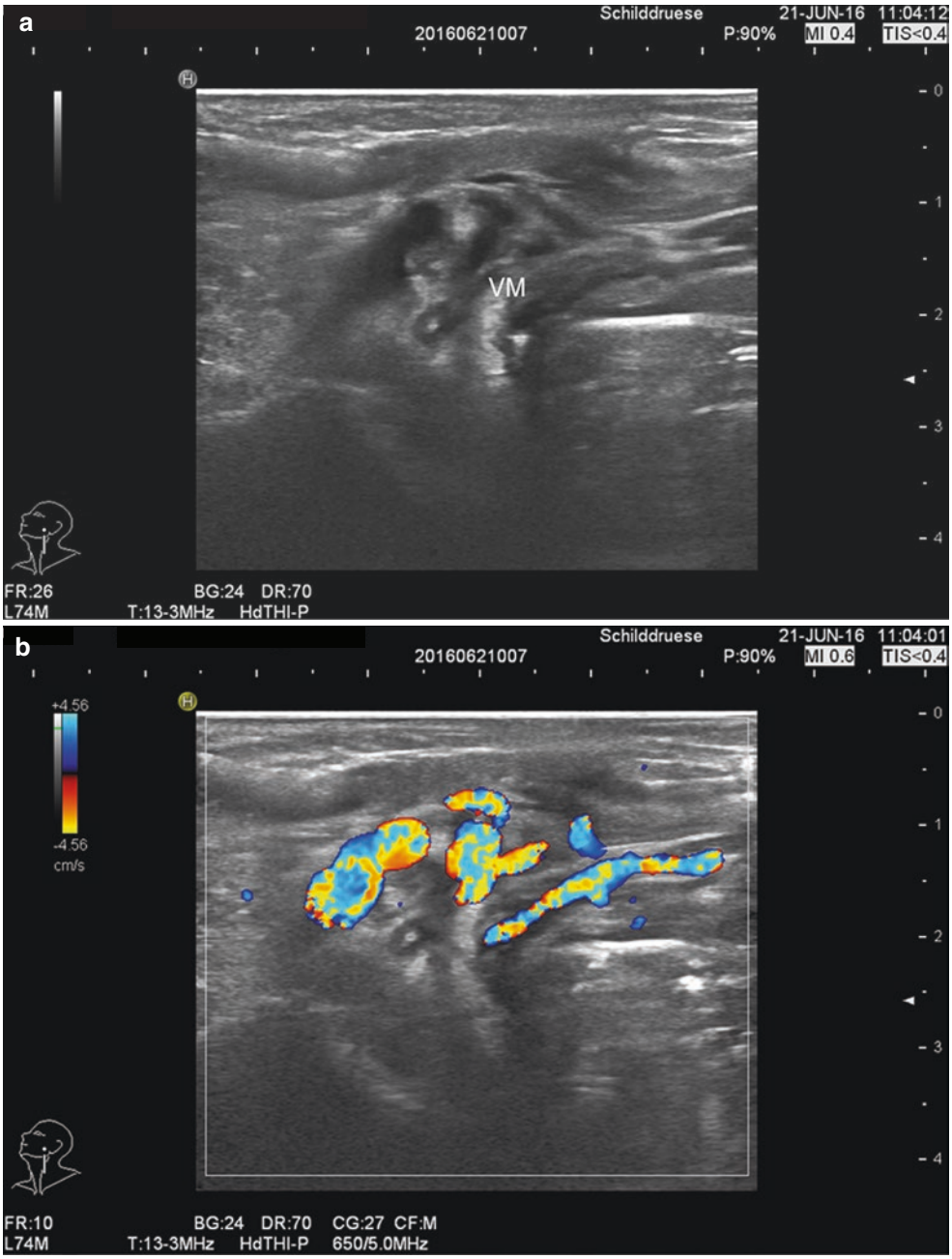

Fig. 6.24 Vascular malformation. (**a**) B-scan shows the vascular malformation (VM) next to the mandible. (**b**) Duplex sonography indicates high vascularization

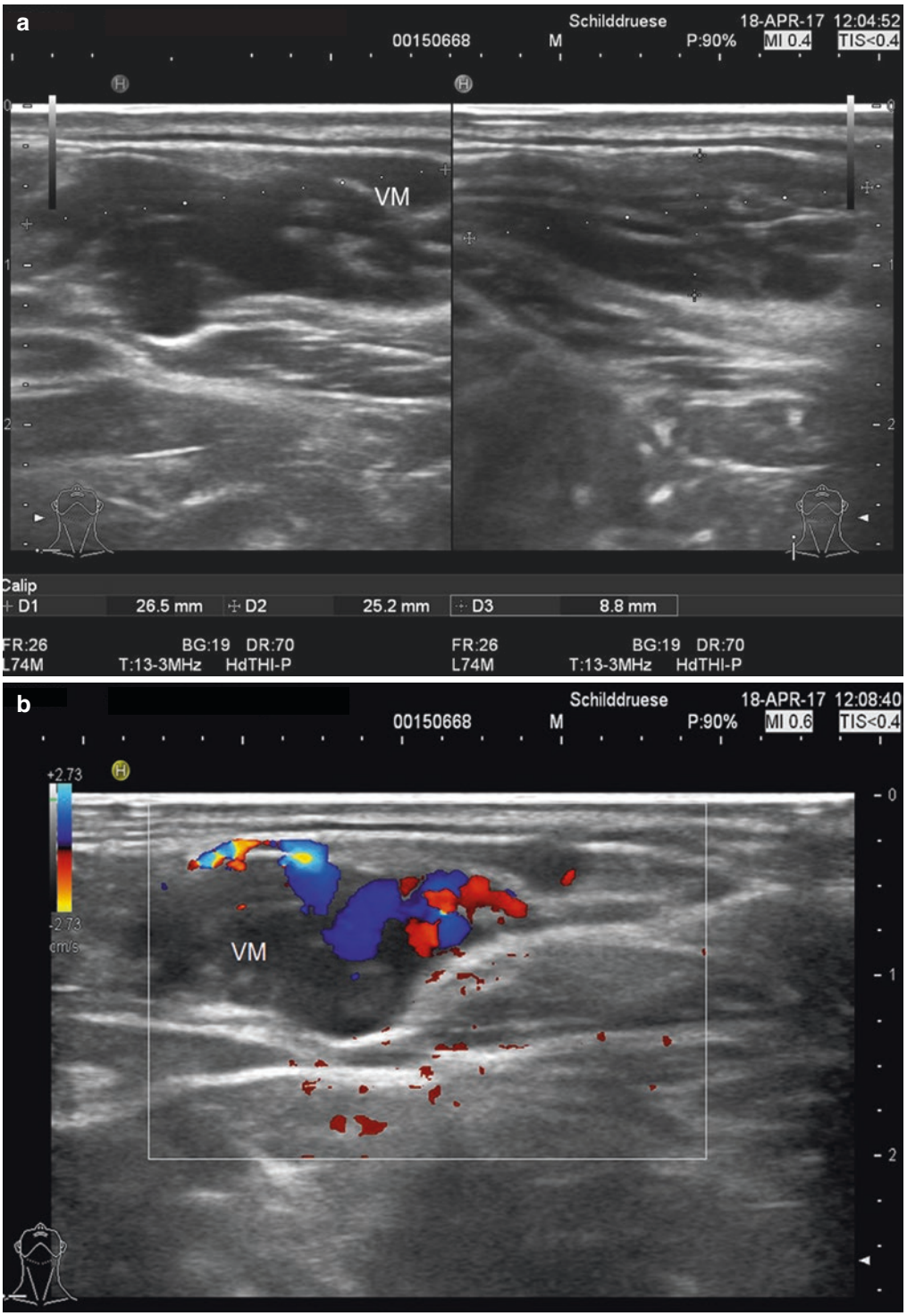

Fig. 6.25 Supraclavicular vascular malformation (VM). (**a**) B-scan. (**b**) Duplex scan. (**c**) Increasing thickness is seen with performance of the Valsalva maneuver (*right*)

Fig. 6.25 (continued)

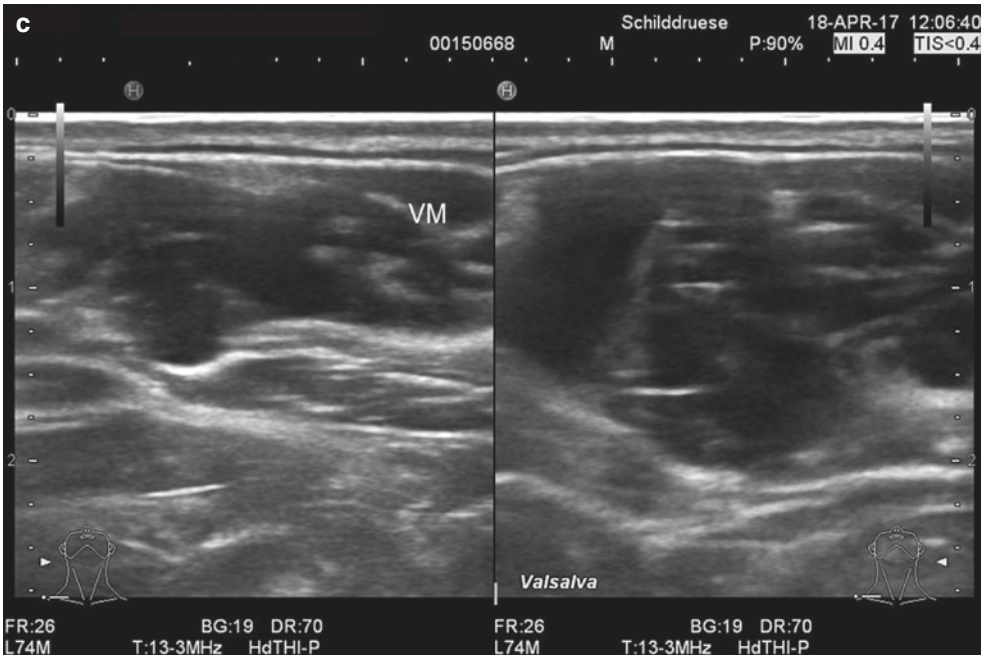

Fig. 6.26 Lymphangioma (LA) of the left neck

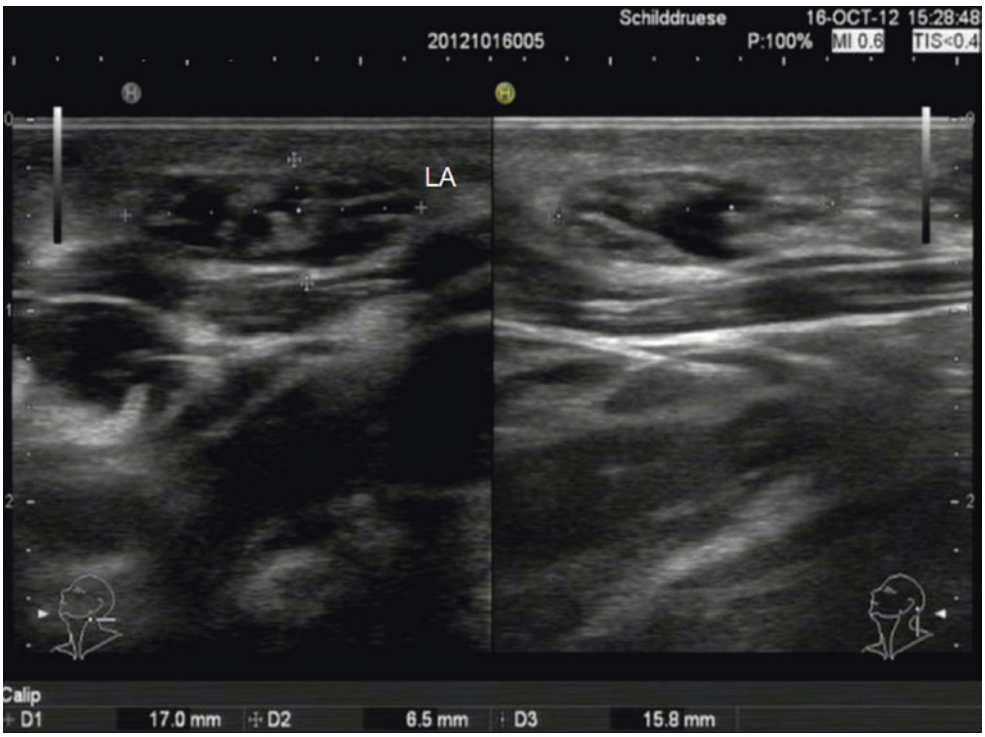

6.4 Branchial Cysts and Thyroglossal Cysts

Branchial cysts result from a failure of the obliteration of the branchial clefts during embryological development. They can occur anywhere in the lateral neck. Thyroglossal cysts are remnants of the thyroglossal duct, which describes the descensus of the thyroid gland from the tongue base via the hyoid to the area in front of the cricoid cartilage. The size of these cysts may differ significantly.

6.4.1 Branchial Cysts

Branchial cysts commonly grow within a few days. They can be detected under the anterior portion of the sternocleido-

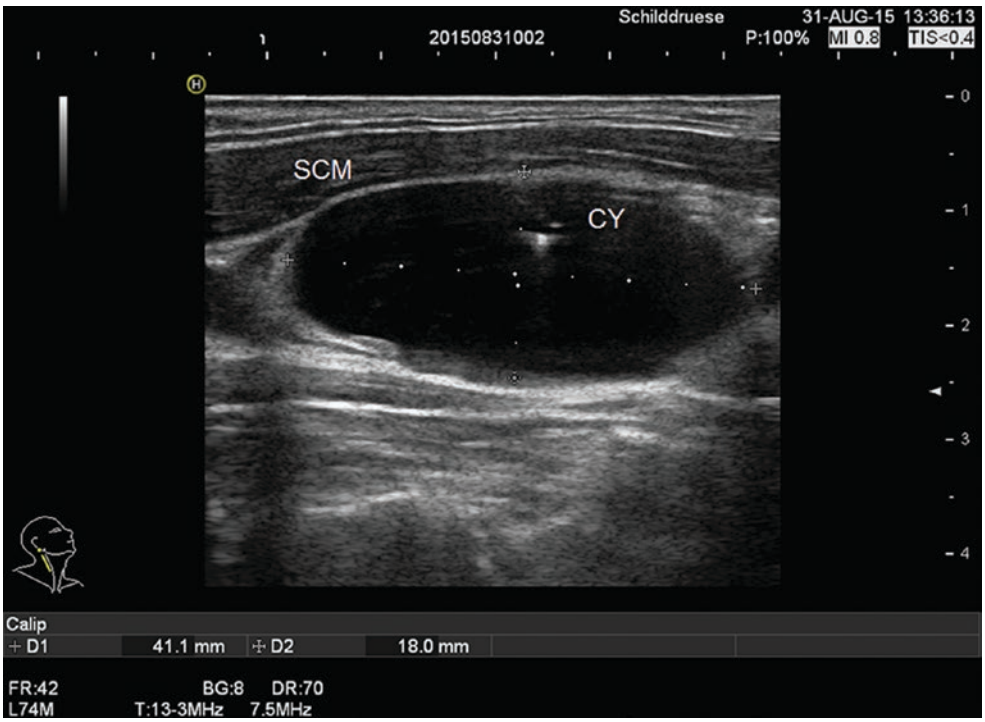

Fig. 6.27 Typical branchial cyst (CY) of the right neck. No structures can be detected within the cyst. The relative enhancement of the echo behind the cyst can be seen. SCM sternocleidomastoid muscle

Fig. 6.28 Often, branchial cysts are filled with thickened secretion. The cyst then appears brighter, but the relative enhancement of the echo behind the cyst can still be detected. ECA external carotid artery, ICA internal carotid artery

mastoid muscle and next to the internal and external carotid artery [3]. Branchial cysts are filled with fluid, which results in a hypoechoic pattern with an acoustic enhancement (Fig. 6.27). A regular capsule can be seen. Sometimes the cystic fluid contains epithelia. Then the pattern is more hyperechoic, but the acoustic enhancement behind the cyst still exists (Fig. 6.28). In case of location next to the mandible, the dorsal part of the submandibular gland can be seen next to the cyst (Fig. 6.29).

Painless cysts can be compressed (Video 6.5). This compression maneuver can be observed while sonography is performed (Fig. 6.30). This finding should be documented,

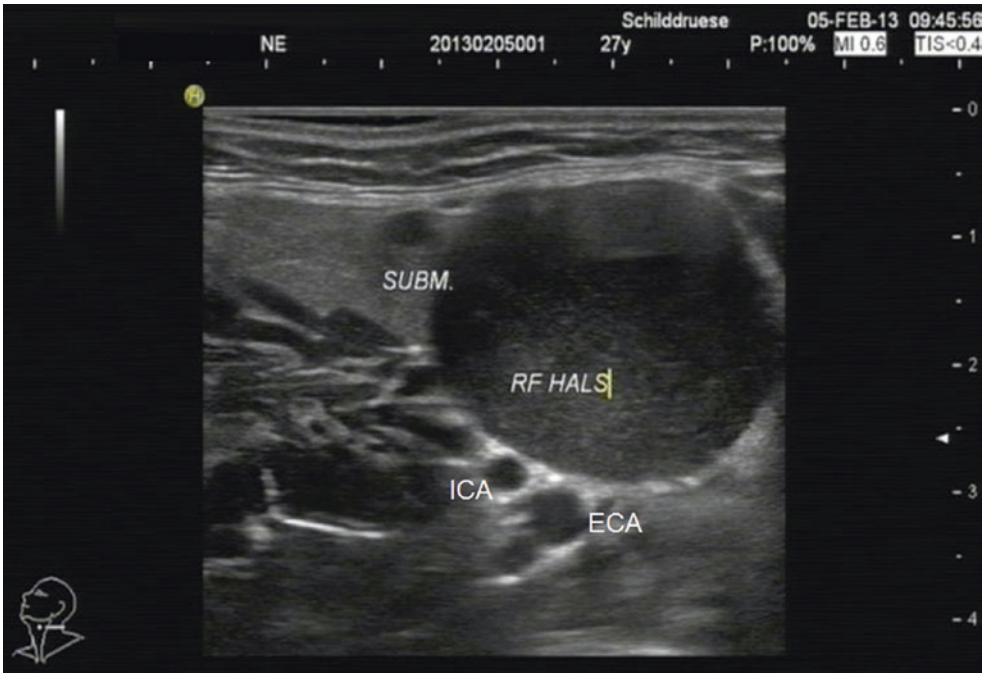

Fig. 6.29 Lateral branchial cysts (RF) can occur in every neck level. This cyst is located directly lateral to the submandibular gland (SM). ECA external carotid artery, ICA internal carotid artery

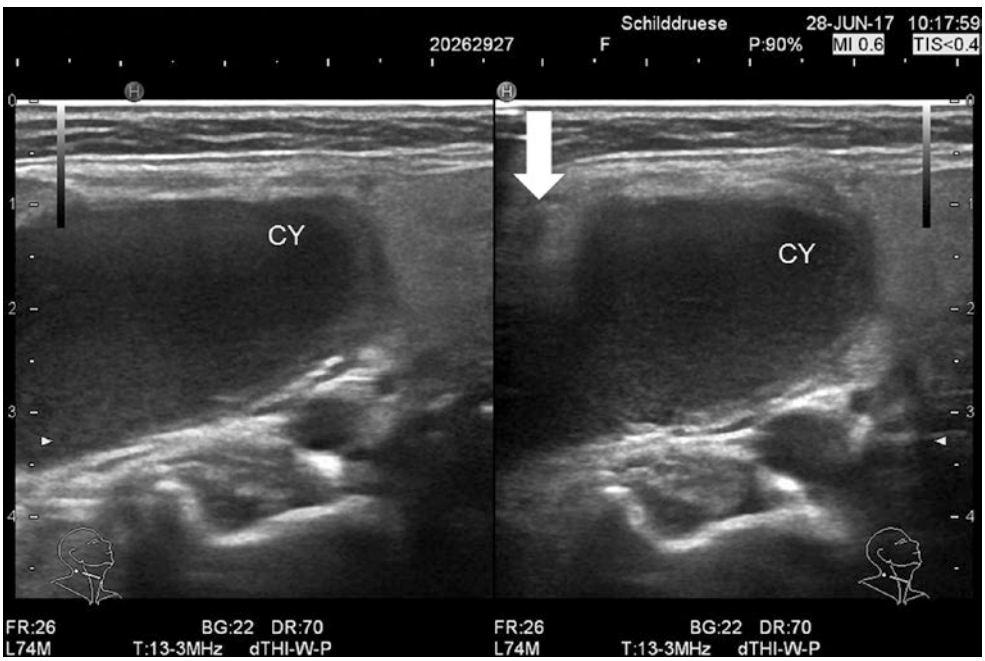

Fig. 6.30 Sonocompression is a typical feature of branchial cysts (CY). Note the difference between the normal cyst (*left*) and the shape of the cyst during compression (*right*). The *arrow* indicates the direction of the compression

because it is a typical feature of branchial cysts (as well as of other cystic tumors).

Commonly, very few blood vessels are detectable in the area of the capsule with the use of color-coded sonography (Fig. 6.31). Some authors additionally describe intratumoral "vessels," which must be interpreted as artifacts. In case of an inflammation of the cyst, the number of blood vessels increases (Fig. 6.32). Furthermore, the echo of the infected cyst is often more heterogenous (Fig. 6.33). Due to the inflammation, the surrounding tissue looks more hyperechoic, as a result of local edema. To relief the cyst in case of acute infection, puncture is a

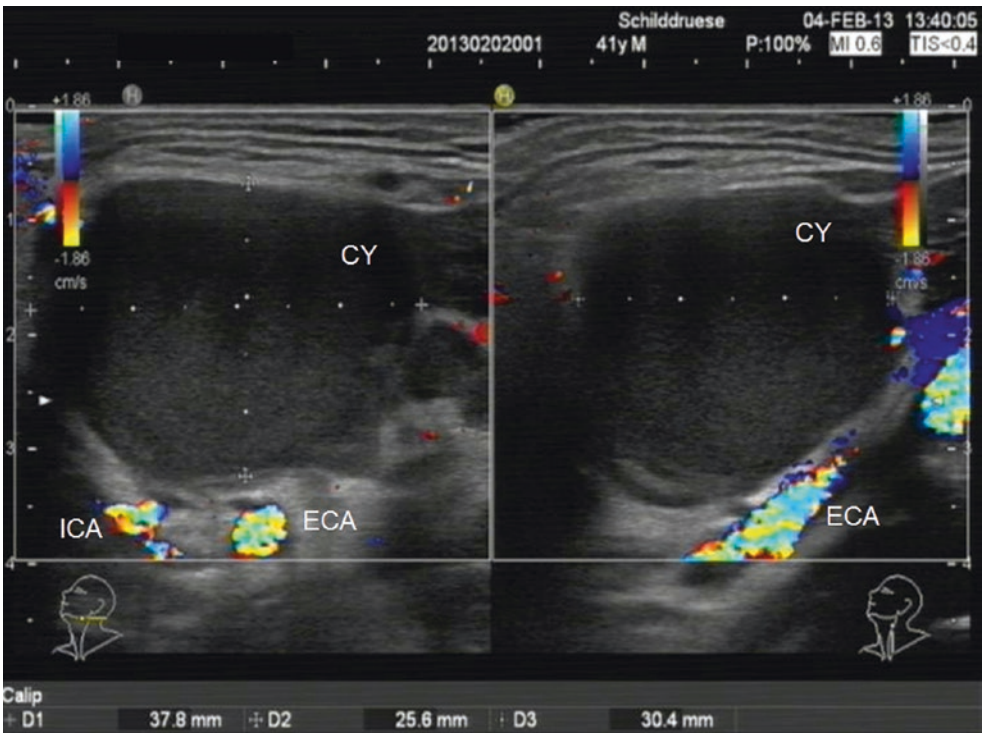

Fig. 6.31 Duplex scan of a lateral branchial cyst (CY). Blood vessels can be detected only in the area of the capsule. ECA external carotid artery, ICA internal carotid artery

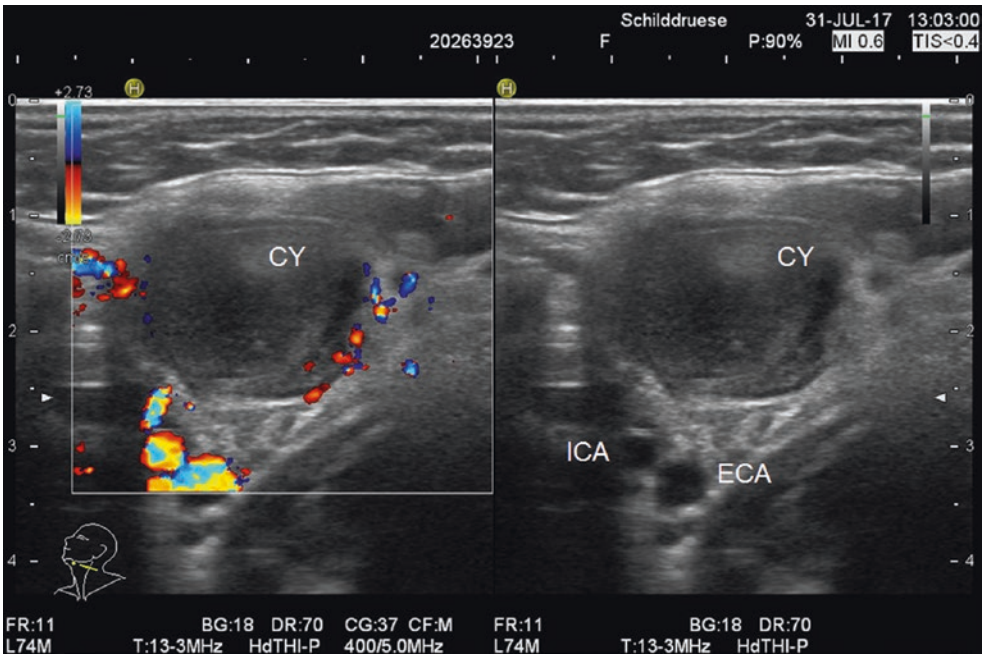

Fig. 6.32 B-scan (*right*) and duplex scan (*left*) of an infected lateral branchial cyst (CY). Note the heterogenous pattern within the cyst and the high number of blood vessels around the cyst. ECA external carotid artery, ICA internal carotid artery

therapeutic option. It can be performed under ultrasound control (Fig. 6.34).

It is important to consider the sonographic characteristics of branchial cysts to avoid overlooking other diseases, especially malignant lymph nodes. If the node's tissue is necrotic, its sonographic appearance may resemble that of a branchial cyst (Fig. 6.35). Therefore, knowledge of the clinical examination of the head and neck region and the patient's history is essential for correct sonographic diagnosis of a branchial cyst.

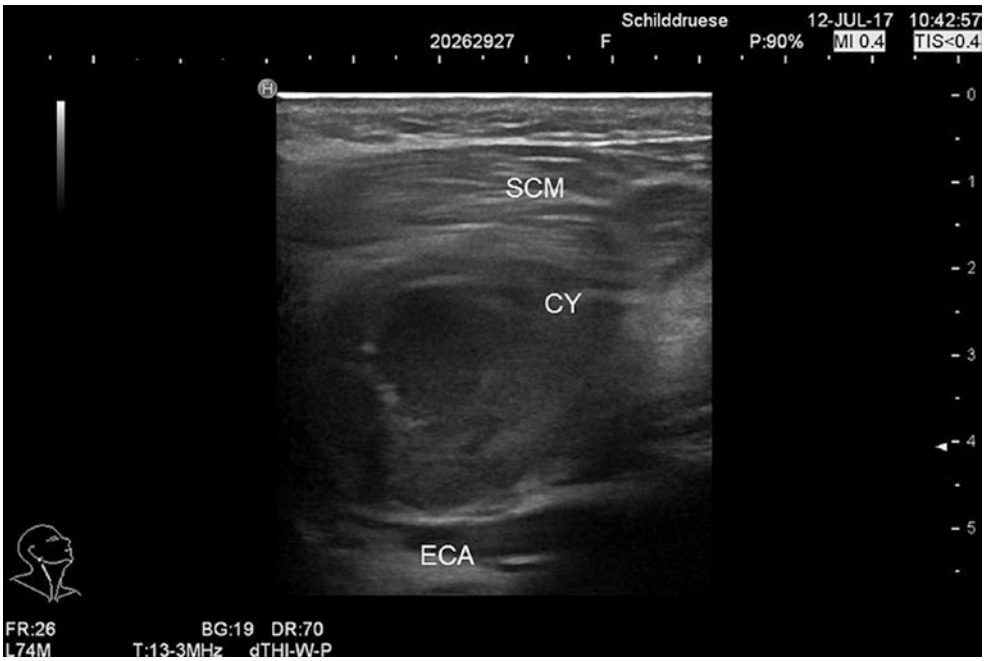

Fig. 6.33 B-scan sonography of an infected lateral branchial cyst (CY). The cyst itself shows a heterogenous pattern, and the surrounding tissue, including the sternocleidomastoid muscle (SCM), is edematous and thickened. ECA external carotid artery

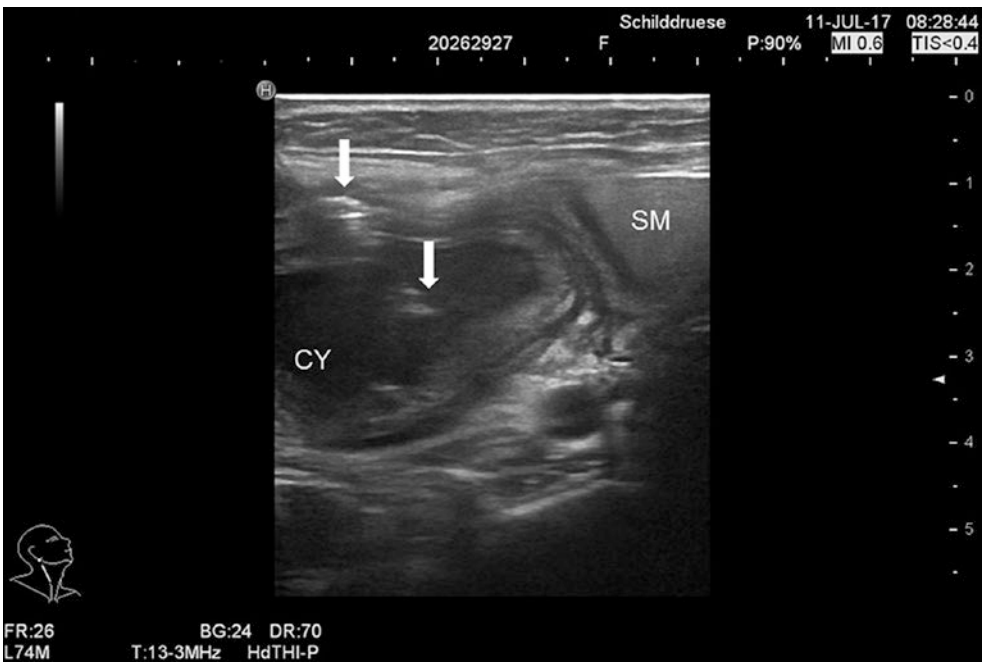

Fig. 6.34 In case of an infection, ultrasound-guided puncture is a therapeutic option. The needle (*arrows*) can be seen easily within the cyst (CY). SM submandibular gland

6.4.2 Thyroglossal Cysts

The most important sonographic characteristic of thyroglossal cysts is their contact with the hyoid bone [6]. The cyst can be located anywhere around the hyoid—under it (Fig. 6.36) or above it (Fig. 6.37). Similar to branchial cysts, the pattern of the cyst is more or less hypoechoic, but an acoustic enhancement can always be seen. Because these cysts usually are much smaller than branchial cysts, a sonographic compression maneuver is difficult to perform. The shape of the cyst may be lobulated (Figs. 6.37 and 6.38), and sometimes intracystic septation can be seen (Fig. 6.39). Blood vessels can be detected only in the area of the smooth capsule and, if present, in the area of the septation. If a cystic duct is present, it also can be seen (Fig. 6.40). In cases of acute inflammation, the surrounding tissue also appears edematous and hyperechoic (Fig. 6.41).

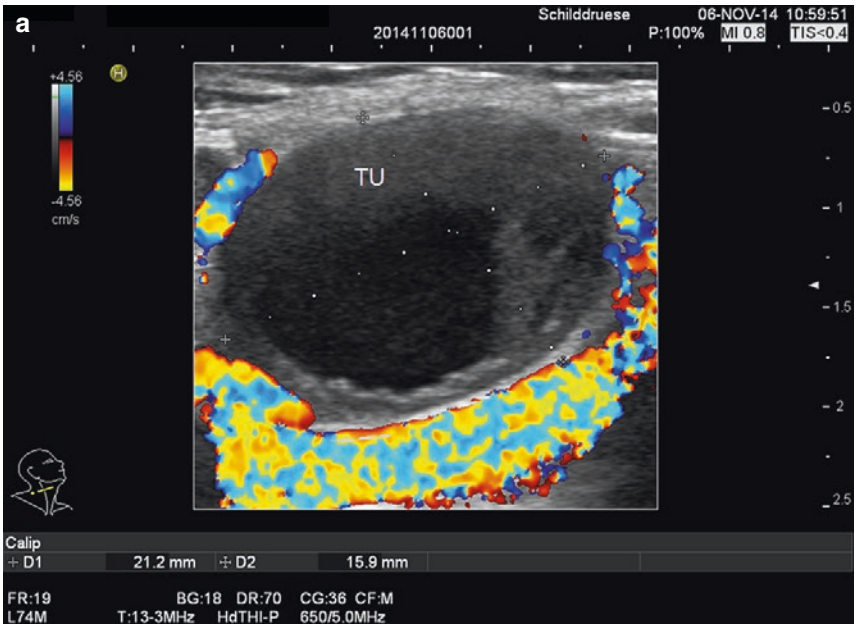

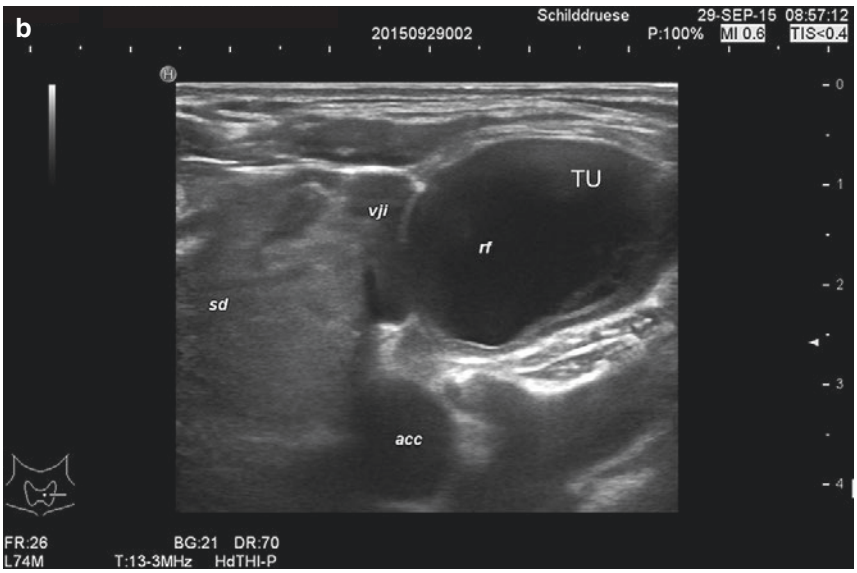

Fig. 6.35 Many tumors (TU) can imitate a branchial cyst. The differential diagnosis always includes a necrotic metastatic lymph node. (**a**): A metastasis of a cancer of unknown origin. (**b**): A metastatic node in a patient with endometrial cancer. CCA common carotid artery, SD thyroid gland, IJV internal jugular vein

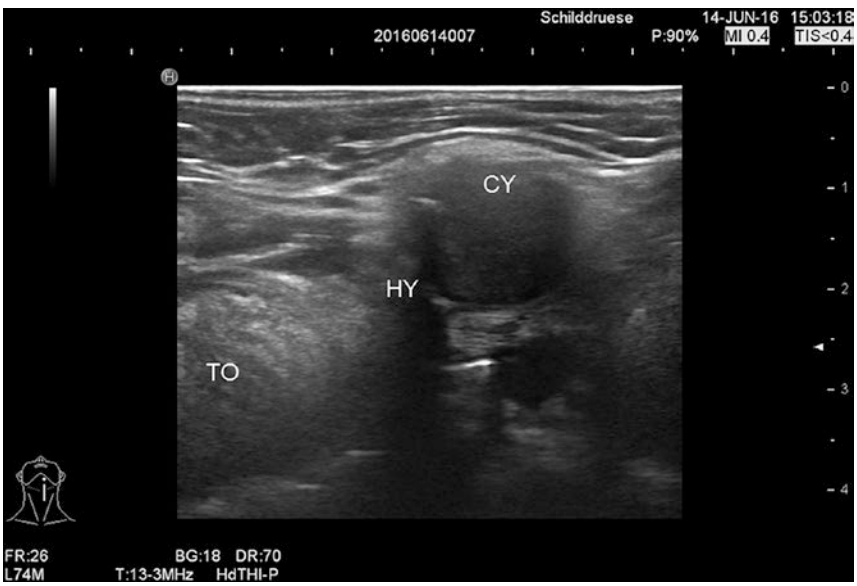

Fig. 6.36 A thyroglossal cyst (CY) always has contact with the hyoid (HY). The cyst has a poor echo as well as (more or less) relative acoustic enhancement of the echo. TO tongue

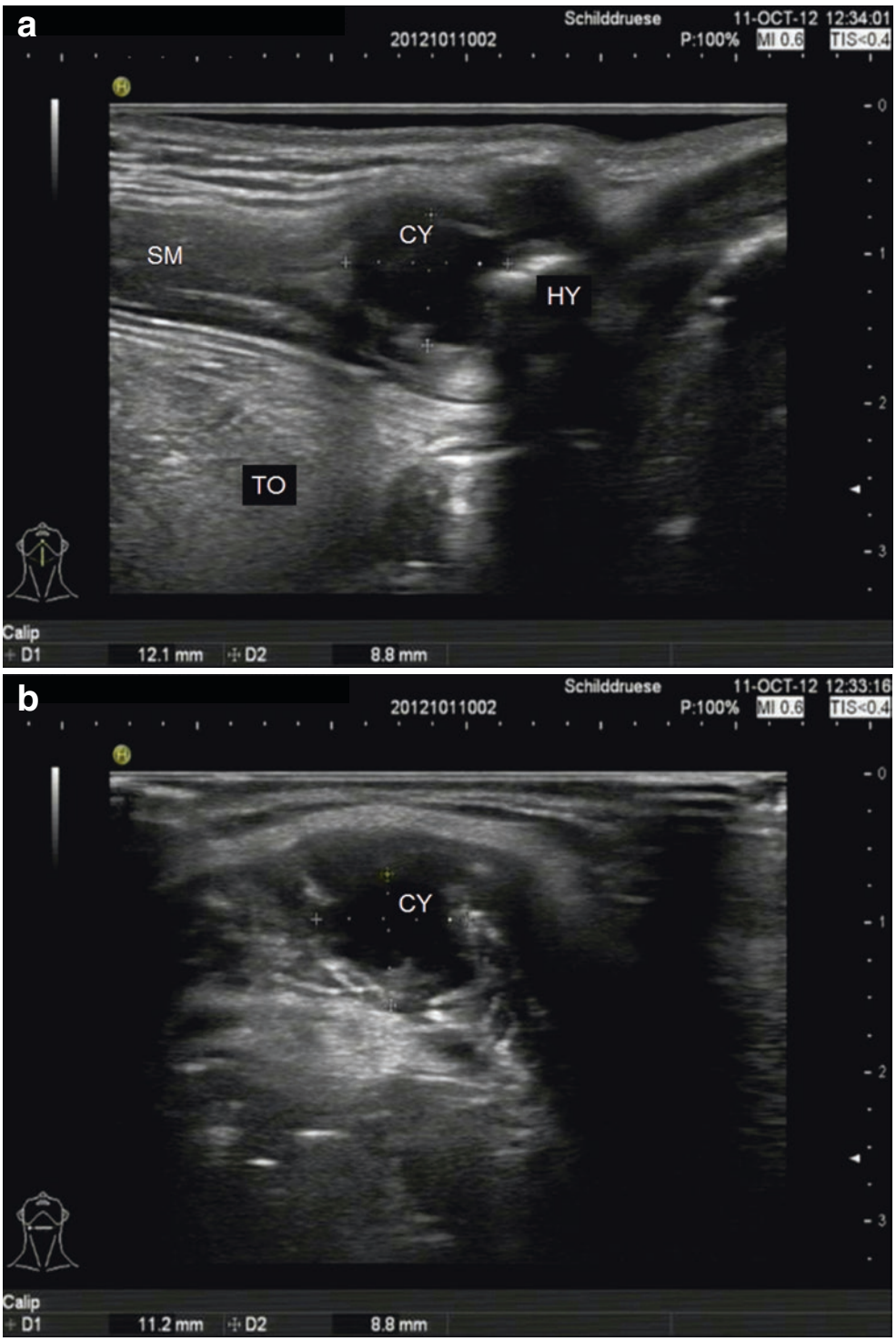

Fig. 6.37 This thyroglossal cyst (CY) is located above the hyoid (HY). The cyst has a poor echo, with some acoustic enhancement. (**a**): Sagittal section. (**b**): Transverse section. SM suprahyoidal muscles, TO tongue

Particular attention should be paid to the tongue base [2]. Often parts of the cyst or even the whole cyst is located in this deep central neck area, where it cannot be palpated (Fig. 6.42). The sonographic appearance of these deep thyroglossal cysts is the same as the appearance of superficial cysts (Video 6.6). These deep cysts are difficult to detect because they are commonly smaller than the thyroglossal cysts located directly under the skin (Fig. 6.43). But even such small and deeply located cysts can be seen with the use of ultrasound, and appropriate surgery can be planned.

Because the thyroglossal duct marks the descensus of the thyroid gland, thyroid tissue often can be found within the cyst [7]. Then the sonographic appearance of the supposed cyst is comparable to the pattern of thyroid gland; this is true

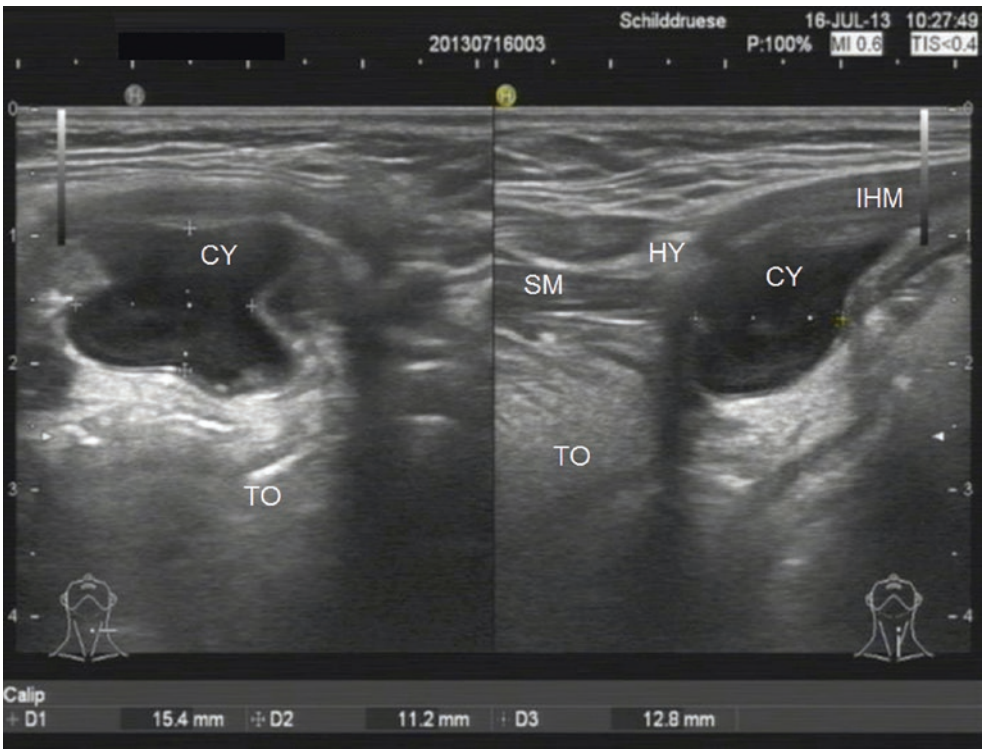

Fig. 6.38 This thyroglossal cyst (CY) with the shape of a butterfly is located paramedian under the infrahyoidal muscles (IHM). HY hyoid, SM suprahyoidal muscles, TO tongue

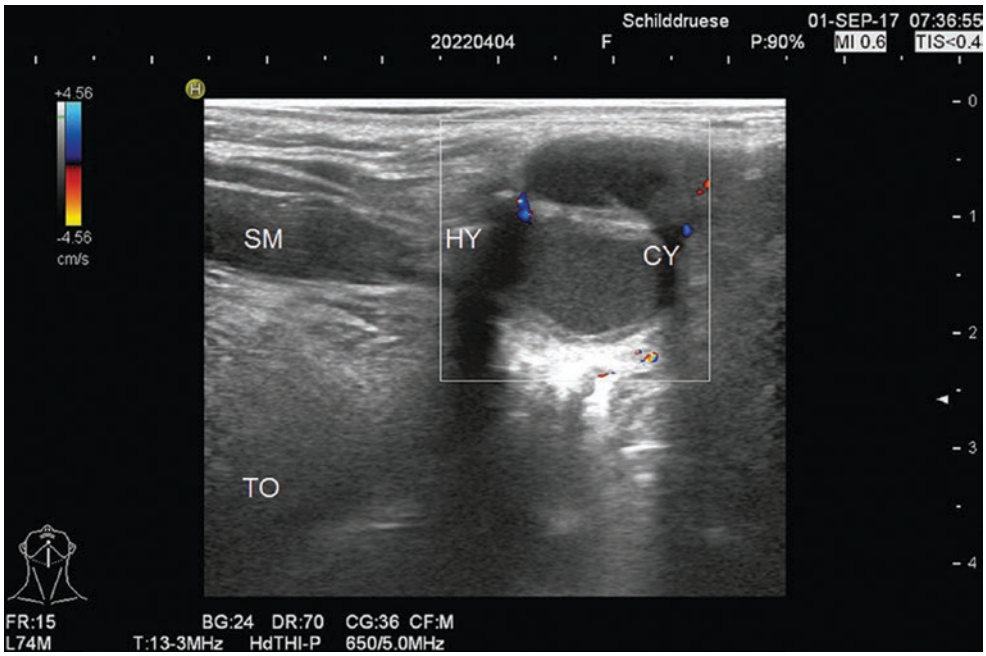

Fig. 6.39 A septated thyroglossal cyst (CY). HY hyoid, SM suprahyoidal muscles, TO tongue

for both B-scan and color-coded sonographic characteristics (Fig. 6.44). Similarly, sometimes thyroid tissue also can be detected in the tongue base area (Fig. 6.45).

If thyroid tissue is seen within a thyroglossal cyst, we must consider the possibility of malignant transformation, just as in the thyroid gland itself. Therefore, we must differentiate these nodules, similar to thyroid nodules, as explained in other chapters. For example, a spongiform nodule next to the hyoid probably indicates a benign process in the thyroglossal cyst (Fig. 6.46). But heterogeneity of the tissue within the thyroglossal cyst and additional microcalcification (Fig. 6.47) is highly suspect for thyroid cancer and needs further evaluation.

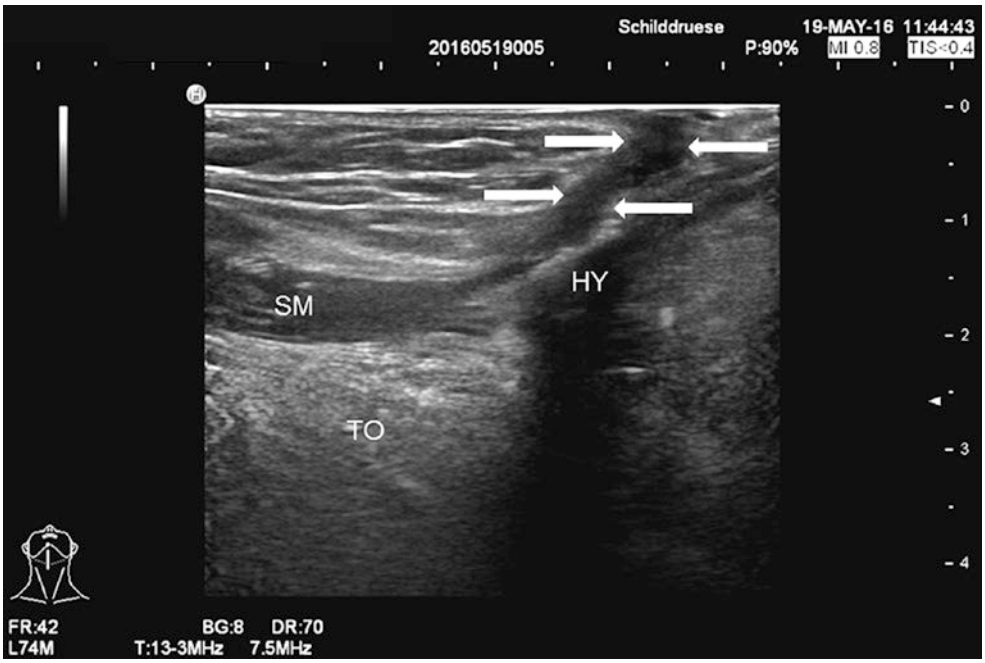

Fig. 6.40 A small, fistulating thyroglossal cyst (*between the arrows*) next to the hyoid (HY). SM suprahyoidal muscles, TO tongue

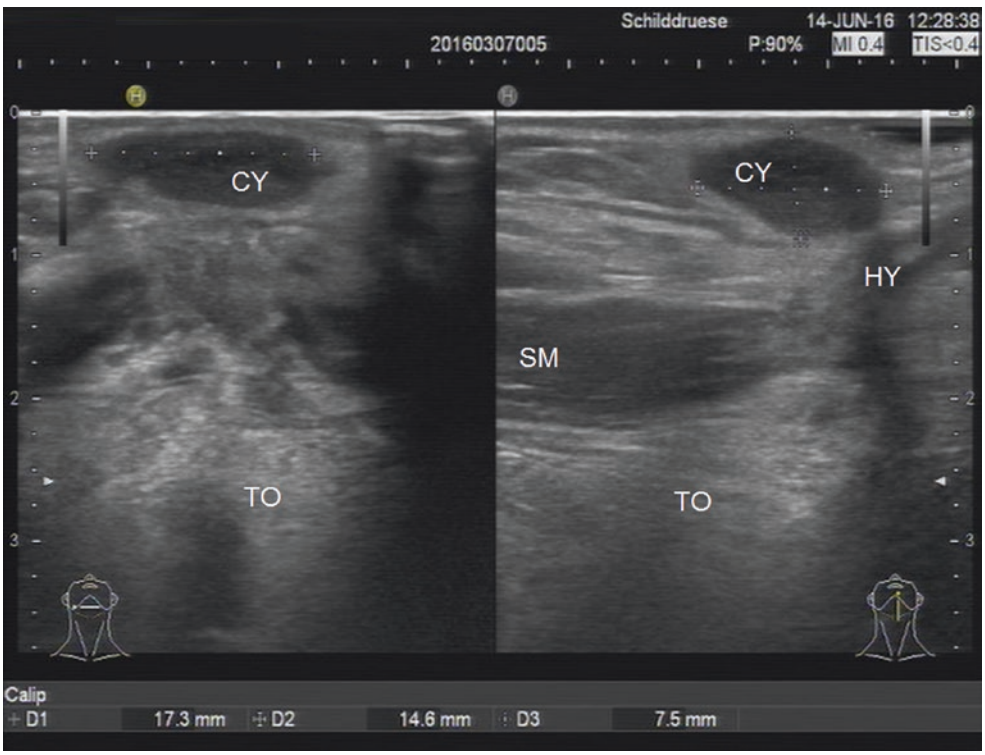

Fig. 6.41 Infected thyroglossal cyst (CY). The tissue is edematous and thickened. HY hyoid, SM suprahyoidal muscles, TO tongue

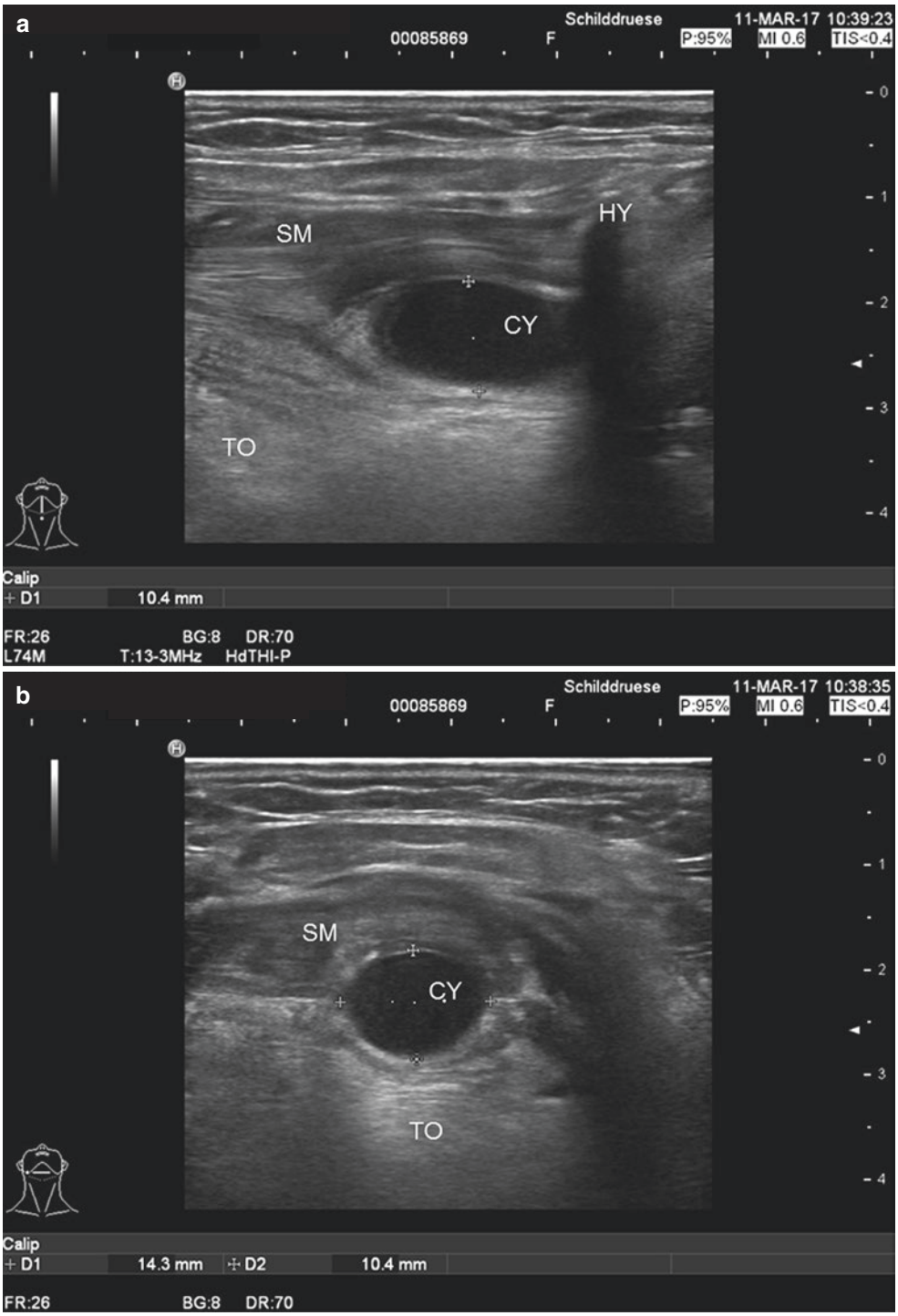

Fig. 6.42 Sagittal view (**a**) and transverse view (**b**) of an infected thyroglossal cyst (CY), which is only located proximal to the hyoid (HY) within the tongue base. SM suprahyoidal muscles, TO tongue

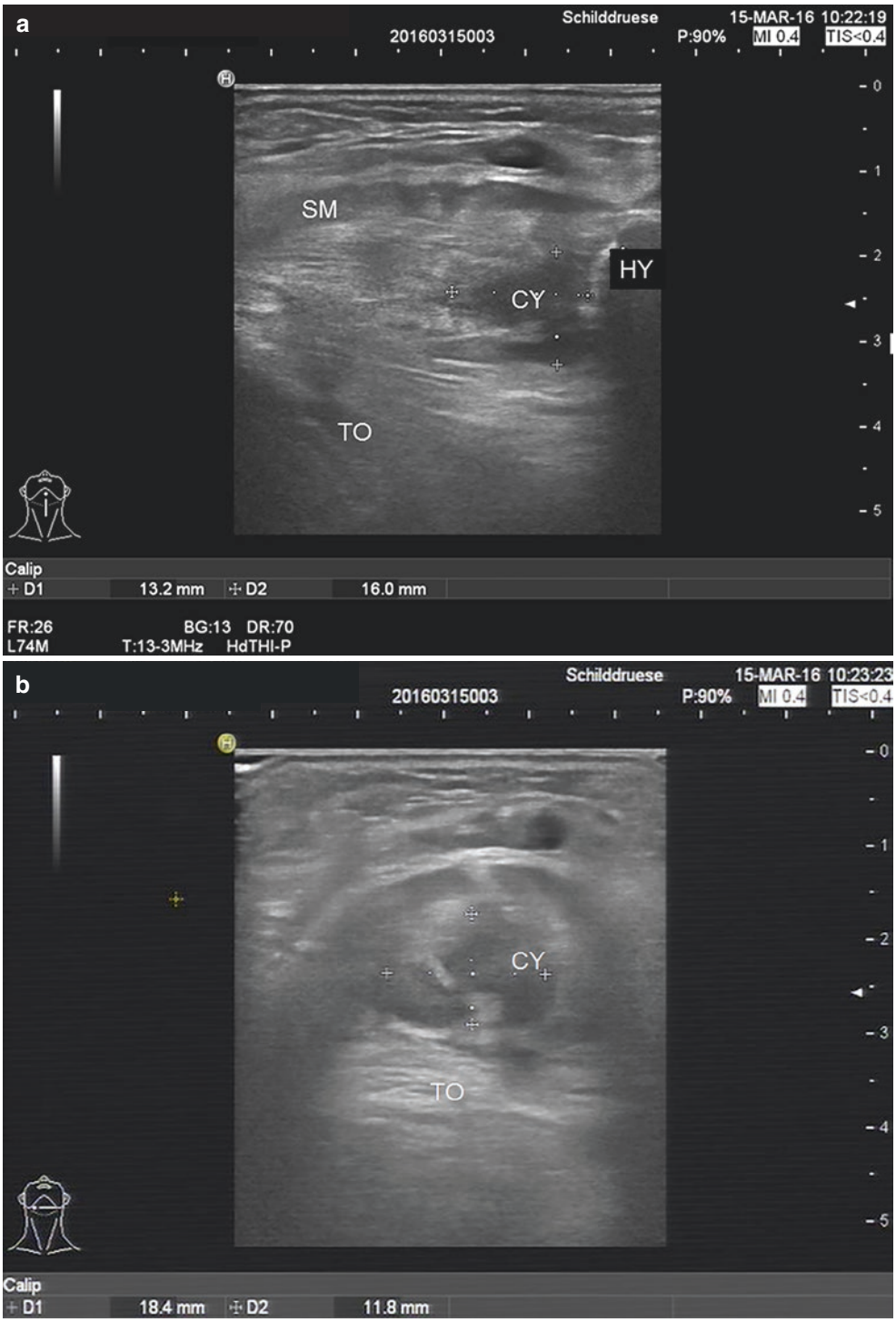

Fig. 6.43 Sagittal view (**a**) and transverse view (**b**) of an infected, irregularly shaped thyroglossal cyst (CY), located within the tongue base. After antibiotic therapy (**c**), the cyst was much smaller and was resected successfully. HY hyoid, SM suprahyoidal muscles, TO tongue

Fig. 6.43 (continued)

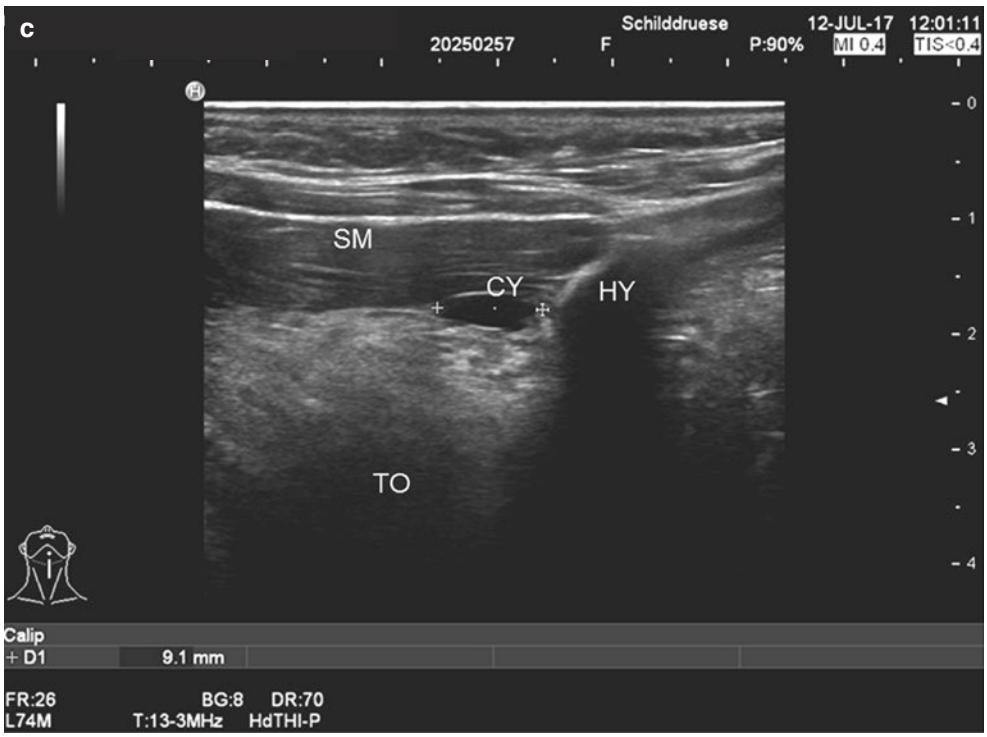

Fig. 6.44 Typically located thyroglossal cyst (CY) containing thyroid tissue. The echo within the cyst is homogenous and comparable to that of the healthy thyroid gland. In contrast to cysts filled with fluid, the detection of blood vessels indicates the presence of solid tissue. HY hyoid, SM suprahyoidal muscles, TO tongue

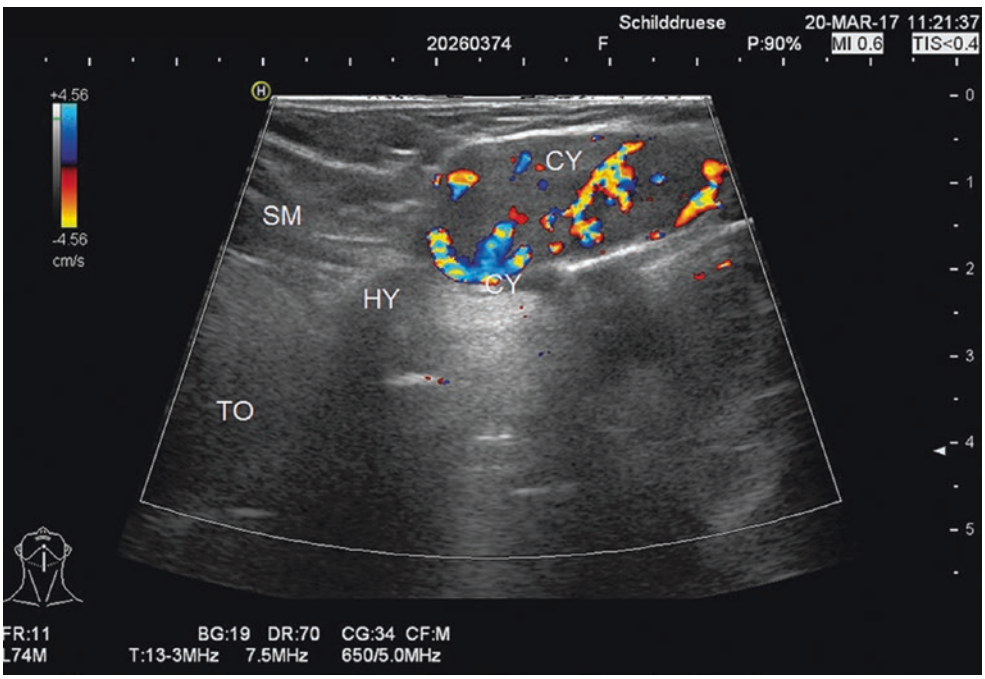

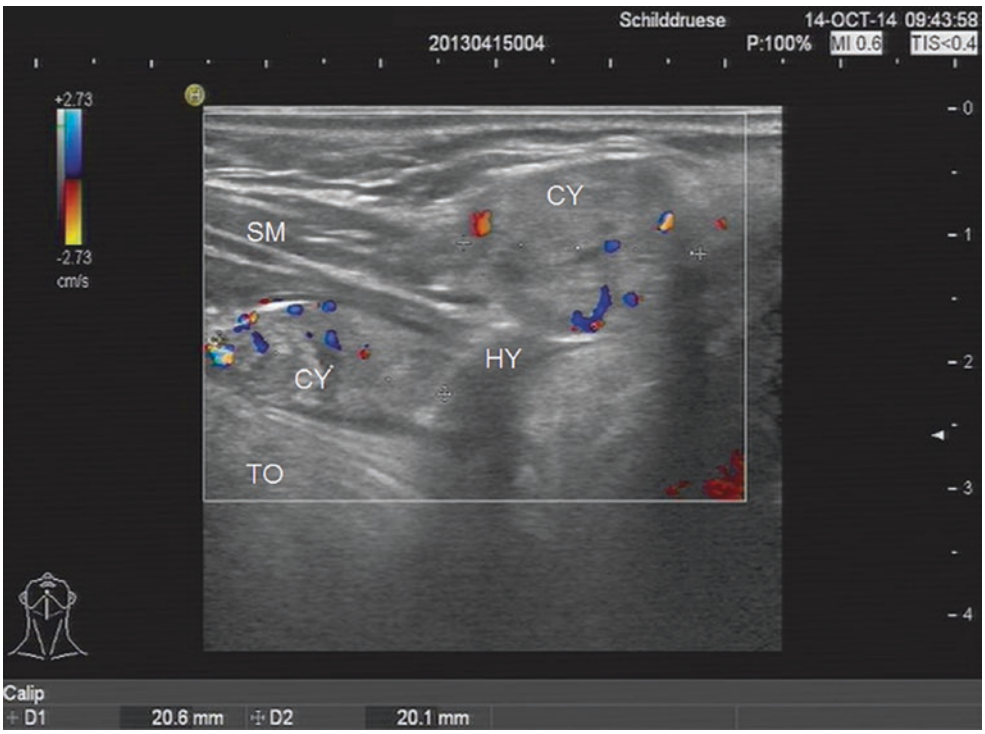

Fig. 6.45 Thyroglossal cyst (CY) distal and proximal to the hyoid (HY), containing thyroid tissue. SM suprahyoidal muscles, TO tongue

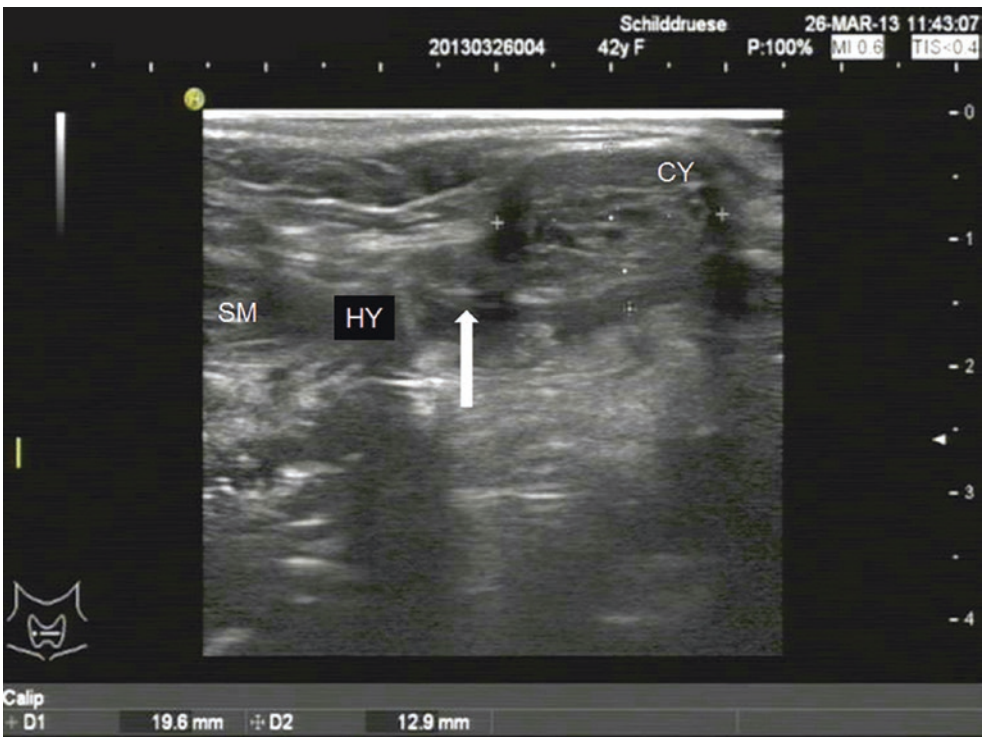

Fig. 6.46 Thyroglossal cyst (CY) in typical location with spongiform tissue inside, characteristic of benign thyroid tissue. Note the contact with the hyoid (*arrow*). SM suprahyoidal muscles

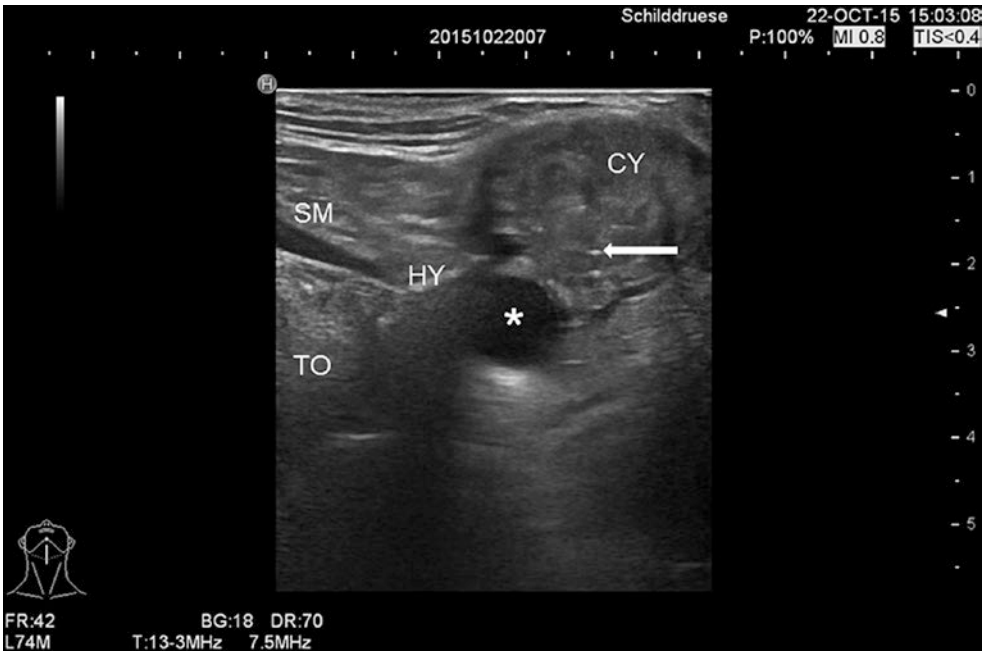

Fig. 6.47 Thyroid tissue in a thyroglossal cyst (CY). The tissue is heterogenous, with a necrotic area (*asterisk*) and microcalcifications (*arrow*). Histological examination revealed papillary thyroid cancer. HY hyoid, SM suprahyoidal muscles, TO tongue

6.5 Solid Tumors of the Neck

Solid tumors of the neck are due to various entities. Most of them are enlarged lymph nodes, and a detailed description of sonographic characteristics of lymph nodes can be found elsewhere in this book. Other, relatively rare tumors of the neck also can be identified correctly by ultrasound.

6.5.1 Carotid Body Tumor

Carotid body tumors can be detected by B-scan plus color-coded sonography with a sensitivity of nearly 90% [8]. The location of the tumor is typically in the area of the bifurcation, which results in a splaying of the internal and external carotid artery (Video 6.7). The tumor appears homogenous and hyperechoic (Fig. 6.48a) and can be easily misdiagnosed as an enlarged lymph node on the basis of its B-scan appearance. With the normal setting of the ultrasound unit, intravascular vessels cannot be seen in the carotid body tumor because of the slow blood flow in small tumor vessels. Therefore, the pulse repetition frequency has to be adjusted for low flow [2]. Then the characteristic hypervascularization of the tumor, which allows us to distinguish carotid body tumor from other tumors in this area, can be seen [9] (Fig 6.48b). Thus, ultrasound should be the first imaging method to detect or to exclude recurrent disease (Fig. 6.49). It is also appropriate for screening of family members of patients with a carotid body tumor, as a familial predisposition is described in 10–50% [9].

Color-coded ultrasound is especially useful in differentiating between a carotid body tumor and anatomic variations in this region (Fig. 6.50). Inflamed lymph nodes also may resemble small carotid body tumors, but these nodes commonly are lateral to the bifurcation, not between both carotid arteries (Fig. 6.51).

6.5.2 Neurinoma

Neurinoma or schwannoma of the neck can originate from several nerves. Similarly to carotid body tumors, neurinoma of the vagal nerve can splay the bifurcation (Fig. 6.52) [2]. Sometimes a connection to the nerve can be identified. The tumor itself has a characteristic heterogenous pattern and a thicker capsule than carotid body tumors (Video 6.8). But the most impressive difference from carotid body tumors is the rarity of blood vessels in the neurinoma (Fig. 6.53).

6.5.3 Rare Tumors

In clinical routine, the head and neck surgeon is confronted with many other tumor entities, but because they are rare, the surgeon may have little experience with ultrasound imaging of such tumors, and the correct diagnosis often depends on other imaging modalities. Nevertheless, ultrasound should always be the first imaging method used to get a first impression of such tumors, which is the requirement for a differentiated indication for further imaging.

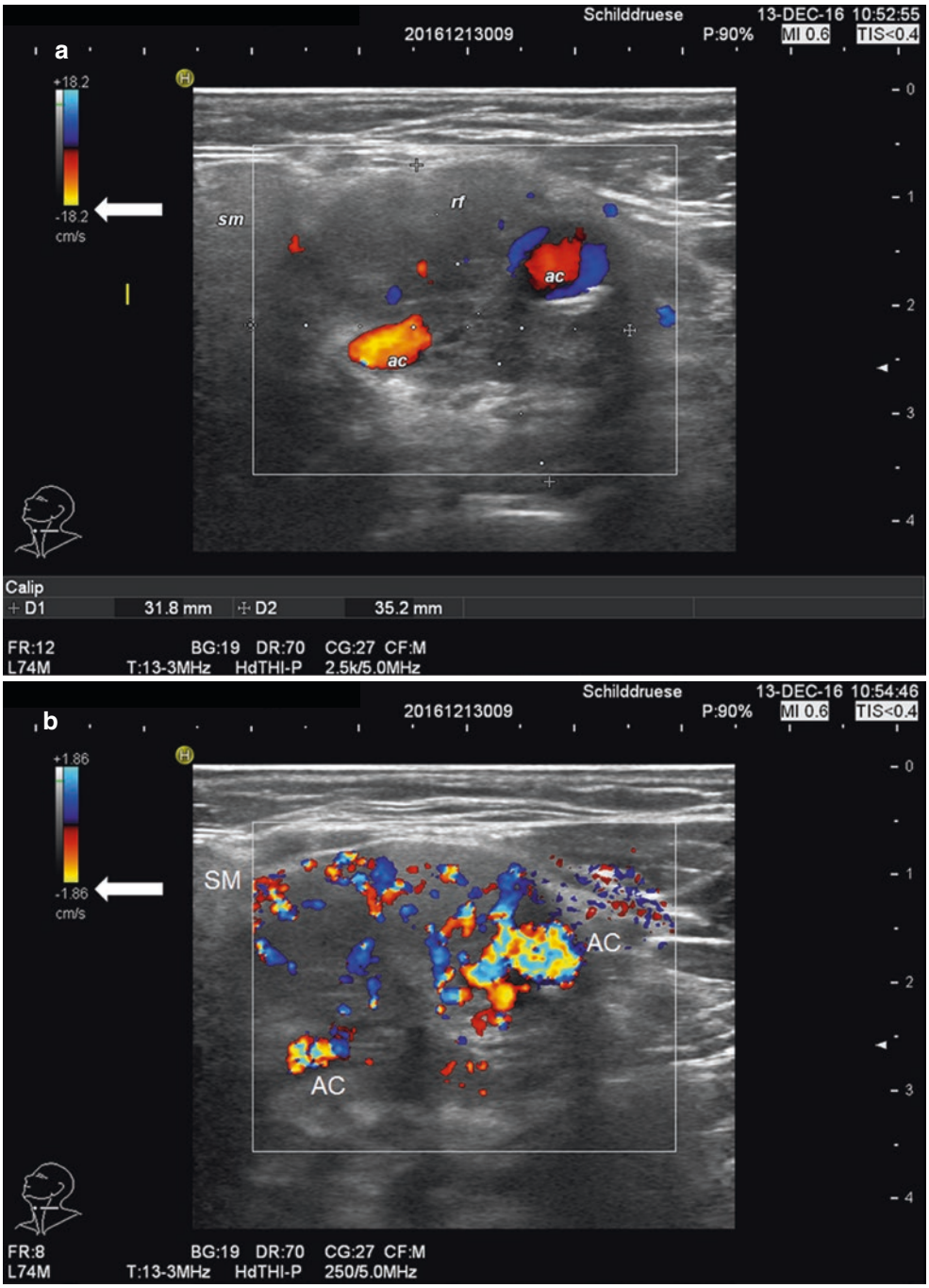

Fig. 6.48 Large carotid body tumor (RF) of the left neck. (**a**) High pulse repetition frequency (PRF), −18.2 cm/s (*arrow*). (**b**) Low PRF, −1.86 cm/s (*arrow*). CA carotid arteries, SM submandibular gland

Metastatic lymph nodes (Fig. 6.54) must be suspected in patients suffering from any malignant disease.

Ectopic thyroid tissue [2] can occur anywhere in the neck and can easily be diagnosed with ultrasound (Fig. 6.55a), even if it is very small (Fig. 6.55b). Other imaging techniques are unnecessary in these patients. Especially if criteria of malignancy can be seen, CT scans with iodized contrast agents are obsolete. Furthermore, ectopic thyroid tissue, which should always be removed, should not be confused with a physiological pyramidal process (Fig. 6.55c).

Other tumors can occur in the laryngeal skeleton (Fig. 6.56) or even next to the spinal column or the skull base. Tumors in the skull base area can be difficult to detect by ultrasound because they are deeply located. If there is suspicion of tumor in the skull base area, we prefer the use of a 5 MHz sector array, which normally is used in abdominal

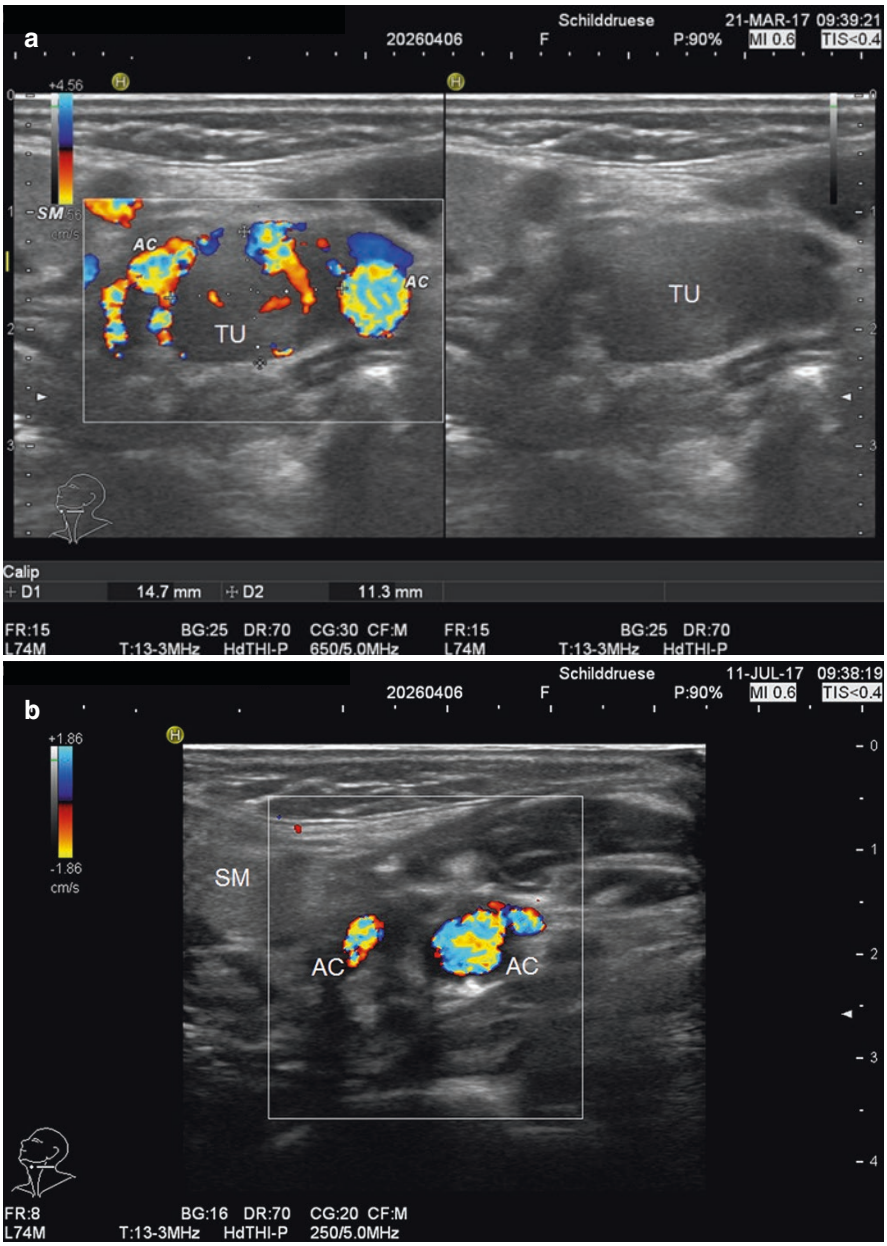

Fig. 6.49 Small carotid body tumor (TU) of the left neck, typically located between both carotid arteries (CA). (**a**) Color-coded sonography (*left*) and B-scan (*right*) showing the preoperative situation. (**b**) Postoperative situation. SM submandibular gland

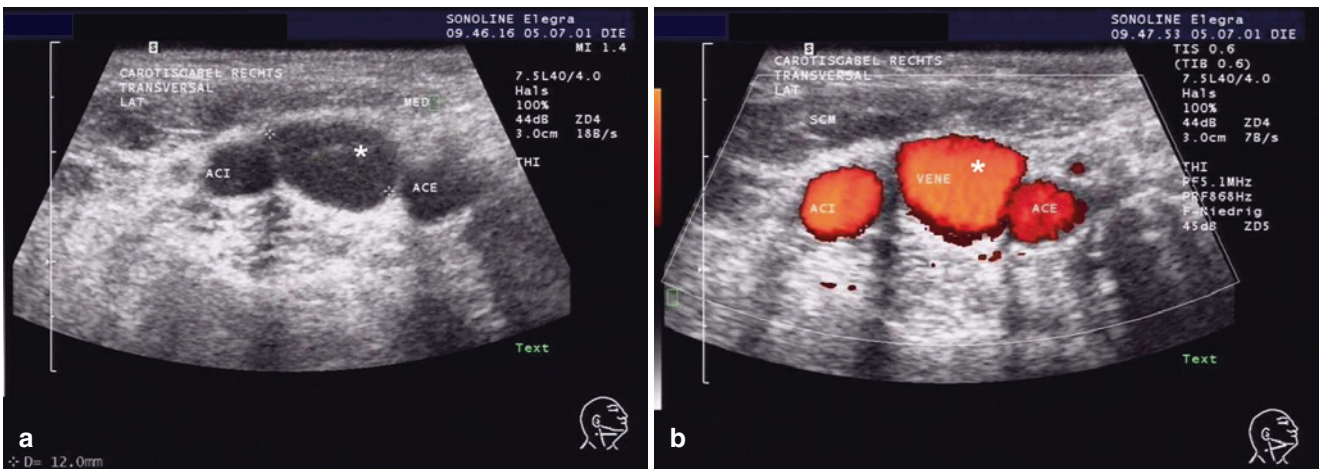

Fig. 6.50 Atypical course of the internal jugular vein (*asterisk*) between the external carotid artery (ACE) and the internal carotid artery (ACI). (**a**) B-scan. (**b**) Duplex scan, power mode

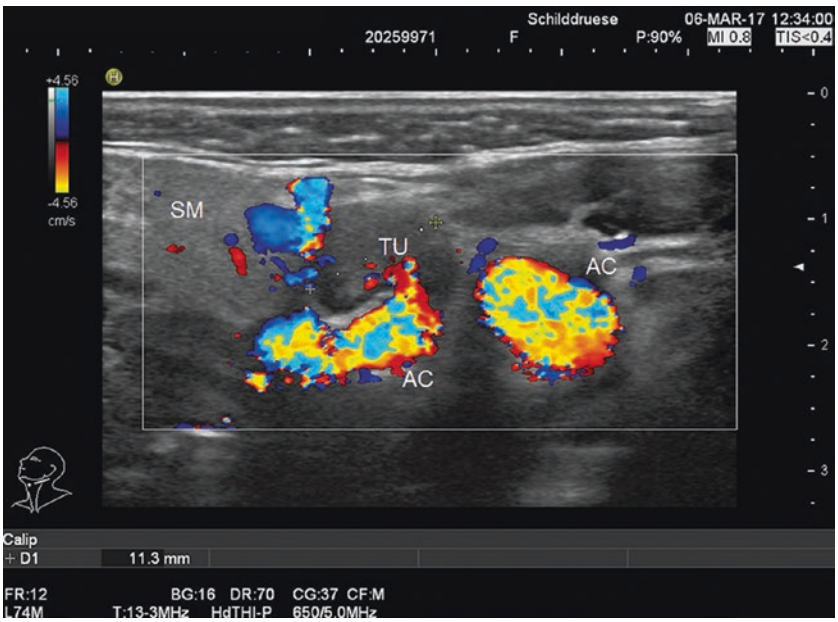

Fig. 6.51 Small tumor (TU) *next to* the bifurcation, not *between* both carotid arteries (CA). This is probably a lymph node. SM submandibular gland

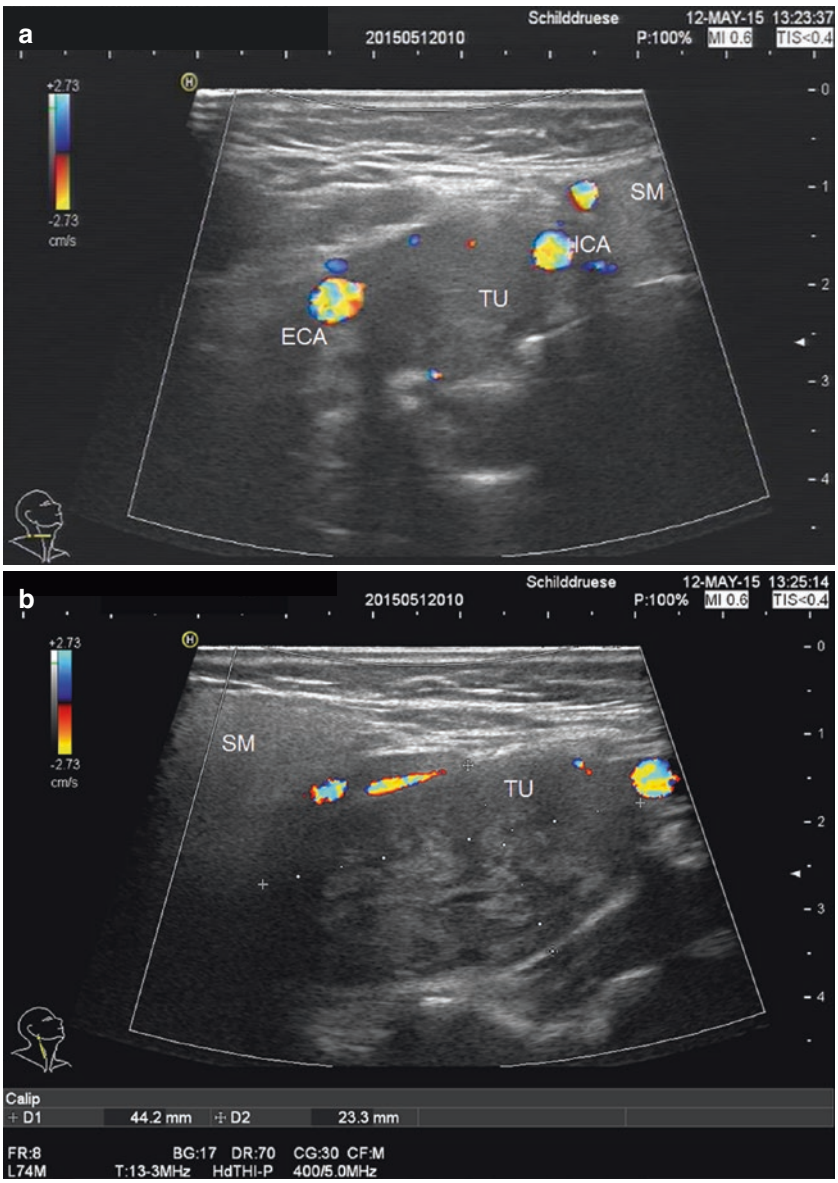

Fig. 6.52 (**a**) Vagal neurinoma (TU) spreading the right bifurcation. Even if a low pulse repetition frequency is used, only rare vascularity can be detected. (**b**) B-scan characteristics of the neurinoma. ECA external carotid artery, ICA internal carotid artery, SM submandibular gland

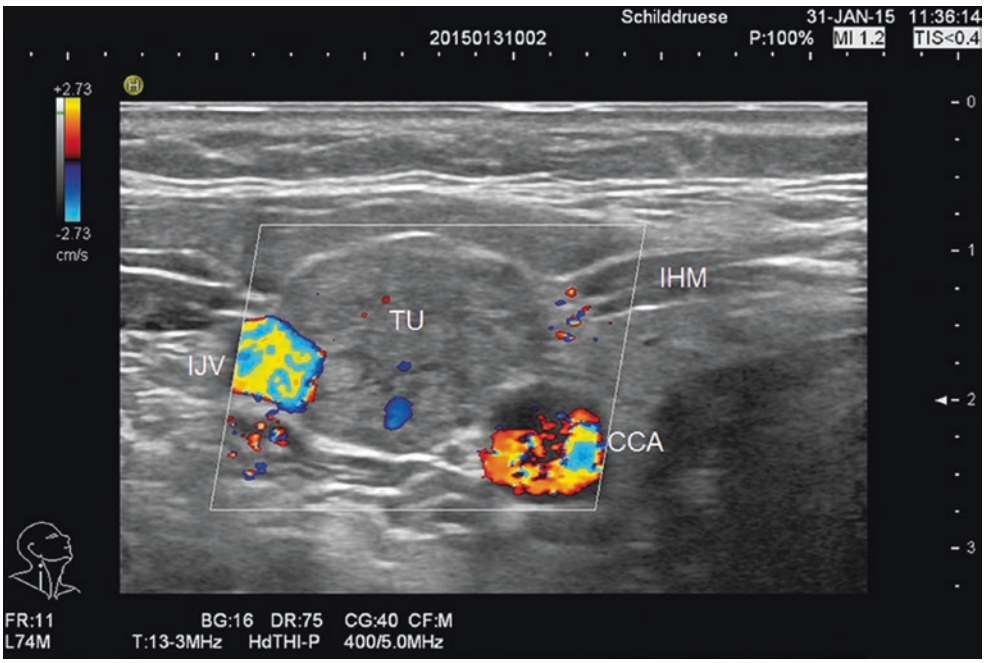

Fig. 6.53 Vagal neurinoma (TU) of the right neck, level IV. CCA common carotid artery, IHM infrahyoidal muscles, IJV internal jugular vein

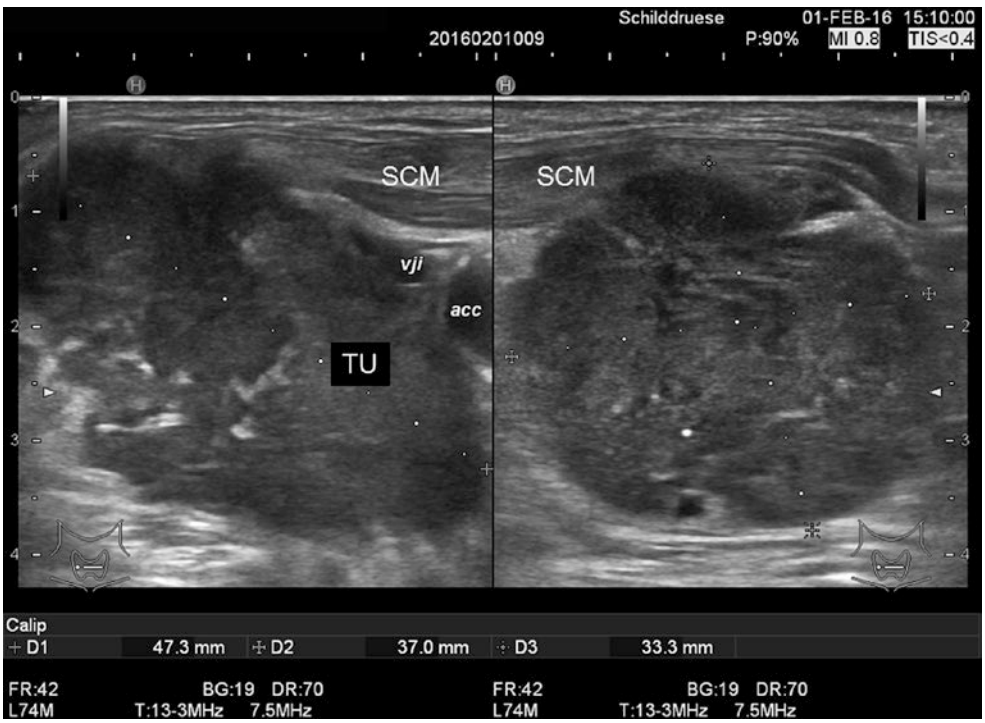

Fig. 6.54 Large metastasis (TU) of a squamous cell carcinoma next to the internal jugular vein (vji) and the common carotid artery (acc). SCM sternocleidomastoid muscle

sonography. Then changes in this area such as skull base metastasis, rare tumors like fibrous tumors (Fig. 6.57), or even an aneurysm of the internal carotid artery (Fig. 6.58) can be detected with ultrasound. Furthermore, jugular vein thrombosis as a cause of neck swelling can be diagnosed very quickly by ultrasound (Video 6.9). All of these tumors appear as hypoechoic lesions.

Even if other imaging methods are needed for complete detection of the tumor extension, ultrasound can give us important initial information about the origin of these tumors or the existence of signs of malignancy (Figs. 6.59, 6.60, 6.61, and 6.62). Therefore, ultrasound should routinely be a part of the clinical examination of patients suffering from swelling in the head and neck region.

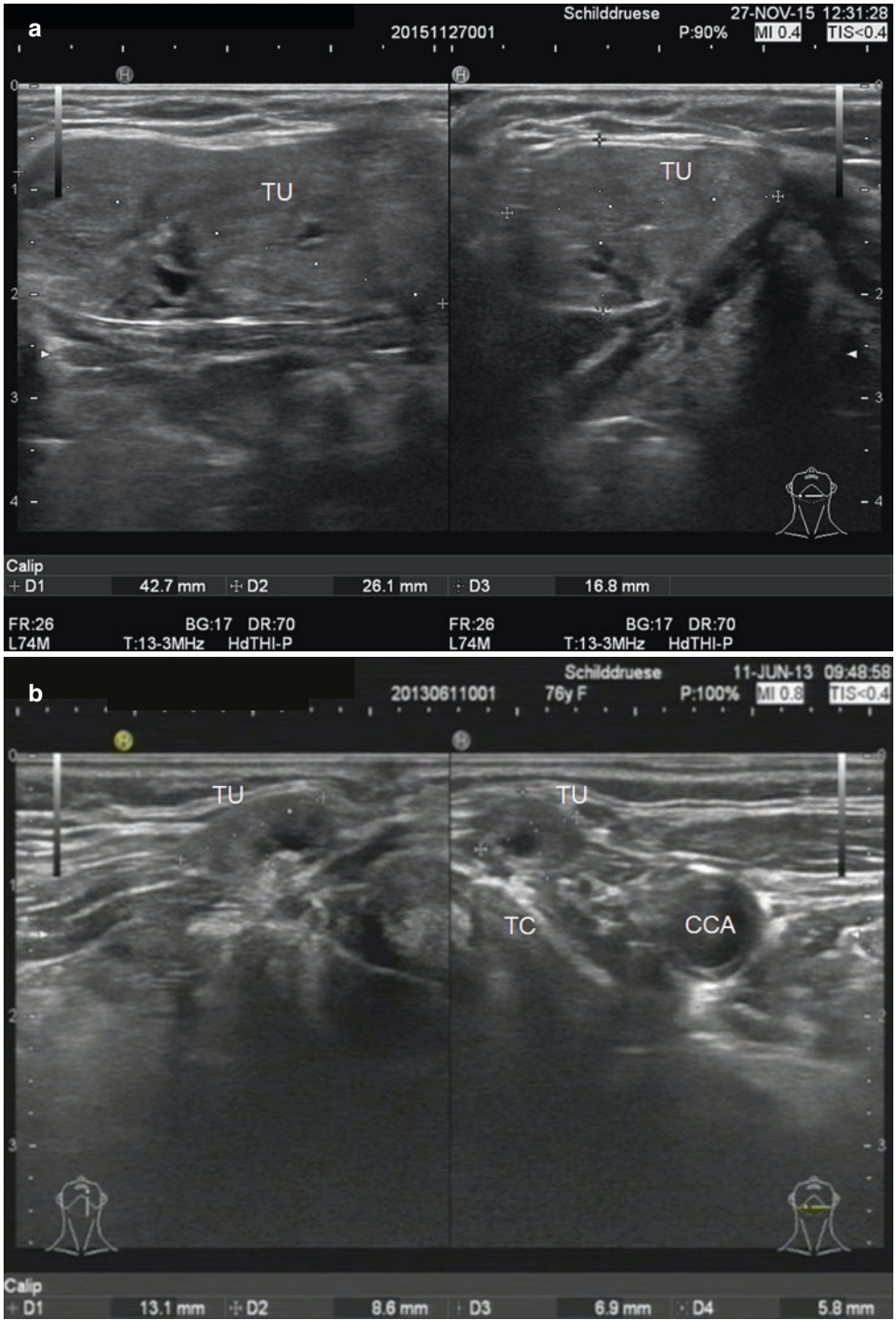

Fig. 6.55 Ectopic thyroid tissue (TU) in the floor of the mouth (**a**) and lateral to the thyroid cartilage (TC) (**b**). Sometimes thyroid tissue in the neck is due to a large pyramidal process (**c**). CCA common carotid artery, HY hyoid

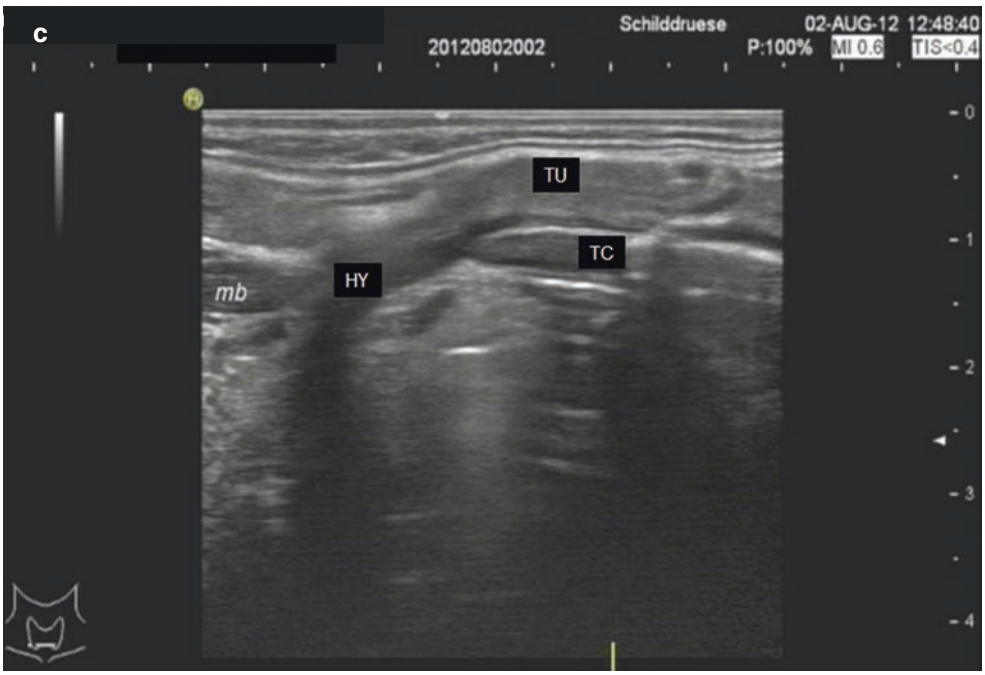

Fig. 6.55 (continued)

Fig. 6.56 Cystic lesion (*arrow*) within the thyroid cartilage (TC). HY hyoid, IHM infrahyoidal muscles. *Inset* shows the corresponding CT scan

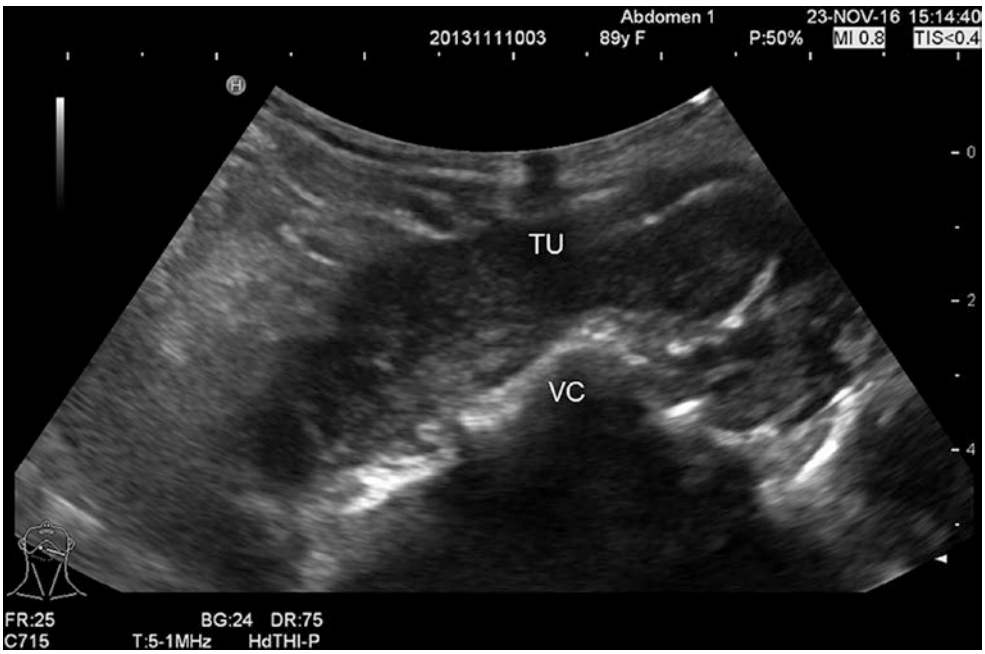

Fig. 6.57 A rare case of a solid fibrous tumor (TU) of the skull base next to the vertebral column (VC)

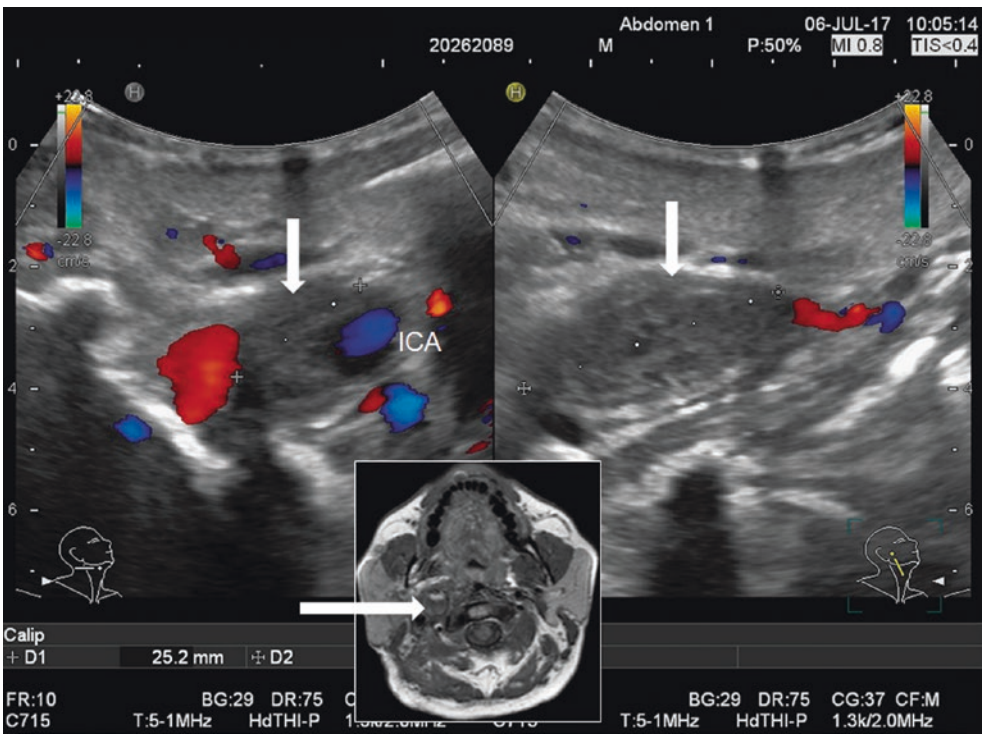

Fig. 6.58 Swelling of the right neck caused by a thrombosed aneurysm (*arrows*) of the internal carotid artery (ICA). Tumors of the skull base can be detected more easily if an abdominal array is used. *Inset* shows CT scan of the aneurysm (from [10])

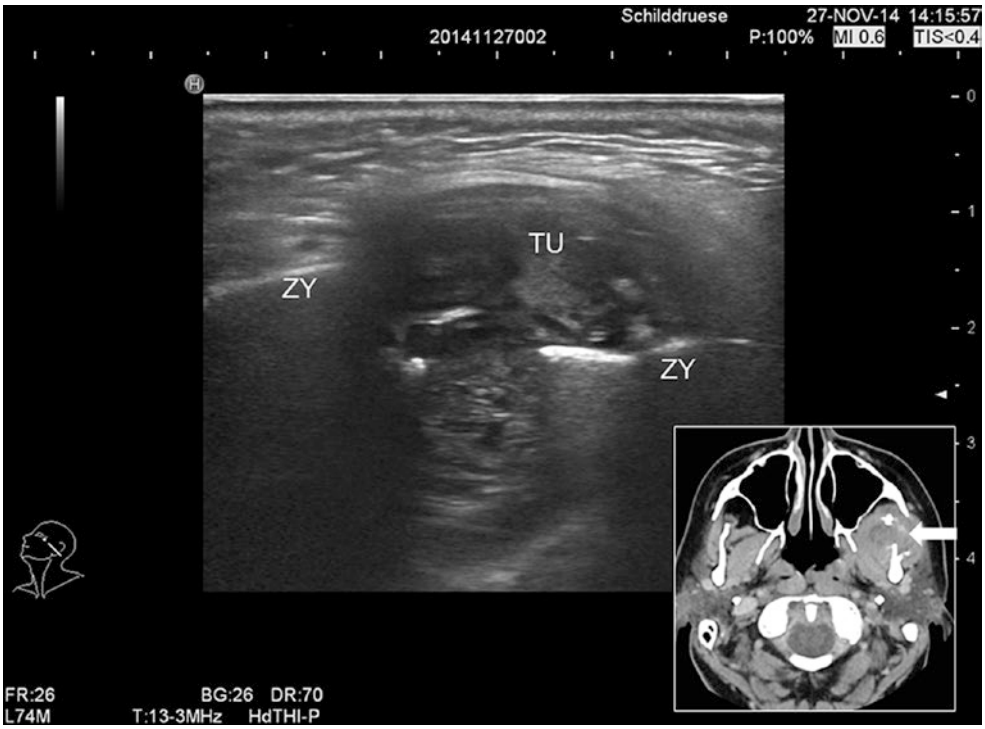

Fig. 6.59 Intraosseous tumor (TU) destroying the zygoma (ZY). Histological examination revealed a Ewing sarcoma. *Inset* shows CT scan of the zygoma

Fig. 6.60 Metastasis (TU) of a squamous cell carcinoma infiltrating the clavicle (CL)

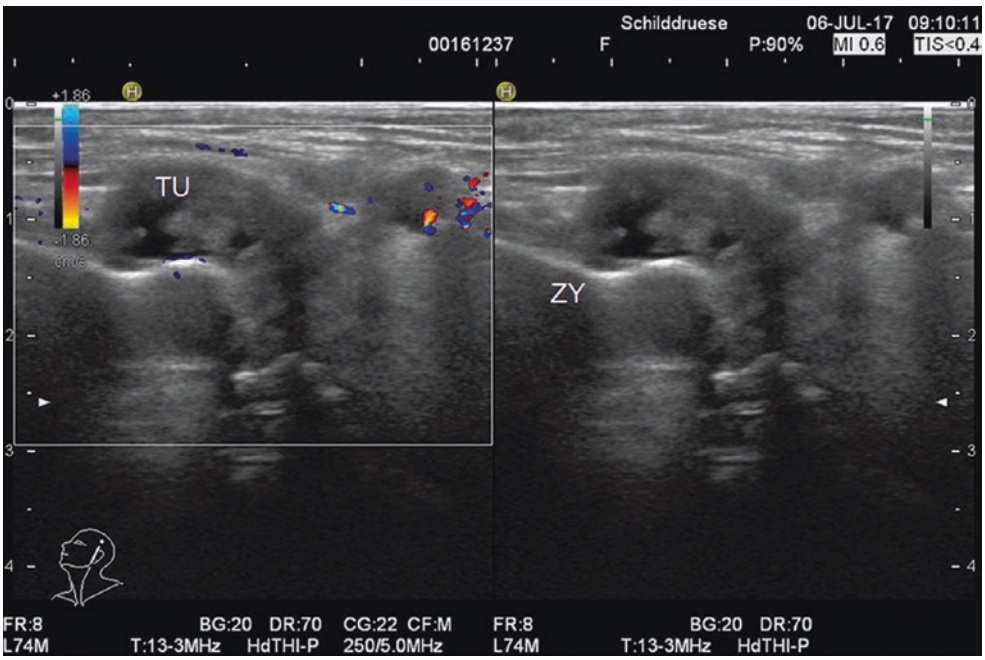

Fig. 6.61 Cancer (TU) of the external auditory canal. Tumor growth can also be detected preauricular next to the zygoma (ZY)

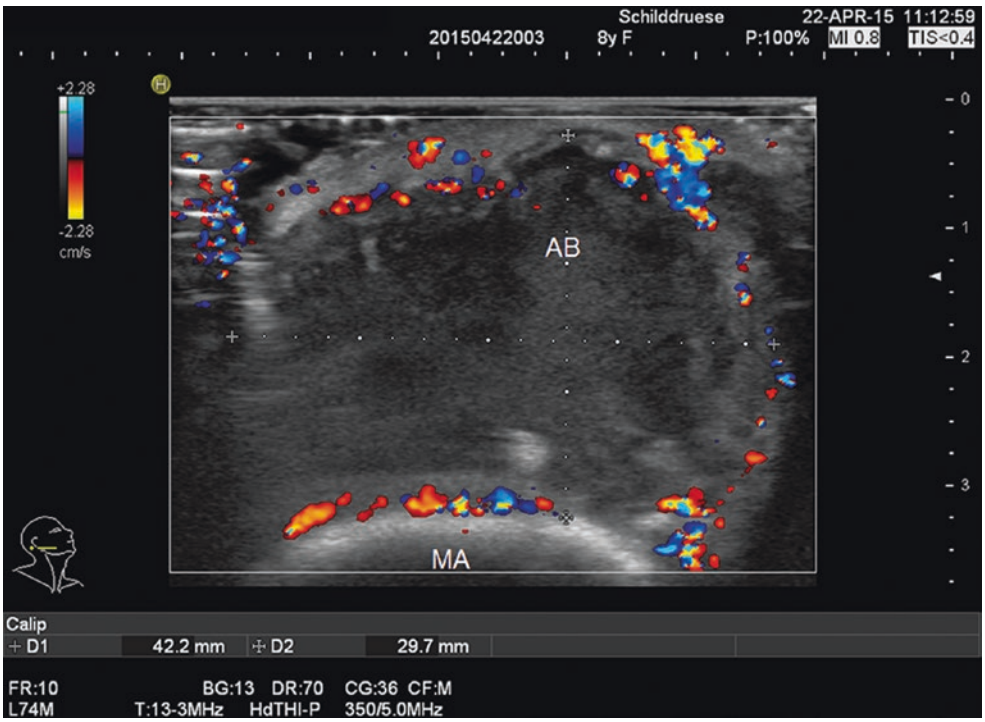

Fig. 6.62 Mastoiditis with a subperiosteal abscess (AB). MA mastoid

6.6 Posttraumatic Changes

6.6.1 Hematoma and Seroma

Most posttraumatic changes involve fractures and hematoma. Fractures such as those of the nose or the mandible are described elsewhere in this book. A hematoma can commonly be detected as a capsulated process without vascularization. If the hematoma is not clotted, it appears nearly echo-free with an acoustic enhancement (Fig. 6.63). If the hematoma is clotted, it appears hypoechoic but commonly not echo-free (Fig. 6.64). Extended hematomas can be detected easily, but the detection of small hematomas requires much more experience (Fig. 6.65).

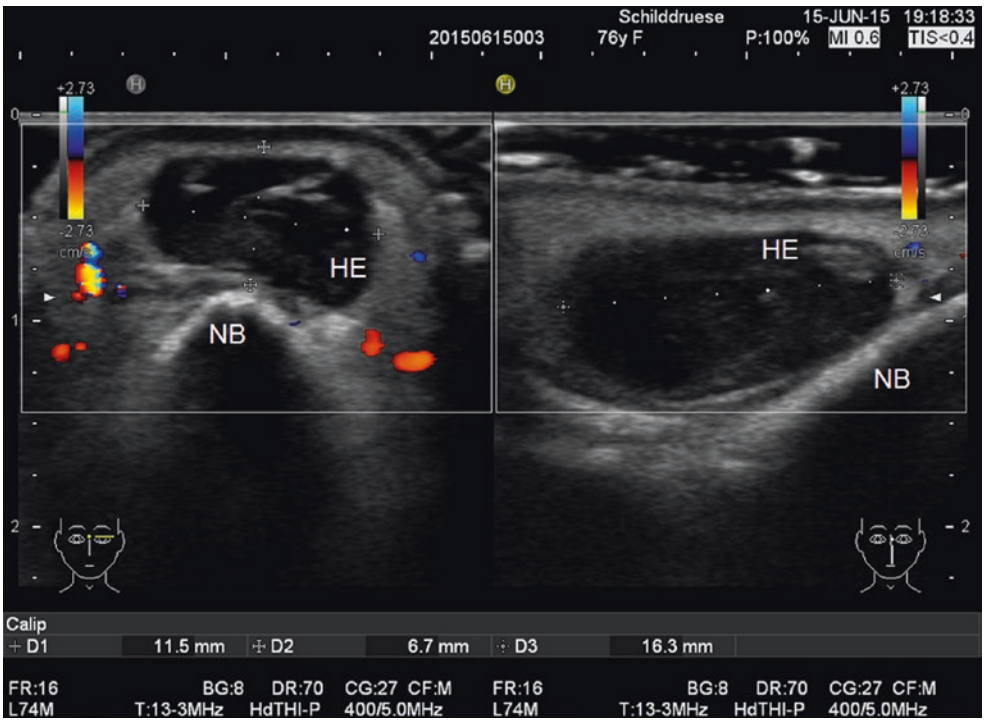

Fig. 6.63 Hematoma (HE) after nasal trauma, without clotting. NB nasal bone

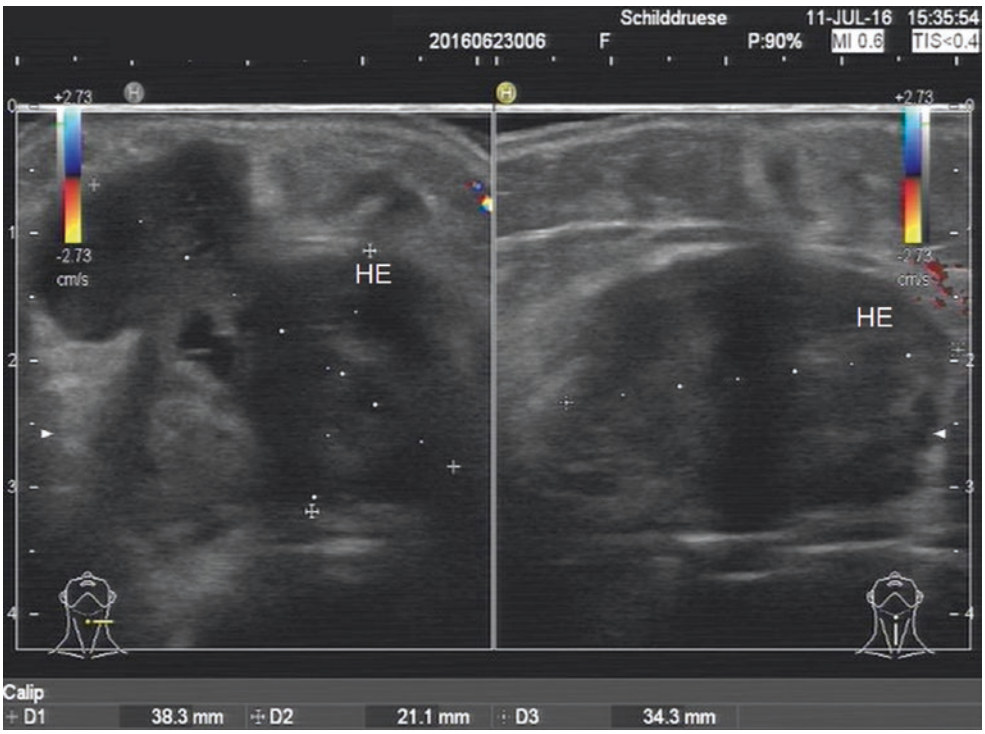

Fig. 6.64 Spontaneous, partially clotted hematoma (HE) of the neck after massive intake of anticoagulants

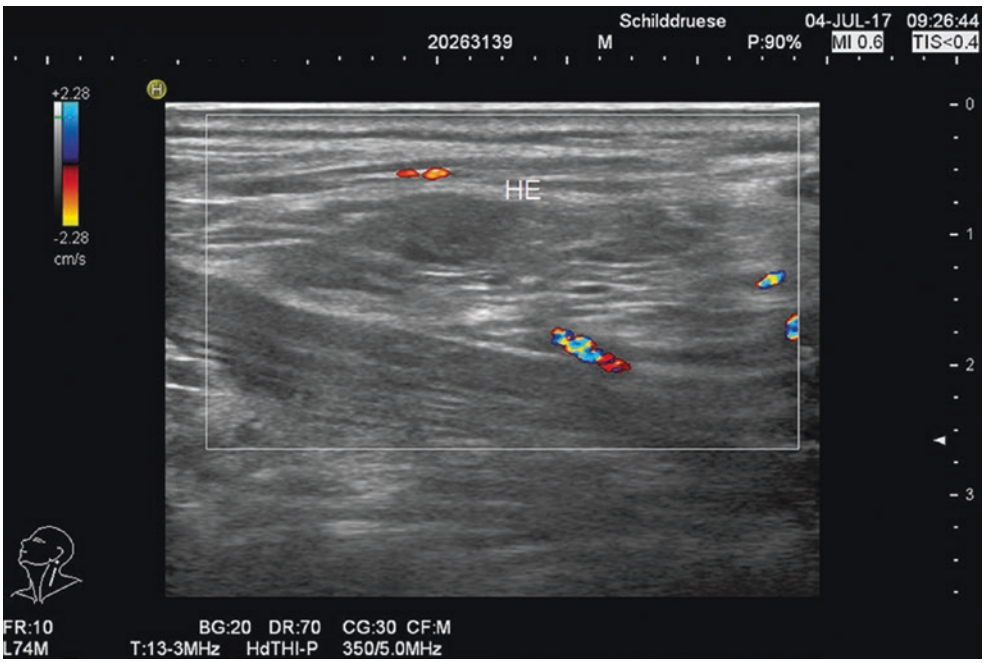

Fig. 6.65 Residual hematoma (HE) of the neck caused by a seat belt, after a car accident

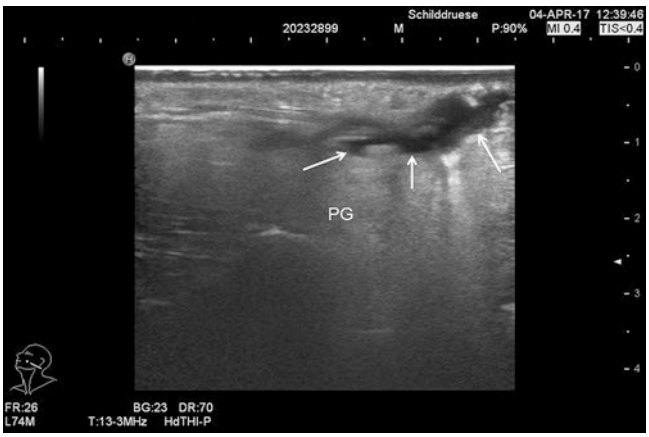

Fig. 6.66 Small seroma (*arrows*) after neck surgery. PG parotid gland

Neck seroma typically appears as a postoperative complication (Video 6.10). Usually it exposes itself as a hypoechoic structure (Fig. 6.66). In rare cases it can be hyperechoic (Fig. 6.67).

6.6.2 Foreign Bodies

Foreign bodies like a drain or a catheter (*see* Video 6.9) can be detected with ultrasound. For example, they may appear as small, hyperechoic structures with acoustic shadow (Fig. 6.68). The detection of foreign bodies such as bullets or swabs has been described, but we have little experience with such foreign bodies.

6.7 Sonographic Changes After Surgery or Radiotherapy

After surgery, the anatomy of the neck may differ from the normal situation. Therefore, the examiner is well advised to know which surgical procedures were performed prior to the ultrasound examination to avoid a false diagnosis. For example, after neck dissection, typical landmarks can be absent (Fig. 6.69), such as muscles, blood vessels, or salivary glands. After laryngectomy, the neopharynx (Video 6.11) typically can be seen between the large vessels of the neck (Fig. 6.70). In case of uncertainty, the neopharynx can be detected while swallowing [2]. Furthermore, after radiotherapy of the neck, the whole neck tissue is thickened owing to lymphedema (Fig. 6.71) (Video 6.12). In this case, the whole picture appears more hyperechoic because of the tissue edema.

The examination of the former tumor region is difficult. For example, after reconstruction procedures with a forearm flap, as shown in Fig. 6.72, it is possible to distinguish between the flap and the surrounding tissue, because the flap is characterized by a typical muscular echo. But the early detection of recurrent cancer requires a very experienced examiner, and one is well advised to perform other imaging techniques as well, such as CT or MRI scans, during follow-up or if other rare postoperative changes are seen (Fig. 6.73).

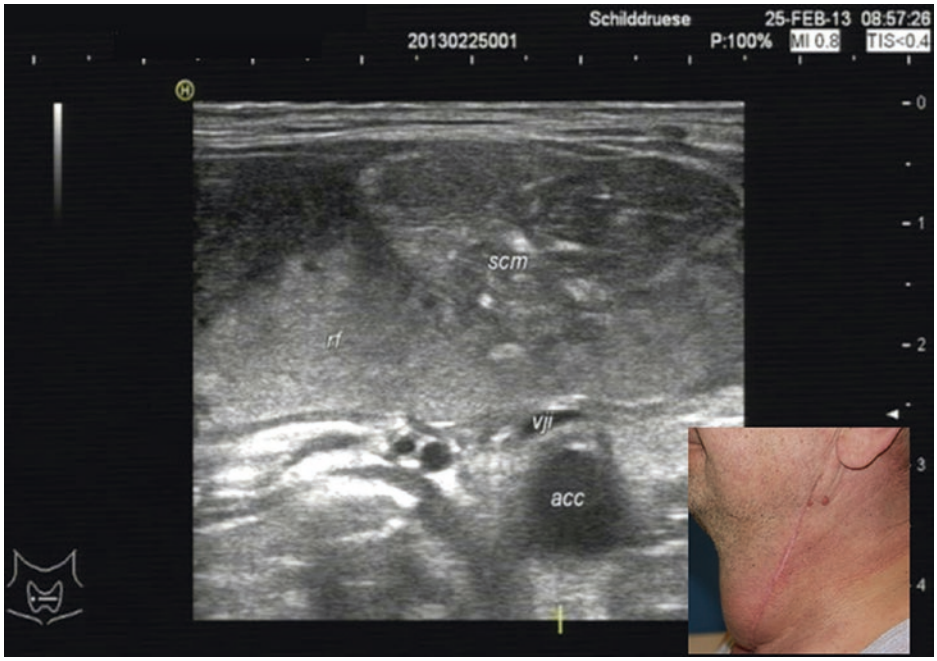

Fig. 6.67 Large seroma of the neck (RF) around the sternocleidomastoid muscle (SCM) after neck dissection and radiotherapy. Note the strong relative enhancement of the echo. CCA common carotid artery, IJV internal jugular vein

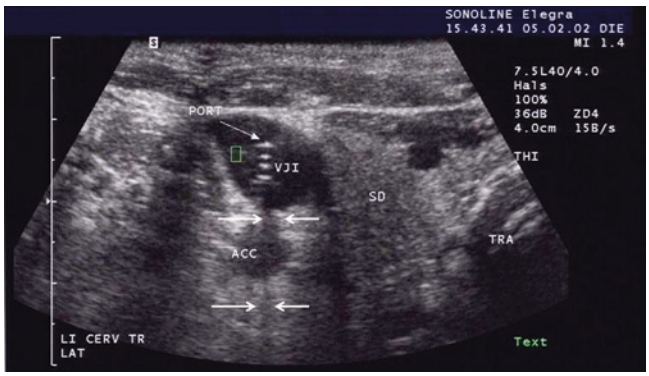

Fig. 6.68 Internal jugular vein (VJI) catheter (PORT). Note the reverberation artifacts caused by the foreign body and the acoustic shadow (*between arrows*); ACC common carotid artery, SD thyroid gland, TRA trachea

Fig. 6.69 Floor of the mouth after neck dissection including removal of the anterior portion of the left digastric muscle. DIG right digastric muscle

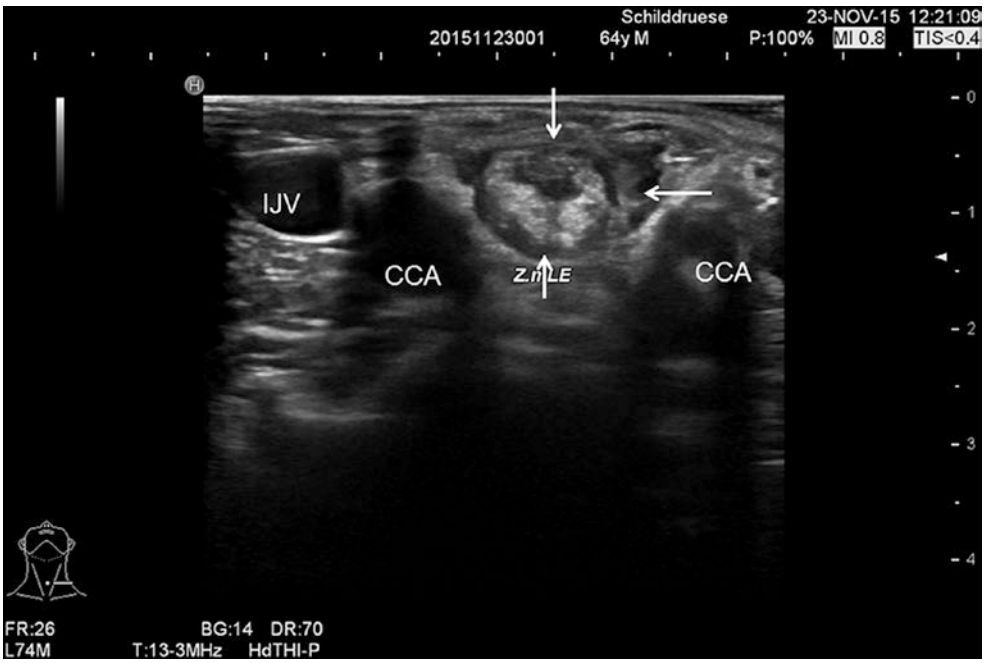

Fig. 6.70 Neopharynx (*between arrows*) after laryngectomy. CCA common carotid artery, IJV internal jugular vein

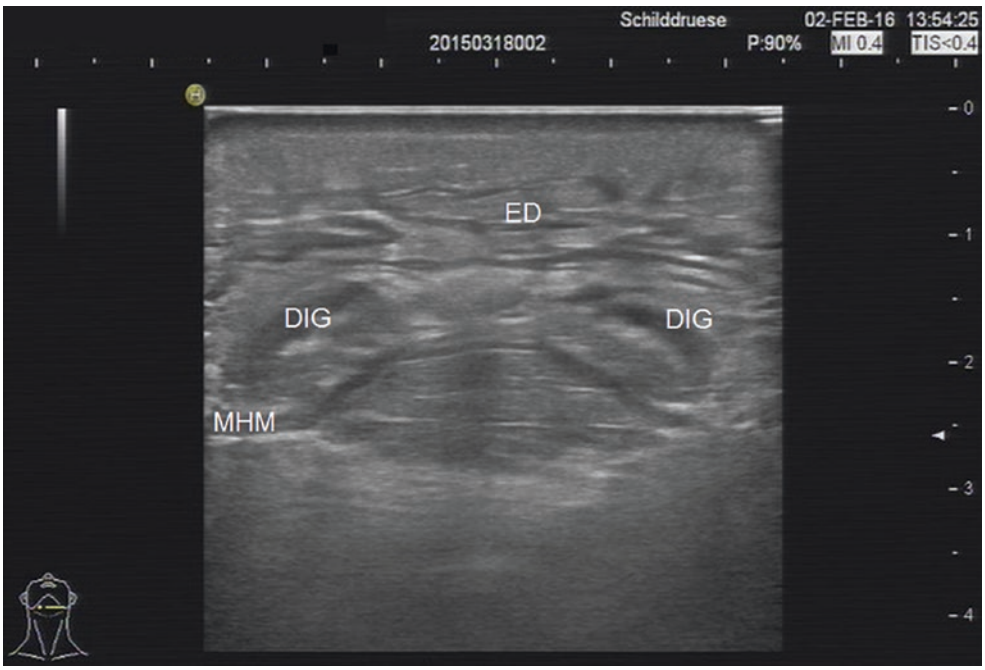

Fig. 6.71 A distinct edema (ED) of the floor of the mouth after radiotherapy. DIG digastric muscles, MHM mylohyoid muscle

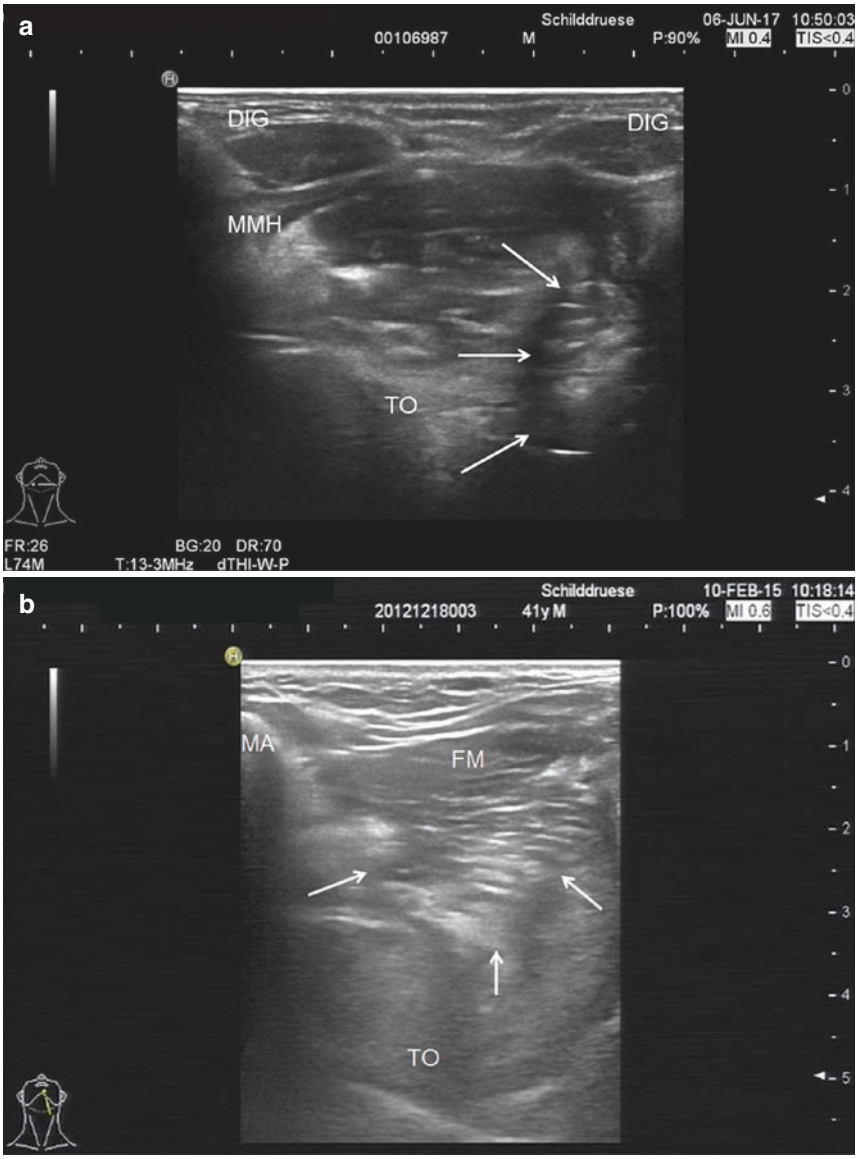

Fig. 6.72 Sonography of the floor of the mouth (FM) and the tongue (TO) after tumor resection followed by reconstruction with a radial forearm flap (*arrows*), using a frontal section (**a**) and sagittal section (**b**). The echo of the flap differs from the echo of the tongue. DIG digastric muscle, MA mandible, MMH mylohyoid muscle

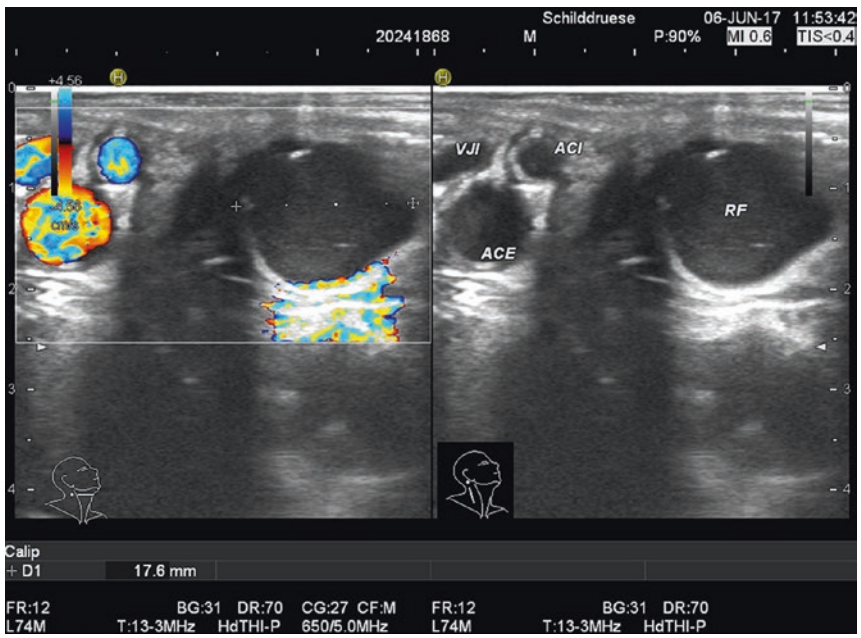

Fig. 6.73 Cystic lesion (RF) after lateral pharyngotomy. ACE external carotid artery, ACI internal carotid artery, VJI internal jugular vein

References

1. Orloff LA. Head and neck ultrasonography. 2nd ed. San Diego: Plural Publishing; 2017.
2. Welkoborsky HJ, Jecker P, Maurer J, Mann WJ. Ultraschalldiagnostik Kopf-Hals. Stuttgart: Thieme; 2013.
3. Jecker P, Maurer J, Mann WJ. Ultrasound characteristics of lateral cervical space-occupying lesions. Ultraschall Med. 2001;22:130–5. German.
4. Peer S. The place of sonography in the diagnostic work-up of haemangiomas and vascular malformations. Handchir Mikrochir Plast Chir. 2009;41:70–7. German.
5. Costache A, Dumitru M, Tweedie D, Sarafoleanu C, Anghel I. Adult cervical lymphangioma - ultrasonography, surgical removal, and pathology results. Case report. Med Ultrason. 2015;17:411–3.
6. Choi HI, Choi YH, Cheon JE, Kim WS, Kim IO. Ultrasonographic features differentiating thyroglossal duct cysts from dermoid cysts. Ultrasonography. 2018;37:71–7.
7. Inarejos Clemente E, Oyewumi M, Propst EJ, Ngan BY, Greer ML. Thyroglossal duct cysts in children: Sonographic features every radiologist should know and their histopathological correlation. Clin Imaging. 2017;46:57–64.
8. Jin ZQ, He W, Wu DF, Lin MY, Jiang HT. Color Doppler ultrasound in diagnosis and assessment of carotid body tumors: comparison with computed tomography angiography. Ultrasound Med Biol. 2016;42:2106–13.
9. Tong Y. Role of duplex ultrasound in the diagnosis and assessment of carotid body tumour: a literature review. Intractable Rare Dis Res. 2012;1:129–33.
10. Podzimek J, Jecker P, Daliri A. Seltene Ursache für eine Schwellung im Bereich der Gl. parotis. HNO. 2018;66:702–4.

7 Sonography of the Oropharynx, Hypopharynx, Larynx, and Cervical Esophagus

Peter Jecker

7.1 Tumors of the Oral Vestibule, the Floor of the Mouth, the Tongue, and the Tonsils

Tumors of the oral vestibule can be detected easily with ultrasound [1–3]. In this region, we often see benign tumors, such as cysts of the small salivary glands of the lip. These are commonly hypoechoic and homogenous with a relative signal enhancement (Figs. 7.1 and 7.2). Their margins are regular. In contrast, malignant tumors in this area sometimes show irregular margins (Fig. 7.3).

Alveolar cysts (Fig. 7.4) show the typical characteristics of cysts of other regions. These cysts in the maxillary area can be detected better by ultrasound than by other imaging methods.

Another cystic tumor that often can be seen is a ranula (Fig. 7.5). A ranula is located next to the mandible, where the sublingual gland is normally seen. As with other cysts, the margin is regular, and the ranula itself is hypoechoic with a relative signal enhancement. The same pattern can be seen with other cystic lesions of the mouth floor (Fig. 7.6).

In contrast to benign lesions, malignant tumors of the mouth floor often show irregular margins (Fig. 7.7). With ultrasound, infiltration of the tongue or other surrounding structures can be seen early in the diagnostic process [1]. Commonly, these tumors are less hypoechoic than cysts and sometimes are inhomogeneous. They are located next to the mouth floor muscles. Complications such as tumor extension toward the contralateral side of the mouth floor can be seen with ultrasound (Fig. 7.8).

Tongue cancer shows a similar ultrasound finding (Figs. 7.9, 7.10, and 7.11). In contrast to mouth floor cancer, tongue tumors do not necessarily contact the mouth floor muscles. Their sonographic appearance is similar to cancer of other neck regions. Because they are sometimes located in deeper regions of the neck, the use of low frequencies is advantageous. We sometimes recommend the use of an abdominal curved array to detect the whole tumor (Fig. 7.11).

In contrast to the tongue and the mouth floor, the tonsillar region is more difficult to examine because ultrasound must be performed in a more or less oblique plane caudal to the jaw angle. Therefore, the examiner must be well trained to detect pathological processes (such as tumors) of the tonsil with ultrasound. There is no reason to perform ultrasound of the tonsils in patients with tonsillitis or tonsillar abscesses; these diseases should be diagnosed clinically. Furthermore, in our experience, small abscesses cannot be excluded with ultrasound alone, so we prefer to use CT scans in unclear clinical situations.

Normally, the tonsils can be seen lateral to the tongue and behind the submandibular gland. In younger patients, the tonsils are characterized by an onion-like pattern (Fig. 7.12). In older patients, they become atrophic and therefore are more difficult to detect.

Unilateral growth or hyperplasia of the tonsil is frequently seen clinically. Then, the different size can be documented with ultrasound. The normal hyperplastic tonsil (Figs. 7.13 and 7.14; Video 7.1) and cancer of the tonsil (Figs. 7.15, 7.16, and 7.17; Video 7.2) or malignant lymphoma (Figs. 7.18 and 7.19) are characterized by a hypoechoic pattern of the organ. The differential diagnosis can be confirmed if lymph nodes are present with patterns typical of cancer or lymphoma. Furthermore, the extent of tumor growth especially details such as infiltration of the tongue or the mouth floor (Fig. 7.17) or tumor growth along the pharynx (Fig. 7.20) can be seen well by ultrasound. In some cases, ultrasound will show tumor growth toward the large vessels of the neck (Fig. 7.21). In these patients, duplex scan should be used to differentiate between the internal and external carotid artery, which is essential for the therapeutic strategy.

Electronic Supplementary Material The online version of this chapter (https://doi.org/10.1007/978-3-030-12641-4_7) contains supplementary material, which is available to authorized users.

P. Jecker (✉)
Department of Otorhinolaryngology and Plastic Head and Neck Surgery, Klinikum Bad Salzungen GmbH, Bad Salzungen, Germany
e-mail: peter.jecker@klinikum-badsalzungen.de

© Springer Nature Switzerland AG 2019

H. J. Welkoborsky, P. Jecker (eds.), *Ultrasonography of the Head and Neck*, https://doi.org/10.1007/978-3-030-12641-4_7

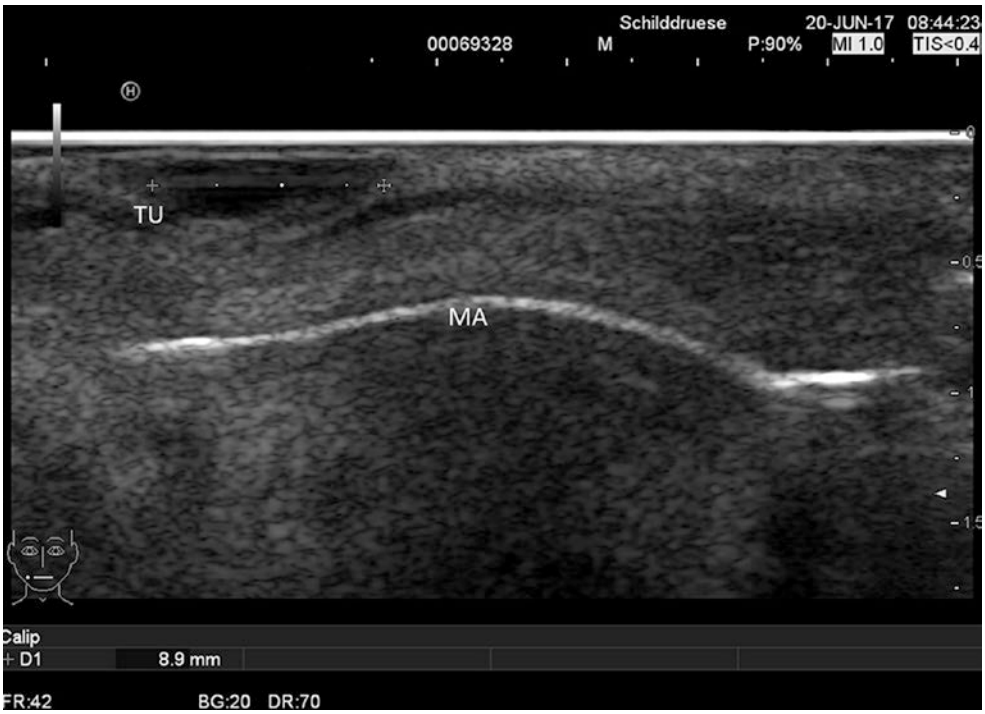

Fig. 7.1 Salivary cyst (TU) of the lower lip. The cyst is hypoechoic and the borders are regular. MA mandible

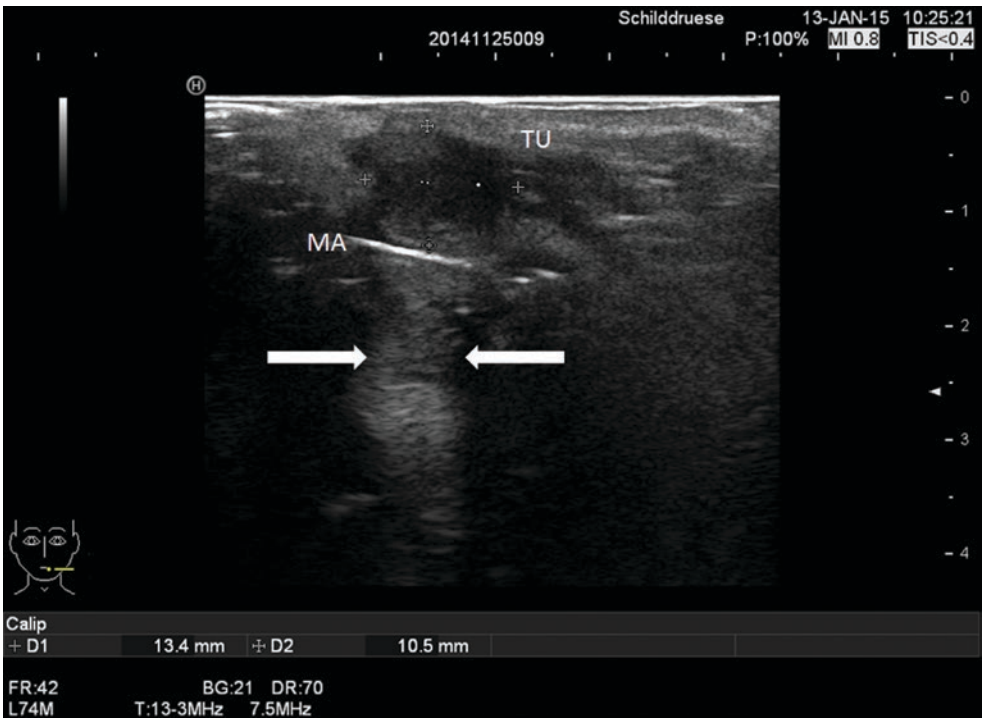

Fig. 7.2 Salivary cyst (TU) of the lower lip. Note the relative acoustic enhancement (*between arrows*). MA mandible

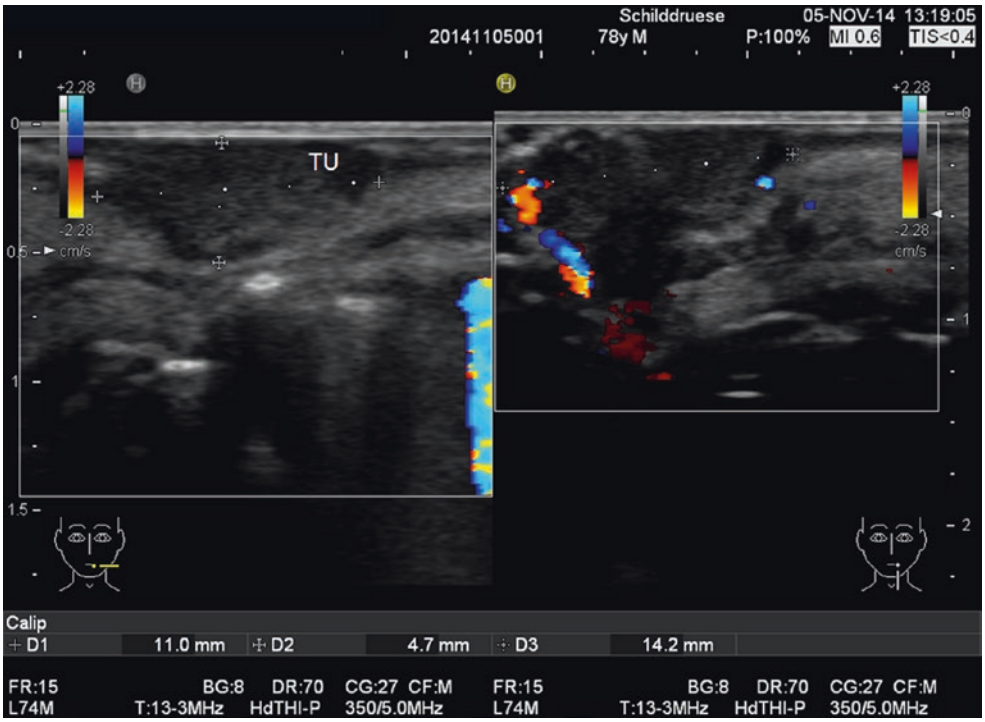

Fig. 7.3 Cancer (TU) of the lower lip. The tumor is heterogeneous and the borders are irregular

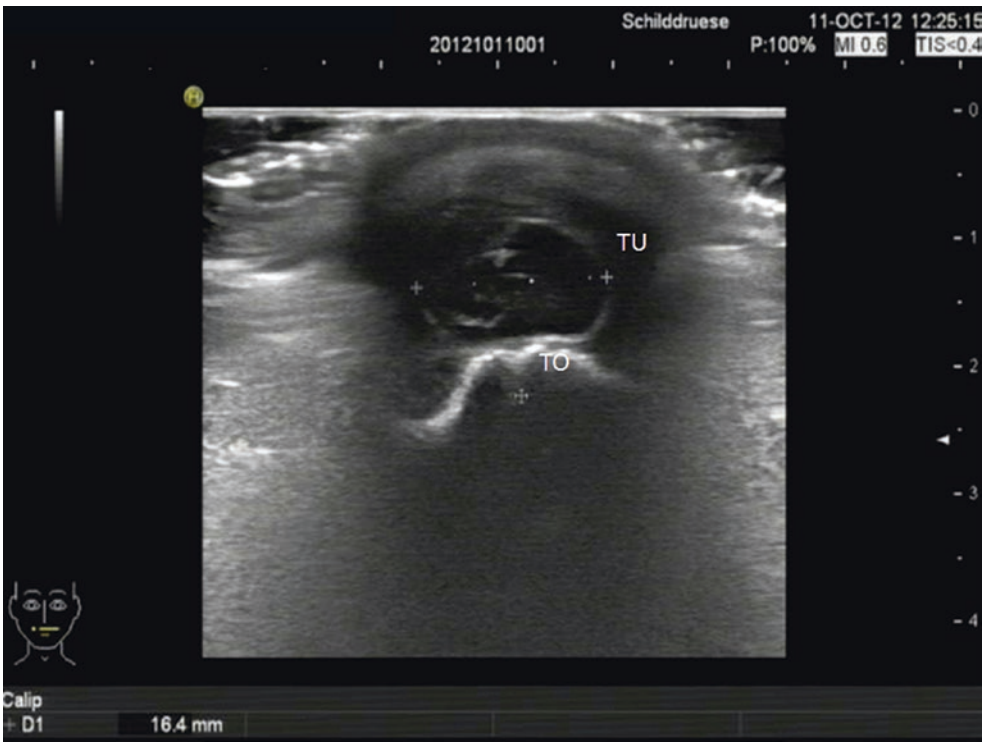

Fig. 7.4 Alveolar cyst (TU) of a maxillary tooth (TO)

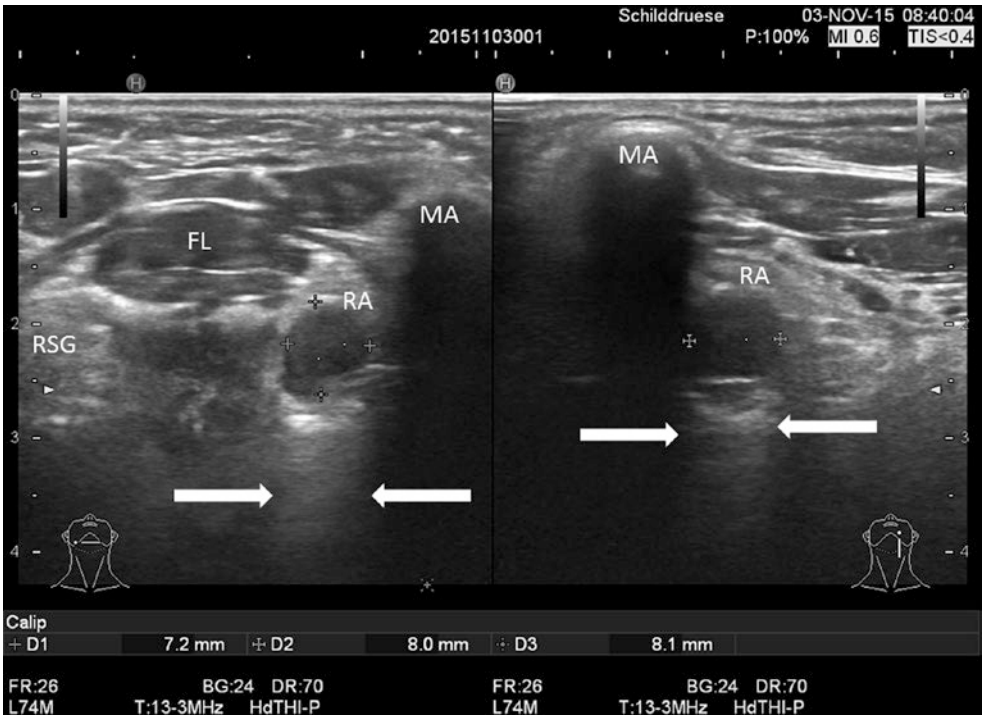

Fig. 7.5 Ranula (RA) of the left mouth floor. This cyst is typically located in the area of the sublingual gland. Note the relative acoustic enhancement (*between arrows*). FL floor of the mouth, MA mandible, RSG right sublingual gland

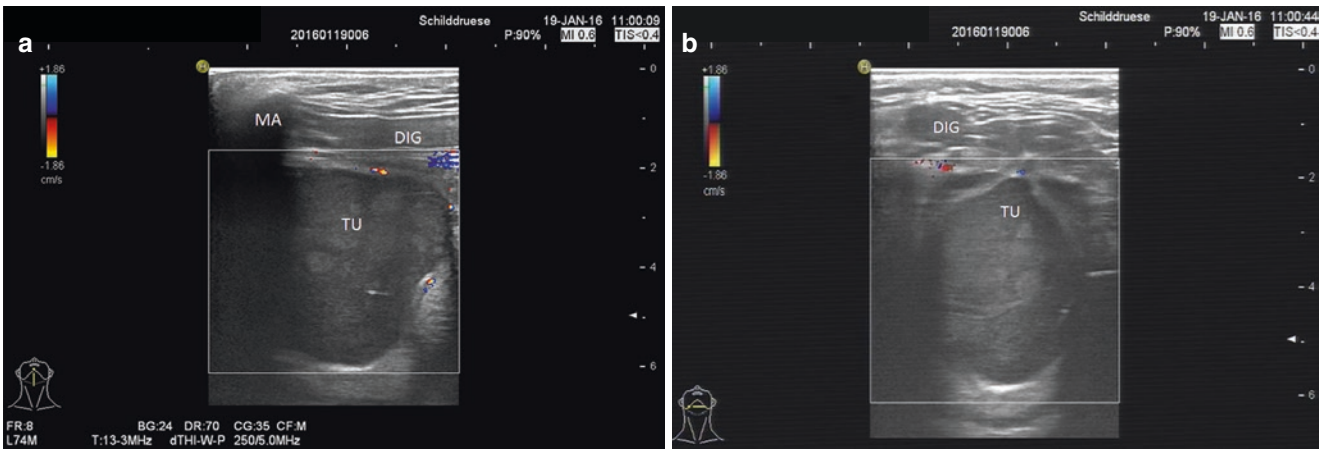

Fig. 7.6 Large cystic tumor (TU) of the mouth floor, in sagittal (**a**) and frontal (**b**) plane. DIG digastric muscle, MA mandible

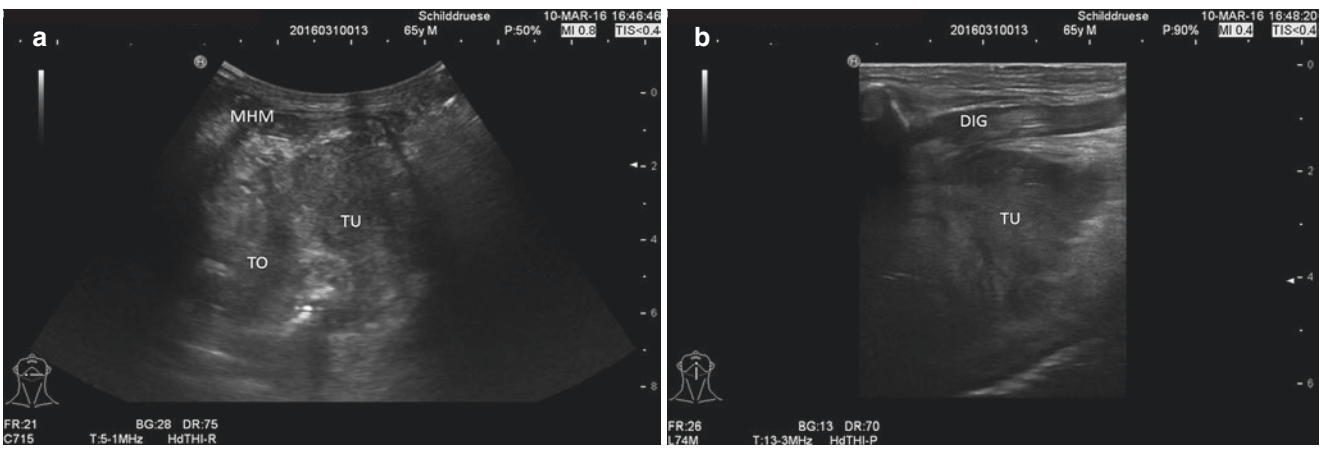

Fig. 7.7 Cancer (TU) of the left mouth floor, infiltrating the tongue (TO), in sagittal (**a**) and frontal (**b**) plane. DIG digastric muscle, MHM mylohyoid muscle

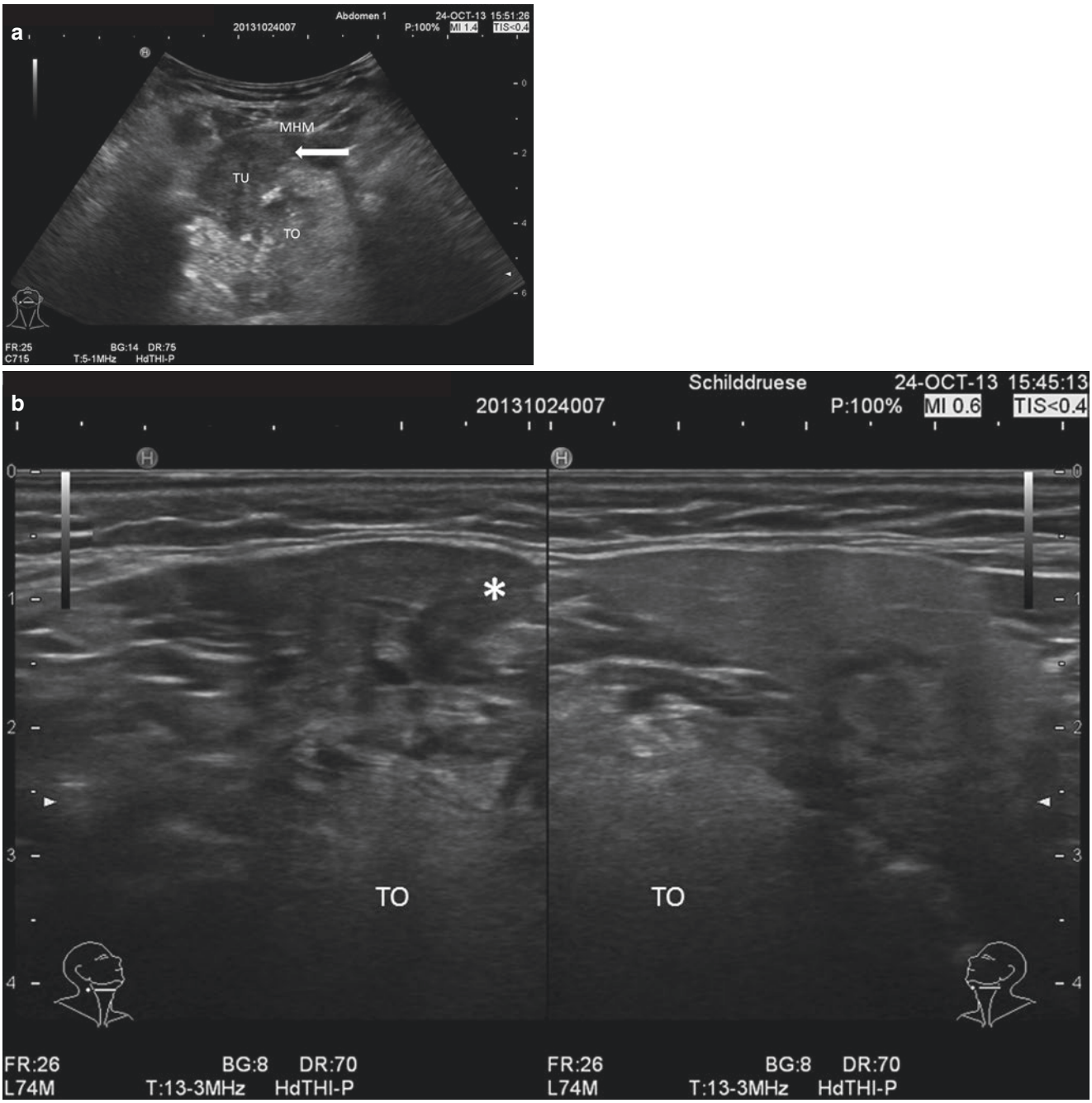

Fig. 7.8 Cancer (TU) of the right mouth floor (**a**), which crosses the midline (*arrow*). The tumor is infiltrating Wharton's duct, resulting in chronic sialadenitis (*asterisk*) of the right submandibular gland (**b**). MHM mylohyoid muscle, TO tongue

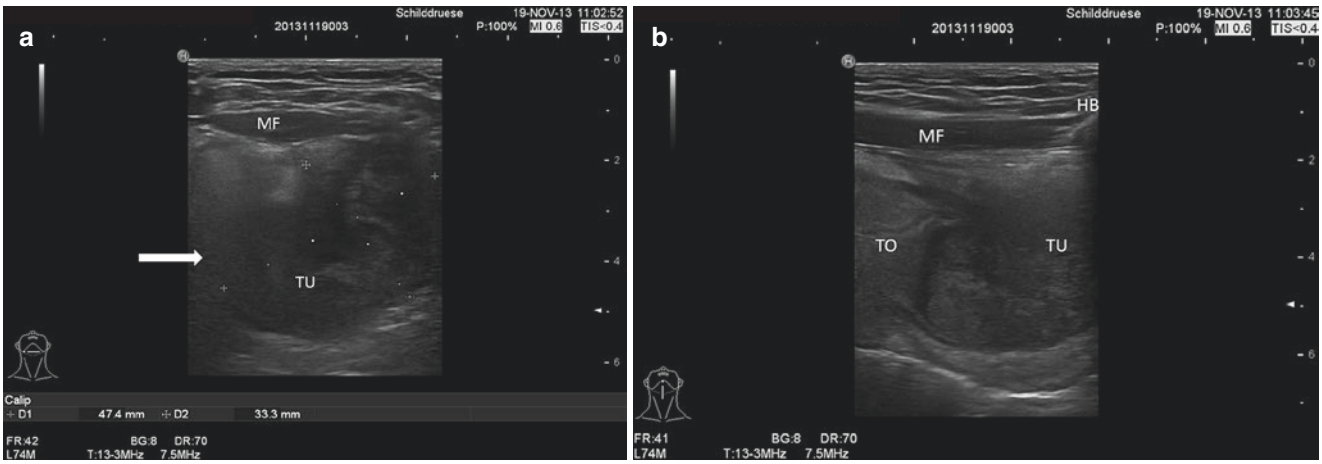

Fig. 7.9 Left side tongue cancer (TU) exceeding the midline (*arrow*), in frontal (**a**) and sagittal (**b**) plane. HB hyoid bone, MF mouth floor, TO tongue

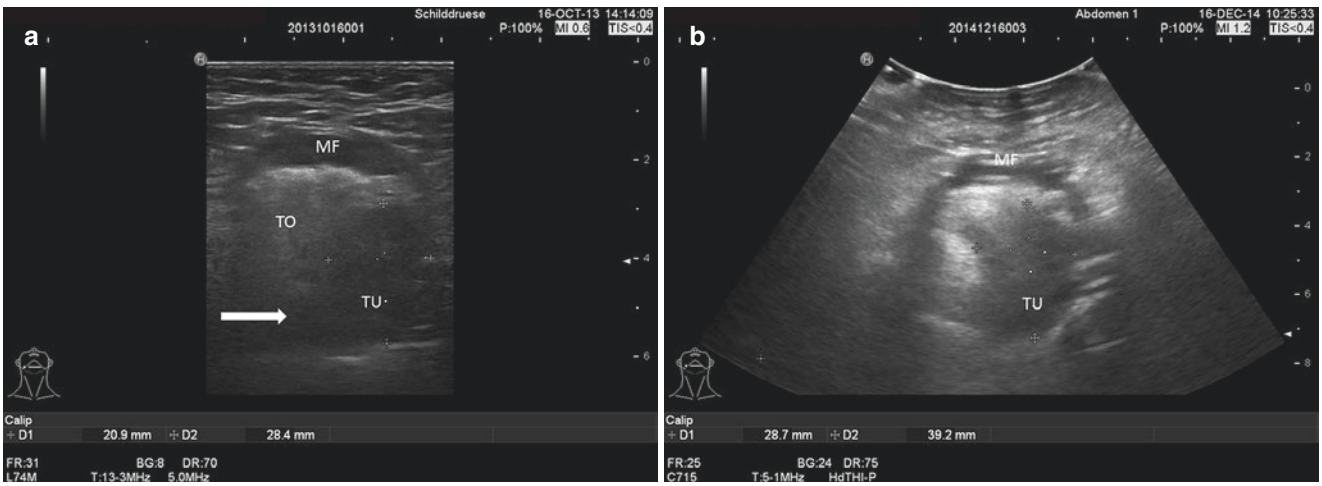

Fig. 7.10 Left side tongue cancer (TU) exceeding the midline (*arrow*), before (**a**) and after (**b**) radiotherapy, in the same patient. The tumor seems to be larger after therapy. Note that different arrays were used. MF mouth floor, TO tongue

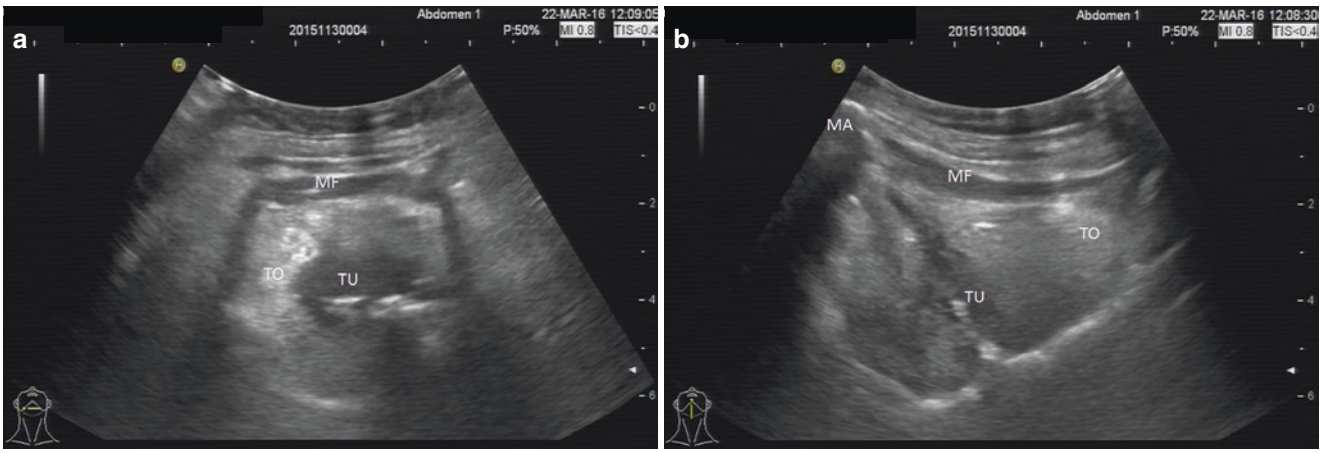

Fig. 7.11 Cancer (TU) in the midline of the tongue after radiotherapy, in frontal (**a**) and sagittal (**b**) plane. A 5-MHz curved array was used for better tumor detection. MA mandible, MF mouth floor, TO tongue

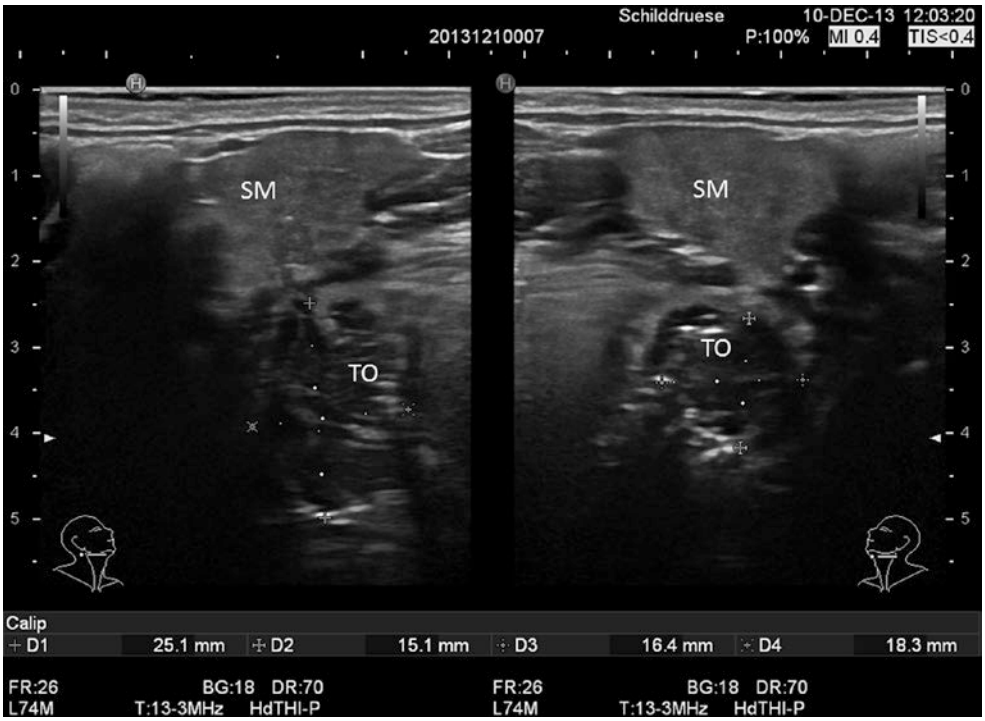

Fig. 7.12 Hyperplastic tonsils (TO, right greater than left) in a child. Note the typical onion-like pattern of childhood. SM submandibular gland

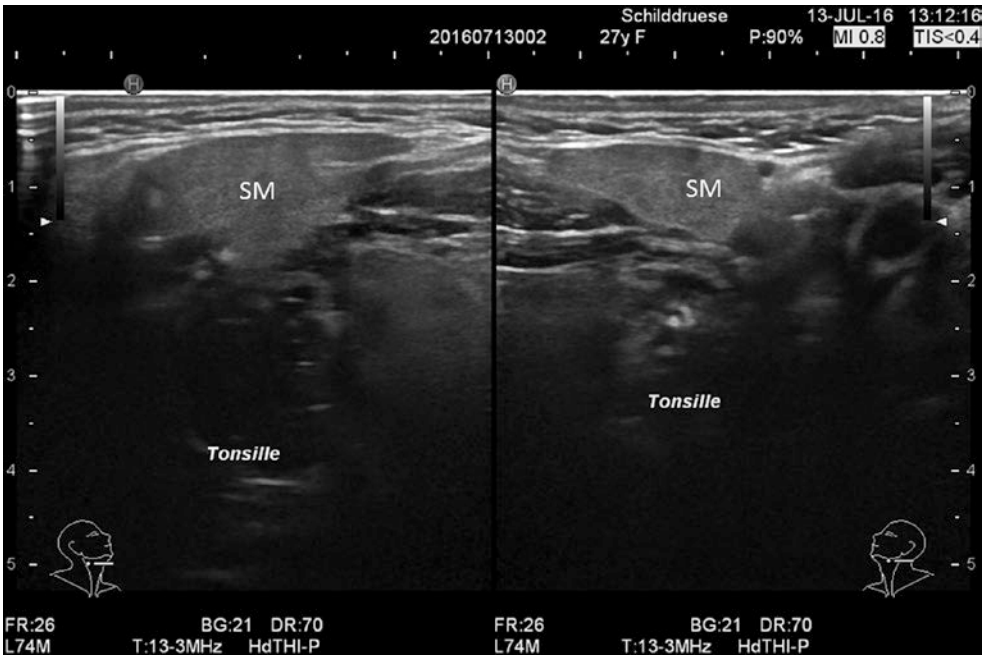

Fig. 7.13 Massive hyperplasia of the right tonsil (tonsille) in an adult patient. SM submandibular gland

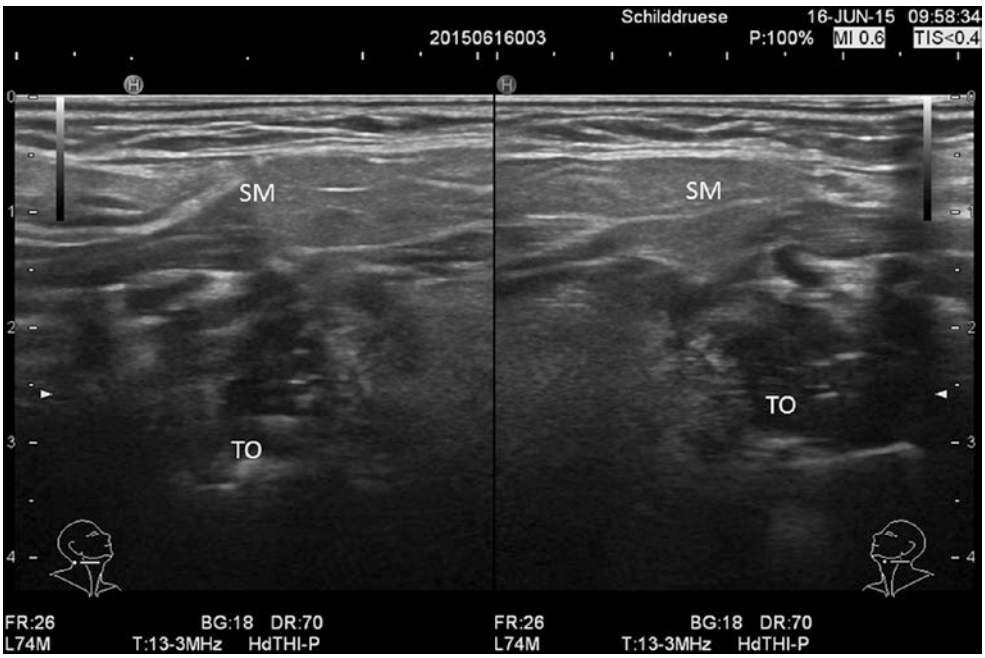

Fig. 7.14 Moderate hyperplasia of the left tonsil (TO) in an adult patient. SM submandibular gland

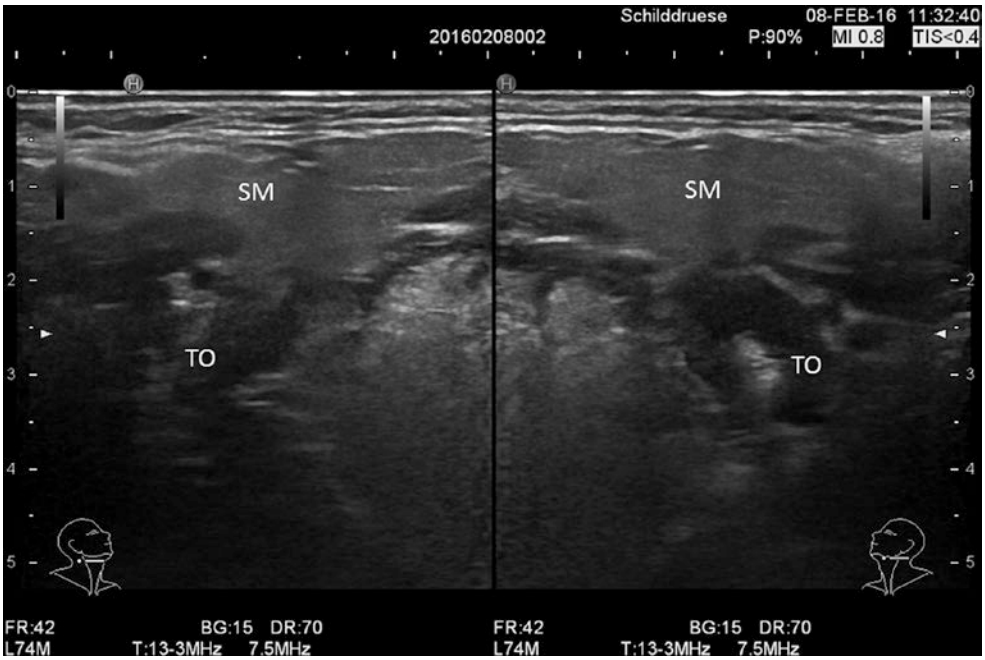

Fig. 7.15 T2 cancer of the left tonsil (TO). SM submandibular gland

Fig. 7.16 T4 cancer of the left tonsil (TO). LN reactive lymph node, SM submandibular gland

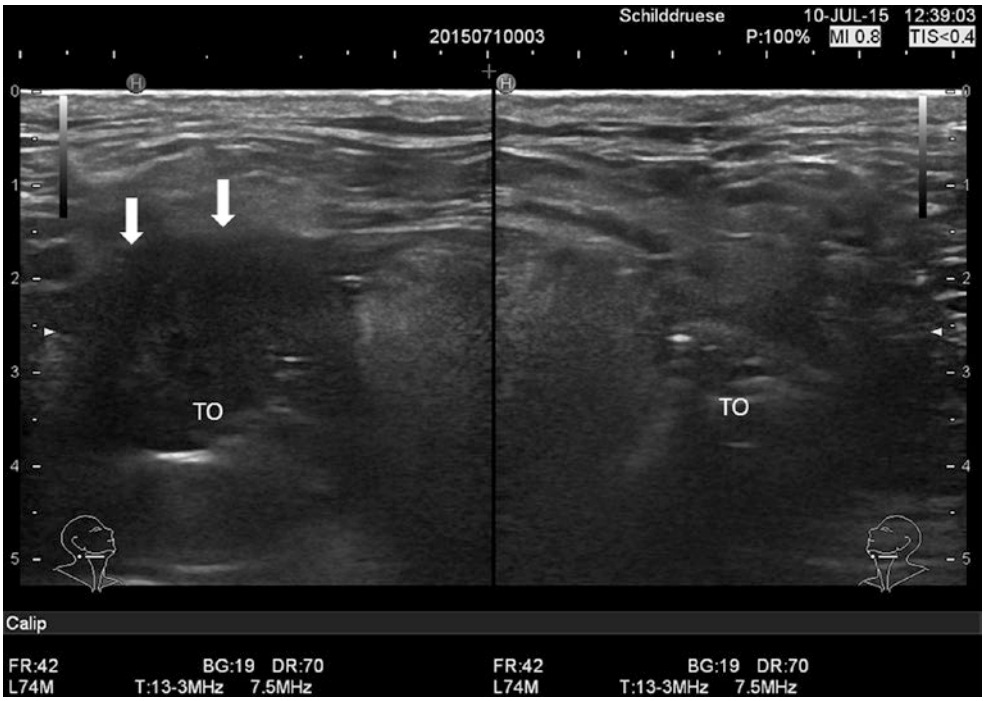

Fig. 7.17 Cancer of the right tonsil (TO) with infiltration of the mouth floor and the submandibular gland (*arrows*)

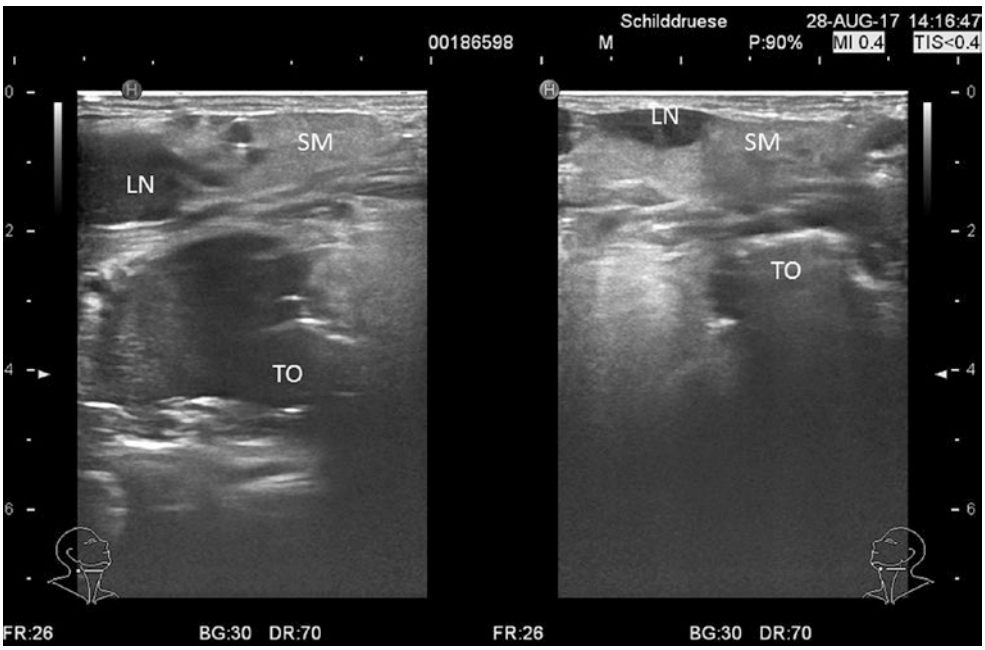

Fig. 7.18 Malignant lymphoma of the right tonsil (TO) with multiple lymph nodes (LN) in the neck. SM submandibular gland

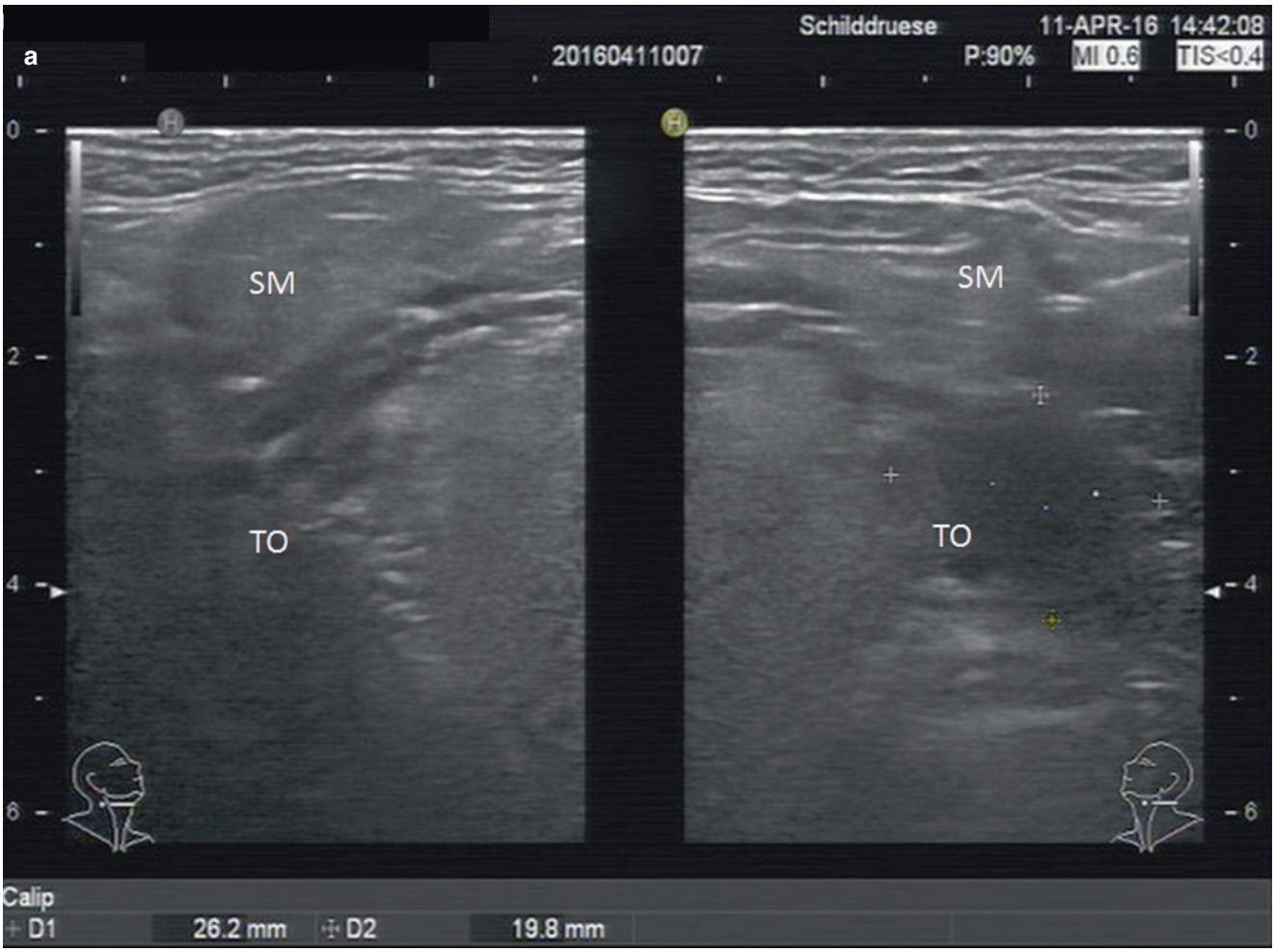

Fig. 7.19 (**a**) Non-Hodgkin lymphoma of the left tonsil. (**b**) The diagnosis is supported by the typical pattern of lymph nodes (LN) next to the submandibular gland. SM submandibular gland, TO tonsil

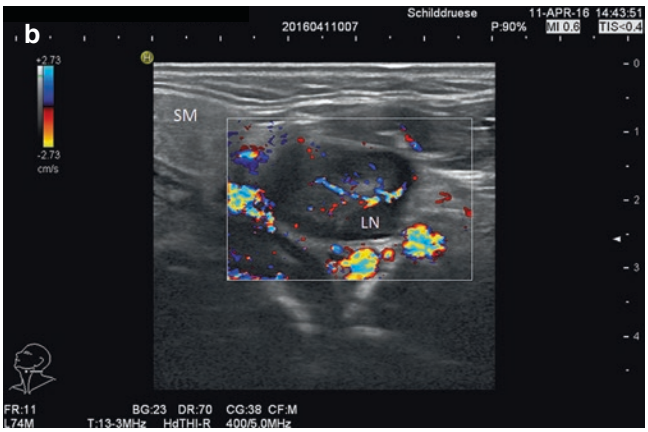

Fig. 7.19 (continued)

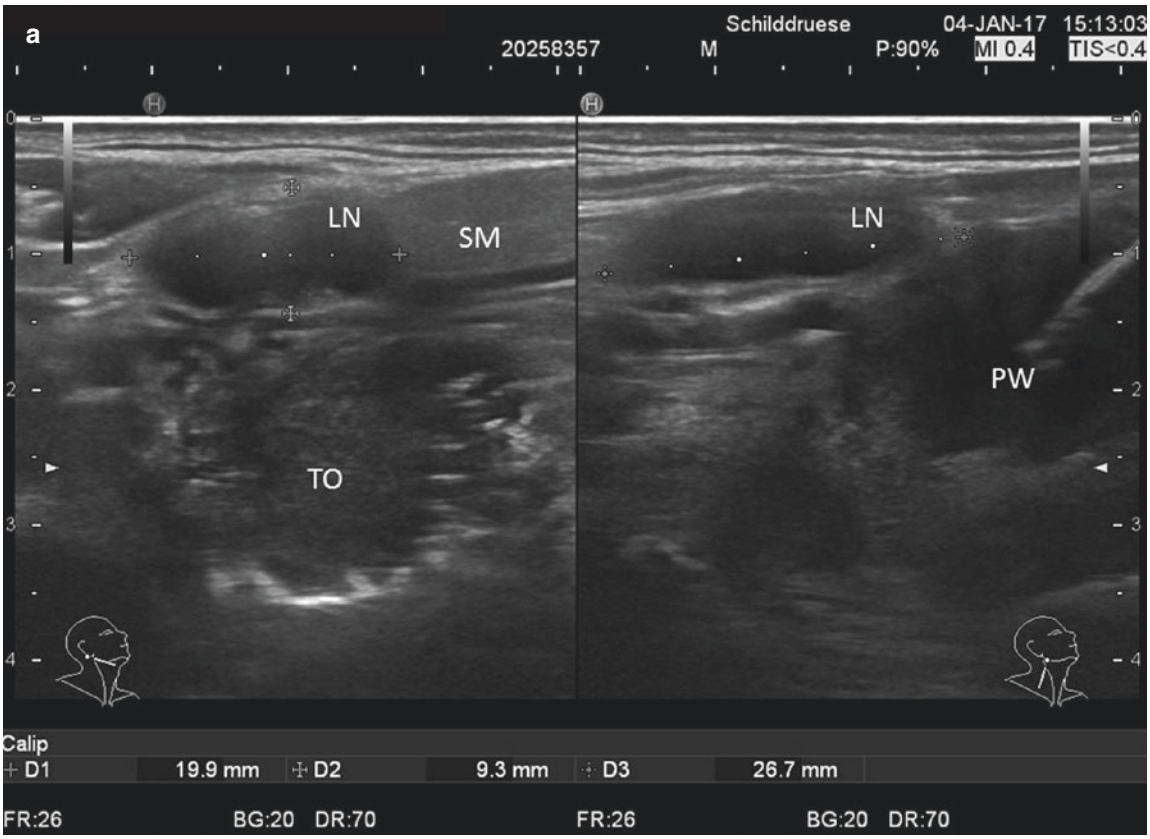

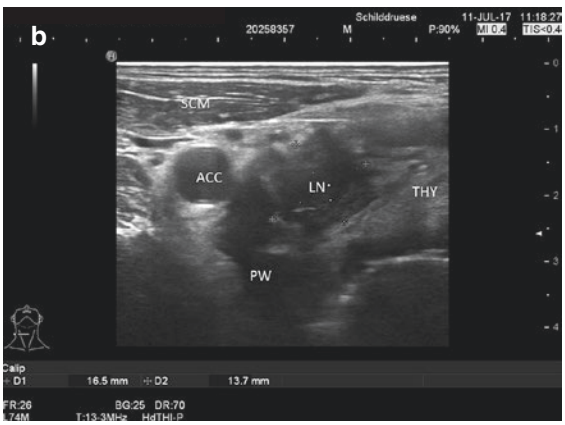

Fig. 7.20 T4 cancer of the right tonsil (TO) (**a**) and the pharyngeal wall (PW) (**b**) with metastatic lymph nodes (LN). ACC common carotid artery, SCM sternocleidomastoid muscle, SM submandibular gland, THY thyroid

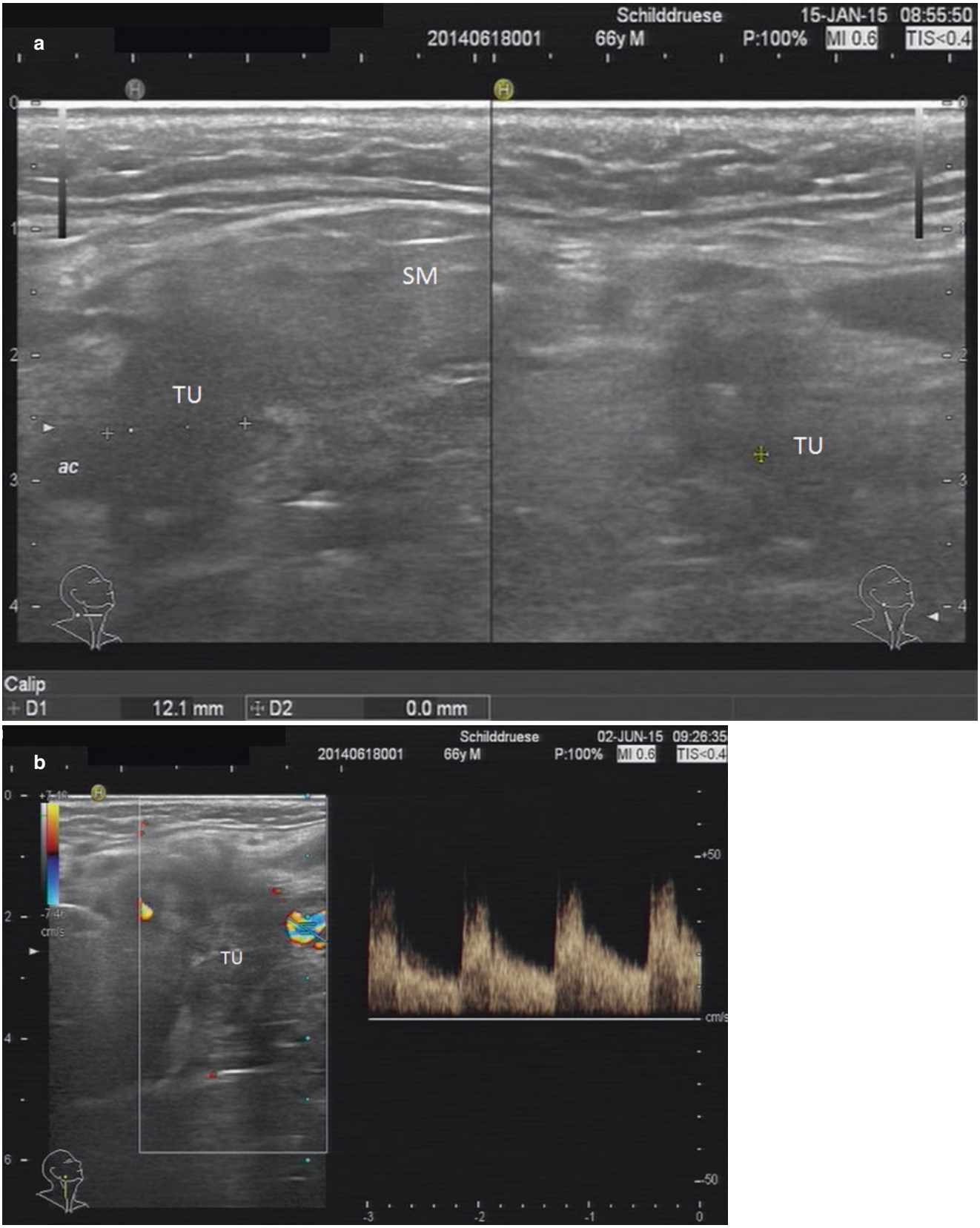

Fig. 7.21 (**a**) Recurrent cancer (TU) next to the pharynx and the carotid artery (ac). (**b**) Using pulsed-wave (pw) Doppler, the internal carotid artery can be identified next to the tumor

7.2 Tumors of the Tongue Base and the Vallecular Region

Similar to tonsillar hyperplasia, hyperplasia of the tongue base is frequently seen clinically. Using ultrasound, the tongue base is hypoechoic, and its size is symmetrical on both sides (Fig. 7.22; Video 7.3). Unilateral enlargement of the tongue base can be well documented with ultrasound (Figs. 7.23 and 7.24). Furthermore, tumors of the tongue base (Fig. 7.25) and even the extent of thyroid tissue at the tongue base (Figs. 7.26 and 7.27) can be estimated with ultrasound. But of course, the correct diagnosis always depends on the clinical aspect, because many pathologies in this region show a similar sonographic appearance.

Similar to the tongue base, the vallecular region is sometimes difficult to inspect during clinical examination. Depending on the patient's neck anatomy, pathologies of this region can be visualized by ultrasound on both sides

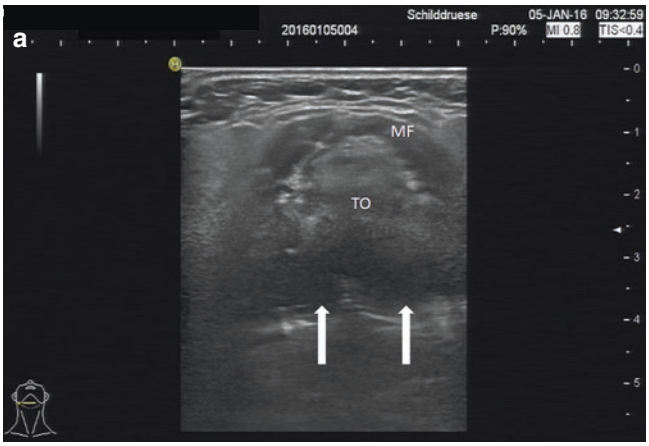

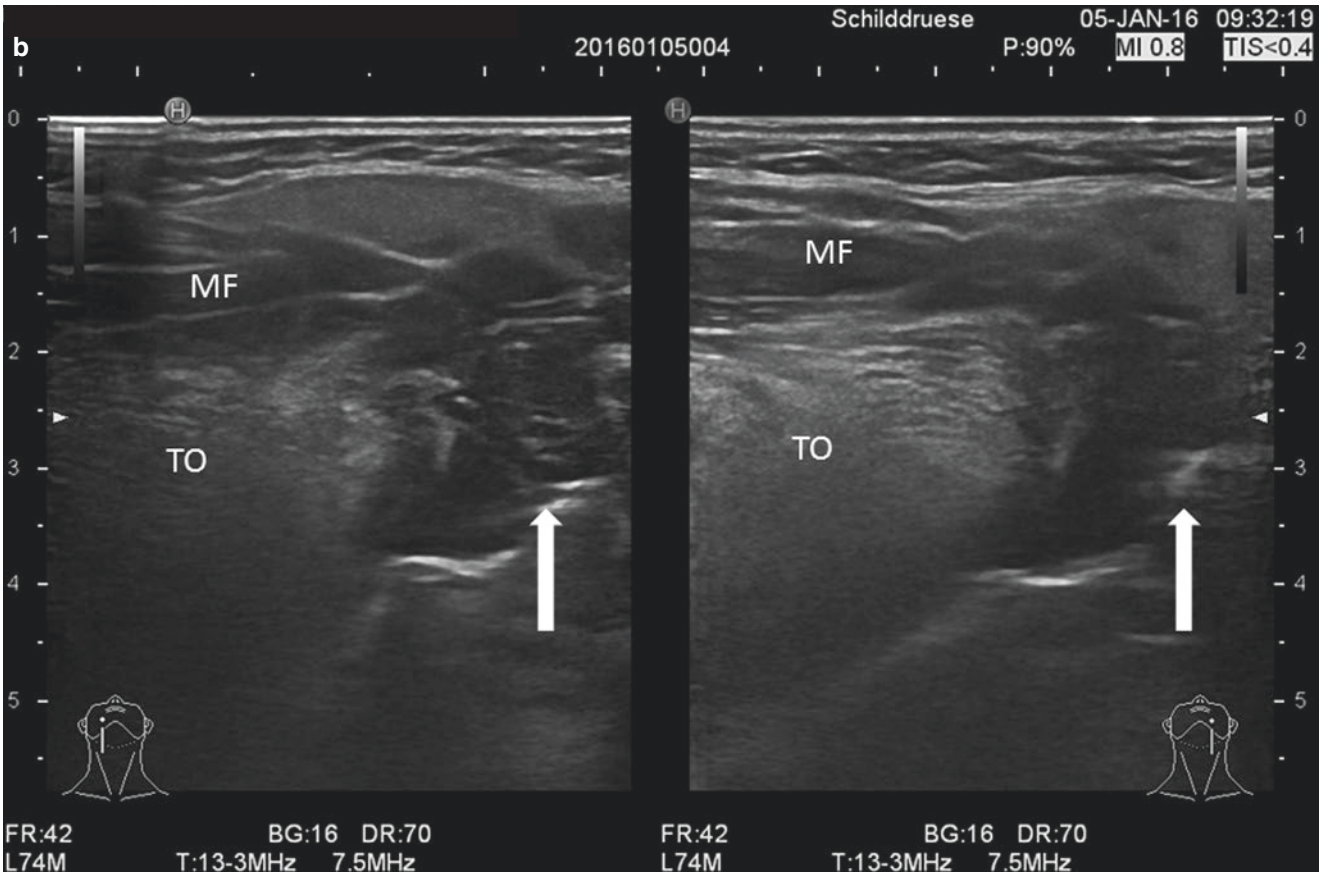

Fig. 7.22 Symmetric hyperplasia of the tongue base (*arrows*). (**a**) Frontal plane. (**b**) Two sagittal planes beside the midline. MF mouth floor, TO tongue

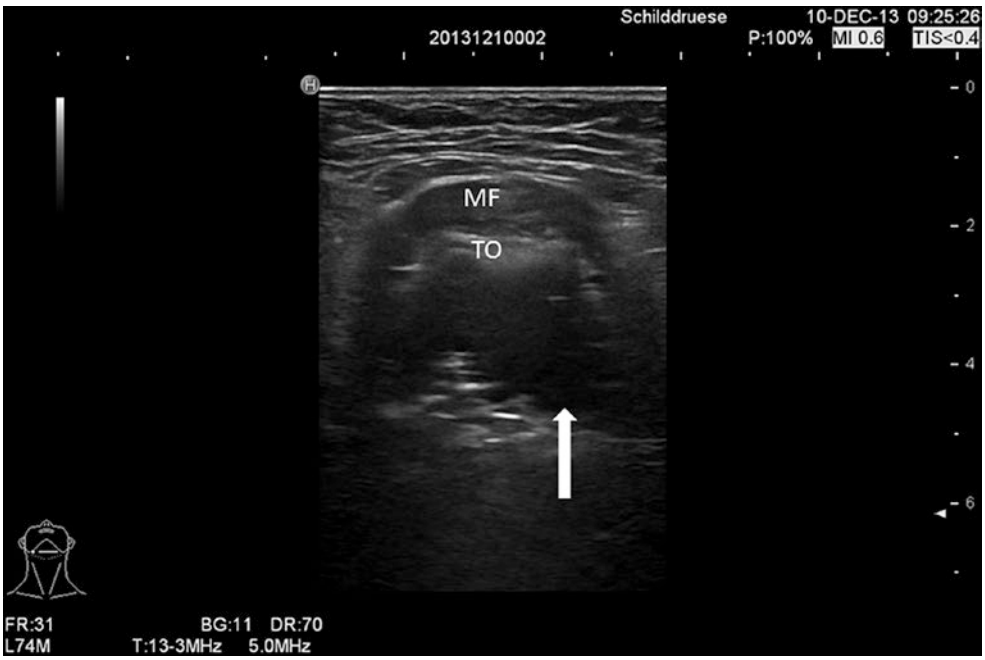

Fig. 7.23 Moderate hyperplasia of the left tongue base (*arrow*). MF mouth floor, TO tongue

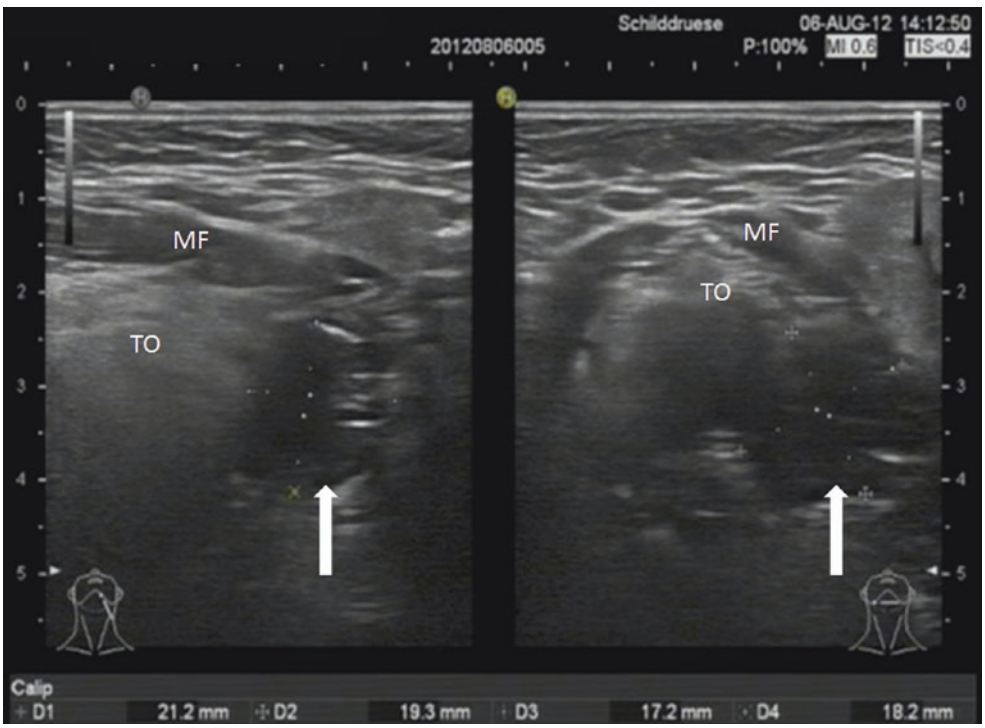

Fig. 7.24 Massive hyperplasia of the left tongue base (*arrow*). MF mouth floor, TO tongue

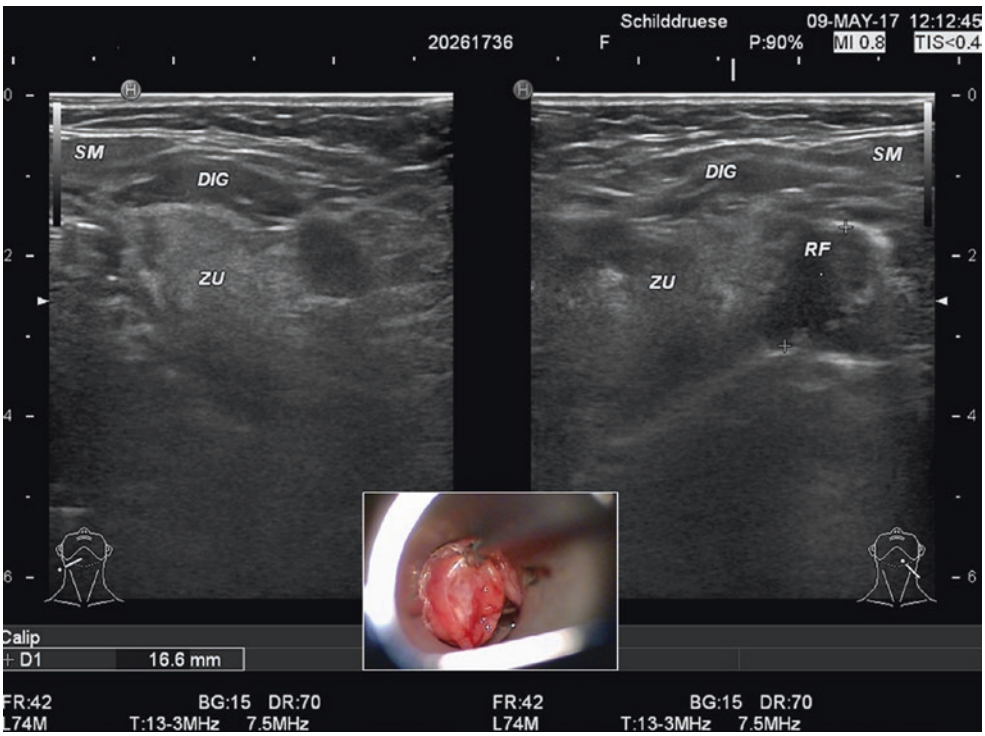

Fig. 7.25 T1 cancer of the left tongue base (RF). The image shows both sides of the tongue base in an oblique plane and the intraoperative situs (*inset*). DIG digastric muscle, SM submandibular gland, ZU tongue

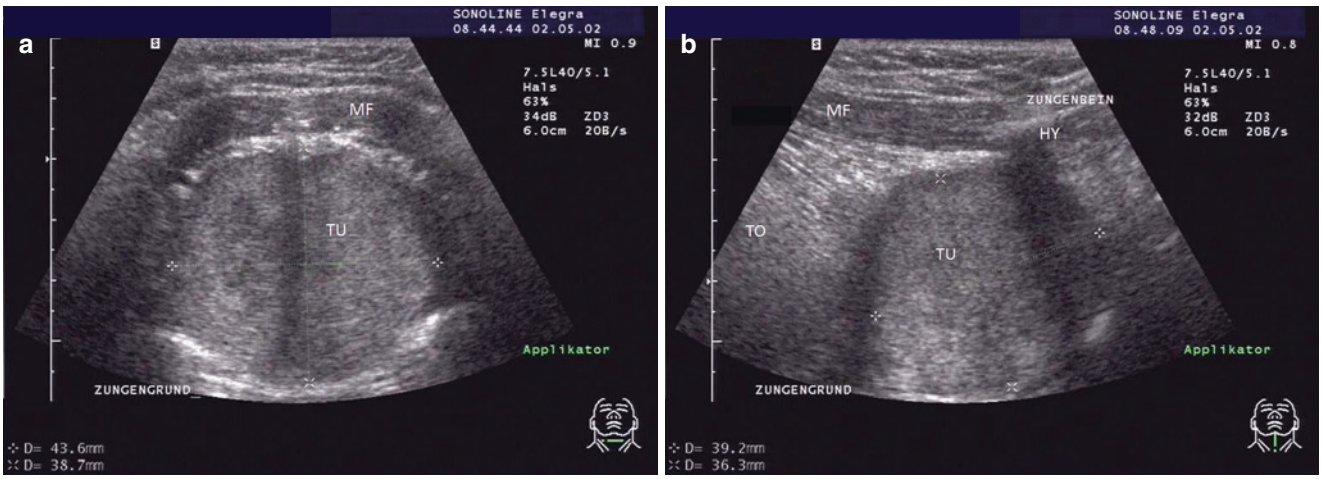

Fig. 7.26 Goiter (TU) of the tongue base in a frontal plane (**a**) and a sagittal plane (**b**). HY hyoid, MF mouth floor, TO tongue

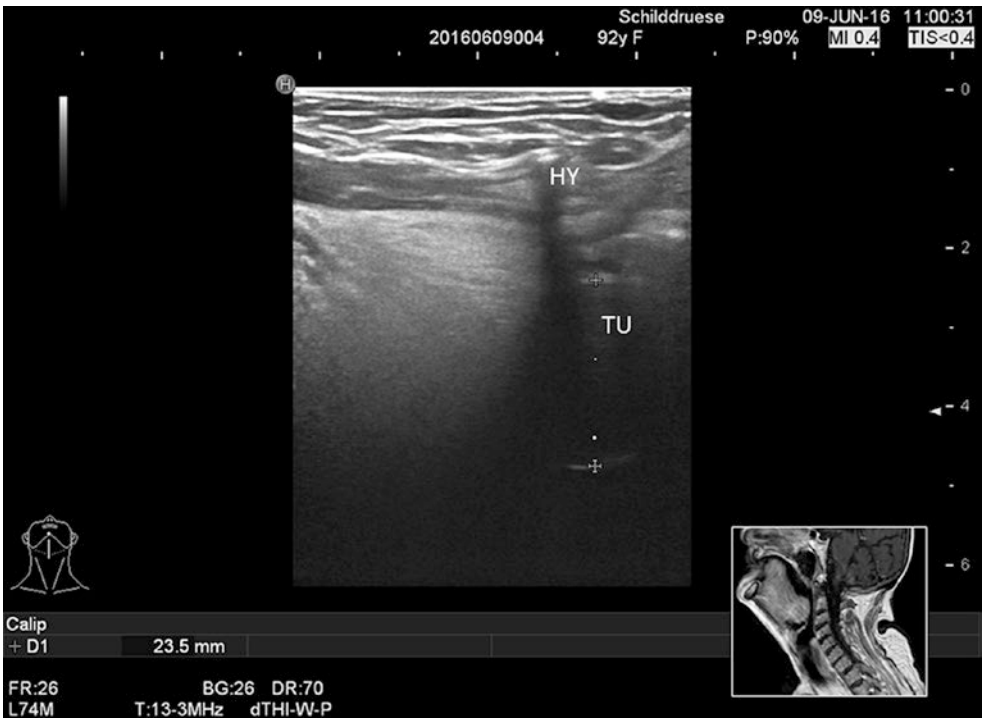

Fig. 7.27 Goiter (TU) of the tongue base, hypoechoic. HY hyoid. *Inset* shows corresponding MRI

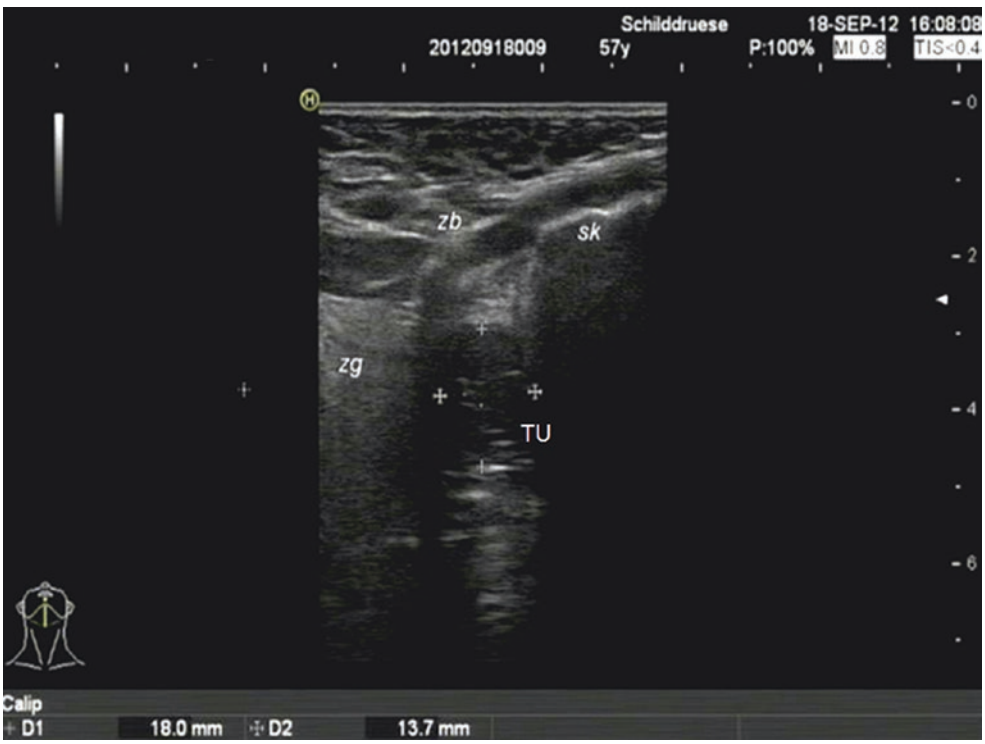

Fig. 7.28 Vallecular cyst (TU) visible between the hyoid (ZB) and the thyroid cartilage (SK). ZG tongue base

next to the acoustic shadow of the hyoid (Figs. 7.28 and 7.29). We detect mainly vallecular cysts in this region (Video 7.4). These cysts are commonly hypoechoic, with a relative signal enhancement. It is impossible to differentiate this cyst from an epiglottic cyst (Fig. 7.30) based only on ultrasound.

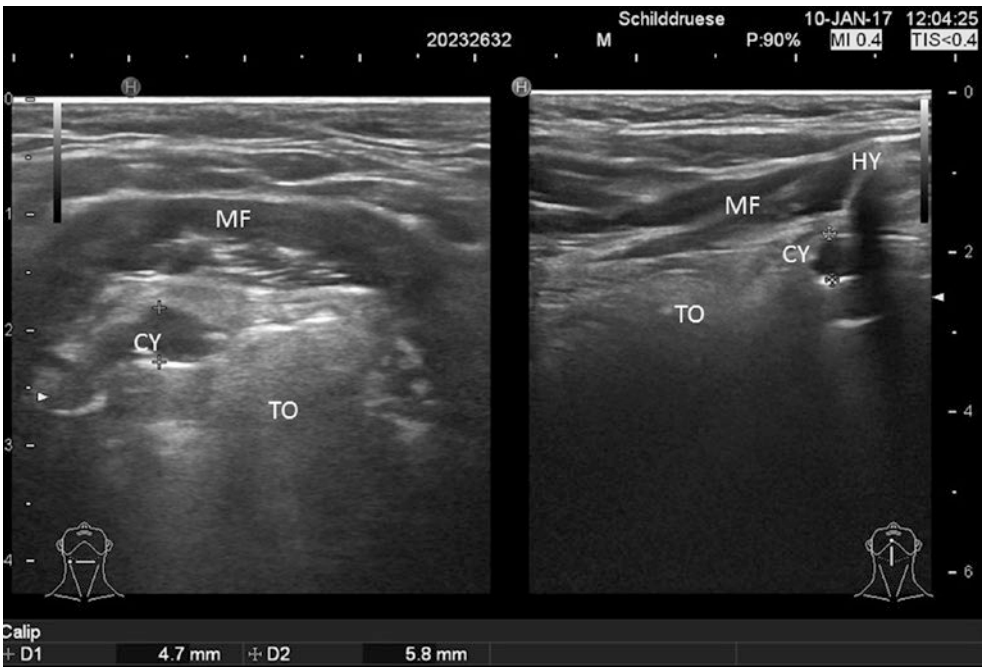

Fig. 7.29 Small vallecular cyst (CY). HY hyoid, MF mouth floor, TO tongue base

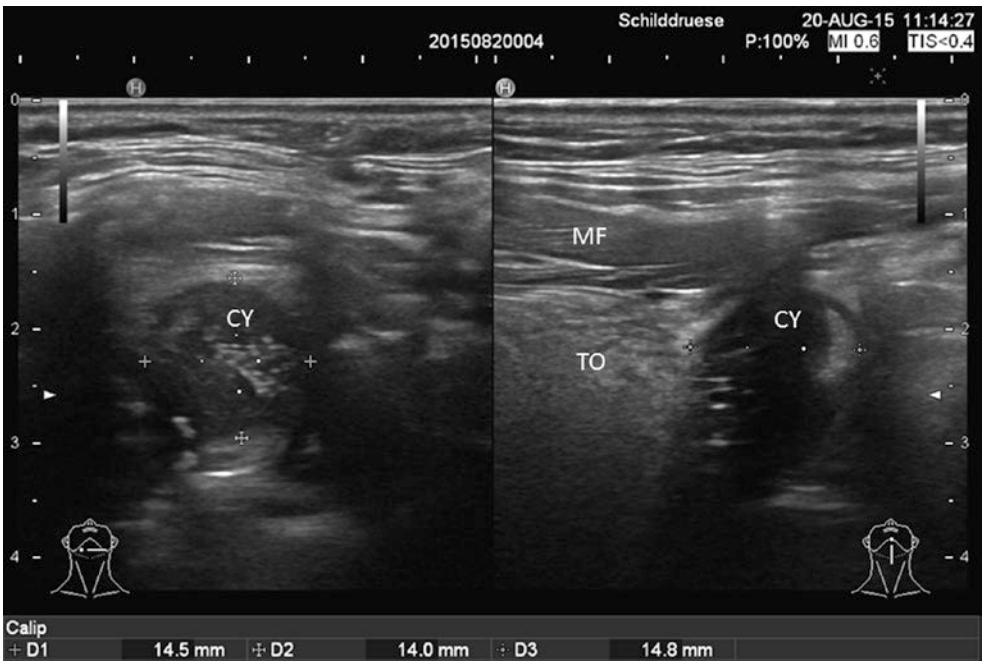

Fig. 7.30 Large epiglottic cyst (CY). MF mouth floor, TO tongue base

7.3 Tumors of the Larynx

Laryngeal tumors are detectable via endoscopic examination. Ultrasound of these tumors is difficult because major tumor parts often are located within the organ. It also becomes more difficult to view intralaryngeal structures with increasing age of the patient, owing to greater calcification of the cartilages. Nevertheless, the examiner should always try to detect the tumor using ultrasound because major interindividual differences exist in the calcification of the cartilages [4]. Additionally, other single structures like the epiglottis or the hypopharynx also can be evaluated with ultrasound.

Epiglottic changes can be seen through a sonographic window between the hyoid and the thyroid cartilage (Fig. 7.31). Parts of the epiglottis might be overlapped by the acoustic shadow of the hyoid, however, making the detection of small tumors impossible. Similarly, processes of the larynx can be seen with ultrasound in cases of extralaryngeal growth, such as external laryngoceles (Fig. 7.32) or even larynx cancer infiltrating supraglottic structures or the tongue base (Fig. 7.33). If such processes are detected with ultrasound, typical benign characteristics, such as homogeneity and regular margins (Fig. 7.32), or malignant characteristics like heterogeneity and irregular margins (Fig. 7.33) become visible.

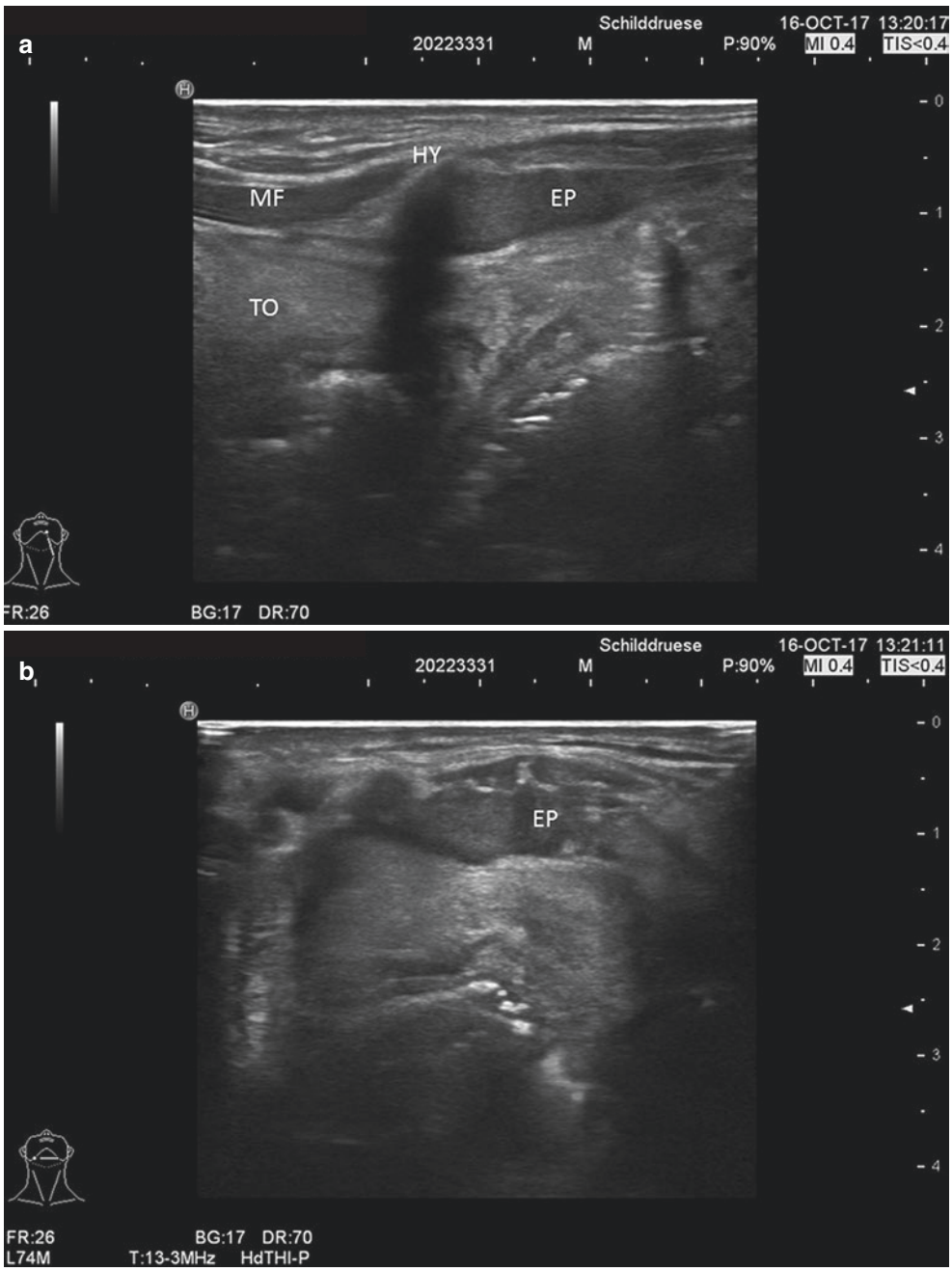

Fig. 7.31 Acute epiglottitis (EP) with swelling of the left side, sagittal plane (**a**) and frontal plane (**b**). HY hyoid, MF mouth floor, TO tongue base

Major impedance differences between a tumor and healthy laryngeal tissue allow the detection of intralaryngeal processes [5]. This is possible above all for intralaryngeal cysts (Figs. 7.34 and 7.35). We often can see only parts of these cysts by endoscopy, but ultrasound allows the complete detection of the cyst, so we can optimize the planning of therapy (Video 7.5).

Additionally, with the ultrasound devices used today in routine sonography, intralaryngeal cancer growth can be seen with ultrasound. Similar to cysts, the tumor itself is hypoechoic, with or without acoustic enhancement, which depends on the tumor structure (Fig. 7.36). Sometimes it is possible to detect specific features of the tumor growth, such as infiltration of the cartilages (Fig. 7.37, Video 7.6) or even tumor breakthrough (Fig. 7.38).

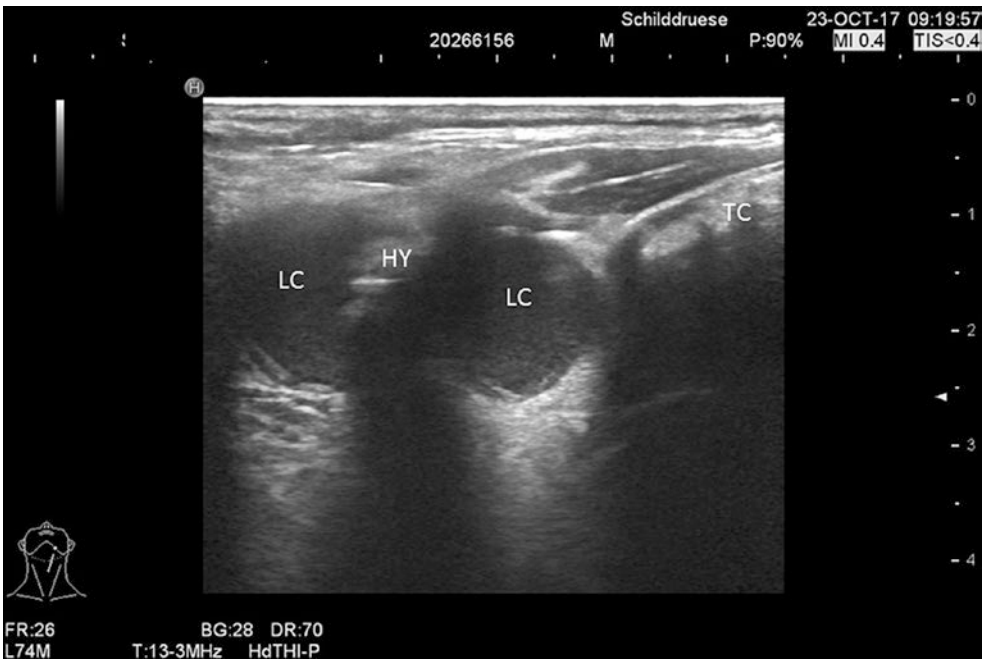

Fig. 7.32 External laryngocele (LC) with retrohyoidal extension. HY hyoid, TC thyroid cartilage

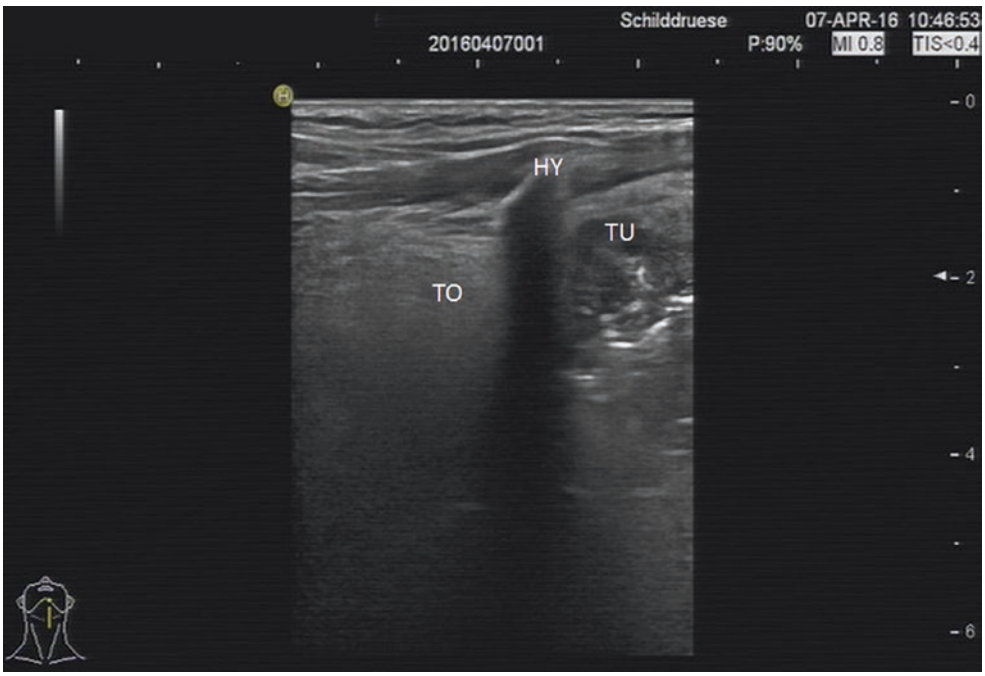

Fig. 7.33 Supraglottic cancer (TU). TO tongue base, HY hyoid

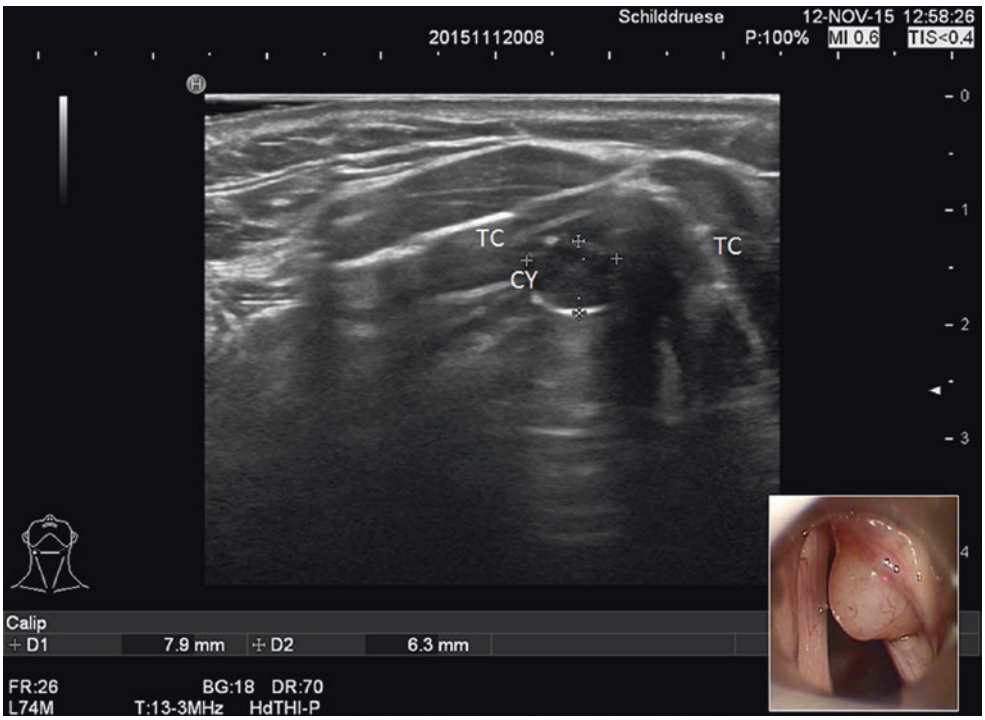

Fig. 7.34 Inner laryngocele (CY) of the right Morgagni's sinus. The cyst appears homogenous and hypoechoic, with a relative acoustic enhancement and regular margins. TC thyroid cartilage. *Inset* shows intraoperative situs

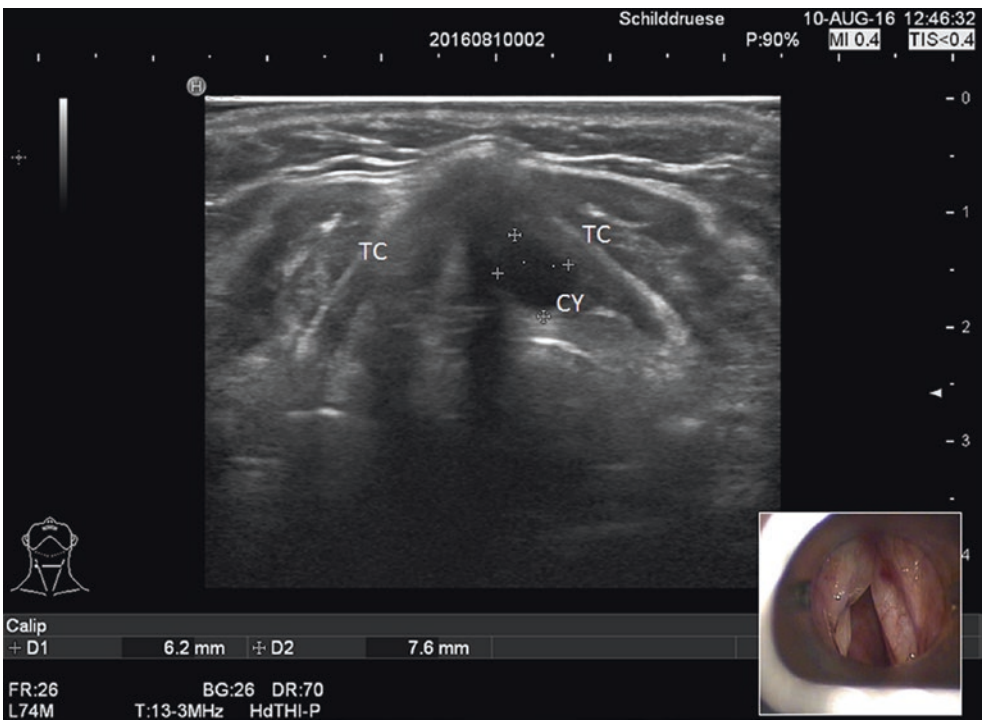

Fig. 7.35 Small cyst (CY) of the left vestibular fold. TC thyroid cartilage. *Inset* shows intraoperative situs

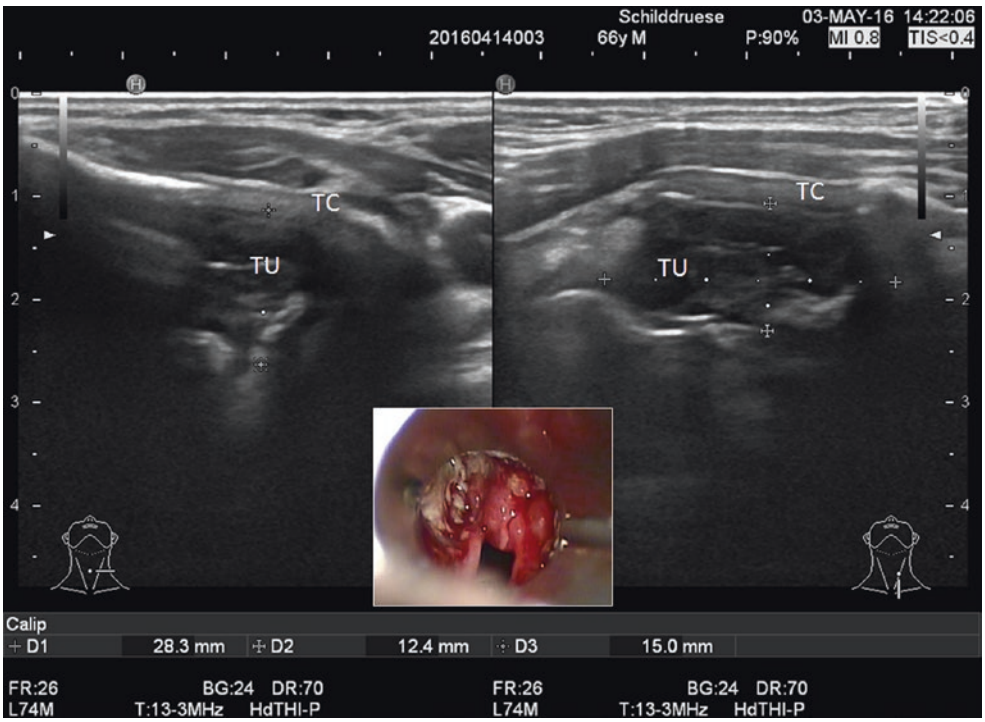

Fig. 7.36 Larynx cancer (TU) with contact to the thyroid cartilage (TC). *Inset* shows intraoperative situs

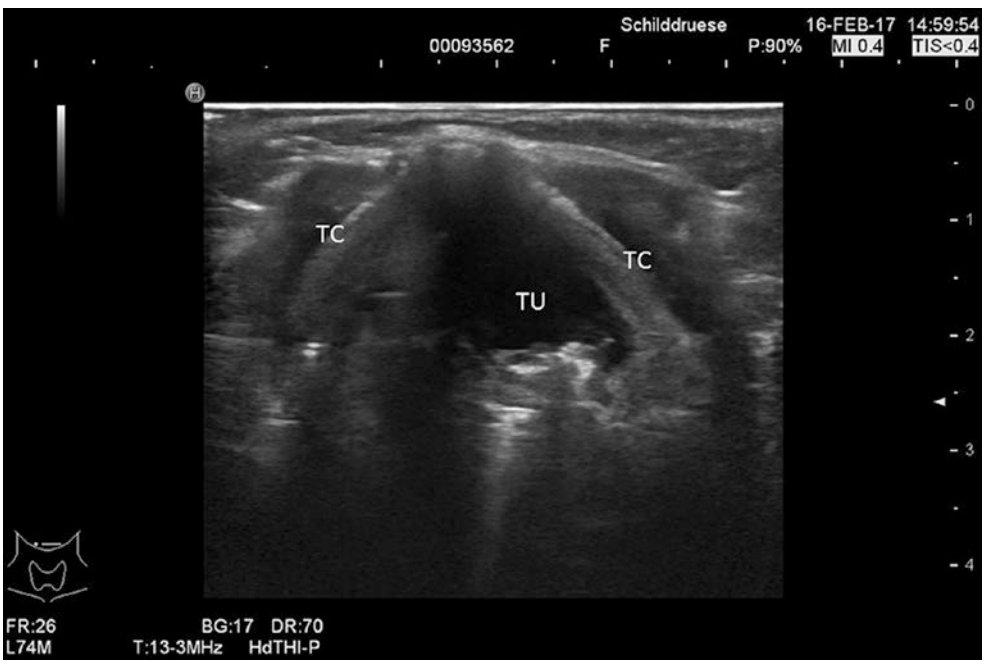

Fig. 7.37 Cancer (TU) of the left ventricular fold. The tumor seems to infiltrate the thyroid cartilage (TC)

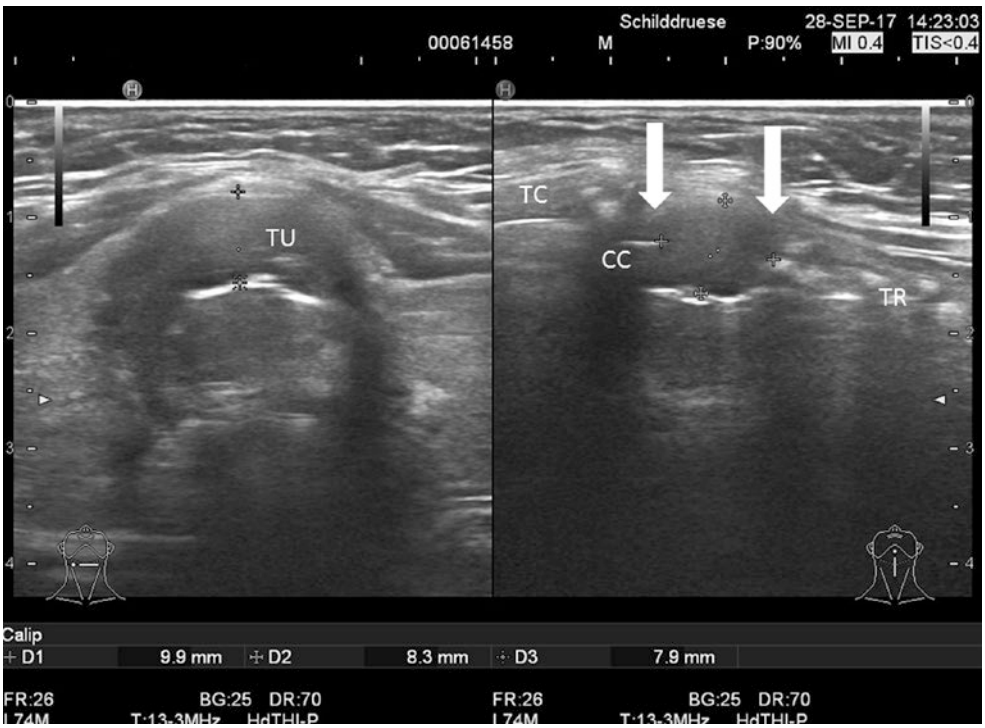

Fig. 7.38 Adenoid cystic carcinoma (TU) of the anterior subglottic mucosa. The examination in a sagittal plane (*right*) indicates destruction (*arrows*) of the cricoid cartilage (CC). TC thyroid cartilage, TR trachea

Destruction of the cartilage and tumor growth outside of the larynx into the surrounding tissue can be seen without problems (Fig. 7.39). With major destruction of the cartilage, the view of intralaryngeal parts of the tumor becomes better (Fig. 7.39b).

7.4 Tumors of the Hypopharynx and the Cervical Esophagus

Infiltration of the hypopharynx by laryngeal cancer or primary hypopharynx cancer also can be seen by ultrasound. In our experience, this is possible for T2 tumors or larger but is difficult for T1 tumors. Typically, the tumors are detectable medial to the thyroid gland (Fig. 7.40), which often is moved laterally by the tumor. The tumor itself is hypoechoic and inhomogeneous, sometimes infiltrating the thyroid gland. The same can be seen in cases of cancer of the proximal esophagus (Fig. 7.41). The tumor can clearly be identified, since the typical stratified pattern of the esophagus no longer exists [6]. Instead of this typical pattern of the healthy organ, the tumor is characterized as a hypoechoic mass, sometimes infiltrating the thyroid gland. Usually the whole extension of the tumor cannot be seen because major parts may be covered by the acoustic shadow of the clavicle.

Similarly, a Zenker diverticulum can sometimes be seen in the left hypopharynx, next to the thyroid gland (Fig. 7.42).

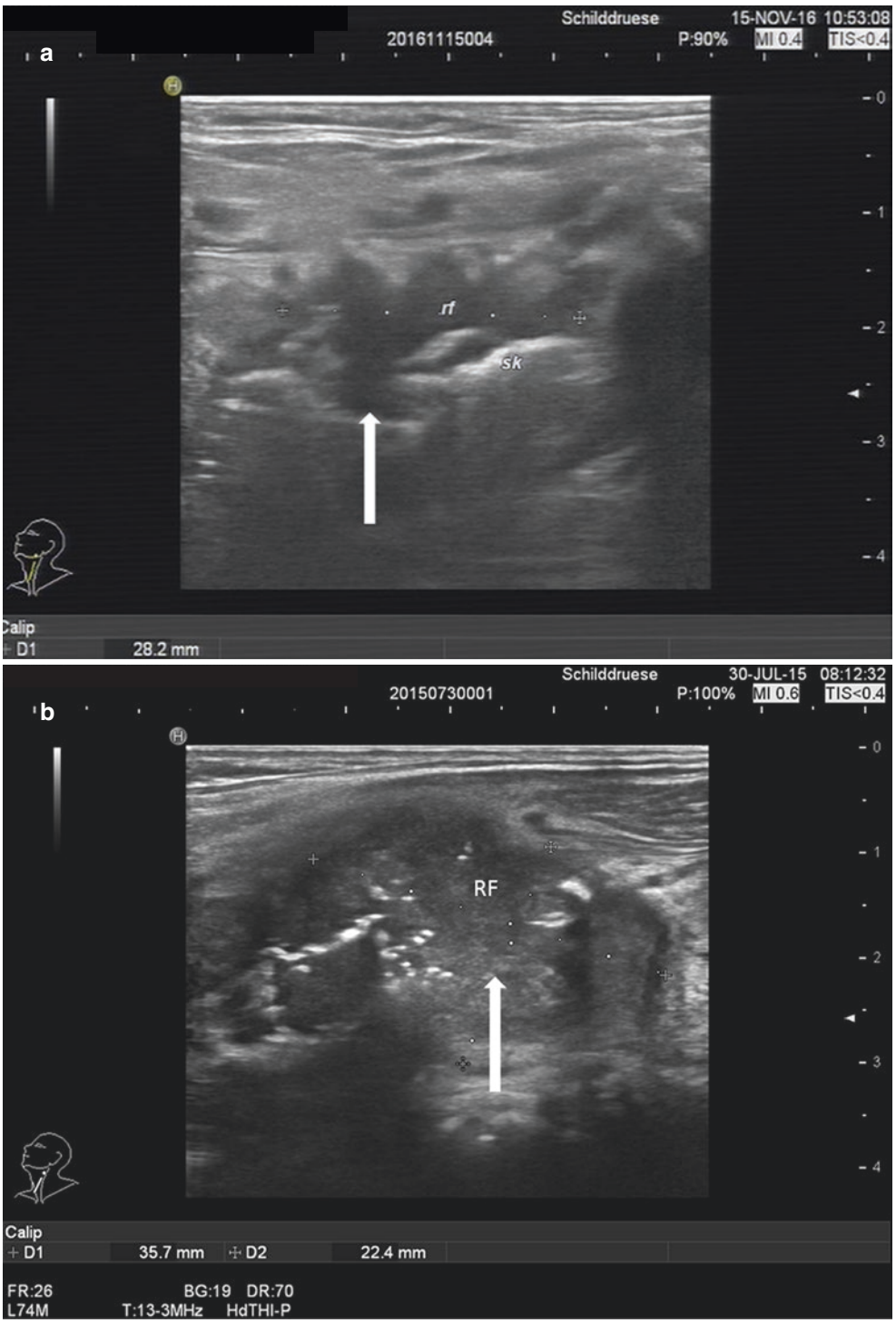

Fig. 7.39 Detection of special situations with ultrasound. (**a**, **b**) Tumor (RF) breaks through thyroid cartilage (sk) (*arrows*). (**b**, **c**) Tumor growth outside of the larynx (*arrows*). (**d**, **e**) Infiltration of the sternocleidomastoid muscle (SCM) (*arrows*) and the thyroid gland (THY). CCA common carotid artery. *Inset* shows corresponding CT

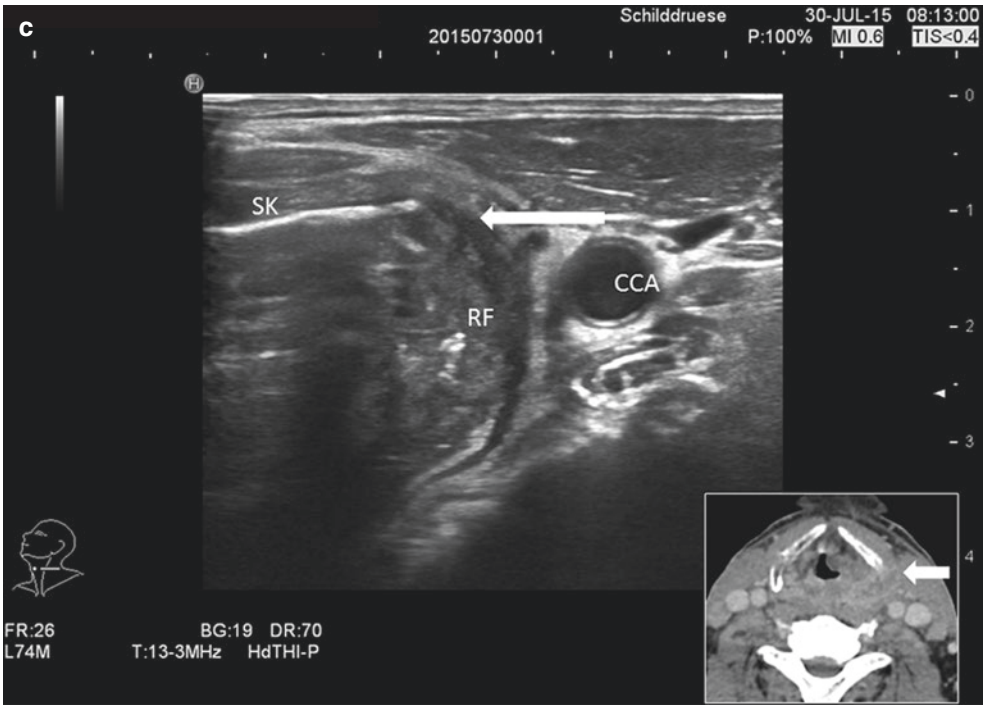

Fig. 7.39 (continued)

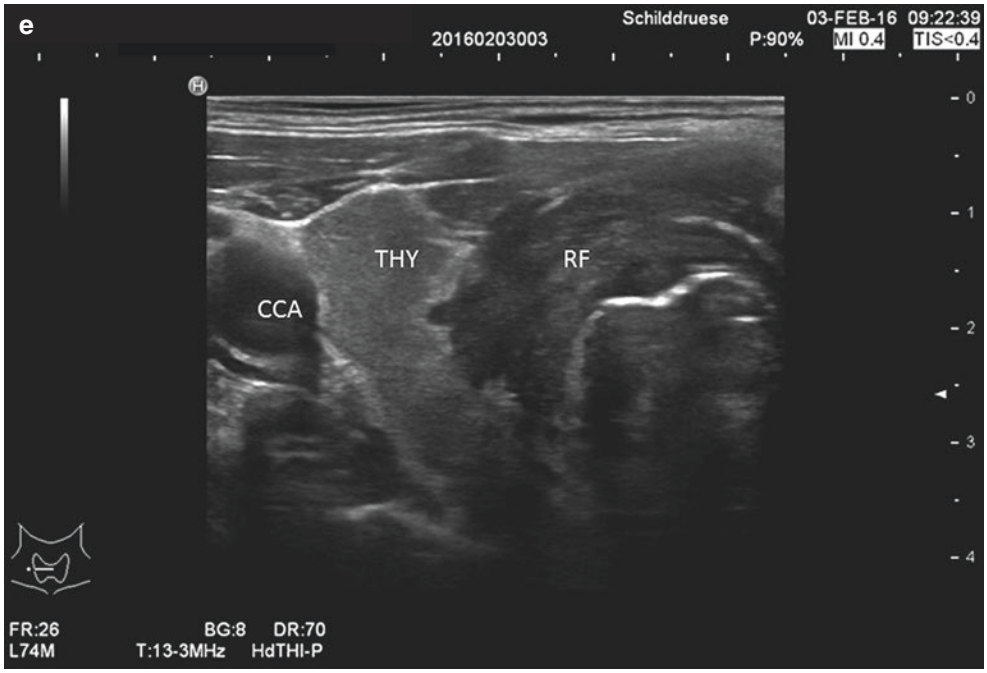

Fig. 7.39 (continued)

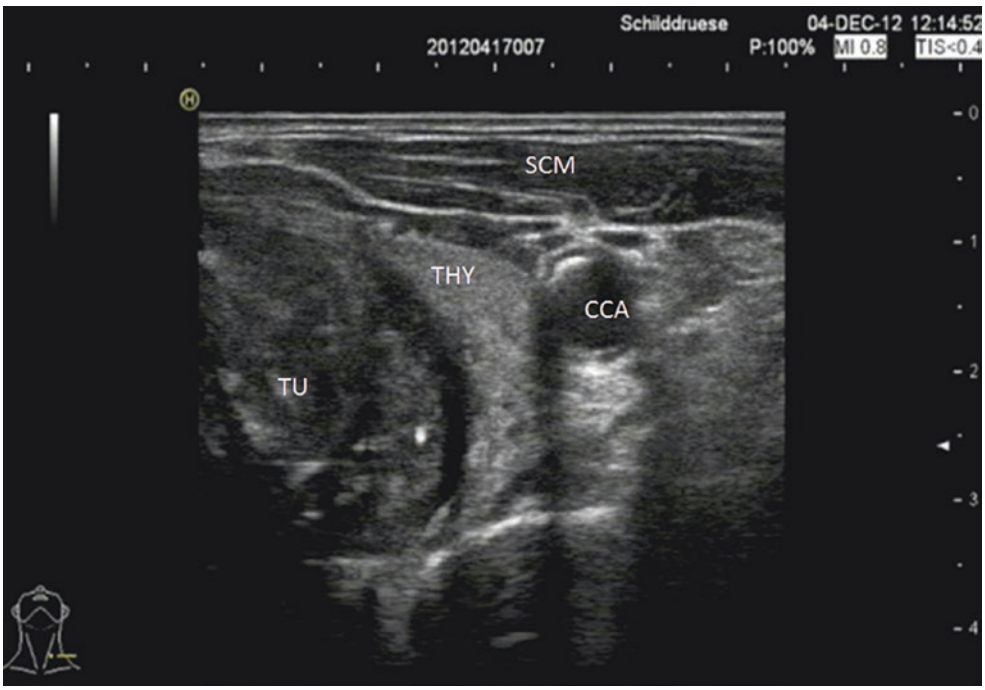

Fig. 7.40 Hypopharynx cancer. The tumor (TU) typically moves the thyroid gland (THY) to the side. CCA common carotid artery, SCM sternocleidomastoid muscle

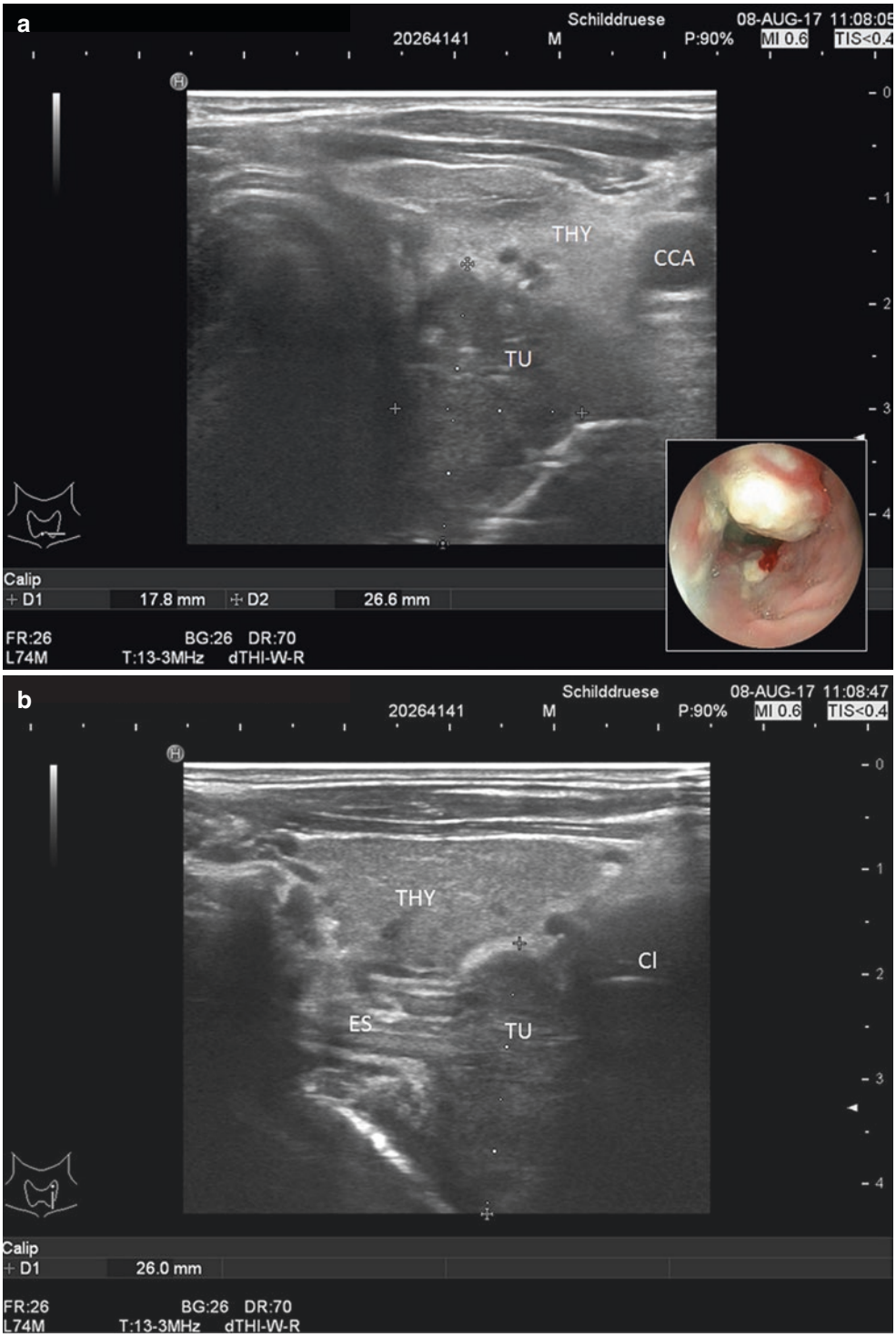

Fig. 7.41 Esophageal cancer (TU), infiltrating the thyroid gland (THY), seen in frontal plane (**a**) and sagittal plane (**b**). CCA common carotid artery, CL clavicle, ES cranial esophagus. *Inset* shows endoscopic finding

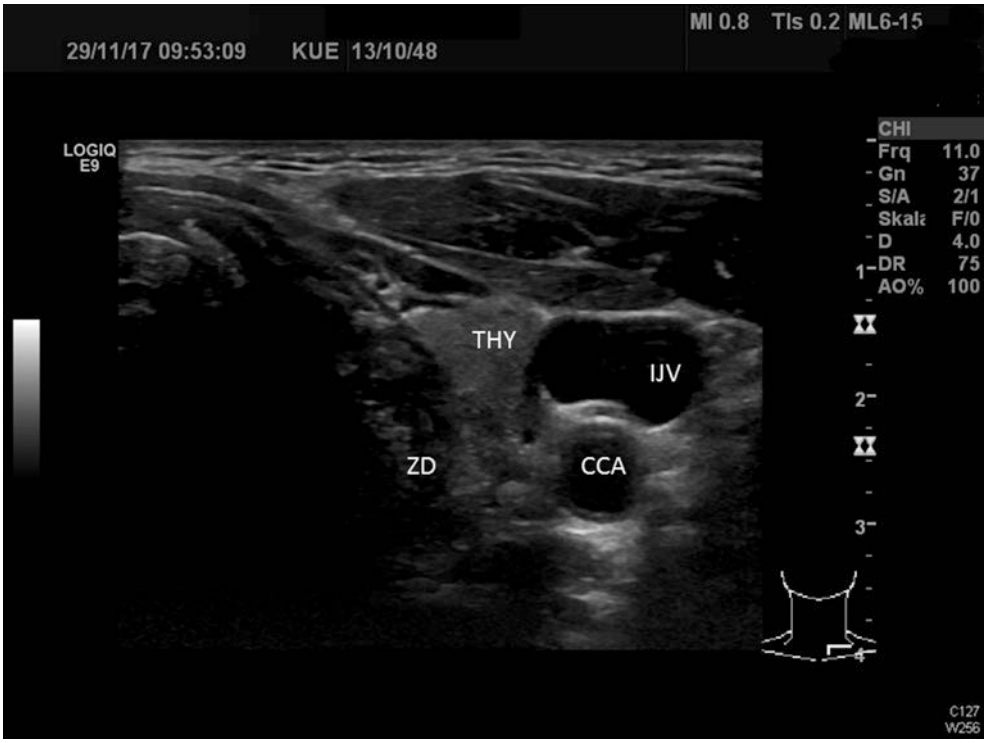

Fig. 7.42 Zenker diverticulum (ZD). CCA common carotid artery, IJV internal jugular vein, THY thyroid

References

1. Welkoborsky HJ, Jecker P, Maurer J, Mann WJ. Ultraschalldiagnostik Kopf-Hals. Stuttgart: Thieme; 2013.
2. Orloff LA. Head and neck ultrasonography. 2nd ed. San Diego: Plural Publishing; 2017.
3. Coquia SF, Hamper UM, Holman ME, DeJong MR, Subramaniam RM, Aygun N, Fakhry C. Visualization of the oropharynx with transcervical ultrasound. AJR Am J Roentgenol. 2015;205:1288–94.
4. Bozzato A, Zenk J, Gottwald F, Koch M, Iro H. Influence of thyroid cartilage ossification in laryngeal ultrasound. Laryngorhinootologie. 2007;86:276–81. German.
5. Gomaa MA, Hammad MS, Mamdoh H, Osman N, Eissawy MG. Value of high resolution ultrasonography in assessment of laryngeal lesions. Otolaryngol Pol. 2013;67:252–6.
6. Jecker P, Seidel J, Mann WJ. Staging of esophageal cancer using ultrasound. Radiologe. 2007;47:115–8. German.

Sonography of Parapharyngeal Masses

8

Courtney M. Tomblinson and Michael L. Hinni

8.1 Introduction

Lesions of the parapharyngeal space (PPS) can be primary or secondary. Primary lesions are limited in number, owing to the paucity of tissues contained within the region. PPS tumors account for only 0.5% of head and neck neoplasms [1]. Of these, 80% are benign and almost half arise from the salivary gland, namely, pleomorphic adenoma [2, 3]. The second most frequently encountered PPS tumors are neurogenic tumors, followed by paraganglioma [4, 5].

8.2 Anatomic Boundaries of the Parapharyngeal Space

The PPS is a potential space that forms an inverted pyramid, extending from the skull base along the inferior surface of the petrous temporal bone superiorly to the greater cornu of the hyoid bone inferiorly [6]. Some authors consider the parapharyngeal space caudal to the mandibular angle to be obliterated and thus regard the styloglossus muscle as a landmark for the inferior boundary [5]. The medial boundary is formed by the superior constrictor muscle and pharyngobasilar fascia. From anterior to posterior, the lateral boundary is formed by the medial pterygoid muscle, mandibular ramus, deep lobe of the parotid gland, and posterior belly of the digastric muscle. The prevertebral fascia forms the posteromedial boundary.

The PPS includes both pre-styloid and post-styloid components, separated by the tensor-vascular-styloid fascia, which extends from the styloid process to the tensor veli palatini [6–8]. Two other fascial layers have been described, the stylopharyngeal aponeurosis or aileron and the cloison sagittale, but controversy exists about their course and how they divide the compartments of the PPS [5]. Given the debate in the literature, these structures are likely to be inconsistent and vary among patients.

The carotid sheath comprises all three layers of the deep cervical fascia and represents a limited barrier between the PPS (laterally) and the retropharyngeal space (medially) [9–11]. This intimate relationship allows for processes traversing one of these spaces to easily enter the other [1].

Anteriorly, the PPS is contiguous with both the masticator and sublingual spaces, with implications for the spread of infection.

8.2.1 Pre-styloid Compartment

The pre-styloid compartment consists predominantly of fat through which traverse the inferior alveolar nerve, lingual nerve, auriculotemporal nerve, and ascending pharyngeal artery. The deep lobe of the parotid gland is directly lateral to the pre-styloid compartment. Salivary gland tumors, the most common parapharyngeal mass, arise in the pre-styloid compartment, displacing the great vessels posteriorly [12], as shown in Fig. 8.1.

8.2.2 Post-styloid Compartment

The post-styloid compartment, consisting largely of structures in the carotid sheath, contains the carotid artery, internal jugular vein, cranial nerves IX–XII, sympathetic chain, and deep lymph nodes.

C. M. Tomblinson
Department of Radiology and Radiological Sciences, Vanderbilt University Medical Center, Nashville, TN, USA

M. L. Hinni (✉)
Department of Otolaryngology–Head and Neck Surgery, Mayo Clinic, Phoenix, AZ, USA
e-mail: hinni.michael@mayo.edu

© Springer Nature Switzerland AG 2019

H. J. Welkoborsky, P. Jecker (eds.), *Ultrasonography of the Head and Neck*, https://doi.org/10.1007/978-3-030-12641-4_8

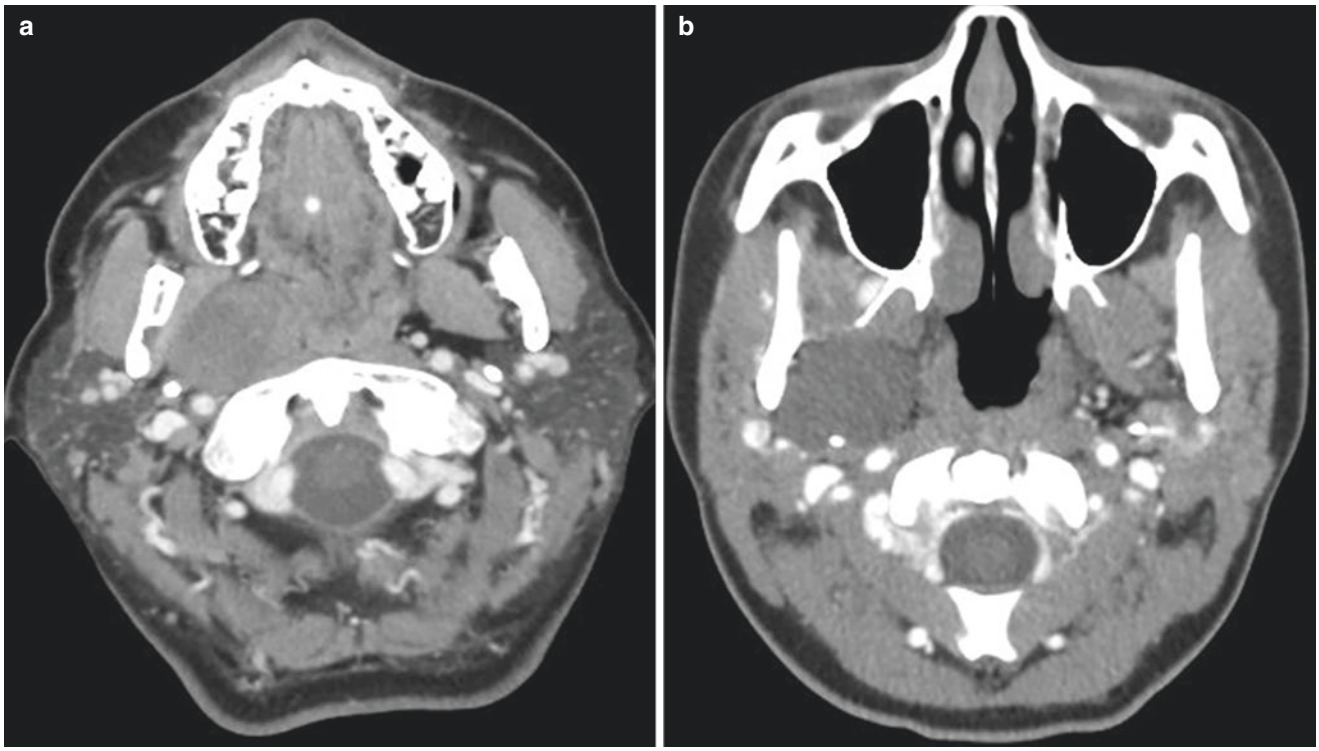

Fig. 8.1 Two patients with right parapharyngeal pleomorphic adenoma. Comparison of parapharyngeal fat plane surrounding the mass (**a**) versus no definitive fat plane with the deep lobe of the parotid (**b**). In both cases, the great vessels are displaced posteriorly, signaling the pre-styloid origin of the tumor. The most common pre-styloid compartment tumor is a benign mixed tumor

8.2.3 Variations in Nomenclature

Historically, the nomenclature of the PPS has remained complex and nonuniform, depending on the era of the study and variance between anatomic descriptions [5, 12–15]. For the purposes of this text, *PPS* is synonymous with the *lateral pharyngeal cleft*, *lateral pharyngeal space*, *pharyngomasticatory space*, *pharyngomaxillary space*, *pterygomaxillary space*, and *pterygopharyngeal space*.

8.2.4 Controversy in Anatomic Boundaries

There is significant controversy over the anatomic boundaries and contents of the PPS. Some experts prefer to divide the PPS into pre-styloid and post-styloid compartments, whereas others consider the post-styloid compartment a distinct entity, equivalent to the carotid space [6]. Specifically, the distinction between the pre-styloid and post-styloid compartments is important to surgeons as they evaluate landmarks for entering the carotid sheath, with the great vessels and cranial nerves lying immediately deep to the complex fascia surrounding this space [5].

Furthermore, fascial defects in the posterior PPS establish continuity with the carotid space. The carotid space and its associated pathologies are sometimes considered to be included in the PPS or to be an extension of it.

For the purposes of this discussion, we will consider both the pre-styloid and post-styloid compartments to be part of the PPS. Lesions in these spaces affect both imaging considerations and surgical approach. It is important to recognize that the literature remains divided on this understandably complex anatomic categorization.

Table 8.1 Primary and secondary lesions of the parapharyngeal space

Primary
Schwannoma
Neurofibroma
Paraganglioma
Lipoma
Vascular malformation
Branchial cleft cyst
Ectopic salivary tumor
Secondary
Deep lobe parotid tumor
Nodal metastasis
Abscess
Carotid artery pseudoaneurysm

8.3 Evaluation of Parapharyngeal Space Masses

Parapharyngeal masses can be primary (arising from structures within the PPS) or secondary (arising from structures external to the PPS but encroaching on it) (Table 8.1). Combined with location in the pre-styloid or post-styloid compartments, this distinction allows the imager to significantly limit the differential diagnosis for the clinician and affects surgical approach. Displacement of the parapharyngeal fat is key (Fig. 8.2). Pre-styloid masses displace the parapharyngeal fat and great vessels posteriorly and often laterally. Post-styloid masses displace the parapharyngeal fat anteromedially. Similarly, masticator space masses push the PPS contents posteriorly. An oropharyngeal squamous cell carcinoma arising from the pharyngeal mucosal space will push the parapharyngeal fat laterally.

8.3.1 Clinical Evaluation

Most patients harboring a parapharyngeal mass present with a neck or intraoral mass (84%), with dysphagia (51%) or ear pressure/pain (36%) the next most common presenting symptoms. Less common symptoms include odynophagia, tinnitus, hoarseness, or obstructive sleep apnea [2, 16, 17]. Many patients are asymptomatic because of the insidious growth in the setting of a benign mass. Frequently, parapharyngeal masses are found incidentally on imaging for other purposes.

8.3.2 Physical Examination

Often, PPS tumors are occult on exam if they are too small to result in mass effect (generally <3 cm). Because of the bony structures surrounding the PPS laterally (mandibular ramus) and superiorly (skull base), tumors tend to grow inferiorly and medially. This medial displacement may result in palatal depression and/or uvular deviation to the contralateral side (Fig. 8.3). Hughes et al. reported that 66% of patients in their series had palate displacement, 58% had a palpable mass posterior to the mandibular angle, and only 28% had both [2]. A different series, by Miller et al., noted 59% with an intraoral mass and 20% with a neck mass [18]. Bimanual palpation may allow assessment of mass mobility if the mass is large enough. Unfortunately, these tumors are generally too deep to assess for mobility and compressibility, factors that help the clinician decide the likelihood of malignancy in other areas of the head and neck.

Cranial neuropathies of the glossopharyngeal, vagus, spinal accessory, or hypoglossal nerves may result from primary involvement of the nerve (glomus vagale, vagal schwannoma, or neurofibroma) or secondarily from extrinsic compression (branchial cleft cyst or salivary gland tumor) [19]. Often, this manifests as hoarseness in patients with vagus nerve involvement. Of the patients with cranial neuropathy in the Hughes et al. series [2], almost half were related to malignancy. Facial pain and jaw pain in combination with a cranial neuropathy raise concern for malignancy [2, 18].

8.3.3 Family History

In the setting of a newly identified paraganglioma, the clinician should elicit a family history, in search of a hereditary syndrome involving paraganglioma. Although most paragangliomas are sporadic, bilateral paragangliomas can be either sporadic or hereditary. Bilateral carotid body tumors occur in 5–14% of sporadic tumors and 26–33% of familial cases [5].

8.4 Diagnostic Imaging

For parapharyngeal masses, the goals of imaging include evaluating the inherent properties of the tumor (size, location, vascularity, and echotexture or signal characteristics), lesion extent and resectability, and relationship to important structures, such as the carotid artery.

Ultrasonography is quick, readily available, inexpensive, noninvasive, and without the radiation exposure of CT scans. This makes ultrasound a logical first step in evaluation of head and neck masses, particularly in children and in patients with large masses. Contrast-enhanced CT is fast, less expensive, and more accessible than MRI. CT can also be performed in patients with contraindications to MRI, such as implanted medical devices or hardware. MRI affords much higher contrast resolution of soft tissues, although at the expense of both time and cost. Pre-contrast T1-weighted nonfat-saturated images are very useful for assessing the fat displacement in the PPS [6]. Most authors agree that, overall, MRI is superior to CT for evaluation of parapharyngeal masses [20–22].

Despite radiation exposure and need for sedation, some authors advocate for CT over ultrasound in the evaluation of pediatric parapharyngeal abscess because of ultrasound's low sensitivity (33%) and low positive predictive value (50%) in one series [23].

Pan et al. compared ultrasound to MRI for evaluation of nasopharyngeal carcinoma invasion into the PPS; the reported sensitivity of ultrasound was 97.8%, with 41.7% specificity [24]. They also concluded that MRI is superior for defining the full extent of invasion and delineating boundaries of the nasopharynx. MRI has been shown to be superior to PET/CT in the setting of nasopharyngeal carcinoma [25].

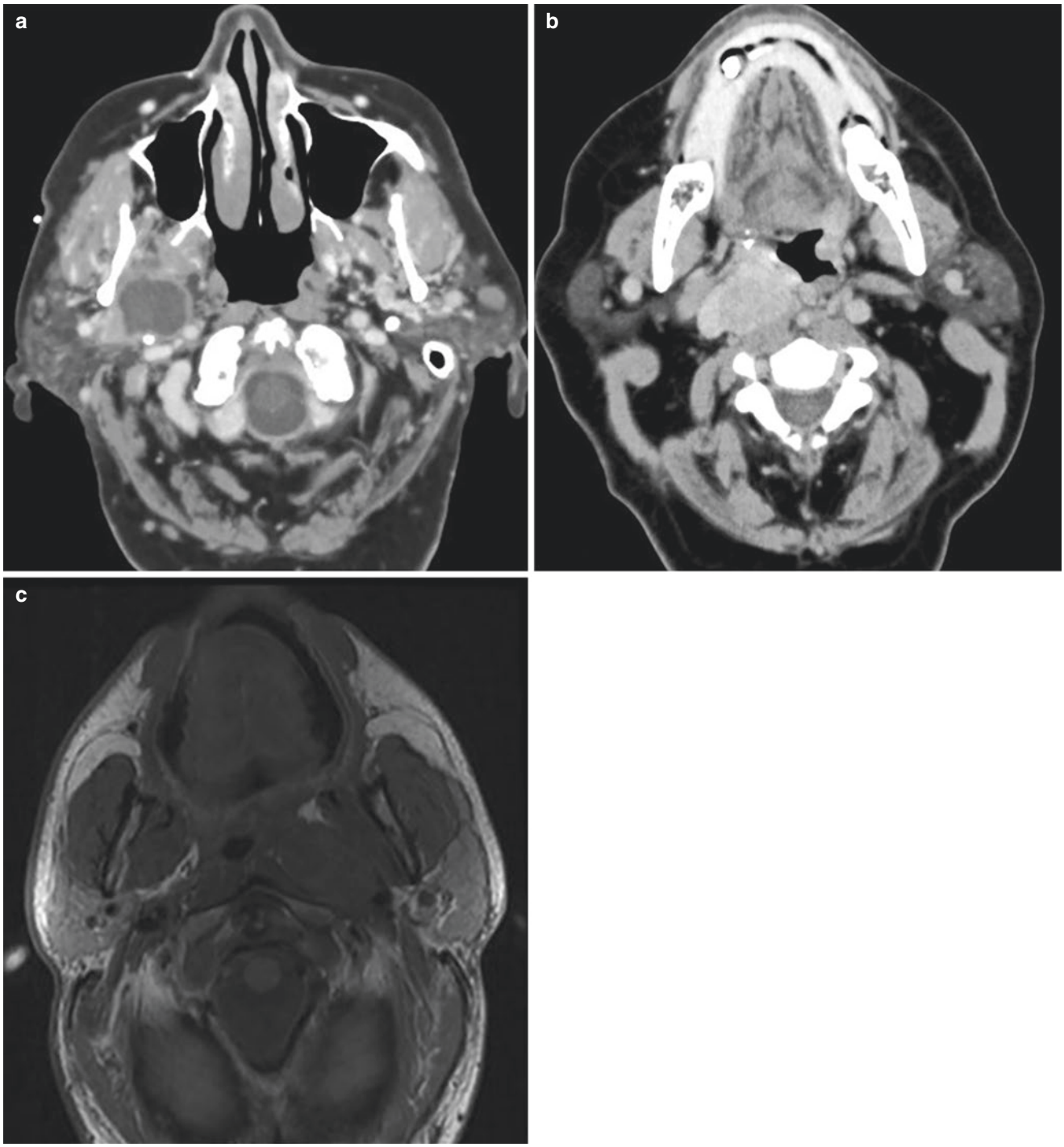

Fig. 8.2 Three patients with different parapharyngeal tumors, each resulting in variable displacement of the parapharyngeal fat, which serves as a key to the space of origin. (**a**) Contrast CT reveals a predominantly cystic right parapharyngeal lesion contiguous with the deep lobe of the parotid gland, displacing parapharyngeal fat medially toward the nasopharynx. At resection, this was proven to be an oncocytic cystadenoma. (**b**) In this 80-year-old woman, a solidly enhancing homogeneous mass displaces the parapharyngeal fat laterally and posteriorly on CT scan. This was a glomus vagale tumor. (**c**) Axial T1-weighted noncontrast MRI demonstrates a circumscribed mass in the left parapharyngeal space, displacing the parapharyngeal fat anteriorly. This represents a vagal schwannoma

Fig. 8.3 Before (*left*) and after (*right*) parapharyngeal tumor resection via a combined transcervical-transparotid approach. The underlying lesion was myoepithelial carcinoma

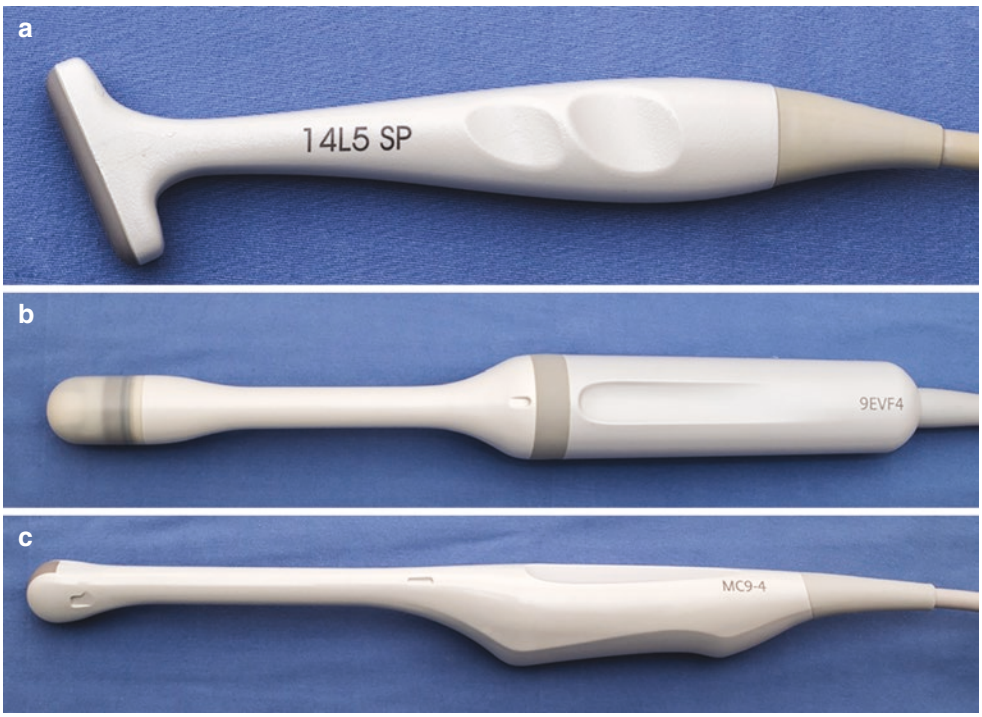

Fig. 8.4 Ultrasound transducers. (**a**) Small-part, high-frequency "hockey stick" transducer, typically used in thyroid and musculoskeletal imaging. (**b**) 3D endocavitary transducer; this probe has a large footprint but allows for 3D volumetric acquisition. (**c**) Smaller 2D endocavitary probe. Both endocavitary transducers allow for beam steering and can reach more lateral tumors

Catheter angiography may be useful in discerning paraganglioma and for pre-op embolization to minimize blood loss during surgery.

In^{111}-pentetreotide and newer Ga^{68}-DOTA-conjugated peptides bind to somatostatin receptors in paragangliomas with pooled sensitivity of 89% and >95%, respectively [26]. The conjugated peptides are relatively new, and further studies are needed to draw more substantial conclusions. These nuclear studies can be particularly useful to localize lesions outside the head and neck if there is concern about multifocality or a hereditary syndrome.

8.5 Sonographic Technique

Sonographic evaluation of the PPS can be challenging, given the deep location and bony structures with only a narrow window between them. To optimize visualization, select a

high-frequency linear transducer with a small footprint to begin. The authors recommend transducer frequencies of 7–15 MHz, found within a small-part linear probe, similar to one often used for thyroid imaging (Fig. 8.4a). The high-frequency transducers intrinsically possess better axial resolution to discern structures along the beam path. A small footprint allows the sonographer to slide into the notch posterior to the mandibular ramus and anterior to the most cranial portion of the sternocleidomastoid muscle and mastoid tip [9, 24]. This interval can be opened further by turning the patient's head slightly away from the transducer or by protrusion of the mandible. Alternative to the small parts probe, a pediatric probe (also with a small footprint) may be useful.

Patients should be imaged in the semi-upright position with a bed incline of approximately 70°, with the head resting on a pillow and the neck mildly extended. This position is the same for either an external percutaneous approach or an intraoral endocavitary approach. If planning to pursue an intraoral approach, administration of topical anesthetic spray (Cetacaine™ - 14% benzocaine, 2% butamben, 2% tetracaine hydrochloride) is helpful to diminish the gag reflex (Fig. 8.5). While allowing adequate time for the anesthetic to take effect, attempt a percutaneous scan from an external approach. To locate the PPS, begin in a longitudinal plane posterior to the angle of the mandible, orienting the transducer medially and anteriorly. Identify the great vessels and then angle slightly more anterior. At this point, one may see the deep lobe of the parotid in view. This is the pre-styloid compartment; it can be exceptionally difficult to visualize, depending on the age and body habitus of the patient. Turn the probe into the transverse plane and attempt a similar trajectory.

After completing an external percutaneous approach through either a retromandibular or submandibular window, one may consider an intraoral examination in the appropriate clinical setting [27, 28]. The intraoral sonogram allows for identification of structures that may be obscured with an external approach and can assist in preoperative planning, particularly if a transoral surgery is considered. For intraoral sonography, we recommend either the small-part probe (similar to the probe used for thyroid assessment) or an endocavitary probe (such as those used for prostate or endovaginal ultrasound) (Fig. 8.4). The 3D endocavitary probes allow for beam steering, related to the phased firing of piezoelectric crystals in the array. This is useful for tumors that may be more lateral in the PPS, where a straight beam may not reach the lesion, such as a mass in the deep lobe of the parotid gland.

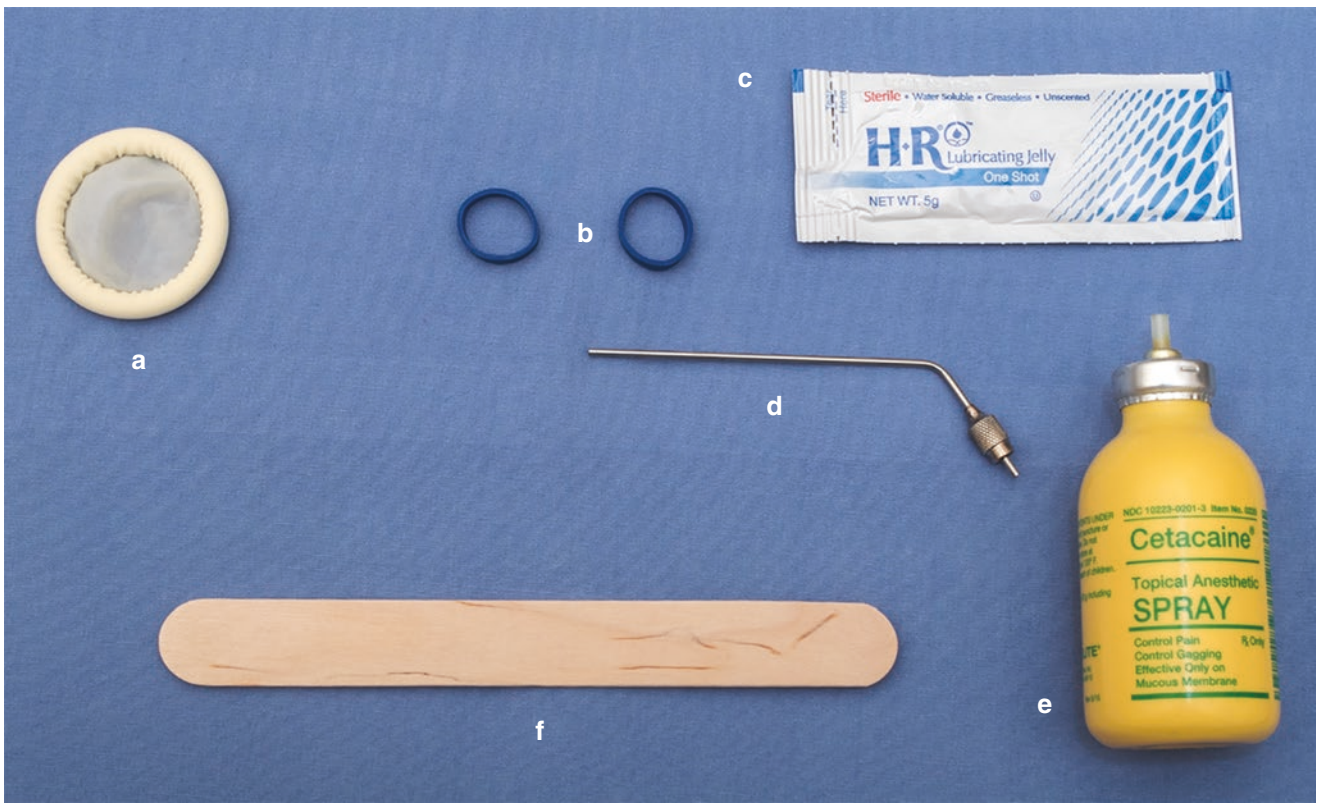

Fig. 8.5 Ancillary supplies for intraoral sonography. (**a**) Latex sheath to cover the ultrasound probe. (**b**) Sterile rubber bands to secure the sheath in place. (**c**) Sterile lubricant to create contact interface on the latex sheath. (**d**) Spray tip for topical anesthetic. (**e**) Topical anesthetic for the oropharynx. (**f**) Tongue depressor, if needed

Place gel on the selected transducer. Apply a latex sheath, and use a medical-grade rubber band to keep the sheath taut. Apply a scant amount of lidocaine gel to the external surface of the sheath. Next, instruct the patient to lay his or her head against the pillow, still in the semi-upright position. With the mouth open, gently direct the ultrasound probe toward the anesthetized side of the oropharynx. Instruct the patient to breathe through the mouth while the transducer is in the oropharynx. The most superficial structure encountered will be the pharyngeal mucosa, a thin, echogenic band. Scanning in the craniocaudal direction can give an appreciation of the orientation of the pterygoid musculature and great vessels [29]. This approach is particularly helpful for medial parapharyngeal masses, but it may prove more challenging in patients with a strong gag reflex and for masses suspected to arise from the deep lobe of the parotid gland.

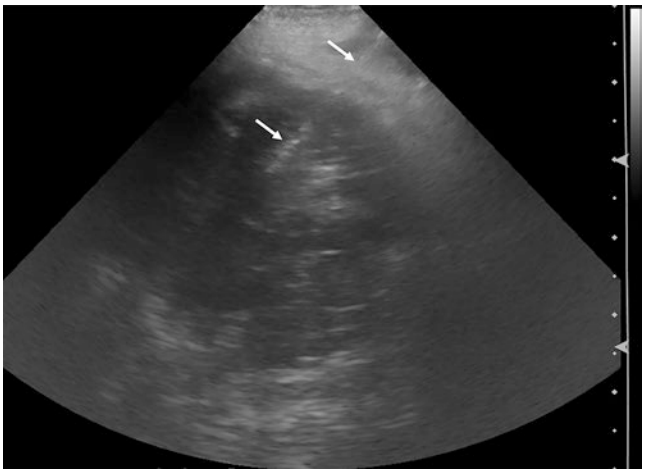

Fig. 8.6 Grayscale image demonstrating the linear echogenic needle in-plane during biopsy of a large right parapharyngeal mass. Pathology showed myoepithelial carcinoma (same patient as Fig. 8.3)

8.5.1 Grayscale Images

Grayscale sonographic images are obtained to assess the margins, echogenicity, internal characteristics, and adjacent soft tissue structures.

8.5.2 Doppler Images

Color Doppler images allow assessment of relative vascularity, feeding vessels, and relationship of parapharyngeal masses to adjacent vascular structures. Spectral Doppler can be used to evaluate waveforms in the lesion to determine if arterial or venous supply is present.

8.5.3 Sonographic Approach

For large or lateral parapharyngeal masses, such as those arising from the deep lobe of the parotid gland, an external percutaneous approach from either a retromandibular or submandibular location may be feasible. In children, a submental approach has been demonstrated for evaluation of peritonsillar and parapharyngeal abscesses [30]. Smaller or more medial lesions may necessitate intraoral sonography using an endocavitary probe, as described above.

8.5.4 Biopsy and Intervention

Sonography has been a useful adjunct in guidance for fine needle aspiration (FNA) [31]. Ultrasound-guided FNA is a safe method for acquiring tissue. After finding a trajectory and sterilizing the overlying skin, a 25-gauge noncutting needle attached to a 10-mL syringe is passed toward the lesion. The tip of the needle should be kept in the plane of the ultrasound beam at all times (Fig. 8.6). Longer needles may be necessary to reach the PPS, depending on the depth and size of the lesion. Once the needle tip is within the lesion, gentle suction can be applied to the syringe, with the needle gently and fluidly moved through the mass four or five times [5]. The contents are placed on a glass microscope slide and affixed in 70% ethanol or air-dried, depending on local pathologist preference.

Dim et al. reported the use of endoscopic ultrasound-guided FNA to diagnose a ganglioneuroma in a 75-year-old man with a history of lung cancer [32]. Under general anesthesia, an endocavitary probe equipped with core needle biopsy successfully diagnosed a pleomorphic adenoma of the PPS after an unsuccessful percutaneous attempt [28]. In this case, the tumor was so large that it presumably compressed the right internal carotid artery over a long period of time and resulted in carotid dissection and stroke, which led to cross-sectional imaging and identification of the parapharyngeal tumor.

Wong et al. describe their experience with three patients in whom different histologic types of tumor were diagnosed via intraoral ultrasound-guided biopsy [33]. In addition to FNA, ultrasound-guided core biopsy has also shown to be an effective diagnostic tool without a significantly increased complication rate [5].

Percutaneous ultrasound-guided drainage of head and deep neck abscess has been found to be a safe and effective treatment in select patients, with decreased length of hospital stay and avoidance of surgical complications [34, 35]. However, if the etiology of recurrent deep fluid collection is an underlying congenital lesion, such as branchial cleft cyst, then definitive surgical treatment is recommended [36].

Ultrasound can be used as an adjunct in PPS foreign body removal and has been reported to decrease operation time [37].

Preoperative embolization of feeding vessels to paraganglioma has been an adjunct to minimize blood flow to tumors in an attempt to decrease blood loss at the time of surgery [38].

8.6 Space-Based Differential Diagnosis

When evaluating imaging findings of a parapharyngeal mass, several questions should be asked to assist in narrowing the differential diagnosis:

- Is the mass primary or secondary? To answer this question, look for a rim of parapharyngeal fat circumferentially around the mass. If there is one (as in Fig. 8.1a), you are likely to be dealing with a primary PPS lesion. If not (as in Fig. 8.1b), you are most likely dealing with an external mass encroaching upon or invading the PPS.
- What direction is the parapharyngeal fat displaced (*see* Fig. 8.2)? If the fat is medial, the lesion arises from the parotid gland. If the fat is posterior, the lesion arises from the masticator space. If the fat is lateral, the lesion arises from the oropharyngeal mucosa or tonsil. If the fat is anterior, the lesion arises from the carotid space.
- Where are the great vessels? Together or separated? If the internal carotid artery (ICA) and internal jugular vein (IJV) are splayed, you may be dealing with a vagal schwannoma or glomus tumor. To distinguish between them, look at vascularity with color Doppler ultrasound and/or MRI (see below). If the great vessels are displaced together in an abnormal direction, the cause could be related to several entities, also discussed below.

8.7 Primary Lesions

Primary lesions of the PPS arise from fat, salivary gland rests, neural or venous structures, or congenital remnants.

8.7.1 Schwannoma

Schwannomas of the PPS most commonly affect the vagus nerve (12% of PPS masses) and the cervical sympathetic chain (6%) [18]. Similar to other neurogenic tumors, schwannomas present as a slowly enlarging neck mass, with or without nerve deficits.

Neurogenic tumors appear as fusiform, hypoechoic, well-circumscribed oval masses contiguous with the adjacent nerve. Posterior acoustic enhancement is common. The entering and exiting nerves can be thickened, and this appearance can result in a tapering of the oval mass [19]. Striations within the nerve fascicles may be visible.

The imaging characteristics of schwannomas of the sympathetic chain and the vagus nerve are similar, but some clues allow us to pinpoint the nerve of origin. The sympathetic chain lies posteromedial to the carotid sheath, so a sympathetic chain schwannoma will usually displace the great vessels anterolaterally. The superior aspect of the sympathetic chain lies slightly medial to the anterior margin of the carotid sheath. Though most schwannomas of the sympathetic chain displace the ICA anterolaterally, the mass can slip between the sheath and the pharyngeal wall, resulting in posterior displacement of the ICA, giving the appearance of origin in the pre-styloid compartment [5] (Fig. 8.7).

The vagus nerve, on the other hand, lies within the carotid sheath between the ICA and IJV, so a vagal schwannoma will displace the IJV laterally, while the ICA is pushed medially, so a separation of these vessels is seen on imaging (Fig. 8.8) [39, 40]. To further distinguish a vagal schwannoma from a glomus vagale, one can use color Doppler flow on ultrasound and MRI to assess for flow voids in a glomus tumor.

8.7.2 Neurofibroma

Even with advanced imaging techniques, differentiating schwannoma from neurofibroma remains difficult. Neurofibromas are typically echogenic and often display a *target sign* of alternating hyperechoic and hypoechoic bands [29]. When the nerve of origin is in question, it has been shown that the high spatial resolution of sonography can assist in tumor localization to the vagus nerve [19]. The same group also found that the appearance of the normal vagus nerve changes depending on transducer frequency. At lower frequencies of 7.5–10 MHz, the nerve appeared cord-like and centrally hypoechoic, but at higher frequencies of 13–15 MHz, the hypoechoic parallel fascicles were visibly separated by a hyperechoic sheath [19].

8.7.3 Paraganglioma

Paragangliomas are a type of neuroendocrine tumor with slow growth, which occasionally present as palpable, pulsatile masses. Three main types (in order of incidence) exist in the head and neck: glomus vagale, carotid body tumor, and glomus jugulare. Paragangliomas have an elevated incidence in high-altitude populations; this increase is postulated to result from the effect of chronic hypoxia on chemoreceptors [41,

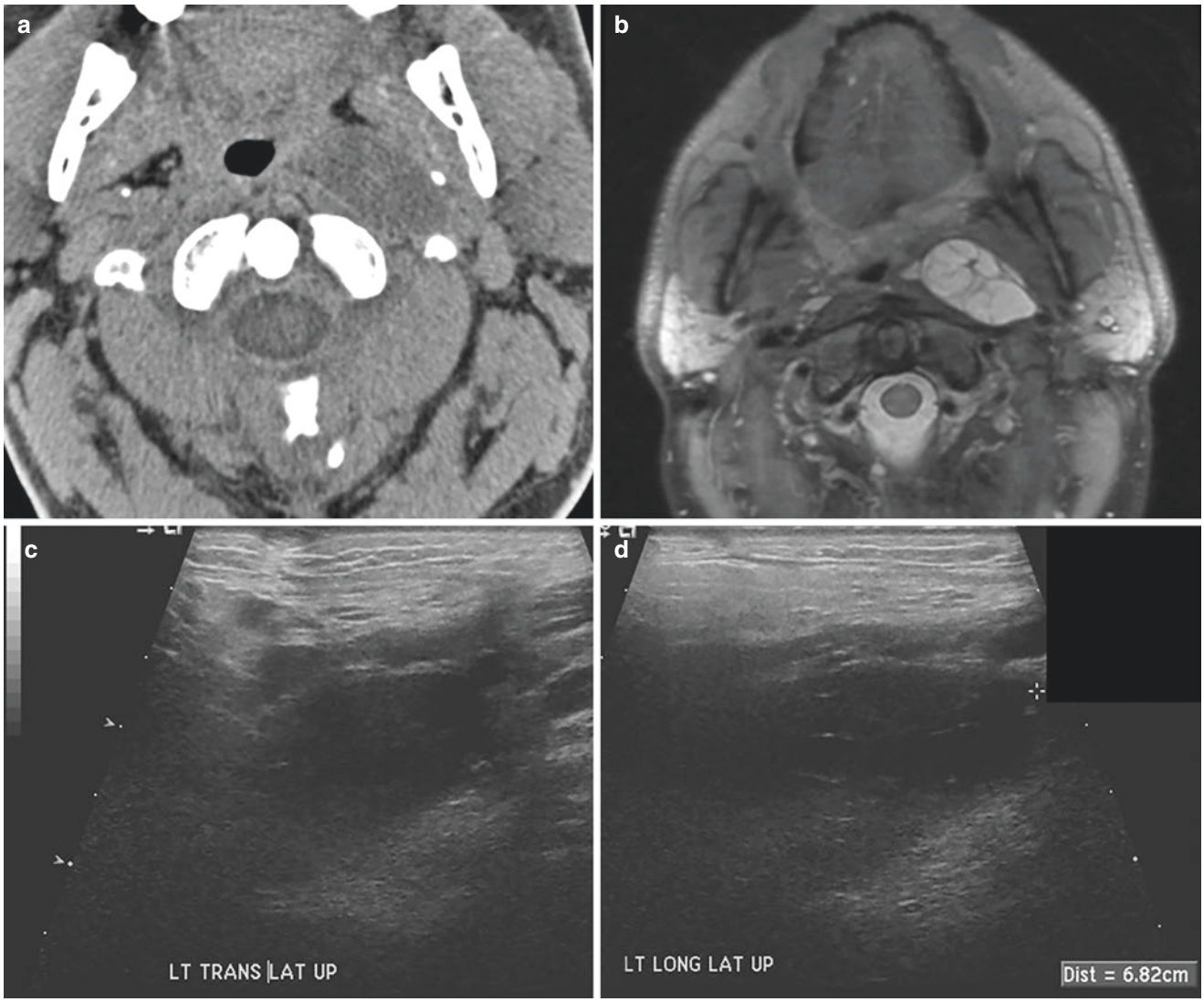

Fig. 8.7 Schwannoma with cystic degeneration. (**a**) Axial noncontrast CT demonstrates a well-circumscribed cystic mass in the left parapharyngeal space and medial to the styloid process. The parapharyngeal fat is displaced anteriorly. (**b**) Axial T2-weighted MRI demonstrates a multiseptated, well-circumscribed cystic mass anteromedial to the carotid artery. This finding raises suspicion of a sympathetic chain schwannoma because the sympathetic chain can be more medial than posterior in the upper parapharyngeal space (PPS). (**c** and **d**) Grayscale sonographic images in the transverse and longitudinal planes demonstrate thin septations throughout the mass, corresponding to the multicystic appearance on MRI

42]. On physical exam, most paragangliomas are immobile in the cephalocaudal direction. Vocal cord paralysis was seen in 66% of patients in one series [18]. Paragangliomas have a high rate of bilaterality, so when a single paraganglioma is identified, regardless of symptoms, evaluation of the contralateral neck should be undertaken to exclude a second tumor [5].

On ultrasound, paragangliomas are well-defined, round or oval, hypoechoic masses. They may have bands of internal hyperechogenicity related to intervening stroma [29]. Tubular, hypoechoic structures represent vessels coursing through the mass. Color Doppler imaging demonstrates a rich vascular bed surrounding and within the tumor, corresponding to their avid enhancement on cross-sectional imaging.

Glomus vagale is typically located within 2 cm of the skull base. Similar to other paragangliomas, which are richly hypervascular lesions, the glomus vagale contains flow voids on MRI. These two features allow differentiation from vagal schwannoma, which are not located as superiorly in the PPS and do not possess flow voids (*see* Fig. 8.8) [7]. Glomus vagale may present with vocal cord paralysis or aural fullness due to pressure on the nearby eustachian tube [11].

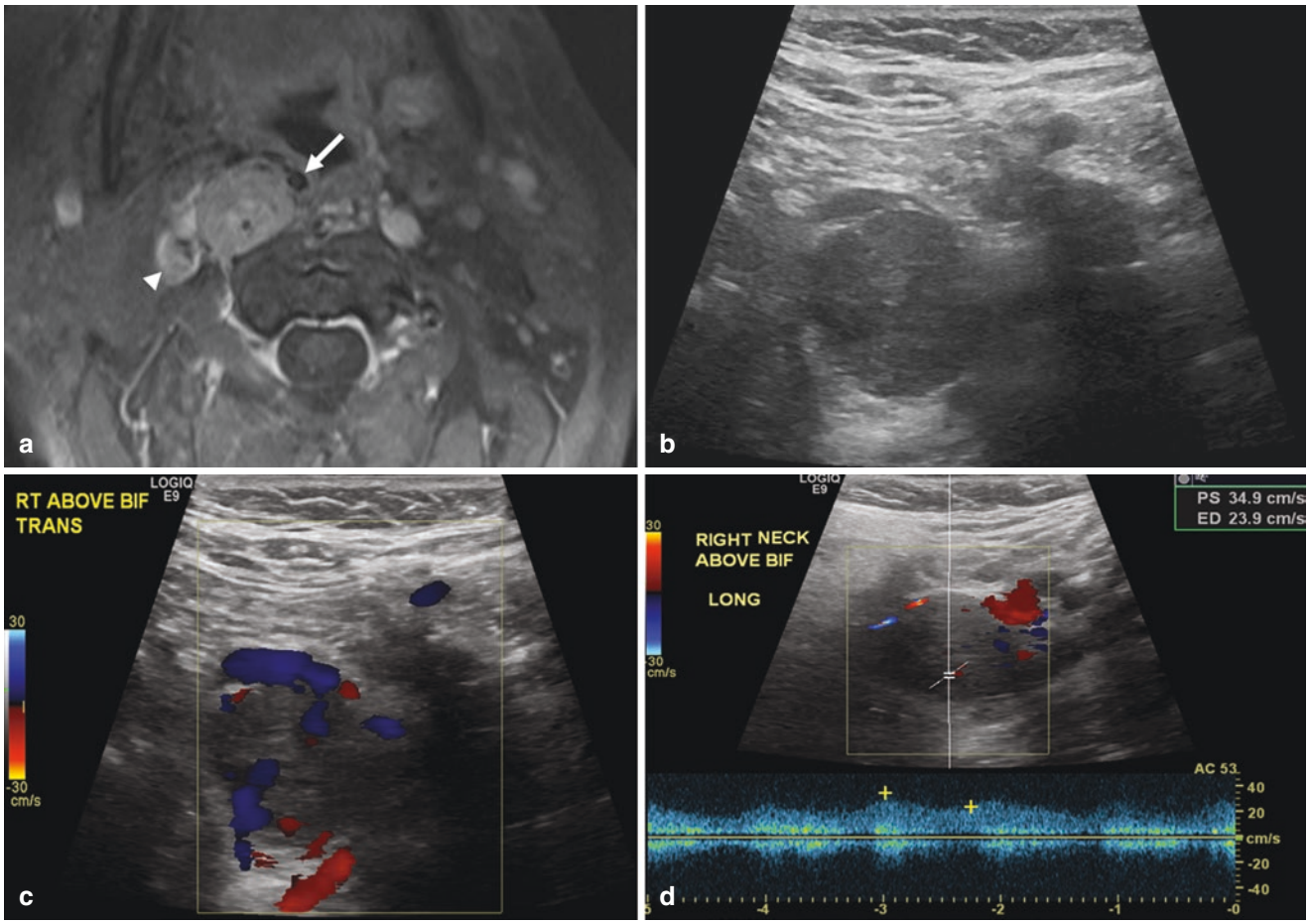

Fig. 8.8 A case highlighting a diagnostic imaging dilemma of vagal paraganglioma versus schwannoma. (**a**) Both tumors may result in displacement of the carotid artery medially (*arrow*) and the internal jugular vein posterolaterally (*arrowhead*). Typically, a glomus vagale will be within 2 cm of the skull base near the nodose ganglion. This lesion is within centimeters of the carotid bifurcation, lower than would be expected for a glomus vagale, but not in the appropriate location for a carotid body paraganglioma. (**b**) Grayscale sonogram demonstrates a well-circumscribed mass deep in the neck with a vessel overlying the superficial margin. A color Doppler image (**c**) and spectral image (**d**) confirm robust internal phasic flow. The adjunctive findings on MRI suggested glomus vagale, but the patient was lost to follow-up without tissue diagnosis

Carotid body tumors originate in the carotid body at the crux of the bifurcation. Because of the inherent location of the carotid body, tumors of this neuroendocrine organ result in splaying of the internal and external carotid arteries, a classic appearance on imaging known as the *lyre sign* (Fig. 8.9).

Sonography demonstrates an overall hyperechoic mass, possibly containing striations or hyperechoic feathering. Some lipomas are well defined within a pseudocapsule, but others are poorly defined. No significant flow is appreciated on color Doppler imaging.

8.7.4 Lipoma

The principal tissue type of the PPS is fat, which may serve as origin for a lipoma. Although 13% of all lipomas occur in the head and neck, only 1–2% occur in the PPS [18, 43, 44]. These tumors are soft, pliable, and insidious. They may displace adjacent parapharyngeal structures, such as the great vessels, but do not compress them.

8.7.5 Vascular and Lymphatic Malformations

Vascular malformations of the PPS are exceptionally rare, reported as less than 1% of PPS tumors [13]. Previously, many of these lesions were reported as "hemangioma," although we now recognize many of these to be classified elsewhere as we gain a greater appreciation of the breadth of benign vascular lesions [45]. Lesions can be further

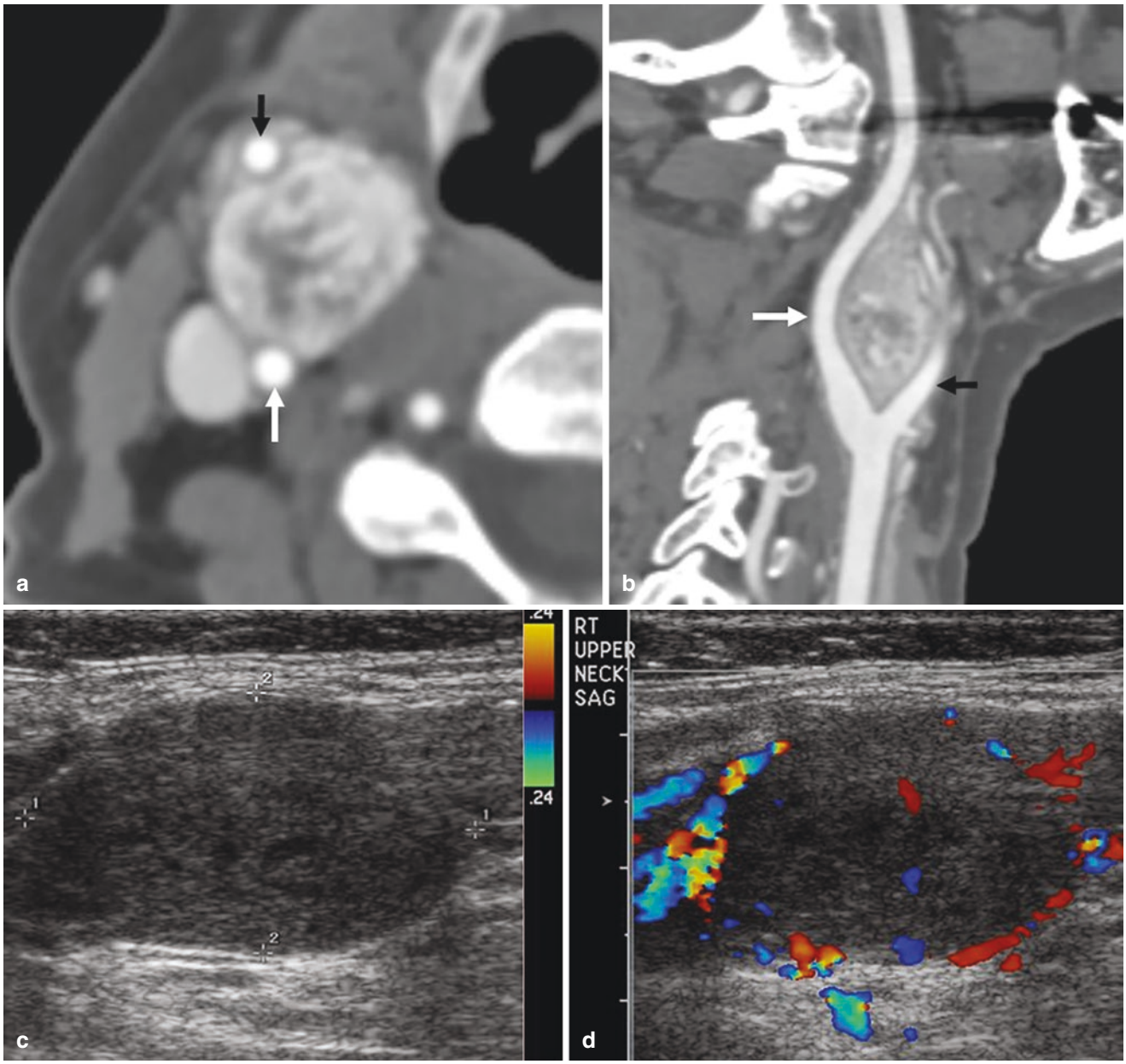

Fig. 8.9 Carotid body paraganglioma. Axial (**a**) and sagittal (**b**) maximum intensity projection CT angiography demonstrates splaying of the external carotid artery (*black arrow*) and internal carotid artery (*white arrow*), known as the *lyre sign*. The external carotid artery is displaced anteriorly, while the internal carotid artery is displaced posteriorly. (**c**) Grayscale sonographic image demonstrates an ovoid, hypoechoic mass with tubular anechoic structures inside. (**d**) Color Doppler image demonstrates positive internal flow, which was noted to be intensely pulsatile on real-time imaging. This lesion was resected, and pathology confirmed paraganglioma

subdivided into high-flow and low-flow vascular malformations. Vascular malformations typically are multiseptate, with heterogeneous echogenicity with intervening hyperechoic trabecular bands. Low-flow lesions, such as a venous malformation, demonstrate scant internal flow (Figs. 8.10 and 8.11). Hemangiomas may be intensely hypervascular, demonstrating a tangle of small blood vessels [29].

Primary lymphatic malformations of the PPS are rarely reported. More likely, these lesions are transspatial and involve the PPS secondarily. Historically, these lesions were called *cystic hygroma*, but that nomenclature has fallen out of favor. Composed of dilated lymphatic vessels, these lesions do not involute but rather expand or contract depending on cycles of repetitive internal hemorrhage, inflammation and/or superinfection, and the volume of lymphatics.

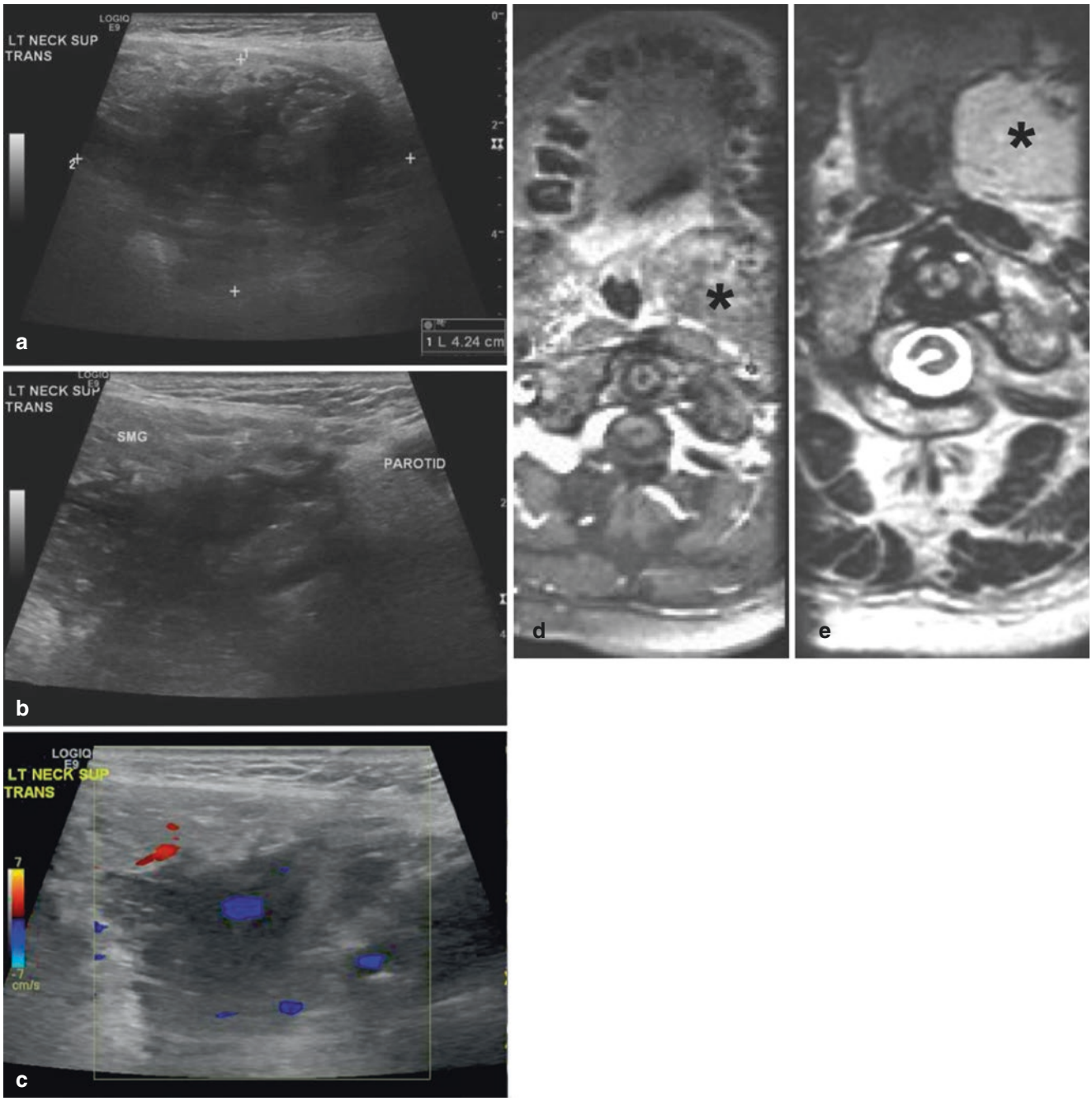

Fig. 8.10 Vascular malformation. (**a** and **b**) Grayscale ultrasound images from an external approach near the mandibular angle demonstrate a mixed echogenicity mass with irregular borders and the suggestion of internal debris and/or septation. (**c**) Low-velocity flow was present internally on color Doppler images. No shadowing stones were identified. (**d**) An axial T1-weighted post-contrast image demonstrates a large mass (*asterisk*) with heterogeneous enhancement in the left parapharyngeal space. The great vessels are posterior to the mass. (**e**) Axial T2-weighted MRI demonstrates that the mass (*asterisk*) is uniformly T2-hyperintense. This mass was a vascular malformation and was observed with serial imaging

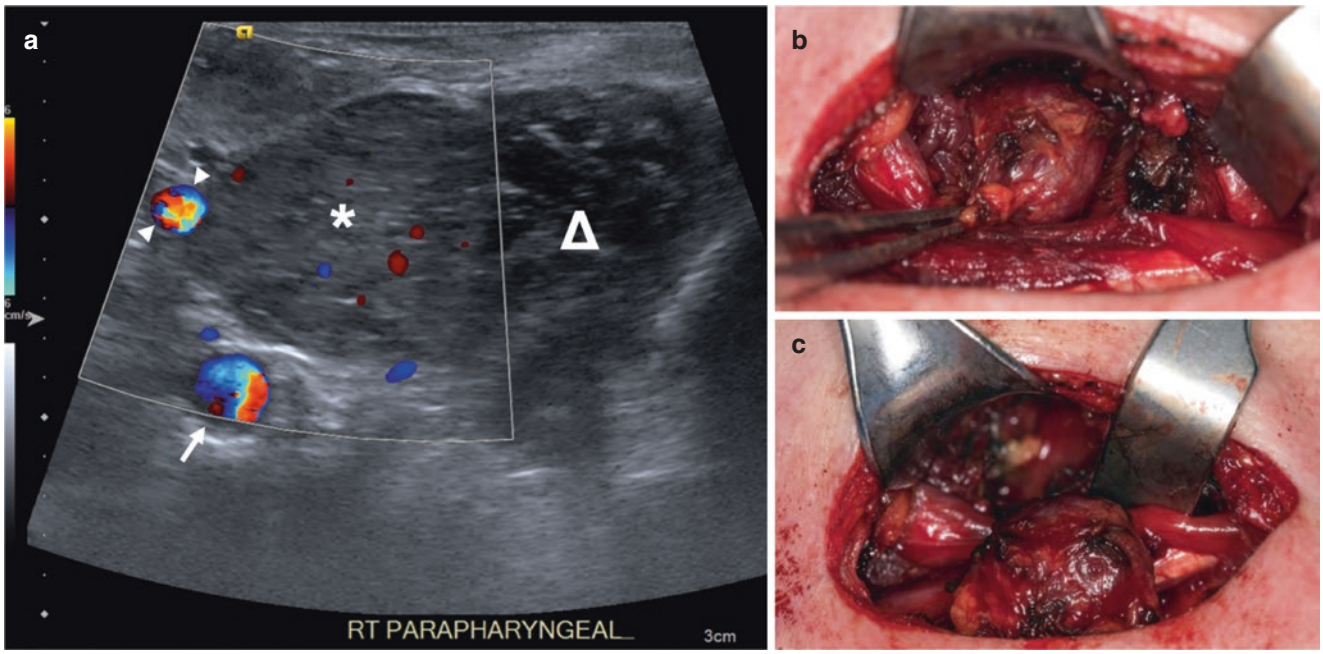

Fig. 8.11 (**a**) Venous malformation of the right parapharyngeal space visualized with intraoral sonography. Note the relationship of the internal maxillary artery (*white arrowheads*) and internal carotid artery (*white arrow*) abutting the posterolateral aspect of the mass (*asterisk*). The relationship of the mass to the medial pterygoid muscle (*triangle*) is also appreciated. (**b** and **c**) Intraoperative photographs demonstrate the tumor in its native location in the parapharyngeal space (**b**) and after extirpation (**c**) with a view into the parapharyngeal cavity

Aygenc et al. described an infant with an in utero sonographic diagnosis of a cystic neck mass, later evaluated by ultrasound at 28 months of age showing a right parapharyngeal hypoechoic, multilocular cystic mass containing septa; it was treated with surgical excision, and no recurrence had occurred 1 year later [46].

At sonography, lymphatic malformations are ill-defined, generally hypoechoic lymphatic channels with traversing hyperechoic septations. Because of the debris within the lymphatic channels, low-level echoes may be present in the cystic components. Posterior acoustic enhancement is common. These lesions are relatively avascular.

8.7.6 Branchial Cleft Cyst

Branchial cleft cysts (BCCs) in the PPS represent remnants of the second branchial apparatus [19, 47, 48]. A second BCC can occur anywhere along its course from the tonsillar fossa, between the internal and external carotid arteries, to the skin overlying the sternocleidomastoid muscle [6, 48] and is the most common type of BCC found in the PPS [5].

Sonographic findings of BCC are comparable to other benign-appearing cysts elsewhere in the body, with well-defined margins, hypoechoic or anechoic echotexture, round or ovoid shape, and posterior acoustic enhancement. Low-level echoes in the dependent portion of the cyst correspond to debris or proteinaceous fluid. If bouts of prior inflammation and/or infection have occurred, the wall of the cyst may be thickened and hypervascular. Generally, no internal flow on color Doppler imaging is present in a noninflamed cyst (Fig. 8.12).

8.8 Secondary Lesions

8.8.1 Salivary Gland Tumors

Salivary gland tumors, comprised largely of pleomorphic adenoma or benign mixed tumors, are the most common mass of the PPS and represent 40–50% of PPS masses [3]. Only 10–12% of pleomorphic adenomas arise from the deep lobe [49]. Salivary gland tumors may arise from either the deep lobe of the parotid gland or de novo from salivary gland rests or minor salivary glands inherent to the PPS. Deep lobe

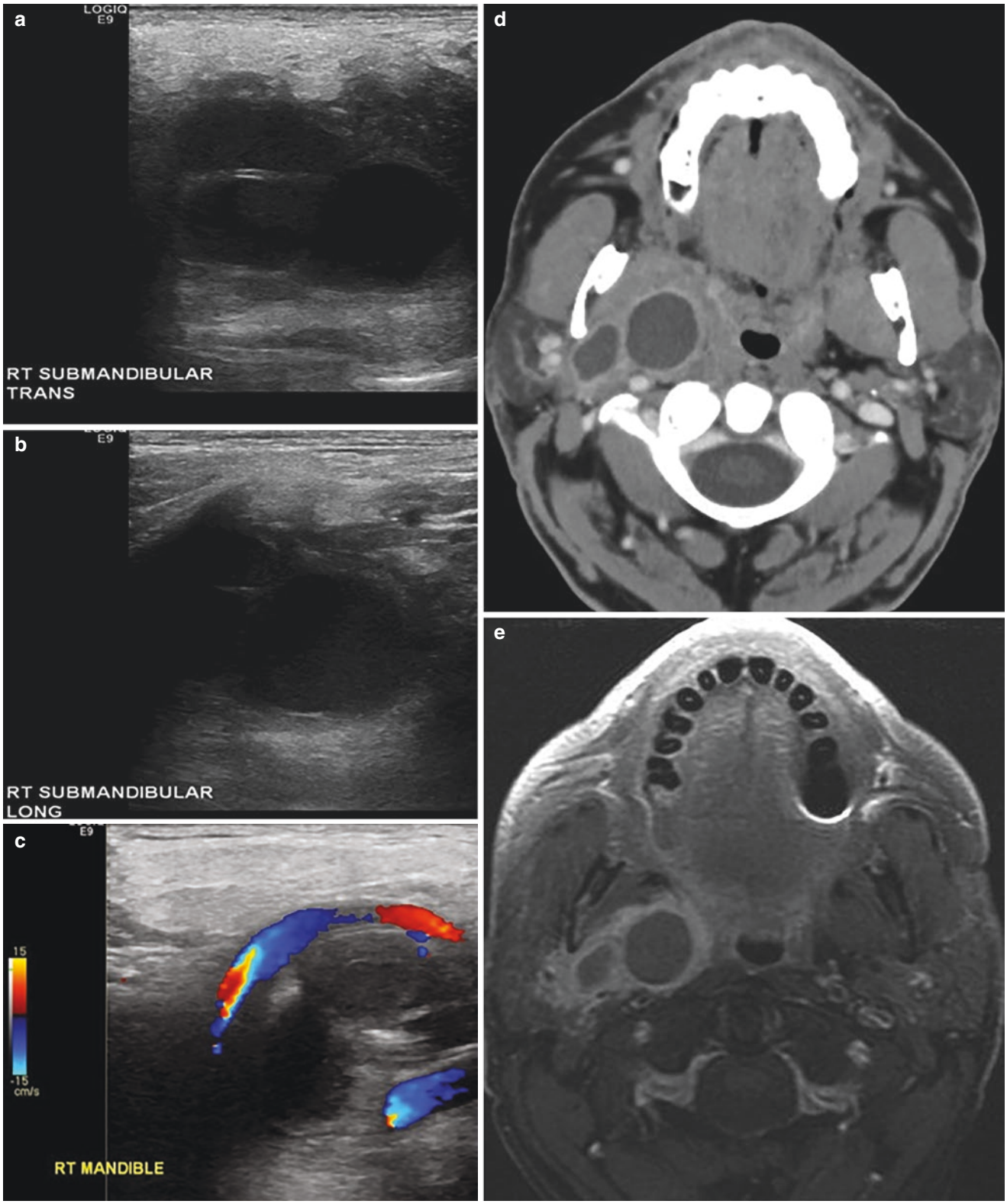

Fig. 8.12 Branchial cleft cysts. (**a** and **b**) Grayscale images from a submandibular approach demonstrate multiple adjacent cystic structures, some of which contain layering debris. Though well-circumscribed, there is wall thickening (particularly in **b**), related to underlying repeat inflammation. (**c**) Color Doppler image at a similar level shows no internal flow, although several large vessels traverse the nearby tissues. The deep vessel was thought to represent the internal carotid artery. (**d**) Axial contrast-enhanced CT demonstrates avid enhancement of the cyst wall with thickening. Central low-density contents are seen within the cyst. (**e**) Axial T1-weighted post-contrast images demonstrate similar findings

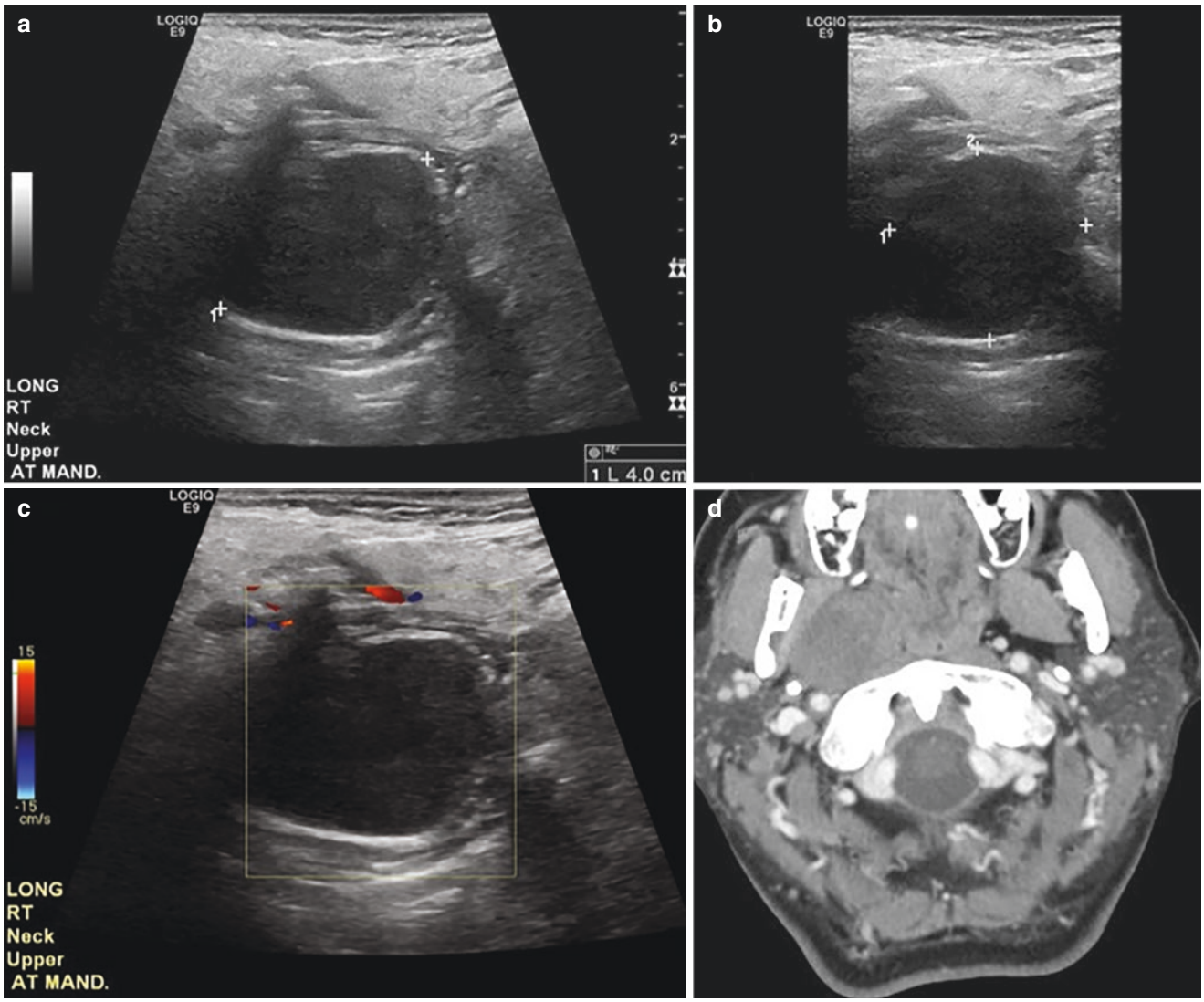

Fig. 8.13 Pleomorphic adenoma arising in ectopic salivary gland tissue. (**a** and **b**) Longitudinal and transverse grayscale images from a retromandibular approach depict a well-circumscribed, hypoechoic (nearly anechoic) mass. Real-time scanning and cine clips through the mass demonstrate that this mass is definitively hypoechoic. Posterior acoustic enhancement is present. The tail of the parotid gland can be seen in the superficial zone. (**c**) Color Doppler images show an avascular lesion. (**d**) Axial contrast-enhanced CT demonstrates a well-circumscribed, slightly hypodense soft tissue mass in the right parapharyngeal space, separate from the parotid gland. A small, compressed band of hypodense fat is present circumferentially around the mass

masses in the pre-styloid compartment encroach on the PPS, displacing the parapharyngeal fat medially and the great vessels posteriorly.

Salivary gland tumors may also arise from ectopic salivary gland rests or minor salivary glands. The key to distinguishing deep lobe or ectopic origin is identification of the parapharyngeal fat on cross-sectional imaging or a clear plane of separation between the mass and the deep lobe of the parotid gland on ultrasound [50]. Deep lobe tumors that have expanded beyond the borders of the parotid space and medially into the PPS will displace the parapharyngeal fat medially and lack a fat cleft surrounding the mass circumferentially. In contrast, ectopic salivary gland tumors arising within the PPS proper will contain a fat cleft surrounding the mass and distinct from the margin of the deep lobe of the parotid gland. This is best appreciated on T1-weighted nonfat-saturated MR sequences.

On ultrasound, benign mixed tumors are round, homogeneous, and well circumscribed, although they may be lobulated when greater than 1.5–2 cm [5]. These lesions can appear very hypoechoic and may display posterior acoustic enhancement, confounding the diagnosis with

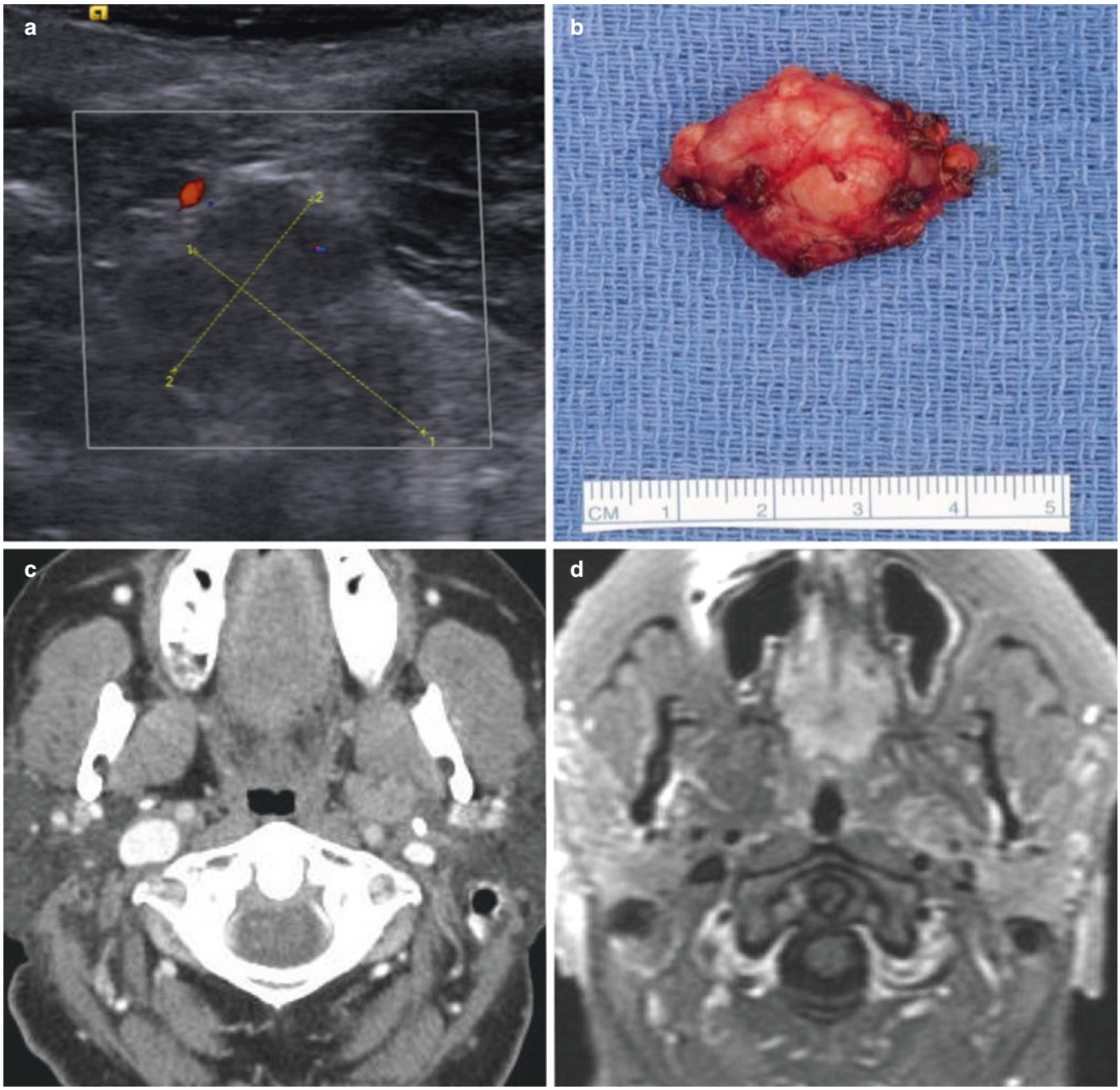

Fig. 8.14 Salivary gland tumor. (**a**) Intraoral color Doppler endosonography via the left oropharynx demonstrates a lobulated, hypoechoic mass with minimal internal flow. The margins of the lesion (particularly the deep margin) are poorly defined. (**b**) Gross pathologic specimen shows a mass that is firm and glistening white-yellow, similar in appearance to other salivary gland neoplasms. (**c**) Axial contrast-enhanced CT demonstrates a space-occupying lesion in the left prestyloid parapharyngeal space, displacing the parapharyngeal fat medially. At a minimum, the posterolateral aspect of the mass abuts the deep lobe of the parotid gland. (**d**) Axial T1-weighted MRI after gadolinium administration demonstrates clear continuity of the lesion with the deep lobe of the parotid gland, indicative of salivary gland origin. Though most parapharyngeal salivary gland tumors are benign, this lesion was an acinic cell carcinoma

that of a simple cyst, but cross-sectional imaging or biopsy can confirm the solid nature of these lesions (Figs. 8.13 and 8.14). When assessing tumors of the parotid gland for benign versus malignant features, poorly defined margins had higher diagnostic value than increased tumor vascularity [51]. Rarely, a malignant salivary gland tumor may demonstrate poorly defined margins on ultrasound (Fig. 8.14) or invasion into adjacent musculature, such as the pterygoid muscles or the posterior belly of the digastric muscle. Additionally, the presence of enlarged regional lymph nodes raises the index of suspicion of a malignant tumor.

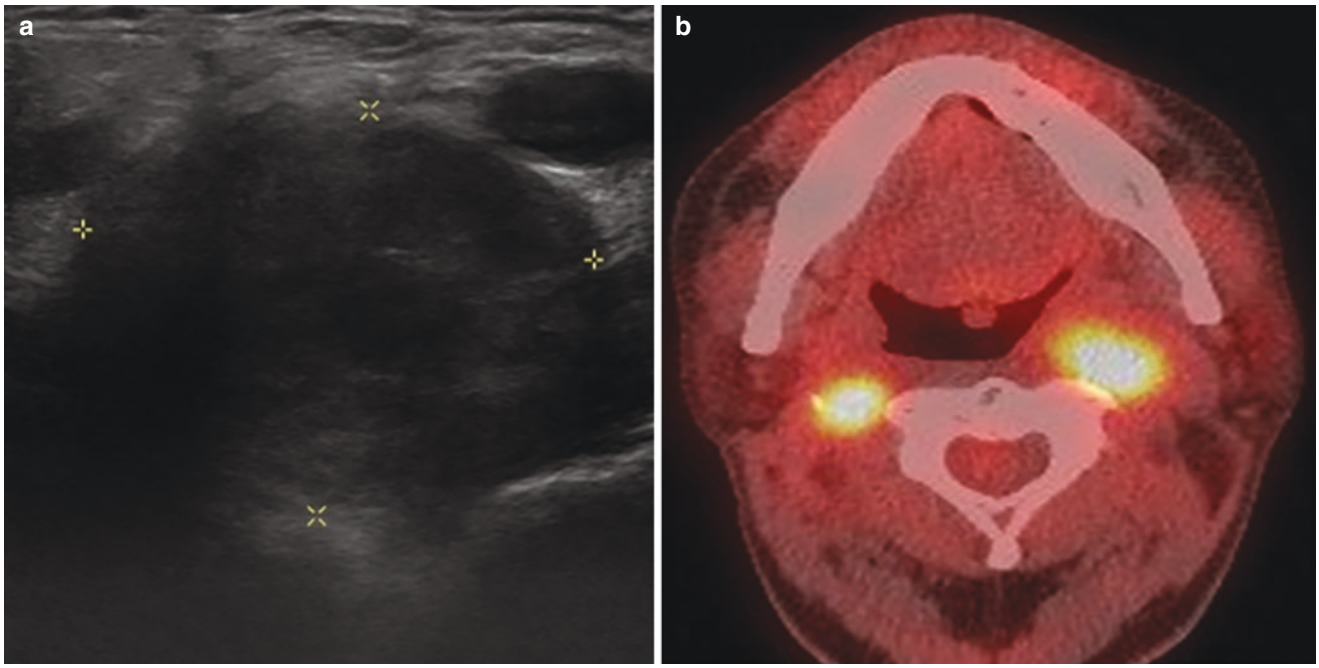

Fig. 8.15 Bilateral papillary thyroid carcinoma metastases. (**a**) Grayscale ultrasound in a longitudinal plane demonstrates an ovoid, prominently hypoechoic mass whose cranial end and deep margins are obscured. This metastatic lymph node was present in the left post-styloid compartment. (**b**) Axial fused ^{18}F-FDG PET/CT demonstrates bilateral hypermetabolic parapharyngeal masses (left greater than right). Additional hypermetabolic foci were present in the mediastinum and lungs in this patient with metastatic papillary thyroid carcinoma

8.8.2 Nodal Metastasis

Pathologic lymph nodes within the carotid space or post-styloid PPS are mostly often seen in the setting of squamous cell carcinoma, papillary thyroid carcinoma, or lymphoma. Variable incidence of metastatic PPS lymph nodes ranges from 0.09% to 3.4% [1, 52]. Furthermore, the rich lymphatic bed in the region contains many anastomotic channels between the PPS and the retropharyngeal space, which connect with the node of Rouvière in the retropharyngeal space [52–55]. If large enough, a parapharyngeal nodal metastasis may become clinically apparent as a neck mass, or it may be found incidentally as part of the imaging work-up for an underlying malignancy.

The normal sonographic appearance of a lymph node shows an oval shape with a reniform, mildly hypoechoic cortex and hyperechoic fat in the hilum. Normal small-caliber hilar vessels are present (absent peripheral vascularity). The cortical margin is smooth and symmetric.

Abnormal lymph nodes demonstrate loss of normal architecture, asymmetric cortical thickening, and replacement of the fatty hilum. The cortical margins of a node replaced with tumor are biconvex and very hypoechoic. Sometimes, the margins of the node may appear shaggy (Fig. 8.15). Additional discerning features can point toward an origin of the primary tumor from which the metastases arose: Microcalcifications are common in papillary thyroid carcinoma, and nodal necrosis is often present in the setting of squamous cell carcinoma.

8.8.3 Abscess

Owing to easy communication with surrounding spaces, the PPS is also susceptible to infection and even abscess formation. Dental infections may spread from the anteriorly positioned masticator space [56], and tonsillar cellulitis may progress to peritonsillar abscess and spill through the superior constrictor muscle laterally into the PPS [6, 14, 30, 57]. Bassiony et al. found the ultrasound to be a valuable addition in the diagnosis of superficial infections but inferior to MRI when evaluating deep fascial spaces such as the PPS [56]. Cadaveric studies by Grodinsky revealed that injection of dye into the PPS spread through the alar fascia into the "danger space," highlighting the importance of the PPS as a potential route of passage for aggressive processes to the mediastinum [15].

As with abscesses in any other location, these collections appear centrally hypoechoic, with a variable amount of wall thickening. Layering debris may also be present within the abscess. Peripheral hypervascularity on color Doppler images may correlate with the degree of surrounding inflammatory changes in the pharyngeal and parapharyngeal soft tissues. Contrast-enhanced CT scans should be considered to delineate the extent and location of the great vessels in relation to the abscess and for planning purposes if surgery is indicated. Alternatively, these lesions can be treated with endoscopic or external ultrasound-guided drainage in the appropriate setting, under sedation or anesthesia [34, 35, 58, 59]. The use of sonography allows vessels in the needle path to be visualized in real time.

8.8.4 Carotid Artery Aneurysm and Pseudoaneurysm

Aneurysm of the extracranial carotid artery is rare but significant. The etiology for most is atherosclerosis, usually located near the carotid bifurcation. Fifty percent arise in the internal carotid artery, 48% in the common carotid artery, and only 2% in the external carotid artery. On imaging, carotid artery aneurysm appears as focal dilatation of the vessel wall, with or without internal thrombosis [60].

Pseudoaneurysm may occur after penetrating trauma and typically occurs in younger patients. On ultrasound, pseudoaneurysms are characterized as a saccular outpouching arising from the carotid artery, with a thin neck leading to the pseudoaneurysm sac. Color Doppler flow demonstrates turbulence in the sac with a classic to-and-fro waveform.

8.9 Treatment

Treatment of lesions in the PPS depends on the tumor's malignant potential and inherent characteristics (size, location, and vascularity), the clinical presentation of the patient, and the expected risk of observation versus treatment. As surgical technique has evolved over the past several decades, much debate exists regarding various approaches—transcervical, transparotid, transmandibular, and, more recently, transoral (see below). Some authors advocate endoscopic assistance for transcervical approaches (for tumors as large as 7 cm) [61] or for a transoral approach [62].

For an asymptomatic patient with a large neurogenic tumor involving a cranial nerve, a careful risk-benefit consideration must be undertaken by both the patient and surgeon, as chances for dysfunction of the nerve after resection are not insignificant. This risk is weighed against the reported 10% malignant degeneration rate for neurofibromas, versus 1% for schwannomas [11]. Complete surgical resection of nerve sheath tumors may require sacrifice of the involved nerve.

8.9.1 Surgical Approaches

The transcervical approach to the PPS is the most direct and safest means of accessing most tumors. For larger tumors, combining the transcervical approach with a transparotid approach may prevent injury to the facial nerve and additional exposure, preventing tumor spillage. This is also true for tumors affecting the lower cranial nerves, such as the vagal schwannoma or glomus tumors, which are often situated in the superior PPS and are more fixed. For these tumors, removal via a transcervical approach alone may be particularly challenging without the added exposure afforded by parotidectomy.

Transmandibular approaches are seldom needed, generally only for fixed malignant masses that may involve the great vessels or skull base. This approach comes with significantly more morbidity, including tracheostomy, malocclusion or loss of teeth, dysphagia and dysarthria, and a prolonged hospital stay. This approach should be employed only after the transcervical approach has been explored [63].

Pioneered in recent decades and first reported in 1988 by Goodwin, transoral surgery provides an alternate route to the PPS [63, 64]. This approach may be appropriate for small tumors, but it is limited by visualization of a small field and potential for neurovascular injury. Larger tumors may be resected safely and adequately in experienced hands. Dallan et al. emphasize the importance of the stylopharyngeus and styloglossus muscles as cardinal points for orientation in the PPS [63]. They also report that identifying the ICA and IJV on the lateral surface of the superior pharyngeal constrictor muscle is key to a safe and successful surgery and feel that this approach exposes patients to a risk of lack of bleeding control that is similar (not increased) to an external approach.

Numerous clinicians very recently have begun utilizing transoral robotic surgery (TORS) to resect select PPS tumors in the pre-styloid compartment, with high local control and low complication rates [65, 66]. TORS has been reported to have rates of carotid injury, wound dehiscence, and postoperative transoral bleeding that are similar or decreased when compared with open procedures, making TORS a reasonable choice when clinically appropriate [67].

Andrews and colleagues reported successful extirpation of metastatic lymph nodes in the PPS in six patients, using intraoperative ultrasound guidance for methylene blue dye instillation [68]. The advantages of intraoperative ultrasound guidance in the setting of transoral surgery are to assess feasibility of the operation and define relationships to the ICA.

8.10 Conclusions

Ultrasound is a powerful adjunct to cross-sectional imaging in the evaluation of parapharyngeal masses. Most parapharyngeal masses are benign, but cranial neuropathy may indicate a lesion arising from a cranial nerve (vagal schwannoma, glomus vagale, or neurofibroma) or perineural malignancy. Both external and intraoral sonographic approaches are quick, inexpensive, noninvasive, and well tolerated. The internal characteristics of the lesion, combined with its relationship to surrounding structures such as the great vessels, can allow appropriate surveillance or preoperative planning.

References

1. Batsakis JG, Sneige N. Parapharyngeal and retropharyngeal space diseases. Ann Otol Rhinol Laryngol. 1989;98:320–1.
2. Hughes KV 3rd, Olsen KD, McCaffrey TV. Parapharyngeal space neoplasms. Head Neck. 1995;17:124–30.
3. Khafif A, Segev Y, Kaplan DM, Gil Z, Fliss DM. Surgical management of parapharyngeal space tumors: a 10-year review. Otolaryngol Head Neck Surg. 2005;132:401–6.
4. Pang KP, Goh CH, Tan HM. Parapharyngeal space tumours: an 18 year review. J Laryngol Otol. 2002;116:170–5.
5. Som PM, Curtin HD. Head and neck imaging. 5th ed. St. Louis: Elsevier; 2011.
6. Gupta A, Chazen JL, Phillips CD. Imaging evaluation of the parapharyngeal space. Otolaryngol Clin N Am. 2012;45:1223–32.
7. Gamss C, Gupta A, Chazen JL, Phillips CD. Imaging evaluation of the suprahyoid neck. Radiol Clin N Am. 2015;53:133–44.
8. Warshafsky D, Goldenberg D, Kanekar SG. Imaging anatomy of deep neck spaces. Otolaryngol Clin N Am. 2012;45:1203–21.
9. Gervasio A, D'Orta G, Mujahed I, Biasio A. Sonographic anatomy of the neck: The suprahyoid region. J Ultrasound. 2011;14:130–5.
10. Harnsberger HR, Osborn AG. Differential diagnosis of head and neck lesions based on their space of origin. 1. The suprahyoid part of the neck. AJR Am J Roentgenol. 1991;157:147–54.
11. Heeneman H, Maran AG. Parapharyngeal space tumours. Clin Otolaryngol Allied Sci. 1979;4:57–66.
12. Curtin HD. Separation of the masticator space from the parapharyngeal space. Radiology. 1987;163:195–204.
13. Chrzanowski DS, Powers CN, Reiter ER. Parapharyngeal space hemangioma in a pediatric patient. Otolaryngol Head Neck Surg. 2005;133:455–7.
14. Gaughran GR. The lateral pharyngeal cleft. Ann Otol Rhinol Laryngol. 1959;68:1082–96.
15. Grodinsky M. Retropharyngeal and lateral pharyngeal abscesses: an anatomic and clinical study. Ann Surg. 1939;110:177–99.
16. Datarkar AN, Deshpande A. Giant parapharyngeal space pleomorphic adenoma of the deep lobe of parotid presenting as obstructive sleep apnoea: a case report & review of the diagnostic and therapeutic approaches. J Maxillofac Oral Surg. 2015;14:532–7.
17. Shi X, Tao L, Li X, Wu H, Huang W, Chen X, et al. Surgical management of primary parapharyngeal space tumors: a 10-year review. Acta Otolaryngol. 2017;137:656–61.
18. Miller FR, Wanamaker JR, Lavertu P, Wood BG. Magnetic resonance imaging and the management of parapharyngeal space tumors. Head Neck. 1996;18:67–77.
19. Giovagnorio F, Martinoli C. Sonography of the cervical vagus nerve: normal appearance and abnormal findings. AJR Am J Roentgenol. 2001;176:745–9.
20. Lloyd GA, Phelps PD. The demonstration of tumours of the parapharyngeal space by magnetic resonance imaging. Br J Radiol. 1986;59:675–83.
21. Muraz E, Delemazure AS, Mourrain-Langlois E, Bourget K, Malard O, Frampas E. Peripharyngeal space tumors: can magnetic resonance and multidetector-row computed tomography help predict location, malignancy and tumor type? Diagn Interv Imaging. 2016;97:617–25.
22. Som PM, Sacher M, Stollman AL, Biller HF, Lawson W. Common tumors of the parapharyngeal space: refined imaging diagnosis. Radiology. 1988;169:81–5.
23. Kalmovich LM, Gavriel H, Eviatar E, Kessler A. Accuracy of ultrasonography versus computed tomography scan in detecting parapharyngeal abscess in children. Pediatr Emerg Care. 2012;28:780–2.
24. Pan D, Zhu SY, Xu YB, Wu YF, Lun HM, Wei YY. Sonographic findings of nasopharyngeal carcinoma and its involvement in the parapharyngeal space. J Ultrasound Med. 2013;32:1041–7.
25. Ng SH, Chan SC, Yen TC, Chang JT, Liao CT, Ko SF, et al. Staging of untreated nasopharyngeal carcinoma with PET/CT: comparison with conventional imaging work-up. Eur J Nucl Med Mol Imaging. 2009;36:12–22.
26. Varoquaux A, Fakhry N, Gabriel S, Garcia S, Ferretti A, Chondrogiannis S, et al. Retrostyloid parapharyngeal space tumors: a clinician and imaging perspective. Eur J Radiol. 2013;82:773–82.
27. Rebol J, Takac I, Bumber Z. Intraoral sonographic evaluation of parapharyngeal space tumors. J Clin Ultrasound. 2001;29:302–5.
28. Riskalla A, Arora A, Vaz F, O'Flynn P. Novel use of ultrasound-guided endo-cavitary probe to evaluate an impalpable parapharyngeal mass. J Laryngol Otol. 2010;124:328–9.
29. Orloff LA. Head and neck ultrasonography: essential and extended applications. 2nd ed. San Diego: Plural Publishing; 2017.
30. Bandarkar AN, Adeyiga AO, Fordham MT, Preciado D, Reilly BK. Tonsil ultrasound: technical approach and spectrum of pediatric peritonsillar infections. Pediatr Radiol. 2016;46:1059–67.
31. King AD, Ahuja AT, King W, Metreweli C. Sonography of peripheral nerve tumors of the neck. AJR Am J Roentgenol. 1997;169:1695–8.
32. Dim DC, Nugent SL, Peng HQ. Ganglioneuroma presenting as a paraesophageal mass lesion diagnosed by endoscopic ultrasound-guided fine needle aspiration cytology: a case report. Acta Cytol. 2010;54:321–4.
33. Wong KT, Tsang RK, Tse GM, Yuen EH, Ahuja AT. Biopsy of deep-seated head and neck lesions under intraoral ultrasound guidance. AJNR Am J Neuroradiol. 2006;27:1654–7.
34. Cable BB, Brenner P, Bauman NM, Mair EA. Image-guided surgical drainage of medial parapharyngeal abscesses in children: a novel adjuvant to a difficult approach. Ann Otol Rhinol Laryngol. 2004;113:115–20.
35. Chang KP, Chen YL, Hao SP, Chen SM. Ultrasound-guided closed drainage for abscesses of the head and neck. Otolaryngol Head Neck Surg. 2005;132:119–24.
36. Nusbaum AO, Som PM, Rothschild MA, Shugar JM. Recurrence of a deep neck infection: a clinical indication of an underlying congenital lesion. Arch Otolaryngol Head Neck Surg. 1999;125:1379–82.
37. Friedrich RE. Ultrasonographically supported removal of foreign bodies of the eye lid and parapharyngeal space in a 13-year-old boy subjected to shot injuries in early childhood. GMS Interdiscip Plast Reconstr Surg DGPW. 2013;2:Doc19.
38. White JB, Link MJ, Cloft HJ. Endovascular embolization of paragangliomas: a safe adjuvant to treatment. J Vasc Interv Neurol. 2008;1:37–41.

39. Anil G, Tan TY. Imaging characteristics of schwannoma of the cervical sympathetic chain: a review of 12 cases. AJNR Am J Neuroradiol. 2010;31:1408–12.
40. Saito DM, Glastonbury CM, El-Sayed IH, Eisele DW. Parapharyngeal space schwannomas: preoperative imaging determination of the nerve of origin. Arch Otolaryngol Head Neck Surg. 2007;133:662–7.
41. Astrom K, Cohen JE, Willett-Brozick JE, Aston CE, Baysal BE. Altitude is a phenotypic modifier in hereditary paraganglioma type 1: evidence for an oxygen-sensing defect. Hum Genet. 2003;113:228–37.
42. Rodriguez-Cuevas S, Lopez-Garza J, Labastida-Almendaro S. Carotid body tumors in inhabitants of altitudes higher than 2000 meters above sea level. Head Neck. 1998;20:374–8.
43. Pensak ML, Gluckman JL, Shumrick KA. Parapharyngeal space tumors: an algorithm for evaluation and management. Laryngoscope. 1994;104:1170–3.
44. Ulku CH, Uyar Y. Parapharyngeal lipoma extending to skull base: a case report and review of the literature. Skull Base. 2004;14:121–5; discussion 5.
45. Dasgupta R, Fishman SJ. ISSVA classification. Semin Pediatr Surg. 2014;23:158–61.
46. Aygenc E, Fidan F, Ozdem C. Lymphatic malformation of the parapharyngeal space. Br J Oral Maxillofac Surg. 2004;42:33–5.
47. Piccin O, Cavicchi O, Caliceti U. Branchial cyst of the parapharyngeal space: report of a case and surgical approach considerations. Oral Maxillofac Surg. 2008;12:215–7.
48. Shin JH, Lee HK, Kim SY, Park HW, Khang SK, Choi CG, et al. Parapharyngeal second branchial cyst manifesting as cranial nerve palsies: MR findings. AJNR Am J Neuroradiol. 2001;22:510–2.
49. Morita N, Miyata K, Sakamoto T, Wada T. Pleomorphic adenoma in the parapharyngeal space: report of three cases. J Oral Maxillofac Surg. 1995;53:605–10.
50. Chotai NC, Tang P, Gopinathan AN. Imaging of parotid gland primitive neuroectodermal tumor. J Cancer Res Ther. 2010;6:327–9.
51. Gerwel A, Kosik K, Jurkiewicz D. US in preoperative evaluation of parotid gland neoplasms. Otolaryngol Pol. 2015;69:27–33.
52. Som PM, Biller HF, Lawson W, Sacher M, Lanzieri CF. Parapharyngeal space masses: an updated protocol based upon 104 cases. Radiology. 1984;153:149–56.
53. Aygenc E, Kaymakci M, Karaca C, Ozdem C. Papillary thyroid carcinoma metastasis to the parapharyngeal space. Eur Arch Otorhinolaryngol. 2002;259:322–4.
54. Carrau RL, Myers EN, Johnson JT. Management of tumors arising in the parapharyngeal space. Laryngoscope. 1990;100:583–9.
55. Saydam L, Kalcioglu T, Demirkiran A, Gurer M. Occult papillary thyroid carcinoma presenting as a parapharyngeal metastasis. Am J Otolaryngol. 1999;20:166–8.
56. Bassiony M, Yang J, Abdel-Monem TM, Elmogy S, Elnagdy M. Exploration of ultrasonography in assessment of fascial space spread of odontogenic infections. Oral Surg Oral Med Oral Pathol Oral Radiol Endod. 2009;107:861–9.
57. Keren G, Lison M, Graif M, Barzilay Z. Ultrasound diagnosis of parapharyngeal abscesses in a young infant. Eur J Pediatr. 1982;139:206–7.
58. Balekuduru A, Dutta AK, Subbaraj SB. Endoscopic ultrasound-guided transoral drainage of parapharyngeal abscess. Dig Endosc. 2016;28:756.
59. Duque CS, Guerra L, Roy S. Use of intraoperative ultrasound for localizing difficult parapharyngeal space abscesses in children. Int J Pediatr Otorhinolaryngol. 2007;71:375–8.
60. Som PM, Dorfman GS, Reede DL, Solodnik P, Sacher M. The bull's-eye sign of extracranial cervical aneurysms. J Comput Tomogr. 1988;12:81–5.
61. Pilolli F, Giordano L, Galli A, Bussi M. Parapharyngeal space tumours: video-assisted minimally invasive transcervical approach. Acta Otorhinolaryngol Ital. 2016;36:259–64.
62. Wang J, Li WY, Yang DH, Jin XF, Niu YY. Endoscope-assisted transoral approach for parapharyngeal space tumor resection. Chin Med J. 2017;130:2267–8.
63. Dallan I, Lenzi R, Bignami M, Battaglia P, Sellari-Franceschini S, Muscatello L, et al. Endoscopic transnasal anatomy of the infratemporal fossa and upper parapharyngeal regions: correlations with traditional perspectives and surgical implications. Minim Invasive Neurosurg. 2010;53:261–9.
64. Goodwin WJ Jr, Chandler JR. Transoral excision of lateral parapharyngeal space tumors presenting intraorally. Laryngoscope. 1988;98:266–9.
65. O'Malley BW, Quon H, Leonhardt FD, Chalian AA, Weinstein GS. Transoral robotic surgery for parapharyngeal space tumors. ORL J Otorhinolaryngol Relat Spec. 2010;72:332–6.
66. Arshad H, Durmus K, Ozer E. Transoral robotic resection of selected parapharyngeal space tumors. Eur Arch Otorhinolaryngol. 2013;270:1737–40.
67. Weinstein GS, O'Malley BW, Magnuson JS, Carroll WR, Olsen KD, Daio L, et al. Transoral robotic surgery: a multicenter study to assess feasibility, safety, and surgical margins. Laryngoscope. 2012;122:1701–7.
68. Andrews GA, Kwon M, Clayman G, Edeiken B, Kupferman ME. Technical refinement of ultrasound-guided transoral resection of parapharyngeal/retropharyngeal thyroid carcinoma metastases. Head Neck. 2011;33:166–70.

Pediatric Sonography of the Neck: Characteristic Findings

9

Jürgen Weidemann and Gabriele H. A. Engelcke

9.1 Introduction

As with head and neck ultrasound in adults, it is useful to analyze pathologies in children on the basis of anatomical spaces and morphological (cystic, solid, vascular) components, including lymph node involvement (Tables 9.1, 9.2, 9.3, and 9.4) [1, 2]. In addition, pediatric age-related pathologies such as embryological remnants and malformations should be considered; some of them may also occur in adulthood [3], and individual findings may indicate a syndromic disease that may require further investigation. For example, port wine stains may occur in a Sturge-Weber syndrome, or large facial hemangiomas may be part of a PHACE(S) syndrome (see below).

Most pediatric pathologies are accessible with a standard linear probe, with no need for special pediatric ultrasound probes. Small hockey-stick probes can help longitudinal thyroid imaging on small, short necks. They are also useful in vascular punctures in the context of catheter systems.

It is advisable to document midline transversal images from the submandibular space (including both submandibular glands), the thyroid, the jugulum (thymus, dermoid cysts), lateral lymph node stations along the carotid sheath, and coronal images of both parotid glands. Depending on the clinical findings, other specific examinations may be indicated, such as examining the posterior cervical regions (for lymphomas) and bone boundaries (for tumors such as eosinophilic granuloma of the mandible, odontogenic abscesses, and cysts).

Table 9.1 Differential diagnosis of cystic lesions

Suprahyoid
Parotid space
First branchial cyst
Parotid retention cyst
Tumor
Benign (pleomorphic adenoma; Warthin tumor)
Malignant (mucoepidermoid carcinoma)
Lymph node necrosis
Lymphatic malformation
Submandibular space
Second branchial cyst
Ranula
Dermoid/epidermoid
Thyroglossal duct cyst
Vallecular cyst
Lymph node necrosis
Lymphatic malformation
Infrahyoid
Midline
Thyroglossal duct cyst
Dermoid/epidermoid
Lateral
Second/third/fourth branchial cyst
Lymphatic malformation
Laryngocele
Cystic lymphadenopathy (inflammatory or malignant)
Teratoma
Thymic cyst
Lacking definition by the hyoid
Cystic lymphatic malformation
Cystic lymphadenopathy (inflammatory or malignant)

Welcome the child and the parents and keep eye contact during the examination. Even infants respond to a calming direct response. Always explain the process and the objectives of the investigation. If necessary, infants can be calmed with a sweet pacifier and older children with some videos on mobile devices. The child also can hold a favorite plush toy. Bend the child's head slightly overstretched on a pillow. Use warm ultrasound gel. Explain your findings in simple terms at the end of the examination.

Electronic Supplementary Material The online version of this chapter (https://doi.org/10.1007/978-3-030-12641-4_9) contains supplementary material, which is available to authorized users.

J. Weidemann (✉) · G. H. A. Engelcke
Department of Pediatric Radiology, Kinder- und Jugendkrankenhaus Auf der Bult, Hannover, Germany
e-mail: weidemann@hka.de

© Springer Nature Switzerland AG 2019

H. J. Welkoborsky, P. Jecker (eds.), *Ultrasonography of the Head and Neck*, https://doi.org/10.1007/978-3-030-12641-4_9

Table 9.2 Differential diagnosis of solid lesions

Suprahyoid
Parotid space
Lymph node
Lymphofollicular proliferation (HIV)
Malignoma
Submandibular space
Lymph node
Infrahyoid
Midline
Thyroid nodule (adenoma, carcinoma)
Dermoid/epidermoid
Lateral
Lymph adenopathy
Teratoma
Lacking definition by the hyoid
Ectopic thymic tissue (occasionally found cranially to the mediastinal thymus)
Reactive or malignant lymph node enlargement
Malignant tumors
In infants: neuroblastomas, lymphomas, rhabdomyosarcomas
In older children: mainly lymphomas and thyroid carcinomas
Fibromatosis colli

Table 9.3 Differential diagnosis of vascular anomalies[a]

Vascular tumors
Benign (hemangioma)
Locally aggressive or borderline vascular tumors (hemangioendothelioma, kaposi sarcoma, others)
Malignant vascular tumors (angiosarcoma, epithelioid hemangioendothelioma, others)
Vascular malformations
Simple vascular malformations
Capillary malformations
Lymphatic malformations
Venous malformations
Arteriovenous malformations (high-flow lesion)
Arteriovenous fistula (high-flow lesion)
Combined vascular malformations (defined as two or more vascular malformations found in one lesion)
Of major named vessels (anomalies of origin, course, number, length, diameter, communication, persistence of embryonal vessel)
Associated with other anomalies (e.g., Sturge-Weber syndrome)

[a]Classification according to the International Society for the Study of Vascular Anomalies (ISSVA) [7]

Table 9.4 Differential diagnosis of lymph node lesions

Cystic
Viral and bacterial lymph node enlargement with presence of purulent foci and fistulas
Solid
Viral and bacterial lymph node enlargement without presence of purulent foci and fistulas
Lymphomas
Calcification
Atypical mycobacterial infections (*Mycobacterium avium-intracellulare-scrofulaceum* [MAIS] complex)
Lymph node metastasis of thyroid carcinoma

Key Points

- Child-friendly examination conditions
- Standardized approach and documentation
- Assignment of pathology based on morphological components, anatomical region, and possible embryonic genesis
- Possible syndromic connection

9.2 Suprahyoid Space

9.2.1 Parotid and Submandibular Spaces

Inflammatory Lesions of the Salivary Glands

The most common diseases of the salivary glands are *acute inflammations,* which are often viral or, more rarely, bacterial. Typical viral pathogens are mumps, mononucleosis, and cytomegalovirus. The salivary glands are painfully swollen and show an increased hypoechoic tissue pattern with increased vascularization in color duplex.

Bacterial infections may occur in children, especially involving the parotid gland. Most patients are children who are preterm, less than 1 year old, or immunosuppressed. The infections are most likely the result of diverted inflammation of the oral cavity or, rarely, of stone obstruction, especially for the submandibular gland. The most common pathogen is *Staphylococcus aureus*. In addition to edematous changes, sonographic findings can range from enlargements of intraglandular and extraglandular lymph nodes to abscesses. In the case of stones, extensions of the excretory ducts may also be found.

Chronic recurrent parotitis is the most common form of *chronic inflammation* in children, typically aged 3–6 years. The disease affects only the parotid gland. The cause is unknown. The disease can occur on one or both sides. The gland is intermittently swollen and painful, with concomitant fever. Multiple hypoechoic (lymphofollicular) foci with a diameter of 2–4 mm are typical (Fig. 9.1). The condition is treated supportively and heals spontaneously in adolescence or adulthood in most cases.

Other forms of chronic salivary gland inflammation are caused by granulomatous diseases (*Mycobacterium avium* infection, actinomycosis, histoplasmosis) or occur in the context of autoimmune diseases (such as Sjögren's syndrome or Heerfordt's disease). Lymphofollicular proliferation may develop as part of HIV disease. Sonographically, there are multiple hypoechoic, partly echo-free (cystic) nodules.

Neoplasms

Most masses of the salivary glands are caused by vascular tumors (infantile hemangiomas and lymphatic vascular

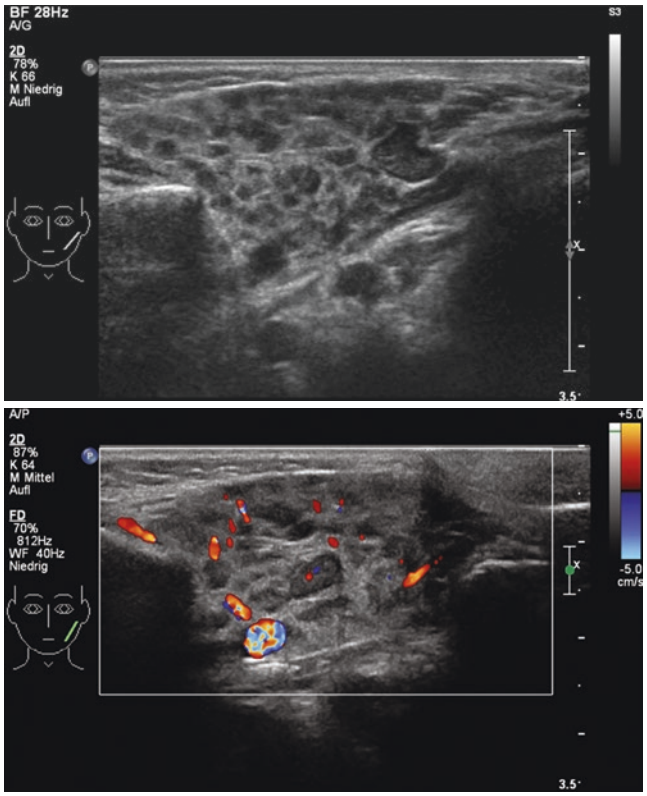

Fig. 9.1 Chronic recurrent parotitis. A 2-year-old girl. The gland was intermittently swollen and painful, with concomitant fever. Multiple hypoechoic (lymphofollicular) foci

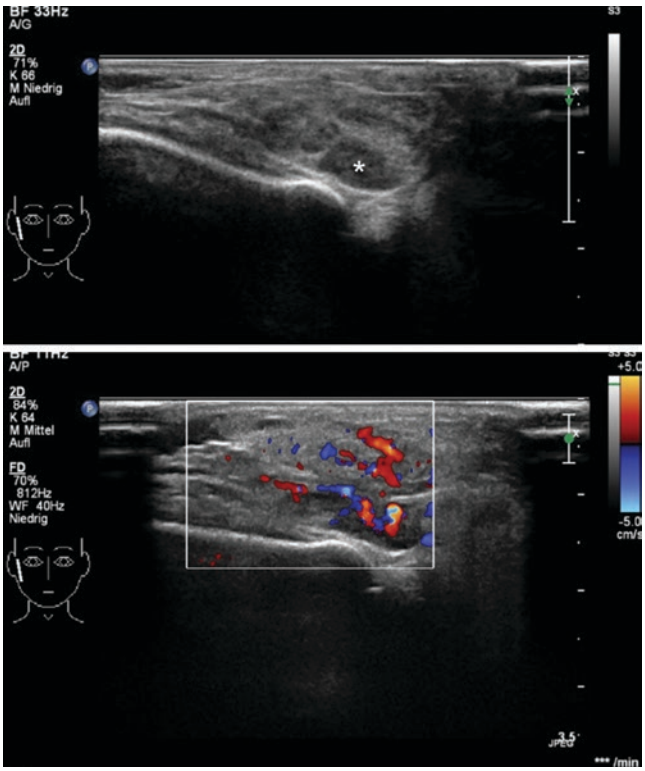

Fig. 9.2 Infantile hemangioma of parotid gland. An 11-week-old girl. Note the hypoechoic islands (*asterisk*) of vascular tissue in the gland. (*See* Video 9.1)

malformations); the gland is typically only partially involved. Infantile hemangiomas are true neoplasms, usually occurring early after birth and showing rapid proliferative activity in the first year of life, with a tendency to spontaneous regression in subsequent years. Sonographically, predominantly lobulated, hypoechoic areas with vigorous vascularization are found in the proliferative phase (Fig. 9.2; Video 9.1). Single, focal calcifications are possible. In the regression phase, vascularization and hypoechoic lobules are regressed. A proportion of hyperechoic adipose tissue often remains. Lymphatic vascular malformations appear as cystic masses with individual septa. Hemorrhage into individual cysts is possible and leads to a more inhomogeneous sonographic picture.

Solid epithelial tumors (benign and malignant) are rare in childhood but match the image of the adult. Differential diagnoses include malformations of the first pharyngeal arch, as they do not always show a clear cystic picture because of intermittent inflammation (Fig. 9.3; Videos 9.2 and 9.3).

Other tumors that may affect this region are neurofibromas, lipomas, more rarely rhabdomyosarcomas, lymphomas (in the salivary gland as MALT lymphoma due to Sjögren's syndrome or HIV), tongue-bottom thyroid glands, leukemias, and metastases.

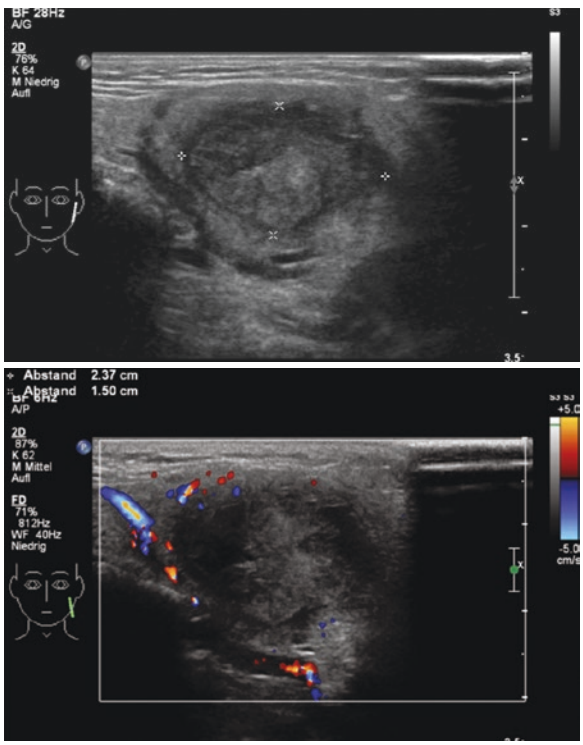

Fig. 9.3 Cystic malformation of the first pharyngeal arch. A 15-month-old girl. Detritus/pus in the parotid gland. (*See* Videos 9.2 and 9.3)

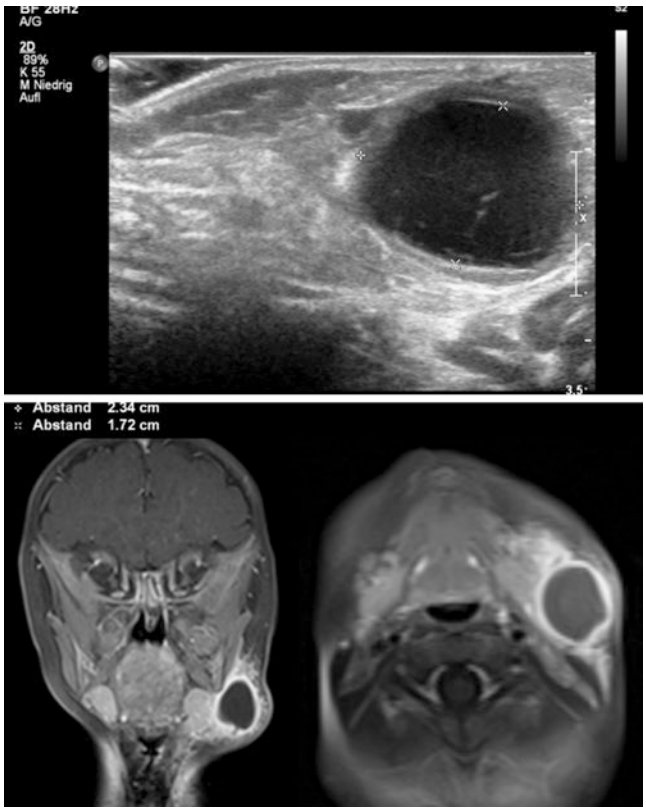

Fig. 9.4 Cyst of the second branchial arch. A 9-month-old boy. Cyst dorsolateral to the submandibular gland with mild inflammatory changes. A fat-saturated contrast-enhanced T1-weighted MRI (*bottom*) shows inflammatory enhancement surrounding the cyst

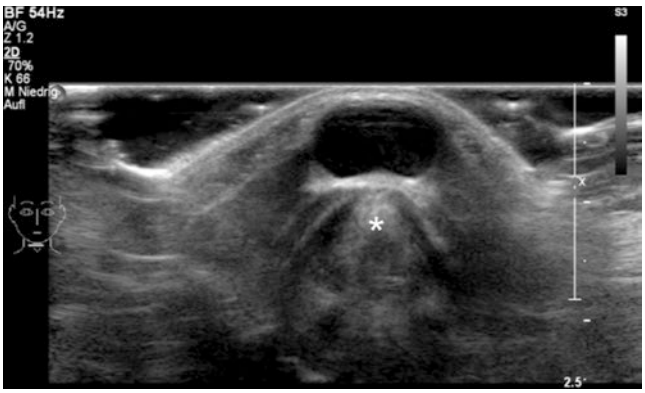

Fig. 9.5 Median cervical cyst. A 4-year-old girl. Cyst slightly below the hyoid bone in front of the larynx (*asterisk*) without recognizable signs of inflammation. (*See* Video 9.4)

Fig. 9.6 Mucoid retention cyst (ranula). A 6-year-old boy. Cyst adjacent to the right sublingual gland (view from below, floor of mouth). (*See* Video 9.5)

Suprahyoid Cystic Lesions

Cysts of the first branchial arch occur in the parotid gland (as in Fig. 9.3). Parts of a cystic lymphatic malformation may affect the parotid glands (*see* Table 9.1). Tumors and inflammation can lead to cystic changes in the intraglandular lymph nodes of the parotid gland; the submandibular gland has no intraglandular lymph nodes. Cysts of the second branchial arch are typically dorsolateral to the submandibular gland and may appear with or without inflammatory changes (Fig. 9.4).

In the midline, the median cervical cyst should be mentioned as the remnant of the thyroglossal duct. This is usually in the middle or left paramedian at the level of the hyoid bone or a little further caudal (Fig. 9.5; Video 9.4). Sublingual cysts around the floor of the mouth may correspond to a dermoid/epidermoid cyst or mucoid retention cyst of the sublingual gland, called a *ranula* (Fig. 9.6; Video 9.5). Dorsal to the mylohyoid muscle, descending ranulas are also called *diving ranulas*. Tumors and inflammation can lead to cystic changes of the lymph nodes. Cysts located on the dorsal root of the tongue may correspond to retention cysts of the valleculae and may lead to airway obstruction.

9.2.2 Masticator Space

Muscular tumors (sarcomas), as well as local odontogenic inflammation and cysts, can affect the masticator space. The odontogenic origin is not always sonographically palpable and therefore should be verified, if necessary, with further imaging techniques. For example, bony alterations should be verified with CT scans (Fig. 9.7). Vascular malformations (lymphatic or lymphatic-venous) may affect this space proportionally.

Key Points

- Lateral cervical cyst originates from the second pharyngeal arch.
- Median neck cyst appears along the course of the thyroglossal duct, mostly around the level of the hyoid bone.
- Inflammatory and malignant lymph node changes, including intraglandular lymph nodes of the parotid gland.

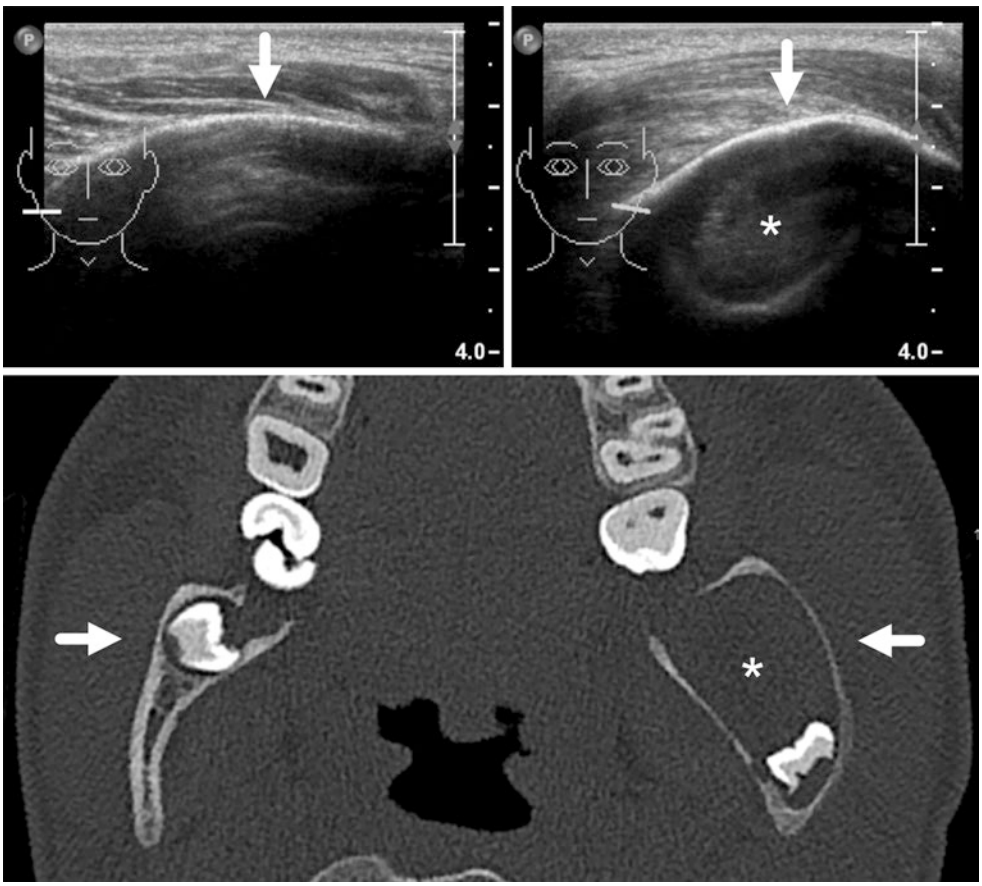

Fig. 9.7 Odontogenic cyst. A 12-year-old boy. Cyst (*asterisk*) with bony expansion on the left side (semitransparent thin bony border). A CT scan (*bottom*) verifies the nature of the bony alteration

- Hemangiomas and vascular malformations (lymphatic and lymphatic-venous) may involve the parotid gland.
- The masticatory muscles and the lower jaw can be affected by tumors or odontogenic cysts.

9.3 Infrahyoid Space

The *thyroid gland* may be completely absent (Fig. 9.8; Video 9.6), or only a single thyroid lobe may be missing (Fig. 9.9), more often on the left. In any case, the course of the thyroglossal duct from the floor of the mouth to the thymus should be examined in order to avoid overlooking ectopic thyroid tissue. Congenital hypothyroidism may be caused by hypoplasia of the thyroid gland or by goiter, in cases of congenital metabolic disturbances of the child or mother. A normal-sized thyroid gland, however, may be present in the context of a pseudohypoparathyroidism or a trisomy 21, despite a demonstrated hypothyroidism.

An inflammatory cyst may be due to cysts of the 3rd and 4th branchial cleft, usually found in the left upper thyroid lobe. Acute inflammations of the thyroid are otherwise rare and usually are due to these cystic malformations. The detection of a typical cyst, however, often fails because of the inflammatory changes.

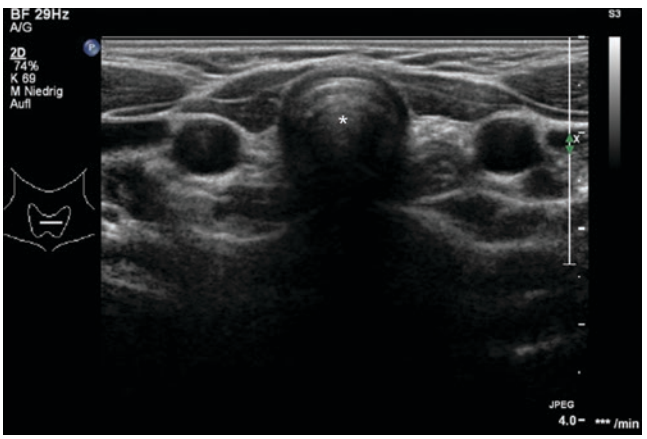

Fig. 9.8 Complete thyroid aplasia. A 10-year-old girl. Absent thyroid gland tissue in normal position around the trachea (*asterisk*). (*See* Video 9.6)

More common are autoimmune-mediated inflammations of the thyroid gland. Hashimoto's thyroiditis is the most common thyroid disease of the child and adolescent (Fig. 9.10). It occurs frequently in association with type 1

diabetes. There may be over-function in the acute phase or under-function in the chronic phase. Sonography shows a swollen gland with increased vascularization in the acute phase, with multiple hypoechoic nodules ranging in size from 1 to 6 mm. The parenchyma appears increasingly septate and lobulated. A spontaneous regression is possible, or nodular remodeling with shrinkage of the gland may occur.

Grave's disease (Fig. 9.11) is caused by autoantibodies that bind directly to thyroid-stimulating hormone (TSH) receptors. The disease causes thyroid enlargement, exophthalmos, and hyperthyroidism. In addition to an inhomogeneously hypoechoic, swollen parenchyma, ultrasound shows increased vascularization in color duplex.

De Quervain's thyroiditis is a rare focal inflammation of the thyroid gland most likely due to a viral infection.

Thyroid nodules are rare in childhood. The distinction between benign versus malignant is based on morphological criteria (with limited safety!) and the time course [4–6]. Unclear lesions require a biopsy. The criteria for malignancy are primarily solid lesions with inhomogeneous margins, internal calcification (especially microcalcifications) (Fig. 9.12), a shape taller than it is wide, the absence of a hypoechoic halo, internal vascularization in color duplex (Fig. 9.13), and pathological lymph nodes in the neighborhood. Benign lesions include follicular adenoma (round, well-defined, often with hypoechoic halo, no internal vascularization in color duplex) (Fig. 9.14) or degenerative (colloid) cysts (complex internal structure, echo-rich comet-tail artifact typical) (Fig. 9.15; Video 9.7). Multinodular goiter is rare in childhood but may require regular control to exclude focal malignant development.

Papillary thyroid carcinoma is the most common thyroid carcinoma in childhood and adolescence (80%). It metastasizes lymphogenously. Follicular thyroid carcinoma comprises 17% of thyroid carcinomas in these patients; it may have hematog-

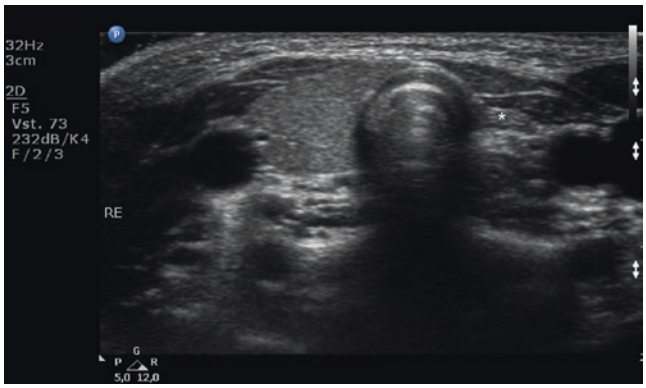

Fig. 9.9 Hemiaplasia of the thyroid gland. A 5-year-old girl. Almost complete absence of thyroid tissue on the left side (*asterisk*)

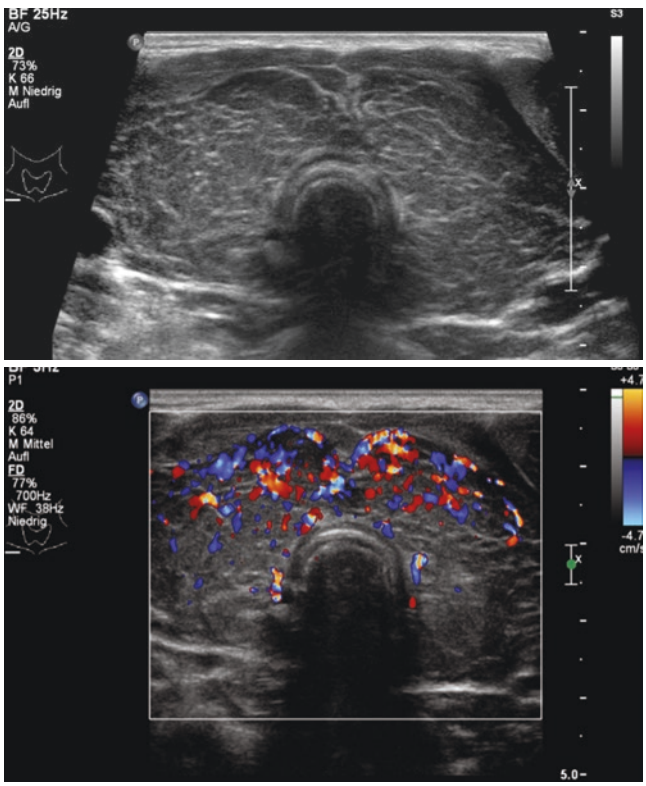

Fig. 9.10 Hashimoto's thyroiditis. A 14-year-old boy. Multiple hypoechoic nodules in a swollen, septated, and lobulated thyroid gland. Hypervascularization in color duplex

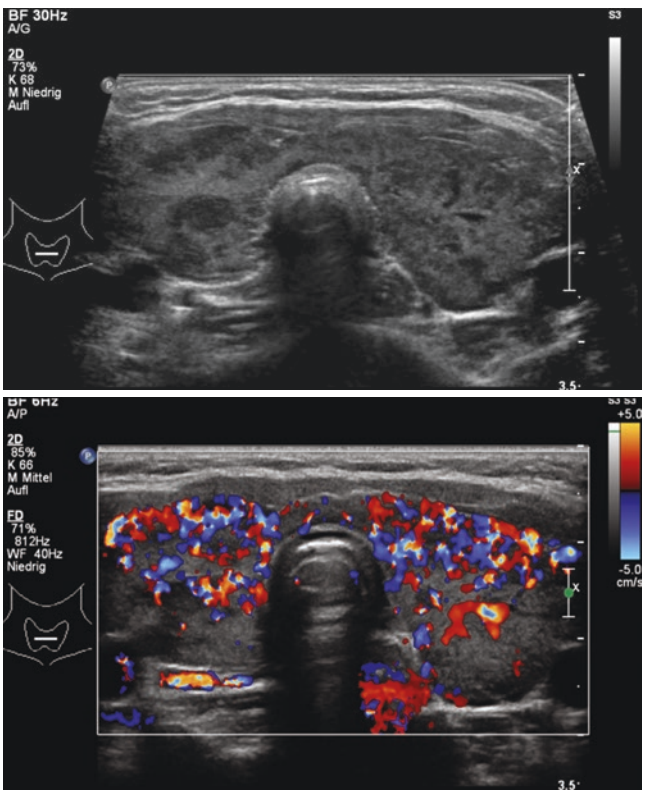

Fig. 9.11 Grave's disease. An 11-year-old girl. Thyroid gland with hypoechoic, swollen parenchyma. Hypervascularization in color duplex

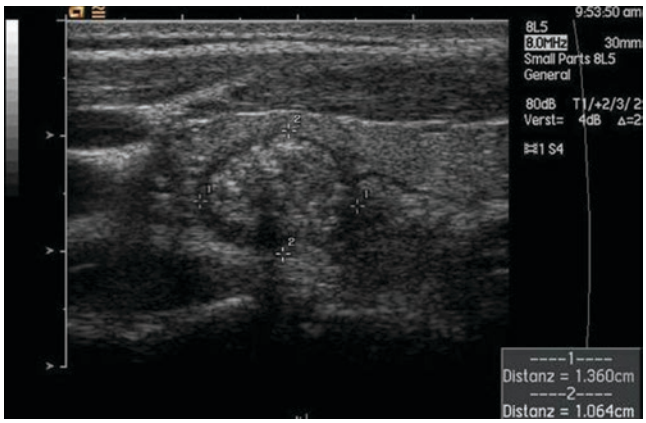

Fig. 9.12 Papillary thyroid carcinoma with microcalcifications. (*Courtesy of* Tilman Rohrer, Department of Pediatrics, Saarland University Medical Center, Homburg/Saar, Germany)

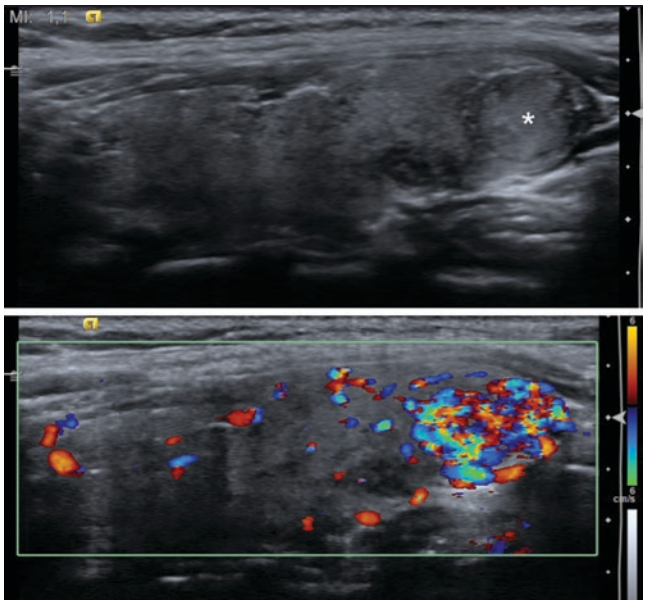

Fig. 9.13 Papillary thyroid carcinoma (*asterisk*) in the lower pole of left lobe (longitudinal section) with internal vascularization in color duplex. (*Courtesy of* Tilman Rohrer, Department of Pediatrics, Saarland University Medical Center, Homburg/Saar, Germany)

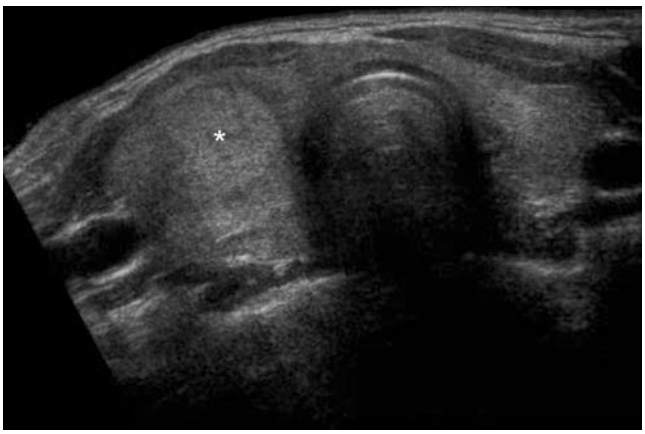

Fig. 9.14 Follicular adenoma (*asterisk*) without microcalcifications. No abnormal internal vascularization in color duplex (not shown). (*Courtesy of* Tilman Rohrer, Department of Pediatrics, Saarland University Medical Center, Homburg/Saar)

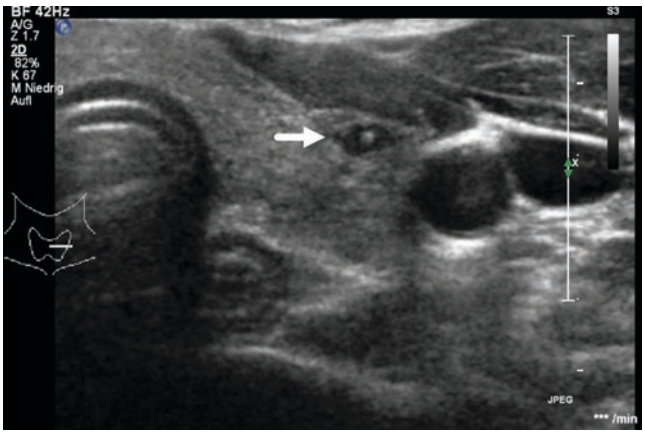

Fig. 9.15 Colloid cyst. A 17-year-old girl. Cyst (*arrow*) with typical echo-rich comet-tail artifact inside. (*See* Video 9.7)

enous spread. Medullary thyroid carcinoma is less common, is associated with multiple endocrine neoplasia type II (MEN II), and is often metastatic to the lymph nodes and lungs upon discovery. Other tumors of the thyroid are lymphomas (e.g., in the context of Hashimoto's thyroiditis) and teratoma.

The four *parathyroids* are usually indistinguishable from the isoechogenic thyroid parenchyma. In children with secondary hyperparathyroidism due to renal insufficiency and in rare cases of primary hyperparathyroidism due to an adenoma (Fig. 9.16), the glands may become visible as hypoechoic nodules. Characteristic is an enlargement of the pole-supplying vessel of the inferior thyroid artery. Sometimes the corresponding gland is ectopic (e.g., mediastinal) and can be searched for using MRI.

Rare, cervically located (bronchogenic/esophageal) foregut cysts can be detected sonographically. Laryngoceles can appear as air-filled or fluid-filled paralaryngeal pouches of the laryngeal ventricle.

Key Points

- An ectopic thyroid gland can be found along the thyroglossal duct.
- Hashimoto's thyroiditis is the most common form of autoimmune thyroiditis and occurs more commonly in type 1 diabetes mellitus.
- Third and fourth branchial cleft cysts may occur as focal thyroid-infiltrating inflammation.

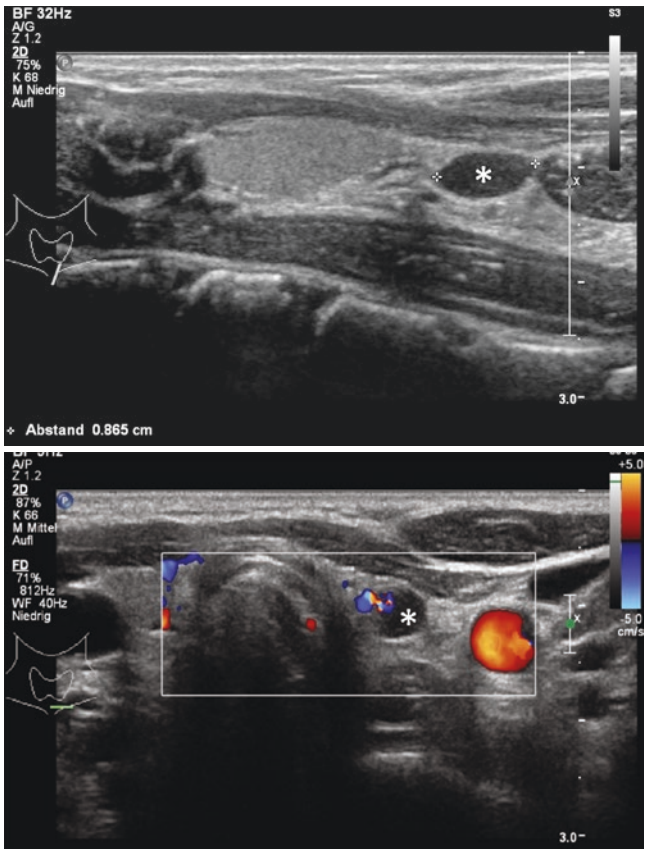

Fig. 9.16 Parathyroid adenoma. An 11-year-old girl. Primary hyperparathyroidism associated with multiple endocrine neoplasia type I (MEN I). Hypoechoic adenoma (*asterisk*). Note the pole-supplying vessel

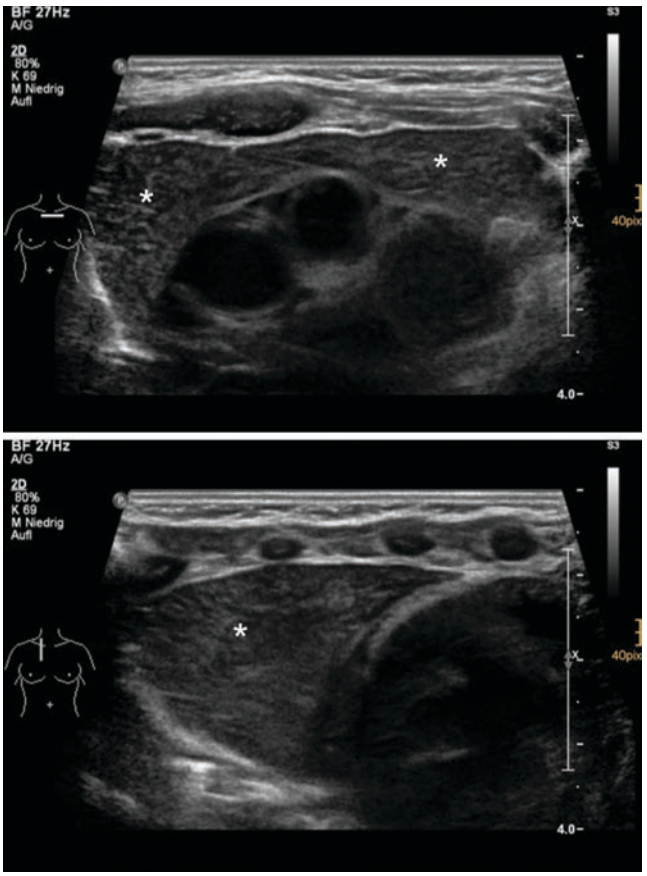

Fig. 9.17 Normal thymus. A 6-month-old boy. Cross and longitudinal sections of typical thymus tissue (*asterisks*)

- Thyroid nodules are rare in childhood. Possible signs of malignancy are primarily solid lesions, inhomogeneous margins, internal calcification (especially microcalcifications), taller-than-wide shape, absence of a hypoechoic halo, internal vascularization in color duplex, and pathological lymph nodes in the neighborhood.
- Papillary, follicular, and medullary thyroid carcinomas are found in childhood; medullary carcinomas occur mainly in the context of multiple endocrine neoplasia type II (MEN II).
- Parathyroid enlargement occurs as part of primary hyperparathyroidism (adenoma) or secondary hyperparathyroidism (renal insufficiency).

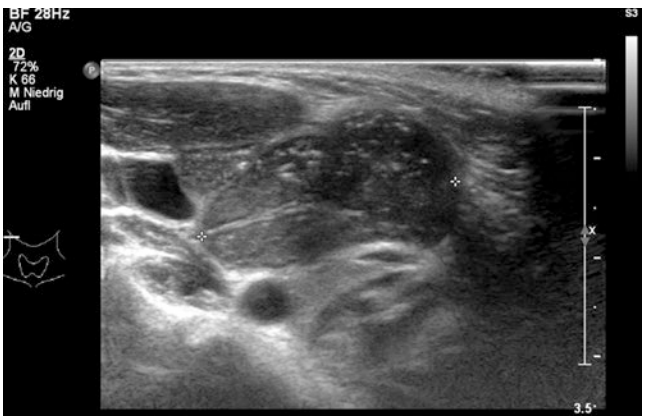

Fig. 9.18 Ectopic thymus tissue. A 3-year-old boy. Thymus tissue nestles between the muscles and the vessels of the neck without a bigger mass effect. (*See* Video 9.8)

9.4 Lacking Definition by the Hyoid

Branchial cleft cysts are noticeable as cystic, often infected lesions. In most cases, the lesions originate from the second arch, in rarer cases from the first arch [3]. Cysts of the third and fourth arch are much less common.

The *thymus* develops from outpourings of the third and fourth pharyngeal pouches and migrates during development along the carotid sheath into the upper mediastinum (Fig. 9.17). Ectopic thymic tissue, although clinically unremarkable, can occasionally be found during cervical sonography and must be differentiated from other lesions (Fig. 9.18; Video 9.8). Sonographically, the ectopic thymus tissue corresponds to the typical echo pattern of the orthotopic thymus,

with its sharply defined shape and soft structure without mass effect on neighboring structures. Thymic cysts may occur along the developmental route and (similar to the branchial cleft cysts) can be transformed by inflammation.

Dermoid or epidermoid cysts appear primarily as painless midline cysts. They occur most often in the area of the floor of the mouth or the suprasternal area (Fig. 9.19; Video 9.9).

Cervical teratomas show up as partly solid, partly cystic masses in the anterior and lateral cervical region, with a space-occupying effect on the respiratory tract.

Vascular anomalies can be classified into vascular tumors and vascular malformations according to the International Society for the Study of Vascular Anomalies (ISSVA) [7] (*see* Table 9.3). Infantile hemangiomas, by far the most common vascular tumors, have a typical echo pattern and time course (Figs. 9.20 and 9.21). Larger hemangiomas in the tri-

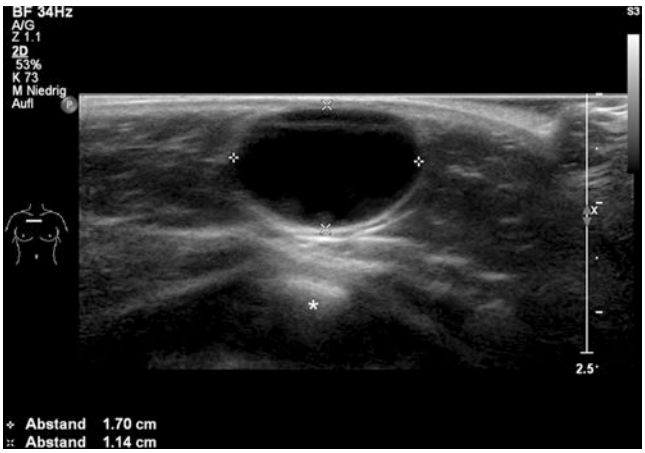

Fig. 9.19 Dermoid cyst. A 7-month-old girl. Cyst of the jugulum near the sternum (*asterisk*). No signs of inflammation. (*See* Video 9.9)

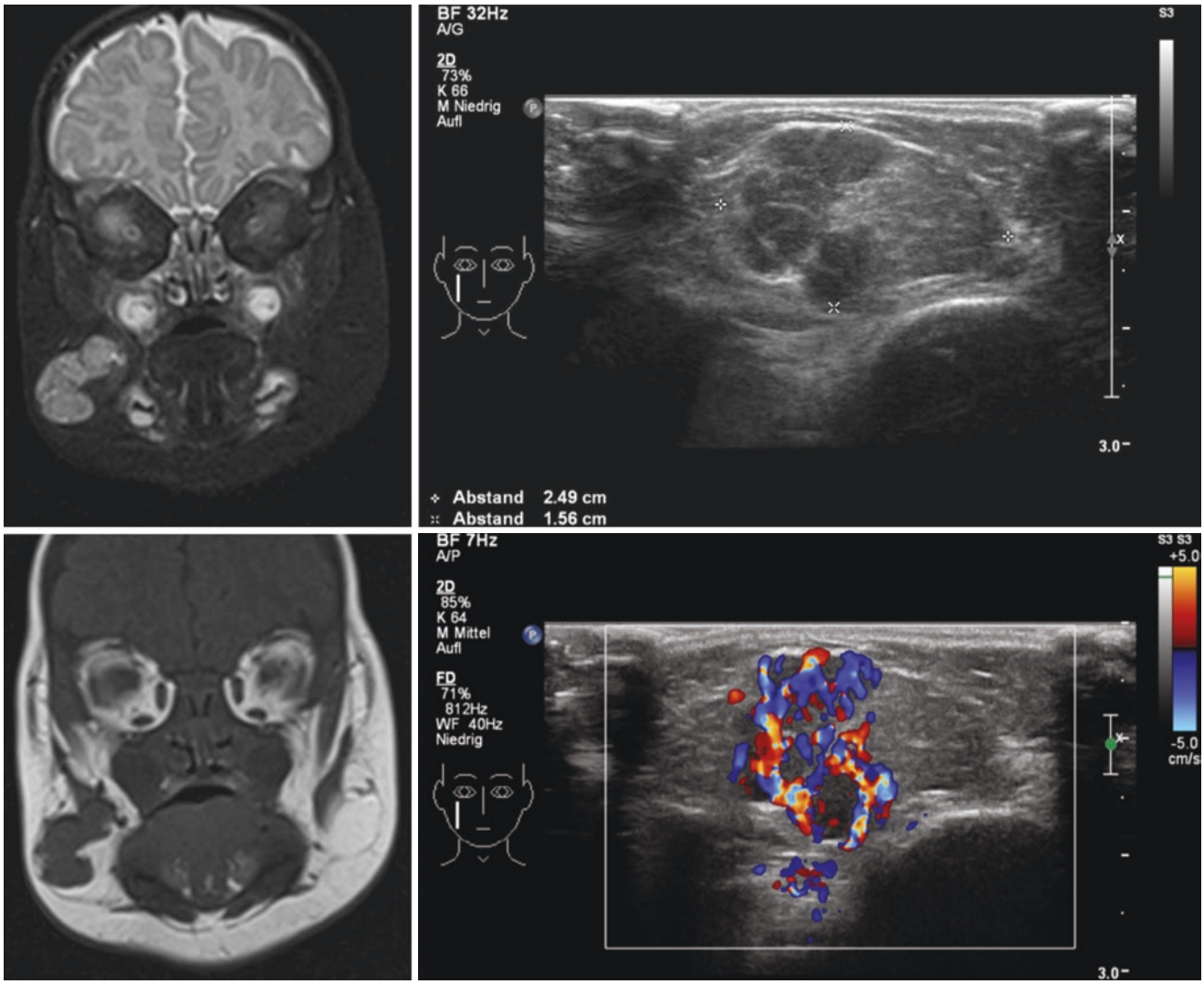

Fig. 9.20 Infantile hemangioma of the right cheek. A 2-month-old girl. Note the hypoechoic vascular part and the more hyperechoic fatty part of the hemangioma. A fat-saturated T2-weighted MRI (*upper left*) and a T1 without fat suppression (*lower left*) show the vascular and fatty parts of the lesion

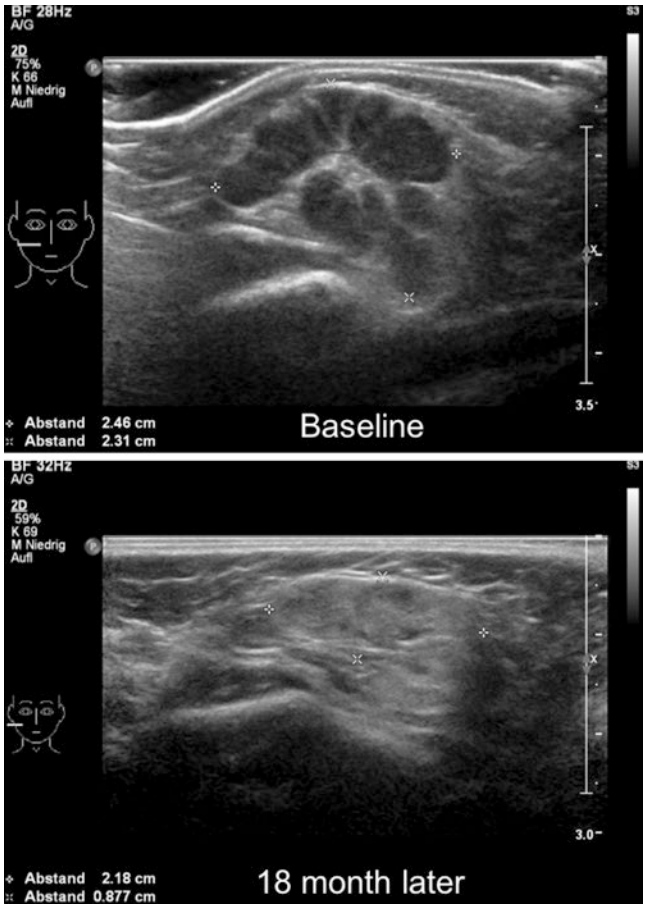

Fig. 9.21 Same infantile hemangioma as in Fig. 9.20. Note the fatty transformation 18 months later (after propranolol therapy)

geminal area may occur as part of a PHACES syndrome (posterior fossa malformations, hemangioma, arterial anomalies, coarctation of the aorta and cardiac defects, eye anomalies, and sternal anomalies). These lesions should be distinguished from capillary vascular malformations in this area occurring in connection with a Sturge-Weber syndrome (associated with intracranial leptomeningeal capillary malformation and frequently choroidal or scleral angiomatosis anomalies leading to seizures and glaucoma.

Vascular malformations are further classified as high-flow and low-flow lesions (Figs. 9.22 and 9.23) and by the involved vascular components (arterial, venous, lymphatic). Malformations can extend over several fascia spaces. Assessment of the spread to deeper regions of the midface and neck may require the use of MRI (Fig. 9.24). Phleboliths and bleeding into cystic or cavernous portions of a vascular malformation can modify the sonographic image.

Abnormalities of the lymph nodes (*see* Table 9.4) are among the most common findings in sonography of the child's neck [8]. Reactive lymph node enlargement is often found as a result of inflammation of the pharynx or tonsils (Fig. 9.25; Video 9.10). Most unilateral pyogenic inflammations are caused by *Staphylococcus aureus* or group A beta-hemolytic streptococci (Video 9.11) [9]. These should be distinguished from peritonsillar abscesses (Video 9.12, compared with the inconspicuous tonsil shown in Video 9.13). Bilateral lymph node inflammation is often caused by viruses, such as Epstein-Barr virus (EBV) (Fig. 9.26). In these cases, sonography shows regionally enlarged lymph nodes with preserved oval shape and hilus differentiation, with more or less edematous surrounding reaction (cellulitis). Purulent intranodal foci may occur in primary bacterial infiltration and mycobacteriosis (Fig. 9.27; Video 9.14). Calcifications and chimney-like fistulas can occur during mycobacterial infections (Fig. 9.28). Pathological lymph nodes in the context of lymphoma often show a roundish form, a hypoechoic parenchyma with loss of hyperechoic hilus, and a marked activity in FDG PET (Figs. 9.29 and 9.30). Color duplex may show increased flow centrally and peripherally. Supraclavicular lymph node enlargement is highly suspicious for malignancy (Fig. 9.30). Additional bony lesions associated with atypical lymph nodes may indicate Langerhans cell histiocytosis (Fig. 9.31).

Fibromatosis colli typically occurs as lateral neck swelling with accompanying torticollis in infants between weeks 2 and 8. Focal swelling is typically found in the caudal third of the sternocleidomastoid muscle (Fig. 9.32; Video 9.15 with normal sternocleidomastoid muscle and Video 9.16 with fibromatosis). The echotexture is irregularly fibromatous here. In the acute phase, an increased vascularization can be seen in color duplex. The cause of the disease is not fully understood; birth traumas may play a role but are not a necessary prerequisite. The lesion typically heals spontaneously. Fibromatous shortening of the muscle can be avoided by concomitant physiotherapy.

Carcinomas in the head and neck region account for 5% of all childhood cancers. The most common malignant tumors in children under the age of 6 are neuroblastomas (Fig. 9.33), lymphomas, and rhabdomyosarcomas. In the age group of 7–13 years, lymphomas, thyroid carcinomas, and rhabdomyosarcomas are the most common. After puberty, lymphomas are the most common malignant tumors. The morphology of lymph node metastases often corresponds to that of the original tumors or the lymphoma picture. Ultimately, any tissue of the neck can be the site of origin of a mass (Figs. 9.34, 9.35, 9.36, and 9.37; Videos 9.17, 9.18, and 9.19).

Iatrogenic lesions are most commonly hematomas after punctures or thrombosis along central vascular access routes.

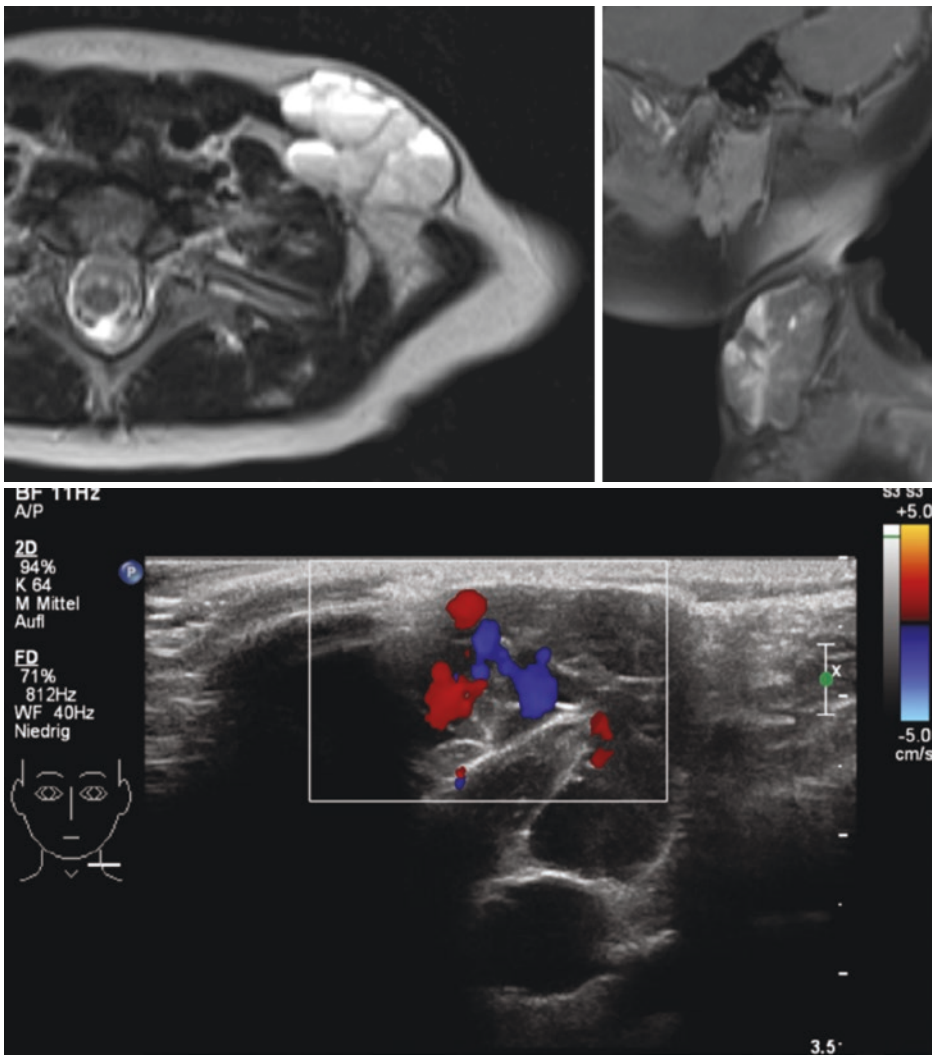

Fig. 9.22 Venous hemangioma (low-flow lesion). A 23-month-old girl. MRI shows fluid-fluid levels and sparse contrast enhancement of the lesion. Color duplex shows sparse flow signal in some of the vessels

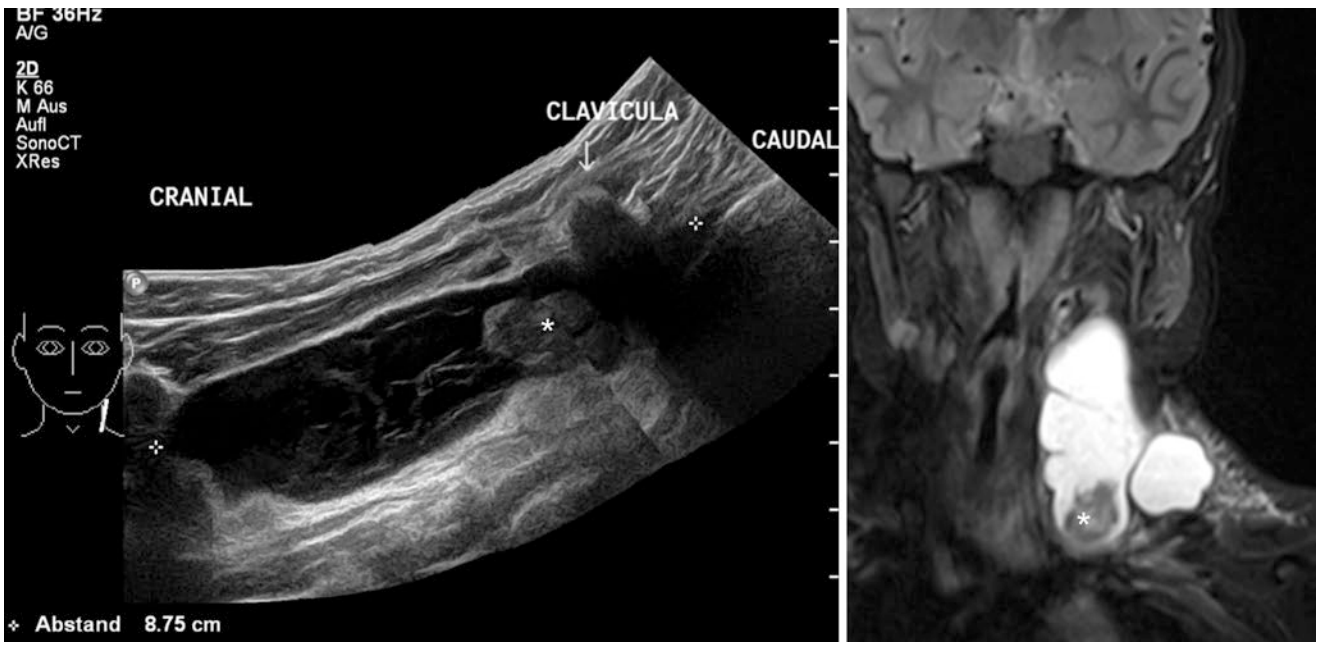

Fig. 9.23 Lymphatic malformation. A 6-year-old boy. Note the thrombus (*asterisk*) as a possible consequence of a hemorrhage. A fat-saturated T2-weighted MRT (right) shows the cystic nature of the lesion and the thrombus

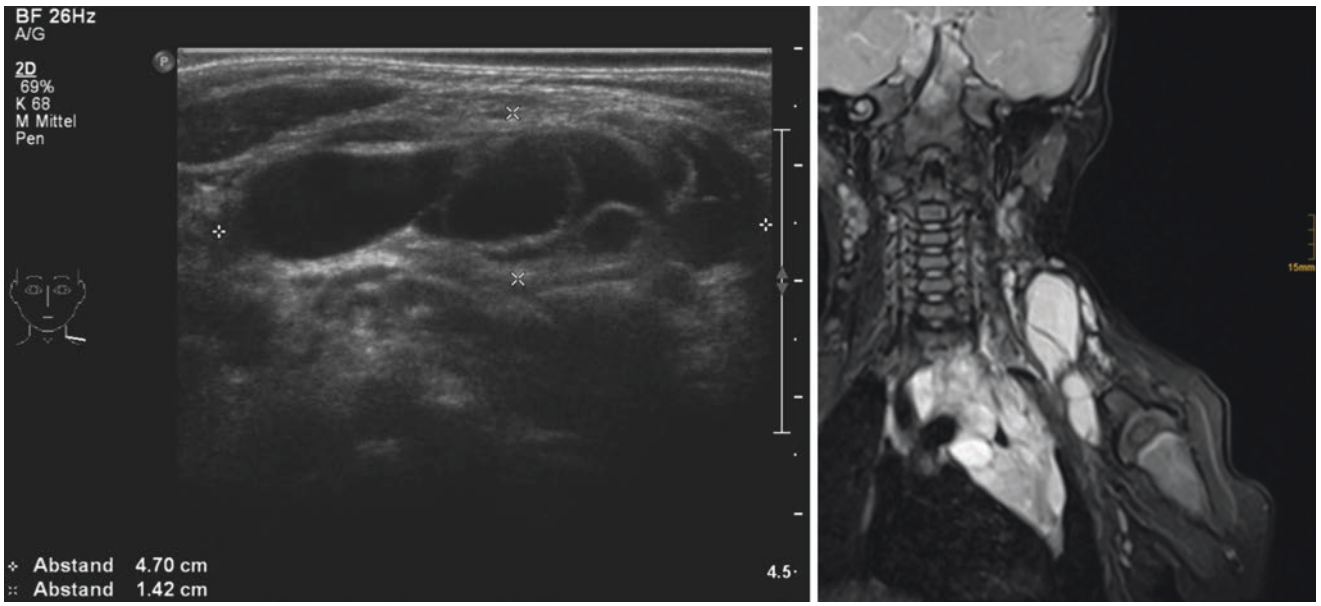

Fig. 9.24 Lymphatic malformation. An 11-month-old boy. The deeper mediastinal parts can be seen only on MRI

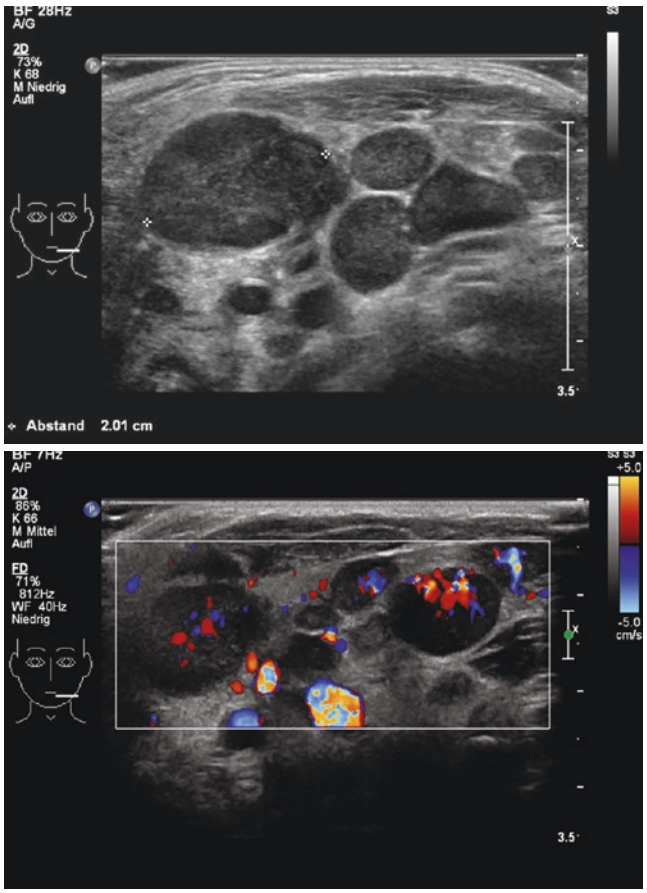

Fig. 9.25 Reactive cervical lymphadenopathy. A 5-year-old boy. The lymph nodes are still oval. The vascular architecture is preserved. (*See* Videos 9.10–9.13)

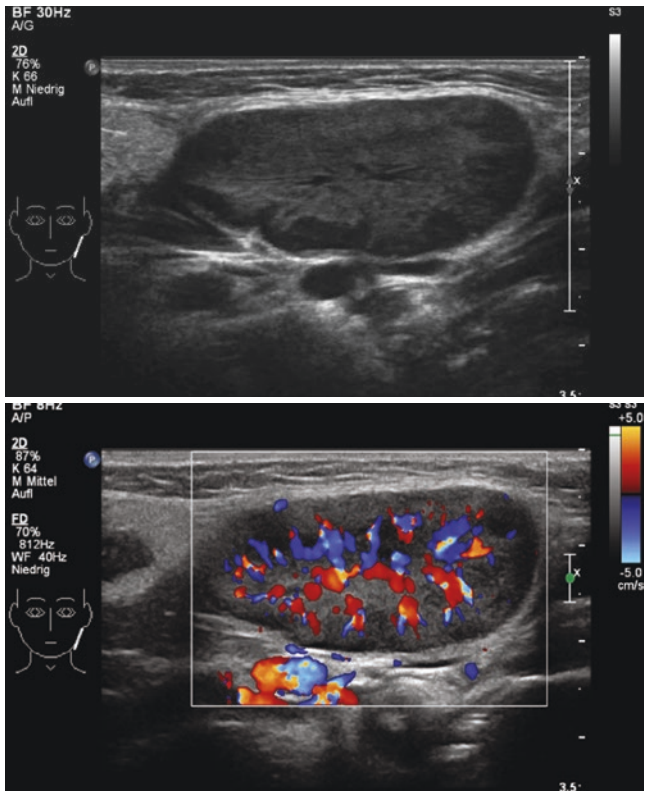

Fig. 9.26 Epstein-Barr virus (EBV) infection. A 10-year-old boy. Increased vascularization with preserved vessel architecture

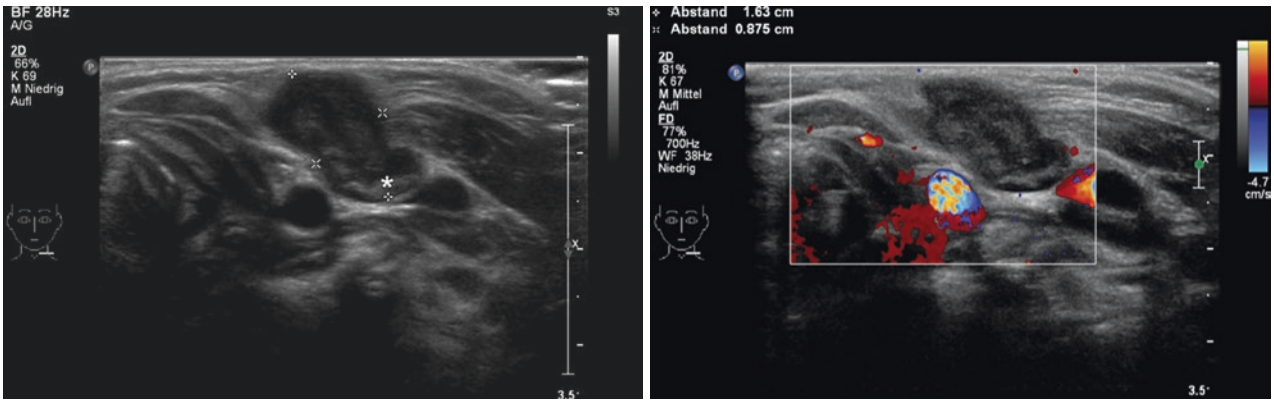

Fig. 9.27 Atypical mycobacteriosis. A 3-year-old boy. Purulent intranodal inflammation of a lymph node (*asterisk*) with the beginning of a chimney-like fistula due to atypical mycobacterial infection. (*See* Video 9.14)

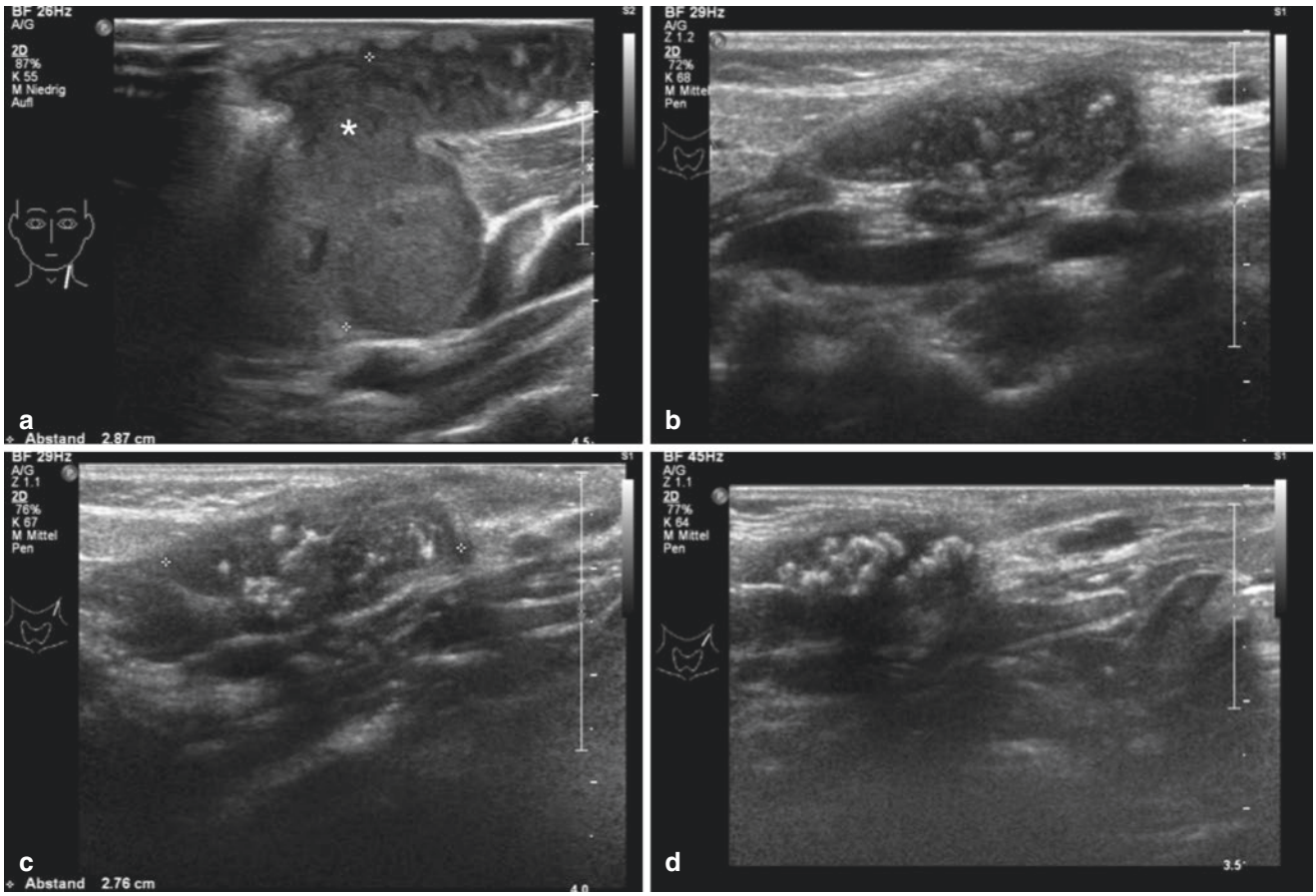

Fig. 9.28 Proven lymph node infection with *Mycobacterium avium*. A 4-year-old girl. Several weeks of neck swelling. The first ultrasound (**a**) shows a swollen lymph node with a chimney-like abscess (*asterisk*). After drainage without lymph node removal, a decrease in the size of the lymph node with increasing calcification occurs over a period of 9 months (**b**) 12 months (**c**) and 33 months (**d**)

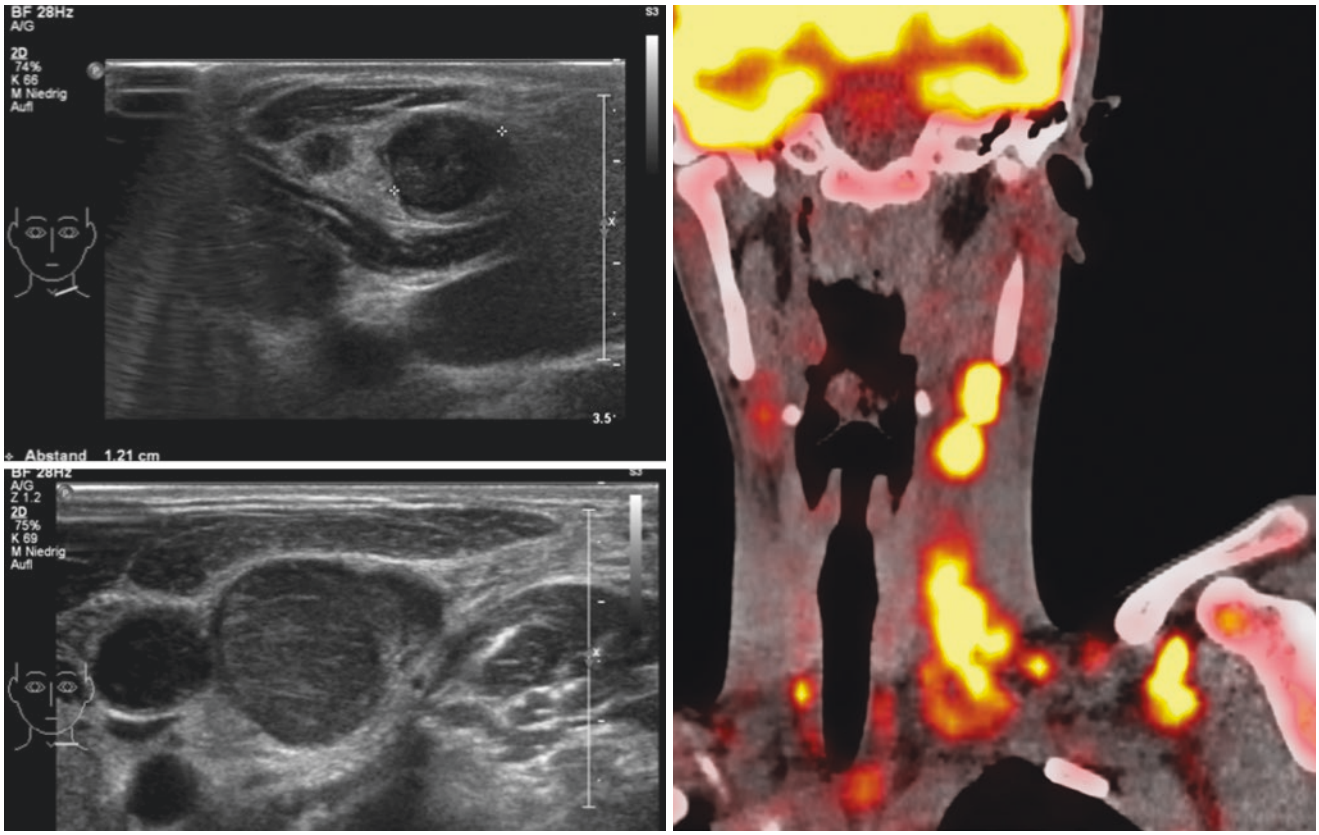

Fig. 9.29 Nodular sclerosis classical Hodgkin lymphoma (NSCHL). A 16-year-old boy. Lymph nodes show a roundish form with loss of hyperechoic hilus. (PET/CT image *courtesy of* Department of Nuclear Medicine, Hannover Medical School, Germany)

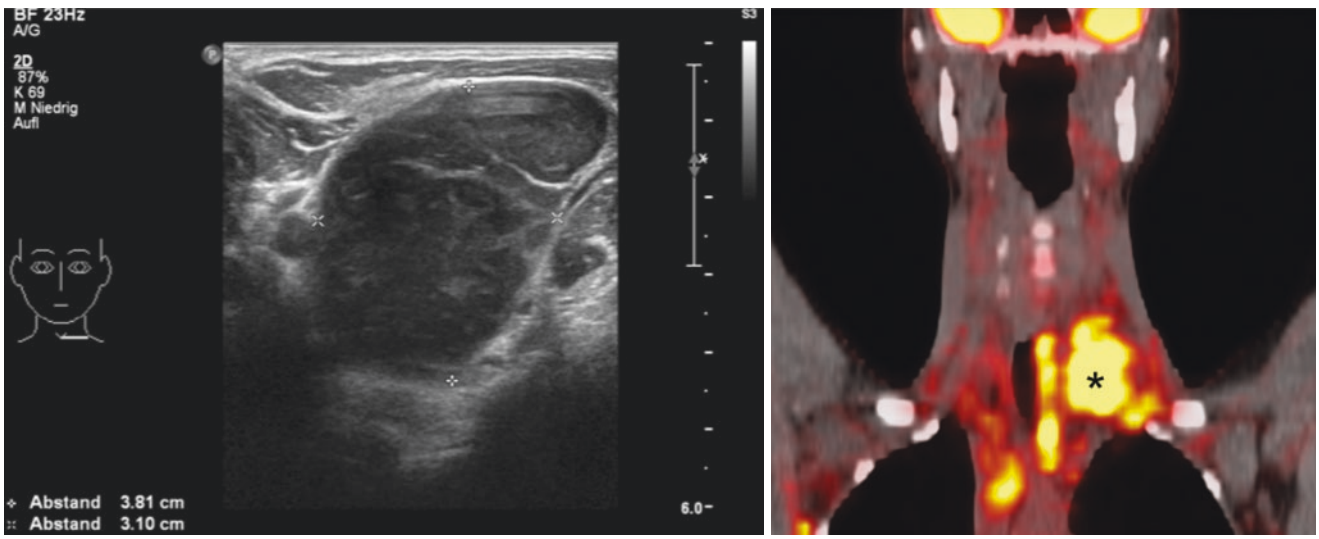

Fig. 9.30 Nodular sclerosis classical Hodgkin lymphoma (NSCHL). A 15-year-old boy. Supraclavicular lymph node enlargement (*asterisk*) is highly suspicious for malignancy. (PET/CT image *courtesy of* Department of Nuclear Medicine, Hannover Medical School, Germany)

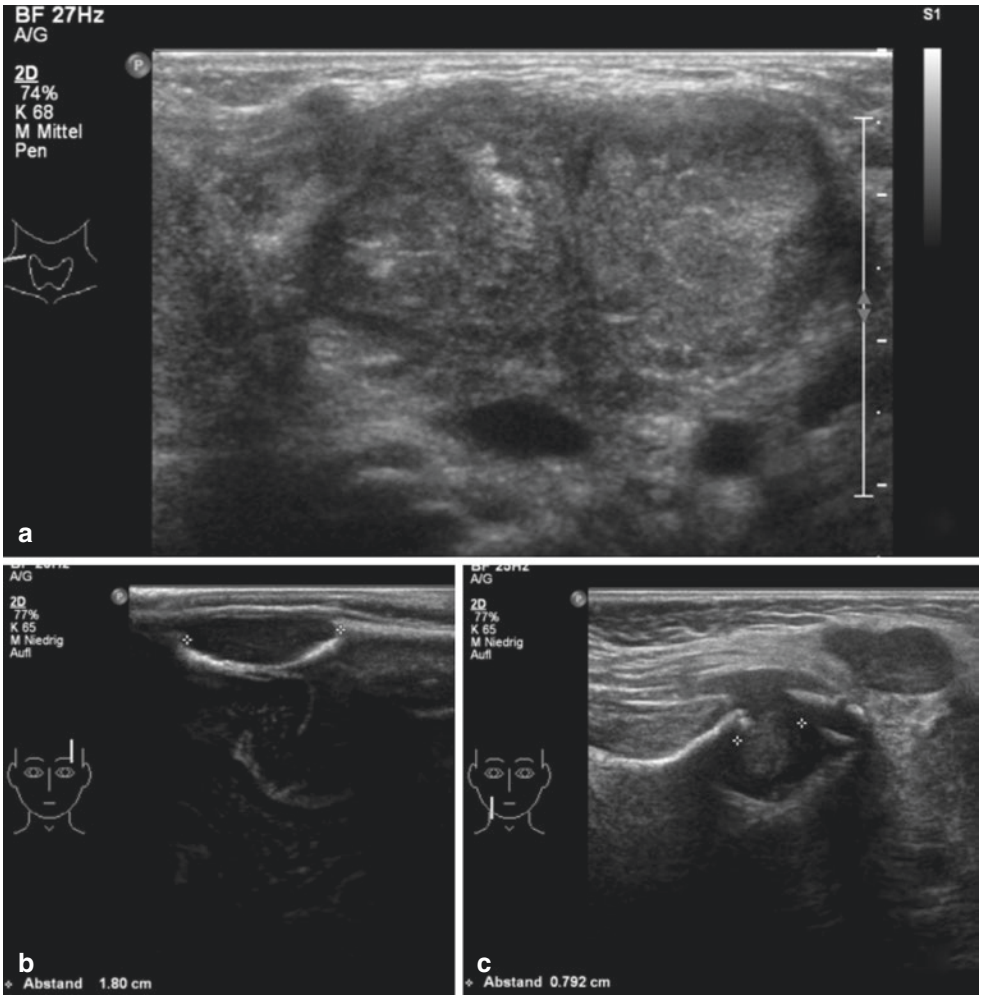

Fig. 9.31 Langerhans cell histiocytosis. A 3-year-old boy. Two weeks of neck swelling. Inhomogeneous hyperechoic lymph node (**a**). Bony lesions with soft tissue were found in the skull (**b**) and lower jaw (**c**)

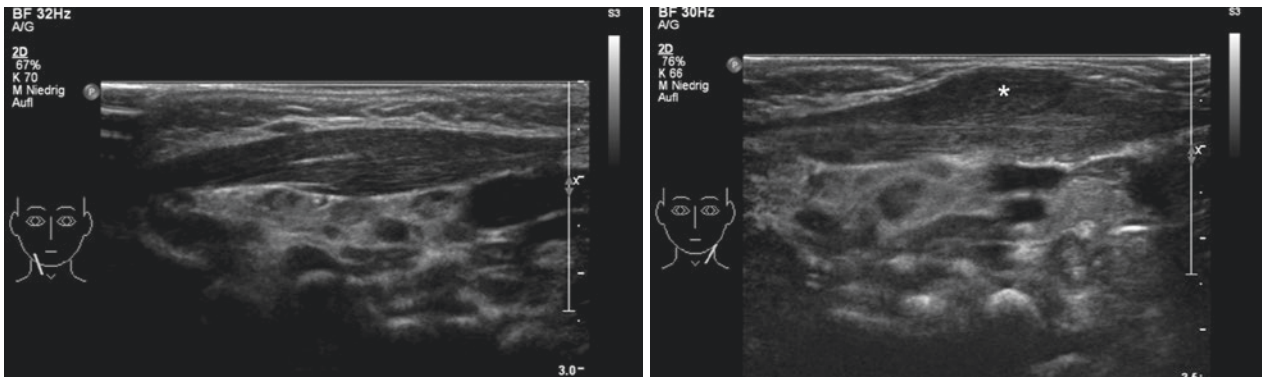

Fig. 9.32 Fibromatosis colli. A 4-week-old girl. Mild torticollis and palpable neck tumor. Focal enlargement (*asterisk*) of the left sternocleidomastoid muscle. (*See* Videos 9.15 and 9.16)

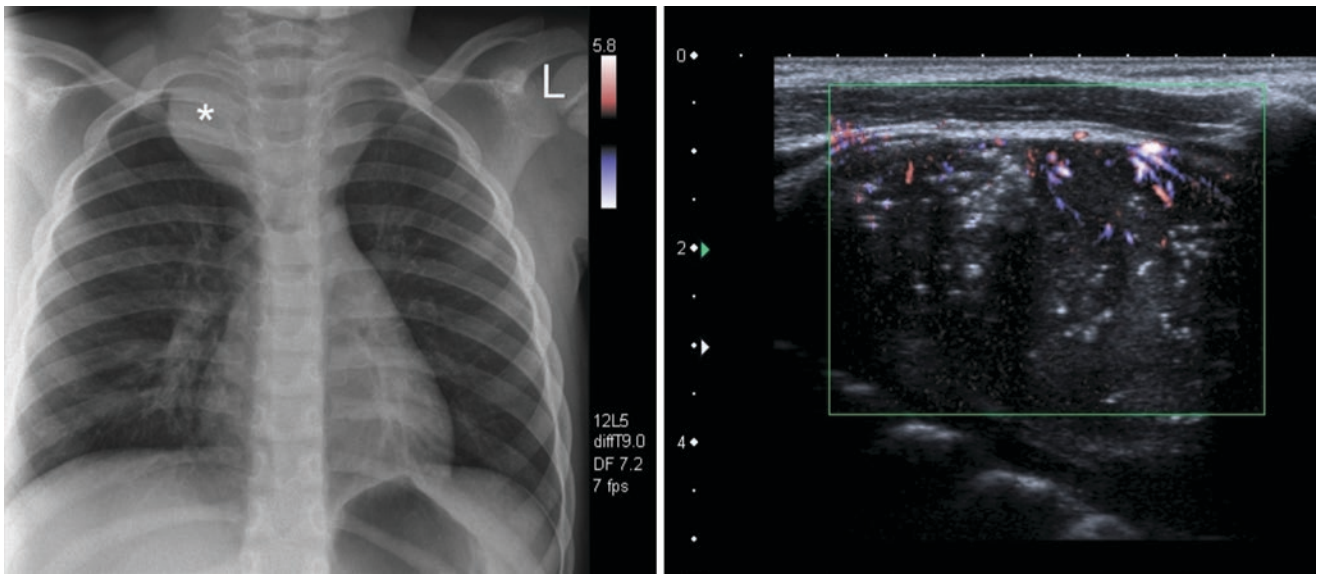

Fig. 9.33 Ganglioneuroma. A 4-year-old boy. The radiograph shows a mass of the upper mediastinum (*asterisk*). Ultrasound shows focal calcifications in a soft-tissue mass. (Ganglioneuromas may demonstrate calcifications)

Fig. 9.34 Lipoma of the neck. A 10-year-old girl. Typical pattern of subcutaneous fatty tissue. (*See* Video 9.17)

Key Points

- Cystic mass lesions may be caused by branchial cleft cysts, cystic/necrotic inflammatory or malignant lymph nodes, or by cystic lymphatic vascular malformations.
- Ectopic thymic tissue may occasionally be found cranially to the mediastinal thymus.
- Viral and bacterial lymph node enlargements are among the most common masses in the necks of children. Decisive for the differential diagnosis and therapy are form, vascularization, presence of purulent foci, and fistulas.
- Malignant tumors in infants are usually neuroblastomas, lymphomas, or rhabdomyosarcomas; in older children, these tumors are mainly lymphomas or thyroid carcinomas.
- Vascular anomalies and masses can be classified as tumors and vascular malformations according to the International Society for the Study of Vascular Anomalies (ISSVA).
- Fibromatosis colli typically occurs as a lateral neck swelling with accompanying torticollis in infants between weeks 2 and 8, caused by fibrosis of the caudal third of the sternocleidomastoid muscle.

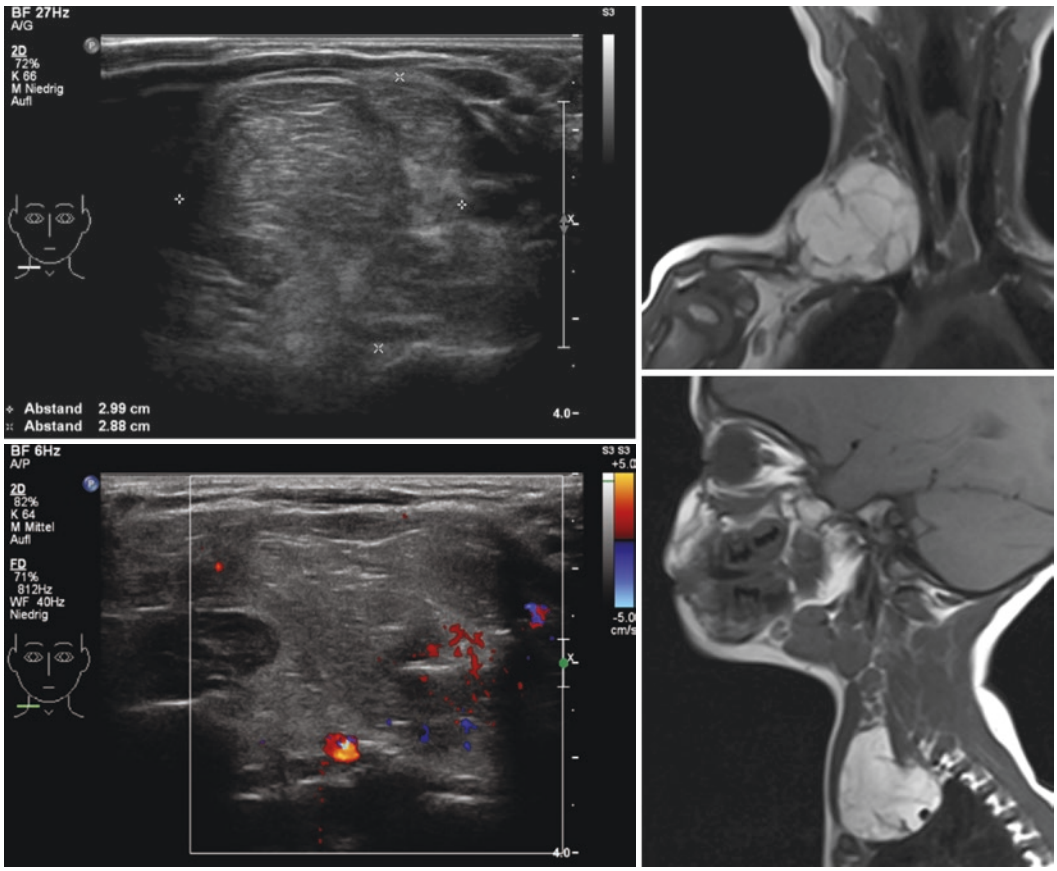

Fig. 9.35 Lipomatous tumor. A 21-month-old girl. Fatty tissue with some septations and inhomogeneous texture. A T1-weighted MRT without fat suppression (right) confirms the fatty nature of the lesion. (*See* Video 9.18)

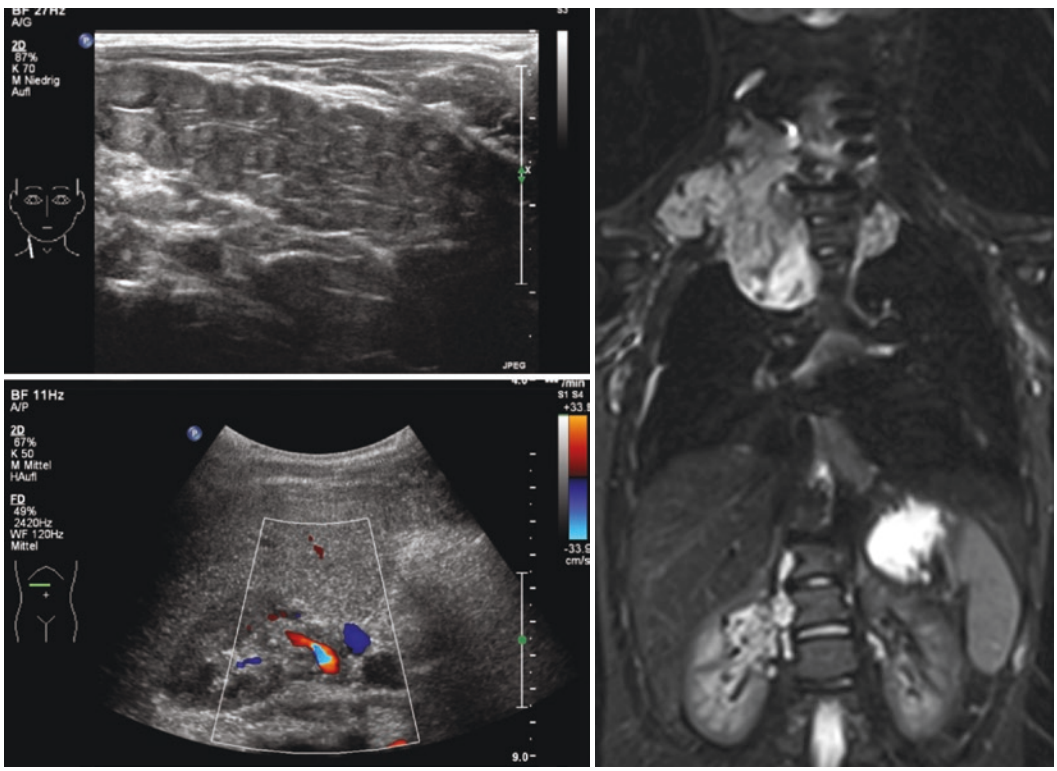

Fig. 9.36 Neurofibroma. A 5-year-old girl. Neurofibromatosis 1 (NF 1). Nodular tumors around the right vagal nerve and amorphous tissue in the right renal hilum. A fat-saturated T2-weighted MRT (right) shows the full extension of both lesions. (*See* Video 9.19)

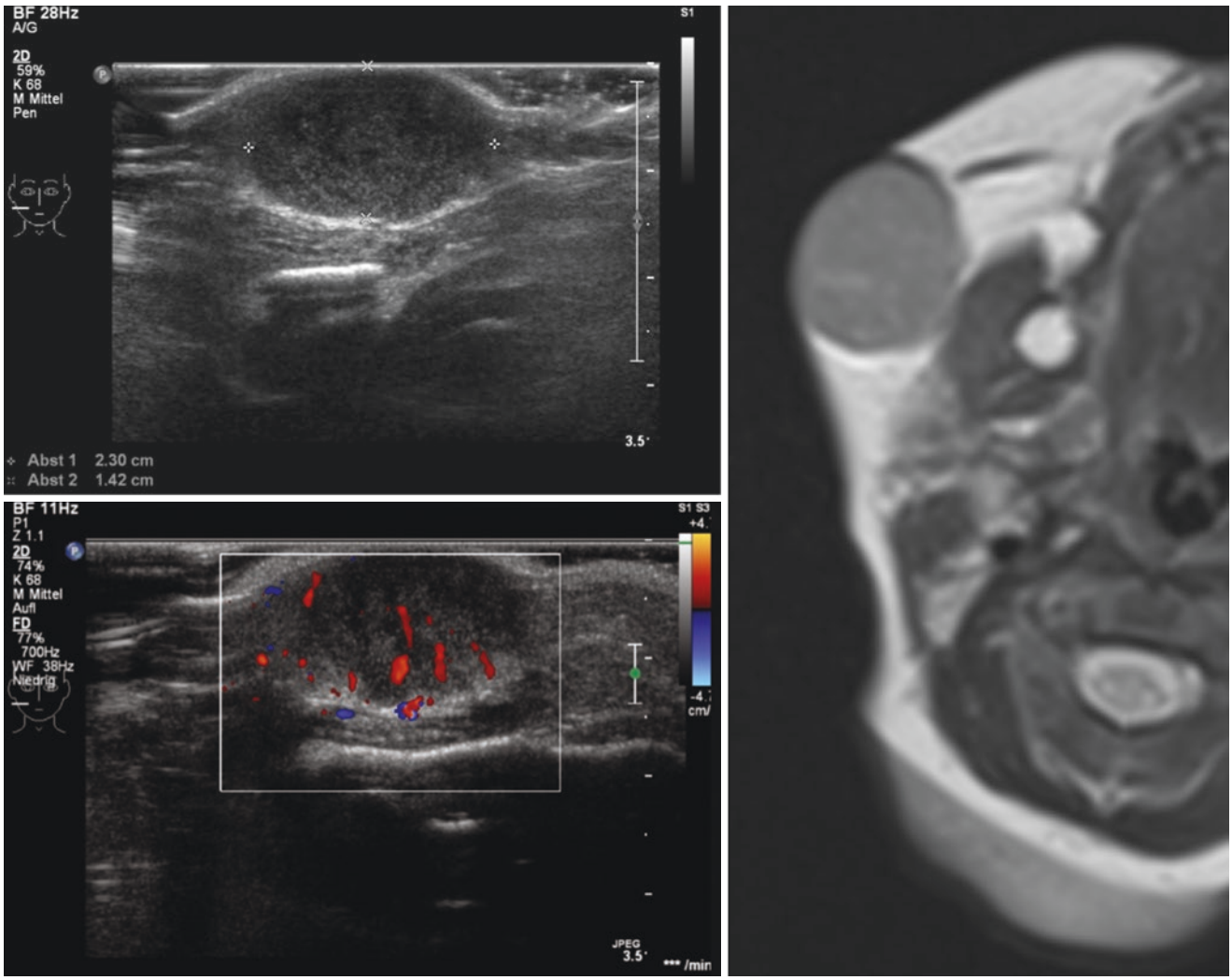

Fig. 9.37 Infantile myofibroma. A 1-month-old girl. Oval soft-tissue tumor without a vascular hilum as in a lymph node. The sonographic picture is nonspecific; other soft-tissue tumors (sarcomas) would be possible. A T2-weighted MRT without fat suppression (*right*) also shows an unspecific soft-tissue signal

References

1. Koch B, Hamilton BE, Hudgins P, Harnsberger HR. Diagnostic imaging: head and neck. 3rd ed. Philadelphia: Elsevier; 2016.
2. Rumack C, Wilson S, Charboneau JW, Levine D. Diagnostic ultrasound: pediatrics. 4th ed. Philadelphia: Elsevier; 2014.
3. Koch BL. Cystic malformations of the neck in children. Pediatr Radiol. 2005;35:463–77.
4. Richman DM, Benson CB, Doubilet PM, Peters HE, Huang SA, Asch E, et al. Thyroid nodules in pediatric patients: sonographic characteristics and likelihood of cancer. Radiology. 2018;288:591–9.
5. Mussa A, De Andrea M, Motta M, Mormile A, Palestini N, Corrias A. Predictors of malignancy in children with thyroid nodules. J Pediatr. 2015;167:886–92.
6. Avula S, Daneman A, Navarro OM, Moineddin R, Urbach S, Daneman D. Incidental thyroid abnormalities identified on neck US for non-thyroid disorders. Pediatr Radiol. 2010;40:1774–80.
7. ISSVA Classification of Vascular Anomalies ©2018 International Society for the Study of Vascular Anomalies. Available at http://www.issva.org/classification. Accessed 16 Sept 2018.
8. Restrepo R, Oneto J, Lopez K, Kukreja K. Head and neck lymph nodes in children: the spectrum from normal to abnormal. Pediatr Radiol. 2009;39:836–46.
9. Golriz F, Bisset GS 3rd, D'Amico B, Cruz AT, Alade KH, Zhang W, Donnelly LF. A clinical decision rule for the use of ultrasound in children presenting with acute inflammatory neck masses. Pediatr Radiol. 2017;47:422–8.

Sonography of the Large Neck Vessels and of Tumors with Suspected Infiltration of the Large Neck Vessels

10

Hans J. Welkoborsky

Exact knowledge of vascular anatomy and vascular ultrasonography is crucial for head and neck surgeons. Blood vessels in the neck can be altered either by diseases of the vessels (e.g., atherosclerosis, thrombosis, malformations) or by tumors in the neck. Furthermore, some diseases show characteristic vascular sonographic pattern. This chapter demonstrates vascular anatomy, sonographic, and Doppler/duplex sonographic characteristics of particular vessels. Sonographic criteria of atherosclerosis and carotid artery stenosis are also detailed, as well as infiltration of large vessels in the neck by a given tumor.

10.1 Introduction

For ENT surgeons, knowledge of vascular ultrasonography in the entire neck, with both its normal and pathological findings, is of great importance. Besides diseases of the neck vessels themselves, neck masses, lymph node diseases, and other diseases can alter the neck vessel anatomy. Furthermore, some neck diseases develop an infiltrative growth pattern involving the large vessels, especially the carotid artery and the internal jugular vein. Another indication for vessel sonography in the neck is the assessment of tumor vascularization and perfusion. With modern ultrasound equipment and high-resolution multiband transducers, it is possible to visualize blood vessels down to a diameter of about 1 mm. This chapter focuses on the description of ultrasound characteristics of diseases of the large neck vessels themselves and on estimation of vessel infiltration by a given tumor.

10.2 Anatomical Remarks

The large blood vessels in the neck are the common carotid artery, the carotid artery bifurcation, the external and internal carotid arteries, the vertebral arteries, the internal jugular vein, and the facial vein. Most of these vessels are easy accessible for ultrasound imaging, as they are fairly superficial in the neck and create significant acoustic impedance differences.

The carotid artery is one of the large vessels supplying the brain with blood. The right common carotid artery arises from the branches of the brachiocephalic trunk. It arises in the neck in one compartment together with the internal jugular vein, beneath the sternocleidomastoid muscle. In the vicinity of the second to fourth cervical vertebra (in most cases at the level of the third cervical vertebra), it bifurcates into the external and internal carotid artery. The left common carotid artery arises directly from the aortic arch and enters the neck in the vicinity of the seventh cervical vertebra. It arises in the neck also together with the internal jugular vein and bifurcates into the external and internal carotid artery (Fig. 10.1). The external carotid artery courses on both sides medial-cranially and is responsible (with its branches) for the blood supply of the neck soft tissues, the face, salivary glands, oral cavity, larynx, parts of the thyroid gland, and tongue. The largest branches of the external carotid artery (from caudal to cranial) are the ascending pharyngeal artery, superior thyroid artery (with the superior laryngeal artery), lingual artery, external maxillary artery, occipital artery, sternocleidomastoid branches, facial artery, and posterior auricular artery. The external carotid artery terminates with the internal maxillary and with the superficial temporal arteries as their terminal branches. Many branches of the external carotid artery are assessable by ultrasonography, at least at their origin when they arise from the main vessel. In cases of internal carotid artery occlusion, the branches of the external carotid artery become important collateral pathways, especially the branches that communicate with the ophthalmic

Electronic Supplementary Material The online version of this chapter (https://doi.org/10.1007/978-3-030-12641-4_10) contains supplementary material, which is available to authorized users.

H. J. Welkoborsky (✉)
Department of Otorhinolaryngology, Head and Neck Surgery, KRH Nordstadt Clinic–Academic Hospital, Hannover, Germany
e-mail: hans-juergen.welkoborsky@krh.eu

© Springer Nature Switzerland AG 2019

H. J. Welkoborsky, P. Jecker (eds.), *Ultrasonography of the Head and Neck*, https://doi.org/10.1007/978-3-030-12641-4_10

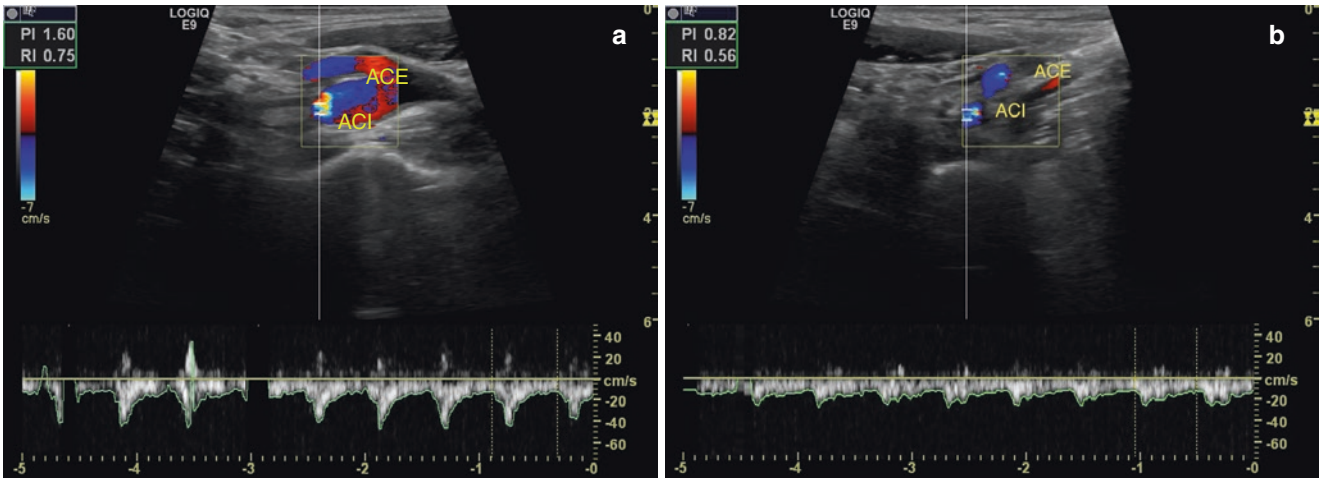

Fig. 10.1 Carotid artery bifurcation. (**a**) The common carotid artery (CCA) bifurcates into the external carotid artery (ACE), which is located usually anteriorly in the transverse section, and the internal carotid artery (ICA), which is located more dorsally. (**b**) In the axial section, the external carotid artery appears more superficial than the internal carotid artery

artery (i.e., the facial artery, angular artery, trochlear artery, meningeal artery).

The internal carotid artery does not have any branches in the neck. The vessel courses after the bifurcation more dorsal-cranially and passes the skull base through the carotid artery canal. The vessel then crosses the petrous bone and the lateral aspect of the sphenoid bone up to the cavernous portion in the vicinity of the cavernous sinus with the carotid artery siphon. In this area, the ophthalmic artery with the superior and posterior ethmoid arteries arises from the vessel. The internal carotid artery then forms a part of the circle of Willis, joins the posterior communicating artery, and terminates into the anterior and middle cerebral arteries. Sonographically, the internal carotid artery can be assessed from the bifurcation up to the inframandibular space.

The internal jugular vein can be assessed by ultrasound along its entire length from the supraclavicular fossa to the area of the posterior belly of the digastric muscle. In many cases, the facial vein and its junction with the internal jugular vein are visible, which is important from a clinical point of view, as many lymph nodes are located in this area, which is a preferred site for lymph node metastases arising from malignant tumors of the floor of the mouth, oral cavity, tonsils, tongue, oropharynx, and salivary glands (Fig. 10.2).

The vertebral arteries are other large vessels in the neck that are accessible for ultrasound examination. The right and left vertebral arteries arise directly from the subclavian arteries. They ascend and enter the costotransverse foramen at the level of the seventh or (more frequently) the sixth cervical vertebra. They course through the transverse foramina of the transverse processes of the cervical vertebra up to the second cervical vertebra; then, behind the atlas, pass the dura; and enter the intracranial space via the foramen magnum. Along the way, they give several branches to the deep neck and

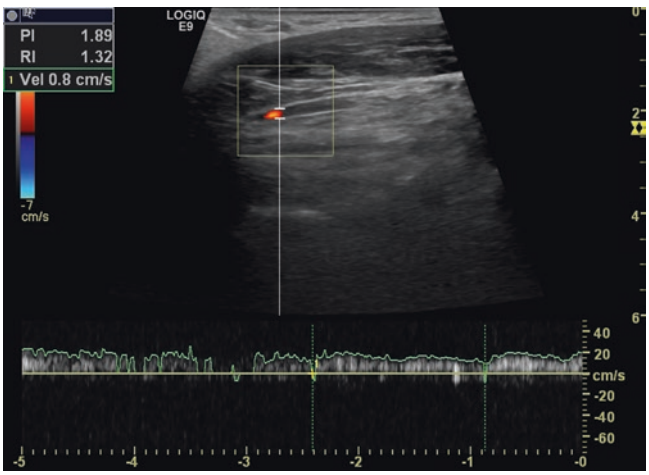

Fig. 10.2 Internal jugular vein in longitudinal section. It is more challenging to visualize the internal jugular vein than arteries because this vessel can easily be compressed, even with slight pressure of the ultrasound transducer. Performing a Valsalva maneuver often helps to better display the vein. (*See* Video 10.1.) Note the Doppler signal of the vein, which indicates a permanently low flow; no pulsation is visible. In some cases, the facial vein can also be seen, forming an angle with the internal jugular vein in which some lymph nodes are located

nuchal muscles, which form an anastomosis to the occipital artery from the external carotid artery (occipital-vertebral anastomosis). During the intracranial course of the vessels, branches include the posterior and anterior spinal arteries and the posterior inferior cerebellar artery, supplying blood to the medulla, cerebellum, and parts of the inner ear. Both vertebral arteries then unite to form the basilar artery, which maintains part of the blood supply of the posterior cerebral fossa, parts of the cerebellum, parts of the temporal lobes, and the occipital lobes. Ultrasound examination of the vertebral arteries is more challenging than that of the carotid

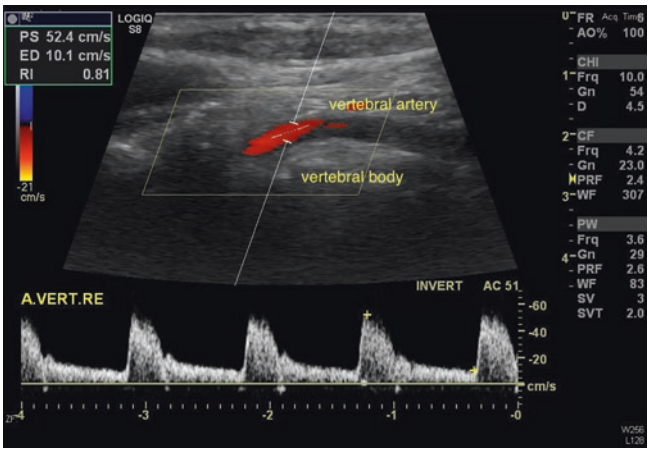

Fig. 10.3 The visualization of the vertebral artery is more challenging than that of the carotids because the vessel courses through the foramen transversarium in the transverse processes of the cervical spine and can be visualized only in the intravertebral segments . Courtesy of Dr. Silke Hörnschemyer-Decker, Dept. of Neurology, Nordstadt Clinic, Academic Hospital, Hannover, Germany

arteries, as its exposition is limited by its anatomy. In contrast to the examination of the carotid arteries, the vertebral arteries cannot be visualized continuously along their entire cervical length, but only in the intervertebral segments and at the atlas-loop portion (Fig. 10.3). In slim patients, the origin of the vessel from the subclavian arteries also can be visualized.

10.3 Technical Remarks

For examination of the large blood vessels in the neck and assessment of the perfusion of some neck masses, the ultrasound machine to be used must be equipped with the possibilities of B-mode sonography, C (color)-mode sonography, and D (Doppler)-mode sonography. Most recently, the B-flow mode was introduced in many modern ultrasound machines. This is an angle-independent measurement. Echo amplitudes of short, successive acoustic pulses are compared to each other by subtraction. Thus, echoes from moving particles (i.e., blood flow) can be differentiated from other tissues. The difference is visualized in a B-mode picture. The advantages of this technique are a more precise visualization of blood flow and no aliasing phenomenon.

The combination of B-mode and D-mode sonography is called "duplex," and the combination of B-mode, C-mode, and D-mode sonography is called "triplex." To estimate tumor perfusion, it is important that the equipment can detect even slow-flow blood velocities (2–5 cm/s).

Duplex- and triplex-mode ultrasound examinations of the large vessels in the neck and of neck masses with close relation to the large vessels are preferably performed with the patient sitting or lying. Small multifrequency ultrasound transducers with an appropriate frequency band of 7–12 MHz are suitable for B-mode sonography.

Examination of the carotid arteries and jugular vein includes transverse (axial) and longitudinal scans of the vessels. The patient is placed in a supine position with rotation of the head of about 45° to the contralateral side. First, conventional B-mode sonography is performed for identification and orientation of the large vessels (Fig. 10.4). This technique makes it possible to evaluate the morphology of the vessel, such as intima-media thickness, atherosclerotic plaques, or aneurysms. With additional C-mode, a two-dimensional color-coded flow image is superimposed over the B-mode image, allowing the visualization of flow velocities and flow direction (Fig. 10.5).

The transducer is now moved more distally, to the carotid artery bifurcation, to identify the internal and external carotid artery. The external carotid artery is frequently smaller than the internal carotid artery and has branches, so that its identification should not be a problem. From each section, a representative B-mode image is taken, along with spectral analysis (Doppler mode). The spectral cursor is placed inside the vessel parallel to the vessel's wall and in the center of the blood flow. The angle of insonation should be adjusted to the vessel's course and should be kept to 60° or lower.

The carotid artery appears in axial planes as a round shape with a hypoechoic center and a more hyperechoic border, in which different layers, representing the tissue layers (intima, adventitia, muscularis), can be identified (Fig. 10.6). The structure is not compressible; it does not change its shape when compressed by the ultrasound transducer.

The internal jugular vein is located lateral to the carotid artery. In axial planes, it is seen as a hypoechoic triangular-shaped structure. The borders are much thinner than those of the carotid artery, and no distinct tissue layers can be identified (Fig. 10.7). The jugular vein is compressible. For better visualization of the vessel, the patient is asked to perform a Valsalva maneuver, which causes the vessel to enlarge; it can then easily be identified (Video 10.1). The vagal nerve can be seen between the carotid artery and the jugular vein, laterally and attached to the artery.

The pulsation of the carotid artery and jugular vein is different: the artery displays a systolic pulse and no diastolic pulsation, whereas the jugular vein displays a larger systolic pulse followed by a diastolic pulse of small amplitude ("double pulse") (Video 10.2). The examination is then continued in the second plane (transverse scans) by rotating the transducer about 90°. The vessels appear now with a band-like hypoechoic shape.

The examination of the vertebral artery is more challenging. The transducer should be directed posteriorly, looking for the vessel in the vertebral canal of the vertebral bodies.

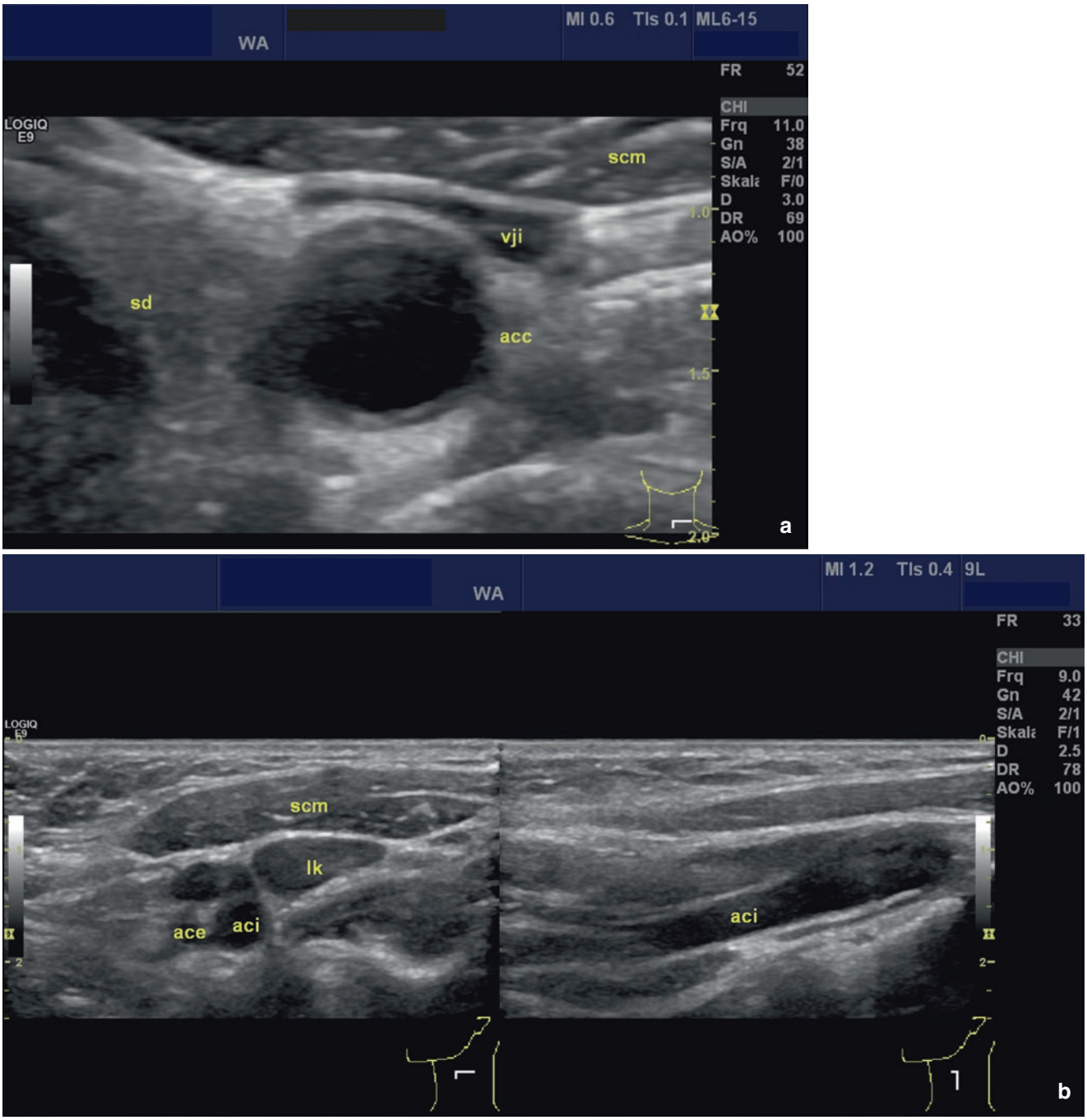

Fig. 10.4 B-scan sonography in axial (**a**; **b**, *left*) and longitudinal (**b**, *right*) sections of the caudal parts of the neck. In the median parts of the neck, landmarks include the sternocleidomastoid muscle (SCM) and the common carotid artery (acc), with the carotid artery bifurcation (**b**, *left*). In the cranial parts of the neck can be seen the sternocleidomastoid and digastric muscles and the external carotid artery (ECA) and internal carotid artery (ICA). Note that the external carotid artery is smaller than the internal carotid artery and has some branches. In this area, some lymph nodes (lk) typically occur. SD thyroid gland, IJV internal jugular vein

This is easier in tall and slim patients. The vessel's patency, flow direction, and flow velocity are recorded (Fig. 10.8).

Both the common carotid artery (CCA) and the internal carotid artery (ICA) are low-resistance vessels; both have a significant diastolic flow, but it is greater in the ICA. In contrast, the external carotid artery (ECA) is a high-resistance vessel that exhibits almost no diastolic flow, so the Doppler spectrum of these vessels has significant morphologic and sound differences. The blood flow velocity in the CCA is about 45–60 cm/s, in the ECA 60–90 cm/s, and in the ICA 55–90 cm/s (Fig. 10.9; Video 10.3). Peak systolic velocities of more than 100 cm/s must be considered pathologic [1–3].

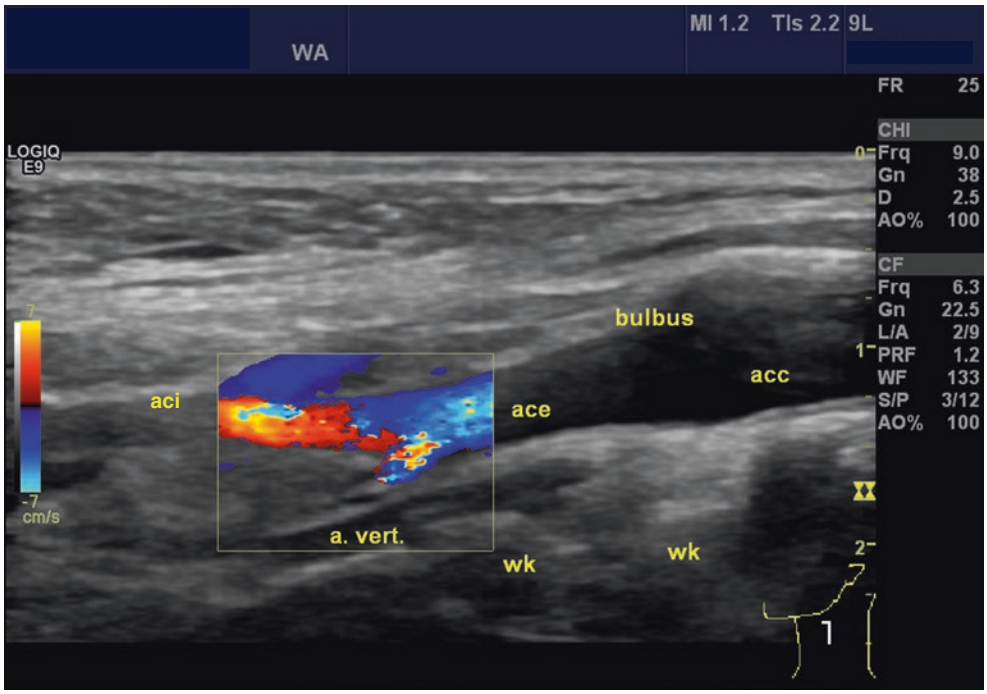

Fig. 10.5 Color-coded duplex sonography of the internal carotid artery, carotid artery bifurcation, and ICA. Note that red color means bloodstream toward the transducer, whereas blue color means bloodstream away from the transducer. Yellow or orange can signify some turbulence. (a) vert vertebral artery, acc common carotid artery, ECA external carotid artery, ICA internal carotid artery, bulb carotid artery bulb, wk. vertebral bodies

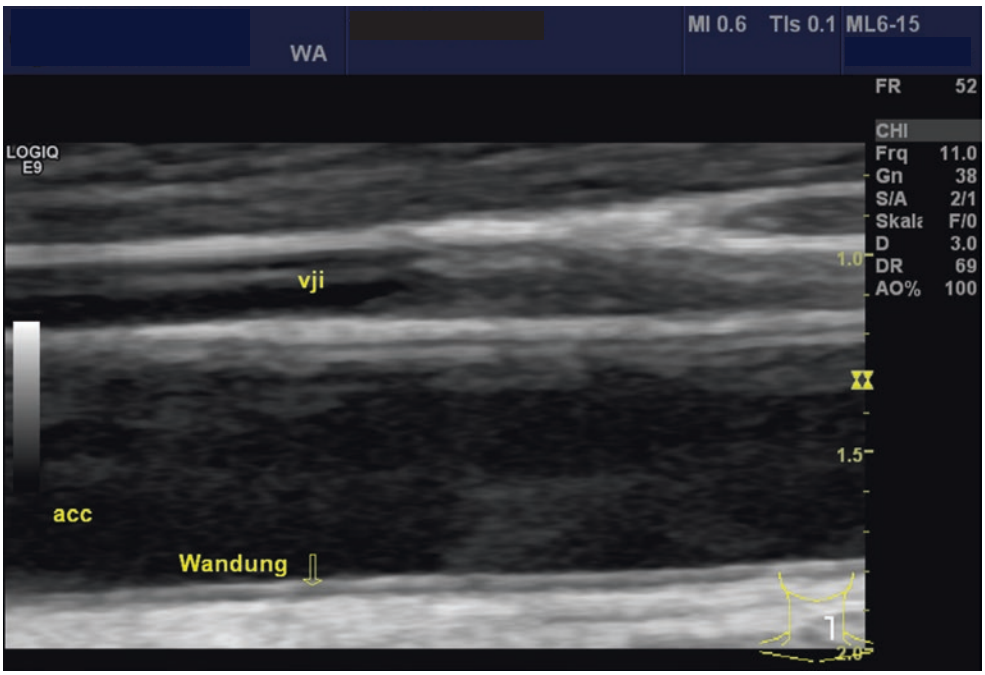

Fig. 10.6 High-resolution section of the common carotid artery (acc), in which the tissue layers (intima, muscularis, adventitia) can be identified. IJV, internal jugular vein; Wandung, vessel wall

The vertebral artery is also a low-resistance vessel in which the Doppler waveform resembles that of the ICA. However, normal peak systolic velocities in the vertebral artery are lower than in the ICA and are more variable than in the CCA or ICA. They normally range between 20 and 40 cm/s, and peak systolic velocities below 10–20 cm/s are considered to be abnormal [1]. Peak systolic velocities exceeding 40 cm/s might be due to an occlusion or stenosis of the contralateral vertebral artery; velocities may be normal in the dominant vertebral artery in cases of significant asymmetries of these arteries.

For accurate examination of the carotid artery, flow velocities are to be measured in the proximal, middle, and distal (just proximal to the carotid artery bifurcation) parts of the CCA; in the proximal, middle, and distal parts of the ICA; and in the proximal part of the ECA. The following hemodynamic parameters are derived from the single measurements and used for interpretation: peak systolic velocity

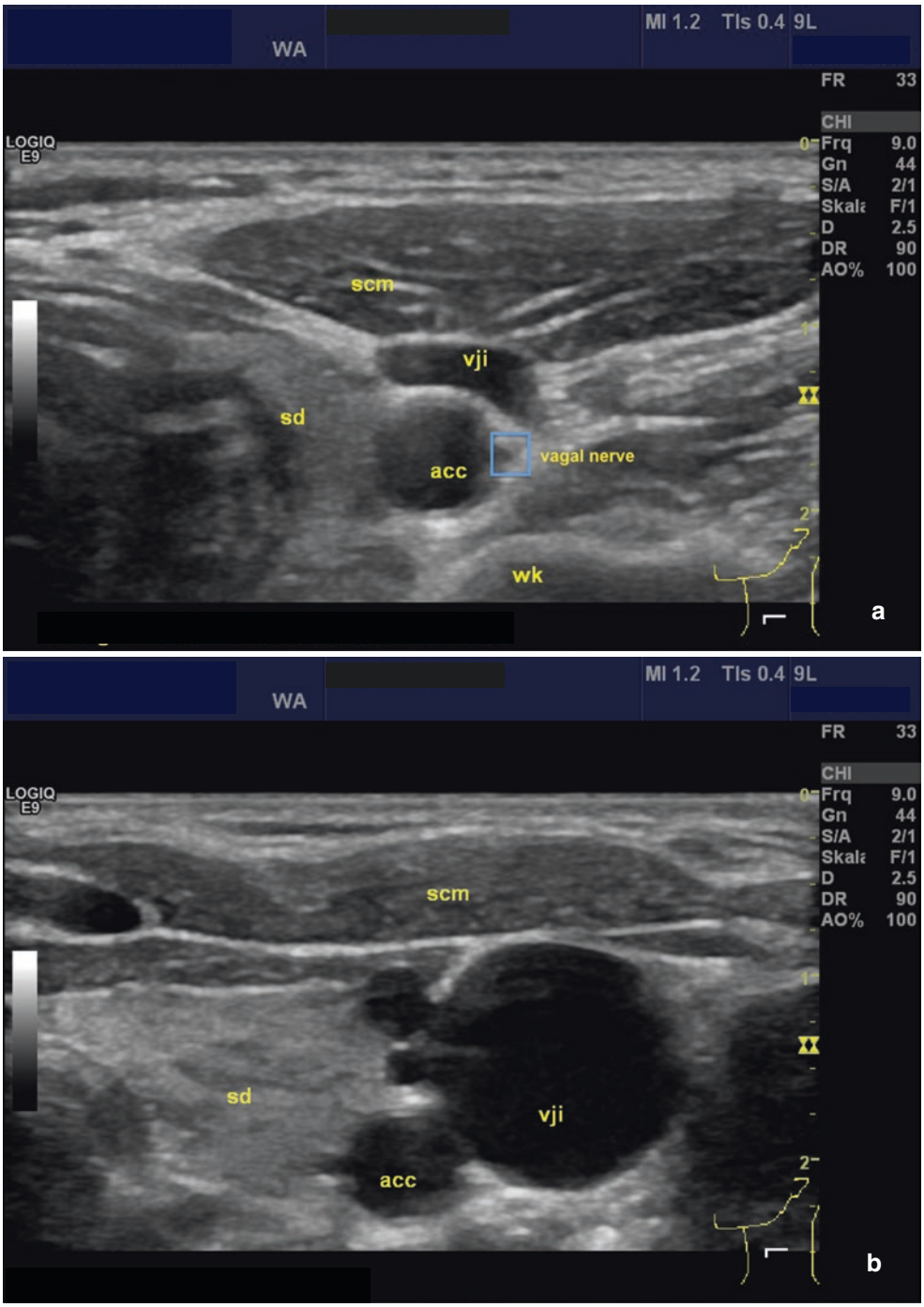

Fig. 10.7 (**a**) The internal jugular vein (IJV) has a triangular shape in axial sections and a band-like shape in transverse section. Here the vessel is located anterior to the carotid (acc). Note that the vagal nerve appears as a small, round, hypoechoic structure between the carotid artery and the jugular vein. The vein is compressed by the ultrasound transducer. (**b**) Following a Valsalva maneuver, the internal jugular vein "blows up" and gets a roundish shape in axial sections. This maneuver is suitable for purposes of orientation or in cases in which an infiltration of the vein is suspected

(PSV), end-diastolic velocity (EDV), mean flow velocity (MFV), peak systolic and end-diastolic ICA/CCA velocity ratios, resistance index (defined as (PSV-EDV)/PSV), pulsatility index (defined as (PSV-EDV)/MFV) and spectral characteristic [4–6].

To estimate tumor perfusion, the ultrasound machine must be able to detect slow blood flow velocities. The mass is visualized in conventional B-mode, and the vessels supplying the tumor with blood are detected by color-coded C-mode. Peak systolic velocities are variable (Table 10.1); those of

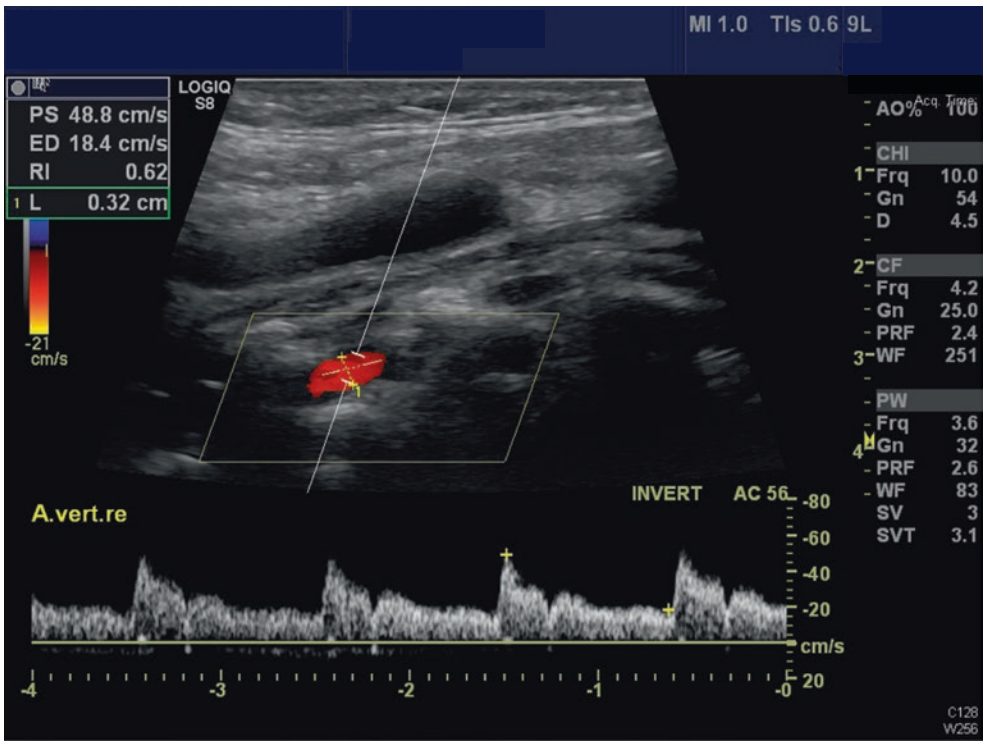

Fig. 10.8 Color duplex sonography of a right vertebral artery in a healthy person. The vessel is identified in the intravertebral segments. Patency and blood flow are recorded (Courtesy of Dr. Silke Hörnschemeyer-Decker, Dept. of Neurology, Nordstadt Clinic, Hannover, Germany)

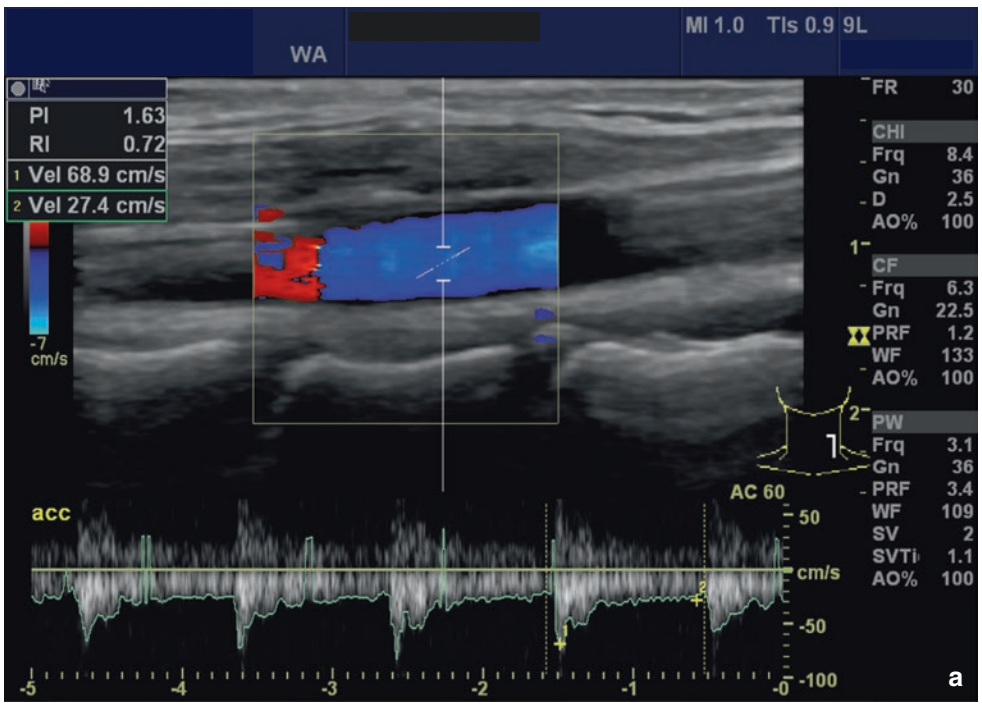

Fig. 10.9 Doppler spectrum of the common carotid artery (**a**, **b**) internal carotid artery (**c**) and external carotid artery (**d**). (Figures 10.9 a-c: Courtesy of Dr. Silke Hörnschemeyer-Decker, Dept. of Neurology, Nordstadt Clinic, Hannover, Germany). Note that the external carotid artery is a high-resistance vessel with a very low end-diastolic flow, whereas the internal carotid artery is a low-resistance vessel with a higher end-diastolic flow. The Doppler spectrum of the common carotid artery comprises both

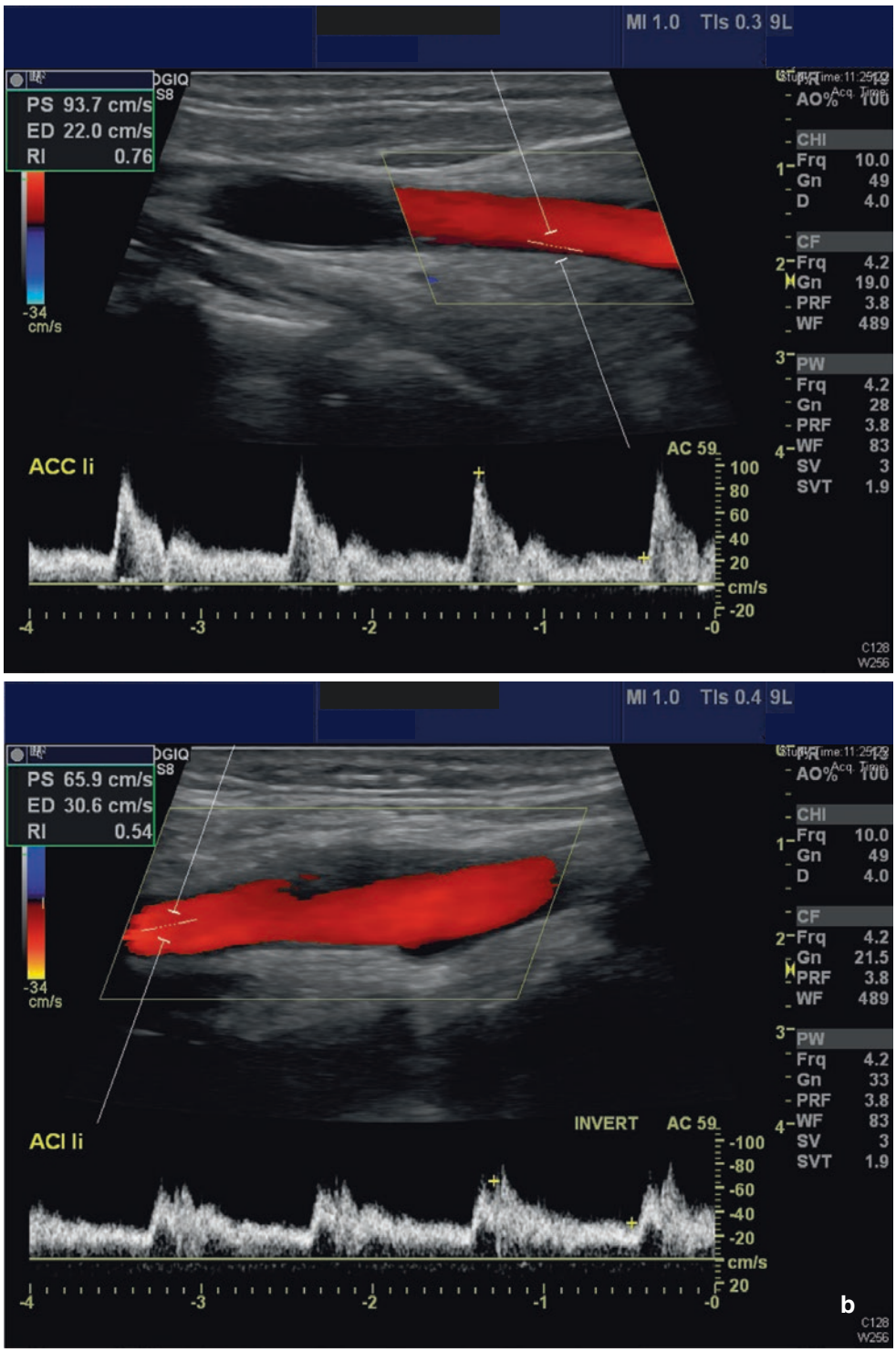

Fig. 10.9 (continued)

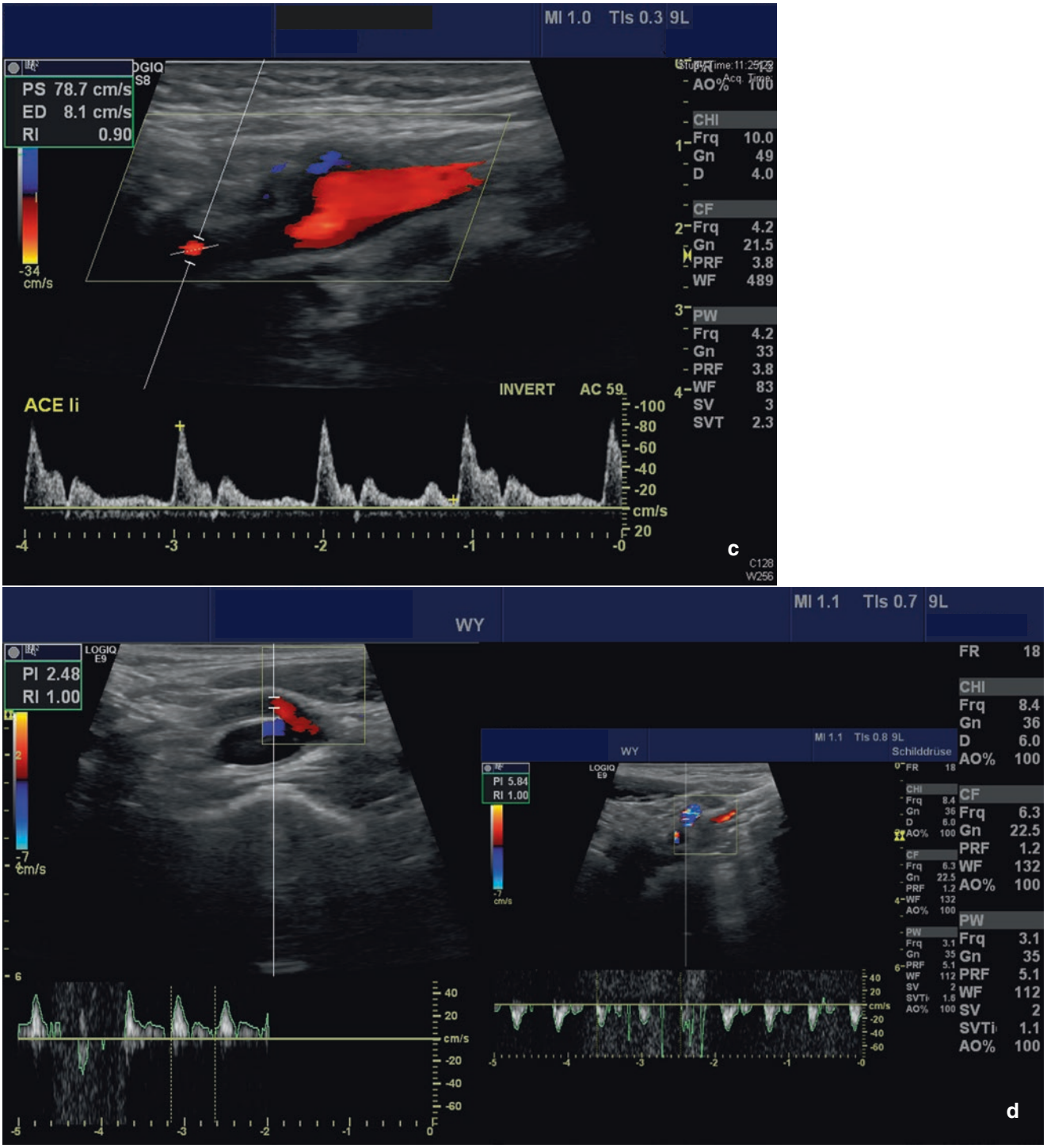

Fig. 10.9 (continued)

Table 10.1 Normal peak systolic blood flow velocities in different extracranial vessels and vessels for blood supply of cervical masses

Vessel	Peak systolic velocity (PSV)
Common carotid artery (CCA)	45–60 cm/s
Internal carotid artery (ICA)	55–90 cm/s
External carotid artery (ECA)	60–90 cm/s
Vertebral artery	20–40 cm/s
Tumor vessels	Variable; 2.5–10–30 cm/s

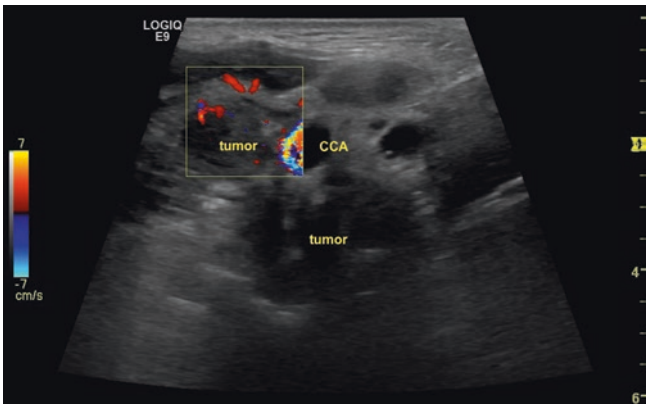

Fig. 10.10 Visualization of small vessels supplying a neck mass with blood. The vascularization comes from the periphery into the mass. By Doppler sonography, peak systolic velocities of 2.5–5 cm/s in these small vessels can be estimated

2.5–10 cm/s can also be observed in the small tumor vessels as velocities exceeding 20 cm/s (Fig. 10.10; Video 10.4).

10.4 Indications for Ultrasound Imaging of the Large Neck Vessels

Basically the indications for ultrasound examinations of the extracranial vessels and vertebral arteries, according to the latest advice from the American Institute of Ultrasound in Medicine (AIUM) and the society of radiologists in ultrasound (SRU) [7], can be divided into neurological and non-neurological indications:

- Neurological indications
  - Hemispheric neurologic symptoms, such as stroke, transient ischemic attacks, and amaurosis fugax
  - Unexplained or non-hemispheric neurologic symptoms
  - Cervical bruit
- Non-neurologic indications
  - Diseases of the large vessels themselves
    - Suspected carotid artery dissection or pseudoaneurysms
    - Suspected arteriovenous malformations (arteriovenous shunts)
    - Atherosclerotic plaques and suspected carotid artery stenosis
    - Follow-up in patients with proven carotid artery disease
    - Suspected subclavian steal syndrome
    - Follow-up after cerebrovascular revascularization, carotid endarterectomy, carotid stenting, or carotid-to-subclavian bypass
  - Other indications
    - Pulsatile neck masses
    - Preoperative examination before major cardiovascular surgery
    - Intraoperative monitoring of vascular surgery
    - Large neck masses with suspected vessel infiltration
    - Estimation of the perfusion of a given neck mass

The last two points are not advised by the AIUM and SRU, but for head and neck surgeons, it is of great importance to determine the relation between a given tumor and the large neck vessels and to estimate suspected tumor infiltration of the vessels, in order to decide whether the tumor can be resected with little risk for the patient. As many neck masses, such as lymph node metastases, reactive neck lymph nodes, and masses related to malignant lymphoma, paraganglioma, and hemangioma, have a characteristic perfusion pattern, it is reasonable to conclude that duplex and triplex examination of these lesions provides very important information that will influence therapeutic strategy.

The following sections focus on the description of typical sonographic findings in diseases of the large vessels themselves and on ways to exclude infiltration by examining the relation between given tumors and the large vessels.

10.5 Diseases of the Large Neck Vessels

10.5.1 Carotid Artery Pathology

Carotid ultrasonography is the most useful imaging technique in the evaluation of patients with symptomatic and asymptomatic carotid artery stenosis. Carotid sonography provides data on the extent, site, and degree of stenosis, according to the distribution of abnormal blood flow patterns within, proximal to, and distal to a narrowed arterial segment. Carotid artery ultrasonography has been shown to achieve a sensitivity of 92–100% and specificity of 93–100% to assess the degree of stenosis, which is comparable to or even better than other imaging techniques, such as CT scans. Conventional angiography attains important information about the diameter of the vessel, whereas ultrasonography provides important information on the length

of the lesion and on blood flow; the two methods partially correlate [8].

Magnetic resonance angiography (MRA) is reported to achieve a higher overall accuracy of 70–99% for diagnosis of a stenosis, compared with ultrasound, but the techniques are comparable for detecting complete or incomplete carotid artery occlusion. As ultrasonography provides additional information about the vessel's wall and morphology, some authors conclude that the combination of ultrasound and MRA seems most accurate in diagnosing carotid artery diseases [9]. Ultrasound examinations provide important information regarding the severity of stenosis, but the correlation between its results and the results of conventional intra-arterial angiography and CT angiography is uncertain in many cases [10]. In a Cochrane meta-analysis, the threshold of ultrasound-determined peak systolic velocity >130 cm/s showed a sensitivity of 98% and a specificity of 95% for grading an ICA stenosis of >50% in angiography, and a peak systolic velocity >200 cm/s revealed a sensitivity of 90% and a specificity of 94% in diagnosing an angiographic stenosis >70% [11].

Several studies have been conducted to answer the question whether the degree of carotid stenosis in asymptomatic patients predicts the risk for a transient ischemic attack or a stroke. In general, the overall annual risk of a stroke is about 3–4% in patients with asymptomatic stenosis of 80–99% and below 1% in patients with a stenosis <80% [12].

Atherosclerotic plaques are the most common cause for carotid artery stenosis. An atherosclerotic plaque is defined as an area of a focal wall protrusion greater than 1.5 mm or a focal vessel wall thickening of more than 50% greater than the surrounding wall thickness [1] (Fig. 10.11). If an atherosclerotic plaque is present, the maximal carotid plaque thickness is determined by measurement in the highest plaque prominence in any of the three carotid artery segments assessed in multiangled images [1]. The plaque size, plaque surface, and plaque composition can be determined by B-mode sonography, and three additional morphologic parameters can be evaluated:

- The intima-media thickness (IMT)
- The carotid plaque burden and total plaque area (TPA)
- The three-dimensional estimation of plaque volume

TPA and three-dimensional plaque volume are highly correlated with the risk of cardiovascular disease and stroke.

Morphologically, several features are determined by a combination of B-mode ultrasonography and duplex sonography [13]:

- *Plaque size*. It is measured in axial and longitudinal scans. It correlates directly with the degree of stenosis and has some impact as an independent predictor for future cerebrovascular events and as a predictor for myocardial infarction.
- *Plaque ulceration and plaque surface irregularities*. The estimation of plaque surface irregularities is sometimes challenging by B-mode sonography, but it has some predictive value for the stroke risk.

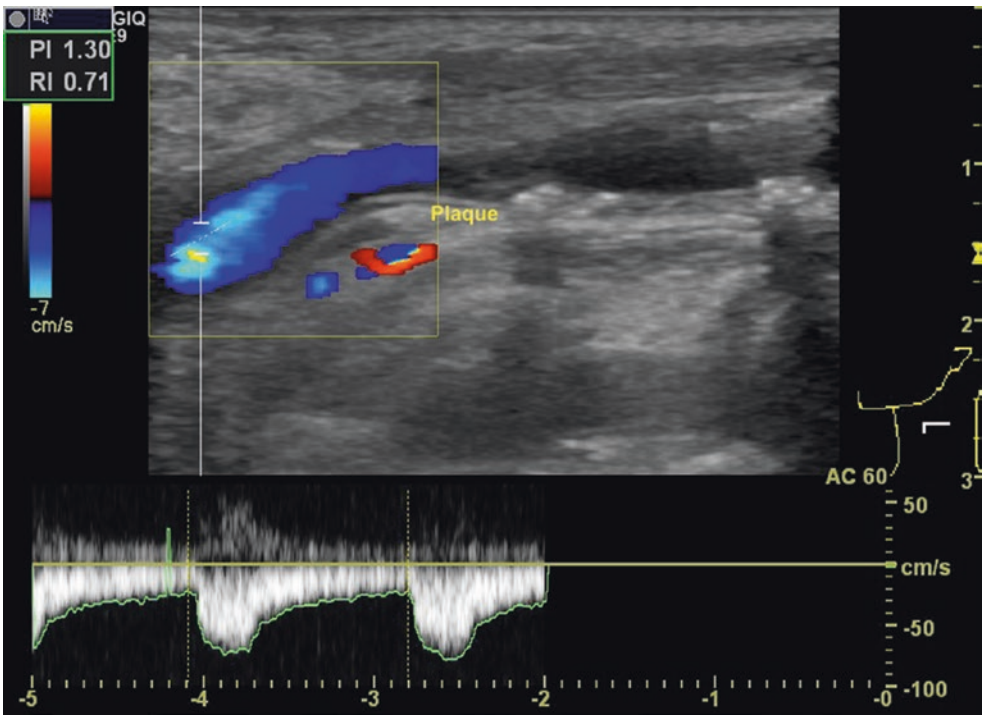

Fig. 10.11 Atherosclerotic plaque in the ICA with a focal wall protrusion >1.5 mm and a focal thickening more than 50% greater than the surrounding wall thickness

- *Plaque echogenicity*. The basic difference is between hyperechoic (echodense) and hypoechoic (echolucent) plaques. Hyperechoic plaques contain more calcium and are therefore calcified. In B-mode sonography, they are seen as bright areas attached to the vessel's lumen, with acoustic shadowing (Fig. 10.12). Hypoechoic plaques contain more lipid or blood. They are seen as masses that are hypoechoic compared with the surrounding tissue, and they lack acoustic shadowing (Fig. 10.13). Several studies revealed that hypoechoic, lipid-rich plaques are associated with the risk of plaque progression and with increased risk for future cerebrovascular events. In cases of inflammatory lesions, hypoechoic plaques also occur with a smooth or slightly irregular surface [14]. Calcified hyperechoic plaques may induce instability at the border with soft tissues in the vessel's wall, with a risk for plaque rupture, but several investigations have shown that plaques with a higher calcification percentage have a smaller lipid-rich necrotic core, which probably decreases plaque vulnerability [1].
- *Distal turbulence intensity in the carotid bifurcation* [13]. According to a meta-analysis and review of the literature [15], there is some evidence that some plaque features, including echolucency, neovascularization, ulceration, and intraplaque motion, are associated with high risk for ischemic symptoms, but the sensitivity and specificity of sonography in detecting lipid-rich necrotic core, intra-

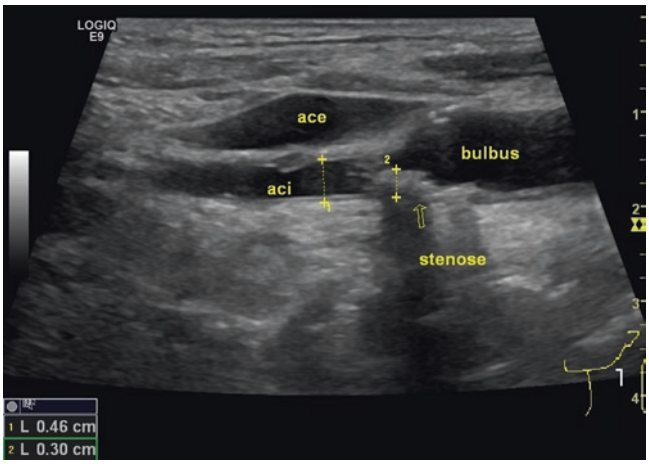

Fig. 10.12 Hyperechoic (echodense) plaque in the internal carotid artery (ICA). The plaque contains calcium and appears as a bright area attached to the vessel's lumen. Note the acoustic shadowing behind the plaque, a sign of calcification

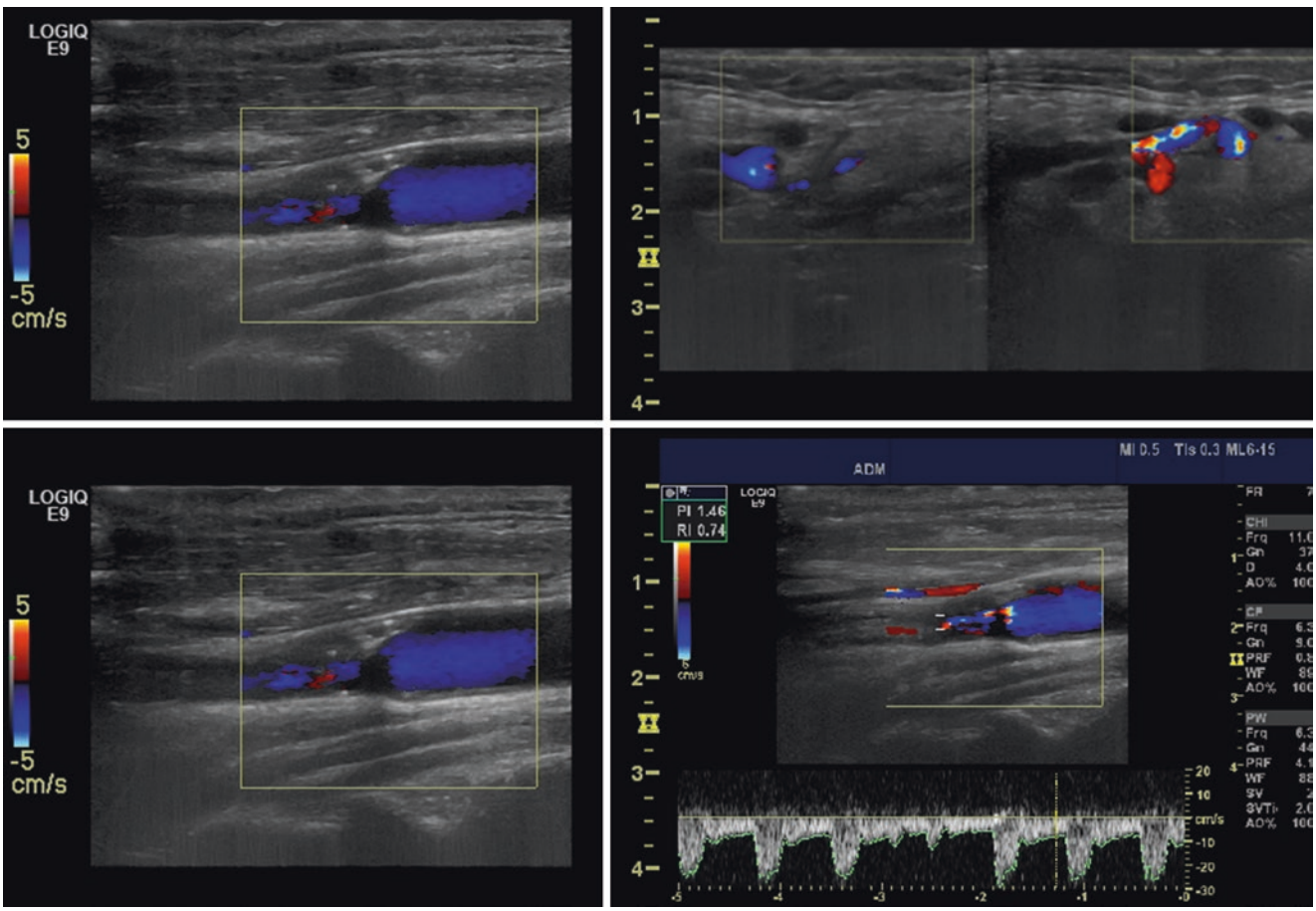

Fig. 10.13 Hypodense (echolucent) plaque in the ICA. It displays as a hypoechoic mass attached to the vessel's lumen. Longitudinal planes (*left*), axial plane (*top right*), and Doppler spectrum (*bottom right*)

plaque hemorrhage, and ulceration (predictors for risk stratification) are limited, so additional MRI is recommended in some cases [16].

Carotid Intima-Media Thickness (IMT)

Much effort has been made in the past to investigate carotid IMT and to elucidate its potential impact on atherosclerosis and vascular events. The IMT measurements are performed in longitudinal (transverse) scans (Fig. 10.14), with measurements performed at the following standardized carotid artery segments [1]:

- The near and the far wall of the carotid segment from 10 mm to 20 mm proximal to the tip of the flow divider into the CCA
- The near and the far wall of the carotid artery bifurcation, beginning at the tip of the flow divider and extending 10 mm proximal to the flow divider tip
- The near and the far wall of the proximal 10 mm of the ICA

It is important to note that the IMT is measured out of plaque areas. A total carotid IMT is calculated as a composite measure (the mean of the twelve sites described above). Although several studies have established a clear association between IMT, plaque size, and vascular events and between a decrease of IMT influenced by the intake of medications and a decrease of risk for vascular events, normal values for IMT in different populations and age groups are lacking, and the importance of these findings in regard to clinical practice is still unclear. As a result, IMT and plaque measurement are regarded only as useful tools in estimation of risks of vascular events in patients with risk factors. An increased CCA wall thickness especially might be associated with rapid progression of carotid stenosis [17]. It is considered that the advantage of B-mode ultrasonography lies in its cost-effectiveness and lack of patient inconvenience, so that it can be applied for risk assessment and monitoring of drug therapy [1, 18].

Carotid Artery Stenosis

There are three basic pathogenetic mechanisms for cerebral ischemia caused by a carotid artery stenosis due to atherosclerotic plaques: (1) embolization, in which parts of the plaque flow from the carotid artery into the intracerebral vessels; (2) thrombosis of the carotid artery due to plaque and propagation of thrombosis to the intracerebral vessels; and (3) downregulation of cerebral perfusion due to blood flow impairment.

B-mode and color Doppler sonography is used to estimate carotid artery stenosis, but blood flow velocities and other criteria used for diagnostic purposes and estimation of the degree of stenosis vary significantly between different laboratories and different studies. These differences may be due to differences in the study population, the sonographer's expertise, the variability of vascular anatomy, and the ultrasound equipment [4–6, 19, 20]. Much effort has been made to search for a perfect ultrasonic classification in assessing carotid artery stenosis. A multiparametric approach that has been implemented includes as its criteria the maximal peak systolic velocity (PSV), end-diastolic velocity, and the ICA-to-CCA ratio [4, 5, 21, 22]. According to the North American Symptomatic Carotid Endarterectomy Trial (NASCET), a carotid stenosis is defined as an occlusion of more than 20% of the vessel's lumen, and a *significant* stenosis is defined as an occlusion of more than 50% [23]. Doppler velocity criteria can successfully be applied for classifying the severity of an ICA stenosis. On the other hand, the simplified greyscale/mosaic protocol has a high negative predictive value for detection of carotid artery stenosis with an occlusion of more than 50% [23]. The correlation between the parameter "maximum peak systolic velocity" and artery stenosis is moderate [23]. Additional criteria that could be used include the prestenotic flow in the CCA and the extent of poststenotic disturbances (Video 10.5) [5]. By using this multiparametric approach, the correlation between sonography and conventional angiography in describing the degree of stenosis can be improved [5]. A meta-analysis of 19 publications revealed a significant variability of these Doppler velocity stenosis criteria, compared with conventional angiography in both native and stented ICAs [6].

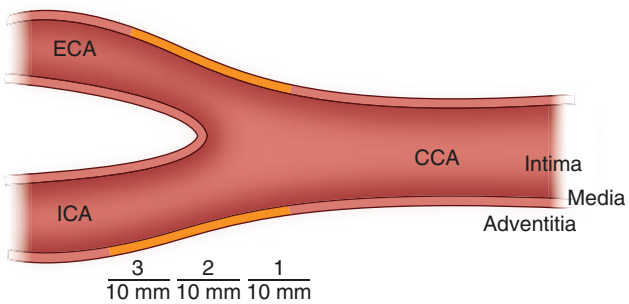

Fig. 10.14 Sites for measuring the carotid intima-media-thickness (IMT). (1) In a segment of 10–20 mm proximal to the flow divider in the CCA. (2) In the carotid artery bifurcation up to 10 mm proximal to the flow divider. (3) The near and the far wall in the proximal 10 mm of the ICA [1]

Three-dimensional ultrasound imaging of the vessel is useful to recognize carotid stenosis. Together with flow pattern, this technique might be important for planning an operative procedure in the future [24].

According to the AIUM and SRU (Society of Radiologists in Ultrasound) consensus recommendations, carotid artery stenosis can be graded according to the sonographic characteristics listed in Table 10.2a, b [7, 25]:

- Minimal carotid artery stenosis (<40%)
- Mild carotid artery stenosis (40–59%) (Fig. 10.15)
- Moderate carotid artery stenosis (60–79%) (Fig. 10.16)
- Severe carotid artery stenosis (80–99%) (Fig. 10.17)
- ICA occlusion (100%)

B-mode and duplex sonography is also highly useful in cases in which endarterectomy or insertion of a stent has been performed. In these cases, duplex sonography reveals information about the revascularization and eventual restenosis [26]. Patients who have received a carotid artery stent or carotid artery angioplasty for carotid stenosis or aneurysm should undergo careful long-term follow-up and surveillance, which can be ensured by both duplex sonography and transcranial Doppler (TCD) sonography [27, 28], dynamic techniques that are noninvasive and cause no radiation exposure. By B-mode and duplex sonography, the position of the stent and its patency can be estimated (Fig. 10.18). TCD provides information about the cerebral hemodynamic status [27, 29]. Duplex sonography can be used to estimate restenosis after stent implantation; the risk is about 6% after 2 years [30, 31]. In a long-term follow-up, increasing peak systolic velocities and ICA/CCA ratios correlate with evolving restenosis in the stented carotid artery [32]. In patients following carotid arterioplasty, carotid duplex ultrasound identifies

Table 10.2a Grade of ICA stenosis according to NASCET [23]

Grade of stenosis (%)		10	20–40	50	60	70	80	90	Occlusion
Main criteria	B-mode sonography	+++	+						
	Color-coded sonography	+	+++	+	+	+	+	+	+++
	Systolic peak flow velocity in the maximum of the stenosis (cm/sec) ca. (=circa)			200	250	300	350–400	100–500	
	Systolic poststenotic peak velocity					>50	<50	<30	
	Collateral vessels and precursors (periorbital arteries/ACA)					(+)	++	+++	+++
Additional criteria	Diastolic prestenotic blood flow deceleration (CCA)					(+)	++	+++	+++
	Poststenotic flow disturbances/turbulences			+	+	++	+++	(+)	
	End-diastolic peak velocity in the maximum of the stenosis (cm/sec)			<100	<100	>100	>100		
	"Confetti" sign				(+)	++	++		
	Stenosis index (ICA/CCA)			≥2	≥2	≥4	≥4		

Table 10.2b Grading and sonographic and Doppler characteristics of carotid artery stenosis [1, 7, 25]

Grade	Sonographic characteristics	Systolic blood flow velocity
Minimal (<40%)	Small atherosclerotic plaque and/or thickening of the intima/media	<120 cm/s
Mild (40–59%)	Larger atherosclerotic plaques	Local increase of peak and mean flow velocities Systolic blood flow velocity >120 cm/s
Moderate (60–79%)	Atherosclerotic plaques occlude more than 50% of the vessel's lumen Distortion of normal flow in addition to an increase of peak and flow velocities	120 cm/s through 250 cm/s with systolic flow deceleration in the poststenotic segment of the vessel
Severe (80–99%)	Only a minor vessel lumen is visible by B-mode and color Doppler sonography	Peak flow velocities exceeding 250 cm/s (up to 500 cm/s!) Prestenotic and poststenotic blood flow velocity is significantly reduced compared with the unaffected contralateral side Retrograde flow via the ophthalmic artery may occur
Complete occlusion (100%)	No lumen can be detected inside the vessel by either B-mode or color Doppler sonography	Absence of any signal A low-velocity signal along with predominant reversed signal component and absence of diastolic flow can be detected at the presumed origin of the ICA (stump flow) The blood flow of the CCA is reduced and a retrograde flow in the ophthalmic artery may occur. Elevated diastolic flow velocity in the ECA may occur, indicating collateral supply via the ophthalmic artery

CCA common carotid artery, *ECA* external carotid artery, *ICA* internal carotid artery

severe recurrent stenosis, but it also can identify carotid arteries that will appear normal on arteriography [28]. Hence, TCD sonography and color duplex sonography are useful in the diagnosis and risk stratification of patients with carotid artery disease [29]. In conclusion, ultrasonographic techniques are noninvasive examinations with low cost and good availability for the initial diagnosis and follow-up of many carotid artery diseases [33].

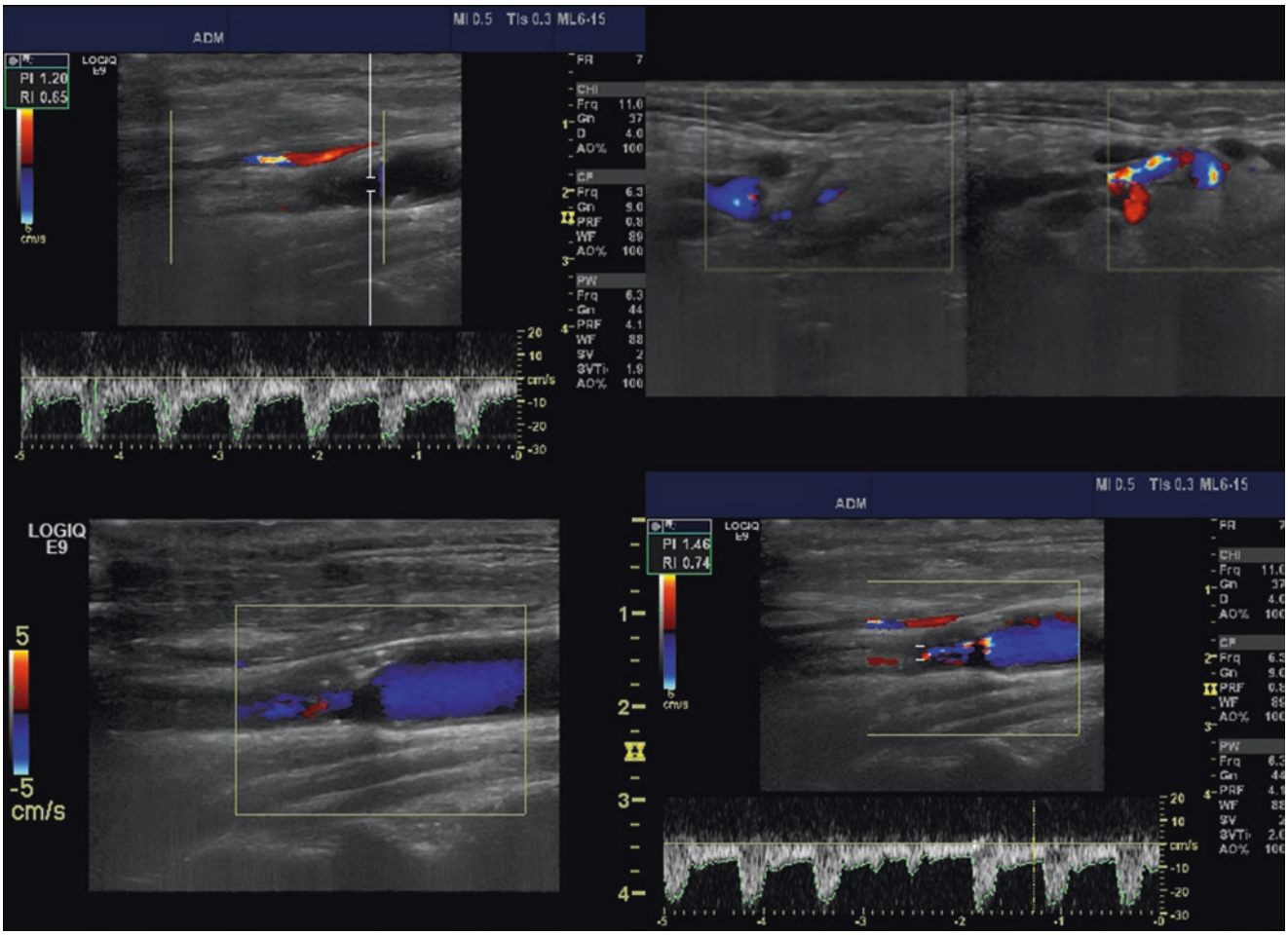

Fig. 10.15 Mild carotid artery stenosis (40–59%). *Top left*, *bottom left*, and longitudinal view of the carotid artery with a plaque narrowing the vessel's lumen by about 50%. *Top left*, *bottom right*: the prestenotic and poststenotic blood flow velocity is measured by Doppler. *Top right*, axial plane

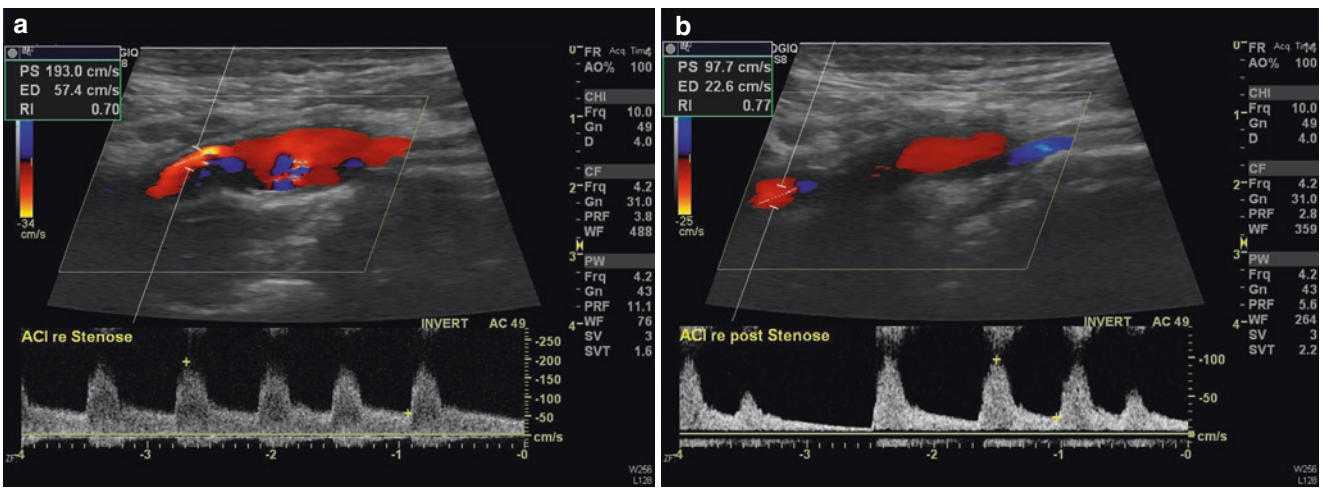

Fig. 10.16 Moderate carotid artery stenosis. The systolic blood flow velocity in the stenosis is about 200 cm/sec (**a**). The systolic blood flow velocity in the poststenotic segment of the vessel is about 100 cm/sec (**b**). (Courtesy of Dr. Silke Hörnschemeyer-Decker, Dept. of Neurology, Nordstadt Clinic, Academic Hospital, Hannover, Germany)

10.5.2 Carotid Artery Dissection/Aneurysm

Carotid artery dissection can occur in the intracranial or extracranial part of the vessel, conditions known as two different disease entities. Extracranial dissection is known to be one of the most frequent causes for a stroke in young people [34]. The cause of the dissection might be traumatic, infectious, or iatrogenic. Sonographically, the lumen of the vessel can be tapered, and sometimes a floating intimal flap is seen. The false lumen can lead to a narrowing of the true

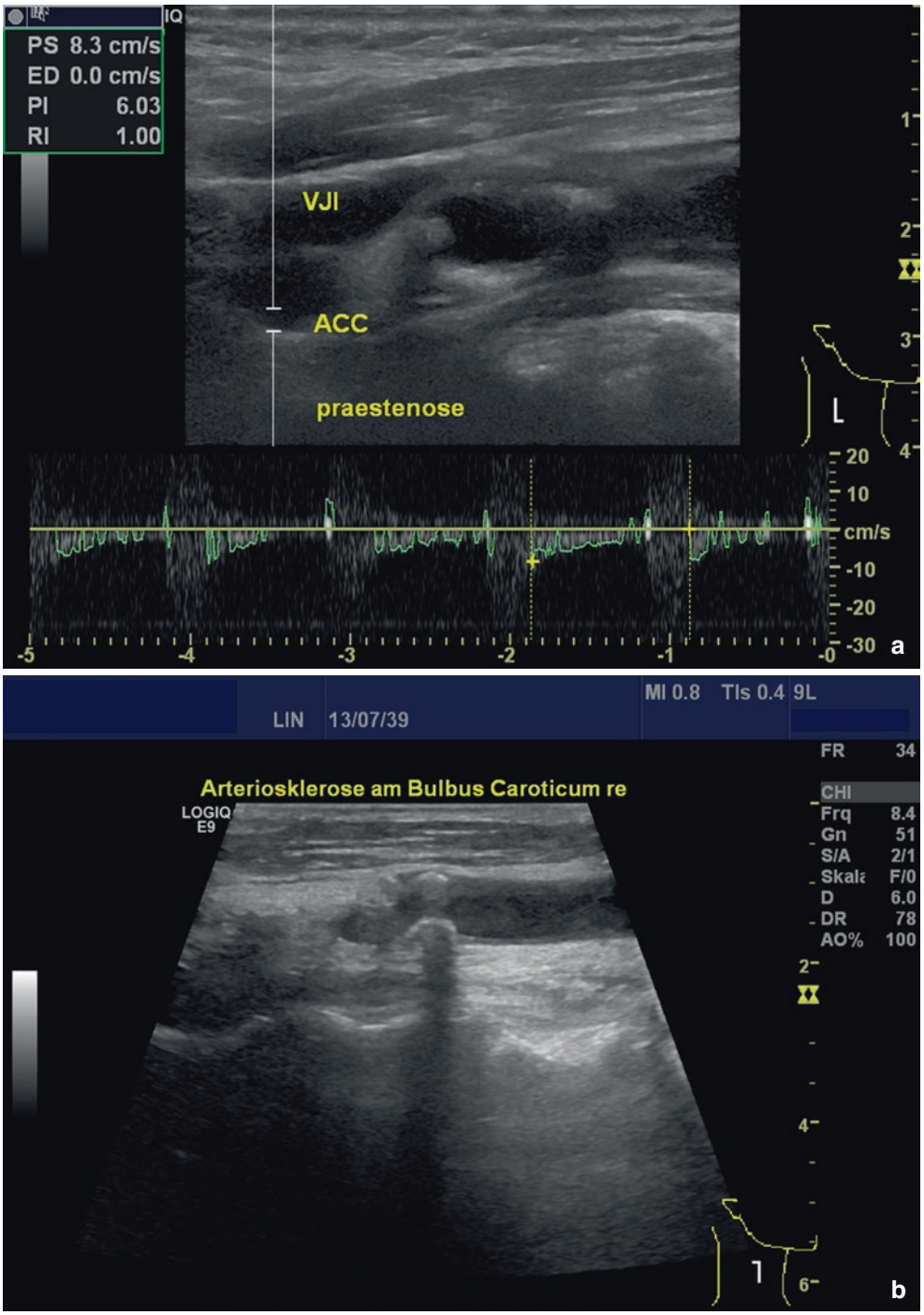

Fig. 10.17 Severe carotid artery stenosis (80–99%). (**a**) The plaque narrowing the lumen of the vessel significantly in a longitudinal plane. The Doppler is recorded prestenotically. (**b**) Atherosclerotic plaque in longitudinal plane. (**c**) Duplex of the vessel with the Doppler in the stenosis reveals a systolic blood flow velocity of more than 600 cm/sec. (**d**) The systolic blood flow velocity in the poststenotic segment of the vessel is 50 cm/sec. (Fig. 10.17. (**c**) and (**d**): Courtesy of Dr. Silke Hörnschemeyer-Decker, Dept. of Neurology, Nordstadt Clinic, Academic Hospital, Hannover, Germany)

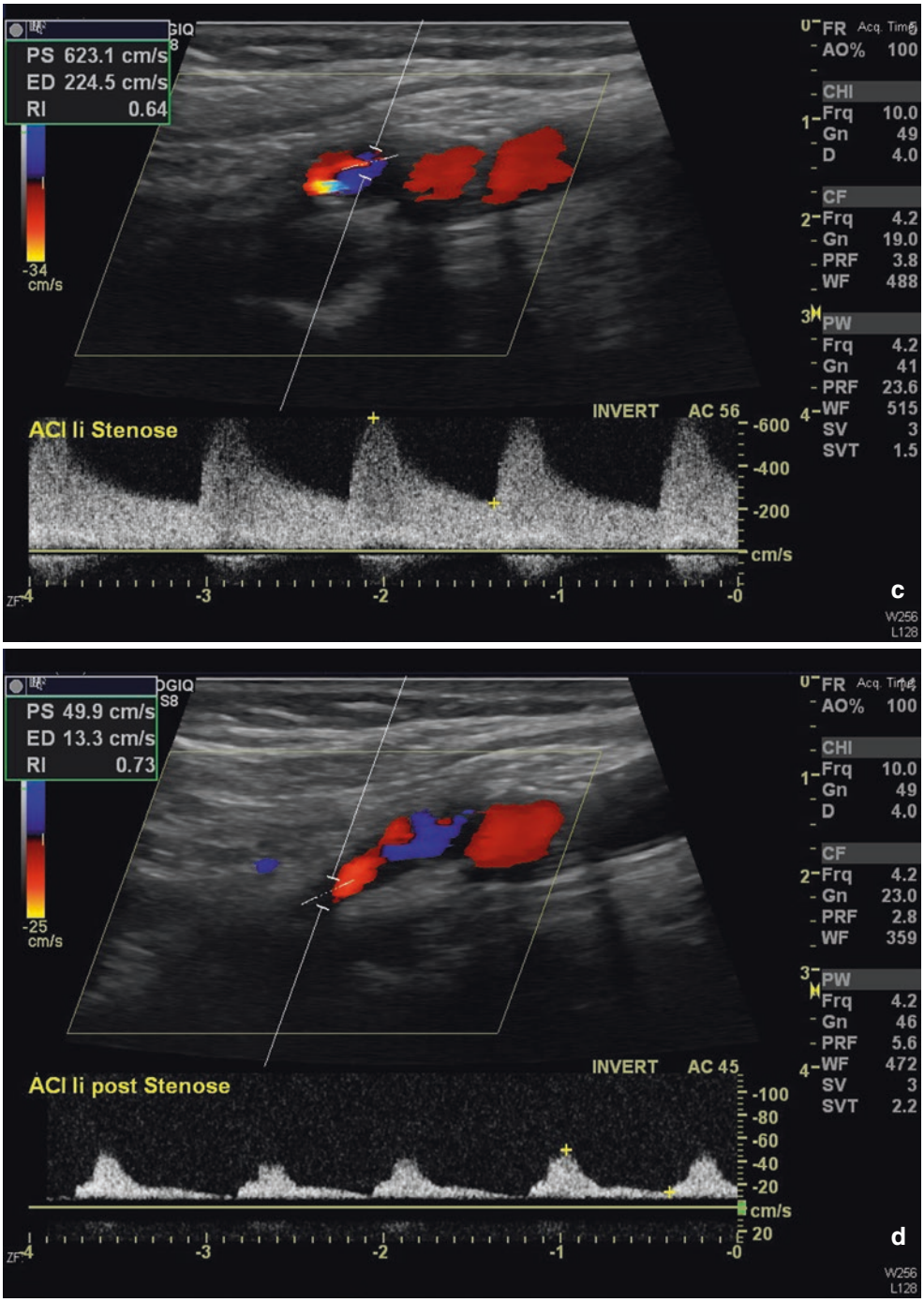

Fig. 10.17 (continued)

lumen (Fig. 10.19). Duplex sonography can reveal either forward, reverse, or bidirectional flow. Doppler sonography may show complex flow dynamics that are significantly dependent on the presence of a thrombus inside the false lumen, the existence of an entry and exit flap, and the extent of the dissection [1]. If surgery is indicated and performed, monitoring is possible during recanalization and in the postoperative period using B-mode, color-coded, and Doppler sonography [34]. As a differential diagnosis, carotid artery dissection must be separated from vascular abnormalities such as carotid webs [35], which are extremely rare but can cause quite similar sonographic and duplex sonographic characteristics [35]. Sonography (especially duplex and TCD sonography) is also suitable to pro-

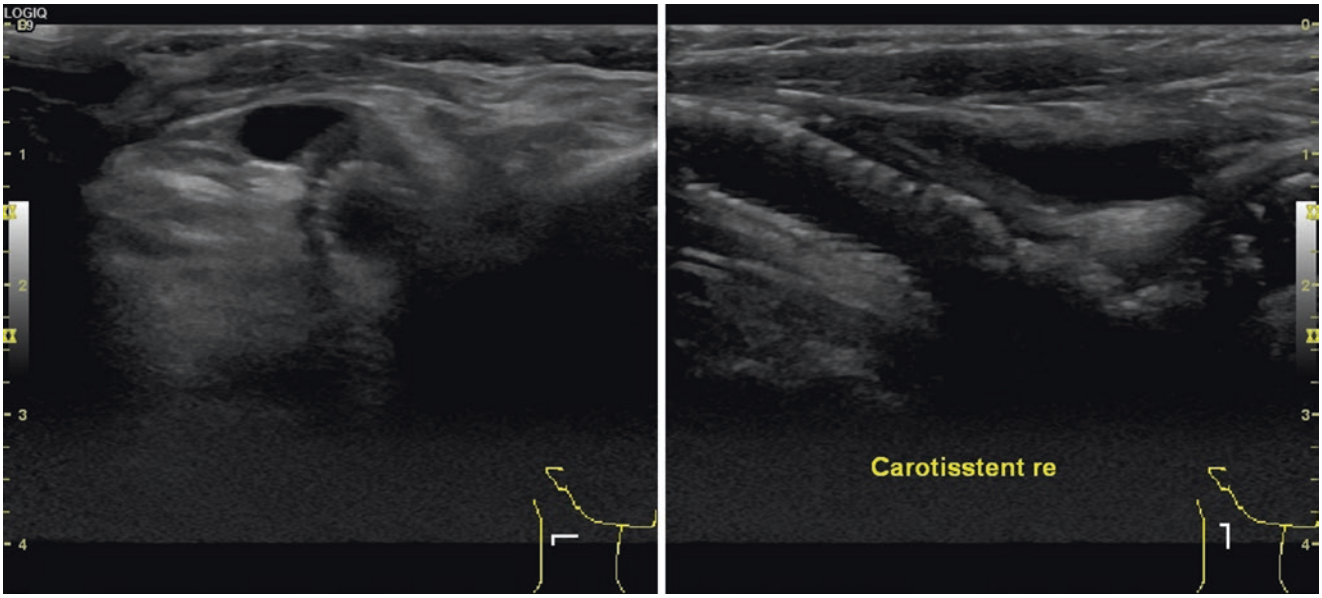

Fig. 10.18 Carotid artery following stent implantation in axial (*left*) and longitudinal section (*right*). The stented vessel is patent

vide an insight into the patient's cerebral perfusion status, such as following carotid artery stenting [27, 29]. In some cases of vertebral artery dissection, duplex and TCD sonography provides important information regarding that vessel's wall and the size of the aneurysm [36].

10.5.3 Thrombosis of the Internal Jugular Vein (Including Lemierre Syndrome)

Thrombosis of the internal jugular vein occurs mainly as a result of cancer, central venous or Swan-Ganz catheters, or injuries, as part of the ovarian hyperstimulation syndrome, or as part of an autoimmune disease (e.g., Behçet's disease). When it occurs as a septic thrombosis owing to a primary ear, nose, or throat infection, the disease is called *Lemierre syndrome* [37–41]. Lemierre syndrome is very rare, with an incidence reported to be lower than one in a million [42]. Multivariate analysis revealed the following risk factors for an internal jugular vein thrombosis: older age, female sex, and ovarian hyperstimulation syndrome [40].

Microvascular head and neck reconstruction with venous draining of the flap into the internal jugular vein can also cause thrombosis, even several days postoperatively [43]. B-mode ultrasound and color-coded ultrasound can be applied as a useful tool to assess the patency of the flap's vessels and anastomosis.

Lemierre syndrome is typically caused by an infection with *Fusobacterium necrophorum*; the portal of entry is often located in the oropharynx rather than in other pharyngeal structures such as the hypopharynx or the floor of the mouth [42, 44]. The infection leads first to a phlebitis, with thrombosis following.

Thrombosis of the internal jugular vein can have life-threatening complications, including sepsis, pulmonary embolism, and post-thrombotic syndrome [40]. The mortality rate was reported to be 90% in the pre-antibiotic era [38]. Therapy for Lemierre syndrome consists of intravenous antibiotics for about 10–14 days, followed by oral antibiotics for up to 6 weeks [44]. Anticoagulative agents are also recommended [38] and represent the main therapy in cases of aseptic internal jugular vein thrombosis.

Diagnosis of internal jugular vein thrombosis can be made rapidly by B-mode and color-coded sonography. The thrombus appears as a hypoechoic mass inside the vessel's lumen, attached to the vessel's wall. In cases of thrombophlebitis, a significant thickening of the vessel's wall can occur. The vein is often dilated distally to the thrombus; in cases of complete occlusion, it shows no blood flow proximal to the thrombus [39, 42, 44] (Fig. 10.20; Video 10.6). Additional investigation of the internal jugular vein on the opposite side is also recommended, as well as an examination of the proximal parts of the vessel and the subclavian vein, as some thrombosis can extend proximally into the subclavian vessels [39]. In these cases, CT angiography delineates the extension of the thrombosis better than B-mode sonography and color-coded sonography alone [39]. In cases of incomplete vessel occlusion, color-coded sonog-

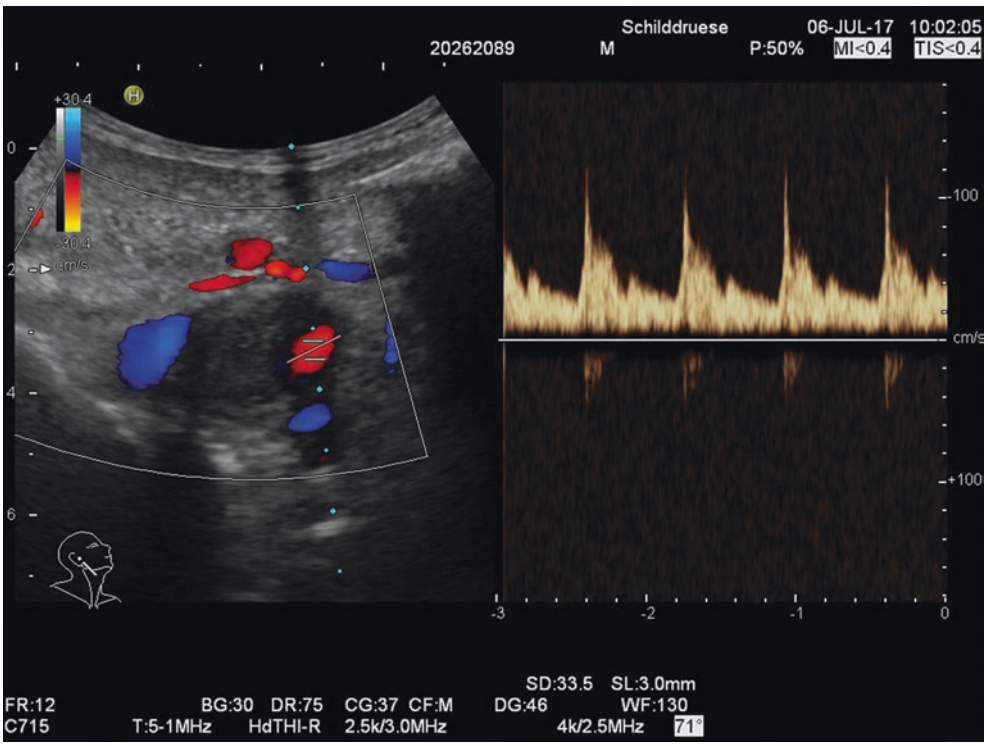

Fig. 10.19 Carotid artery dissection. (*Courtesy of* Peter Jecker, MD, PhD; *also see* Chap. 6)

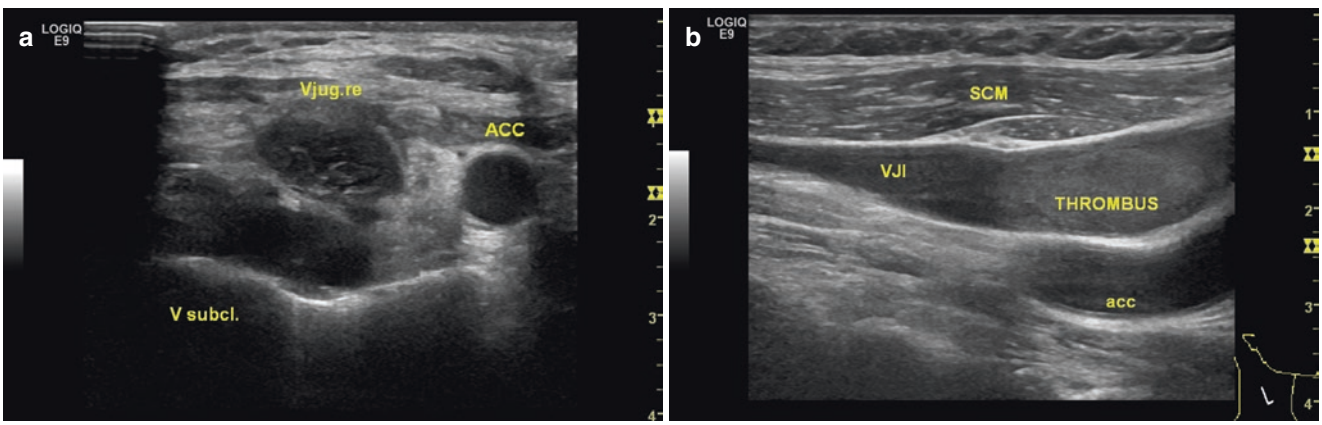

Fig. 10.20 Septic thrombosis of the internal jugular vein (IJV) as a result of a peritonsillar abscess (Lemierre syndrome). The thrombus displays as a mass inside the vessel's lumen. (**a**) Axial plane. (**b**) The thrombus inside the vessel in the longitudinal plane

raphy reveals the hypoechoic thrombus, which is surrounded by some blood flow.

B-mode sonography, color-coded sonography, and, if possible, the B-flow mode are essential to monitor recanalization during therapy and in the post-therapeutic follow-up. In patients with bilateral idiopathic internal jugular vein thrombosis, cancer (especially lung cancer) or malignant lymphoma must be excluded [40].

10.6 Infiltration of Large Neck Vessels by Malignant Tumors

The diagnostic accuracy of ultrasound in the detection of lymph node metastases is unmistakable in the literature. One of the most important issues for ultrasound application in the head and neck is the estimation of suspected vessel infiltration by a tumor in patients with very large metastases

Table 10.3 Direct and indirect sonographic signs of vessel infiltration

Direct signs
Direct infiltration of the vessel's wall
Visible tumor parts inside the vessel's lumen
Lack of shifting between tumor and vessel estimated by dynamic sonopalpation
Indirect signs
Cranio-caudal contact zone between vessel and tumor of >3 cm
Tumor surrounding the vessel by >180°

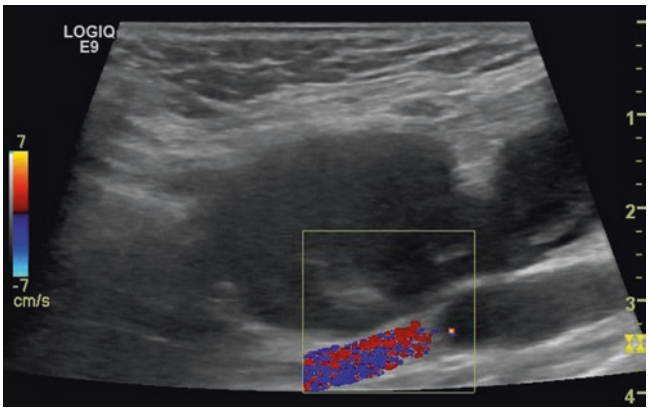

Fig. 10.21 Indirect sign of vessel infiltration by a malignant tumor: cranio-caudal contact zone of >3 cm. In this case, a particular tissue layer between the vessel and tumor is visible, which makes an infiltration unlikely

[45]. Taken together, B-mode sonography, duplex sonography, and TCD sonography are more effective than CT scans in this setting in excluding invasion of the carotid artery by metastases [46].

10.6.1 Sonographic Criteria for Vessel Infiltration

Sonographically, there are direct and indirect signs of vessel infiltration by a given tumor, which are listed on Table 10.3. The indirect signs are illustrated by Figs. 10.21 and 10.22.

Ultrasound is also suitable for detecting extracapsular spread of cervical lymph node metastases, with a specificity of 81.8% and a sensitivity of 78.6% [47]. However, subclinical infiltration of the carotid sheath, which is rare, is hard to recognize by sonography [48]. Color Doppler sonography is useful to detect the coexistence of sclerotic plaques in the carotid arteries, which may have consequences for the therapeutic procedure [49].

The suspected vessel infiltration can be grouped in five stages, as explained in Table 10.4 and illustrated by Fig. 10.23. In stages II and III, dynamic sonopalpation is required to estimate the likelihood of vessel infiltration, eventually followed by TCD sonography with and without manual compression of the ipsilateral ICA or balloon occlusion of the ipsilateral ICA to estimate the contralateral blood supply to the brain by the contralateral carotid artery where appropriate [50].

10.6.2 Dynamic Sonopalpation

Dynamic sonopalpation takes advantage of the dynamic nature of ultrasound examination. It is indicated in all cases where vessel infiltration by a given tumor is suspected (stages II through IV), before contemplating therapeutic strategy. The technique of this examination is quite easy: the mass is visualized on the ultrasound screen in both transverse and longitudinal sections, and the indirect and direct signs of vessel infiltration are determined. The tumor is then palpated and moved by the examiner's hand under direct view (Video 10.7). Whether the vessel shifts towards the tumor is documented. A shifting indicates no vessel infiltration, and the tumor can therefore be resected with low risk to the vessel. On the other hand, lack of shifting indicates vessel infiltration. Additional examinations, such as TCD sonography, are required to determine eventual cross flows or anastomosis, which would allow the vessel to be resected with a low risk for a stroke [50].

10.6.3 Transcranial Doppler Sonography

Transcranial Doppler (TCD) sonography is an ultrasound technique for assessment of blood flow velocities and blood flow directions and in some cases for detection of emboli in intracranial arteries [51]. It is performed by insonating the intracranial vessels through various skull "windows" and cranial foramina. The aim of this examination is to detect occlusions and narrowing of major intracranial artery trunks and to estimate collateral flow through anterior and posterior communicating arteries [52] without using other tests (such as the balloon occlusion test) that have a potential risk for development of symptomatic ischemia [53–55]. For TCD sonography, a low-frequency ultrasound transducer of 1.5 through 3 MHz is used, with which thin bony structures can be penetrated to insonate the intracranial vessels. It is important to note that this examination is done without visual guidance [1, 56]. The insonation of intracranial vessels is performed via a temporal, suboccipital, orbital, and submandibular window, through which different intracranial vessels can be assessed [27] (Table 10.5).

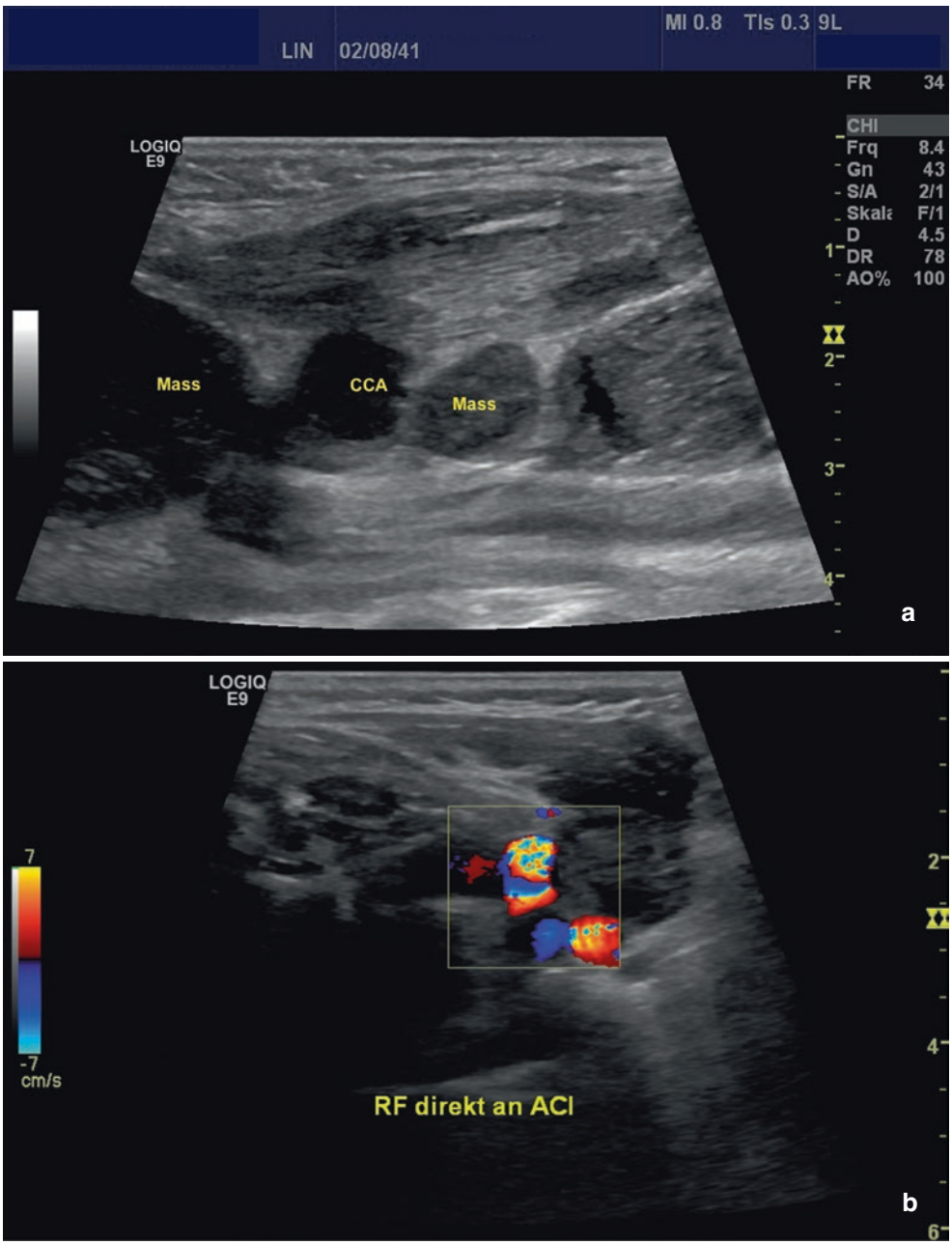

Fig. 10.22 Indirect sign of vessel infiltration by a malignant tumor. (**a**) Surrounding of the vessel by the tumor of more than 180°. (**b**) Color Doppler. The vessel is, although surrounded by the tumor, patent, and there is a tiny tissue layer between tumor and vessel

Table 10.4 Sonographic stages of vessel infiltration by a neck tumor and required actions

Stage	Sonographic characteristic	Action required
Stage 0	No signs of vessel infiltration by the tumor	The tumor can be resected with no risk or only low risk of vessel injury
Stage I	Sharply demarked tissue layer between the tumor and the vessel; good shifting of the tumor toward the vessel estimated by dynamic sonopalpation	The tumor can be resected with low risk of vessel injury or a stroke
Stage II	Unsharp tissue layer between tumor and the vessel	Dynamic sonopalpation is required to estimate the vessel infiltration When there is a significant shifting of the tumor toward the vessel, the tumor can be resected with low risk for vessel injury
Stage III	Unsharp tissue layer between tumor and the vessel; no significant shifting between the tumor and the vessel estimated by dynamic sonopalpation	Vessel infiltration by the tumor is highly probable Transcranial Doppler sonography with compression test is required to estimate a cross flow prior to surgical intervention
Stage IV	Tumor masses inside the vessel's lumen	Vessel infiltration is proven Transcranial Doppler sonography with compression test; if this is not possible, more invasive tests (e.g., balloon occlusion test) are required prior to surgery to estimate a cross flow and therefore the risk that the patient will suffer a stroke

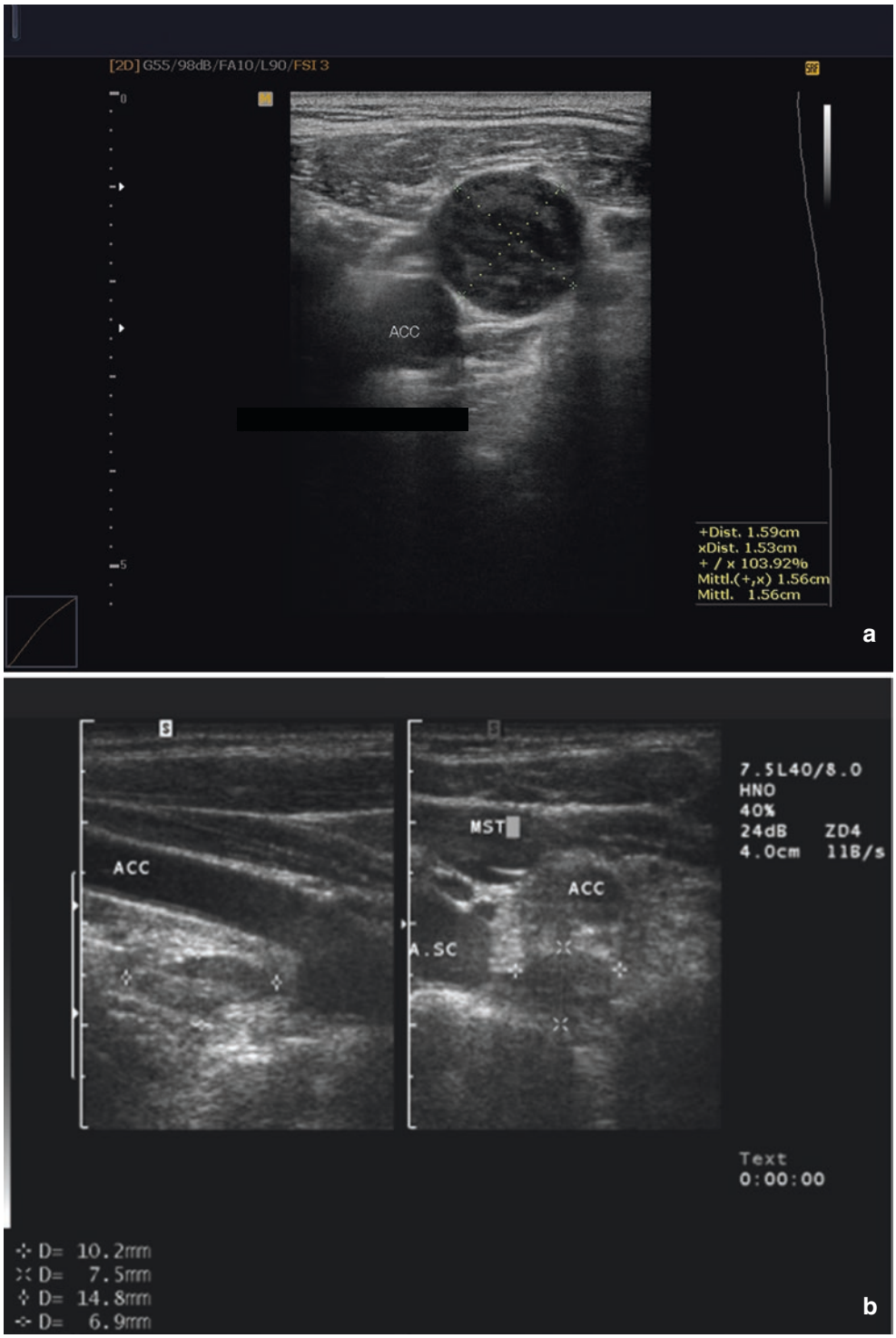

Fig. 10.23 Stages of vessel infiltration by a malignant tumor. (**a**) Stage I: sharply demarcated tissue layer between tumor and vessel. (**b**) Stage IV: tumor masses inside the vessel's lumen

For identification of the vessels assessed, the distance of the signal from the probe, flow velocity, flow direction (toward or away from the probe), waveforms of the Doppler signal, and pulsatility indices are used. Some authors have defined normal values for easier identification of particular vessels and for better interpretation of results [1, 57, 58] (Table 10.6).

The indications for TCD sonography examinations comprise mainly of neurological diseases [1, 29, 33, 51, 56, 57]:

- Assessment and follow-up of intracranial stenosis and vessel occlusion
- Assessment of patients with vasospasm in subarachnoid hemorrhage

Table 10.5 "Windows" for transcranial Doppler sonography (TCD) and vessels that can be assessed [27]

"Window" for TCD	Vessels That Can Be Assessed
Temporal approach	Internal carotid artery Middle cerebral artery Anterior cerebral artery Posterior cerebral artery
Orbital approach	Ophthalmic artery Siphon of internal carotid artery
Suboccipital approach (via foramen magnum)	Vertebral arteries Basilar artery
Submandibular approach	Distal parts of the extracranial internal carotid artery

Table 10.6 Normal distances, blood flow velocities, and flow direction of some intracranial vessels, assessed by TCD [1, 58]

Vessel	Distance to transducer, mm	Mean blood flow velocity, cm/s	Flow direction
Middle cerebral artery	40–60	40–80	Toward transducer
Anterior cerebral artery	60–75	40–60	Away from transducer
Posterior cerebral artery	60–70	30–50	Bidirectional
Vertebral artery	50–80	30–50	Away from transducer
Basilar artery	80– >100	30–50	Away from transducer
Ophthalmic artery	30–50	20–30	Toward transducer
Internal carotid artery	60–70	30–50	Away from transducer or bidirectional, depending whether temporal or orbital is measured

TCD transcranial Doppler

- Detection of microemboli during carotid artery or cardiac surgery
- Assessment of cerebral vasomotor reactivity
- Detection of intracranial aneurysms
- Detection of right-to-left shunts
- Investigation of patients with sickle cell disease to evaluate stroke risk
- Investigation of arteriovenous malformations
- Adjunct in diagnosis of brain death
- Evaluation of positional vertigo or syncope
- Evaluation of collateral pathways for intracranial blood flow

For head and neck surgeons, it is of great importance to know whether there is a collateral blood flow and a cross flow from the collateral carotid artery into the ipsilateral vessel in cases of a tumor with suspected carotid artery infiltration. TCD sonography is performed when dynamic sonopalpation reveals a suspicion of vessel wall infiltration, because that vessel probably will need to be sacrificed during operative therapy (Fig. 10.24). The TCD results, together with a manual compression test or balloon occlusion, are then strong indicators to estimate the risk of a stroke [50]. The examination begins initially without any manipulation. In the second step, the ipsilateral carotid artery can be compressed, and it is observed whether there is a cross flow from the contralateral side into the median cerebral artery. When there is lack of cross flow, or if the patient develops neurological symptoms, the compression is released. If there is no cross flow or collateral flow in TCD, a nonfunctional anastomosis via the communicating arteries is probable [59]. Then the risk for a stroke is very high, and the vessel probably cannot be sacrificed. If TCD reveals a cross flow or collateralization, that is a sign of a functional collateral pathway in the circle of Willis [59], and it may be possible to resect the vessel with a low risk of stroke [9, 60]. Mean blood flow velocity reduction of 30% or less during compression or balloon occlusion indicates a low risk for developing neurological symptoms, but mean blood flow velocity reductions of more than 50% indicate a high risk for developing neurological symptoms [61]. Balloon occlusion has been proven to be a little more accurate in predicting the occurrence of cerebral ischemic lesions when the vessel has to be sacrificed [62]. In conclusion, TCD with and without compression offers a noninvasive source of valuable information about perfusion status in patients with large neck tumors infiltrating the CCA and/or ICA. TCD with a carotid compression test is a valid method for predicting interhemispheric flow and clinically relevant hemodynamics [54]. The results are comparable to those obtained by more invasive techniques such as balloon occlusions [62–64].

10.7 Ultrasound Characteristics of Large Neck Vessels Following Surgery or Radiotherapy

Both surgery and radiation therapy lead to alterations of the anatomy in the neck. Sonographic orientation can be challenging because of an increase of scar and fibrous tissue and the excision of some structures during surgery. The CCA, which is usually not affected by an operation, is the best anatomic landmark for orientation.

Radiotherapy has a significant impact on the carotid artery [65, 66]. In general, radiotherapy leads to an increase of scar tissue and fibrosis in the neck and to increases of intima-media thickness (IMT), plaque size, and plaque volume in all segments of the carotid artery [67–69] (Fig. 10.25). The increase in IMT seems dose-related; the higher the radiation dose, the higher the risk for increased

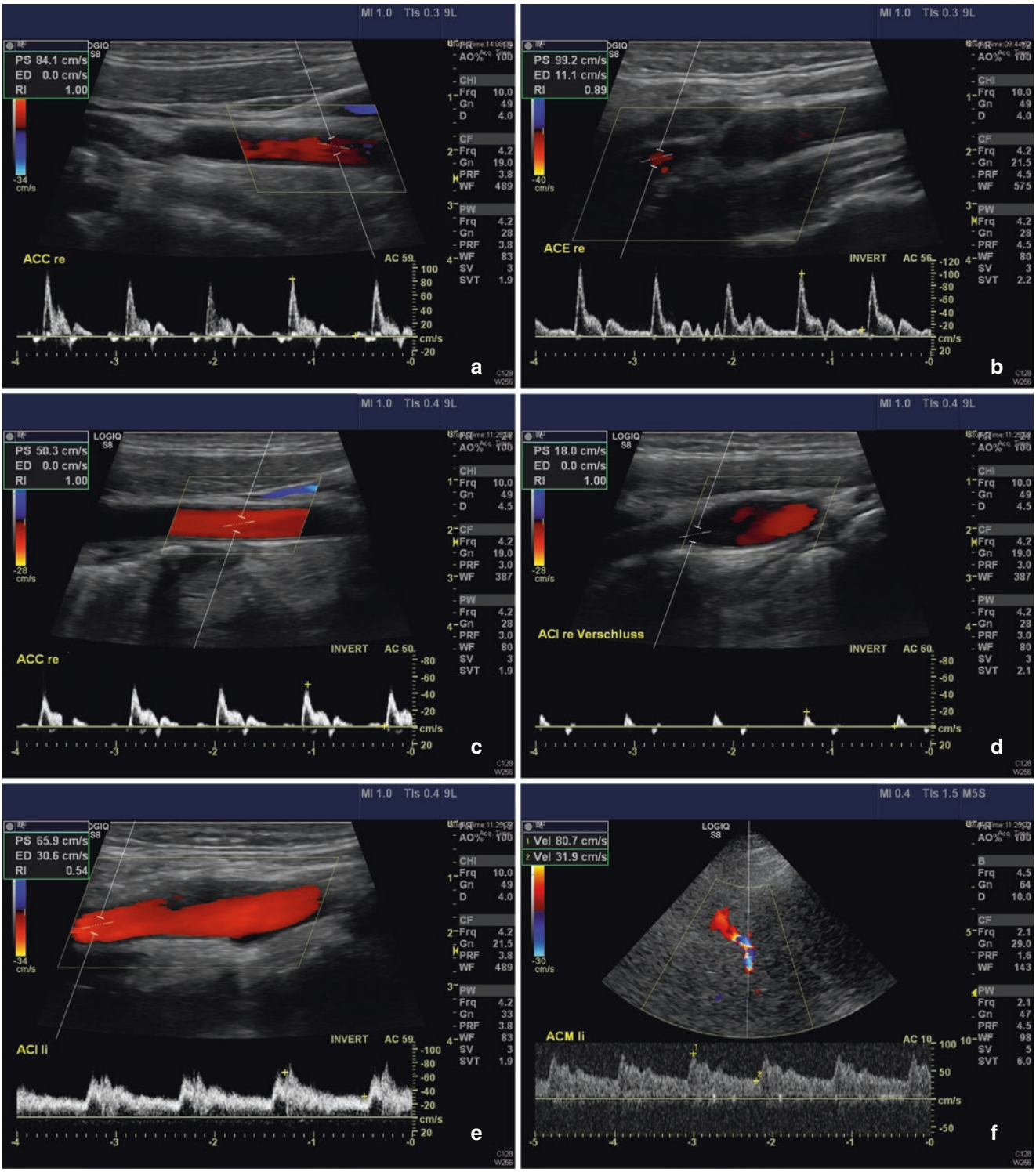

Fig. 10.24 Transcranial Doppler (TCD) sonography to estimate cross flow in the medial cerebral artery in cases with occlusion of the ipsilateral internal carotid artery. (**a**) Stenosis of the common carotid artery on the right side with blood flow prestenotically (longitudinal plane). (**b**) Blood flow in the ipsilateral external carotid artery by duplex and Doppler. (**c**) Blood flow in the common carotid artery is prestenotically normal. (**d**) Internal carotid artery on the right side is distally occluded, and distal to the carotid bifurcation, there is a complete obstruction of the vessel. (**e**) Duplex sonography reveals normal blood flow in the contralateral (left-sided) internal carotid artery. Only some flat, fibrotic plaques occur in the vessel. In this case, blood flow in the medial cerebral artery on the left side is normal (**f**), and a moderately good cross flow with collateration of the median cerebral artery (MCA) on the left side (**g**) that occurs via the left anterior communicating artery (or ramus) (ACA) can be detected (**h**), which retrogradely fills the right ACA (**i**) (Courtesy of Dr. Silke Hörnschemeyer-Decker, Dept. of Neurology, Nordstadt Clinic, Hannover, Germany). (**j**) and (**k**) MRI shows the occluded carotid artery on the right side in axial view and with vessel reconstruction

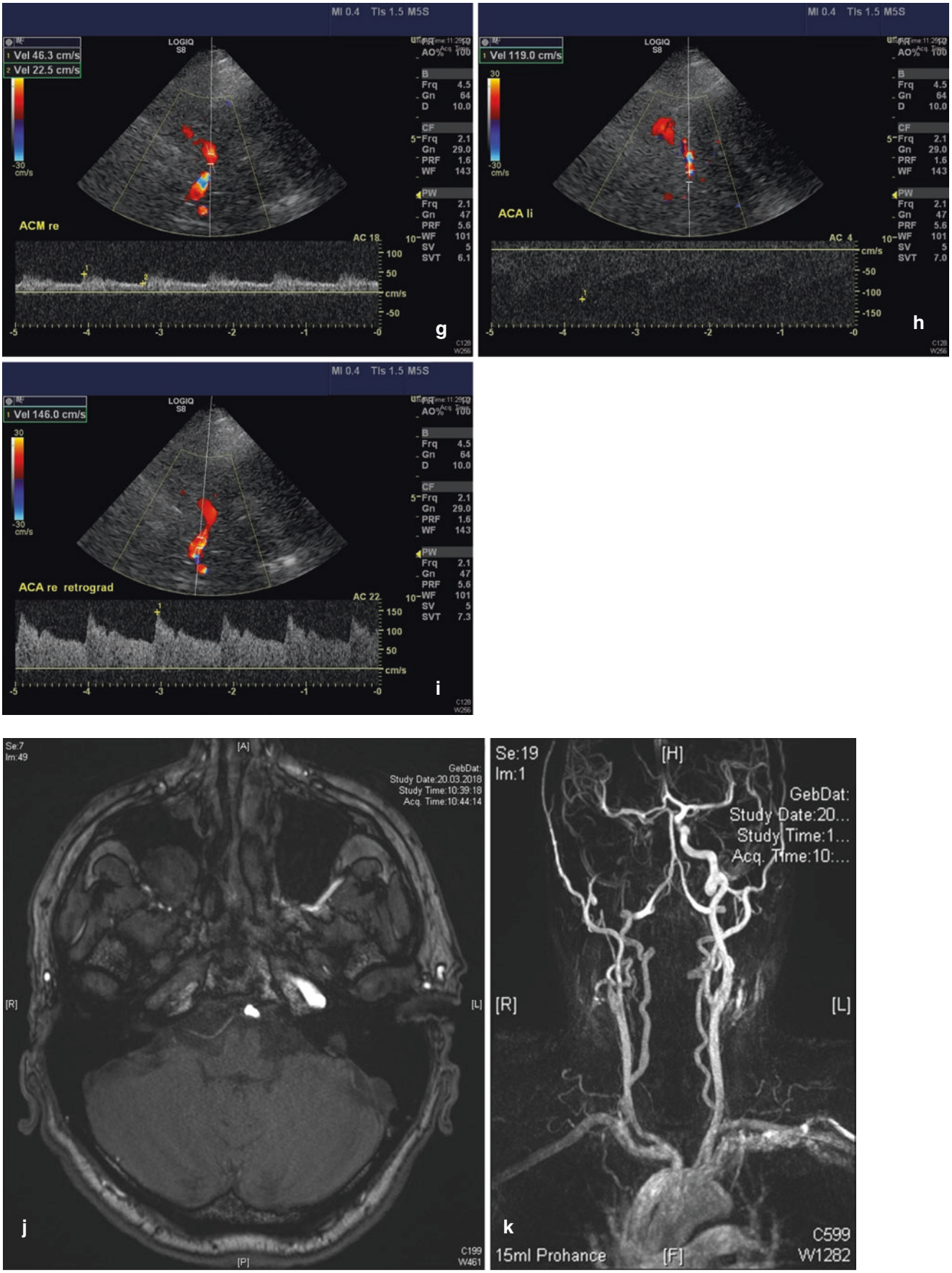

Fig. 10.24 (continued)

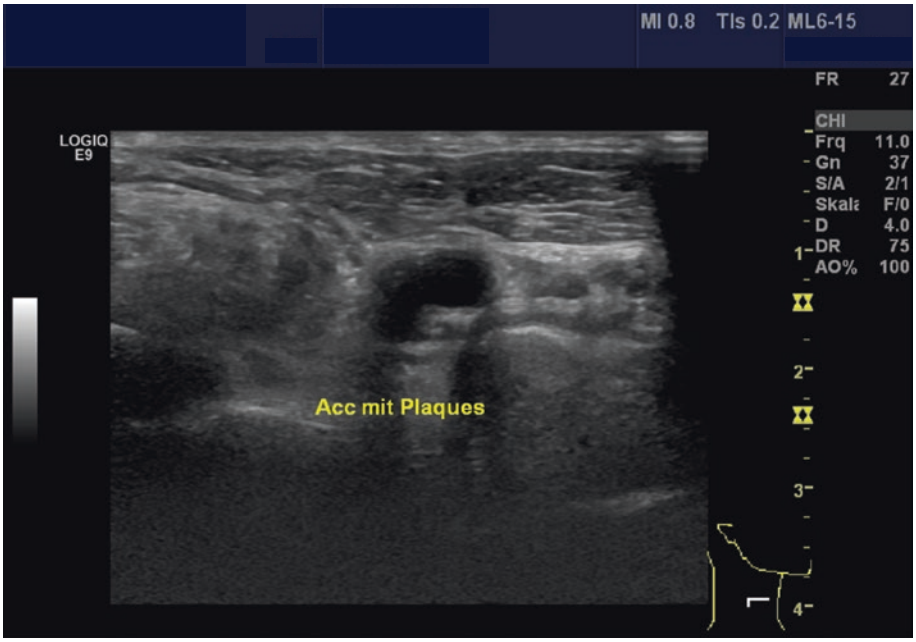

Fig. 10.25 Ultrasound of the neck following radiation therapy. Note the increase of scar tissue and fibrosis. The internal jugular vein is missing, as it has been removed during a neck dissection. The common carotid artery is seen with an increased intima-media thickness and a calcified plaque

IMT and plaque formation. Therefore it is important to keep in mind that after radiation therapy of the neck, patients have a higher risk of carotid artery disease, especially accelerated atherosclerosis, so they need intensive follow-up and surveillance. Parallel to changes in the carotid artery wall and decrease of vessel diameter, hemodynamic changes occur, with a decrease of blood flow volume following radiotherapy [70]. If the carotid artery was spared by using intensity-modulated radiotherapy, these pathologic conditions can be significantly decreased, with both better blood flow volume and decreased risk of progressive atherosclerosis [71]. Carotid IMT has been proven to be a strong biomarker for early diagnosis of vascular changes and risk of cerebrovascular events after radiation therapy of the neck. In these patients, long-term follow-up including B-mode and duplex sonography is required for early detection and surveillance of vessel disease.

10.8 Examination of Vessels Prior to Microvascular Flap Surgery

Another indication for vessel ultrasound is the identification of the afferent and efferent vessels prior to intended microvascular tissue transfer. An example is the microvascular forehand flap, which has the radial artery as its feeder vessel. This is the microvascular flap that is currently most often used for reconstruction of larger defects in the head and neck, so it is very common. The examination can be performed preoperatively and intraoperatively. With this test, which is called the Allen test, the existence and patency of the anastomosis between the superficial palmar arterial arch and the profound palmar arterial arch in the ipsilateral hand is assessed (Fig. 10.26; Video 10.8). The existence of an anastomosis between the radial and ulnar artery is required before the flap (which is usually pedicled at the radial artery) can be harvested. The profound palmar arterial arch is a prolongation of the radial artery and courses beneath the long flexor strings. It is identified on the ultrasound screen, and then the radial artery is compressed under continuous observation of the blood flow in the palmar arch. The test is positive if there is significant blood flow during compression. It is advantageous to perform pulse oximetry with a sensor at the index finger during the test, because this provides additional information about the pulsation, oxygen saturation, and perfusion of the nail bed during compression of the radial artery. It is very likely that the blood supply of the second and third finger is sufficient and the anastomosis is intact when no significant decrease of the pulsation curve occurs. The flap can then be harvested.

Postoperatively, duplex sonography helps to evaluate the blood supply of an incorporated flap and assess the patency of the flap's vessels.

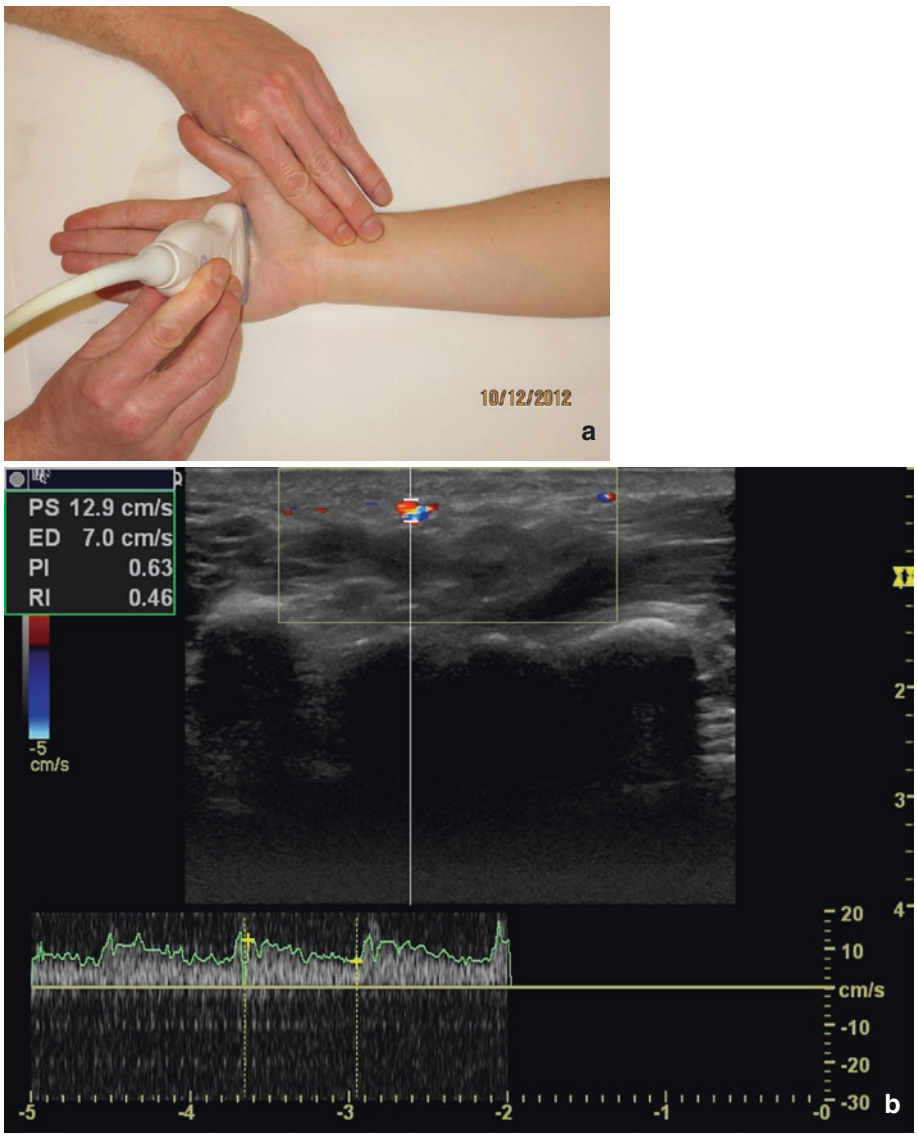

Fig. 10.26 (**a**) Before harvesting a forehand flap, the Allen test is performed to assess the profound palmar artery arch for collateral blood supply of the first three fingers during compression of the radial artery. (**b**) Duplex sonography reveals a good blood flow in the profound palmar arterial arch

References

1. Rundek T, Simonetto M, Campo N, Cabral DE. Vascular ultrasound, carotid and transcranial Doppler imaging. In: Orloff LA, editor. Head and neck ultrasonography: essential and extended applications. 2nd ed. San Diego: Plural Publishing; 2016. p. 395–443.
2. Kochanowicz J, Turek G, Rutkowski R, Mariak Z, Szydlik P, Lyson T, Krejza J. Normal reference values of ratios of blood flow velocities in internal carotid artery to those in common carotid artery using Doppler sonography. J Clin Ultrasound. 2009;37:208–11.
3. Shaalan WE, Wahlgren CM, Desai T, Piano G, Skelly C, Bassiouny HS. Reappraisal of velocity criteria for carotid bulb/internal carotid artery stenosis utilizing high-resolution B-mode ultrasound validated with computed tomography angiography. J Vasc Surg. 2008;48:104–12.
4. Mozzini C, Roscia G, Casadei A, Cominacini L. Searching the perfect ultrasonic classification in assessing carotid artery stenosis: comparison and remarks upon the existing ultrasound criteria. J Ultrasound. 2016;19:83–90.
5. Von Reutern GM, Goertler MW, Bornstein NM, Del Sette M, Evans DH, Hetzel A, et al. Grading carotid stenosis using ultrasonic methods. Stroke. 2012;43:916–21.
6. Beach KW, Leotta DF, Zierler RE. Carotid Doppler velocity measurements and anatomic stenosis: correlation is futile. Vasc Endovasc Surg. 2012;46:466–74.
7. American Institute of Ultrasound in Medicine. AIUM practice parameter for the performance of an ultrasound examination of the extracranial cerebrovascular system. https://www.aium.org/resources/guidelines/extracranial.pdf. Accessed 5 July 2018.
8. Harmon L, Boccalandro F. Comparison of carotid artery dimensions and lesion length measured by B-mode ultrasonography and

quantitative angiography in patients with severe stenosis undergoing percutaneous revascularization. J Clin Ultrasound. 2014;42:270–6.
9. Hoksbergen AW, Majoie CB, Hulsmans FJ, Legemate DA. Assessment of the collateral function of the circle of Willis: three-dimensional time-of-flight MR angiography compared with transcranial color-coded duplex sonography. AJNR Am J Neuroradiol. 2003;24:456–62.
10. Zavanone C, Ragone E, Samson Y. Concordance rates of Doppler ultrasound and CT angiography in the grading of carotid artery stenosis: a systematic literature review. J Neurol. 2012;259:105–18.
11. Jahromi AS, Cina CS, Liu Y, Clase CM. Sensitivity and specificity of color duplex ultrasound measurement in the estimation of internal carotid artery stenosis: a systematic review and meta-analysis. J Vasc Surg. 2005;41:962–72.
12. Lovrencic-Huzjan A, Rundek T, Katsnelson MJ. Carotid disease and stroke. Stroke Res Treat. 2012;2012:264752.
13. Wong EY, Nikolov HN, Rankin RN, Holdsworth DW, Poepping TL. Evaluation of distal turbulence intensity for the detection of both plaque ulceration and stenosis grade in the carotid bifurcation using clinical Doppler ultrasound. Eur Radiol. 2013;23:1720–8.
14. Maggi P, Perilli F, Lillo A, Carito V, Epifani G, Bellacosa C, Pastore G, Regina G. An ultrasound-based comparative study on carotid plaques in HIV-positive patients vs. atherosclerotic and arteritis patients: atherosclerotic or inflammatory lesions? Coron Artery Dis. 2007;18:23–9.
15. Brinjikji W, Rabinstein AA, Lanzino G, Murad MH, Williamson EE, DeMarco JK, Huston J 3rd. Ultrasound characteristics of symptomatic carotid plaques: a systematic review and meta-analysis. Cerebrovasc Dis. 2015;40:165–74.
16. Brinjikji W, Huston J 3rd, Rabinstein AA, Kim GM, Lerman A, Lanzino G. Contemporary carotid imaging: from degree of stenosis to plaque vulnerability. J Neurosurg. 2016;124:27–42.
17. Diomedi M, Scacciatelli D, Misaggi G, Balestrini S, Balucani C, Sallustio F, et al. Increased common artery wall thickness is associated with rapid progression of asymptomatic carotid stenosis. J Neuroimaging. 2014;24:473–8.
18. Ibrahim P, Jashari F, Bajraktari G, Wester P, Henein MY. Ultrasound assessment of carotid plaque echogenicity response to statin therapy: a systematic review and meta-analysis. Int J Mol Sci. 2015;16:10734–7.
19. Arous EJ, Baril DT, Robinson WP, Aiello FA, Hevelone ND, Arous EJ, et al. Institutional differences in carotid artery duplex diagnostic criteria result in significant variability in classification of carotid artery stenosis and likely lead to disparities in care. Circ Cardiovasc Qual Outcomes. 2014;7:423–9.
20. Farrell MB, Choi JY, Ziu E, Cockroft KM. Characteristics of accredited transcranial Doppler ultrasound laboratories in the United States. J Neuroimaging. 2017;27:210–6.
21. Arous EJ, Simos JP, Flahive JM, Beck AM, Stone DH, Hoel AW, et al. National variation in preoperative imaging, carotid duplex ultrasound criteria, and threshold for surgery for asymptomatic carotid artery stenosis. J Vasc Surg. 2015;62:937–44.
22. Doyle AJ, Stone JJ, Carnicelli AP, Chandra A, Gillespie DL. CT angiography–derived duplex ultrasound velocity criteria in patients with carotid artery stenosis. Ann Vasc Surg. 2014;28:1219–26.
23. Högberg D, Dellagrammaticas D, Kragsterman B, Björck M, Wanhainen A. Simplified ultrasound protocol for the exclusion of clinically significant carotid artery stenosis. Ups J Med Sci. 2016;121:165–9.
24. Igase K, Kumon Y, Matsubara I, Arai M, Goishi J, Watanabe H, et al. Utility of 3-dimensional ultrasound imaging to evaluate carotid artery stenosis: comparison with magnetic resonance angiography. J Stroke Cerebrovasc Dis. 2015;24:148–53.
25. Grant EG, Benson CB, Moneta GL, Alexandrov AV, Baker JD, Bluth EI, et al. Carotid artery stenosis: grayscale and Doppler ultrasound diagnosis – Society of Radiologists in ultrasound consensus conference. Ultrasound Q. 2003;19:190–8.
26. Reichmann BL, Hellings WE, van der Worp HB, Algra A, Brown MM, Mali WP, de Borst GJ. Flow velocities in the external carotid artery following carotid revascularization. Eur J Vasc Endovasc Surg. 2013;46:411–7.
27. Spacek M, Sorrell VL, Veselka J. Transcranial Doppler ultrasound in the current era of carotid artery stenting. Ultraschall Med. 2015;36:337–41.
28. Chahwan S, Miller MT, Pigott JP, Whalen RC, Jones L, Comerota AJ. Carotid artery velocity characteristics after carotid artery angioplasty and stenting. J Vasc Surg. 2007;45:523–6.
29. Kargiotis O, Safouris A, Magoufis G, Georgala M, Roussopoulou A, Stamboulis E, et al. The role of neurosonology in the diagnosis and management of patients with carotid artery disease: a review. J Neuroimaging. 2018;28:239–51.
30. Pizzolato R, Hirsch JA, Romero JM. Imaging challenges of carotid artery in- stent restenosis. J Neurointerv Surg. 2014;6:32–41.
31. Barros P, Felgueiras H, Pinheiro D, Guerra M, Gama V, Veloso M. Restenosis after carotid artery stenting using a specific designed ultrasonographic protocol. J Stroke Cerebrovasc Dis. 2014;23:1416–20.
32. Lal BK, Hobson RW 2nd, Tofighi B, Kapadia I, Cuadra S, Jamil Z. Duplex ultrasound velocity criteria for the stented carotid artery. J Vasc Surg. 2008;47:63–73.
33. Tsivgoulis G, Alexandrov AV. Ultrasound in neurology. Continuum (Minneap Minn). 2016;22:1655–77.
34. Vicenzini E, Toscano M, Maestrini I, Petolicchio B, Lenzi GL, Di Piero V. Predictors and timing of recanalization in intracranial carotid artery and siphon dissection: an ultrasound follow-up study. Cerebrovasc Dis. 2013;35:476–82.
35. Fu W, Crockett A, Low G, Patel V. Internal carotid artery web: Doppler ultrasound with CT angiography correlation. J Radiol Case Rep. 2015;9:1–6.
36. Lee S, Choi HS, Jang J, Jung SL, Ahn KJ, Kim BS, et al. Progression of vertebral artery dissection: vessel wall enhancement and aneurysm dilation. Can J Neurol Sci. 2016;43:715–6.
37. Fabiani A, Pittiruti M, Russo S, Sanson G. Early-onset thrombosis of internal jugular vein associated with introducer catheter for heart catherization in cardiac surgery. J Vasc Access. 2015;16:57–63.
38. Schubert AD, Hotz MA, Caversaccio MD, Arnold A. Septic thrombosis of the internal jugular vein: Lemierre's syndrome revisited. Laryngoscope. 2015;125:863–8.
39. Kumar M, Singh R, Sawlani KK, Kumar S. A typical presentation of Lemierre syndrome: role of imaging. BMJ Case Rep. 2013;2013:pii: bcr2012007647. https://doi.org/10.1136/bcr-2012-007647.
40. Gbaguidi X, Janvresse A, Benichou J, Cailleux N, Levesque H, Marie I. Internal jugular vein thrombosis: outcome and risk factors. QJM. 2011;104:209–19.
41. Bilici M, Pehlivan Y, Kimyon G, Kisacik B. Internal jugular vein thrombosis in Behcet's disease: a rare complication. BMJ Case Rep. 2014;2014:bcr2013200261. https://doi.org/10.1136/bcr-2013-200261.
42. Gupta N, Kralovic SM, McGraw D. Lemierre syndrome: not so forgotten. Am J Crit Care. 2014;23:176–9.
43. Kim EK, Lee SS. Internal jugular vein thrombosis after microvascular head and neck reconstruction in a hemodynamically unstable patient. J Craniofac Surg. 2013;24:255–6.
44. Prakashchandra SP, Patel AK, Patel K, Doshi RK, Patel NA. Grave complication of pharyngitis: Lemierre syndrome. J Clin Diagn Res. 2015;9:TD03–4.
45. Puri R, Srinath VS, Chakravati AL. Duplex colour Doppler sonography – role in neck metastasis. Indian J Otolaryngol Head Neck Surg. 2002;54:171–4.
46. Zaragoza L, Sendra F, Solano J, Garrido V, Martinez-Morillo M. Ultrasonography is more effective than computed tomography

in excluding invasion of the carotid wall by cervical lymphadenopathies. Eur J Radiol. 1993;17:191–4.
47. Steinkamp HJ, Beck A, Werk M, Rademaker J, Felix R. Extracapsular spread of cervical lymph node metastases; diagnostic relevance of ultrasound examinations. [Article in German]. Ultraschall Med. 2003;24:323–30.
48. Chaturverdi P, Vaishampayan SS, Nair S, Nair D, Pawar P, Kane S. Routine removal of the carotid sheath as part of neck dissection is unnecessary if grossly uninvolved as seen intra-operatively. Int J Oral Maxillofac Surg. 2012;41:576–80.
49. Falkowski A, Wilk G, Mokrzynski S, Dul P, Otoloczko-Grabarek A, Huzarski T, Kowalczyk R. Colour Doppler ultrasound in preoperative assessment of the neck vessels in patients with tumours of the oral cavity and the neck region. Med Sci Monit. 2004;10:63–6.
50. Keller E, Ries F, Gruenwald F, Honisch C, Rosanowski F, Pavics L, et al. Multimodal carotid occlusion test for determining risk of infarct before therapeutic internal carotid artery occlusion. (German). Laryngorhinootologie. 1995;74:307–11.
51. Liberman AL, Zandieh A, Loomis C, Raser-Schramm JM, Wilson CA, Torres J, et al. Symptomatic carotid occlusion is frequently associated with microembolization. Stroke. 2017;48:394–9.
52. Hoksbergen AW, Fülesdi B, Legemate DA, Csiba L. Collateral configuration of the circle of Willis: transcranial color-coded duplex ultrasonography and comparison with postmortem anatomy. Stroke. 2000;31:1346–51.
53. Krejza J, Baumgartner RW. Clinical applications of transcranial color-coded duplex sonography. J Neuroimaging. 2004;14:215–25.
54. Hetzel A, von Reutern G, Wernz MG, Droste DW, Schumacher M. The carotid compression test for therapeutic occlusion of the internal carotid artery. Comparison of angiography with transcranial Doppler sonography. Cerebrovasc Dis. 2000;10:194–9.
55. Elias AE, Chaudhary N, Pandey AS, Gemmete JJ. Intracranial endovascular balloon test occlusion: indications, methods, and predictive value. Neuroimaging Clin N Am. 2013;23:695–702.
56. Schoysman L, Tshibanda JF, Otto B, Spynger M, Nchimi A. Transcranial color-coded sonography in the management of patients with cervical and intracranial arterial stenosis (French). Rev Med Liege. 2014;69:146–50.
57. Alexandrov AV, Sloan MA, Tegeler CH, Newell DN, Lumsden A, Garami Z, et al. Practice standards for transcranial Doppler (TCD) ultrasound. Part II. Clinical indications and expected outcomes. J Neuroimaging. 2012;22:215–24.
58. Tegeler CH, Crutchfield K, Katsnelson M, Kim J, Tang R, Passmore Griffin L, et al. Transcranial Doppler velocities in a large, healthy population. J Neuroimaging. 2013;23:466–72.
59. Liu J, Wang H, Zhang M, Sui X, Li F, Liu Z, et al. What influenced the lesion patterns and hemodynamic characteristics in patients with internal carotid artery stenosis? A retrospective study. Neurol Neurochir Pol. 2018;52:9–14.
60. Hoksbergen AW, Legemate DA, Csiba L, Csati G, Sito P, Fülesdi B. Absent collateral function of the circle of Willis as risk factor for ischemic stroke. Cerebrovasc Dis. 2003;16:191–8.
61. Eckert B, Thie A, Carvajal M, Groden C, Zeumer H. Predicting hemodynamic ischemia by transcranial Doppler monitoring during therapeutic balloon occlusion of the internal carotid artery. AJNR Am J Neurordiol. 1998;19:577–82.
62. Sorteberg A, Sorteberg W, Bakke SJ, Lindegaard KF, Boysen M, Nornes H. Varying impact of common carotid artery digital compression and internal carotid artery balloon occlusion on cerebral hemodynamics. Head Neck. 1998;20:687–94.
63. Mann WJ, Beck A, Schreiber J, Maurer J, Amedee RG, Gluckman JL. Ultrasonography for evaluation of the carotid artery in head and neck cancer. Laryngoscope. 1994;104:885–8.
64. Maurer J, Ungersböck K, Amedee RG, Mann WJ, Perneczky A. Transcranial Doppler ultrasound recording with compression test in patients with tumors involving the carotid arteries. Skull Base Surg. 1993;3:11–5.
65. Shariat M, Alias NA, Biswal BM. Radiation effects on the intima-media thickness of the common carotid artery in post-radiotherapy patients with head and neck malignancy. Postgrad Med J. 2008;84:609–12.
66. Thalhammer C, Husmann M, Glanzmann C, Studer G, Amann-Vesti BR. Carotid artery disease after head and neck radiotherapy. Vasa. 2015;44:23–30.
67. Gianicolo ME, Gianicolo EA, Tramacere F, Andreassi MG, Portaluri M. Effects of external irradiation of the neck region on intima media thickness of the common carotid artery. Cardiovasc Ultrasound. 2010;8:8.
68. Toprak U, Aytas I, Ustuner E, Habiboglu R, Aslan N, Pasoglu E, Karademir A. Sonographic assessment of acute changes in plaque size and echogenicity and in intima-media thickness of carotid arteries after neck radiation therapy. Clin Ultrasound. 2012;44:23–30.
69. Gujral DM, Chahal N, Senior R, Harrington KJ, Nutting CM. Radiation-induced carotid artery atherosclerosis. Radiother Oncol. 2014;110:31–8.
70. Mohammadkarim A, Mokhtari-Dizaji M, Kazemian A, Saberi H. Hemodynamic analysis of radiation-induced damage in common carotid arteries by using color Doppler ultrasonography. Ultrasonography. 2018;37:43–9.
71. Choi HS, Jeong BK, Jeong H, Song JH, Kim JP, Park JJ, et al. Carotid sparing intensity modulated radiotherapy on early glottic cancer: preliminary study. Radiat Oncol J. 2016;34:26–33.

Sonography of Major Salivary Glands

11

Andreas Knopf

Major salivary glands represent a melting pot of inflammatory, neoplastic, and dysontogenetic diseases. Diagnostic approaches are of major clinical impact to achieve both sufficient radicality of epithelial malignancy and a minimum of functional loss in benign lesions. Whereas B-mode ultrasound demonstrates high sensitivity and specificity in the identification of sialolithiasis, B-mode ultrasound and color-coded duplex sonography fail to reliably distinguish inflammatory and neoplastic conditions. Recent advances in elastography increased precision of diagnostic regimens in inflammatory conditions but require great personal expertise. Modern diagnostic algorithms including elastography and contrast-enhanced ultrasound result in significantly higher precision in the identification of glandular malignancy. However, complex algorithms are not part of the daily ultrasonographic routine, and detailed anamnesis and clinical examination remain mandatory in these cases.

11.1 Introduction

Major salivary glands represent a melting pot of inflammatory, neoplastic, and dysontogenetic diseases [1–3]. Final treatment regimens range from wait and scan concepts to ablative surgery and subsequent facial reconstruction. The close relation of major salivary glands to vascular and neuronal structures—particularly the facial, hypoglossal, and lingual nerves—gives rise to the necessity of a reliable preoperative lesional estimation to manage the balancing act between sufficient radicality and a minimum of functional loss. High-resolution ultrasound provides detailed information about the lesional localization, size, shape, homogeneity, and pattern of vascularity [4]. More recently, modern ultrasound techniques including strain and shear-wave elastography or contrast-enhanced ultrasound (CEUS) have been applied to increase diagnostic sensitivity and specificity, but these techniques are not part of today's routine in major salivary gland ultrasound. MRI represents an appropriate alternative to head and neck ultrasound [4–6] and is the diagnostic technique of choice when complete ultrasonographic visualization fails [5]. CT scans are indicated when a growing tumor is suspicious for osseous destruction. The diagnostic impact of other imaging techniques (such as glandular scintigraphy in Sjögren's syndrome) has decreased in the past decades, owing to the increased sensitivity and specificity of high-resolution B-mode ultrasound [7, 8]. Nevertheless, no imaging technique is currently able to reliably distinguish among the variety of salivary gland diseases, so it is vital to associate salivary gland imaging with the patient's detailed history and clinical examination [9, 10].

11.2 Inflammatory Diseases

Inflammatory diseases of major salivary glands can be divided into infectious and autoimmune conditions. Other diseases become clinically apparent as inflammation, but their etiopathogenesis is poorly understood. Traditionally, the clinical course of salivary gland inflammation differentiates between acute and chronic disease, but a substantial proportion of autoimmune diseases that are summarized as chronic sialadenitis show an acute and self-limiting early disease stage referring to acute sialadenitis. Therefore, classification in this chapter will reflect etiopathogenetic considerations.

A. Knopf (✉)
Department of Otorhinolaryngology–Head and Neck Surgery, University of Freiburg, Freiburg, Germany

© Springer Nature Switzerland AG 2019

H. J. Welkoborsky, P. Jecker (eds.), *Ultrasonography of the Head and Neck*, https://doi.org/10.1007/978-3-030-12641-4_11

11.2.1 Infectious Sialadenitis

Bacterial Sialadenitis

There are different mechanisms resulting in a bacterial infection of major salivary glands. Bacteria ascending via salivary ducts represent one of the most important mechanisms. Dysfunctional saliva drainage and irrigation due to obstructive sialadenitis, duct ectasia, duct cysts, dehydration, and Sjögren's syndrome are preconditions in bacterial sialadenitis [11]. Usually, patients present reddened, enlarged, and painful salivary glands. Pus can be expressed at the ductal orificium after palpation. However, in parotid gland sialadenitis, purulent drainage fails if bacterial infection primarily affects intra-parotideal lymph nodes. Cutaneous foci frequently result in the affection of the lymphatic basin of the parotid gland. Hematogenous and lymphatic spread in salivary glands can be diagnosed in mycobacteria and mycobacteria other than tuberculosis (MOTT). Both mycobacteria and MOTT often demonstrate severe resistance to common antibiotics, sometimes with organ fistulation. Abscess formation complicates bacterial sialadenitis in all pathomechanisms. Bacterial smear usually identifies *Staphylococcus aureus* and species of the oral flora [12].

B-mode ultrasound visualizes uncomplicated sialadenitis as diffuse and inhomogeneous enlargement of the glandular tissue [12]. Strand-like hypoechogenicity refers to congested lymphatic septa (Fig. 11.1). Echo-free strands referring to congested Wharton's and Stenson's duct can be identified in obstructive sialadenitis. Peripheral concrements show cortical reflex and acoustic shadow with subsequent proximal duct dilatation (see Sect. 11.4.1) [13]. Color-coded duplex sonography (CDS) shows glandular hypervascularity (Fig. 11.2). Intraglandular abscess shows irregular borders and marked hypoechogenicity (Fig. 11.3). Inhomogeneity is due to different amounts of purulent areas. CDS demonstrates peripheral vascularity and an avascular core (Fig. 11.4). Cold abscesses with intraglandular fistula often occur in mycobacterial/MOTT sialadenitis (Fig. 11.5). Usually, bacterial sialadenitis is completed by reactive intra-parotideal and/or cervical lymphadenopathy.

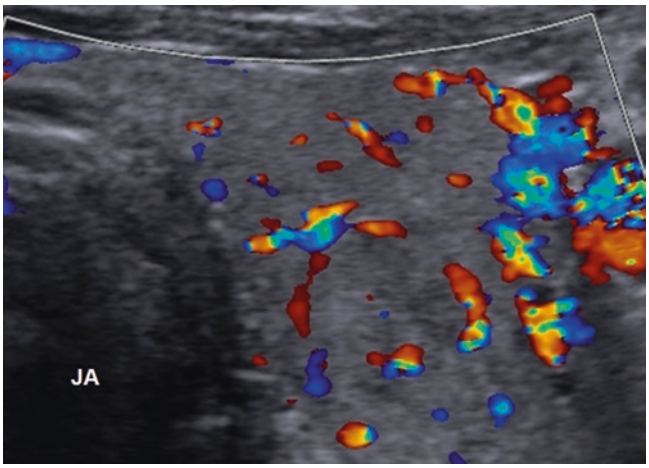

Fig. 11.2 Color-coded duplex sonography of bacterial sialadenitis shows marked hypervascularity of the entire left parotid gland, with hypoechoic lymphatic septa. JA jaw angle

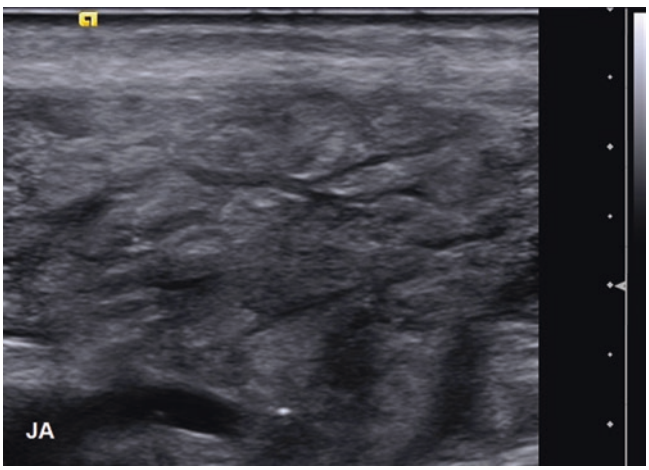

Fig. 11.1 B-mode ultrasound of bacterial sialadenitis shows diffuse enlargement of the entire left parotid gland with hypoechoic lymphatic septa. JA jaw angle

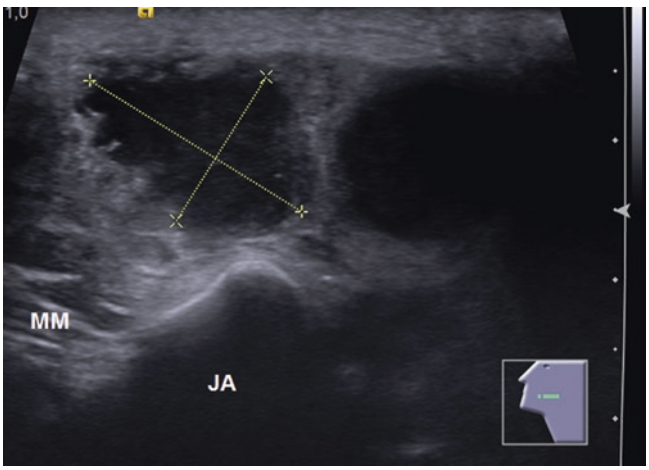

Fig. 11.3 B-mode ultrasound of left parotid gland abscesses visualizes hypoechoic or echo-free lesions with irregular borders. JA jaw angle, MM masseter muscle

Viral Sialadenitis

Various viruses may infect the major salivary glands. Epstein-Barr virus (EBV), cytomegalovirus (CMV), HIV, and mumps viruses are the most frequent pathogens [14, 15]. CMV, EBV, and mumps infections result in acute sialadenitis, but HIV-induced sialadenitis usually presents a chronic clinical course [14]. In contrast to bacterial sialadenitis, viral infection usually demonstrates oligo-sialadenitis. B-mode ultrasound and CDS can visualize diffuse and inhomogeneous enlargement of the glandular tissue with strand-like hypoechogenicity with marked hypervascularity, comparable to bacterial sialadenitis (Fig. 11.6). However, CMV and EBV demonstrate a predilection for cervical lymph nodes and therefore parotid gland infection referring intra-parotideal lymph nodes (Fig. 11.7). Interestingly, the sonographic appearance of HIV infection differs significantly from the other viral infections, demonstrating echo-free areas referring to lymphoepithelial lesions (Fig. 11.8). CDS and CEUS validate cystic areas without macro- or micro-perfusion (Fig. 11.9). Cystic areas were visualized soft in strain elastography (Fig. 11.10). Sonography in HIV-induced sialadenitis cannot be distinguished from Sjögren's syndrome or mucosa-associated lymphoid tissue (MALT) lymphoma; differential diagnosis is mandatory in these cases [11, 16–18].

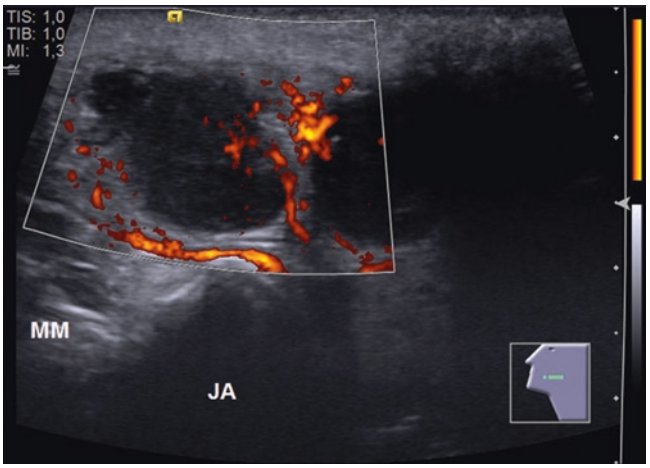

Fig. 11.4 Color-coded duplex sonography (CDS) of left parotid gland abscesses demonstrates peripheral hypervascularity of avascular echo-free areas. JA jaw angle, MM masseter muscle

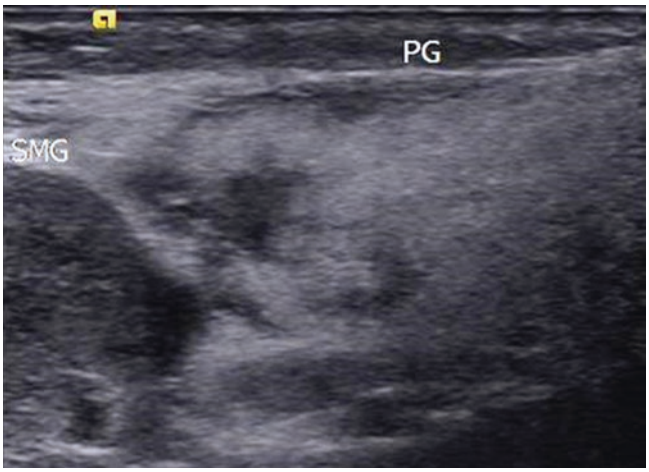

Fig. 11.6 Oligo-sialadenitis of the parotid gland (PG) and submandibular gland (SMG) in mumps infection. B-mode ultrasound shows hypoechoic lymphatic septa of the parotid gland and hypoechogenicity of the submandibular gland

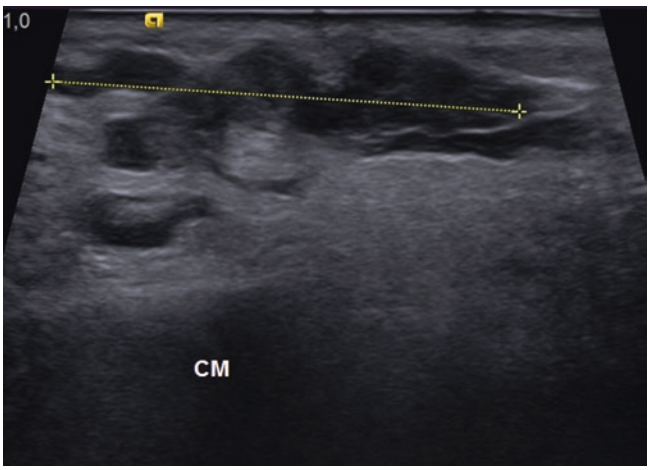

Fig. 11.5 B-mode sonography of parotid gland tuberculosis shows echo-free fistulae in central glandular parts. CM collum mandibulae

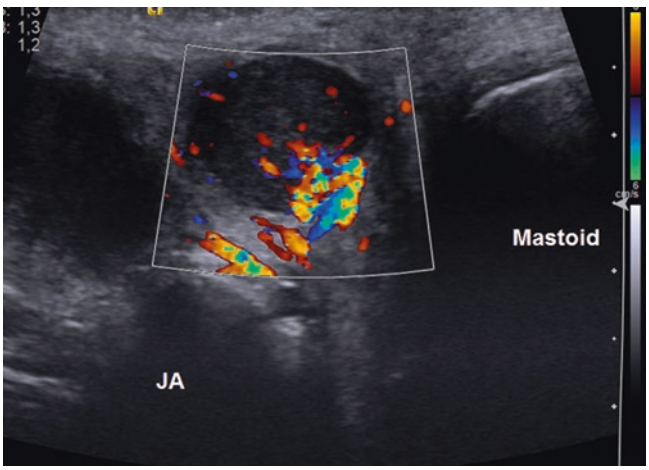

Fig. 11.7 Color-coded duplex sonography of intra-parotideal lymph node EBV infection. Hypoechoic lymph nodes show hilus hypervascularity. JA jaw angle

11.2.2 Autoimmune Sialadenitis

Sjögren's Syndrome

Sjögren's syndrome represents the most important rheumatic disorder affecting the head and neck, with a prevalence of 1–2% in the adult population, a female predominance of approximately 8:1, and a mean age of onset usually in the fourth to fifth decade of life [11, 19, 20]. Sjögren's syndrome can be present without another underlying inflammatory condition (primary Sjögren's syndrome), or it may be coupled with an underlying inflammatory disease (secondary Sjögren's syndrome). Autoantibodies induce chronic epithelialitis, particularly of serous salivary glands. Therefore, the parotid and lacrimal glands are predominantly affected, but sialadenitis also includes submandibular, sublingual, and minor salivary glands [11, 17]. Chronic glandular inflammation results in an insidious destruction of salivary gland tissue and progressive sicca symptoms. Acute and self-limiting enlargements of major salivary glands, particularly of the parotid gland, represent typical symptoms of early disease stages, but they are dramatically underdiagnosed [11, 17]. Bilateral, hypoechoic lesions of the submandibular and

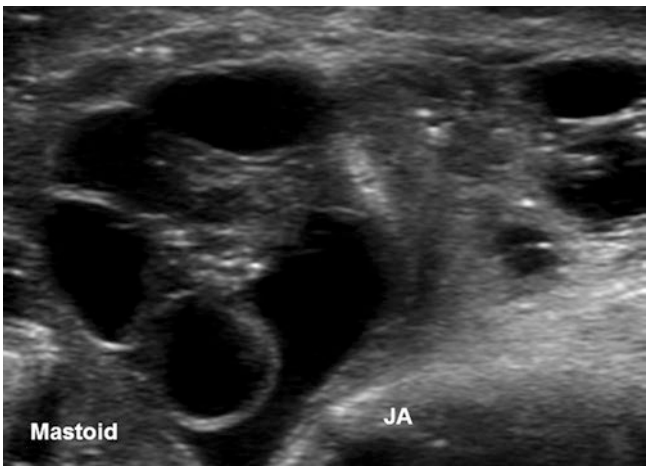

Fig. 11.8 B-mode ultrasound of lymphoepithelial lesions in HIV infection demonstrates multiple intra-parotideal echo-free areas. JA jaw angle

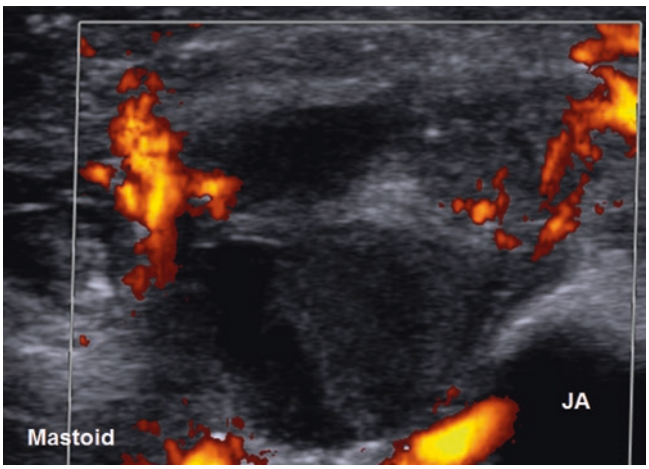

Fig. 11.9 Color-coded duplex sonography of lymphoepithelial lesions in HIV shows peripheral hypervascularity and avascular echo-free areas. JA jaw angle

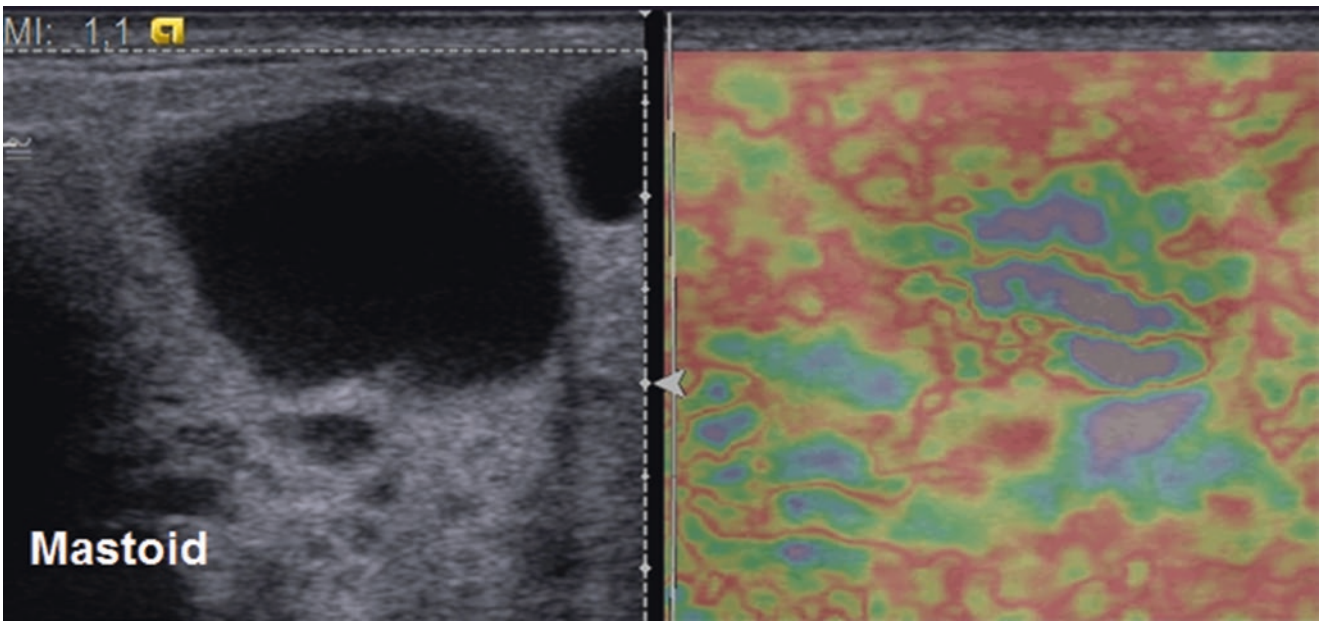

Fig. 11.10 Strain elastography of lymphoepithelial lesions in HIV infection. Echo-free areas are visualized soft (*blue*) in contrast to hardened parotid gland tissue (*red*). Red areas in the lymphoepithelial lesion refer to compression phenomenon to incompressible liquids

parotid gland are pathognomonic B-mode criteria for Sjögren's syndrome, but they occur in only 40% of cases [17]. Hypoechoic lesions can be scored by lesional diameter (0 = normal, homogeneous gland; 1 = mild inhomogeneity, hypoechoic areas of 2 mm; 2 = evident inhomogeneity, hypoechoic areas of 2–6 mm; 3 = gross inhomogeneity, hypoechoic areas of 6 mm; 4 = adipose degeneration of gland, with adipose tissue echogenicity and parenchymal atrophy (Fig. 11.11) [21–23]. Grade 1 (mild affection) and grade 4 (burned-out gland) can hardly be distinguished from healthy glands (grade 0) by untrained physicians. The maximum diameter of the submandibular gland is often less than

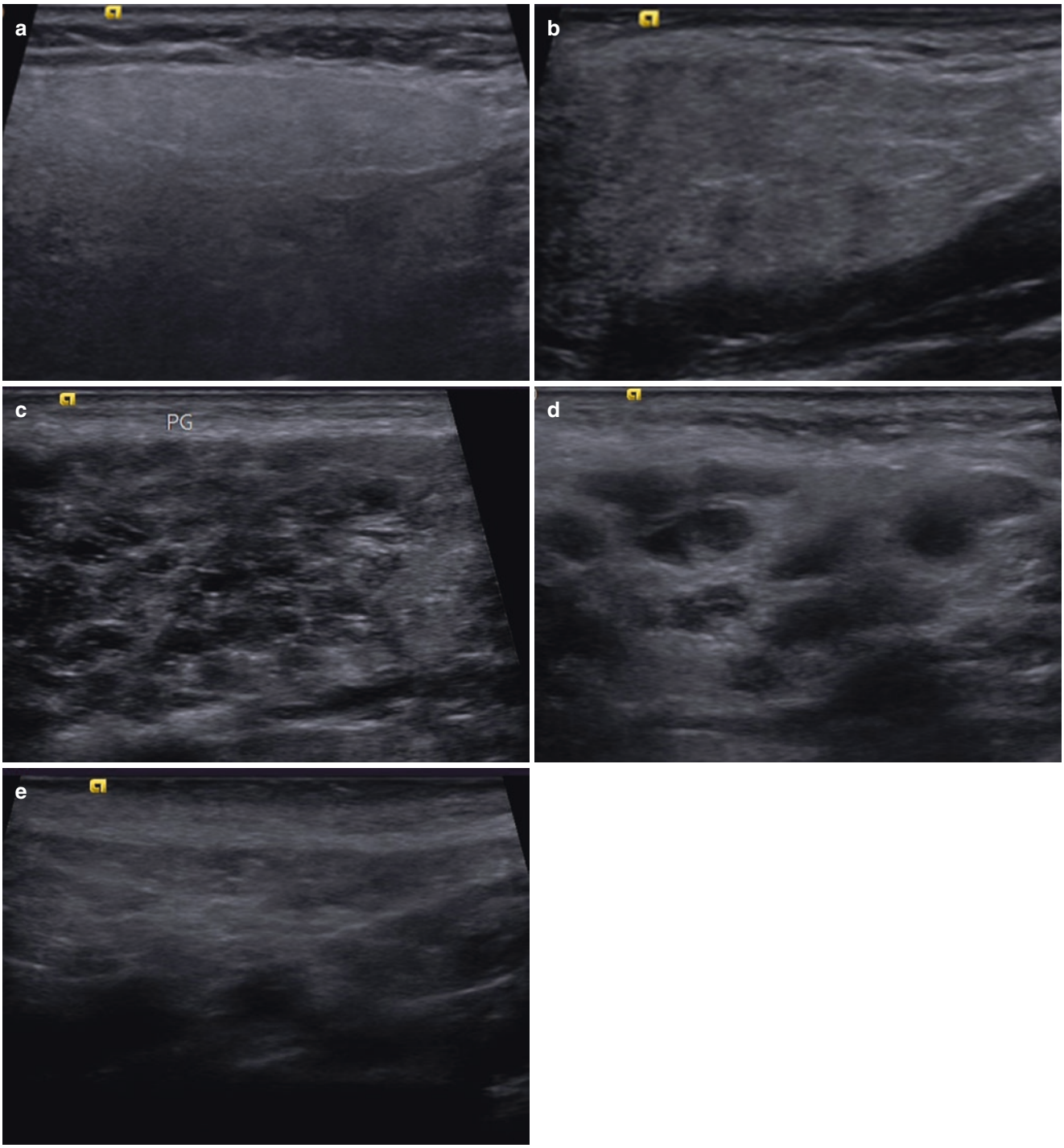

Fig. 11.11 B-mode scoring in Sjögren's syndrome ranging from normal parotid gland (PG) tissue (grade 0, **a**) through increasing inhomogeneity (grades 1–3, **b–d**) to a hyperechoic, burned-out parotid gland (grade 4, **e**)

3 centimeters (Fig. 11.12). In addition, marked hypoechogenic lesions (grade 3) cannot be distinguished from sarcoidosis, MALT lymphoma, or HIV-induced lymphoepithelial lesions, so open parotid gland biopsy is required in these cases [11, 16–18]. Strain elastography visualizes progressive hardened glands, sometimes including soft cystic areas (Fig. 11.13) [24]. Highly inflammatory salivary glands show hypervascularity in CDS. Although literature reports sensitivity and specificity higher than 90%, glandular assessment via B-mode sonography, CDS, or strain elastography requires great personal expertise [17, 24, 25]. Therefore, shear-wave elastography was established as a diagnostic tool that reliably identifies different disease stages in a quantitative manner (Fig. 11.14), though it is not widely available and is restricted to specialized centers. Shear-wave velocities greater than 2.4 m/s indicate Sjögren's syndrome [17, 26].

Sarcoidosis

Sarcoidosis is a granulomatous disease that is based on a dysfunction in T-cell regulation. The incidence in Caucasians is estimated to be about 20–40 cases per 100,000 inhabitants. Sarcoidosis affects patients in the second to fourth decade of life and shows a balanced gender distribution. Lungs and mediastinal lymph nodes are predominantly affected. Cervical lymph nodes represent an extrathoracic hot spot region [11, 18]. There are notable differences in the clinical

Fig. 11.12 B-mode sonography demonstrates downscaled submandibular gland in grade 3–4 submandibular gland Sjögren's syndrome

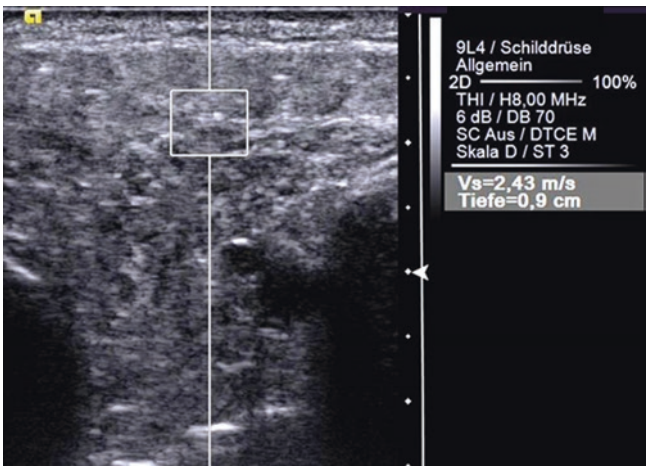

Fig. 11.14 Shear-wave elastography in grade 3 parotid gland Sjögren's syndrome shows velocities higher than 2.4 m/s

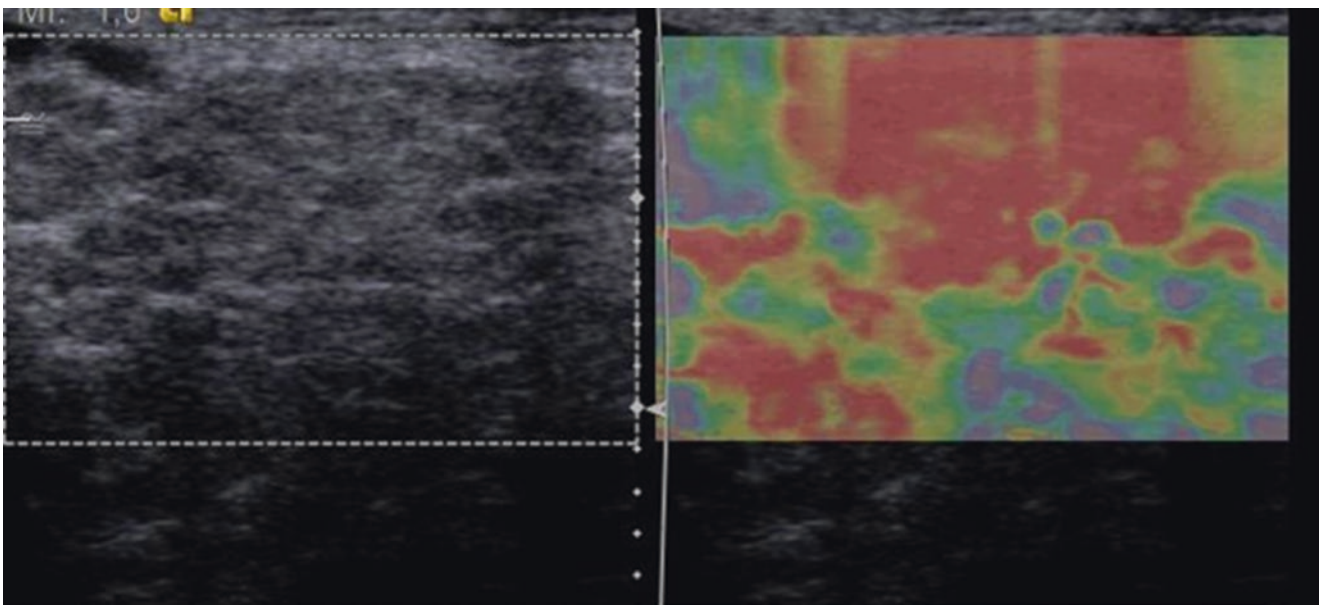

Fig. 11.13 Strain elastography in grade 3 Sjögren's syndrome, visualizing hardened (*red*) submandibular gland tissue

course of patients with pulmonary sarcoidosis compared with their extrathoracic counterparts. Pulmonary sarcoidosis is often incidentally diagnosed via chest x-ray and has a chronic clinical course. Heerfordt's syndrome represents acute sarcoidosis. Although Heerfordt's syndrome (syn. *Febris uveoparotid*), which includes fever, parotitis, uveitis, and facultative facial nerve palsy, is traditionally attributed to the head and neck region, cervical and intra-parotideal lymph node manifestations are the most frequent head and neck symptoms in both acute and chronic sarcoidosis [11, 18]. Subsequently, B-mode ultrasound frequently diagnoses enlarged cervical and intra-parotideal lymph nodes with hilus hypervascularity in CDS (Fig. 11.15). In addition, intraparenchymatous manifestations of the parotid in a submandibular gland occur in a minor proportion of patients. B-mode criteria and CDS cannot distinguish these cases from Sjögren's syndrome or MALT lymphoma (Fig. 11.15) [11, 16–18]. In all cases, histological proof of granulomatous inflammation and subsequent clinical differential diagnosis (e.g., tuberculosis) is mandatory.

IgG4-Associated Sialadenitis

Mikulicz-Radecki first described systemic disease including the lacrimal and submandibular glands in 1892. Later, a hardened, indolent, and tumor-like submandibular gland was described as Küttner's tumor [27]. In 2001, Hamano et al. demonstrated for the first time increased serum IgG4 levels in sclerosing pancreatitis [28]. Today, IgG4-associated diseases involve 14 organ systems, including lacrimal and salivary glands (Mikulicz syndrome, Küttner's tumor) [29]. Interestingly, salivary gland manifestation has shown a strong predilection for the submandibular gland; involvement of the parotid, sublingual, and minor salivary glands are rare events [2, 3, 11, 17]. B-mode ultrasound usually visualizes a downscaled submandibular gland with maximum diameter often less than 3 cm. An intraglandular, irregular border and hypoechogenicity represent the B-mode sonographic correlate of chronic inflammation (Fig. 11.16). CDS shows irregular intralesional vascularity of the hypoechoic region (Fig. 11.17). B-mode sonography and CDS show significant overlap with submandibular gland carcinoma, so diagnostic submandibulectomy represents the surgical approach of choice [3].

11.2.3 Radiation-Induced Sialadenitis

Radiation-induced sialadenitis occurs in both transcutaneous radiotherapy of head and neck cancer and radioiodine (^{131}I) therapy of well-differentiated thyroid cancer [30, 31].

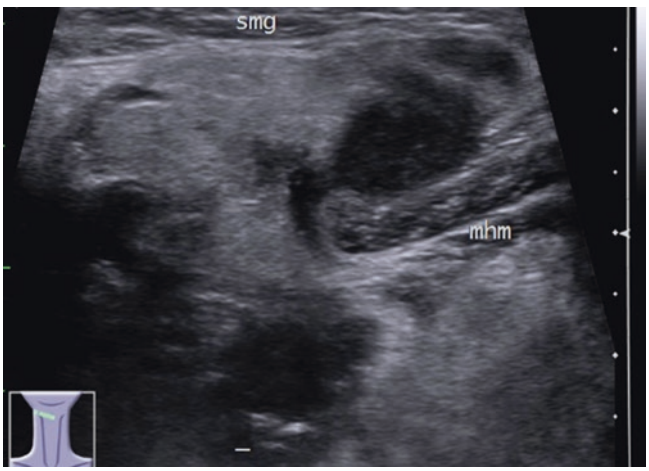

Fig. 11.16 B-mode sonography of IgG4-associated disease shows irregular-bordered, hypoechoic lesions in the anterior part of the right submandibular gland. mhm *m. mylohyoideus*, smg submandibular gland

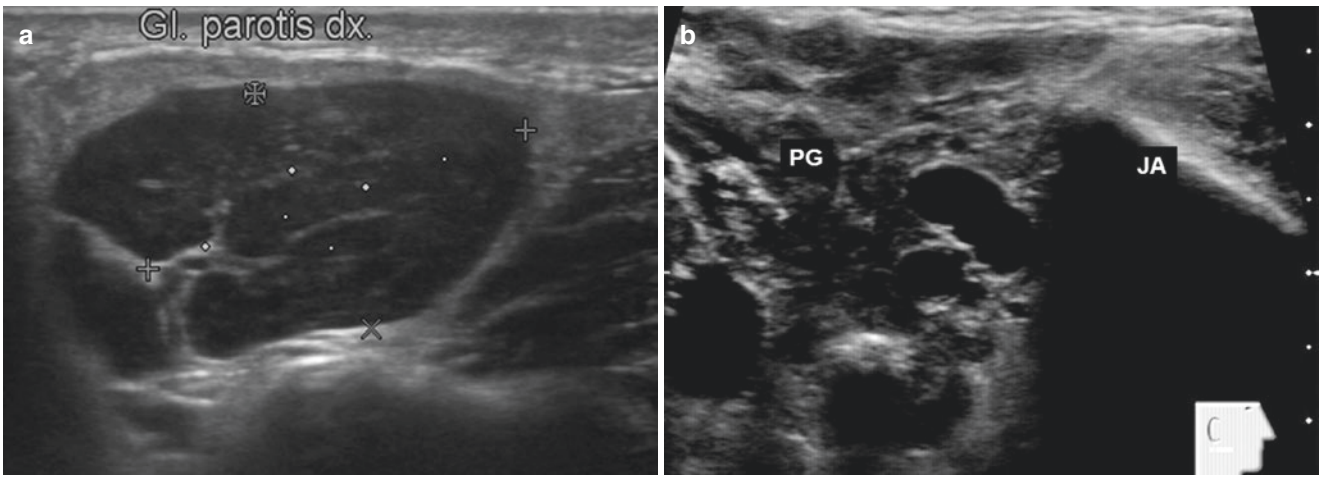

Fig. 11.15 B-mode sonography of parotid gland sarcoidosis visualizes a large intra-parotideal lymph node with marked hilus structure (**a**) or a parenchymatous manifestation with multiple echo-free areas (**b**). JA jaw angle, PG parotid gland

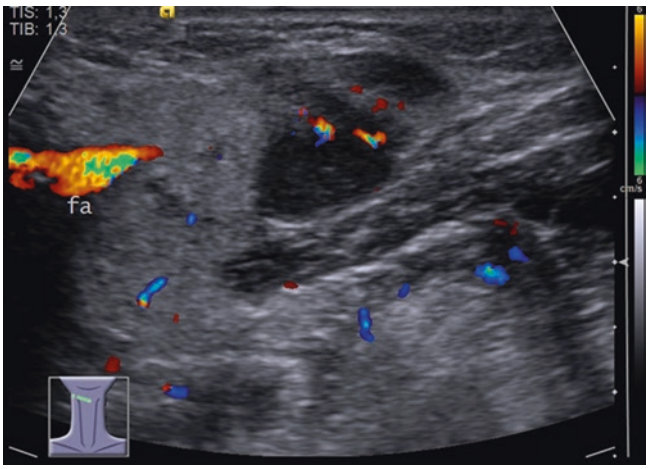

Fig. 11.17 Corresponding color-coded duplex sonography of IgG4-associated disease shows irregular intralesional vascularity

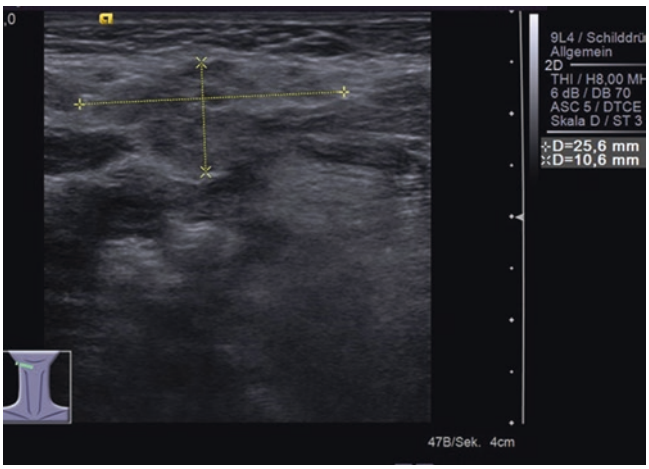

Fig. 11.19 B-mode sonography in chronic radiation-induced sialadenitis visualizes a downscaled and inhomogeneous right submandibular gland

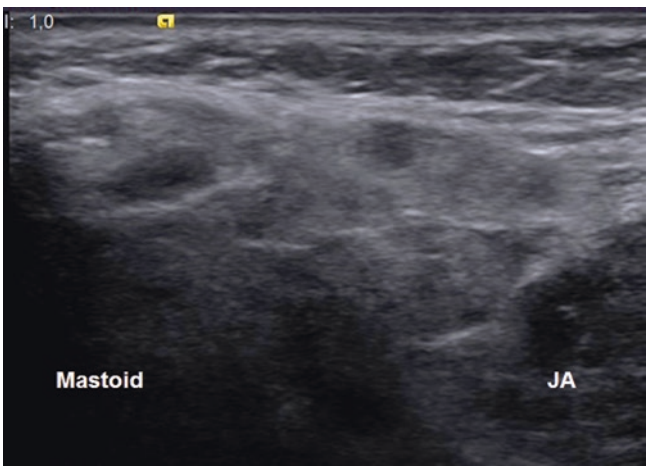

Fig. 11.18 B-mode sonography in acute radiation-induced sialadenitis of the right parotid gland demonstrates diffuse glandular enlargement and hypoechoic lesions. JA jaw angle

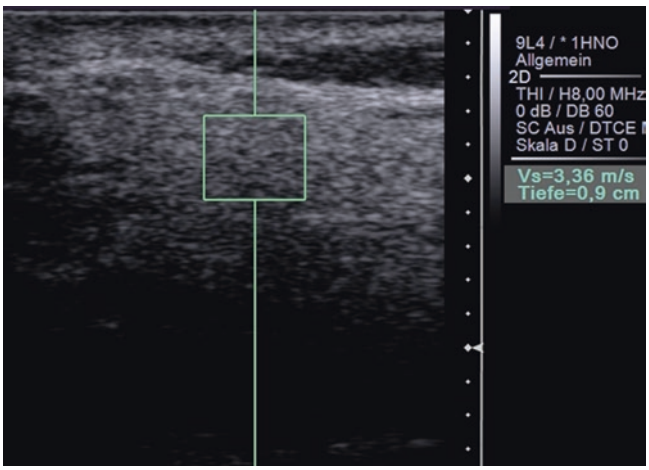

Fig. 11.20 Shear-wave elastography in chronic radiation-induced sialadenitis shows shear-wave velocities of the right parotid gland higher than 2 m/s

Transcutaneous radiotherapy with cumulative doses greater than 30 gray causes permanent salivary gland dysfunction from damage to epithelial and connective tissue elements such as blood vessels, from direct damage of salivary acini and ducts, or both [31, 32]. The ^{131}I accumulates in the salivary glands, giving rise to transient or permanent salivary gland damage [30, 33]. Serous salivary tissue of the parotid gland demonstrates particularly high sensitivity to transcutaneous ^{131}I radiation therapy. In acute sialadenitis, B-mode ultrasound demonstrates enlarged salivary glands with diffuse hypoechoic inhomogeneity (Fig. 11.18). CDS shows hypervascularized glandular tissue. However, chronic tissue destruction occurs more often and can be seen as hyperechoic, sclerosing, and down-scaled salivary glands (Fig. 11.19). Strain elastogram shows salivary glands that are harder than circumjacent tissue. More recently, acoustic structure quantification and shear-wave elastography were established to reliably identify radiation-induced salivary damage. Shear-wave velocities >2 m/s indicate chronic glandular tissue destruction (Fig. 11.20) [34–36].

11.2.4 Chronic Recurrent Parotitis

Chronic recurrent parotitis represents a nonobstructive parotitis that can be divided into juvenile and adult forms. The etiopathogenesis is still unknown; dysontogenetic duct ectasia and autoimmune conditions are discussed. In nearly all

patients, the condition becomes clinically apparent with a painful, unilateral, or bilateral swelling of the parotid gland after bacteria superinfection. B-mode ultrasound visualizes hypoechoic and echo-free lesions, referring to intraparotideal lymph nodes and ductal ectasia (Fig. 11.21). Peripheral hypervascularity occurs in acute bacterial superinfection (Fig. 11.22). Strain elastography attributes the soft tissue pattern to echo-free areas (Fig. 11.23). More recently, shear-wave elastography was suggested as reliable diagnostic tool for the assessment of disease severity and progression [37]. However, there is no ultrasonographic proof of chronic recurrent parotitis, so a detailed history of the clinical course may be required for the diagnostic workup, and differential diagnosis of lymphoepithelial lesions is necessary in the adult form.

11.3 Sialadenosis

Sialadenosis is defined as noninflammatory and nonneoplastic swelling of major salivary glands. Underlying conditions range from dystrophic, endocrine, neurogenic, or medication-associated conditions to anorexia or bulimia [38]. There is no typical sonographic appearance. Mostly, B-mode ultrasound visualizes a hyperechoic, slightly inhomogeneous, bilateral enlargement of the parotid glands

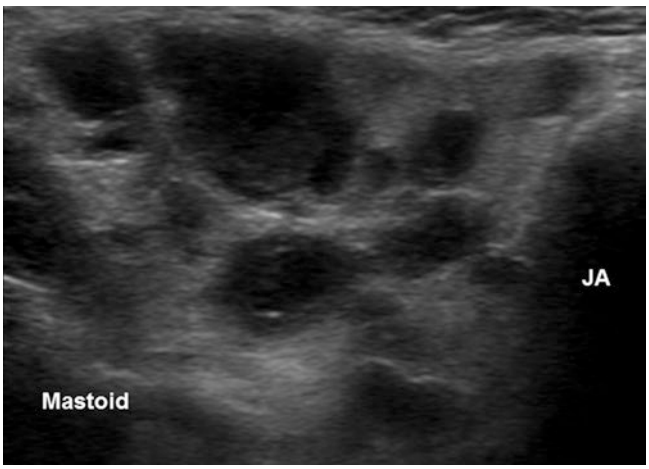

Fig. 11.21 B-mode sonography in chronic recurrent parotitis shows multiple hypoechoic lesions in an enlarged right parotid gland. JA jaw angle

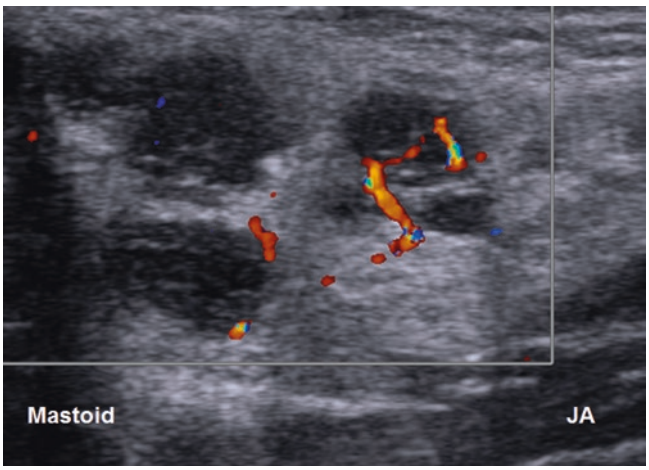

Fig. 11.22 Color-coded duplex sonography in chronic recurrent parotitis attributes hypoechoic areas to intra-parotideal lymph nodes with hilus vessels and duct ectasia with peripheral vascularity. JA jaw angle

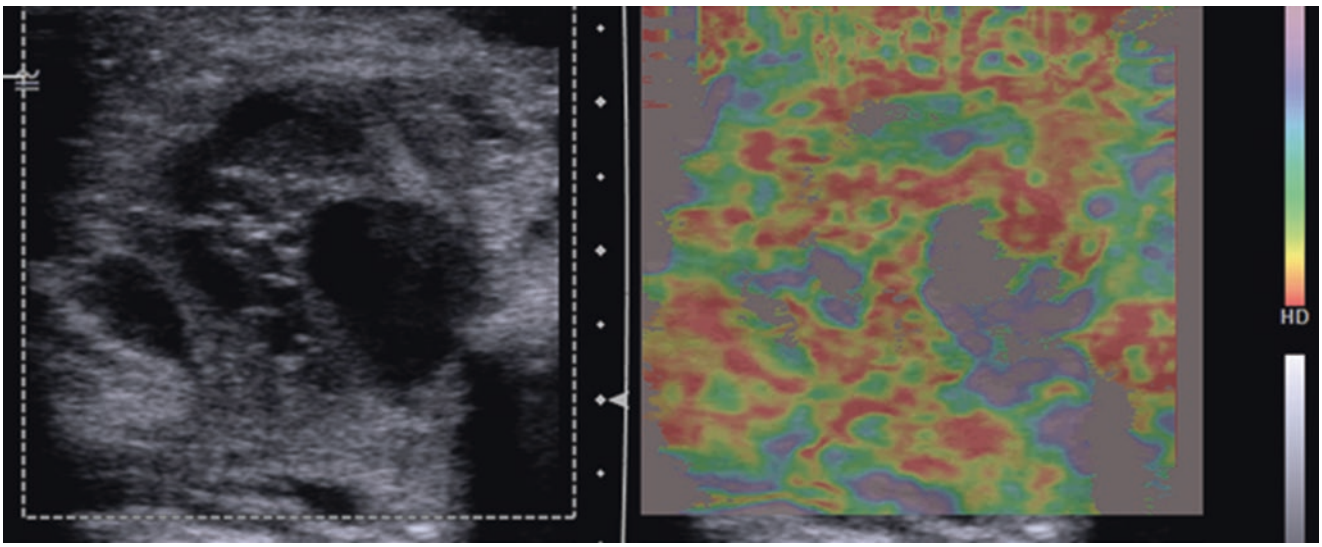

Fig. 11.23 Strain elastography in chronic recurrent parotitis validates color-coded duplex sonography and visualizes avascular areas as soft (*blue*) and vascularized hypoechoic areas as hard (*red*)

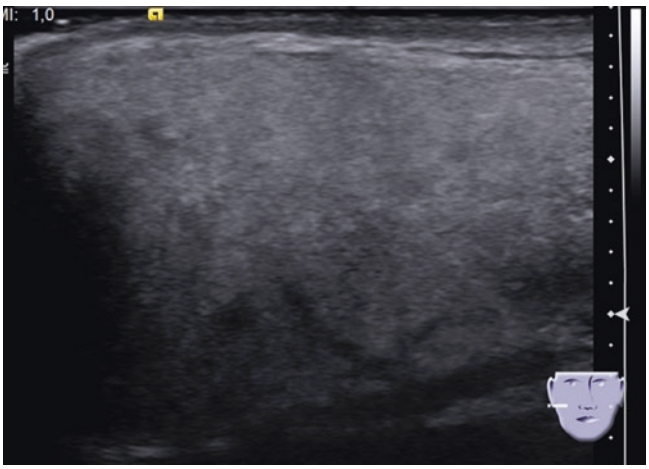

Fig. 11.24 B-mode sonography of parotid gland sialadenosis shows diffuse enlargement of the pre-auricular parotid gland, with regular echotexture

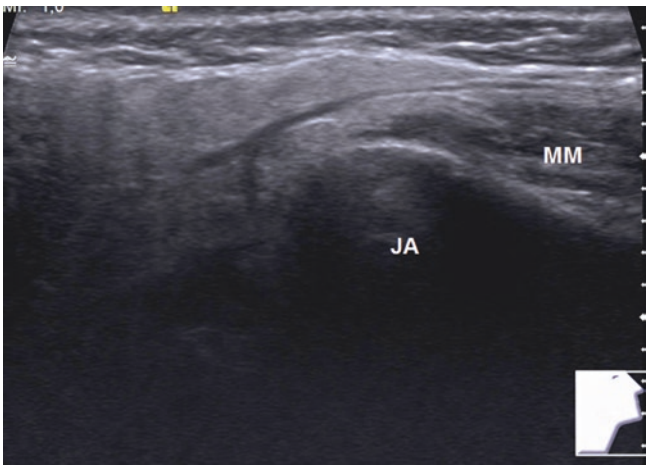

Fig. 11.25 Stenosis of Stenson's duct papilla with proximal duct dilatation. JA jaw angle, MM masseter muscle

(Fig. 11.24) [4]. A detailed history, clinical examination, and laboratory testing are needed to exclude a broad variety of chronic parotid gland diseases.

11.4 Duct-Associated Disease

11.4.1 Obstructive Sialadenitis

Stenosis and stricture of salivary ducts, as well as ductal concrements (sialolithiasis), result in obstructive sialadenitis. Stenosis and stricture may be due to dysontogenetic, posttraumatic, post-inflammatory, and iatrogenic conditions; sialolithiasis represents the most important etiopathogenetic condition (Fig. 11.25) [39]. About 90% of sialolithiasis affects the submandibular gland; concrements of the parotid or sublingual glands occur infrequently. Concrements can be diagnosed in the glandular hilus, in the central part, and in the peripheral parts of the Wharton's and Stenson's duct. The diagnostic setup in obstructive sialadenitis comprises sonography, MR sialography, and sialendoscopy [40]. Concrements larger than 2 mm can usually be diagnosed via B-mode ultrasound, which has an estimated diagnostic sensitivity of 94%, with 100% specificity [3, 41]. A history of digestion-associated swelling of the affected gland with B-mode visualization of cortical concrement reflex, dorsal acoustic shadows, and pre-stenotic ductal dilatation validate the hypothesis of sialolithiasis (Fig. 11.26). Bacterial ascensus with subsequent sialadenitis is frequently diagnosed (Fig. 11.27). Intraductal application of contrast enhancers and elastographic assessment is currently under consideration but is not part of a standardized diagnostic approach [42, 43].

11.4.2 Duct Cysts

Salivary gland duct cysts are nonneoplastic lesions with an epithelium lining inside, so they can therefore be differentiated from sialocele after facial injury [44]. True salivary gland cysts are acquired as a result of ductal obstruction [44]. The vast majority of lesions originate in the main body of the superficial parotid gland lobe or are associated with Stenson's duct (Fig. 11.28). A substantial proportion of these parotid gland cysts are diagnosed due to bacterial superinfection. Dysontogenetic cysts show predilection for the sublingual gland (ranula) and can be diagnosed by inspection of the floor of the mouth (Fig. 11.29). Some of these cysts exhibit transcervical extension, perforating the mylohyoid muscle or coiling its posterior border (Fig. 11.30). Cysts appear hypoechoic or echo-free because of differences in liquid viscosity. Intralesional vascularization fails to be diagnosed in CDS, but hypervascularization of the circumjacent tissue can occur after inflammation (Fig. 11.31).

11.5 Neoplasms

The incidence of salivary gland tumors is estimated to be about 40 cases per million inhabitants, representing 3% of all head and neck neoplasms [45, 46]. Pleomorphic adenomas and Warthin's tumors (syn. *cystadenolymphoma*) are the most frequent entities, but a variety of other benign lesions are also reported [2, 45–48]. The vast majority of salivary gland lesions originate in the parotid gland, but the relative number of major salivary gland malignancies increases from the parotid and submandibular glands to the sublingual gland [46]. Salivary gland malignancy is estimated to be about nine

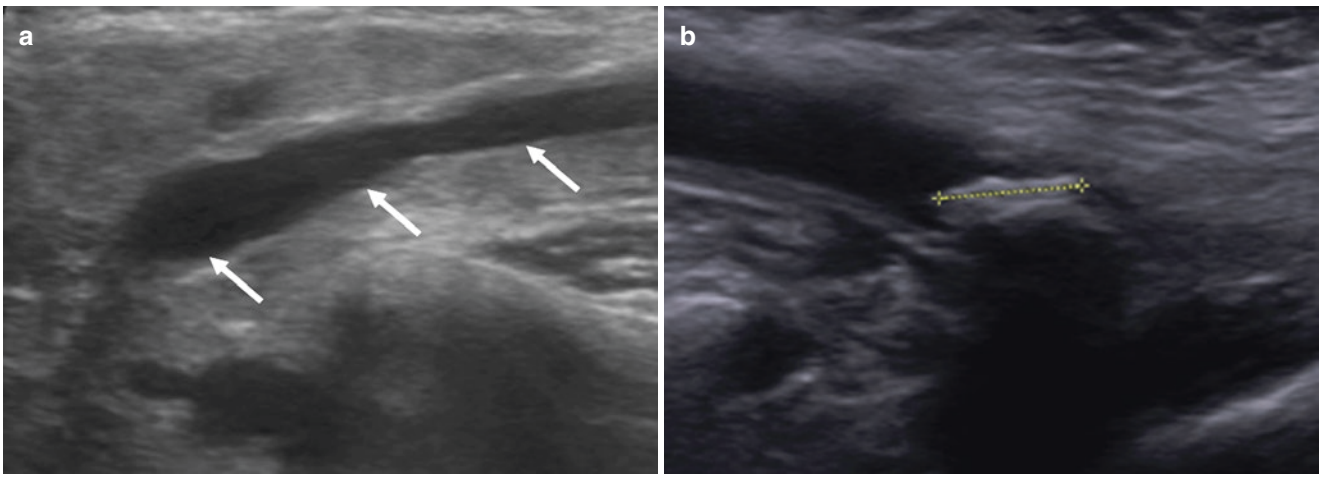

Fig. 11.26 (**a**) Proximal duct dilatation (*arrows*) due to distal sialolithiasis of the right submandibular gland. (**b**) Concrement shows cortical reflex with dorsal acoustic shadow

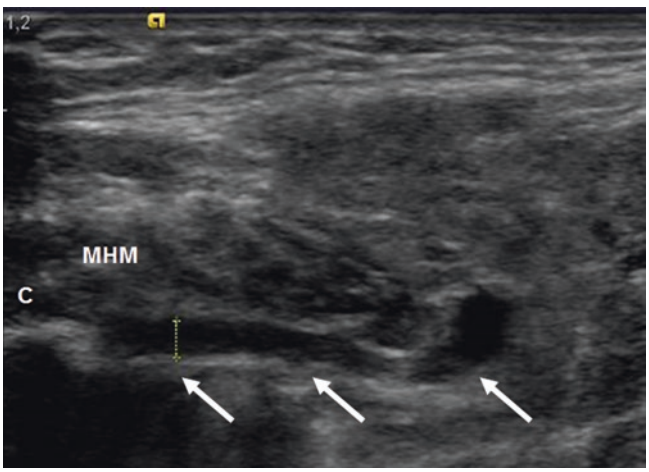

Fig. 11.27 B-mode ultrasound shows bacterial superinfection in sialolithiasis of the left submandibular gland. Seen are diffuse glandular inhomogeneity with hypoechoic lymphatic septa, and a peripheral concrement (C) with proximal duct dilatation (*arrows*). MHM—mylohyoid muscle

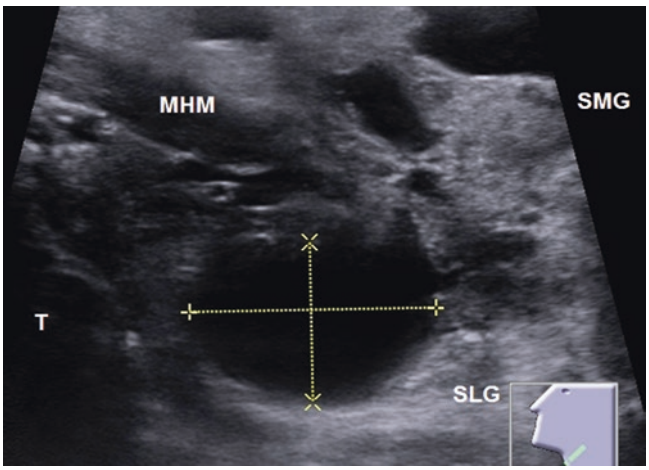

Fig. 11.29 B-mode ultrasound shows an intraoral echo-free lesion (ranula). MHM mylohyoid muscle, SLG sublingual gland, SMG submandibular gland, T tongue

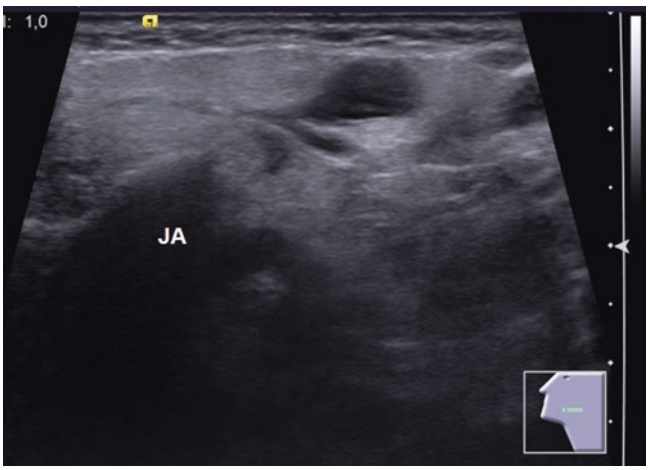

Fig. 11.28 B-mode sonography of an intra-parotideal duct cyst visualizes an echo-free lesion in the central part of the left parotid gland. JA jaw angle

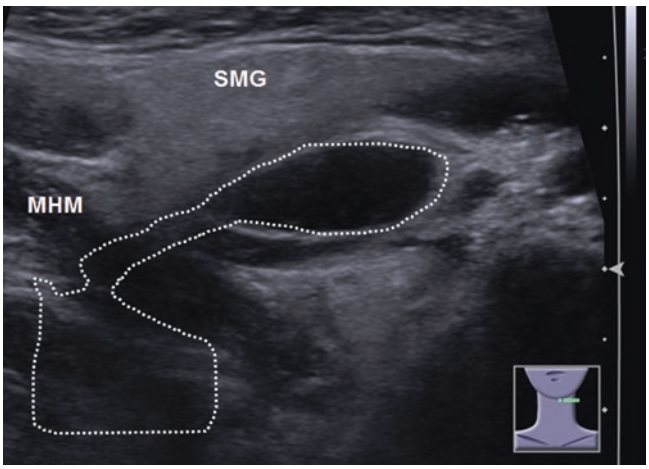

Fig. 11.30 B-mode ultrasound of a ranula with cervical extension bypassing the mylohyoid muscle (MHM). SMG submandibular gland

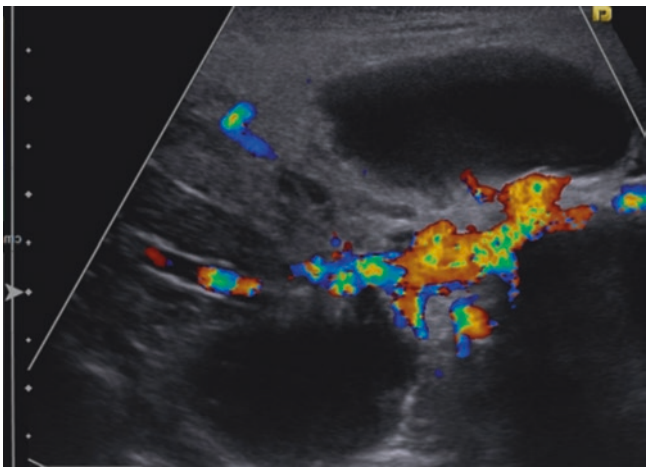

Fig. 11.31 Corresponding color-coded duplex sonography validates the ranula by demonstrating the avascularity of the echo-free lesion

cases per million inhabitants; mucoepidermoid carcinoma is the most common primary cancer [2, 45, 47]. In contrast to the submandibular and sublingual glands, the parotid gland harbors lymph nodes, so it represents an organ of locoregional metastasis [2, 49]. Salivary gland lymphoma or other malignancies occur infrequently [2].

11.5.1 Benign Tumors

Pleomorphic Adenoma

Pleomorphic adenomas are the most frequent tumor entity of the major salivary glands. In contrast to Warthin's tumors, multilocularity in pleomorphic adenomas exclusively occurs after prior parotid gland surgery, most likely linked to an iatrogenic rupture of the tumor's pseudo-capsule [2]. The risk of intraoperative tumor dissemination and the risk of malignant transformation highlight the necessity of reliable preoperative tumor identification in order to optimize treatment regimens. B-mode ultrasound characterizes pleomorphic adenomas as being sharply bordered and lobulated tumors with moderate to strong acoustic enhancement [3, 45, 50, 51]. Echogenicity varies because of different extents of epithelial and stromal components (Fig. 11.32) [3, 45, 52–54]. CDS usually visualizes poor intralesional vascularization (Fig. 11.32b) [3, 45, 50, 52–54]. More recently, strain and shear-wave elastography, as well as CEUS, have been used to increase the preoperative identification and differentiation of pleomorphic adenomas. Strain elastography shows a pleomorphic adenoma that is harder than the circumjacent glandular tissue ("dense core") (Fig. 11.32a) [53, 55]. Interestingly, analysis of shear-wave velocities demonstrates heterogeneous results, with a high rate of measurement dropout [53]. There are two explanations for these contradictory results: first, lesional tissue heterogeneity results in an inappropriate standard deviation in the measured region of interest, causing value exclusion. Second, shear-wave velocities are markedly higher than the measurement range of the ultrasound device [53]. In accordance with findings in CDS, CEUS demonstrates poorly microvascularized tumors (Fig. 11.32b, c) [52, 54, 56].

Miliary seeding of pleomorphic adenoma after surgical intervention appears as tumor multilocularity in the submandibular triangle or the parotid region, including subcutaneous tissue and head and neck muscles. Tumors demonstrate well-defined borders, a round or lobulated shape, and often marked hypoechogenicity (Fig. 11.33). Tumor seeding is often much wider than expected from the initial surgical attempt (Fig. 11.34).

Monomorphic Adenoma

Monomorphic adenomas represent a heterogeneous group of salivary gland tumors. Warthin's tumor is the most important monomorphic adenoma, accounting for approximately the half of all benign tumors [2, 57]. Today's balanced distribution of pleomorphic adenoma and Warthin's tumors refers most likely to an increased patients' age, nicotine abuse, improved diagnostic applications, and a general demographic change toward an older population [2, 57]. Interestingly, Warthin's tumor does not affect the sublingual or submandibular gland, but de novo unilateral or bilateral parotideal multilocularity occurs in 5–10% of cases [2]. In addition, a substantial proportion of Warthin's tumors show an eccentric growing pattern in level IIa that impedes the differentiation to cervical lymph nodes or branchial cleft cysts [3, 58]. These findings refer to the hypothesis of an inclusion of glandular cells in parotid gland lymph nodes during embryogenesis [59–61]. Other histological subtypes of monomorphic adenoma, such as oncocytoma, basal cell adenoma, or myoepithelioma, occur infrequently [2]. However, pretherapeutic differentiation might be of high clinical impact, because oncocytoma and basal cell adenoma also demonstrate miliary seeding after surgical rupture of the tumor capsule [2]. B-mode ultrasound visualizes a round, oval, or polycyclic tumor with well-defined borders (Fig. 11.35). Monomorphic adenoma appears as a hypoechoic tumor with moderate to strong acoustic enhancement (Fig. 11.35a). Echo-free areas occur in cystic parts of Warthin's tumor. Complex cysts can be seen due to septal segmentation [3, 52–54]. Monomorphic adenoma usually shows peripheral and/or central hypervascularity, which can be validated with a fast and strong perfusion in CEUS (Fig. 11.35b, c) [52–54]. Particularly in Warthin's tumor, strain elastography shows soft and hard areas representing solid and cystic parts ("half and half") (Fig. 11.35a) [53, 55]. Other monomorphic adenomas appear harder as the circumjacent glandular tissue [53]. Sonographic findings after miliary seeding of basal cell adenoma and oncocytoma are often similar to pleomorphic adenoma.

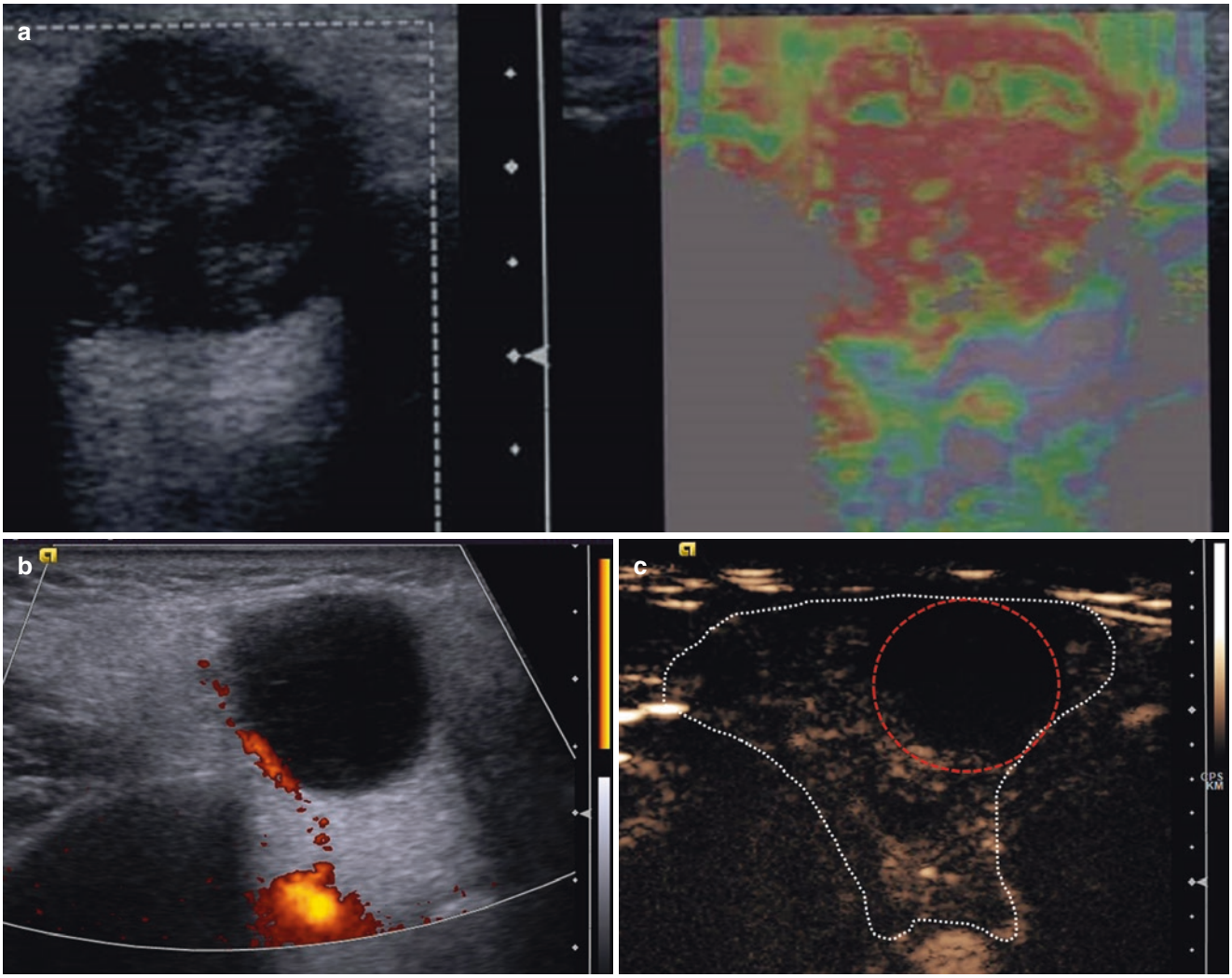

Fig. 11.32 (**a**) B-mode ultrasound of pleomorphic adenoma demonstrates a hypoechoic intra-parotideal lesion with regular borders that appears hard (*red*) in strain elastography. (**b**, **c**) Hypovascularity and hypoperfusion are visualized in color-coded duplex sonography and contrast-enhanced ultrasound. The *white line* outlines the parotid gland; the *red line* indicates the tumor

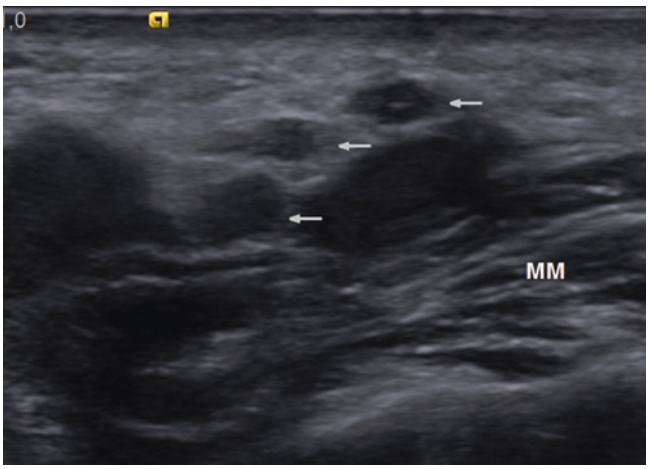

Fig. 11.33 B-mode sonography of miliary seeding of pleomorphic adenoma. Hypoechoic tumors (*arrows*) originated in the subcutaneous tissue after parotidectomy. MM masseter muscle

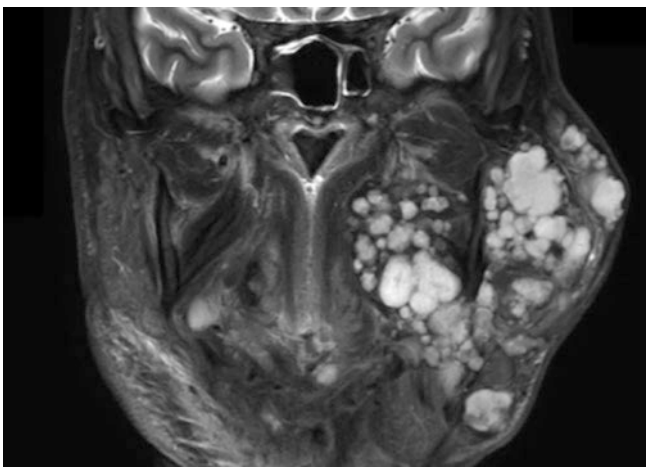

Fig. 11.34 Coronal magnetic resonance (MR) tomography of miliary seeding of pleomorphic adenoma

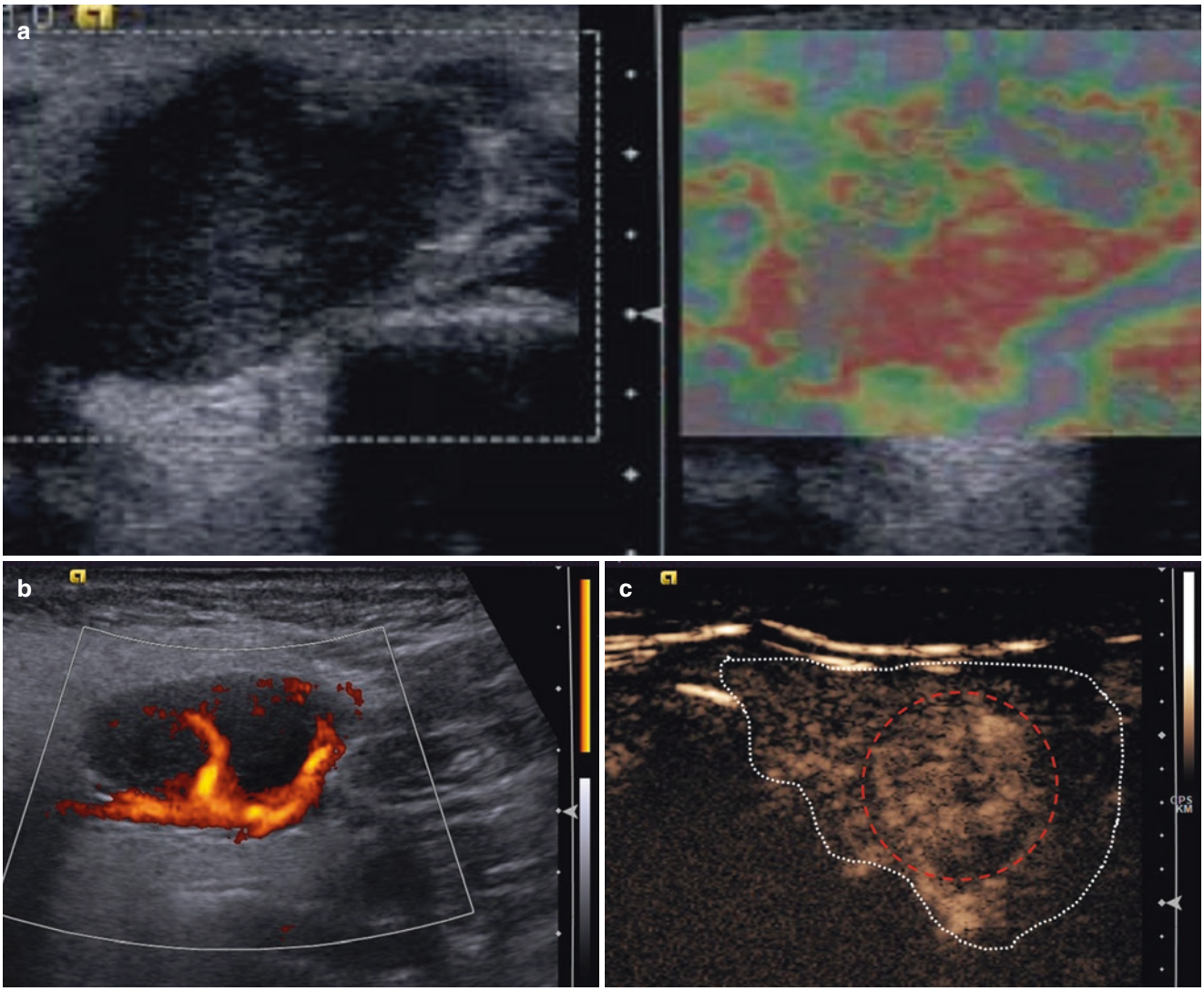

Fig. 11.35 (**a**) B-mode ultrasound of Warthin's tumor demonstrates a hypoechoic intra-parotideal lesion with regular borders that appears with hard (*red*) and soft (*blue*) areas in strain elastography. (**b**, **c**) Hypervascularity and hyperperfusion are visualized in color-coded duplex sonography and contrast-enhanced ultrasound. The *white line* outlines the parotid gland; the *red line* indicates the tumor

11.5.2 Malignant Tumors

Primary and Secondary Epithelial Malignancy

Carcinomas of major salivary glands occur infrequently, with an incidence estimated to be about nine cases per million inhabitants [2, 45, 47]. The broad variety of salivary gland carcinomas comprises 24 histological subtypes listed by the World Health Organization (WHO). Cancer of the parotid gland represents almost 15% of all parotid gland lesions and can be divided into primary carcinoma and secondary carcinoma (intra-parotideal lymph node metastasis) [2]. Lymph node metastasis most commonly involves cutaneous malignancy, such as squamous cell carcinoma, malignant melanoma, and Merkel cell carcinoma [62, 63]. A dramatic increase of metachronous intra-parotideal metastasis in recent decades is likely the result of the increased elderly population and failure to recommend elective parotidectomy and neck dissection in cases of cutaneous squamous cell carcinoma [2, 64]. The proportions of primary carcinomas increase from about 20% for the parotid gland to about 50% for the submandibular gland and about 95% for sublingual glands [65]. Mucoepidermoid, adenoid cystic, acinic cell, and adenocarcinoma, as well as carcinoma ex pleomorphic adenoma are the most common histological subtypes [2, 65]. The clinical appearance differs dramatically between different histological subtypes. Whereas a minor proportion of low-grade mucoepidermoid, myoepithelial, or adenoid cystic carcinomas exhibit lymph node metastases, lymph node positivity is frequently diagnosed in high-grade mucoepidermoid carcinoma and carcinoma ex

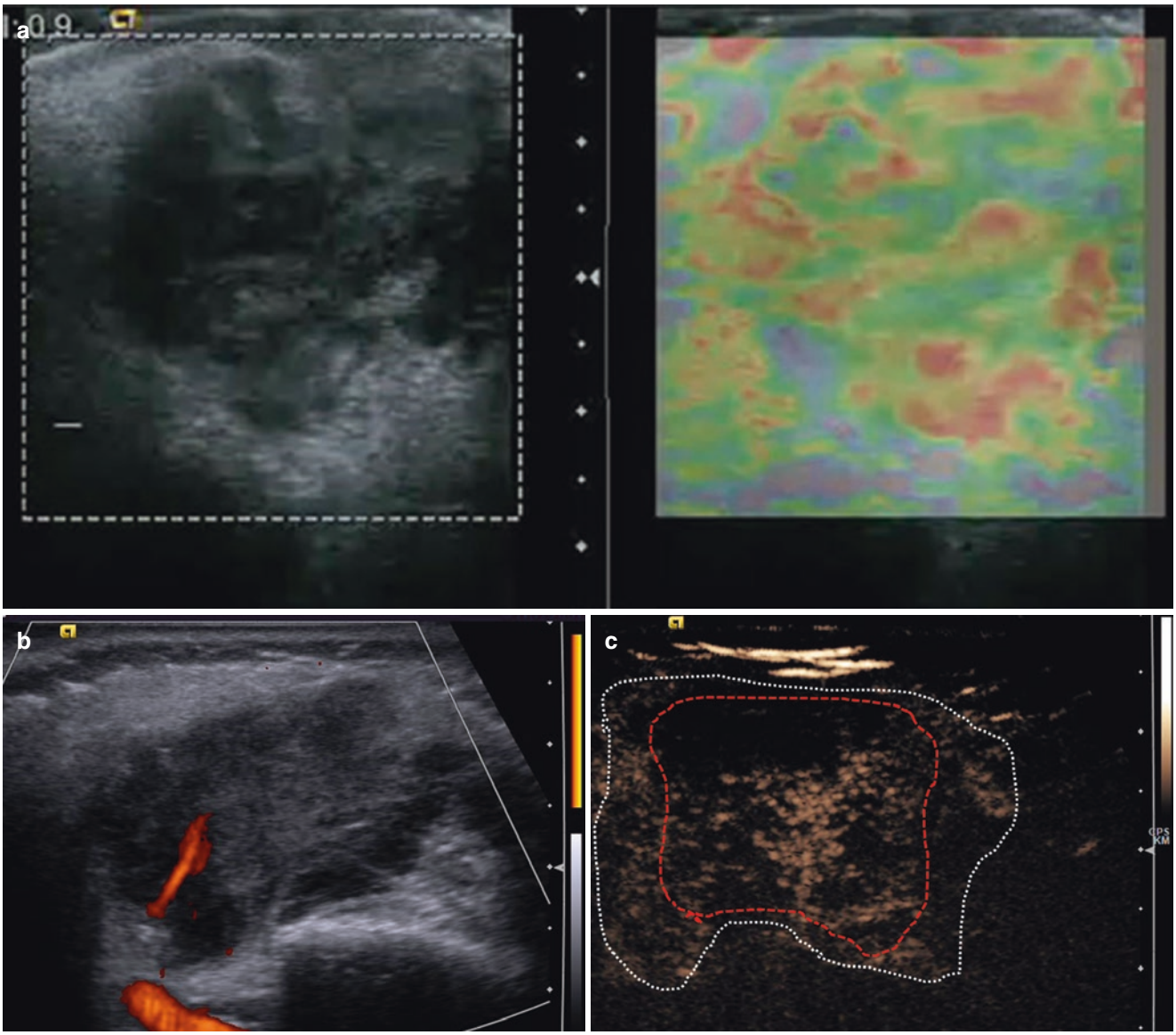

Fig. 11.36 (**a**) B-mode ultrasound of parotid gland carcinoma shows an inhomogeneous intra-parotideal lesion with irregular borders, which appears with irregular hard areas in strain elastography. (**b**) Slight vessel formation is visualized in color-coded duplex sonography, (**c**) Contrast enhanced ultrasound shows hyperperfused and hypoperfused areas. The *white line* outlines the parotid gland; the *red line* indicates the tumor

pleomorphic adenoma [2]. Adenoid cystic carcinomas show striking differences from other parotid gland carcinomas. The growth pattern of adenoid cystic carcinoma is rather slow, but perineural invasion can frequently be seen and results in a higher proportion of facial nerve palsy at the time of diagnosis [2]. Hematogenous metastases (particularly pulmonary metastases) occur frequently, whereas lymphatic metastatic spread is infrequent. Therefore, pulmonary and abdominal CT scan is a mandatory part of the initial and follow-up staging [2].

Overall, facial nerve palsy can be diagnosed in 8% of all patients with parotid gland malignancy, with a pronounced occurrence in squamous cell carcinomas and their metastases [2]. Preoperative ultrasonographic identification of salivary gland malignancy is of major clinical impact in managing the balancing act between sufficient radicality and a minimum of facial nerve alteration. Irregular tumor borders, missing acoustic enhancement, and the occurrence of cervical lymph nodes in B-mode ultrasound—as well as irregular ("chaotic") vessel formation in color-coded duplex sonography—are highly suspicious for salivary gland malignancy (Fig. 11.36) [3, 52, 54]. Inhomogeneous elastography visualizing a mixture of hard and soft areas ("garland sign") occurs significantly more often in salivary gland malignancy (Fig. 11.36a). The impact of shear-wave techniques is discussed controversially [54, 66]. Unfortunately, the vast

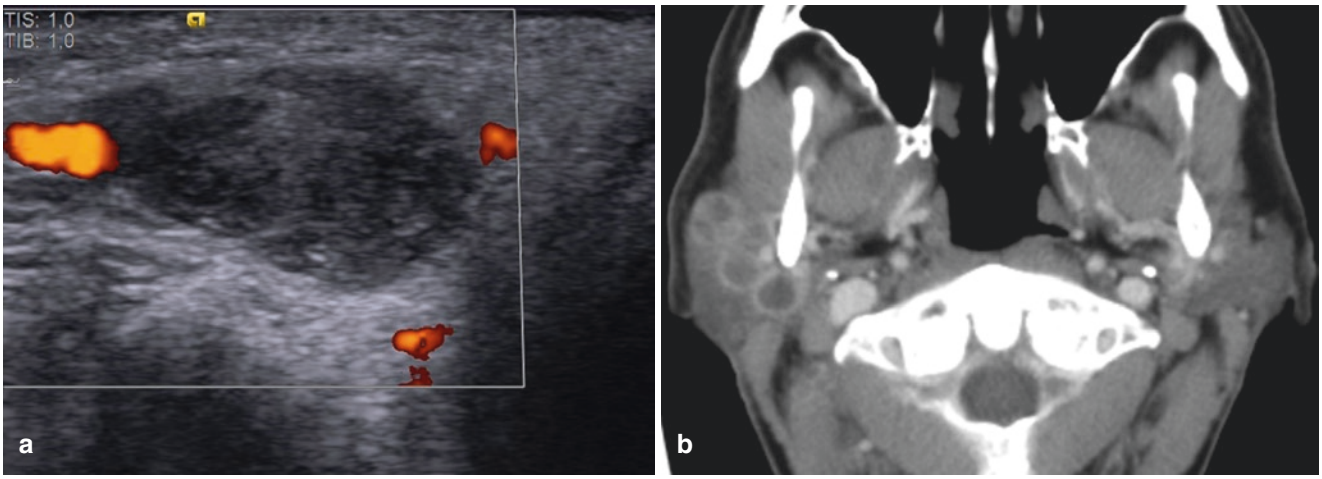

Fig. 11.37 Color-coded duplex sonography (**a**) and axial CT scan (**b**) of intra-parotideal metastasis of cutaneous squamous cell carcinoma. Color-coded duplex sonography shows an inhomogeneous, hypoechoic tumor with well-defined borders and capsular vascularity

majority of salivary gland carcinoma does not demonstrate a "typical" ultrasonographic appearance and will be underdiagnosed [3, 52, 54]. In these cases, hypoperfusion in CEUS of hypervascularized tumors after CDS (and vice versa) can often be attributed to malignant lesions (Fig. 11.36b, c). CEUS as part of an ultrasonography-based algorithm significantly improves diagnostic sensitivity and specificity in the identification of salivary gland cancer, but it is not part of today's sonography routine [3, 52, 54, 67–69]. Therefore, the occurrence of ipsilateral cervical lymph nodes, parotid gland masses with a history of ipsilateral cutaneous malignancy, irregular tumor borders, and facial nerve alteration are highly suspicious for salivary gland malignancy (Fig. 11.37) [3, 54].

Lymphoma

Manifestations of major salivary gland lymphoma can be seen in both mucosa-associated lymphoid tissue and parotid gland lymph nodes [1–3, 17]. The parotid gland represents the most frequent tumor site, where lymphoma accounts for approximately 3% of all lesions [2]. Diffuse large B-cell lymphoma (DLBCL) and mucosa-associated lymphoid tissue (MALT) lymphoma represent the most frequent entities [2, 3]. Glandular MALT lymphoma often refers to Sjögren's syndrome [11, 17, 70]. Patients with Sjögren's syndrome have a 44-fold increased risk of developing salivary or extrasalivary lymphoma, 48–75% of which cases are MALT lymphoma [71]. There is a broad ultrasonographic appearance of salivary gland lymphoma. Some lymphomas show B-mode characteristics of benign or malignant parotid gland lesions. Others can be diagnosed as enlarged intra-parotideal lymph node or are hidden in lymphoepithelial lesions of Sjögren's syndrome (Fig. 11.38). Interestingly, facial nerve alteration is a rare event [2]. Open biopsy and "diagnostic" submandibulectomy and parotidectomy are the diagnostic approaches of choice because of the lack of specificity of symptoms and ultrasonographic findings and the broad variety of differential diagnoses.

11.6 Pseudotumors of Major Salivary Glands

A few types of inflammatory, dysontogenetic, and neoplastic lesions can be clinically mistaken for major salivary gland tumors. Some of these lesions originate in salivary gland structures; others refer to circumjacent tissue. The lesions most often misinterpreted as salivary gland tumors represent lymph nodes originating in level I or IIa. Limited space between the floor of the mouth, the mandible, and the submandibular gland impede rough differentiation between a submandibular gland tumor and level I cervical lymph nodes [3]. B-mode assessment of the relative contact between the lesion and the submandibular gland can give a rough estimate of the lesional origin [3]. Tumors with less than 40% relative contact with the submandibular gland (referring to the entire tumor circumference) are cervical lymph nodes than submandibular gland tumors (Fig. 11.39) [3]. In some cases, CDS clearly identifies hilar vessel formation or vascularization apart from the submandibular gland, suggesting lymph node disease (Fig. 11.40). In addition, tumor masses in level IIa must be differentiated as eccentric Warthin's tumor or cervical lymph node (Fig. 11.41) [58]. Unfortunately, Warthin's tumor shares many B-mode and CDS criteria with cervical lymph nodes, so sonographic differentiation may be illusive at this point. Tumor diagnosis is based on total extirpation, with awareness of the necessity of extracapsular dis-

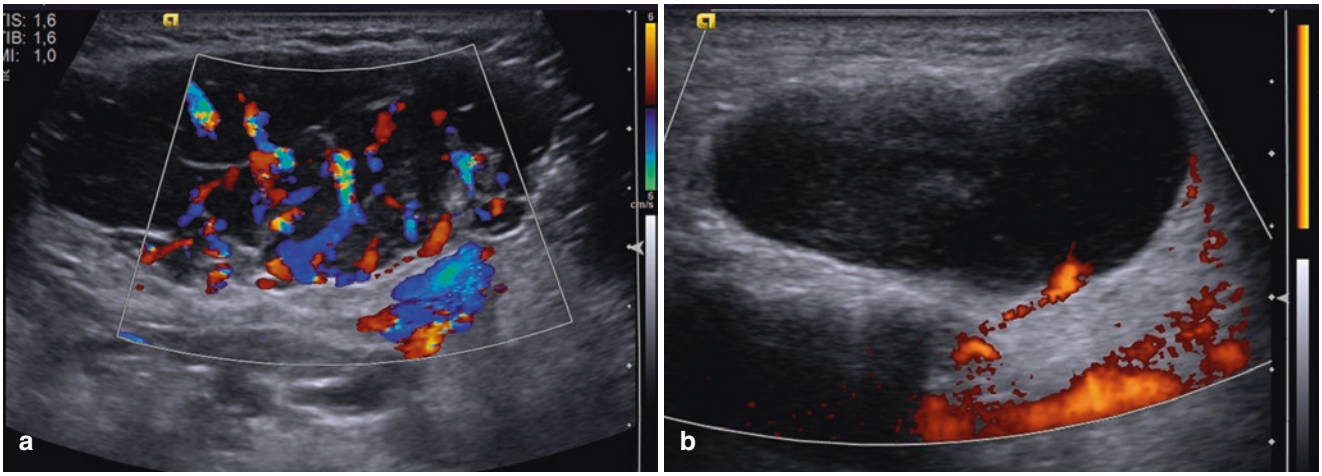

Fig. 11.38 (**a**) Color-coded duplex sonography shows grade 3 Sjögren's syndrome of the right parotid gland, with septal hypervascularity referring to mucosa-associated lymphoma. (**b**) Diffuse large B-cell lymphoma (DLBCL) is visualized echo-free with well-defined borders and slight hilus vascularization

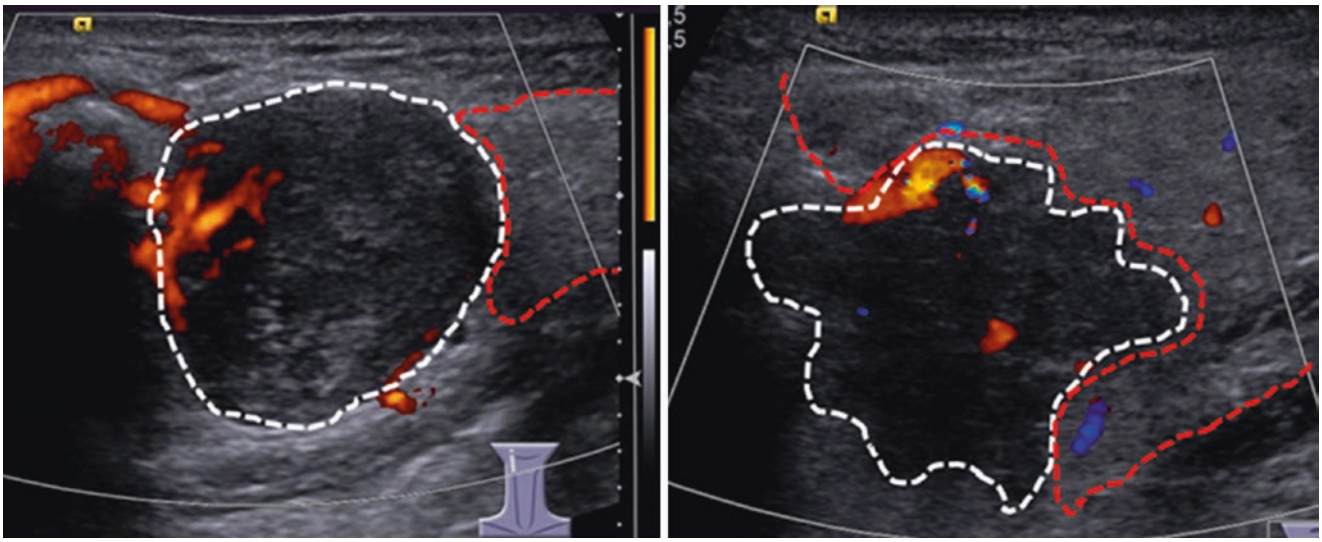

Fig. 11.39 Color-coded duplex sonography demonstrates the relative contact between the lesion (*white line*) and the submandibular gland (*red line*), referring to its own circumferences. Relative contact less than 40% (*left*) refers to an extra-glandular lymph node; more than 40% (*right*) refers to a submandibular gland tumor

section. Application of continuous neuromonitoring might be suitable in these cases [58].

Another lesion in level IIa/b that requires differentiation is the first branchial cleft cyst. Second to fourth branchial cleft cysts represent typical differential diagnoses of head and neck masses, but first branchial cleft cysts occur infrequently [72]. B-mode ultrasound demonstrates a hypoechoic or echo-free lesion in the caudal and deep part of the parotid gland, superiorly lying on the posterior belly of the digastric muscle (Fig. 11.42) [73]. Intralesional macrovascularization and microvascularization are absent. Ductal structures passing the gland profound to the facial nerve often fail to be diagnosed (Fig. 11.43) [73]. An extension into the parapharyngeal space can be diagnosed with MRI, which is indicated when cysts are not fully visualized via ultrasound (Fig. 11.44).

Vessel-associated disease, including hemangioma, lymphangioma, and vessel malformation, also shows manifestations in the parotid region or submandibular triangle. In B-mode ultrasound, hemangioma shows hypoechoic lesions sometimes resembling lipoma. CDS visualization ranges from a low-flow pattern to striking hypervascularity due to the underlying vessel supply (Fig. 11.45). Though hemangioma appears hard on palpation, lymphangioma and vessel

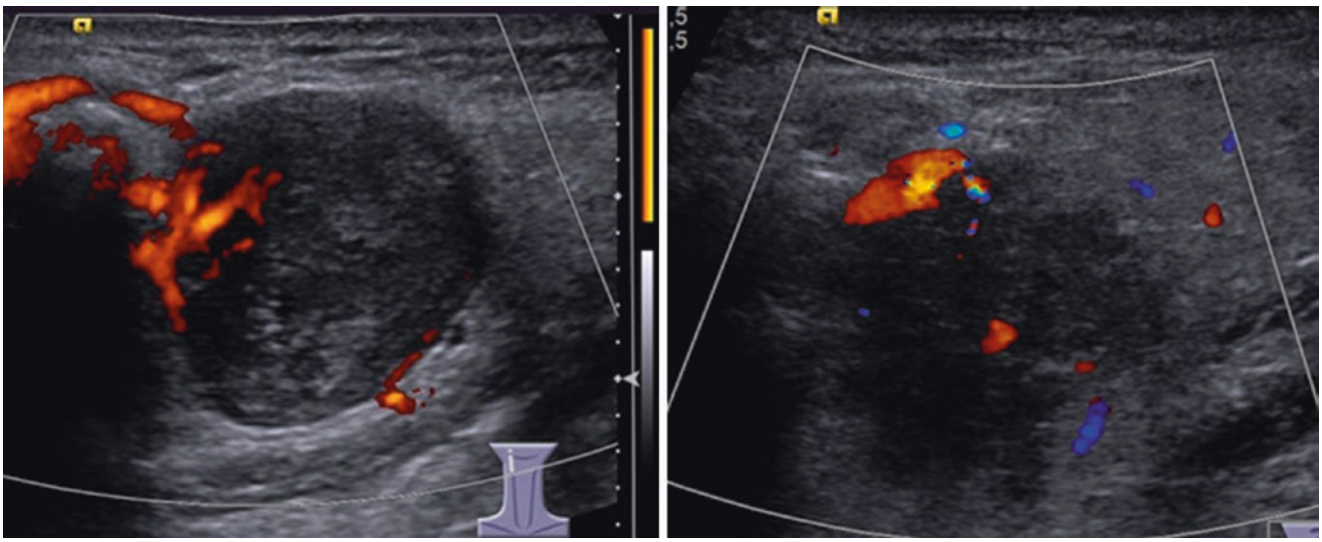

Fig. 11.40 Color-coded duplex sonography visualizes hilus vessel supply via facial vein branches (*left*), suggesting a level Ib lymph node. Irregular submandibular gland vascularization (*right*) refers to submandibular gland adenoid cystic carcinoma

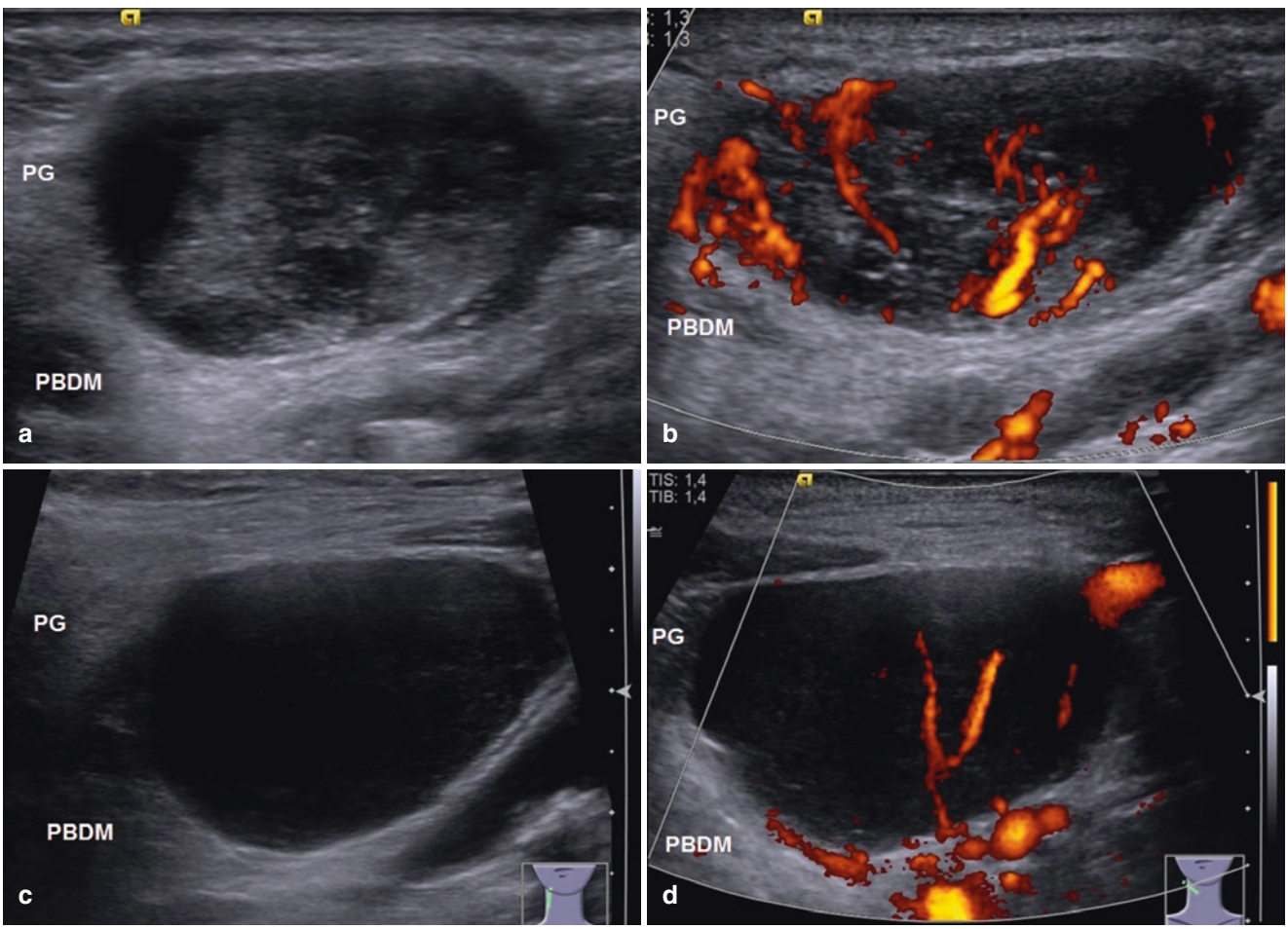

Fig. 11.41 Differential diagnoses of parotid gland pseudo-tumors. (**a**) Eccentric Warthin's tumor is visualized in B-mode ultrasound as an inhomogeneous tumor with well-defined borders. (**b**) Color-coded duplex sonography shows peripheral and central hypervascularity. (**c**) In the same region, B-mode ultrasound visualized non-Hodgkin lymphoma as an echo-free tumor with well-defined borders. (**d**) Color-coded duplex sonography excludes branchial cleft cyst, but eccentric Warthin's tumor remains a potential differential diagnosis. PBDM posterior belly of the digastric muscle, PG parotid gland

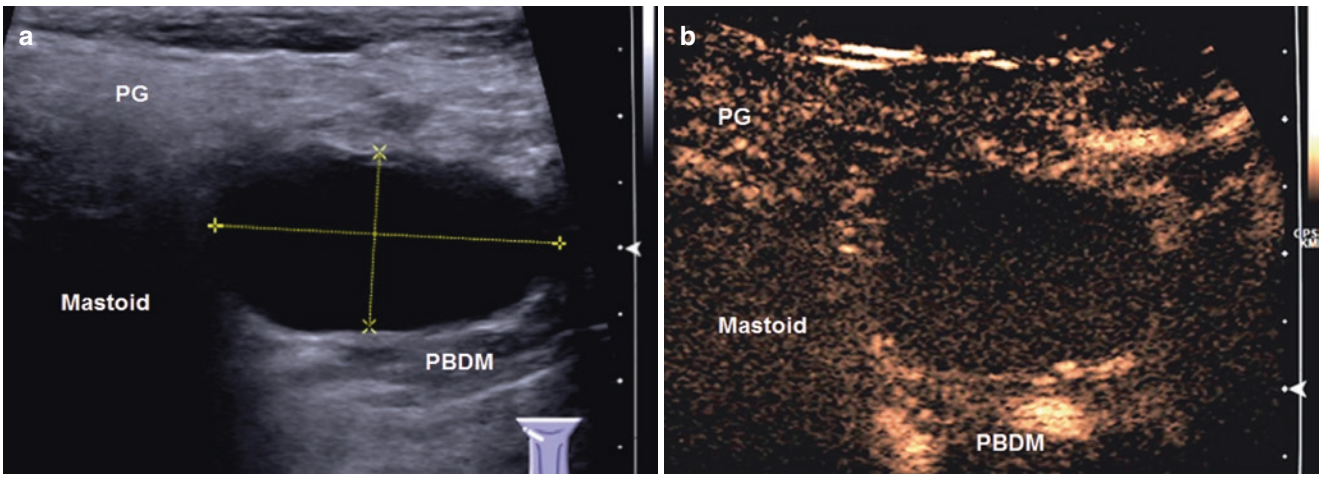

Fig. 11.42 B-mode ultrasound of a first branchial cleft cyst shows an echo-free lesion in the caudal and profound part of the parotid gland (**a**) without perfusion in contrast-enhanced ultrasound (**b**). PBDM posterior belly of the digastric muscle, PG parotid gland

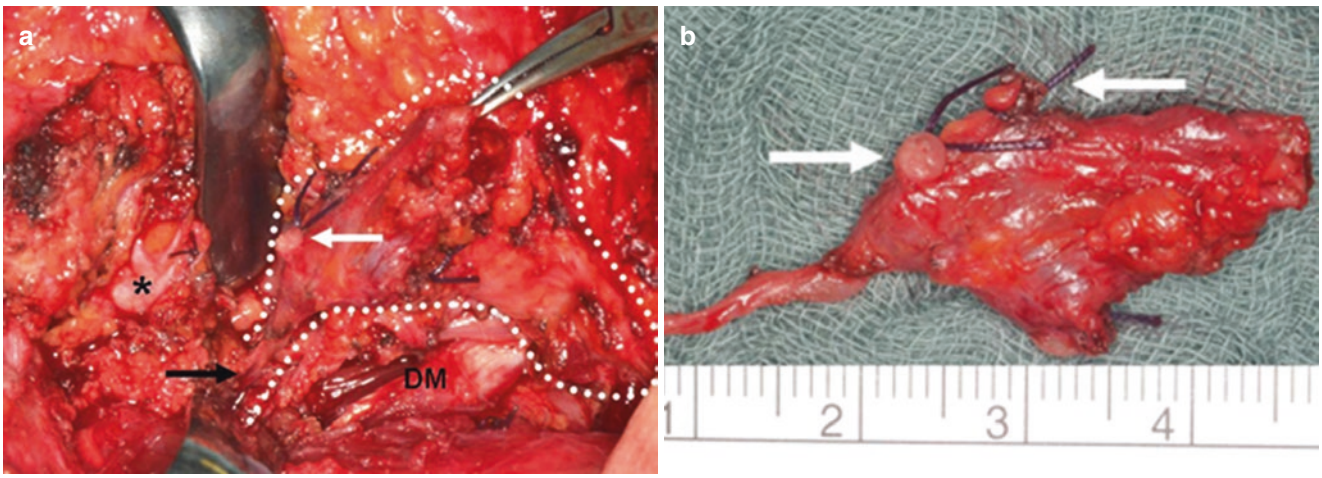

Fig. 11.43 (**a**) Intraoperative situs in surgery for extirpation of a first branchial cleft cyst (*white dotted line*). Shown are the duct (*black arrow*), facial nerve (*black star*), and the superficial temporal artery (*white arrow*). (**b**) Extirpated first branchial cleft cyst. DM digastric muscle [73]

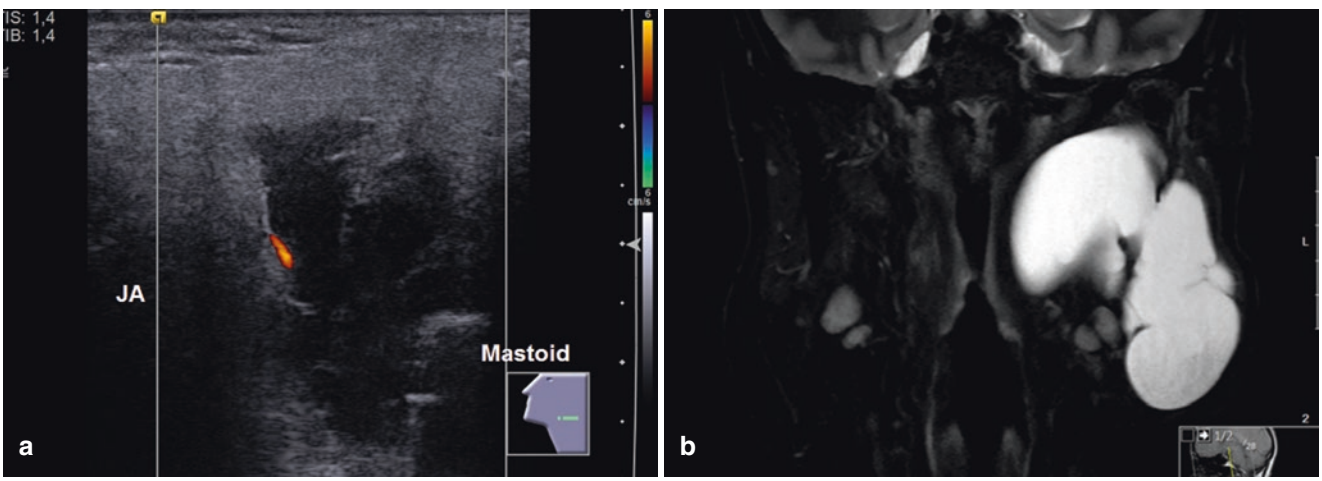

Fig. 11.44 (**a**) Color-coded duplex sonography demonstrates avascular, echo-free lesion of the left parotid gland that cannot be completely visualized by ultrasound. (**b**) Corresponding coronal MRI shows parapharyngeal extension of a first branchial cleft cyst. JA jaw angle

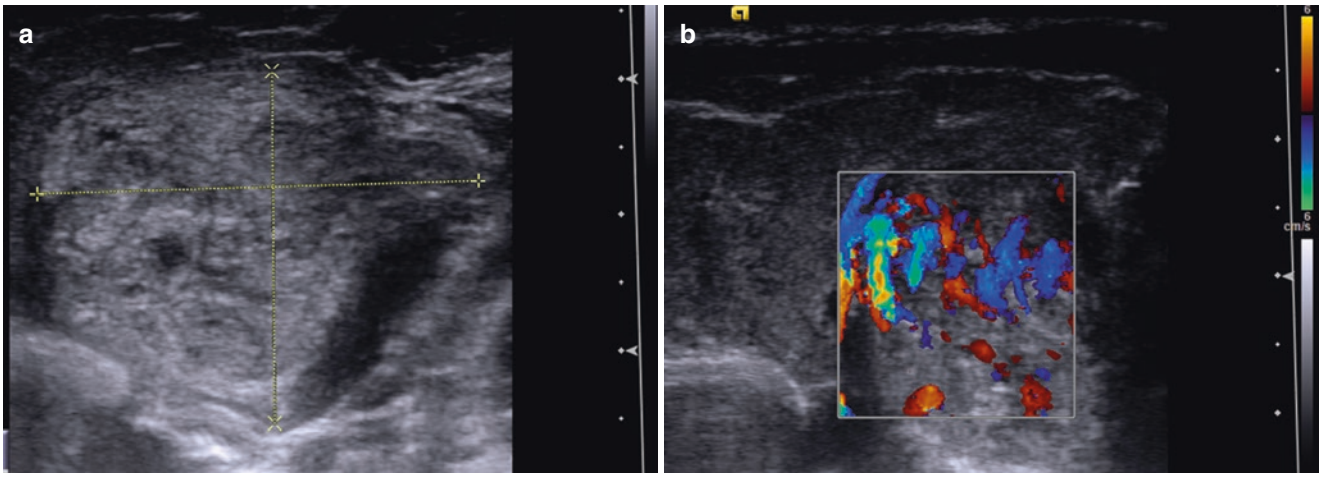

Fig. 11.45 Hemangioma. (**a**) B-mode ultrasound shows an inhomogeneous tumor of the parotid gland capsule. (**b**) Strong hypervascularity is seen in color-coded duplex sonography

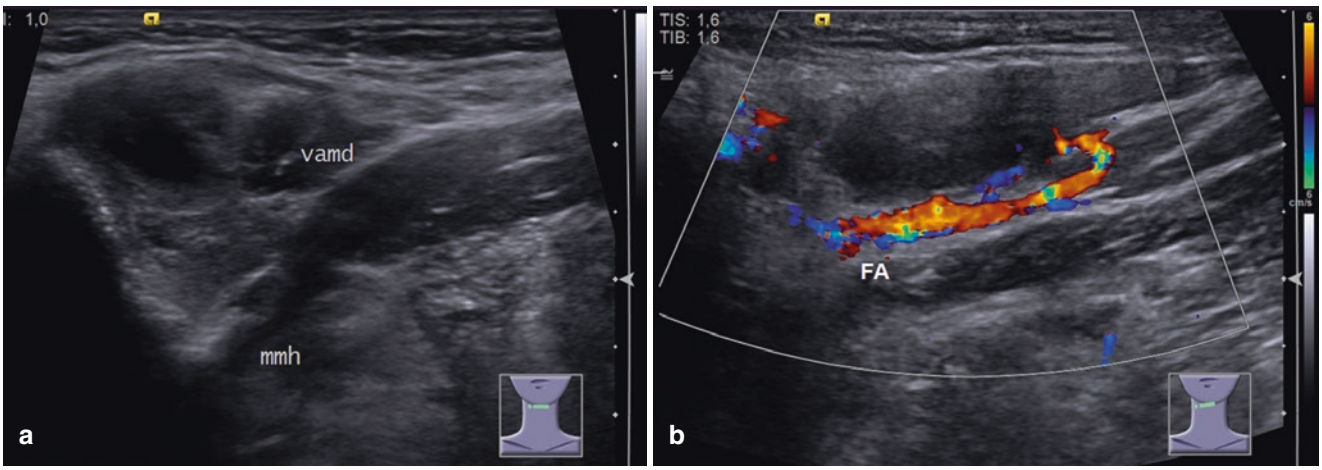

Fig. 11.46 Submandibular lymphangioma. (**a**) B-mode ultrasound shows an echo-free tumor with intralesional septa. (**b**) Color-coded duplex sonography excludes intralesional vascularization. FA facial artery, mmh mylohyoid muscle

malformation appear soft. Both show echo-free areas in B-mode ultrasound, with differing extent of intralesional septa [74]. Though CDS fails to visualize vascularization in lymphangioma (Fig. 11.46), the acquisition of a valid vascularization pattern can be difficult in vessel malformation, particularly in venous low-flow variants. In these cases, contrast-enhanced ultrasound shows vessel perfusion with high sensitivity (Fig. 11.47). However, angio-MRI should be performed to exclude deep neck extension (Fig. 11.48) [75].

Masseter muscle hypertrophy also represents a pseudotumor of the parotid gland that is usually associated with dysgnathia. B-mode ultrasound reveals unilateral or bilateral masseter muscle hypertrophy without any glandular pathology (Fig. 11.49).

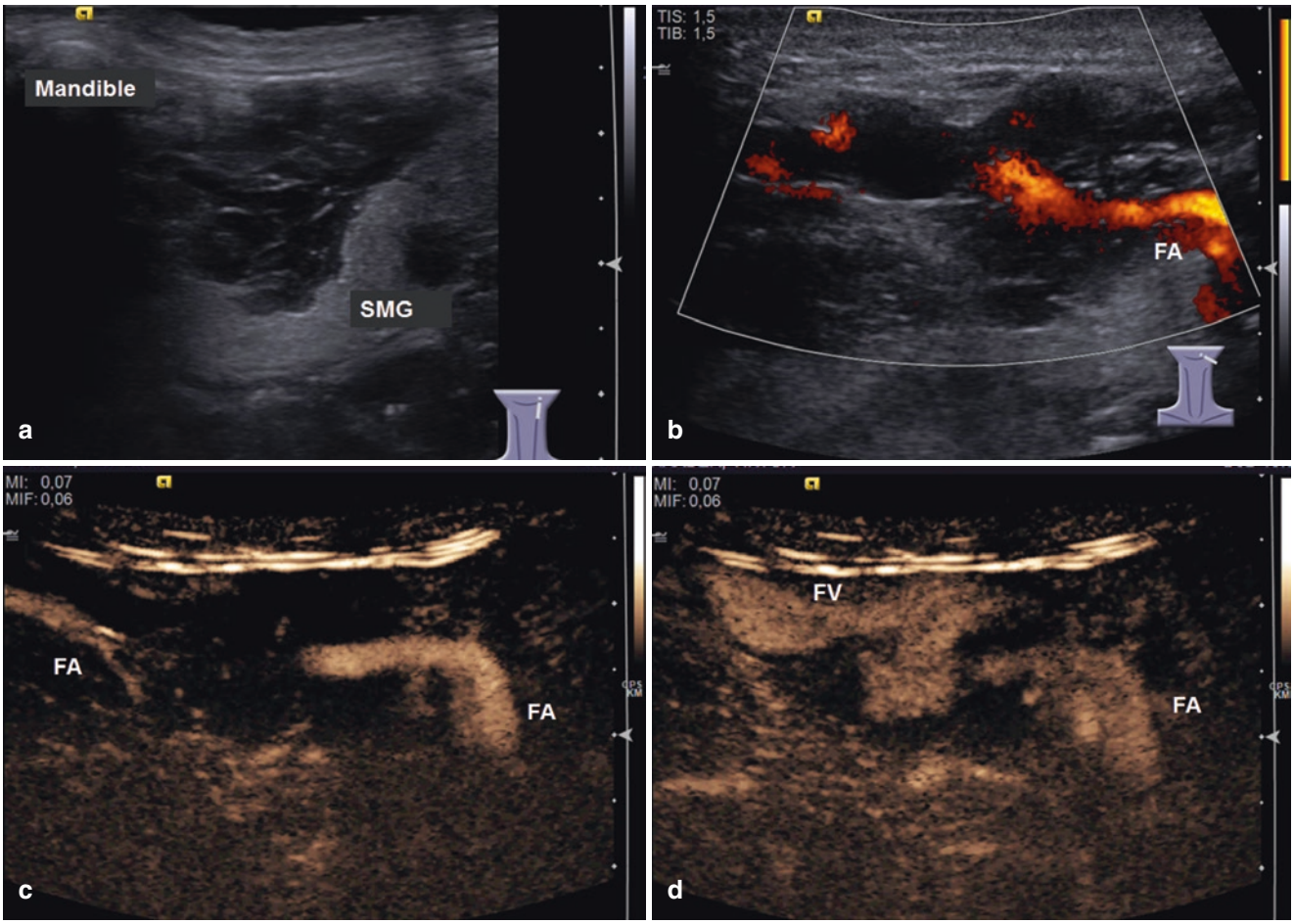

Fig. 11.47 Vessel malformation. (**a**) B-mode ultrasound visualized this submandibular low-flow vessel malformation as an echo-free lesion with intralesional septa comparable to those of lipoma. (**b**) Color-coded duplex sonography fails to visualize lesional vascularity. (**c**) Early-phase contrast-enhanced ultrasound does not show lesional perfusion. (**d**) Late-phase contrast-enhanced ultrasound visualizes perfusion by facial vein (FV) supply. FA facial artery, SMG submandibular gland

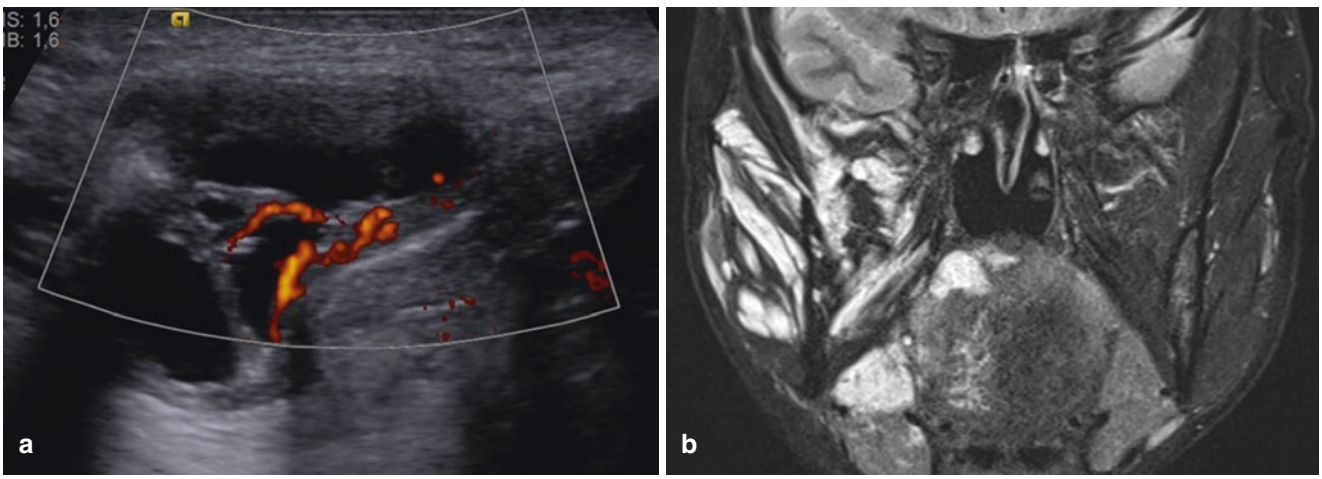

Fig. 11.48 (**a**) Color-coded duplex sonography demonstrates an avascular, echo-free lesion of cavernous hemangioma that cannot be completely visualized by ultrasound. (**b**) Corresponding coronal angio-MRI demonstrates broad transcervical extension

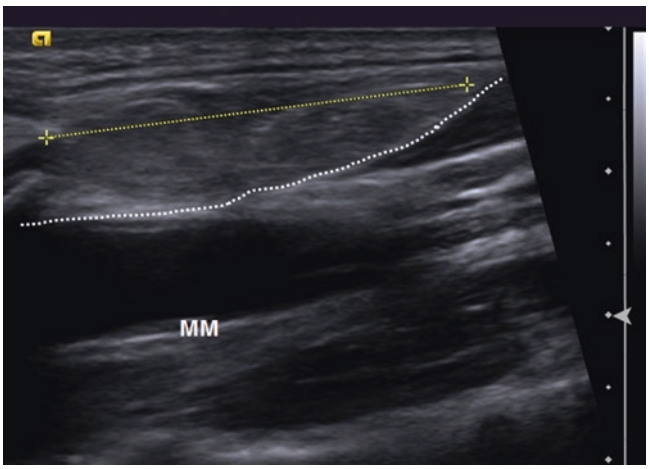

Fig. 11.49 B-mode sonography of masseter muscle hypertrophy in the pre-auricular region, profound to the parotid gland (*white line*). MM masseter muscle

References

1. Hofauer B, Chaker A, Strenger T, Bas M, Mansour N, Knopf A. Swelling of the submandibular and parotid glands: a description of possible differential diagnoses. HNO. 2016;64:333–48. German.
2. Knopf A, Szyper M, Mansour N, Sonnenberg J, Hofauer B, Niedermeyer H. A critical review of 20 years of parotid gland surgery. Acta Otolaryngol. 2016;136:711–6.
3. Knopf A, Cortolezis N, Bas M, Mansour N, Hofauer B. Multimodal ultrasonographic algorithm in the differentiation of submandibular masses. Acta Otolaryngol. 2017;137:640–5.
4. Zengel P, Schrotzlmair F, Reichel C, Paprottka P, Clevert DA. Sonography: the leading diagnostic tool for diseases of the salivary glands. Semin Ultrasound CT MR. 2013;34:196–203.
5. Lee YY, Wong KT, King AD, Ahuja AT. Imaging of salivary gland tumours. Eur J Radiol. 2008;66:419–36.
6. Christe A, Waldherr C, Hallett R, Zbaeren P, Thoeny H. MR imaging of parotid tumors: typical lesion characteristics in MR imaging improve discrimination between benign and malignant disease. AJNR Am J Neuroradiol. 2011;32:1202–7.
7. Milic VD, Petrovic RR, Boricic IV, Marinkovic-Eric J, Radunovic GL, Jeremic PD, et al. Diagnostic value of salivary gland ultrasonographic scoring system in primary Sjögren's syndrome: a comparison with scintigraphy and biopsy. J Rheumatol. 2009;36:1495–500.
8. Cornec D, Jousse-Joulin S, Saraux A, Devauchelle-Pensec V. Salivary gland ultrasound to diagnose Sjögren's syndrome: a claim to standardize the procedure. Rheumatology (Oxford). 2015;54:199–200.
9. Rudack C, Jörg S, Kloska S, Stoll W, Thiede O. Neither MRI, CT nor US is superior to diagnose tumors in the salivary glands--an extended case study. Head Face Med. 2007;3:19.
10. de Ru JA, van Leeuwen MS, van Benthem PP, Velthuis BK, Sie-Go DM, Hordijk GJ. Do magnetic resonance imaging and ultrasound add anything to the preoperative workup of parotid gland tumors? J Oral Maxillofac Surg. 2007;65:945–52.
11. Knopf A, Bas M, Chaker A, Strassen U, Pickhard A, Stark T, et al. Rheumatic disorders affecting the head and neck: underestimated diseases. Rheumatology (Oxford). 2011;50:2029–34.
12. Lakshmi NM, Azeem Mohiyuddin SM, Mohammadi K, Devnikar AV, Prasad KN. Parotid abscess in children – a tertiary rural hospital experience. Int J Pediatr Otorhinolaryngol. 2015;79:1988–90.
13. Terraz S, Poletti PA, Dulguerov P, Dfouni N, Becker CD, Marchal F, Becker M. How reliable is sonography in the assessment of sialolithiasis? AJR Am J Roentgenol. 2013;201:W104–9.
14. Francis CL, Larsen CG. Pediatric sialadenitis. Otolaryngol Clin N Am. 2014;47:763–78.
15. Wilson KF, Meier JD, Ward PD. Salivary gland disorders. Am Fam Physician. 2014;89:882–8.
16. Hofauer B, Chaker A, Thurmel K, Knopf A. Manifestations of autoimmune disorders in otorhinolaryngology: classical symptoms and diagnostic approach. HNO. 2017;65:695–708.
17. Knopf A, Hofauer B, Thürmel K, Meier R, Stock K, Bas M, Manour N. Diagnostic utility of Acoustic Radiation Force Impulse (ARFI) imaging in primary Sjoegren's syndrome. Eur Radiol. 2015;25:3027–34.
18. Knopf A, Lahmer T, Chaker A, Stark T, Hofauer B, Pickhard A, et al. Head and neck sarcoidosis, from wait and see to tumor necrosis factor alpha therapy: a pilot study. Head Neck. 2013;35:715–9.
19. Carsons S. A review and update of Sjögren's syndrome: manifestations, diagnosis, and treatment. Am J Manag Care. 2001;7:S433–43.
20. Patel R, Shahane A. The epidemiology of Sjögren's syndrome. Clin Epidemiol. 2014;6:247–55.
21. Makula E, Pokorny G, Rajtar M, Kiss I, Kovacs A, Kovacs L. Parotid gland ultrasonography as a diagnostic tool in primary Sjögren's syndrome. Br J Rheumatol. 1996;35:972–7.
22. Makula E, Pokorny G, Kiss M, Voros E, Kovacs L, Kovacs A, et al. The place of magnetic resonance and ultrasonographic examinations of the parotid gland in the diagnosis and follow-up of primary Sjögren's syndrome. Rheumatology (Oxford). 2000;39:97–104.
23. Hocevar A, Ambrozic A, Rozman B, Kveder T, Tomsic M. Ultrasonographic changes of major salivary glands in primary Sjögren's syndrome. Diagnostic value of a novel scoring system. Rheumatology (Oxford). 2005;44:768–72.
24. Hofauer B, Mansour N, Heiser C, Gahleitner C, Thuermel K, Bas M, Knopf A. Sonoelastographic modalities in the evaluation of salivary gland characteristics in Sjögren's syndrome. Ultrasound Med Biol. 2016;42:2130–9.
25. Mansour N, Hofauer B, Knopf A. Ultrasound elastography in diffuse and focal parotid gland lesions. ORL J Otorhinolaryngol Relat Spec. 2017;79:54–64.
26. Hofauer B, Mansour N, Heiser C, Wirth M, Strassen U, Loeffelbein D, et al. Reproducibility of Acoustic Radiation Force Impulse imaging in thyroid and salivary glands with experienced and inexperienced examiners. Ultrasound Med Biol. 2016;42:2545–52.
27. Mulholland GB, Jeffery CC, Satija P, Cote DW. Immunoglobulin G4-related diseases in the head and neck: a systematic review. J Otolaryngol Head Neck Surg. 2015;44:24.
28. Hamano H, Kawa S, Horiuchi A, Unno H, Furuya N, Akamatsu T, et al. High serum IgG4 concentrations in patients with sclerosing pancreatitis. N Engl J Med. 2001;344:732–8.
29. Kleger A, Seufferlein T, Wagner M, Tannapfel A, Hoffmann TK, Mayerle J. IgG4-related autoimmune diseases: polymorphous presentation complicates diagnosis and treatment. Dtsch Arztebl Int. 2015;112:128–35.
30. Haugen BR, Alexander EK, Bible KC, Doherty GM, Mandel SJ, Nikiforov YE, et al. 2015 American Thyroid Association management guidelines for adult patients with thyroid nodules and differentiated thyroid cancer: the American Thyroid Association guidelines task force on thyroid nodules and differentiated thyroid Cancer. Thyroid. 2016;26:1–133.
31. Epstein JB, Thariat J, Bensadoun RJ, Barasch A, Murphy BA, Kolnick L, et al. Oral complications of cancer and cancer therapy: from cancer treatment to survivorship. CA Cancer J Clin. 2012;62:400–22.
32. Baum BJ, Bodner L, Fox PC, Izutsu KT, Pizzo PA, Wright WE. Therapy-induced dysfunction of salivary glands: implications for oral health. Spec Care Dentist. 1985;5:274–7.
33. Lee HN, An JY, Lee KM, Kim EJ, Choi WS, Kim DY. Salivary gland dysfunction after radioactive iodine (I-131) therapy in patients following total thyroidectomy: emphasis on radioactive iodine therapy dose. Clin Imaging. 2015;39:396–400.

34. Jeong SH, Hong HS, Lee EH. Diagnostic utility of acoustic structure quantification for evaluation of radiation sialadenitis after radioactive iodine therapy. Ultrasound Med Biol. 2016;42:2553–61.
35. Badea AF, Tamas SA, Ciuleanu E, Chioreanu I, Baciut G, Lupsor PM, Badea R. ARFI quantitative elastography of the submandibular glands. Normal measurements and the diagnosis value of the method in radiation submaxillitis. Med Ultrason. 2013;15:173–9.
36. Badea I, Tamas-Szora A, Chiorean I, Crisan M, Ciuleanu E, Baciut G, Badea M. Acoustic Radiation Force Impulse quantitative elastography: a new noninvasive technique for the evaluation of parotid glands. A preliminary study in controls and in patients with irradiated nasopharyngeal carcinoma. Med Ultrason. 2015;17:308–14.
37. Zengel P, Reichel CA, Vincek T, Clevert DA. Ultrasound elastography in diagnosis and follow-up for patients with chronic recurrent parotitis. Clin Hemorheol Microcirc. 2017;67:389–97.
38. Sanan A, Cognetti DM. Rare parotid gland diseases. Otolaryngol Clin N Am. 2016;49:489–500.
39. Koch M, Iro H, Zenk J. Stenosis and other non-sialolithiasis-related obstructions of the major salivary gland ducts. Modern treatment concepts. HNO. 2010;58:218–24.
40. Zenk J, Iro H, Klintworth N, Lell M. Diagnostic imaging in sialadenitis. Oral Maxillofac Surg Clin North Am. 2009;21:275–92.
41. Katz P, Hartl DM, Guerre A. Clinical ultrasound of the salivary glands. Otolaryngol Clin N Am. 2009;42:973–1000.
42. Zengel P, Schrotzlmair F, Schwarz F, Paprottka P, Kramer M, Berghaus A, Clevert DA. Elastography: a new diagnostic tool for evaluation of obstructive diseases of the salivary glands; primary results. Clin Hemorheol Microcirc. 2012;50:91–9.
43. Zengel P, Berghaus A, Weiler C, Reiser M, Clevert DA. Intraductally applied contrast-enhanced ultrasound (IA-CEUS) for evaluating obstructive disease and secretory dysfunction of the salivary glands. Eur Radiol. 2011;21:1339–48.
44. Vinayachandran D, Sankarapandian S. Salivary duct cyst: histopathologic correlation. J Clin Imaging Sci. 2013;3:3.
45. Dumitriu D, Dudea SM, Botar-Jid C, Baciut G. Ultrasonographic and sonoelastographic features of pleomorphic adenomas of the salivary glands. Med Ultrason. 2010;12:175–83.
46. Pinkston JA, Cole P. Incidence rates of salivary gland tumors: results from a population-based study. Otolaryngol Head Neck Surg. 1999;120:834–40.
47. Biorklund A, Eneroth CM. Management of parotid gland neoplasms. Am J Otolaryngol. 1980;1:155–67.
48. Drivas EI, Skoulakis CE, Symvoulakism EK, Bizaki AG, Lachanas VA, Bizakis JG. Pattern of parotid gland tumors on Crete, Greece: a retrospective study of 131 cases. Med Sci Monit. 2007;13:CR136–40.
49. Seifert G, Hennings K, Caselitz J. Metastatic tumors to the parotid and submandibular glands--analysis and differential diagnosis of 108 cases. Pathol Res Pract. 1986;181:684–92.
50. Bialek EJ, Jakubowski W, Zajkowski P, Szopinski KT, Osmolski A. US of the major salivary glands: anatomy and spatial relationships, pathologic conditions, and pitfalls. Radiographics. 2006;26:745–63.
51. Bialek EJ, Jakubowski W, Karpinska G. Role of ultrasonography in diagnosis and differentiation of pleomorphic adenomas: work in progress. Arch Otolaryngol Head Neck Surg. 2003;129:929–33.
52. Knopf A, Mansour N, Chaker A, Bas M, Stock K. Multimodal ultrasonographic characterisation of parotid gland lesions--a pilot study. Eur J Radiol. 2012;81:3300–5.
53. Mansour N, Stock KF, Chaker A, Bas M, Knopf A. Evaluation of parotid gland lesions with standard ultrasound, color duplex sonography, sonoelastography, and acoustic radiation force impulse imaging – a pilot study. Ultraschall Med. 2012;33:283–8.
54. Mansour N, Bas M, Stock KF, Strassen U, Hofauer B, Knopf A. Multimodal ultrasonographic pathway of parotid gland lesions. Ultraschall Med. 2017;38:166–73.
55. Klintworth N, Mantsopoulos K, Zenk J, Psychogios G, Iro H, Bozzato A. Sonoelastography of parotid gland tumours: initial experience and identification of characteristic patterns. Eur Radiol. 2012;22:947–56.
56. Matsuzuka T, Suzuki M, Saijo S, Ikeda M, Matsui T, Nomoto Y, et al. Stiffness of salivary gland and tumor measured by new ultrasonic techniques: virtual touch quantification and IQ. Auris Nasus Larynx. 2015;42:128–33.
57. Mantsopoulos K, Koch M, Klintworth N, Zenk J, Iro H. Evolution and changing trends in surgery for benign parotid tumors. Laryngoscope. 2015;125:122–7.
58. Knopf A, Heiser C, Karasoy O, Hofauer B, Bier H, Mansour N. Bipolar dissection technique in parotid gland surgery. Acta Otolaryngol. 2017;137:1210–4.
59. Teymoortash A, Werner JA, Moll R. Is Warthin's tumour of the parotid gland a lymph node disease? Histopathology. 2011;59:143–5.
60. Teymoortash A, Werner JA. Tissue that has lost its track: Warthin's tumour. Virchows Arch. 2005;446:585–8.
61. Seifert G, Bull HG, Donath K. Histologic subclassification of the cystadenolymphoma of the parotid gland. Analysis of 275 cases. Virchows Arch A Pathol Anat Histol. 1980;388:13–38.
62. Strassen U, Hofauer B, Jacobi C, Knopf A. Management of locoregional recurrence in cutaneous squamous cell carcinoma of the head and neck. Eur Arch Otorhinolaryngol. 2017;274:501–6.
63. Knopf A, Bas M, Hofauer B, Mansour N, Stark T. Clinicopathological characteristics of head and neck Merkel cell carcinomas. Head Neck. 2017;39:92–7.
64. Franzen A, Buchali A, Lieder A. The rising incidence of parotid metastases: our experience from four decades of parotid gland surgery. Acta Otorhinolaryngol Ital. 2017;37:264–9.
65. Bradley PJ. Frequency and histopathology by site, major pathologies, symptoms and signs of salivary gland neoplasms. Adv Otorhinolaryngol. 2016;78:9–16.
66. Zengel P, Notter F, Reichel CA, Clevert DA. Does Virtual Touch IQ elastography help to improve the preoperative diagnosis of parotid tumors: a prospective trial. Clin Hemorheol Microcirc. 2017;67:425–34.
67. Badea AF, Bran S, Tamas-Szora A, Floares A, Badea R, Baciut G. Solid parotid tumors: an individual and integrative analysis of various ultrasonographic criteria. A prospective and observational study. Med Ultrason. 2013;15:289–98.
68. Abdel Razek AA, Ashmalla GA, Gaballa G, Nada N. Pilot study of ultrasound parotid imaging reporting and data system (PIRADS): inter-observer agreement. Eur J Radiol. 2015;84:2533–8.
69. Wei X, Li Y, Zhang S, Li X, Wang H, Yong X, et al. Evaluation of microvascularization in focal salivary gland lesions by contrast-enhanced ultrasonography (CEUS) and Color Doppler sonography. Clin Hemorheol Microcirc. 2013;54:259–71.
70. Ambrosetti A, Zanotti R, Pattaro C, Lenzi L, Chilosi M, Caramaschi P, et al. Most cases of primary salivary mucosa-associated lymphoid tissue lymphoma are associated either with Sjoegren syndrome or hepatitis C virus infection. Br J Haematol. 2004;126:43–9.
71. Kassan SS. Immunogenetics of Sjögren's syndrome. Ann Med Interne (Paris). 1998;149:45–8.
72. D'Souza AR, Uppal HS, De R, Zeitoun H. Updating concepts of first branchial cleft defects: a literature review. Int J Pediatr Otorhinolaryngol. 2002;62:103–9.
73. Gahleitner C, Scherer E, Knopf A. A specific type of cyst. HNO. 2013;61:958–60.
74. Sun RW, Tuchin VV, Zharov VP, Galanzha EI, Richter GT. Current status, pitfalls and future directions in the diagnosis and therapy of lymphatic malformation. J Biophotonics. 2017. https://doi.org/10.1002/jbio.201700124. [Epub ahead of print].
75. Guneyli S, Ceylan N, Bayraktaroglu S, Gucenmez S, Aksu K, Kocacelebi K, et al. Imaging findings of pulmonary granulomatosis with polyangiitis (Wegener's granulomatosis): lesions invading the pulmonary fissure, pleura or diaphragm mimicking malignancy. Wien Klin Wochenschr. 2016;128:809–15.

Ultrasound of the Thyroid Gland

12

Tomislav Novosel and Peter Jecker

12.1 Introduction: The Thyroid Examination

To simplify the thyroid ultrasound (US) examination and to make it more practical and systematic (according to thyroid ultrasound features), it is reasonable to group the examination into two parts: the general thyroid examination and special thyroid examination.

Before using US to go deep into thyroid problems, it is important to have a general overview. The first step should be to measure the thyroid size (width, length, height). While obtaining these measurements, the examiner will acquire the first impression of the thyroid: Is it normal in size, small, or enlarged? Is it substernal? Does it have nodules? Is the thyroid tissue homogenous or heterogeneous? On the basis of these findings, it is possible to start to diagnose pathology.

A more thorough, special thyroid US examination is important to completely evaluate thyroid nodules, to find the presence or absence of pretracheal and paratracheal lymph nodes, and to perform elastography of thyroid nodules.

A substantial US report regarding thyroid nodules should always begin with the position of the nodules in the thyroid: the upper pole, the lower pole, the middle third of the thyroid, or the isthmus. To complete the evaluation, the following US characteristics should be considered [1, 2]:

- The number of nodules in the thyroid
- The size of each nodule
- The echogenicity of the nodules (hypoechoic, hyperechoic, isoechoic, anechoic, homogeneous, heterogeneous, cystic, solid, posterior enhancement, spongiform)
- The presence of calcification (microcalcifications, coarse calcifications, peripheral rim calcification [eggshell phenomenon])
- The form of the nodules (round, oval, irregular, "taller-than-wide" phenomenon)
- Regularity of the borders
- Halo effect
- Comet-tail sign
- Vascularization of the nodules (peripheral ring of flow, internal flow)

Thyroid US can also estimate the nature of lymph nodes surrounding thyroid. The appearance and form of lymph nodes suggest whether they might be suspicious. Oval lymph nodes with hilum represent benign lymph nodes, whereas lymph nodes without hilum and with extensive internal flow are very suspicious and must be further investigated by performing fine needle aspiration biopsy [3]. It is not usual to find lymph nodes in the pretracheal or paratracheal compartment, so it is essential to investigate all lymph nodes found in this area. But it should be expected to find such lymph nodes in patients with autoimmune thyroid disease (Hashimoto thyroiditis); the characteristics of Hashimoto thyroiditis are discussed in a later section of this chapter.

A relatively new US method to help distinguish soft from hard thyroid nodules is elastography. Soft nodules are more likely to have a benign etiology, whereas hard nodules have a higher rate of malignancy [4]. Elastography findings alone are not currently enough to make a decision about surgery, but it is a helpful diagnostic tool to decide whether fine needle aspiration biopsy should be performed.

Electronic Supplementary Material The online version of this chapter (https://doi.org/10.1007/978-3-030-12641-4_12) contains supplementary material, which is available to authorized users.

T. Novosel (✉) · P. Jecker
Department of Otorhinolaryngology and Plastic Head and Neck Surgery, Klinikum Bad Salzungen GmbH, Bad Salzungen, Germany
e-mail: Tomislav.novosel@klinikum-badsalzungen.de

© Springer Nature Switzerland AG 2019

H. J. Welkoborsky, P. Jecker (eds.), *Ultrasonography of the Head and Neck*, https://doi.org/10.1007/978-3-030-12641-4_12

12.2 Evaluation of Thyroid Nodules

As noted above, many factors need to be evaluated in the US examination of thyroid nodules; the findings have important clinical implications.

12.2.1 Size (Small Nodules, Large Nodules, Large Goiter)

Measuring the size of the thyroid and thyroid nodules is important not only to get a first impression but also to start to decide whether further nodule evaluation is needed. Recent reports have recommended that thyroid nodules smaller than 1 cm should not be further investigated (Fig. 12.1). Large thyroid nodules (Fig. 12.2), especially ones larger than 4 cm, present a higher incidence of developing thyroid cancer. Large thyroid goiter (Fig. 12.3)—especially substernal and retrosternal goiter—can cause difficult swallowing and shortness of breath; smaller nodules can have a similar effect, especially if they are located close to the trachea or esophagus. Nevertheless, nodule size is not predictive of malignancy [5].

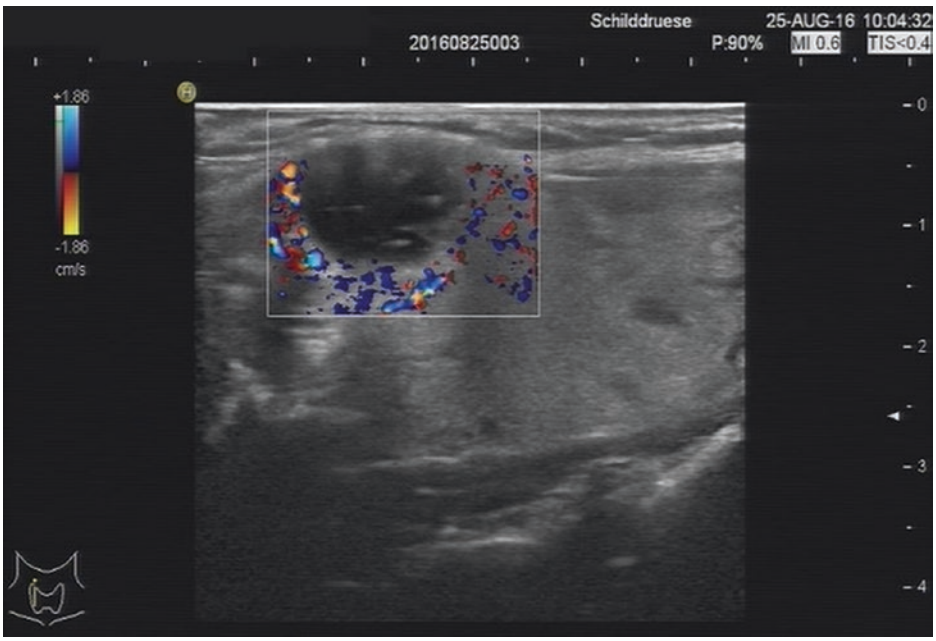

Fig. 12.1 Small hypoechoic thyroid nodule in upper pole of the right thyroid lobe

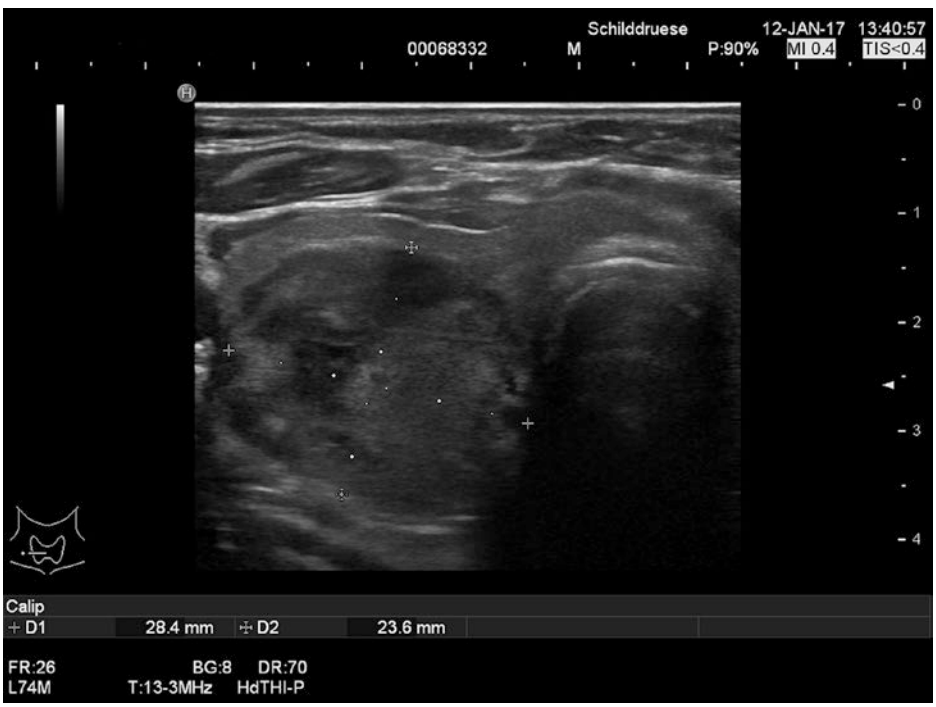

Fig. 12.2 A large, heterogeneous, isoechoic thyroid nodule with hypoechoic areas in the middle of the right thyroid lobe

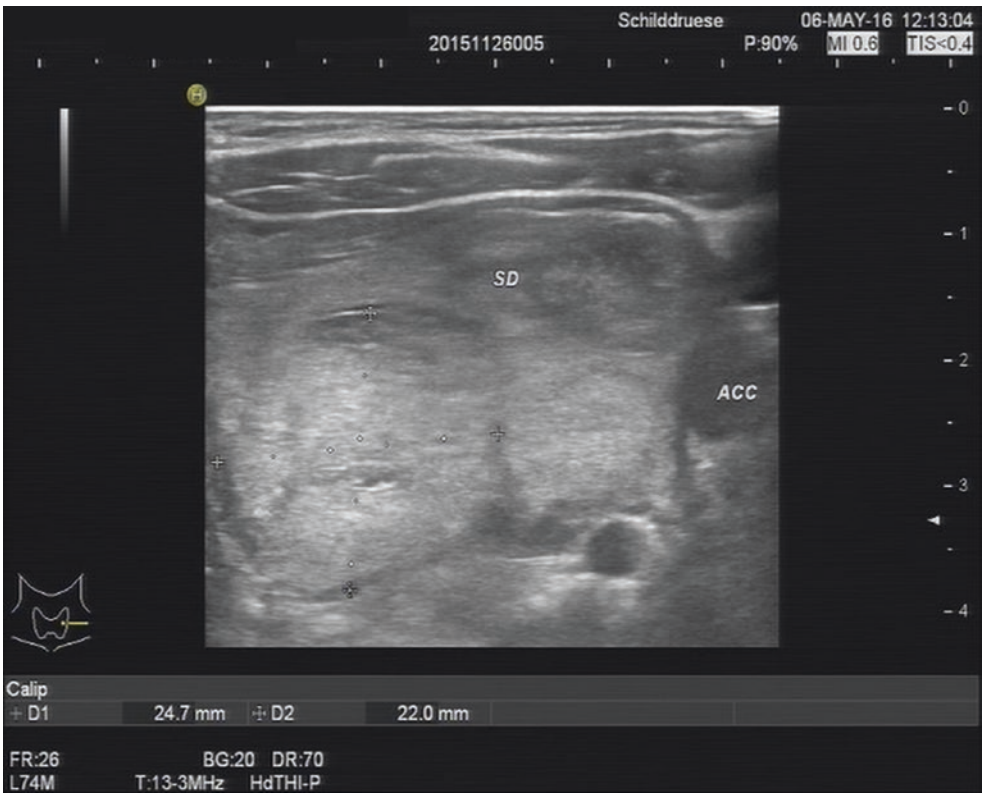

Fig. 12.3 Large, multinodular goiter of the left thyroid lobe

Fig. 12.4 Small, hypoechoic nodule of the left thyroid lobe without suspicious ultrasound characteristics

12.2.2 Echogenicity (Hyperechoic, Hypoechoic, Isoechoic)

The term *echogenicity* is used to illustrate the ability to return the US signal coming from the probe to the tissue and back to the probe. The quality of the signal can be characterized as *hypoechoic* (lower echogenicity, a darker image) (Fig. 12.4; Video 12.1), *hyperechoic* (higher echogenicity, a lighter image) (Fig. 12.5), *isoechoic* (the same echogenicity as the surrounding tissue) (Fig. 12.6; Video 12.2),

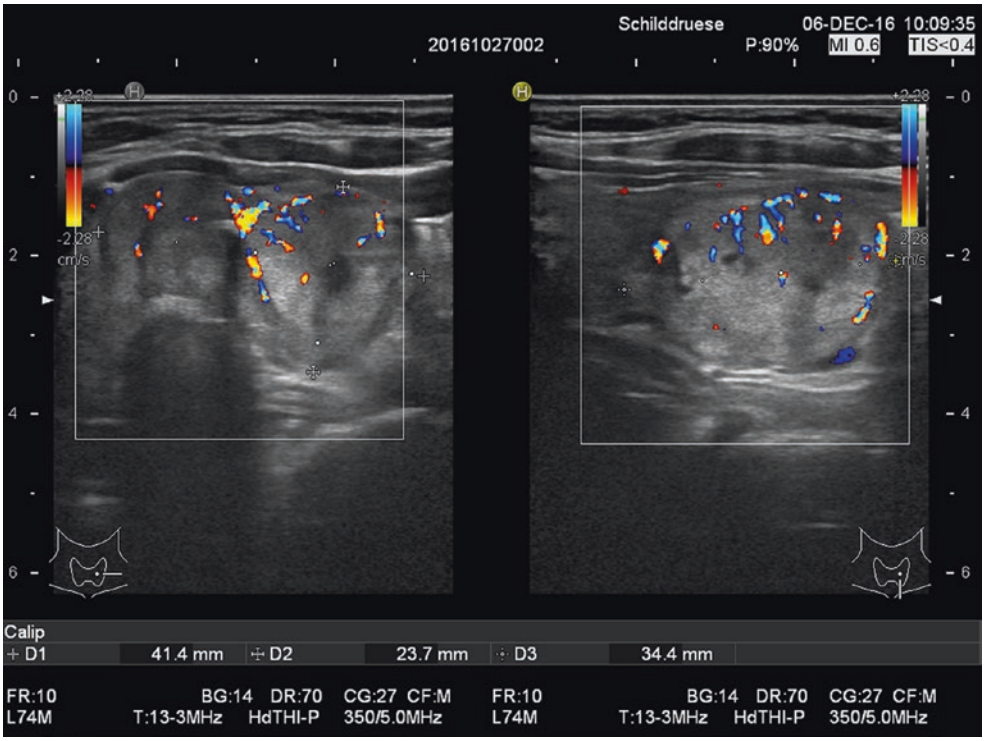

Fig. 12.5 Hyperechoic thyroid nodule in the left lobe of the thyroid, with a small, isoechoic nodule in the isthmus

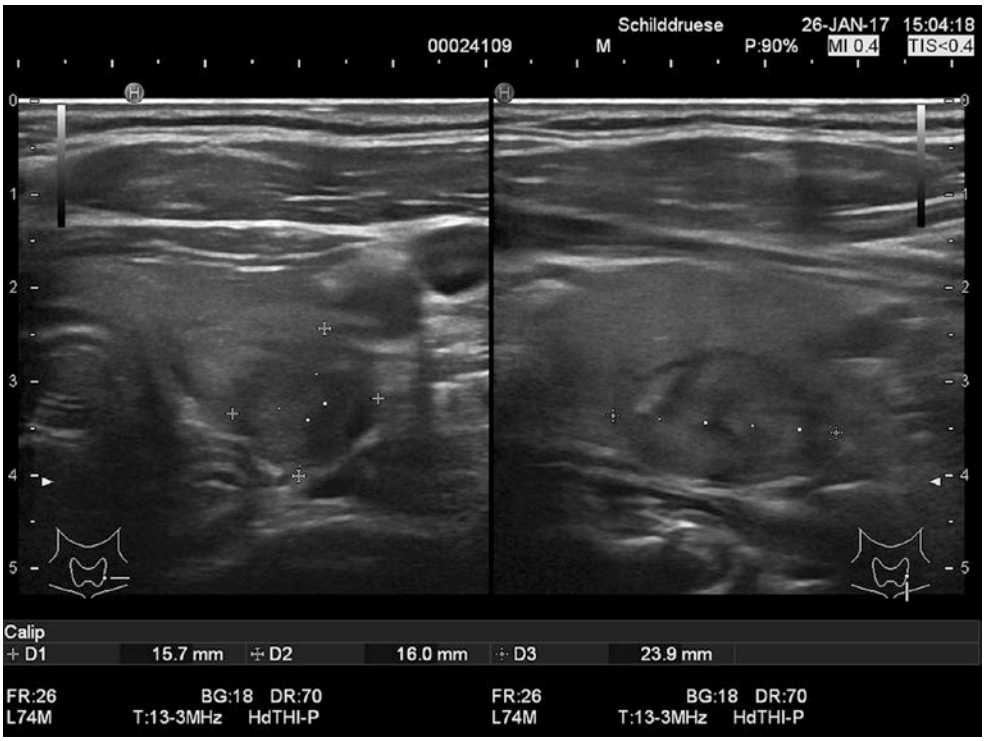

Fig. 12.6 Relatively small, isoechoic nodule in the lower pole of the left thyroid lobe, with well-defined margins

and *anechoic* (without echogenicity, completely dark) (Fig. 12.7). Echogenicity of a thyroid nodule is important because it can be a predictor of thyroid disease. Most thyroid carcinomas are hypoechoic, and almost all hyperechoic nodules are benign, but to decide whether a particular nodule is benign, malignant, or suspicious for malignancy, we must also consider other US characteristics and perform fine needle biopsy to prove the diagnosis, because benign thyroid nodules can also be hypoechoic [6].

Fig. 12.7 Typical presentation of a thyroid cyst in the upper pole of the right thyroid lobe; the cyst is completely anechoic, with posterior enhancement

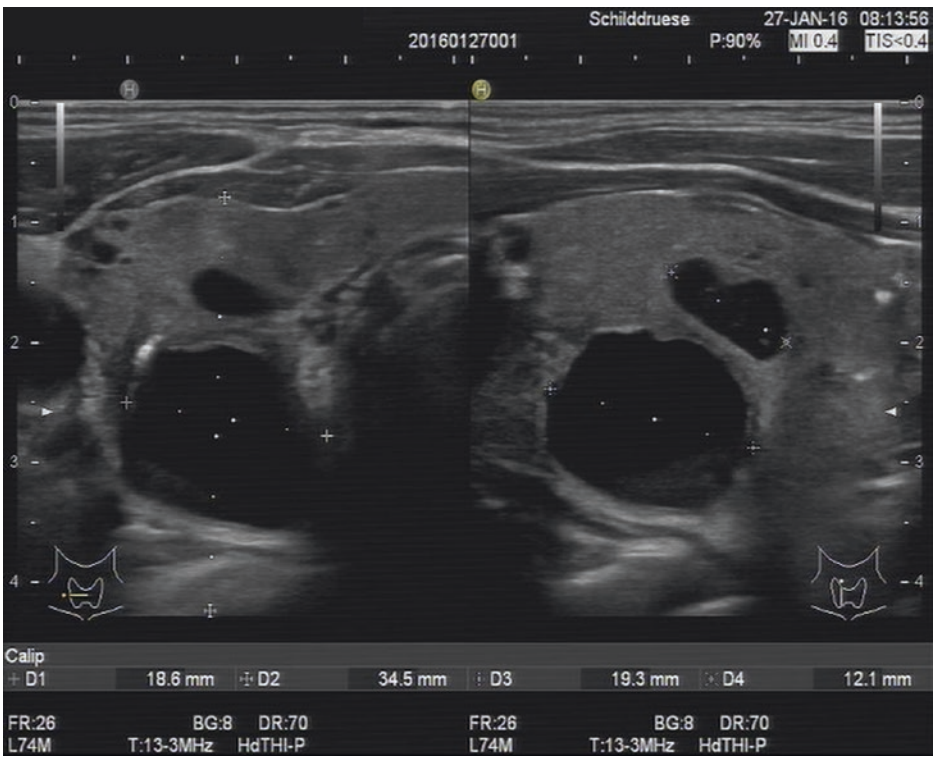

Fig. 12.8 Two small cysts of the right thyroid lobe, both anechoic; the bigger cyst shows posterior enhancement, but the smaller cyst does not

12.2.3 Content and Echo Structure (Cyst, Partly Cystic Nodule, Solid Nodule, Comet-Tail Sign, Calcifications)

Thyroid *cysts* appear as homogenous hypoechoic or anechoic nodules; they typically have a hyperechoic rim behind them (called *posterior enhancement*), but this rim is not always present. Thyroid cysts are actually enlarged, fluid-filled parts of the thyroid gland. The cysts can range in size from small (Fig. 12.8) to large (Fig. 12.9), or they can be partly cystic (Video 12.3) and partly solid (Fig. 12.10). Another classic US feature of one variant of thyroid cyst (the colloid cyst

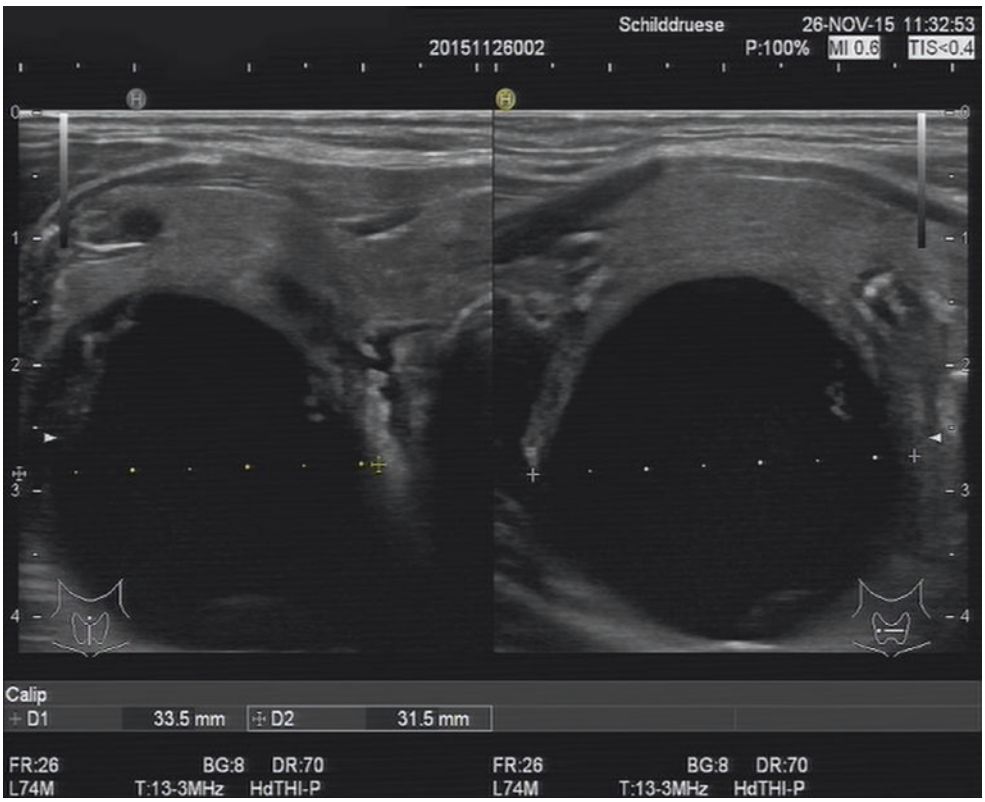

Fig. 12.9 Large thyroid cyst of the right thyroid pole; the cyst is anechoic with posterior enhancement

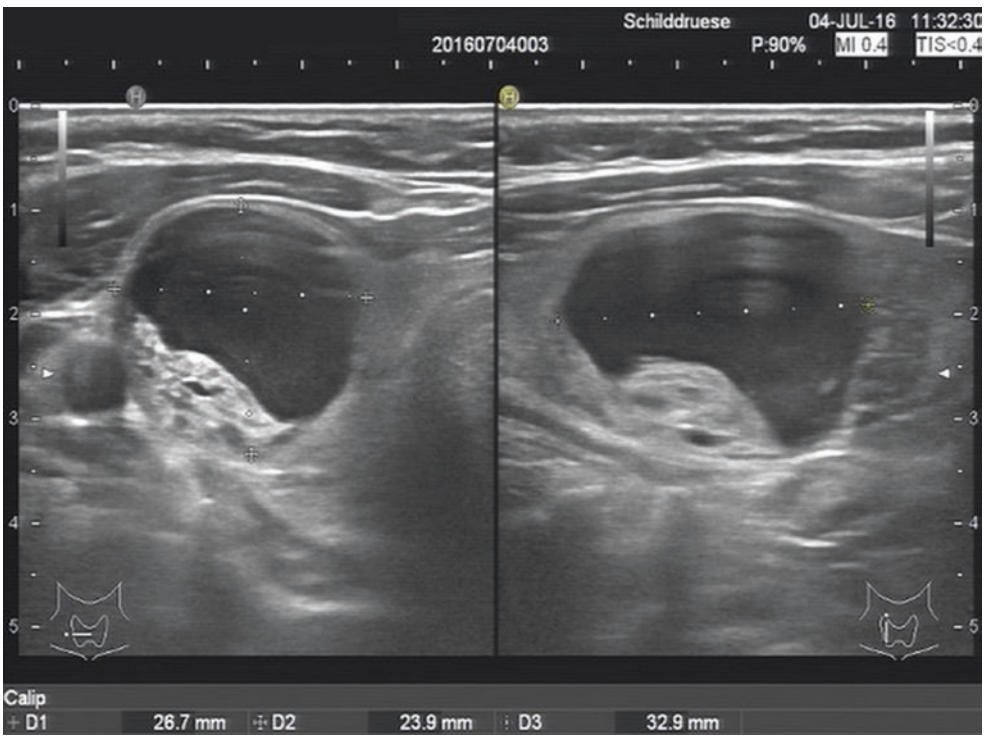

Fig. 12.10 Partly cystic thyroid nodule of the right thyroid lobe, with a solid, hyperechoic component in the lower lateral part of the nodule

[Video 12.4]) is the so-called comet-tail sign (Fig. 12.11). This US feature is a form of reverberation artifact characteristic of benign thyroid nodules.

Pure thyroid cysts are associated with benign etiologies. Partially cystic thyroid nodules with a solid component have a greater possibility of malignancy, and further evaluation is required.

Solid thyroid nodules (Fig. 12.12) can be hypoechoic, hyperechoic, or isoechoic. Many thyroid nodules have calcification. It is very important to differentiate microcalcifica-

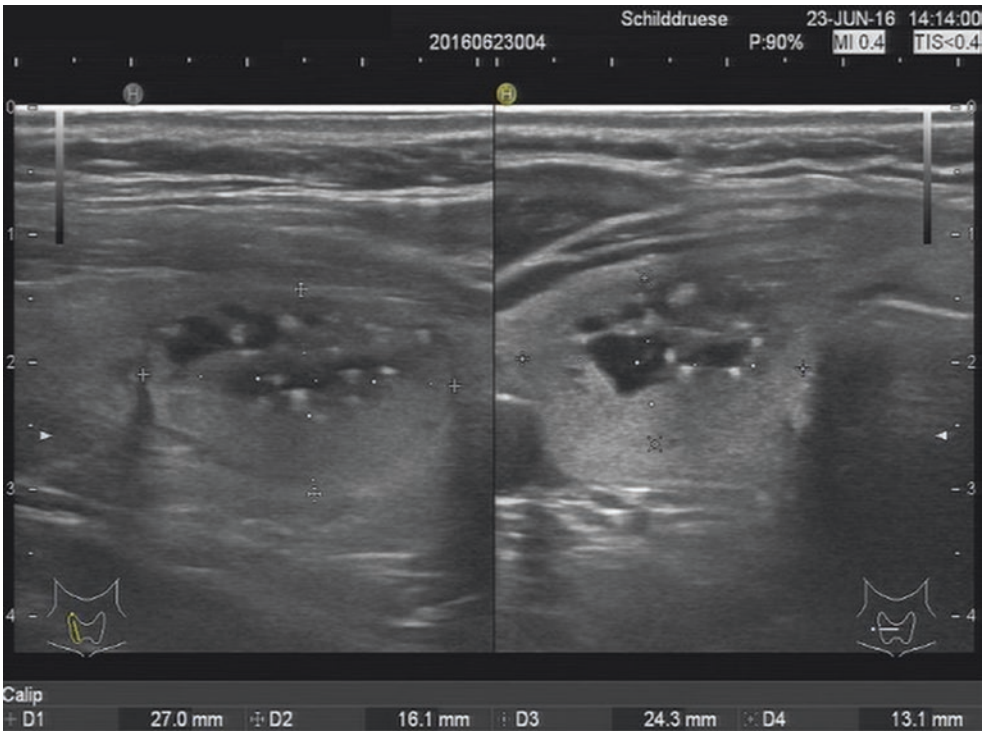

Fig. 12.11 Partly cystic, partly solid thyroid nodule of the right thyroid lobe. In the upper (cystic) part of the nodule can be seen a lot of small, hyperechoic areas (reverberation artifact), called the comet-tail sign

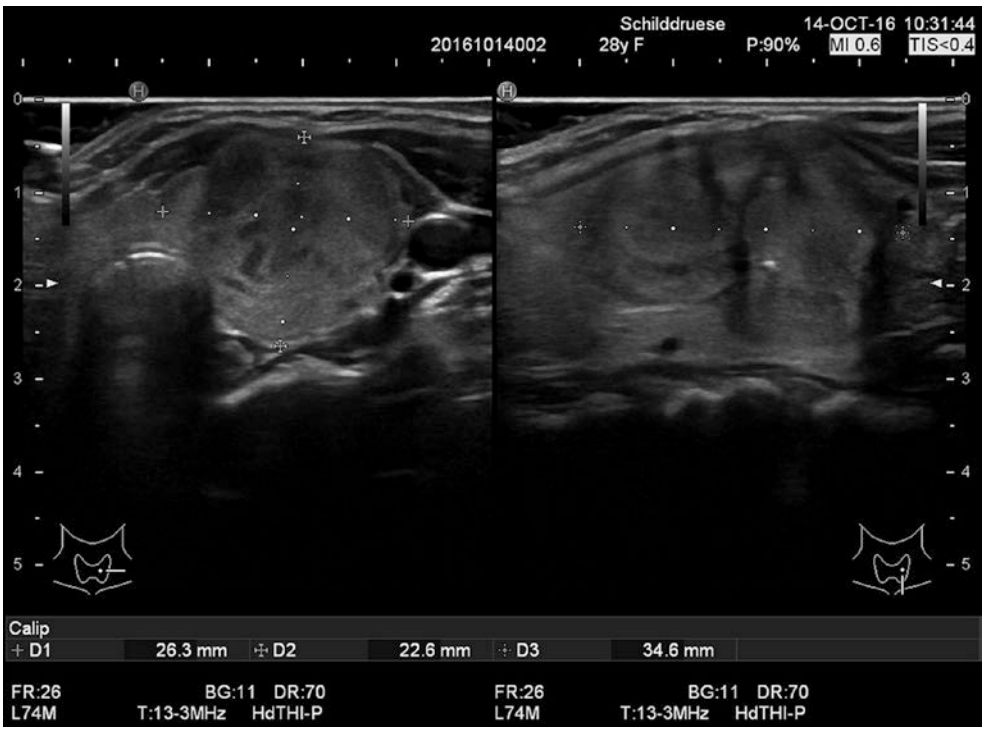

Fig. 12.12 Solid, heterogeneous thyroid nodule in the upper part of the left thyroid lobe, in contact with the isthmus and trachea

tion (Fig. 12.13) from coarse calcification (Figs. 12.14 and 12.15). Microcalcifications belong to group of suspicious US features that also include irregular margins and hypervascularity. The round, laminated calcifications called *psammoma bodies* are one of the most specific features of thyroid malignancy. It is important not to mistake the comet-tail sign for this kind of microcalcification.

Coarse calcifications usually can be seen in thyroid goiter (a benign thyroid condition), but they can also be present in malignant thyroid nodules, with or without microcalcifications. Unlike

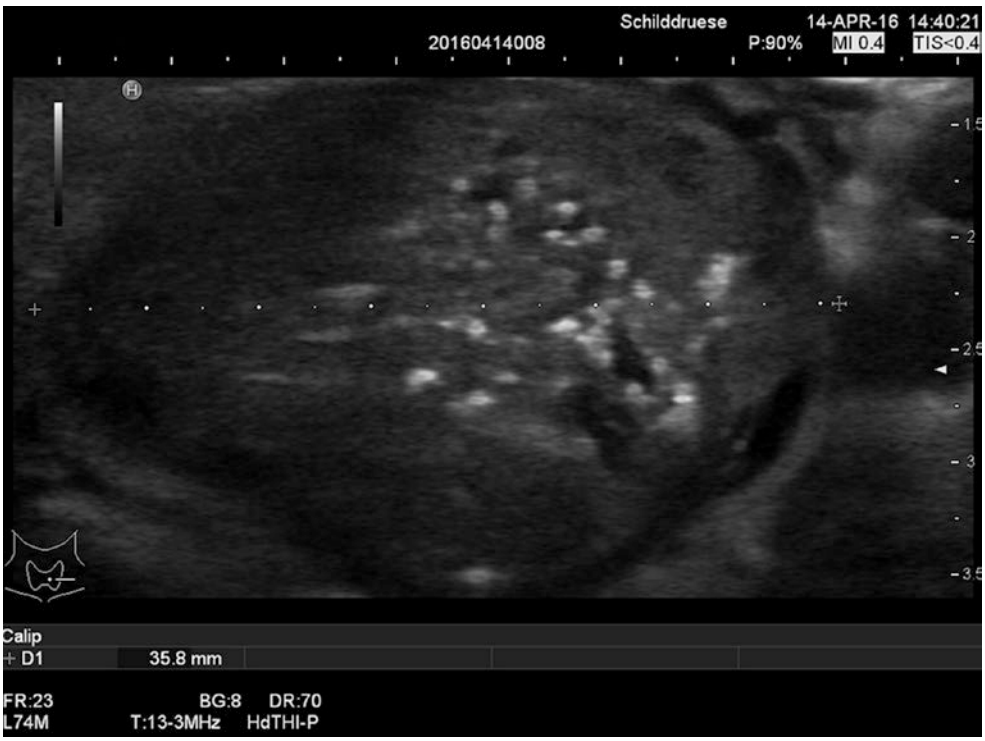

Fig. 12.13 A large, heterogeneous nodule of the left thyroid lobe with suspicious ultrasound characteristics (microcalcifications, seen as a lot of small, hyperechoic spots)

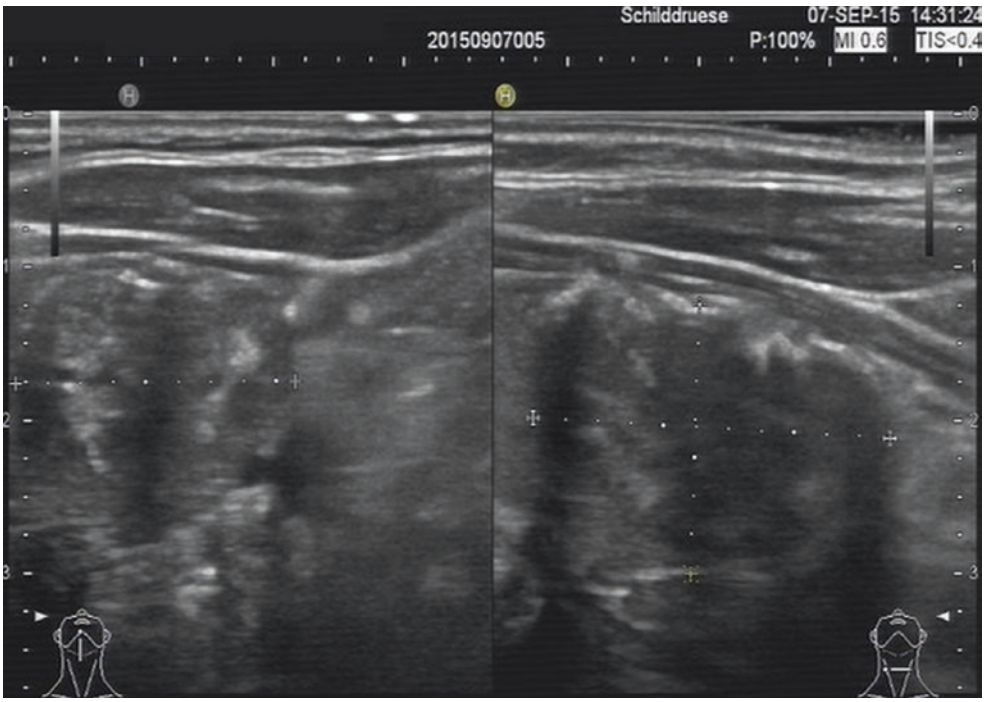

Fig. 12.14 Several coarse calcifications in the pyramidal lobe of the thyroid. Behind every calcification can be seen posterior acoustic shadowing; the area behind the calcification cannot be interpreted

microcalcifications, coarse calcification always produces posterior acoustic shadowing, which is easy to recognize.

Eggshell calcification of thyroid nodules is another suspicious US characteristic. Some authors describe the eggshell phenomenon as more useful in diagnosing thyroid malignancy than hypoechogenicity or a taller-than-wide shape of thyroid nodules.

A homogeneous nodule without suspicious US features or a thyroid nodule with a spongiform pattern (Fig. 12.16) generally indicates a benign etiology [7–10].

Fig. 12.15 A small nodule in the upper pole of the left thyroid lobe. At the upper edge of the nodule is visible a hyperechoic rim, presenting coarse calcification. Behind the calcification, everything is dark (hypoechoic) because of posterior acoustic shadowing, so nothing is detectable

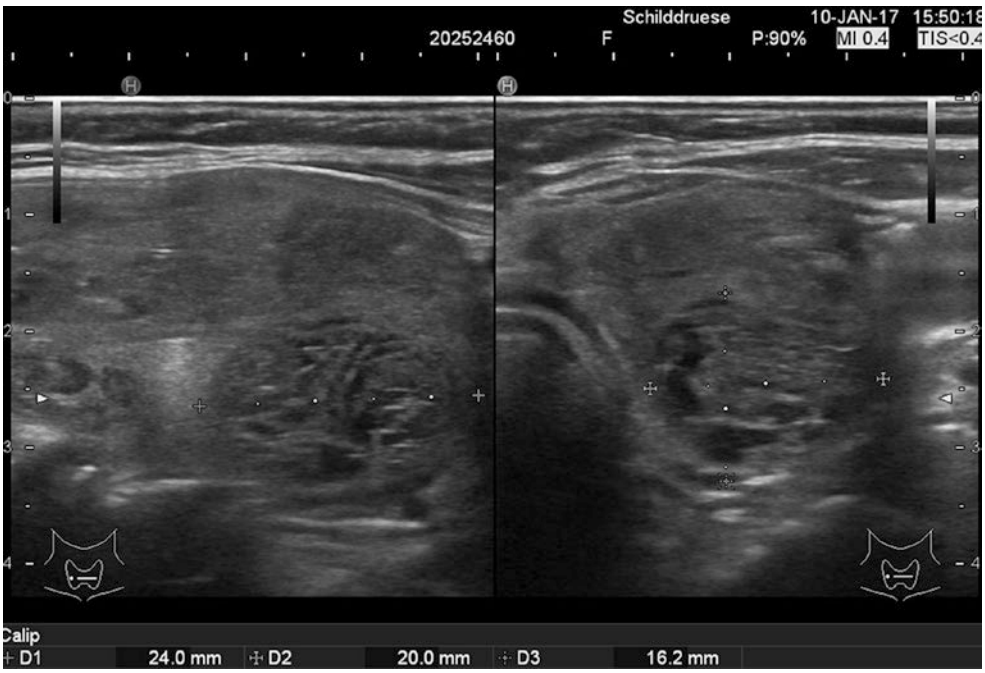

Fig. 12.16 Heterogeneous nodule in the lower pole of the left thyroid lobe, with characteristic spongiform pattern

12.2.4 Margins (Regular, Suspicious, Irregular)

The margins of thyroid nodules are excellent predictors of the nature of thyroid disease. Benign thyroid nodules usually have regular, well-defined margins (Fig. 12.17). On the other hand, suspicious thyroid nodules have irregular borders (Fig. 12.18; Video 12.5). In such cases, this US feature serves as a negative diagnostic factor explaining the potentially more aggressive behavior of the nodule, with infiltration of the surrounding tissue (extrathyroidal extension).

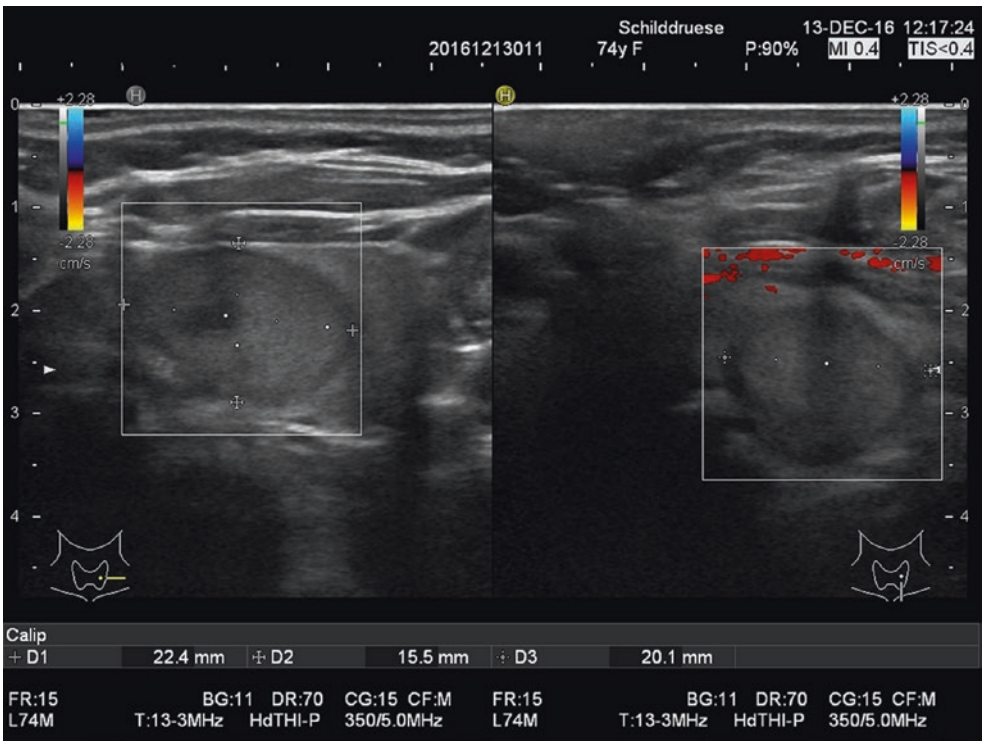

Fig. 12.17 A relatively small, isoechoic thyroid nodule with regular margins and "halo effect" (hypoechoic rim)

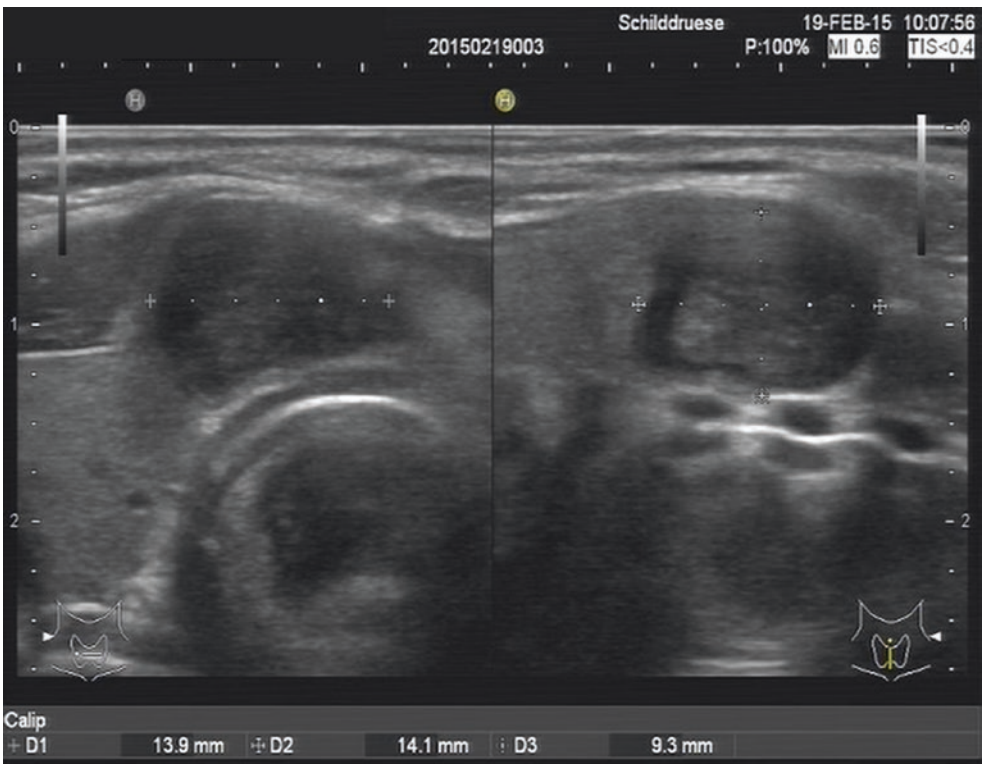

Fig. 12.18 Thyroid nodule in the isthmus with irregular margins, especially in the upper part of the nodule

Sometimes it is not easy to evaluate whether a nodule has regular or irregular margins, especially when it is positioned near the capsule of the thyroid close to the strap muscles. We advocate performing a fine needle aspiration biopsy (Video 12.6) when the margins of a nodule are clearly irregular or if it is uncertain whether they may be irregular (Fig. 12.19) [11].

12.2.5 Form (Round, Oval, Irregular, Taller than Wide)

It is usually hard to assess whether thyroid nodules are likely to be benign or malignant on the basis of their shape. Almost all thyroid nodules—both benign and malignant—are round (Fig. 12.20) or oval (Fig. 12.21) in shape, and the margins

Fig. 12.19 Thyroid nodule with suspicion of irregular margins. The upper part of the nodule is not visible. It is also hard to find the border with strap muscles. This is a highly suspicious nodule

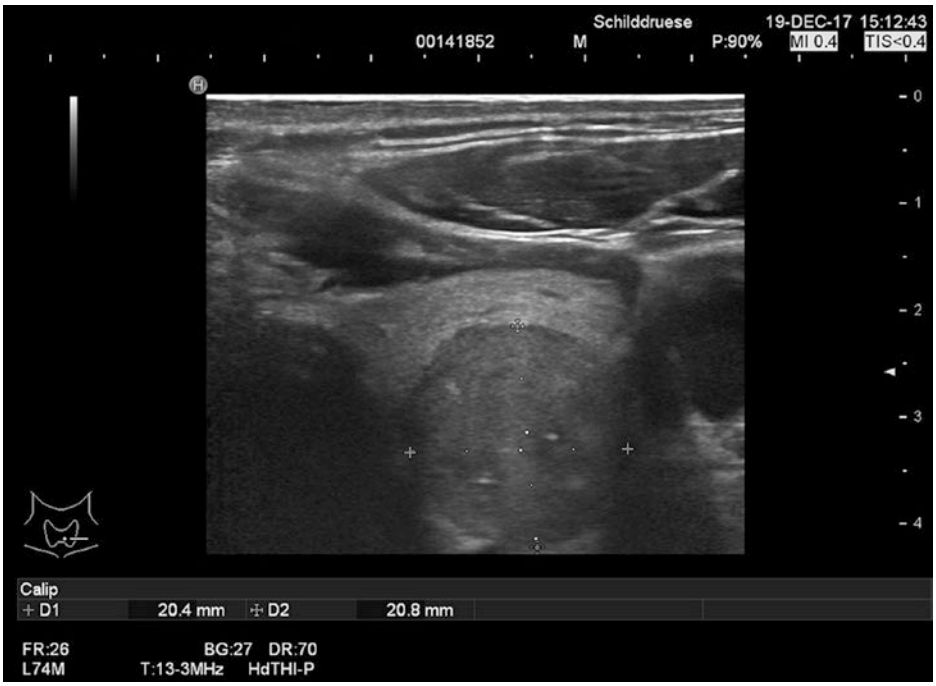

Fig. 12.20 Mildly hypoechoic, round nodule of the left thyroid lobe, with well-defined margins

are almost always regular. A possibility of malignancy is suggested by a nodule with an irregular shape, which can represent extranodular infiltration, especially with synchronous, ill-defined margins (Fig. 12.22). An enlarged thyroid with irregular nodules also may represent a large multinodular thyroid goiter, however (Fig. 12.23). Round and oval nodules are more likely to be benign, especially if other suspicious US criteria are negative, but one special shape of thyroid nodule, called "taller than wide," indicates a higher rate of thyroid malignancy [12, 13] (Fig. 12.24).

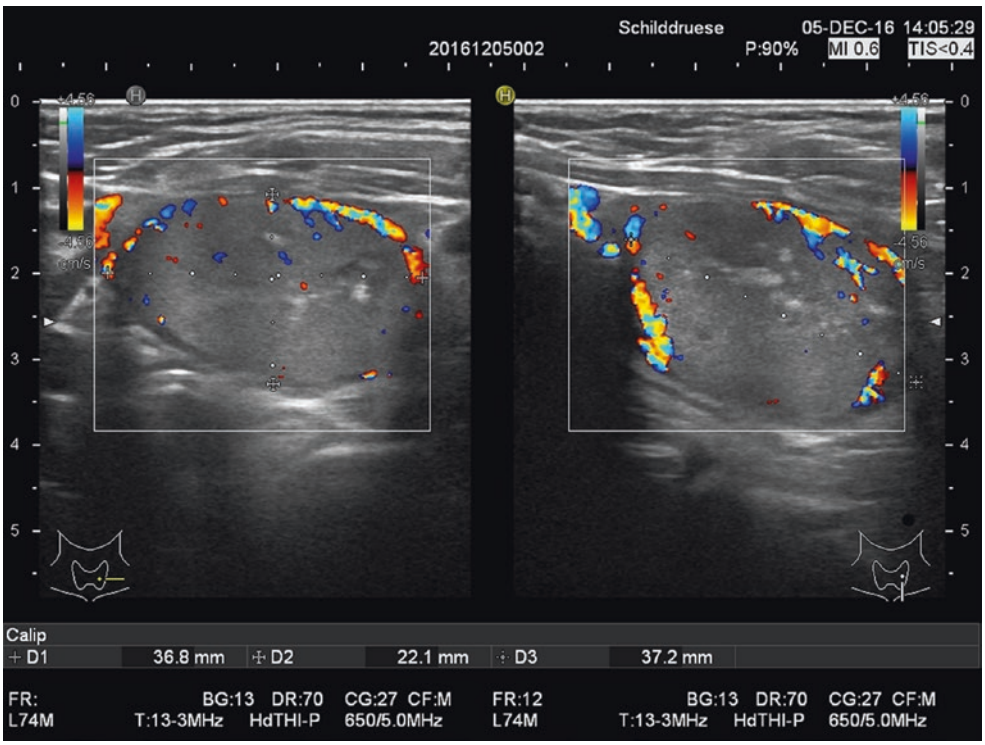

Fig. 12.21 Oval, isoechoic nodule of the left thyroid lobe, with well-defined margins and peripheral vascularity; it has no suspicious ultrasound characteristics

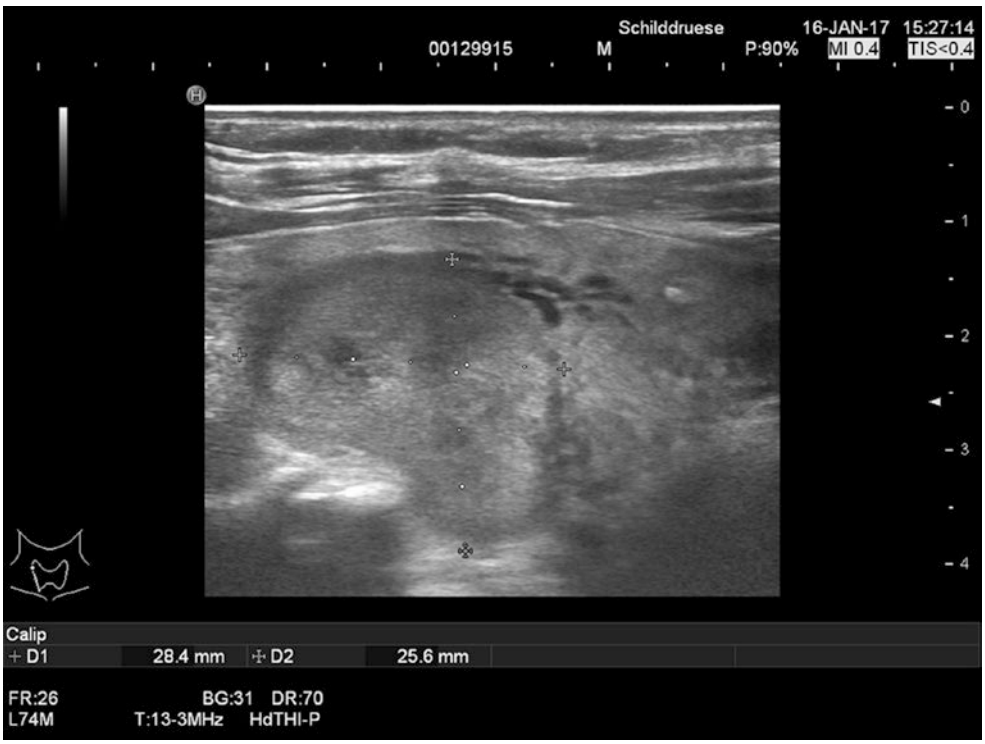

Fig. 12.22 Heterogeneous thyroid nodule with irregular shape and ill-defined margins. (Pathology report: thyroid cancer)

Fig. 12.23 Large, relatively homogeneous nodule with irregular shape and well-defined margins (thyroid goiter)

Fig. 12.24 Isoechoic nodule of the right thyroid lobe with "halo effect." It also is taller than wide (a suspicious ultrasound characteristic)

12.2.6 Vascularity (Peripheral Ring of Flow, Internal Flow)

Using color Doppler during a thyroid ultrasound examination can be very useful in detecting thyroid malignancy (Video 12.7). Peripheral ring of flow is associated with benign thyroid etiology (Fig. 12.25). When internal flow is positive, the nodule is highly suspicious for malignancy (Fig. 12.26). This interpretation is also valid for lymph nodes. In that case, lymph nodes with increased color Doppler flow are very suspicious for metastatic disease. While performing thyroid US examinations, it is very valu-

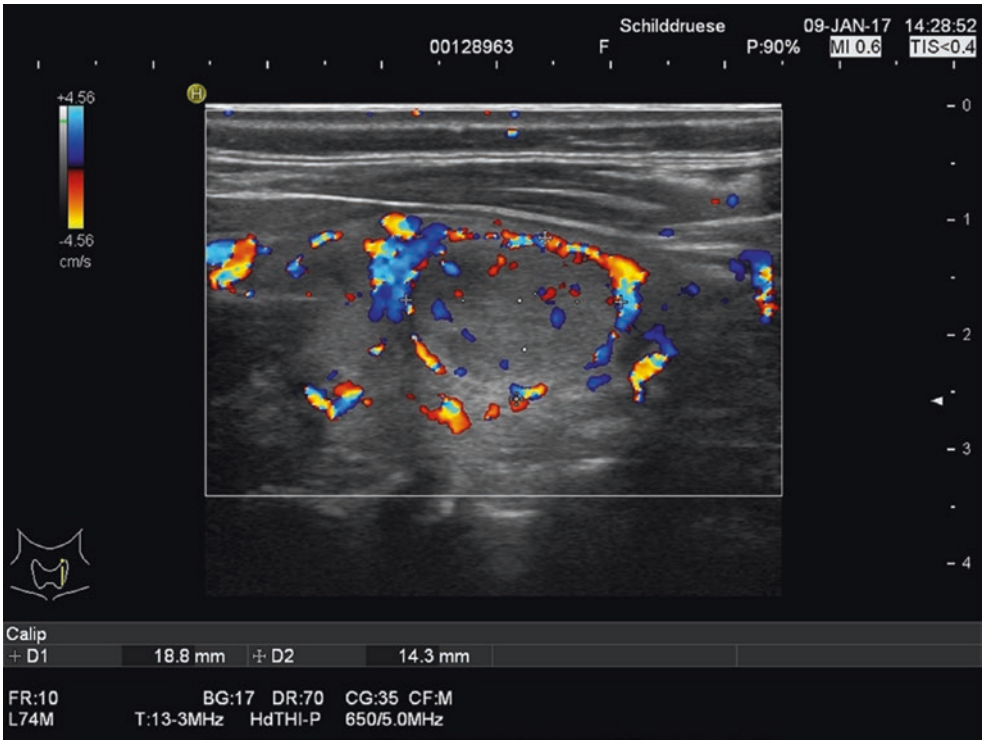

Fig. 12.25 Isoechoic thyroid nodule in a lower pole of the left thyroid lobe, with peripheral ring of flow

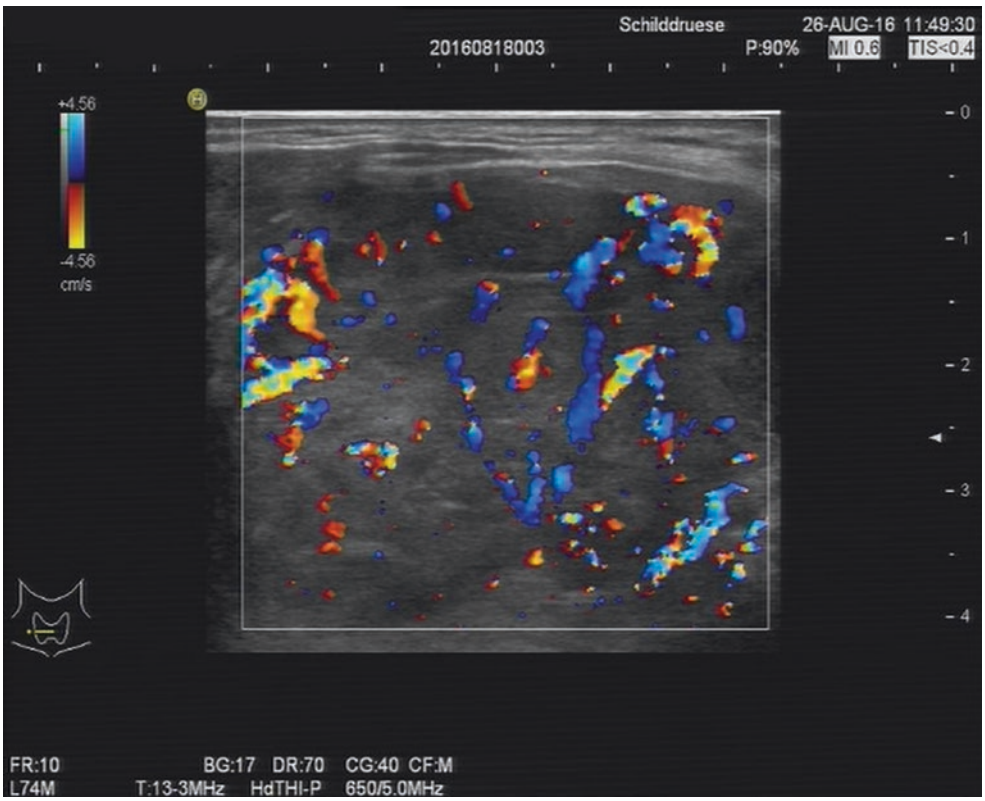

Fig. 12.26 A large, heterogeneous thyroid nodule with positive internal flow, very suspicious for malignancy

able to assess lymph nodes around the thyroid and paratracheal, prelaryngeal, and pretracheal lymph nodes to exclude or confirm potential metastatic disease. Enlarged lymph nodes in these levels can be the first sign of malignant disease.

Pure thyroid cysts are completely avascular, anechoic thyroid nodules (Fig. 12.27). The absence of vascularity can be proven using color Doppler [14].

12.2.7 Elastography

Elastography is a dynamic imaging technique that can help to distinguish differences in firmness between thyroid nodules and surrounding thyroid tissue. To get feedback on whether the thyroid nodule is soft or hard, it is important to use the US probe to compress the thyroid gland. The US device can measure tissue modification that happens under the compression of the probe, and the elasticity of the thyroid nodule can be interpreted and presented on a color scale. It has been empirically noted that thyroid masses related to malignant etiology are more likely to be hard (Fig. 12.28), whereas soft thyroid nodules (Fig. 12.29) tend to be benign. On our US machine, hard thyroid nodules can be seen as blue (Fig. 12.28), and soft nodules can be seen as red or green (Fig. 12.29) on the color scale [15]. This additional diagnostic information can help with decision-making (Video 12.7).

12.3 Thyroiditis

Thyroiditis is a group of inflammatory thyroid diseases with various causes. It is important to describe thyroiditis as a special entity dissociated from thyroid nodal diseases. The main difference between these two groups of thyroid disorders is that thyroid nodal disease is a localized change of thyroid tissue, whereas thyroiditis is usually a diffuse change affecting the whole thyroid gland.

Thyroiditis can be classified as one of several types:

- Chronic lymphocytic thyroiditis (Hashimoto thyroiditis) (Fig.12.30; Video 12.8)
- Subacute lymphocytic thyroiditis (postpartum thyroiditis and sporadic painless thyroiditis)
- Granulomatous thyroiditis (de Quervain's thyroiditis) (Fig. 12.31; Video 12.9)
- Microbial inflammatory thyroiditis (suppurative thyroiditis, acute thyroiditis)
- Invasive fibrous thyroiditis (Riedel's struma, Riedel's thyroiditis) (Fig. 12.32)

The changes of thyroiditis can be detected with US, and the diagnosis then can be determined, especially in patients with Hashimoto thyroiditis (the most common type, caused by thyroid antibodies). The thyroid changes will be more or less visible and are often pathognomonic. In Hashimoto thyroiditis, the thyroid is of small or normal size, and a lot of

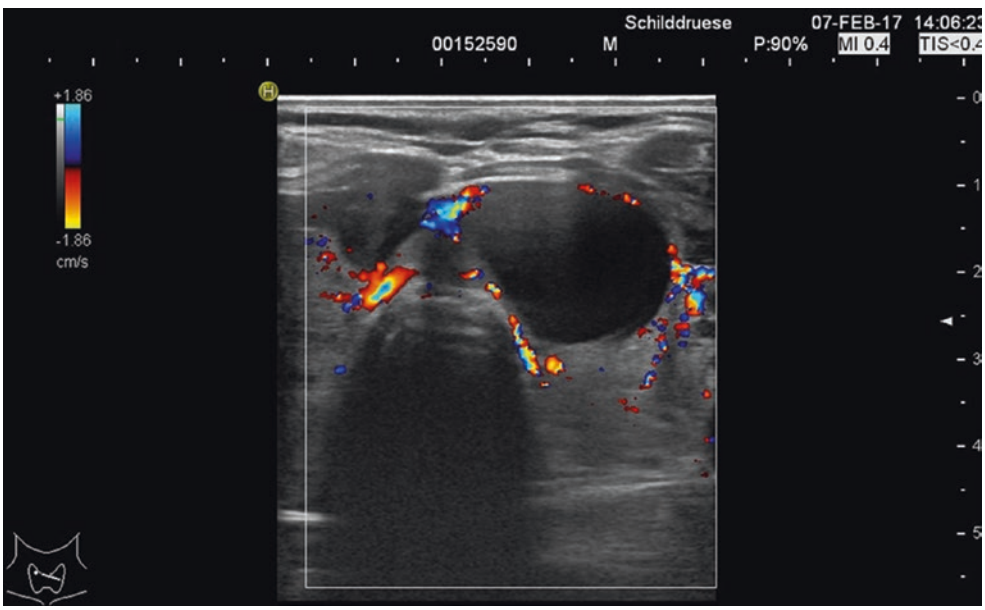

Fig. 12.27 Pure thyroid cyst, an avascular thyroid nodule

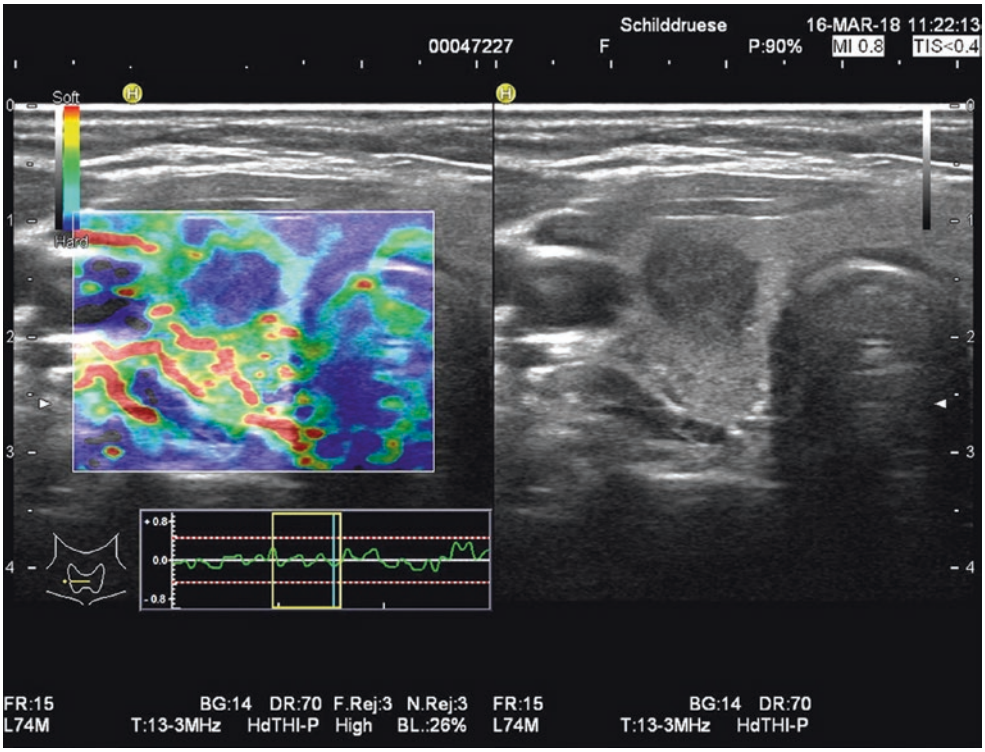

Fig. 12.28 Hypoechoic thyroid nodule with ill-defined margins; elastography (*left*) shows it to be hard (mostly blue). (Pathology report: follicular thyroid cancer)

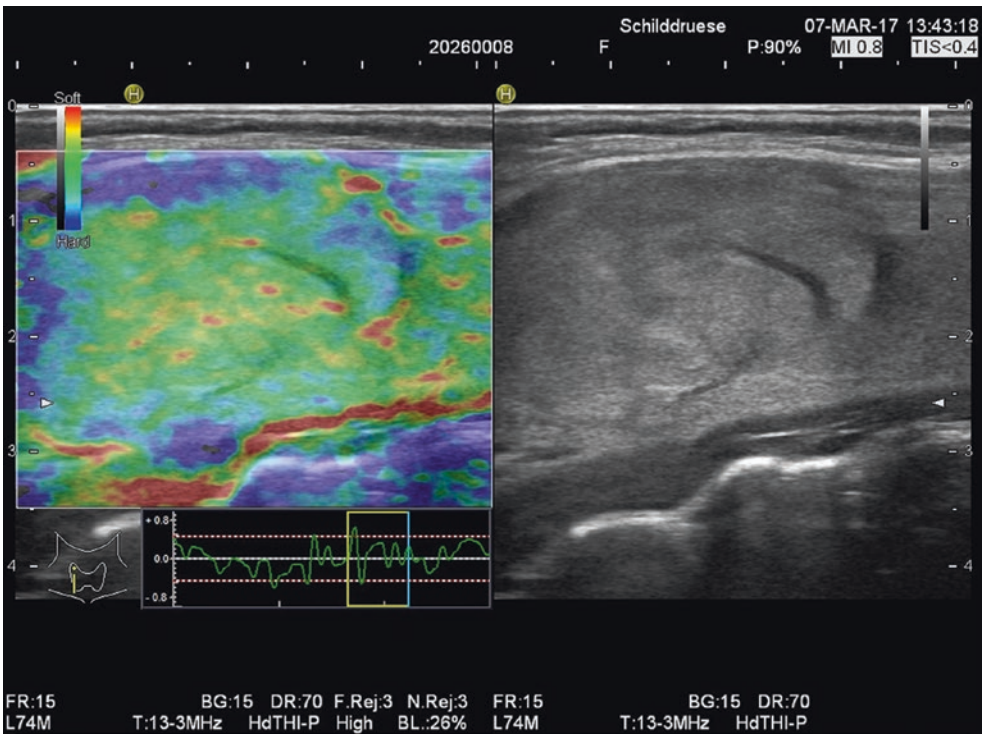

Fig. 12.29 A large, isoechoic nodule of the right thyroid lobe, without suspicious ultrasound characteristics; it is soft on elastography (mostly green)

Fig. 12.30 Thyroid of normal size, diffusely changed with many hypoechoic areas and hyperechoic lines—typical findings for Hashimoto thyroiditis

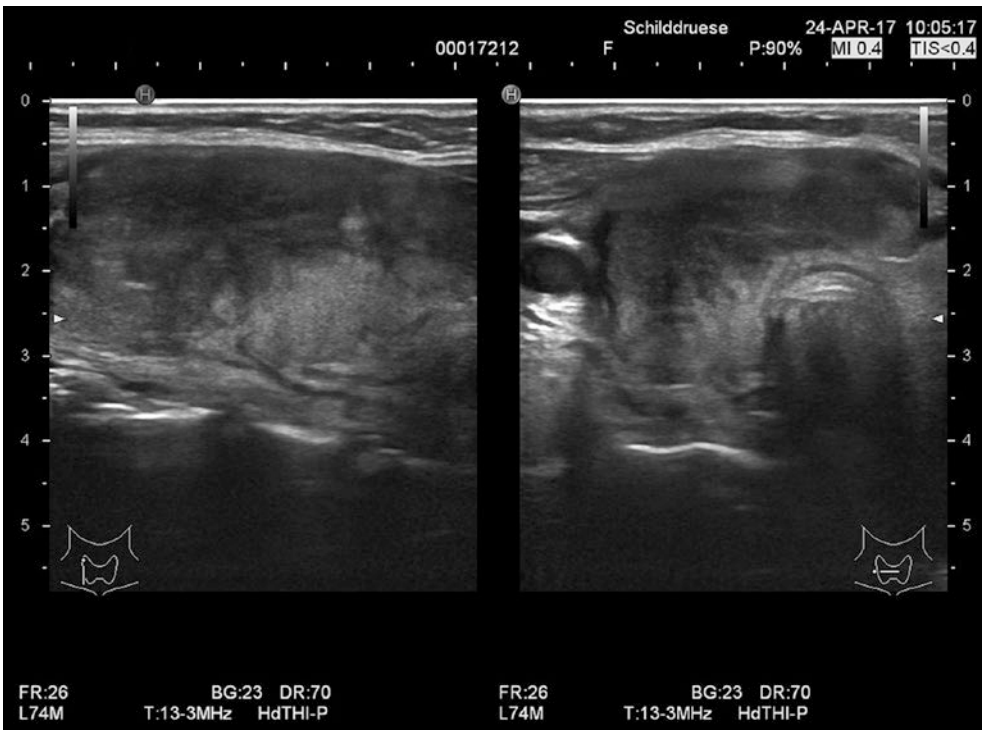

Fig. 12.31 Enlarged, heterogeneous right thyroid lobe with many hypoechoic areas of different sizes, which can be separated with small, hyperechoic part of the thyroid tissue, typical finding for de Quervain's thyroiditis

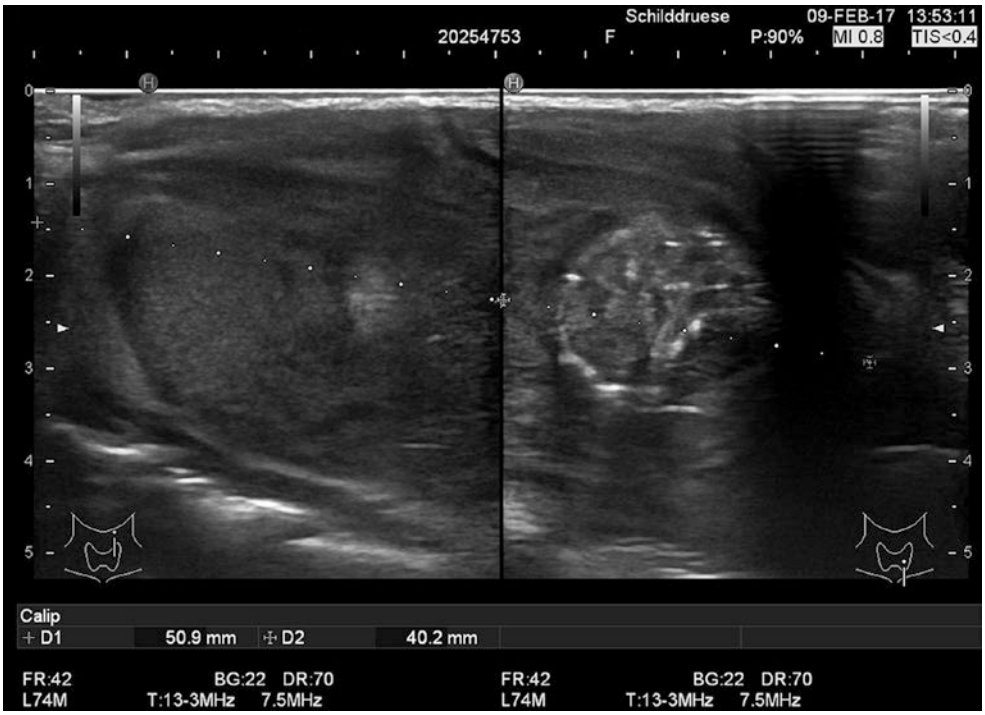

Fig. 12.32 Heterogeneous thyroid tissue with suspicious nodule in the lower pole of the left lobe. (Pathology report: Riedel's thyroiditis)

small, hypoechoic areas are surrounded by hyperechoic lines. Because this pattern sometimes gives an impression of thyroid nodules, it is called pseudonodular.

12.4 Graves' Disease

Graves' disease is an autoimmune thyroid disease characterized by positive specific thyroid-stimulating antibodies causing the production of an excessive amount of thyroid hormones. This condition is diagnosed with scintigraphy, positive thyroid antibodies, and specific thyroid US (Fig. 12.33). Although thyroid US can be specific, the first diagnostic tool after the diagnosis of hyperthyroidism should be thyroid scintigraphy. Performing US, we can usually see an enlarged, inhomogeneous thyroid, which may be hyperechoic, or a normal-size thyroid with diffuse changes (heterogeneous echotexture). The diffuse changes can be more or less visible depending on the stage of the disease [16].

12.5 Thyroid Nodule Guidelines and Classification

12.5.1 American Thyroid Association (ATA) Guidelines

In 2015, the American Thyroid Association (ATA) had presented guidelines for adult patients with thyroid nodules and differentiated thyroid cancer [17]. The part of the guidelines related to US can help us to determine the probability of thyroid malignancy using sonography. Five groups of nodules were described in regard to potential malignancy:

1. Benign (suspicion less than 1%): *Cyst* (Fig. 12.7)
   Pure cystic lesions do not express a high probability of malignancy. Because they are filled with liquid, there are not many cells capable of malignant alteration. They can usually be seen as a hypoechoic or anechoic nodule with or without posterior enhancement.
2. Very low suspicion (less than 3%): Spongiform nodules; partly cystic nodule without suspicious features (Fig. 12.16)
   Spongiform thyroid nodules (also known as "honeycomb" or "puff pastry") are thyroid changes without suspicious US features, usually organized in bundles of small, hypoechoic echogenic fields separated with hyperechoic palisades.
3. Low suspicion (5–10%):
   - Hyperechoic solid nodules with regular margin (Fig. 12.5)
   - Isoechoic solid nodules with regular margin (Fig. 12.6)
   - Partly cystic nodules with eccentric area (Fig. 12.10)
     Hyperechoic and isoechoic thyroid nodules do not have high potential for malignant alteration, especially when the nodules have regular margins. These kinds of nodules are easy to recognize. They can be situated in every part of the thyroid. Hyperechoic nodules are not as common as isoechoic. Nodules with partly cystic

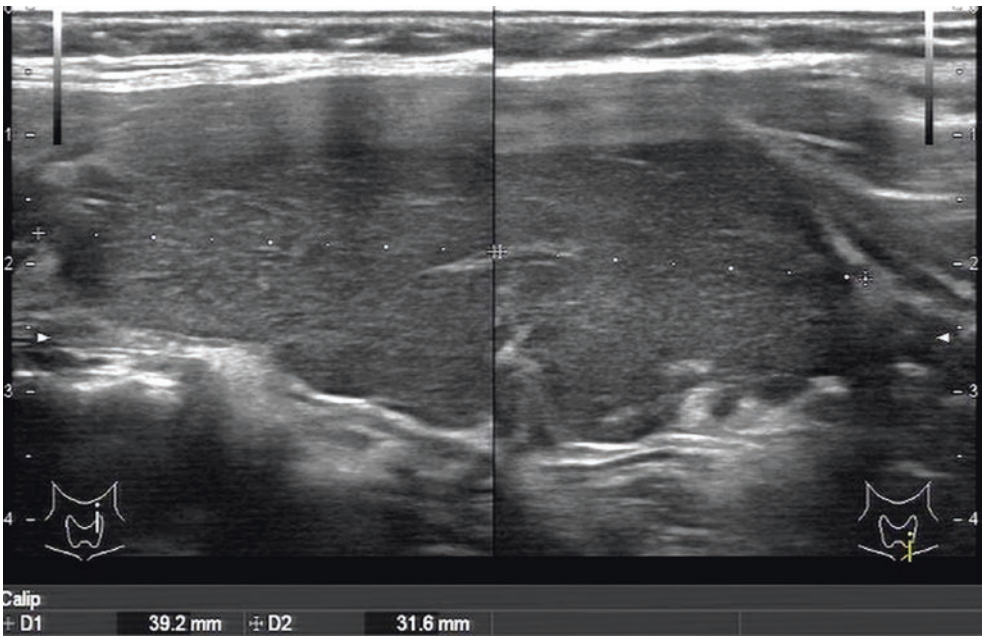

Fig. 12.33 Enlarged, heterogeneous left thyroid lobe with diffuse changes, relatively hyperechoic with many hyperechoic lines and no nodule—typical findings for Graves' disease

areas also belong in this group of nodules with low suspicion. The parts of the nodule that are not cystic have almost the same tendency to malignancy as a purely solid nodule with the same US characteristics.

4. Intermediate suspicion (10–20%): Hypoechoic solid nodules with regular margin (Figs. 12.1 and 12.4)

   Although hypoechoic nodules bear intermediate suspicion for thyroid cancer, only a minority of hypoechoic nodules are actually positive for malignancy (of course, without other suspicious US features). It is common to see a lot of hypoechoic nodules in clinical practice.

5. High suspicion (more than 70–90%):
   - Hypoechoic nodules with microcalcifications and irregular margin (Fig. 12.13)
   - Hypoechoic nodules with irregular margins (Fig. 12.18; Video 12.10)
   - Hypoechoic nodules that are taller than wide (Fig. 12.24)
   - Hypoechoic nodule with irregular margins and extrathyroidal extension (Fig. 12.19)
   - Hypoechoic nodule with interrupted rim calcification with soft-tissue extrusion, irregular margins, and surrounding suspicious lymph nodes

   To this group of thyroid nodules with high suspicion for thyroid cancer are assigned all the thyroid nodules with any suspicious US characteristic. Some of the unfavorable ultrasound features, like hypoechoic nodule with irregular margins and extrathyroidal extension, bear very high suspicion for malignancy. It is crucial to point out that all nodules with any of the abovementioned characteristics must be further examined, and these patients will probably have to undergo thyroid surgery.

The ATA risk stratification does take into consideration elastography and thyroid nodule vascularity [17, 18].

12.5.2 Thyroid Imaging Reporting and Data System (TIRADS) Classification

TIRADS is a classification system proposed by the American College of Radiology (ACR), which recommends which thyroid nodules require fine needle aspiration (FNA) biopsy and how often US follow-up is needed [19]. The recommendations are the result of a scoring system based on US findings. Five groups are designated as TIRADS 1 through TIRADS 5, with higher scores reflecting a higher probability of malignancy and a need for FNA biopsy. The following is a list of US features with the corresponding scores:

- *Composition*: Cystic or completely cystic, 0 points; spongiform, 0 points; mixed cystic and solid, 1 point; solid or almost completely solid, 2 points
- *Echogenicity*: Anechoic, 0 points; hyperechoic or isoechoic, 1 point; hypoechoic, 2 points; very hypoechoic, 3 points
- *Shape*: Wider than tall, 0 points; taller than wide, 3 points
- *Margin*: Smooth, 0 points; ill-defined, 0 points; lobulated or irregular, 2 points; extrathyroidal extension, 3 points
- *Echogenic foci*: None, 0 points; large comet-tail artifact, 0 points; macrocalcifications, 1 point; peripheral (rim) calcifications, 2 points; punctate echogenic foci, 3 points

The scoring divides nodules into the five TIRADS groups, with recommendations:

- *TIRADS1*: 0 points—benign, no FNA required
- *TIRADS2*: 2 points—not suspicious, no FNA required
- *TIRADS3*: 3 points—mildly suspicious; FNA if ≥2.5 cm, follow-up if ≥1.5 cm
- *TIRADS4*: 4–6 points—moderately suspicious; FNA if ≥1.5 cm, follow-up if ≥1 cm
- *TIRADS5*: ≥7 points or more—highly suspicious; FNA if ≥1 cm, follow-up if ≥0.5 cm

References

1. Ghervan C. Thyroid and parathyroid ultrasound. Med Ultrason. 2011;13:80–4.
2. Xie C, Cox P, Taylor N, LaPorte S. Ultrasonography of thyroid nodules: a pictorial review. Insights Imaging. 2016;7:77–86.
3. Tavares MR, Cruz JA, Waisberg DR, Toledo SP, Takeda FR, Cernea CR, et al. Lymph node distribution in the central compartment of the neck: an anatomic study. Head Neck. 2014;36:1425–30.
4. Cantisani V, Lodise P, Grazhdani H, Mancuso E, Maggini E, Di Rocco G, et al. Ultrasound elastography in the evaluation of thyroid pathology. Current status. Eur J Radiol. 2014;83:420–8.
5. Shin JJ, Caragacianu D, Randolph GW. Impact of thyroid nodule size on prevalence and post-test probability of malignancy: a systematic review. Laryngoscope. 2015;125:263–72.
6. Park M, Park SH, Kim EK, Yoon JH, Moon HJ, Lee HS, Kwak JY. Heterogeneous echogenicity of the underlying thyroid parenchyma: how does this affect the analysis of a thyroid nodule? BMC Cancer. 2013;13:550.
7. Popoveniuc G, Jonklaas J. Thyroid nodules. Med Clin North Am. 2012;96:329–49.
8. Wu H, Zhang B, Li J, Liu Q, Zhao T. Echogenic foci with comet-tail artifact in resected thyroid nodules: not an absolute predictor of benign disease. PLoS One. 2018;13:e0191505.
9. Virmani V, Hammond I. Sonographic patterns of benign thyroid nodules: verification at our institution. AJR Am J Roentgenol. 2011;196:891–5.
10. Campanella P, Ianni F, Rota CA, Corsello SM, Pontecorvi A. Quantification of cancer risk of each clinical and ultrasonographic suspicious feature of thyroid nodules: a systematic review and meta-analysis. Eur J Endocrinol. 2014;170:R203–11.
11. Yoon JH, Han K, Kim EK, Moon HJ, Kwak JY. Diagnosis and management of small thyroid nodules: a comparative study with six guidelines for thyroid nodules. Radiology. 2017;283:560–9.
12. Brito JP, Gionfriddo MR, Al Nofal A, Boehmer KR, Leppin AL, Reading C, et al. The accuracy of thyroid nodule ultrasound to predict thyroid cancer: systematic review and meta-analysis. J Clin Endocrinol Metab. 2014;99:1253–63.
13. Intenzo CM, Dam HQ, Manzone TA, Kim SM. Imaging of the thyroid in benign and malignant disease. Semin Nucl Med. 2012;42:49–61.
14. Sultan LR, Xiong H, Zafar HM, Schultz SM, Langer JE, Sehgal CM. Vascularity assessment of thyroid nodules by quantitative color Doppler ultrasound. Ultrasound Med Biol. 2015;41:1287–93.
15. Veer V, Puttagunta S. The role of elastography in evaluating thyroid nodules: a literature review and meta-analysis. Eur Arch Otorhinolaryngol. 2015;272:1845–55.
16. Pishdad P, Pishdad GR, Tavanaa S, Pishdad R, Jalli R. Thyroid ultrasonography in differentiation between Graves' disease and Hashimoto's thyroiditis. J Biomed Phys Eng. 2017;7:21–6.
17. Haugen BR, Alexander EK, Bible KC, Doherty GM, Mandel SJ, Nikiforov YE, et al. 2015 American Thyroid Association management guidelines for adult patients with thyroid nodules and differentiated thyroid cancer: the American Thyroid Association guidelines task force on thyroid nodules and differentiated thyroid cancer. Thyroid. 2016;26:1–133.
18. Kim JY, Jung SL, Kim MK, Kim TJ, Byun JY. Differentiation of benign and malignant thyroid nodules based on the proportion of sponge-like areas on ultrasonography: imaging-pathologic correlation. Ultrasonography. 2015;34:304–11.
19. Grant EG, Tessler FN, Hoang JK, Langer JE, Beland MD, Berland LL, et al. Thyroid ultrasound reporting lexicon: white paper of the ACR Thyroid Imaging, Reporting and Data System (TIRADS) Committee. J Am Coll Radiol. 2015;12:1272–9.

Ultrasound of the Parathyroid Glands

13

Julia E. Noel and Lisa A. Orloff

Ultrasound is an invaluable diagnostic tool in the evaluation of patients with parathyroid disease and may be used in conjunction with nuclear medicine studies or as a single imaging modality in appropriate cases. This chapter focuses on pertinent ultrasound applications in hyperparathyroidism, most importantly sonographic techniques and characteristics that facilitate accurate identification of abnormal glands. Anatomic and embryologic considerations will be reviewed. Ultrasound-guided interventions that aid in the diagnosis, intraoperative localization, and therapeutic management of adenomatous or hyperplastic glands are also described.

13.1 Introduction and History

The clinical findings of hyperparathyroidism were recognized long before the discovery of the parathyroid glands themselves. Historically, tetany and seizures manifesting after total thyroidectomy were originally attributed to the accumulation of toxins not being metabolized by the now-absent thyroid gland. Parathyroid glands were first described in humans in 1880 [1]. However, it was not until the early 1900s, with the ability to determine serum calcium, that the relationship between the glands and calcium homeostasis became evident. The use of parathyroid extract, parathyroid transplantation, and calcium supplementation thereafter became increasingly routine following thyroid surgery [2].

Hyperparathyroidism became recognized as a distinct entity after parathyroid tissue transplantation (which had become successful in treating post-thyroidectomy hypocalcemia) failed to treat patients with fibrocystic bone disease. Later autopsies of these same patients revealed enlarged parathyroid glands [3]. Further investigation of the correlation between calcium metabolism and the renal condition led to an understanding of the differing etiologies of hyperparathyroidism, which ultimately had a profound impact on surgical indications and approaches. Before the availability of reliable preoperative localization technology, the approach to parathyroidectomy was a bilateral, four-gland exploration. Attempts at localizing disease via arteriography and cervical venous phlebotomy were inconsistent and prone to significant morbidity [4]. Modern parathyroid surgery has been revolutionized by the development of radiographic studies and real-time parathyroid hormone detection. Instead of an empirical bilateral approach, the preferred surgical treatment for primary hyperparathyroidism is now a focused exploration. A unilateral or single-quadrant approach allows for shorter operative time, preservation of normal glands, and minimally invasive techniques or incisions.

In fact, a defining characteristic of minimally invasive parathyroid surgery is the preoperative localization of diseased glands. Successful surgery hinges upon the reliable identification of pathology to limit dissection. This chapter reviews in depth the significant contribution of ultrasound in the identification and management of parathyroid disease.

13.2 Office-Based Ultrasound and Practical Applications

Ultrasound is highly efficacious in the detection of parathyroid adenomas, with sensitivities reported between 70% and 93% [5–9]. When used in combination with radionuclide scanning, preoperative imaging strategies have a 97% sensitivity and 100% specificity in localizing disease [10]. It has been suggested that when sestamibi and ultrasound imaging correlate, intraoperative parathyroid hormone (PTH) confirmation of adenoma removal may not be necessary, as the cure rate remains exceptionally high [11, 12]. When the studies are discordant, however, intraoperative PTH continues to be a useful adjunct to confirm the successful removal of pathologic gland(s) [13, 14].

J. E. Noel · L. A. Orloff (✉)
Department of Otolaryngology–Head and Neck Surgery, Stanford University School of Medicine, Stanford, CA, USA
e-mail: lorloff@stanford.edu

© Springer Nature Switzerland AG 2019

H. J. Welkoborsky, P. Jecker (eds.), *Ultrasonography of the Head and Neck*, https://doi.org/10.1007/978-3-030-12641-4_13

Ultrasound may be used as a single imaging modality in the localization of enlarged parathyroid glands. Specifically, surgeon-performed ultrasound has been reported to have a high success rate, detecting adenomas in 87% of patients [8]. It has been suggested, therefore, that the surgeon may reserve radionuclide studies for negative ultrasounds or reoperative cases. Numerous studies have also addressed the financial aspect of preoperative imaging, reporting that performing ultrasound alone is more cost-effective than including sestamibi scanning [15, 16]. Emphasis should, again, be placed on the experience of the operator, as it has been shown that the presence of concomitant thyroid disease and incorrect localization are the most common reasons for discrepancies between preoperative imaging and intraoperative findings [17]. This same study found that second-look ultrasound by experienced ultrasonographers was able to identify the candidate lesion in 66% of initially negative studies.

Preoperative four-dimensional (4D) CT has also emerged as an accurate method of localization. As a single modality, specificity for localizing an adenoma to the correct side of the neck is 84%, with an accuracy of 83% [18]. When combined with ultrasound, the sensitivity of lateralization increases to 94% [19]. Economic studies have determined that 4D CT is also cost-effective, with the sequence of cervical ultrasound followed by 4D CT identified by numerous groups as the least costly regimen for evaluation [16]. In practice, these three imaging strategies are complementary and take advantage of different features of a parathyroid adenoma. Ultrasound detects a mass structure in the context of surrounding anatomy, whereas sestamibi scanning and 4D CT highlight functional retention of a radioisotope or contrast material. Only ultrasound, however, offers imaging devoid of ionizing radiation exposure.

Office-based ultrasound is a useful tool that can be performed at the time of initial evaluation for identification of parathyroid disease. Often, patients will present to a surgeon having already undergone another localization study, and ultrasound can be performed to correlate prior findings in the context of the surrounding structures. In-office ultrasound also allows for fine-needle aspiration (FNA) of candidate lesions for parathyroid hormone washout, which is not advised in routine cases but proves particularly useful in situations of discordant imaging or reoperative cases. The limitations of ultrasound as they pertain to patient anatomy, thyroid disease, and ectopic glandular locations must be recognized. It is particularly challenging to perform an effective evaluation in a patient with a large body habitus or one whose neck extension is restricted by prior surgery, radiation, or pain. Adenomas in the mediastinal compartment or in the paratracheal or paraesophageal grooves may not be readily visible because of both depth and attenuation from nearby bony and cartilaginous structures. The presence of thyroid pathology—particularly multinodular goiter and lymphocytic thyroiditis, along with central compartment lymphadenopathy—additionally accounts for a significant number of missed lesions and inaccurate localization [20, 21].

Finally, consideration must be given to the logistics of introducing ultrasound techniques to the office setting. A significant amount of training and financial investment are required, and the visit length must be extended to accommodate this additional evaluation. Furthermore, coordination between the radiology and pathology departments is required to establish a collegial multidisciplinary approach [22]. As the diagnostic and therapeutic applications of ultrasound in endocrine diseases continue to expand, however, it becomes increasingly important for the surgeon to become facile with this technology.

13.3 Indications for Parathyroid Ultrasound

Ultrasound is an integral diagnostic tool in parathyroid gland evaluation, which may provide independent localization of abnormalities or may corroborate findings of radionuclide scanning. This tool may prove useful at numerous stages in the diagnosis and management of parathyroid disease, so it is important to recognize the indications for its use.

In the preoperative setting, all patients with suspected hyperparathyroidism on laboratory and clinical evaluation in whom surgical intervention is being considered are candidates for neck ultrasound. In cases of primary hyperparathyroidism (80% of which are attributable to a single adenoma), ultrasound is often critical to precisely localizing the enlarged gland [23]. Identifying relationships of the gland to normal neck structures can then facilitate a minimally invasive parathyroidectomy (Fig. 13.1). Primary parathyroid hyperplasia is suspected when both the ultrasound and sestamibi scan fail to identify a candidate adenoma, as multiple hyperplastic glands may be too small for detection by either imaging modality. Similarly, because hyperplastic change is often asymmetric, the identification of more than one candidate gland on ultrasound can also indicate primary hyperplasia (Fig. 13.2). In either case, these features prepare the surgeon for the possibility of a bilateral exploration. In patients with suspected secondary or tertiary hyperparathyroidism, in whom multigland hyperplasia is expected, ultrasound may often detect enlarged glands (Fig. 13.3). The order of exploration can then be determined based on gland size, with the potential aid of intraoperative PTH levels.

Evaluation of the thyroid gland is of paramount importance in planning for parathyroid surgery (Fig. 13.4). It is ideal to perform simultaneous central compartment surgery because revision operations present an increased risk of morbidity [24]. Coexistent thyroid disease, therefore, may prompt additional diagnostic measures, such as FNA, and

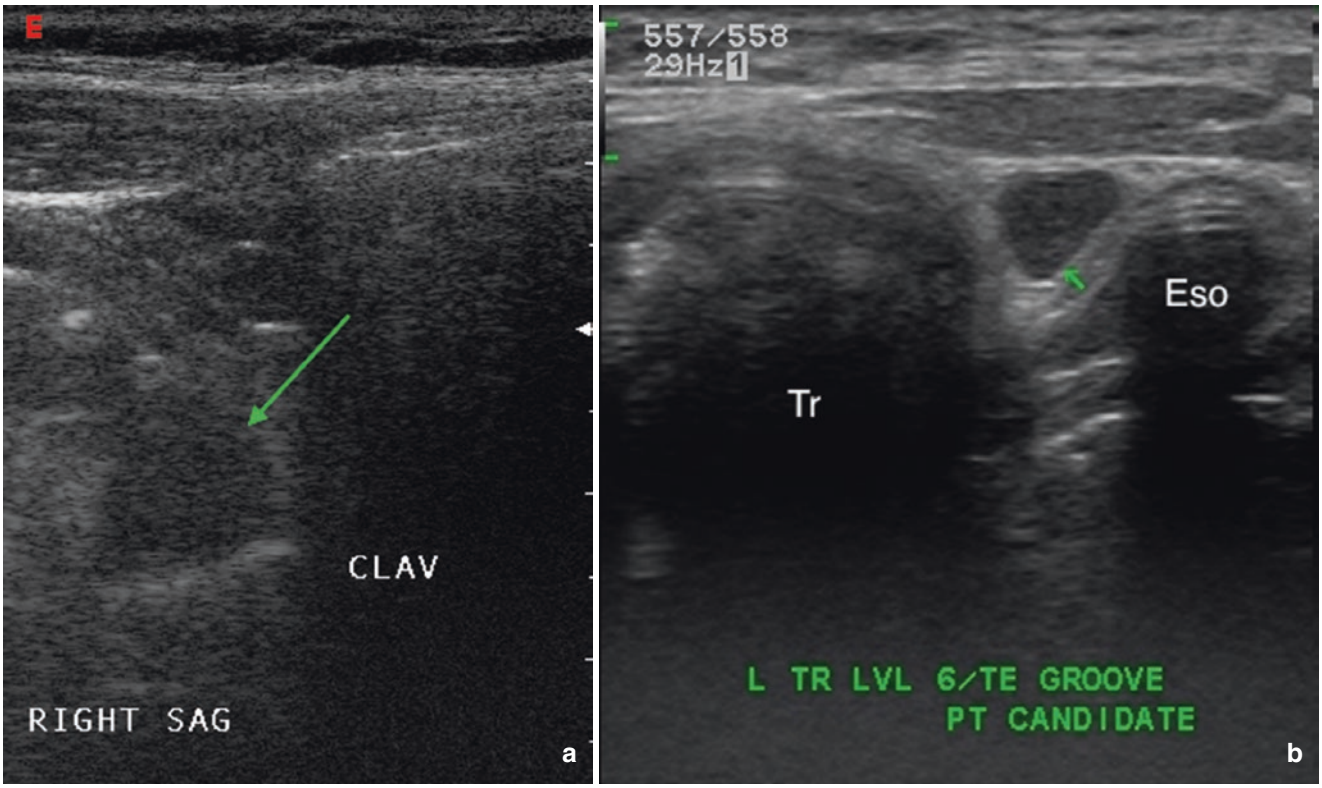

Fig. 13.1 Identifying relationships of an enlarged parathyroid gland to normal neck structures facilitates surgical localization. (**a**) Sagittal view of a right inferior parathyroid adenoma (*arrow*) in an obese patient, with clavicle (CLAV) just inferior. (**b**) Transverse view of left inferior parathyroid adenoma (*small arrow*) within the tracheoesophageal groove. Eso esophagus (with temperature probe shadowing artifact), Tr trachea

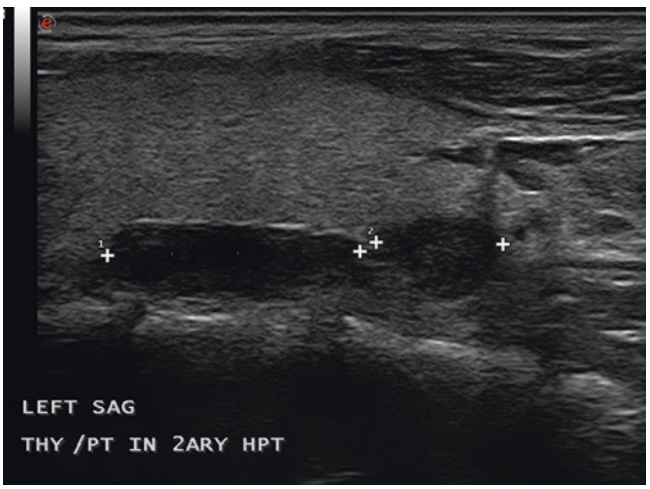

Fig. 13.2 Asymmetric parathyroid hyperplasia (left sagittal view). The superior parathyroid gland is more enlarged and elongated than the inferior gland

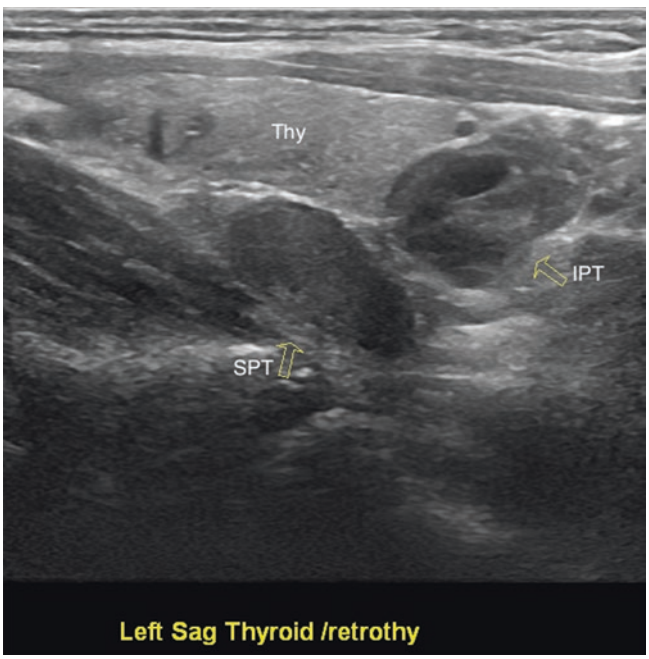

Fig. 13.3 Tertiary parathyroid hyperplasia (*arrows*). Note how the superior parathyroid gland (SPT) points inferodorsally, whereas the inferior gland (IPT) points inferoventrally. This orientation is characteristic and helps distinguish superior from inferior parathyroid glands. Thy thyroid

may be addressed at the time of parathyroidectomy. Ultrasound also prepares the surgeon for unexpected or aberrant anatomy. Though identification of the recurrent laryngeal nerve(s) is not always necessary during parathyroidectomy, understanding nerve anatomy will help to

avoid unnecessary injury and postoperative voice and swallowing issues. A nonrecurrent right inferior laryngeal nerve, though present in only 0.5% of cases, is suspected when the right subclavian artery arises directly from the aortic arch rather than from an innominate artery [25, 26]. This vascular relationship is typically readily visible on ultrasound (Fig. 13.5).

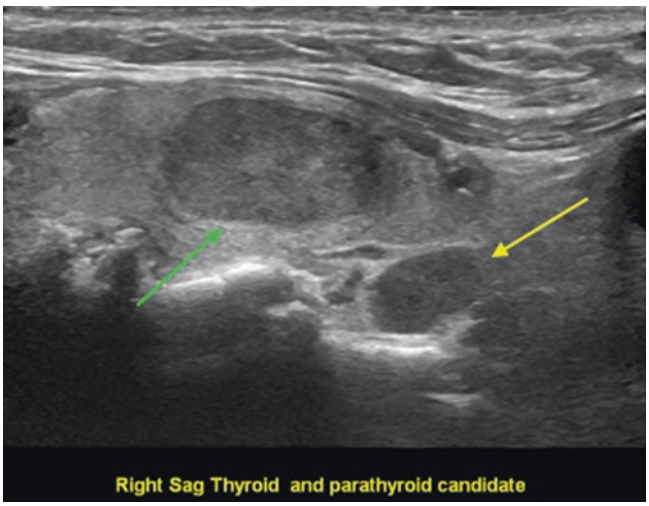

Fig. 13.4 Thyroid gland evaluation during parathyroid ultrasound. Right sagittal view of thyroid nodule (*green arrow*) and parathyroid adenoma (*yellow arrow*)

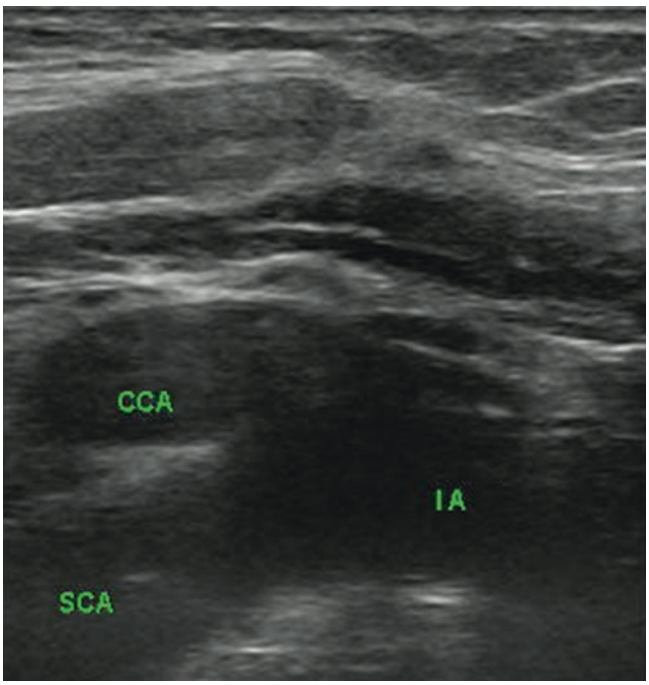

Fig. 13.5 Identification of normal right-sided vascular anatomy, including bifurcation of the innominate artery (IA) into the subclavian artery (SCA) and common carotid artery (CCA), predicts normal recurrent laryngeal nerve anatomy

In the intraoperative setting, ultrasound can be repeated once the patient is supine and in the operative position. With the patient relaxed and the neck in ideal extension, the target gland(s) may be reconfirmed and localized in the context of the surrounding anatomy. This localization aids incision planning and facilitates efficient dissection, especially in patients with parathyroid hyperplasia or reoperative disease. Occasionally, in the case of an unidentified adenoma, an enlarged gland not initially detected may become apparent on this evaluation and will alter the surgical plan.

13.4 Ultrasound Technique

Ultrasound of the neck should begin with proper patient positioning. The patient is supine with a pillow beneath the neck and shoulders to provide support, while the head rests on the exam table, allowing for comfortable neck extension (Fig. 13.6). Extension brings the low central neck and superior mediastinal contents more cephalad and can expose pathology that may otherwise be hidden behind the clavicles or in the thoracic inlet.

Prior knowledge of a localizing lesion on a radionuclide study does not preclude a complete thyroid and parathyroid examination. The sequence of scanning is at the discretion of the sonographer, but should be methodical and thorough. Initial evaluation may begin with the central neck. The transducer is held perpendicular to the skin in a transverse

Fig. 13.6 Proper patient positioning with support and comfortable neck extension

orientation, while potential areas for parathyroid pathology are examined. One approach is to begin cephalad at the hyoid bone on the right side. Moving caudally, the central compartment is scanned from the carotid sheath to the larynx and trachea. The esophagus can be easily differentiated from true pathology by asking the awake patient to swallow. At the thoracic inlet, normal vascular (and nerve) anatomy is confirmed by observing branching of the right innominate artery into the right subclavian and common carotid arteries (*see* Fig. 13.5). An identical evaluation is then performed on the left central compartment. The transducer is then rotated 90° so that the central neck can be evaluated in the sagittal plane. Beginning at the carotid sheath on one side, slow movement is made medially toward the trachea and then continues to the contralateral carotid sheath. The patient's head is turned away from the transducer as needed.

If not already done at the outset, the thyroid gland itself is evaluated at the conclusion, beginning with the right superior lobe in a transverse orientation and moving caudally. An identical examination is performed on the left side, followed by evaluation in the sagittal plane. The isthmus and the presence of a pyramidal lobe should be noted. While moving cephalad in the midline, the arytenoid cartilages will become visible within the larynx, and movement of the vocal folds may also be assessed at this juncture [27, 28]. This is accomplished by asking the patient to temporarily halt respiration, at which time the normal vocal folds adduct in a symmetric fashion, meeting in the midline to close the glottis (Fig. 13.7). When normal respiration resumes, symmetric abduction will be observed. Vocal fold motion can also be evaluated by having the patient phonate or hum, but this view is often more challenging owing to the vertical laryngeal excursions associated with speech.

Following a thorough evaluation of the central neck and thyroid, the lateral neck is also examined in a systematic manner. This examination allows detection of ectopic enlarged parathyroid glands, abnormal lymph nodes, and other unexpected masses or salivary gland pathology.

Detection of mediastinal and ectopic parathyroid adenomas can pose a particular challenge. Adjusting to a lower transmitted frequency allows for increased depth of penetration and may reveal lesions in the prevertebral, retropharyngeal, or retroesophageal spaces. Directing the transducer in a longitudinal fashion and fanning from a lateral position will also decrease impedance from the carotid artery, larynx, and trachea. Moving into the thoracic inlet, the sonographer can tilt the transducer away from perpendicular or can position one corner into the sternal notch for improved visualization of the superior mediastinum.

13.5 Parathyroid Anatomy and Embryology

Recognition of the embryologic development and anatomy of the parathyroid glands is valuable in anticipating the most common locations of parathyroid disease and guiding a systematic survey for ectopic sites. Most humans have two superior and two inferior glands, but cadaver studies have shown that 3–6% of individuals have fewer glands, or more than four [29]. The superior parathyroid

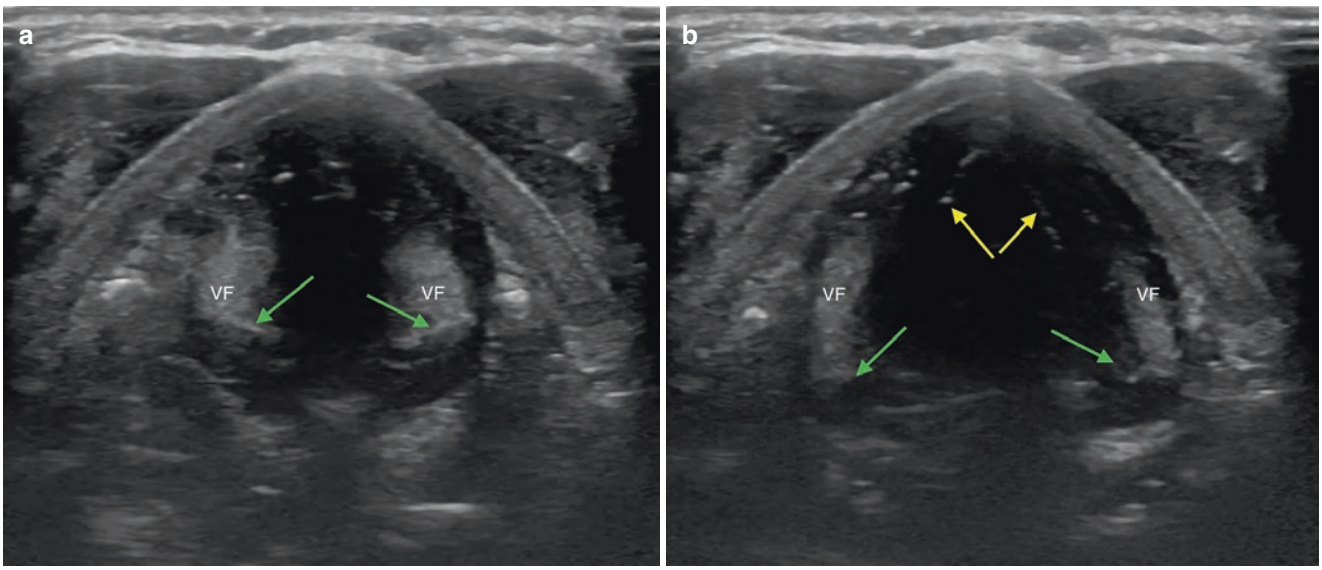

Fig. 13.7 Laryngeal ultrasound. (**a**) Halted respiration, with adducted vocal folds (VF) and arytenoids (*arrows*). (**b**) Resumed respiration, with symmetric abduction of the vocal folds (VF) and arytenoids (*green arrows*); the *yellow arrows* indicate the free edges of the vocal folds

glands arise from the fourth pharyngeal pouch, and the inferior parathyroid glands arise from the third pharyngeal pouch. After parenchymal differentiation, the glands detach from the pharynx and begin their caudal descent during the seventh week of gestation. The superior glands are associated with the thyroid during their caudal migration and typically are found at the posterolateral aspect of the superior lobe, either on the glandular surface or within the perithyroidal fascia. The inferior glands travel with the thymus, which also arises from the third pharyngeal pouch, and detach proximally at the inferior and posterior aspect of the thyroid. Regardless of descent or ectopy, the glands maintain a consistent relationship with the recurrent laryngeal nerve in the coronal plane. The superior parathyroid glands are dorsal to the nerve, regardless of latitude within the neck, and the inferior glands lie ventral to the plane of the nerve [25].

When evaluating for parathyroid disease, it is critical to acknowledge potential ectopic as well as eutopic locations. Superior glands are less likely to be ectopic than inferior glands, but tend to be deep (Fig. 13.8) and may be found in the carotid sheath, retropharyngeal, retroesophageal, retrotracheal, and parapharyngeal spaces. Rarely, the superior parathyroid may descend into the posterior mediastinum. The inferior parathyroid glands, because of their longer migration, have a more variable, yet still more superficial, location. If it fails to migrate with the thymus, the gland may be found as cephalad as the hyoid bone or carotid bifurcation or as caudal as the anterior/superior mediastinum. Intrathyroidal parathyroid glands (Fig. 13.9) occur rarely (0.2% of the time); they are more likely to be inferior rather than superior glands [30].

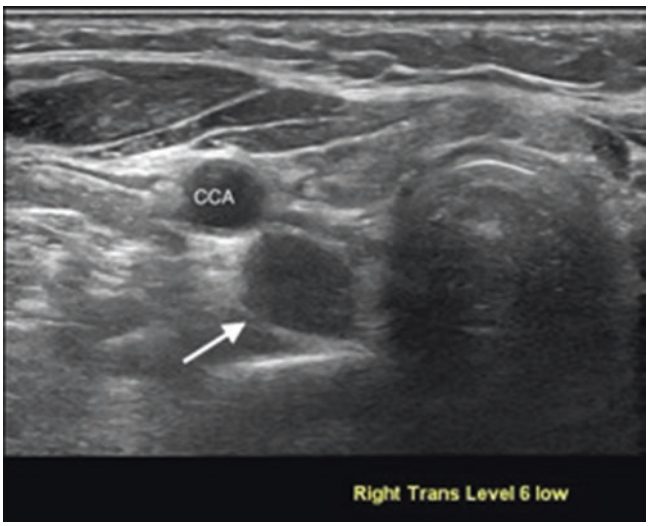

Fig. 13.8 A deep descended superior parathyroid adenoma (*arrow*), which is entirely deep to the plane of the common carotid artery (CCA), in a right transverse view

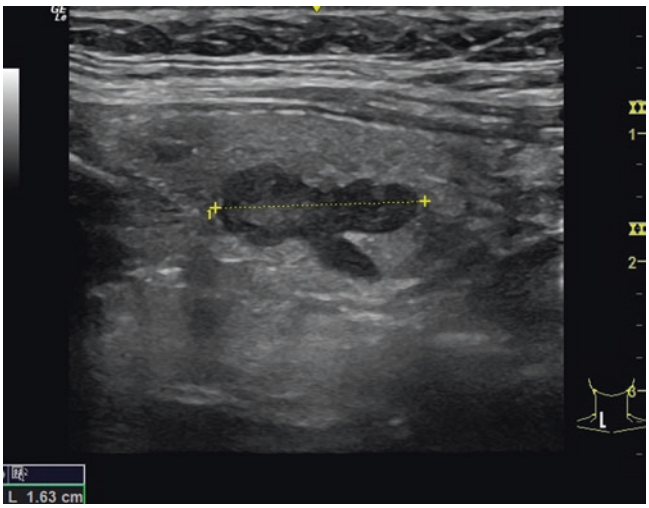

Fig. 13.9 Intrathyroidal parathyroid gland (right sagittal view). Despite its irregular shape, this lesion was confirmed to be a parathyroid adenoma

The vascular supply of the parathyroid glands is important to consider when undertaking parathyroid or thyroid surgery. With eutopic glands, the inferior thyroid artery most commonly provides the majority of the vascular supply. However, the superior thyroid artery may give significant contributions to the superior glands or, less often, the inferior glands. Occasionally, the inferior glands may derive their blood supply from branches directly off the subclavian artery or the aorta [31, 32].

13.6 Sonographic Characteristics of Parathyroid Glands

Normal parathyroid glands are quite small, measuring approximately 6 mm × 4 mm and weighing 30–60 mg [30, 33]. They are indistinguishable from surrounding structures in the neck by imaging studies, generally including ultrasound. Enlarged glands or adenomas typically appear as homogenous, ovoid structures that are hypoechoic relative to the thyroid gland because of their dense cellularity and lipid-rich content (Fig. 13.10). Less commonly, enlarged parathyroids may take on a cystic or lobulated appearance with echogenicity similar to the thyroid gland or may even appear anechoic. The capsule is generally more hyperechoic but is so thin that it is often imperceptible.

A parathyroid gland is easily mistaken for a lymph node, which also presents as an ovoid and hypoechoic mass, but key sonographic features differentiate the two entities. A lymph node has a central, echogenic, fatty hilum that a parathyroid gland lacks (Fig. 13.11). On power Doppler, a lymph node will demonstrate arborizing

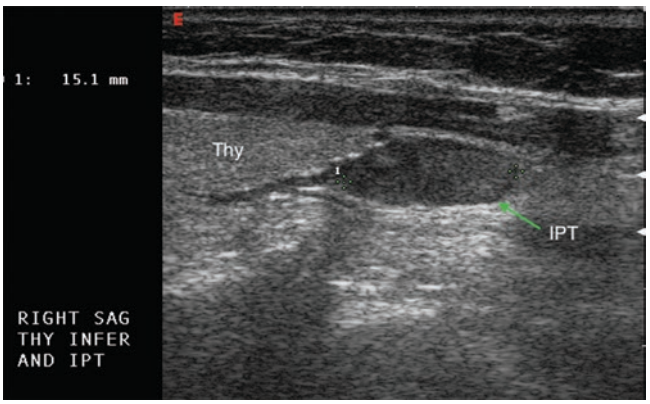

Fig. 13.10 Typical parathyroid adenoma (*arrow*, right sagittal view). IPT inferior parathyroid, Thy thyroid

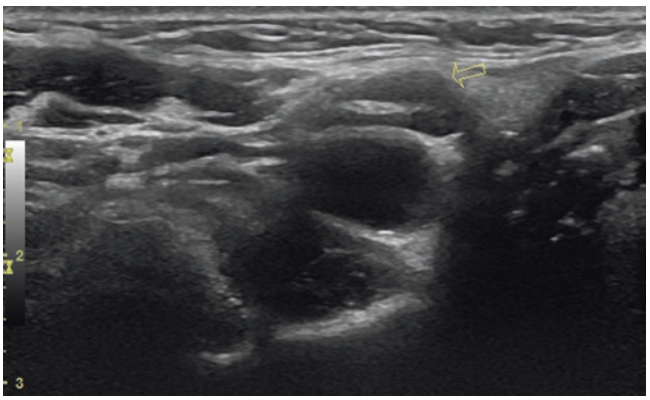

Fig. 13.11 A normal lymph node (*arrow*) has a central, echogenic, fatty hilum, which a parathyroid gland lacks

flow through the hilar pedicle, but a parathyroid adenoma typically has a single feeding vessel from the superior pole that terminates shortly after entering the adenoma (Fig. 13.12) [34–36]. It is particularly difficult to make this differentiation in patients with chronic lymphocytic thyroiditis, who often have multiple small, reactive paratracheal nodes that may not have a prominent central hilum (Fig. 13.13). This vascular pattern also becomes important in identifying truly intrathyroidal glands, wherein the adenoma is entirely encapsulated within the thyroid tissue. Though the echogenicity of the gland may provide some indication, a thyroid nodule may also appear hypoechoic and ovoid [37]. Therefore, if suspicion for an intrathyroidal adenoma is high and a candidate lesion is noted, the next step is to perform an ultrasound-guided FNA of the lesion with testing of the needle rinse for parathyroid hormone [21, 38].

In cases of secondary and tertiary hyperparathyroidism with multiglandular disease, hyperplastic glands are often detectable via ultrasound with 62.5% sensitivity and 85.7% specificity [39]. Correlation has been demonstrated between the degree of parathyroid hormone elevation and the ability to visualize enlarged glands [39]. Ultrasound has additionally been described as a tool to monitor response to calcimimetics and guide the decision to proceed with parathyroidectomy. Glands responsive to medical therapy may show cystic degeneration, volume decrease, and loss of vascularity [40].

Finally, a parathyroid malignancy must be considered in cases where the parathyroid hormone is more than three times greater than normal levels, the serum calcium is over 14 mg/dL, serum alkaline phosphatase is elevated, or there is a palpable neck mass. Irregular, indistinct borders with invasion into adjacent structures on ultrasound are suspicious for parathyroid carcinoma (Fig. 13.14). Other features may include a heterogeneous appearance or intralesional calcification [41–43].

13.7 Extended Applications for Parathyroid Ultrasound

A number of adjunctive interventions performed with the aid of ultrasound imaging are worthy of mention. FNA has been previously discussed as a means to investigate a candidate lesion for concentrated PTH on needle rinse with saline, in complex cases. Routine FNA of parathyroid glands is not recommended, especially with larger-gauge needles, because of concern for implantation of parathyroid cells. Still, prior study has suggested that ultrasound localization followed by verification with lesional aspiration and parathyroid hormone washings carries a sensitivity of 95% [44]. Parathyroid hormone levels from direct aspiration of a targeted parathyroid gland are expected to be significantly elevated above serum level, and often above the limits of testing. Nodular thyroid glands or multiple reactive central lymph nodes may represent coexisting malignant pathology, and also often make it difficult to distinguish a parathyroid adenoma [17, 20]. In such cases, ultrasound-guided FNA of the suspicious lesion may be pursued to confirm the presence of pathology and assist with preoperative planning.

Intralesional methylene blue dye injection has also been described as a complementary method of localization to facilitate minimally invasive parathyroidectomy [45, 46]. A small amount (0.1 cc is sufficient) of 1% methylene blue is infiltrated into the adenoma under ultrasound guidance until a flush is seen within the lesion. After the incision is made, the contrasting color makes the tract and lesion readily visible (Fig. 13.15). This technique must be used with caution, however, as the dye may disperse into surrounding tissues and render differentiation of important

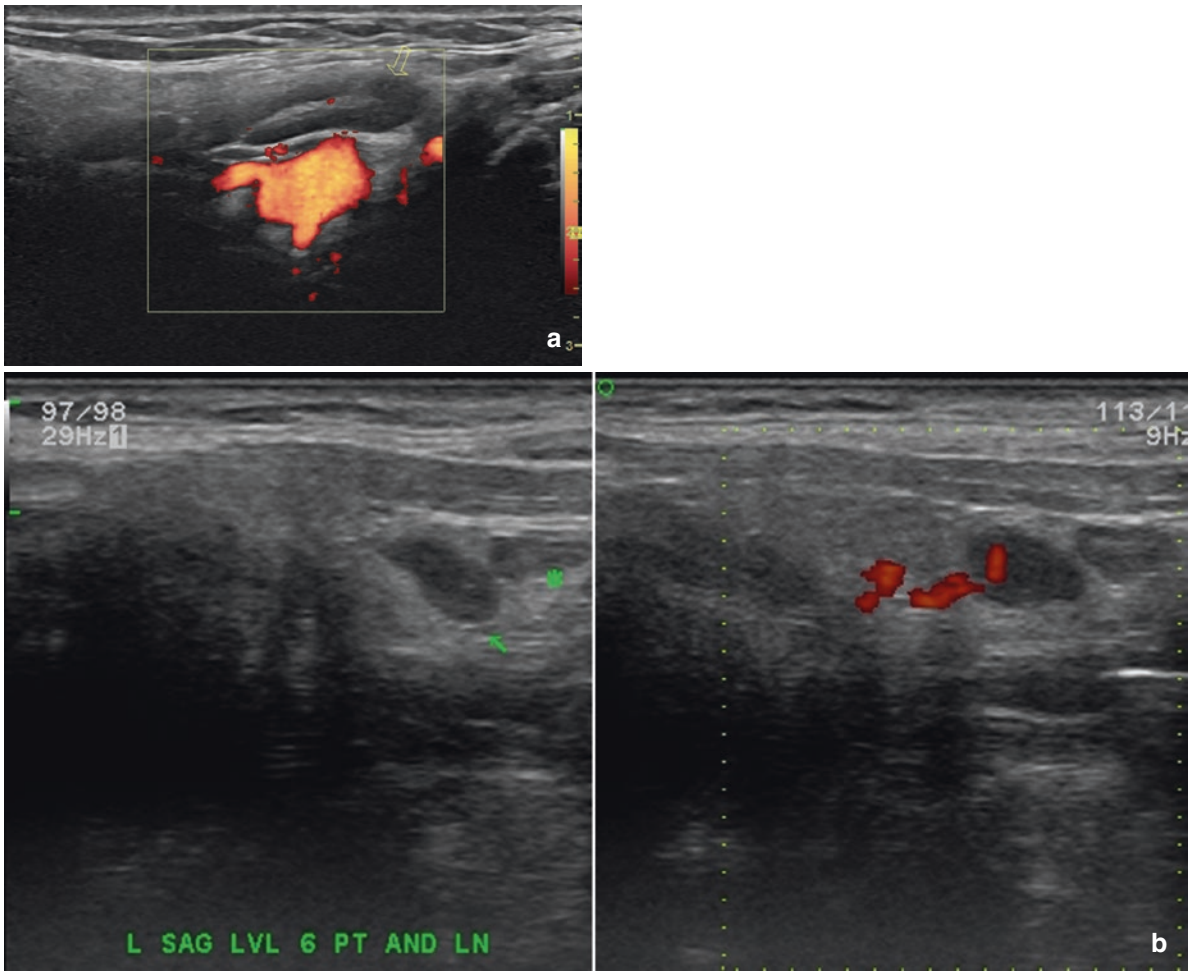

Fig. 13.12 Contrast between polar blood flow into a parathyroid adenoma and the absence of visible flow or hilar pattern of flow in a benign lymph node on power Doppler. (**a**) Very slight hilar blood flow in a normal lymph node (*arrow*). (**b**) Left inferior parathyroid adenoma (*arrow*) and adjacent lymph node (*asterisk*) without (left) and with (right) power Doppler; note polar flow into adenoma

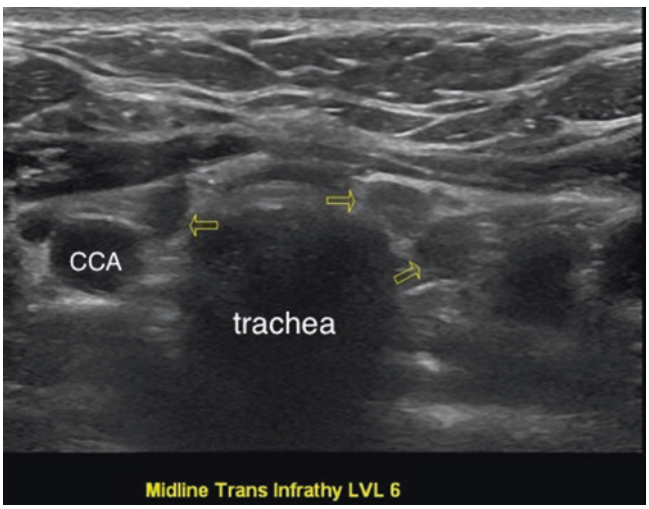

Fig. 13.13 Multiple small, reactive paratracheal lymph nodes (*arrows*) with barely visible or invisible central hila, associated with chronic lymphocytic thyroiditis (midline transverse view). CCA right common carotid artery

nearby neurovascular structures challenging. Authors have suggested that this strategy may be most appropriate in the reoperative neck [47].

Ultrasound may also be used for therapeutic intervention. Sonographically guided percutaneous ethanol ablation of parathyroid adenomas has been described and reported to result in normocalcemia in 65% of patients [48]. However, hypercalcemia can recur several years after treatment, requiring more definitive intervention. Furthermore, there is a risk of chemical injury to the recurrent laryngeal nerve [49, 50]. Patients with secondary or tertiary hyperparathyroidism, especially those not suitable for surgery, may also undergo ethanol ablation, but the long-term results are inferior to those of surgical management, and these patients are also subject to recurrent symptomatic hypercalcemia [51, 52]. Ethanol ablation in the postoperative setting, as an adjunct to subtotal parathyroidectomy, also has been described [53].

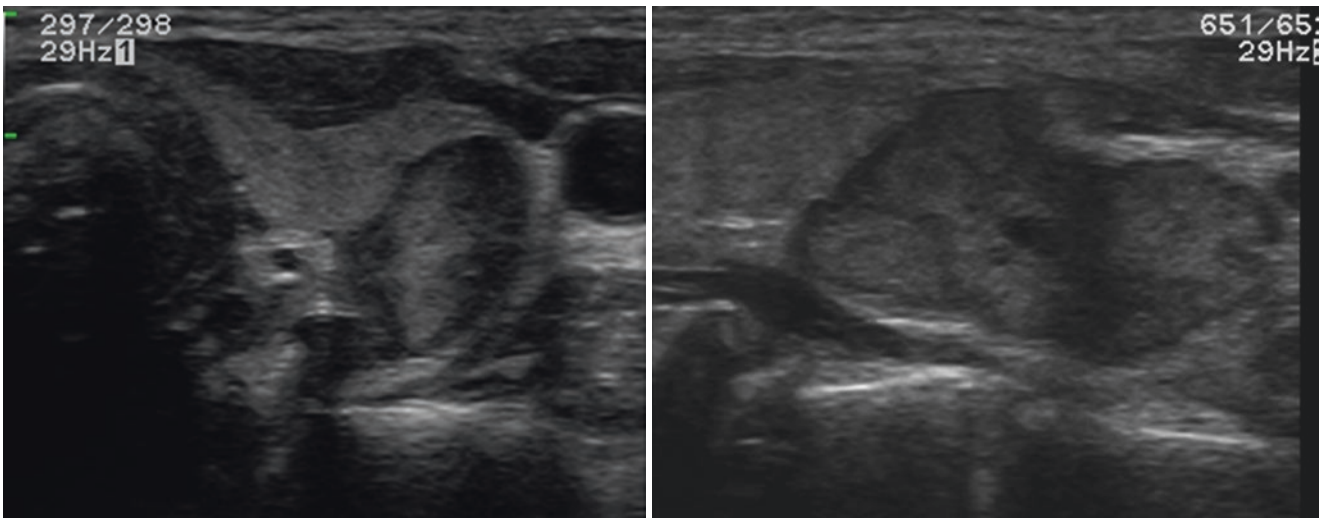

Fig. 13.14 Parathyroid carcinoma (left transverse and sagittal views). Large, hypoechoic mass with irregular borders and infiltration into the adjacent thyroid

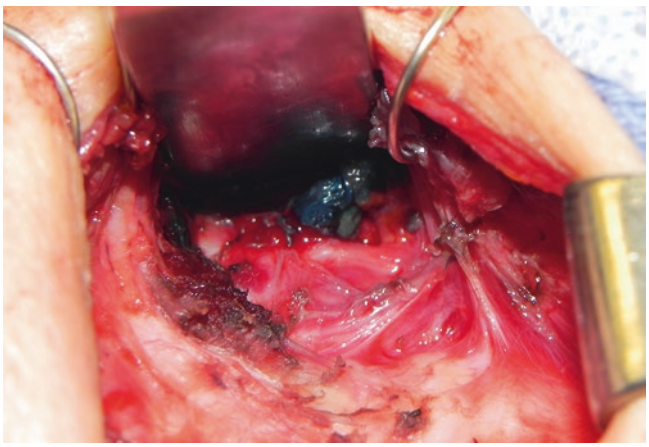

Fig. 13.15 The methylene blue staining of the lesion in the center of this photo makes this parathyroid adenoma readily visible because of its contrasting color compared with surrounding tissues

13.8 Summary

Ultrasound is a critical component in the evaluation of parathyroid pathology. Providing a noninvasive, convenient, radiation-free, and inexpensive way in which to identify diseased glands and anatomic relationships, ultrasound may be used in a complementary fashion or as a single imaging modality. Improved preoperative localization afforded by its technology has played an important role in targeting dissection and increasing the accuracy of parathyroidectomy. Furthermore, sonographic guidance may be applied to additional diagnostic or therapeutic procedures, and, in select cases, may provide a safer alternative to surgery for the correct patient. Specifically, surgeon-performed ultrasound has emerged as a highly effective adjunct to the preoperative clinical evaluation to determine expected anatomy and the location of disease relative to critical structures. Familiarity with sonographic technology and interpretation is, therefore, indispensable to the parathyroid surgeon.

References

1. Giddings CEB, Rimmer J, Weir N. History of parathyroid gland surgery: an historical case series. J Laryngol Otol. 2009;123:1075.
2. Toneto MG, Prill S, Debon LM, Furlan FZ, Steffen N. The history of the parathyroid surgery. Rev Col Bras Cir. 2016;43:214–22.
3. Kalra S, Baruah MP, Sahay R, Sawhney K. The history of parathyroid endocrinology. Indian J Endocrinol Metab. 2013;17:320–2.
4. Bilezikian JP, Doppman JL, Powell D, Wells SA, Heath DA, Ketcham AS, et al. Preoperative localization of abnormal parathyroid tissue. Cumulative experience with venous sampling and arteriography. Am J Med. 1973;55:505–14.
5. Smith RB, Evasovich M, Girod DA, Jorgensen JB, Lydiatt WM, Pagedar NA, Spanos WC. Ultrasound for localization in primary hyperparathyroidism. Otolaryngol Head Neck Surg. 2013;149:366–71.
6. Levy JM, Kandil E, Yau LC, Cuda JD, Sheth SN, Tufano RP. Can ultrasound be used as the primary screening modality for the localization of parathyroid disease prior to surgery for primary hyperparathyroidism? A review of 440 cases. ORL J Otorhinolaryngol Relat Spec. 2011;73:116–20.
7. Bennedbæk FN, Karstrup S, Hegedüs L. Percutaneous ethanol injection therapy in the treatment of thyroid and parathyroid diseases. Eur J Endocrinol. 1997;136:240–50.
8. Untch BR, Adam MA, Scheri RP, Bennett KM, Dixit D, Webb C, et al. Surgeon-performed ultrasound is superior to 99Tc-sestamibi scanning to localize parathyroid adenomas in patients with primary hyperparathyroidism: results in 516 patients over 10 years. J Am Coll Surg. 2011;212:522–9; discussion 529–31.
9. Schenk WG, Hanks JB, Smith PW. Surgeon-performed ultrasound for primary hyperparathyroidism. Am Surg. 2013;79:681–5.

10. Mohammadi A, Moloudi F, Ghasemi-Rad M. The role of colour Doppler ultrasonography in the preoperative localization of parathyroid adenomas. Endocr J. 2012;59:375–82.
11. Najafian A, Kahan S, Olson MT, Tufano RP, Zeiger MA. Intraoperative PTH may not be necessary in the management of primary hyperparathyroidism even with only one positive or only indeterminate preoperative localization studies. World J Surg. 2017;41:1500–5.
12. Smith N, Magnuson JS, Vidrine DM, Kulbersh B, Peters GE. Minimally invasive parathyroidectomy: use of intraoperative parathyroid hormone assays after 2 preoperative localization studies. Arch Otolaryngol Head Neck Surg. 2009;135:1108–11.
13. Barczynski M, Konturek A, Cichon S, Hubalewska-Dydejczyk A, Golkowski F, Huszno B. Intraoperative parathyroid hormone assay improves outcomes of minimally invasive parathyroidectomy mainly in patients with a presumed solitary parathyroid adenoma and missing concordance of preoperative imaging. Clin Endocrinol. 2007;66:878–85.
14. Patel KN, Caso R. Intraoperative parathyroid hormone monitoring. Surg Oncol Clin N Am. 2016;25:91–101.
15. Solorzano CC, Carneiro-Pla D. Minimizing cost and maximizing success in the preoperative localization strategy for primary hyperparathyroidism. Surg Clin North Am. 2014;94:587–605.
16. Lubitz CC, Stephen AE, Hodin RA, Pandharipande P. Preoperative localization strategies for primary hyperparathyroidism: an economic analysis. Ann Surg Oncol. 2012;19:4202–9.
17. Chandramohan A, Sathyakumar K, Irodi A, Abraham D, Paul MJ. Causes of discordant or negative ultrasound of parathyroid glands in treatment naïve patients with primary hyperparathyroidism. Eur J Radiol. 2012;81:3956–64.
18. Hinson AM, Lee DR, Hobbs BA, Fitzgerald RT, Bodenner DL, Stack BC. Preoperative 4D CT localization of nonlocalizing parathyroid adenomas by ultrasound and SPECT-CT. Otolaryngol Head Neck Surg. 2015;153:775–8.
19. Kutler DI, Moquete R, Kazam E, Kuhel WI. Parathyroid localization with modified 4D-computed tomography and ultrasonography for patients with primary hyperparathyroidism. Laryngoscope. 2011;121:1219–24.
20. Kebapci M, Entok E, Kebapci N, Adapinar B. Preoperative evaluation of parathyroid lesions in patients with concomitant thyroid disease: role of high resolution ultrasonography and dual phase technetium 99m sestamibi scintigraphy. J Endocrinol Investig. 2004;27:24–30.
21. Cho M, Oweity T, Brandler TC, Fried K, Levine P. Distinguishing parathyroid and thyroid lesions on ultrasound-guided fine-needle aspiration: A correlation of clinical data, ancillary studies, and molecular analysis. Cancer Cytopathol. 2017;125:674–82.
22. Nagarkatti SS, Mekel M, Sofferman RA, Parangi S. Overcoming obstacles to setting up office-based ultrasound for evaluation of thyroid and parathyroid diseases. Laryngoscope. 2011;121:548–54.
23. Bilezikian JP, Bandeira L, Khan A, Cusano NE. Hyperparathyroidism. Lancet. 2018;391:168–78.
24. Roh JL, Kim JM, Park CI. Central compartment reoperation for recurrent/persistent differentiated thyroid cancer: patterns of recurrence, morbidity, and prediction of postoperative hypocalcemia. Ann Surg Oncol. 2011;18:1312–8.
25. Mohebati A, Shaha AR. Anatomy of thyroid and parathyroid glands and neurovascular relations. Clin Anat. 2012;25:19–31.
26. Brauckhoff M, Walls G, Brauckhoff K, Thanh P, Thomusch O, Dralle H. Identification of the non-recurrent inferior laryngeal nerve using intraoperative neurostimulation. Langenbeck's Arch Surg. 2002;386:482–7.
27. Tsui PH, Wan YL, Chen CK. Ultrasound imaging of the larynx and vocal folds: recent applications and developments. Curr Opin Otolaryngol Head Neck Surg. 2012;20:437–42.
28. Miles KA. Ultrasound demonstration of vocal cord movements. Br J Radiol. 1989;62:871–2.
29. Akerström G, Malmaeus J, Bergström R. Surgical anatomy of human parathyroid glands. Surgery. 1984;95:14–21.
30. Lappas D, Noussios G, Anagnostis P, Adamidou F, Chatzigeorgiou A, Skandalakis P. Location, number and morphology of parathyroid glands: results from a large anatomical series. Anat Sci Int. 2012;87:160–4.
31. Kaufman C, Ray CE Jr, Kumpe D, Keller FS. Vascular anatomy of the parathyroid gland and its relevance to interventional radiology [abstract]. Cardiovasc Intervent Radiol. 2011;34:660.
32. Nobori M, Saiki S, Tanaka N, Harihara Y, Shindo S, Fujimoto Y. Blood supply of the parathyroid gland from the superior thyroid artery. Surgery. 1994;115:417–23.
33. Hojaij F, Vanderlei F, Plopper C, Rodrigues CJ, Jácomo A, Cernea C, et al. Parathyroid gland anatomical distribution and relation to anthropometric and demographic parameters: a cadaveric study. Anat Sci Int. 2011;86:204–12.
34. Mazzeo S, Caramella D, Lencioni R, Viacava P, De Liperi A, Naccarato AG, et al. Usefulness of echo-color Doppler in differentiating parathyroid lesions from other cervical masses. Eur Radiol. 1997;7:90–5.
35. Lane MJ, Desser TS, Weigel RJ, Jeffrey RB. Use of color and power Doppler sonography to identify feeding arteries associated with parathyroid adenomas. AJR Am J Roentgenol. 1998;171:819–23.
36. Mohammadi A, Moloudi F, Ghasemi-Rad M. Preoperative localization of parathyroid lesion: diagnostic usefulness of color doppler ultrasonography. Int J Clin Exp Med. 2011;5:80–6.
37. Heller MT, Yip L, Tublin ME. Sonography of intrathyroid parathyroid adenomas: are there distinctive features that allow for preoperative identification? Eur J Radiol. 2013;82:e22–7.
38. Owens CL, Rekhtman N, Sokoll L, Ali SZ. Parathyroid hormone assay in fine-needle aspirate is useful in differentiating inadvertently sampled parathyroid tissue from thyroid lesions. Diagn Cytopathol. 2008;36:227–31.
39. Anari H, Bashardoust B, Pourissa M, Refahi S. The diagnostic accuracy of high resolution ultrasound imaging for detection of secondary hyperparathyroidism in patients with chronic renal failure. Acta Med Iran. 2011;49:527–30.
40. Meola M, Petrucci I, Colombini E, Barsotti G. Use of ultrasound to assess the response to therapy for secondary hyperparathyroidism. Am J Kidney Dis. 2011;58:485–91.
41. Tamler R, Lewis MS, LiVolsi VA, Genden EM. Parathyroid carcinoma: ultrasonographic and histologic features. Thyroid. 2005;15:744–5.
42. Owen RP, Silver CE, Pellitteri PK, Shaha AR, Devaney KO, Werner JA, et al. Parathyroid carcinoma: a review. Head Neck. 2011;33:429–36.
43. Thompson LDR. Parathyroid carcinoma. Ear Nose Throat J. 2009;88:722–4.
44. Abraham D, Sharma P, Bentz J, Gault P, Neumayer L, McClain D. Utility of ultrasound-guided fine-needle aspiration of parathyroid adenomas for localization before minimally invasive parathyroidectomy. Endocr Pract. 2007;13:333–7.
45. Candell L, Campbell MJ, Shen WT, Gosnell JE, Clark OH, Duh QY. Ultrasound-guided methylene blue dye injection for parathyroid localization in the reoperative neck. World J Surg. 2014;38:88–91.
46. Ryan WR, Orloff LA. Intraoperative tumor localization with surgeon-performed ultrasound-guided needle dye injection. Laryngoscope. 2011;121:1651–5.

47. Haciyanli M, Koruyucu MB, Erdoğan NK, Dere O, Sarı E, Kumkumoğlu Y, et al. Successful localization of abnormal parathyroid gland using ultrasound-guided methylene blue dye injection in the reoperative neck. Indian J Surg. 2015;77:1094–7.
48. Vergès B, Cercueil JP, Jacob D, Vaillant G, Brun JM. Treatment of parathyroid adenomas with ethanol injection under ultrasonographic guidance. [Article in French]. Ann Chir. 2000;125:457–60; discussion 460–1.
49. Mauz P, Stiegler M, Holderried M, Brosch S. Complications of ultrasound guided percutaneous ethanol injection therapy of the thyroid and parathyroid glands. Ultraschall der Medizin – Eur J Ultrasound. 2005;26:142–5.
50. Stratigis S, Stylianou K, Mamalaki E, Perakis K, Vardaki E, Tzenakis N, et al. Percutaneous ethanol injection therapy: a surgery-sparing treatment for primary hyperparathyroidism. Clin Endocrinol. 2008;69:542–8.
51. Schamp S, Dünser E, Schuster H, Kramer-Deimer J, Kettenbach J, Funovics M, et al. Ultrasound-guided percutaneous ethanol ablation of parathyroid hyperplasia: preliminary experience in patients on chronic dialysis. Ultraschall Med. 2004;25:131–6.
52. Fletcher S, Kanagasundaram NS, Rayner HC, Irving HC, Fowler RC, Brownjohn AM, et al. Assessment of ultrasound guided percutaneous ethanol injection and parathyroidectomy in patients with tertiary hyperparathyroidism. Nephrol Dial Transplant. 1998;13:3111–7.
53. Chen HH, Lin CJ, Wu CJ, Lai CT, Lin J, Cheng SP, Yang TL. Chemical ablation of recurrent and persistent secondary hyperparathyroidism after subtotal parathyroidectomy. Ann Surg. 2011;253:786–90.

14 Sonography of the Paranasal Sinuses, Soft Tissues of the Face, Orbit, and Bony Structures of the Face

Hans J. Welkoborsky

Ultrasonography of the soft tissues in the face, of the paranasal sinuses, and of the orbit is not as common as examinations of the neck, thyroid glands, or salivary glands. One reason for this lies in the anatomy that makes ultrasonographic imaging sometimes impossible. The first part of this chapter focusses on anatomical and technical remarks for ultrasonography of the face and paranasal sinuses. Both common techniques, A-mode and B-mode sonography, are described with their diagnostic accuracy and their advantages and limitations. The second part of the chapter describes typical sonographic characteristics of particular diseases, e.g., acute and chronic sinusitis, inflammatory diseases of facial soft tissues, and masses of the soft tissues. The third part of the chapter details sonography of the orbit and its adnexa.

14.1 Introduction

Ultrasonographic examinations of the soft tissues in the face, of the paranasal sinuses, and of the orbits are not as common as examinations of the neck or salivary glands. One reason lies in the anatomy: the soft tissue layers in the face are usually relatively thin. Underneath these soft tissues, the bony structures that mainly form the face are predominant and reflect more than 90% of all ultrasound energy. The bony structures surround the paranasal sinuses, and in healthy conditions, they are filled with air, which does not reflect sufficient sound energy to create interpretable images [1]. Pathologic conditions in the soft tissues of the face and in the paranasal sinuses and orbits, however, sometimes create fairly typical ultrasound characteristics that make this technique suitable to be applied in this area, rather than other imaging techniques.

Of the paranasal sinuses, only the maxillary sinuses and the frontal sinuses are accessible for ultrasound. Studies published on this issue are rare, and some date from 20 years ago or even earlier, but many of these studies have shown good correlations between plain x-ray, CT scans, and ultrasound findings in a population of patients with acute and chronic sinus disease [2–6]. The sphenoid sinus and the anterior ethmoid sinuses are usually withdrawn from ultrasound examinations because of the very thick bony structures that lie between the ultrasound transducer and the sinus. On the other hand, the posterior ethmoid cells can be assessed by using the eyeball as a water path for ultrasound imaging of these structures, which lie deep in the head. Ultrasound of the middle and inner ear is not possible with the currently available technology and equipment, because the thickness of the temporal bone prevents most ear structures from being visualized by ultrasonography [1].

The soft tissues of the face are relatively superficial, so they are easily accessible for ultrasonography. Ultrasound also provides some important information about pathologic conditions of the bones, such as bony fractures of the zygoma, the infraorbital or supraorbital rim, or the nasal skeleton, and it can therefore contribute to differential diagnosis. With its easy accessibility in institutions equipped for ultrasonography, it can serve as a first-line assessment for screening of trauma and infectious or tumorous conditions and pathologies, rather than more complex imaging techniques such as CT scans. This advantage is especially important in the office setting or for patients for whom radiation exposure should be avoided, such as children and pregnant women. This chapter focuses on the indications, technique, and typical findings of ultrasonography in the soft tissues of the face, the paranasal sinuses, and the orbit.

14.2 Anatomical Remarks

The soft tissue layers in the face consist of the skin, the subcutaneous adipose tissue, and flat muscles. Underneath these relatively thin, soft tissues are located the bony structures, which create a more significant acoustic mismatch. The soft

H. J. Welkoborsky (✉)
Department of Otorhinolaryngology, Head and Neck Surgery, KRH Nordstadt Clinic–Academic Hospital, Hanover, Germany
e-mail: hans-juergen.welkoborsky@krh.eu

© Springer Nature Switzerland AG 2019

H. J. Welkoborsky, P. Jecker (eds.), *Ultrasonography of the Head and Neck*, https://doi.org/10.1007/978-3-030-12641-4_14

tissues, which are located superficially, are easily accessible for ultrasound imaging, but only the superficially located bony structures can be examined by sonography. Therefore only fractures and other bony discontinuities of the nasal skeleton, the mandible, or the orbital walls can be visualized, along with bony swellings such as those due to a bony tumor.

The frontal sinuses are slightly curved; their expansion underlies significant interindividual variations. The anterior bony wall of the frontal sinuses can easily be examined by ultrasonography, along with parts of the sinus floor. Secretions, mucosal swellings, or cystic lesions create typical ultrasound findings in both A-mode and B-mode ultrasonography and can therefore be diagnosed with high accuracy. The maxillary sinuses are shaped like a pyramid with its base directed to the cheek. The roof of the sinus is the orbital floor with the infraorbital rim. As in the frontal sinuses, the anterior maxillary sinus wall and the sinus contents can be easily examined. The anterior and posterior ethmoid sinuses are located between the orbits. They can be visualized only in part, using the eyeball as a water path so that the sound can pass [3].

Of the midface bony structures, the infraorbital, supraorbital, and lateral orbital rims can be visualized, along with parts of the mandible and the bones of the nose.

14.3 Technical Remarks

For ultrasound examination of the soft tissue of the face, high-frequency array transducers of 7.5 MHz or above are appropriate. Alternatively, multiband transducers of 7.5–12 MHz might be used. For dermatologic purposes such as estimation of skin infiltration by a tumor, transducers of even higher frequencies (15–20 MHz) should be used. One should keep in mind that the depth of sound penetration decreases with the increase of the transducer's frequency, so the resolution of a high-frequency transducer is excellent in the superficial parts but worse in the deeper tissue layers, as discussed in Chap. 2. For examination of the paranasal sinuses, ultrasound transducers of lower frequencies (3.5 or 5 MHz) are appropriate.

Imaging of the facial bones and soft tissue is performed with the patient lying in a supine position, but ultrasonography of the paranasal sinuses ideally should be performed with the patient sitting upright with anteflexion of the head (Fig. 14.1). This position ensures that if the patient has fluid in the sinus lumen, this fluid has some contact with the anterior bony sinus wall, which is essential for its detection.

Basically, ultrasonography of the paranasal sinuses can be performed in two different technical ways: A-mode sonography (amplitude-mode) or B-mode sonography (brightness or grayscale mode). Ultrasonography of the paranasal sinuses is usually performed using B-mode sonography, but A-mode sonography is historically anchored in Europe as part of the diagnostics of paranasal sinus diseases, especially in an office setting. A-mode sonography can detect mucosal swellings, cysts, and fluid retention in both the maxillary and frontal sinuses. The technique is reliable and simple, which is the reason for its wide application, mainly in Europe [7, 8].

In healthy patients, the echo of the anterior wall of the maxillary and frontal sinuses normally can be detected. It is usually not possible to visualize the posterior wall or to examine the sinus lumen in an air-filled sinus (Fig. 14.2). During acute and chronic sinusitis, with swollen mucosa or retention of fluid, which conducts the ultrasound waves, a second echo from the posterior wall can be visualized.

14.4 Ultrasonography of the Paranasal Sinuses

The main indications for ultrasonography of the paranasal sinuses are detailed in Table 14.1.

14.4.1 Acute Sinusitis

Acute sinusitis is a usually clinical diagnosis, based on the combination of the symptoms: history of rhinitis or acute upper respiratory tract infection, frontal headache that is intensified when the head is bent forward or downward, and sometimes some pus visible in the nasal cavity. Ultrasonography can support this diagnosis. Both A-mode and B-mode sonography are suitable. A-mode sonography shows a broadening of the anterior wall echo in cases without fluid retention and an echo of the posterior wall in cases with fluid retention (pus) (Fig. 14.3). It is important to note that the examination should be performed with the patient in an upright position with the chin directed to the sternum, so that retained fluid is in contact with the anterior sinus wall and thus with the ultrasound transducer. If the patient is supine, fluid retention could be overlooked.

B-mode sonography also shows the anterior bony wall with a broadening of the swollen mucosa behind it. If there is no fluid retention, the posterior wall cannot be visualized (Fig. 14.4). In cases with pus, the posterior wall can be seen.

Some investigations have compared the diagnostic accuracy of ultrasound with that of other imaging techniques in the diagnosis of acute sinusitis. Early studies were performed using A-mode ultrasonography. Zagolski and Strek [8] found a concordance between CT scans and A-mode ultrasound in 58.8% of cases with acute sinusitis and in 85% of cases with chronic sinusitis. The limitation of the technique is that only fluid retention, mucosal swelling, and some cysts can be detected by A-mode sonography without a direct anatomical

Fig. 14.1 (**a**–**d**) Ultrasound examination of the paranasal sinuses with A-mode sonography: The patient is sitting in an upright position with a slightly anteflexion of the head. The ultrasound transducer is placed on the maxillary sinuses and frontal sinuses on both sides. The transducer is moved around the sinus silhouette to detect even minor fluid retentions, cysts, or mucosal swellings in the sinus lumen. The patient's head can be moved in a more anterior position when fluid retention is suspected, so that the fluid comes in contact with the anterior sinus wall, which creates an echo. (**e**–**l**) B-mode ultrasonography of the paranasal sinuses. This patient is also sitting in an upright position with a slightly anteflexion of the head. The anatomical structures can easily be examined by the ultrasound transducer. The examination is performed in two planes, usually in axial and longitudinal planes

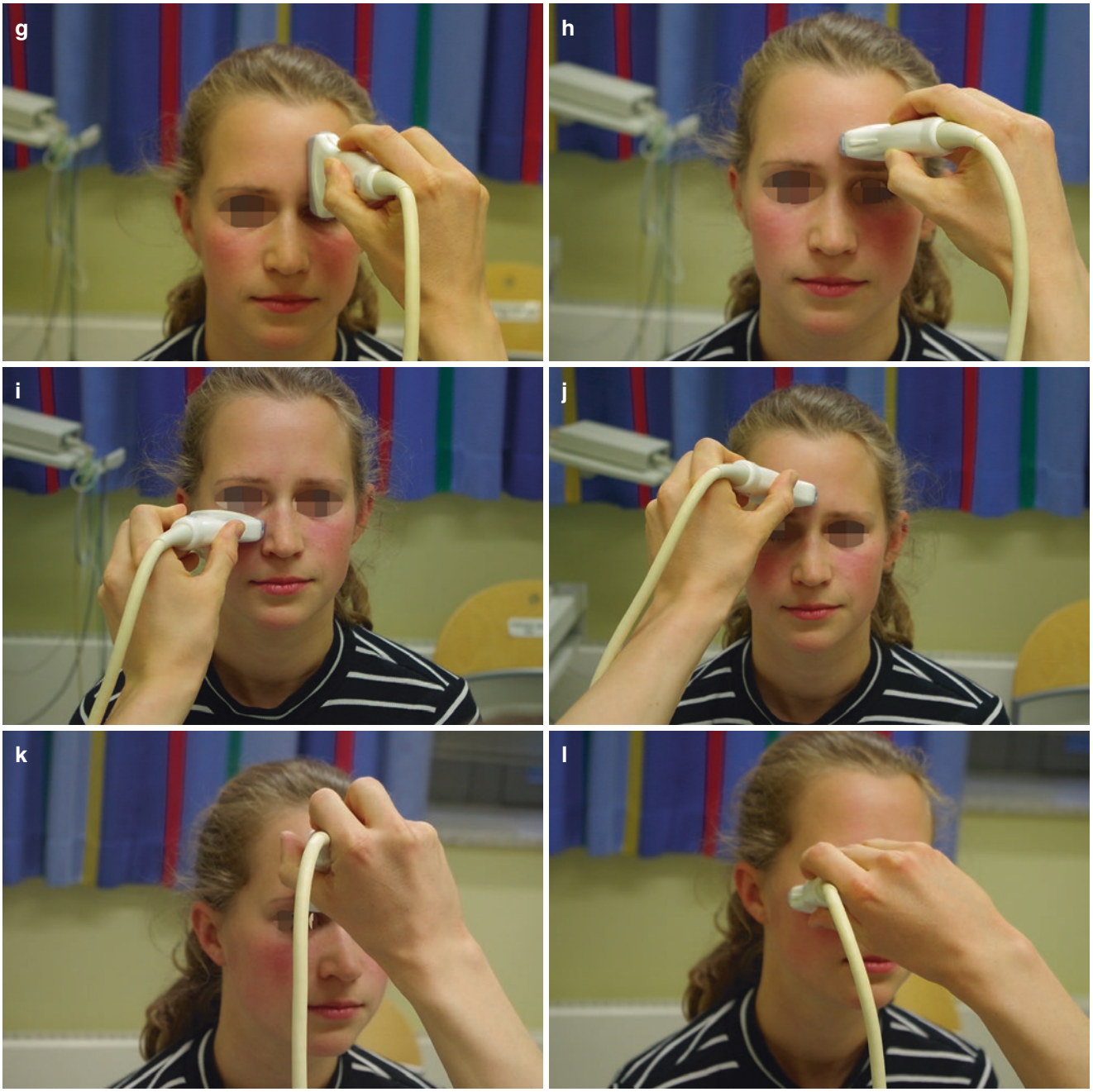

Fig. 14.1 (continued)

context. Others have applied A-mode ultrasonography in patients with asthma to estimate a probable sinus disease. They found at least minimal mucosal thickening in the paranasal sinuses in 74% of the patients. A-mode sonography demonstrated a sensitivity of 70% but a specificity of only 22% for detecting mucosal hyperplasia [9]. For B-mode sonography, rates of concordance between ultrasound, x-ray, and CT scans of 62.5% to 92% were reported [2]. In the setting of an ICU, ultrasound can be used as a bedside diagnostic tool to detect sinusitis [10, 11]; the sensitivity and specificity of 100% are in accordance with other publications [2, 8, 10–14].

A pretty good correlation between ultrasound results and CT scans has also been described for diagnosing acute sinusitis in the maxillary sinus in the pediatric population [15–17]. Some authors described evidence that the loss of a posterior wall echo during therapy of an acute sinusitis correlates well with a decrease of clinical symptoms [17]. Benninger et al. [18] developed an animal model for ultrasound visualization of fluid in the maxillary sinus during microgravity and

Table 14.1 Main indications for A-mode and B-mode sonography of the paranasal sinuses

A-Mode sonography	B-Mode sonography
Confirmation of fluid retention (i.e., acute sinusitis)	Confirmation of fluid retention (i.e., acute sinusitis)
Cysts; mucoceles	Cysts; mucoceles
Confirmation of mucosal swelling (i.e., chronic sinusitis)	Confirmation of mucosal swelling (i.e., chronic sinusitis)
Polyps; tumors	Paranasal sinus tumors
Therapy monitoring (i.e., during antibiotic therapy of an acute sinusitis)	Tumors of the soft tissues of the face and the bony sinus borders
Postoperative care following functional endoscopic sinus surgery	Therapy monitoring (i.e., during antibiotic therapy of an acute sinusitis or chemotherapy of a malignant tumor)
	Suspected bony fractures if x-ray exposure must be avoided
	Postoperative care following functional endoscopic sinus surgery
	Localization of foreign bodies in the maxillary sinus
	Intraoperative application during endonasal endoscopic skull base surgery

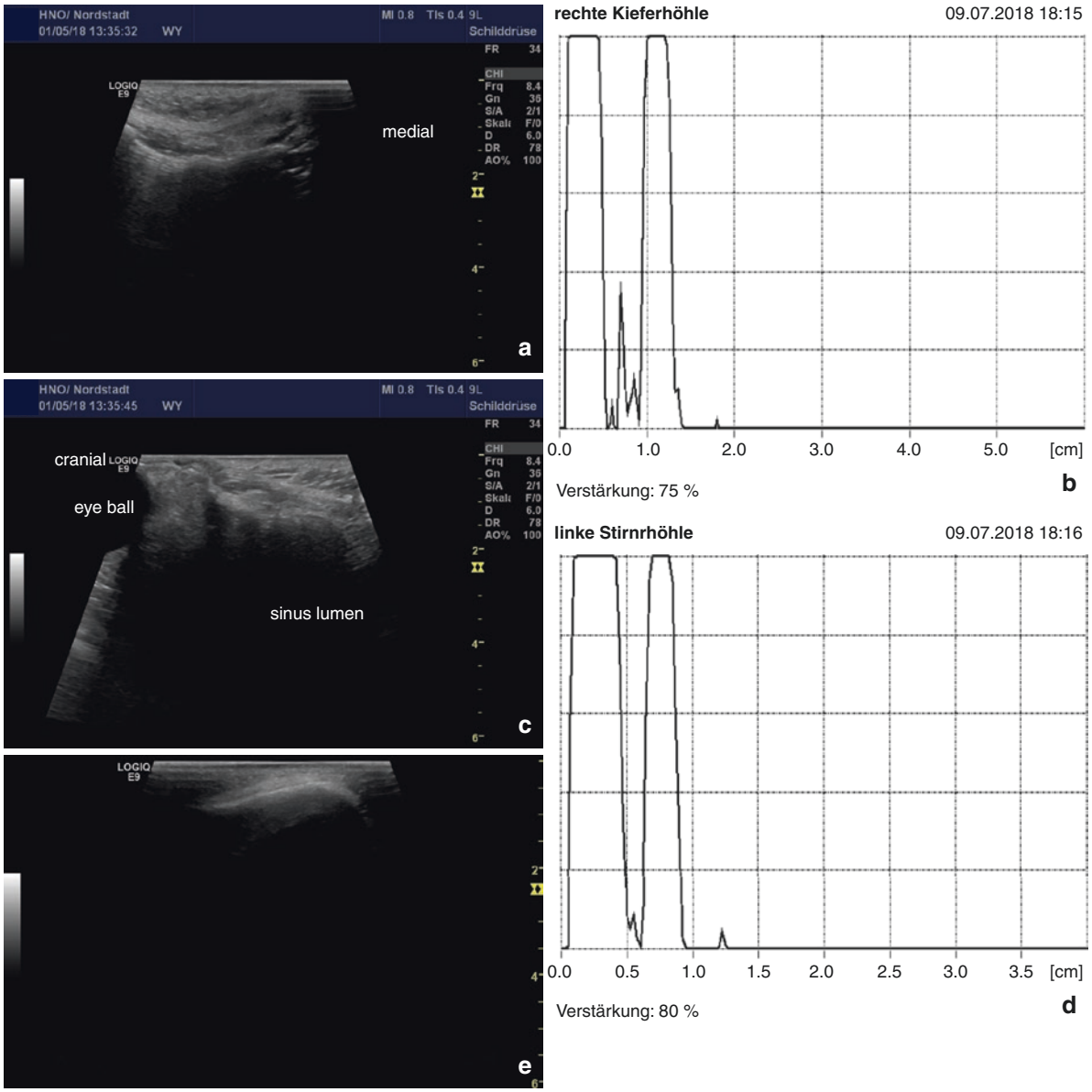

Fig. 14.2 A-mode and B-mode ultrasound of the maxillary sinus in axial and longitudinal section (**a**–**c**) and of the frontal sinus in axial section (**d**, **e**) in a healthy person. The anterior bony wall creates an echo. If there is no fluid retention and no cyst (as in this case), the posterior wall is not visible. The anterior wall of the frontal sinus is slightly curved

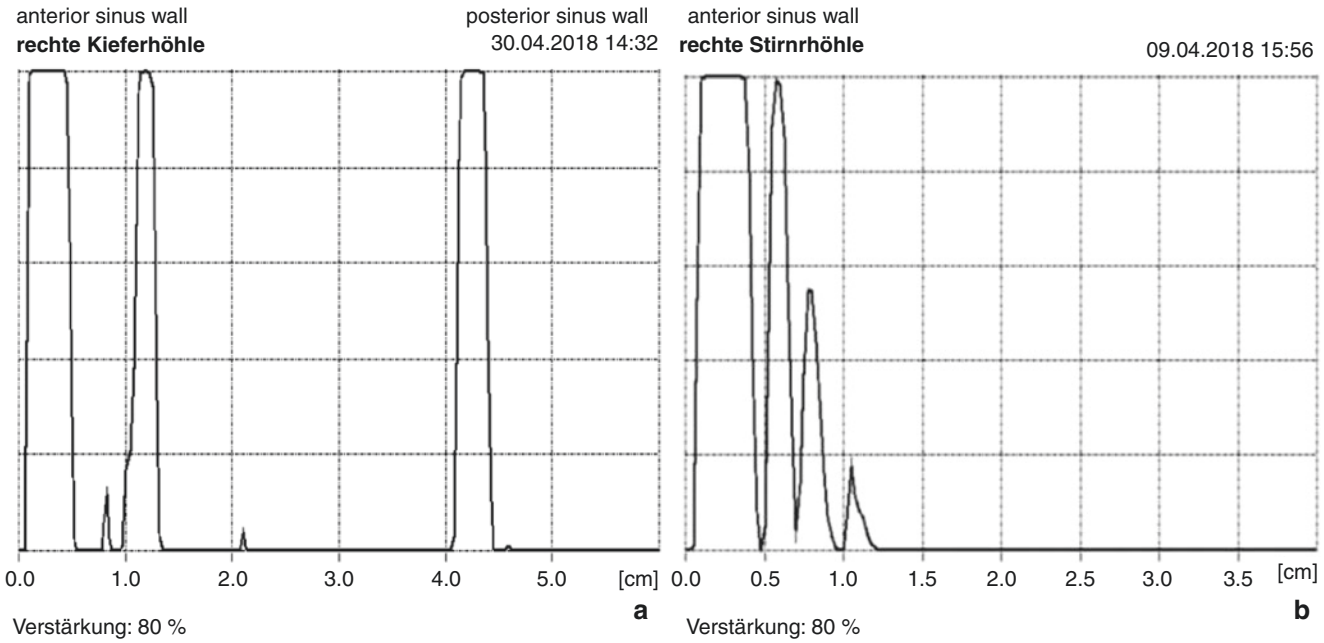

Fig. 14.3 (**a**) A-mode sonography in a patient with acute maxillary sinusitis and fluid retention. A broadening of the anterior wall echo is visible, along with the echo of the posterior wall. (**b**) This patient with frontal sinusitis has no fluid retention, so only the broadening of the anterior wall is visible, not the echo of the posterior wall

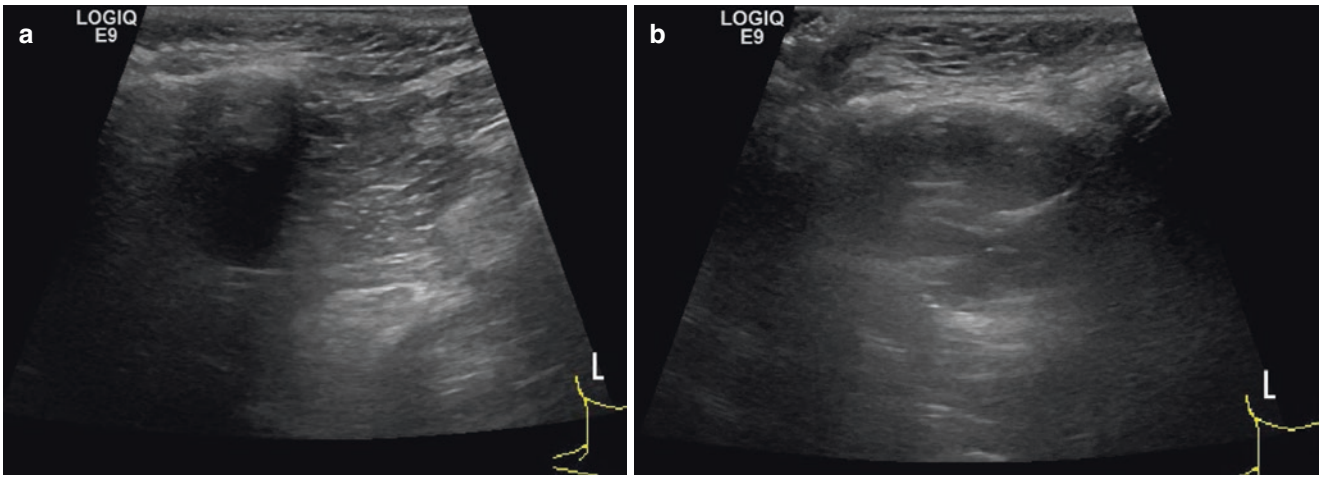

Fig. 14.4 (**a**) B-mode sonography of the maxillary sinus in a patient with acute sinusitis and fluid retention. The swollen mucosa inside the sinus creates a broadening of the anterior wall and the fluid inside the sinus lumen is visible. (**b**) In cases with no fluid retention, only the broadening of the anterior wall due to the swollen mucosa can be displayed, not an echo of the posterior wall

postulated diagnostic criteria for acute bacterial rhinosinusitis in the microgravity environment. Ultrasound has also been applied to help in the localization of foreign bodies in the maxillary sinuses [19].

Thus one can conclude that ultrasound of the paranasal sinuses is a rapid, painless, nonionizing, reproducible, and low-cost imaging technique to confirm a clinical diagnosis of an acute sinusitis [20, 21], which can be applied when ionizing exposure is contraindicated. Further applications for this technique include clinical follow-up and monitoring of antibiotic therapy. In such cases, ultrasound might reduce the need for further radiological imaging and may help to reduce unnecessary antibiotic treatment [21].

14.4.2 Chronic Sinusitis

Chronic sinusitis is also basically a clinical diagnosis [7], suggested by a combination of some of the following symptoms: nasal obstruction, postnasal drip, rhinorrhea,

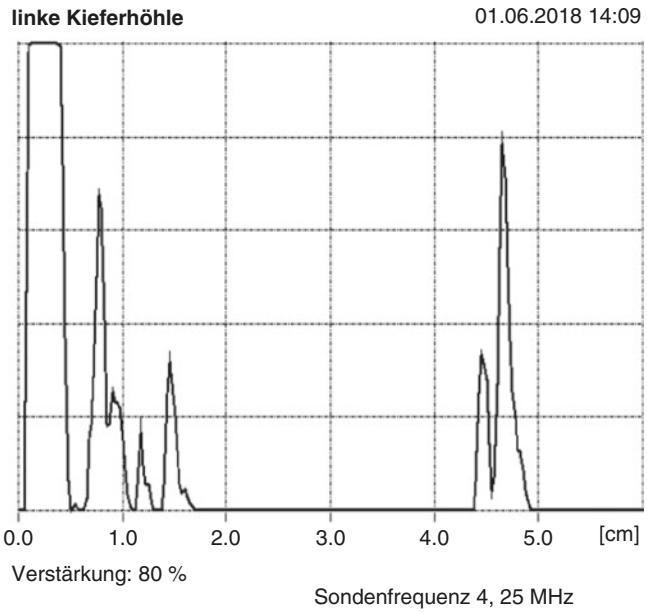

Fig. 14.5 A-mode sonography in a patient with a cyst in the maxillary sinus. In this case, the anterior wall echo is visible. The cystic fluid also creates an echo of the posterior wall of the cyst. According to the depth of the posterior wall, the diameter of the cyst can be determined; it is about 3 cm in this case

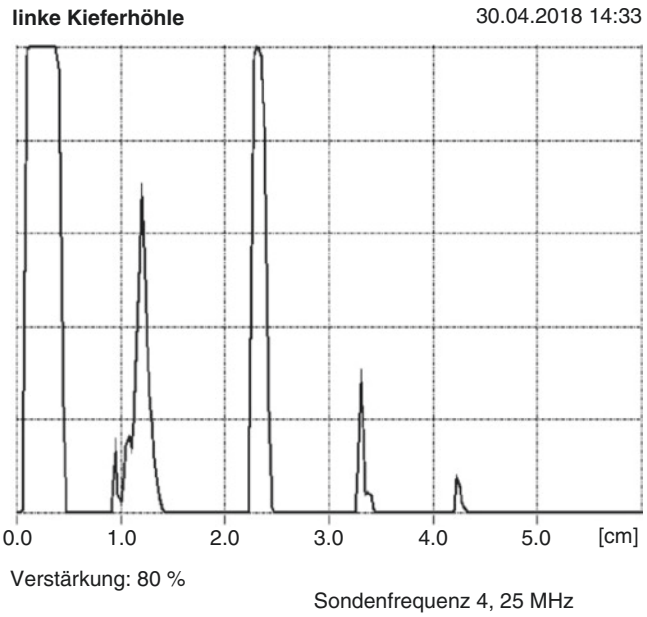

Fig. 14.6 A-mode sonography in polypoid sinusitis. The polyps create some single echoes behind the anterior wall echo

frontal headache or oppression feeling, and recurrent episodes of acute sinusitis. In some cases, patients also suffer from an allergy. The findings in A-mode and B-mode ultrasonography are unspecific. In cases with mucosal swellings, the echo of the anterior sinus wall appears broadened. In cases of fluid retention, the posterior wall is seen. In patients with nonpolypoid chronic rhinosinusitis, A-mode sonography was proven to be helpful in identifying intrasinusoidal liquid contents rather than hypertrophic mucous membranes [7]. Cystic lesions lead to a quite characteristic sonographic appearance in both A-mode (Fig. 14.5) and B-mode sonography: first the anterior wall echo appears, then the echo of the posterior wall of the cyst, and finally the echo of the posterior sinus wall can appear [12]. In cases of polyps, some irregular structures with higher echogenicity appear inside the sinus lumen in B-mode ultrasonography. A-mode sonography sometimes only reveals some single echoes behind the anterior wall echo (Fig.14.6). Different investigators have had difficulty reproducing results, however, especially for A-mode ultrasonography, so some authors conclude that A-mode sonography should not be recommended to diagnose fluid retention or mucosal swelling in patients with chronic mucosal changes [9]. The results for B-mode sonography in chronic nonpolypoid sinusitis are better at detecting mucosal swelling or fluid retention.

The sustained increase in demand for more detailed and precise imaging of the paranasal sinuses to investigate anatomy and the skull base has led to a wide application of CT or cone beam scans in the diagnosis of chronic sinusitis. When operative therapy is planned, CT or cone beam scans of the paranasal sinuses and skull base is mandatory to estimate the olfactory gap and to exclude some anatomical abnormalities of the skull base. In such cases, sonography is only an additive to confirm the suspected diagnosis of a chronic sinusitis, and it has some justification in monitoring of therapy or in the postoperative care of patients following functional endonasal sinus surgery for early detection of fluid retention [8, 12].

14.4.3 Cysts and Mucoceles

Cysts in the paranasal sinuses have a quite characteristic sonographic finding. In B-mode sonography, they appear as a hypoechoic mass only when the cyst is attached to the anterior sinus wall and therefore gets contact to the ultrasound transducer [1, 22, 23]. Some hyperechoic inclusions can occur, representing debris or large protein molecules in the cystic fluid. If the anterior sinus wall is missing, the lesion appears as a round or roundish, well-demarcated mass, the contents of which frequently have a higher echogenicity (Fig. 14.7). In A-mode sonography, the anterior sinus wall echo is followed by an anechoic area. The posterior wall of the cyst causes a second or third echo.

Mucoceles are large, cystic lesions that show some infiltrating growth pattern. They are usually of sinugenic origin; spontaneous mucoceles are extremely rare. In most cases, a history of head injury, paranasal sinus surgery, or recurrent severe sinus inflammations can be determined. Mucoceles

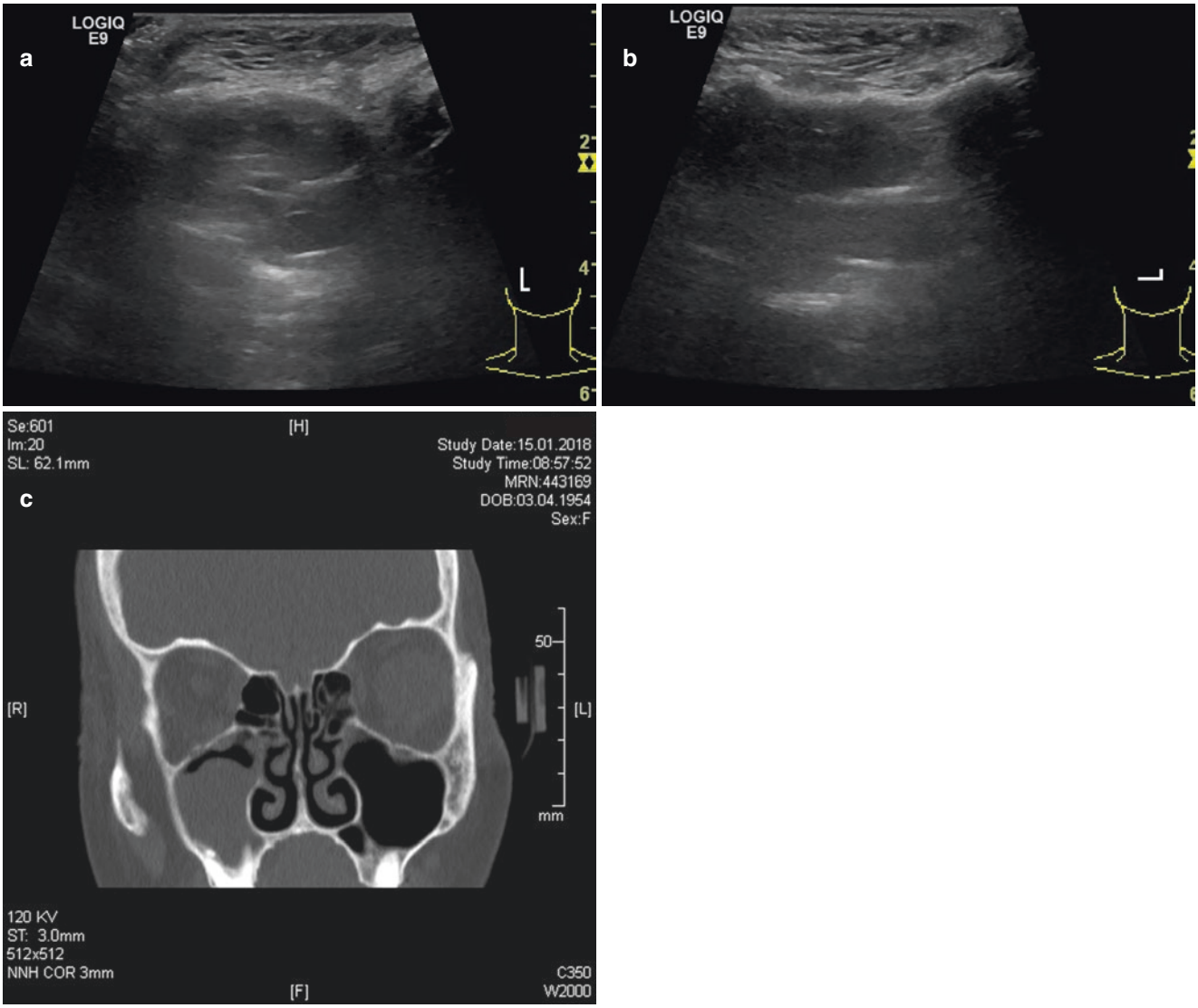

Fig. 14.7 (**a**) B-mode sonography (axial image) in a patient with a cyst in the maxillary sinus. (**b**) Longitudinal image of the same patient. The anterior sinus wall is visible, and the cyst is seen as a roundish, hypoechoic mass. (**c**) CT scan (coronal scan) of the same patient

display as hypoechoic or anechoic masses with clear borders. In most cases, additional finely granulated echoes can be seen inside the lesion, which are due to protein molecules and cell debris in the mucocele content. The echogenicity is often more homogeneous than that of abscesses. A posterior enhancement is apparent in most mucoceles [4, 24]. Dehiscence of the bony walls, enabling the mucocele to grow into neighboring structures, can be detected in many cases (Fig. 14.8).

Color-coded duplex sonography does not reveal any intralesional vessels in either cysts or mucoceles. In contrast to abscesses, usually no hypervascularity is also seen in the vicinity of the mucocele or cyst.

Meningoceles or *meningoencephaloceles* are intracranial lesions that protrude through the skull base through a bony gap. They consist of meninges that surround parts of the central nervous system like a shell. They also contain cerebrospinal fluid. Lesions with extension into the paranasal sinuses and orbit can be visualized by B-mode sonography. Here the bony gap is visible, and the lesion is seen as a hypoechoic mass with some areas of higher echogenicity surrounded by a more hyperechoic, band-like structure, which corresponds to the meninges (Fig. 14.9).

14.4.4 Postoperative Care

Repeated use of ultrasonography takes advantage of its dynamic character and lack of patient inconvenience and radiation exposure. Thus it is suitable for application in postoperative care following paranasal sinus surgery, to exclude fluid retention and to monitor healing. It is also

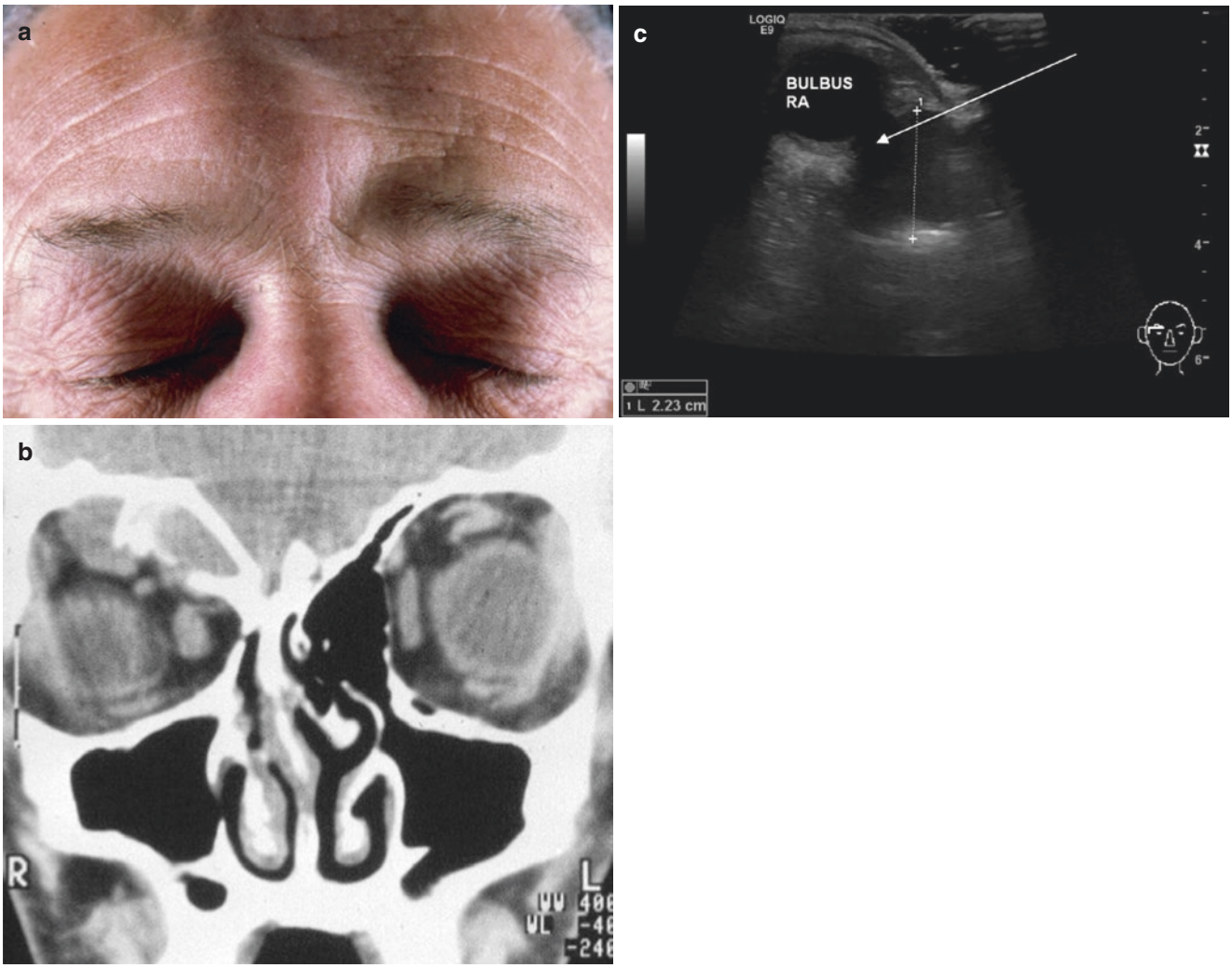

Fig. 14.8 Mucocele of the right frontal sinus. (**a**) Clinical picture shows protrusion of the anterior wall of the sinus. (**b**) In the CT scan, the erosion of the bone is visible. (**c**) B-mode sonography reveals a gap in the bony sinus wall (*arrow*) and the extension of the mucocele into the orbit. The mucocele itself presents as a hypoechoic mass with some complex echogenicity inside the lesion

better than other imaging techniques for monitoring of therapy with topical corticoids. Both A-mode and B-mode sonography can be used for monitoring of therapy and healing, to estimate signs of fluid retention and mucosal swelling [8].

14.4.5 Paranasal Sinus Tumors

Both benign and malignant tumors can occur in paranasal sinuses. Frequent tumors of the paranasal sinuses are inverted papillomas, squamous cell carcinoma, adenocarcinoma, adenoid cystic carcinoma, and malignant lymphoma. Malignant melanoma and sarcomas are less frequent.

There is no typical ultrasound finding for particular tumors. A-mode sonography is limited in the diagnosis of a paranasal sinus tumor. In many cases it reveals only some echoes appearing inside the sinus (when the tumor is limited to the particular sinus), and A-mode sonography cannot detect infiltration into the surrounding tissues; nor does it show other important sonographic features, such as echogenicity or vascularization. Therefore A-mode ultrasonography cannot be recommended as a diagnostic technique if a tumor is suspected.

The diagnostic accuracy of B-mode sonography in patients with paranasal sinus tumors is higher than that of A-mode sonography. Liu et al. [25] found that ultrasound detected 78.1% of tumors, compared with a detectability rate of 96.9% for CT scans. However, sonography showed a higher detectability of tumors in the nasal vestibule and on the wings of the nose, compared with CT [25]. These authors concluded that sonography should be applied especially in these indications (Fig. 14.10).

In many tumorous lesions of the paranasal sinuses, B-mode sonography reveals a hypoechoic mass with

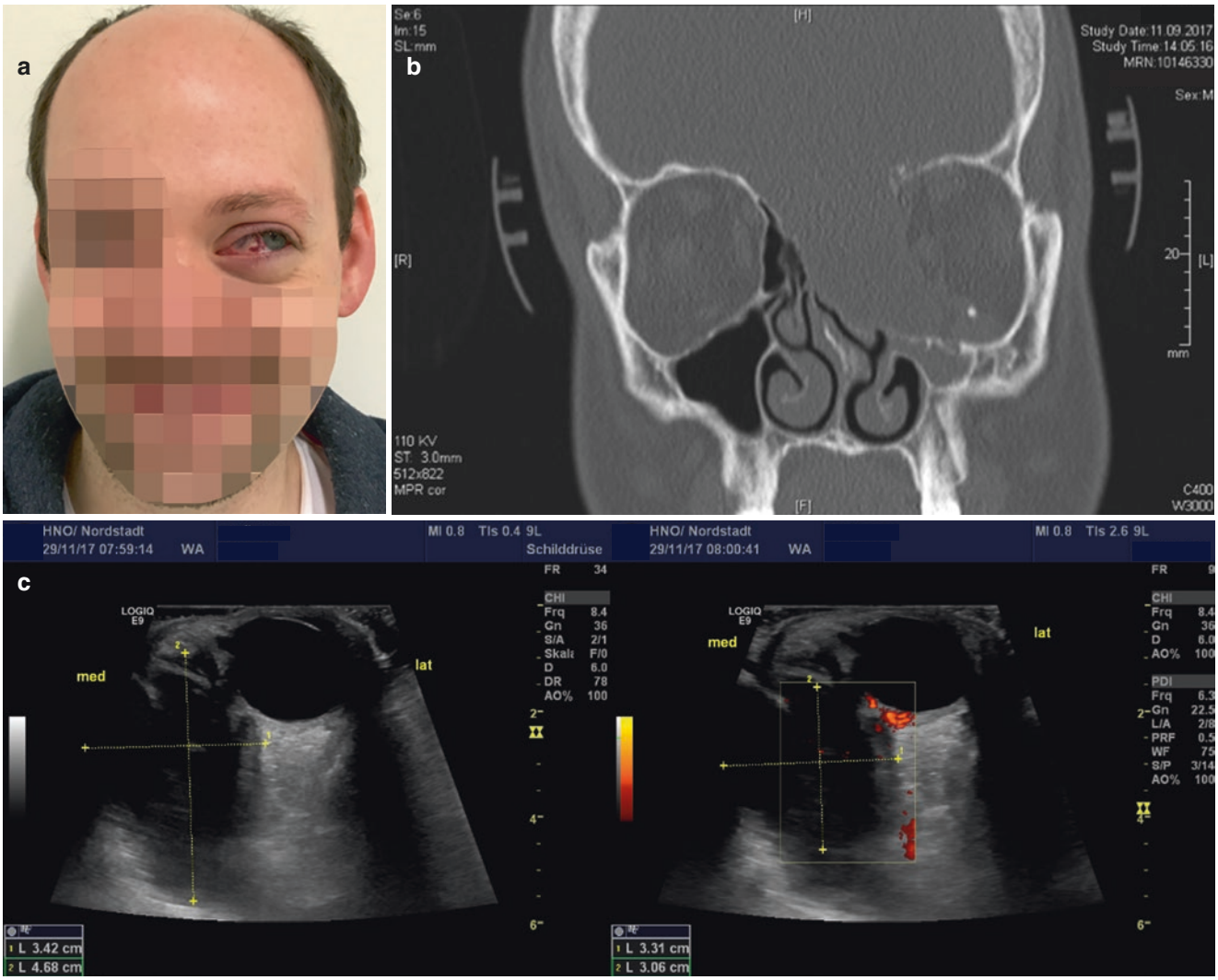

Fig. 14.9 Patient with a meningoencephalocele of the left skull base with involvement of the paranasal sinuses and the orbit. (**a**) The eye bulb is displaced and deviated to the left side. (**b**) The CT scan shows the bony gap in the frontal skull base, with prolapse of the meninges and some intracranial structures into the ethmoid sinuses and into the orbit. (**c**) B-mode sonography reveals a hypoechoic or anechoic mass that is surrounded by a capsule-like structure, which represents the meninges. Blood vessels are visible only in this region

frequent areas of higher or complex echogenicity inside the sinus lumen. Hypoechoic or echo-complex masses with inhomogeneous echogenicity are common, depending on histology. Other sonographic features, including shape, internal echogenicity, calcification, bone infiltration, or borders can be estimated, and an examination of the neck in patients with malignant tumors can be used to exclude cervical lymphadenopathy. If the tumor has infiltrated the surrounding tissue, B-mode sonography shows an infiltrative growth pattern, and the stage of the infiltration can be estimated. Even T-staging of a maxillary tumor is possible by sonography in some cases [26].

A cytologic or histologic examination is required when sinus tumors or metastasis is suspected. Color-coded duplex sonography is advantageous for estimating tumor vascularization and for differential diagnostic purposes [22, 25]. A higher vascularization can be detected for some tumors, such as metastases of renal cancer.

14.5 Ultrasonography of the Bony Structures in the Midface

Because of the high acoustic mismatch of bony structures, ultrasound waves are reflected almost completely. Therefore the intact bone appears as a hyperechoic, band-like structure. Fractures lead to a disruption of continuity at the surface of the bone. With modern ultrasound

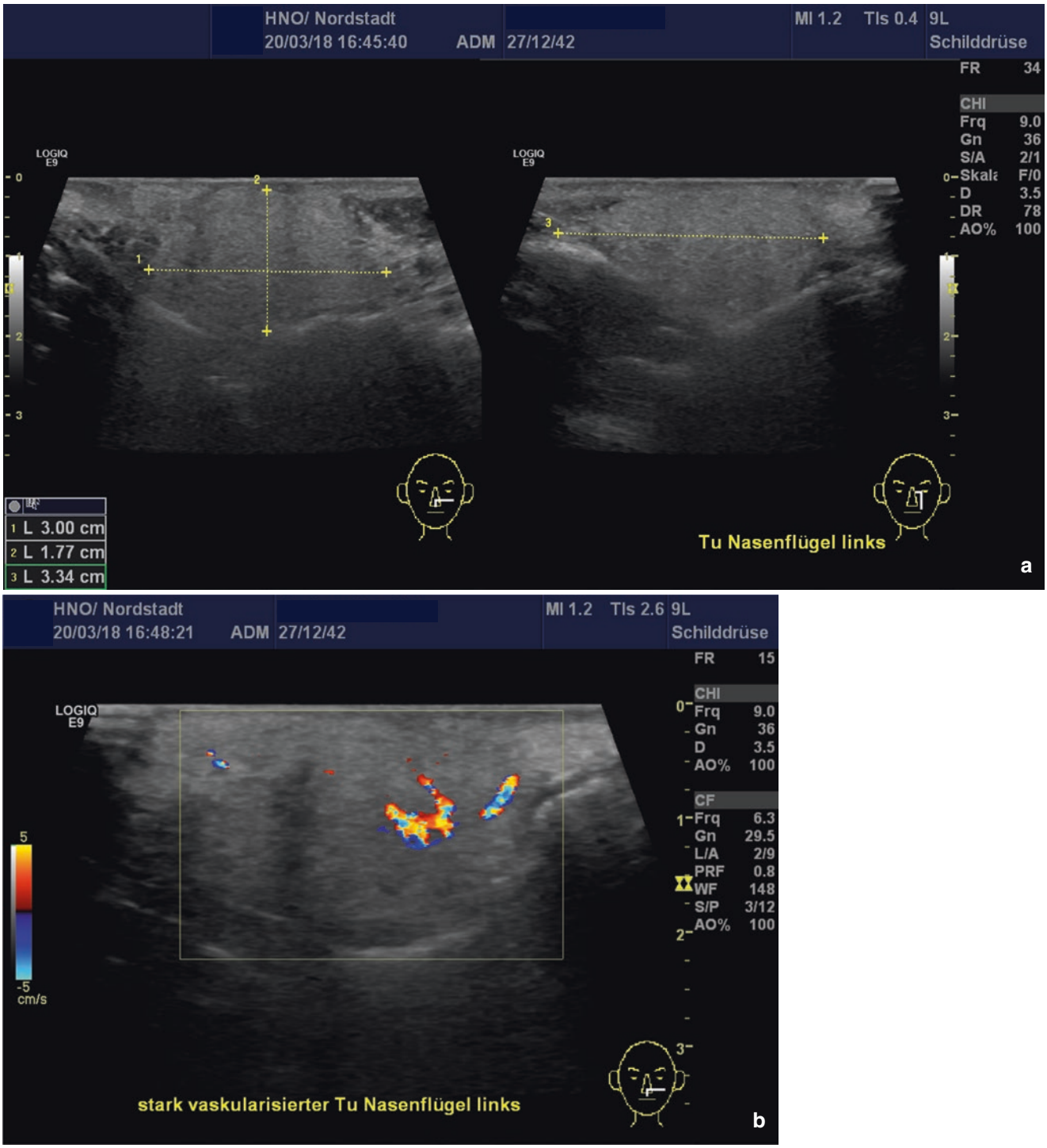

Fig. 14.10 Tumor of the nasal wing. (**a**) Sonographically the tumor presents as an unsharp-bordered echo-complex mass, which lies on the underlying cartilage. Histologically this was an angiolymphoma. (**b**) Duplex sonography visualizes some relatively large intralesional vessels

equipment with multiband linear array transducers (7–15 MHz) or a hockey stick probe, it is possible to distinguish between fractures that are dislocated or not dislocated [27]. Owing to the curved shape of the bones, small ultrasound transducers with ultrasound gel are required for accurate examination.

14.5.1 Fractures of the Nasal Bones

The bony nasal pyramid can be investigated by B-mode sonography. For fracture identification, ultrasound achieves a diagnostic accuracy as high or even higher than that of conventional x-ray and CT scans, reaching a sensitivity of nearly

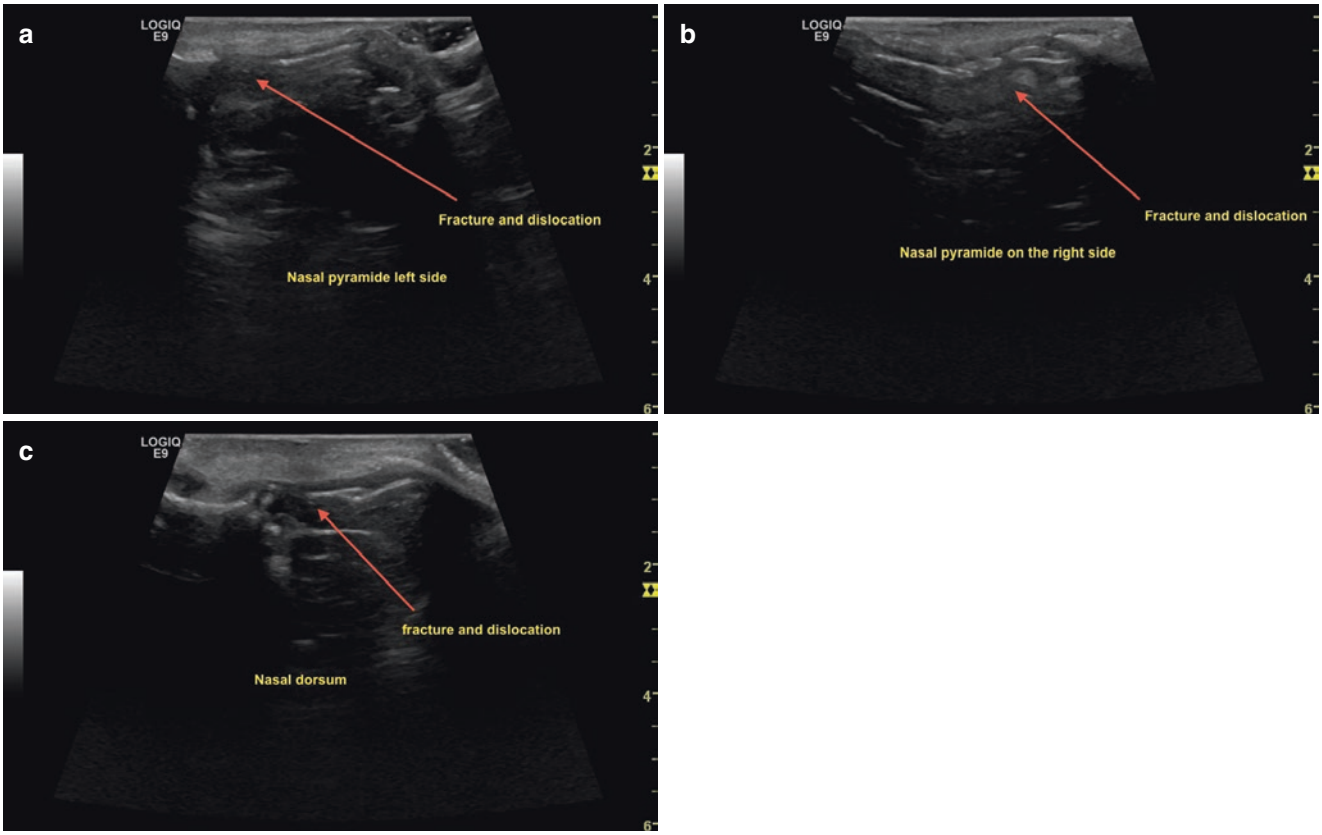

Fig. 14.11 Nasal bone fracture. The fracture is clearly detectable by a discontinuity of the bone and a dislocation of the bone fragments. Lateral right (**a**) left (**b**) and nasal dorsum (**c**). The dislocation of the bones is clearly visible

100% [8, 27–29], so that conventional radiography can be replaced by ultrasound [30]. Fractures of the nasal bones are especially easy to visualize by a discontinuity of the bone, as these structures are located superficially. A dislocation and its severity also can be assessed (Fig. 14.11). One advantage of ultrasound compared with x-ray is also that it allows evaluation of the soft tissues overlying the bones. This is important, because the soft tissues often show a significant swelling from posttraumatic hematoma. With ultrasound, it is possible to distinguish between a fracture and a pseudo-deviation of the nose due to a hematoma [28]. Sonography is also highly recommended when a nasal fracture is suspected in a child or a pregnant woman [31].

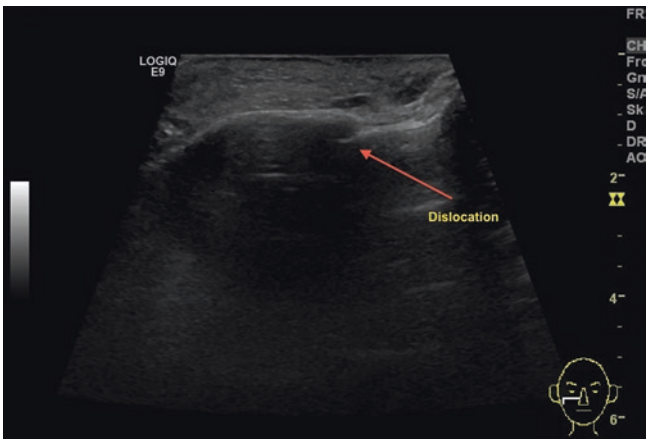

Fig. 14.12 Fracture of the zygoma/infraorbital rim

14.5.2 Fractures of the Zygoma, Maxillary Sinus Wall, and Frontal Bone

Fractures of the maxillary sinus, the frontal bone, and the zygomatic arch are easily assessable with ultrasound. In all cases, ultrasound is able to penetrate a soft tissue swelling. The sensitivity and overall diagnostic accuracy of ultrasound in detecting fractures of these bones and the mandible are more than 90% [32–34], which justifies the use of ultrasonography in detecting maxillofacial fractures [33, 35]. Fractures always are seen as a discontinuity of the hyperechoic bone. Indications for an operation can also be made by ultrasound, depending on the degree of dislocation of the bony fragments (Fig. 14.12). This is particularly important in

fractures of the frontal bone and/or the anterior wall of the frontal sinus. In these cases, the ultrasound examination achieves a high degree of agreement with CT scans and is even better than conventional x-ray.

In conclusion, ultrasound is suitable for fracture diagnosis, with the advantage of no radiation exposure. It is also suitable for intraoperative application to determine the results of repositioning, with a chance for correction if the reposition is inadequate. The limitation of this technique lies in the inadequate visualization of deeper bony structures or in quantifying the degree and severity of fracture fragment dislocation, for which a conventional or cone beam CT scan is required [35].

Fig. 14.13 Abscess formation in the nasal slope. B-mode sonography, axial plane. The lesion is seen as a hypoechoic mass beneath the skin with unsharp borders. The underlying bone is intact. Axial plane

14.5.3 Tumorous Lesions of the Bones

Bony tumors frequently occurring in the head are fibrous dysplasia, hemangioma, and osteoma; malignant conditions like osteosarcoma are very rare. Sonographically, most of these lesions appear as a circumscribed, hypoechoic enlargement and swelling of the bone, with some echo-complex areas. When the compacta of the bone is involved, the result is a discontinuity and disturbance of the smooth surface.

14.6 Ultrasonography of the Soft Tissues in the Face and Mastoid

14.6.1 Abscesses

Abscesses in the soft tissues of the face are usually of dental or sinugenic origin or are caused by a skin infection (folliculitis). Their location may be adjacent to the mandible (for dentogenic origin) or to the anterior wall of the maxillary sinus (for sinugenic origin). In cases of dermatologic origin, the abscess can occur at any location in the face. For sonographic examination, only B-mode ultrasonography is suitable. Abscesses are characterized sonographically like other fluid-filled processes, by a visible rim, decreased echogenicity, and posterior enhancement. The echo itself might be heterogeneous (Fig. 14.13). Color-coded sonography often reveals hypervascularity in the vicinity of the abscess. Sonography can be used for guidance of a needle for aspiration of abscess contents under direct view.

14.6.2 Benign Lesions

Benign lesions are often located superficially and have their origin in the cutis and subcutaneous adnexa. *Atheromas* are the most frequent lesion in this group. They arise from the sebaceous glands and appear as clearly bordered, hypoechoic masses located beneath the skin or at the skin level. In many cases, some fine, granulated acoustic echoes can be seen inside the lesion, which may be due to cell debris or large protein molecules in the lesion's content (Fig. 14.14).

Pilomatrixoma (also known as *epithelioma calcificans Malherbe*) is a benign tumor that arises from the hair follicles or sebaceous glands; it occurs frequently in the head and neck region of children [36]. Histologically, cystic areas with necrotic cells and calcifications are predominant, in some cases with some foreign-body giant cells. Depending on the degree of calcification, the lesion may feel tough or even hard upon palpation. The sonographic appearance of this tumor differs depending on the particular subtype, especially on the degree of calcification. Highly calcified lesions display as echo-complex or hyperechoic masses with a distinct border to the dermis and with a posterior enhancement. In highly calcified lesions, however, the border toward the deeper tissue layers may be worse, so this lesion can be misinterpreted as a malignant tumor. Tumors with minor calcification appear as hypoechoic, well-bordered masses with minor dorsal enhancement [36]. Color-coded duplex sonography reveals no or little vascularization (Fig. 14.15).

Tumors of the connective tissue are *fibromas*. Other benign mesenchymal tumors include *myoma*, *neurinoma*, *lipoma*, or *hemangioma*. Fibroma, myoma, and neurinoma usually display as hypoechoic or echo-complex masses that sometimes have unclear borders (especially in the case of fibromas, which do not have a capsule). The underlying bony structures are not involved or infiltrated. Neurinomas often contain some pseudocystic lesions, which may be due to degenerative processes. Lipomas show a characteristic feather-like pattern. Color-coded duplex sonography reveals only minor vascularization in these lesions.

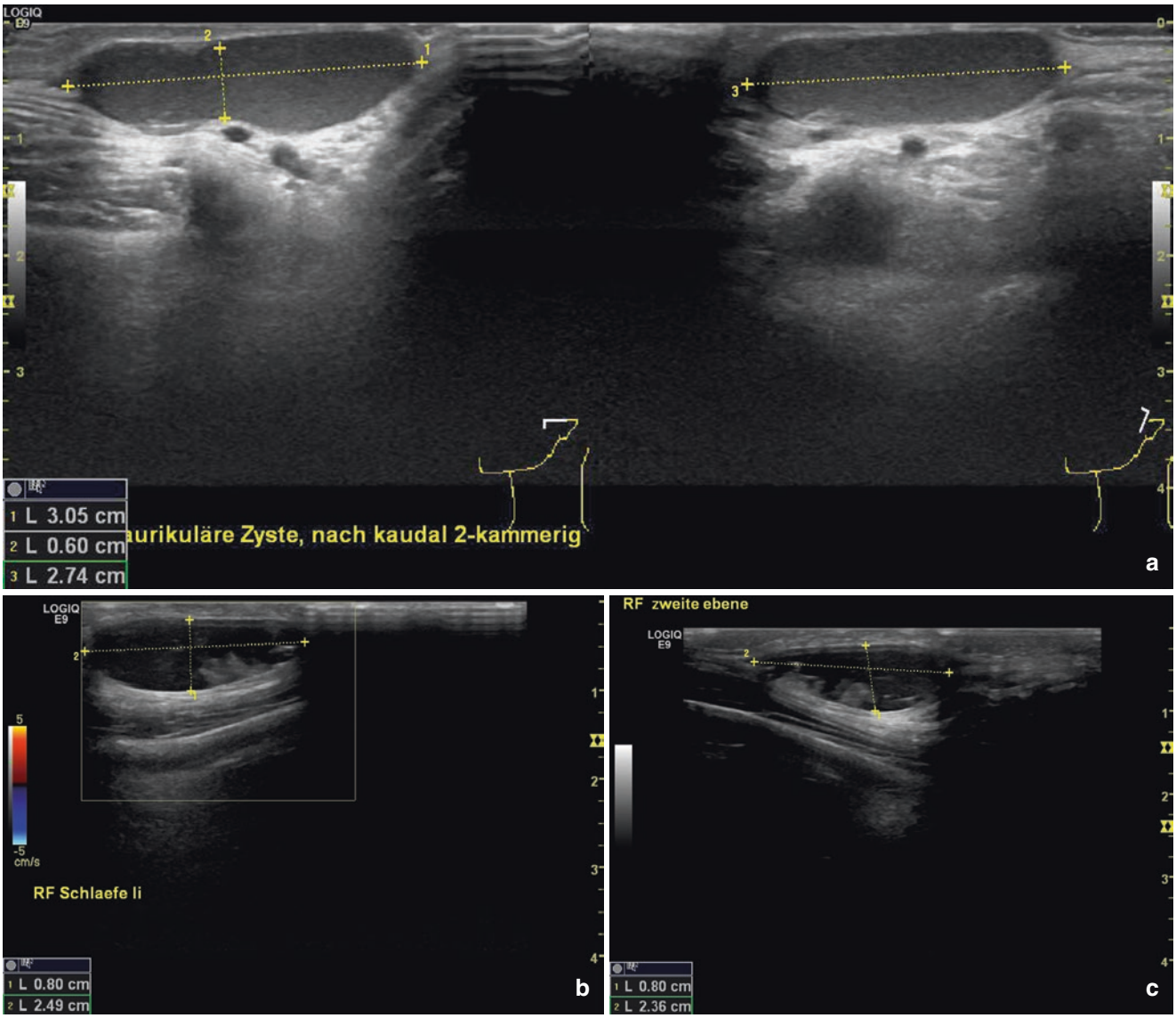

Fig. 14.14 Subcutaneous masses in the temporal region. (**a**) Atheroma. B-mode sonography in axial (*left*) and longitudinal (*right*) view. The lesion is clearly shaped and well-bordered, hypoechoic with some more complex echogenicity inside, which is probably due to cell debris or large protein molecules in the cystic fluid. (**b**, **c**) A dermoid in the temporal region, seen in axial (**b**) and longitudinal (**c**) views, which show some irregular structures inside the mass

Lymph nodes often appear in the parotid gland, in the submandibular space, and on the mastoids (Fig. 14.16). Lymph nodes in the parotid gland and submandibular space are discussed in Chap. 11.

With the current technology, the anatomic structures of the middle and inner ear are usually not assessable by ultrasound [1], but the surface of the bony structures can easily be assessed, including the periosteum (Fig. 14.17). Lymph nodes sometimes appear on the mastoid in cases of acute inflammation and can then mimic an acute mastoiditis. The lymph node displays as a hypoechoic mass that is usually oval-shaped and well-bordered, with a hilar structure.

14.6.3 Malignant Lesions

Most malignant tumors found in the face are malignant conditions of the skin, of which the most frequent are basal cell carcinoma and squamous cell carcinoma of the skin. Ultrasound can be applied to estimate the depth of infiltration of a tumor. For this purpose, ultrasound transducers with a frequency exceeding 15 MHz are required for adequate visualization of the infiltrated tissue layers. Ultrasound is also used for staging purposes.

Malignant tumors of the soft tissues of the face are rare lesions that usually comprise different kinds of sarcoma. Sonographically hypoechoic or echo-complex lesions are

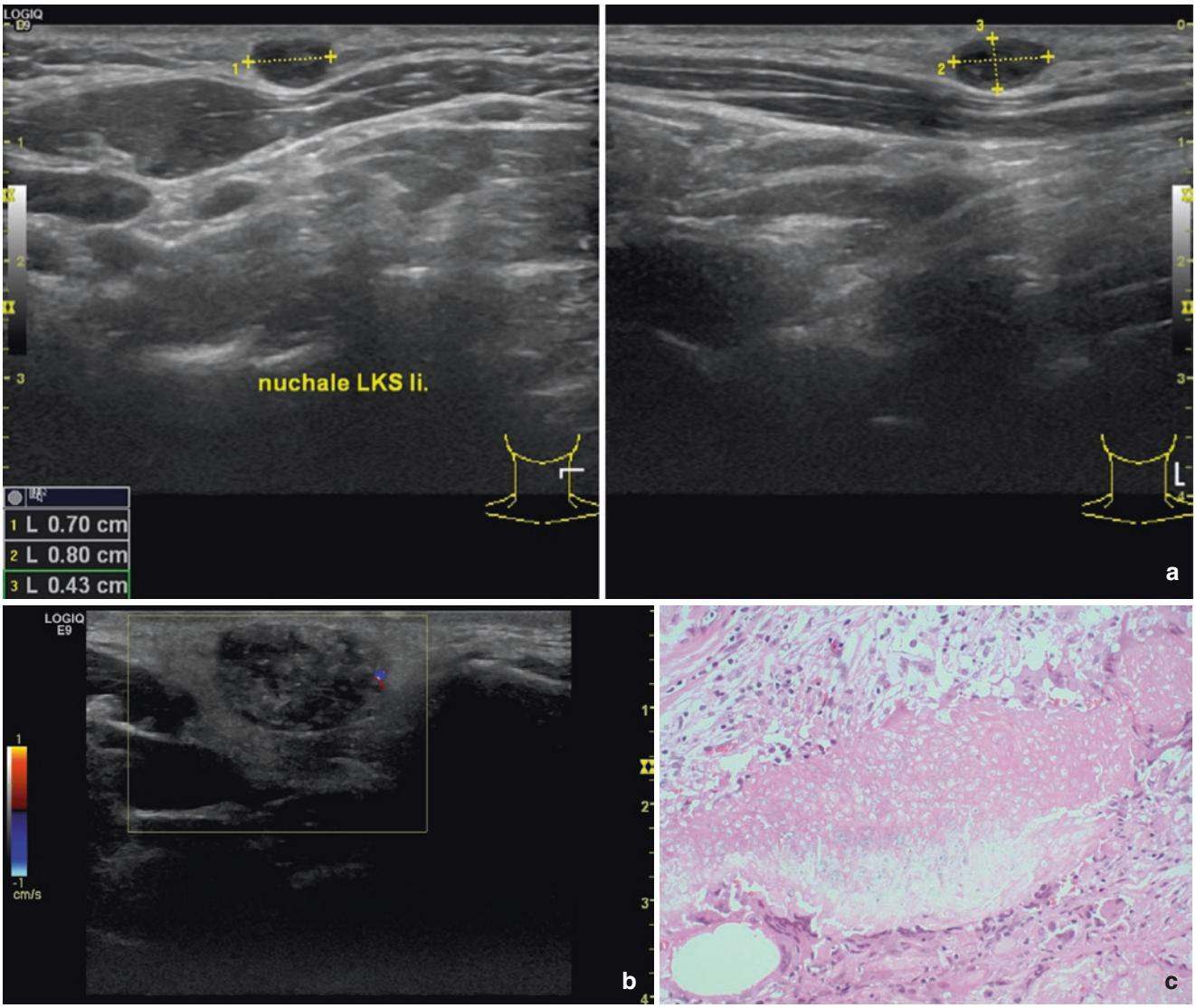

Fig. 14.15 Pilomatrixoma. (**a**) Sonography shows this benign cutaneous tumor to be a well-bordered, hypoechoic subcutaneous mass that contains some echo-complex areas, representing calcification zones. (**b**) Color duplex sonography reveals no vessels inside the lesion. (**c**) Histology confirms the benign condition and the calcification. (*Courtesy of* Prof. Dr. L. Wilkens, Dept. of Pathology, Nordstadt Clinic, Academic Hospital, Hannover, Germany)

visible with signs of infiltration and sometimes signs of central necrosis. The degree of acoustic echogenicity correlates with the degree of fibrous tissue.

Frequent malignant lesions of the paranasal sinuses, which sometimes can also spread to the orbit, are histologically squamous cell carcinoma, adenocarcinoma, sinunasal undifferentiated carcinoma (SNUC), or adenoid cystic carcinoma. Malignant melanoma or metastases of primary tumors of other types are less frequent. Sonographically these tumors are seen as hypoechoic masses that may show signs of an infiltrative growth pattern, for example, to the extraocular muscles [25]. The deeper parts of the orbit cannot be assessed by ultrasonography alone, so CT or MRI scans are superior in their diagnostic accuracy. Duplex sonography reveals various vascularization patterns; the vessels usually course from the periphery into the lesion.

14.7 Sonography of the Orbit and Its Adnexa

The sustained increase in demand for precise imaging of the paranasal sinuses and orbit, to investigate even very small structures in thin slices, has led to wide application of CT scans (both conventional scans and, increasingly, cone beam CT scans) and/or MRI for all kinds of orbital diseases, including acute and chronic inflammations, pathologic masses and tumors, and bony fractures. CT

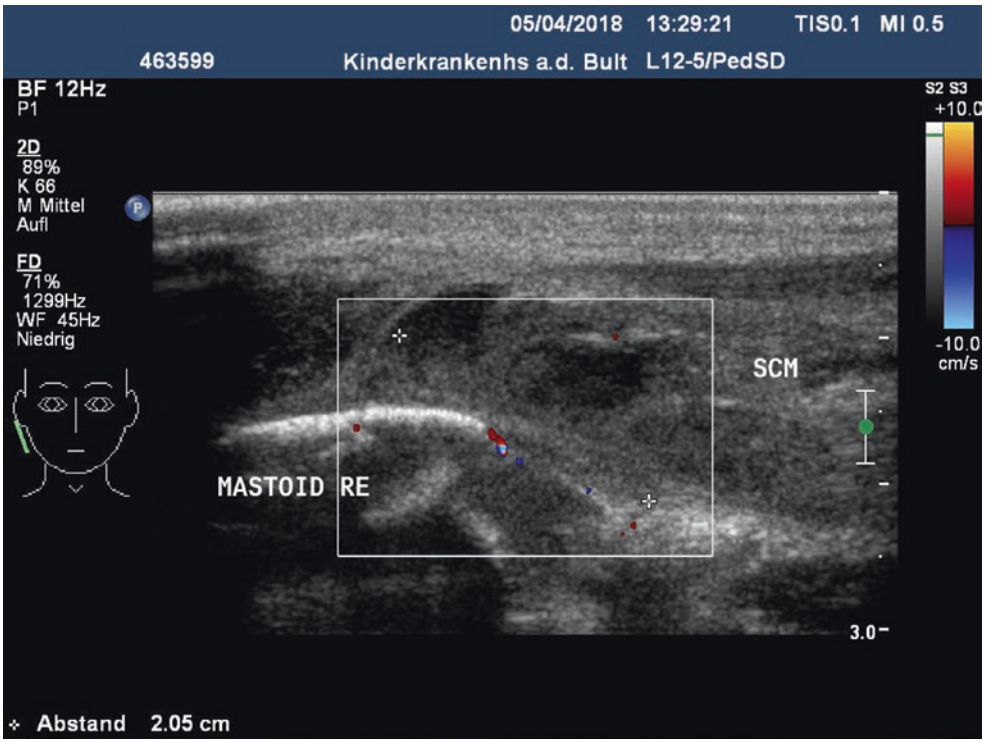

Fig. 14.16 In cases of lymphadenitis of the mastoid lymph nodes, the node can easily be visualized with B-mode sonography. This node is hypoechoic, with worse demarcation indicating the acute inflammation

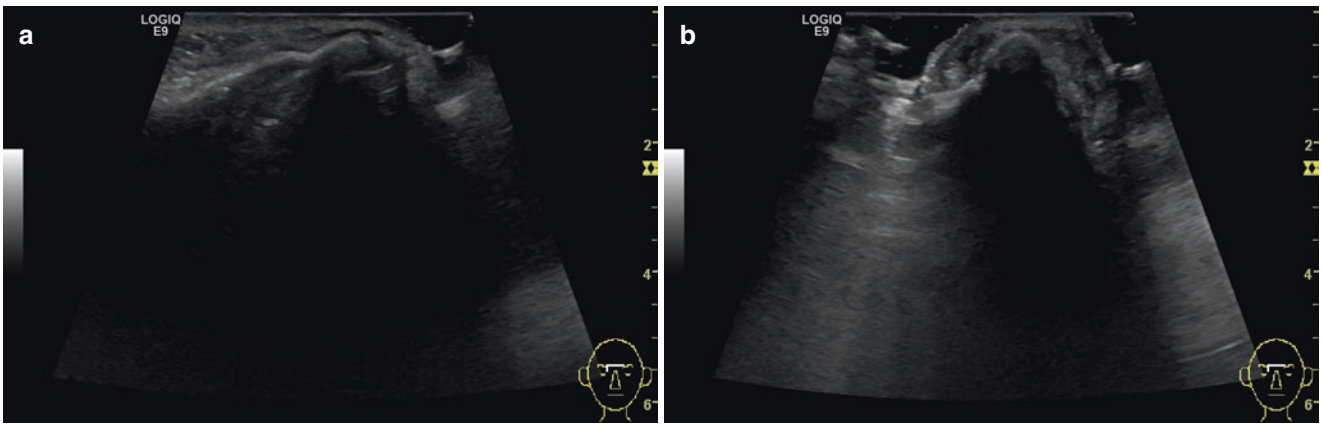

Fig. 14.17 Tumorous mass originating from the nasal bone. Histologically it was a granulomatous tumor-like inflammation. B-mode sonography, longitudinal (**a**) and axial (**b**) plane

scans and MRI are currently regarded as the "gold standard" for imaging of the paranasal sinuses and orbit. They are complementary, as the two techniques are sensitive to different tissue properties, and images obtained with these techniques differ significantly. Ultrasound examinations, on the other hand, are of minor importance, but ultrasound imaging is more sensitive than CT or MRI for examining superficial soft tissue diseases or tumors of the anterior orbit, the lacrimal glands, or the soft tissue of the orbit and eyelids. Ultrasonography therefore can give very valuable diagnostic information. In these cases, ultrasound is complementary to other imaging techniques applied [1, 22, 37]. Another indication for ultrasound is for use in patients who should not be exposed to ionizing radiation (especially children and pregnant women). The following subchapter demonstrates some typical ultrasound findings in frequent diseases of the orbits and their adnexa.

14.7.1 Technical Remarks

B-mode ultrasound examinations of the orbit are preferably performed with the patient sitting or lying. Small-part multifrequency ultrasound transducers with a frequency band of 7–12 MHz are suitable, but if the infiltration of a tumor into

the skin layers is to be examined, transducers of even higher frequency (20 MHz) should be used. For precise imaging, the ultrasound transducer is covered by a gel and set up onto the closed eye (Fig. 14.18). This transducer position is appropriate for investigating superficial anatomical structures such as the eyelids, lacrimal glands, and bony orbital rims [38, 39]. The eyeball can be used as a water-filled adapter that improves contrast for examining the deeper parts of the orbit or adjacent paranasal sinuses [3, 39]. In this way, it is possible to investigate the insertion zones of the extraocular muscles, the retrobulbar adipose tissue, the eyeball layers, and the anterior parts of the optic nerve [40, 41]. The orbital apex and adjacent structures usually evade from sonographic evaluation, however.

Fig. 14.18 Position of the ultrasound transducer for ultrasound examination of the orbit and the orbital floor, for axial images (**a**–**d**) and longitudinal images (**e**, **f**)

14.7.2 Ultrasound Anatomy

Sonographically, the eyelids are seen as tiny, band-like, hyperechoic structures. Small nodular lesions such as tumors of the eyelids can be detected. Ultrasound with very-high-resolution transducers is sensitive (as in ultrasonography of the skin) to investigate the infiltration depth of malignant tumors, including basal cell carcinoma of the eyelids, which might have consequences when contemplating the therapeutic procedures [42]. The cornea displays as a hypoechoic, sickle-shaped structure in the dorsal part of the eyeball, which is commonly surrounded by a slightly more hyperechoic limbus, caused by an impedance gap between the skin and cornea. The anterior eye chamber is located behind the cornea. The lens, the iris, and the ciliary body can be identified more dorsally (Fig. 14.19).

The normal vitreous body displays sonographically as an anechoic structure with dorsal enhancement. The sclera, choroidea, and retina can be visualized at its dorsal border, but ultrasonography usually does not provide certain differentiation of these structures in nonpathogenic conditions [40]. Ultrasound transducers with a very high frequency are more sensitive and offer better visualization of the eyeball layers. With their use, and by reducing the distal amplification (time-compensated gain, TCG), the choroidea appears slightly more hypoechoic than the retina or the sclera [39]. In cases of retinal detachments, however, the retina displays as a separated membrane, which is easily visible in the ultrasound image [41].

The optic nerve papilla can usually be identified by a protrusion in the dorsal border of the eyeball. Moving the ultrasound transducer and varying the sound direction make it possible to identify the optic nerve, which appears as a band-like, hypoechoic structure with a thickness of 4–5 mm, dorsal to the eyeball center [39] (*see* Fig. 14.19b). The optic nerve is surrounded by a dural sheath and cerebrospinal fluid, which

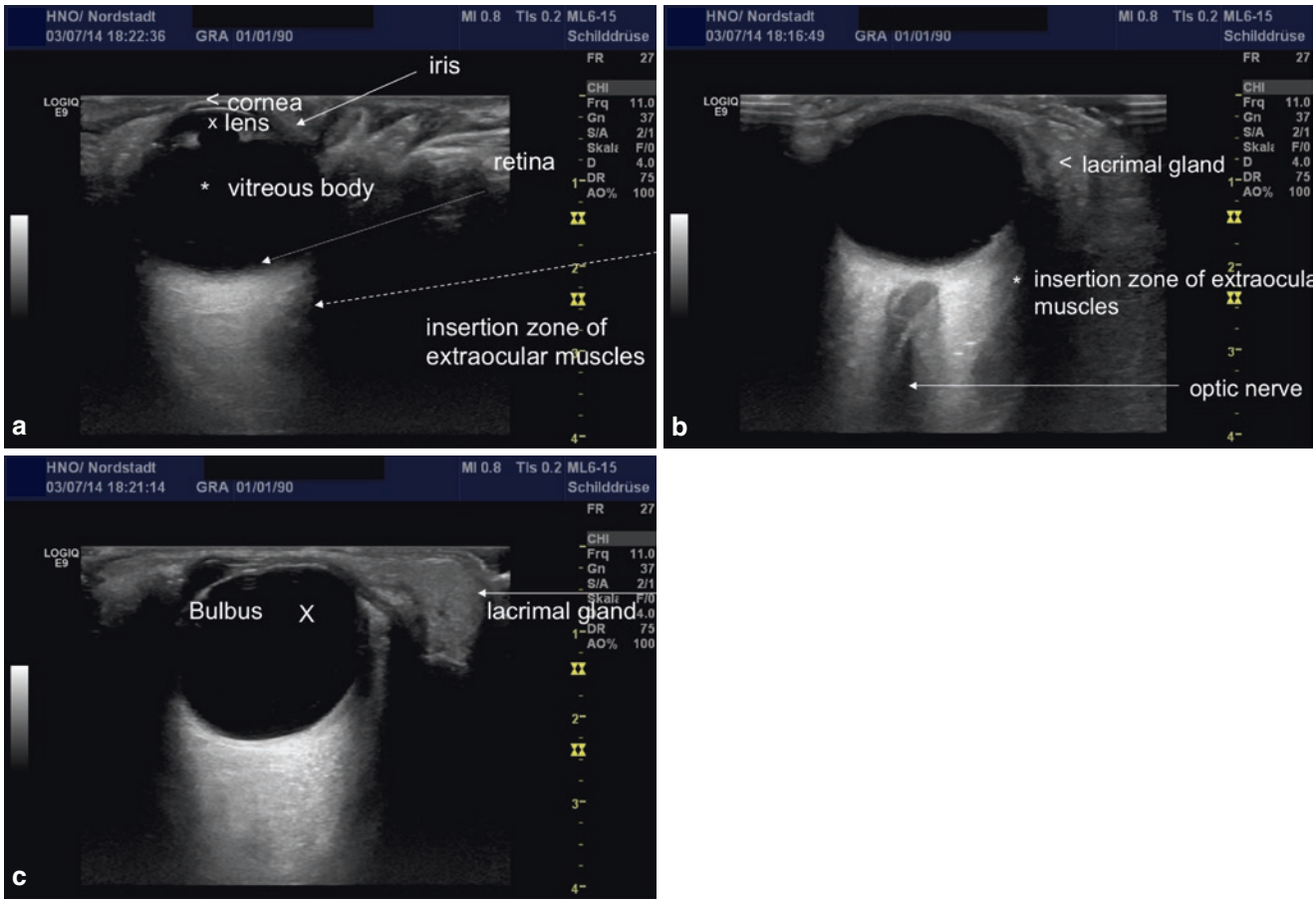

Fig. 14.19 Normal sono-anatomy of the orbit. (**a**) In axial sections of the orbit, the cornea, the lens, the iris, and the insertion zone of the extraocular muscles can be visualized. The differentiation of different layers in the eye fundus is often not possible in healthy conditions. By using ultrasound transducers with very high frequency, differentiation of different tissue layers is possible. (**b**) The optic nerve is seen as a band-like structure. (**c**) The lacrimal gland has an echogenicity similar to the salivary glands. (**d**, **e**) Sonography of the infraorbital rim and orbital floor. The bone displays a band-like pattern with no discontinuities

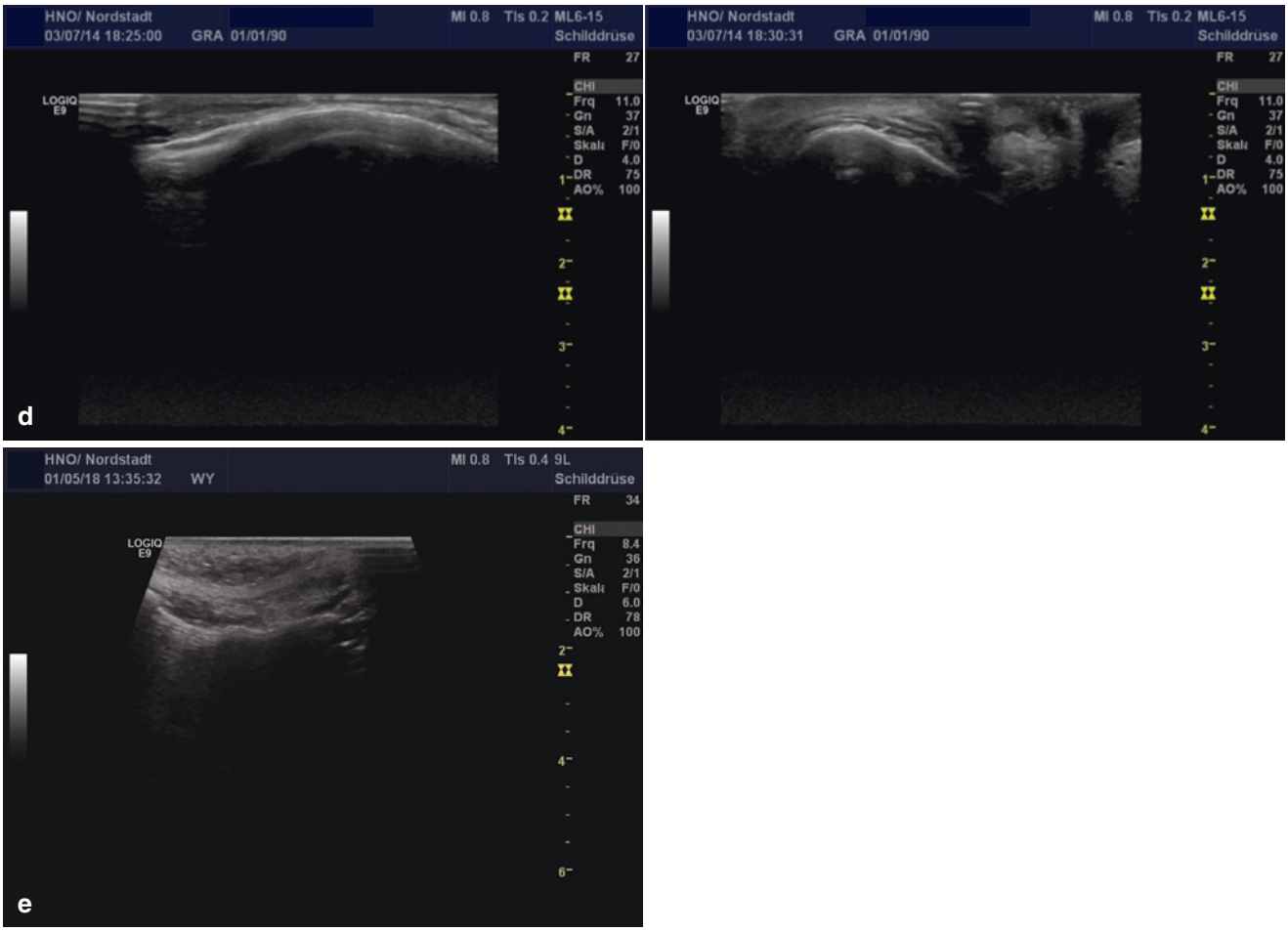

Fig. 14.19 (continued)

causes an impedance gap and provides better contrast between the nerve and adjacent, more hyperechoic adipose tissue. Measurement of the nerve's diameter provides important information about severity and possible deterioration in patients with demyelinating diseases [43, 44]. The extraocular eye muscles appear as band-like or spindle-shaped, hypoechoic structures, which are surrounded by the hyperechoic adipose tissue and show longitudinal stripping, a characteristic sonographic sign for muscles. Ultrasound provides the best visualization of the insertion zones of the rectus muscles, but the oblique muscles cannot be differentiated because of their close relation to the adjacent rectus muscles [39]. The intraconal parts of the orbit are usually hard to investigate by ultrasound. Thus, CT and MRI scans provide better visualization of the posterior orbital compartments.

Color-coded duplex sonography is suitable for measuring the blood circulation in the choroidea or central retinal and optic nerve vessels [39]. This technique is also sensitive for investigation of a suspected cavernous sinus fistula [45]. Increased intracerebral pressure manifests as a swollen papilla (choked papilla), which can easily be recognized [46].

Sonographically, the lacrimal glands appear as well-demarcated structures with homogeneous echogenicity in the lateral parts of the eyelids. Their axial extension is about 1 cm, and their echogenicity is quite similar to that of the thyroid gland or salivary glands (*see* Fig. 14.19c). Ultrasound has the highest sensitivity for recognizing tumors or abscesses of the lacrimal glands, as well as a subperiosteal abscess condition in the area of the medial canthus [40, 47].

The diagnostic evaluation of bony structures by ultrasound is challenging, as it is only sensitive for investigation of the bony orbital rims (*see* Fig. 14.19d). Fracture lines and significant dislocations are visible, but it is not possible to assess the extension and severity of an orbital fracture by ultrasonography alone, and CT scans often offer much better visualization of the entire orbit, midface, and skull base [47].

14.7.3 Ultrasound Examination of Particular Orbital Diseases

Hereditary Malformations (Coloboma, Teratoma, and Dermoids)

Coloboma is regarded as a development-related schistasis of the eyeball. According to the severity, ectatic coloboma with a bulging of the eyeball wall or coloboma cysts can be differentiated. Sonography is highly sensitive in recognition of a coloboma, which is commonly accompanied by a microphthalmos [39, 40].

Teratoma and dermoids are regarded as hereditary tumors, which frequently occur in the first years of life. Sonographically, dermoids appear as hypoechoic, sharply bordered cystic masses with dorsal enhancement, typically located in the bony orbital rim [39, 40]. Teratoma, on the other hand, contains both hyperechoic and hypoechoic areas; the hyperechoic structures commonly present with calcifications [39, 40].

Inflammatory Diseases

Acute inflammations and chronic inflammations of the orbit can be differentiated. The chronic inflammations comprise Graves' orbitopathy and the idiopathic orbital inflammatory disease, orbital pseudotumor, the sonographic characteristics of which are detailed below. It is reasonable to differentiate between acute and chronic inflammations originating in the orbit itself and those spreading into the orbit from other anatomical regions (especially from the adjacent paranasal sinuses).

Acute Inflammations

The acute inflammatory diseases of the orbit can either originate directly in the orbital structures themselves (e.g., dacryocystitis, lid phlegmon) or they can be an orbital complication in which the orbit is secondarily involved by the spreading of an acute inflammation of the paranasal sinuses. Sonography is sensitive and makes it possible to differentiate between preseptal and postseptal extension of the disease. Preseptal disease involves the space anterior to the orbital septum, whereas postseptal inflammations involve the space behind it and usually spread into the intraconal and retrobulbar compartment.

Depending on the classification used to describe the orbital complications of an acute sinusitis, at least four stages of the disease can be differentiated [48]: In stage I of the disease, an inflammatory concomitant swelling of the upper and/or lower lid occurs. Sonographically, stage I is characterized by a relaxation of the soft tissue of the eyelids, and because of the acute inflammatory process, the tissue appears generally more hypoechoic. Circumscribed hypoechoic or anechoic structures, indicating abscess formation, are not visible. In this stage the inflammation is usually limited to the preseptal or extraconal spaces. Subperiosteal abscess, which is regarded as stage II of the disease, appears as a circumscribed, hypoechoic or anechoic structure with dorsal enhancement between the orbital lamina and orbital soft tissue (Fig. 14.20). The medial rectus muscle and the eye bulb itself are frequently displaced laterally, and the disease is extended to the peribulbar and intraconal spaces [39]. Color-coded duplex sonography reveals only minor intralesional perfusion, with areas of perfusion losses. Orbital phlegmon (stage III to IV) is characterized by a diffuse relaxation of the soft tissue in the entire orbit, preseptally and postseptally. The tissue appears partly hypoechoic and hyperechoic, but circumscribed abscess formations usually cannot be detected. Orbital complications can also be caused by aggressive mycosis, most commonly an *Aspergillus* infection or perhaps a *Mucor* species. These infections frequently occur in patients with chronic disease or immune deficiency (Fig. 14.21).

Acute inflammations of the eyelids can be caused by small injuries of the lid skin. The sonographic characteristics are similar to those of the concomitant inflammatory swelling

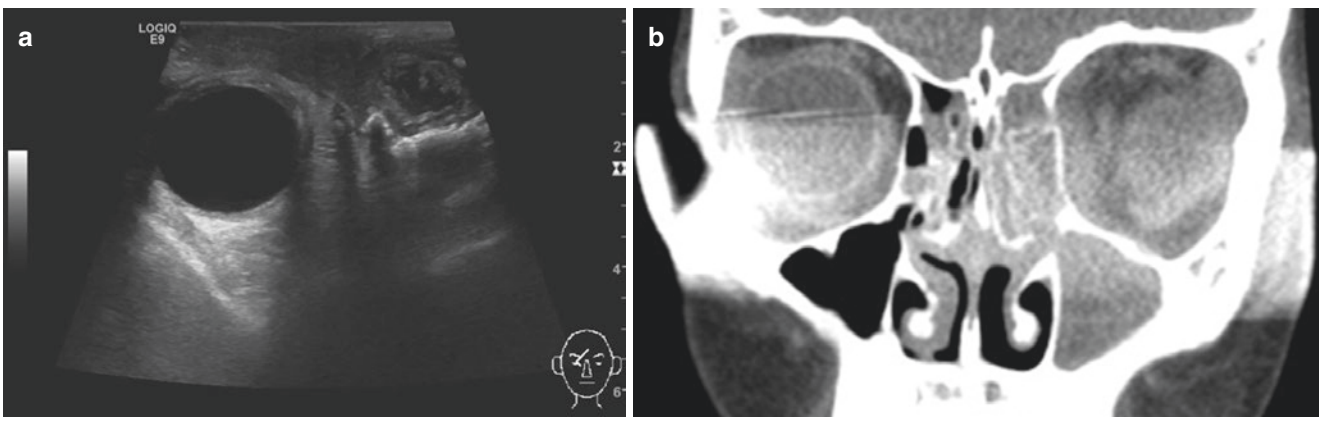

Fig. 14.20 Sinugenic orbital complication. (**a**) Sonography reveals swollen soft tissue of the upper and lower lids, along with a zone of necrotic and melting tissue, representing formation of an abscess. (**b**) This diagnosis was confirmed by the CT scan and intraoperatively

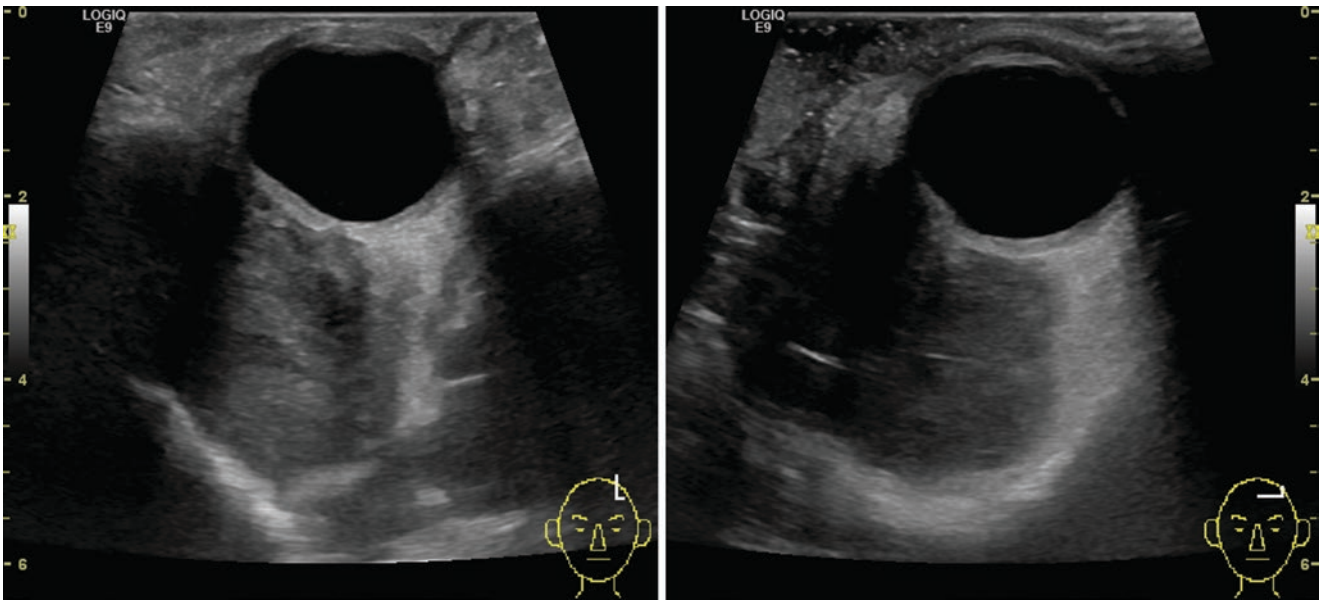

Fig. 14.21 Invasive mycosis of the paranasal sinuses, spreading into and infiltrating the left orbit. The mycosis impresses as a hypoechoic, unsharp-bordered mass with an infiltrative growth pattern and echo-complex and necrotic areas that resemble a malignant tumor. The lesion has affected the eye bulb. Dorsal enhancement

due to an acute sinusitis. The findings are usually limited to the preseptal compartment and do not extend to the retrobulbar or intraconal spaces. Abscess conditions in the eyelid are characterized by irregular structures with dorsal enhancement; they are fairly superficial in most cases.

An acute dacryoadenitis is clinically characterized by a swelling, reddening, and paragraph shape (S-shape) of the upper lid. The sonographic appearance is characteristic, with relaxation of all the lacrimal gland tissue in the lateral lid and orbital area with some hypoechoic and hyperechoic parts. Some irregular structures may indicate microabscess formation.

Graves' Ophthalmopathy

Ultrasonography is sensitive in recognizing the proliferation of adipose tissue in the retrobulbar compartment and the peribulbar area of the eyebrows [49]. Thickened extraocular muscles also can be identified (Fig. 14.22). However, the retrobulbar area is hard to investigate by ultrasound alone, and ultrasound does not provide the possibility to estimate the predominant kind of Graves' ophthalmopathy in a particular patient; it can be either an adipose tissue type, in which the proliferation of retrobulbar adipose tissue is predominant, or a muscle type, with thickening of the extraocular muscles. Both types can be responsible for exophthalmos with an increase of intraorbital pressure. In some cases, both pathogenetic characteristics occur together ("mixed type"). In these cases, MRI scans are preferable [47], but ultrasound is suitable for monitoring during immunosuppressive therapy and for estimation of the disease activity [38, 49].

Orbital Tumors

Tumors originating in the orbit and its adnexa must be distinguished from tumors that originate in the paranasal sinuses and infiltrate secondarily into the orbit.

Benign Lesions and Pseudotumors

One of the most frequent benign lesions in the orbit is idiopathic orbital inflammatory disease (orbital pseudotumor). The etiology of this condition is not completely clear. An autoimmunologic cause has been discussed or an association with immunoglobulin G (IgG)-related diseases. The mass is sonographically characterized by a hypoechoic process limited to the surrounding tissue and which is adjacent to the extraocular muscles and cannot be clearly divided from them. Differential diagnosis thus must exclude a muscle tumor and a malignant lymphoma. Some blood vessels are detectable by color-coded duplex sonography, but no distinct perfusion pattern can be identified (Fig. 14.23). The sonographic characteristics of this disease are quite similar to those of a malignant lymphoma, which always must be excluded histologically or cytologically. Sonography can be applied to obtain material for cytologic examinations by fine-needle aspiration biopsy under direct view [50].

Mucoceles are also pseudotumors. They usually originate in the paranasal sinuses and infiltrate the orbit. They are seen as hypoechoic or anechoic masses with clear borders. In most cases, additional intralesional echoes with fine granules can be seen, which are probably due to protein molecules and cell debris in the mucocele content. Dehiscence of the

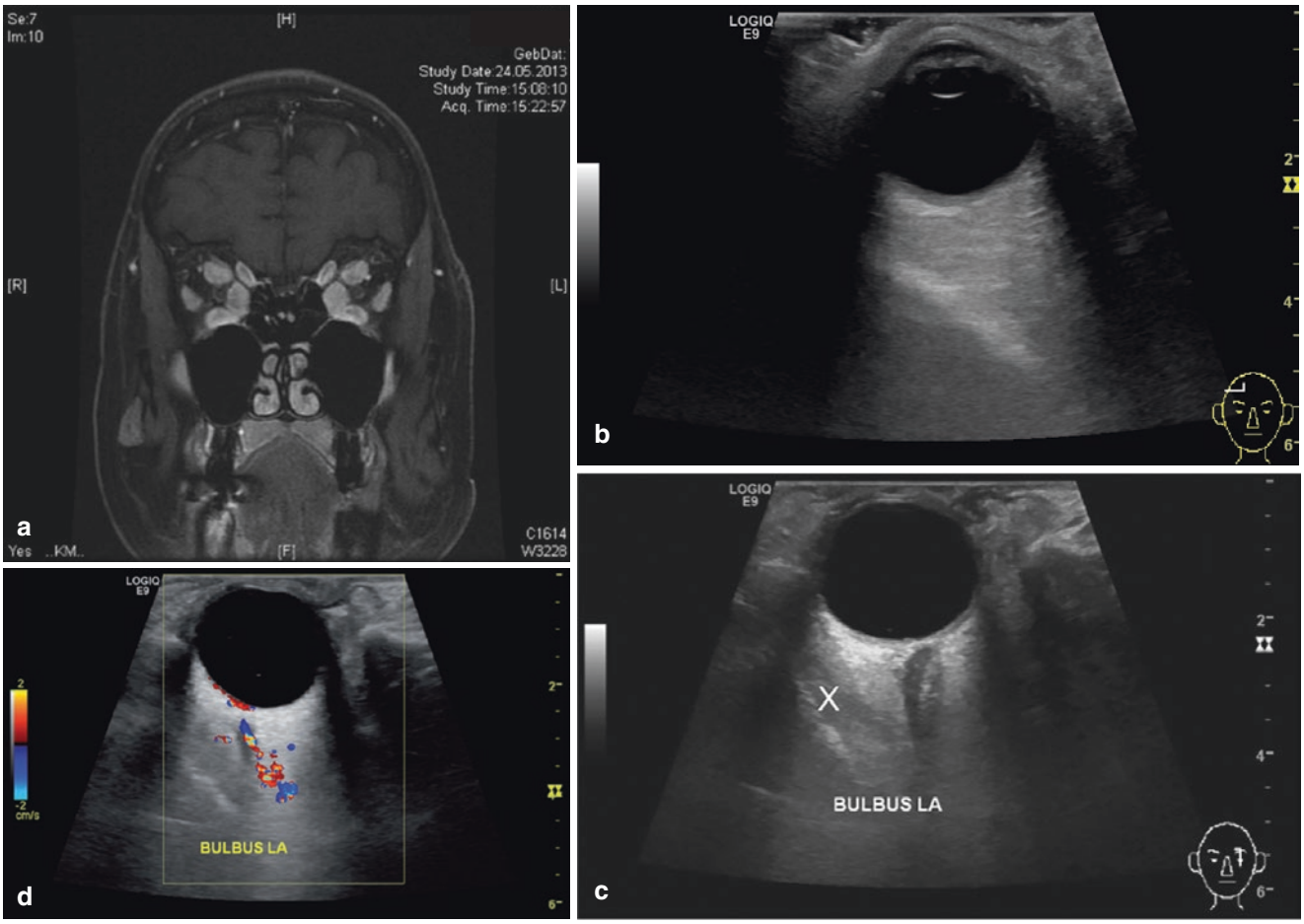

Fig. 14.22 Graves' orbitopathy. (**a**) MRI (coronal plane) shows the enlarged extraocular muscles, along with the proliferated adipose tissue. (**b**, **c**) B-mode sonography reveals enlarged extraocular muscles (X), swollen eyelids, and increased adipose tissue. (**d**) Color duplex sonography shows some vascularization in the retrobulbar compartment

bony walls, which enables the mucocele to grow into the orbit, can be detected in many cases [24, 51] (Fig. 14.24). Color-coded duplex sonography does not reveal any intralesional vessels.

Cavernous hemangiomas, regarded being the most frequent benign orbital tumors, are either retrobulbar or peribulbar in location. They can be identified by sonography only when they are located peribulbar or anteriorly in the orbit. They usually appear as hypoechoic masses with inhomogeneous echogenicity and sometimes with worse demarcation toward the adjacent adipose tissue. Color-coded duplex sonography helps in identification of the afferent and draining blood vessels. The masses present with a dense and irregular blood vessel pattern, which shows high blood flow velocity. Thrombosed hemangiomas have a significantly worse perfusion. Sonography is suitable for interstitial laser therapy of hemangioma, permitting placement of the laser transducer straight into the lesion under direct visual control. The coagulation effect can be seen in real time.

Lymphangiomas represent hereditary lesions in most cases [52]. They appear sonographically as clearly separated, hypoechoic, septated masses with several anechoic impressive inclusions, corresponding to lymph cysts. Color-coded duplex sonography reveals perfusion patterns in the tumor capsule, along with the septa. Intralesional bleeding can lead to fluid levels and sedimentation owing to the blood constituents inside the lymph cysts [40]. Surgical excision is the therapy of choice. A minor invasive therapy procedure is sclerosing of the lesions, in which sclerosing agents are administered intralesionally under sonographic control [52].

Meningioma in the orbit originates in most cases from the meninges of the optic nerve. The nerve is often surrounded by the tumor. Sonographically, the tumor is seen as a hypoechoic, clear-bordered mass with some vascularization in the meninges (Fig. 14.25). It has a very tight connection to the optic nerve, which often cannot be separated from the tumor mass.

The most frequent benign tumor of the lacrimal glands is the *pleomorphic adenoma*, which show sonographic conditions

quite similar to those of pleomorphic adenoma of the salivary glands (Fig. 14.26). The tumor appears as a hypoechoic, polycyclic-bordered, intraglandular mass with clear borders and dorsal acoustic enhancement. Color-coded duplex sonography reveals only minor perfusion of these masses, with detectable blood vessels mostly in the tumor's capsule.

Osteomas usually originate in the paranasal sinuses (ethmoid sinuses, frontal sinuses) and grow secondarily in the orbit. They are benign and slowly growing masses. Sonographically, the osteoma is a hyperechoic or echo-complex mass that cannot be separated from the bone. When it grows into the orbit, the eyeball can be displaced (Fig. 14.27).

Malignant Tumors

Malignant tumors of the inner orbit can be of many types:

- Retinoblastoma
- Rhabdomyosarcoma
- Metastases of primary tumors in other sites
- Carcinoma of the lacrimal glands (adenocarcinoma, adenoid cystic carcinoma)
- Carcinoma of the eyelids and conjunctiva (basal cell carcinoma, squamous cell carcinoma)
- Malignant melanoma
- Malignant lymphoma

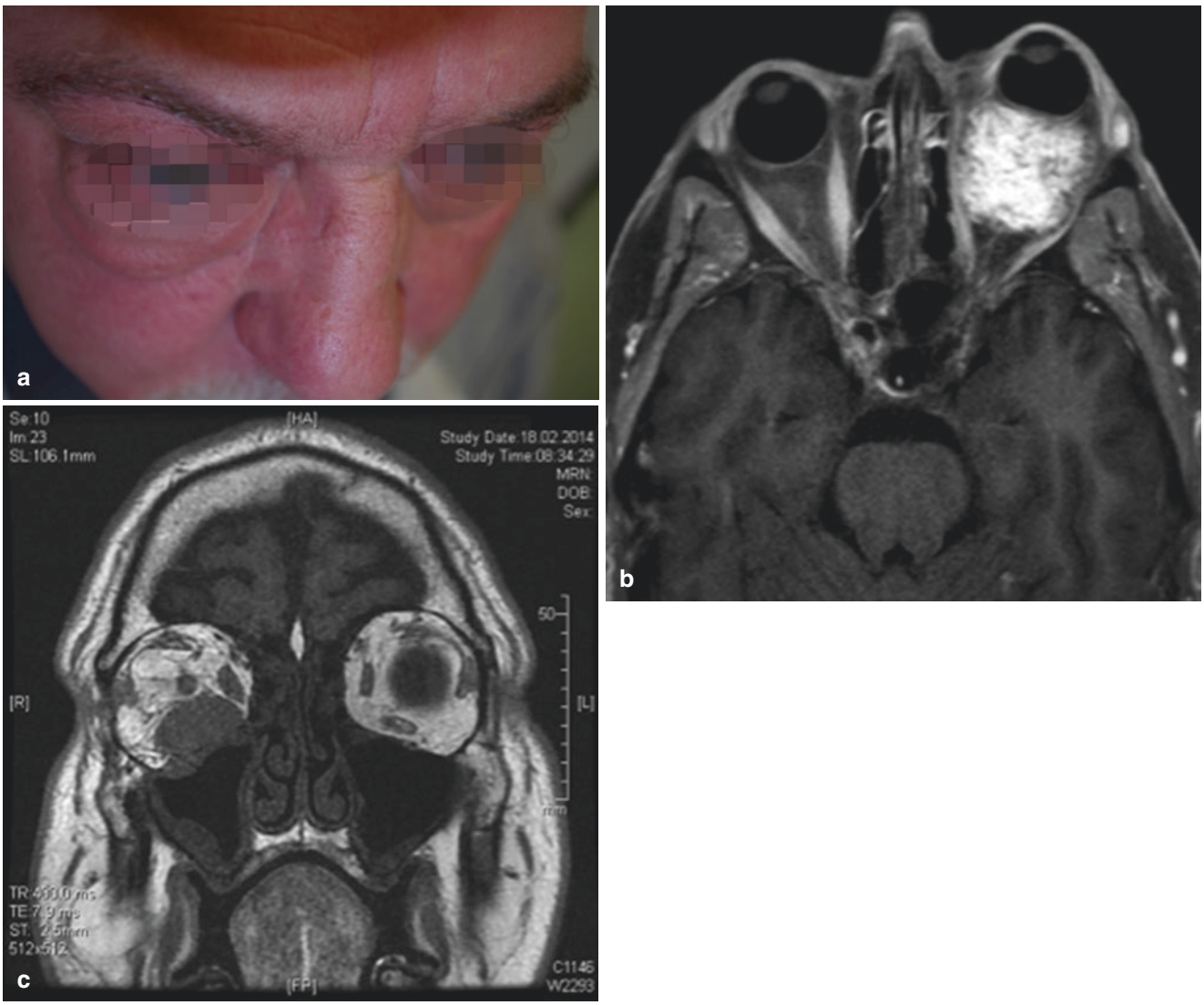

Fig. 14.23 Idiopathic orbital disease (orbital pseudotumor). (**a**) The clinical photo shows lower lid swelling and slight exophthalmos. (**b**) (axial) and (**c**) (coronal), MRI scans show the tumor in the caudal compartments intraconally. (**d**) B-mode sonography reveals a clearly bordered and sharply shaped hypoechoic mass without signs of an infiltrative pattern. (**e**) Color duplex sonography shows fairly good vascularization. (**f**) Histology confirms an idiopathic orbital disease (orbital pseudotumor). (*Courtesy of* Prof. Dr. L. Wilkens, Dept. of Pathology, Nordstadt Clinic, Academic Hospital, Hannover, Germany)

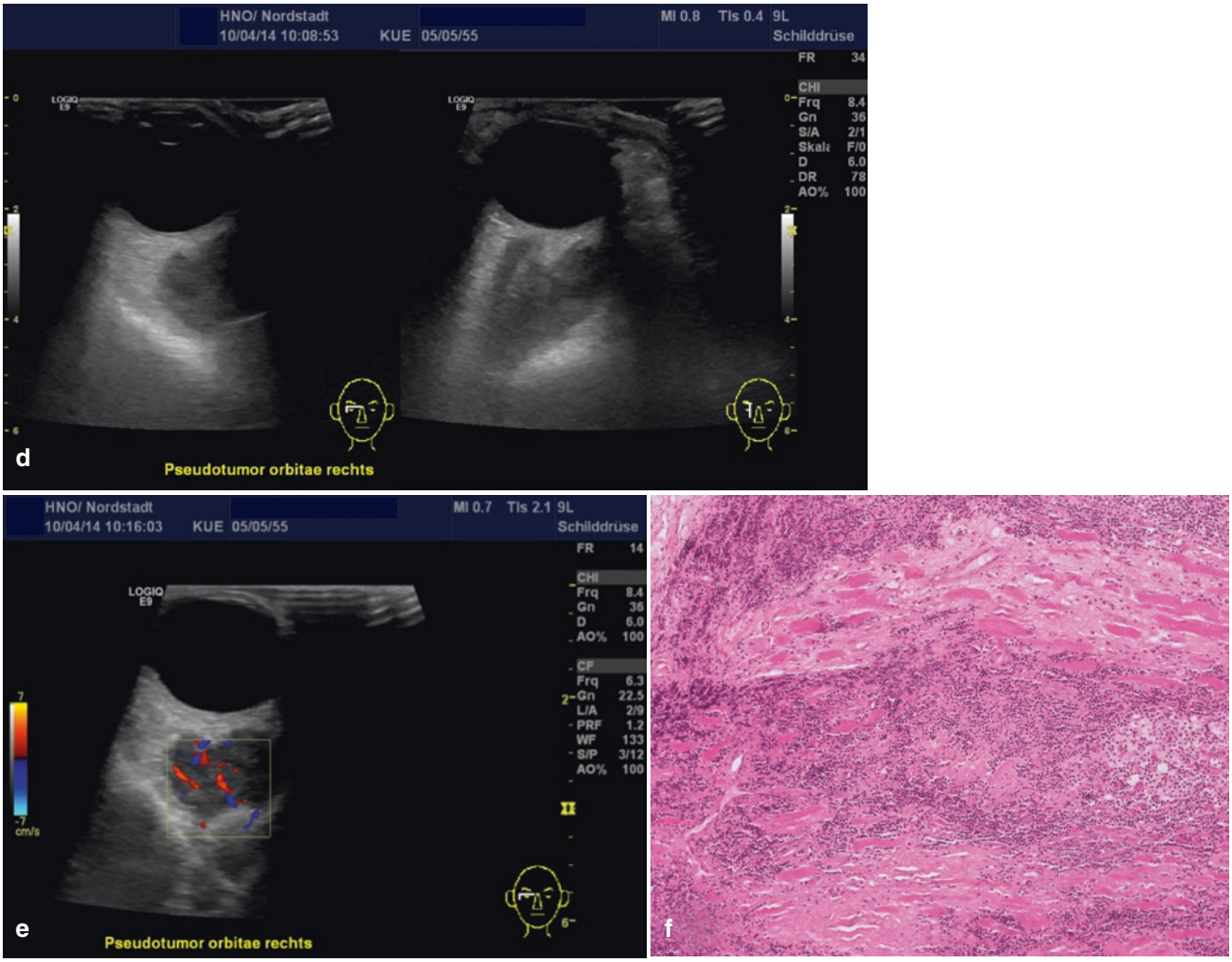

Fig. 14.23 (continued)

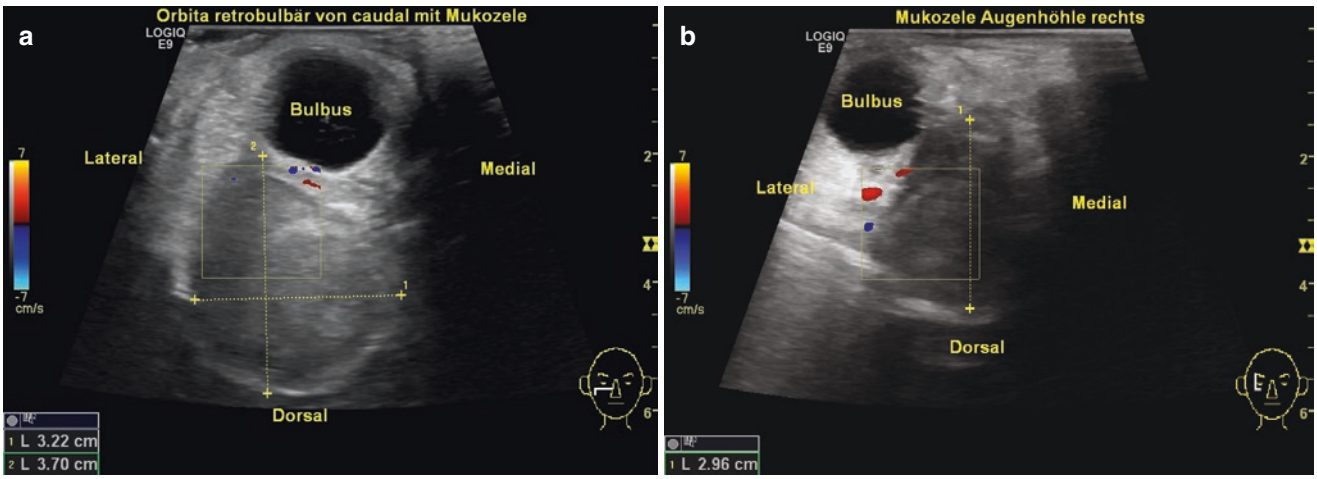

Fig. 14.24 Mucocele of the right orbit. (**a**) B-mode sonography (axial plane) reveals a clearly shaped and bordered hypoechoic mass with dorsal enhancement in this case. The eye bulb is cranially displaced. No signs of an infiltrative pattern. Some more complex echoes inside the lesion represent cell debris and large protein molecules in the mucocele content. (**b**) B-mode sonography in an axial section of another mucocele, originating in the ethmoid sinus and affecting the orbit from medial

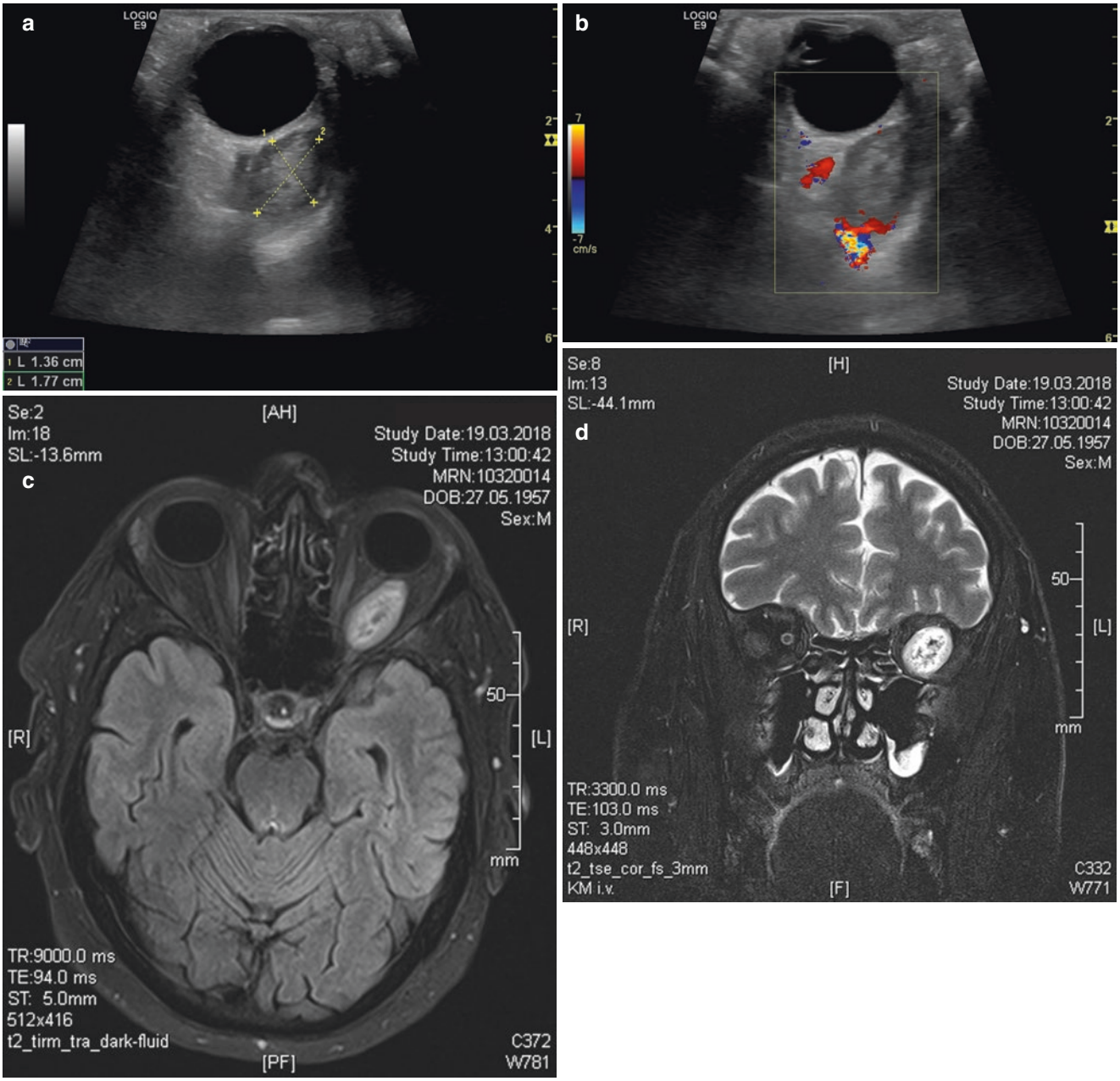

Fig. 14.25 Meningioma in the orbit. (**a**) B-mode sonography reveals a hypoechoic, partially echo-complex mass that is located directly in the vicinity of the optic nerve. The lesion cannot be divided from the nerve, indicating that it originates in the optic nerve meninges. (**b**) Color duplex sonography reveals some vascularization in the tumor capsule. (**c**, **d**) MRI scans in axial and coronal planes also show the tumor, which surrounds the optic nerve

Sonographically, the *retinoblastoma* is characterized by a well-perfused, hyperechoic mass that is directed toward the vitreous body. Calcifications occur frequently; they can be identified by intralesional hyperechoic irregular structures with dorsal sound mitigation, sound extinction, or acoustic shadowing [53].

Rhabdomyosarcoma originates in the extraocular muscles, impressing as hypoechoic masses that cannot be differentiated from the muscles. The tumor is poorly demarcated from the adjacent tissue and shows signs of an infiltrative pattern. Color-coded duplex sonography reveals numerous blood vessels [40].

Intraorbital metastases frequently originate from breast cancer, gastrointestinal cancer, kidney cancer, or thyroid cancer. Hence, they do not have a uniform sonographic appearance. Hypoechoic or echo-complex masses with inhomogeneous echogenicity are common. A cytologic or histologic examination is required when metastasis is suspected.

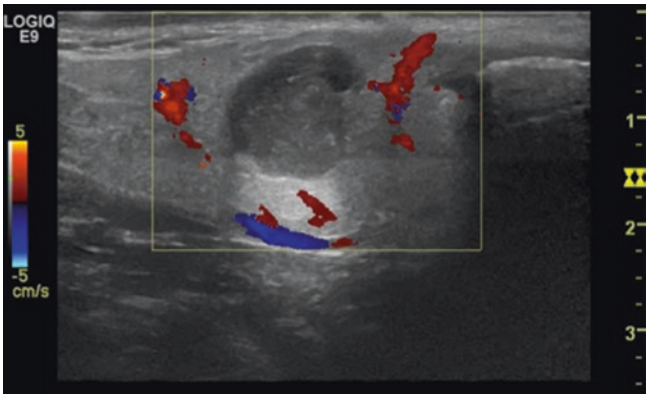

Fig. 14.26 Pleomorphic adenoma of the lacrimal gland. The sonographic characteristics are similar to those of the salivary glands. The tumor is hypoechoic with polycyclic borders and dorsal enhancement, with some more echo-complex areas. Color duplex reveals rare vascularization in the tumor capsule

With ultrasound, it is possible to examine a suspected infiltration of the intraorbital structures in real time; both the eyeball and the tumor are visualized, and the patient is asked to move the eye. If there is a tissue layer between the tumor and the surrounding tissue, infiltration is not likely. Color-coded duplex sonography is advantageous when tumors of higher vascularization are suspected.

Frequent tumors of the lacrimal glands include adenocarcinoma, adenoid cystic carcinoma, and carcinoma ex pleomorphic adenoma (which arises from the benign pleomorphic adenoma, discussed above). There are no specific sonographic characteristics, but most of these tumors appear as hypoechoic lesions with sometimes unsharp borders, inhomogeneous echogenicity, and signs of an infiltrative growth pattern. The same is true for tumors of the eyelids.

Malignant melanoma of the uvea or retina displays sonographically sometimes as a clearly bordered mass that is hypoechoic or has complex echogenicity. In cases of retinal melanoma, the tumor masses protrude into the eyeball and can easily be visualized.

Malignant lymphoma of the orbit is seen sonographically as hypoechoic, roundish, or oval masses in the lacrimal glands or peribulbar area, with clear borders [50]. Color-coded duplex sonography reveals diffuse perfusion in most cases. Sonography is sensitive for monitoring during chemotherapy or radiation therapy [42, 54, 55].

Fractures

Sonography is suitable for investigation of the soft tissue, eyelids, or peribulbar compartments in orbital injuries, but generally only the superficial bony walls (lateral and

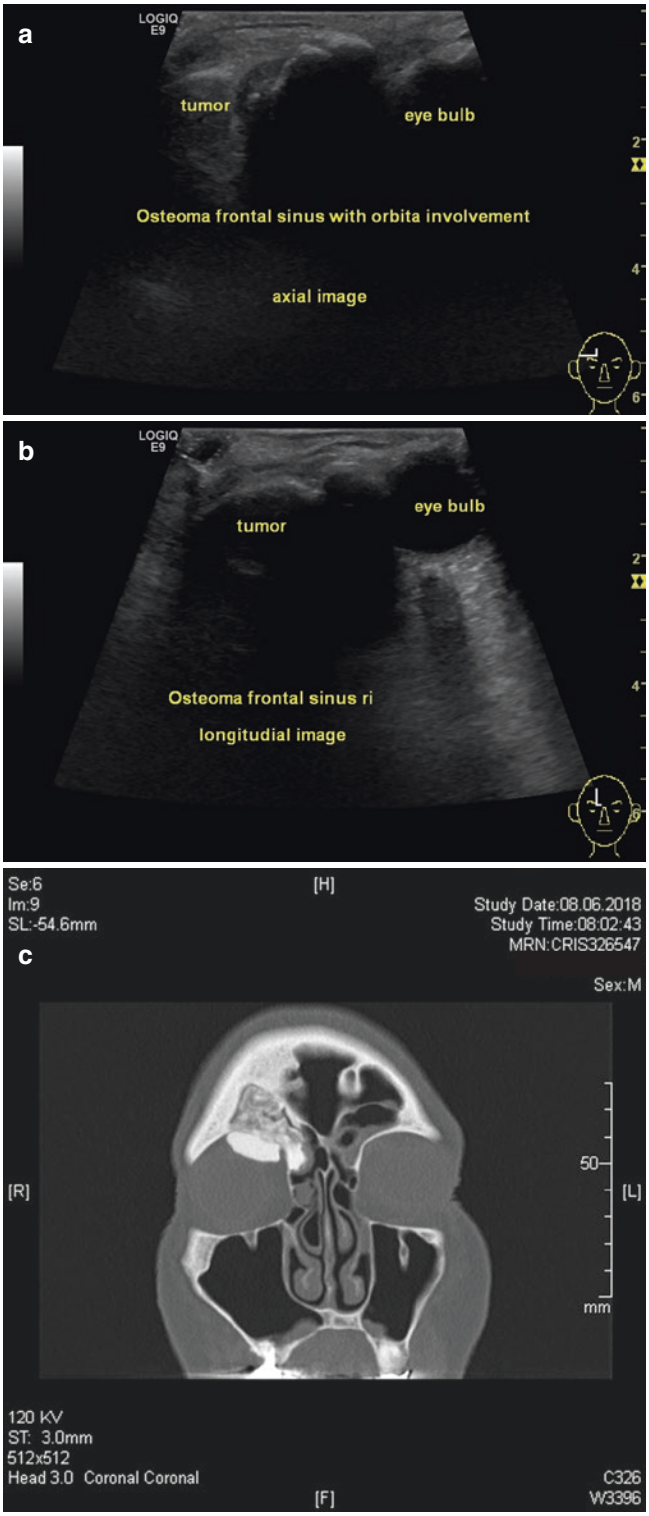

Fig. 14.27 Osteoma of the frontal sinus invading the orbit. (**a**, **b**) The eyeball is displaced by the tumor, which is seen as a hyperechoic mass. Note the complete sound extinction behind the tumor, which is of bony origin. (**c**) The coronal CT scan confirms the bony structure of the tumor

medial orbital walls, infraorbital rim, and supraorbital rim) can be evaluated. The extension and depth of the injury cannot be evaluated sonographically, so CT scans are more sensitive and superior for these purposes [56, 57]. Sonographically, dislocated fractures are seen as a discontinuity and disruption of the affected bones and frequently a "stair," so the degree of dislocation can be evaluated (Fig. 14.28). The diagnostic accuracy of sonography in the detection of blowout fractures was reported to be 86% in older studies in the literature, with a sensitivity of 85% or greater compared with CT scans or direct surgical exploration [56]. In blowout fractures, adipose tissue and inferior rectus muscle prolapsed into the maxillary sinus can be visualized. In another study of patients with isolated orbital floor fracture, ultrasonography showed a sensitivity of 95%, a specificity of 100%, and an overall diagnostic accuracy of 98% in detecting prolapse of orbital content into the maxillary sinus, compared with CT scans. The authors concluded that a valuable indication for ultrasound is the application in patients who should not be exposed to ionizing radiation (children, pregnant women) [57, 58]. In cases of deep and extensive bony fractures and in patients with impaired eye motility or vision loss, a CT scan is mandatory, however [57], because sonography has a lower sensitivity in detection of these severe and complex fractures.

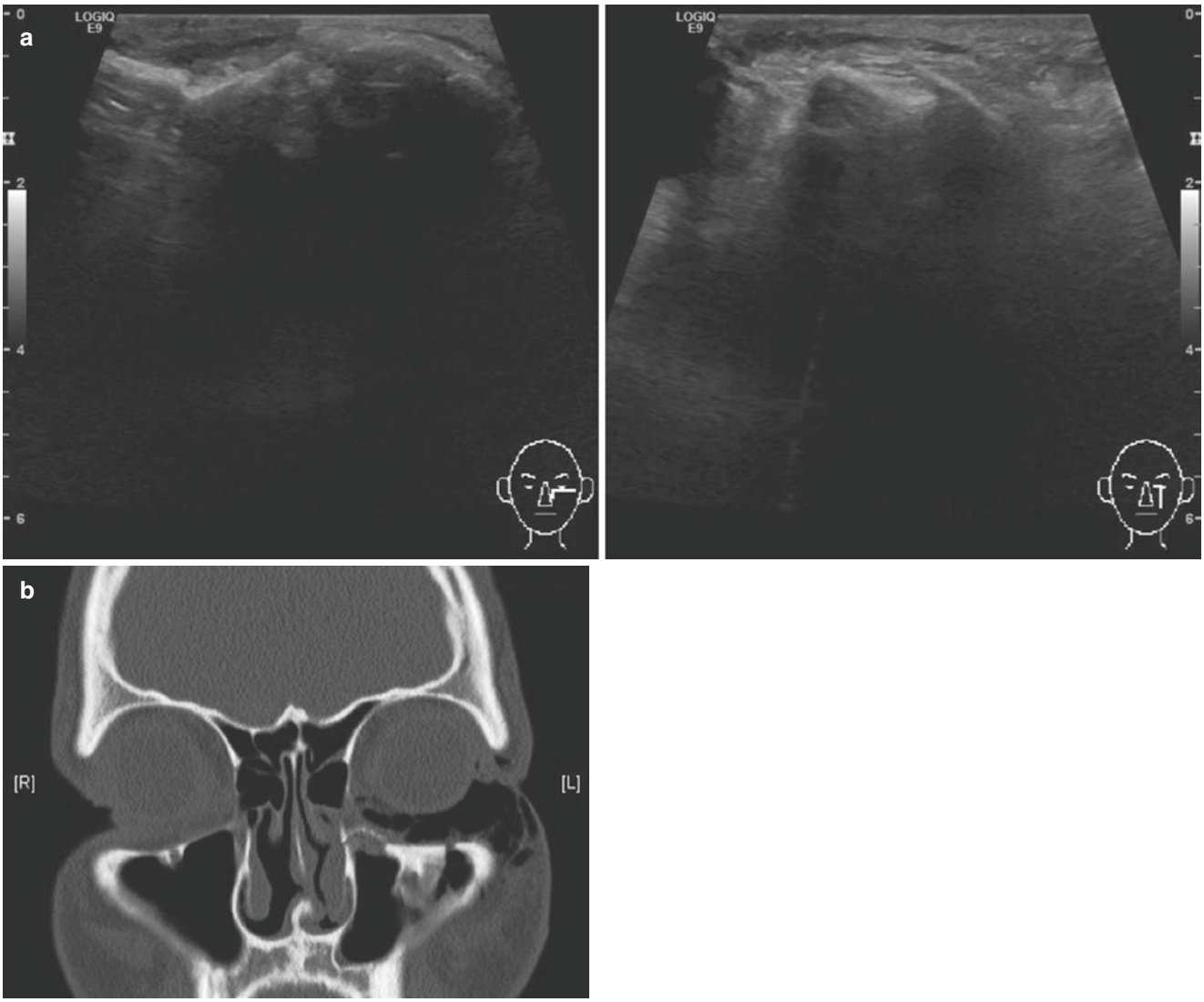

Fig. 14.28 Fracture of the infraorbital rim. The continuity of the bone is disrupted. (**a**) The degree of dislocation can be estimated, but the deeper structures of the orbit cannot be visualized by sonography alone. (**b**) CT scan shows the fracture extent. Sonography can be used postoperatively for reposition control

Ultrasound is most suitable to be applied intraoperatively to control the repositioning of bone fractures, and it can also provide most valuable information for localizing intraorbital or intrabulbar foreign bodies [59, 60].

14.8 Intraoperative Applications During Neuroendoscopic Skull Base Surgery

In recent years, several studies have described the intraoperative endonasal application of B-mode ultrasonography during neuroendoscopic transsphenoidal pituitary gland surgery [61]. The advantage of this technique is the clear identification of the carotid arteries, the anterior and middle cerebral arteries, and the chiasmatic cistern. It is also possible to recognize residual tumor in real time using sagittal and coronal sonography images [62–64]. Some authors have reported that the image resolution is far better than what can be achieved with current intraoperative clinical MRI technology and the system can be applied easily. With ultrasound guidance, it is possible to perform safer and more radical surgery, which may have a positive influence on the postoperative functional and oncological outcome. Additional studies on this promising application are under way.

References

1. Jecker P. Ultrasonography of the face, paranasal sinuses, and ear. In: Orloff L, editor. Head and neck ultrasonography. 2nd ed. San Diego: Plural Publishing; 2016. p. 323–41.
2. Peng J, Cai X, Gong J, Zou H, Chen Q, Chen J. Use of diagnostic ultrasound of sinus in the paranasal sinus disease. [Article in Chinese]. Lin Chuang Er Bi Yan Hou Ke Za Zhi. 1999;13:81–2.
3. Gianoli GJ, Mann WJ, Miller RH. B-mode ultrasonography of the paranasal sinuses compared with CT findings. Otolaryngol Head Neck Surg. 1992;107:713–20.
4. Riechelmann H, Mann W. Ultrasonography of paranasal sinus lesions. Rhinol Suppl. 1992;14:136–40.
5. Jannert M, Andreasson L, Benthin M, Dahl P. Ultrasonography of the paranasal sinuses. A new computerized equipment using LCD-display and capture mode. Rhinology. 1987;25:133–7.
6. Mann W, Burny A, Schlenter W. Ultrasonography in paranasal sinus disease. Ann Otolaryngol Chir Cervicofac. 1981;98:299–303.
7. Belic B, Erdevicki L, Stojanovic J, Stojanovic S, Arsenijevic S, Stankovic P. A-mode ultrasonography and roentgenography in diagnosing chronic nonpolypoid maxillary rhinosinusitis. Acta Chir Jugosl. 2009;56:139–44.
8. Zagolski O, Strek P. Ultrasonography of the nose and paranasal sinuses. Pol Merkur Lekarski. 2007;22:32–5.
9. Pfister R, Lütolf M, Schapowal A, Glatte B, Schmitz M, Menz G. Screening for sinus disease in patients with asthma: a computed tomography-controlled comparison of A- mode ultrasonography and standard radiography. J Allergy Clin Immunol. 1994;94:804–9.
10. Lichtenstein D, Bidermann P, Meziere G, Gepner A. The sinusogram, a real time ultrasound sign of maxillary sinusitis. Intensive Care Med. 1998;24:1057–61.
11. Bektas F, Soyuncu S, Yigit O. Acute maxillary sinusitis detected by bedside emergency department ultrasonography. Int J Emerg Med. 2010;3:497–8.
12. Vento SI, Ertama LO, Hytönen ML, Malmberg CH. A-mode ultrasound in the diagnosis of chronic polypous sinusitis. Acta Otolaryngol. 1999;119:916–20.
13. Druce HM. The use of ultrasound as an imaging technique in the diagnosis of sinusitis. N Engl Reg Allergy Proc. 1988;9:109–12.
14. Teppo H, Revonta M. Ultrasound device helps in ruling out maxillary sinus fluid in acute rhinosinusitis: how we do it. Clin Otolaryngol. 2011;36:491–4.
15. Mori A, Nakayama T, Tsukidate T, Hirabayashi H, Haruna S. Comparison of B- mode ultrasonography and computed tomography in the evaluation of maxillary sinusitis in pediatric patients. [Article in Japanese]. Nihon Jibiinkoka Gakkai Kaiho. 2014;117:26–33.
16. McQuilla L, Crane LA, Kempe A. Diagnosis and management of acute sinusitis by pediatricians. Pediatrics. 2009;123:e193–8.
17. Revonta M, Kuuliala I. The diagnosis and follow-up of pediatric sinusitis: Water's view radiography versus ultrasonography. Laryngoscope. 1989;99:321–4.
18. Benninger MS, McFarlin K, Hamilton DR, Rubinfeld I, Sargsyan AE, Melton SL, et al. Ultrasonographic evaluation of sinusitis during microgravity in a novel animal model. Arch Otolaryngol Head Neck Surg. 2010;136:1094–8.
19. Aras MH, Miloglu O, Barutcugil C, Kantarci M, Ozcan E, Harorli A. Comparison of the sensitivity for detecting foreign bodies among conventional plain radiography, computed tomography and ultrasonography. Dentomaxillofac Radiol. 2010;39:72–8.
20. Ghatasheh M, Smadi A. Ultrasonography versus radiography in the diagnosis of maxillary sinus. East Mediterr Health J. 2000;6:1083–6.
21. Puhakka T, Heikkinen T, Mäkelä MJ, Alanen A, Kallio T, Korsoff L, et al. Validity of ultrasonography in diagnosis of acute maxillary sinusitis. Arch Otolaryngol Head Neck Surg. 2000;126:1482–6.
22. Jecker P. Ultraschalluntersuchung der Nasennebenhöhlen und der Orbita. In: Welkoborsky HJ, Jecker P, Maurer J, Mann WJ, editors. Ultraschall im Kopf-Hals- Bereich. Stuttgart: Thieme Verlag; 2013. p. 121–31.
23. Jecker P. Diagnostic use of ultrasound for examination of the nose and the paranasal sinuses. [Article in German]. Ultraschall Med. 2005;26:501–16.
24. Thompson LD. Paranasal sinus mucocele. Ear Nose Throat J. 2012;91:276–8.
25. Liu JJ, Gao Y, Wu YF, Zhu SY. Sonography for diagnosis of benign and malignant tumors of the nose and paranasal sinuses. J Ultrasound Med. 2014;33:1627–34.
26. Gao Y, Yan X, Lai M, Guo P, Wu Y, Zhu S. T-Staging of maxillary sinus carcinoma: comparison of ultrasonography and computed tomography. Discov Med. 2016;21:469–77.
27. Lee IS, Lee JH, Woo CK, Kim HJ, Sol YL, Song JW, Cho KS. Ultrasonography in the diagnosis of nasal bone fractures: a comparison with conventional radiography and computed tomography. Eur Arch Otorhinolaryngol. 2016;273:413–8.
28. Nemati S, Jandaghi AB, Banan R, Aghajanpour M, Kazemnezhad E. Ultrasonography findings in nasal bone fracture; 6-month follow-up: can we estimate time of trauma? Eur Arch Otorhinolaryngol. 2015;272:873–6.
29. Mohammadi A, Ghasemi-Rad M. Nasal bone fracture – ultrasonography or computed tomography? Med Ultrason. 2011;13:292–5.
30. Atighechi S, Baradaranfar MH, Karimi G, Dadgarnia MH, Mansoorian HR, Barkhordari N, et al. Diagnostic value of ultrasonography in the diagnosis of nasal fractures. J Craniofac Surg. 2014;25:e51–3.
31. Javadrashid R, Khatoonabad M, Shams N, Esmaeili F, Jabbari KH. Comparison of ultrasonography with computed tomography

in the diagnosis of nasal bone fractures. Dentomaxillofac Radiol. 2011;40:486–91.
32. Friedrich RE, Heiland M, Bartel-Friedrich S. Potentials of ultrasound in the diagnosis of midfacial fractures. Clin Oral Investig. 2003;7:226–9.
33. Adeyemo WL, Akadiri OA. A systematic review of the diagnostic role of ultrasonography in maxillofacial fractures. Int J Oral Maxillofac Surg. 2011;40:655–61.
34. Menon RP, Chowdhury SK, Semi RS, Gupta V, Rahman S, Balasundaram T. Comparison of ultrasonography with conventional radiography in the diagnosis of zygomatic complex fractures. J Craniomaxillofac Surg. 2016;44:353–6.
35. Ogunmuyiwa SA, Fatusi OA, Ugboko VI, Ayoola OO, Maaji SM. The validity of ultrasonography in the diagnosis of zygomaticomaxillary complex fractures. Int J Oral Maxillofac Surg. 2012;41:500–5.
36. Graß SK, Deichmüller CM, Brandis A, Welkoborsky HJ. Pilomatrixoma – an important differential diagnosis of facial masses. [Article in German]. Laryngorhinootologie. 2015;94:29–33.
37. Hande PC, Talwar I. Multimodality imaging of the orbit. Indian J Radiol Imaging. 2012;22:227–39.
38. Rose GE, Verity DH. Neuro-ophthalmology of orbital disease. Handb Clin Neurol. 2011;102:467–91.
39. Dudea SM. Ultrasonography of the eye and orbit. Med Ultrason. 2011;13:171–4.
40. Gaßner I, Mair M. Sonographie von Bulbus oculi und Orbita. Kind Radiologie. 2006;3:34–9.
41. Gaßner I, Mair M. Bulbus oculi und Orbita. In: Hofmann V, Deeg KH, Hoyer PF, editors. Ultraschalldiagnostik in Pädiatrie und Kinderchirurgie. Stuttgart: Thieme Verlag; 2005. p. 191ff.
42. Ciocalteu AM, Ardeleanu S, Checherita IA. The role of ultrasonography exam in orbital-ocular tumors. Rev Med Chir Soc Med Nat Iasi. 2011;115:1113–8.
43. Fernandez-Dominguez J, Garcia-Rodriguez R, Mateos V. Transorbital echography for assessment of optical nerve atrophy in demyelinating diseases: a pilot study. Rev Neurol. 2012;54:587–92.
44. Karami M, Janghorbani M, Dehghani A, Riahinejad M. Orbital Doppler evaluation of blood flow velocities in optic neuritis. Korean J Ophthalmol. 2012;26:116–22.
45. Shokoohi H, Taheri MR, Boniface KS, Abdulmohsen A, Janet L. Orbital ultrasound in the selective screening of a dural-cavernous sinus fistula. Eur J Emerg Med. 2013;20:137–9.
46. Foster T, Tayal VS, Saunders T, Norton J. Emergency ultrasound optic nerve sheath measurement to detect increased intracranial pressure in head injury patients: preliminary study of interobserver variability in normal human subjects. Acad Emerg Med. 2003;10:487–8.
47. Welkoborsky HJ. Ultrasonography of the orbit. In: Welkoborsky HJ, Wiechens B, Hinni ML, editors. Orbit surgery. Stuttgart: Thieme Publishers; 2017. p. 59–66.
48. Graß S, Welkoborsky HJ. Orbital complications. In: Welkoborsky HJ, Wiechens B, Hinni ML, editors. Orbit surgery. Stuttgart: Thieme Publishers; 2017. p. 89–97.
49. Chang SH, Papageorgiu K, Ang M, King AJ, Goldberg RA. High-resolution ultrasound as an effective and practical tool to analyze eyebrow profile expansion in thyroid-associated periorbitopathy. Ophthalmic Plast Reconstr Surg. 2013;29:382–5.
50. Orlandi D, Sconfineza LM, Lacelli F, Bertolotto M, Sola S, Mauri G, et al. Ultrasound-guided core-needle biopsy of extra-ocular orbital lesions. Eur Radiol. 2013;23:1919–24.
51. Wagner LH, Reich SS, Johnson BB. Frontal sinus mucocele diagnosed by fundus examination and B-mode ultrasonography. JAMA Ophthalmol. 2015;133:e151159.
52. Aslan A, Büyükkaya R, Tan S, Erdogan C, Hakyemez B. Efficacy of ultrasonography in lymphatic malformations: diagnosis, treatment and follow-up: a case report. Med Ultrason. 2013;15:244–6.
53. Chawla B, Hada M, Kashyap S, Bakhshi S. Orbital retinoblastoma in an adult. Orbit. 2013;32:146–8.
54. Alkatan HM, Alaraj A, El-Khani A, Al-Sheikh O. Ocular adnexal lymphoproliferative disorders in an ophthalmic referral center in Saudi Arabia. Saudi J Ophthalmol. 2013;27:227–30.
55. Rasmussen PK, Coupland SE, Finger PT, Graue GF, Grossniklaus HE, Honavar SG, et al. Ocular adnexal follicular lymphoma: a multicenter international study. JAMA Ophthalmol. 2014;132:851–8.
56. Jenkins CN, Thuau H. Ultrasound imaging in assessment of fractures of the orbital floor. Clin Radiol. 1997;52:708–11.
57. Johari M, Ghavimi MA, Mahmoudian H, Javadrashid R, Mirakhor Samani S, Fouladi DF. A comparable study of the diagnostic performance of orbital ultrasonography and CBCT in patients with suspected orbital floor fractures. Dentomaxillofac Radiol. 2016. https://doi.org/10.1259/dmfr20150311.
58. Jank S, Emshoff R, Etzelsdorfer M, Strobl H, Nicasi A, Norer B. The diagnostic value of ultrasonography in the detection of orbital floor fractures with a curved array transducer. Int J Oral Maxillofac Surg. 2004;33:13–8.
59. Srirangam R, Gokhale SK, Kulkarni AU, Gadre KS. Unusual intraorbital foreign body. BMJ Case Rep. 2012;2012. pii: bcr1220115377. https://doi.org/10.1136/bcr-12-2011-5377.
60. Patel SN, Langer PD, Zarbin MA, Bhagat N. Diagnostic value of clinical examination and radiographic imaging in identification of intraocular foreign bodies in open globe injury. Eur J Ophthalmol. 2012;22:259–68.
61. Solheim O, Selbekk T, Løvstakken L, Tangen GA, Solberg OV, Johansen TF, et al. Intrasellar ultrasound in transsphenoidal surgery: a novel technique. Neurosurgery. 2010;66:173–85; discussion 185–6.
62. Ishikawa M, Ota Y, Yoshida N, Iino Y, Tanaka Y, Watanabe E. Endonasal ultrasonography-assisted neuroendoscopic transsphenoidal surgery. Acta Neurochir (Wien). 2015;157:863–8; discussion 868.
63. Ota Y, Mami I. Ultrasonography imaging during nasal endoscopic transsphenoidal surgery. ORL J Otorhinolaryngol Relat Spec. 2013;75:27–31.
64. Marcus HJ, Vercauteren T, Ourselin S, Dorward NL. Intraoperative ultrasound in patients undergoing transsphenoidal surgery for pituitary adenoma: systematic review [corrected]. World Neurosurg. 2017;106:680–5.

Endoscopic Ultrasound

15

Christoph Arens and Nikolaos Davaris

15.1 Introduction

In recent years, endoscopic ultrasound (EUS), also known as *endosonography*, has been established as a useful diagnostic tool, especially in gastroenterology and pneumology. Both its indications and clinical applications have been continuously evolving. With most endoscopic imaging techniques divided into horizontal and vertical planes, EUS belongs to the latter group, that enables an examination of a tissue in depth [1]. In otorhinolaryngology, EUS can combine the advantages of both endoscopy and sonography, providing important information in areas that are difficult to examine by transcervical ultrasound alone, such as the adult larynx [1]. It can be particularly valuable for evaluating the infiltration depth of malignant tumors in various anatomic areas.

15.2 Technical Remarks, Equipment, and Methods

EUS can be performed using miniature probes, echoendoscopes, or conventional ultrasound transducers, depending on the area to be examined. Echoendoscopes are available in two imaging planes, curved linear ("linear") array or radial array [2]. In linear array probes, the piezoelectric crystals are arranged in a linear formation within the transducer, producing a rectangular beam. In modern radial array probes, the piezoelectric crystals are arranged in a fixed annular pattern; older devices use a rotating disc. Consequently, the ultrasound field produced is radial (360°). The optical sensor and suction channel can be located proximally or distally to the transducer. Miniature probes (miniprobes) are placed throughout the channels of (or attached to) standard endoscopes. Small conventional L-shaped ultrasound probes (hockey stick probes) are suitable for echoendoscopic examination of the oral cavity, the oropharynx, and the outer ear.

The selected scanning frequency depends on the required accuracy and imaging depth needed. A high scanning frequency can provide very precise details in the vicinity of the probe and therefore predominately in the superficial tissue layers, but it cannot penetrate deeper into the tissue, which results in poorer resolution. As early as 1994, EUS probes of 7.5 MHz were used during microlaryngoscopy, for example [3]. Multiband miniprobes with a frequency range of 10–30 MHz (high-frequency EUS) are ideal for ultrasound examination of the larynx, trachea, hypopharynx, and esophagus. They have a diameter of 2–5 millimeters and can pass through most stenoses [4]. Different manufacturers provide a variety of devices with different technical specifications, such as echoendoscope channel diameter, ultrasound radial field (mostly 110–180°), or the scanning frequency (ranging from 5 to 20 MHz).

For intraoperative examination of the oral cavity, a small conventional ultrasound transducer ("hockey stick") or a linear array echoendoscope can be used after flooding the cavity with saline solution. Gauze swabs in the oropharynx prevent the leak of saline solution. In an office setting, the ultrasound probe can be placed in an examination glove or in a rubber sheath filled with ultrasound gel. This approach is usually well tolerated for the examination of the vestibule of the mouth, lips, tongue, buccal and palatal mucosa, the tonsillar region, and the floor of the mouth. A semisolid acoustic coupling medium can be regarded as a favorable alternative to ultrasound gel, which moves around and often loses contact with the tissue [5]. This intraoral approach can be limited in some cases by the gag reflex and the patient's discomfort or pain [6].

Examination of the nasal cavity can be performed intraoperatively with a radial array probe or miniprobe, which is inserted through the nostril after flooding the nasal cavity with saline solution. Gauze swabs in the nasopharynx or a balloon, as described by Noda et al. [7], prevents water

C. Arens (✉) · N. Davaris
Department of Otorhinolaryngology, Head and Neck Surgery, University Hospital Magdeburg, Otto-von-Guericke University, Magdeburg, Germany
e-mail: christoph.arens@med.ovgu.de

© Springer Nature Switzerland AG 2019

H. J. Welkoborsky, P. Jecker (eds.), *Ultrasonography of the Head and Neck*, https://doi.org/10.1007/978-3-030-12641-4_15

leakage. The paranasal sinuses can also be visualized, which makes this technique suitable even during endoscopic sinus surgery [7].

Although the indications are limited, EUS also can be performed to visualize the external acoustic meatus using small-diameter, radial array probes after filling the ear canal with a saline solution. A linear array probe or a "hockey stick" transducer can be used to examine the outer ear.

Ultrasonographic examination of the upper trachea, larynx and hypopharynx is performed during microlaryngoscopy after placing the endotracheal tube near the carina and flooding the lumen with a saline solution to allow acoustic coupling to the mucosa [8, 9]. Air bubbles are removed by suction and softly tapping on the cricoid. To evaluate the posterior larynx, the orotracheal tube is loaded up with a laryngoscope [1]. Alternatively, a water-filled balloon can be used around the transducer of the echoendoscope.

15.3 Sonographic Characteristics of Particular Structures and Clinical Applications

15.3.1 Outer Ear and External Acoustic Meatus

The cartilage of the external acoustic meatus and the outer ear appears hyperechoic, whereas most tumors display as hypoechoic to isoechoic masses (Fig. 15.1).

EUS has also been used to demonstrate middle ear effusion, but the use of this method is limited in clinical practice [10].

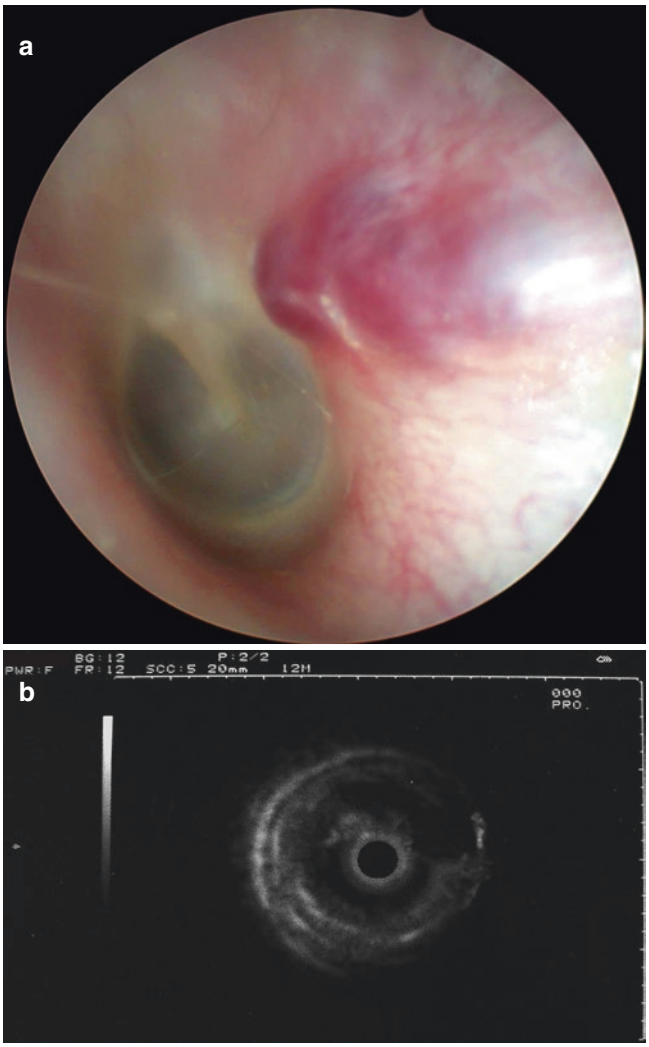

Fig. 15.1 (**a**, **b**) Hemangioma of the outer ear duct. The tumor appears hypoechoic to anechoic. The bony structures are hyperechoic

15.3.2 Nasal Cavity, Paranasal Sinuses, and Nasopharynx

Important anatomical structures such as the nasal septum, the nasal turbinates, and the lamina papyracea can be recognized by endosonography. These structures appear as hyperechoic lines, whereas the mucosa has a homogenous isoechoic to hypoechoic pattern. The walls of the paranasal sinuses can also be visualized as hyperechoic lines. In cases of extensive defects of the lamina papyracea, the periorbital adipose tissue can be distinguished as an isoechoic to hyperechoic area (Figs. 15.2 and 15.3) [7].

Submucosal glandular or nasolabial cysts appear as an anechoic, roundish pattern. Hemangiomas and most solid tumors appear isoechoic or hypoechoic, and EUS can help to estimate the depth of infiltration [11].

The nasopharynx is difficult to assess and displays an irregular shape. Lymphatic tissue is mostly hyperechoic. The surrounding bony structures lead to a complete reflex-

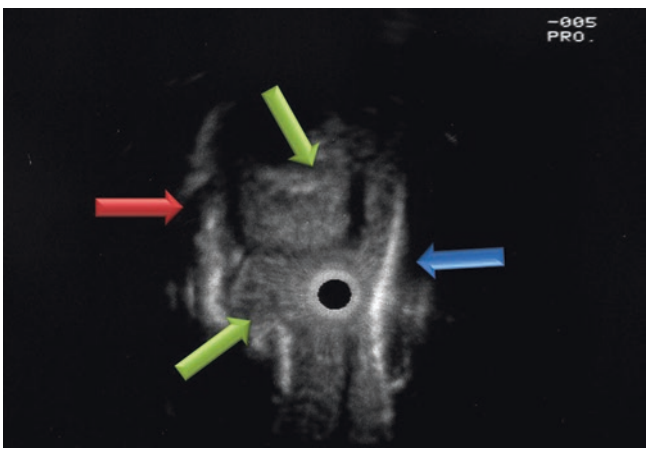

Fig. 15.2 Endosonography of the nasal cavity, displays the semilunar hiatus (*red arrow*), the conchae (*green arrows*), and the nasal septum (*blue arrow*)

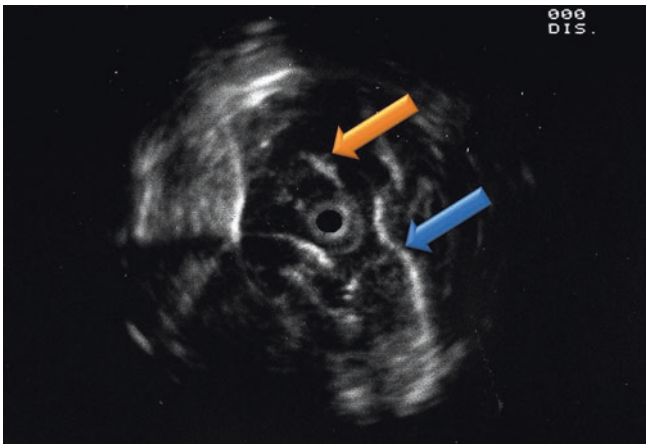

Fig. 15.3 A miniprobe is surrounded by hypoechoic nasal polyps (*orange arrow*). The *blue arrow* indicates the nasal septum

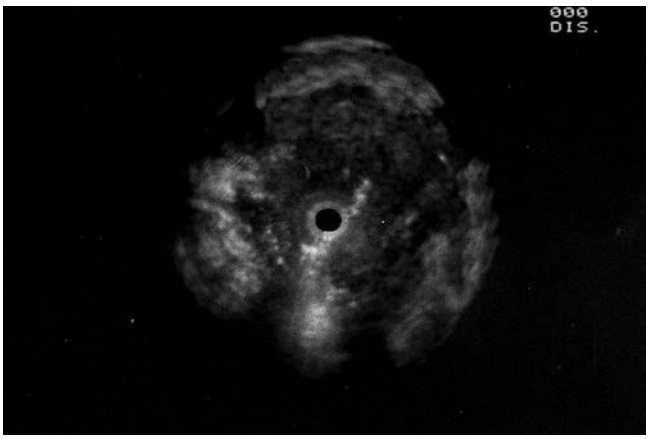

Fig. 15.5 Hypoechoic nasopharyngeal cancer. Artefacts are caused by air bubbles around the probe

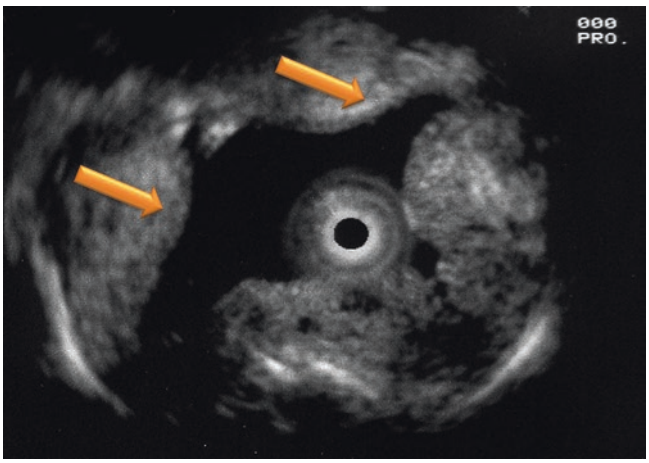

Fig. 15.4 In this nasopharynx, the probe is attached to the lymphatic tissue of the adenoids. *Orange arrows* mark the velum palatinum

ion and can be visualized as a sharp edge. Cystic lesions have an anechoic appearance and can easily be detected (Fig. 15.4).

Nasopharyngeal cancer can be examined in a nasopharynx flooded with saline solution. It usually presents as an exophytic and hypoechoic mass, that can be easily delineated from the surrounding tissue (Fig. 15.5).

15.3.3 Oral Cavity and Oropharynx

The oral mucosa usually appears isoechoic with a homogenous pattern. In the buccal mucosa, a hyperechoic aspect is attributed to the mandibular bone, whereas the sublingual glands lead to acoustic shadowing in the floor of the mouth [6]. Cysts and ranula can be easily visualized, appearing anechoic with a posterior sound enhancement. Lipomas are mostly ellipsoid in shape, appearing slightly hyperechoic with characteristic linear echogenic striations parallel to the skin (featherlike pattern) [12].

Invasive carcinomas appear mostly as hypoechoic to nearly anechoic masses. The intraoral ultrasound examination can provide precise information about the depth of infiltration, the tumor extension, and the depth of the margins in the tongue or in the mucosa of the buccal area and mouth floor, avoiding possible artifacts caused by air bubbles or the mandibula (Figs. 15.6, 15.7, 15.8, and 15.9) [6, 13]. The tumor thickness can be measured. Modern ultrasound transducers can identify carcinomas with a thickness of 1 mm. A thickness less than 2 mm is associated with an extension into the lamina propria. A thickness greater than 6 mm is associated with the infiltration of the muscular layer [6, 14]. According to a recent meta-analysis, the sonographic intraoral examination of tumor thickness is highly accurate with a resolution of 0.5 mm [15].

15.3.4 Larynx

Ossification of the laryngeal cartilage in adults and intraluminal air usually do not allow adequate examination of the larynx by transcervical ultrasound. On the other hand, EUS can provide precise information about laryngeal lesions as small as 3 mm. Adequate knowledge of the sonographic anatomy of the larynx is a prerequisite for endolaryngeal ultrasound examination and recognition of pathological features. Endosonographic examination of the larynx is usually performed using a radial echoendoscope (miniprobe), similar to the examination of the trachea. Anatomical structures such as the vocal ligament, the thyroarytenoid (vocal) muscle, the ventricular fold, the preepiglottic and paraglottic spaces, and the epiglottis can easily be identified [4].

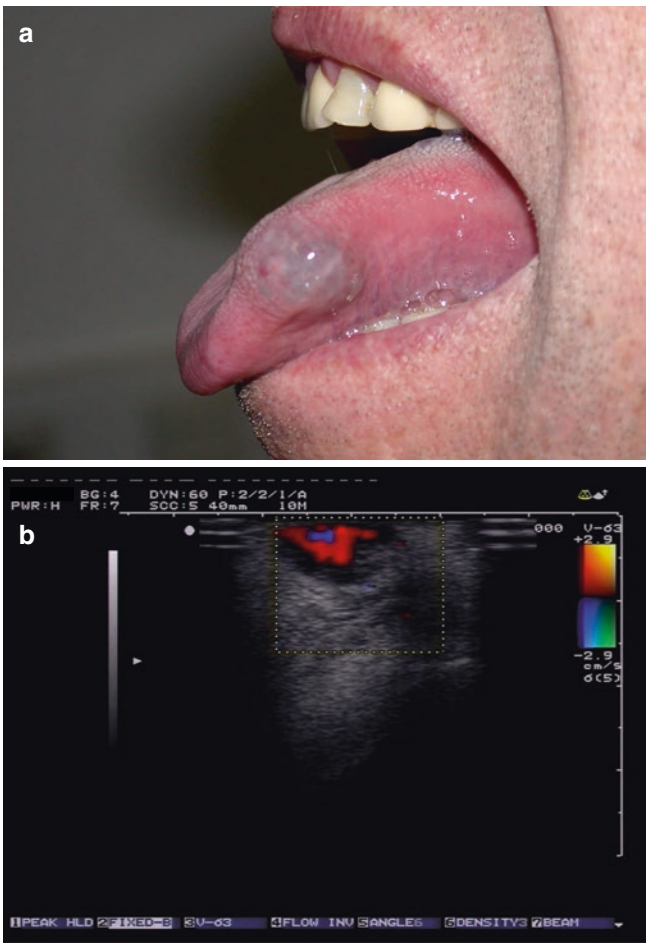

Fig. 15.6 (**a**) Typical purple appearance of a hemangioma of the left tongue. (**b**) Colored duplex mode during endosonography confirms a high perfusion of the lesion

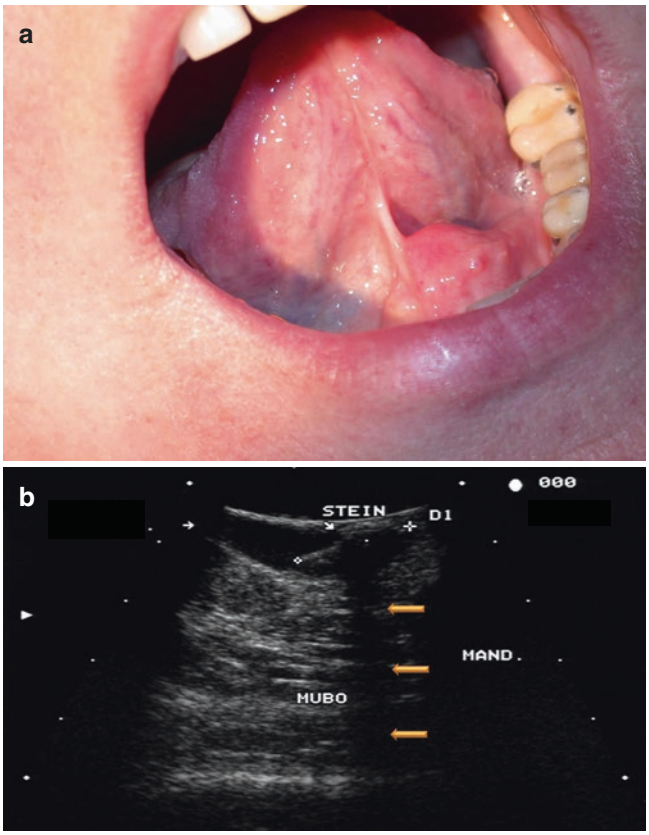

Fig. 15.7 (**a**) Endoscopic picture reveals a sialolithiasis of the submandibular duct. (**b**) Endosonography presents a complete reflection of the ultrasound beam by the stone. Orange arrows indicate distal shadowing

The vocal folds normally appear hypoechoic because of the vocalis muscle and the paraglottic space, whereas the epithelium and the vocal ligament appear hyperechoic. This hyperechoic pattern is enhanced through significant differences in impedance between the tissue and the intraluminal water [1]. The ventricular folds and preepiglottic space have a slightly denser echo than the vocal folds, possibly due to the greater amount of tissue containing seromucous glands and fat [1, 8]. The inner and outer perichondrium of the cricoid and thyroid cartilage appears hyperechoic. The elastic cartilage in some areas is hypoechoic, but in adults it is mostly isoechoic to hyperechoic because of ossification [16]. The cricoid appears as a closed ring, whereas the thyroid cartilage has a triangular shape (Figs. 15.10, 15.11, and 15.12).

Tumors can usually be identified by endoscopic examination. In the EUS examination carcinomas usually appear as hypoechoic masses, with clear margins [4]. In exophytic carcinomas or those near the anterior commissure, it can be difficult to distinguish between an infiltrative growth pattern and lesions just touching the vocal folds. EUS can be used to detect carcinomas with a minimal extension of 3 mm, but smaller tumors are hardly visible (Fig. 15.13) [1]. Identification of thyroid cartilage infiltration by a carcinoma is a crucial issue and of great importance for the therapeutic procedure. It is seen as an interruption of the inner perichondrium, which then appears blurred and hypoechoic (Fig. 15.14). However, precancerous lesions and microinvasive cancer can be better assessed by digital chromoendoscopy and optical coherence tomography (SIN I-III, T1 < 3 mm). In a prospective study, the authors were able to demonstrate that EUS has a higher accuracy (89 vs. 77%) in comparison to CT or MRI. Only the specificity (93 vs. 89%) and positive predictive value (89 vs. 83%) did not present a significant difference between EUS and MRI [17].

The identification of small, benign lesions such as polyps or vocal fold nodules is usually difficult with EUS alone, but laryngeal cysts or Reinke's edema can be identified, appearing as anechoic or hypoechoic masses with a clear border (Fig. 15.15).

EUS is also helpful for the grading of laryngeal stenoses, before and after surgery [8].

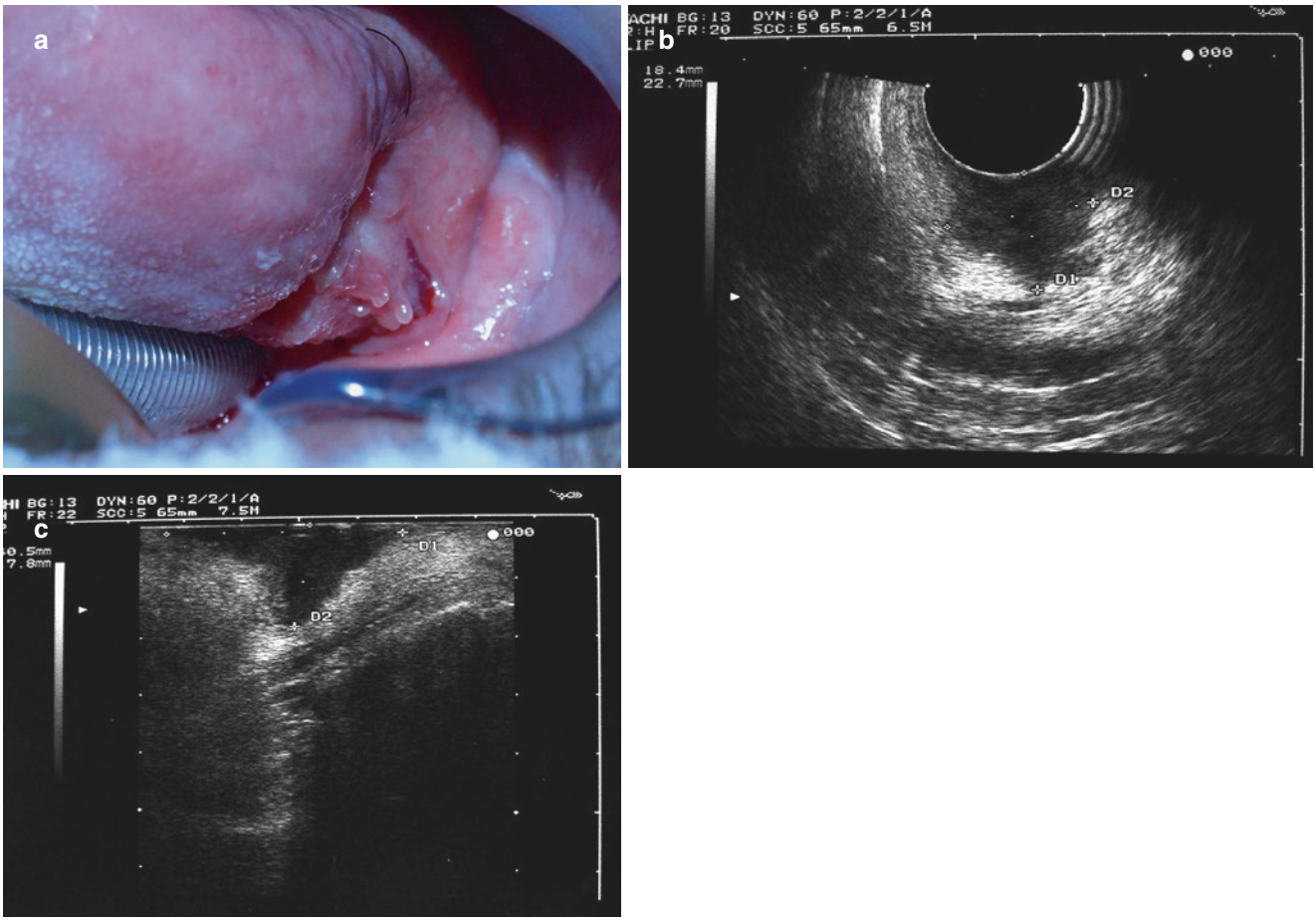

Fig. 15.8 Tongue cancer. (**a**) Clinical image of a squamous cell carcinoma of the tongue. (**b**) and (**c**) show the tumor in two different planes. The lesion appears irregular and hypoechoic. The infiltration depth and boarding structures can easily be assessed

15.3.5 Trachea

The trachea has a horseshoe shape, which leads to its typical appearance in EUS (Fig. 15.16). The examination is usually performed using a radial echoendoscope and starts moving upward inferiorly and continuously, until reaching the cricoid cartilage. The elastic cartilages of the trachea can be used as anatomical landmarks. They appear hypoechoic, whereas the inner and outer perichondrium appears hyperechoic. The mucosa is isoechoic with a homogenous echogenicity [4, 16].

Lesions in the tracheal mucosa or in the membranous portion of the trachea can be identified by the examination, and cartilage involvement can also be assessed [4]. Carcinomas mostly appear hypoechoic, and their size and depth of infiltration can be measured. Additionally, EUS can be used to measure the degree of tracheal stenoses before and after therapy [16].

15.3.6 Hypopharynx

Examination of the hypopharynx is performed intraoperatively. The superficial mucosa appears hyperechoic, and the muscularis layer is hypoechoic. Tumors usually can be well visualized after endoscopic detection when the hypopharynx is flooded with saline solution. This technique is suitable to measure the depth of tumor infiltration (Fig. 15.17) [19].

In most cases, carotid arteries and possible lymph nodes also can be identified [4].

15.3.7 Proximal Esophagus

In echoendoscopic evaluation of the esophagus, five tissue layers can be identified. Examination is usually performed with a radial echoendoscope. The superficial mucosa appears hyperechoic and the deeper mucosal layer is

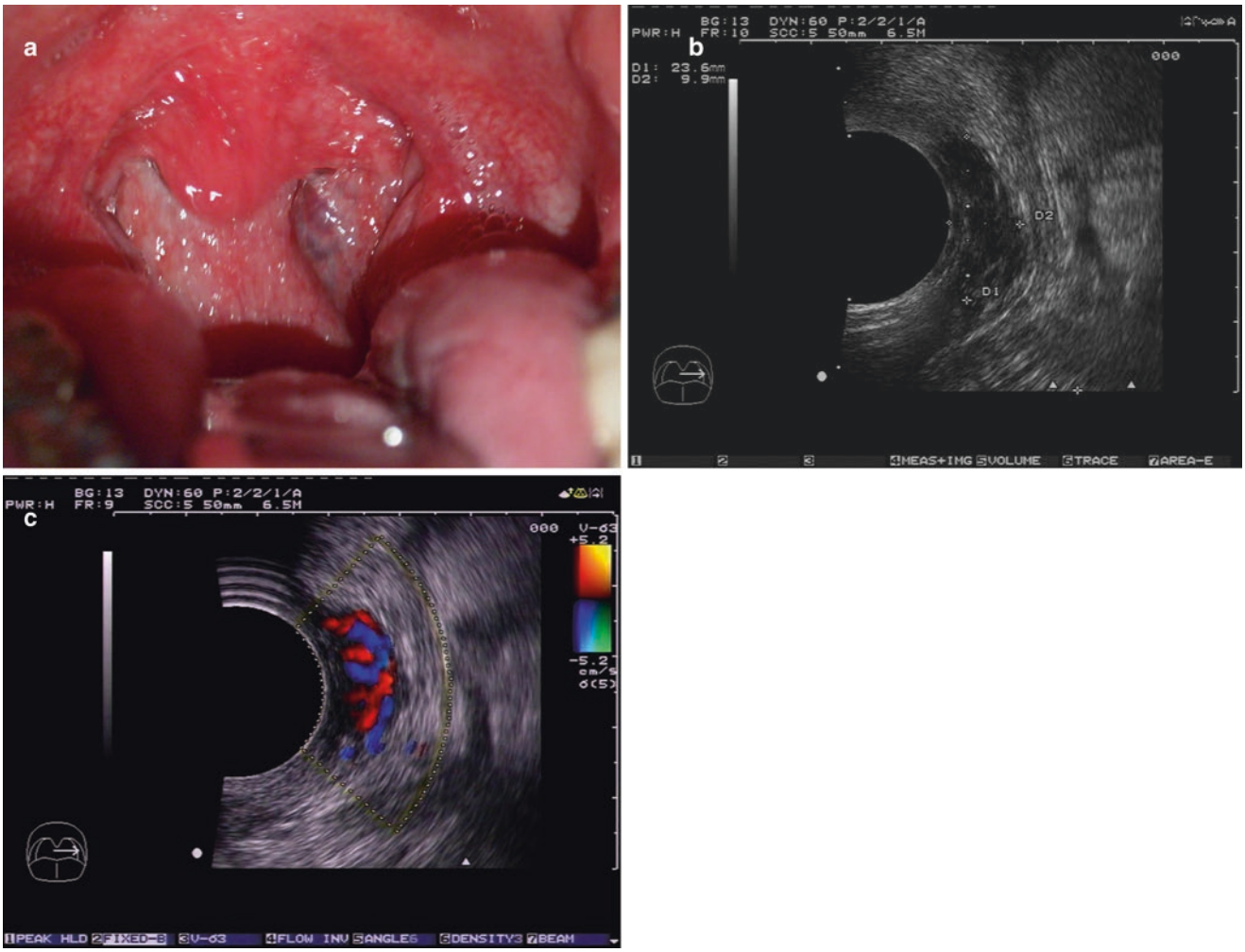

Fig. 15.9 (**a**) Clinical image of an hemangioma of the left oropharynx. (**b**) Endosonographic B-mode image presents a sharp delineated hypoechoic mass. (**c**) Colored duplex mode demonstrated high perfusion of the lesion indicating an hemangioma

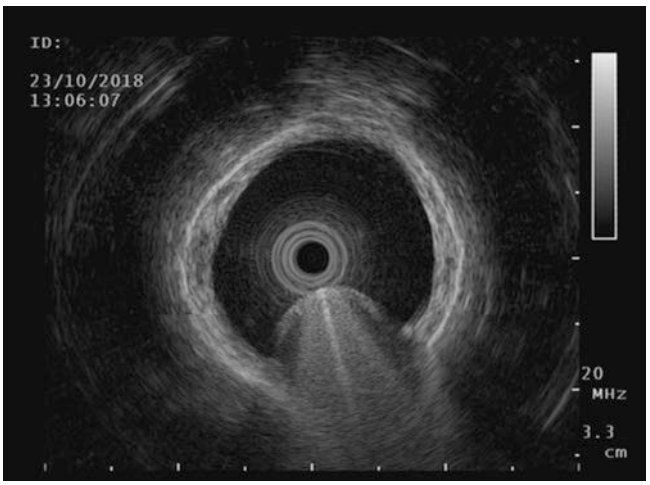

Fig. 15.10 Almost completely closed cricoid ring, with hyperechoic cartilage

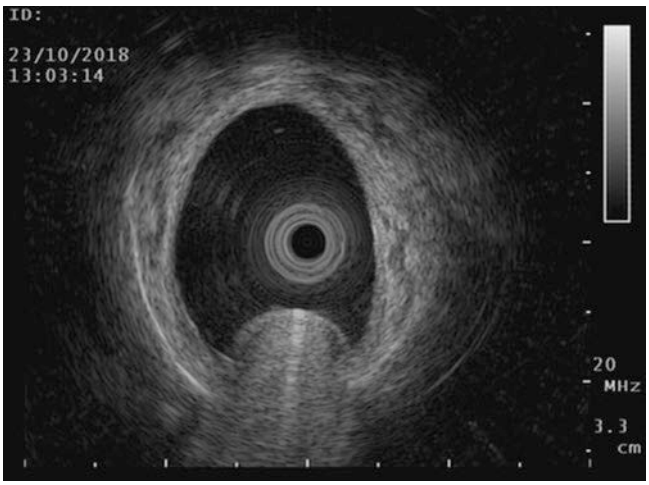

Fig. 15.11 Cricoid ring that opens anteriorly through the cricothyroid ligament

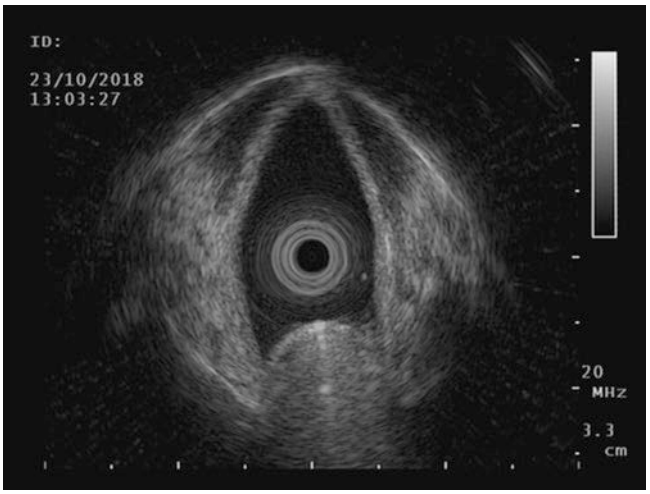

Fig. 15.12 V-shaped thyroid cartilage. The vocal folds appear hypoechoic, whereas the elastic cone shows a hyperechoic signal

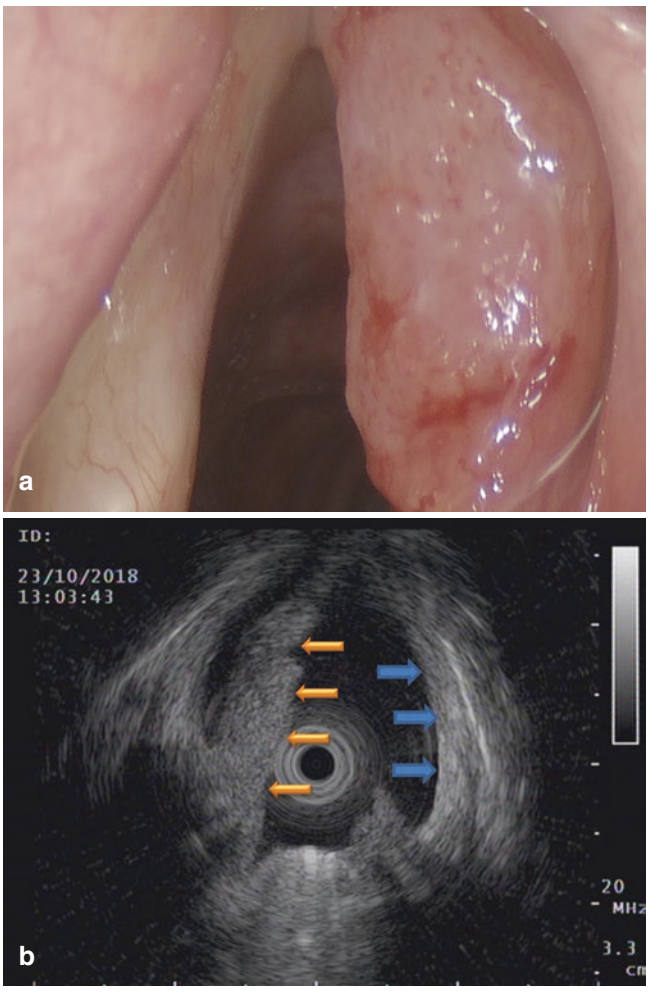

Fig. 15.13 Tumor of the left vocal fold. (**a**) Clinical image. (**b**) In EUS, the *orange arrows* point at the tumor; the *blue arrows* indicate the Morgagni ventricle

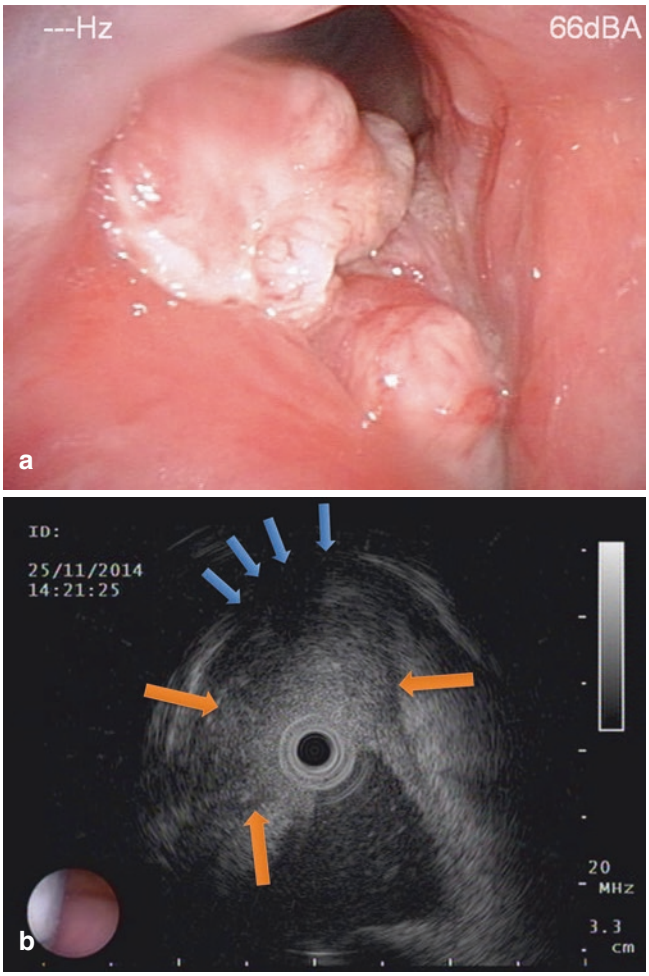

Fig. 15.14 Recurrent T4 laryngeal cancer. (**a**) Clinical image. (**b**) In EUS, *blue arrows* indicate infiltration of the thyroid cartilage; the *orange arrows* indicate the tumor

hypoechoic. The next tissue layer is hyperechoic and corresponds to the submucosa, followed by the muscularis propria (hypoechoic) and the serosa (hyperechoic) [18].

The thyroid gland can be identified as a hyperechoic structure on either side of the trachea, and the thymus can sometimes be visualized distal to the thyroid. The left and right internal jugular veins course medially to the thyroid gland, and the left and right carotid arteries can also be visualized. Furthermore, paraesophageal and paratracheal lymph nodes and tumors can be identified in this area (Figs. 15.18 and 15.19) [18].

EUS-guided fine-needle aspiration and core biopsies can easily be performed. The application of linear ultrasound probes is recommended for fine-needle aspiration, as the needle remains in the imaging beam, allowing precise guidance and placement. Core biopsies, on the other hand, are preferentially performed with radial array echoendoscopes [19].

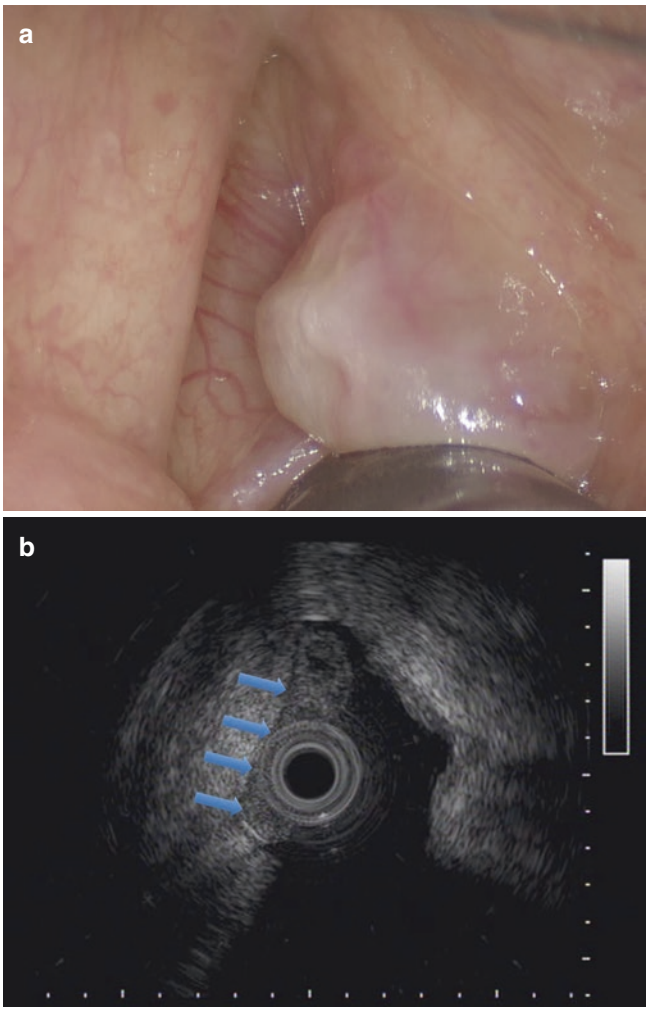

Fig. 15.15 Reinke's edema. (**a**) Clinical image. (**b**) In EUS, *blue arrows* point at a right-sided Reinke's edema extending to the supraglottic area

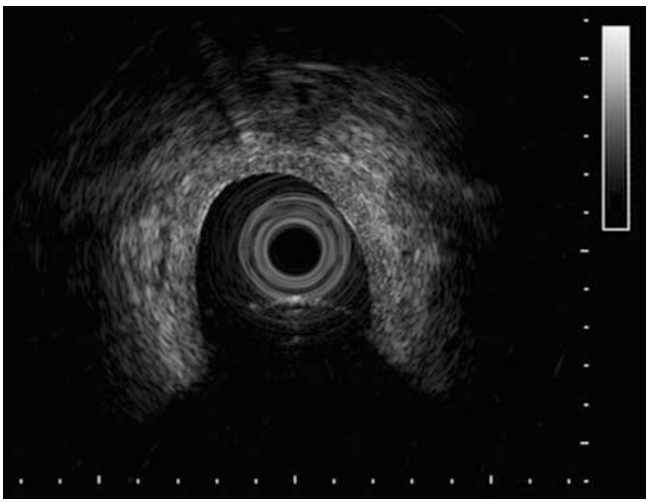

Fig. 15.16 Typical horseshoe-shape appearance of the trachea on EUS

Fig. 15.17 Endoscopic ultrasound (EUS) examination of the right piriform sinus with a visible hypoechoic lymph node (LK)

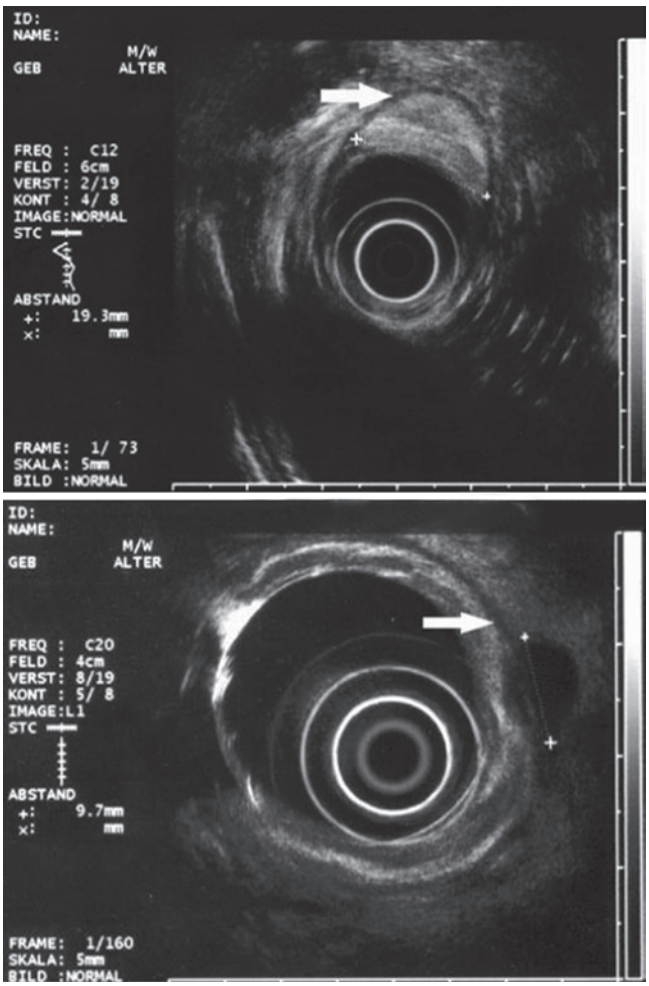

Fig. 15.18 Lipoma of the esophagus. Clear delineated echogenic tumor of the tunica submucosa. *Arrow* indicates lamina muscularis propria

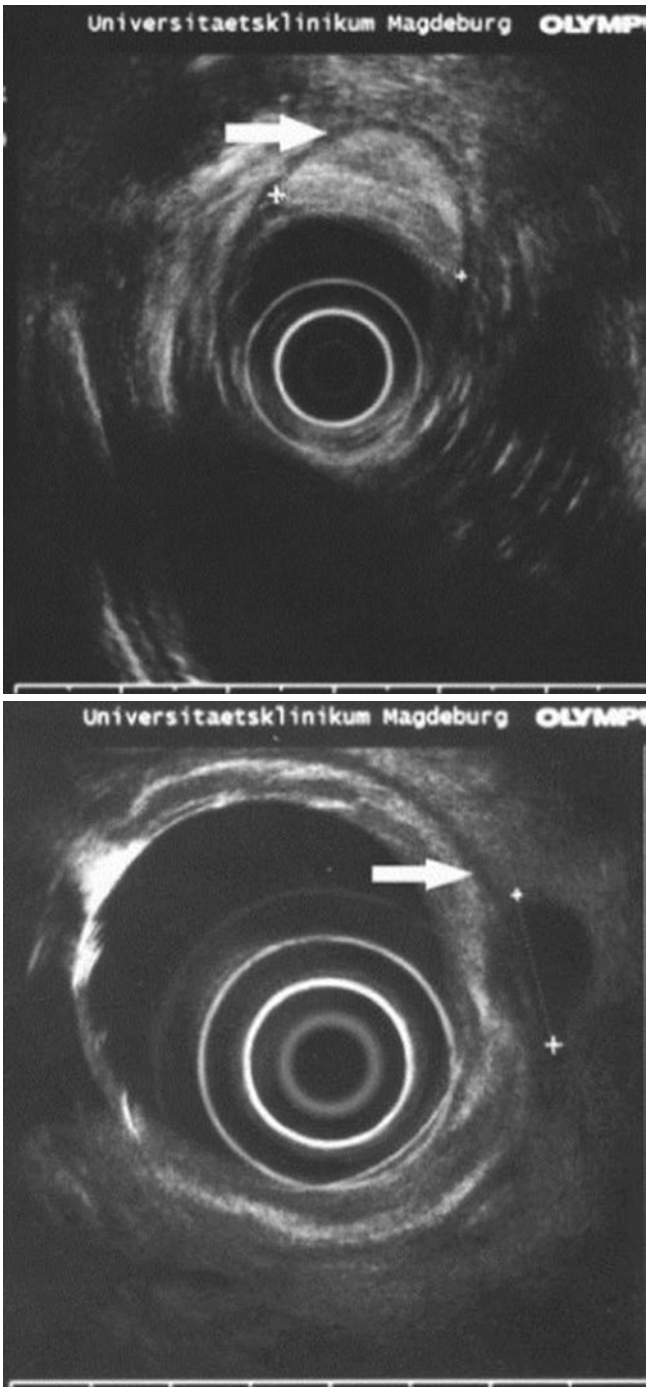

Fig. 15.19 Hypoechoic tumor (between markers) of the lamina muscularis propria (*arrowhead*). It is most likely a leiomyoma. Differential diagnosis should include a gastrointestinal stromal tumor (GIST)

15.4 Conclusion

Endoscopic ultrasound proves to be a reliable imaging tool for the investigation of lesions in the head and neck region and can easily be performed during microlaryngoscopy, panendoscopy or even in an ambulatory setting. It offers higher image resolution than CT scans or MRI and allows complete sonographic evaluation of whole organs as well as pathological conditions, especially head and neck cancer.

References

1. Arens C, Kraft M. Endoscopic ultrasound of the larynx. Curr Opin Otolaryngol Head Neck Surg. 2016;24:128–34.
2. Mallery S. Endosonographic instrumentation. In: Shami VM, Kahaleh M, editors. Endoscopic ultrasound. New York: Humana Press; 2010. p. 3–32.
3. Zech M, Scherer M, Maier H, Heppt W. Endosonographie des larynx. Eur Arch Otorhinolaryngol. 1994;251:480–1.
4. Kraft M, Mende S, Arnoux A, Arens C. Anatomical landmarks for endosonography of the larynx. Head Neck. 2010;32:326–32.
5. Sugiura K, Iwai T, Oguri S, Tohnai I. Intraoral ultrasonography with wrapped acoustic coupling medium. Br J Oral Maxillofac Surg. 2017;55:202–4.
6. Shintani S, Yoshihama Y, Ueyama Y, Terakado N, Kamei S, Fijimoto Y, et al. The usefulness of intraoral ultrasonography in the evaluation of oral cancer. Int J Oral Maxillofac Surg. 2001;30:139–43.
7. Noda K, Tamura M, Doi K, Kubo T. Ultrasonography in a nasal cavity filled with water during endoscopic sinus surgery. Ann Otol Rhinol Laryngol. 2002;111:836–41.
8. Arens C, Glanz H. Endoscopic high-frequency ultrasound of the larynx. Eur Arch Otorhinolaryngol. 1999;256:316–22.
9. Tamura E, Kitahara S, Kohno N. Clinical assessment of intralaryngeal ultrasonography. Laryngoscope. 2001;111:1767–70.
10. Wu CH, Hsu CJ, Hsieh FJ. Preliminary use of endoluminal ultrasonography in assessment of middle ear with effusion. J Ultrasound Med. 1998;17:427–30.
11. Pruna X, Inaraja L, Gallardo E, Serra J, Casamitjana F, Serrano A. Value of sonography in the assessment of space-occupying lesions of the anterior nasal fossa. J Clin Ultrasound. 2000;28:14–9.
12. La'porte SJ, Juttla JK, Lingam RK. Imaging the floor of the mouth and the sublingual space. Radiographics. 2011;31:1215–30.
13. Helbig M, Flechtenmacher C, Hansmann J, Dietz A, Tasman AJ. Intraoperative B-mode endosonography of tongue carcinoma. Head Neck. 2001;23:233–7.
14. Angelelli G, Moschetta M, Limongelli L, Albergo A, Lacalendola E, Brindicci F, et al. Endocavitary sonography of early oral cavity malignant tumors. Head Neck. 2017;39:1349–56.
15. Klein Nulent TJW, Noorlag R, Van Cann EM, Pameijer FA, Willems SM, Yesuratnam A, et al. Intraoral ultrasonography to measure tumor thickness of oral cancer: a systematic review and meta-analysis. Oral Oncol. 2018;77:29–36.
16. Arens C, Eistert B, Glanz H, Waas W. Endolaryngeal high-frequency ultrasound. Eur Arch Otorhinolaryngol. 1998;255:250–5.
17. Kraft M, Bruns N, Hügens-Penzel M, Arens C. Clinical value of endosonography in the assessment of laryngeal cancer. Head Neck. 2013;35(2):195–200.
18. Cooper ST, Sanders MK. Radial endoscopic ultrasound. In: Shami VM, Kahaleh M, editors. Endoscopic ultrasound. New York: Humana Press; 2010. p. 63–90.
19. Arens C, Weigt J, Schumacher J, Kraft M. Ultrasound of the larynx, hypopharynx and upper esophagus [in German]. HNO. 2011;59(2):145–54.

Contrast-Enhanced Ultrasonography: Clinical Applications

16

Julian Küstermeyer

16.1 Introduction

Contrast-enhanced ultrasound (CEUS) is an emerging diagnostic technique. It was first described in the 1990s as a combination of using a contrast agent with established ultrasound techniques. It allows analysis of perfusion patterns in greater detail than conventional sonographic modalities. Today, a number of contrast agents with different properties are available for a variety of indications. Since the technique's beginnings two decades ago, contrast agents have steadily improved. Besides its diagnostic features, therapeutic options are given by using targeted contrast agents, which release specific drugs locally. Meanwhile, cardiac, vascular, and abdominal examinations with CEUS have become accurate tools in clinical routines, especially in Europe and Asia [1]. For some years now, CEUS applications have also become more and more valuable in the field of head and neck sonography, even though international guidelines initially were only available for CEUS in the liver. A consensus initiative of the World Federation for Ultrasound in Medicine and Biology (WFUMB) and the European Federation of Societies for Ultrasound in Medicine and Biology (EFSUMB) first published recommendations for these guidelines in 2012 [2]. Currently there are no internationally approved guidelines regarding the use of CEUS for extrahepatic applications, except the European guidelines from 2012 [3]. They include recommendations and indications for CEUS applications in the head and neck: assessment of the carotid artery or neck abscesses, monitoring of tumor therapy, and follow-up of flap transplants, lymph nodes, and the salivary glands [4].

In summary, the application of CEUS in the head and neck to date has meant off-label use in many diseases, but the European guidelines explicitly recommend its use for some particular indications in the head and neck. Many studies report an improvement of diagnostic accuracy by using CEUS in the head and neck, and there appear to be a variety of promising applications for future clinical routines.

16.2 Basics and Technical Remarks

Contrast agents used for CEUS consist of microbubbles with diameters of about 3 μm, which is comparable to the scale of erythrocytes. Most of these commercially available microbubble contrast agents comprise a core of gas coated with lipid or protein layers. Earlier generations of microbubbles consisted of an air-filled core, which was not as durable as the current gas-filled bubbles. Their physicochemical properties prevent them from leaking from intact blood vessels into the surrounding tissues and circulating freely inside the systemic vasculature. Unlike contrast agents used for CT or MRI, microbubbles do not diffuse through the endothelium of blood vessels. Therefore, the microbubbles also help to detect the perfusion of very small vessels. Other conventional ultrasound modalities, such as color-coded duplex sonography, allow solely the detection of vascularization, whereas CEUS allows detection of perfusion. Also, ultrasound contrast agents are used extravascularly in body cavities; for example, they can be used to detect sialolithiasis in the salivary ducts.

Microbubbles are prepared by shaking a dry mixture with a saline solution. The application is mostly intravenous, in a dosage of about 1–5 mL through a venous catheter. Afterwards, the bubbles can be detected for about 5 minutes until they disrupt and are metabolized, primarily by the lung and (to a smaller degree) by the liver.

Electronic Supplementary Material The online version of this chapter (https://doi.org/10.1007/978-3-030-12641-4_16) contains supplementary material, which is available to authorized users.

J. Küstermeyer (✉)
Department of Otorhinolaryngology, Head and Neck Surgery, KRH Nordstadt Clinic–Academic Hospital, Hannover, Germany
e-mail: julian.kuestermeyer@krh.eu

© Springer Nature Switzerland AG 2019

H. J. Welkoborsky, P. Jecker (eds.), *Ultrasonography of the Head and Neck*, https://doi.org/10.1007/978-3-030-12641-4_16

Unrelated to CEUS, the effective pressure to which a tissue is exposed can be calculated as the mechanical index (MI)—a unitless number in which higher values mean increased pressure. In most areas worldwide, manufacturers need to equip ultrasound scanners with an indication of the mechanical index in order to control it and avoid adverse effects like cavitation. The US Food and Drug Administration (FDA), for example, stipulates that diagnostic ultrasound scanners work with a maximum MI of 1.9 [5]. CEUS is often performed at low mechanical indices, which are defined as less than 0.3 [6]. Low mechanical indices are suitable to induce oscillations of the microbubbles without disrupting them, whereas high mechanical indices will lead to bursting of microbubbles.

Ultrasound transducers emit acoustic pressure, changing from positive to negative like a sinusoidal function. Microbubble contrast agents scatter ultrasound according to the applied amplitude of pressure, measured as the mechanical index, and show vibrations. These properties make these agents significantly more reflective than physiological tissue, and so they enhance both B-mode images and flow-mediated Doppler signals [7]. Microbubbles change their configuration between compression and expansion, according to the sinusoidal pressure applied. In contrast to normal tissue, which shows a linear behavior to pressure, microbubbles present different kinetics. They respond asymmetrically, with a more extensive changing of radius during the negative-pressure phase than in the positive-pressure phase [8, 9]. Because of this property, microbubbles begin to show nonlinear characteristics like harmonic oscillations—or overtones, when the exposed mechanical force exceeds a specific limit (Fig. 16.1). By reaching a certain amount of acoustic pressure, the bubbles finally begin to disrupt. These contexts are crucial for understanding most of the current CEUS techniques. Modern ultrasound scanners use these physical effects to cancel the linear signals from tissue and detect the nonlinear responses from the microbubbles.

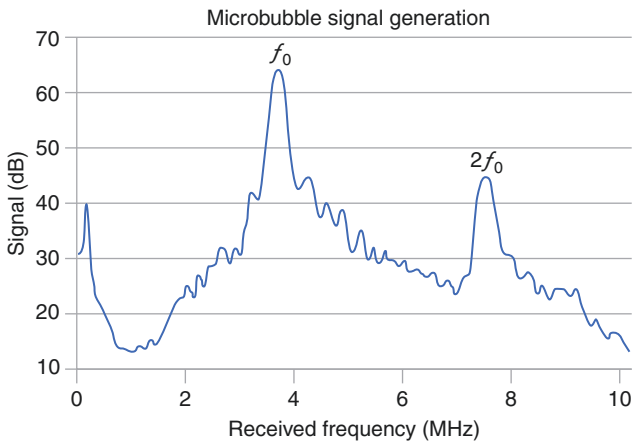

Fig. 16.1 Microbubbles' response is dependent on the received ultrasound frequency with a peak at 4 MHz and a second peak (equal to harmonic overtones) at double the frequency

There are two different methods for utilizing these characteristics. First is harmonic imaging, which filters the harmonic oscillations, preferably at double the transmitted frequency. Second is pulse-inversion imaging, which uses the nonlinear kinetics of the microbubbles. When two pulses are sent rapidly to tissue, the second pulse mirrors the first pulse, according to a sinusoidal function. Therefore, the sum of both pulses is zero. Since microbubbles respond with an asymmetrical echo, the first echo does not mirror the second (Fig. 16.2). This technical issue allows separation of tissue signals from microbubble signals [8–11]. Pulse-inversion imaging enables higher image resolutions and a greater bandwidth of the transducer than with harmonic imaging [12].

16.2.1 Safety Considerations

Extensive use of ultrasound contrast agents over the years has proven them to be very safe. Reports of side effects and severe adverse reactions are rare. The composition of the gas-filled bubbles causes a gentle metabolism. Microbubbles are not nephrotoxic and do not interact with the thyroid gland, so preliminary blood screening tests are not necessary. The incidence of hypersensitivity and anaphylactoid reactions is far lower than for contrast agents used for CT scans. The rate of adverse effects is described as 0.0098% for SonoVue®, which is the most widely used agent [13].

Microbubbles should not be used for diagnosis in patients with severe coronary artery disease and pulmonary hypertension, and patients who have experienced unstable ischemic heart disease in the prior 7 days should be excluded. Pregnancy is a contraindication for using ultrasound contrast agents, as is breastfeeding in some regions.

Although the application of microbubbles in the pediatric context is not officially approved, it is widely accepted [14]. For some indications, it even allows for reduced exposure to ionizing radiation.

Facilities for shock management and resuscitation should be available during the use of ultrasound contrast agents [15, 16].

16.2.2 Regulatory Status

Different ultrasound contrast agents are marketed worldwide with varying configurations and approved indications (Table 16.1). Approval status differs across various regions

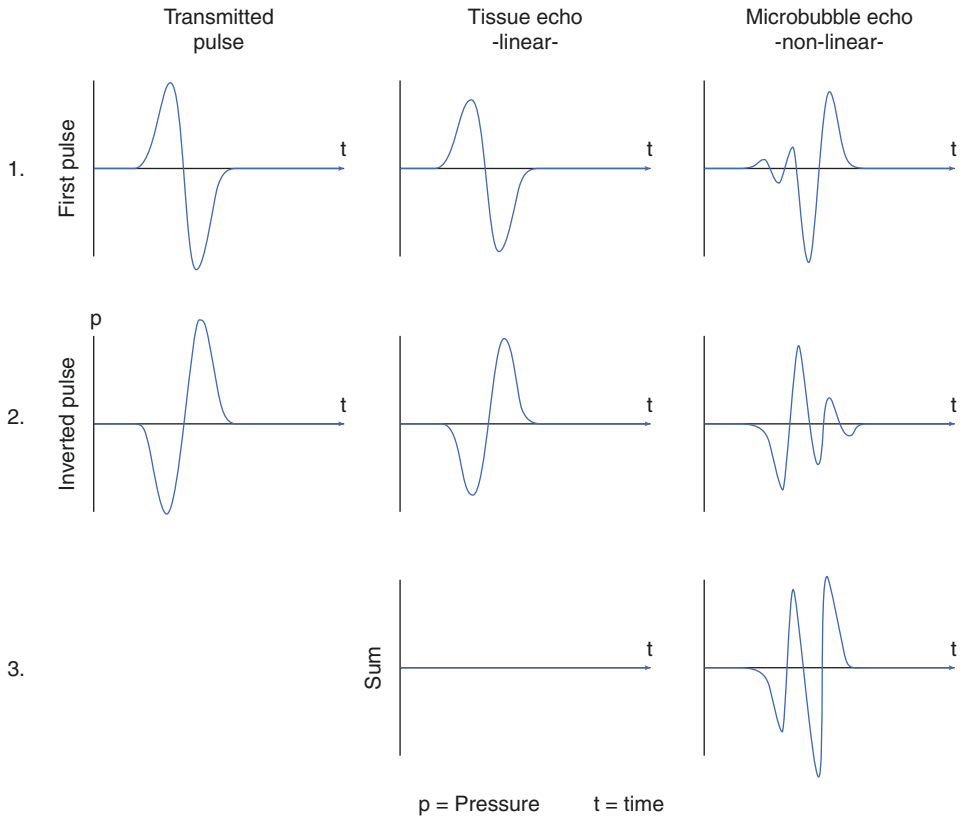

Fig. 16.2 The theoretical background of pulse-inversion techniques: two pulses are transmitted rapidly to tissue and microbubbles. The second pulse is an inverted copy of the first pulse. Tissue responds with linear echoes, which summarize results to zero. Microbubbles show nonlinear kinetics, resulting in increased echoes when summarized

Table 16.1 Regulatory status of available ultrasound contrast agents

Brand name (manufacturer)	Inner gas	Outer shell	Approved indications	Marketed in
Definity/Luminity® (Lantheus Medical Imaging)	Perflutren	Lipid	Cardiology, liver[a], kidney[a], vessels[a]	USA, Canada, Europe, Australia, parts of Asia
Optison® (GE Healthcare)	Perflutren	Albumin	Cardiology	USA, Europe
SonoVue®/Lumason® (Bracco Imaging)	Sulfur hexafluoride	Phospholipid	Cardiology, breast[a], liver[a], vessels[a]	USA, New Zealand, Europe, Brazil, parts of Asia
Sonazoid® (GE Healthcare)	Perflubutane	Lipid	Liver[a], breast[a]	Japan, South Korea

[a]Only in certain countries

and countries, with SonoVue® being the leading agent in general use [4, 17].

16.3 Clinical Applications of CEUS in Head and Neck Sonography

As explained above, CEUS in the head and neck is still an experimental modality without an international consensus regarding indications and particular recommendations. The European CEUS guidelines for extrahepatic indications also encourage the use of contrast-enhanced sonography for some indications involving the head and neck. Furthermore, experts worldwide publish more and more results of CEUS studies affecting such indications. They often provide valuable diagnostic pathways or suggestions for using CEUS in everyday routines.

16.3.1 Salivary Gland Tumors

Tumors of the salivary glands are uncommon and represent only about 3% of all head and neck neoplasms [18]. Nevertheless, they are a very heterogeneous group. In more than 80% of all cases, the tumors occur in the parotid gland; more than 80% of those are benign lesions. The incidence of malignant tumors is estimated at about 15% [19]. The most frequent benign salivary gland tumor is pleomorphic adenoma, with 70–80% of all cases, followed by cystadenolymphomas, also known as Warthin's tumor (5–12%). The most

common malignant tumor is mucoepidermoid carcinoma, followed by squamous cell carcinoma, acinic cell carcinoma, lymphoma, and metastases [20]. Detailed pretherapeutic characterization of those neoplasms is useful for determining the surgical procedure and choosing the right level of radicality. Histopathological examination is still the gold standard for confirming the diagnosis of salivary gland tumors, but some authors report improvement of the differentiation of those heterogeneous pathologies by using CEUS.

Pleomorphic Adenoma

The incidence of pleomorphic adenoma is higher in women than in men, with a peak in the fifth decade and accumulation in the superficial lobe [20]. Though pleomorphic adenoma is a benign entity, it can cause some complications. It can create pressure that injures the facial nerve, or it can transform into a carcinoma. Furthermore, if the capsule is damaged during surgical excision, there is a high risk of local recurrences, since spreading of the tumor cells leads to a multilocular appearance of pleomorphic adenoma in the primary location. Hence, a complete resection with clear margins should be performed as early as possible.

Pleomorphic adenoma shows characteristic perfusion patterns. Qualitative analysis reveals a rich capsular perfusion with only slight perfusion in the center of the tumor (Fig. 16.3 and Video 16.1). Examining the time-intensity curve of a pleomorphic adenoma shows some specific features when compared with other entities (Fig. 16.4) [21–23].

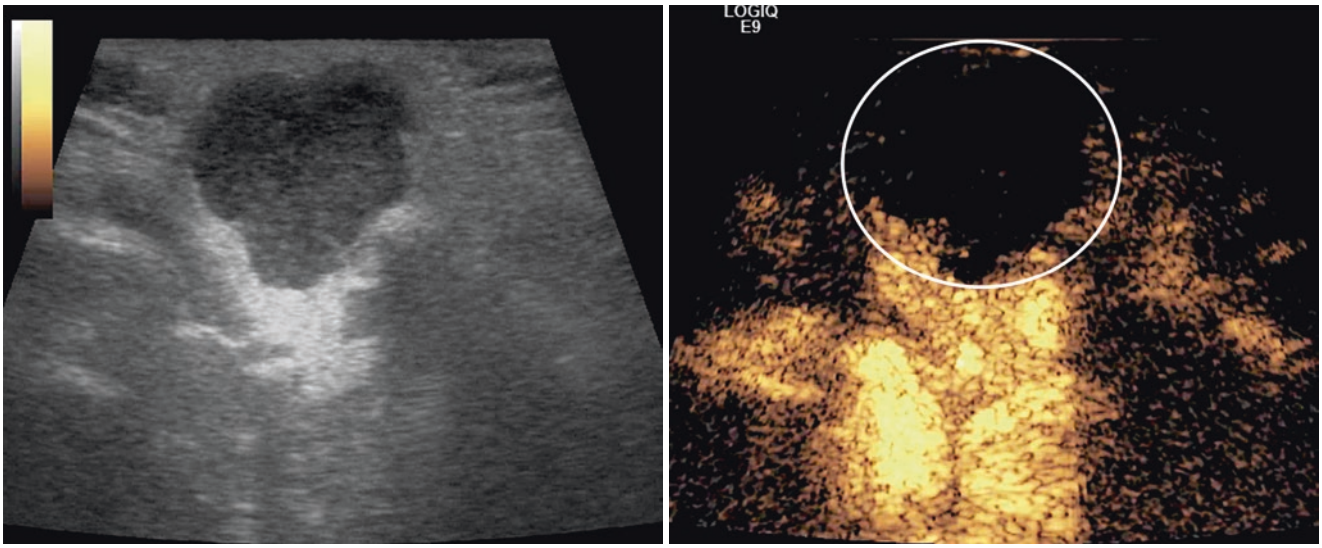

Fig. 16.3 A pleomorphic adenoma displayed in B-mode sonography (left) and contrast-enhanced ultrasound (CEUS) (right). B-mode shows characteristic features including the sharply demarcated border, the polylobular configuration, posterior acoustic enhancement, and the typical localization inside the lateral parotid lobe. CEUS distinguishes the hyperperfused capsule, especially in the deep areas of the tumor. In the center of the tumor, CEUS detects no signs of significant perfusion (*see also* Video 16.1)

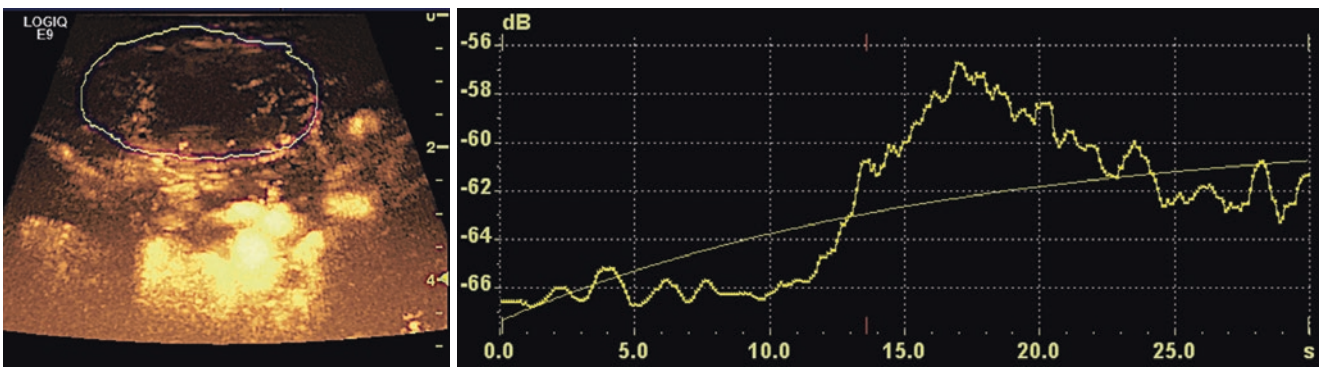

Fig. 16.4 A time-intensity curve of a pleomorphic adenoma shows the perfusion intensity dependent on the time after application of the contrast agent. The time to peak (TTP) is about 17 seconds

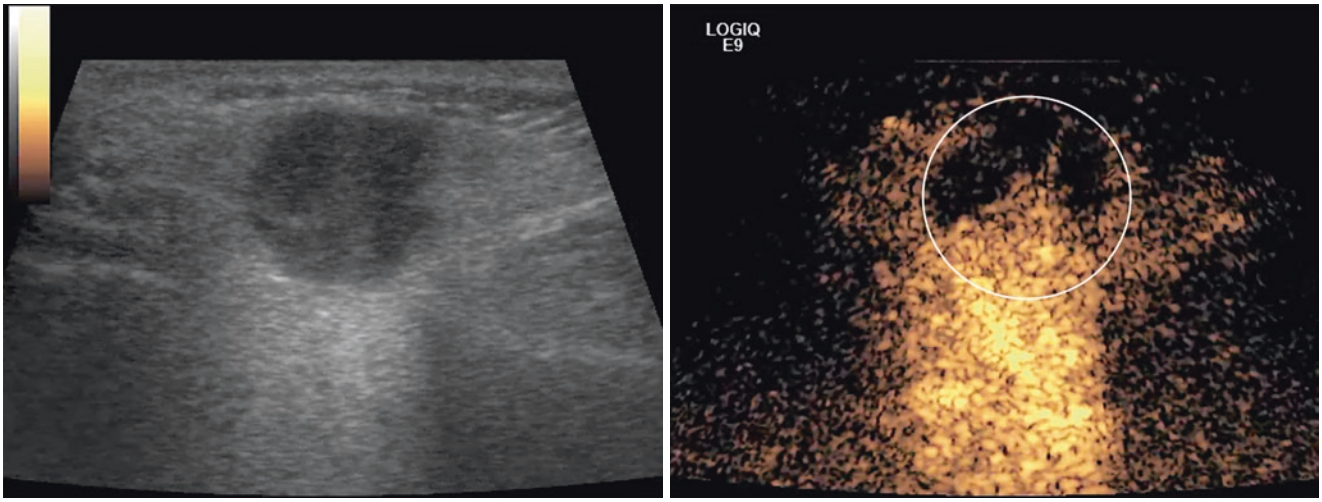

Fig. 16.5 A carcinoma ex pleomorphic adenoma in B-mode (left) and CEUS (right). B-mode shows the same characteristic features as the pleomorphic adenoma (Fig. 16.3). Qualitative perfusion analysis by CEUS detects the hyperperfused capsule and, in addition, perfusion in the center of the tumor. The perfusion originates from the depth and reaches the central areas of the tumor

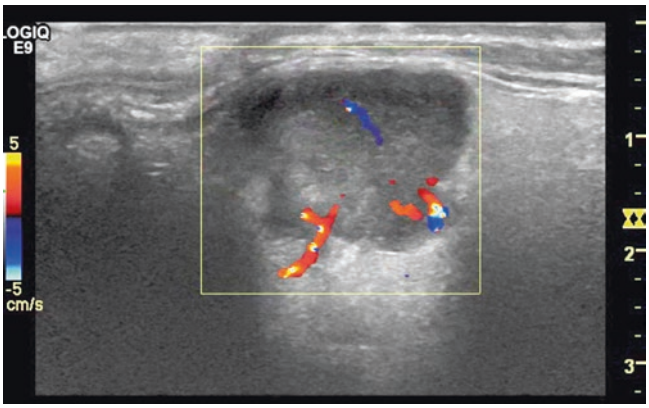

Fig. 16.6 Color-coded duplex sonography of a carcinoma ex pleomorphic adenoma after application of a contrast agent shows hypervascularization of the capsule and in the center of the tumor, with B-mode features similar to those of a benign pleomorphic adenoma

Carcinoma Ex Pleomorphic Adenoma

Malignant transformation into a carcinoma ex pleomorphic adenoma has been reported to occur in 3–4% of all cases [24]. In B-mode sonography, the malignant tumor presents almost the same characteristics as the pleomorphic adenoma (*see* Fig. 16.3). Analogous to other malignant tumors, this entity shows increased perfusion, which can be detected by CEUS (Figs. 16.5, 16.6, and 16.7). Besides the highly perfused capsule, as in pleomorphic adenoma, perfusion can also be observed in the center of the tumor. Quantitatively, the perfusion shows different properties, with a shorter time to peak (TTP), as discussed below.

Cystadenolymphoma (Warthin's Tumor)

Cystadenolymphoma is also known as Warthin's tumor, named after Aldred Scott Warthin, an American pathologist. It is the second most common benign tumor entity of the salivary glands, usually occurring in men, with a peak in the sixth decade. Lesions can be bilateral and multicentric. Cases of extraglandular tumors have also been described. Cystadenolymphomas appear most commonly in the parotid tail region. A relation to cigarette smoking is known [20, 25]. Warthin's tumors show some characteristic sonographic features that help to differentiate them from other entities (Figs. 16.8 and 16.9 and Video 16.2).

Table 16.2 shows different properties of the two most frequent benign salivary gland tumors.

16.3.2 Inflammatory Diseases of the Salivary Glands

Besides neoplasms, inflammatory diseases of the salivary glands are prevalent. In most cases, the combination of clinical examination, B-mode sonography, and, if applicable, color-coded duplex sonography leads to the right diagnosis. For example, acute parotitis, the most frequent inflammatory alteration of the salivary glands in the elderly, shows very characteristic features. Some authors have reported studies using CEUS for obstructive salivary gland diseases. The contrast agent can be applied intraductally to detect sialolithiasis and monitor the effectiveness of therapeutic procedures [26, 27]. The European CEUS guidelines mention this scope of application [4].

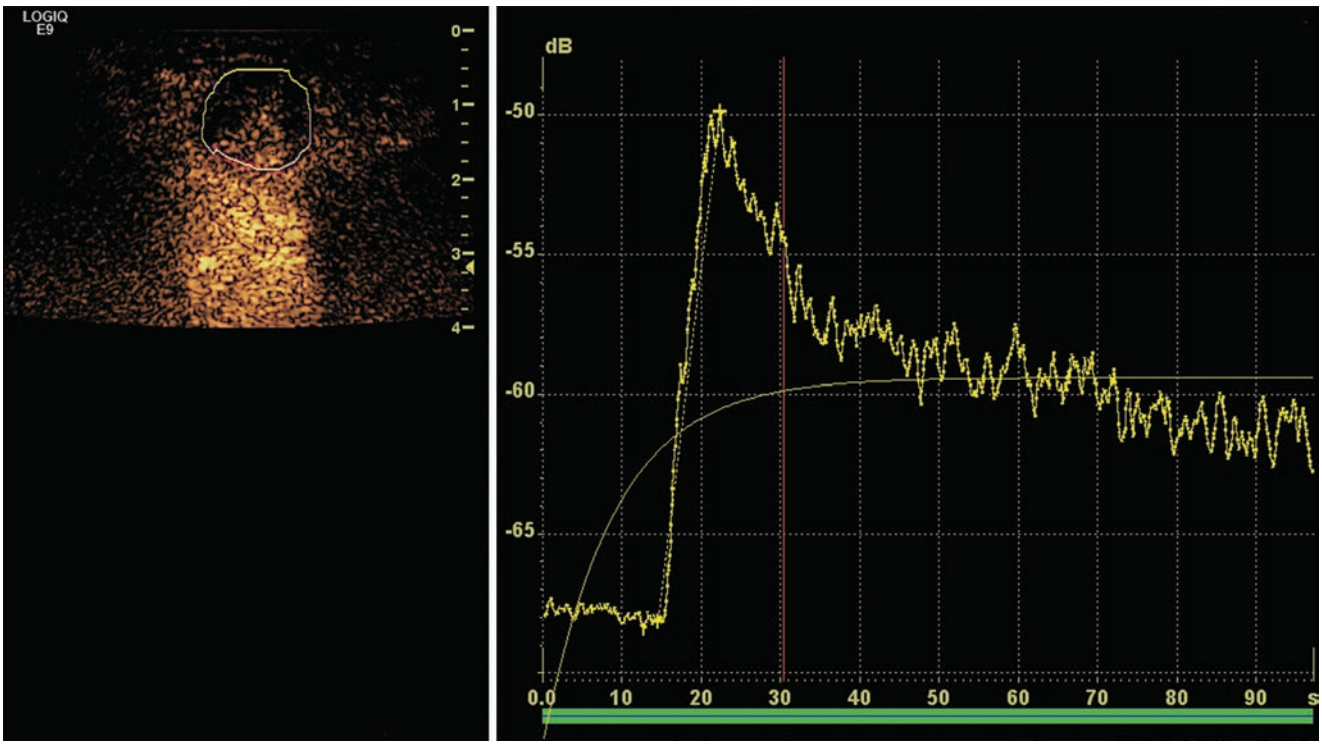

Fig. 16.7 A time-intensity curve of a carcinoma ex pleomorphic adenoma shows the perfusion intensity dependent on the time after application of the contrast agent. The time to peak (TTP) is about 20 seconds. A steep increase begins after 15 seconds

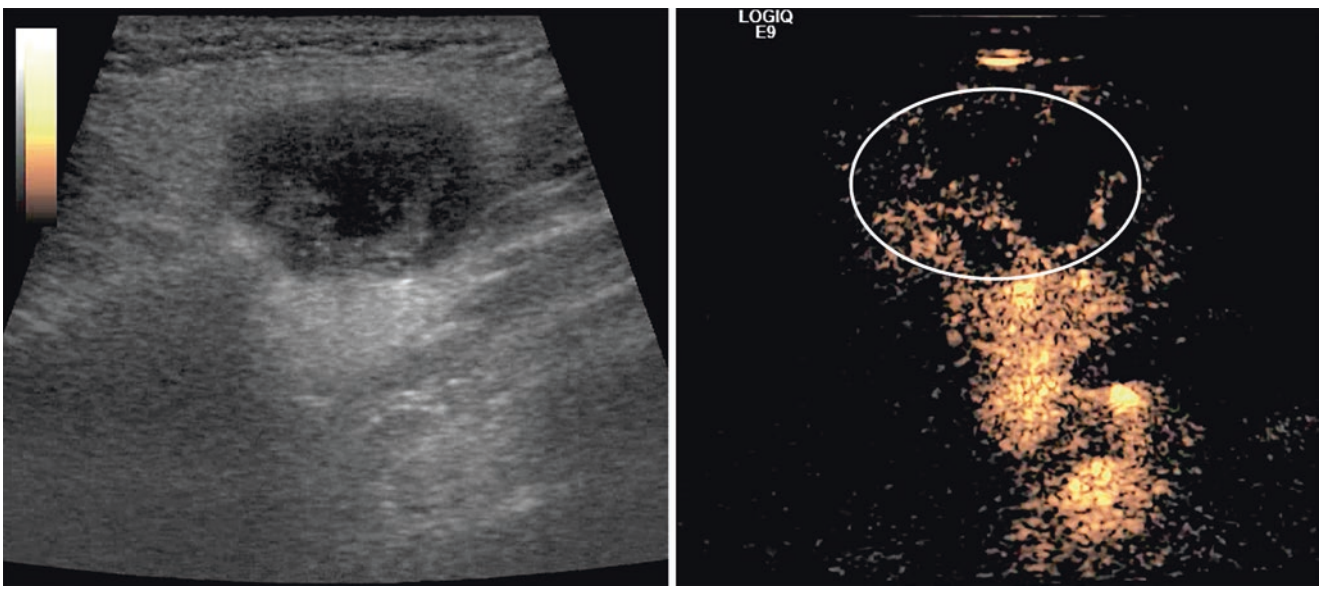

Fig. 16.8 A Warthin's tumor in B-mode (left) and CEUS (right). B-mode shows characteristic features including the sharply demarcated border, a mixed echogenicity with hypoechoic zones, and slight posterior acoustic enhancement. CEUS detects the septal perfusion in the center of the tumor inside the hyperechoic zones and reveals no perfusion inside the cystic areas (*see also* Video 16.2)

Sjögren's Syndrome

Sjögren's syndrome is an autoimmune disease affecting primarily the salivary and lacrimal glands; it leads to dryness in the mouth and eyes. Sonographic examination of the parotid glands typically presents findings with multiple echoic lesions. Loss of function is characterized by decreased vascularization and perfusion (Figs. 16.10 and 16.11).

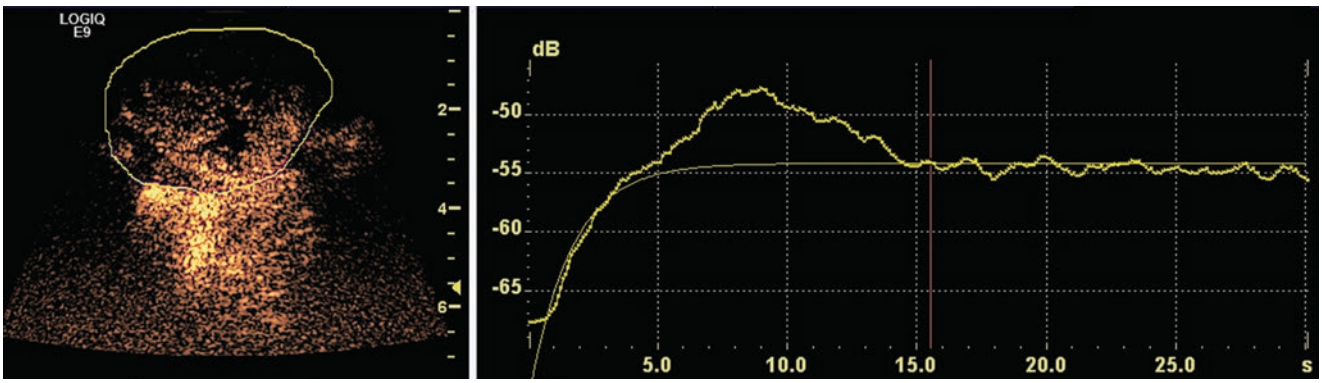

Fig. 16.9 A time-intensity curve of a Warthin's tumor shows the perfusion intensity dependent on the time after application of the contrast agent. The time to peak (TTP) is about 9 seconds. The perfusion analysis reveals a higher area under the curve (AUC) compared with pleomorphic adenomas (*see* Fig. 16.4)

Table 16.2 Characteristics of pleomorphic adenoma and Warthin's tumor

Parameter	Pleomorphic adenoma	Warthin's tumor
Demarcation/outlining	Sharply demarcated border; polylobular configuration	Sharply demarcated border; oval, hypoechoic zones
Posterior acoustic enhancement	+++	+
Vascularization/color-coded duplex sonography	Hypervascularized capsule in the depth; seldom detectable vessels in the tumor's center	Septal vascularization mainly in the center inside hyperechoic zones; vascularized capsule possible
Contrast-enhanced ultrasound (CEUS)	Hyperperfused capsule, low perfusion in the center	Septal perfusion, cystic areas without perfusion

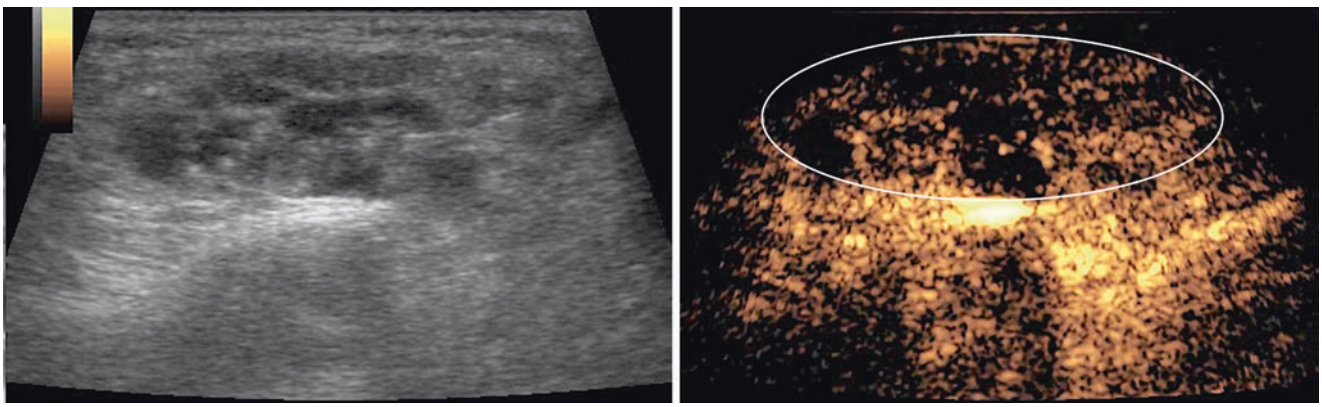

Fig. 16.10 A parotid gland in B-mode (left) and CEUS (right), with characteristic multiple alterations for Sjögren's syndrome. B-mode sonography typically shows various hypoechoic zones. CEUS demonstrates multiple areas with no perfusion disseminated all over the salivary gland

16.3.3 Quantitative Analysis Based on Time-Intensity Curves

Besides qualitative analysis, quantitative examinations based on time-intensity curves (TICs) can be used to assess perfusion characteristics. The literature describes different ways to distinguish between pathologies. Most studies compare various parameters in the TIC, such as the area under the curve (AUC), time to peak (TTP), mean transit time (MTT), and intensity changes (Δi). Some studies point out that in pleomorphic adenoma, the TTP is significantly longer than in Warthin's tumors [24, 28]. Other studies describe significant differences of the AUC between benign and malignant tumors, as well as between pleomorphic adenoma and Warthin's tumors (*see* Figs. 16.4, 16.7, and 16.9) [29]. These differences of perfusion can also be detected by comparing multiple regions of interest inside the assessed tumors [22].

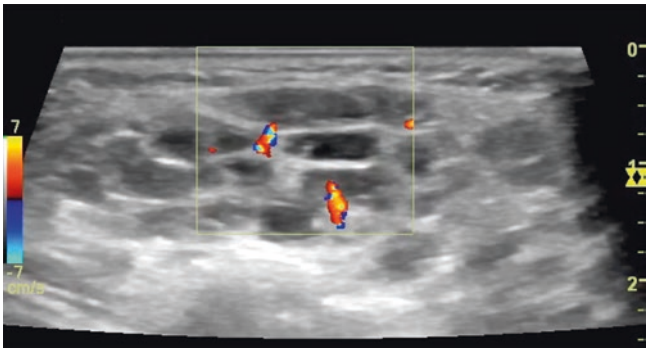

Fig. 16.11 The same parotid gland as in Fig. 16.10, with Sjögren's syndrome: color-coded duplex sonography detects intense hypervascularized areas between the hypoechoic zones

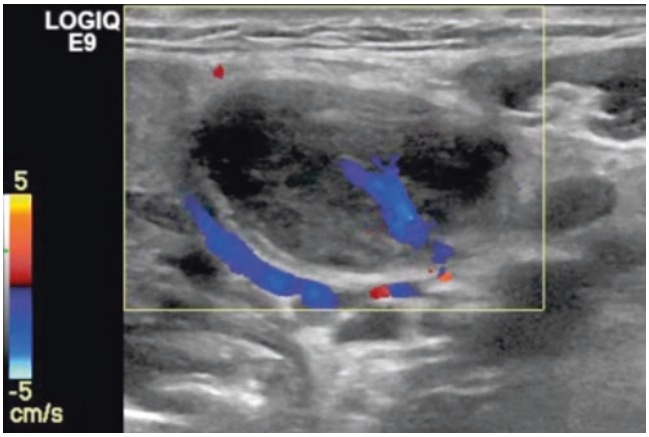

Fig. 16.12 Color-coded duplex sonography shows a reactive lymph node after application of a microbubble contrast agent. The vascularized hilum, which spreads centrifugally, can be detected. Further, the capsule is hypervascularized. The examination of the center reveals no signs of vascularization independent from the hilar vessels

Using CEUS to differentiate salivary gland tumors is still controversial, however. Some authors even see no benefit of distinguishing salivary gland tumors by CEUS [30].

16.3.4 Lymph Nodes

Lymphadenopathy of unclear etiology is a frequent reason for consulting a head and neck specialist. Early and accurate diagnosis is crucial for selecting the right therapy and preventing time delay in cases of malignant entities. Hence, the question regarding the node's malignancy is the central focus. Various studies have analyzed vascular patterns of lymphadenopathy by using CEUS, with the aim of distinguishing between benign and malignant nodes. Their results differ according to the modalities utilized and the parameters examined. Many studies describe color-coded duplex sonographic examinations that used microbubble contrast agents [31–37]. Their authors controversially discuss whether the application of contrast-enhanced color-coded duplex sonography increases diagnostic accuracy. Other reports have assessed low mechanical index B-mode sonography in combination with microbubbles [38–40].

Perfusion patterns of malignant tumors differ from those of benign alterations. Malignant tumors secrete angiogenic factors, which lead to neoangiogenesis. The resulting de novo vessels differ from physiological vessels. They build chaotic branches and penetrate the lymph node's capsule, and they also create porous vessels with high rates of leakage. CEUS helps to detect those properties by analyzing the perfusion patterns. Nevertheless, existing guidelines do not recommend the use of CEUS for routine discrimination between benign and malignant lymph nodes. Only in particular clinical settings can CEUS increase the diagnostic benefit [4].

Inflammatory Reaction

Infectious and inflammatory diseases in most cases lead to collateral reactive lymphadenopathy. Their preserved physiological morphology and vascularization can help to identify benign lymph nodes. Reactive lymph nodes appear characteristically with sharply demarcated borders and a single hilum structure, which contains vessels spreading from the center to the periphery (centrifugal). This vascularization can be detected by CEUS and contrast-enhanced color-coded duplex sonography (Figs. 16.12 and 16.13 and Video 16.3) [41].

Malignant Lymphomas

Malignant lymphomas represent a category with a vast variety of entities. The polymorphic appearance makes it hard to differentiate this kind of lymphadenopathy with universal sonographic features. Furthermore, lymph nodes affected by a lymphoma have perfusion characteristics quite similar to those of reactive nodes. Therefore, the differentiation of benign lymph nodes and malignant lymphomas is not yet possible with high rates of sensitivity and specificity [4, 39, 41, 42].

Typical sonographic findings in lymphoma are sharply demarcated borders and clear, identifiable hilum structures. These are often hypervascularized in color-coded duplex examinations, with often well-sorted vessels and a centrifugal perfusion. The CEUS shows a homogeneous and intense hyperperfusion (Figs. 16.14 and 16.15).

Carcinoma Metastasis

Compared with benign lymphadenopathies and the formerly described lymphomas, lymph nodes affected by carcinoma

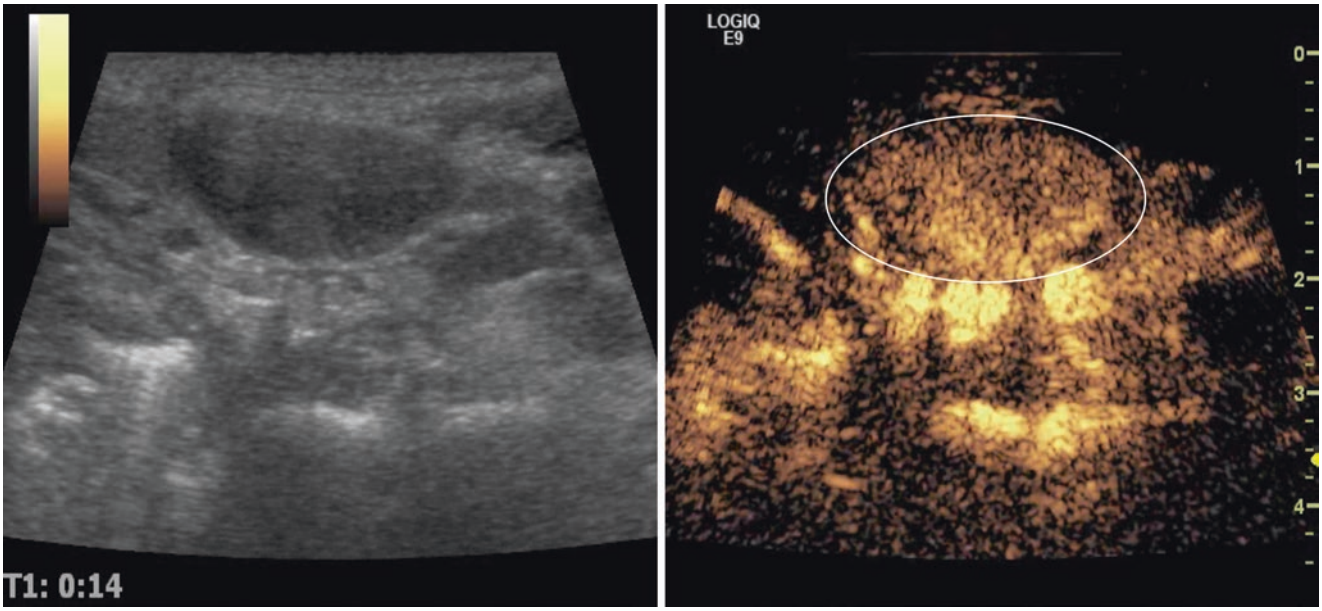

Fig. 16.13 The same reactive lymph node as shown in Fig. 16.12 in B-mode (left) and CEUS (right): B-mode shows characteristic features including an oval configuration and a sharply demarcated border. The hilum is not well distinguished because of the low mechanical index mode. CEUS reveals intense homogeneous enhancement in the whole lymph node with centrifugal perfusion kinetics (*see also* Video 16.3)

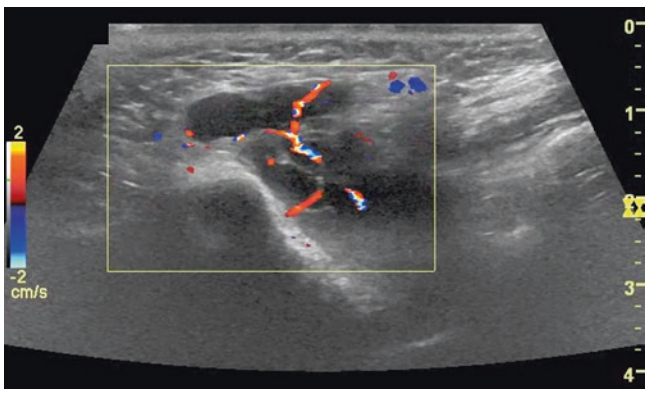

Fig. 16.14 Color-coded duplex sonography shows a lymph node, affected by a non-Hodgkin lymphoma, after application of a microbubble contrast agent. The very prominent hilum is strongly hypervascularized. The detectable flow crosses the node's entire diameter, with noticeable branching

metastasis show very characteristic features. Because of the induced neoangiogenesis, which causes the creation of leaky and chaotically arranged de novo vessels, necrotic zones typically can be detected (Figs. 16.16 and 16.17 and Video 16.4).

Besides qualitative features, some authors describe quantitative markers to distinguish between benign and malignant alterations. Their analyses of time-intensity curves revealed a significantly shorter time to peak (TTP) in malignant lymph nodes than in reactive ones. Furthermore, the area under the curve (AUC) as a marker for perfusion intensity was significantly greater in reactive lymphadenopathy than in malignant alterations [39, 40].

16.3.5 Paragangliomas

Paragangliomas are highly vascularized tumors. Their occurrence is ubiquitous in all body regions. In the head and neck, paragangliomas appear as glomus caroticum, glomus jugulare, and glomus vagale tumors. Glomus caroticum tumors are particularly accessible by ultrasound examinations.

Interventional radiologists usually embolize glomus caroticum tumors prior to a surgical resection, to reduce intraoperative bleeding. Digital subtraction angiography (DSA) allows occlusion of feeder vessels under radioscopy. This modality provides qualitative analysis of perfusion patterns in real time, but the embolization effect is not measured quantitatively. The disadvantages of DSA for head and neck specialists are the limited quantitative information about perfusion and the dependence on radiologists to perform the examination.

Some studies have demonstrated the benefit of using CEUS in the assessment of carotid paraganglioma. In particular, monitoring of the embolization effect with CEUS is a promising technique. It combines the advantages of noninvasiveness and quantitative analysis, and it is a tool in the hands of the head and neck specialist (Figs. 16.18, 16.19, 16.20 and 16.21 and Video 16.5) [43, 44].

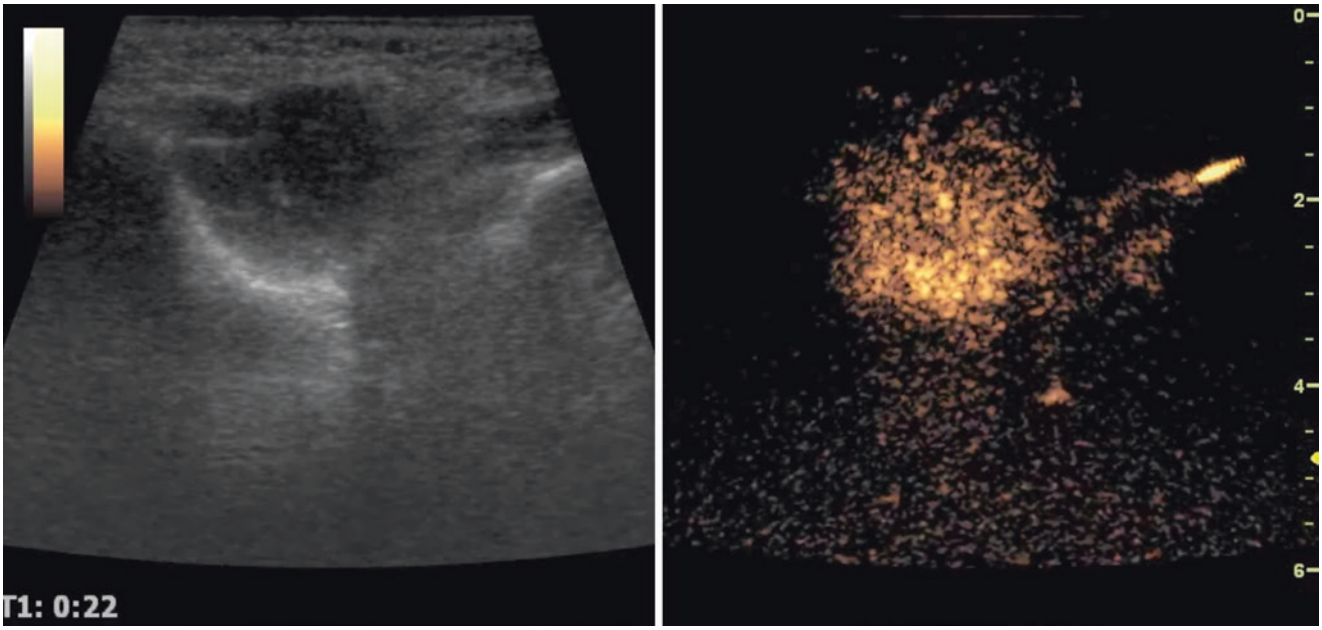

Fig. 16.15 The same lymph node as shown in Fig. 16.14, affected by a non-Hodgkin lymphoma, in B-mode (left) and CEUS (right). B-mode displays an enlarged lymph node near the mandible. CEUS detects an intense enhancement with a maximum in the depth. Remarkably, the surrounding tissue shows almost no perfusion, compared with the lymphoma

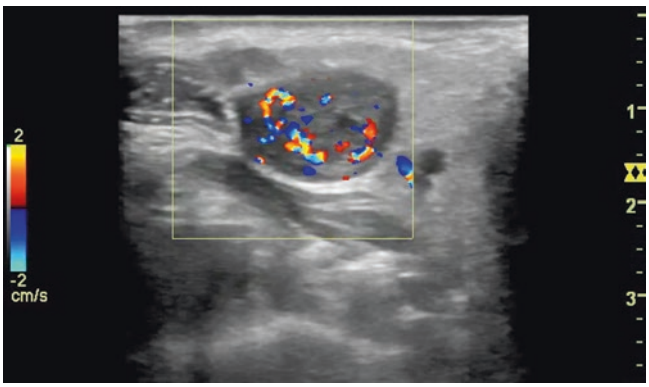

Fig. 16.16 A carcinoma metastasis in color-coded duplex sonography after application of a microbubble contrast agent. The tumor's extreme hypervascularization with chaotically arranged vessels is ubiquitous

16.3.6 Differential Diagnosis of Thyroid Alterations

Thyroid nodules can be detected in 19–68% of examined patients with modern ultrasound techniques [45], but only 5% of clinically identified nodules are malignant [46]. Distinguishing between benign and malignant alterations is thus very important to prevent time delay in the treatment of thyroid cancer and, furthermore, to reduce potential harm due to overtreatment.

The American Thyroid Association (ATA) published guidelines for the management of thyroid nodules in adults [45]. These describe ultrasonographic patterns of nodules in detail concerning B-mode sonography and color-coded duplex sonography. Scoring of suspicious nodules with an algorithm system helps to estimate the risk of malignancy and decide between wait-and-see, ultrasound-guided fine-needle aspiration, or surgery. Recommendations for using CEUS are still missing. Another guideline was created in 2016 by the American Association of Clinical Endocrinologists, the American College of Endocrinology, and the Associazione Medici Endocrinologi [47]. It even advises against the use of CEUS.

Features of high-risk malignant nodules are "a solid hypoechoic nodule or solid hypoechoic component of a partially cystic nodule with one or more of the following features: irregular margins (infiltrative, microlobulated), microcalcifications, taller than wide shape, rim calcifications with small extrusive soft tissue component, evidence of extrathyroidal extension" [47].

The first papers about studies using CEUS to improve diagnostic accuracy in examining thyroid nodules were published in the early 2000s [48–50]. Meanwhile, studies about contrast-enhanced sonography of the thyroid gland have been published increasingly, especially in the past few years [46, 51–59].

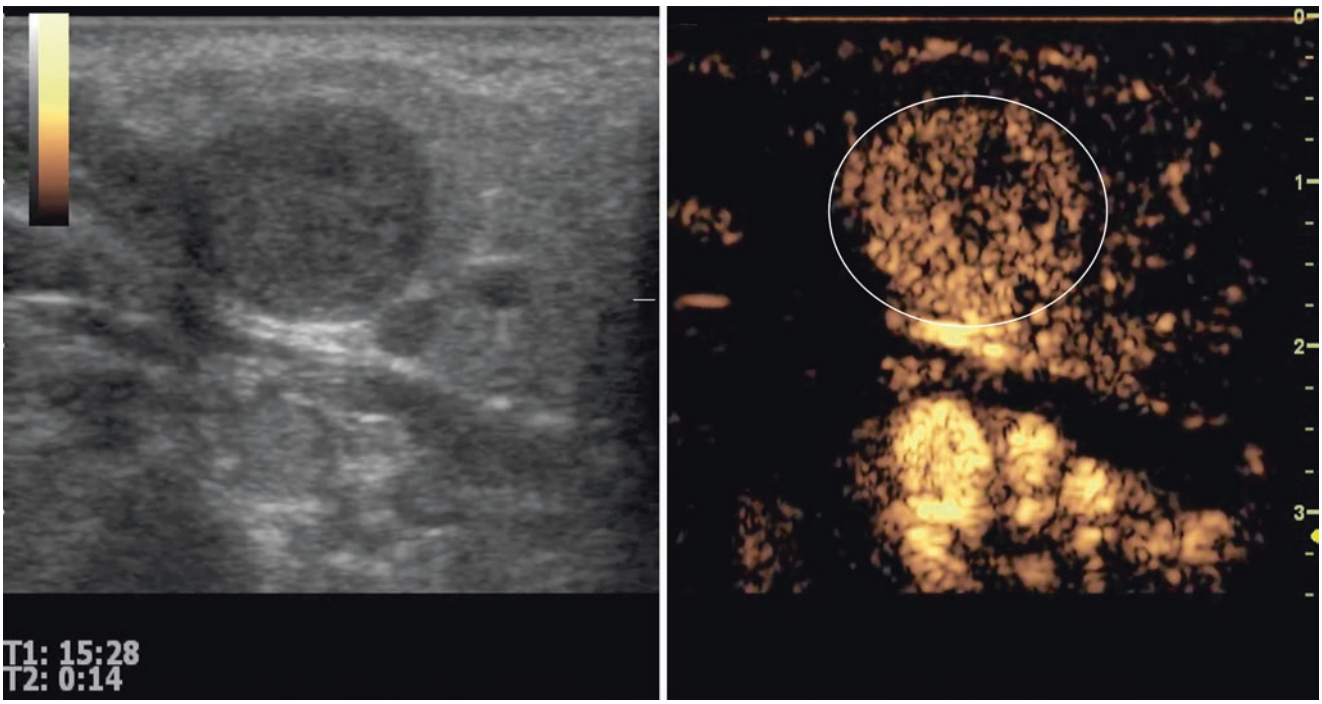

Fig. 16.17 The same carcinoma metastasis as shown in Fig. 16.16 in B-mode (left) and CEUS (right). B-mode shows a round, enlarged lymph node inside the parotid gland. CEUS detects intense, inhomogeneous enhancement, including areas without perfusion, corresponding to necrotic tumor zones (*see also* Video 16.4)

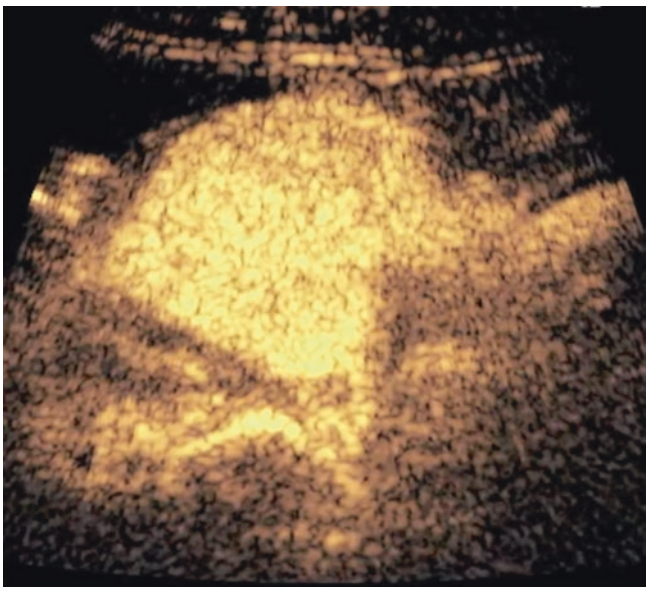

Fig. 16.18 CEUS examination of a paraganglioma at the carotid bifurcation. The tumor shows intense, homogeneous perfusion in all areas. Because of the hyperperfusion, distinguishing between tumor and carotid arteries is not possible

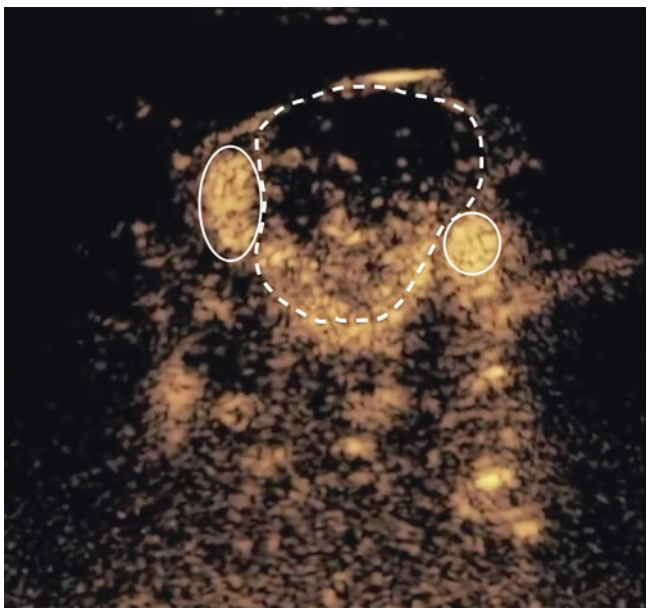

Fig. 16.19 CEUS examination of the same paraganglioma as shown in Fig. 16.18, after embolization of a feeder vessel. The tumor now presents inhomogeneous perfusion, especially with a decrease in the superficial areas. The external carotid artery (*left circle*) and the internal carotid artery (*right circle*) are demarcated from the tumor (*dotted line*) (*see also* Video 16.5)

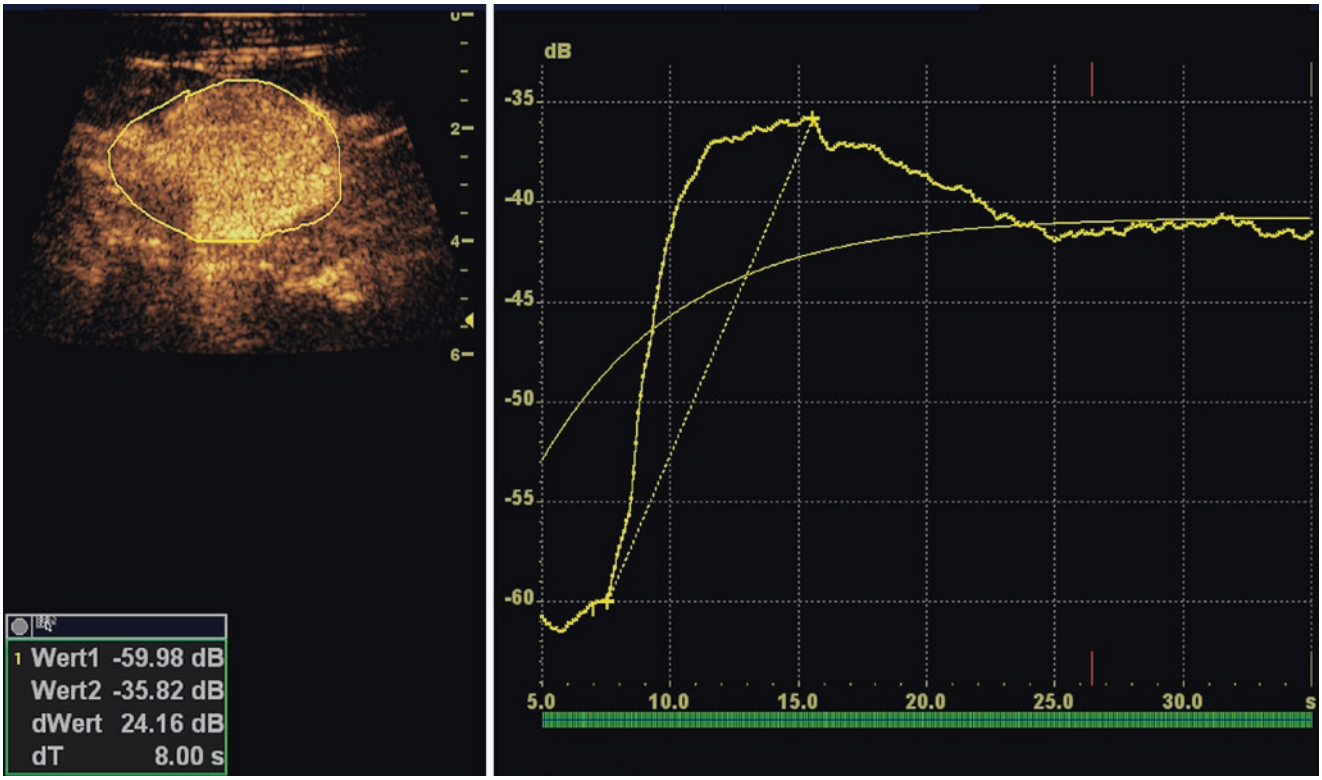

Fig. 16.20 The time-intensity curve of the glomus tumor shown in Fig. 16.18. In the early wash-in phase, the perfusion intensity increases by about 24 dB. The time to peak (TTP) is about 15 seconds

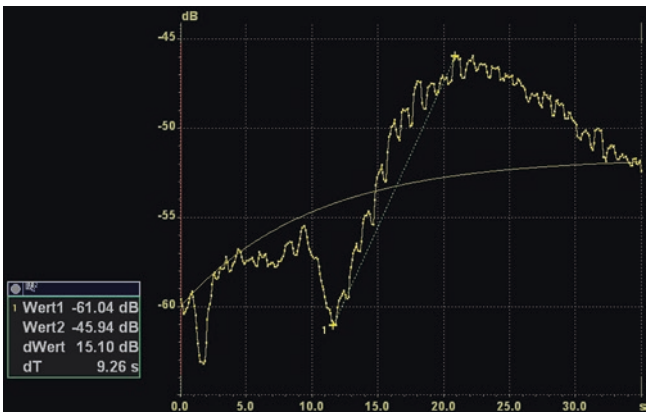

Fig. 16.21 Time-intensity curve of the same tumor as shown in Fig. 16.19, after embolization of a feeder vessel. The perfusion intensity decreases compared with Fig. 16.20. The time-intensity curve confirms the embolization effect. It rises by only about 15 dB, and the time to peak (TTP) is longer, at about 21 seconds

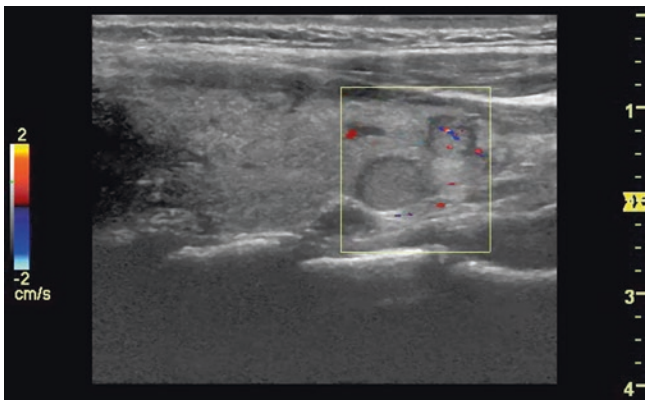

Fig. 16.22 Color-coded duplex scan of a thyroid gland with two nodules. The lower left nodule (a thyroid adenoma) is sharply demarcated, with a surrounding halo sign and homogeneous echogenicity. The upper right nodule (a thyroid papillary carcinoma) shows no regular borders, with an irregular ring structure, homogeneous echogenicity, and hypervascularization compared with the adjacent parenchyma

Qualitative analysis of thyroid nodules' perfusion patterns aims at a description (homogeneous, heterogeneous, hyper-enhancement, hypo-enhancement, and iso-enhancement) and a comparison with the surrounding gland tissue. Some authors conclude that heterogeneous hypo-enhancement of nodules is a criterion for a higher risk of malignancy [54, 56, 59]. Additional criteria that seem to help in predicting malignancy are irregular, hyper-enhancement ring perfusion and no-enhancement ring perfusion (Figs. 16.22, 16.23, and 16.24 and Video 16.6) [56, 59].

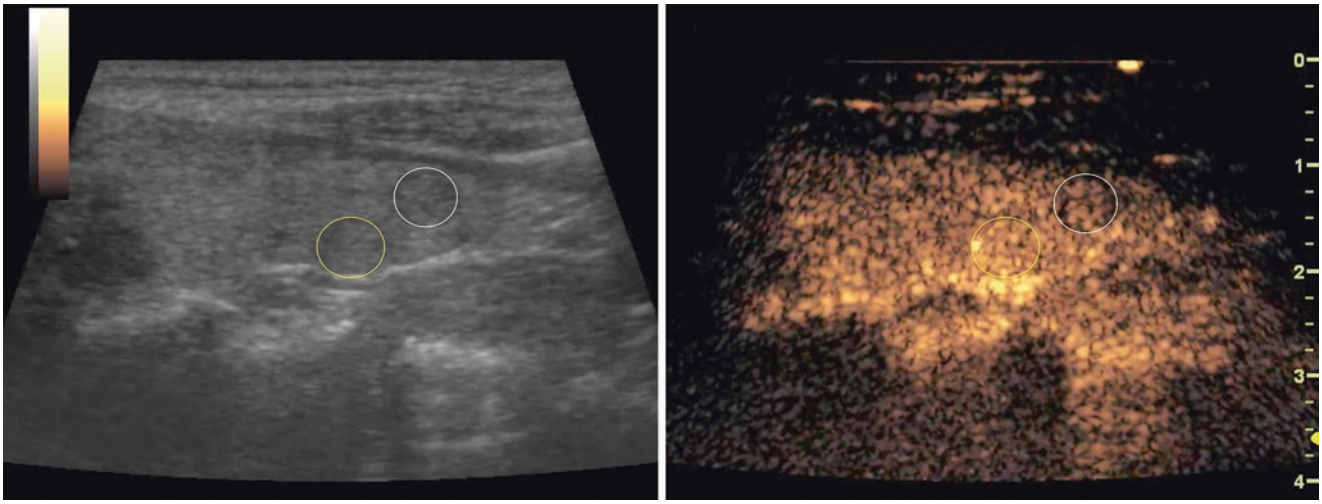

Fig. 16.23 CEUS scan of the same thyroid nodules as shown in Fig. 16.22. The lower left nodule (a thyroid adenoma) shows a homogeneous hyperperfusion. CEUS detects noticeably inhomogeneous low enhancement of the upper right nodule (thyroid papillary carcinoma)

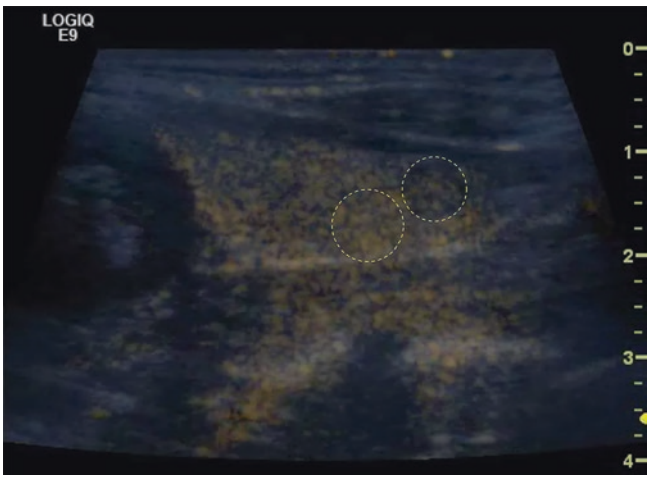

Fig. 16.24 CEUS scan in hybrid presentation of gray scale and contrast enhancement in overlay mode of the same thyroid nodules as shown in Fig. 16.22; the same perfusion patterns are demonstrated (*see also* Video 16.6)

Quantitative assessment by analyzing time-intensity curves of thyroid nodules revealed significant differences when looking at the washout phase. Most malignant nodules showed an inhomogeneous, polyphasic washout phase [46, 53, 60].

16.3.7 Tumor Response Assessment

Extensive tumors in the head and neck that exclude a surgical therapy option are often alternatively treated by chemotherapy. In the clinical routine, radiologic imaging modalities such as CT and MRI scans, combined with endoscopic examinations including histopathological examination of specimens, have been used for therapy monitoring, rather than ultrasound. For other tumor sites such as renal cell carcinoma or sarcoma, however, CEUS has been proven to be a suitable monitoring tool during tumor therapy [61, 62]. Noninvasive CEUS monitoring of extensive tumor disease of the head and neck also seems to be appropriate, and ENT specialists can perform the examination on their own. Through application of CEUS, the therapeutic effect of chemotherapy can be shown qualitatively and quantitatively. In addition to the morphologic analysis of tumor size by imaging techniques such as CT and MRI, CEUS allows a more detailed functional examination of the tumor's vitality by perfusion analysis.

CEUS can analyze the therapeutic effect qualitatively and quantitatively by using time-intensity curves and determination of the area under the curve (AUC) (Figs. 16.25, 16.26, 16.27, 16.28, 16.29, and 16.30).

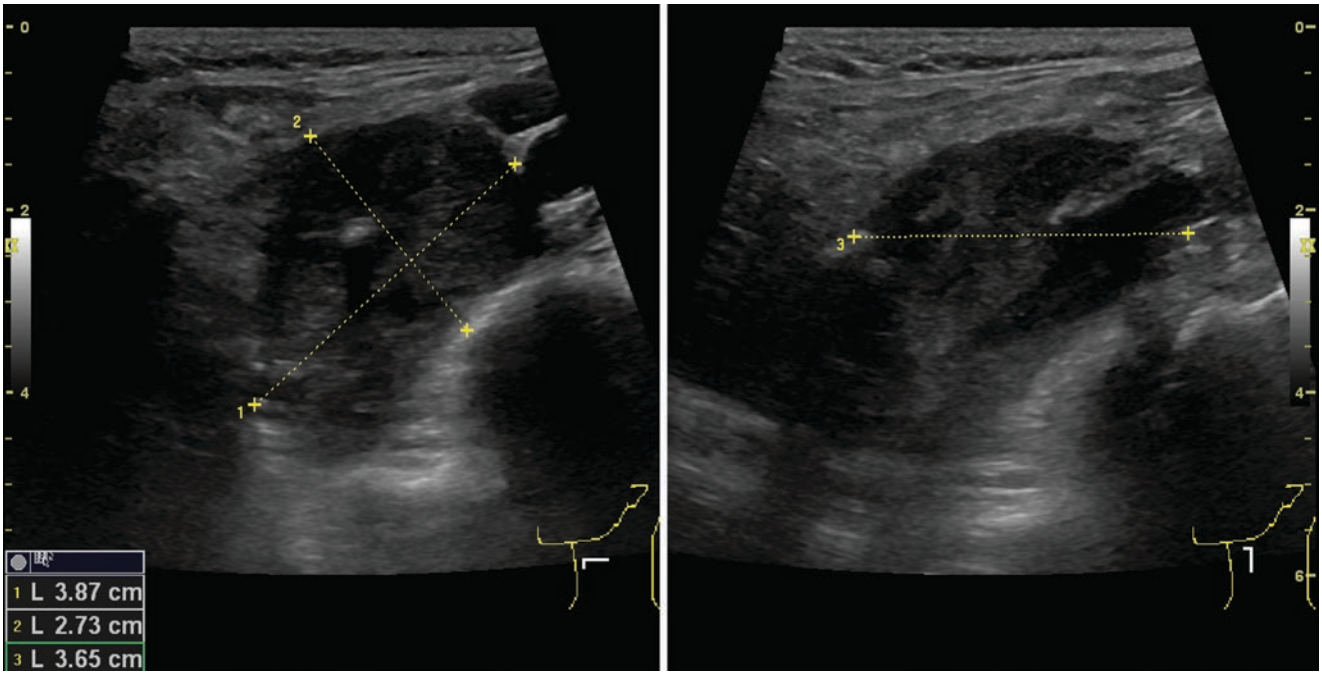

Fig. 16.25 B-mode scan of an oropharyngeal squamous cell carcinoma with irregular borders and mixed echogenicity

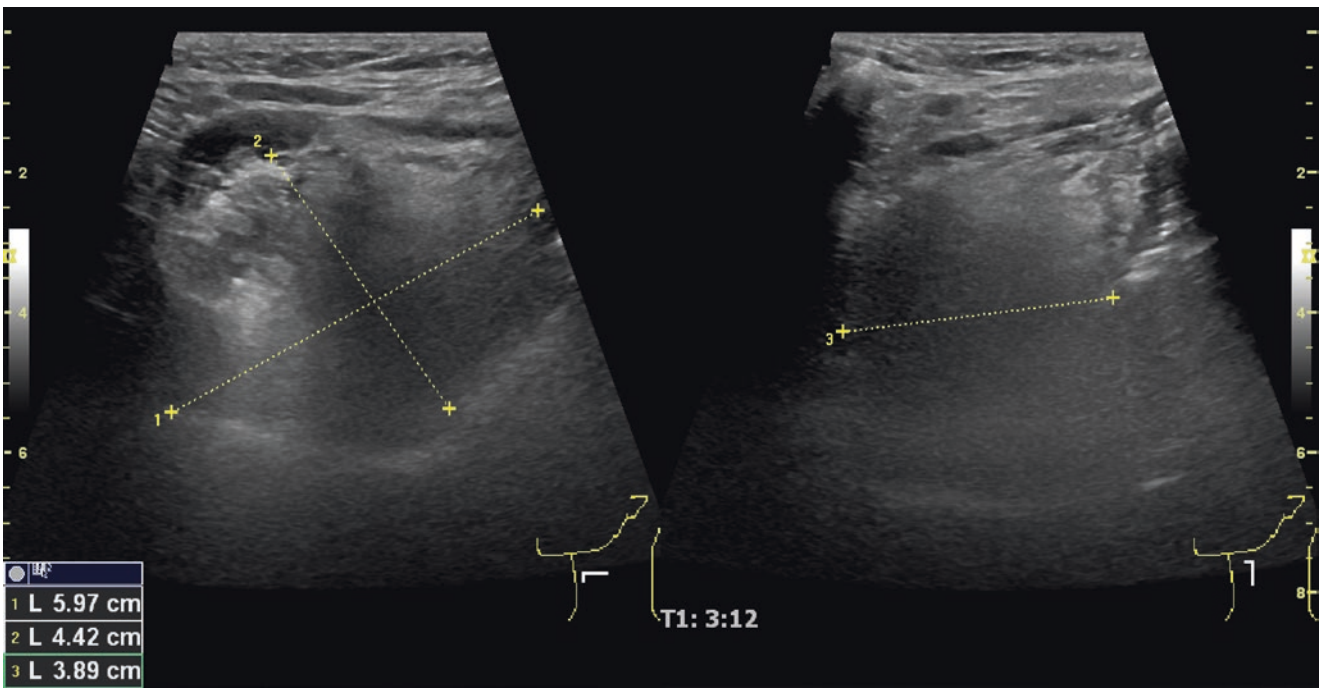

Fig. 16.26 B-mode scan of the same oropharyngeal carcinoma as shown in Fig. 16.25, after two cycles of induction chemotherapy. In the primary tumor site, scarred tissue can be detected, with larger margins than before therapy

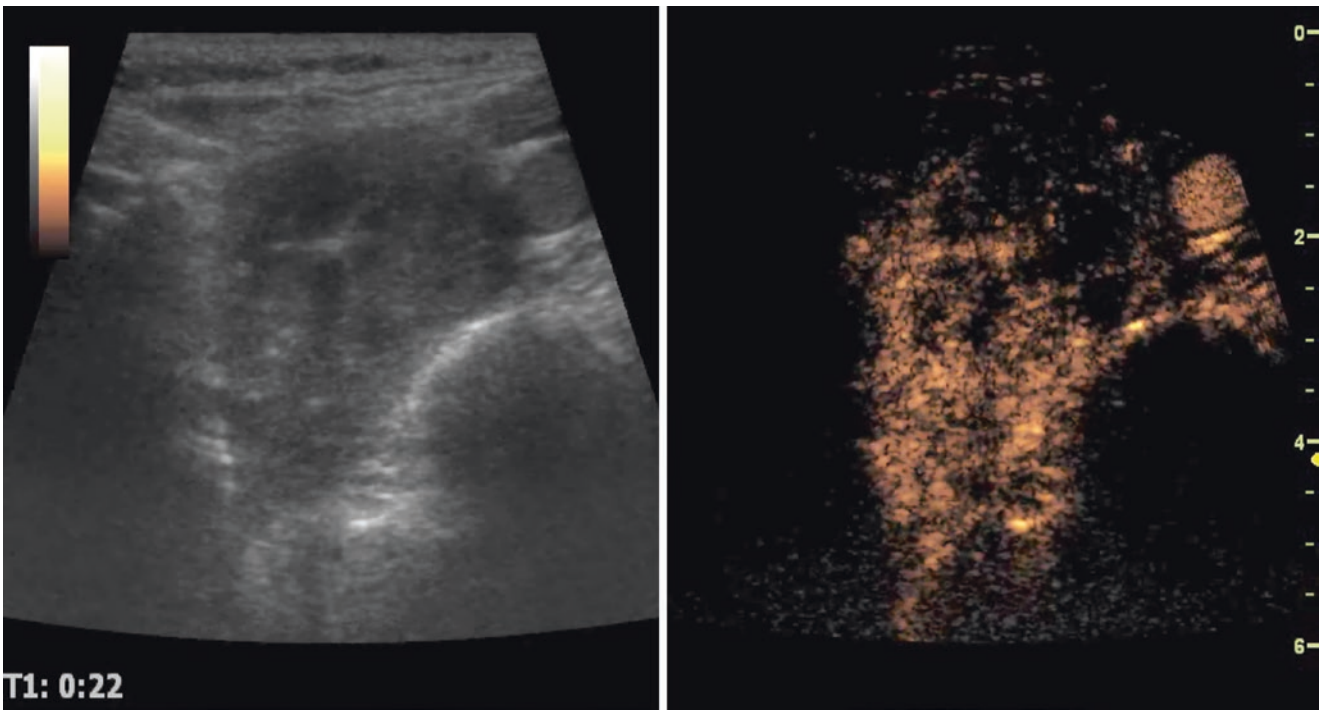

Fig. 16.27 CEUS scan of the same tumor as shown in Figs. 16.25 and 16.26, before induction therapy. Examination of the tumor reveals a heterogeneous hyperperfusion with necrotic no-flow areas

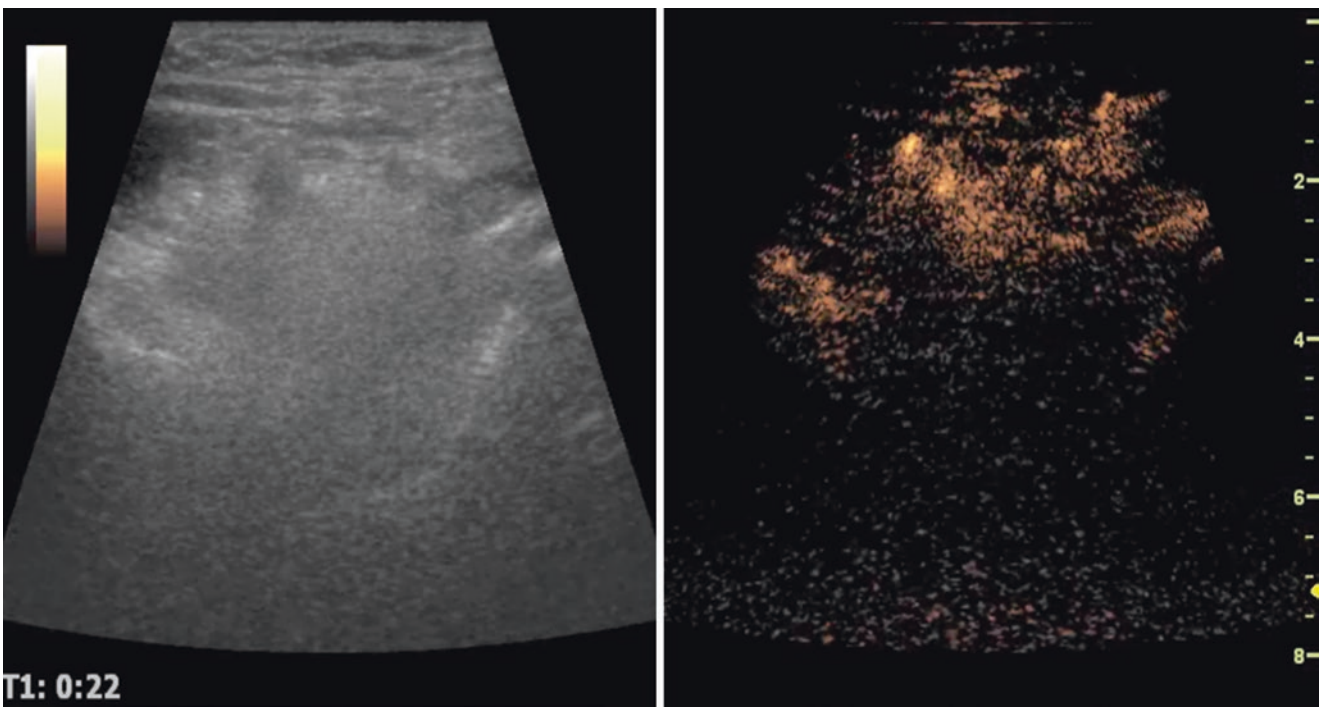

Fig. 16.28 CEUS scan of the same tumor as shown in Figs. 16.25 and 16.26, after two cycles of induction chemotherapy. Assessment of the perfusion reveals a heterogeneous perfusion pattern with no-flow areas corresponding to devitalized primary tumor parenchyma

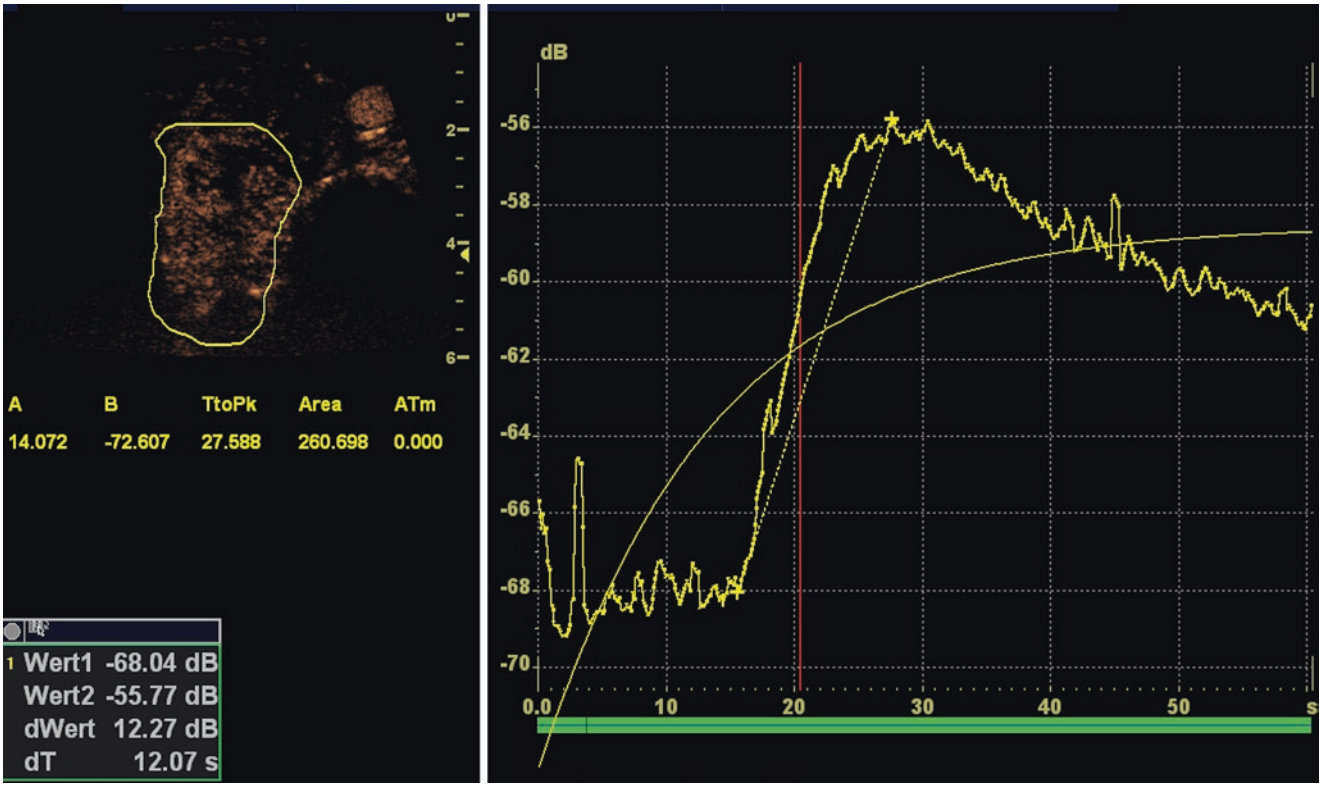

Fig. 16.29 Time-intensity curve of the same tumor as shown in Figs. 16.25–16.28 and 16.30, before induction chemotherapy. The area under the curve is about 260 [dB × sec]

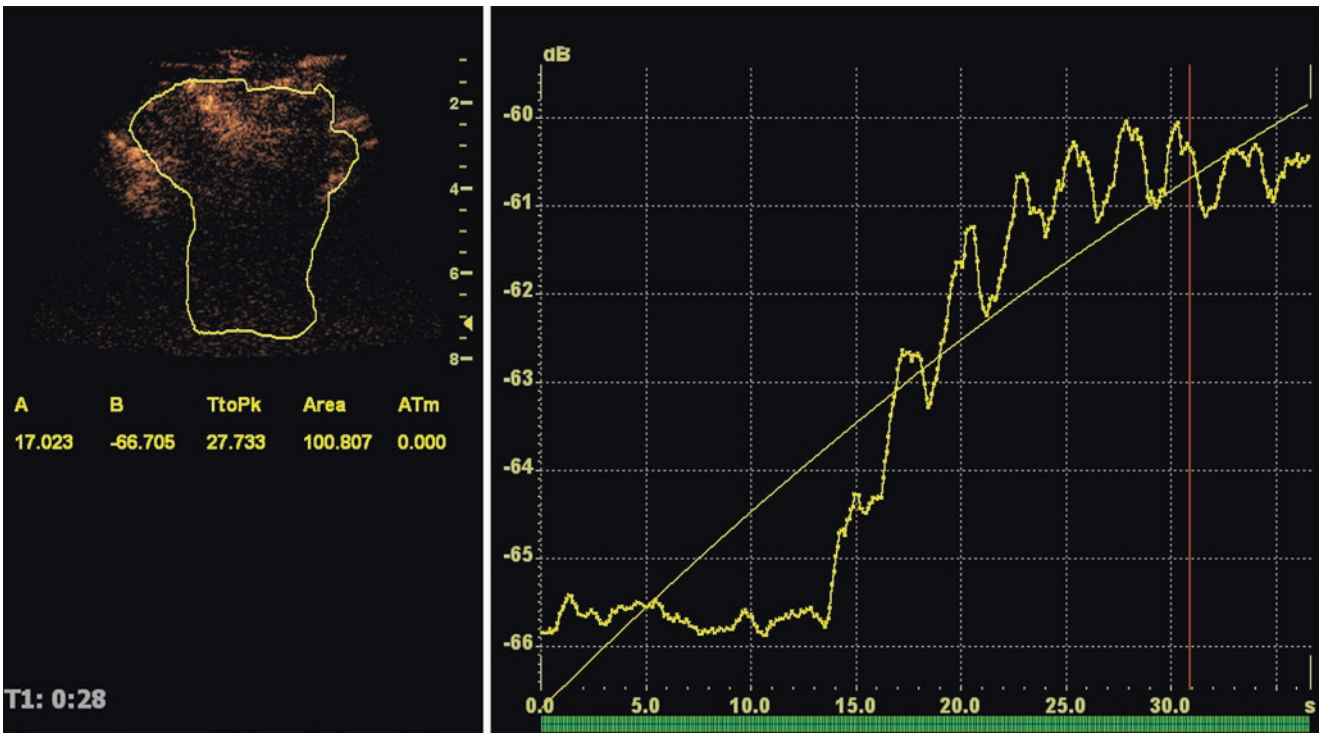

Fig. 16.30 Time-intensity curve of the same tumor as shown in Figs. 16.25–16.28 and 16.31, after two cycles of induction chemotherapy. The area under the curve is about 100 [dB × sec]

References

1. Chung YE, Kim KW. Contrast-enhanced ultrasonography: advance and current status in abdominal imaging. Ultrasonography. 2014;34:3–18.
2. Claudon M, Dietrich C, Choi B, Cosgrove D, Kudo M, Nolsøe C, et al. Guidelines and Good Clinical Practice Recommendations for Contrast Enhanced Ultrasound (CEUS) in the Liver – Update 2012. Ultraschall Med. 2013;34:11–29.
3. Nolsøe CP, Lorentzen T. International guidelines for contrast-enhanced ultrasonography: ultrasound imaging in the new millennium. Ultrasonography. 2016;35:89–103.
4. Piscaglia F, Nolsøe C, Dietrich C, Cosgrove D, Gilja O, Bachmann Nielsen M, et al. The EFSUMB guidelines and recommendations on the clinical practice of Contrast Enhanced Ultrasound (CEUS): update 2011 on non-hepatic applications. Ultraschall Med. 2012;33:33–59.
5. Meltzer RS. Food and Drug Administration ultrasound device regulation: the output display standard, the "mechanical index," and ultrasound safety. J Am Soc Echocardiogr. 1996;9:216–20.
6. von Herbay A, Haeussinger D, Gregor M, Vogt C. Characterization and detection of hepatocellular carcinoma (HCC): comparison of the ultrasound contrast agents SonoVue (BR 1) and Levovist (SH U 508A). Ultraschall Med. 2007;28:168–75.
7. Blomley MJK, Cooke JC, Unger EC, Monaghan MJ, Cosgrove DO. Science, medicine, and the future: Microbubble contrast agents: a new era in ultrasound. BMJ. 2001;322:1222.
8. Burns PN. Basics. In: Weskott H-P, editor. Contrast-enhanced ultrasound. 2nd ed. Bremen: UNI-MED; 2013. p. 16–24.
9. Lindner JR. Microbubbles in medical imaging: current applications and future directions. Nat Rev Drug Discov. 2004;3:527–33.
10. Qin S, Caskey CF, Ferrara KW. Ultrasound contrast microbubbles in imaging and therapy: physical principles and engineering. Phys Med Biol. 2009;54:R27–57.
11. Postema M, Gilja OH. Contrast-enhanced and targeted ultrasound. World J Gastroenterol. 2011;17:28–41.
12. Ignee A, Atkinson NSS, Schuessler G, Dietrich CF. Ultrasound contrast agents. Endosc Ultrasound. 2016;5:355–62.
13. Solivetti FM, Elia F, Musicco F, Bonagura AC, Di Leo N, Iera J, et al. Anaphylactic shock induced by sulphur hexafluoride in an individual with no history of heart disease: case report and literature review. Ultraschall Med. 2012;33:597–8.
14. Torres A, Koskinen SK, Gjertsen H, Fischler B. Contrast-enhanced ultrasound using sulfur hexafluoride is safe in the pediatric setting. Acta Radiol. 2017;58:1395–9.
15. Torzilli G. Adverse effects associated with SonoVue® use. Expert Opin Drug Saf. 2005;4:399–401.
16. Tang C, Fang K, Guo Y, Li R, Fan X, Chen P, et al. Safety of sulfur hexafluoride microbubbles in sonography of abdominal and superficial organs: retrospective analysis of 30,222 cases. J Ultrasound Med. 2017;36:531–8.
17. Appis AW, Tracy MJ, Feinstein SB. Update on the safety and efficacy of commercial ultrasound contrast agents in cardiac applications. Echo Res Pract. 2015;2:R55–62.
18. Dumitriu D, Dudea SM, Botar-Jid C, Baciut G. Ultrasonographic and sonoelastographic features of pleomorphic adenomas of the salivary glands. Med Ultrason. 2010;12:175–83.
19. Pinkston J, Cole P. Incidence rates of salivary gland tumors: results from a population-based study. Otolaryngol Head Neck Surg. 1999;120:834–40.
20. David E, Cantisani V, De Vincentiis M, Sidhu PS, Greco A, Tombolini M, et al. Contrast-enhanced ultrasound in the evaluation of parotid gland lesions: an update of the literature. Ultrasound. 2016;24:104–10.
21. Gou JM, Chen Q, Zhou Q, Liu YX. Quantitative diagnosis of salivary gland tumors with contrast-enhanced ultrasound--a preliminary study. Oral Surg Oral Med Oral Pathol Oral Radiol. 2013;116:784–90.
22. Küstermeyer J, Klingelhöfer G, Welkoborsky H-J. [Analysis of perfusion parameters within salivary gland tumors using contrast enhanced ultrasound]. [Article in German]. Laryngorhinootologie. 2016;95:688–93.
23. Knopf A, Mansour N, Chaker A, Bas M, Stock K. Multimodal ultrasonographic characterisation of parotid gland lesions--a pilot study. Eur J Radiol. 2012;81:3300–5.
24. Fischer T, Paschen C, Slowinski T, Alkhameri A, Berl J, Klingebiel R, et al. Differentiation of parotid gland tumors with contrast-enhanced ultrasound. Fortschr Röntgenstr. 2009;182:155–62.
25. Pinkston JA, Cole P. Cigarette smoking and Warthin's tumor. Am J Epidemiol. 1996;144:183–7.
26. Zengel P, Berghaus A, Weiler C, Reiser M, Clevert DA. Intraductally applied contrast-enhanced ultrasound (IA-CEUS) for evaluating obstructive disease and secretory dysfunction of the salivary glands. Eur Radiol. 2011;21:1339–48.
27. Siedek V, Rytvina M, Klotz LV, Berghaus A, Clevert D-A, Strieth S. Validation of contrast-enhanced ultrasound-derived intensity-time gradients in submandibular gland sialolithotomy patients. Eur Arch Otorhinolaryngol. 2013;270:1941–6.
28. Wei X, Li Y, Zhang S, Li X, Wang H, Yong X, et al. Evaluation of microvascularization in focal salivary gland lesions by contrast-enhanced ultrasonography (CEUS) and Color Doppler sonography. Clin Hemorheol Microcirc. 2013;54:259–71.
29. Klotz LV, Ingrisch M, Eichhorn ME, Niemoeller O, Siedek V, Gürkov R, et al. Monitoring parotid gland tumors with a new perfusion software for contrast-enhanced ultrasound. Clin Hemorheol Microcirc. 2014;58:261–9.
30. Badea AF, Bran S, Tamas-Szora A, Floareş A, Badea R, Baciut G. Solid parotid tumors: an individual and integrative analysis of various ultrasonographic criteria. A prospective and observational study. Med Ultrason. 2013;15:289–98.
31. Moritz JD, Ludwig A, Oestmann J-W. Contrast-enhanced color doppler sonography for evaluation of enlarged cervical lymph nodes in head and neck tumors. Am J Roentgenol. 2000;174:1279–84.
32. Schade G. [Experiences with using the ultrasound contrast medium Levovist in differentiation of cervical lymphomas with color-coded duplex ultrasound]. [Article in German]. Laryngorhinootologie. 2001;80:209–13.
33. Jecker P, Engelke JC, Westhofen M. [Possible application of a signal enhancer for duplex ultrasound in otorhinolaryngology]. [Article in German]. Laryngorhinootologie. 2008;77:289–93.
34. Dudea SM, Lenghel M, Botar-Jid C, Vasilescu D, Duma M. Ultrasonography of superficial lymph nodes: benign vs. malignant. Med Ultrason. 2012;14:294–306.
35. Zenk J, Bozzato A, Steinhart H, Greess H, Iro H. Metastatic and inflammatory cervical lymph nodes as analyzed by contrast-enhanced color-coded Doppler ultrasonography: quantitative dynamic perfusion patterns and histopathologic correlation. Ann Otol Rhinol Laryngol. 2005;114:43–7.
36. Schulte-Altedorneburg G, Demharter J, Linné R, Droste DW, Bohndorf K, Bücklein W. Does ultrasound contrast agent improve the diagnostic value of colour and power Doppler sonography in superficial lymph node enlargement? Eur J Radiol. 2003;48:252–7.
37. Schröder RJ, Mäurer J, Hidajat N, Willam C, Hell B, Weber S, et al. [Signal-enhanced color-coded duplex sonography of reactively and metastatically enlarged lymph nodes]. [Article in German]. Rofo. 1998;168:57–63.

38. Rubaltelli L, Khadivi Y, Tregnaghi A, Stramare R, Ferro F, Borsato S, et al. Evaluation of lymph node perfusion using continuous mode harmonic ultrasonography with a second-generation contrast agent. J Ultrasound Med. 2004;23:829–36.
39. Yu M, Liu Q, Song HP, Han ZH, Su HL, He GB, et al. Clinical application of contrast-enhanced ultrasonography in diagnosis of superficial lymphadenopathy. J Ultrasound Med. 2010;29:735–40.
40. Dudau C, Hameed S, Gibson D, Muthu S, Sandison A, Eckersley RJ, et al. Can contrast-enhanced ultrasound distinguish malignant from reactive lymph nodes in patients with head and neck cancers? Ultrasound Med Biol. 2014;40:747–54.
41. Weskott H-P. Ultrasound in the diagnostic management of malignant lymphomas. Radiologe. 2012;52:347–59.
42. Nakase K, Yamamoto K, Hiasa A, Tawara I, Yamaguchi M, Shiku H. Contrast-enhanced ultrasound examination of lymph nodes in different types of lymphoma. Cancer Detect Prev. 2006;30:188–91.
43. Rübenthaler J, Lutz J, Reiser M, Clevert DA. [Paraganglioma of the head and neck: follow-up of interventional procedures with CEUS]. [Article in German]. Ultraschall Med. 2015;36:541–3.
44. Küstermeyer J, Deichmüller CC, Albers M, Graß SK, Welkoborsky HJ. Quantifizierung des präoperativen Embolisationseffektes bei Glomus caroticum Tumoren durch kontrastverstärkte Sonographie. [Abstract.] 88th Annual Meeting of the German Society of Oto-Rhino-Laryngology, Head and Neck Surgery; 2017. https://doi.org/10.3205/17hno088.
45. Haugen BR, Alexander EK, Bible KC, Doherty GM, Mandel SJ, Nikiforov YE, et al. 2015 American Thyroid Association Management Guidelines for Adult Patients with Thyroid Nodules and Differentiated Thyroid Cancer: The American Thyroid Association Guidelines Task Force on Thyroid Nodules and Differentiated Thyroid Cancer. Thyroid. 2016;26:1–133.
46. Nemec U, Nemec SF, Novotny C, Weber M, Czerny C, Krestan CR. Quantitative evaluation of contrast-enhanced ultrasound after intravenous administration of a microbubble contrast agent for differentiation of benign and malignant thyroid nodules: assessment of diagnostic accuracy. Eur Radiol. 2012;22:1357–65.
47. Gharib H, Papini E, Garber JR, Duick DS, Harrell RM, Hegedüs L, et al. American Association of Clinical Endocrinologists, American College of Endocrinology, and Associazione Medici Endocrinologi Medical Guidelines for clinical practice for the diagnosis and management of thyroid nodules--2016 update. Endocr Pract. 2016;22:622–39.
48. Argalia G, De Bernardis S, Mariani D, Abbattista T, Taccaliti A, Ricciardelli L, et al. Ultrasonographic contrast agent: evaluation of time-intensity curves in the characterisation of solitary thyroid nodules. Radiol Med. 2002;103:407–13.
49. Bartolotta TV, Midiri M, Galia M, Runza G, Attard M, Savoia G, et al. Qualitative and quantitative evaluation of solitary thyroid nodules with contrast-enhanced ultrasound: initial results. Eur Radiol. 2006;16:2234–41.
50. Spiezia S, Farina R, Cerbone G, Assanti AP, Iovino V, Siciliani M, et al. Analysis of color Doppler signal intensity variation after Levovist injection: a new approach to the diagnosis of thyroid nodules. J Ultrasound Med. 2001;20:223–31.
51. Jin L, Xu C, Xie X, Li F, Lv X, Du L. An algorithm of image heterogeneity with contrast-enhanced ultrasound in differential diagnosis of solid thyroid nodules. Ultrasound Med Biol. 2017;43:104–10.
52. Cantisani V, Consorti F, Guerrisi A, Guerrisi I, Ricci P, Di Segni M, et al. Prospective comparative evaluation of quantitative-elastosonography (Q-elastography) and contrast-enhanced ultrasound for the evaluation of thyroid nodules: preliminary experience. Eur J Radiol. 2013;82:1892–8.
53. Friedrich-Rust M, Sperber A, Holzer K, Diener J, Grünwald F, Badenhoop K, et al. Real-time elastography and contrast-enhanced ultrasound for the assessment of thyroid nodules. Exp Clin Endocrinol Diabetes. 2010;118:602–9.
54. Jiang J, Shang X, Zhang H, Ma W, Xu Y, Zhou Q, et al. Correlation between maximum intensity and microvessel density for differentiation of malignant from benign thyroid nodules on contrast-enhanced sonography. J Ultrasound Med. 2014;33:1257–63.
55. Molinari F, Mantovani A, Deandrea M, Limone P, Garberoglio R, Suri JS. Characterization of single thyroid nodules by contrast-enhanced 3-d ultrasound. Ultrasound Med Biol. 2010;36:1616–25.
56. Zhang Y, Luo Y-K, Zhang M-B, Li J, Li J, Tang J. Diagnostic accuracy of contrast-enhanced ultrasound enhancement patterns for thyroid nodules. Med Sci Monit. 2016;22:4755–64.
57. Li F, Wang Y, Bai B, Wang S, Liu S. Advantages of routine ultrasound combined with contrast-enhanced ultrasound in diagnosing papillary thyroid carcinoma. Ultrasound Q. 2017;33:213–8.
58. Zhou X, Zhou P, Hu Z, Tian SM, Zhao Y, Liu W, et al. Diagnostic efficiency of quantitative contrast-enhanced ultrasound indicators for discriminating benign from malignant solid thyroid nodules. J Ultrasound Med. 2017;22:4755.
59. Ma J-J, Ding H, Xu B-H, Xu C, Song L-J, Huang B-J, et al. Diagnostic performances of various gray-scale, color Doppler, and contrast-enhanced ultrasonography findings in predicting malignant thyroid nodules. Thyroid. 2014;24:355–63.
60. Schleder S, Janke M, Agha A, Schacherer D, Hornung M, Schlitt HJ, et al. Preoperative differentiation of thyroid adenomas and thyroid carcinomas using high resolution contrast-enhanced ultrasound (CEUS). Clin Hemorheol Microcirc. 2015;61:13–22.
61. Williams R, Hudson JM, Lloyd BA, Sureshkumar AR, Lueck G, Milot L, et al. Dynamic microbubble contrast-enhanced US to measure tumor response to targeted therapy: a proposed clinical protocol with results from renal cell carcinoma patients receiving antiangiogenic therapy. Radiology. 2011;260:581–90.
62. Lassau N, Lamuraglia M, Vanel D, Le Cesne A, Chami L, Jaziri S, et al. Doppler US with perfusion software and contrast medium injection in the early evaluation of isolated limb perfusion of limb sarcomas: prospective study of 49 cases. Ann Oncol. 2005;16:1054–60.

Future Developments of Sonography

17

Hans J. Welkoborsky

Ultrasonography and its related techniques, such as elastography, contrast-enhanced ultrasonography, targeted therapy, and molecular imaging, are emerging techniques that will improve both the diagnostic accuracy and indications for ultrasound applications in the future. Of the numerous advances and promising developments in ultrasonography, this chapter will focus on the detailed discussion of new developments in data acquisition by matrix transducers, three- and four-dimensional ultrasound, computerized analysis and diagnosis, molecular imaging, targeted therapy with application of ultrasound, and real-time elastography (strain elastography as well as shear wave elastography). This chapter describes each issue and briefly discusses its potential future application in and impact on clinical medicine.

17.1 Introduction

Ultrasound and its related applications (i.e., Doppler sonography, duplex sonography, contrast-enhanced ultrasonography [CEUS], 3D sonography, elastography) are emerging techniques that allow more precise imaging of pathologic conditions and also open up possibilities for novel applications and indications [1, 2]. The development of microbubbles for CEUS imaging and their ability to enhance the permeability of the surrounding tissue for transportation of drugs, for example, make them feasible for both molecular imaging and targeted therapy [3–5]. Technical developments lead to new methods for data acquisition with matrix transducers, and the use of plain or diverging wave transmission enables ultrafast frame rates, leading to a novel imaging mode valuable for ultrafast imaging and monitoring of therapy [6]. A combination of 3D ultrasound and a robot can lead to new methods to reconstruct arteries, which are of great value for diagnosis of stenosis and planning of therapy [7, 8]. Real-time elastography can be applied in various locations in the upper digestive tract as an adjunct to endosonography for better characterization of masses [9], probably combined with high-resolution endosonography, which allows (in combination with the Doppler technique and Nakagami imaging) a functional assessment of the vocal cords [10]. These are only some examples of the emerging character of sonography technique, which will determine its clinical applications in the future.

This chapter focuses on some future developments in ultrasound that may have significant impact on its application, indications, and diagnostic accuracy, as well as on concepts for molecular imaging and targeted therapy. Of the numerous innovations in this field, the chapter will focus on future developments in data acquisition and data processing, 3D and 4D ultrasound, computerized analysis of ultrasound imaging, molecular imaging, targeted therapy, and elastography.

17.2 New Developments in Data Acquisition

The latest innovations in computer technology and in transducer technology have opened new horizons for ultrasound imaging in the near future. In harmonic imaging, fundamental signals are rejected, and second harmonic signals are extracted. Tissue harmonic signals have a narrower and lower clutter noise. The aim is to get pure transmitted ultrasound waves that are free of artifacts and homogeneous, without decreasing the frame rate. The result is higher spatial and contrast resolution with reduced artifacts [11]. Additional technical features, including quadrature signal processing, multibeam receivers, or multiharmonic compounding, are related to powerful computer platforms and make ultrasound quicker and more real-time. Several ultrasound machines are

H. J. Welkoborsky (✉)
Department of Otorhinolaryngology, Head and Neck Surgery, KRH Nordstadt Clinic–Academic Hospital, Hannover, Germany
e-mail: hans-juergen.welkoborsky@krh.eu

© Springer Nature Switzerland AG 2019

H. J. Welkoborsky, P. Jecker (eds.), *Ultrasonography of the Head and Neck*, https://doi.org/10.1007/978-3-030-12641-4_17

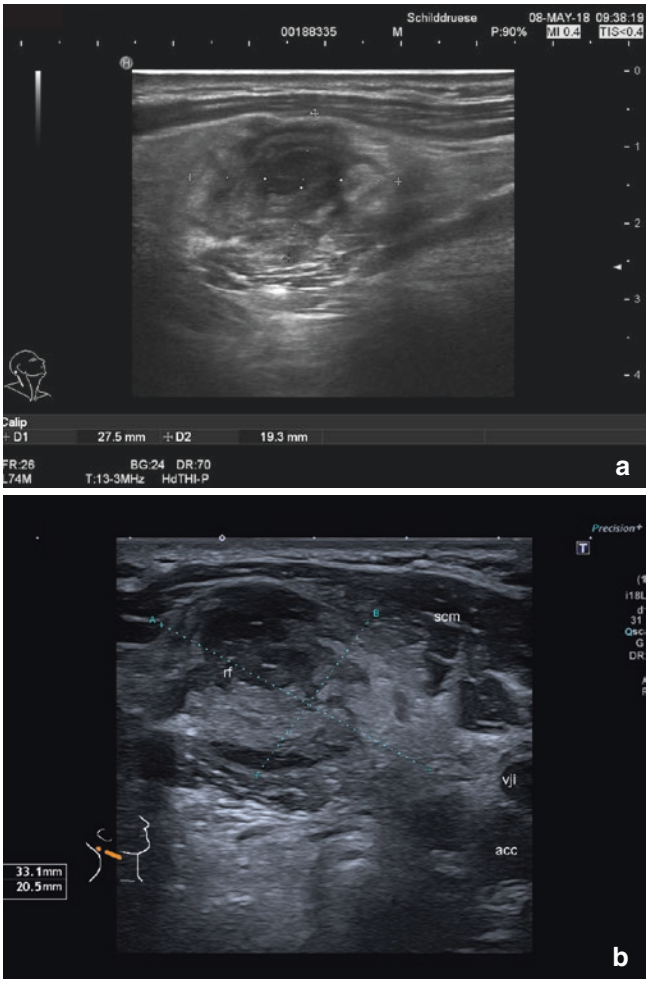

Fig. 17.1 Example of more detailed and clearer visualization of structures in a patient with a neck lymph node metastasis of a hypopharyngeal cancer. (**a**) Image from a conventional transducer of a modern ultrasound machine. (**b**) Image of the same lesion from a matrix transducer with the latest technology. The transducer leads to more precise evaluation, such as of the infiltration of large blood vessels

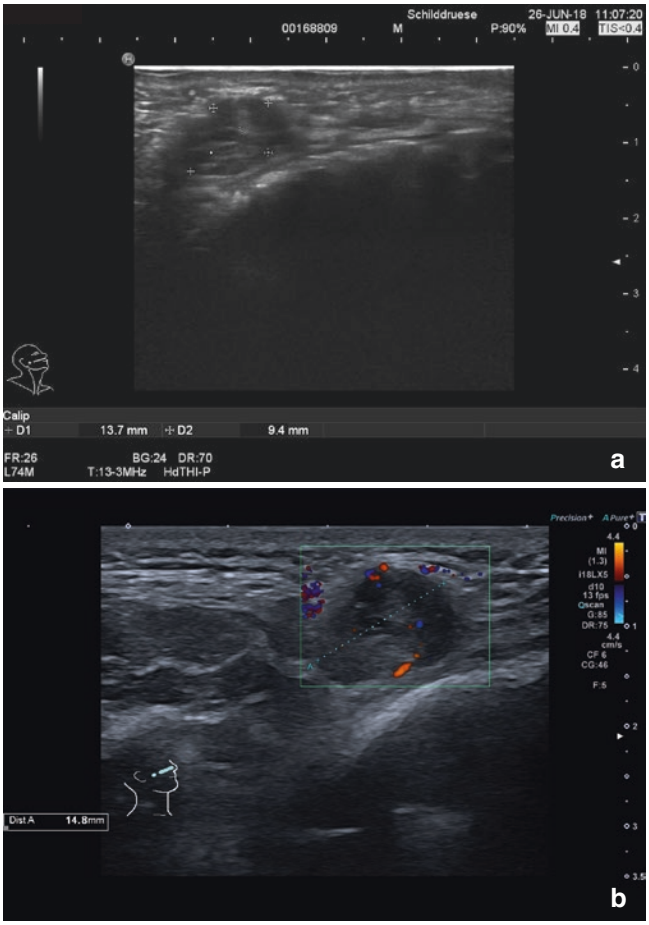

Fig. 17.2 Another example of the much more precise visualization of structures with a matrix transducer, in a patient with an adenoid cystic cancer of the cheek. (**a**) Image with a conventional transducer. (**b**) Image with a matrix transducer using the latest technology

already available that provide these technical features (Figs. 17.1 and 17.2).

Innovations in transducer technology include the introduction of matrix transducers in clinical applications. The characteristic of a matrix transducer is the apposition of the piezoelectric crystals. Instead of 120–190 crystals in conventional transducers, which swing back and forth, a matrix transducer may have 64 rows with 128 crystals each, so that more than 8000 elements are incorporated [12]. With this technique, it is possible to perform 3D ultrasound in real time (4D) unaffected by motion artifacts [13, 14]. Even in miniature probes for transesophageal echocardiography, more than 2000 elements can be incorporated in matrix transducers [15]. With the rapid computer processors, it is possible to create ultrasound waves in all rows in real time, which leads to more precise images and to a rapid calculation of 3D volume, for instance. In addition to conventional ultrasound diagnostics, a new application of this technique is biplane imaging, in which the examiner can investigate a region of interest in one plane, while the computer creates an orthogonal cross-section in real time. This technical innovation can be applied not only in abdominal and obstetric ultrasound but also in head and neck ultrasound.

Another promising future development in ultrasound is the increase of frame rates to visualize ultrafast processes or disruption of contrast agents. In experiments, a theoretical resolution of 6 μm was achieved [12]. Other examples for applications of matrix transducers with ultrafast frames are real-time shear wave elastography or 3D elastography, or its combination as real-time 3D shear wave elastography [16, 17], or three-dimensional molecular imaging, such as imaging of angiogenesis in a tumor using microbubbles targeted at vascular endothelial growth factor receptors (VEGFRs) [18]. Focused ultrasound with microbubbles can open the blood-brain barrier and can therefore achieve accumulation

and distribution of nanoparticle-loaded microbubbles in the brain for therapeutic purposes [19].

New algorithms reduce blurring effects and lead to a higher resolution, which is especially important in applications that need high computing capacity, such as 3D ultrasound [20]. Other progress in computer technology leads to the possibility of correcting refraction in 3D ultrasound using an iterative approach that traces propagation paths [21].

Ultrafast ultrasound microscopy can be applied for noninvasive characterization of disorders such as cartilage degeneration and for cartilage assessment. High-frequency transducers of 40 MHz are used for this application. A moderate correlation of chondrocyte number with backscatter amplitude and envelope statistics was found, so the technique may have potential for future cartilage assessment [22].

Another ultrasound innovation is the development of photoacoustic imaging. The principle of this technique is that ultrafast optical (i.e., laser) impulses are released down in the tissue, which create ultrasound waves with high-contrast and high-resolution images within deep tissues. Much effort is currently underway to development appropriate probes for photoacoustic imaging [23].

In conclusion, future developments will focus on further refinement of both ultrasound matrix transducers (including their possible use in real-time 3D ultrasound and elastography) and of software for more accurate evaluation and post-processing of ultrasound data, enabled by the integration of ultrafast computer technology in the ultrasound equipment.

17.3 3D/4D Ultrasound

One of the disadvantages of ultrasonography is that three-dimensional structures (both normal anatomy and masses) are displayed two-dimensionally [24]. Much effort therefore has been devoted to developing techniques for 3D ultrasonography. Some authors have reported software solutions for 3D reconstruction of anatomy based on two-dimensional images, as a tool to study anatomical spatial relationships and the structure of pathologic masses [24–28], but acoustic artifacts caused the 3D reconstruction of boundaries of arterial vessels to be displayed inadequately [27].

In the past several years, new developments in both transducer and computer technologies led to the introduction of new matrix samples with more than 1000 independent channels to create ultrafast images [29]. Based on these developments, real-time 3D ultrasound (4D ultrasound) was introduced in many applications. The principle of 3D ultrasound is that gray-scale images are processed by very fast repeated scans of multiple planes to get one surface-rendering image along with three perpendicular plane images. For more precise 3D imaging, new techniques in post-processing and computer calculation, such as automatic dynamic range adjustment, have been developed to further enhance the quality of 3D ultrasound [30]. The 4D images (i.e., real-time 3D images) are generated by very fast repeating of 3D images [31]. One question raised was the safety of this procedure. Pooh et al. investigated eventual safety problems and postulated that the thermal and the mechanical index should not exceed 1 for investigation of a fetus, and ultrasound exposure time should be shorter than 30 minutes [31]. The lowest spatial peak temporal average intensity of the ultrasound to suppress cell grow in cell cultures was 240 mW/cm^2 in experimental studies [31], which is usually not reached in routine diagnostic studies. Below this intensity, no ultrasound effect on cultured cells has been reported.

Ultrafast 3D real-time ultrasound (4D ultrasound) with a matrix array has been used for mapping the stiffness, time motion, and flow in the heart and carotid, achieving a high-contrast and high-resolution image [29], for 3D imaging of the subglottic airway and subglottic stenosis [32], and to visualize tongue movements in newborns for functional investigation [33]. Other applications have included the study of anatomical spatial relationships and use of the 3D image for optimal needle position in nerve blocks [26], intracardiac echosonography (4D intracardiac echo [ICE]), and 3D visualization of the prostate gland for mapping of biopsies or targeted imaging [34, 35]. By real-time 3D ultrasound, it is possible to more precisely recognize carotid artery stenosis, carotid artery plaques, and blood flow pattern, which may significantly influence the therapeutic strategy in patients [36, 37], and real-time 3D ultrasound elastography using plane-wave imaging has been proven to be feasible in breast cancer [38].

Recent developments in transducer technology have made it possible to create ultrafast 3D images of the human skin using a 120 MHz probe. This technique, called 3D ultrasound microscopy, has an ultrahigh resolution of the surface skin tissue layers for detecting and estimating cutaneous pathologies, with a significant impact on the knowledge of the human skin structure [39].

One of the most promising developments is the combination of endoscopic imaging with real-time 3D ultrasonography. This image fusion will enhance the possibilities of minimally invasive procedures and is suitable for intraoperative monitoring [40].

Another exciting project is the combination of real-time 3D ultrasound with the use of a robot, opening new horizons for 3D imaging of arteries, for example, which might be of great value for vessel reconstruction [7]. It also opens new possibilities for intraoperative applications such as navigation and monitoring.

As a result, it is reasonable to conclude that real-time 3D ultrasound will dominate ultrasound imaging in the future and will increase the indications and applications for ultrasound.

17.4 Computerized Ultrasound Image Analysis

Ultrasound and duplex sonography are complex, evolving technologies that allow the assessment of nearly all soft tissues and parenchymatous organs. Duplex sonography provides additional information on volumetric blood flow in numerous healthy and pathologic conditions. Ultrasound offers many advantages, including lack of radiation exposure, convenience, high diagnostic accuracy, dynamic procedure, and low cost, but ultrasound approaches are specialized techniques that require intensive training and experience by the examiner. Furthermore, results are often examiner-dependent, and interpretation sometimes appears inconsistent. Methods to evaluate ultrasound findings that are more reliable and objective probably can be facilitated by computerized analysis [41, 42]. Therefore much effort has been made to develop computer-aided diagnosis (CAD) systems for ultrasound examinations, using either the man-made ultrasound features or deep learning systems [43], consisting of software that is regarded as able to learn better and faster than a human examiner with no prior experience [44]. In the first clinical trials, deep learning software systems were applied for classification of breast cancer and proved highly accurate (even with comparably few training cases), and their fast evaluation speed made their use feasible for real-time image analysis [44]. Rodríguez-Cristerna et al. conducted a study of conventional CAD systems for breast ultrasound. They combined CAD with a breast imaging/reporting and data system and found that their approach had an increased sensitivity with unchanged high specificity, which significantly improved the performance of CAD systems in the classification of breast lesions [45]. Other authors described automated breast ultrasound techniques that produced a full 3D scan of the breast automatically, with lesion segmentation; this system reduced operator dependency and facilitated double reading and comparison with past exams [46].

In conclusion, the computer-based automated interpretation of ultrasound findings is a fascinating issue. The probable indications might be the classification of cancers (e.g., breast, prostate) and of salivary gland tumors and the computing of distances such as those between masses and large vessels in the neck when a vessel infiltration is suspected. However, several advantages of ultrasound—dynamic procedure, direct correlation of findings with intraoperative findings, and interpretation of pathologic findings by an experienced clinician—remain very important issues that will probably limit the clinical application of computerized, automated interpretation.

17.5 Molecular Imaging

Like targeting therapy, molecular imaging is a most promising future development in ultrasound, to make possible the diagnosing and monitoring of pathological processes on a molecular level [47, 48]. The principle of this technique is the conjugation of targeting ligands with microbubbles. These conjugates are then used as contrast agents and lead to an ultrasound enhancement of the targeted structures, particularly in the field of neoangiogenesis, due to the strictly intravascular presence of the microbubbles [47, 49, 50]. The targeted microbubbles are held in place, while the unbound ones are eliminated; subsequent ultrasound imaging can then visualize the highly reflectant microbubbles that are left behind, leading to the enhancement [51]. A problem for application in vivo might be that they may contain immunogenic components (such as biotin-avidin constructs), so much effort has been made to attach the microbubbles with components of minimal immunogenicity [47]. For application in vivo, targeting microbubbles have been described with three important characteristics: (1) low degree of nonspecific bubble retention in more than one nonreticuloendothelial tissue, (2) effective for real-time imaging, and (3) effective for acoustic quantification of molecular targets [49, 52].

The potential clinical applications for molecular imaging include molecular profiling and therapy monitoring of cancer (e.g., by VEGFR2-targeted microbubbles for assessment of angioneogenesis in cancer [18]), visualization of ischemic zones in transient myocardial ischemia, monitoring of disease activity in inflammatory processes, drug delivery, and diagnosis of atherosclerosis [48, 50, 53]. The combination of 3D ultrasound and molecular imaging using VEGFR2-targeted microbubbles led to feasible, highly reproducible, accurate 3D assessment of tumor angiogenesis in a murine model of human colon cancer [18]. Molecular imaging was recently applied for staging of prostate cancer [54].

In conclusion, molecular imaging by ultrasound, in combination with new endoscopic probes and new endoscopic technology, has the potential for early detection of cancer, particularly of early-stage premalignant lesions [55]. The development of nano ultrasound contrast agents (nUCAs) will enable the particles to leave the intravascular space and provide more molecular information about particular diseases [56] and will increase the wider implementation of individualized diagnosis and therapy [53].

17.6 Targeted Therapy

Ultrasound-mediated targeted therapy is regarded as one of the most promising strategies in modern therapy [57]. To make targeted therapy possible, new transducers have been developed. These capacitive micromachined ultrasonic transducer (cMUTs) embed two types of arrays. One of the main features is the possibility of implementing two different gap heights on the same wafer [57]. The principle of targeted therapy is the conjugation of ligands to the surface of microbubbles to target specific biomarkers of a disease or a specific process [50, 58, 59]. The technique is thought

to have significant therapeutic potential in various fields, including tumor therapy, cardiovascular diseases, CNS diseases, diseases of the skeletomuscular system, and stem cell therapy [60–62]. Targeting therapy can facilitate the delivery of nucleic acid-loaded and targeted nanobubbles for tumor therapy [63] or microbubbles loaded with the neuroprotector kallidinogenase in patients with acute cerebral infarction, for promotion of proliferation of neuroblasts and vascular regeneration (and therefore functional improvement) after a stroke [62].

The propagation of ultrasound waves with higher energy, intensity, and frequency can induce thermal, mechanical, and chemical effects that can be applied for therapeutic purposes in a great variety of diseases [64]. The therapeutic potential lies in the fact that high-intensity focused ultrasound can enable the focused and localized deposition of high-energy doses deep in the tissue without harming the adjacent tissue [65]. Since its first experimental descriptions, high-intensity focused ultrasound has been applied for thermal ablation of pancreatic cancer or prostate cancer [66, 67]. Zhang et al. reported an experimental study in which methotrexate (MTX)-loaded nanobubbles were used for ultrasound imaging and for targeted therapy of residual tumor cells [68]. They conjugated the active tumor-targeting monoclonal anti-HLA-G antibodies onto the surface of MTX-loaded nanobubbles and demonstrated that this method enhanced the ultrasound imaging both in vivo and in vitro. In vivo histopathology and immunohistochemical analysis showed the lowest proliferation index and the highest apoptotic index, along with a coagulative necrosis. The authors concluded that the targeted MTX-loaded nanobubbles provided an excellent opportunity for efficient, imaging-guided, noninvasive, high-intensity, focused ultrasound synergistic therapy to kill residual cancer cells and to prevent tumor recurrences [68]. Park et al. [69] applied pulsed high-intensity ultrasound for enhancement of the effect of cetuximab, a drug targeting epidermal growth factor receptor. They treated human colon cancer xenografts in a mouse model and found a positive enhancement of the antitumor effect of cetuximab mediated by ultrasound [69].

In a recent study, Apfelbeck et al. [70] reported on fusion of contrast-enhanced ultrasound (CEUS) with MRI images in patients with prostate cancer, who were treated by high-intensity focused ultrasound (HIFU). After the treatment and in the first 24 hours, CEUS showed a significant reduction of microcirculation in the treated area, but signs of perfusion persisted in the prostate capsule. The combination of CEUS and MRI images was shown to be helpful in detecting residual tumor, which could be a target for HIFU treatment, and in monitoring the therapeutic success [70].

Other experimental applications have included minimally invasive ultrasound-mediated drug delivery through a transient formation of pores in cell membranes, disruption of the blood-brain barrier for intracerebral application of drugs [64, 71], and delivery of plasmid-DNA in liver cells of canines [72].

In conclusion, it is likely that future functional analyses will be complemented by molecular ultrasound imaging, to visualize markers of inflammation and angiogenesis. HIFU has been shown to have a promising therapeutic effect in many tumors, and it benefits from integration with MRI. Oscillating microbubbles can open biological barriers and can therefore provide delivery of drugs or nucleic acids [71]. Molecular therapy with targeted nanobubbles or microbubbles shows promising prospects for clinical applications, which probably can help to reduce drug dosages, toxicity, and side effects [59].

17.7 Elastography

Ultrasound elastography is a method for noninvasive measurements of tissue stiffness and mechanical properties [73, 74]. Basically, two different ultrasound elastography techniques are available: (1) real-time strain elastography, in which the examiner alters the pressure of the ultrasound transducer a bit to create different echoes depending on the tissue's stiffness, and (2) shear wave elastography (SWE), in which shear waves are simultaneously sent into the tissue [74, 75]. For strain elastography, strain ratios for a tissue are calculated, whereas the mean elasticity value and elasticity ratio of the lesion to fat are calculated for SWE [75].

Both elastography techniques have been applied recently to a variety of diseases, including liver fibrosis and portal hypertension [73, 76], chronic pancreatitis [78], and benign and malignant breast lesions [75], and they have been used in the differentiation of thyroid nodules and lymph nodes [77, 79] and for examination of the muscle-tendon unit [80]. In most of these studies, elastography increased the diagnostic accuracy of ultrasound. In the examination conducted by Seo et al. [75], strain and shear wave elastography were compared in their diagnostic accuracy for differentiating benign and malignant breast lesions; they found that both elastography techniques had a similar diagnostic performance and, combined with B-mode ultrasound, they resulted in a higher diagnostic performance [75]. Batur et al. [81] published a novel application for elastography. They found significant differences in the stiffness of the optic nerve in normal individuals and patients with optic neuritis and postulated that elastography can be regarded as an adjunctive tool for confirming the diagnosis [81].

In conclusion, elastography yields significant additional information about the mechanical characteristics of particular tissues, and it is very likely that real-time elastography—either strain or shear wave elastography—will play an increasingly important role in future ultrasound imaging [82].

References

1. Vizzutti F, Arena U, Marra F, Pinzani M. Elastography for the non-invasive assessment of liver disease: limitations and future developments. Gut. 2009;58:157–60.
2. Ohana M, Moser T, Moussaouï A, Kremer S, Carlier RY, Liverneaux P, Dietemann JL. Current and future imaging of the peripheral nervous system. Diagn Interv Imaging. 2014;95:17–26.
3. Kang ST, Yeh CK. Ultrasound microbubble contrast agents for diagnostic and therapeutic applications: current status and future design. Chang Gung Med J. 2012;35:125–39.
4. Deshpande N, Needles A, Willmann JK. Molecular ultrasound imaging: current status and future directions. Clin Radiol. 2010;65:567–81.
5. Oyen WJ, Bodei L, Giammarile F, Maecke HR, Tennvall J, Luster M, Brans B. Targeted therapy in nuclear medicine--current status and future prospects. Ann Oncol. 2007;18:1782–92.
6. Tanter M, Fink M. Ultrafast imaging in biomedical ultrasound. IEEE Trans Ultrason Ferroelectr Freq Control. 2014;61:102–19.
7. Janvier MA, Merouche S, Allard L, Soulez G, Cloutier G. A 3-D ultrasound imaging robotic system to detect and quantify lower limb arterial stenoses: in vivo feasibility. Ultrasound Med Biol. 2014;40:232–43.
8. Ten Kate GL, van den Oord SC, Sijbrands EJ, van der Lugt A, de Jong N, Bosch JG, et al. Current status and future developments of contrast-enhanced ultrasound of carotid atherosclerosis. J Vasc Surg. 2013;57:539–46.
9. Dietrich CF, Săftoiu A, Jenssen C. Real time elastography endoscopic ultrasound (RTE-EUS), a comprehensive review. Eur J Radiol. 2014;83:405–14.
10. Tsui PH, Wan YL, Chen CK. Ultrasound imaging of the larynx and vocal folds: recent applications and developments. Curr Opin Otolaryngol Head Neck Surg. 2012;20:437–42.
11. Imamura T, Kurita K, Shikata H, Kawagishi T. Evolution and revolution of system architecture with new generation technology. In: Medical review, Toshiba Medical Systems;2016:1–5 https://mfl.ssl.cdn.sdlmedia.com/636364554593809137UQ.pdf.
12. Desailly Y, Pierre J, Couture O, Tanter M. Resolution limits of ultrafast ultrasound localization microscopy. Phys Med Biol. 2015;60:8723–40.
13. La Torre R, Bevilacqua E, D'Ambrosio V, Pasquali G, Aliberti C, Ventriglia F, Giancotti A. Matrix array transducer for the examination of fetal heart. Clin Exp Obstet Gynecol. 2014;41:581–2.
14. Wigen MS, Fadnes S, Rodriguez-Molares A, Bjastad T, Eriksen M, Stensaeth KH, et al. 4D Intracardiac ultrasound vector flow imaging--feasibility and comparison to phase-contrast MRI. IEEE Trans Med Imaging. 2018. https://doi.org/10.1109/TMI.2018.2844552 [Epub ahead of print].
15. Yu Z, Blaak S, Chang ZY, Yao J, Bosch JG, Prins C, et al. Front-end receiver electronics for a matrix transducer for 3-D transesophageal echocardiography. IEEE Trans Ultrason Ferroelectr Freq Control. 2012;59:1500–2.
16. Gennisson JL, Provost J, Deffieux T, Papadacci C, Imbault M, Pernot M, Tanter M. 4-D ultrafast shear-wave imaging. IEEE Trans Ultrason Ferroelectr Freq Control. 2015;62:1059–65.
17. Wang M, Byram B, Palmeri M, Rouze N, Nightingale K. On the precision of time-of- flight shear wave speed estimation in homogeneous soft solids: initial results using a matrix array transducer. IEEE Trans Ultrason Ferroelectr Freq Control. 2013;60:758–70.
18. Wang H, Kaneko OF, Tian L, Hristov D, Willmann JK. Three-dimensional ultrasound molecular imaging of angiogenesis in colon cancer using a clinical matrix array ultrasound transducer. Investig Radiol. 2015;50:322–9.
19. Baghirov H, Snipstad S, Sulheim E, Berg S, Hansen R, Thorsen F, et al. Ultrasound-mediated delivery and distribution of polymeric nanoparticles in the normal brain parenchyma of a metastatic brain tumour model. PLoS One. 2018;13:e0191102.
20. Ma R, Zhou X, Zhang S, Yin T, Liu Z. A 3D reconstruction algorithm for magneto- acoustic tomography with magnetic induction based on ultrasound transducer characteristics. Phys Med Biol. 2016;61:8762–78.
21. Lindsey BD, Smith SW. Refraction correction in 3D transcranial ultrasound imaging. Ultrason Imaging. 2014;36:35–54.
22. Männicke N, Schöne M, Gottwald M, Göbel F, Oelze ML, Raum K. 3-D high- frequency ultrasound backscatter analysis of human articular cartilage. Ultrasound Med Biol. 2014;40:244–57.
23. Reinhardt CJ, Chan J. Development of photoacoustic probes for in vivo molecular imaging. Biochemistry. 2018;57:194–9.
24. Fenster A, Landry A, Downey DB, Hegele RA, Spence JD. 3D ultrasound imaging of the carotid arteries. Curr Drug Targets Cardiovasc Haematol Disord. 2004;4:161–75.
25. Fenster A, Bax J, Neshat H, Cool D, Kakani N, Romagnoli C. 3D ultrasound imaging in image-guided intervention. Conf Proc IEEE Eng Med Biol Soc. 2014;2014:6151–4.
26. Gebhard RE, Eubanks TN, Meeks R. Three-dimensional ultrasound imaging. Curr Opin Anaesthesiol. 2015;28:583–7.
27. Yeom E, Nam KH, Jin C, Paeng DG, Lee SJ. 3D reconstruction of a carotid bifurcation from 2D transversal ultrasound images. Ultrasonics. 2014;54:2184–92.
28. Wang Y, Erpelding TN, Jankovic L, Guo Z, Robert JL, David G, Wang LV. In vivo three-dimensional photoacoustic imaging based on a clinical matrix array ultrasound probe. J Biomed Opt. 2012;17:061208.
29. Provost J, Papadacci C, Arango JE, Imbault M, Fink M, Gennisson JL, et al. 3D ultrafast ultrasound imaging in vivo. Phys Med Biol. 2014;59:L1–13.
30. Lee Y, Kang J, Yoo Y. Automatic dynamic range adjustment for ultrasound B-mode imaging. Ultrasonics. 2015;56:435–43.
31. Pooh RK, Maeda K, Kurjak A, Sen C, Ebrashy A, Adra A, et al. 3D/4D sonography - any safety problem. J Perinat Med. 2016;44:125–9.
32. Or DY, Karmakar MK, Lam GC, Hui JW, Li JW, Chen PP. Multiplanar 3D ultrasound imaging to assess the anatomy of the upper airway and measure the subglottic and tracheal diameters in adults. Br J Radiol. 2013;86:20130253.
33. Burton P, Deng J, McDonald D, Fewtrell MS. Real-time 3D ultrasound imaging of infant tongue movements during breast-feeding. Early Hum Dev. 2013;89:635–41.
34. Long JA, Daanen V, Moreau-Gaudry A, Troccaz J, Rambeaud JJ, Descotes JL. Prostate biopsies guided by three-dimensional real-time (4-D) transrectal ultrasonography on a phantom: comparative study versus two-dimensional transrectal ultrasound-guided biopsies. Eur Urol. 2007;52:1097–104.
35. Schalk SG, Demi L, Smeenge M, Mills DM, Wallace KD, de la Rosette JJ, et al. 4-D spatiotemporal analysis of ultrasound contrast agent dispersion for prostate cancer localization: a feasibility study. IEEE Trans Ultrason Ferroelectr Freq Control. 2015;62:839–51.
36. Igase K, Kumon Y, Matsubara I, Arai M, Goishi J, Watanabe H, et al. Utility of 3-dimensional ultrasound imaging to evaluate carotid artery stenosis: comparison with magnetic resonance angiography. J Stroke Cerebrovasc Dis. 2015;24:148–53.
37. Chiu B, Shamdasani V, Entrekin R, Yuan C, Kerwin WS. Characterization of carotid plaques on 3-dimensional ultrasound imaging by registration with multicontrast magnetic resonance imaging. J Ultrasound Med. 2012;31:1567–80.
38. Hendriks GA, Holländer B, Menssen J, Milkowski A, Hansen HH, de Korte CL. Automated 3D ultrasound elastography of the breast: a phantom validation study. Phys Med Biol. 2016;61:2665–79.
39. Kumagai K, Koike H, Nagaoka R, Sakai S, Kobayashi K, Saijo Y. High-resolution ultrasound imaging of human skin in vivo by

using three-dimensional ultrasound microscopy. Ultrasound Med Biol. 2012;38:1833–8.
40. Yang L, Wang J, Ando T, Kubota A, Yamashita H, Sakuma I, et al. Vision-based endoscope tracking for 3D ultrasound image-guided surgical navigation. Comput Med Imaging Graph. 2015;40:205–16.
41. Thomas KN, Lewis NC, Hill BG, Ainslie PN. Technical recommendations for the use of carotid duplex ultrasound for the assessment of extracranial blood flow. Am J Physiol Regul Integr Comp Physiol. 2015;309:R707–20.
42. Tang A, Cloutier G, Szeverenyi NM, Sirlin CB. Ultrasound elastography and MR elastography for assessing liver fibrosis: part 2, diagnostic performance, confounders, and future directions. AJR Am J Roentgenol. 2015;205:33–40.
43. Huang Q, Zhang F, Li X. Machine learning in ultrasound computer-aided diagnostic systems: a survey. Biomed Res Int. 2018;2018:5137904.
44. Becker AS, Mueller M, Stoffel E, Marcon M, Ghafoor S, Boss A. Classification of breast cancer in ultrasound imaging using a generic deep learning analysis software: a pilot study. Br J Radiol. 2018;91:20170576.
45. Rodríguez-Cristerna A, Gómez-Flores W, de Albuquerque Pereira WC. A computer- aided diagnosis system for breast ultrasound based on weighted BI-RADS classes. Comput Methods Prog Biomed. 2018;153:33–40.
46. Agarwal R, Diaz O, Lladó X, Gubern-Mérida A, Vilanova JC, Martí R. Lesion segmentation in automated 3D breast ultrasound: volumetric analysis. Ultrason Imaging. 2018;40:97–112.
47. Tranquart F, Arditi M, Bettinger T, Frinking P, Hyvelin JM, Nunn A, et al. Ultrasound contrast agents for ultrasound molecular imaging. Z Gastroenterol. 2014;52:1268–76.
48. Abou-Elkacem L, Bachawal SV, Willmann JK. Ultrasound molecular imaging: moving toward clinical translation. Eur J Radiol. 2015;84:1685–93.
49. Yeh JS, Sennoga CA, McConnell E, Eckersley R, Tang MX, Nourshargh S, et al. Quantitative ultrasound molecular imaging. Ultrasound Med Biol. 2015;41:2478–96.
50. van Rooij T, Daeichin V, Skachkov I, de Jong N, Kooiman K. Targeted ultrasound contrast agents for ultrasound molecular imaging and therapy. Int J Hyperth. 2015;31:90–106.
51. Ibsen S, Shi G, Schutt C, Shi L, Suico KD, Benchimol M, et al. The behavior of lipid debris left on cell surfaces from microbubble based ultrasound molecular imaging. Ultrasonics. 2014;54:2090–8.
52. Yeh JS, Sennoga CA, McConnell E, Eckersley R, Tang MX, Nourshargh S, et al. A targeting microbubble for ultrasound molecular imaging. PLoS One. 2015;10:e0129681.
53. Wang S, Hossack JA, Klibanov AL. Targeting of microbubbles: contrast agents for ultrasound molecular imaging. J Drug Target. 2018;26:420–34.
54. Boustani AM, Pucar D, Saperstein L. Molecular imaging of prostate cancer. Br J Radiol. 2018;91:20170736.
55. Ahmed S, Strand S, Weinmann-Menke J, Urbansky L, Galle PR, Neumann H. Molecular endoscopic imaging in cancer. Dig Endosc. 2018. https://doi.org/10.1111/den.13199 [Epub ahead of print].
56. Zlitni A, Gambhir SS. Molecular imaging agents for ultrasound. Curr Opin Chem Biol. 2018;45:113–20.
57. Gross D, Coutier C, Legros M, Bouakaz A, Certon D. A cMUT probe for ultrasound- guided focused ultrasound targeted therapy. IEEE Trans Ultrason Ferroelectr Freq Control. 2015;62:1145–60.
58. Ninomiya K, Noda K, Ogino C, Kuroda S, Shimizu N. Enhanced OH radical generation by dual-frequency ultrasound with TiO2 nanoparticles: its application to targeted sonodynamic therapy. Ultrason Sonochem. 2014;21:289–94.
59. Yang F, Chen ZY, Lin Y. Advancement of targeted ultrasound contrast agents and their applications in molecular imaging and targeted therapy. Curr Pharm Des. 2013;19:1516–27.
60. Yang C, Li Y, Du M, Chen Z. Recent advances in ultrasound-triggered therapy. J Drug Target. 2018;27:1–18. https://doi.org/10.1080/1061186X.2018.1464012.. [Epub ahead of print]
61. Qian L, Thapa B, Hong J, Zhang Y, Zhu M, Chu M, et al. The present and future role of ultrasound targeted microbubble destruction in preclinical studies of cardiac gene therapy. J Thorac Dis. 2018;10:1099–111.
62. Liang Y, Chen J, Zheng X, Chen Z, Liu Y, Li S, Fang X. Ultrasound-mediated kallidinogenase-loaded microbubble targeted therapy for acute cerebral infarction. J Stroke Cerebrovasc Dis. 2018;27:686–96.
63. Wu M, Zhao H, Guo L, Wang Y, Song J, Zhao X, et al. Ultrasound-mediated nanobubble destruction (UMND) facilitates the delivery of A10-3.2 aptamer targeted and siRNA-loaded cationic nanobubbles for therapy of prostate cancer. Drug Deliv. 2018;25:226–40.
64. Phenix CP, Togtema M, Pichardo S, Zehbe I, Curiel L. High intensity focused ultrasound technology, its scope and applications in therapy and drug delivery. J Pharm Pharm Sci. 2014;17:136–53.
65. Jenne JW, Preusser T, Günther M. High-intensity focused ultrasound: principles, therapy guidance, simulations and applications. Z Med Phys. 2012;22:311–22.
66. Wu F. High intensity focused ultrasound: a noninvasive therapy for locally advanced pancreatic cancer. World J Gastroenterol. 2014;20:16480–8.
67. Crouzet S, Rouviere O, Martin X, Gelet A. High-intensity focused ultrasound as focal therapy of prostate cancer. Curr Opin Urol. 2014;24:225–30.
68. Zhang X, Zheng Y, Wang Z, Huang S, Chen Y, Jiang W, et al. Methotrexate-loaded PLGA nanobubbles for ultrasound imaging and synergistic targeted therapy of residual tumor during HIFU ablation. Biomaterials. 2014;35:5148–61.
69. Park MJ, Kim YS, Yang J, Sun WC, Park H, Chae SY, et al. Pulsed high-intensity focused ultrasound therapy enhances targeted delivery of cetuximab to colon cancer xenograft model in mice. Ultrasound Med Biol. 2013;39:292–9.
70. Apfelbeck M, Clevert DA, Ricke J, Stief C, Schlenker B. Contrast enhanced ultrasound (CEUS) with MRI image fusion for monitoring focal therapy of prostate cancer with high intensity focused ultrasound (HIFU)1. Clin Hemorheol Microcirc. 2018;69:93–100.
71. Rix A, Lederle W, Theek B, Lammers T, Moonen C, Schmitz G, Kiessling F. Advanced ultrasound technologies for diagnosis and therapy. J Nucl Med. 2018;59:740–6.
72. Noble ML, Kuhr CS, Graves SS, Loeb KR, Sun SS, Keilman GW, et al. Ultrasound-targeted microbubble destruction-mediated gene delivery into canine livers. Mol Ther. 2013;21:1687–94.
73. Kennedy P, Wagner M, Castéra L, Hong CW, Johnson CL, Sirlin CB, Taouli B. Quantitative elastography methods in liver disease: current evidence and future directions. Radiology. 2018;286:738–63.
74. Dietrich CF, Bibby E, Jenssen C, Saftoiu A, Iglesias-Garcia J, Havre RF. EUS elastography: how to do it? Endosc Ultrasound. 2018;7:20–8.
75. Seo M, Ahn HS, Park SH, Lee JB, Choi BI, Sohn YM, Shin SY. Comparison and combination of strain and shear wave elastography of breast masses for differentiation of benign and malignant lesions by quantitative assessment: preliminary study. J Ultrasound Med. 2018;37:99–109.
76. Roccarina D, Rosselli M, Genesca J, Tsochatzis EA. Elastography methods for the non-invasive assessment of portal hypertension. Expert Rev Gastroenterol Hepatol. 2018;12:155–64.
77. Ahn HS, Lee JB, Seo M, Park SH, Choi BI. Distinguishing benign from malignant thyroid nodules using thyroid ultrasonography: utility of adding superb microvascular imaging and elastography. Radiol Med. 2018;123:260–70.
78. Kuwahara T, Hirooka Y, Kawashima H, Ohno E, Ishikawa T, Yamamura T, et al. Usefulness of shear wave elastography as a

quantitative diagnosis of chronic pancreatitis. J Gastroenterol Hepatol. 2018;33:756–61.
79. You J, Chen J, Xiang F, Song Y, Khamis S, Lu C, et al. The value of quantitative shear wave elastography in differentiating the cervical lymph nodes in patients with thyroid nodules. J Med Ultrason (2001). 2018;45:251–9.
80. Lima KMME, Costa Júnior JFS, Pereira WCA, Oliveira LF. Assessment of the mechanical properties of the muscle-tendon unit by supersonic shear wave imaging elastography: a review. Ultrasonography. 2018;37:3–15.
81. Batur M, Batur A, Çilingir V, Seven E, Çinal A, Bora A, Yaşar T. Ultrasonic elastography evaluation in optic neuritis. Semin Ophthalmol. 2018;33:237–41.
82. McQueen AS, Bhatia KS. Head and neck ultrasound: technical advances, novel applications and the role of elastography. Clin Radiol. 2018;73:81–93.

Index

A
Abdominal sonography, 124–127
Abnormalities of lymph nodes, 196
Abscesses, 70, 71, 183, 184, 303
Acoustic impedance, 8, 9
Actinomycosis, 66
Acute sinusitis, 292, 294–296
Acute bacterial rhinosinusitis, 296
Acute dacryoadenitis, 311
Acute epiglottitis (EP), 156
Acute inflammations, 188, 191, 310, 311
Acute radiation-induced sialadenitis, 242
Acute sinusitis, 292, 294, 296
Adenoid cystic carcinomas, 160, 249
Allen test, 230, 231
Alveolar cysts, 139, 141
American Institute of Ultrasound in Medicine (AIUM), 4
American Thyroid Association (ATA) guidelines, 276, 277
A-mode ultrasonography, 292, 293, 295, 297, 299
Amplitude-scan (A-scan) ultrasonography, 1–3
Ancillary supplies for intraoral sonography, 172
Anechoic thyroid nodules, 262, 263, 273
Anterior ethmoid sinuses, 291
As low as reasonably achievable (ALARA), 9
Aspiration of liquids, 43
Atheroma, 96, 97, 100, 303
Atherosclerosis, 205, 217, 230
Atherosclerotic plaques, 215
Attenuation, 9
Atypical lipoma, 103
Atypical mycobacteriosis, 199
Autoantibodies, 192, 238
Autoimmune-mediated inflammations, 191
Autoimmune sialadenitis
  IgG4-associated sialadenitis, 241, 242
  sarcoidosis, 240, 241
  Sjögren's syndrome, 238–240

B
Bacterial infections, 188
Bacterial sialadenitis, 236
Basalioma, 105
Benign tumors, 104, 139
  monomorphic adenomas, 246
  pleomorphic adenomas, 246, 247
  and pseudotumors, 311–313, 316
  soft tissues in face and mastoid, 303, 304, 306
Bilateral carotid body tumors, 169
Bilateral papillary thyroid carcinoma metastases, 183
B-mode (brightness-mode) ultrasonography, 2, 7, 10, 12, 53, 61, 207, 215, 217, 218, 223, 230, 236–238, 240–243, 245, 248, 254, 292, 295, 297–299, 318
B-mode grayscale sonography, 58
Bony structures of face, 291
  anatomical remarks, 292
  in midface
    frontal bones, fractures of, 302, 303
    maxillary sinus wall, fractures of, 302, 303
    nasal bones, fractures of, 301, 302
    tumorous lesions of bone, 303
    zygoma, fractures of, 302, 303
Branchial cleft cysts (BCCs), 179, 180, 194, 251, 253
Branchial cysts, 110–115
Brightness-mode (B-mode) ultrasonography, *see* B-mode (brightness-mode) ultrasonography
B-scan sonography, 113, 114, 123, 208

C
Calcifications, 42, 43, 196
Capacitive micromachined ultrasonic transducer (cMUTs), 352
Carcinoma ex pleomorphic adenoma, 335, 336
Carcinoma metastasis, 338–341
Carcinomas in head and neck region, 196
Carotid artery, 150, 205, 207, 209
  aneurysm, 184, 220, 222
  bifurcation, 206
  dissection, 220, 221, 223
  pathology
    atherosclerotic plaques, 215
    B-mode ultrasonography, 215
    carotid IMT, 217–220, 222
    carotid ultrasonography, 214
    duplex sonography, 215
    hyperechoic (echodense) plaque, 216
    hypodense (echolucent) plaque, 216
    magnetic resonance angiography, 215
Carotid artery stenosis, 215, 217–220, 222
Carotid body paraganglioma, 177
Carotid body tumors, 123, 176
Carotid intima media thickness (IMT), 217
Carotid ultrasonography, 214
Catheter angiography, 171
Catheterization
  stenotic salivary ducts, treatment of, 45, 46
  vascular access/cannulas, 46–48
Cavernous hemangiomas, 312
Central/anterior lymphadenopathy
  HNSCC, 82
  thyroid cancer, 82
Cerebral ischemia, 217

© Springer Nature Switzerland AG 2019

H. J. Welkoborsky, P. Jecker (eds.), *Ultrasonography of the Head and Neck*, https://doi.org/10.1007/978-3-030-12641-4

Cervical esophagus, 160
Cervical lymph node (CLN), 53, 57–61, 69, 72, 83
  Doppler US and CEUS, 55
  fine-needle aspiration (FNA) cytology, 78
  plain Greyscale US, 54
  supplemental characteristics, 56
Cervical metastases, 86
Cervical teratomas, 195
Cetuximab, 353
CEUS, *see* Contrast-enhanced ultrasound (CEUS)
Chronic glandular inflammation, 238
Chronic inflammation, 188
Chronic lymphocytic thyroiditis, 273, 285
Chronic radiation-induced sialadenitis, 242
Chronic recurrent parotitis, 188, 189, 242, 243
Chronic sinusitis, 292, 296, 297
CLN diseases, *see* Cervical lymph node (CLN)
Coarse calcifications, 266
Coarse rim calcification, 11
Cold abscesses, 70, 71, 236
Collar stud abscess, 61, 84
Colloid cyst, 10, 193
Coloboma, 310
Color-coded duplex sonography (CDS), 4, 53, 123, 209, 223, 236–238, 242, 243, 246, 250–253, 255, 298, 300, 309, 310, 312, 313, 335, 338, 339
Color Doppler sonography, 69, 173, 176, 179, 184, 217, 271
Color duplex sonography, 58, 211
Color-flow Doppler, 12
Colour-coded Doppler sonography, 3
Comet-tail artifact, 10
Comet-tail sign, 265, 266
Common carotid artery (CCA), 208, 209, 211
Communicating carotid artery, 209
Complete thyroid aplasia, 191
Computer-aided diagnosis (CAD) systems, 352
Congenital hypothyroidism, 191
Contrast-enhanced ultrasound (CEUS), 53, 55, 235, 250, 353
  clinical applications
    inflammatory diseases of the salivary glands, 335–338
    lymph nodes, 338, 339
    paragangliomas, 339, 341, 342
    salivary gland tumors, 333–335
    thyroid alterations, differential diagnosis of, 340, 342, 343
    time-intensity curves, quantitative analysis, 337, 338
    tumor response assessment, 343–346
  contrast agents, 331
  harmonic imaging, 332
  head and neck squamous cell carcinoma (HNSCC), 76
  low mechanical indices, 332
  mechanical index (MI), 332
  microbubbles, 332
  pulse-inversion imaging, 332, 333
  regulatory status, 332, 333
  safety considerations, 332
Core biopsy (CB), 44, 45, 173
Cranial neuropathies, 169
Cutaneous metastases, 105
Cyst of second branchial arch, 190
Cystadenolymphoma, 333, 335–337
Cystic hygroma, 177
Cystic lesion, 129, 137
Cystic lymphatic malformation, 190
Cystic malformation, 189
Cystic/necrotic lymphadenopathy
  inflammatory lymphadenopathies, 84
  malignant lymphadenopathies, 84, 85, 88

D
Delphian lymph node, 82
Dental infections, 183
De Quervain's thyroiditis, 192
Dermoid cyst, 195
Dermoids, 310
Diffuse large B-cell lymphoma (DLBCL), 250
Diffuse lipomatosis, 103
Digital subtraction angiography (DSA), 339
Distal sialolithiasis, 245
Distal turbulence intensity in carotid bifurcation, 216
Distinct edema (ED), 136
Diving ranulas, 190
Doppler effect, 11–13
Doppler ultrasonography, 53, 55, 69, 207, 218
Duct-associated disease
  duct cyst, 244
  obstructive sialadenitis, 244, 245
Duct cysts, 244
Duplex sonography, 207, 215, 218, 224, 230
Dynamic sonopalpation, 224
Dysontogenetic cysts, 244

E
Echoencephalography, 1
Echogenic thin layer, 61
Echogenicity, 49, 72, 246, 261–263, 312
Echo-reflection methods, 1
Ectopic thymus tissue, 194
Ectopic thyroid tissue, 124, 128
Eggshell calcification, 267
Elastography, 273, 274, 353
Embryological remnants, 187
Endoscopic ultrasound (EUS)
  equipment, 321, 322
  hypopharynx, 325, 328
  larynx, 323, 324, 326, 327
  methods, 321, 322
  nasal cavity, 322
  nasopharynx, 322, 323
  oral cavity and oropharynx, 323–326
  outer ear and external acoustic meatus, 322
  paranasal sinuses, 322
  proximal esophagus, 325, 327–329
  technical remarks, 321, 322
  trachea, 325, 328
Endosonography, *see* Endoscopic ultrasound (EUS)
End-stage non-tuberculous mycobacterial infection, 68
Epidermoid cysts, 195
Epiglottic cyst, 154, 155
Epithelioma calcificans Malherbe, 303
Epstein-Barr virus (EBV) infection, 69, 88, 198, 237
Epstein Barr virus (EBV)–triggered lymphadenopathy
  characteristics, 68
  Doppler ultrasonographic assessment of intranodal vascular resistance, 68–70
  plain grayscale ultrasonography, 68
  qualitative/quantitative elastographic assessment, 70
Esophageal cancer, 164
European Federation for Ultrasound in Medicine (EFSUM), 4
Exophytic carcinomas, 324
External carotid artery (ECA), 205–208
External laryngocele (LC) with retrohyoidal extension, 157
External percutaneous approach, 172, 173
Extracapsular spread (ECS), 72
Extracorporeal shock wave lithotripsy (ESWL), 48, 50

Extracranial carotid artery, 184
Extracranial dissection, 220
Extracranial vessels, 214

F
Facial nerve palsy, 241, 249
Fibromas, 303
Fibromatosis colli, 196, 201
Fine-needle aspiration (FNA), 173, 262, 269, 280, 285
Fine-needle aspiration cytology (FNAC), 43, 44, 76, 78, 82
Fistulas, 106, 107
Follicular adenoma, 192, 193
Forehand flap, 231
Foreign bodies, 134
Four-dimensional (4D) CT, 280
4D ultrasound, 351
Frontal sinuses, 299
  anatomical remarks, 292
  technical remarks, 292

G
Ganglioneuroma, 173, 202
Glomus vagale, 169, 170, 174–176, 339
Goiter, 153, 154
Granulomatous diseases, 188
Granulomatous thyroiditis, 273
Graves' disease, 192, 276
Graves' ophthalmopathy, 311, 312
Grayscale image, 173
Grey-scale obstetric scans, 2
Grayscale sonographic images, 173

H
Hashimoto's thyroiditis, 192, 193, 259
Head and neck squamous cell carcinoma (HNSCC), 53, 72
  central/anterior lymphadenopathy, 82
  CEUS, 76
  characteristics, 71
  Doppler ultrasonographic assessment of intranodal vascular resistance, 75, 76
  lateral lymphadenopathy, 83
  plane grayscale ultrasonography, 71–74
  posterior lymphadenopathy, 84
  USFNA and USCB, 76
Heerfordt's syndrome, 241
Hemangioma, 107, 177, 251, 254, 303, 322, 324, 326
Hematoma, 133
Hemiaplasia of thyroid gland, 192
Hereditary malformations, 310
Heterogeneous texture of a lymph node, 72
High-end ultrasound systems, 4
High-intensity focused ultrasound (HIFU), 353
High-intensity ultrasound, 1
Hilar vascularization, 58, 79, 81
History of ultrasound, 4
  A-scan ultrasonography, 1–3
  B-mode (brightness-mode) ultrasonography, 2, 3
  colour-coded Doppler sonography, 3
  colour-coded duplex sonography, 4
  head and neck examination, 4
  high-intensity ultrasound, 1
  hyperphonography, 1
  maxillary and frontal sinus, gray scale imaging, 2
  middle-ear effusions, 1
  neurologic diagnosis for endocranial space-occupying lesions, 1
  small parts transducers, 3
  transcranial sonography, 3
  two-dimensional plane, 3
HIV infection, 238
Hot abscesses, 70, 71
HPV-driven cervical metastases, 88
HPV-positive head and neck squamous cell carcinoma, 85
Hyoid, lacking definition by, 194–196
  atypical mycobacteriosis, 199
  dermoid cyst, 195
  ectopic thymus tissue, 194
  Epstein-Barr virus (EBV) infection, 198
  fibromatosis colli, 201
  ganglioneuroma, 202
  infantile hemangioma, 195, 196
  infantile myofibroma, 204
  langerhans cell histiocytosis, 201
  lipoma of the neck, 202
  lipomatous tumor, 203
  lymphatic malformation, 197, 198
  neurofibroma, 203
  nodular sclerosis classical Hodgkin lymphoma (NSCHL), 200
  normal thymus, 194
  reactive cervical lymphadenopathy, 198
  venous hemangioma, 197
Hypercalcemia, 286
Hyperechoic (echodense) plaque, 216
Hyperechoic thyroid nodules, 261, 262, 276
Hyperparathyroidism, 279
Hyperphonography, 1
Hyperplastic tonsils, 145
Hypodense (echolucent) plaque, 216
Hypoechoic (echolucent) plaques, 216
Hypoechoic nasopharyngeal cancer, 323
Hypoechoic thyroid nodules, 260–263, 269, 274, 276, 277
Hypoechoic tumor, 329
Hypopharyngeal cancer, 350
Hypopharynx cancer, 160, 163

I
Idiopathic orbital disease, 313
IgG4-associated sialadenitis, 241, 242
Indeterminate cervical lymph node, 76, 77
Infantile hemangioma, 189, 195, 196
Infantile myofibroma, 204
Infected atheroma of cheek, acute, 101
Infectious mononucleosis, 68, 70
Infectious sialadenitis
  bacterial sialadenitis, 236
  viral sialadenitis, 237
Inflammatory changes of neck, 95
Inflammatory diseases, 310
  acute inflammations, 310, 311
  autoimmune sialadenitis
    IgG4-associated sialadenitis, 241, 242
    sarcoidosis, 240, 241
    Sjögren's syndrome, 238–240
  chronic recurrent parotitis, 242, 243
  Graves' ophthalmopathy, 311, 312
  infectious sialadenitis
    bacterial sialadenitis, 236
    viral sialadenitis, 237
  radiation-induced sialadenitis, 241, 242
  salivary glands, 188, 335–338
Inflammatory lymphadenopathies, 84

Inflammatory reaction, 338, 339
Infrahyoid space, 191–194
Inhomogeneity, 236
Intensity-modulated radiotherapy, 230
Internal carotid artery (ICA), 174, 205, 206, 208, 209
Internal jugular vein, 206, 207, 210
Interventional ultrasonography
  catheterization (*see* Catheterization)
  destruction of tissues, 44–46
  echogenicity, 49
  long-axis technique, 41, 42
  punctures
    aspiration of liquids, 43
    cytologic examinations, 43, 44
    histologic examinations, 44
    therapeutic liquids, instillation of, 43
    tissue consistency, testing of, 42, 43
  short-axis technique, 42
  sialolithiasis, treatment of (*see* Sialolithiasis, treatment of)
Intima media thickness (IMT), 217, 227
Intraglandular abscess, 236
Intramuscular (MU) lipoma, 104
Intranodal necrosis, 70
Intraoral echo-free lesion, 245
Intraoral endocavitary approach, 172
Intraoral ultrasound-guided biopsy, 173
Intraorbital metastases, 315
Intraosseous tumor, 131
Intra-parotieal duct cyst, 245
Intrathyroidal parathyroid gland, 284
Invasive fibrous thyroiditis, 273
Isoechoic thyroid nodules, 260–262, 265, 268, 270–272, 274, 276

J
Jugular vein thrombosis, 127, 222, 223

L
Langerhans cell histiocytosis, 196, 201
Large carotid body tumor, 124
Large cystic tumor, 142
Large neck vessels
  anatomical remarks, 205–207
  disease
    carotid artery dissection/aneurysm, 220, 221
    carotid artery pathology (*see* Carotid artery pathology)
    thrombosis of the internal jugular vein, 222, 223
  indications for ultrasound examinations, 214
  microvascular flap surgery, 230
  technical remarks
    B-mode sonography, 207
    B-scan sonography, 208
    CCA, 208, 209
    color duplex sonography, 211
    color-coded duplex sonography, 209
    common carotid artery, 211
    communicating carotid artery, 209
    Duplex- and triplex-mode ultrasound, 207
    flow velocities, 209
    ICA, 208, 209
    internal jugular vein, 207, 210
    small vessels, 214
    transducer, 207
    tumor perfusion, 210
  ultrasound characteristics of, 227, 230
  vessel infiltration, malignant tumors
    dynamic sonopalpation, 224
    sonographic criteria, 224–226
    transcranial Doppler (TCD) sonography, 224, 226, 227
Large thyroid goiter, 260
Larger hemangiomas, 195
Laryngeal tumors, 156–161
Larynx cancer, 159
Laser therapy, 44
Lateral cervical compartment, 25
Lateral lymphadenopathy
  HNSCC, 83
  non-tuberculous lymphadenopathy, 83
  thyroid cancer, 83
  tuberculous lymphadenopathy, 84
Latrogenic lesions, 196
Lead zirconate titanate (PZT), 8
Left parotid gland abscesses, 236
Left side tongue cancer, 144
Lemierre syndrome, 222
Lipoma, 97, 102, 176, 202, 303, 328
Lipomatous tumor, 203
Lower jugular metastasis, 84
Lymphadenitis, 306
Lymphadenopathy, 338
Lymphangioma, 110, 251, 312
Lymphatic malformations, 108, 177, 179, 197, 198
Lymphatic vascular malformations, 189
Lymph node (LN) abscess, 98
Lymph node in neck
  CEUS, 53, 55
  cystic/necrotic lymphadenopathy
    inflammatory lymphadenopathies, 84
    malignant lymphadenopathies, 84, 85, 88
  Doppler US, 53, 55
  Epstein Barr virus (EBV)–triggered lymphadenopathy
    characteristics, 68
    Doppler ultrasonographic assessment of intranodal vascular resistance, 68–70
    plain grayscale ultrasonography, 68
    qualitative/quantitative elastographic assessment, 70
  malignant lymphoma, 148, 316, 338–340
    characteristics, 78
    Doppler ultrasonographic assessment of intranodal vascular resistance, 79
    plane grayscale ultrasonography, 79
    qualitative elastographic assessment, 79
    right tonsil, 148
    USFNA and USCB, 80
  non-tuberculous mycobacteria (NTM) lymphadenopathy, 66
    characteristics, 64, 65
    Doppler ultrasonographic assessment of intranodal vascular resistance, 66, 67
    plain grayscale ultrasonography, 65, 66
    qualitative/quantitative elastographic assessment, 67
  plain Greyscale US, 53, 54
  reactive lymphadenopathy, 84
    characteristics, 53
    plain grayscale ultrasonography, 53, 57, 58
    qualitative elastographic assessment, 58
    quantitative elastographic assessment, 60
  regional differential diagnosis, 81, 82
    central/anterior lymphadenopathy (*see* Central/anterior lymphadenopathy)
    lateral lymphadenopathy, 82–84
    posterior lymphadenopathy, 84

suppurative lymphadenopathy
characteristics, 70
plain grayscale ultrasonography, 70, 71
qualitative/quantitative elastographic assessment, 71
thyroid carcinoma lymph node metastases, 88
characteristics, 76, 77
qualitative/quantitative elastographic assessment, 77
USFNA and USCB, 78
tuberculous lymphadenopathy, 84
characteristics, 60
Doppler ultrasonographic assessment of intranodal vascular resistance, 61
plain grayscale ultrasonography, 60, 61
posterior lymphadenopathy, 84
qualitative/quantitative elastographic assessment, 62
USCB, 63
USFNA, 63
Lymph node lesions, 188
Lymph node (LN) abscess, 98
Lymphoepithelial lesions, 238
Lymphofollicular proliferation, 188
Lymphoma, 139, 250
Lymphoma nodes, 88
Lymphomatous cervical lymph node, 79
Lymphomatous node, 79, 81
Lyre sign, 176

M
Madelung disease, 99
Magnetic resonance angiography (MRA), 215
Major salivary glands
duct-associated disease
duct cyst, 244
obstructive sialadenitis, 244, 245
inflammatory diseases (*see* Inflammatory diseases)
neoplasms (*see* Neoplasms)
pseudotumors, 250, 251, 254
sialadenosis, 243
Malformations, 196
Maligant melanoma, 316
Malignant lesions
orbital tumors, 313, 315, 316
soft tissues in face and mastoid, 304, 305
Malignant lymphadenopathies, 84
EBV, 88
HPV-positive HNSCC, 85
lymphoma nodes, 88
N2a or N3 metastases, 88
thyroid carcinoma lymph node metastases, 88
Malignant lymphoma, 148, 316, 338–340
characteristics, 78
Doppler ultrasonographic assessment of intranodal vascular resistance, 79
plane grayscale ultrasonography, 79
qualitative elastographic assessment, 79
right tonsil, 148
USFNA and USCB, 80
Malignant tumors
lymphoma, 250
primary and secondary epithelial malignancy, 248–250
Masseter muscle hypertrophy, 254, 256
Massive hyperplasia, 145, 152
Masticator space, 190, 191
Mastoiditis with subperiosteal abscess, 132
Matrix transducers, 349–351
Maxillary sinus, 292, 295, 296, 302
Maximum peak systolic velocit, 217
Mechanical index (MI), 332, 338
Mediastinal and ectopic parathyroid adenomas, 283
Medullary thyroid carcinoma, 193
Meningioma, 312, 315
Meningoceles, 298
Meningoencephalocele, 298, 300
Metastatic disease, infiltration of skin, 104, 105
Metastatic lymph nodes, 124
Methotrexate (MTX)-loaded nanobubbles, 353
Microbial inflammatory thyroiditis, 273
Microcalcifications, 76, 78, 183, 193
Microvascular flap surgery, 230
Microvascular head and neck reconstruction, 222
Middle jugular metastasis, 84
Mild carotid artery stenosis, 219
Miniature probes (miniprobes), 321, 323
Minimally invasive parathyroidectomy, 285
Minimally invasive techniques, 279
Mini-papillotomy, 48
Mirror image artifact, 11
Moderate carotid artery stenosis, 219
Moderate hyperplasia, 146, 152
Molecular imaging, 352
Molecular therapy, 353
Monomorphic adenomas, 246
Morgagni's sinus, 158
Mouth floor, tumors of, 139, 142, 143
Mucocele, 297–299, 311, 314
Mucoepidermoid carcinoma, 246, 248
Mucoid retention cyst, 190
Mucosa-associated lymphoid tissue (MALT) lymphoma, 237, 250
Multinodular goiter, 192
Multiple endocrine neoplasia type II (MEN II), 193
Muscular tumors, 190
Mycobacteria other than tuberculosis (MOTT), 236
Mycobacterium avium, 199
Myoma, 303

N
Nasal bone fracture, 302
Nasal cavity, 322
Nasal wing, tumors of, 301
Nasolabial cysts, 322
Nasopharyngeal carcinoma (NPC), 88, 323
Nasopharynx, 322, 323
Necrosis, 88, 89
Neopharynx, 136
Neoplasms, 188, 189
benign tumors
monomorphic adenomas, 246
pleomorphic adenomas, 246, 247
malignant tumors
lymphoma, 250
primary and secondary epithelial malignancy, 248–250
Neurinomas, 123, 303
Neuroendoscopic skull base surgery, 318
Neuroendoscopic transsphenoidal pituitary gland surgery, 318
Neurofibroma, 104, 174, 203
Neurogenic tumors, 174
Nodal metastasis, 183
Nodular sclerosis classical Hodgkin lymphoma (NSCHL), 200
Non-Hodgkin lymphoma, 148, 339, 340
Nonpolypoid chronic rhinosinusitis, 297

Nonrecurrent right inferior laryngeal nerve, 282
Non-tuberculous cervical lymph nodes, 65, 66
Non-tuberculous disease, 67
Non-tuberculous lymphadenopathy, 54–56, 83–85
Non-tuberculous mycobacteria (NTM) lymphadenopathy, 66
  characteristics, 64, 65
  Doppler ultrasonographic assessment of intranodal vascular resistance, 66, 67
  plain grayscale ultrasonography, 65, 66
  qualitative/quantitative elastographic assessment, 67

O
Obstructive sialadenitis, 45, 244, 245
Odontogenic cyst, 191
Odontogenous abscess, 99
Oligo-sialadenitis of the parotid gland (PG), 237
Oral vestibule, tumors of, 139
Orbit and its adnexa, sonography of, 305, 306
  fracture, 316–318
  hereditary malformations, 310
  inflammatory disease, 310, 311
  orbital tumors, 311–313, 315, 316
  technical remarks, 306, 307
  ultrasound anatomy, 308, 309
Oropharyngeal squamous cell carcinoma, 169
Osteomas, 313, 316
Ovarian hyperstimulation syndrome, 222

P
Papillary thyroid cancer (PTC), 83, 192, 193
Paragangliomas, 4, 169, 171, 174–176, 339, 341, 342
Paranasal sinuses, 1, 2, 291, 300
  acute sinusitis, 292, 294, 296
  A-mode sonography, 293, 295
  B-mode sonography, 295
  chronic sinusitis, 296, 297
  cysts, 297
  EUS, 322
  indications for ultrasonography, 292
  invasive mycosis, 311
  mucoceles, 297, 298
  postoperative care, 298
  technical remarks, 292
  tumors, 299, 300
Parapharyngeal pleomorphic adenoma, 168
Parapharyngeal space (PPS) masses, 167
  anatomic boundaries of
    carotid space, 168
    lateral boundary, 167
    medial boundary, 167
    nomenclature, 168
    post-styloid compartment, 168
    post-styloid components, 167
    pre-styloid components, 167
  diagnostic imaging, 169, 171
  evaluation of
    clinical, 169
    family history, 169
    parapharyngeal tumors, 169, 170
    physical examination, 169
    primary and secondary lesions, 168, 169
  parapharyngeal pleomorphic adenoma, 168
  primary lesions
    BCC, 179
    lipoma, 176
    lymphatic malformations, 177, 179
    neurofibroma, 174
    paragangliomas, 174–176
    schwannomas, 174
    vascular malformations, 176
  secondary lesions
    abscess, 183, 184
    carotid artery aneurysm, 184
    nodal metastasis, 183
    pseudoaneurysms, 184
    salivary gland tumors, 179, 181, 182
  sonographic evaluation
    biopsy and intervention, 173, 174
    color Doppler images, 173
    external percutaneous approach, 172, 173
    grayscale sonographic images, 173
    intraoral endocavitary approach, 172
    pre-styloid compartment, 172
    3D endocavitary probes, 172
    transducer, 171–173
  space-based differential diagnosis, 174
  treatment
    asymptomatic patient with a large neurogenic tumor, 184
    surgical approaches, 184
    transcervical approaches, 184
    transoral approach, 184
Parathyroid adenoma, 194, 284, 286, 287
Parathyroid carcinoma, 287
Parathyroid enlargement, 194
Parathyroid glands, ultrasound
  applications, 285, 286
  history, 279
  indications for, 280, 282
  office-based ultrasound and practical applications, 279, 280
  parathyroid anatomy and embryology, 283, 284
  sonographic characteristics of, 284–285, 287
  techniques
    laryngeal ultrasound, 283
    mediastinal and ectopic parathyroid adenomas, 283
    patient positioning, 282
    transducer, 282, 283
    vocal fold motion, 283
Parathyroid hormone (PTH), 279, 280, 285
Parathyroidectomy, 279
Parathyroids, 193
Parotid gland carcinoma, 249
Parotid gland pseudo-tumors, 252
Parotid gland sarcoidosis, 241
Parotid gland sialadenosis, 244
Parotid spaces
  inflammatory lesions of salivary glands, 188
  neoplasms, 188, 189
  suprahyoid cystic lesions, 190
Pediatric sonography of neck
  hyoid, lacking definition by, 194–196
  infrahyoid space, 191–194
  suprahyoid space (*see* Suprahyoid space)
Percutaneous ultrasound-guided drainage, 173
Peripheral hypervascularity, 184
Peripheral vascularization, 75, 78
Phleboliths and bleeding, 196
Phlegmon, 99
Piezoelectric crystals, 8
Pilomatrixoma, 303, 305
Plain grayscale ultrasonography, 53, 54

EBV, 68
non-tuberculous mycobacteria (NTM) lymphadenopathy, 65, 66
reactive lymphadenopathy, 57, 58
suppurative lymphadenopathy, 70, 71
tuberculous lymphadenopathy, 60, 61
Plane grayscale ultrasonography
HNSCC, 71–74
malignant lymphoma nodes, 79
Plaque echogenicity, 216
Plaque size, 215
Plaque ulceration and plaque surface irregularities, 215
Pleomorphic adenoma, 167, 173, 181, 244, 246, 247, 312, 316, 334, 337
Polypoid sinusitis, 297
Positive end-expiratory pressure (PEEP), 46
Posterior enhancement artifact, 11, 12, 263
Posterior fossa malformations, hemangioma, arterial anomalies, coarctation of aorta and cardiac defects, eye anomalies, sternal anomalies (PHACES syndrome), 187, 196
Posterior lymphadenopathy
HNSCC, 84
tuberculous lymphadenopathy, 84
Posttraumatic changes
foreign bodies, 134
hematoma, 133
seroma, 134
Power Doppler ultrasonography, 12, 53, 70, 75, 79
Preseptal disease, 310
Primary epithelial malignancy, 248–250
Primary hyperparathyroidism, 280
Primary parathyroid hyperplasia, 280
Principles of ultrasound physics
artifacts in imaging, 9, 10
comet-tail artifact, 10
mirror image artifact, 11
posterior enhancement artifacts, 11
reverberation artifact, 10
shadowing artifact, 11
Doppler effect, 11–13
in tissues
acoustic impedance, 8, 9
attenuation, 9
contact coupling, 9
reflection, 8, 9
refraction, 8
sound speed/velocity, 8
spatial resolution, 9
transmission, 8, 9
untrasound waves
generation and reception, 8
sound waves, 7
Psammoma bodies, 266
Pseudoaneurysm, 184
Pseudohypoparathyroidism, 191
Pseudotumors, 250, 251, 254, 311–313, 316
PTC skip metastasis, 85
Pulse repetition frequency (PRF), 108
Pulsed-wave (pw) Doppler, 26, 108
Purulent intranodal foci, 196

R
Radiation-induced sialadenitis, 241, 242
Radiation therapy, 227, 230
Ranula, 139, 142, 190, 245, 246
Reactive cervical lymphadenopathy, 198
Reactive hyperplasia, 53
Reactive lymphadenitis, 68
Reactive lymphadenopathy, 84
characteristics, 53
plain grayscale ultrasonography, 53, 57, 58
qualitative elastographic assessment, 58
quantitative elastographic assessment, 60
Real-time elastography, 349, 353
Recurrent T4 laryngeal cancer, 327
Reinke's edema, 328
Retinoblastoma, 315
Reverberation artifact, 10
Rhabdomysarcoma, 315

S
Salivary cyst, 140
Salivary gland lymphoma, 246
Salivary gland tumors, 179, 181, 182, 333–335
carcinoma ex pleomorphic adenoma, 335, 336
cystadenolymphoma, 333, 335–337
incidence of, 333
pleomorphic adenoma, 334
Sarcoidosis, 240, 241
Sarcomas, 190
Schwannomas, 123, 174–176, 184
Secondary epithelial malignancy, 248–250
Secondary hyperparathyroidism, 193, 280, 285
Septic thrombosis of internal jugular vein, 223
Seroma, 134
Shadowing artifact, 11
Shear-wave elastography (SWE), 235, 240, 242, 243, 246, 249, 353
Sialadenosis, 243
Sialendoscopy, 48
Sialolithiasis, 245
extraction of stones, 48, 49
fragmentation of stones, 48
stones for drainage, mobilization of, 47, 48
Sinugenic orbital complication, 310
Sjögren's syndrome, 235, 237–240, 250, 336–338
Skin tumors and subcutaneous tissue
atheroma, 96, 97
fistulas, 106
hemangioma, 107
infiltration of skin by metastatic disease, 104, 105
lipomas, 97, 102
lymphatic malformations, 108
vascular malformations, 107, 108
venous malformations, 108
Skull base metastasis, 127
Small carotid body tumor, 125
Small parts transduce, 3
Small parts transducers, 3
Snell's law, 9
Soft tissue inflammation, 95
Soft tissues in face, 291
anatomical remarks, 291
and mastoid
abscesses, 303
benign lesions, 303, 304, 306
malignant lesions, 304, 305
technical remarks, 292
Solid epithelial tumors, 189
Solid lesions, 188
Solid thyroid nodules, 265

Solid tumors of neck
carotid body tumors, 123
cystic lesion, 129
ectopic thyroid tissue, 124, 128
external auditory canal, cancer of, 132
intraosseous tumor, 131
large metastasis, 127
in laryngeal skeleton, 124
mastoiditis with subperiosteal abscess, 132
metastatic lymph nodes, 124
neurinoma, 123
right neck, swelling of, 130
squamous cell carcinoma, 131
Sonocompression, 112
Sonographic changes after surgery/radiotherapy, 134–137
Spatial resolution, 9
Spectral Doppler US, 58
Sphenoid sinus, 291
Squamous cell carcinoma, 106, 131, 183
Steinkamp/Solbiati index, 53, 58, 73, 74
Stenotic salivary ducts, treatment of, 45, 46
Stenson's duct, 244
Strain elastography, 235, 237, 238, 240, 242, 243, 246
Strand-like hypoechogeneity, 236
Sturge-Weber syndrome, 187, 196
Subacute lymphocytic thyroiditis, 273
Subcutaneous masses, 304
Subcutaneous process, 106
Submandibular lymphangioma, 254
Submandibular metastasis, 83
Submandibular spaces
inflammatory lesions of salivary glands, 188
neoplasms, 188, 189
suprahyoid cystic lesions, 190
Submental approach, 173
Submental cervical lymph node, 82
Submucosal glandular cyst, 322
Superficial tumor, 105
Suppurative lymphadenopathy
characteristics, 70
plain grayscale ultrasonography, 70, 71
qualitative/quantitative elastographic assessment, 71
Supraclavicular vascular malformation, 109
Supraglottic cancer, 157
Suprahyoid cystic lesions, 190
Suprahyoid space
masticator space, 190, 191
parotid and submandibular spaces
inflammatory lesions of salivary glands, 188
neoplasms, 188, 189
suprahyoid cystic lesions, 190
Suspicious cervical lymph node, 76, 77
Swan-Ganz catheters, 222
Symmetric hyperplasia, 151

T
T1 cancer of left tongue base, 153
T4 cancer of right tonsil, 149
Teratoma, 310
Tertiary hyperparathyroidism, 280, 285
Tertiary parathyroid hyperplasia, 281
Three-dimensional ultrasound, 218, 349, 351
Thrombosis of internal jugular vein, 222, 223
Thymic cysts, 195
Thymus, 194
Thyroglossal cyst, 114–123
Thyroid cancer, 78, 82, 83, 260, 276, 277
Thyroid carcinoma lymph node metastases, 88
characteristics, 76, 77
qualitative/quantitative elastographic assessment, 77
USFNA and USCB, 78
Thyroid, colloid cyst within, 10
Thyroid cysts, 263, 265
Thyroid gland, 191
Thyroid Imaging Reporting and Data System (TIRADS) classification, 277, 278
Thyroid nodules, 192, 194
Thyroid ultrasound
Graves' disease, 276
nature of lymph nodes, 259
thyroid nodules, evaluation of
content and echo structure, 263, 265–267
echogenicity, 261–263
elastography, 273, 274
heterogeneous thyroid nodule with irregular shape, 270
internal flow, 271, 272
isoechoic nodule, 271
large nodules, 260
large, relatively homogeneous nodule with irregular shape, 271
large thyroid goiter, 260
margins, 268, 269
oval nodule, 270
peripheral ring of flow, 271, 272
pure thyroid cyst, 273
round nodule, 269, 270
small nodules, 260
taller than wide, 270
thyroid nodules guidelines and classification
American Thyroid Association (ATA), 276, 277
TIRADS, 277, 278
thyroid size measurement, 259
thyroiditis, 273, 276
US characteristics, 259
Thyroiditis, 273, 276
Thyroid-stimulating hormone (TSH) receptors, 192
Tissue differentiation technology, 3
Tongue base, tumors of, 151
Tongue cancer, 139, 144, 325
Tonsillar cellulitis, 183
Tonsillar hyperplasia, 151
Tonsils, tumors of, 139, 146, 147
Transcervical approaches, 184
Transcervical-transparotid approach, 171
Transcranial Doppler (TCD) sonography, 218, 221, 224, 226–228
Transcranial sonography, 3
Transcutaneous radiotherapy, 242
Transmandibular approaches, 184
Transoral approach, 184
Transoral robotic surgery (TORS), 184
Transparotid approaches, 184
Triplex-mode ultrasound, 207
Tuberculous cervical lymph nodes (TCLN), 60–65, 67
Tuberculous inflammation, 64
Tuberculous lymphadenopathy, 84
characteristics, 60
Doppler ultrasonographic assessment of intranodal vascular resistance, 61
plain grayscale ultrasonography, 60, 61
posterior lymphadenopathy, 84
qualitative/quantitative elastographic assessment, 62
USCB, 63

USFNA, 63
Two-dimensional ultrasound mode (2D mode), 10
Typical lipoma, 101
Typical parathyroid adenoma, 285

U
Ultrafast ultrasound microscopy, 351
Ultrasound
anatomy of neck and head
anterior mouth floor, 34
aortic arch, 19
brachiocephalic artery, 19
carotid artery, 19
carotid bifurcation with a calcified plaque, 29
carotid bulb, 27
cervical plexus, 19, 24
cheek, 36, 39
common carotid artery (CCA), 28
cricoid cartilage (CC), 18, 19
device setting and starting examination, 15
esophagus, 15, 18, 19
external carotid artery (ECA), 30
external jugular vein (EJV), 26
facial artery, 32, 34
hilus-like structure, 33
infrahyoid muscles, 15
isthmus of the thyroid (IST), 17
jaw angle, 32
jugular fossa, 18, 19, 22
jugulofacial vein angle (JVA), 27
lateral neck compartments, 23, 26, 30
left thyroid lobe area, 17
lower medial cervical compartment, 16
masseter muscle, 38, 39
medial neck compartment, 15
mouth floor, 35
omohyoid muscle (OHM), 27
parotid gland, 33, 35, 36
retromandibular vein, 38
submandibular gland, 32, 33
supraclavicular artery, 19
supraclavicular region, 18, 23, 24
thyroid, 15
thyroid cartilages, 18
tongue, 33, 36
tonsils, 35, 37
venous valve, 26
vertebral artery, 31
vertebral vein, 31
future
CEUS imaging, 349
computerized ultrasound image analysis, 352
data acquisition, new developments in, 349–351
elastography, 353
4D ultrasound, 351
molecular imaging, 352
targeted therapy, 352, 353
3D ultrasound, 349, 351
Ultrasound elastography (USE), 77
Ultrasound-guided core biopsy (USCB), 53
head and neck squamous cell carcinoma (HNSCC), 76
malignant lymphoma nodes, 80
thyroid carcinoma lymph node metastases, 78
tuberculous lymphadenopathy, 62
Ultrasound-guided fine-needle aspiration (USFNA), 53
head and neck squamous cell carcinoma (HNSCC), 76
malignant lymphoma nodes, 80
thyroid carcinoma lymph node metastases, 78
tuberculous lymphadenopathy, 62
Unilateral/single-quadrant approach, 279
Upper jugular metastasis, 83

V
Vagal neurinoma, 126, 127
Vagal paraganglioma, 176
Vallecular cyst, 154, 155
Vallecular region, tumors of, 151
Valsalva maneuver, 108, 207, 210
Vascular access/cannulas, 46–48
Vascular anomalies, 188
Vascular malformations, 107, 108, 176, 178, 190, 196
Vascular ultrasonography, 205
Venous hemangioma, 197
Venous malformation, 108, 179
Ventriculograms, 1
Vessel malformation, 255
Viral sialadenitis, 237
Vocal cord paralysis, 175
V-shaped thyroid cartilage, 327

W
Warthin's tumor, 244, 246, 248, 250, 252, 333, 336, 337
World Federation of Ultrasound in Medicine and Biology (WFUMB), 4

Z
Zenker diverticulum (ZD), 160, 165